MEDSI 2016

MECHANICAL ENGINEERING DESIGN OF SYNCHROTRON RADIATION EQUIPMENT AND INSTRUMENTATION



COSMOCAIXA Science Museum
Barcelona, Spain

September 11-16, 2016

Hosted by
ALBA Synchrotron Light Source
www.medsi2016.org

www.albasynchrotron.es

MEDSI
2016
11-16 September 2016
BARCELONA

Dear Colleagues,

The 9th edition of the Mechanical Engineering Design for Synchrotron Radiation Equipment & Instrumentation, ***MEDSI***, was held in Barcelona (Spain) between September 11th and 16th hosted by ALBA Synchrotron Light Source. MEDSI is a biennial conference addressed to worldwide experts on covering all engineering fields of accelerators and beamlines technology. This conference is a fruitful opportunity to showcase and exchange cutting-edge developments in mechanical design and engineering of synchrotron-based instrumentation, as well as an excellent opportunity for networking, sharing information and ideas among different professionals and also to present the ultimate developments.

This edition in Barcelona was held in Cosmocaixa, the Science Museum of Barcelona. The nice venue offered to delegate's very welcoming and pleasant spaces for the entire event: tutorials, regular sessions and industrial exhibition in a merged orientation organization between sessions, posters, sponsors and breaks, enhancing delegates interaction. Furthermore, the welcome reception at Observatory Fabra and the Conference Dinner at Drassanes Maritime Museum together whit a wonderful weather, providing the delegates the chance to enjoy one of the most magical places of Barcelona.

The event program included about 42 oral contributions and 125 posters, covering all engineering disciplines for Synchrotrons. This ***MEDSI'16*** with an unprecedented number of delegates (more than 300), contributions (175 submitted abstracts) and sponsors (up to 33 private companies supporting us), was the most successful edition so far. In addition to these rewarding outcomes, this was the first course that the conference was edited by the JACoW platform, with a great implementation which promotes the conference to the highest publication scientific excellence.

It has been a great pleasure for the organizers to prepare this event and we would like to express our deep gratitude to all our delegates for their engagement and rich involvement, but specially to all those who have contribute to the conference, without which it couldn't have been possible. Thank you to the Scientific Committee, for such a quality selection. Also to the Local Organizing Committee, for the unmeasurable dedication and prominent organization. To the Editorial Team, for dealing with the challenge of implementing successfully the publication for the first time. And last, but not less, to the International Organizing Committee for their support and confidence.

We are very excited about next ***MEDSI'18*** in such beautiful place like Paris.



Yolanda Ruiz
Engineering Division Secretary
Local Organizing Committee

Ana Belén Martinez
Communication and Outreach
Office Head
Local Organizing Committee

David Lopez
Software Engineer (Computing Division)
JACoW Editor's Head
Local Organizing Committee

Joan Casas
Head of Engineering Division
Scientific Committee chair
Local Organizing Committee

Carles Colldelram
Transversal Section Head
(Engineering Division)
Scientific Committee chair
Local Organizing Committee Chair

Marcos Quispe
Transversal Section Head Deputy
Scientific Committee chair
Local Organizing Committee

Contents

Preface **i**
Group Photo . . . ii
Foreword . . . iii
Contents . . . v
Committees . . . viii

Papers **1**
MOPE01 – Stabilization Methods for Force Actuators and Flexure Hinges . . . 1
MOPE02 – Studies on Flow-Induced Vibrations for the New High-Dynamics DCM for Sirius . . . 8
MOPE05 – Mechanical Design of Secondary Source Slits for Hard X-ray Beamlines at Taiwan Photon Source . . . 12
MOPE07 – Ground Motions Measurements for Synchrotron . . . 15
MOPE08 – The LNLS Metrology Building . . . 17
MOPE09 – Preliminary Design and Test of Damping Mechanism for Reducing Vibration of TPS SR Vacuum Chamber . . . 20
MOPE10 – Dynamic Analysis and Measurement of Ground Motion for the Solaris - National Synchrotron Radiation Centre in Cracow . . . 24
MOPE11 – Preliminary Active Vibration Elimination Study of the TPS Girder System . . . 26
MOPE13 – The 20m/s CERN Fast Vacuum Wire Scanner Conceptual Design and Implementation . . . 29
MOPE15 – Cam Mover Alignment System Positioning with Wire Position Sensor Feedback for CLIC . . . 32
MOPE16 – Development of the RIXS Manipulator . . . 35
MOPE17 – OCTOGLIDE - Table Positioning Device for Diffraction Applications . . . 38
MOPE18 – Real-Time Motor Control System for Beamlines . . . 41
MOPE19 – Mechatronics Concepts for the New High-Dynamics DCM for Sirius . . . 44
MOPE20 – Ultra Stiffness And Ultra Low Wawing LM Guide . . . 48
MOPE22 – Mechanical Design of the MID Split-and-Delay Line at the European XFEL . . . 50
MOPE23 – An Assembling Calibration Method of XBPM Diamond Blades in TPS . . . 54
MOPE24 – The Precision Adjustment Holder for Montel Mirrors . . . 57
MOPE26 – Front End Photon Shutter Water Leak to Vacuum at the Canadian Light Source . . . 60
MOPE27 – The Influences of Material Properties to Micro Damages on Vacuum Chamber CF Flanges . . . 63
MOPE28 – Vacuum System of SESAME Storage Ring . . . 71
MOPE29 – Vacuum System of HLS-II Storage Ring . . . 74
MOPE30 – The Development of CuCrZr High Heat Load Absorber in TPS . . . 77
MOPE31 – Dynamic Performance of a Support System for BBA Components in SXFEL . . . 80
MOPE32 – Preliminary Design and Analysis of the FODO Module Support System for the APS-U Storage Ring 83
MOPE34 – Preliminary Design of the Magnet Support and Alignment Systems for the Aps-U Storage Ring . . . 87
MOPE37 – Diamond Multi-Bend Achromats for Low Emittance and New Insertion Devices . . . 90
MOPE38 – Milliprobe Scanner Station . . . 93
MOPE40 – Designing the Flash II Photon Diagnostic Beamline and Components . . . 96
MOPE41 – Design and Construction of a PW Experimental System of HV Chamber Adaptable, Modular and Stable 99
MOPE42 – Experimental and Numerical Study of the ALBA LINAC Cooling System . . . 102
MOPE43 – Hydraulic Failure Caused by Air in Pipelines of the Experimental Area Ring of ALBA Synchrotron Light Source: Research, Simulations and Solutions . . . 105
TUAA01 – Precision Mechanical Design of a Miniature Dynamic Mirror Bender for the SSRF Beamline Upgrade Project . . . 108
TUAA02 – Earth, Wind, and Fire: The New Fast Scanning Velociprobe . . . 112
TUBA01 – The Design of a Precision Mechanical Assembly for a Hard X-ray Polarizer . . . 116
TUBA03 – The Generic Mirror Chamber for the European XFEL . . . 121
TUBA04 – Mechanical Design and Development of Compact Linear Nanopositioning Flexure Stages with Centimeter-Level Travel Range and Nanometer-Level Resolution . . . 124
TUCA02 – Structural Dynamic Modelling and Measurement of SwissFEL Bunch Compressor . . . 128
TUCA03 – Estimation of the Temperature Fluctuations Harshness Regarding Stability of Structures in the Nanometer Range . . . 133
TUCA05 – The New High Dynamics DCM for Sirius . . . 141
TUCA06 – The Girders System for the New ESRF Storage Ring . . . 147
TUPE01 – DMM Thermal Mechanical Design . . . 152

TUPE02 – Experimental Validated CFD Analysis on Helium Discharge . . . 156
TUPE04 – Coherent Soft X-Ray EPU Vacuum Chamber Thermal Analysis for Synchrotron Radiation Protection 159
TUPE05 – Numerical Simulation of the ALBA Synchrotron Light Source Cooling System Response for Failure Prevention . . . 162
TUPE06 – Thermo-Fluid Numerical Simulation of the Crotch Absorbers' Cooling Pinholes for ALBA Storage Ring 165
TUPE08 – Finite Element Analysis of a Photon Absorber Based on Volumetric Absorption of the Photon Beam 169
TUPE09 – Thermo-Fluid Study of the UPC Race-Track Microtron Cooling System . . . 173
TUPE10 – A Thermal Exploration of Different Monochromator Crystal Designs . . . 176
TUPE11 – Study on Thermal Mechanical Design and Optimization Analysis for the ALBA Infrared Microspectroscopy Beamline (MIRAS) Extraction Mirror Based on Finite Element Analysis . . . 179
TUPE12 – Developing White Beam Components of TPS Beamline 24A . . . 183
TUPE13 – Numerical Simulation of the ALBA Synchrotron Light Source Cooling System Response to Pump Start-Up and Shut-Down . . . 187
TUPE14 – Study, Design and Optimization Analysis of the ALBA LOREA Dipole Vacuum Chamber and Crotch Absorbers Based on Finite Element Analysis . . . 191
TUPE15 – Thermal Management and Crystal Clamping Concepts for the New High-Dynamics DCM for Sirius . 194
TUPE16 – Design of A Leaf Spring Bender for Double Laue Crystal Monochromator at SSRF . . . 198
TUPE18 – Design and FEA of a 3D Printed Detector Window Frame . . . 201
TUPE19 – Application of a NEG Coated Chamber at the Canadian Light Source . . . 205
TUPE21 – CLSI BMIT's Super-Conducting Wiggler Cryogenic Safety Improvements* . . . 209
TUPE22 – Low-Order Aberrations Correction of Extreme Ultraviolet Imaging Objective with Deformable Multilayer Mirrors . . . 213
TUPE23 – Glidcop Brazing in Sirius' High Heat Load Front-End Components . . . 216
TUPE25 – Metallurgical Evaluation of Dissimilar Metal Joints for Accelerator Vacuum Chamber Construction at the Advanced Photon Source Upgrade Project . . . 220
TUPE26 – Carbon-Steel/poliethylene Radiation Enclosures for the Sirius Beamlines . . . 223
TUPE28 – Characterization of the Acoustic Field Generated by the Single-Axis Acoustic Levitator . . . 226
TUPE29 – Integration of a Stripline Kicker Prototype for CLIC Project Into ALBA Storage Ring . . . 230
TUPE31 – Manufacturing of Photon Beam-Intercepting Components from CuCrZr . . . 233
TUPE32 – A Girder-Free Magnet Support System Design . . . 236
TUPE33 – NSLS-II Beam Aperture Slit Vibration Studies . . . 239
TUPE36 – Ground Vibration Monitoring for SXFEL Construction at SSRF . . . 242
TUPE38 – Progress and Mechanical Engineering of FEL Projects at SINAP . . . 246
TUPE40 – Cryo-Ready Undulator U15: Passing SOLEIL's 2 Meters Threshold in Useful Magnetic Length . . . 249
TUPE41 – Design and Development of a System of Hybrid Type to Measure the Magnetic Field of a Cryogenic Undulator . . . 251
TUPE44 – Optimization for the APS-U Magnet Support Structure . . . 254
WEAA02 – X-Ray Absorber Design and Calculations for the EBS Storage Ring . . . 257
WEAA03 – Thermal Stability of the New ESRF Extremely Brilliant Source . . . 262
WEAA04 – Novel Numerical Method for Calculating the Shadow Projection and Collisions of a Multi-Axis Goniometer at Diamond . . . 267
WEBA01 – Nostradamus and the Synchrotron Engineer: Key Aspects of Predicting Accelerator Structural Response . . . 272
WEBA03 – Recent Progress on the Design of High-Heat-Load Components . . . 277
WEBA04 – A Discussion on Utilization of Heat Pipes and Vapour Chamber Technology as a Primary Device for Heat Extraction from Photon Absorber Surfaces . . . 280
WECA03 – Experience With the Commissioning of the U15-Undulator for SwissFEL-Aramis Beamline and New Developments for the Athos Beamline . . . 283
WECA04 – Horizontal-Gap Vertically-Polarizing Undulator (HGVPU) Design Challenges and Resolutions . . . 288
WECA05 – Superconducting RF System Plans at CLS . . . 293
WECA06 – Mechanical Engineering Solutions for COXINEL Project . . . 299
WECA07 – Engineering Challenges of the VMXi Beamline . . . 304
WEPE01 – Combined Fixed Mask, Photon Shutter, Safety Shutter, and Collimator Design for BXDS IVU at the CLS 309
WEPE02 – Performance Evaluation of Fast Closing Shutter System at the SPring-8 Front-end . . . 312
WEPE03 – Beamline Front Ends at the 2.5-GeV Photon Factory Storage Ring . . . 315

WEPE04 – Design of X-Ray Beam Position Monitor for High Heat Load Front Ends of the Advanced Photon Source Upgrade . . . 318
WEPE05 – Innovative Design of Radiation Shielding for Synchrotron Light Sources . . . 321
WEPE06 – High Heat Load Front Ends for Sirius . . . 324
WEPE07 – A High Heat Load Front-End for the Superconducting Wiggler Beamline at SSRF . . . 327
WEPE09 – Designing the Photon Beamline Frontends in the PETRAIII Extension Project . . . 330
WEPE10 – Mechanical Design of Pulse-by-Pulse X-Ray Beam Position Monitor Using Diamond Heat Sink . . . 333
WEPE14 – Minimizing Grating Slope Errors in the IEX Monochromator at the Advanced Photon Source . . . 336
WEPE15 – High Frequency UHV Mechanical X-Ray Beam Chopper . . . 339
WEPE18 – APS 2-ID Beamline, Upgrade to Canted Configuration . . . 342
WEPE22 – F-Switch: Novel 'Random Access' Manipulator for Large Numbers of Compound Refractive Lenses 345
WEPE24 – Live Animal Imaging Program at Bio-Medical Imaging and Therapy Facility at the Canadian Light Source 348
WEPE26 – Upgrade the Beamline PF-AR NW14A for the High-Repetition-Rate X-Ray Pump-Probe Experiments 351
WEPE28 – Minimizing Experimental Setup Time and Effort at Aps Beamline 1-Id Through Instrumentation Design 353
WEPE29 – A Novel Filter Auto-Mounter for the BioXAS Beamlines at the CLS . . . 357
WEPE30 – Introduction to Neutron Scattering Instruments - How are they Different? . . . 360
WEPE36 – Design, Construction and Commissioning of Two Highly Integrated Experimental Stations for Micro-Focusing Macromolecular Crystallography Beamlines at NSLS-II . . . 363
WEPE37 – Upgrade of the Super Advanced X-Ray Spectrometer (SAXES) of the RIXS Endstation for Better Resolution and Larger Detector Size . . . 367
WEPE38 – The Mechanics of the Vekmag Experiment . . . 370
WEPE39 – Fabrication, Assembly, and Metrology Methods to Optimize an Adjustable Exit Slit for a Soft X-ray Beamline . . . 374
WEPE40 – Two-rotation Mechanism for an in Vacuum Beamstop . . . 378
THAA02 – Mechanical Engineering of a Cryo STXM at CLS . . . 381
THAA03 – Mechanical Design of New Dual Pinhole Mini-Beam Collimator With Motorized Pitch and Yaw Adjuster Provides Lower Background for X-Ray Crystallography at GMCA@APS . . . 387
THAA04 – Upgrading a Transmission SAX/WAX Beamline to Allow High Quality GISAX/GIWAX Experiments for Soft Matter Thin Films . . . 390
THBA01 – An Endstation with Cryogenic Coils Contributing to a 0.5 Tesla Field and 30-400k Sample Thermal Control . . . 396
FRAA01 – Engineering Challenges on the I14 Nanoprobe Beamline . . . 398
FRAA03 – Mechanical Design of MIRAS, Infrared Microspectroscopy Beam Line at ALBA Synchrotron . . . 403
FRBA01 – A New Crystal Bender for the ID31 Laue-Laue Monochromator . . . 409
FRBA02 – The Nanobender: A New X-Ray Mirror Bender With Nanometer Figure Correction . . . 413
FRBA03 – Design of the Diamond Light Source DMM for the VMXi Beamline . . . 420

Appendices **425**
List of Authors . . . 425
Institutes List . . . 432
Participants List . . . 440

MEDSI 2016 Committees

Scientific Programme Committee

Chair

Carles Colldelram, *ALBA-CELLS*
Joan Casas, *ALBA-CELLS*
Marcos Quispe, *ALBA-CELLS*

Members

Josep Campmany, *ALBA-CELLS*
Antonio Carballedo, *ALBA-CELLS*
Alejandro Crisol, *ALBA-CELLS*
Artur Gevorgyan, *ALBA-CELLS*
Nahikari González, *ALBA-CELLS*
Joaquín González, *ALBA-CELLS*
Jon Ladrera, *ALBA-CELLS*
Marta Llonch, *ALBA-CELLS*
Óscar Matilla, *ALBA-CELLS*
Raquel Monge, *ALBA-CELLS*
Josep Nicolás, *ALBA-CELLS*
Yuri Nikitin, *ALBA-CELLS*
Liudmina Nikitina, *ALBA-CELLS*
Llibert Ribó, *ALBA-CELLS*

Local Organizing Committee

Chair

Carles Colldelram, *Head of Transversal Section at the Engineering Division, ALBA-CELLS*

Members

Joan Casas, *Head of Engineering Division, ALBA-CELLS*
David López, *JACoW Editor in Chief, ALBA-CELLS*
Marcos Quispe, *Transversal Section Deputy Head at the Engineering Division, ALBA-CELLS*
Ana Belén Martínez, *Communications & Outreach, ALBA-CELLS*
Yolanda Ruiz, *Engineering Division Secretary, ALBA-CELLS*

International Organizing Committee

James Kay, *MEDSI IOC Chairman, Diamond Light Source*
Sushil Sharma, *Brookhaven National Laboratory*
Deming Shu, *APS/Argone National Laboratory*
Nicholas M. Kelez, *Linac Coherent Light Source SLAC National Accelerator Laboratoty*
Yves Dabin, *European Synchrotron Radiation Facility*
June-Rong Chen, *National Synchrotron Radiation Research Center (NSRRC)*
Tino Noll, *Max-Born-Institut*
Robert M. Duarte, *Lawrence Berkeley National Laboratory*
Sunao Takahashi, *SPring-8/JASRI*
Lin Zhang, *LCLS/SLAC*
Brad Mountford, *Australian Synchrotron*
Keihan Tavakoli, *SOLEIL Synchrotron*
Lixin Yin, *Shanghai Synchrotron Radiation Facility*
Regis T. Neuenschwander, *Brazilian Synchrotron Light Laboratory*
Brian Norsk Jensen, *MAX IV Laboratory*
Carles Colldelram, *ALBA-CELLS*
Martin Dommach, *European XFEL*
Gordon Barkway, *Canadian Light Source*

JACoW Editorial Team

Isidre Costa, *ALBA-CELLS*
David López, *ALBA-CELLS*
Montserrat Prieto, *ALBA-CELLS*
Volker RW Schaa, *GSI*

ISBN: 978-3-95450-188-5 doi:10.18429/JACoW-MEDSI2016-MOPE01

STABILIZATION METHODS FOR FORCE ACTUATORS AND FLEXURE HINGES

Carles Colldelram[1*], Josep Nicolas[2], Claude Ruget[1]
[1]CELLS, Cerdanyola del Vallès, Spain
[2]SLAC, Stanford, California, United States

Abstract

In the framework of the design of an adaptive optics x-ray mirror bender a stabilization system for ultra-low spring-constant force springs actuators and flexure hinges with nanometre resolution has been conceived. For this purpose its force resolution is better than 10^{-2}N. Since the actuator must preserve the force at this level and provide both pulling or pushing force the spring force was initially transmitted by a lever arm which was pivoting about a bearing articulation but its friction is up to the level of the required force. We present a novel method to compensate the stiffness of the corrector spring as well as a stabilized flexure, substituting the bearing, allowing to a obtain a system able to introduce a variable force on a which its force insensible to movements of the application point in a range of about 1 mm and a frictionless, torque-free articulation in a range of a 1º. The method is based on a combination of magnets with the flexure, in a way that the elastic force exerted by the flexure is compensated by the force of the magnet. Preliminary results show that it is possible to stabilize the torque exerted by the flexure below 0.005 N·m, in a range of 1 degree.

INTRODUCTION

The Nanobender [1,2], Fig. 1, is an instrument conceived to bend X-Ray mirrors to the required focusing curvature and also correct the optics surface errors by means a force actuator. The role of the actuator is to apply a force to introduce a controlled deformation of the mirror substrate that compensates the surface errors of the mirror.

From the deformation model, it turns that to allow compensating surface errors below one nanometer, the forces have to be tunable in a range of up to 20 N or more, and with a resolution of 10^{-2} N or better. To preserve the induced deformation, and thus the corrected figure, the forces applied by the corrector must be stable also within that range.

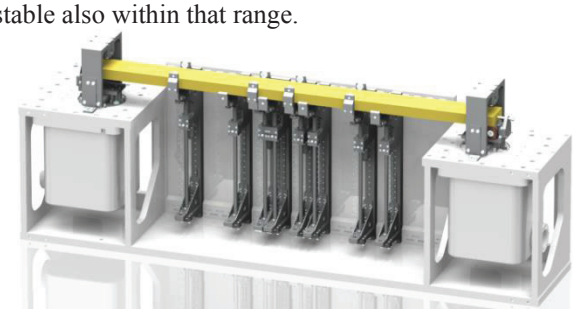


Figure 1: Nanobender.

* ccolldelram@cells.es

For a properly designed actuator, free of friction and parasitic forces, the main source of potential instability comes from mirror transport requirements. Since the mirror has to be moved from the metrology bench to the beamline, or even to a different laboratory, mirror systems must be prepared for transport.

In order to transport safely the mirror, the actuator contact to the mirror must be released. Considering that actuators are applying stress to the mirror, a shock on the transport crate could provoke that some actuator exceeded transitorily the fracture limit of the mirror. Releasing the contact of the actuator from the mirror implies that the repeatability of their relative position is limited to a few tens of microns.

Moreover the original corrector includes and articulation solved by a deep grove ball bearing, that although it has very low friction behaviour could be completely solved by means an also stabilized flexure applying the same compensating principle as for the force mechanism.

The actuator we propose incorporates a mechanism that preserve the force exerted by the actuator for small changes of such position. The working principle of such mechanism is described in this paper.

The paper is divided in two main sections: First the force compensating mechanism for the force actuation and second the stabilized flexure for the articulation.

STABLE-TUNABLE FORCE ACTUATOR

Description

The actuator is sketched in Fig. 2. This corrector have been patented [3]. In this case a pushing actuator is considered. The mechanism can be divided in the four following parts:

1. The frame of the actuator, which is the part of the actuator that supports the other parts of the mechanism, and is mounted on the main frame of the bender.
2. The transmission chain, which includes the lever arm and the contact to the mirror, is the part that transmits the forces exerted by the spring and the magnets, which have different application points, onto a single contact point to the mirror. The transmission also has articulations that absorb all the parasitic components of the forces, which would affect the performance of the system. Although the transmission chain is articulated, it is in practice static, because the reaction force induced

Content from this work may be used under the terms of the CC BY 3.0 licence (© 2016). Any distribution of this work must maintain attribution to the author(s), title of the work, publisher, and DOI.

ISBN: 978-3-95450-188-5 doi:10.18429/JACoW-MEDSI2016-MOPE01

Content from this work may be used under the terms of the CC BY 3.0 licence (© 2016). Any distribution of this work must maintain attribution to the author(s), title of the work, publisher, and DOI.

by the mirror equilibrates the forces exerted by actuator components.

3. The spring and its adjustment system, which allows regulating the force exerted by the actuator. One end of the spring is connected to the lever arm, where it applies a traction force. The other end of the spring is connected to the nut of a lead screw., driven by a stepper motor. Since the lever arm position does not change. The elongation of the spring can be adjusted by changing the position of the nut; this is, by turning the lead screw. This allows, therefore, adjusting the force exerted by the actuator. The spring adjustment system also includes fixations, guides and articulations to minimize friction and parasitic components of the force.
4. The magnet-puller and its adjustment system. It consists in a couple of magnets, set up in attraction, separated by a small gap each other. One of the magnets is attached to the lever arm, and the other magnet attached to the frame, by a fixation system that allows for adjusting its position. This allows adjusting the gap, and correspondingly, the pulling force this part of the system applies to the lever arm.

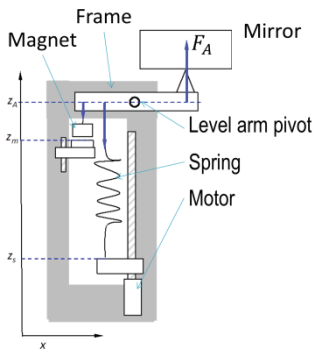


Figure 2: Layout of papers.

Both the magnetic structure and the spring mechanism are pulling the lever arm, and the total force is the contribution of the two mechanisms. On the other hand, if one considers a variation of the position of the mirror, for instance assuming it moves up, the spring will be less stretched, and therefore will exert a smaller force. The gap in the magnet structure will also decrease but in this case, the force will increase. By properly choosing the spring constant and the magnet strength it is possible to find a range where both contributions compensate each other and the total force is independent of the position of the mirror (see Fig 3). This is analysed in detail in the following section.

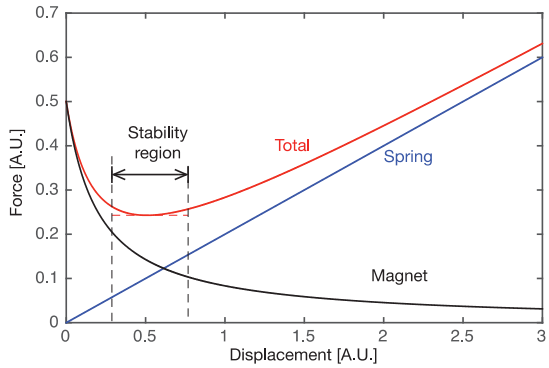


Figure 3: Illustration of the stabilization principle. The spring force has a linear dependence on the mirror displacement, while the magnetic force is given by an inverse law. The sum of the two forces has a minimum around which the force is independent of the displacement.

Analysis

The force applied by the lever arm on the mirror (F_A) is given by the following expression:

$$F_A = \frac{r_S F_S + r_m F_m}{r_A} \quad (1)$$

Here, F_S and F_m are the forces made by the spring system and the magnet system respectively. r_S, r_m, r_A are the distances of the application points on these forces to the pivot point. For simplicity, we have considered that all the forces are parallel each other (vertical) and orthogonal to the lever arm, and that the application points are aligned at the horizontal line defined by the pivot point. Figure 2 provides the sign convention considered in the equation, since both r_S and F_S are negative, their product is positive, and since r_A is positive, the resulting force contribution of the spring to the mirror is positive. The same argument applies to the magnet system.

The force exerted by the spring is proportional to the elongation of the spring, it can be written as follows.

$$F_S = -k_S(z_A - z_S - L_S) \quad (2)$$

Here L_S is the length at rest of the spring, counted from the attachment to the lever arm, to the attachment to the nut

The force made by the magnet system is inversely proportional to some power of the gap between the magnet and the metal block (d). The precise exponent depends on the geometry of the magnet. However for a diameter much larger than the gap between magnet and metal block, the exponent is close to one. Therefore the force can be written as.

$$F_m = -\frac{F_{max}}{d/d_m + 1} \quad (3)$$

ISBN: 978-3-95450-188-5 doi:10.18429/JACoW-MEDSI2016-MOPE01

F_{max} and d_m are constants that parameterize the force dependence with distance.

F_{max} is the maximum force made by the magnet (for gap zero), and d_m is the gap for which the force has decreased to one half of the maximum. The expression is valid only for positive gaps, In that case F_m is negative according to the sign convention given in Figure 2.

An example of values for F_{max} and d_m are 8 N, and 0.5 mm respectively, which correspond to disk-shaped magnets, with diameter 15 mm, height 1 mm, and magnetization N35.

Spring-like Description of the Magnet

In order to provide a comprehensive description of the stabilization mechanism, it is worth expressing the magnetic force in terms of a spring constant. This can be done in a small region by making use of the Taylor expansion of the magnetic force, as follows:

$$F_m = -\frac{F_{max}}{d_0/d_m+1} + \frac{F_{max}}{d_m(d_0/d_m+1)^2}(d-d_0) \quad (4)$$

This can be expressed more compactly as:

$$F_m = F_{m0} - k_m(d-d_0) \quad (5)$$

Where:

$$F_{m0}(d_0) = -\frac{F_{max}}{d_0/d_m+1} \quad (6)$$

and

$$k_m(d_0) = -\frac{F_{max}}{d_m}\frac{1}{(d_0/d_m+1)^2} \quad (7)$$

k_m has units of spring constant, and unlike elastic systems, it takes negatives values. It can be adjusted by properly selected the point d_0, between $-\frac{F_{max}}{d_m}$ and zero.

Force Stability

By combining expressions (1), (2) and (5), one can write the total force as:

$$F_A = -\frac{r_S}{r_A}k_S(z_A - z_S - L_S) + \frac{r_m}{r_A}F_{m0}(d_0) - \frac{r_m}{r_A}k_m(d_0)(z_A - z_m - L_m - d_0) \quad (8)$$

Here we have expressed the gap of the magnetic structure as a function of the coordinates of its ends, as given in Figure 3.1. One can re-arrange the terms as follows:

$$F_A = -\frac{r_S k_S + r_m k_m}{r_A}z_A + \frac{r_S}{r_A}k_S(z_S + L_S) + \frac{r_m}{r_A}F_{m0} + \frac{r_m}{r_A}k_m(z_m + L_m + d_0) \quad (9)$$

The expression has four main terms, which express the dependence on z_A, z_S and z_m, one can see that the dependence on z_A vanishes for:

$$r_S k_S + r_m k_m = 0 \quad (10)$$

When this condition holds, the force exerted by the actuator does not depend on the position of the actuation point. This is equivalent to a system with null stiffness.

By replacing k_m by its explicit expression one can find the magnetic gap that produces such condition.

$$d_0 = +\sqrt{\frac{r_m F_{max} d_m}{r_S k_S}} - d_m \quad (11)$$

There is solution only for positive values of d_0, this is:

$$\frac{F_{max}}{d_m} > \frac{r_S}{r_m}k_S \quad (12)$$

This condition means, essentially, that the maximum equivalent stiffness of the magnet structure must be as big as the stiffness of the spring.

The gap between magnets can be adjusted by adjusting the position of the magnet attached to the frame, this is z_m. The system includes a dedicated mechanism for this adjustment. Tuning z_m affects the total force applied by the actuator..

Force Tuning

Once the magnetic gap is adjusted to cancel the dependence of force on z_A, one can tune the total force of the actuator by adjusting the spring elongation. This is done by moving the lower end of the spring (z_S). Note that adjusting z_S does not change the equilibrium between the spring constants of the spring system and of the magnetic system, so the force stability is preserved for the full range of forces available for the actuator.

Range of Stabilization

The spring-like approximation of the magnet structure is valid within a small region around d_0, the error of the approximation is dominated by the quadratic term of the corresponding Taylor series.

$$\delta F_m = \frac{F_{max}}{d_m^2(d_0/d_m+1)^3}(d-d_0)^2 \quad (13)$$

Which after some manipulations can be written as:

$$\delta F_m = F_m(d_0)\frac{k_m(d_0)}{k_{m,max}}\left(\frac{d-d_0}{d_m}\right)^2 \quad (14)$$

So the error increases more rapidly when the magnet force is near its maximum, and when the maximum spring constant is constant.

The range of validity, for a given threshold is:

Content from this work may be used under the terms of the CC BY 3.0 licence (© 2016). Any distribution of this work must maintain attribution to the author(s), title of the work, publisher, and DOI.

ISBN: 978-3-95450-188-5 doi:10.18429/JACoW-MEDSI2016-MOPE01

Content from this work may be used under the terms of the CC BY 3.0 licence (© 2016). Any distribution of this work must maintain attribution to the author(s), title of the work, publisher, and DOI.

$$\delta z_A = d_m \sqrt{\frac{k_{m,max}}{k_m(d_0)}} \sqrt{\frac{\delta F_m}{F_m(d_0)}} \quad (15)$$

The first factor is the characteristic length of the magnets, the longer it is, the smoother the decay of the field. The second term is the ratio of the spring constant to the maximum achievable by the magnets. It indicates that to have a wide stabilization range, the spring should be weak in comparison to the magnet. Finally, the third term is just the ratio between the force tolerance and the force contribution of the spring.

Summarizing, one needs strong magnets and use their weak field part, in order to have a large stability range.

Experimental Set Up

Figure 4 shows a picture of the experimental setup done to test the working principle of the force correction. The setup is shown in Figure 4.1. In this setup, the force at the application point is measured by a high resolution load cell, capable of measuring a maximum force of 50 N, and with resolution better than 10-3 N. Changes in the position of the application point are simulated by steering a motorized linear stage. Rigidly connected to the load cell. The load cell is connected to the transmission, which collects the force exerted by the spring and by the magnet system. The gap between the magnets is adjusted by a manual linear stage, while the elongation of the spring is actuated by a motorized linear stage.

In order to test the stability provided by the system, we scan the position of the force application point by scanning the linear stage on the top, and record the force measured for the load cell for each position. The same experiment is repeated for different elongations of the spring, which are adjusted by steering the linear stage in the bottom in figure 4.

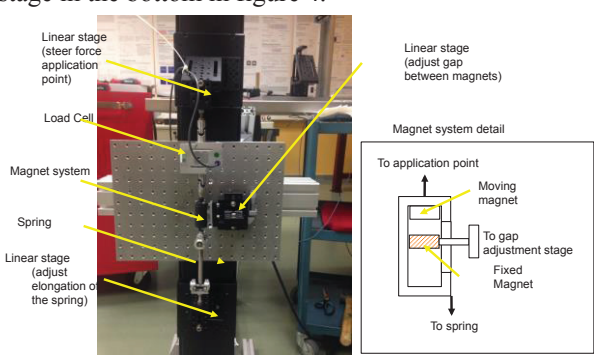


Figure 4: Picture of the experimental setup. A detail of the transmission system is given in the box at the right.

The corresponding results are given in the plot in in Fig. 5. There the deviation from the nominal force is represented as a function of the position of the application point. One can see that the deviation presents a minimum, and that in a range about 2.3 mm the force drift is below 0.02 N. Note also that the position of such minimum does not depend on the nominal force. This means that once the magnet gap is optimized, the nominal force can be tuned by changing the elongation of the spring, while preserving the null-stiffness position.

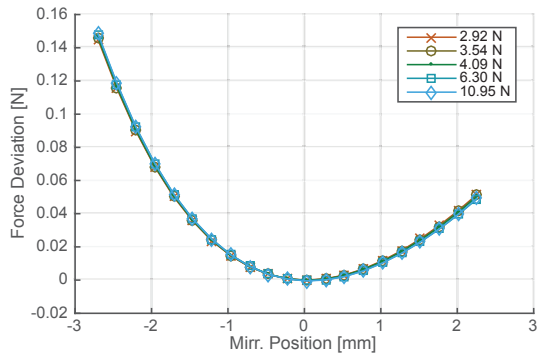


Figure 5: Force deviation from the nominal force as a function of the position of the force actuation point. Curves for different nominal forces, between 2.92N and 10.95 N, are represented. They all show a similar behaviour.

REDUCED RANGE, ZERO TORQUE & FRICTIONLESS ARTICULATION

Description

Flexures give a high performing solution when it is needed to achieve a short range and precise rotation as it give full rigidity in all axis, by its massive geometry, les in the movement one. Also thanks to its simplicity, and avoiding rolling elements as compared with bearings for instance, their thickness compared with the narrowing minimizes the rotation axis wobbling and they are naturally frictionless. Nevertheless they introduce a spring-like rotational torque which in some high accurate application may become a drawback. This torque is governed by the flexion theory equations on the narrowing cross section but as a flexure by definition is a reduced range articulation around its nominal stable position, or zero, thus could be simplified as a torsional spring, with a torque, angle dependent, of a constant rotational K value and of the turned angle.

Conceptual Design

The stabilized flexure is sketched in the Fig. 6. It has been patented [4]. It consists in a basic flexure made in four independent parts to facilitate the manufacturing as well as adjusting its rigidity. In this case the system is stabilized with two pairs of magnets but can be done as well with a single pair. The difference is that with two pair the flexure could be stabilized at its nominal free position or nominal zero.

The articulation has a fixed part or a base which hold two of the magnets and the fixed region of the flexures. It includes as well a rotating part which includes other two magnets and the bendable zone of the flexures. This flexure articulation is split into two different parts placed at each side, extreme, of the rotation axis. In

ISBN: 978-3-95450-188-5 doi:10.18429/JACoW-MEDSI2016-MOPE01

order to make it work the four magnet are paired and in attraction.

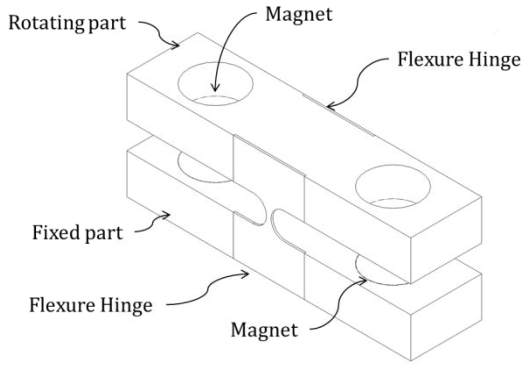


Figure 6: Stabilized flexure.

The articulation is dimensioned in such a way that the rigidity of the flexure is twice the equivalent magnet "equivalent" rigidity, which includes two set of them, but magnets, in attraction, could have a negative k value which could never be in the case of springs or spring-like system like a flexure. The flexure rigidity and the magnet would have the same rigidity, instead of half, in the case of designing it with a single set of magnets. The two magnetic arrangements they are trying to move the flexure from its free, or nominal zero position, but it preserves its free position as both magnets pairs are in opposite side of the flexure thus cancelling them the total resultant torque.

If the rotating part is twisted by means and external force or torque then the flexure is stressed increasing its resistance to the rotation with a returning torque. The gap in the two magnetic arrangements is increasing in one side and decreasing in the other, this make the attraction force is increasing in one arrangement and is decreasing at the other which make that the total flexure torque increase is compensated by the magnets torque variation thus no torque variation of the whole system. By properly choosing the spring constant, flexure spring constant, and the magnet strength, it is possible to find a range where both torques variations compensates each other and the total torque remains zero as at the free or nominal position. This means in this zero torque range the flexure will remain at the target angle from the zero.

Analysis

The total torque $T(\theta)$ introduced on the articulation is given by the following expression and plotted in the Fig. 7:

$$T(\theta) = M_{F_{m1}} - M_\theta + M_{F_{m2}} \tag{16}$$

Where $M_{F_{m1}}$ is the torque introduced by the left side flexure magnet; M_θ is the torque of the flexure and $M_{F_{m2}}$ is the torque of the right flexure magnet.

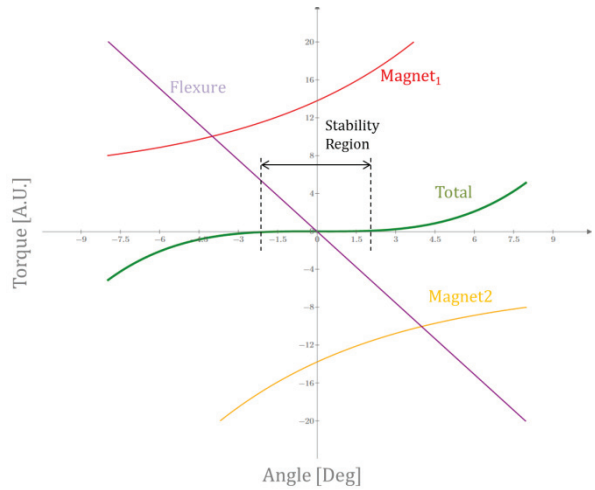


Figure 7: Graph of the stabilization principle. The flexure torque has a linear dependence while the magnetic law is given by an inverse law. The sum of the three torques is zero around its nominal free zero position and it is preserved zero in an angle range around this point where the torque is independent of the angle.

The torque exerted by the flexure is proportional to the rotation angle, and it can be written as follows:

$$M_\theta = k_\theta \theta \tag{17}$$

The magnet forces are although they have an angle interdependence they work in opposite sense, thus they are expressed like:

$$M_{F_{m1}} = F_{m1} D \tag{18}$$

and

$$M_{F_{m2}} = -F_{m2} D \tag{19}$$

Previous equation can be figure out from the system lay-out shown in next Fig. 8.

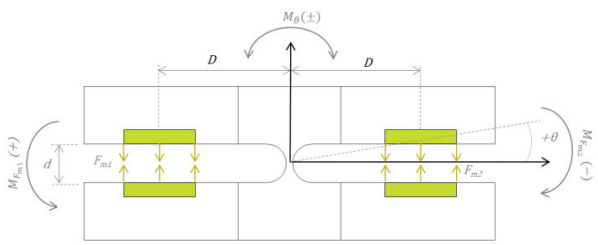


Figure 8: Sketch of the system dynamics.

In order to have the system equation dependent of a single variable, the angle θ, the magnet gap distance, and thus the magnet force equation, must be expressed in terms of this variable, thus the gap can be expressed as:

$$d_1 = d_0 - D sin\theta \tag{20}$$

Content from this work may be used under the terms of the CC BY 3.0 licence (© 2016). Any distribution of this work must maintain attribution to the author(s), title of the work, publisher, and DOI.

ISBN: 978-3-95450-188-5 doi:10.18429/JACoW-MEDSI2016-MOPE01

Content from this work may be used under the terms of the CC BY 3.0 licence (© 2016). Any distribution of this work must maintain attribution to the author(s), title of the work, publisher, and DOI.

and

$$d_2 = d_0 + Dsin\theta \quad (21)$$

Where d_0 is the initial setting of the magnet gap where it achieve the required rigidity to make the system self-compensate the torques variation with the angle as described below:

Following equation 3 as the force actuator for the flexure F_{max} is the maximum force made by the magnet (for gap zero), and d_m is the gap for which the force has decreased to one half of the maximum. The expression is valid only for positive gaps, In that case F_m is Positive according to the sign convention given in Figure 8.

An example of values for F_{max} and d_m are 14,2 N, and 0.9mm respectively, which correspond to disk-shaped magnets, with diameter 8 mm, height 3 mm, and magnetization N45.

Each magnet have an opposite behavior, thus the system have two different F_m forces working on, F_{m1} and F_{m2}, which only have the same value at the nominal zero. An example of stabilized flexure with two flexures of 0,5 mm Aluminum sheet and Ø5 mm circles at the flexible point gives the following stabilization graph, Fig. 10:

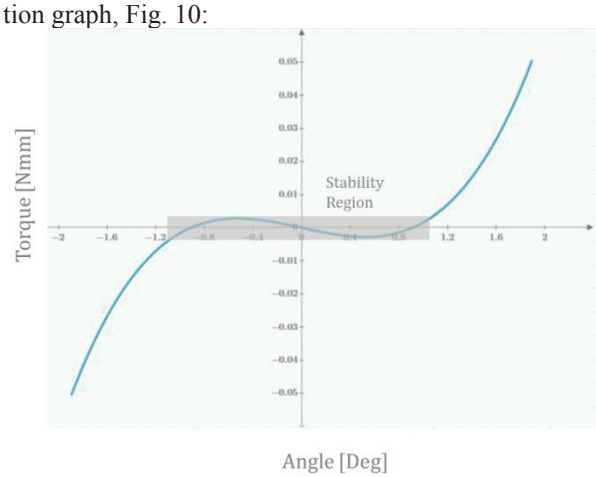


Figure 9: Calculation for specific flexure.

Torque Variation Compensation

The same spring-like mathematical expression of a magnet developed in previous section is applicable for the compensated flexure. By combining the expressions (16), (18), (19), (20), (21) and (5) the final torque can be expressed like:

$$T(\theta) = -2\, k_m D^2 Sin\theta - k_\theta \theta \quad (22)$$

The expression has only two terms. k_m must take negative values to make the system work as will be demonstrated below.

The principle that makes the system have a self-compensated torque is that from a stable position, the nominal zero, whatever rotation in the working range introduces a self-compensated Torque Variation which variation is zero thus achieving a new stable position in whatever position in the working range. Torque variation means, and seeing figure 3, just the derivative of this equation 12:

$$\frac{\partial T(\theta)}{\partial \theta} = -2\, k_m D^2 Cos\theta - k_\theta \quad (23)$$

This derivate, equation is zero when there is a negligible variation of the torque, thus $\frac{\partial T(\theta)}{\partial \theta} = 0$ and given that $Cos\theta = 1$ for θ values around zero gives:

$$k_m = \frac{k_\theta}{-2D^2} \quad (24)$$

This equation means that the magnets stiffness must be as rigid as the flexure. The negative sign just shows that k_m could take negative values. The constant two just shows that this have two magnet set, if the system is set up with one magnet this constant 2 would not appear. As expected the distance of the magnet to the flexure center, D, plays a role in the rigidity as the force of the magntet by this distances is the torque exerted by the magnet sets, this means the stabilization could be adjusted by means d_0& D.

The gap between magnets can be adjusted by adjusting the position of the magnet attached to the frame, this is d_0. Tuning d_0 affects the total force applied by the actuator.

It is possible to arrive to the same conclusion by replacing k_m by its explicit expression at the equation 12 one can find the magnetic gap that produces such condition:

$$d_m \sqrt{\frac{F_{max}}{d_m} \frac{-2\, D^2 Cos\theta}{k_\theta}} - d_m = d_0 \quad (25)$$

There is solution only for positive values of d_0, this is:

$$\frac{F_{max}}{d_m} > \frac{k_\theta}{-2\, D^2} \quad (26)$$

CONCLUSIONS

With this actuator it is clear that a set up could be designed to introduce a controlled adjustable force and making it insensible to displacements of the force application force, thus a system which allows an accurate adjustment in a optics laboratory and then dismantle the mirror and remount it on site achieving the same correction fine tuning forces with in independence of the mechanical mounting errors.

The compensated flexure is able to stabilize a flexure in such a way that the linear torque introduced by the flexions of the hinge is completely cancelled in a articulation type, flexure, which it is intrinsically frictionless and thus obtaining the almost perfect articulation for a reduced range of about 1°. A final set up with the

ISBN: 978-3-95450-188-5 doi:10.18429/JACoW-MEDSI2016-MOPE01

flexure have to be mounted in the next steps to evaluate the proximity of a real compensated articulation to zero torque and its range bandwidth.

ACKNOWLEDGEMENT

The authors thanks all involved members on the design and hardware set up. Especially Dr. Pablo Pedreira in doing the measurements Jose Ferrer for the fine-tuned set up.

REFERENCES

[1] J. Nicolas, "Nanometer figure correction of x-ray mirrors using multiple spring actuators", Proc. SPIE 9965, Adaptive X-Ray Optics IV, 996503 (Oct. 2016); doi:10.1117/12.2239533.

[2] J. Nicolas, "Dispositivo para curvar espejos", Oficina Española de Patentes y Marcas, No. P201530735, May. 2016.

[3] J. Nicolas, "Dispositivo y metodo de aplicación de fuerza en un objeto", Oficina Española de Patentes y Marcas, No. P201630506, Apr. 2016.

[4] C. Colldelram, "Dispositivo de articulación", Oficina Española de Patentes y Marcas, No. P201631142, Sep. 2016.

Content from this work may be used under the terms of the CC BY 3.0 licence (© 2016). Any distribution of this work must maintain attribution to the author(s), title of the work, publisher, and DOI.

ISBN: 978-3-95450-188-5 doi:10.18429/JACoW-MEDSI2016-MOPE02

STUDIES ON FLOW-INDUCED VIBRATIONS FOR THE NEW HIGH-DYNAMICS DCM FOR SIRIUS

R. M. Caliari*, O.R. Bagnato, L. de Souza Jr, F. R. Francisco, R. R. Geraldes, R. L. Parise, M. Saveri Silva, and D. O. Tavares, Brazilian Synchrotron Light Laboratory, Campinas, Brasil
T. A. M. Ruijl, MI-Partners, Eindhoven, Netherlands

Abstract

The monochromator is known to be one of the most critical optical elements of a synchrotron beamline, since it directly affects the beam quality with respect to energy and position. Naturally, the new 4th generation machines, with emittances in the range of order of 100 pm rad, require even higher stability performances, in spite of the still conflicting factors such as high power loads, power load variation, and vibration sources. A new high-dynamics DCM (Double Crystal Monochromator) is under development at the Brazilian Synchrotron Light Laboratory for the future X-ray undulator and superbend beamlines of Sirius, the new Brazilian 4th generation synchrotron [1, 2]. The disturbances induced by the coolant flows are known to be among the most detrimental influences to a DCM performance, however, quantitative force numbers are not commonly investigated. According to the novel dynamic concept, these forces should be predictably translated into stability performance. Therefore, experimental setups that allow the indirect measurement of such forces in conditions close to those of operation were designed. The results comparing different indirect cooling profiles and manufacturing processes (brazing and additive manufacturing) are shown.

INTRODUCTION

The goal of this work is to present the flow-induced vibrations experiments, an indirect measurement of the force frequency spectrum for the cooling vibrations disturbances at the new high stability monochromator for Sirius [1]. Details about the full system can be found in [3].

DCM CLOSED LOOP CONTROL

The new high-dynamics monochromator introduced in the present conference is a high ending mechatronics system [4], in which the system stability, in particular, is only possible because of a high-bandwidth closed loop control. As it is highlighted in Fig. 1, in order to achieve a nanometric positioning resolution and stability it is essential to understand the disturbances actuating on each element of the closed loop control, so that the effects of each disturbance can be analysed already at project level. Therefore, one must know the frequency domain characteristics and energy content of each component.

A preliminary work has already been dedicated to floor vibration characterization at Sirius [5], whereas amplifier and quantization noise, delays, non-linearities and other disturbances from the chosen equipment are well-known (see [6]). Flow-induced vibrations, on the other hand, are a more difficult subject, to which this work is dedicated.

* ricardo.caliari@lnls.br

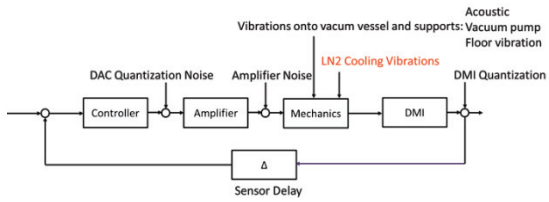


Figure 1: Block diagram of a generic representation of the main disturbances of the closed loop control.

LIQUID NITROGEN COOLING

Due to the high power load that reaches the first crystal in the DCM, liquid nitrogen (LN_2) or water-cooling is generally necessary. An important development front was conducted in this subject to match the LN_2 cooling requirements with the high-dynamics and metrology methods [7].

The problems associated with flow-induced vibrations are known since very long [8], and their negative influence in the performance of monochromators has already been identified and characterized [8, 9]. Indeed, previous works presented vibration results as position vs. frequency plots [10] or acceleration levels (or arbitrary units) in time plots [11, 12]. The state-of-the-art DCMs typically live under given conditions, passively dealing with them by means of mechanical improvements to damp the vibrations and tuning flow and working pressure for each system.

However, in order to guarantee higher bandwidth dynamic control and set the appropriate designing targets for the project, quantitative data of disturbance forces in conditions close to that of real operation should be available. Thus, the force Power Spectral Density (PSD) from the flow-induced vibrations should be characterized.

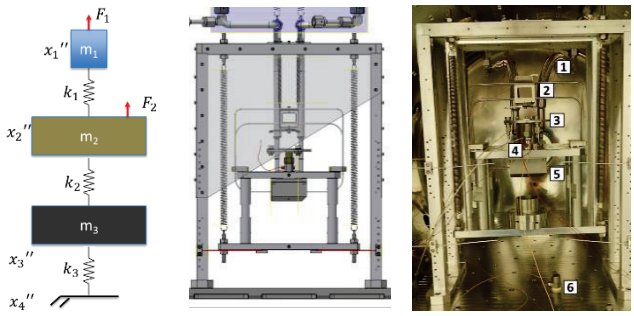
DYNAMIC MODEL

Discrete Structure Model

The first step was the development of a 1D lumped-mass model, as depicted in Fig. 2(a). The purpose was to design an experimental setup that would be sensitive enough to the expected small force levels. The first approximation was that the flow-induced disturbance forces would be in the range of 1 to 10 mN. These values guided the definition of masses and stiffness for the setups. It was soon realized that the PSD noise floor of the metrology instruments together with parasitic disturbances, such as floor vibrations, would prevent the full frequency range of interest (from about out 5 Hz to 2 kHz), from being evaluated with a single setup.

Content from this work may be used under the terms of the CC BY 3.0 licence (© 2016). Any distribution of this work must maintain attribution to the author(s), title of the work, publisher, and DOI.

ISBN: 978-3-95450-188-5 doi:10.18429/JACoW-MEDSI2016-MOPE02



(a) (b) (c)

Figure 2: Dynamic project phases: (a) 1D lumped-mass model; (b) 3D CAD model, with dynamic simulations and model validation; (c) full instrumented setup, assembled on a UHV chamber, where: 1: LN_2 lines, 2: cooling block, 3: interferometer, 4 and 6: accelerometers, 5: manifold.

Therefore, this evaluation would need to be done with different sensors in different setups for two separate frequency regions. In the DCM the low-stiffness pipes that are used prevent the cooling system from fighting against the metrology architecture. In this case, this mechanical property of the pipes allowed for the design of the experiment in those two regions, namely, before and after the mechanical decoupling of the mass of interest, which could be the copper cooling blocks (m1) or the LN_2 manifold (m2) of the DCM, from the rest of the structure. Indeed, by using the assembly stiffness and measuring displacement, vibration forces in the low frequency range (before decoupling) could be found. Likewise, by using the mass and measuring acceleration, vibration forces in the high frequency range (after decoupling) can be obtained. Fig. 3 depicts the basic dynamics of a second order system, showing the dominant regions of stiffness and mass, which defines the concept that has been used.

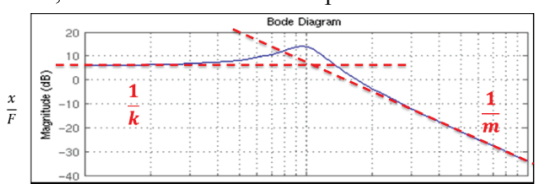


Figure 3: Bode Diagram for a second order system, showing the frequency range proportional to the stiffness (1/k) and the one proportional to the mass (1/m).

Dynamic Simulation and Previous Evaluation

As mentioned, two force PSD levels are of interest, namely, F1, the vibration disturbance force in the cooling blocks, and F2, the force in the LN_2 manifold. Fig. 4 shows MIMO Frequency Response Functions for this system, through which an iterative method was applied, in order to achieve the ideal setup configurations, namely, convenient attenuation of the parasitic disturbances to assure reliable quantitative data in the measurements. It also shows the progress of the model: "First model" represents the initial target values, "Updated model" uses the values after final mechanical design and FEA analysis, and "Measured parameters model" uses the measured stiffness and mass for each body. It can be seen that the real setup is in very good agreement with the designed model. Finally, it represents the MIMO FRF for case 1 at Table 1, where the working cases are summarized. Looking at the first output in Fig. 5, i.e. the first row with the sensitivity of the displacement measurements by the interferometer, one can see that, in the frequency range of interest, the inputs from Acc1 (floor acceleration) and F2 are attenuated, whereas F1 is not.

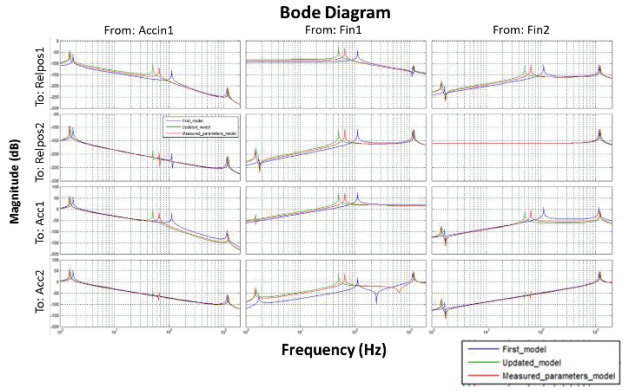
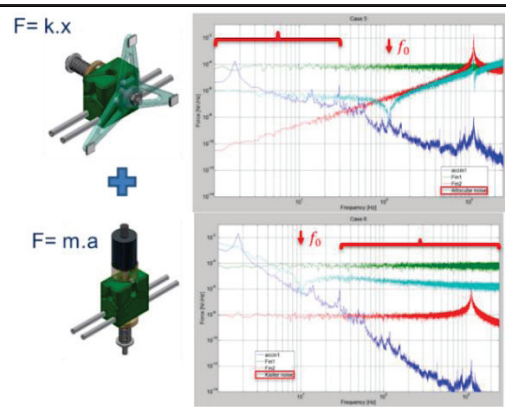


Figure 4: MIMO System FRF. Inputs: Acc1, floor acceleration; F1, forces at the cooling block; and F2 forces at the manifold. Outputs: displacement 1 (w.r.t m2) and 2 (w.r.t m3) and accelerations at m1 and m2.

Table 1: Setup Matrix Information

Case	Measured output	Measured force	Frequency range
1	Relpos1	F1	5 – 40 Hz
2	Acc1	F1	70 – 2 kHz
3	Relpos2	F2	5 – 40 Hz
4	Acc2	F2	10 – 2 kHz



(a) (b)

Figure 5: Force measurement, using stiffness and position in (a) and acceleration and mass in (b).

In Fig. 5, from the transfer functions, the disturbances and instruments characteristics, a final dynamic analysis was made, in which can be seen the simulated force level of each disturbance or force, as well as the sensor noise level. The goal of this analysis was to ensure that the force magnitude of interest was at least one order of magnitude higher than all other values, in order to take the values as reliable data, as already mentioned.

Content from this work may be used under the terms of the CC BY 3.0 licence (© 2016). Any distribution of this work must maintain attribution to the author(s), title of the work, publisher, and DOI.

ISBN: 978-3-95450-188-5 doi:10.18429/JACoW-MEDSI2016-MOPE02

Content from this work may be used under the terms of the CC BY 3.0 licence (© 2016). Any distribution of this work must maintain attribution to the author(s), title of the work, publisher, and DOI.

EXPERIMENT

Instrumentation Description

The previous dynamic analysis showed that the selection of the appropriate sensor or instrument is essential to have the reliable force results. The Fabry-Perot interferometer from AttoCube was used to measure displacement, with resolution of 1 pm and acquisition bandwidth of 10 MHz [6]. The operational conditions, cryogenic temperatures and UHV, were the most critical obstacles. As a complementary measurement instrument, Kistler 8786A5 accelerometer sensors were used. They were chosen for their relative small mass and low noise floor at the required frequency range. The operational conditions were a problem once again, since these sensors have non-linear behaviours with temperature and are definitely not cryogenic compatible. Thus, cartridge resistances and thermocouples were used to make localized closed-loop temperature control, keeping them at room temperature, despite the cryogenic conditions of the setup.

The experiment automation was designed in a National Instruments cRIO platform. The FPGA was essential to read the interferometer's HSSL protocol [13]. A NI USB-4431 24 bit ADC was preferred to read the accelerometer signals and ensure a lower digitizer influence. Finally, FMB Oxford Series F Cryocooler was chosen because of its proven dynamic stability. The auxiliary vacuum vessel and its instrumentation, which were needed due to the low temperatures, is a fully automated system that was recently developed in-house exactly for this sort of application. It is called Multipurpose Vacuum Chamber.

Setup Validation and Calibration

Before the final assembly of the parts, it was necessary to measure the real parameters to validate and calibrate the dynamic model. The mass of each part was measured in a precision weighing scale, whereas the stiffness values were indirectly determined in auxiliary tests in which the displacement caused by known masses was measured. Then, the final alignment of the setup was made using auxiliary level sensors, what was necessary because of the flexible extension springs used to decouple the system from the outside vibrations influences, as shown in Fig. 2. Finally, after the final assembly, the background signal levels of the sensors were measured to ensure the reliability of the collected data and proper post-processing analyses.

PARALLEL DEVELOPMENT

To achieve the right vibration and thermal performances in the DCM. The well-known brazing of OFHC Copper and 316L Stainless Steel, using Palcusil-10 are the first production approaches. Nevertheless, 3D printing technology is also under validation, to make the optimal cooling design possible. The first leak test results of the 3D parts are showed on Table 2. Unfortunately, the only process with a successful prototype regarding UHV application (target leak: $\leq 1.0 \cdot 10^{-11}$ mbar.l/s) has failed in producing the final design. However, this is still work in-progress.

Table 2: Leak Test Results of 3D-printed Prototypes

Material	Supplier	Leak test result [mbar.l/s]	Approved
CoCr	UNICAMP	$1.0 \cdot 10^{-4}$	Not OK
SS – PH1	UNICAMP	$1.0 \cdot 10^{-1}$	Not OK
SS – 316L	Höganäs	$1.0 \cdot 10^{-11}$	OK

In addition, the development of a low-vibration flexible hose with an internal mesh is under evaluation (Fig. 6). Since F2 also includes the contribution of the vibrations from the hoses, their design should be optimized. This development based on the results shown on [10].



Figure 6: Flexible hose with internal mesh to reduce turbulence and vibration levels in the cooling lines.

RESULTS

The experiments are still in progress and the first results are according to the initial force estimates, i.e., in the mN range in the PSD plot, as shown in Fig. 7. Considering Fig. 4, the first low-frequency peak, at about 7 Hz, should come from input1-output1 and the last peak, at about 80 Hz, should be the first resonance frequency of input1-output2.

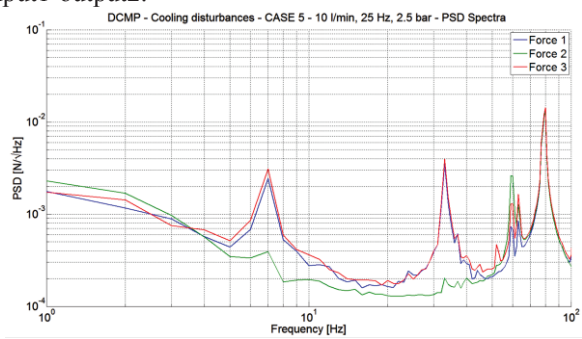


Figure 7: First results for case 1. Forces 1, 2 and 3 come from three simultaneous interferometer readings that measure the displacement of the cooling block. The correlated data provide distance, pith and roll data.

CONCLUSIONS

The proposed approach has been successfully validated and the forces actuating on the first crystal of the high-dynamics DCM for Sirius can be extracted from the PSD measurements and feed back into the dynamic model of the DCM. Simultaneously, different cooling designs are being evaluated to guide the design targets for the final DCM system.

ACKNOWLEDGEMENT

The authors would like to gratefully acknowledge the funding by the Brazilian Ministry of Science, Technology, Innovation and Communication and the contributions of LNLS and MI-Partners teams.

ISBN: 978-3-95450-188-5 doi:10.18429/JACoW-MEDSI2016-MOPE02

REFERENCES

[1] A. Rodrigues *et al*, "Sirius Status Report", in *Proc. IPAC'16*, Busan, Korea, May 2016, paper WEPOW001, pp. 2811-2814.

[2] L. Liu, F. H. de Sá, and X. R. Resende, "A new optics for Sirius," in *Proc. IPAC'2016*, pp. 3413–3415.

[3] R. Geraldes *et al*, "The new high dynamics DCM for Sirius", presented at MEDSI 2016, Barcelona, Spain, Sep. 2016, this conference.

[4] R. Geraldes *et al*, "Mechatronics Concepts for the New High-Dynamics DCM for Sirius", presented at MEDSI 2016, Barcelona, Spain, Sep. 2016, this conference.

[5] A. Rodrigues *et al*, "Sirius Accelerators Status Report", in *Proc. IPAC'15*, Richmond, VA, USA, May 2015, paper TUPWA006.

[6] K. Thurner *et al*, "Fiber-based distance sensing interferometry", *Applied Optics*, vol. 54, no. 10, Apr. 2015

[7] M. Saveri Silva *et al*, "Thermal management and crystal clamping concepts for the new high dynamics DCM for Sirius", presented at MEDSI 2016, Barcelona, Spain, Sep. 2016, this conference.

[8] S. Kaneko *et al*, *Flow-Induced Vibrations: Classifications and Lessons from Practical Experiences*, London, UK: Elsevier, 2014.

[9] P. Kristiansen, J. Horbach, R. Doehrmann, and Joachim Heuer, "Vibration Measurements of high-heat-load monochromators for DESY PETRA III extension", *Journal of Synchrotron Radiation*, vol. 22, pp. 879-885, Jul. 2015.

[10] S. Alcock, "Off-line characterization & optimization of monochromators", presented at ESRF DCM Workshop, Grenoble, France, May 2014.

[11] H. Yamazaki, "SPring-8 Standard Monochromators (SSMs)", presented at ESRF DCM Workshop, Grenoble, France, May 2014.

[12] J. Nicolas *et al*, "Characterization of the dynamic performance of DCMs at Alba", presented at DCM Workshop, May 2014.

[13] N. Inami *et al, "*Real-time motion control and data acquisition system for scanning X-ray microscopy using programmable hardware", *Journal of Physics*, vol. 502, no. 1, Jul. 2014.

Content from this work may be used under the terms of the CC BY 3.0 licence (© 2016). Any distribution of this work must maintain attribution to the author(s), title of the work, publisher, and DOI.

ISBN: 978-3-95450-188-5 doi:10.18429/JACoW-MEDSI2016-MOPE05

MECHANICAL DESIGN OF SECONDARY SOURCE SLITS FOR HARD X-RAY BEAMLINES AT TAIWAN PHOTON SOURCE

H. Y. Yan†, C. H. Chang, D. J. Wang, C. Y. Chen, J. M. Lin, C. Y. Huang, D. G. Liu, S. H. Chang
National Synchrotron Radiation Research Center, Hsinchu, Taiwan

Abstract

The secondary source slits have been developed for specific hard X-ray beamlines at Taiwan Photon Source. Especially for Coherent X-ray Scattering and X-ray Nanoprobe beamlines, severe specifications of the slits are more necessary to define proper beam sizes in horizontal and vertical directions at sample. The opening size of each pair of slits assembled orthogonally is usually needed to range within several microns, so the UHV-compatible piezo-driven stages with closed-loop system were adopted for the purposes of fine adjustment, precise positional accuracy and repeatability. To reduce X-ray scattering effect, the rectangular single-crystal film was bonded on the edge of the slit blade. The machined rotary weak-link structure and piezo-driven actuators were used to slightly adjust parallelism of each pair of the blades with the method of single-slit diffraction. To enhance structural and thermal stability, the granite plinths with specified shape were designed and the precise temperature controlling system will be set up recently. The overall design, mechanical specifications and procedure of testing for secondary source slits will be introduced in this paper.

INTRODUCTION

As small beam size is more required in hard X-ray beamlines at accelerators of synchrotron radiation around the world, the specifications of slits system become more critical. For example, the beam size between 1 - 10 μm both in horizontal and vertical directions at sample was design for the Coherent X-ray Scattering beamline at Taiwan Photon Source (TPS). The quality of beam spot with small size is influenced by unstable situation very easily, so mechanical stability of slits system needs to be considered comprehensively. For these reasons, the necessity of designing a new type of mono beam secondary source slits was taken into account. Recently we have developed a new type of stable slits system with severe specifications, such as the smallest opening size and parallelism between two blades on each pair of slits. The following sections will introduce design of secondary source slits, testing procedure and result, and precise temperature controlling system respectively.

DESIGN OF SECONDARY SOURCE SLITS

To achieve the expected performance, some commercial components used widely were adopted in the mono beam secondary source slits for their mature developing experience. And the specific design for accurate adjustment and mechanical stability were completed. Fig. 1 and Fig. 2 show the schematic 3-D drawing and on-site view of secondary source slits installed in the Coherent X-ray Scattering beamline and located at 40.52 m from the center of two Insertion Devices respectively. Considering the optical design, the slits system is uncooled type because of locating after the Double Crystal Monochromator (DCM).

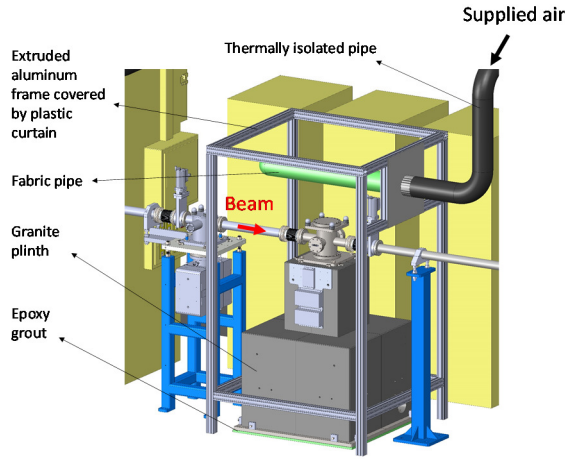


Figure 1: Schematic 3-D drawing of secondary source slits.

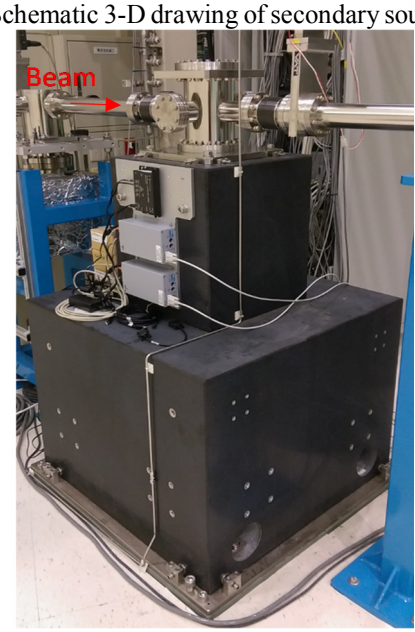


Figure 2: On-site view of secondary source slits installed in the Coherent X-ray Scattering beamline at TPS.

Specifications

Fig. 3 shows a 3-D model of main mechanism for secondary source slits. Gap between blades of each slit is maintained to produce zero beam. Two sets of piezo-driven actuator were adopted for their accurate size for each step and compatibility of ultra-high vacuum (UHV). Piezo stages with closed-looped system function for controlling opening size of each pair of slits, and their positional accuracy and repeatability are both less than 100 nm. Picomotors are used to adjust parallelism between blades of each

Content from this work may be used under the terms of the CC BY 3.0 licence (© 2016). Any distribution of this work must maintain attribution to the author(s), title of the work, publisher, and DOI.

ISBN: 978-3-95450-188-5 doi:10.18429/JACoW-MEDSI2016-MOPE05

slit, and size for each step is less than 30 nm. Tungsten carbide is taken as material of blades. Specifically, rectangular single-crystal film is bonded on the edge of the slit blade to reduce X-ray scattering effect. The overall specifications of secondary source slits are specified in Table 1.

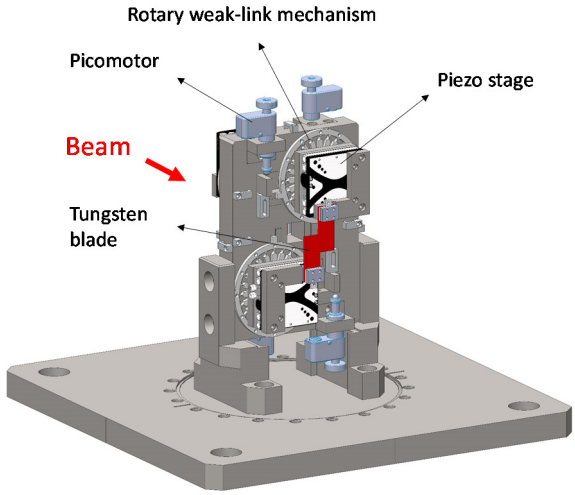


Figure 3: A 3-D model of main mechanism for secondary source slits.

Table 1: The Overall Specifications of Secondary Source Slits

Item	Specification
Vacuum	$\leq 10^{-9}$ mbar
Helium leak rate	$\leq 5\times10^{-10}$ mbar·l/s
Material	Tungsten carbide (Type WF20: 86.4% WC, 11.5% Co, 2.1% Others) GaAs single crystal
Maximum opening size	13 mm (H) × 13 mm (V)
Position resolution	≤ 0.006 μm
Position repeatability	≤ 0.018 μm
Positional accuracy	≤ 0.2 μm
Parallelism between blades	≤ 1 μm
Range of rotary adjustment	± 0.21 degree

Design of Mechanical Stability

The rotary weak-link mechanism [1] was developed for slightly rotary movement with high stiffness and stability, so it is very suitable for adjustment of parallelism of two blades of each slit. The rotary weak-link structure is shaped with complex axisymmetric geometry and has 3 mm of thickness. Except for wire electrical discharge machining (WEDM), ordinary machining methods are not able to realize the design.

SOLIDWORKS Simulation software was used as a tool of finite-element analysis to verify the statistical mechanics of rotary weak-link mechanism. The boundary conditions consist of the centric constraint and torque forced by picomotor. SUS630 H900 stainless steel was chosen as material of rotary weak-link mechanism for its high yielding stress. Result of finite-element analysis is shown in Fig. 4. This graph describes the maximum von Mises stress is about a half of yielding stress set as 1000 GPa while a 0.8 N-m of torque is applied. The actuated rotary movement is about 0.42 degree, which is taken as design value. Moreover, loading capacity of picomotors also needs to be considered. When a 0.8 N-m of torque is produced, reactive force is still under the loading capacity of picomotors.

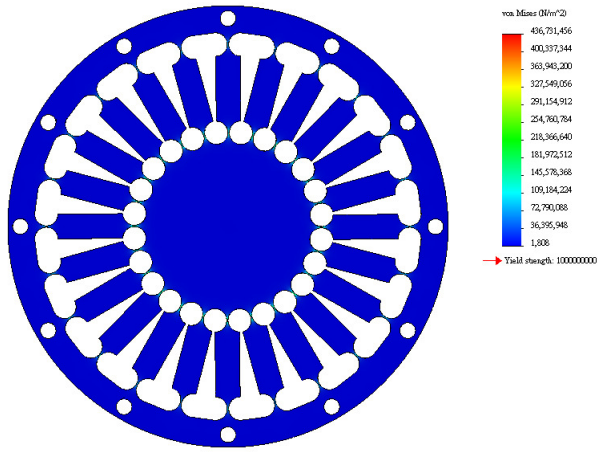


Figure 4: Result of finite-element analysis for rotary weak-link mechanism.

TESTING PROCEDURE AND RESULT

The parallelism between horizontal or vertical pair of blades is hard to measure because of its small opening size. Optical microscope, especially in high magnification, cannot be used due to limitation of depth of field. To overcome the difficulty of verifying the parallelism, the method of single-slit diffraction was used for its convenient observation. Based on the equation of Fraunhofer single-slit:

$$y = \frac{m\lambda D}{a} \quad (1)$$

Symbols y, m, λ, and a from above equation mean displacement from centreline for minimum intensity, order, wavelength of light, distance from slit and screen, and width of slit respectively. Helium-Neon laser with 543 nm of wavelength was used as the source of light in the testing system. Obviously if the displacement from centreline for first minimum intensity which means m equals one is measured, the width of slit can be calculated. Scanning from one side to the other is then made to observe variation of width.

Fig. 5 shows the diffraction pattern observed in the test of parallelism for horizontal slit. After adjusting rotary weak-link structure, the smallest variation of parallelism was about 0.3 μm less than that of specifications. This result represents not only the testing system is convenient for adjustment of parallelism, but the weak-link mechanism is effective for slightly rotary adjustment.

Content from this work may be used under the terms of the CC BY 3.0 licence (© 2016). Any distribution of this work must maintain attribution to the author(s), title of the work, publisher, and DOI.

ISBN: 978-3-95450-188-5 doi:10.18429/JACoW-MEDSI2016-MOPE05

Content from this work may be used under the terms of the CC BY 3.0 licence (© 2016). Any distribution of this work must maintain attribution to the author(s), title of the work, publisher, and DOI.

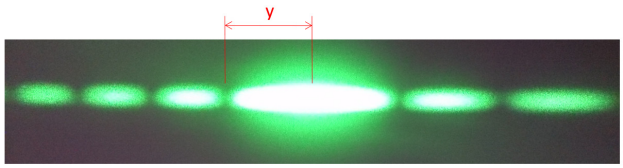


Figure 5: Diffraction pattern observed in the test of parallelism for horizontal slit.

PRECISE TEMPERATURE CONTROLLING SYSTEM

To minimize fluctuation of surrounding temperature for secondary source slits, a precise temperature controlling system is adopted. The system of secondary source slits is planned to be enclosed by a extruded-aluminum frame covered by double layers of plastic curtain and isolated from environment. A compact-type air handling unit (AHU) with coil-type heat exchangers shown in Fig. 6 supplies air with very stable temperature into the enclosed area. According to previous on-site test of this type of AHU in other beamline at TPS, variation of temperature for supplied air in exit port of AHU is within ±0.02 ℃. It is also verified that variation of temperature of supplied air in inlet port of enclosed area is within ±0.03 ℃.

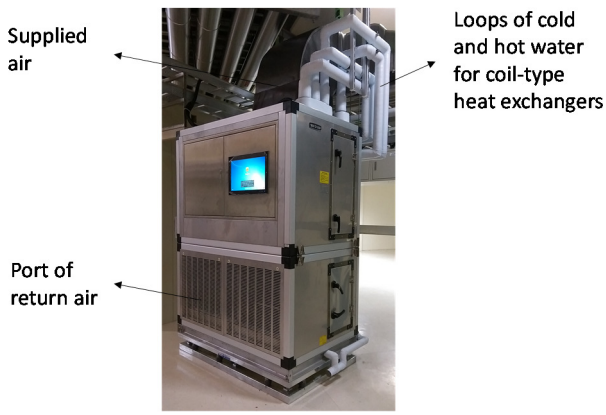


Figure 6: A compact-type air handling unit for precise temperature controlling system.

CONCLUSION

A system of mono beam secondary source slits has been designed, fabricated, tested, and installed on the Coherent X-ray Scattering beamline at TPS. UHV-compatible piezo-driven actuators were used to control opening sizes in horizontal and vertical directions and adjustment of parallelism between two blades on each pair of slits respectively. A set of testing procedure based on single-slit diffraction was realized to measure the parallelism between blades, and the design value of parallelism was reached successfully. To reduce the influence of ambient temperature, a precise temperature controlling system will be applied to provide air with constant temperature for enclosed system of secondary source slits. On-site test will be made to acquire more results during the beam time of TPS. According to the results, upgrade will be considered to reach better performance for system of secondary source slits in the future.

REFERENCES

[1] D. Shu *et al.*, "Development and applications of a two-dimensional tip-tilting stage system with nanoradian-level positioning resolution", *Nucl. Instr. And Meth. A* , vol. 649, pp. 114-117, 2011.

ISBN: 978-3-95450-188-5 doi:10.18429/JACoW-MEDSI2016-MOPE07

GROUND MOTIONS MEASUREMENTS FOR SYNCHROTRON

D. Ziemianski†, Cracow University of Technology, Kraków, Poland
M. P. Nowak, Solaris, Kraków, Poland

Abstract

For more than two decades, ground vibration measurements were made by different teams for feasibility studies of linear accelerators. Recent measurements were performed in the SPS tunnel and at different CERN sites on the surface. The devices to measure vibrations of magnitude ranging in nanometres, the analysis techniques and the results are critically discussed and compared with the former measurements. The implication of the measured integrated R.M.S. displacements for the Crab cavities cavern are mentioned.

The equipment used in this study consists of 2 state-of-the-art Guralp broadband triaxial seismometers. Models CMG-T60-0004 (Guralp Systems) performed measurements in three directions V, N/S and E/W.

The first analysis was to evaluate the power spectral density for each direction of sensors and event. The power spectral density is calculated from the auto power spectrum.

The power spectral density shows a typical curve for the geophones with the micro seismic peak between 0.2 and 0.4 [Hz]. It is important to point that ground vibrations should not be ignored in planning accelerator facility. Actually it is one of the limiting factor in the optimization of future accelerators.

SENSORS

Each author should submit the PDF file and all source files (text and figures) to enable the paper to be reconstructed if there are processing difficulties.

Models CMG-T60-0004 (Guralp Systems) performed measurements in three directions V, N_S and E_W. The geophones measure velocity with a sensitivity of about 2000 [V/(m/s)] and a frequency range between 30 [s] and 100 [Hz].

Geophones were adjusted to have the vertical direction parallel to the gravitation force. Longitudinal north-south and east west directions for geophones were pointed in the same directions. The results obtained from these sensors are dependent on good operational conditions and give a good signal to noise ratio only if all conditions are correct. The geophones need to be well protected against fluctuation in temperature and turbulent airflow.

In order to have a constant temperature for the geophones during operation, they were located and switched on 1 hour before any measurement was started. Then they had time to reach thermal equilibrium, this also reduces the DC offset from the measurement.

RESULTS

The first analysis was to evaluate the power spectral density for each direction of sensors and event. The ground motions at several locations measured in are plotted in (Figure 1). These locations are divided into three groups. The first group (red lines) is the synchrotron bunker, the second group (green lines) is the experimental hall and the third group (black lines) is the tunnel linac.

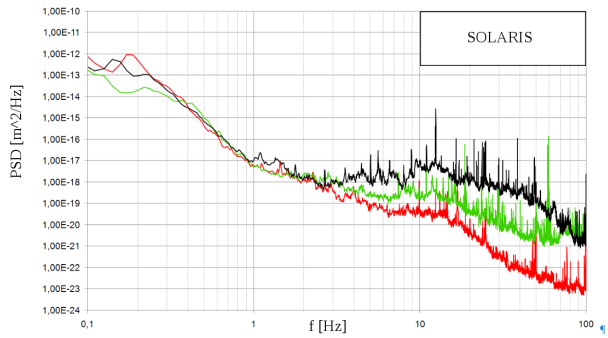


Figure 1: PSD for SOLARIS synchrotron.

RMS Integrated is used to sum up the total vibration of the PSD. It gives the RMS (Root Mean Square) value of the total vibration The integrated RMS ground motion in vertical direction for all these locations are plotted in (Figure 2). The (Table 1) show the value Integrated RMS value at 1 [Hz].

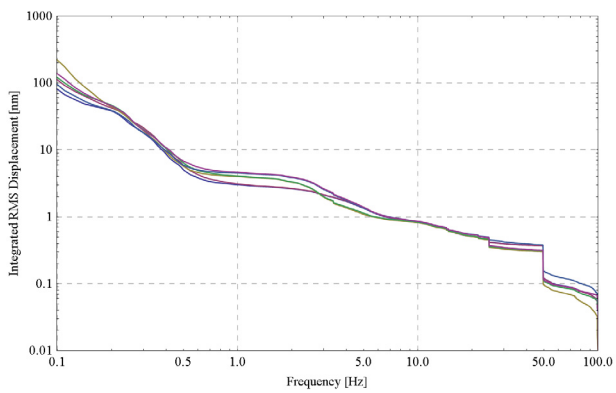


Figure 2: Ground motion all measured locations.

† dziemianski@pk.edu.pl

Content from this work may be used under the terms of the CC BY 3.0 licence (© 2016). Any distribution of this work must maintain attribution to the author(s), title of the work, publisher, and DOI.

ISBN: 978-3-95450-188-5 doi:10.18429/JACoW-MEDSI2016-MOPE07

Content from this work may be used under the terms of the CC BY 3.0 licence (© 2016). Any distribution of this work must maintain attribution to the author(s), title of the work, publisher, and DOI.

Table 1: The Value Integrated RMS Value at 1 [Hz]

RMS Integraded values	**@1 Hz [nm]**
SOLARIS	4,8
CLEX experiment (Bld.2013)	13,3
AEGIS experiment (Bld.193)	13,0
PSI particle accelerator	11,8
CMS experiment	6,8
CesrTA particle accelerator	3,8
LSS4 Caver-SPS Accelerator	4,1
TT1 tunnel (ISR)	2,3
LHC tunnel (DCUM584)	1,9

CONCLUSIONS

The ground motion spectrum can be separated in two main regions. The low frequency region below about 2 Hz which is dominated by natural motions sources like ocean waves and earth tides, and the high frequency region above 2 Hz which is dominated by cultural motion sources like traffic, industry, transformers, pumps and people walking. The power spectral density graphs above clearly shows the distinction between these two regions. In the low frequency region, all locations have a similar ground motion dominated by well correlated natural motions. In higher frequencies the ground motion is dominated by the local cultural noise, and the highest ground motions occur at locations with high cultural activity.

Measurements performed at one location several times during a day show varying levels of ground motions, with a highest cultural noise during daytime.

ISBN: 978-3-95450-188-5 doi:10.18429/JACoW-MEDSI2016-MOPE08

THE LNLS METROLOGY BUILDING*

H. G. P. Oliveira†, L. Sanfelici, C. Esper-Neto, P. T. Fonseca, R. R. Geraldes, B. C. Meyer, M. A. Pereira, G. L. Rodrigues, L. G. Silva, LNLS, Campinas, Brazil
L. Buccianti, M. H. A. Costa, C. Prudente,
Biotec Soluções Ambientais, São José dos Campos, Brazil

Abstract

The increasing demands of instrumentation projects for SIRIUS require more sensitive equipment to be developed and characterized in the micro and nanometer scale. To achieve this level of precision it is necessary to work within a controlled environment, minimizing instabilities and disturbance effects such as temperature variation and vibrations. Based on metrology labs as those at BESSY, ESRF, DLS and others, a new facility is currently under final construction stage at the LNLS, which will be dedicated to high precision optical and mechanical metrologies. This work describes in detail the project of the new LNLS Metrology Building.

INTRODUCTION

Sirius [1] is a 3 GeV synchrotron light source that is currently being built by the Brazilian Synchrotron Light Laboratory (LNLS), with a high brilliance beam which size could be as small as 9.5x3.5 μm and with a natural emittance of 0.25 nm·rad. Most of its beamlines have the requirements for a micrometric beam size up to 50 μm. To achieve these specifications, it is necessary to work with high-end mechanical and optical elements able to guarantee the stability and precision, like the new high-dynamics monochromator under developing at LNLS, aiming a final stability of 10 nrad at the Bragg angle [2]. Moreover, besides the designing and machining steps, it is necessary to validate the mechanisms as a whole, which is achieved with precision metrology. Also, to make reliable measurements, several parameters must be taken into account, like the accuracy and uncertainties of the measurement equipment, the test setup and the environmental disturbances, which could be temperature stability, air convection and turbulence, air cleanness, atmospheric pressure and humidity, and vibration [3]. This paper describes the main design aspects of the new LNLS Metrology Building, with four rooms: Assembly 1 and Assembly 2 for general assemblies, vacuum tests and dimensional analysis, a Mechanical Metrology Lab (MML) and an Optical Metrology Lab (OML); with an advanced environmental control and vibrational stability by means of a high precision HVAC system and inertial blocks with special foundations. The building itself is an 840 m² thermally isolated shed kept within ±1,5°C. Inside there are two 100 m^2 inertial bases and, around them, the mentioned four rooms were erected. The assembly rooms have relaxed environmental requirements (±0,5°C and ±10% RH), whereas both of the metrology laboratories are more restrict (±0,1°C and ±5% RH). The optical lab is also an ISO7 cleanroom.

The authors recommend being with the poster when reading this paper, as they are complementary documents.

INERTIAL BASES

In 2013, a study was held at LNLS in order to define the Sirius tunnel floor foundation, aiming for a high level of stability. First, the site soil geophysics conditions and natural vibration were analysed. Then, two special blocks prototypes were proposed and constructed, based on the MAXIV and DLS ring floor foundation. Several vibrational tests were carried out on the prototypes. Both bases perform very well concerning external vibration attenuation, but the MAX-based performed better (faster) on dissipating vibrations generated internally, which led to the choice of this foundation type to be used at Sirius.

As vibrational issues are an important matter for metrology purposes, it was decided that the LNLS metrology building would be erected around these inertial bases, being the assembly rooms around the DLS-based floor and the metrology laboratories around the MAXIV-based foundation.

CONCEPT

The LNLS Metrology Building was designed following a layer-based architecture, in which the outer layers have a proper environmental control that contributes for the stability of the inner ones. The goal of this architecture is to provide the laboratories (inner layers) a highly stable environment, minimizing the influence of the large thermal and humidity variations that may naturally occur outside the building. There are three layers: the machine room (MR), the building itself and the laboratories, that can be seen in Figure 1. Each layer has one or more rooms controlled by independent air handling units (AHUs). The environmental requisites for each room are presented in Table 1:

Table 1: Environmental Parameters

Room	T [°C]	RH [%]	Clean Room Class
Building	23±1.5	-	-
Assembly 1	22±1.0	50±10	-
Assembly 2	22±0.5	50±10	-
Mech. Metrology	22±0.1	50±5	-
Gowning Room and Buffers	22±0.1	50±5	ISO 8
Opt. Metrology	22±0.1	50±5	ISO 7

* Work supported by the Brazilian Ministry of Science, Technology, Innovation and Communication
† henrique.oliveira@lnls.br

Content from this work may be used under the terms of the CC BY 3.0 licence (© 2016). Any distribution of this work must maintain attribution to the author(s), title of the work, publisher, and DOI.

ISBN: 978-3-95450-188-5 doi:10.18429/JACoW-MEDSI2016-MOPE08

Content from this work may be used under the terms of the CC BY 3.0 licence (© 2016). Any distribution of this work must maintain attribution to the author(s), title of the work, publisher, and DOI.

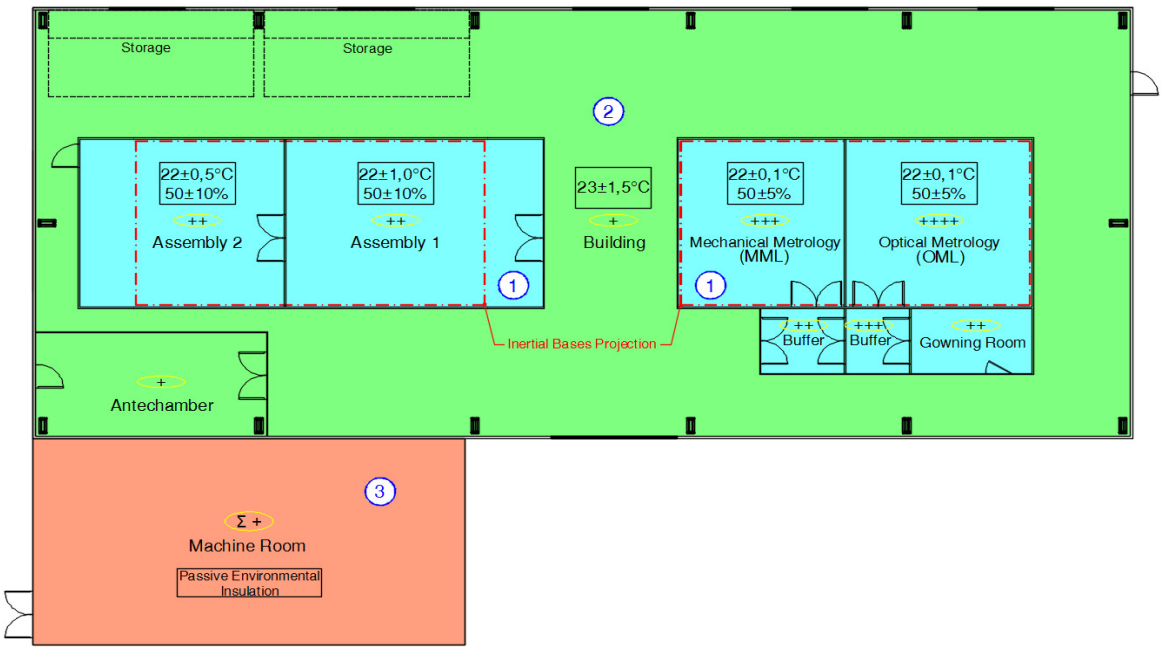


Figure 1: HVAC system architecture based on layers.

The MR operates admitting external air, working as a source of fresh air to make the necessary volume renewal. It is made of 100 mm thick Polyurethane (PU) isopanels walls and roof tiles for passive thermal insulation and it has an air exchange rate of 7 volumes/h. Three AHUs are installed in the MR, responsible for the shed conditioning and pre-treating the other AHUs air intake.

The building is also insulated with the same PU panels at walls and roof and, moreover, it has an active temperature control provided by the AHUs at the MR, with a maximum of temperature variation of ±1,5 °C, providing passive stability to the inner layer. Also, the AHUs designated to the laboratories are installed inside the building, suspended at the ceiling in order to not touch the flour around the inertial bases to prevent vibration coupling. Worth to mention that, regardless of being in the building layer, the labs AHUs fresh air supply comes from the unit named FC-CAP, at the MR.

The metrology laboratories and assembly rooms are where the fine environmental control take place and, despite of being physically separated, constitute the inner layer. The rooms and laboratories wall is made of 50 mm Polystyrene isopanels, for passive thermal insulation. The assembly rooms have a shared AHU, but the temperature control is independent, as the air is reheated directly on the diffusers. The mechanical and optical metrology rooms have individual AHUs, since the control is challenging and much finer than the others, and also because the optical lab is an ISO7 clean room.

HVAC SYSTEM

The core of the whole Metrology Building construction is the high precision HVAC system, which is the responsible for achieving the environmental parameters established for each area. For the system dimensioning, the following parameters for the city of Campinas, Brazil, at 685 m of altitude, were considered in Table 2.

Table 2: External Environmental Conditions

Season	Dry Bulb Temp.[°C]	Wet Bulb Temp.[°C]	Relative Humidity
Summer	33.0	11.0	48.7%
Winter	24.0	10.2	92.0%

Equipment

In all fronts of the HVAC system, only high-end equipment is being used. For the production of chilled water, two Trane air-cooled chillers are being employed, with 50 RT of cooling capacity each one. Both were planned to operate simultaneously, but in case of failure, the system can manage to operate with only one most part of the year. For the chilled water circuit, the system counts with Grundfos vertical pumps, installed in concrete inertial bases. Either the chillers and the pumps bases are supported by vibration attenuators. Also, there is a 15000 l tank for thermoaccumulation and regulation for chilled water, insulated with a 75 mm thick PU layer. All this equipment is located on an open area, outside the building.

Inside the MR, there is a filtering cabinet (G4 class) with a fan for external air intake and humidifiers.

The entire HVAC systems is composed by six customized AHUs from Trox. To supply the main shed (system 1), there are two AHUs (FC1.1 and FC1.2) that may work in parallel or, in case of failure, alone. The assembly rooms (system 2) share the same AHU (FC2), as their environmental requirements are more relaxed, and each one of the metrology labs has its own AHU (FC3 and FC4, systems 3 and 4). Also, it has a fan-coil (FC CAP) dedicated to the fresh air intake of FCs 2, 3 and 4.

ISBN: 978-3-95450-188-5 doi:10.18429/JACoW-MEDSI2016-MOPE08

Pressure Arrangement and Exchange Rates

Besides general architecture, Figure 1 also shows the pressure cascade that must be followed to insure cleanliness and temperature stability. Either the area is classified or not, the pressure balancing for each room must be within the tolerances shown in Table 3.

Table 3: Pressure Limits

Symbol	Min. [Pa]	Nominal [Pa]	Max [Pa]
0 (atm)	-5	**0**	5
∑ **+**	n.a.	**15***	n.a.
+	10	**15**	20
++	25	**30**	35
+++	40	**45**	50
++++	55	**60**	65

The symbol used at the MR (∑+) indicates a positive pressure, but without defined tolerances. It does not have an effective control, but it ensures that the air flows from inside the room to the external ambient.

Table 4 indicates the exchange rates for each area. The actual value must be within 10% and 20% of the nominal.

Table 4: Rooms' Exchange Rate

Room	Volume [m³]	Exchange Rate (vol/h)
Machine Room	151.3	7
Building/Shed	4711.7	8
Assembly 1	238.7	15
Assembly 2	190.1	20
Mech. Metrology	142.6	25
Opt. Metrology	159.3	35

Filtering System

The main requirement for a high class filtering system is the optical metrology clean room specified as class 10.000 (ISO 7). Still, there is a long "chain" of filters through the entire system to guarantee a high quality supplied air for all the areas. Figure 2 shows it in detail:

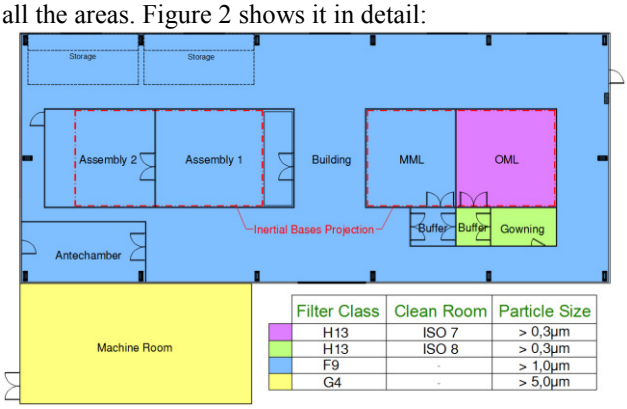


Figure 2: Filtering specs for each area.

Temperature and Humidity Control

Each fan-coil system has a cooling and a heating capacity to control both temperature and humidity for the supplied area. There are four controlled areas and an automation panel for each one, with a high number of sensors and actuators, concentrating information on an individual Siemens PLC for each panel. All parameters are available at a local supervisory, which is integrated with the LNLS Building Monitoring System (BMS). The automation panels and the IT rack are powered by an UPS circuit, as well as sensitive instrumentation inside the labs, following the same strategy intended for the Sirius building and beamlines.

For the shed temperature control, sensors are localized on the return ducts, and its readings implies on a signal sent to 2-way valves and/or heaters. The other areas have a quite different control strategy. The temperature sensors are at the air supply duct and its control point is set lightly below the desired temperature, because the fine adjustment is made by heaters located inside each air diffuser. Precision temperature transmitters are strategically positioned inside the rooms and send signal to the PLC, which controls solid state relays in order to define the power output supplied to the heaters. For the humidity control, the sensors are in the return ducts and the system acts through the coil control valve if it needs to condensates the water vapour, or at the humidifiers if the air is too dry.

STATUS AND FUTURE WORK

By now, the LNLS Metrology Building is at the final steps of its entirely conclusion. The first automation panel arrived at September 2, which enable the shed conditioning (second layer). The OML should be ready at September 12, and the other areas until the end of the month. Even with the complete installation, it will be necessary three more months to make general tests and the fine tuning of the HVAC system, so the Metrology Building should be fully functional by the end of 2016. Until there, the LNLS team is expanding its metrology capacity by acquiring new equipment such as capacitive sensors, CMM, laser trackers, AFM, long trace profiler, micro-interferometer, Fizeau interferometer, optical tables, among others [4,5].

ACKNOWLEDGEMENT

The LNLS team would like to thank to many colleagues around the world which contributed to the development of the Metrology Building - ESRF, ALBA, Diamond, BESSY, among others.

REFERENCES

[1] L. Liu, F. H. de Sá, and X. R. Resende, "A new optics for Sirius," in *Proceedings of IPAC'2016*, pp. 3413–3415.

[2] R. R. Geraldes *et al*, "The new high dynamics DCM for Sirius", presented at MEDSI 2016, Barcelona, Spain, Sep. 2016.

[3] V. V. Yashchuk *et al.*, "Advanced environmental control as a key component in the development of ultrahigh accuracy *ex situ* metrology for x-ray optics", *Optical Engineering*, vol. 54, no. (10), p.104104, Oct. 2015.

[4] B. Meyer, "Conceptual design report (CDR): Metrology equipment of the LAMOX", unpublished.

[5] M. Idir *et al.*, "Current Status of the NSLS-II optical metrology laboratory", *Nuclear Instruments and Methods in Physics Research A*, vol. 710, pp. 17-23, May 2013.

Content from this work may be used under the terms of the CC BY 3.0 licence (© 2016). Any distribution of this work must maintain attribution to the author(s), title of the work, publisher, and DOI.

ISBN: 978-3-95450-188-5 doi:10.18429/JACoW-MEDSI2016-MOPE09

PRELIMINARY DESIGN AND TEST OF DAMPING MECHANISM FOR REDUCING VIBRATION OF TPS SR VACUUM CHAMBER

K. H. Hsu†, H.C. Ho, C.K.Kuan, C.M. Cheng, W.Y. Lai, S.Y. Perng, T.C. Tseng, D.G. Huang, M.L. Chen, C.J. Lin, H.S. Wang, National Synchrotron Radiation Research Center, Hsinchu, Taiwan (R.O.C)

Abstract

Since flow-induced vibration of vacuum chamber effects of the stability of the electron beam storage ring in Taiwan Photon Source (TPS), a damping mechanism was designed and installed to reduce vibration. The damping mechanism is composed of a clamper of vacuum chamber, a fixed fixture on the girder and a sandwiched stainless steel support with damping materials inside. Different kinds of materials were applied in the damping mechanism for vacuum chamber. The vibration of vacuum chamber were obtained and compared. The design and vibration measurement results of damping mechanism for vacuum chamber are presented in this paper.

INTRODUCTION

Taiwan Photon Source (TPS), a third-generation accelerator, was constructed with a circumference of 518.4m with 24 girder magnet assembled (GMA). It reached its goal of 500mA in 2015. However, it was found that the vibration of vacuum chamber is major especially in the upstream of the dipole magnets. The source of vacuum chamber vibration are thought to be generated by cooling water passing through the pipe as shown in figure 1.The vibration of vacuum chamber affect the motion of electron beam due to eddy current effect [1]. In order to reduce the vibration of vacuum chamber, the damping mechanism was designed.



Figure 1: cooling pipe of vacuum chamber.

DESIGN OF DAMPING MECHANISM

Due to limited space between the touch sensor module and quadruple magnet on the girder, the damping mechanism is designed as a thin support as shown in figure 2 .The damping mechanism was composed of a clamper of vacuum chamber, a fixed fixture on the girder and a sandwiched stainless steel support with damping material inside. The clamper is designed to clamp the vacuum chamber with two M8 bolts with two sets of screws to adjust the vacuum chamber from the top surface. The fixture is fixed on the girder with two M16 bolts, and linked with the stainless steel sandwiched support with three m8 bolts. The thickness of stainless steel is 2mm. The sandwiched stainless are mounted with six M8 bolts with damping material inside. The six bolts are fastened lightly at the last step of assembling the damping mechanism in order to prevent from deforming the vacuum chamber.

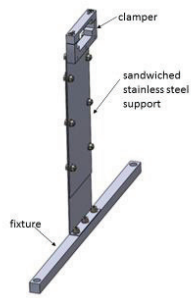


Figure 2: Design of damping mechanism for vacuum chamber.

MATERIALS IN DAMPING MECHANISM

Since it is difficult to obtain commercial passive damping material in Taiwan, only 3 types of material applied in the damping mechanism were chosen to study the performance of vibration reduction. These materials for our test are listed in Table 1 and Figure 3.

Table 1: Testing Materials

Material	Thickness (mm)	Loss factor	Storage module(Mpa)
3M ISD 112	0.127	1.0	0.22
Nitto D-300N	1.5	N/A	N/A
3M 4026	1.6	N/A	N/A



Figure 3: Different materials (from right: 3M ISD112, Nitto D-300N and 3M 4026).

3M ISD112, a kind of viscoelastic damping polymers, is used in many engineering designs to reduce vi-

† khhsu@nsrrc.org.tw

Content from this work may be used under the terms of the CC BY 3.0 licence (© 2016). Any distribution of this work must maintain attribution to the author(s), title of the work, publisher, and DOI.

ISBN: 978-3-95450-188-5 doi:10.18429/JACoW-MEDSI2016-MOPE09

bration [2]. Another material, Nitto D-300N, composed of aluminum layer, synthetic rubber adhesive and release liner, is claimed to having high performance in damping minimization [3]. However, the damping properties of D-300N are not available from the material supplier. The other material, 3M 4026, a kind of double coated urethane foam tape for bonding various types of surfaces together, which cannot be claimed as a damping material [4]. Thus, there is no damping properties in the specification of 3M 4026 either. Being the case, the performance of these 3 materials which applied in damping mechanism are compared and discussed.

EXPERIMENTAL SETUP

In order to know if it has the same results in different vacuum chamber, we set up both tests in the R13 and R20 cell. Since the vibration of vacuum chamber we measured may alter at different time points due to the variation of the girder vibration, the girder vibration measured is set to be the denominator of the transmissibility. The transmissibility is defined as the ratio of the vibration of vacuum chamber to that of girder as in equation (1). Thus, both the vibration of vacuum chamber and girder are measured simultaneously with digital FFT analyser. The two PCB 393B31accelerometers (sensitivity: 10V/g) were mounted on the vacuum chamber and the girder respectively in the same direction as shown in figure 4. The X and Y direction are defined as the horizontal and vertical respectively. We measured 4 conditions (free, ISD112, D300N, 3M4026) in each direction to study the effectiveness of the vibration suppression. The condition named "free" means that the vibration of vacuum chamber is measured without damping mechanisms. The condition named ISD112/D300N/3M4026 means that the vibration measurement of vacuum chamber with 3M ISD112/Nitto D300N/ 3M 4026 damping mechanism are executed. The bandwidth range of vibration measurement is 0-300Hz and the 4096 points are recorded in each frame. The spectrum of vibration are linear averaged with 10 frames. The averaged vibration spectrum of each condition are obtained twice to check the consistency of the data.

$$\text{Tramsimissibility} = \frac{the\ vibration\ of\ vacuum}{the\ vibration\ of\ the\ girder}. \quad (1)$$

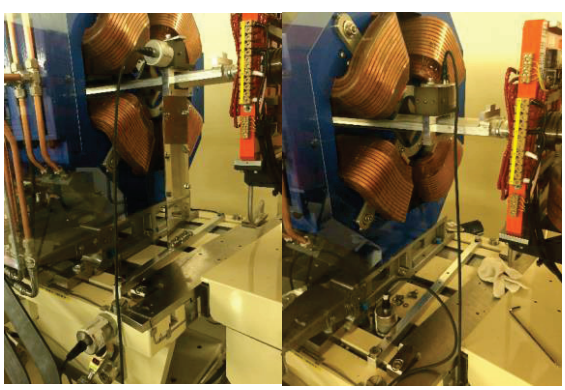


Figure 4: The experimental setup.

EXPERIMENTAL RESULTS

Since both the vibration spectrum of the vacuum chamber and girder are measured, the transmissibility spectrum of R13 and R20 vacuum chamber, supported by damping mechanism with different damping material, to the girder in X and Y direction are shown in Figure 5 to 8.



Figure 5: The transmissibility spectrum of R13 in X direction.

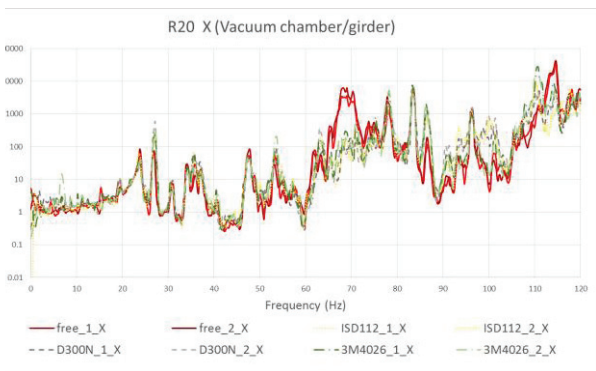


Figure 6: The transmissibility spectrum of R20 in X direction.

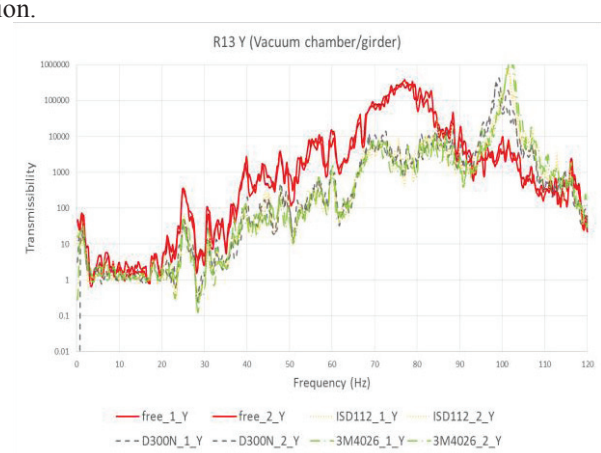


Figure 7: The transmissibility spectrum of R13 in Y direction.

Content from this work may be used under the terms of the CC BY 3.0 licence (© 2016). Any distribution of this work must maintain attribution to the author(s), title of the work, publisher, and DOI.

ISBN: 978-3-95450-188-5 doi:10.18429/JACoW-MEDSI2016-MOPE09

Content from this work may be used under the terms of the CC BY 3.0 licence (© 2016). Any distribution of this work must maintain attribution to the author(s), title of the work, publisher, and DOI.

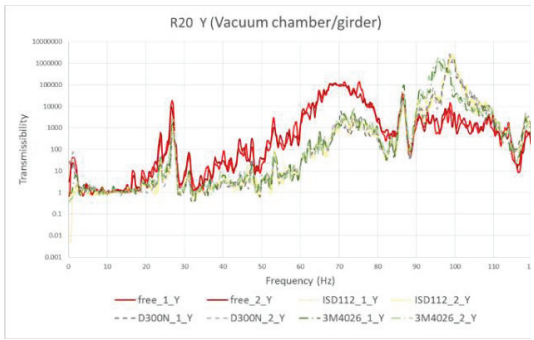


Figure 8: The transmissibility spectrum of R13 in Y direction.

From these transmissibility spectrum, it was found that the results with the same condition measured twice are similar. Nevertheless, the results in different cells (R13& R20) are different even with the same damping mechanism and material in the same direction. In X direction, the transmissibility spectrum are similar with different conditions; in Y direction the spectrum of "free" condition are significantly different from other condition from 20 to 90Hz.

For the legibility to compare with different damping material, the transmissibility of those damping material divided by that of no damping mechanism (free), is called transmissibility ratio. The transmissibility ratio spectrum of different materials are shown in figure 9 and 10. When the transmissibility ratio is smaller than 1, the damping mechanism reduces the vibration of vacuum chamber. In Y direction, the vibration of vacuum chamber with damping mechanism are reduced effectively from 40Hz to 80Hz.

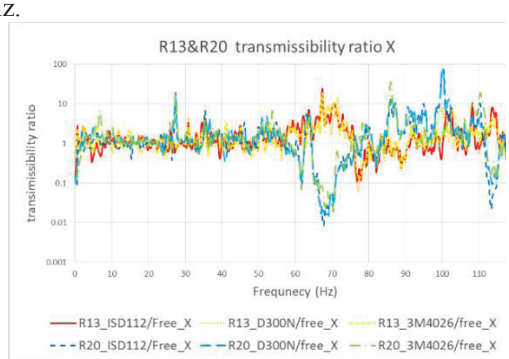


Figure 9: The transmissibility ratio spectrum in X direction.

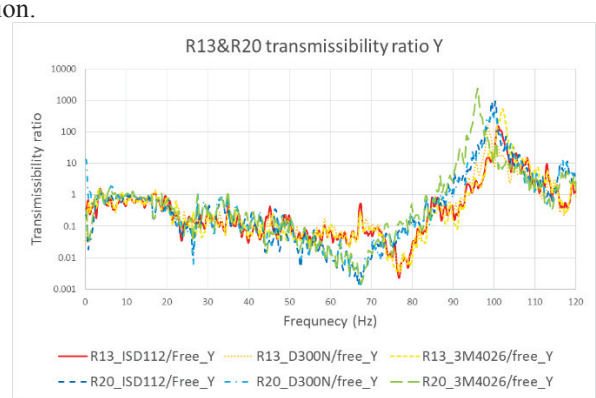


Figure 10: The transmissibility ratio spectrum in Y direction.

The transmissibility of averaged integrated displacement RMS with different materials from 4Hz to 100Hz in R13 and R20 are shown in Figure 11 and 12. As shown in the result, we can find that the vibration of vacuum chamber reduce more in the vertical direction. 3M4026 reduce vibration more effectively than other material in R13 (21%), but it has the opposite results in R20 (55%). On the contrary, it is meaningless to reduce the vibration in horizontal direction.

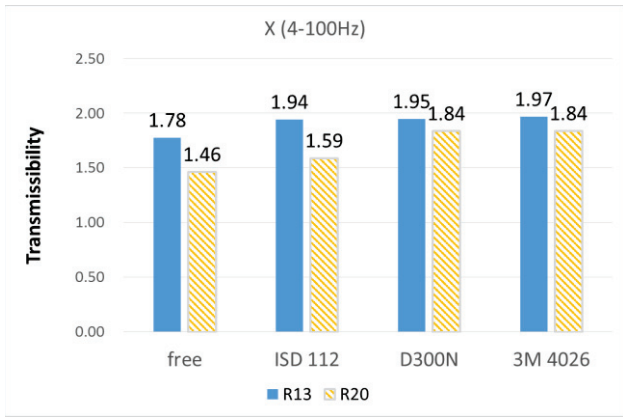


Figure 11: Comparison of the transmissibility of different materials in damping mechanism for vacuum chamber in X direction in R13 and R20.

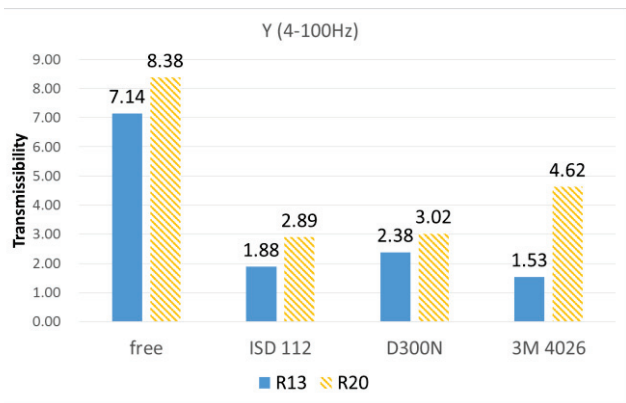


Figure 12: Comparison of the transmissibility of different materials in damping mechanism for vacuum chamber in Y direction in R13 and R20.

SUMMARY

In this paper, the damping mechanism for TPS SR vacuum chamber was designed and installed in the entire TPS storage ring. As the test results, this damping mechanism reduce the vibration of vacuum chamber in vertical direction from 20% to 55% especially from 40Hz to 80Hz. Nevertheless, the vibration of vacuum chamber in horizontal direction is not been suppressed effectively. Different materials applied in damping mechanism reduce the vibration similarly.

ISBN: 978-3-95450-188-5 doi:10.18429/JACoW-MEDSI2016-MOPE09

REFERENCES

[1] *Observation of Beam Orbit Fluctuation with Forced-Vibrating Magnets and Vacuum Chambers,* MEDSI, Illinois U.S.A 2002 pp.147-155.

[2] 3M website. http://goo.gl/yp54iZ.

[3] Nitto website. http://goo.gl/LGgHMt.

[4] 3M website. http://goo.gl/A3vXZ.

Content from this work may be used under the terms of the CC BY 3.0 licence (© 2016). Any distribution of this work must maintain attribution to the author(s), title of the work, publisher, and DOI.

ISBN: 978-3-95450-188-5 doi:10.18429/JACoW-MEDSI2016-MOPE10

DYNAMIC ANALYSIS AND MEASUREMENT OF GROUND MOTION FOR THE SOLARIS - NATIONAL SYNCHROTRON RADIATION CENTRE IN CRACOW

D. Ziemianski†, Cracow University of Technology, Cracow, Poland
M. Nowak[1], National Synchrotron Radiation Centre SOLARIS, Cracow, Poland

Abstract

The paper presents the results of the ground motion measurements and dynamic analysis performed in The Polish synchrotron radiation facility Solaris. The analysis has been carried out within the framework of the installation experimentals lines inside SOLARIS bilding and accelerator tunnel. The equipment used in this study consists of 4 seismic, high sensitivity, ceramic flexural ICP accelerometer. Models 393B31. (PCB) , which performed measurements in one vertical directions. The first analysis was to evaluate the power spectral density for each sensors and event. The power spectral density is calculated from the auto power spectrum. The power spectral density shows a typical curve with the micro seismic peak between 0.2 and 0.4 [Hz]. It is important to point that ground vibrations should not be ignored in planning accelerator facility. All over the measurement, the RMS integrated level in the vertical direction at 1 [Hz] were calculated and presented in paper.

SENSORS

Four mono-axial seismic accelerometers were used to measure the ground motion, with a sensitivity of about 1000 [mV/m/s2].The mass of each transducer is 635 [g] and 771[g] (PCB 393831, ENDEVCO 86). The usable frequency range of a sensor is from about 0.1 Hz up to 1/3 to 1/2 of the natural resonance frequency (700/370 [Hz]). In order to increase the frequency, either the stiffness should be increased or the mass decreased. Since decreasing mass also decreases sensitivity, increasing stiffness is preferable. In most cases, a combination of the two approaches is required.

The accelerometers were glued on the floor with wax. The natural frequency of an umounted sensor is different from that of a mounted sensor, because the mounted sensor has a stiffness determined by the stiffness of the structure in which it is mounted. Attaching the sensor to a structure can lower the natural frequency by a substantial amount.

† dziemianski@pk.edu.pl

EVOLUATION OF ACCELEROMETER

In addition to seismometers, seismic accelerometers can be a suitable motion transducer for the SOLARIS measurement. The signal and noise of two different seismic accelerometers has been evaluated. These are PCB393831 (Figure 1) and Endevco Model 86 (Figure 2).

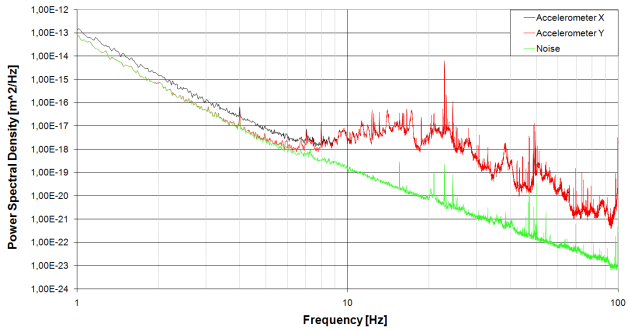


Figure 1: Integrated RMS signal and noise PCB393831.

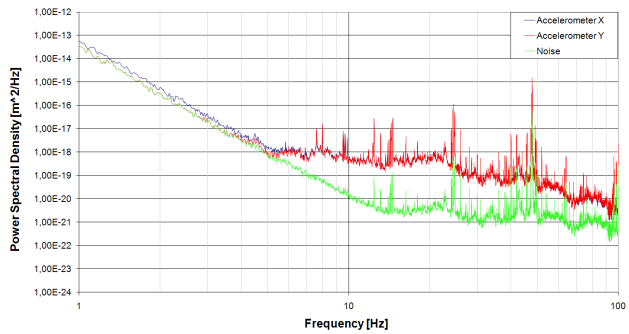


Figure 2: Integrated RMS signal and noise Endevco Model 86.

Two curves show that all accelerometers tested are able to measure above 7 Hz according to the signal to noise ratio. For the SOLARIS measurement this is not sufficient. The motion should be measured down to 1 Hz. However, seismic accelerometers can be used as a supplement to seismometers at high frequencies.

INTEGRATED RMS VALUES

Integrated RMS is used to sum up the total vibration in a spectrum. As the name indicates it give the RMS (Root Mean Square) value of the total vibration.

$$\sigma_{\omega} = \sqrt{\sum_{k_1}^{k_2} \Phi_{\omega}(v)\, dv} \qquad (1)$$

Content from this work may be used under the terms of the CC BY 3.0 licence (© 2016). Any distribution of this work must maintain attribution to the author(s), title of the work, publisher, and DOI.

ISBN: 978-3-95450-188-5 doi:10.18429/JACoW-MEDSI2016-MOPE10

Integrated RMS is a function of k, the frequency, k_1 is the lower value for the summation and k_2 is the upper value for summation. It is usual to plot the integrated RMS as a graph where k_2 is a fixed upper value and k_1 is gradually reduced while the integrated RMS is plotted for each value of k_1. Then it is possible to see the total summation of vibrations from a frequency and down to every lower frequency.

The integrated RMS ground motion at vertical direction for several locations are plotted (Figure 3).

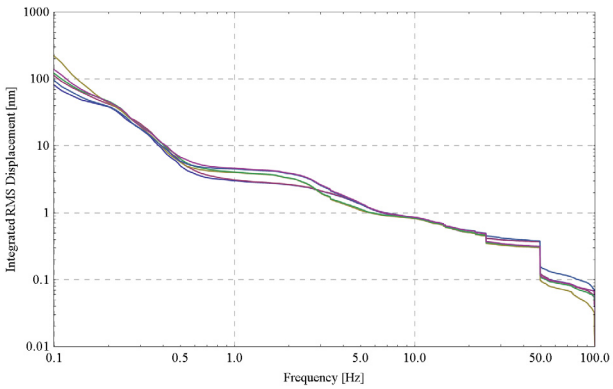


Figure 3: Integrated RMS displacement at vertical direction.

CONCLUSIONS

The power spectral density shows a typical curve for the geophones with the micro seismic peak between 0.2 and 0.3 [Hz]. The amplitude of this peak has a good correlation with ocean wave height and depends also on the distance from the ocean.

Table 1: The value Integrated RMS value at 1 and 10 [Hz]

Location	1 Hz [nm]	10 Hz [nm]
SOLARIS	5,1	0,9
CLEX experiment (Bld.2013)	13,3	11,6
AEGIS experiment (Bld.193)	13,0	12,4
PSI particle accelerator	11,8	11,0
CERN surface	11,7	10,1
CMS experiment	6,8	1,5
CesrTA particle accelerator	3,8	3,0
SOLARIS	5,1	0,9
CLEX experiment (Bld.2013)	13,3	11,6

All over the measurement, the RMS integrated level in the vertical direction at 1 [Hz] do not exceed a maximum of 5.1 [nm]. The values obtained from these measurements do not differ as to the value of the results obtained during the measurements in other locations (Table 1).

Content from this work may be used under the terms of the CC BY 3.0 licence (© 2016). Any distribution of this work must maintain attribution to the author(s), title of the work, publisher, and DOI.

ISBN: 978-3-95450-188-5 doi:10.18429/JACoW-MEDSI2016-MOPE11

PRELIMINARY ACTIVE VIBRATION ELIMINATION STUDY OF THE TPS GIRDER SYSTEM

T.C. Tseng, S.Y. Perng, H.S. Wang, K.H. Hsu,W.Y. Lai, M.L. Chen, H.C. Ho, C.J. Lin, D.G. Huang, C.W. Tsai, C.K. Kuan, National Synchrotron Radiation Research Center, Hsinchu, Taiwan

Content from this work may be used under the terms of the CC BY 3.0 licence (© 2016). Any distribution of this work must maintain attribution to the author(s), title of the work, publisher, and DOI.

Abstract

Taiwan Photon Source (TPS) had delivered the first synchrotron light on the last day of 2014 and is to open to the users from September 2016 after one and half years of commissioning and insertion devices installation. However, the instability is still an obvious problem to the beam quality and the deviation amplification factor of the magnets to the electron beam plays an important contribution role. Since the magnets are firmly installed on the girders and the contribution is mainly transferred from the girder vibration. This study tries to eliminate the obvious vibration frequencies amplitude exerted on the girder from outside sources such as the utility system with the PZT actuators installed on the locking wedges between girder and pedestals. By the amplitude and inverse phase searching iteration, some vibration frequency peaks in phase domain can be eliminated and the instability is also reduced.

INTRODUCTION

The Taiwan Photon Source (TPS) storage ring began the installation at Oct. 2013 as shown in the Figure 1 and had delivered the first synchrotron light on the last day of 2014[1]. After one and half years of commissioning and insertion devices installation, TPS is scheduled to open to the users from September 2016.

However, the instability is still an obvious problem to the beam quality and the deviation amplification factor of the magnets to the electron beam plays an important contribution role[2]. Since the magnets are firmly installed on the girders and the contribution is mainly transferred from the girder vibration.

In order to align the girders precisely and quickly with less manpower, an automatic-tuning girder system was proposed and fulfilled[3,4,5]. This girder system showed prominent adjustability and stability[6]. However, due to the heavy load of magnets the natural frequency as showed in Figure 2 is still not high enough although a locking system has applied. From the vibration spectrum inspection on the girder set and ground, there are frequency peaks other than the natural frequencies from outside sources such as the utility system as shown in the Figure 3.

This preliminary study tries to show the ability to eliminate the obvious vibration frequencies amplitude exerted on the girder system from outside sources. And eventually an active system will be set up to improve the stability.



Figure 1: TPS Storage ring bending section.

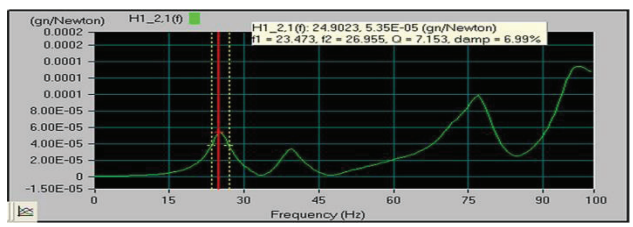


Figure 2: Natural frequency of one girder set with locking system.

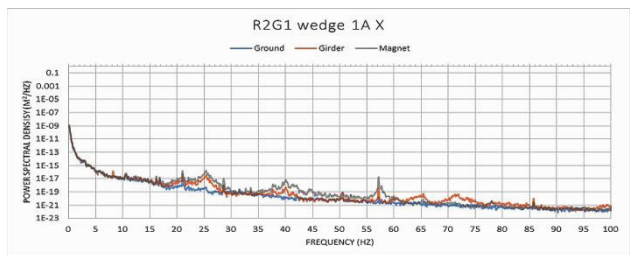


Figure 3: Vibration spectrum measurement around a girder set.

TESTING GIRDER SETUP

An extra testing girder set had been installed at the TPS inner ring lab for the preliminary study instead of the storage girder for convenient. The TPS storage ring girder configuration is shown as in Figure 4. Two modified locking wedges with PZT modular as in Figure 5 are installed at the same side of outside two pedestals as the anti-vibration actuators.

Two 3-axes PCB 356B18 accelerometers are placed on the girder surface top of the outside pedestals. These accelerometers serve as the monitors at the preliminary study stage and will be the feedback sensors for the active system.

A computer with labview program was prepared to control the system. The accelerometer signals are received

ISBN: 978-3-95450-188-5 doi:10.18429/JACoW-MEDSI2016-MOPE11

through an ADLINK PXIe-9529 interface card. And a shaker with function generator output exerted on the girder body to simulated the vibration source as in Figure 6. A Tektronix AFG3022C function generator with 2 output channels to driving the PZT to compensate the vibration derived form the shaker. The AFG3022C will be replaced with an ADLINK PXI-2502 DAQ card for the active system.

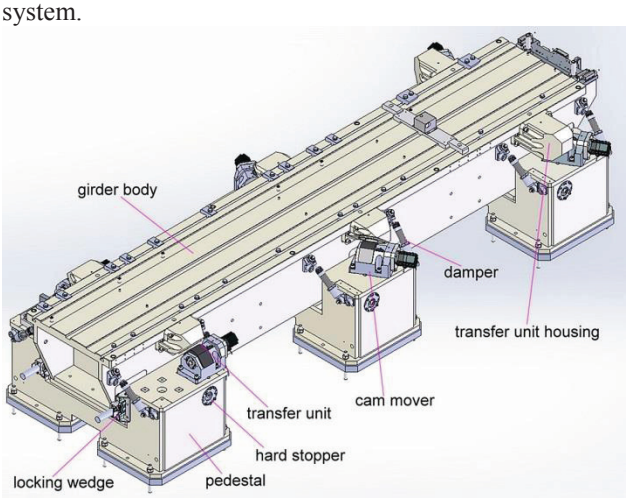


Figure 4: TPS girder configuration.

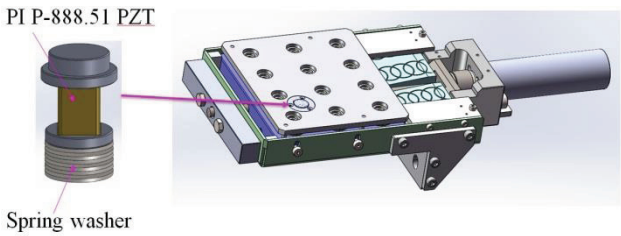


Figure 5: Modified locking wedge with PZT modular.

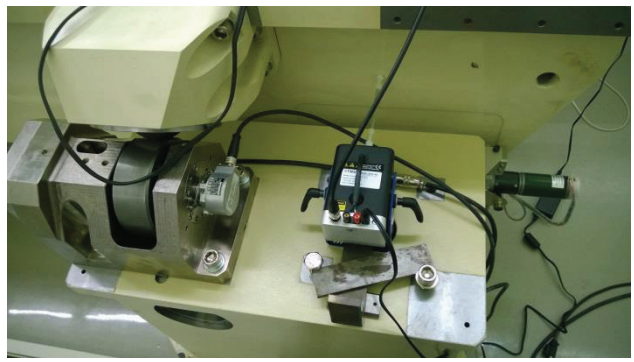


Figure 6: A shaker to simulate the vibration source.

TESTING RESULTS

As shown in Figure 7, by using the function generator to control the shaker, a 27 Hz vibration peak can be detected from the accelerometer in the horizontal transverse direction of one side. The other directions and the accelerometer on the other side are negligible. This result shows the stability of the girder is still quite good. By adjusting the amplitude and phase output of the AFG3022C as shown in Figure 9, the 27Hz peak generated from the shaker can be eliminated as shown in Figure 8.

However, the peaks of 45Hz and 52Hz,the natural frequencies of the girder without magnets installed, cannot be eliminated because they are aroused from the environment white noise without steady phase.

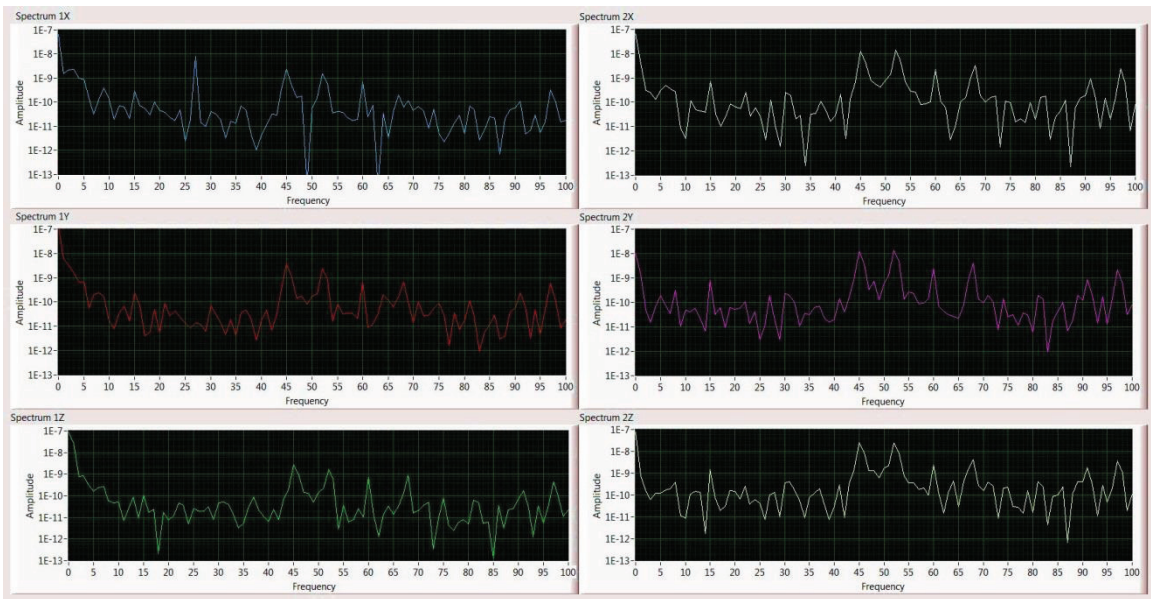


Figure 7: Vibration peak detected while shaker on.

Content from this work may be used under the terms of the CC BY 3.0 licence (© 2016). Any distribution of this work must maintain attribution to the author(s), title of the work, publisher, and DOI.

ISBN: 978-3-95450-188-5 doi:10.18429/JACoW-MEDSI2016-MOPE11

Content from this work may be used under the terms of the CC BY 3.0 licence (© 2016). Any distribution of this work must maintain attribution to the author(s), title of the work, publisher, and DOI.

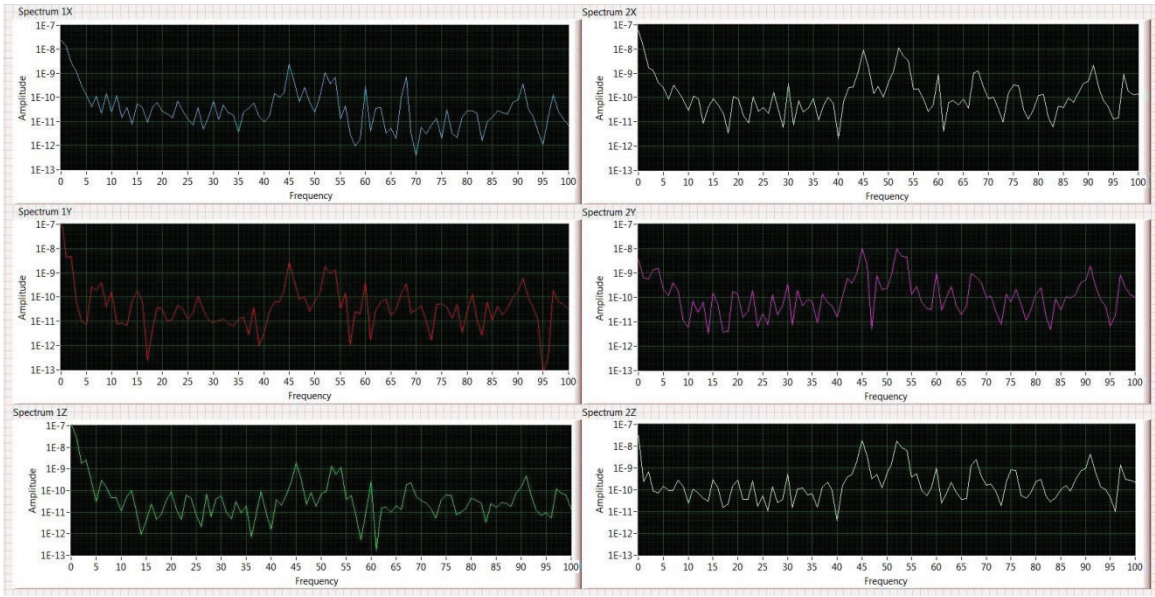


Figure 8: Vibration peak eliminated at one direction.

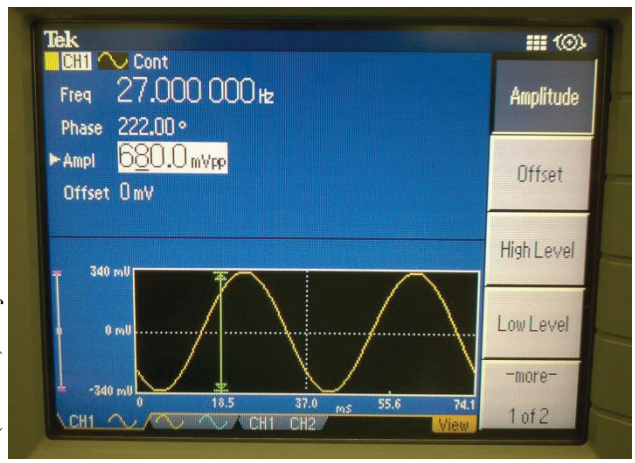


Figure 9: Amplitude and phase adjusting.

CONCLUSION

A testing girder set had been installed at the TPS inner ring lab. Two modified locking wedges with PZT modular were assembled for vibration elimination testing. At the preliminary testing stage, with a shaker to simulate the vibration source, the generated peak can be eliminated via a function generator output to the PZT with the amplitude and phase adjusted. However, the natural frequency peak induced by the environment white noise is hard to reduce or eliminate because the phase is not unique. Furthermore, the PZT arouse vibration peak at other direction indicated a six axes elimination system is demanded. Such a system is under fabrication.

REFERENCES

[1] NSRRC website: http://www.nsrrc.org.tw/english/tps.aspx

[2] TPS design handbook.

[3] T.C. Tseng et al, "A precise 6-axies girder system with cam mover mechanism", MEDSI(2006)

[4] T.C. Tseng et al, "Design and prototype testing of the girder system for TPS", SRI(2008)

[5] T.C. Tseng et al, "Installation And Implementation Of An Auto-Alignment Girder System For TPS Storage Ring", MEDSI(2014)

[6] T.C. Tseng et al, "The Auto-Alignment Girder System of TPS Storage Ring", PAC(2015)

ISBN: 978-3-95450-188-5 doi:10.18429/JACoW-MEDSI2016-MOPE13

THE 20M/S CERN FAST VACUUM WIRE SCANNER CONCEPTUAL DESIGN AND IMPLEMENTATION

J. Herranz†, Proactive Research and Development, Barcelona, Spain
W.Andreazza, N.Chritin, B. Dehning, J. Emery, D.Gudkov, P.Magagnin, S.Samuelsson
J.L. Sirvent Blasco, R. Venness, CERN, Geneva, Switzerland
A.Barjau[1], Universitat Politècnica de Catalunya, Barcelona, Spain

Abstract

In the next years the luminosity of the LHC will be significantly increased. Therefore a much higher accuracy of beam profile measurement than actually achievable by the current wire scanner is required. The new performance demands a wire travelling speed up to 20 m/s and a position measurement accuracy of the order of 1 µm. In order to minimize the error source of the wire position measurement, a challenging concept has been developed which consists of the placement of the motor rotor and the angular position sensor in vacuum. The implementation of this new concept requires the use of a magnetic brake, hybrid vacuum bearings, the design and production of very thin (<0.5mm) wall vacuum chamber regions and the production of titanium components by 3D additive technologies. The implementation of this new concept has required different optimization processes as the structural optimization under dynamic load of the most critical rotating elements or the optimization of the control system and the motion pattern. This contribution gives an overview of the new device design and shows the different technical solution applied to develop the new concept in a successful way.

INTRODUCTION

A wire scanner (Fig. 1) is an electro-mechanical device which measures the transverse beam density profile of a particle beam by means of moving a thin wire across the beam in an intermittent manner. As the wire passes through the beam the interaction generates a cascade of secondary particles. These are intercepted by a scintillator, which couples the photons generated by the incident particle to a photomultiplier (PMT), which provides an electrical signal proportional to the incident photon flux.

The wire is stretched by a fork directly mounted on a shaft. The wire, fork and shaft are located in a vacuum chamber while the actuator is outside that chamber. The actuator provides a motion pattern consisting of three distinct phases (acceleration, constant speed and deceleration) fulfilling a set of requirements in order to achieve a suitable wire speed and position at beam crossing. Therefore the wire is crossing the beam in motion and consequently subjected to dynamic effects.

The strong peak acceleration in the motion pattern induces deflections and vibrations on the measurement chain (shaft, fork and wire) [1], which result in discrepancies between the true position of the wire and the position measured by the position sensor (Fig. 2).

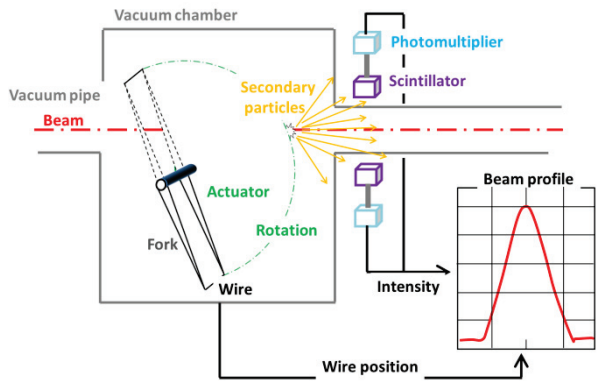


Figure 1: Illustration of the rotating wire scanner instrument.

Errors on the wire position when intersecting the beam have a direct consequence on the profile and position measurement accuracy. Thus, identifying and minimizing the uncertainties and error sources is a priority [2].

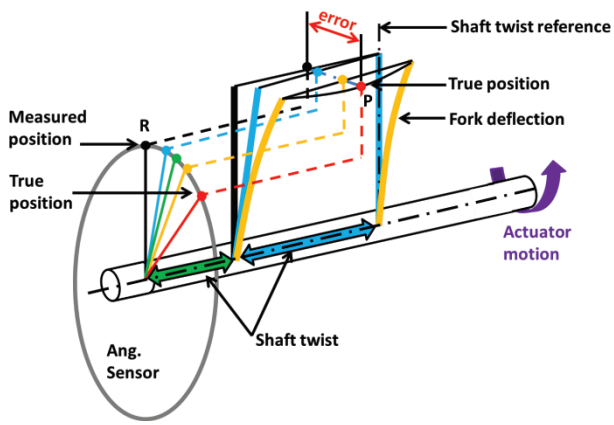


Figure 2: Deflections of the measurement chain for a rotating wire scanner.

The measurement requirement of the transverse beam distribution in the LHC rings [3] established the maximum uncertainty for the beam size determination for the LHC beam to be 1.8%. Minimum LHC beam size is in the range of 160 µm therefore the uncertainty in the beam size determination by the wire scanner has to be lower than 2.8 µm.

Experimental studies have been performed in order to determine wire damage limits due to the beam-wire energy deposition [4]. The conclusions of these studies advocate a wire traveling speed on the range of 20m/s.

†jherranz@proactiverd.com

Content from this work may be used under the terms of the CC BY 3.0 licence (© 2016). Any distribution of this work must maintain attribution to the author(s), title of the work, publisher, and DOI.

ISBN: 978-3-95450-188-5 doi:10.18429/JACoW-MEDSI2016-MOPE13

Content from this work may be used under the terms of the CC BY 3.0 licence (© 2016). Any distribution of this work must maintain attribution to the author(s), title of the work, publisher, and DOI.

CONCEPTUAL DESING DESCRIPTION

The most remarkable feature of the new wire scanner concept is that all the movable components of the system are under vacuum. Although the rotating elements (actuator, angular sensor, shaft, fork and wire) remain the same as in the existing designs (i.e. a fork holding the wire is mounted on a rotating shaft), the mechanical complexity of the system is highly reduced since no kinematical links are required to transmit the motion from the pressure side to the vacuum side. Additionally, all movable parts are mounted in the same shaft, which implies the suppression of the kinematic chain which typically links the wire measuring point to the angular position sensor. Avoiding these kinematic chains represents a conceptual improvement compared to the existing devices from the precision point of view, as there is no mechanical play between the different parts of the measurement chain. Therefore, the position determination of the measuring chain is much more accurate. The main parts of this new wire scanner concept are shown in Fig. 3.

DESIGN IMPLEMENTATION

In the following the main component of the new wire scanner are described.

Actuator

The actuator consists of a frameless electrical motor. In this type of motor, the rotor and stator are independent, which allows a proper embedding of the motor in the system. In the case of the new wire scanner, this type of motor has been chosen because it allows the rotor to be installed in vacuum while the stator remains outside vacuum. In the typical air gap between rotor and stator is located the vacuum barrier, which is a very thin cylindrical shell made from stainless steel. As in a standard motor, the rotor is driven by the rotating magnetic field generated by the stator. The advantage of this configuration is that the rotor (already in vacuum) is connected directly to the shaft. Therefore no mechanical transmission is required, thus avoiding elements which are fatigue-prone.

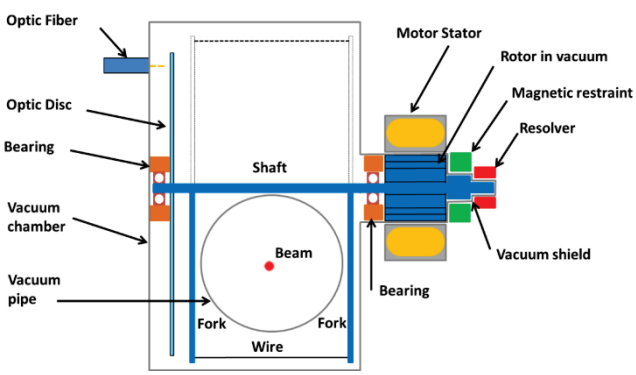


Figure 3: Conceptual design of the Fast Vacuum Wire Scanner.

Shaft

The shaft is the element driving the rotational motion of the system. The rotation torque delivered by the actuator is transmitted to the shaft by the rotor, and provokes its rotation as well as that of all the elements mounted on it.

Resolver, magnetic restrain system, motor-rotor, the two arms and the optical encoder disk are directly mounted on the shaft.

Fork

In previous design of wire scanner instruments [5], the fork could be considered rigid in the transversal direction but it showed flexibility in the longitudinal direction to maintain the tension of the carbon wire and also provide a constant and homogeneous tension during the scan process. However, the measurements and the dynamic models developed along this work, show that longitudinal flexibility on the fork tips may enhance the transversal vibration amplitude of the wire [2]. Therefore, for the new design it has been decided to use a fork concept which is also rigid in the wire longitudinal direction. Consequently, the wire tension is guaranteed only by the wire elasticity and the initial preload tension applied at the first mounting.

Carbon Wire Fixation

To avoid this source of uncertainty in the wire position due to wire tension variations, the wire fixation system mechanically links the wire to the fork.

A suitable brazing will be applied between the ceramic isolator and the fork, as well as between the copper sleeve and the ceramic isolator (see Fig. 4). Thus, the extremities of the carbon wire will be properly bonded to the fork tips but electrically isolated.

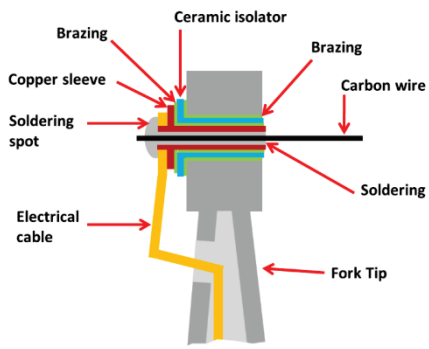


Figure 4: Wire fixation system detail.

Angular Sensor

The angular sensor is the element which serves to determine the angular position of the shaft and therefore the absolute position of the fork. This information is required to perform the beam profile reconstruction (see in the introduction chapter the functional description of the wire scanner). Moreover, the information provided by the angular sensor is needed to feedback the control system in order that the scan follows the suitable motion pattern. In the new design, the function of this angular sensor is achieved by means of two independent angular sensors, a solid rotor resolver for the motor feedback loop and an optical encoder for the beam projection reconstruction.

ISBN: 978-3-95450-188-5 doi:10.18429/JACoW-MEDSI2016-MOPE13

Resolver (motor feedback) This device measures the absolute angular position of the shaft and provides this information to the feedback control loop.

This device is relatively robust and provides angular absolute position without having to go to a home position, i.e., it provides continuous absolute angular position. The resolver device consists of a solid rotor without windings fixed to the shaft and therefore under vacuum. The stator is located on the air side. As in the actuator, a very thin cylindrical shell made of high magnetic permeability stainless steel allows this configuration.

Although the accuracy of this device is relatively low (17 mrad), it shows a high reproducibility, which allows to improve the accuracy by means of a calibration procedure.

Optical disk This part of the angular sensor is based in the incremental angle optical encoder technology and consists of a glass disk with a pattern made of high reflectivity chrome directly mounted on the shaft. An optical fiber drives the light from a laser diode to the optical disk. Using the reflectivity of the chrome pattern, the reflected light is coupled back into the same fiber, and directed to a photodiode through an optical circulator. After proper calibration, this sensor provides a resolution in the range of the requirements, i.e. 2.8 µm at the fork tip.

Magnetic Restrain System

The new conceptual design does not integrate any kind of mechanical link between the rotating parts and any other element that could block the unwanted rotation of the shaft. Bearing friction would not be enough to restrict the rotational momentum produced by the unbalanced weight of the fork. The only way to guarantee the grip of the shaft would be by means of the holding torque provided by the stator. However, in case of an electrical failure (the stator would be unpowered), The shaft could eventually rotate out of control. That situation could bring the wire in front of the beam causing the wire melting or, in the worst case, beam losses that could oblige to dump (or stop) the beam.

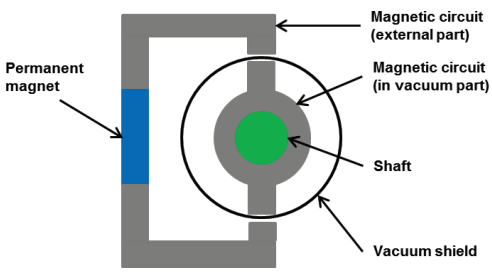


Figure 5: Magnetic restrain system detail.

The conceptual design of the magnetic restraint system, show in Fig. 5, consists on a dipolar magnetic field generated by a permanent magnet, a magnetic frame or yoke located outside the vacuum, and a ferromagnetic piece fixed to the shaft. The magnetic field (circuit) thus produced guaranties a resistive torque which avoids unwanted rotations. This resistive torque is very low compared to the torque that can be provided by the motor, therefore this magnetic restriction cannot stop the rotation of the shaft under the action of the motor.

CONCLUSION

In this paper, the design of the new CERN Fast Vacuum Wire Scanner has been presented. The requirements for this new device, its conceptual design and the design implementation have been discussed. The most relevant component of the device has been described. As of today a first prototype of the devices has been built and installed in the CERN Proton Synchrotron Machine where operation test will be performed along this year.

A digital mock-up of the final device is shown in Fig. 6, where the design and integration of the different parts can be seen.

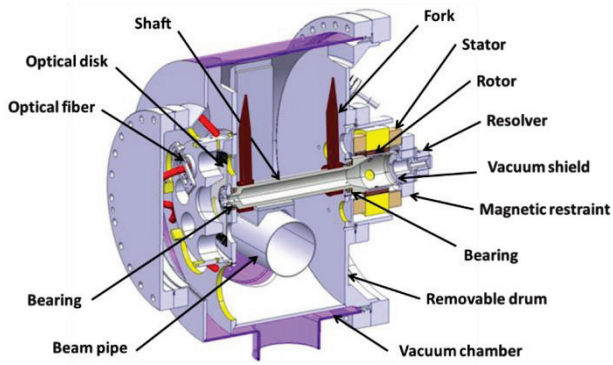


Figure 6: Digital mock-up of the device.

REFERENCES

[1] J.Herranz, Minimisation of the wire position uncertainties of the new CERN vacuum wire scanner, Universitat Politècnica de Catalunya (2016).

[2] J.Herranz, A.Barjau, B.Dehning, Vibration measurements of a wire scanner – experimental setup and models, Journal of Mechanical Systems and Signal Processing (2015).

[3] Sapinski M., 2008, "Model of Carbon Wire Heating in Accelerator Beam", CERN-AB-2008-030 BI, CERN.

[4] Sapinski M., 2008, "Model of Carbon Wire Heating in Accelerator Beam", CERN-AB-2008-030 BI, CERN.

[5] Steinbach Ch., 1985, "A scanning wire beam profile monitor", IEEE Transactions on Nuclear Science. Vol. NS-32, NO. 5, October 1985.

Content from this work may be used under the terms of the CC BY 3.0 licence (© 2016). Any distribution of this work must maintain attribution to the author(s), title of the work, publisher, and DOI.

ISBN: 978-3-95450-188-5 doi:10.18429/JACoW-MEDSI2016-MOPE15

CAM MOVER ALIGNMENT SYSTEM POSITIONING WITH WIRE POSITION SENSOR FEEDBACK FOR CLIC

J. Kemppinen[1, *], Z. Kostka, H. Mainaud Durand, CERN, 1211 Geneva 23, Switzerland
[1]also at Institute of Machine Tools and Manufacturing, ETH Zürich, Zürich, Switzerland

Abstract

Compact Linear Collider (CLIC) is a study of an electron-positron collider with nominal energy of 3 TeV and luminosity of $2 \cdot 10^{34}$ cm^{-2}s^{-1}. The luminosity goal leads to stringent alignment requirements for single quadrupole magnets. Vertical and lateral offset deviations with regards to a given orbit reference in both ends of a quadrupole shall be below 1 µm and quadrupole roll deviation shall be below 100 µrad. Translation in the direction of particle beam is not controlled but mechanically locked.

A parallel kinematic platform based on cam movers was chosen as system for detailed studies. Earlier studies have shown that cam movers can reach the CLIC requirements through an iterative process. The paper presents new modular off-the-shelf control electronics and software including three optional positioning algorithms based on iterations as well as a more advanced algorithm which can reach target position in one movement. The advanced algorithm reads wire position sensors (WPS), calculates quadrupole orientation based on the readings and updates the remaining trajectory during motion. All of the optional positioning methods reach the CLIC positioning requirements within minutes.

INTRODUCTION

CLIC final stage nominal energy is so high that two 21-km-long main linacs are needed, even though a very high acceleration of 100 MV/m is foreseen. Both main linacs are composed of 2.01-m-long modules. The modules are composed of either accelerating structures (AS), main beam quadrupoles (MBQ) or a combination of the two. There are four different types of MBQ which differ from each other only by length. Type 1 is the shortest and type 4 is the longest MBQ. The lengths are 420 mm, 920 mm, 1420 mm and 1915 mm. [1, pp. 393]

Each MBQ is equipped with a beam position monitor (BPM). In order to reach the CLIC luminosity target, all MBQ magnetic centres have to be within 17 µm and all BPMs within 14 µm from straight line fit on any sliding window of 200 m along the linacs, as shown in Fig. 1. The requirements include uncertainties related to linking the MBQ magnetic centre to the alignment sensors, uncertainties of the alignment sensors themselves as well as positioning accuracy of the alignment stage of a single MBQ. The maximum contribution of single MBQ misalignment is defined as ± 1 µm in transversal (x) and vertical (y) offset with regards to a given orbit reference with ± 3 mm travel in each end of the MBQ. In addition, maximum deviation in rotation around the beam (roll) is 100 µrad.

* Juha.Kemppinen@cern.ch

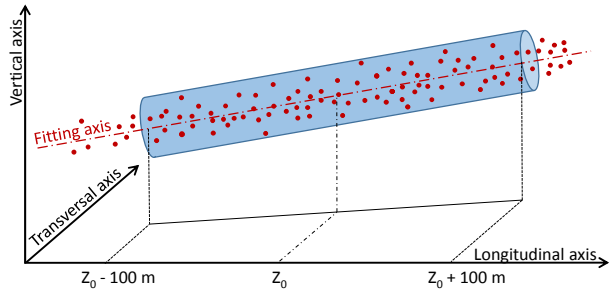


Figure 1: Objectives of CLIC active pre-alignment. [1, pp. 602]

It was demonstrated in an earlier study that the CLIC positioning requirement is reached when a mock-up girder with dummy weights, simulating type 4 MBQ and stabilisation system, is aligned using a parallel kinematics machine (PKM) based on cam movers [2]. In this paper, the same PKM and girder are used but the control electronics have been replaced. The new electronics allowed more advanced motion control. Four different positioning algorithms were developed. They are presented and compared.

The type 4 cam movers and the test setup are presented in the next section. Then, the new control electronics are introduced. Next, the positioning algorithms are described, followed by test results and comparison. Finally, conclusions are drawn.

TEST SETUP

Left side of Fig. 2 shows CLIC type 4 MBQ together with a system that stabilizes its mechanical vibrations. The combination weighs 570 kg. It is mounted on five cam movers which control five degrees of freedom (DOF). Only translation in the direction of beam is not controlled but rather blocked mechanically. The five DOFs are measured redundantly with two stretched wires and two wire position sensors (WPS) around each wire, manufactured by Fogale Nanotech and measuring both x- and y-offsets with 0.1 µm resolution.

Actual type 4 MBQ prototype together with its stabilization system has not been built. Therefore, a mock-up girder was used in the alignment study. Right side of Fig. 2 shows the girder, mounted on CLIC type 4 cam movers (ZCM), manufactured by ZTS VVU Kosice. The same setup was used also previous study [2]. The girder weighs 185 kg. In the previous study, 590 kg of dummy weights were installed on top of the girder, resulting in total load of 775 kg and it was seen to make positioning more difficult. This time, only the girder was installed due to lack of time. Two stretched wires and four WPS sensors are used to measure the girder position.

Content from this work may be used under the terms of the CC BY 3.0 licence (© 2016). Any distribution of this work must maintain attribution to the author(s), title of the work, publisher, and DOI.

ISBN: 978-3-95450-188-5 doi:10.18429/JACoW-MEDSI2016-MOPE15

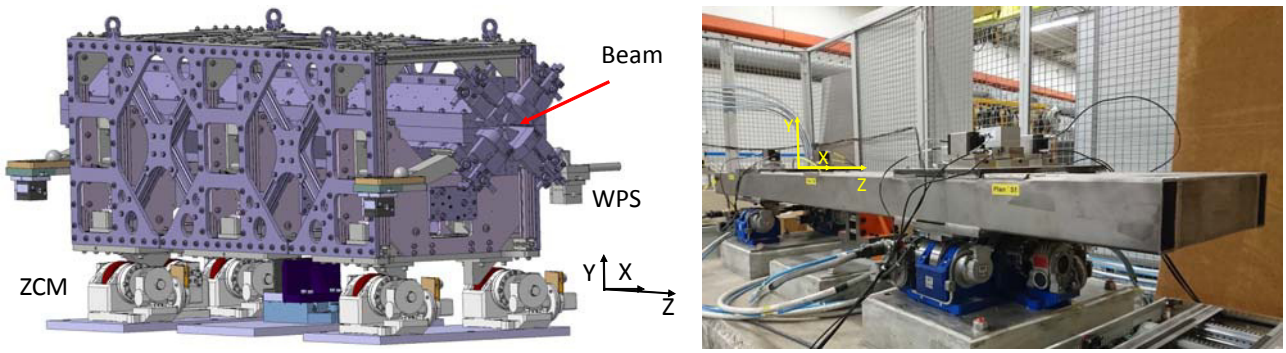


Figure 2: Type 4 MBQ and stabilisation system mounted on cam movers (left) and test setup including ZCMs, follower girder and local coordinate system (right).

Least squares algorithm is used to calculate the controlled five DOFs from the redundant data. The girder position can be thus measured with the uncertainty of approximately 5 µm in absolute and 1 µm in relative but the measurement system is not within the scope of this paper. The goal was to show that the girder can be positioned within 1 µm in offsets and 100 µrad in roll from an alignment sensor feedback. The accuracy of the feedback is not relevant.

CONTROL ELECTRONICS

ZCMs were delivered with dedicated control electronics. Previous study, demonstrating the positioning capability of a PKM based on ZCMs with an iterative algorithm, was conducted using the dedicated electronics crate. There are, however, some drawbacks with this setup. Firstly, it is only possible to set a target angle and parameters of trapezoidal motion profile of the ZCMs. It is not possible to adapt the trajectory during motion. Secondly, the crate is error prone. This prevented long test runs.

In order to exploit the full potential of the ZCMs, new control electronics crate based on commercial, off-the-shelf components was developed in-house. The goal was also that the same control crate could be used to control other cam mover prototypes with small adaptations. National Instruments (NI) cRIO-9068 was chosen as the controller as the hardware setup can be adapted by changing the standardized C modules. Plenty of different modules are available, manufactured by NI and other companies.

This study was carried out with a configuration of five C modules. Two SEA 9521 BiSS interface modules were used to acquire the five absolute encoders. Two SISU-1004 stepper interface modules were used to send steps to the motor drives. In addition, an NI-9207 module was used for fast acquisition of four WPS sensors.

The new electronics enable three software layers. User interface is a regular LabVIEW program running on a host computer. All calculations (kinematics, measurement data processing, trajectory generation) are done in the cRIO-9068 processor and the program is written in LabVIEW Real-Time. Low level program is running on LabVIEW FPGA and it reads the WPSs and encoders as well as sends step signals to stepper motor drives.

POSITIONING ALGORITHMS

CLIC alignment requirement is set for MBQ magnetic centre. In this study, it is assumed that the magnetic centre is coincident to the beam which goes through the MBQ, as indicated in the left side of Fig. 2. The beam line does not exist in the mock-up girder. Therefore, both the positioning algorithms and the WPS readings are transformed to a theoretical beam line which is floating on top of the girder at the same height compared to the ZCMs as in the left side of Fig. 2 and which is rigidly attached to the girder.

The ZCMs are calibrated in a separate setup. The girder has a reference position approximately in the mid-travel in 5 DOF. The ZCMs are driven to the angles corresponding to this reference position. Girder position is then measured and all movements are relative to this reference position. NI SoftMotion is used in motion control of the setup.

Four positioning algorithms were developed and compared. The first one is called Synchronous PTP (point-to-point) and it is the simplest one. Target girder position is transformed to relative motor steps of each ZCM based on a kinematic model. Trajectory is not pre-defined but SoftMotion makes sure that all five cams start and stop at the same time. After the movement is finished, the position is measured with the WPSs. The target position is compared to the measured position and if the deviation is too high, it is added to the target. A new movement is performed and the procedure is repeated. This is done until the target position is reached within limits. This is called iterative approach.

The second algorithm is called Straight-line movement and it is also iterative. Trajectory to the target is calculated before movement and constraints to the trajectory can be applied. However, it is not monitored during motion whether the girder follows the trajectory, only between iterations.

The third algorithm is called Complex movement and it is a combination of the two first ones. The trajectory of first iteration (which is assumed to be the longest movement) is calculated in advance like in Straight-line movement. The following iterations (if needed) are using the Synchronous PTP algorithm. This way the trajectory is well defined during the long movement but no slow trajectory calculations are needed for the shorter iterations.

Content from this work may be used under the terms of the CC BY 3.0 licence (© 2016). Any distribution of this work must maintain attribution to the author(s), title of the work, publisher, and DOI.

ISBN: 978-3-95450-188-5 doi:10.18429/JACoW-MEDSI2016-MOPE15

Content from this work may be used under the terms of the CC BY 3.0 licence (© 2016). Any distribution of this work must maintain attribution to the author(s), title of the work, publisher, and DOI.

In the fourth algorithm, called Predictive movement, trajectory can be constrained. Before movement, the trajectory of the first 4 seconds of movement is calculated. This is divided into 40 intermediate points (one every 100 ms). When movement is started, this buffer of points is consumed. When there are less than 10 points left, the girder position is measured, the position error is taken into account and new ten points are calculated to the buffer. This means that during motion, the trajectory is updated every second. In the end of the movement, slow approach is applied. The goal is to have a smooth positioning without overshoot. It was seen in previous study that, especially with the higher load, changing rotation direction of cams caused jumps in position and made it harder to reach the target.

TESTS

Uncertainties in the kinematic model of the 5 DOF setup, e.g. manufacturing tolerances and uncertainties in assembly and ZCM calibration, cause open-loop positioning error. The error increases with increasing distance from the reference position. Positioning is therefore the most dependent on the feedback near maximum travel in each direction and emphasis of tests was there. A test of 136 sequences was repeated using each of the four positioning algorithms. Each test sequence had a target position where the girder was driven directly from the previous target position, without passing by the reference position.

The 96 first test sequences covered different offset combinations near the maximum travels but while roll was kept at zero. The 40 last sequences covered roll targets while other DOFs were kept at zero. For each sequence, the target was considered reached (and parameters were set so that this was always the case) when offset deviations with regards to alignment sensors were below 1 µm and roll deviation below 5 µm. The roll deviation tolerance was kept lower than CLIC requirement because the system can readily handle it.

All positioning algorithms managed to reach all sequence targets within tolerances. Alignment sensor readings were not saved during motion but ten acquisition were saved after each target was reached. Standard deviation of the ten acquisitions was calculated in order to check that the girder was well stabilised to the target position. The difference between performances of movement types can then be evaluated by comparing the time it takes them to position the girder within tolerance.

Fig. 3 shows a 20 sequence slice of the test. It can be seen that the movement time of Synchronous PTP algorithm is significantly longer than that of the others. Fig. 3 does not take into account the time it takes to calculate trajectory before movement. This is on average 2 % of the total time for Synchronous PTP and Predictive movements and 5 % for Straight line and Complex movements.

After the movement type comparison test, the Predictive movement algorithm was tested with a reduced amount of sequences and three different stop condition parameters: the original, the tightest possible which still reached all positions and a set of parameters which is between them.

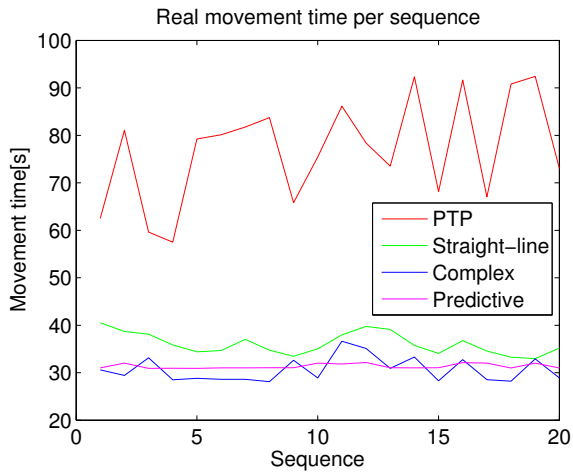


Figure 3: Comparison of execution times of four movement types in 20 test sequences.

Average deviation decreased when stop condition was tightened, but not significantly. A bigger difference can be seen in the maximum deviations, which are approximately 1.0 µm for x-offsets, 0.4 µm for y-offsets and 2.0 µrad for roll with original parameters and 0.5 µm, 0.4 µm and 1.3 µrad correspondingly with the tightest parameters. The positioning takes on average 13 % and up to 65 % longer with the tightest parameters than with the original ones. The parameter set in between is only very little better than the original set but it also takes only 1 % more time on average in positioning.

CONCLUSIONS

It was demonstrated that the CLIC positioning requirements for MBQ alignment stage can be met in one movement by using feedback directly from alignment sensors. This predictive movement was compared to iterative algorithms and it performed well both in level of deviation and in positioning time. A trade-off between positioning accuracy with regards to feedback and positioning time can be made depending on requirements.

When applied to a specific system, the predictive movement algorithm can be made faster, especially if there is very little play in the cam movers. Then overshoot is allowed and more aggressive trajectory can be applied.

REFERENCES

[1] M. Aicheler et al, "A Multi-TeV linear collider based on CLIC technology: CLIC Conceptual Design Report", CERN-2012-007.

[2] J. Kemppinen, S. Griffet, R. Leuxe, H. Mainaud Durand, J. Sandomierski, M. Sosin, "CLIC main beam quadrupole active pre-alignment based on cam movers", in *MEDSI*, 2012.

ISBN: 978-3-95450-188-5 doi:10.18429/JACoW-MEDSI2016-MOPE16

DEVELOPMENT OF THE RIXS MANIPULATOR

H.Joehri†, Leonard Nue, Thorsten Schmitt, Christoph Hess, Luc Patthey,

Sebastian Sonderegger, Paul Scherrer Institut, Villigen, Switzerland

Abstract

The RIXS Manipulator (RIXS = Resonant Inelastic X-ray Scattering) is a further development of the Carving Manipulator.

The carving manipulator has six independent degrees of freedom (three translations and three rotations). All three rotations are exactly in the middle of the sample surface.

The head of the manipulator is in UHV and the sample can be cooled down to 14K.

For the RIXS manipulator there is a new requirement to have a field of view from 0 – 180°. There are mainly two parts in the carving manipulator that set the probe in the shadow of the beam at small angles.

- A bellow
- The bearings

To solve these problems we shifted the bellow behind the pivot point. This gives some strange movements of the bellows and we had to analyse this in a separate test installation.

For the bearings, we developed a goniometer bearing with ceramic bearing shells.

Meanwhile the RIXS manipulator is implemented and in routine operation.

CARVING MANIPULATOR

The RIXS manipulator is a further development of the carving manipulator which is used to position solid samples. It has six degrees of freedom and the kinematics is designed in a way that all tree rotations can be executed without moving the center of the sample (Figure 1).

The head is in a vacuum chamber and the sample can be cooled down to 14°K.

All motors are outside of the vacuum chamber. The rotation of the sample and the movement of the tilt angle are transmitted into the vacuum.

The transmission is realized by shafts and gears (Fig 2).

For the rotation of the sample, one step of the transmission is done by a bellow (Figure 3)

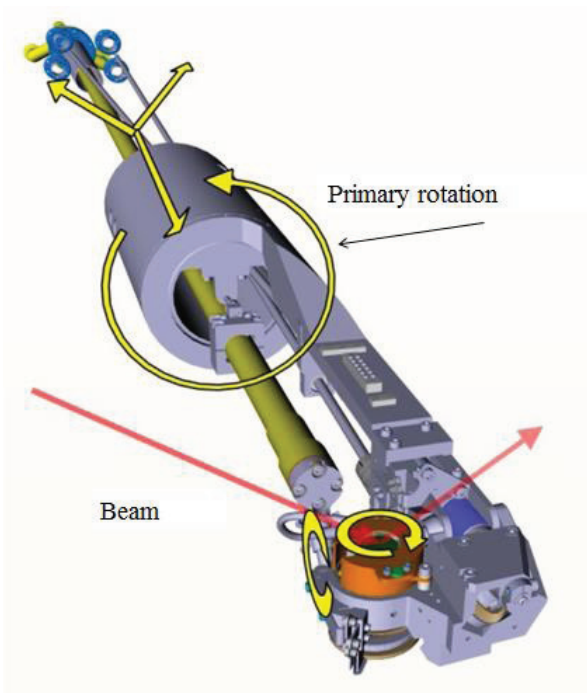


Figure 1: Carving manipulator with 6 degrees of freedom.

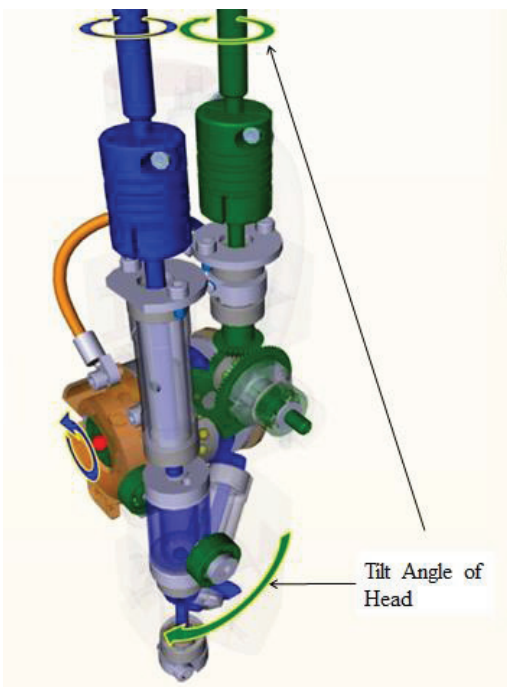


Figure 2: Transmission of sample-rotation (blue) and tilt angle of head (green).

† haimo.joehri@psi.ch

Content from this work may be used under the terms of the CC BY 3.0 licence (© 2016). Any distribution of this work must maintain attribution to the author(s), title of the work, publisher, and DOI.

ISBN: 978-3-95450-188-5 doi:10.18429/JACoW-MEDSI2016-MOPE16

Content from this work may be used under the terms of the CC BY 3.0 licence (© 2016). Any distribution of this work must maintain attribution to the author(s), title of the work, publisher, and DOI.

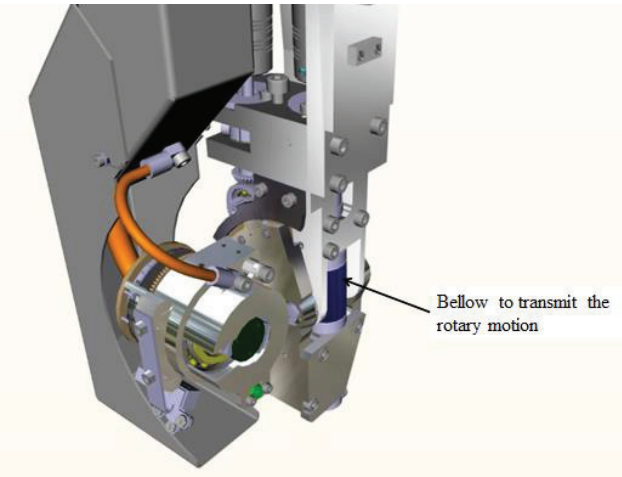


Figure 3: Bellow.

RIXS MANIPULATOR

For the RIXS Manipulator (Resonant Inelastic X-ray Scattering), an angular range of the primary rotation of 0° - 180° is needed. In the Carving Manipulator design, the bellow and the bearing obstructs the beam at small angles (Figure 4). To solve this problem, the bellow is shifted away from the axis and a goniometer bearing was developed.

For the goniometer bearing, shells and balls of ceramics are used (Figure 5).

For the bellow, the tilt rotation results in a combined lateral, axial and angular movement for the bellow, that have been tested in a separate test setup (Figure 6)

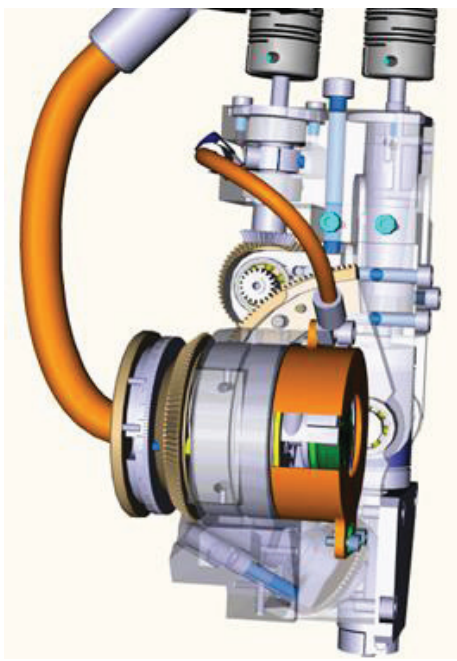


Figure 4: Obstruction of the beam at small angles.

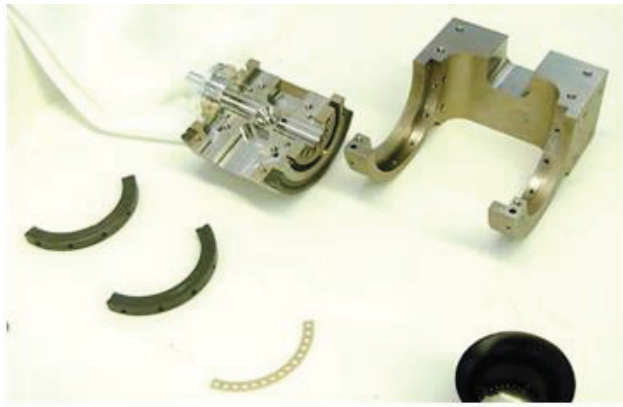


Figure 5: Goniometer Bearing.

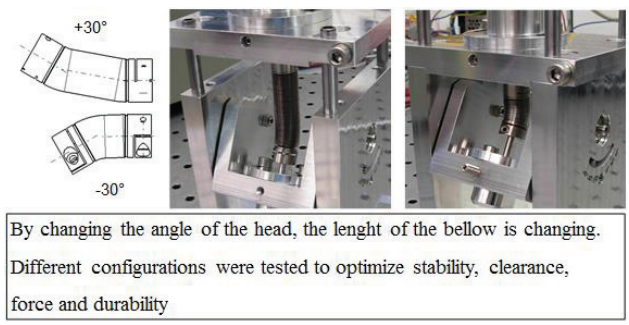


Figure 6: Test of Bellow.

MAIN PARAMETERS

6 independent degrees of freedom
Vacuum : <10E-10 mbar
Cryo : 14° K
Precision : 20µm
Non-magnetic
Gears in PEEK and Titan Grade 5
Mech. Parts : Titan Grade 5
Tilt Angle of Head : +/- 30°

CONCLUSION

With the new design, we realized a primary rotation of 0° to 180°. Photos of the realized manipulator in Figure 7 and 8.

ISBN: 978-3-95450-188-5 doi:10.18429/JACoW-MEDSI2016-MOPE16

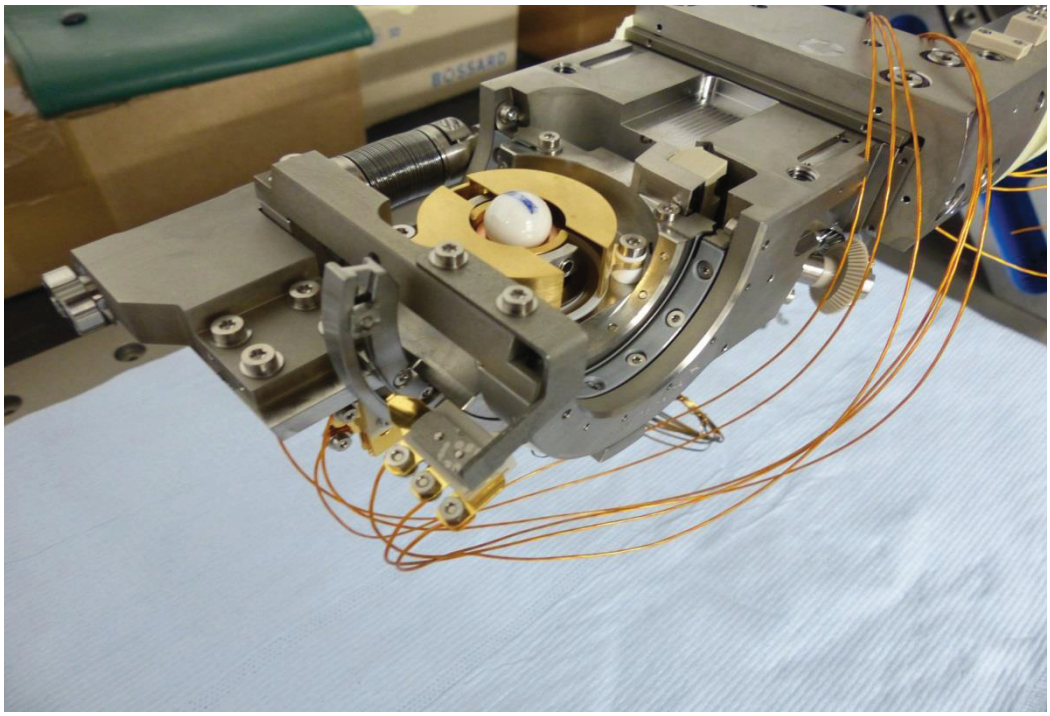


Figure 7: Head of manipulator.

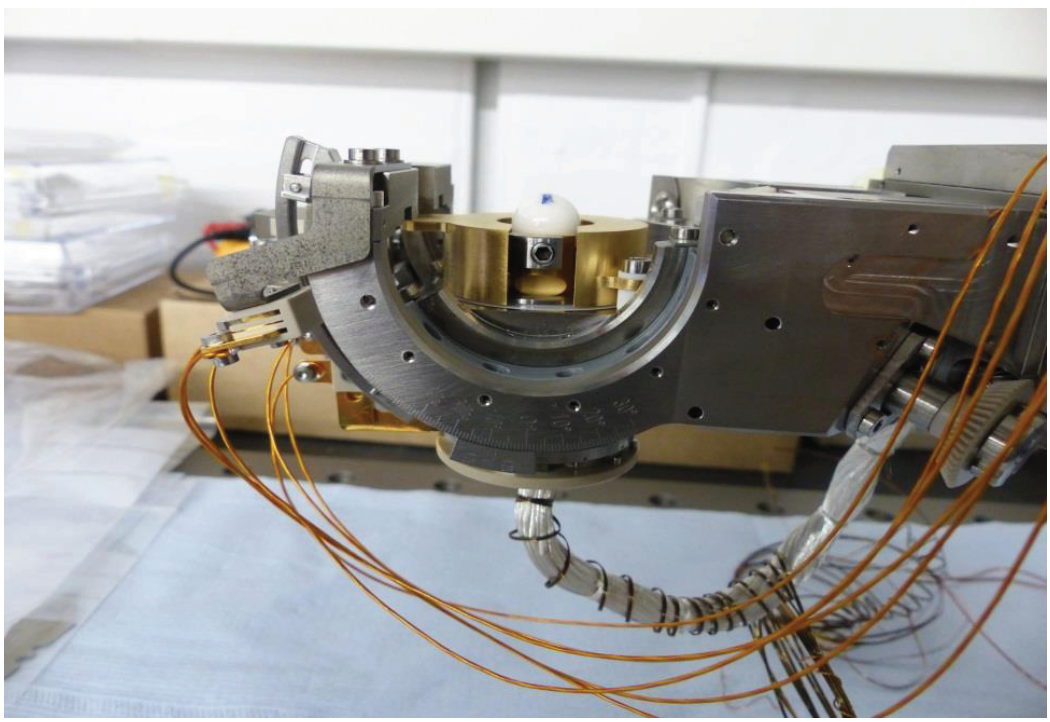


Figure 8: View from the side: No obstruction for the beam.

.

ACKNOWLEDGMENT

We want to thank the whole team, including the mechanics from the workshop for the manufacturing, assembling and measuring of the very precise and complicated parts.

Content from this work may be used under the terms of the CC BY 3.0 licence (© 2016). Any distribution of this work must maintain attribution to the author(s), title of the work, publisher, and DOI.

ISBN: 978-3-95450-188-5 doi:10.18429/JACoW-MEDSI2016-MOPE17

Content from this work may be used under the terms of the CC BY 3.0 licence (© 2016). Any distribution of this work must maintain attribution to the author(s), title of the work, publisher, and DOI.

OCTOGLIDE – TABLE POSITIONING DEVICE FOR DIFFRACTION APPLICATIONS

G. Olea†, N. Huber, HUBER Diffraction GmbH & Co.KG, Rimsting, Germany

Abstract

A new Table Positioning Device (TPD) for high precision and heavy load manipulations has been developed. Conceived as an alternative to the precision hexapods, it fulfils the gap of sample (and/or, instruments) positioning in smaller (height) available working spaces of synchrotron Diffractometers (Dm). The concept is based on a Redundant Parallel Kinematic Structure (Rd-PKS) with four (4) legs having 2dof active joints (actuators). In the Proof of Functionality (PoF) step, a stacked solution has been adopted for the actuators' design using precision XY translation Positioning units (Pu). The symmetrically 6-4(**PP**)PS mechanism – OCTOGLIDE(OG) having eight (8) gliding actuators (**P**) is implying also a pair of wedges–Elevation (El) and socket/ball–Guiding (G) Pu, as passive joints (P and S) forming one of the Positioning modules (Pm). Spatial positions in the working space can be reached without any singularities and planar motions along X or Y axis performed very intuitively with only some of the actuators (decoupled) motions. The first tests of the prototype are revealing both, high precision geometry of motion (straightness, flatness, etc.) and stiffness capabilities.

INTRODUCTION

Diffraction using standard or advanced X-ray methods is still the most common techniques to investigate the structure of various materials [1]. In the synchrotron case, the dedicated machines – Diffractometers (Dm) have been built in a large variety to fulfil the specific requirements (NEWPORT, HUBER, KOHZU, etc). Sometimes, these requirements implied the use of special environmental conditions' instruments. They could be sophisticated, large in size and heavy; but, must be manipulated with high precision (i.e. I07/DLS [2]), too. In order to comply with the actual existent space of standard available Dm machines, the designers of positioning devices must adapt. Till now, the serial stacked solution has been largely used. Each of the motion axes – X, Y and/or Z (translation and/or rotations) has been materialized through standard independent stages to pose the sample (and, instrument) in the right position. However, in the case of more than 3 dof, the available space cannot be enough for packing all axes, or doing the necessary tasks-especially, variable distance rotations around Dm - Center of Rotation(CoR) point, which in this case is fixed. Precision Hexapods has been foreseen as next solution [3]. By being more compact, they are precise and able to freely choose the pivot point (P). However, when the combination of the specifications is including heavy load, and appreciable rotation distance (dP), the design of the products could be a challenge [4], especially the height (250mm). In order to fulfil the gap, a new product has been developed. The specificity of its kinematics, design and performance are now presented.

† go@xhuber.com

KINEMATICS

Topology

The new Table Positioning Device (TPD) is based on a more general parallel kinematic (PK) [5] topology having four (4) legs. This QUADROPOD (QP) family has a good natural static stability, being perfect adapted to the common shape of a working table. With all the actuators at the base, the 6-4(**2**)13 structure is a redundant one (Rd=2) which can be an advantage (power). By choosing DD (or, in-parallel) actuated joints, the dynamic capabilities will increase [6], too.

Mechanism

However, the Figure 1 shows a TPD kinematic structure with 2dof active joints ($\mathbf{P_iP_{i+4}}$, i=1…4) stacked on two levels (i,i+4). In the Prove of Functionality (PoF) step, the standard (electromechanically) motorized stages were an easy way of implementation and the motor / screw mechanical principle (stability) another one. 6-4(**PP**)PS mechanism (6-dof, PPPS-kinematic chains, P-prismatic/linear and S-spherical joints) can be seen as composed from two pair of orthogonal arranged kinematic chains (K_i,K_{i+2}, i=1,2), each having a pair of active joints with motion axis perpendicular on each other ($\mathbf{P_i \perp P_{i+4}}$) and parallel on the opposed ones($\mathbf{P_i \parallel P_{i+2}}$).

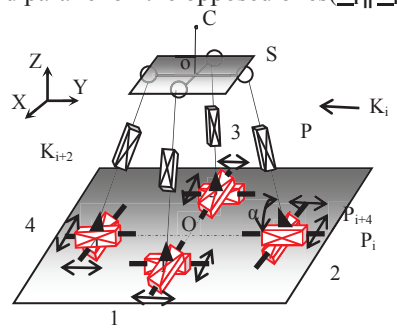


Figure 1: Mechanism kinematics.

By this symmetric arrangement of the eight (8) planar sliding/gliding actuators (OCTOGLIDE), together with the specificity of the passive joints on the next level (P, α

Table 1: Basic Motions

Motion	Actuation	Ki
X	P_i(i=2,4)P_{i+4}(i=1,3)	2
Y	P_i(i=1,3)P_{i+4}(i=2,4)	2
Z	P_{i+4}(i=1,...,4)*	2

* ±X & ±Y sign should apply.

ISBN: 978-3-95450-188-5 doi:10.18429/JACoW-MEDSI2016-MOPE17

fixed angle) the mechanism is able to provide a way of moving the table in one direction with only two (2) couples of opposed pairs, Table 1. Moreover, for horizontal motions - X (or, Y), a displacement in the positive/negative direction implies displacements (4) with exactly the same values, i.e. X=Xi(i=2,4)=Yi(i=1,3).

Following these (decoupled) motions, the control at: a) workshop and b) programming sites is becoming more intuitive (a desire of technicians) and simplified. Note: For the entire mechanism, two joints – P and S types have been used, only.

DESIGN

Concept

Based on the above mechanism, in a modular design concept (specific to PKMs), between a base (B) and table (T) four Positioning modules Pm have been arranged around the centre of the base (O); each of them consisting from a well-defined combination of active and/or passive Positioning units (Pu), Fig. 2.

Active (Ac) Pu have been chosen as compact translational XY stages with high accuracy (and, stiffness) based on screw principle. The first passive Pu is built as Elevation unit (El) based on inclined plane principle. A pair of wedges - W1 and W2 is materializing a precise and compact stiff up / down motion.

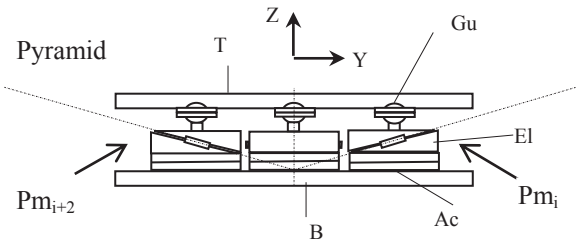


Figure 2: Design concept.

A compact ball & socket design has been chosen for the Guiding unit (Gu) passive positioning based on sliding principle. It consists from a vertical pillar with a high precision ball - B at one end and an adjusted socket - S house (two parts). Through a combined Pm (Pm_i, Pm_{i+2}, i=1,2) motions (and, constrains), precision and stiff : a) translations – X,Y,Z and/or b) rotations - Rx, Ry or Rz can be obtained based on the resulting pyramid principle.

CAD

The above design concept – principle and components has been implemented in specialized software (ProE) to produce functional (solid models) and, manufacturing (drawings) graphical products. The main features of: a) standard (XY) and b) customized (W, SJ) precision used components [7] are included in Table 2.

Table 2: Device Positioning Module

Pu	Principle	Type
Ac	XY	5102.15
El	W1/W2	Z(α=30°)
Gu	B&S	SSJ(ϕ20mm)

A picture of the 3D solid model representing the product (nominal position) with the overall dimensions can be seen in Fig. 3. Note: The height value h=225(<250mm).

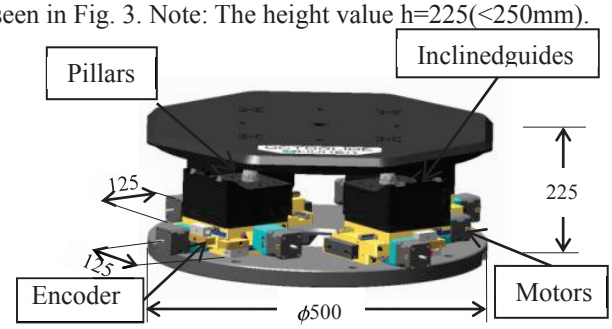


Figure 3: Device layout.

Workspace

In order to characterize a PKM product, its specific features (e.g. workspace) should be determined or, at least evaluated before the production even started. Generally, the multi degrees of freedom Workspace (WS) of a PK device is a complex 6D shape resulting from the total number of pose (translation & rotations) reached by a chosen (center of platform) point taken in to account max/min permitted actuators displacements. The determination is an issue. A more easy way is to determine a 3D shape with constant orientation (Rx=Ry=Rz=0). By using the geometrical features of each guided point intersected in the table's center (geometric method), the OG final rectangular WS shape – double pyramids is coming as an intersection of four partial prisms (Ws_i, i=1,…,4). The overall dimensions are included in Fig. 4. As expected, the shape & size are affected by the actuation and elevation (wedges) maximum strokes. However, there are no singularities inside. A smaller rectangular (cubic) WS_c can be defined as inscribed (l=9.6mm). Note: With an optimum design, it can be enlarged.

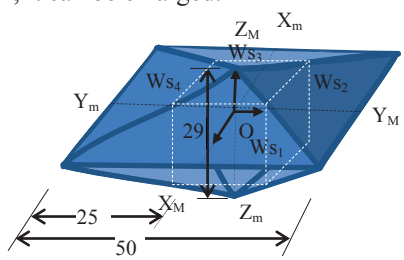


Figure 4: Maximal & inscribed (dashed) workspace.

PROTOTYPE

Manufacturing

An experimental prototype has been built based on the drawings of the above design process. It is mainly consisting from two parts: a) Mechanical device (Md) and b) Controller(C) units. Latter, a PC with the software (graphical interface) has been included. The entire manufacturing process has been based on - standard and specific set of operations like machining, assembly and control based

Content from this work may be used under the terms of the CC BY 3.0 licence (© 2016). Any distribution of this work must maintain attribution to the author(s), title of the work, publisher, and DOI.

ISBN: 978-3-95450-188-5 doi:10.18429/JACoW-MEDSI2016-MOPE17

Content from this work may be used under the terms of the CC BY 3.0 licence (© 2016). Any distribution of this work must maintain attribution to the author(s), title of the work, publisher, and DOI.

on the well-established rules and the specific expertise acquired by the company in precision manufacturing.

Control

In order to produce a motion (positioning) with the desired accuracy, the mechanical (motors), electronic (hardware) and software components must be chosen accordingly and work perfectly together. The main component in the loop (controller) must manage input/output informational flux safely and in time, by being very robust. For OG a digital controller (SMC9300PP) has been built using BISS interface. The dedicated motion software which is using the Invers Positional Problem (IPP) is not taken (yet!) in to account the linear encoders (RESOLUTE) standard components of each of the actuators. It is controlling the device in an open loop, only. A simple graphical interface has been implemented including the menu for the: a) desired point linear & angular (X,Y,Z, Roll, Pitch, Yaw) coordinates, b) Pivot/probe point (X,Y,Z) coordinates and c) maximum translation & rotation (Tmax,Rmax) range visual parameters.

Tests

In order to fully characterize a positioning product, some specific features must be experimentally verified before the small/mass production release. After the OCTOGLIDE prototype has been completed (and the motion control functions integrated) the first investigations started with a set of measurements consisted in to determine: a) range, b) accuracy and c) stability of functional motions. The setup shown in Fig. 5 is mainly based on using a laser interferometer (RENISHAW) - source, retroreflectors, etc., stable table (granite) with an additional frame (Z axis) and PC to record the data.

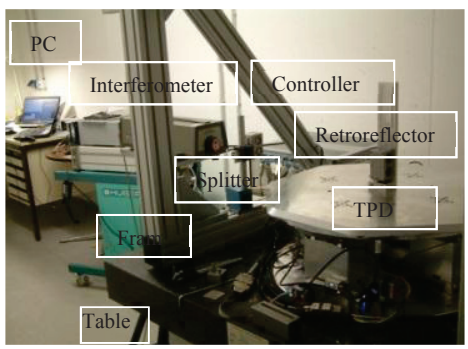


Figure 5: Measurements Set-up.

The basic motions range have been proved to be carried out as expected (designed). The max/min values are the direct result of the actuation values (XY=±25mm), Table 3.

Table 3: Motion Range

Parameter	Unit	Min/Max
X, Y, Z	mm	50, 50, 29
Rx,Ry,Rz	°	11, 11, 18

The measurements to determine the errors (accuracy & geometrical) in both, horizontal /vertical (X/Z) axis with out load has been performed; and, in addition, for rotational motions – roll, pitch and yaw have been performed. The first obtained results proved a good positioning behaviour of the device: a) accuracy (±3,1/4µm) / repeatability (1,5/1,6µm), b) geometric / straightness (flatness) and c) stiffness (0,55Nm/", m=50 kg, r=145 mm) features, Fig. 6 and Table 4.

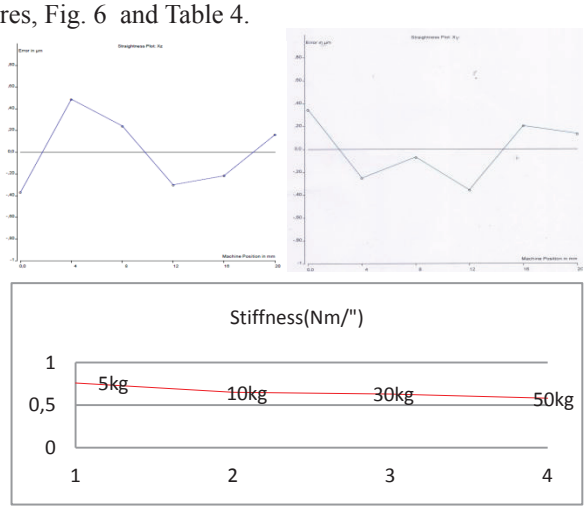


Figure 6: Straight-, flat- and stiffness errors (X).

Table 4: Positional Accuracy

Parameter	Unit	X(Z)
Straightness	µm	0,856 (2,61)
Flatness	µm	0,704 (1,9)
Stiffness	Nm/"	0,55

CONCLUSION

A high precision and heavy load, compact Table Positioning Device (TPD) called OCTOGLIDE, to be used with standard diffractometers in synchrotron X-ray advanced applications has been presented. Built on the Design for Precision (DfP) concept and with specific requirements of using heavy load/size instruments it shows a good behaviour to be considered as a solution for further precise positioning tasks. With minimal design modifications it can be used in other diffraction machines having small working spaces, as well.

REFERENCES

[1] E.J. Mittemeijer and U. Welzel, "*Modern Diffraction Methods"*, J.Wiley & Sons, 2012.

[2] C. Nicklin, *et al.*,"Diamond beamline I07", *J. Sync. Rad.*, 23, pp.1-9, 2016.

[3] "Hexapods 6-Axis Precision Systems", BRO14E, PI GmbH &Co.KG, 2009.

[4] G. Olea *et al.* "Precision Hexapod" *Proc.10th Int. Conf. & Exh.(EUSPEN),* May 2010, pp.379-383.

[5] JP. Merlet, "*Parallel Robots*", 2nd ed., Springer, 2006.

[6] G. Olea *et al.*, "High-precision table positioning device", in *Proc.of 16th EUSPEN,* Nothingham, UK, 2016, pp.499-500.

[7] HUBER GmbH, http://www.xhuber.com

ISBN: 978-3-95450-188-5 doi:10.18429/JACoW-MEDSI2016-MOPE18

REAL-TIME MOTOR CONTROL SYSTEM FOR BEAMLINES

Chia-Feng Chang, NSRRC, 101 Hsin-Ann Road, Hsinchu 300, Taiwan

Abstract

To improve the stability and accuracy of motor control system for Beamline, the beamline with motor adjustment mechanism collocates with the real-time firmware motor control system through the high-definition motor mechanism. Because the real-time motor control system doesn't need to be connected with the computer for a long time, it improves the speed, stability and accuracy of closed loop operation thus promote the controlling ability of motor. As a result, the real-time motor control system will improve the stability and accuracy of the entire motor control system with beamline.

INTRODUCTION

Closed-loop control is a vital part of a control system. The parameters of closed-loop control and the advantage and disadvantage of an analog input/output system will lay influence on the control system results. This text is designed to discuss about the applications for Closed-loop control and analog input/output system, in order to enhance the stability and accuracy of beamline motor control system. Consequently, we adopt analog input/output system, FPGA and closed-loop control for design.

Because the stepper motor equipped with a reducer can analyze mobile platform to 10 nanometers per stepper, with FPGA accompanied to simultaneously trigger the activation of an analog input/output system, the addition of a closed-loop control mode firmware into this hardware structure can enhance the stability of the beamline motor system, and the convenience of real-time adjustment against stability. Thus, the beamline control system will be about stability, accuracy and convenience.

SYSTEM ARCHITECTURE

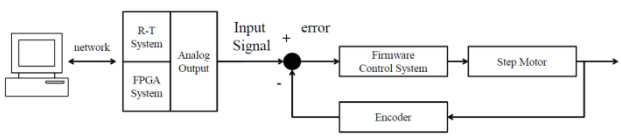


Figure 1: Close-loop Control architecture of Motor control system.

The control system structure in this text is designed by way of R-T closed-loop control (Fig. 1), with the analog input/output module acting as the reading and processing center, and FPGA module and firmware controllers acting as the hardware. The computer end serves to give location orders and besides, the stepper motor serves as the hardware of actual motion and the reading sensor serves to return its actual moving distance for the Encoder.

Control System Description

The hardware related to the control system in the text is composed of three portions: the first is, the computer-controlled center, including the PXI-8108 multi-core processor equipped with R-T module, the analog input/output module, FPGA module; the second is the firmware, the stepper motor control system, responsible for converting the analog output of the analog input/output module into digital forms, and use this data as motion signal; the third is Encoder, which will act according to the moving distance of motion signal after receiving that signal. The information on distance changes can be accessed the value of Encoder Count (Fig. 2).

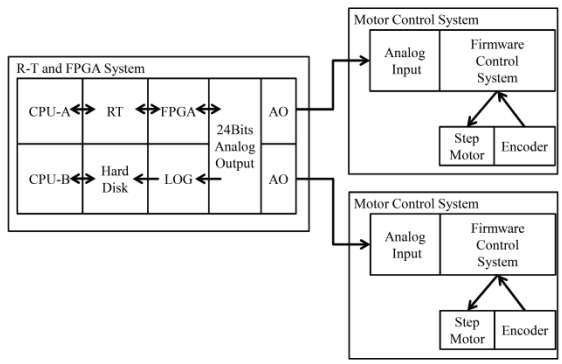


Figure 2: System architecture of R-T control system.

System Process Flow

After the system is activated, R-T System produces voltage signals by way of analog output module, and later synchronizes two sets of voltage signal through FPGA module, to avoid time errors of voltage signal. Then, the analog signals will be converted into digital ones by way of firmware. After signal processing and the user-set distance confirmed, the CPU will take the voltage signals under control, with these signals connected to the voltage input module of the motor-controlled system and the converted voltage signals for the stepper motor, at the same time the apparatus in cooperation will change the length. This way, we repeat the procedure and the closed loop control of the firmware system will continue modification of locations (Fig. 3).

Content from this work may be used under the terms of the CC BY 3.0 licence (© 2016). Any distribution of this work must maintain attribution to the author(s), title of the work, publisher, and DOI.

ISBN: 978-3-95450-188-5 doi:10.18429/JACoW-MEDSI2016-MOPE18

Content from this work may be used under the terms of the CC BY 3.0 licence (© 2016). Any distribution of this work must maintain attribution to the author(s), title of the work, publisher, and DOI.

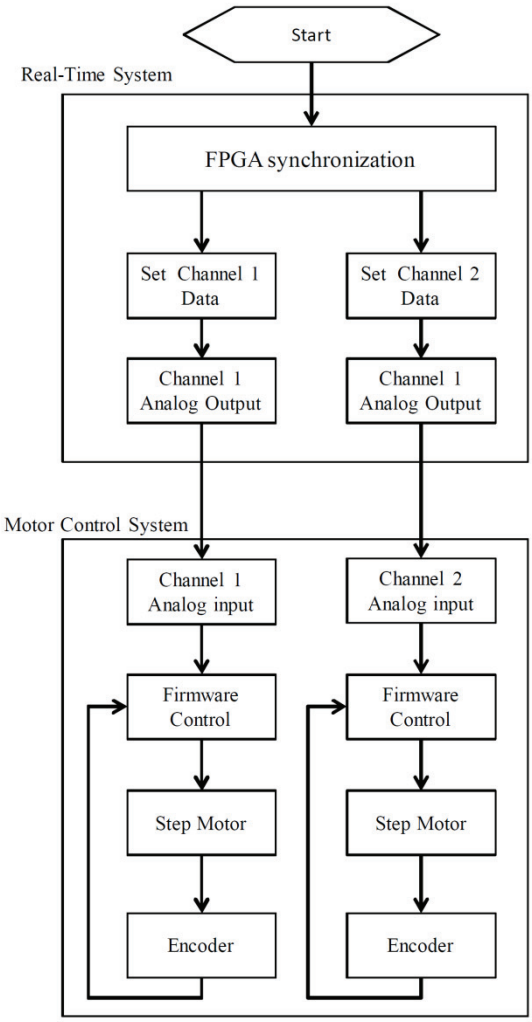


Figure 3: Flow chart of Motor control system.

HARDWARE DESCRIPTION

High-accuracy Data Acquisition Devices

The National Instruments 4461 is high-accuracy data acquisition devices specifically designed for sound and vibration applications. The devices include the hardware and software needed to make precision measurements with microphones, accelerometers, and other transducers that have very large dynamic ranges (Fig. 4).



Figure 4: The picture of high-accuracy data acquisition devices.

FPGA Technology

NI R Series multifunction RIO devices offer the best combination of value and performance by integrating this FPGA technology with eight analog inputs, eight analog outputs, and 96 digital I/O lines, all into a single device that is offered on standard PC form PXI, Using the LabVIEW FPGA Module (Fig. 5) [1-3].



Figure 5: The picture of FPGA Module.

PROGRAM INTERFACE

Program interface applies National Instruments LabVIEW as the layout. One can acquire system information from the graph, including Encoder, analog output waveform and set point information; moreover, the content of the program is composed of high resolution analog output module reading program, data storage, dual-core control and synchronize motion control program (Fig. 6).

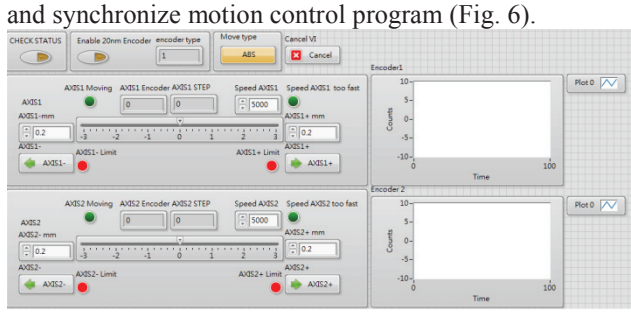


Figure 6: The visual Control interface.

ISBN: 978-3-95450-188-5 doi:10.18429/JACoW-MEDSI2016-MOPE18

FIRMWAVE CONTROL SYSTEM

To enhance stability and instantaneity, the integration of firmware's closed loop controls and motor controllers is used to maintain the accuracy of required locations through reduced time of communication with computers. In the following procedure of firmware's closed loop control, the required location is identified through analog output on the computer. While the location information required by controllers through analog input is digitized by way of the firmware program, the closed loop controlled module of the firmware system will initiate location modification. Since there's the farthest distance between the starting point and the targeted one, the enhanced motion distance will be the likewise farthest. The shorter motion distance is then used to make modifications. While the location is reached within the range of tolerable errors, the closed loop control will run into a status of placidity and the entire system will run stably. In this state of stability, if any displacement takes place, the system will move its structure to a correct position in order to lock in the location (Fig. 7).

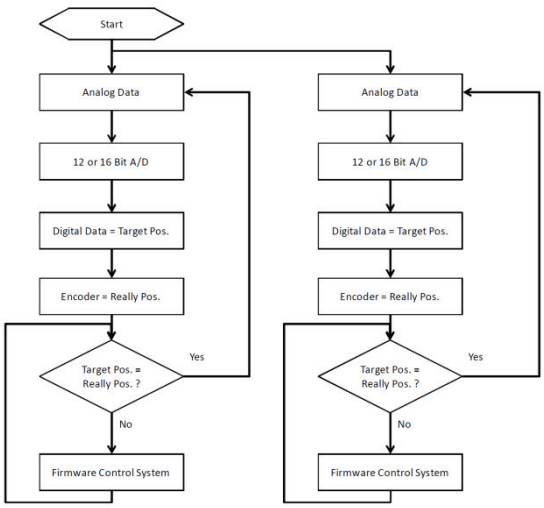


Figure 7: Flow chart of Firmware control system.

BEAMLINE APPLICATION

When the system has been applied into the slits of light beams, and at the same time when the computer has issued a motion order, with system parameters shown on Form 1, each axis will move in the meantime. Although the targeted distance set up by each axis differs, and because of the FPGA multi-tasking, the adjustments of each axis are made at the same time curves rather than at multi-stepping curves. Aside from the time differences, real-time modification can be made.

CONCLUSION

The FPGA hardware module can trigger signals activation and integrate with high-resolution analog input/output module to accompany R-T System, while the software applies the closed loop control module, which can enhance the stability of stepper motor control to a 10-nanometer level. Consequently, the system can effectively enhance the stability and convenience of beamline controlling, and the R-T-FPGA system can reduce signal error caused by deferred time and thus improve the real-time efficiency of signal process.

ACKNOWLEDGEMENT

We would like to thank the staffs at NSRRC, especially those in the Experimental Technique Group and Beamline Group, for assistance in this project.

REFERENCES

[1] NI web page, http://taiwan.ni.com.
[2] Automatic Control System, Benjamin C. Kuo, 1997.
[3] An FPGA-based feedback control system that suppresses the nanoscale resonance, Proceedings of the MEDSI 2014 Conference, Chia-Feng Chang, Melbourne, Australia - October 2014.

Content from this work may be used under the terms of the CC BY 3.0 licence (© 2016). Any distribution of this work must maintain attribution to the author(s), title of the work, publisher, and DOI.

ISBN: 978-3-95450-188-5 doi:10.18429/JACoW-MEDSI2016-MOPE19

Content from this work may be used under the terms of the CC BY 3.0 licence (© 2016). Any distribution of this work must maintain attribution to the author(s), title of the work, publisher, and DOI.

MECHATRONICS CONCEPTS FOR THE NEW HIGH DYNAMICS DCM FOR SIRIUS

R. R. Geraldes†, R. M. Caliari, G. B. Z. L. Moreno, LNLS, Campinas, Brazil
M. J. C. Ronde, T. A. M. Ruijl, R. M. Schneider, MI-Partners, Eindhoven, Netherlands

Abstract

The monochromator is known to be one of the most critical optical elements of a synchrotron beamline, since it directly affects the beam quality with respect to energy and position. Naturally, the new 4th generation machines, with emittances in the range of order of 100 pm rad, require even higher stability performances, in spite of the still conflicting factors such as high power loads, power load variation, and vibration sources. A new high-dynamics DCM (Double Crystal Monochromator) is under development at the Brazilian Synchrotron Light Laboratory for the future X-ray undulator and superbend beamlines of Sirius, the new Brazilian 4th generation synchrotron [1, 2]. Aiming at an inter-crystal stability of a few tens of nrad (even during the Bragg angle motion for flyscans) and considering the limitations of the current DCM implementations, several aspects of the DCM engineering are being revisited. The system concept is chosen such that a control bandwidth in the order of 200 to 300 Hz can be achieved. This requires well-designed system dynamics, which can be realized by applying a fundamentally different architecture than that used in common DCM designs, based on the principles used in ultra-precision systems for semiconductor manufacturing. As a result, a lot of the known disturbances can be attenuated or suppressed, and internally excited modes can be effectively handled. The mechatronics concepts and analyses, including the metrological details, are shown.

INTRODUCTION

In the recent years it has become clear to the synchrotron community that the stability performance of DCMs would turn out to be one of the main bottlenecks in the overall performance of many X-ray beamlines, particularly for the new 4th generation machines, the so called Diffraction Limited Storage Rings (DLSR). Indeed, their performance is typically affected by well-known vibration sources, as the cooling system, the experimental floor and vacuum pumps in the surroundings. In addition, the self-induced disturbances, caused by servo and piezo actuators, for instance, have recently been more carefully investigated [3, 4].

Even though some incremental progress has been achieved in mitigating such disturbances, examples from applications in other industries show that the required stability could not be achieved by these incremental changes, based on the common architecture. A fundamentally different overall system approach is necessary to successfully design and realize such ultra-precision system. This work shows the mechatronics concepts used at the new high-stability DCM for Sirius [5]. More details about the full system and its specifications can be found in [6].

†renan.geraldes@lnls.br

CONCEPTUAL DESIGN

The concepts applied in the present design aim at a high-bandwidth closed-loop control, in which the main target is a control bandwidth of the inter-crystal parallelism in the order of 200 to 300 Hz. Thus, the disturbance rejection capacity of the control loop can suppress errors to the required nm levels, both in stand-still and during flyscan. By a proper design of the mechanics, the internal errors (noise sources) are minimized.

To achieve such a high closed-loop control bandwidth, a very well designed mechanical system, based on a fundamentally different dynamic architecture, is applied, and the use of voice-coil (VC) actuators is crucial. Whereas common DCM systems typically use piezo actuators or other inherently stiff actuators systems (like spindle drives), the use of inherently compliant actuators, as VCs, allows for another dynamic architecture. By this principle, the dynamics of the system can be designed to reach a significant higher closed-loop bandwidth, as only the essential mechanical components will act in the control loop. Namely, by means of a mechanical filter, established by a so-called reaction mass, or balance mass, the non-essential so-called reaction path dynamics can be filtered and, as such, be eliminated from the close-loop dynamics in the sense of control stability and disturbance amplification.

Essential for a successful design of such high-end system is predictive modelling, not only with respect to dynamics, but also thermal and other physical and mechanical aspects. Starting with the right overall architecture and taking all the essential requirements into account, predictive modelling, error-budgeting and proper design principles based on experience are crucial to design such complex high-end system. With respect to dynamics, dynamic system models, lumped-mass as well as FE-models are made. From these models, transfer functions are derived and evaluated to guide the conceptual choices and mechanical design to finally reach the required performance. Based on PSD analysis quantitative error budgeting is applied to finally predict the expected performance.

Dynamic Model and Control Tools

Figure 1 shows a schematic drawing of the DCM, which was used as the basis for a 1D-lumped-mass dynamic model of the system. The chosen degree of freedom to be used in this model was Rx, since pitch requirements are the most critical in terms of stability. Starting with such relative simple lumped-mass model, several

ISBN: 978-3-95450-188-5 doi:10.18429/JACoW-MEDSI2016-MOPE19

concepts can be evaluated and the feasibility can be proven quickly. Of course, the outcome of such model and the reliability of the results is not trivial, but requires experience in predictive modelling and designing high-end systems. By means of transfer functions, the system was evaluated and adaptions to the concepts were made. In parallel, the mechanical design was built and continuously updated, from rough to more detailed versions, whilst more detailed analysis, like simple hand calculations or FE analyses, provided more realistic numbers, so that masses and compliances/stiffness numbers could be refined to improve the dynamic model.

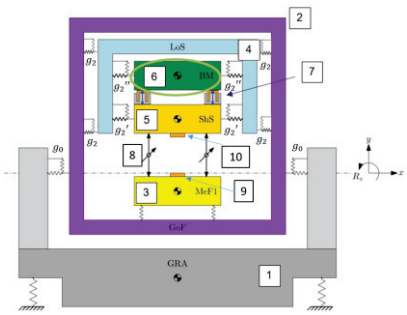


Figure 1: DCM schematic: (1) inertial reference; (2) rotating subsystem; (3) first crystal metrological frame and fixation base; (4) first level translational structure; (5) Second crystal metrological frame and fixation base; (6) reaction mass; (7) VCs; (8) optical interferometers; (9) First crystal; (10) second crystal.

The dynamic model allows for the convenient representation of the system in Bode plots, which reveal the mechanical performance of the system in the frequency domain. It can also be used to verify the control sensitivity of a given input, whether a control input or a disturbance source. Regarding control, the model is also used in analyses of Nyquist plots and phase margin for system stability. By varying specific system parameters, the impact of stiffness, misalignments, imbalance and construction tolerances, for example, can be analyzed, conferring robustness for the control project.

Actuator Concept

Piezoelectric actuators are extensively used in high-precision positioning systems, including the precise adjustment of parallelism between crystals in DCMs. However, as spindle drives with stepper motors, they are position based actuators and stiff by definition. Depending on the control loop and relative positioning of the mechanical parts in a given system, this inherent stiffness can be beneficial. However, in more complex systems, like the DCM, this inherent stiffness also creates a dynamic link that significantly limits the overall dynamic performance. Especially in scanning systems, as the DCM in flyscan, such mechanically stiff connection would couple the motion errors of a guiding system directly to the final positioning performance of the system. Thus, in the case of such an inherently stiff actuation principle (as in piezos) the control loop has to fight against its own inherent stiffness, since the noise in the guiding system becomes visible in the relative position of the crystals during the flyscan motion. Considering the required nm performance, a lean and predictable system, without these unwanted interactions, is clearly needed. Some first-order simulations of the closed-loop bandwidth of the DCM were made for piezo and VC actuators (see Table 1). For the first, due to the mechanical and dynamic interaction of the inherently stiff piezos, the control gain is relatively limited, with a bandwidth in the order of a few tens of Hz. The VCs, on the other hand, without the unwanted mechanical and dynamic coupling, allow for a more robust control, with closed-loop bandwidth that may reach a few hundreds of Hz.

Reaction Mass Concept

The attainable bandwidth will be limited by resonances in the system to be controlled, which can be in the forward-path (ShS), or in the backward-path, i.e., in the structure dynamics. Both the forward and backward path Bode plots for pitch control are depicted in Fig. 2, with and without a reaction mass. It can be seen in the forward-path the intentional decoupling of ShS at low frequencies and the internal resonances above 1 kHz. Indeed, the forward-path has been carefully designed, such that the first internal resonances are above 1.5 kHz. The backward-path, on the other hand, is much more complicate and involves many bodies with internal resonance far below 1 kHz (typically a few hundred Hz), which are back excited by the reaction forces of the actuator, so that they become visible in the control loop and can limit the close-loop bandwidth due stability reasons. Without a reaction mass, Fig. 2(a), the backward-path peaks overcome the forward-path control and limit the closed-loop bandwidth well below 100 Hz. On the other hand, with the reaction mass, Fig. 2(b), the reaction forces act directly against it, which is also decoupled at low-frequencies. Thus, it effectively filters the reaction forces of the actuator with respect to the overall structure, attenuating the backward-path dynamics, so that it does not limit the achievable bandwidth anymore.

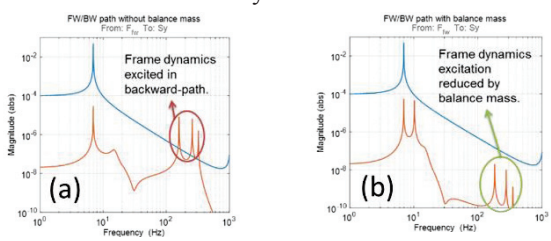


Figure 2: Transfer function for pitch correction in the 2nd crystal of the DMC: forward path in blue and backward path in red. In (a) the reaction force acts against the long stroke frame, whereas in (b), against the balance mass.

Feedback

In order to achieve the high-bandwidth control, the sensor system becomes crucial in the feedback performance. The noise level should be low enough, whereas the sample rate, high enough to achieve the nm performance and the high close-loop bandwidth. Considering the nm per-

Content from this work may be used under the terms of the CC BY 3.0 licence (© 2016). Any distribution of this work must maintain attribution to the author(s), title of the work, publisher, and DOI.

ISBN: 978-3-95450-188-5 doi:10.18429/JACoW-MEDSI2016-MOPE19

Content from this work may be used under the terms of the CC BY 3.0 licence (© 2016). Any distribution of this work must maintain attribution to the author(s), title of the work, publisher, and DOI.

formance and the several mm of stroke that we need, an incremental optical measurement system is an obvious choice. Moreover, considering not only the gap variation of several mm but also the angular motions (pitch and roll), an optical distance measurement interferometers (DMI) seems to be the most elegant solution in this application. By the DMI, subnanometer resolution and stability can be provided at 10 kHz sampling time. Thus, three optical interferometers are combined to measure the gap and the two angles (pitch and roll) between the two metrology frames that support the crystals.

RESULTS

In order to analyze the contribution of various error sources, an error budgeting approach is used, allowing for a complete understanding of the system and identification of the main players, which aids in concept and design choices. For the DCM this approach has been applied for manufacturing tolerances, metrology, alignment and dynamics. All error sources must be considered to predict the final performance of the monochromator.

Table 1 shows a preliminary dynamic error budget for the 1D model (Rx) for different actuator types. Even though it is incomplete, because not all error sources were known, it is very instructive since it shows significant figures that compare the performance of the DCM with the proposed technology to that with the most standard piezo solution, as well as piezo walker actuators.

Table 1: Rx Error Budget for Different Actuators

	Lorenz (VC) [nrad] 3σ	**Piezo Stack** [nrad] 3σ	**Piezo walker** [nrad] 3σ
Bandwidth	200Hz	20Hz	20Hz
Floor vibrations	0.8	2.5	0.9
Amplifier noise	1.4	44.1	2.9
Amplifier DAC quantization	0.2	0.2	0.2
DMI quantization errors	0.2	0.1	0.1
Quadratic sum [nrad] 3σ	1.6	44.1	3.1

Figure 3(a) depicts another interesting analysis tool for the error budget, namely, the cumulative power spectrum. Figure 3(b), on the other hand, shows a stability analysis via Nyquist plots. Both results already belong to the full 6D dynamic model of the system, which was developed in parallel with the mechanical design in order to guide and feedback the development of the conceptual design (conceptual design phase was finished just a few weeks ago). Figure 3(b) shows the open loop Nyquist plot with the system tilted in its outer range and taking misalignments into account. Extensive modelling and error budgeting has been done with respect to alignment and assembly strategy of the system, since assembly and alignment tooling, and interfaces were also part of the conceptual design phase. Simply ignoring them and trying to add them later would never succeed in such complex system design. Finally, to reach the required closed-loop bandwidth in the order of 200 to 300 Hz, the phase loss in the feedback loop is analyzed to define the necessary sample rate of the MIMO controller. As it can be seen in Table 2, by looking at sampling frequency, desired bandwidth and system latency, the phase loss can be calculated and the minimum sampling frequency for a certain system robustness requirement can be determined. For the first prototype of the DCM the MIMO controller will be realized in a real-time XPC target, whereas a high-end motion controller is under evaluation for the final solution.

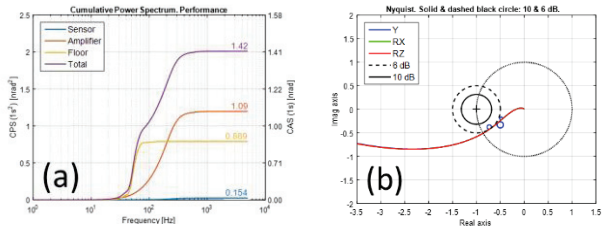


Figure 3: (a) Cumulative Power Spectrum Performance, analysing disturbances individual contributions. (b) Nyquist plot example, with analysis made for misaligment impacts on stability.

Table 2: Phase Loss vs. Sample Frequency

Sampling frequency	**5 kHz**	**10 kHz**	**20 kHz**
Zero-order holder	-5.40º	-2.70º	-1.35º
General delay	-10.80º	-5.40º	-2.70º
Interferometer latency	-0.11º	-0.11º	-0.11º
Total	-16.31º	-8.21º	-4.16º
Spec < -10º	Not Ok	Ok	Ok

CONCLUSION

In this paper a proven dynamic architecture of high-end equipment, as commonly used in semiconductor manufacturing equipment, is applied for a DCM. With a solution based on VC actuators and a balance mass, the present dynamic model predicts that a closed-loop bandwidth above 200 Hz will be achieved in this prototype. This is necessary to reach high disturbance rejection and tracking performance, and thus attain to a few nrad also during flyscan, as required in next generation DCMs. The development of the dynamic model and the use of a set of analysis tools has proven to be essential to accomplish the predictive modelling that such high performance system demands. In conclusion, these concepts and this approach have already started to be applied in other mechanisms of

ISBN: 978-3-95450-188-5 doi:10.18429/JACoW-MEDSI2016-MOPE19

the Sirius beamlines, including mirror systems and sample stages.

ACKNOWLEDGEMENT

The authors would like to gratefully acknowledge the funding by the Brazilian Ministry of Science, Technology, Innovation and Communication and the contribution of LNLS and MI-Partners teams.

REFERENCES

[1] L. Liu, F. H. de Sá, and X. R. Resende, "A new optics for Sirius," in *Proc. IPAC'2016*, pp. 3413–3415.

[2] A. Rodrigues *et al.*, "Sirius Status Report", in *Proc. IPAC'16*, Busan, Korea, May 2016, paper WEPOW001, pp. 2811-2814.

[3] R. Caliari *et al.*, "Studies on flow-induced-vibrations for the new high-dynamics DCM for Sirius", presented at MEDSI 2016, Barcelona, Spain, Sep. 2016, this conference.

[4] P. Kristiansen, J. Horbach, R. Doehrmann, and Joachim Heuer, "Vibration Measurements of high-heat-load monochromators for DESY PETRA III extension", *Journal of Synchrotron Radiation*, vol. 22, pp. 879-885, Jul. 2015.

[5] R. R. Geraldes *et al.*, "Método de controle de grau de liberdade em sistemas mecatrônicos e monocromador de duplo cristal", INPI BR 10 2016 020900 5, Sep. 2016, Patent Pending.

[6] R. Geraldes *et al.*, "The new high dynamics DCM for Sirius", presented at MEDSI 2016, Barcelona, Spain, Sep. 2016, this conference.

Content from this work may be used under the terms of the CC BY 3.0 licence (© 2016). Any distribution of this work must maintain attribution to the author(s), title of the work, publisher, and DOI.

ISBN: 978-3-95450-188-5 doi:10.18429/JACoW-MEDSI2016-MOPE20

ULTRA STIFFNESS AND ULTRA LOW WAVING LM GUIDE

Martí Miret, THK GmbH Sucursal en España Sales Manager, Badalona, Spain

Abstract

Since the launch by THK of the first Linear Motion Guide in 1972, these products have evolved in order to overcome different challenges. A current challenge consists on improving the precision of THK's products up to a nanometric scale. Optimizing the internal design of the block of a linear guide according to concrete specifications can reduce the waving phenomenon caused by the changing load condition of the rolling body in the block. However, this optimization is not enough for improving the precision of the LM Guides in a microscopic level. Increasing the number of effective balls by reducing their diameter, expanding the length of the block and increasing the number of rows in the Guide is a solution that allows a high increase of the rigidity and the reduction of the waving to the desired level.

GEOMETRIC ACCURACY OF MOTION

Straightness and waving are two phenomenons that appear due to the movement of the table of a LM Guide.

Straightness indicates the range of how much the table movement deviates from its ideal line, since this movement should be the straight line.

Waving shows the microscopic wave where it characteristically appears in the rolling motion guidance of the infinite circulation.

As shown in Figure 1, and in order to anticipate the geometric accuracy of the LM Guide, it is important to know how much the table would deform its postural change by the load and the moment influenced to it.

Therefore, it is necessary to know the load distribution of the block interior establishing the theory of the load distribution.

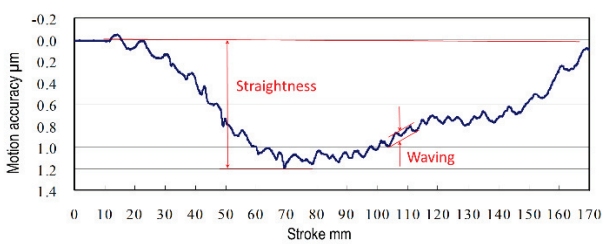


Figure 1: Geometric accuracy of motion.

THEORY OF THE LOAD DISTRIBUTION

This is the theory that consider those respective blocks illustrated in Figure 2 as a single unified system, and varies the external force affecting to the table to a postal change finally by converting the load, elastic deformation, and the contact angle variation where generated at the contact of the rolling body.

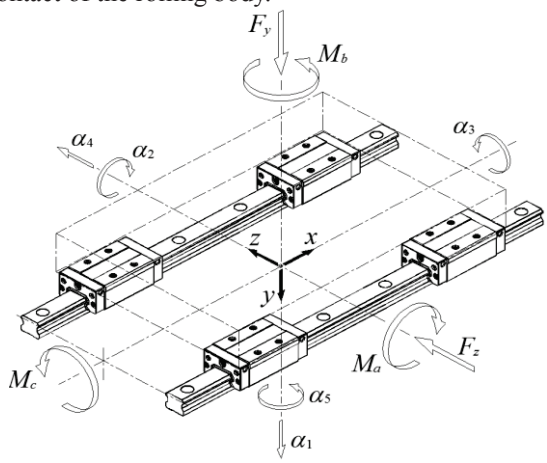


Figure 2: Theory of load distribution.

GENERATING FACTOR OF WAVING

The waving phenomenon occurs due to the movement of the LM block. By this movement, the number of effective balls (balls which are carrying the load) changes increasing and decreasing constantly (Figure 3). This causes a change of the load distribution that creates a changing balance of the load. For this reason appears the factor of waving. The difficulty of correcting this phenomenon is a problem to overcome in order to provide LM Guides of a greater accuracy for ensuring their optimal use in high performance machines.

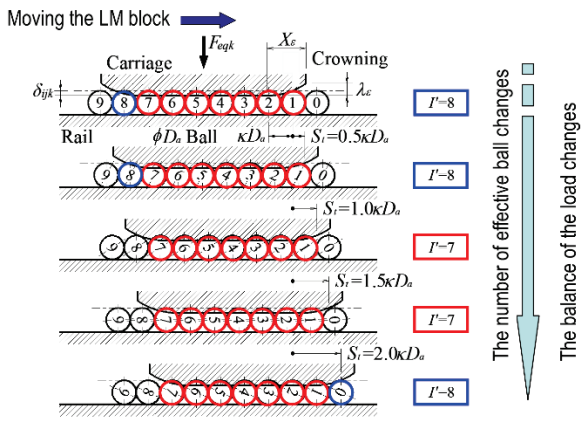


Figure 3: The factor of waving.

OPTIMIZED DESIGN

The initial solution for minimizing the waving consists on determining the optimized design of the block interior for meeting the clients specifications.

Content from this work may be used under the terms of the CC BY 3.0 licence (© 2016). Any distribution of this work must maintain attribution to the author(s), title of the work, publisher, and DOI.

ISBN: 978-3-95450-188-5 doi:10.18429/JACoW-MEDSI2016-MOPE20

PRECISION IMPROVEMENT OF THE LM GUIDE

The merits of the LM Guide include its easy maintenance and the improvement of the machines productivity. Also, it includes a high energy saving and a better improvement of the design with a low total cost.

Changing the load condition of the body in the different stroke generates a waviness phenomenon. Therefore, it was adopted the guidance of the static oil pressure for the high performance machine.

The goal is adding the merit of achieving the ultra-high precision of the LM Guide by realizing the waving of nano-level.

HOW TO MINIMIZE THE WAVING

As previously seen, the objective for achieving a functioning LM Guide, is increasing the number of effective balls in order to have a better distribution of the load. This objective tries to meet the merits of hydrostatic guides with the advantages of caged ball LM Guides (Figure 4).

Therefore, the first action to be taken in order to increase the number of effective balls, is reducing the diameter of the balls. The reduction of the balls by ½ allows increasing the number of effective balls two times.

Also, increasing the number of rows from 4 to 8, allows having contact with the double of balls.

At last, changing the length of the guide's block is another way of increasing the number of effective balls. An expansion of the LM Guide block of two times its standard length, increases the number of effective balls by 2.

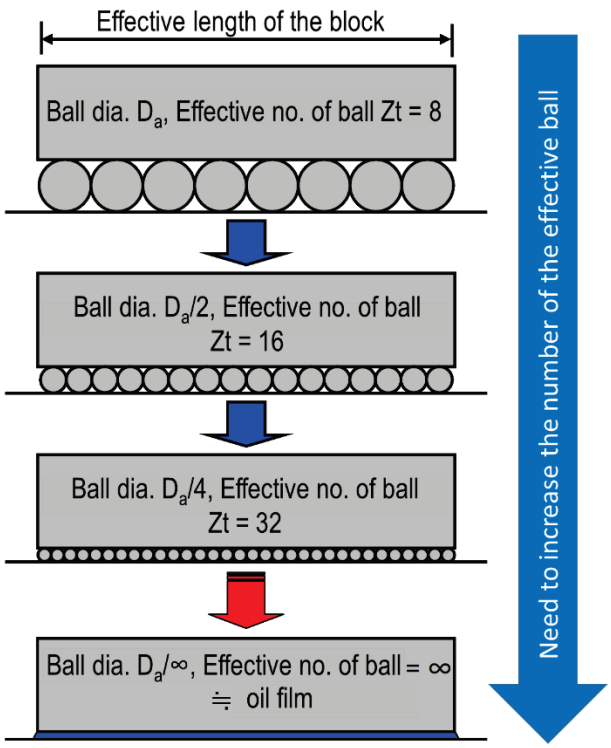


Figure 4: Reduction of the waving.

ADVANTAGES

By the adoption of the previously indicated actions, the SPR/SPS LM Guide meets several advantages.

In the first place, it allows increasing the number of effective balls around 8 times. This has as a consequence a higher accuracy and the achievement of a super-low waving.

These guides allow a high accuracy in a rolling guide that reaches the level of the nanometric scale. The waving phenomenon can be reduced around an 80%.

Also, the SPR/SPS models reach a super high rigidity and a higher load rating. The rigidity of these guides is higher than a roller's guide rigidity.

According to the experimental tests, the measurement of the waving results of 9.5 nm in the vertical direction (Figure 5), and 21 nm in the horizontal direction (Figure 6).

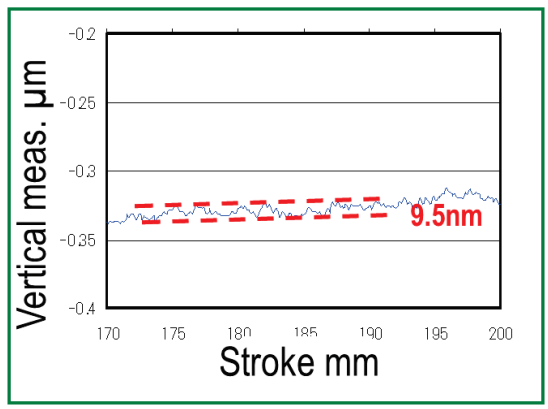


Figure 5: Vertical measurement.

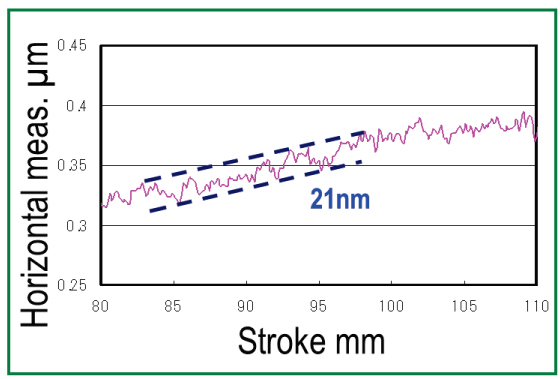


Figure 6: Horizontal measurement.

Content from this work may be used under the terms of the CC BY 3.0 licence (© 2016). Any distribution of this work must maintain attribution to the author(s), title of the work, publisher, and DOI.

ISBN: 978-3-95450-188-5 doi:10.18429/JACoW-MEDSI2016-MOPE22

MECHANICAL DESIGN OF THE MID SPLIT-AND-DELAY LINE AT THE EUROPEAN XFEL

B. Friedrich[1,2], T. Noll[1], W. Lu[3], T. Roth[3], A. Madsen[3], S. Eisebitt[1,2]
[1] Max-Born-Institut, Berlin, Germany, [2] Technische Universität Berlin, Berlin, Germany,
[3] European XFEL, Schenefeld, Germany

Abstract

A new split-and-delay line (SDL) is under development for the Materials Imaging and Dynamics (MID) end station at the European XFEL.[1] The device utilises Bragg reflection to provide pairs of X-ray pulses with an energy of (5 … 10) keV and a continuously tunable time delay of (-10 … 800) ps – thus allowing zero-crossing of the time delay. The mechanical concept features separate positioning stages for each optical element. Those are based on a serial combination of coarse motion axes and a fine alignment 6 DoF Cartesian parallel kinematics[2]. That allows to meet the contradictory demands of a fast long-range travel of up to 1000 mm and in the same time a precise alignment with a resolution in the nanometre range. Multiple laser interferometers monitor the position of the optical elements and allow an active control of their alignment. All optical elements and mechanics will be installed inside an UHV chamber, including the interferometer and about 100 stepper motors.

With this paper we present the mechanical design for the SDL. It will additionally show the design of a prototype of a positioning stage which allows extensive testing of the implemented concepts and techniques.

INTRODUCTION

The intention behind the presented project is the provision of pairs of X-ray pulses with picosecond delay times at the MID end station at the European XFEL. This is to be achieved by a SDL system, which splits the XFEL beam into two branches and merges both after delaying one branch with respect to the other branch. Osaka et al. proofed such a split and delay concept to work with an in-air system for hard X-rays and a delay times up to 220 ps [3]. Earlier, Rosecker er al. developped a SDL working at fixed energy and in air [4].

The SDL under development allows for a window-less integration into the MID beamline and thus places all mechanics into an UHV environment. The SDL is designed to work with an energy in the range of (5 … 10) keV and to achieve a continuously tunable delay time of (-10 … 800) ps. This range also covers the zero crossing of the delay time. The mechanics for the positioning of the optical elements feature a precision in the range of single nanometer and tens of nanoradians, while in the same time allows long-range travel of up to 1000 mm. Full adjustability and an efficient operation will be possible due to the motorisation of most of the controllable dimensions of freedom (DoF) and multiple monitoring and measurement systems.

GENERAL CONCEPT

Bragg reflections of silicon crystals in 220-orientation is utilized to generate the intended beam paths. This, in contrary to grazing incidence mirror optics, is working at high reflection angles, which allow a much shorter and space saving design.

The general concept of the SDL is shown in Fig. 1. It features an upper and a lower branch, in which the incoming beam is divided to by a beam splitter. Both parts of the beam are brought back together at the end of the system by a merger crystal. The two crystals in the upper branch are adjustable in position and angle in order to realise different path length and therefore different delays, and different working energies. The lower branch features two channel cuts, creating a fixed delay to allow also small negative overall delay times.

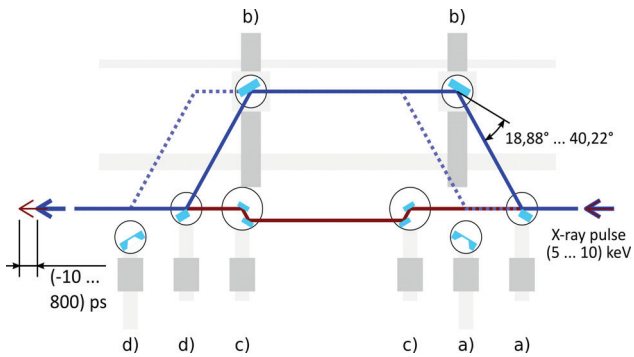


Figure 1: Conceptual view of the SDL indicating the mechanical concept. a) beam splitters; b) upper branch crystals; c) channel cuts; d) beam merger.

Two different splitter and merger stages are foreseen, either using extremely thin crystals and an intensity splitting of the X-ray beam, or the edge of a thick crystal, to split the beam geometrically. The unused version can be translated out of the X-ray beam. Moving all optical elements out of the beam allows the beam to pass through the system without any reflection, i.e. when the SDL is not required for an experiment.

In order to have a most versatile control and evaluation of the system, various measuring and monitoring systems will be integrated. This includes:

- a visible feedback laser, guided parallel to the FEL beam on dedicated mirrors, monitored by nano cameras
- Two 3-axis laser interferometers with sub-nanometre resolution, monitoring the upper branch crystals

Content from this work may be used under the terms of the CC BY 3.0 licence (© 2016). Any distribution of this work must maintain attribution to the author(s), title of the work, publisher, and DOI.

ISBN: 978-3-95450-188-5 doi:10.18429/JACoW-MEDSI2016-MOPE22

- optical encoders with nanometre resolution to track the coarse motions
- beam intensity diodes next to each optical element
- beam position monitors in the upper and lower branch

The mechanics will be installed in an UHV chamber in order to minimize disturbances. This allows for windowless operation, as any window in the coherent X-ray beam would lead to parasitic scattering. To allow for a sufficient controlling of the system, the majority of the controllable DoF are motorized. Due to the vast options of adjustment and the thereby large number of DoF to be controlled, the system features an overall amount of more than 100 in-vacuum stepper motors.

MECHANICAL DESIGN

Figure 2 shows a general view of the SDL with the vacuum chamber containing an optical bench. This bench acts as the supporting structure for the precision mechanics and other components. The chamber sits on a granite block to obtain a high stiffness and eigenfrequencies. For installation and maintenance purposes, one half of the cylindrical shell can get tilted up – providing a wide access to the inner mechanics. In the closed state the chamber features a very high stability due to its cylindrical shape.

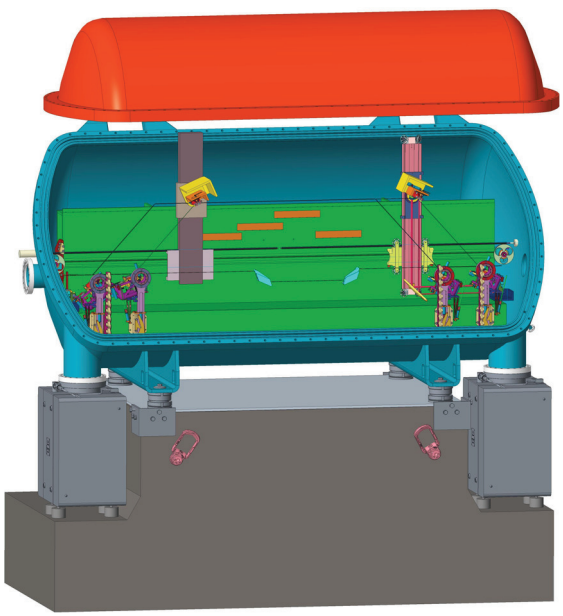


Figure 2: General view of the SDL in its current state of design.

The optical bench is designed for high stiffness. It provides a stable support structure for the installation of the mechanics as well as monitor and measurement systems, as shown in Fig. 3. Decoubling the bench by a minimal amount of connections to the chamber in positions where the chamber rests on the granite, the effects of mechanical or thermal disturbances from the environment onto the precision mechanics are minimised.

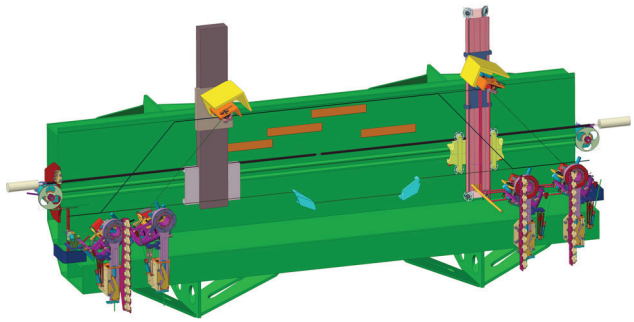


Figure 3: The optical bench as support structure for the precision mechanics and further components.

The system features separate positioning stages mounted to the optical bench for all optical elements. The mechanics of those have to meet two contradictory demands: They must provide a fast long-range travel – in some cases of up to 1000 mm – in order to allow for a positioning according to desired energy, time delay or splitting/merging option. In the same time they must allow a precise alignment with a resolution in the range of single nanometre and tens of nanoradians, in order to select a precise time delay in the order of a few femtoseconds and an overlap of the two split micron sized X-ray beams at the sample position 8m downstream of the SDL. This is achieved by a serial combination of coarse motion axes with a fine alignment stage. Figure 4 shows one beam splitter assembly.

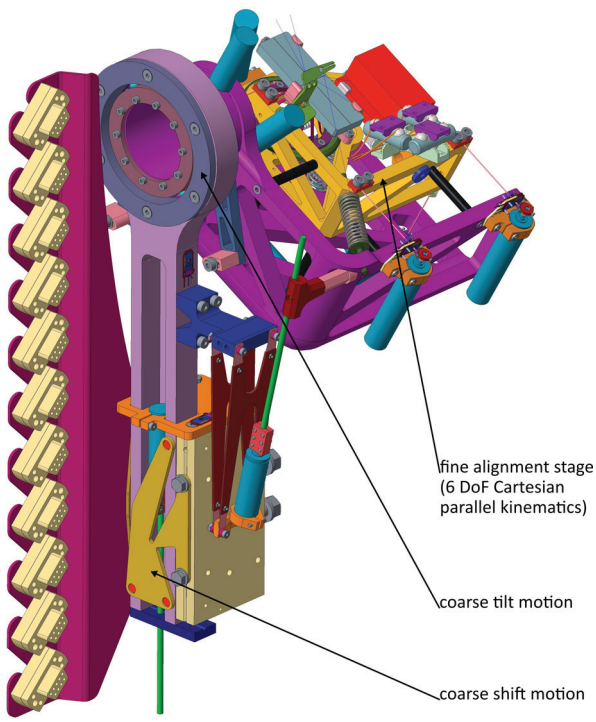


Figure 4: Positioning stage for the beam splitter.

The fine alignment stage is implemented as a 6 DoF Cartesian parallel kinematics. It features a platform supported by a structure of six stainless steel cables. These cables are adjustable in length and preloaded by springs. As these cables are orientated parallel to the

Content from this work may be used under the terms of the CC BY 3.0 licence (© 2016). Any distribution of this work must maintain attribution to the author(s), title of the work, publisher, and DOI.

ISBN: 978-3-95450-188-5 doi:10.18429/JACoW-MEDSI2016-MOPE22

Content from this work may be used under the terms of the CC BY 3.0 licence (© 2016). Any distribution of this work must maintain attribution to the author(s), title of the work, publisher, and DOI.

Cartesian coordinates, the need for complex coordinate transformations is avoided and a simple control scheme can be applied. All cables are coiled on a gear shaft, which is driven by a small stepper motor, thereby allowing for a change in length of each cable. The gear ratio is 154.368. This gives a resolution for their length of about 2,5 nm per full step. Due to the Cartesian orientation of the legs, this is also the linear resolution for the fine alignment stage. The rotary resolution depends on the lever arm, created by the distances between the cables. For the generic design of the fine alignment stage, the three rotary resolutions are about 36 nrad per full step.

A special driving system was developed for the long translations of the upper branch crystals. These translations are driven by a combination of a conventional lead screw for the horizontal translation and a cable system for the vertical translation. A conceptual layout of this is presented in Fig. 5. This implementation allows to have two motors dedicated to individual motions, while in the same time the motors can be installed in a fixed position within the system. This allows for a better cooling scheme and minimizes the thermal impact on crucial mechanical elements.

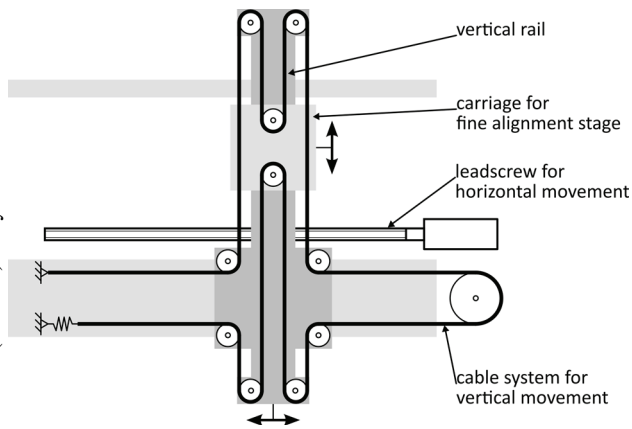


Figure 5: Concept for the driving of the coarse translations of the upper branch positioning stages.

PROTOTYPE

A prototype of a beam splitter positioning stage has been designed and build. Figure 6 shows a photograph of this device. This prototype allows to investigate the capabilities of the mechanical design. First tests of the prototype and the laser interferometer have been conducted in air. It was shown that the mechanics works as intended. However, due to the heavy influence of the air onto the interferometer system, quantitative statements on the achieved accuracy can not be made so far. In order to investigate the capabilities and limits of both components, the test set-up will be transferred into a vacuum environment for further test.

In addition, a thermal camera was used to investigate the thermal behaviour. The camera monitored the area around the lead screw and nut for the vertical shift, while this axis was driven three times over a height of 30 mm (see Fig. 6). On a qualitative level, the results show very clearly the induction of head due to the friction between the nut and the lead screw. This occurs mainly during upwards movements due to the higher force and therefore higher friction in this direction. Accordingly, the temperature degreases while moving downwards. As the relevant temperature differences are in a very small range of less than 1 K, a further optimisation and calibration of the set-up is necessary to allow for quantitative results.

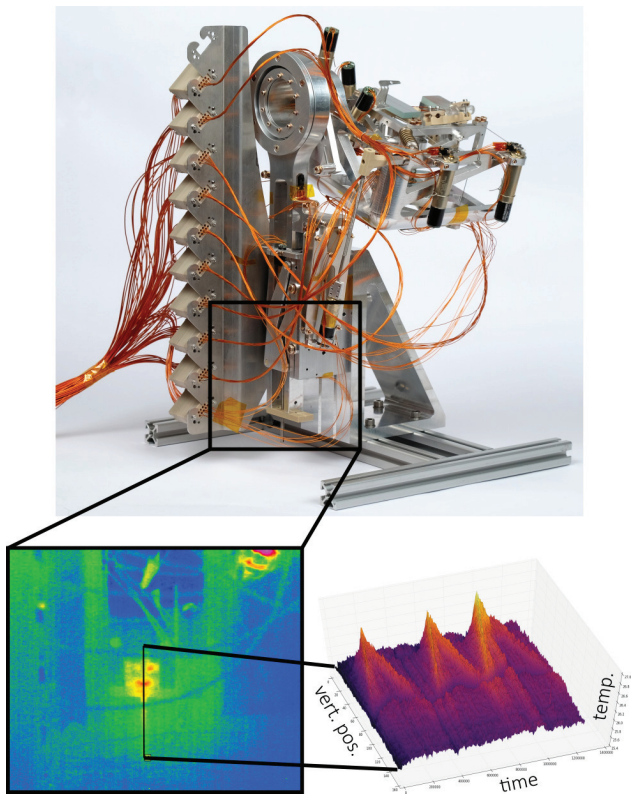


Figure 6: Photograph of the assembled and wired prototype and the results of the thermal investigation.

CONCLUSION

We developed a concept and a corresponding mechanical design for the MID Split-and-Delay line. Advanced mechanical solution were found for crucial points such as the mechanics for the coarse and fine movements. Considering the mechanical design together with the exceptional feedback, control and monitoring systems, that are applied, we are convinced that the system will be able to provide pairs of X-ray pulses with the intended properties.

A prototype of a positioning stage as one of the key mechanical elements was build and is under investigation using a dedicated laser interferometer. First results are promising and will be followed by further investigations with an improved set-up under vacuum conditions.

ISBN: 978-3-95450-188-5 doi:10.18429/JACoW-MEDSI2016-MOPE22

REFERENCES

[1] A. Madsen, J. Hallmann, T. Roth, and G. Ansaldi, "Technical Design Report: Scientific Instrument MID", 2013, doi:10.3204/XFEL.EU/TR-2013-005

[2] T. Noll, K. Holldack, G. Reichardt, O. Schwarzkopf, and T. Zeschke, "Parallel kinematics for nanoscale Cartesian motions", Precision Engineering, vol. 33, no. 3, pp. 291–304, Jul. 2009, doi:10.1016/j.precisioneng.2008.07.001

[3] T. Osaka, T. Hirano, Y. Sano, Y. Inubushi, S. Matsuyama, K. Tono, T. Ishikawa, K. Yamauchi, and M. Yabashi, 'Wavelength-tunable split-and-delay optical system for hard X-ray free-electron lasers', Optics Express, vol. 24, no. 9, p. 9187, May 2016.

[4] W. Roseker, H. Franz, H. Schulte-Schrepping, A. Ehnes, O. Leupold, F. Zontone, S. Lee, A. Robert and G. Grübel, 'Development of a hard X-ray delay line for X-ray photon correlation spectroscopy and jitter-free pump–probe experiments at X-ray free-electron laser sources', J. Synchrotron Rad., vol. 18, no 3, pp. 481-491 (2011)

Content from this work may be used under the terms of the CC BY 3.0 licence (© 2016). Any distribution of this work must maintain attribution to the author(s), title of the work, publisher, and DOI.

ISBN: 978-3-95450-188-5 doi:10.18429/JACoW-MEDSI2016-MOPE23

Content from this work may be used under the terms of the CC BY 3.0 licence (© 2016). Any distribution of this work must maintain attribution to the author(s), title of the work, publisher, and DOI.

AN ASSEMBLING CALIBRATION METHOD OF XBPM DIAMOND BLADES IN TPS

H.C. Ho, C.K.Kuan, W.Y. Lai, S.Y. Perng, T.C. Tseng, D.G. Huang,
M.L. Chen, C.J. Lin, H.S. Wang, K.H. Hsu

NSRRC,Hsinchu 30076, Tiwan, R.O.C

Abstract

Diamond blade type X-ray Beam Position Monitors (XBPM) were adopted to monitor photon position at the beamline front-end in Taiwan Photon Source (TPS) [1]. Due to the thin thickness (125um) and fragile characteristic, the assembling precision of the diamond blades is difficult to measure and influences the accuracy of monitor. A non-contact method was thus developed by using a LED laser with telecentric objective lens and a CCD-array to calibrate the diamond blades assembling configuration within micrometer accuracy. According to the measurement results, XBPM can be correlated to four fiducial points for survey network. This paper describes this method and calibrating results in detail.

INTRODUCTION

XBPM are adopted in synchrotron machine to monitor the photon beam position in beamline frontend [2]. It can eliminate controversy for beam position and stability for machine user. The blade position accuracy will influence the accuracy of the monitor. Due to the thin thickness (125um), vacuum parts and fragile characteristic, the assembling precision of the diamond blades is hard to measure. At the begging, we use non-contact method like telescope and microscope, which may have vision and projection lens error, we need to move and rotate the XBPM, XBPM 3D accuracy error will be over 0.2 mm. Now we developed a new non-contact method by using LED laser with telecentric objective lens and a CCD-array assembling configuration instead of a microscope and accuracy of 5 um. Measurement space can be minimized perfectly and measurement time can be saved. Finally, XBPM can be correlated to four fiducial points for easy survey alignment network installation.

MECHANICAL DESIGN

We hope the measurement accuracy will reach within 5 um with this CCD method and easy blades alignment. During measuring process, moving or rotating the XBPM is forbidden (XBPM weight over 15kg, 240x240 mm). Finally, XBPM measurement data can be correlated to four fiducial holes at about 1/4" for survey alignment network installation. Here is a telecentric objective lens which provides an image of the same size in the so-called telecentric range, which produces a constant accuracy [3]. The line scan camera in the receiver which measures the projected outer contour of the fiducial as shown in Figure 1.

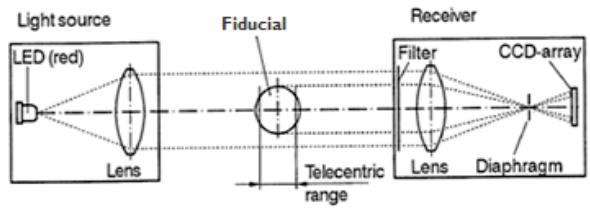


Figure 1: CCD array measurement range of 40 mm, resolution of 0.1 um, and LED wavelength of 670nm.

We make four fiducial holes on the XBPM base template, move the light source and receiver to the fiducial at about 150 mm by using sliders sliding on the rail, and mount and scan fiducial round bar contour. We can make a centre line relative to the rail movement direction by a receiver. Due to the limitation of CCD array area of 40x2 mm, fiducials round bar has a full length which was set up to 75 mm. And the round diameter Ø8 mm concentricity required 2 µm in 55 mm length relative to the hole, the 55mm full length accuracy was controlled within 2 µm. If the measurement range exceeds CCD array range, we can thus move the X-Z stage (450x400 mm travel range) in 1µm resolution. Using a rotatable arm pivot, we can rotate the light source and receiver in 90°. In vertical direction, we measure the blade by using the top surface of the fiducial as a standard point for measurement. In the horizontal direction, the blade is measured by using the side of the fiducial and a side of the blade as a standard point. Scanning step by step, we can measure the gap in the diamond blades and the fiducial centre length. Figure 2 and 3 show the vertical and horizontal sensor scanning.

ISBN: 978-3-95450-188-5 doi:10.18429/JACoW-MEDSI2016-MOPE23

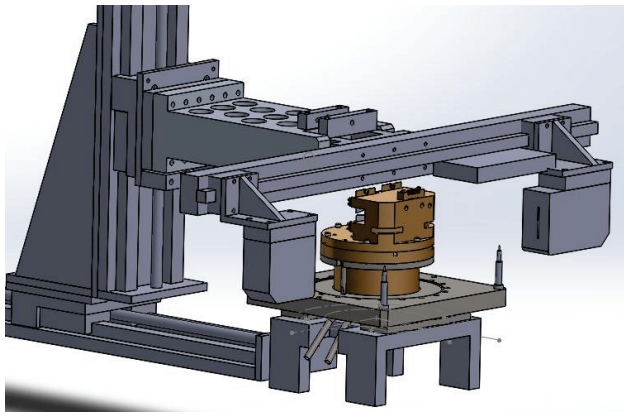


Figure 2: Vertical direction measurement.

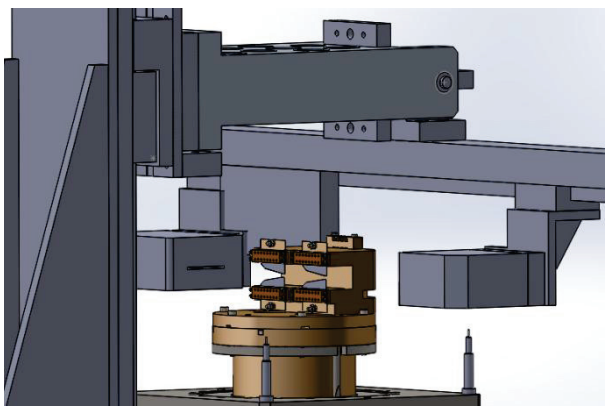


Figure 3: Horizontal direction measurement.

MEASUREMENT

The measurement device was set on the optical table. We use levelling bubble and calliper to set up rail plane and parallel gauge block to reduce misalign for XBPM as shown Figure 4. In order to get a corrected value for the receiver sensor before using, we calibrate receiver sensor with stage and gauge block for its linear as shown in Figure 5.

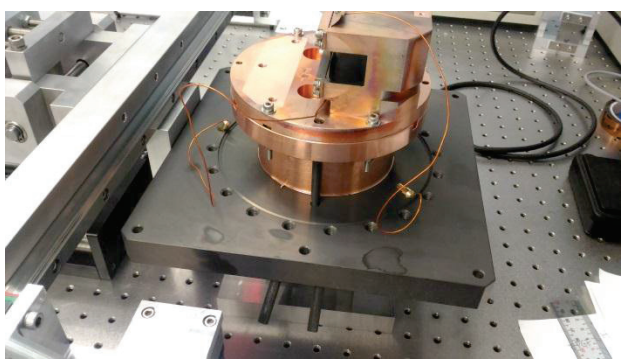


Figure 4: Parallel gauge block to reduce misalign.



Figure 5: Receiver sensor with gauge block gap calibration.

Here is a receiver sensor height calibration compensate linear value as shown in table 1 and Figure 6.

Table 1: Receiver Sensor Compensated Value

Sensor (mm)	Sensor value	Stage linear encoder(mm)	Sensor value-Linear encoder
39.997	0	0	0
39.5074	0.4896	0.498	-0.0084
39.0095	0.9875	1.002	-0.0145
37.9546	2.0424	2.066	-0.0236
35.3216	4.6754	4.728	-0.0526
32.2158	7.7812	7.863	-0.0818
28.6685	11.3285	11.421	-0.0925
20.3553	19.6417	19.771	-0.1293
14.093	25.904	26.048	-0.144
7.4988	32.4982	32.651	-0.1528
0.0084	39.9886	40.172	-0.1834

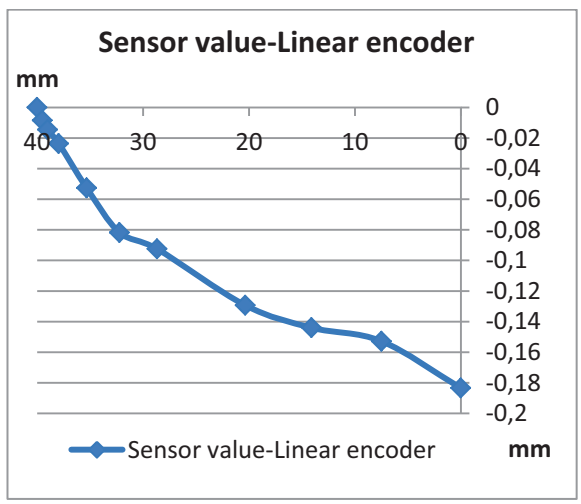


Figure 6: Receiver sensor compensated value.

Content from this work may be used under the terms of the CC BY 3.0 licence (© 2016). Any distribution of this work must maintain attribution to the author(s), title of the work, publisher, and DOI.

ISBN: 978-3-95450-188-5 doi:10.18429/JACoW-MEDSI2016-MOPE23

Table 2: Receiver Sensor Value in Horizontal and Vertical Direction

	#A	#B	#C	#D	#E	#F
Horizontal direction(sensor reading)	33.996 mm	33.992 mm	33.9951 mm	39.9952 mm	39.805 mm	39.9954 mm
Stage position reading (horizontal)	(0 , 0) mm	(0 , 0) mm	(219.979 , 0) mm	(226.057 , 0) mm	(113.644,38.877)mm	(120.277,38.878) mm
Vertical direction(sensor reading)	9.0054 mm	9.0290 mm	9.0021 mm	9.046 mm	38.0001mm	39.039 mm
Stage position reading (verticall)	(0 , 0) mm	(0 , 0) mm	(220.023, -0.001) mm	(220.045,0.001) mm	(108.241,14.500)mm	(113.461,28.999) mm

RESULTS

Each of the horizontal and vertical direction measurement location is as shown in Figure 7, the receiver sensor value is as shown as table 2.

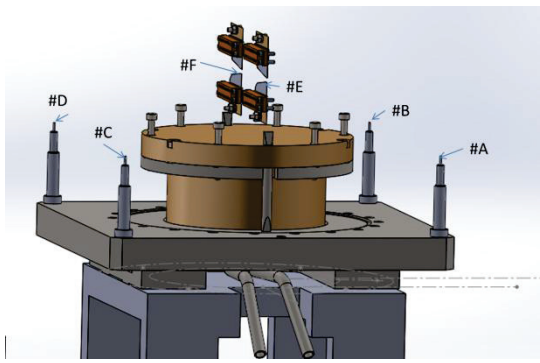


Figure 7: Measurement data locations.

Fiducial hole centre from
#A to #C is 219.978 mm.
#B to #D is 219.9938mm(39.9952mm -33.992mm = 6.0032mm + compensated value 0.06mm =6.0632mm, 226.057mm -6.0632mm = 219.9938 mm).
#A to #E is 115.503mm
#A to #F is 122.336mm
Gap from #E to #F is 122.336mm
Template to blade #E is 98.6146 mm (38mm – 9.0054mm = 28.9946mm + compensated value 0.12mm = 29.1146mm + 14.5mm + fiducial height 55mm = 98.6146 mm)
Template surface to blade #F is 99.6531 mm
Gap from Template surface to #E is 3.025mm
Gap from Template surface to #E to #F is 2.798 mm

We had checked the fiducial holes centre length, the tolerance is within 5μm .The blade height is checked with a calliper, the tolerance is about 0.1 mm(cannot be in contact with blade).

CONCLUSION

The accuracy using this non-contact measurement can be achieved at about 5um. Our system could also reduce a large amount of space, making it more compact as well as save a lot of time while measuring. In the future, we will try to develop a system that could be automatically controlled and measured.

ACKNOWLEDGEMENT

Authors would like to thank the magnet group of NSRRC for providing measurement system ODC2600. The authors would also like to thank MICRO-EPSILON Company for the technical data and measurement principle used in this research.

REFERENCES

[1] I.C. Sheng et al., “Design and Analysis of EPU XBPM in TPS“, MOPPR050, IPAC12, New Orleans, Louisiana, USA (2014).

[2] N. Hubert, et al., “Design of new blade type X-BPM“, WEPD22, IBIC, CA, USA(2014).

[3] Measurement system ODC2600N, MICRO-EPSILON Eltrotec GmbH , Germay.

Content from this work may be used under the terms of the CC BY 3.0 licence (© 2016). Any distribution of this work must maintain attribution to the author(s), title of the work, publisher, and DOI.

ISBN: 978-3-95450-188-5 doi:10.18429/JACoW-MEDSI2016-MOPE24

THE PRECISION ADJUSTMENT HOLDER FOR MONTEL MIRRORS

Bo-Yi Chen†, Gung-Chian Yin, Shi-Hung Chang, Huang-Yeh Chen, Chien-Yu Lee, Bi-Hsuan Lin, Shao-Chin Tseng, Jian-Xing Wu, and Mau-Tsu Tang, National Synchrotron Radiation Research Center, Hsinchu 30076, Taiwan
J. Raynien Kwo, National Tsing-Hua University, Physics Department, Hsinchu 30076, Taiwan
Minghwei Hong, National Taiwan University, Physics Department, Taipei 10617, Tawian

Abstract

The focusing of X-ray nanoprobeat Taiwan Photon Source (TPS) relay upon the special designed Montel mirrors and its adjustment holder, which significantly shorten the length of beamline to 75 meters. Moreover, the focal spot size and working distance are expected to be 40 nm and 55 mm, respectively. To achieve this, the precision adjustment holder was designed and made to align Montel mirrors. The holder includes two major parts: (1) fundamental-position alignment part and (2) relative-position adjustment part.

The fundamental-position alignment part has the ability to adjust the two mirrors together in six degree of freedoms, such as X, Y, Z, pitch, roll, and yaw. These translation stages have several-tens mm travel range and nm resolution, while the rotational stages have around 40 mrad azimuthal angular range and 0.1~0.01 μrad resolution.

The relative-position adjustment part can further adjust the two mirrors to minimize the focal spot. During the pre-alignment process, one of the mirrors can be manual adjusted by micrometer heads (Mitutoyo®) in three translation directions with several mm travel range and micrometers resolution. These micrometer heads also provide this mirror three rotational degree of freedoms with sub-mrad resolution. For the further alignment in vacuum chamber, the additional four piezo-motor (PiezoMotors®) actuators can precisely adjust the other Montel mirror in the Y and Z direction with several nm resolution, and its pitch and roll with 1 urad and 0.05 urad resolution, respectively.

The precision adjustment holder will be installed in TPS-23A endstation and start commission before the end of this year.

MONTEL MIRRORS FOR HARD X-RAY FOCUSING

The Montel mirrors were adopted to focus the hard x-ray down to hundreds even tens of nano-meters in synchrotron beamlines[1-4]. There many nano-focusing optics, such as K-B mirror, Zone Plate, refractive lens, and Montel KB mirror. Different optics have different focusing ability.

According to the study done by Gene E Ice et. al [1], The numerical aperture is limited by the critical angles of the mirrors. Besides, the numerical aperture can be enlarged if more reflections are accompanied for focusing. Therefore, it is very clear that the numerical aperture is enlarged by factor of root 2 theoretically, because the Montel mirrors consists two reflections from identical two plane-ellipse mirrors close to each other. The focus principle is to hit one side of the mirror than the other side.

The Montel KB mirror has better chromatic dependence, higher flux and longer working distance. For the application in TPS-23A, we adapt the Montel mirror as the nano-focusing optics, which gives a larger numerical aperture as well as higher flux than conventional K-Bs.

TPS-23A BEAMLINE

There are two horizontal focusing mirrors and one horizontal DCM in the beamline. In order to preserve the coherent in vertical direction, there no other focusing optics before montel KB mirrors, and it is windowless. Finally, we use montel KB mirror to focus the beam down to 40 nm, and the photon flux can be larger than ten to the power of 10. The length of this beam line is less than 70 m. In order to fully use the symmetrical manner of the Montel mirrors, the horizontal optics is more complicated. The HFM1 focuses the horizontal beam at slits3 and he HFM2 defocuses and pull back the source back to the center of the undulator. With this plan, the source becomes a symmetrical source. The sketch of TPS-23A is shown in Fig. 1.

According to the ray tracing simulation results, if the beam energy is 10 keV and average reflection coefficient is 0.83, the source is 65m up stream to the mirrors, the source size is 12.5 μm x 12.5μm, and the source divergence is 6μrad x 6μrad, we can found that the final spot size is around 40 nm and the divergence is 6.29 mrad. The flux is estimated to be 2x1010 Photon/second.

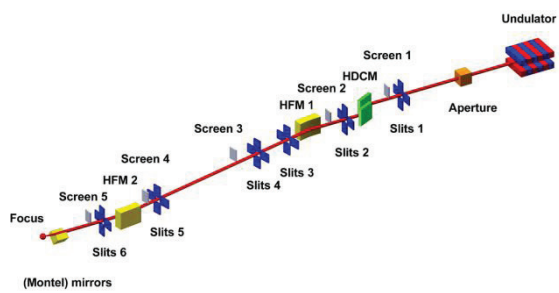


Figure 1: The beamline sketch of TPS-23A.

MONTEL MIRRORS OF TPS-23A

The specification of Montel mirrors adopted in TPS-23A is described as following. The length of the mirror is 110 mm, and the working distance is 55 mm. The very high demand on the slope error is 0.05 μrad, which is the best quality that can be made which is limited by the

Content from this work may be used under the terms of the CC BY 3.0 licence (© 2016). Any distribution of this work must maintain attribution to the author(s), title of the work, publisher, and DOI.

ISBN: 978-3-95450-188-5 doi:10.18429/JACoW-MEDSI2016-MOPE24

Content from this work may be used under the terms of the CC BY 3.0 licence (© 2016). Any distribution of this work must maintain attribution to the author(s), title of the work, publisher, and DOI.

minimum radius of the mirror, which is 20 meter. The material of mirror is silica and coated with rhodium.

The Montel mirrors are placed on the top of mirror holder, as shown in Fig. 2. With the precise alignment of two mirrors, the focal spot size can down to 40 nm. At the same time, the working distance is around 55 mm, which provides the more space and probability to assemble variable detectors, probes and instruments into the endstation.

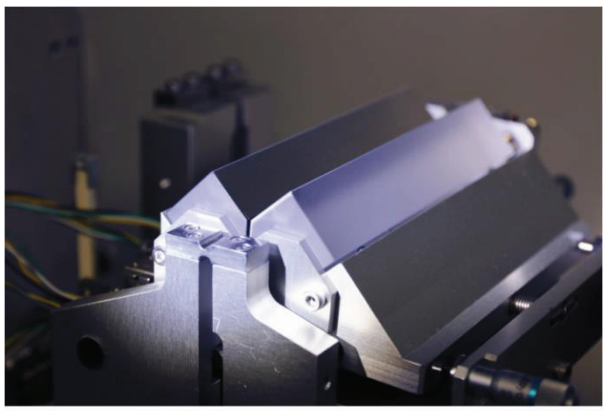


Figure 2: The Montel mirrors of TPS-23A.

TPS-23A ENDSTATION

TPS at NSRRC is already successful for the test operation at the end of 2014. So, at this time our goal is to construct the phase I beamline of TPS. There are seven beamlines in the phase I. And the Nanoprobe project is one of them. This nanoprobe beamline will be delivered at the end of 2016. Due to the cite condition, some part of the TPS storage ring is constructed underground, therefore the length of the beamline is limited. The longest beamline is actually only 75 meters. It is a big challenge to build a modern x-ray nanoprobe beamline with only 75 meters. Therefore, we need a special focusing device, that is Montel mirros.

The X-ray nanoprobe (TPS-23A) is designed to use TPS light source to resolve the atomic, chemical and electronic structures of the semiconductor-based nano-devices in tomographic and nondestructive manners. The Montel KB mirror is adopted to focus the beam down to 40 nm.

Then the end station can provide x-ray probes of imaging, spectroscopy and diffraction, and coherent way. In addition, the station will equipped with SEM, photoluminescense and a stream camera to perform the time-resolved measurement. The sample environment of this beamline is : the sample is in vacuum, and we have a load lock system, the sample can be heat up or cool down, measure some electrical property in our main chamber or preparation chamber. The sketch of TPS-23A endstation is shown in Fig. 3.

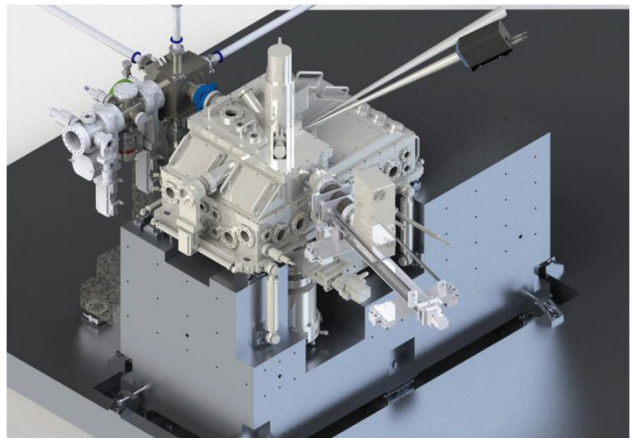


Figure 3: The Sketch of TPS-23A Endstation.

PRECISION ADJUSTMENT MIRROR HOLDER

The idea of Montel nested mirrors has been tested at APS, and a focal spot of 150 nm has been achieved [1]. However, the Montel is not been commonly used as an optics for a nano-focusing beamline for two reasons: first, the gap between the two mirrors is very difficult to control and second, the slope error requirement is very hard to achive. The issue of slop error have been overcome in last two years, by adapting Elastic emission machining(EEM) techniques, which was developed by Osaka University. In this status, the key issue of nano-focusing is how to align and adjust the Montel mirrors. The sketch of the mirror holder is shown in Fig. 4.

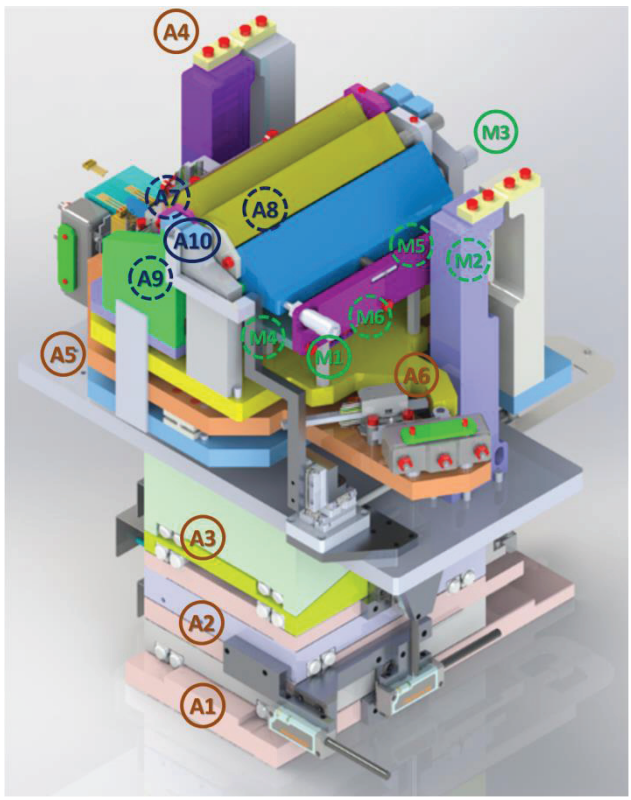


Figure 4: The Sketch of Mirror Holder.

ISBN: 978-3-95450-188-5 doi:10.18429/JACoW-MEDSI2016-MOPE24

As shown in Fig. 4, the mirror holder is designed to precisely adjust the Montel mirror simultaneously and independently in three translation and three rotational directions. The adjustment mechanism A1~A6 can be used to move the two mirrors together in six degree of freedoms. The other four motorized axis: A7~A10 can further align the relative position between two mirrors, which is very important to focus the spot size down to tens of nano-meters. Moreover, to roughly define the position of mirror, one of the mirrors can be manual adjust its position by micrometer heads (Mitutoyo®) in three translation directions with several mm travel range and micro-meters resolution. These micrometer heads also provide this mirror three rotational degree of freedoms with sub-mrad resolution.

Before the holder assembling with the endstation, the relative position of two Montel mirrors should be pre-alignment by the tilt sensor and two optical microscopes, as shown in Fig. 5. The orthogonality of the two mirrors can be adjusted in the range of $90^{o} \pm 15$ min and the gap between two mirrors is less than 10 um. The resolution and travel range of this mirror holder is listed in Table 1.

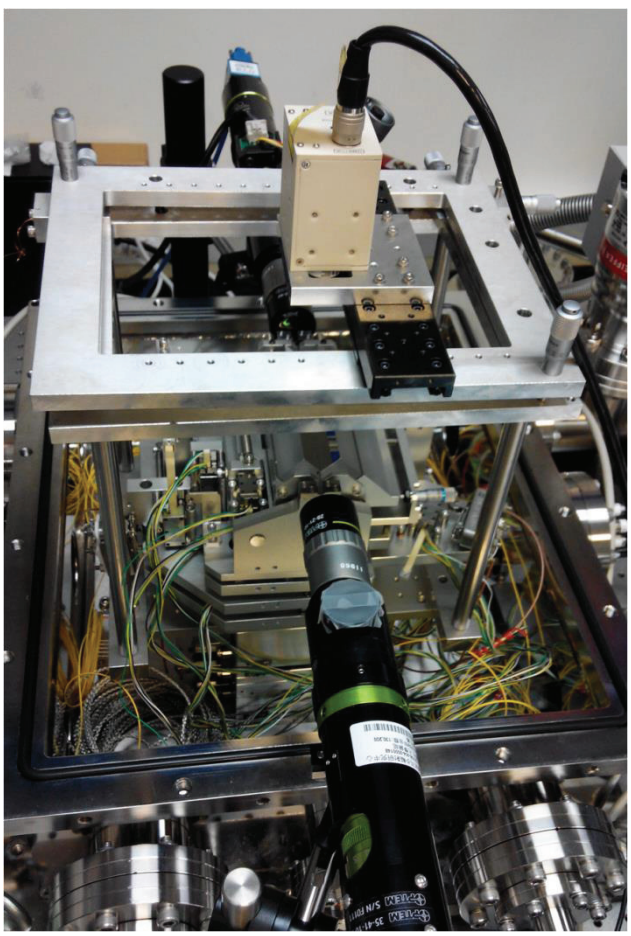


Figure. 5 The Pre-alignment System.

CONCLUSION

In this work, the precision mirror older for the Montel mirrors were designed and made. The two mirrors can be adjusted and aligned simultaneously and independently by micrometers and piezomotors. The adjustable ranges are around 1~24 mm and 1~50 mrad for translation and rotational degree of freedom, respectively. Moreover, the minimum step size is about 1 nm and 0.01 urad .

The precision adjustment holder will be installed in TPS-23A endstation and start commission before the end of 2016.

Table 1: The Resolution and Travel Range of Holder

NO.	Translation/ Rotaiton	Resolution (um/urad)	Travel range (mm/mrad)
A1	Y	0.002	24
A2	X	0.002	10
A3	Z	0.001	10
A4	Pitch	0.01	40
A5	Roll	0.05	50
A6	Yaw	0.01	40
A7	Top-Y	0.01	1
A8	Top-Z	0.01	1
A9	Top-Pitch	0.05	1
A10	Top-Roll	1	1
M1	Top-X	5	1
M2	Top-Yaw	50	10
M3	Top-Y	5	1
M4	Top-Z	5	1
M5	Top-Pitch-II	50	10
M6	Top-Roll-II	100	5

ACKNOWLEDGEMENT

We would like to thank Dr. JÖrg Maser at APS, Prof. K. Yamauchi at Osaka University, and Dr. Gema Martinez-Criado at ESRF for the help in the initial of this project and technical development during the task.

REFERENCES

[1] Gene E. Ice, Rozaliya I. Barabash, and Ali Khounsary, "Nested mirrors for x-rays and neutrons," Published in SPIE Proceedings Vol. 7448: Advances in X-Ray/EUV Optics and Components IV, 2009.

[2] Giacomo Resta, Boris Khaykovich and David Moncton, "Nested Kirkpatrick–Baez (Montel) optics for hard X-rays," Journal of Appl. Crystallography, Vol. 48, pp. 558–564, 2015.

[3] Gung-Chian Yin, Shi-Hung Chang, Bo-Yi Chen, Huang-Yeh Chen, Bi-Hsuan Lin, Shao-Chin Tseng, Chian-Yao Lee, Jian-Xing Wu, Shao-Yun Wu, and Mau-Tsu Tang, "Hard x-ray nanoprobe by Montel KB mirrors at Taiwan Photon Source," Published in SPIE Proceedings, Vol. 9592, 2015.

[4] Wenjun Liu, Gene E. Ice, Lahsen Assoufid, Chian Liu, Bing Shi, Ruben Khachatryan, Jun Qian, Paul Zschack, Jonathan Z. Tischler, and J.-Y. Choic, "Achromatic nested Kirkpatrick–Baez mirror optics for hard X-ray nanofocusing," Journal of Synchrotron Radiation, Vol. 18, pp. 575–579,2011.

Content from this work may be used under the terms of the CC BY 3.0 licence (© 2016). Any distribution of this work must maintain attribution to the author(s), title of the work, publisher, and DOI.

ISBN: 978-3-95450-188-5 doi:10.18429/JACoW-MEDSI2016-MOPE26

FRONT END PHOTON SHUTTER WATER LEAK TO VACUUM AT THE CANADIAN LIGHT SOURCE

G. Henneberg*, G. Barkway, M. J. P. Adam, Canadian Light Source Inc., Saskatoon, Canada

Abstract

A leak in the Hard X-Ray MicroAnalysis (HXMA) front end (FE) Photon Shutter (PSH1) absorber was found and temporarily repaired with no delay in returning the CLS to normal operations. The leak was caused by a large amount of erosion to the interior surface of the cooling channel, due to excessive flow rates (>7.0 m/s). Similar photon shutters currently operating under similar conditions are at risk to fail (19 photon shutters in total). Due to damage they may have sustained operating under similar operating conditions, photon shutters of this design currently in service should be either examined or replaced.

INTRODUCTION

Leak Discovery & Repairs

July 2nd, 2016 Accelerator Operations and Development (AOD) discovered a vacuum event at the Canadian Light Source (CLS) for Storage Ring (SR1) cell 6. Initially, the event was believed to be a air leak located in either the SR1, Soft X-ray for Microcharacterization of Materials Beamline (SXRMB) FE, or the HXMA FE.

A collaborative decision was made to wait to find the exact location of the leak. The mechanical technicians first activated a scroll pump in an attempt to pump down the affected section. Water was discharged from the exhaust of the scroll pump, which indicated the water leak. After determining that the leak had originated in the HXMA FE, the technicians identified which components may have failed. By the afternoon, they had discovered a small pinhole leak on the absorber head of the first HXMA photon shutter (Fig. 1).

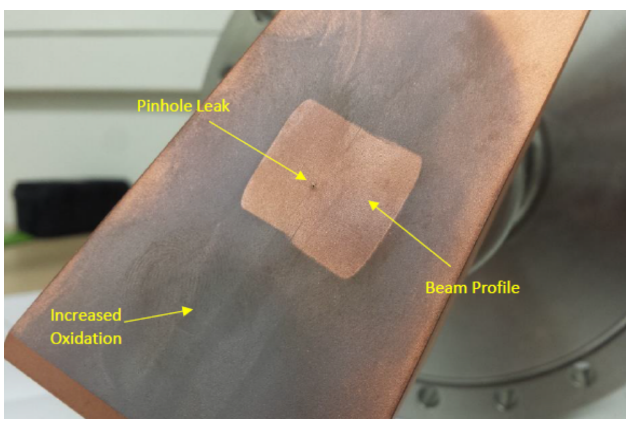


Figure 1: Illustration of the pinhole leak discovered on HXMA PSH1. Leak location is aligned precisely with water jet location of the tube in tube cooled absorber.

* grant.henneberg@lightsource.ca

HXMA Front End Photon Shutter

Estimated heat load for the absorber was found to be 200 W–300 W (for 250 mA ring current). Fortunately, a spare photon shutter previously ordered for the Industry Development, Education, Applications, and Students (IDEAS) beamline was available that satisfied the heat load requirements. The replacement was a Phase II type photon shutter. Technicians oversaw the initial bakeout of affected components (lasting four days). The electron beam was activated to further improve the vacuum quality, using four injections per day to maintain current in the SR1. Equipment testing continued until July 12th, at which point the CLS resumed regular operation. The leak delayed standard start up procedures performed by AOD at the end of the shutdown by seven days, but beam was available to users as scheduled. The PSH1 had been operational since HXMA was commissioned in 2006 (Fig. 2). This type of absorber is similar to a Advanced Photon Source (APS) design and is used to stop bend magnet radiation from the SR1 dipoles when the HXMA Insertion Device (ID) and beamline are turned off. Cooling for the component is provided by running water

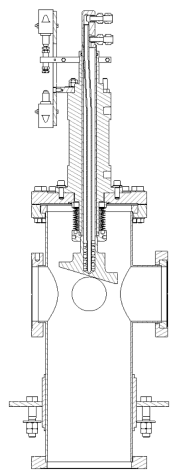


Figure 2: PSH1 absorber style from the front end location of HXMA beamline. The beam path as the absorber is shown is from left to right, with absorption of photon energy along the grazing surface of a tube in tube OFHC absorber.

through the head of the absorber. The leak developed at (or very near) the centre of the absorber's face (Fig. 1). There are six other photon shutters that employ this exact same design currently in use at CLS. There are also 12 photon shutters that are derivatives of this design. Their cooling system and operational parameters are almost identical. Therefore, it is necessary to identify why failure occurred, how it can be prevented, and/or if other components are at risk to fail.

Content from this work may be used under the terms of the CC BY 3.0 licence (© 2016). Any distribution of this work must maintain attribution to the author(s), title of the work, publisher, and DOI.

ISBN: 978-3-95450-188-5 doi:10.18429/JACoW-MEDSI2016-MOPE26

BACKGROUND

PSH1 Cooling

The HXMA PSH1 used cooling water supplied by the SR1 low conductivity cooling water (LCW). The maximum supply pressure is 150 psi, and the return is 35 psi. Table 1 details the flow parameters through the PSH1 at the time of failure. These flow parameters have been employed since 2011 for all PSHs of the same design within the CLS SR1. The cooling water system for the SR1 was not filtered for

Table 1: Flow Parameters through HXMA PSH1at the time of failure. Retrieved from CLS data archive and flow meters for the PSH

Parameter	Value
Flow Rate [kg/s]	0.21
Inner Tube ID [mm]	6.35
Inner Tube OD [mm]	9.525
Outer Tube ID [mm]	20.8
Supply Velocity [m/s]	7.12
Return Velocity [m/s]	0.82
Supply Re	55,000
Return Re	15,000
Pressure Drop [psi]	61

the first eight years of operation. A filter system was put in place in 2013. Since the installation, 24 filter bags of fine grain sediment have been removed from the cooling water system. It is not clear how long the sediment was travelling through the water pipes or the effect it had on the system. The sediment may have promoted erosion in the pipes by acting as an abrasive agent or removing the passivated oxidized layer and increasing corrosion.

INVESTIGATION OF FAILURE

The PSH1 was cut apart to reveal its interior structure (Fig. 3). After visual inspection and discussions, cause was

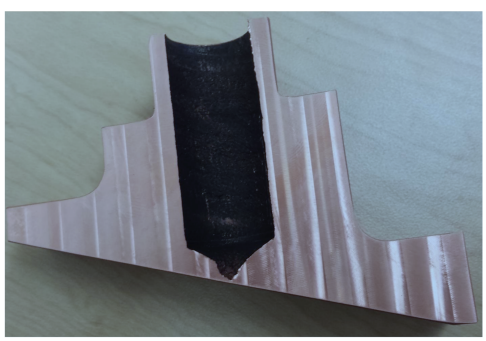


Figure 3: Section cut of failed PSH1, used to investigate extent of damage and location of erosion.

suspected to be degradation of the copper walls due to corrosion, erosion, or impingement damage. Operating conditions of HXMA PSH1 (at >7.12 m/s) exceeded CLS's maximum flow velocity standard of 2.5 m/s [1]. The typical maximum operating velocity of any cooling water channel in the facility is set at max 2.5 m/s.

The HXMA PSH1 is based off of the APS design (Fig. 4). Jeffrey T. Collins, an APS employee, was contacted to determine if this style of photon shutter had a history of leaking. He was the lead author on a paper detailing the heat transfer benefits of using a coil insert for high heat load components [2]. APS has not dealt with such an issue before, but Jeffrey provided CLS with a report on a RF window that had suffered a pinhole water leak into vacuum [3]. The report explains that the RF window's cooling water caused large erosion-corrosion on the copper walls due to excessive flow rates (>5.3 m/s). The inner surface above the coil insert

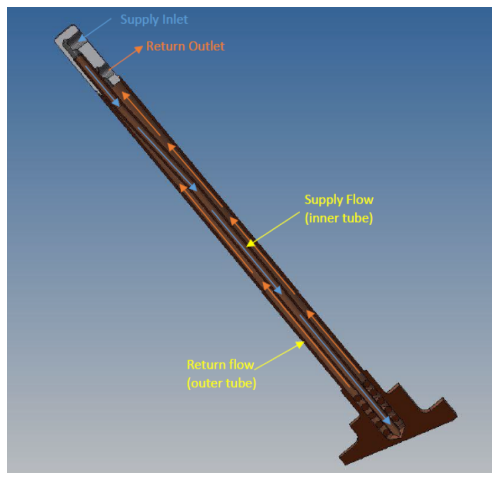


Figure 4: Illustration of the tube-in-tube configuration of PSH1. Cooling water enters from the inner tube and exits the outer tube passage.

has random pitting. There is no distinguishable pattern that suggests the motion of the water was anything but chaotic. Further upstream from the coil insert, the etch marks are thicker, with longer black lines intermixed with the copper. Closer to the coil, however, the etch marks are smaller and closer together.

At the very top of the coil, a hole on the wall of the inner tube formed, allowing water to escape into the return flow without travelling to the base cavity. The hole is roughly 4 mm long and 3 mm wide. The holes sits directly beneath the end of the coil (Fig. 5). There is significant material degradation around the hole and the pipe wall is very thin.

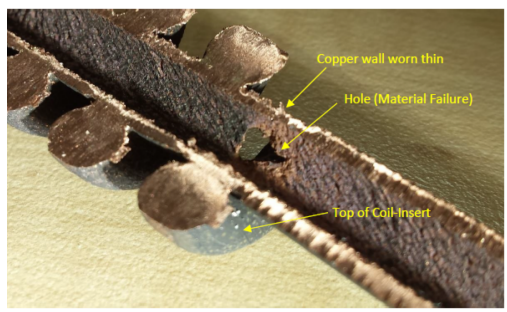


Figure 5: Section cut of eroded inner copper tube.

Content from this work may be used under the terms of the CC BY 3.0 licence (© 2016). Any distribution of this work must maintain attribution to the author(s), title of the work, publisher, and DOI.

ISBN: 978-3-95450-188-5 doi:10.18429/JACoW-MEDSI2016-MOPE26

Content from this work may be used under the terms of the CC BY 3.0 licence (© 2016). Any distribution of this work must maintain attribution to the author(s), title of the work, publisher, and DOI.

DISCUSSION

The large amount of pitting was most likely caused by erosion-corrosion. The velocity of the water (7.2 m/s) was nearly three times the maximum recommended speed [1]. Excessive speed creates high amounts of turbulence that strips away the walls of the pipe. This was evidenced by the extensive pitting inside the inner tube, and smooth surface of the outer tube (where the velocity was reduced to 0.82 m/s). Inside the base cavity, where the supply flow makes contact with the inner absorber cavity, the erosion had a spiral profile. The disfigured surface at the base of the cavity appeared to be eaten away by a high velocity stream or vortex. Large amounts of localized turbulence can attack the pipe wall and absorber, carrying away material leaving a pitted surface [4].

The high velocity jet may have also caused cavitation on the inner surface of the absorber. Cavitation is the implosion of vapour suspended in a liquid against the surface of its container. The implosion of vaporous cavitation bubbles can cause significant pitting [5, 6]. Further analysis is recommended to determine the exact failure mechanism within the HXMA PSH1.

The mechanism causing failure of the sidewall (Fig. 5) is not well understood. Its effect on the system is difficult to determine for the following reasons:

1. 1. The hole formed at an unknown time in the absorbers' operation.
2. 2. The rate at which the hole grew cannot be determined.
3. 3. The flow pattern, velocity, and pressure drop due to the hole are unknown.

It is clear, however, that the location that the hole formed was unique. The hole sat right at the end of the coil, near a change in diameter on the outside of the tube. The pattern of erosion/corrosion on the inside surface changed abruptly on either side of the hole.

The hole may have formed for a multitude of reasons. There may have been localized turbulence as the fluid exited the spiral, increasing the rate of erosion-corrosion. Faulty brazing/soldering work between the coil insert and the tube may have weakened the tube wall. The hole may have formed along the edge where the tube diameter changed creating a larger stress concentration.

CONCLUSION

The HXMA PSH most likely failed due to excessive fluid velocity (7.12 m/s). This was evidenced by the inner pipe's extensive surface damage and the spiral crater that formed at the base of the absorber. The high velocity fluid resulted in erosion and/or erosion-corrosion within the pipe. A troublesome finding was observed with the sidewall hole within the inner pipe. The effects of this hole are not well understood and require further analysis.

The photon shutter's design is susceptible to erosion if excessive flowrates are used. The inner tube was too narrow to supply the necessary flowrate without exceeding CLS's maximum fluid velocity. The narrow tube's outlet created an impinging water jet on the absorber head that may have increased the rate of erosion.

Recommendations

To prevent further degradation in similar photon shutters, flow rate should be evaluated to determine if a lower velocity is adequate (reducing the likelihood of similar HXMA PSH1 failures). Continuing to operate under current conditions may lead to further absorber failures, water leaks, and vacuum leaks. Due to damage they may have sustained operating under similar operating conditions, PSH of this design currently in service should be either examined or replaced at the CLS's earliest convenience. PSHs installed during the Phase II expansion are similar in design and operating conditions; flow velocity settings should be reviewed, but these absorbers may not need replacement.

ACKNOWLEDGMENT

Special thanks to Harley Berndt, Ben Boyachek, Shawn Carriere, Ning Chen, Duane Chipley, Jeff T. Collins, Riley Lander, Linda Lin, Kristin Lunde, Chris Regier, Luke Robson, Bryan Schmiedge, John Swirsky, Jeff Wetzel, Larry Wiebe, Ward Wurtz, and Kevin Wyatt.

REFERENCES

[1] "CLS Photon & Safety Shutter Design Specification, 8.4.41.1 Rev. 0", Canadian Light Source Inc. Saskatoon, Saskatchewan, Canada

[2] J.T. Collins *et al.*, "Enhanced Heat Transfer Using Wire-Coil Inserts for High-Heat-Load Applications", in *Proc. MEDSI'02*, Argonne, Illinois USA, 2002, pp. 409-419

[3] J.T. Collins, "RF Window Failure Analysis & Suggested Corrective Actions", *Argonne National Laboratory, ICMS # 1285316*

[4] Nace International, "Erosion", https://www.nace.org/Corrosion-Central/Corrosion-101/Erosion/

[5] J. M. Coyne, "Flow Induced Failures of Copper Drinking Water Tube", Virgina Polytechnic Institute and State University, 2009

[6] G. W. Vickers and R. Houlston, "Modelling the erosion efficiency of cavitation cleaning jets", *Appl. Sci. Res.*, 1983, 40: 377. doi:10.1007/BF00383042

ISBN: 978-3-95450-188-5 doi:10.18429/JACoW-MEDSI2016-MOPE27

THE INFLUENCES OF MATERIAL PROPERTIES TO MICRO DAMAGES ON VACUUM CHAMBER CF FLANGES

S. Vilcins, M. Holz, M. Lemke, D. Nölle, Chr. Wiebers, DESY, Hamburg, Germany

Abstract

The European-XFEL, a 3.3 km long X-Ray laser facility, powered by a 17.5 GeV superconducting linear accelerator, is located at DESY in Hamburg [1]. For the diagnostics ultra-high vacuum components with high mechanical precision and strict requirements on particle cleanliness had to be developed, designed and produced. For the screen system of the facility, enabling to observe the size and shape of the electron beam, massive vessels, precisely milled out of stainless steel blocks 1.4435 (316L) have been produced. For these chambers all flange-connections are milled into these blocks. This paper will report on micro damages in these integrated knife edges and will present simulations of the damage mechanisms. It will also describe the influences of material properties of two different stainless steel brands, effects on the "knife edge" due to the penetration into the gaskets as well as the non-elastic deformation of the sealing area. The dependence of tightening forces under special conditions, like the very clean conditions in particle free applications due to the non-lubricated conditions will be reported. A "cooking recipe" to avoid such micro damages will be given.

INTRODUCTION

Particle accelerators are used as standard as well as and special diagnostics, also for the European XFEL (E-XFEL) at DESY, Hamburg. A scintillation screen monitor system [2] has been designed for diagnostic purposes in particle beams. For this system two different types of special vacuum chambers have been fabricated. More than 50 vacuum chamber with weights over 50 kg have been fabricated out of massive blocks. These two versions of chambers are varied, one with five and the other with eight Conflat (CF) [3] knife edge flanges allowed attaching other diagnostic devises. In this paper the two types call type A/C and B. For type B see Fig. 1.

The biggest amounts of the chambers have to be assembled and installed in particle reduced environment in different sections of XFEL. The vacuum leak for the UHV system rate has to be below $1*10^{-10}$ mbar l/s and tightened with copper flat gaskets.

The geometry of these chambers had to be chosen so that they match the requirements of independency and stability; therefore a massive stainless steel (SST) block was used.

SST is one of the most commonly used constructional materials for vacuum chambers and other vacuum components in general. Applications like vacuum vessels in linear accelerator or storage ring facilities require ultra-high vacuum (UHV). Finding an appropriate source for the raw material in 316 LN was the first step. The dimensions of these vessels are bigger than all designs at DESY have been in the past. Since it was very difficult to find any supplier for material in 316 LN, a compromise was found to use 316 L.

The raw material was ordered according to DESY material specification for 316 L. Essential a 3.1 certification was sent before the order was placed. In this specification of DESY the boundaries of hardness are between 160 and 200 Brinell Hardness (HB). In the material certification the value for the hardness was a little bit under the minimum bounder of DESY's specifications with 158 HB. The raw material was accepted by DESY. All vacuum chambers were manufactured by outside vendors at two companies. Rest gas analysis was not specified. The final assembling has been done at DESY.

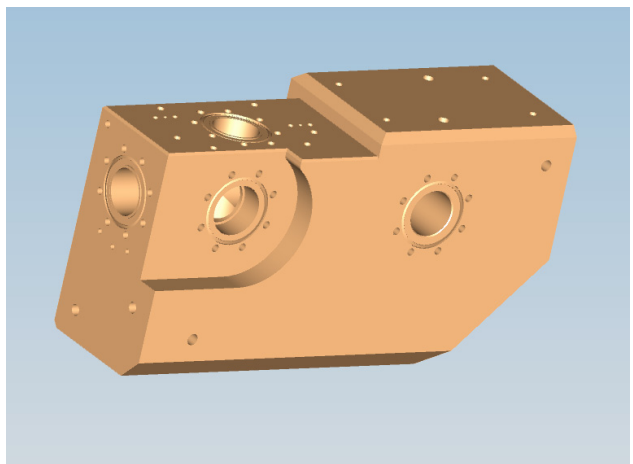


Figure 1: Show a vacuum chamber Type B with adaption ports for other diagnostic devices.

The two prototypes, one for each version, have been successfully tested under UHV conditions at DESY group Machine Diagnostic and Instrumentation (MDI).

After a European wide open call for tender the two versions were placed at two different manufactures in Germany. The cleaned and packaged chambers arrived at DESY and they had to be stored for about 1 year before final assembling. During the final assembling, in a class 5 cleanroom, cleanness problems were detected on one of the attached vacuum window. Due to these problems all chambers had to be dismounted and inspected. During this inspection by chance micro damages on the sealing areas of the CF knife edge were detected. DESY calls this appearance "orange skin" (see Fig. 2). After a few chambers have been cleaned and reassembled the final leak check had shown vacuum tightness problems.

Content from this work may be used under the terms of the CC BY 3.0 licence (© 2016). Any distribution of this work must maintain attribution to the author(s), title of the work, publisher, and DOI.

ISBN: 978-3-95450-188-5 doi:10.18429/JACoW-MEDSI2016-MOPE27

Content from this work may be used under the terms of the CC BY 3.0 licence (© 2016). Any distribution of this work must maintain attribution to the author(s), title of the work, publisher, and DOI.

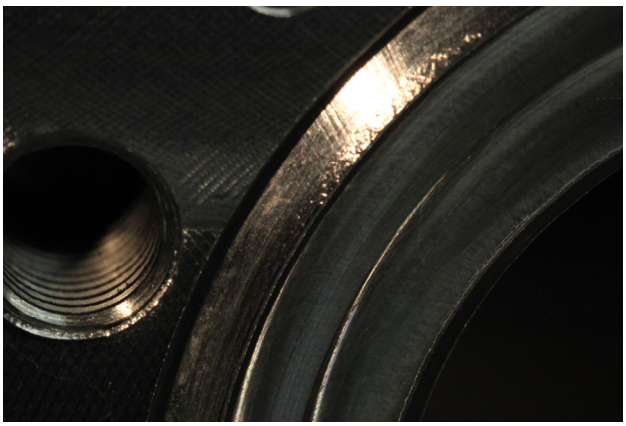


Figure 2: Show of the micro damages ("orange skin) on sealing surface.

The SST material characteristics turned out to be more complicated as expected. The challenge was to produce these massive vacuum chambers without quality problems. Therefore more detailed specifications had to be defined.

GENERAL INFORMATIONS OF SST MATERIAL, MANUFATURING AND VACUUM SEALING TECHNOLOGY

The first industrial development with stainless steel is dating to around 1910. Since the beginning SST has become more and more recognized. The none magnetic properties, durability of surface conditions, good welding properties and exceptional corrosion resistance have made this material group one of the major materials for constructing vacuum systems in accelerator technology.

All institutes worldwide have made their own experiences in building a lot of different accelerators. Most of them have different material specifications. The different accelerators can roughly be classified in warm or cold and linear or circular accelerator. All require different vacuum flange technology, boundary, purity classification and material permeability.

Therefore, there is a need for better knowledge of the intrinsic properties of stainless steels, including corrosion and oxidation resistance, high temperature mechanical strength, material peculiarity and together with all the other characteristics necessary for their use as material.

But even more important are the properties to be processed by various cold and hot forming techniques, like the remelting processes electro-slag or vacuum remelting and the different methods of joining and vacuum brazing. The gasket sealing technologies are defined by the American Vacuum Society [4]. The goal was to seal vacuum connections effectively by compressing a gasket between parts to be sealed.

The choice of the adequate flange/gasket system is driven by the requirements of the vacuum system. Different material selections for gaskets are on the market.

They can be separated into two groups, metal and non-metal gaskets. For both groups there are gaskets for single and multiple use. Another difference is given by the geometry of the gasket. For CF, ISO [5] or KF [6] flange connections flat gaskets are used. Furthermore gaskets with special kinds of geometries are in use for other flange concepts. The last aspect is the vacuum tightening principle. Gaskets can be tightened under pressure or using under shear. Different vacuum qualities are defined by pressure levels, like vacuum ($<1*10^{-7}$ mbar), high vacuum (HV $<1*10^{-8}$ mbar), ultra-high vacuum (UHV $<1*10^{-10}$ mbar) and extreme UHV (XHV better $<1*10^{-10}$ mbar).

An overview of common gaskets in vacuum applications is shown the following two tables. The various types of gaskets can be classified in following groups: The first group, presented in Table 1a, is the soft on hart group. The gasket material is declared as the soft part. The flanges are even been the hart part in these combinations. In Table 1b the gasket materials are made of hard material, too.

Table 1a: Soft on Hard

Type	Material	Multiple use	Pressure level
O-Ring	Natural rubber	yes	vacuum
O-Ring	Rubber	yes	vacuum
O-Ring	PTFE	yes	vacuum
O-Ring	FKM	yes	vacuum/high
O-Ring	FFKM	yes	vacuum/high
Wire	Indium	no	high/UHV
Wire	Lead	no	high/UHV
Wire	Gold	no	UHV/XHV
Wire	Silver	no	UHV/XHV

Table 1b: Hard on Hard

Type	Material	Multiple use	Pressure level
Flat/Profile	Alu	no	UHV/XHV
Flat/Profile	Copper	no	UHV/XHV
Ring	Steel/Alu[1]	yes	UHV/XHV
Flat/Profile	SST	yes	UHV/XHV

[1] A combination with steel spring and cover ring of aluminium (HELICOFLEX®)

Theoretically gas penetration can occur from outside into the evacuated vacuum system with two different mechanisms. Gas can penetrate through the gasket material directly or can pass between surfaces of gasket and the seat of the flange.

ISBN: 978-3-95450-188-5 doi:10.18429/JACoW-MEDSI2016-MOPE27

The sealing process is expressed by:

$$C = 1.93 * 10^4 \sqrt{\frac{T}{M}} \frac{2\pi A^2}{\ln(r_0/r_i)\ 8.12} Ke^{-3\frac{P}{R}} \quad (1)$$

- C is the conductance (of these two ways) in cm^3/sec
- T and M are temperatures in K
- r_0/r_i are outside and inside gasket radius in cm
- K is a factor of surface roughness or surface condition (scratches, dent or waviness…) [7]
- P tightening pressure in kg/cm^2
- R is the sealing factor in kg/cm^2 [7]
- Is the peak to valley value of the surface roughness

ALTERNATIV TEST PROCEDURES

As mention before deformations at the Conflat knife edges had been detected, all chambers were dismounted and were checked visually with the result of the "orange skin" on many knife edges. It was tried to seal the chambers with alternative sealing technologies, like soft copper gaskets, taper sealed (TS) gaskets (hart and soft) and at least aluminium gaskets. But no technology worked. Thus all the vacuum chambers were sent back for refinishing.

After rework of all vessels we tried to seal the chamber a second time with soft annealed copper gaskets and with hard and soft TS gaskets, but we had the same result as before reworking of chambers.

At least aluminium gaskets were chosen. Only the aluminium gasket had sealed the chamber reliably, but this technology was not accepted for the XFEL vacuum-system.

After a lot of different type of gaskets with variable hardness conditions had been tested, DESY made the decision to rebuild all the 50 vacuum chambers for E-XFEL.

HARDNESS CHECK

To find the reason for the "orange skin" one Type B chamber the hardness was checked at DNV GL [8] in Hamburg (see Fig. 3). This first test showed a discriminated value to raw material certification. The results varied between 145 and maximum 154 HB.

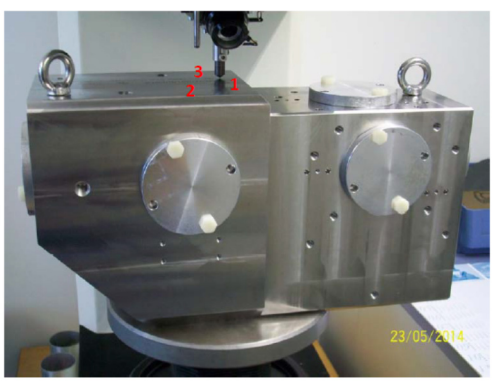


Figure 3: Show of the hardness test of one type B vacuum chamber.

In the second step all the vacuum chambers were tested by mobile hardness measuring. By measuring test parts and comparing them with mobile hardness there was only 0.5 to 1 HB difference. Due to the mobile measurements with a Krautkramer MIC 20 testing device at DESY at most chambers a smaller hardness than certified was detected.

One type A/C chamber with 164 HB had the highest value. The minimum value was 122 HB. The average of 20 chambers type A/C was 135 HB. The type B vessels didn't show different results. The minimum value was 129 HB and one chamber had a maximum of 151 HB. The average of type B was 137 HB.

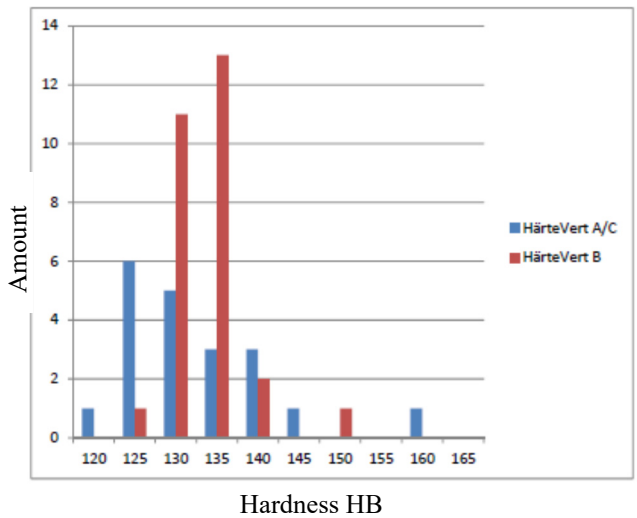


Diagram 1: Show of hardness comparison between type A/C and B.

Moreover the hardness of the raw material was checked, too. The results were in the same bounders of the chambers. Minimum value was 141 HB and maximum was 152 HB. The measurements have been done at DNV GL in Hamburg (see Diagram 1).

MATERIAL ANALYSIS AND INSPECTIONS

This chapter describes same of the test procedures done for checking other material properties. The specific parameter of non-metal parts, embattling into the raw material, determine the grain of purity, and critical grain size had been checked by using different methods and inspections. The results were compared to the material certification and did not fulfil the DESY material specification.

In a following step a part of the knife edge was cut out and was inspected by a 3D microscope. In the Figure 4 the damages of the knife edge is shown by 10 x magnifying.

Content from this work may be used under the terms of the CC BY 3.0 licence (© 2016). Any distribution of this work must maintain attribution to the author(s), title of the work, publisher, and DOI.

ISBN: 978-3-95450-188-5 doi:10.18429/JACoW-MEDSI2016-MOPE27

Content from this work may be used under the terms of the CC BY 3.0 licence (© 2016). Any distribution of this work must maintain attribution to the author(s), title of the work, publisher, and DOI.

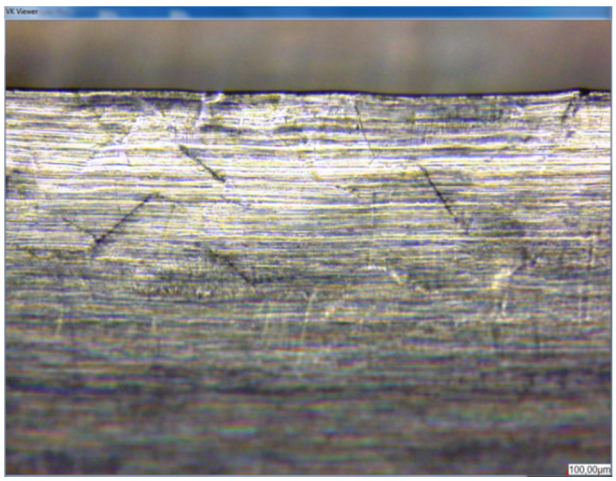


Figure 4: 3D picture of microscope inspected the knife edge of CF flange (rectangle to the 20 ° knife position).

In the Figure 4 crossing lines are burred approx. 0.3 to 0.4 mm deep into the material. The structure of expansion and appearance looks like the stainless steel material grain structure. This visual inspection shows perfectly the "orange skin" surface structure. These massive damages on the CF knife edges are serious problems and have to be understood, therefore more inspection for better understanding these problems were done.

Furthermore copper gaskets (NW 50) were inspected and tested. On the Figure 5 a cross section cut of a tested gasket is shown. The two different cuts are from two different CF knife edges. On the left side the special DESY knife edge is shown and on the right the ISO /T 3669-2 geometry is shown. The difference is the variation of the knife edge angle. DESY had defined a 72° knife edge and in ISO/TS 3669-2 a 90° angle is preferred.

These testes were made at BAM [9] in Berlin because they have adequate equipment for micro hardness soft material testing and preparing.

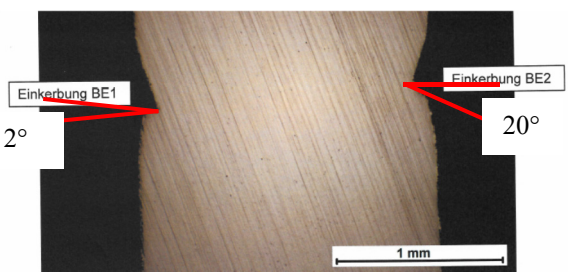


Figure 5: 3D picture of microscope inspected the knife edge of a copper gasket (rectangle to the 20 ° knife position).

In the following Figures 6 and 7 the gradients of hardness curves within the deformed areas are shown. Figure 6 relates to the ISO/TS 3669-2 knife edge angle of 90°. In Figure 7 the DESY 72° knife edge geometry is presented. The numbers present the micro hardness range on the contact zones of the flange to chamber connection with normal copper gaskets (85 HB). For the ISO/TS 3669-2 geometry the maximum value is 122 HV 0.01. But for the DESY geometry this value raised up to 148 HV 0.01.

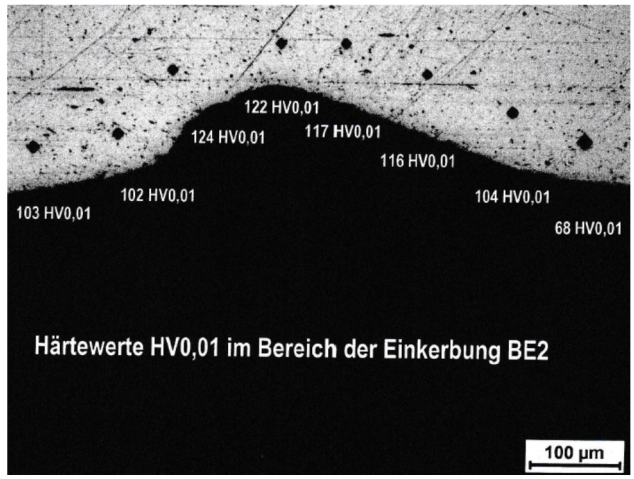


Figure 6: Polished cut image of ISO/TS 3996-2 90° knife edge.

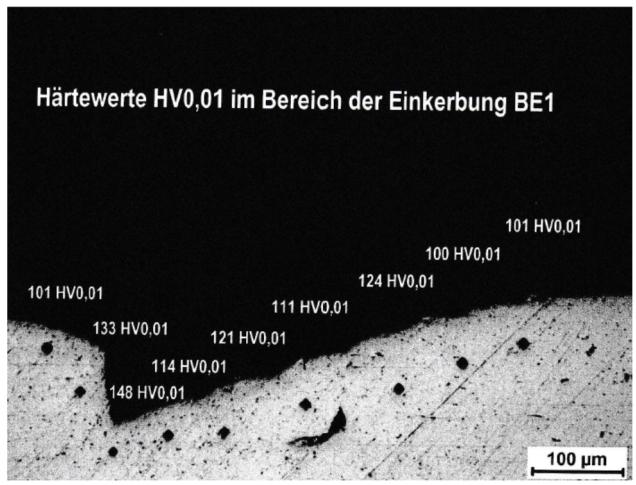


Figure 7: Polished cut image of DESY 72° knife edge contour.

The results of these two different knife edge geometries gave a big breakthrough to understand the orange skin "phenomenon", because these results compared to the measured hardness of the stainless steel blocks have printed out one critical aspect. Due to the assembling process the copper gasket material hardens. The average of the hardness type A/C and B compare to these results quite similar. Even the hardness of copper gaskets is sometimes higher than the average of the booths vessel versions.

FEM ANAYSIS

In a second step a FEM simulation [10] has to elaborate the critical areas of the two different CF flange knife edges. This FEM analysis compares two versions of knife edges geometries are used for UHV flange applications; the ISO/TS 3669-2 standard and the DESY Conflat knife edge geometry (see Figs. 8-10).

ISBN: 978-3-95450-188-5 doi:10.18429/JACoW-MEDSI2016-MOPE27

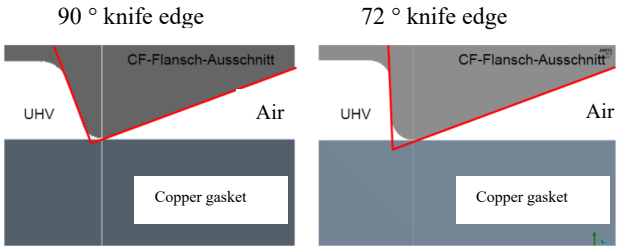


Figure 8: ISO/TS 3669-2 (left) DESY knife edge (right).

Both structures were implicated to FEM simulation process. Various FEM simulations were processed to find optimal simulation attempt. At first the implicit method quadratic formulated finite elements was used. All attempts run into solution errors caused by highly distorted elements. The second approach was to use the explicit solving method taking account of high plastic deformations during the solving process. Again, the solution runs into solver errors due to element shape warnings. The last and successful trail was to use finite elements with mathematical linear formulation, which are more robust against higher deformations. After several evaluations the FEM the program run reliably.

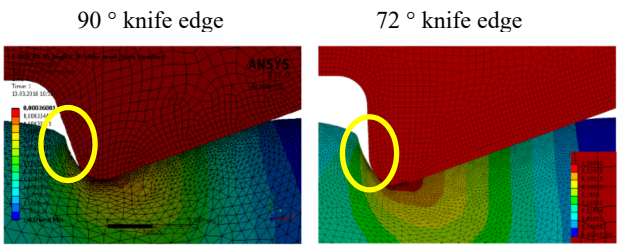


Figure 9: On the left the ISO/TS 3669-2 knife edge is presented and on the right DESY geometry is shown.

Results:

- Both geometries have maximum forces on the radius of the knife edge
- The contact areas are worked out
- A gap onto the vacuum side is shown (marks), related to direction of the knife edge drifting and deforming the gasket

The next Figures 11 and 12 show the knife edges of the flanges under pressure during assembly process. The critical zones are worked out. Differences between the two versions are illustrated. At the DESY geometry the forces on the knife edge are a little bit lower that the ISO geometry. But the steadiness of the DESY knife edge is lower.

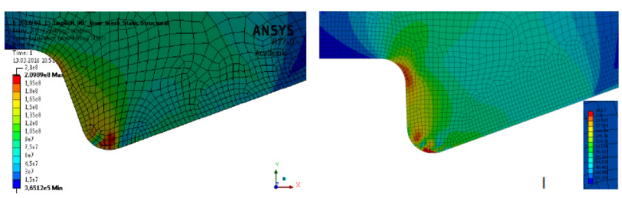


Figure 10: On these two pictures the Mises-stress of both knife edges are compared.

Results:

- Maximum on both knife edge radius form 210 N/mm^2
- Bending of knife edges and friction due to flowage bending of knife edge at the ground radius, higher stress at 72 ° version

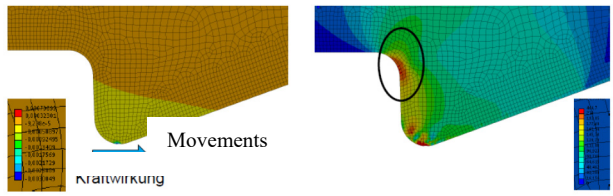


Figure 11: These pictures are shown the direction of forces and the value due to the assembling of flanges.

Results:

- Forces of friction stay against movements
- Both geometries have become forces of same direction
- Forces from vacuum to air side directions

Figure 12 documents the elongation of copper gaskets during assembling. Both copper gaskets show separate deformability behaviour. The plastic deformation to the vacuum side is 0.12 mm and to atmosphere side approx. 0.36 mm. Due to the fact that the allocations of copper material are unequal, the system moves radially to the atmosphere side.

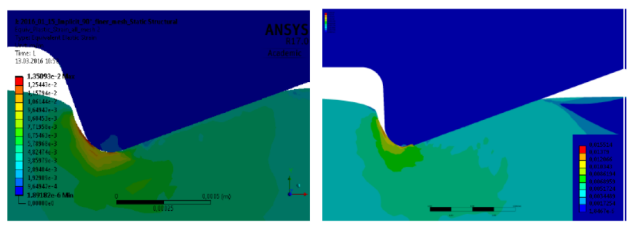


Figure 12: These pictures are shown the elongations of the gaskets in both versions.

Results:

- Selective stress load for the 72° version
- Better stress allocation for the 90° version
- Bigger elongation zone for the 90 ° version

The following Figures 13 and 14 show a comparison with equal scaling between the two geometrical variants for the CF-flanges. In general the stresses in the sealing are nearly identical whereas the stresses in the CF-flanges are different in detail. The edge of the 72°-flange has more concentrated stress-zones compared to the 90°-flange with more homogeneous stress distribution. The stress level up to 470 N/mm² is a direct result of model-problems/a singularity in the contact zone. Stresses up to a level of 320 N/mm² are feasible. The 90°-flange has more "material connection" to the rest of the flange to withstand the forces due to tighten the flange screws.

Content from this work may be used under the terms of the CC BY 3.0 licence (© 2016). Any distribution of this work must maintain attribution to the author(s), title of the work, publisher, and DOI.

ISBN: 978-3-95450-188-5 doi:10.18429/JACoW-MEDSI2016-MOPE27

Content from this work may be used under the terms of the CC BY 3.0 licence (© 2016). Any distribution of this work must maintain attribution to the author(s), title of the work, publisher, and DOI.

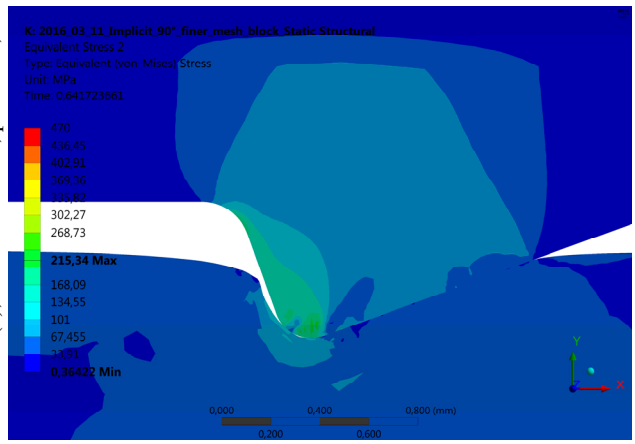


Figure 13: This picture show stress in the ISO/TS 3996-2 knife edge zone.

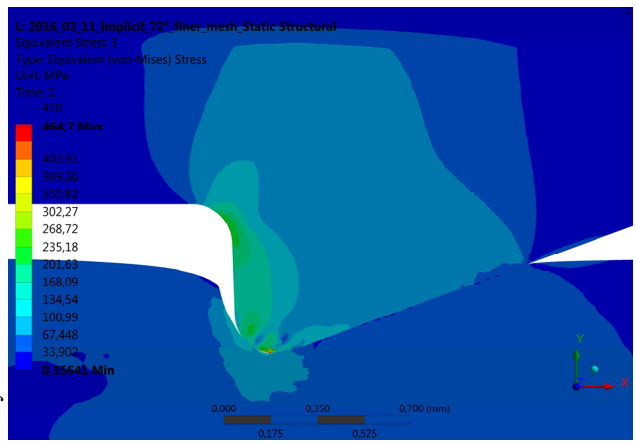


Figure 14: This picture show stress in the DESY 72 ° knife edge zone.

This paper covered only a short overview about this FEM simulation. An internal paper of these FEM simulations is under preparing at DESY [11].

RESULTS

The results are presented in this chapter. After several months ramp-up time of testing, investigations and analysis the new production went smoothly. The newly selected material had a significant higher hardness than the DESY specifications had prescribed.

The FEM simulation results gave a lot of new aspects in several iteration steps all critical forces and zones were pointed out. The FEM simulation gave excellent results for deeper understanding both common knife edge versions used at DESY.

Furthermore the deformations of the copper gaskets are not negligible. The behavior of copper during cold hardening under pressure is a serious problem especially if the minimum boundary of flange material is close to the consistency of copper gaskets after they were assembled under pressure.

All of the hardness tests, analysis and measurements have shown that the raw material certification is not enough for accepting the material. All tolerances were pointed out and had to be integrated in specification for ordering raw materials.

The sealing areas of knife edges receive a lot of power transmission and radial forces. These forces will be never noticed until micro damages on sealing area on the surfaces of flanges happen.

The advantages of Conflat vacuum connections to be used in multiple forms and they can be baked out. The range of temperature limits depends on gasket materials and coated surface of gaskets as reported by Danielson [12].

The disadvantage of Conflat flange connections is that they need much more attention and special care during manufacturing and assembly processes. In order to obtain reliable flange connections, the sealed diameter of the mating knife edges must be absolutely equal to avoid the umbrella effect or staggering of gasket, as reported by Unterlerchner [13]. In the following Figure 15 the umbrella effect is documented. This negative effect produces untitled vacuum leaks.



Figure 15: This picture show a gasket can be twist during assembling.

For customer designed Conflat flange applications a few measures and tolerances have to be attended. The knife edge diameter should better within 0.1 mm, the knife edge radius not bigger than 0.2 mm and the eccentricity should be held be within 0.1 mm related to the flange middle axis. The recess for the gasket should be tolerated to within 0.05 mm related to middle axis of the flanges. The sealed surfaces must not have any marks, scratches or dumps. And the sharp tolerance of sealing surfaces should be within 0.05 mm. And finally the knife edge angles should not be smaller than 90 ° (leaned to ISO/TS 3669-2 standard).

In Figure 16 the risk of getting virtual leaks is pointed out. The pairing flanges are pressed to zero gap. These typical connections are required for XFEL warm beamline connections, because of reduced bellows connections and small gaps between the Conflat flanges.

ISBN: 978-3-95450-188-5 doi:10.18429/JACoW-MEDSI2016-MOPE27

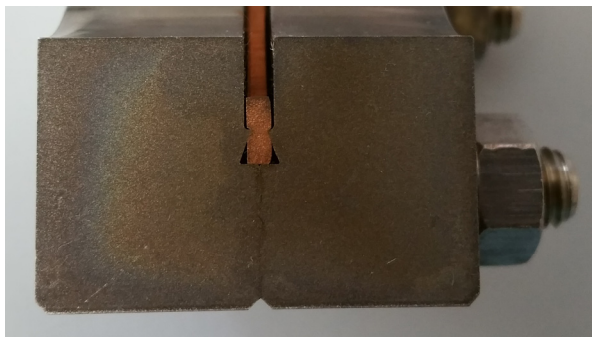


Figure 16: This picture presents a gasket connection between two Conflat flanges with different knife edges.

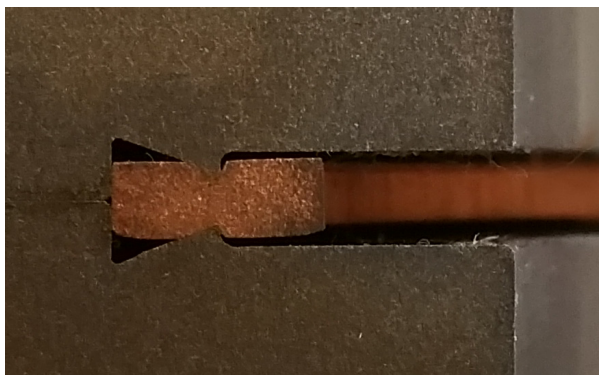


Figure 17: This picture is presenting the pairing of DESY knife edge with IST/TS 3669-2 knife edge.

Figure 17 the different knife edge geometries are presented. This picture represents very clearly the problem during the assembling process, if two different knife angles cut copper gaskets. The gasket tries to twist and the risk to get vacuum leaks increases.

Many gaskets have been badly. They are produced using vibratory grinding and have bad surface roughness. Final processes like etching or polishing are used. In that case gaskets may have micro cracks, shrink holes or the copper grain structure obtrudes. When these gaskets are used for high end applications of UHV, XHV or under cleanroom application leaks are more likely.

A few technologies are existing for bringing more hardness into the surface of high stainless steel alloys, but the penetration of these skin procedures are not deep enough for getting excellent achievements. One process is called Kolsterising® [14] and another is called “Kalt-Nitrieren” [15]. This paper does not cover more details about these two technologies but recent tests at DESY show no reliable improvements [16].

The implementation of quality management for bigger projects or serial production can be controlled more easily. The risk of failure materials gets lower and you will get more reliability.

CONCLUSIONS

The proper material for manufacturing massive vacuum chambers has to be well defined and very painstakingly and carefully inspected before starting serial productions.

The variations of mechanical specifications given in material certifications can be very large. Typical material certifications are made before the raw materials are forged, deformed and annealed. A lot of material specifications are focused on tensile and yield strength, but the hardness of this material mustn`t be ignored. Hardness is a significant property of reliable vacuum tightness, and also for reusing vacuum flange connections. If the hardness of the copper gaskets is under pressure in the order of the stainless steel hardness boundary, serious vacuum problems may appear.

The knife edge with the knife radius is one critical aspect for getting better UHV vacuum connections. However the main important area is the 20 ° surface area, between the knife edge and the shoulder fit of gasket with is terminated vacuum against air. Rework of damage components are very time and costs expensive. FEM analysis gave a better understanding material stresses and forces of several gasket knife edges.

LESSONS LEARNED

Based on the bad experience within this project DESY produced these vacuum chambers a second time. Very big efforts are necessary in order to build new chambers for XFEL within a short time. Not to run into time problems for the XFEL schedule these efforts are necessary. Based on the first design new massive chambers were fabricated and installed in the tunnel.

One lesson learned was to say good bye to constructions of massive blocks like these two designs with integrated Conflat flanges. Running into serious problems in case of having to rework these chambers is one aspect for using vacuum chambers made of standard Conflat flanges with normal standard SST pipes.

For new constructions of diagnostic vacuum chambers, if it cannot be avoided to use massive blocks, the selection of raw material has to be well defined and precisely observed. A lot of specifications are not up to date and should be matched to new technologies or projects. New applications like particle clean environments are the new leading technologies for new accelerator designs. Particle clean components have to be assembled under restricted specifications and the requirements to these parts are much more complicated than in the past. Limited to new conditions like higher cleaned components in high precisions, low residual magnetism and high purity, the specifications for raw materials have to be adapted.

Moreover a lot of different suppliers and producers for Conflat flanges and copper gaskets are on the market, but are they handle out precis specifications to their products?

This worst case event capable to showed that general specifications for vacuum components may often not be precise enough for high technology applications. Many years of experience is necessary, but this cannot be enough. The following steps may help to avoid these bad experiences.

- First clarify, concentrate and be precise about all requirements to the design (incl. all environment conditions, to be bake out, movements, cleanness requirements…)

Content from this work may be used under the terms of the CC BY 3.0 licence (© 2016). Any distribution of this work must maintain attribution to the author(s), title of the work, publisher, and DOI.

ISBN: 978-3-95450-188-5 doi:10.18429/JACoW-MEDSI2016-MOPE27

Content from this work may be used under the terms of the CC BY 3.0 licence (© 2016). Any distribution of this work must maintain attribution to the author(s), title of the work, publisher, and DOI.

- Clarify and require the raw material specifications (find out what is described in your organization …)
- Use standard norms, references or guidelines
- Earliest decision "Make" or "Buy"!
- One big point! Use pipes and standard Conflat flanges if you can!
- Use lessons learned from internal papers, or constructions, if you will get them
- Make a requirement matrix and estimate the technical functions, write out the results
- Before ordering raw material, check very painstakingly and carefully the material properties which will be documented in the 3.1 material raw certification!
- This 3.1 certification should be related to your delivered batch!
- Hardness for secure and reliable UHV or higher vacuum applications should be over 170 HB, better up to 185 HB (results of many different tests)
- N better 0,14 %, Cr not over 17,5 % and Ni more than 12 % (results of many different tests)
- ESR = Electro-Slag-Remelting, forged multidirectional and annealed is mandatory, full austenitic structure
- Early integration of material producers or vendors, manufactures and purchase office
- If you make your own design, build more than one prototype for serial productions.
- According to ASTM E112-13 the grain size shall be better than 3, but for machinability not better than 8!
- Independent material tests of the raw material should be done after delivering the material
- For bigger serial productions make sure that you will have adequate technical descriptions which will cover all the requirements of your scopes.
- Make Quality Audits with suitable vendors or manufactures
- Make a risk analysis and if you can use project management competences
- GOOD LUCK!

to avoid pictures like the following Fig. 18...

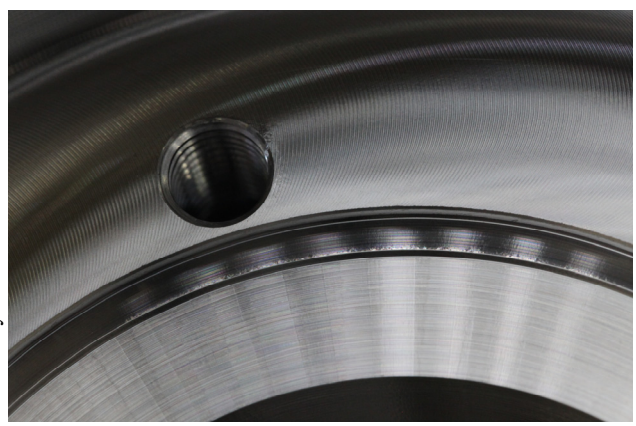


Figure 18: Last picture documents the orange skin micro damages on the scintillation screen monitor vacuum chambers for E-XFEL project.

ACKNOWLEGEMENT

The author would like to thank all the colleagues, suppliers and vendors for their support, motivation, help, constructive and interesting discussion. And also a special thanks to Dr. Andre van Bennekom, Deutsche Stahlwerke for a very interesting discussion to this problem.

REFERENCES

[1] The European XFEL, Hamburg, Germany http://www.xfel.eu/

[2] A. Roth, "Vacuum Sealing Techniques", *American Institute of Physics*, 1994, page 306 ff

[3] K. Kube, Ch. Wiebers, M. Holz, G. Kube, D. Nölle, G. Priebe, H.-C. Schröder, "Scintillating Screen Monitors for Transverse Electron Beam Profile Diagnostics at the European XFEL", DESY, Hamburg, Germany, in *Proc. 2nd International Beam Instrumentation Conference, IBIC'13*, 16-19 September 2013, Oxford, UK.

[4] A. Roth, "Vacuum Sealing Techniques", *American Institute of Physics*, 1994, page 306 ff

[5] ISO standard flange geometry, https://www.lesker.com/newweb/flanges/pdf/kjlced09_sec01_pages210_technicalnotes.pdf

[6] KF standard flange geometry, https://www.lesker.com/newweb/flanges/pdf/kjlced09_sec01_pages210_technicalnotes.pdf

[7] A. Roth, "Nomographic design of vacuum gasket seals", paper, December 1965, Storeq Research Centre, Atomic Energy Commission, Israel, Vacuum, Volume 19, Issue 3, March 1966, Page 113-120

[8] DNV GL, Hamburg, Germany, https://www.dnvgl.de/ueber-uns/index.html

[9] BAM, Bundesanstalt für Materialforschung und –prüfung, Berlin https://www.bam.de/Navigation/DE/Home/home.html

[10] FEM Analysis, **ANSYS, Inc.** ANSYS Workbench V17.0, 2016, http://www.ansys.com/Products/Platform

[11] Martin Lemke, "FEM Analysis CF Flanschschneidengeometrien", DESY, Germany, 2016

[12] P.M. Danielson, "Investigation of gasket coating materials for Ultrahigh-Vacuum seals", *Journal of Vacuum Science and Technology* 7 (3), pp. 449, May 1970

[13] W. Unterlerchner, "Some improvement work on ConFlat joints and their limits of reliability in large-size ultrahigh vacuum systems", *Journal of Vacuum Science and Technology* A5 (2540), 1987

[14] Bodycote, Apeldoorn, Nederland, Specialty Stainless Steel Processes (S3P), http://www.bodycote.com/en/services/heat-treatment/specialty-stainless-steel-processes.aspx

[15] Dreistegen, Monschau, Germany, Randschichtdiffusion http://www.dreistegen.com/pages/rsd.html

[16] K. Wittenburg, "The OTR Vessel Issues", DESY, Hamburg, Germany, MDI/WP17 Internal Report 1, 2016, http://winweb.desy.de/mdi/Reports2016/OTR_Chamber_Issue_final.pdf

ISBN: 978-3-95450-188-5 doi:10.18429/JACoW-MEDSI2016-MOPE28

VACUUM SYSTEM OF SESAME STORAGE RING

M. Al-Najdawi, E. Huttel, F. Makahleh, M. Shehab, H. Al-Mohammad

SESAME Light Source, P.O. Box 7, Allan 19252, Jordan

Abstract

SESAME (Synchrotron-light for Experimental Science and Applications in the Middle East) is a third-generation synchrotron light source under construction near Amman (Jordan).The storage ring has 16 Dipole arc chambers, 8 short and 8 long straight chambers. The general layout and detailed design of the vacuum chambers, crotch absorbers, RF bellows, injection and RF sections will be presented in this contribution, also the testing of the chambers prototype, bake out process and final installation.

STORAGE RING VACUUM SYSTEM

The storage ring is divided into 16 cells, each cell contains a dipole arc chamber and a straight chamber (long or short) closed by UHV RF shielded gate valve.

There are two types of the vacuum cells, an arc chamber with long straight with a total length of 9.35m and an arc chamber with short straight with a total length of 7.3 m. The overall length is 133.2 m. Lumped absorbers are used to absorb the unwanted synchrotron radiation (SR), there are four types of the absorbers based on the location they are installed.

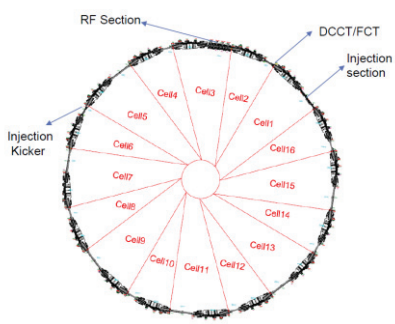
Diode sputter ion pumps (SIP) are installed near the absorbers with an overall nominal pumping speed of 20500 l/s, also, a NEG pumps are installed near the absorber with the highest SR absorption (higher outgassing)

Valves are installed upstream and downstream of each long straight, 16 in total.

Bellows are installed upstream and downstream of each short and long straight and upstream and in addition up and downstream of the septum.

Inverted magnetron Gauges are installed one at each dipole and each long straight chamber, whereas in the RF section at each of the four cavities

Figure 1 shows the general storage ring vacuum layout and a list of the installed pumps.



Ion pumps	105 Pumps
Dipole chamber	2 X 300L/S
	2 X 150L/S
Long Straight	3 X 150L/S
Short straight	2 X150L/S
RF Section	4 x 150L/S
NEG pumps	16
IMG	27
Dipole chamber	16
Long straight	7
RF section	4
RF Valves	16
RF Bellows	34

Figure 1: General storage ring vacuum layout.

Crotch Absorber Design

The crotch absorber design follows the same design implemented for the ANKA and SLS [1] light sources, it consist of two parts with 8.8° vertical tooth inclination and 5° horizontal tooth angle and 10mm tooth width. The thermal load has been applied in a conservative way such that the maximum power intensity on each teeth of the absorber has been applied on the whole subjected area the FWHM Area.

FEA analyses for all absorber have been done for a 2.5 GeV 400 mA e-beam; corresponding to 240 kW SR Power. The most critical absorber 2 with the tip located at 641 mm from the source point is exposed to a surface power density of 45.8 W/mm2. At this location the maximum stress is 175 MPa, the maximum strain is 0.15% and the maximum temperature is 300 °C. Figure 2 shows the FEA results for absorber 2 and Table 1 lists the parameter for all absorbers.

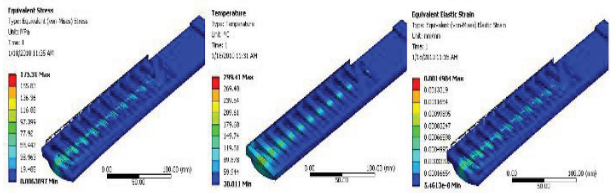


Figure 2: FEA results for absorber 2.

Table 1: Parameter of the SR Absorber

Abs.	Angle [°]	Power [kW]	Lin.Pow. Density [W/mm]	Temp. Max [°C]	Strain [%]
1	6	4.1	41	192	0.14
2	11	7.5	58	300	0.14
3	5	3.2	25	142	0.04
4	0.5	0.4	11	75	0.01

RF Shielded Bellows

The RF bellow design is similar to SLS and ALBA design with some modifications, the bellow has a compact design with a free length of 115 mm and has a sleeve made of 316L stainless steel sheet and 19 fingers made of beryllium copper sheets (0.4 mm thinness). The bellow has a cover made of aluminium; the benefit from the cover is to limit the compression and expansion of the bellow (15mm compression, 3mm expansion and ±2 mm in all transvers directions) also to protect the bellow body from any damage. Figure 3 shows the design concept of the bellow.

Content from this work may be used under the terms of the CC BY 3.0 licence (© 2016). Any distribution of this work must maintain attribution to the author(s), title of the work, publisher, and DOI.

ISBN: 978-3-95450-188-5 doi:10.18429/JACoW-MEDSI2016-MOPE28

Content from this work may be used under the terms of the CC BY 3.0 licence (© 2016). Any distribution of this work must maintain attribution to the author(s), title of the work, publisher, and DOI.

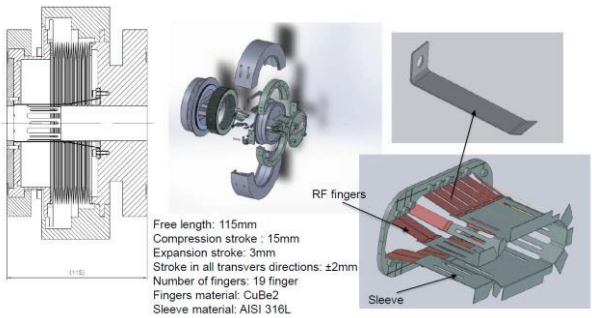


Figure 3: RF bellow design.

Special Straight Sections

There are three special straight sections in the storage ring, the injection, RF and kicker sections. The injection section consists of the injection septum; which has an internal thin walled stainless steel pipe for the incoming beam and pipe made of mild steel for the stored beam. There will be a horizontal fluorescent screen with a motorized linear actuator to monitor the injected and stored beam, a Bunch by bunch feedback kicker and a vertical scraper are also installed in the same section. Figure 4 shows the layout of the injection section.

The second special section is the RF section. Four cavities (Elettra cavity design) will be installed in this section with a downstream and upstream transition parts to have a smooth transition from the key shape arc chamber to the cavity circular shape tube. Between the cavities there will be transition tubes with absorbers and RF shielded bellows at both ends. Figure 5 shows the layout of the RF section, Absorber and the upstream transition parts.

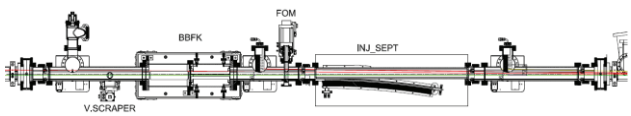


Figure 4: Injection section layout.

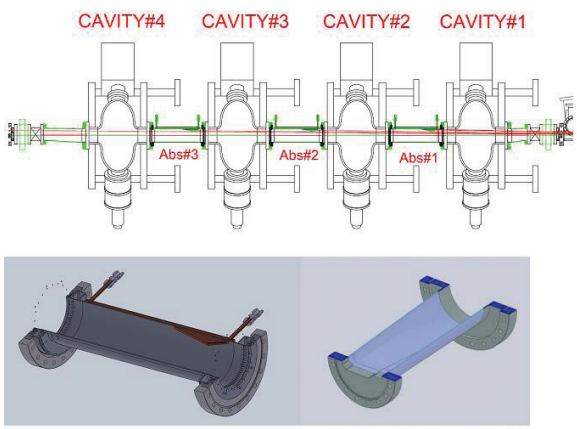


Figure 5: RF section layout, transition centre absorber and the upstream transition parts.

Vacuum Pressure Simulation

To simulate and calculate the vacuum pressure profile in the storage ring, we have used a coupled simulation using SynRad+ [2] to simulate the beam and Molflow [3] to calculate and simulate the vacuum pressure profile. The simulation started by having a simplified model for the internal volume of the chamber and having an empty block for the absorbers. After defining the beam parameters, the simulation started and an outgassing map will be generated for each absorber where the beam hit. Figure 6 shows SynRad+ simulation and the generated outgassing map. After exporting these maps to Molflow we defined the pumps sizes and starting the simulation. Three different vacuum simulations were performed for the most desorbed gases (H2, CO and CO2) and taking advantage of the linear behaviour of the ultra-high vacuum systems, the partial pressure were summed at the end .Figure 7 shows the pressure profile for a complete sector (two arc chambers with a short straight section) at first injection, after 100Ah with nominal current 100 mA, after 500 Ah 300 mA and after 1000Ah 400 mA.

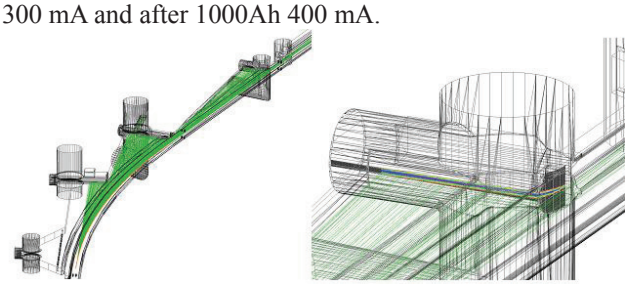


Figure 6: SynRad+ simulation model.

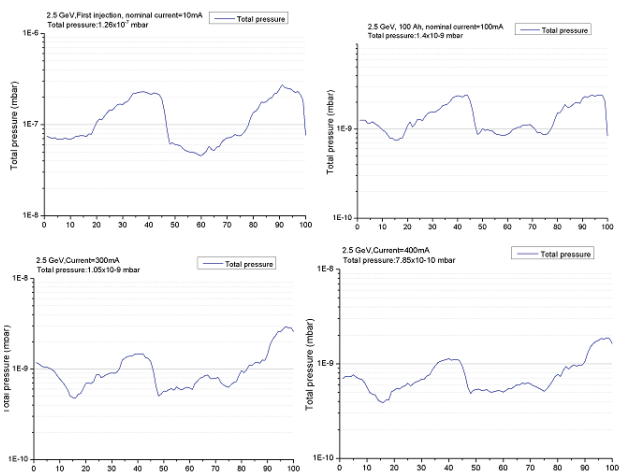


Figure 7: The pressure profile at first injection, after 100Ah 100 mA, 500 Ah 300 mA and after 1000Ah 400 mA.

THE STORAGE RING VACUUM SYSTEM INSTALLATION

The prototype chamber was installed and tested with all magnets and girder at CERN in March 2015 and the real installation of the series vacuum chambers started in February 2016.

The installation started by mounting the arc chamber on a test girder and all vacuum components , gauges, valves were installed, then a roughing pump station were connected to the chamber and pumped down, after that a

ISBN: 978-3-95450-188-5 doi:10.18429/JACoW-MEDSI2016-MOPE28

helium leak detector had been connected to the system and a leak check was performed. After the leak check and our leak rate target 1x10-10 mbar l/s achieved, the chamber was moved to the bake out oven using a skeleton, another leak check and an RGA scan was performed.

The bake out process started at room and the temperature gradually increasing by 25 ^{0}C/ h up to 200 ^{0}C for 72 hours. During the cooldown at 150 ^{0}C the ion pumps were flushed many times. After the complete cool down a leak check and an RGA scan were performed using secondary electron multiplier (SEM) for higher accuracy results.

After all tests the chamber was moved under vacuum to the storage ring tunnel for final installation.

The long straight chamber were installed and connected to the arc chamber by the RF bellows, a leak check has been done then an in-situ bake out performed at 200 ^{0}C for 72 hours, after finishing the bake out process, another leak check was performed.

While the 16 RF gate valves are located up and down stream of the long straight section only; the short straights are connected directly to the arc chambers without gate valves. First, the short straight had been installed in the ring without connecting. Then bake out had been performed and after cool down to room temperature the short straight, the downstream and upstream arc chambers were vented by nitrogen, then the RF bellows installed and the whole assembly pumped down again, ion pumps turned on and the NEG pumps were activated.

Figure 8 shows some pictures of the assembly of the storage ring vacuum system and Figure 9 shows a flow chart of the assembly and bake-out procedure being followed for the storage ring vacuum system installation.



Source of photos © SESAME.

Figure 8: A photos during the assembly, bake-out and installation of the storage ring vacuum chambers.

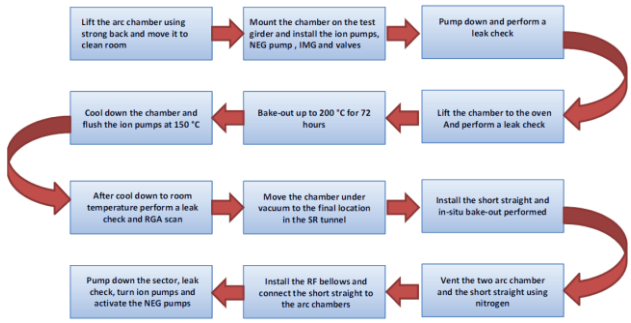


Figure 9: The flow chart of the assembly, bake-out and installation procedure.

ACKNOWLEDGEMENT

The author would like to thank SESAME installation team, especially the vacuum team for all the effort and hard work they give during the installation of the vacuum system.

REFERENCES

[1] S.Hermle, E.Huttel, D.Einfeld,G.Heidenreich, Layout of the Absorbers for ANKA.

[2] R. Kersevan (1993), SYNRAD, a Monte Carlo syn chrotron radiation ray-tracing program, Proceedings of the 1993. Particle Accelerator Conference, vol.5, p 3848-3850.

[3] R. Kersevan, J-L Pons (2009), “Introduction to Molflow+”, JVST A27 (2009), p1017-10.

Content from this work may be used under the terms of the CC BY 3.0 licence (© 2016). Any distribution of this work must maintain attribution to the author(s), title of the work, publisher, and DOI.

ISBN: 978-3-95450-188-5 doi:10.18429/JACoW-MEDSI2016-MOPE29

VACUUM SYSTEM OF HLS-II STORAGE RING*

Y. Wang, X. Pei, W. Wei, L. Fan, Y. Hong B. Zhang†,
National Synchrotron Radiation Laboratory, USTC, Hefei, China

Abstract

Hefei Light Source (HLS) has been operated for more than twenty-five years. From 2010 to 2014, the upgrading project of HLS has been carried out and the new machine is called HLS-II. The main improvement include: the emittance is reduced to 40 nm·rad, 3 new insertion devices (2 IVU and 1 EPU undulators) are added and the injection energy increases to 800 MeV. The typical life time is 300 mins at 300mA, 800 MeV. The average pressure of static and dynamic vacuum are below 2×10^{-8} Pa and 1.2×10^{-7} Pa respectively. The design, installing and commissioning of the vacuum system of the storage ring are detailed stated in in this paper.

INTRODUCTION

The 800MeV electron storage ring of the National Synchrotron Radiation Laboratory (NSRL) is a dedicated VUV and soft X-ray synchrotron radiation light source. The construction of NSRL facility began on November, 1983 and was completed in 1989. HLS comprises of 200 MeV injector, 800 MeV storage ring, 12 beamlines and 15 experimental stations by 2010. In order to supply synchrotron light with higher brightness and stability to the users, the upgrading project of HLS has been carried out during 2010-2014[1]. The main changes of the new HLS (HLS-II) include: The energy of the injector increases to 800 MeV, so the electrons can be injected to the storage ring with full energy. The lattice of the storage ring was changed from TBA to DBA. The beam emittance decreased to 40 nm·rad. A group of multifunctional sextuple magnets are employed and thus the long and short straight section are both lengthened. Five insertion device were installed in the storage ring.

LAYOUT OF THE STORAGE RING

The circumstance of the storage ring is 66.13 m, as shown in Fig. 1. It consists of four DBA cells and each cell has 2 dipoles, 4 quadrupole and 4 sextupole magnets. The synchrotron light is emitted along the direction of 0°and 15° with the beam orbit. There are 8 long straight sections and their length account for 38% of the ring. Insertion devices are located in 6 LSS. Injector and RF cavity are located in the other 2 LSS.

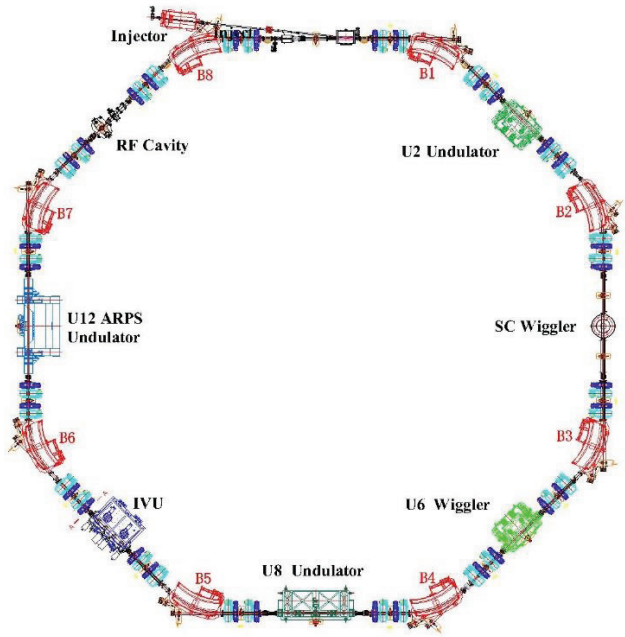


Figure 1: Layout of HLS-II storage ring.

VACUUM SYSTEM DESIGN

The storage ring's circumference is 63.66 meters. The main vacuum pipes are made of 316LN stainless steel by welding. The section is octagonal as shown in Fig.2. To reduce the surface degassing and the magnetic permeability induced by welding, the chambers are baked at 900 °C in the vacuum furnace. After this treatment, vacuum chambers of the total leak rate, outgassing rate and magnetic permeability are below 2×10^{-8} Pa L/s , 2×10^{-11} Pa L/s cm^2 and 1.02 respectively, which meet the design requirements. Considering the convenience of installing, commissioning and maintenance, 3 RF-shielded all-metal gate valves are used to separate the storage ring into three cells. 20 UHV gauges are distributed in the storage ring to monitor the vacuum and for the interlock protection system.

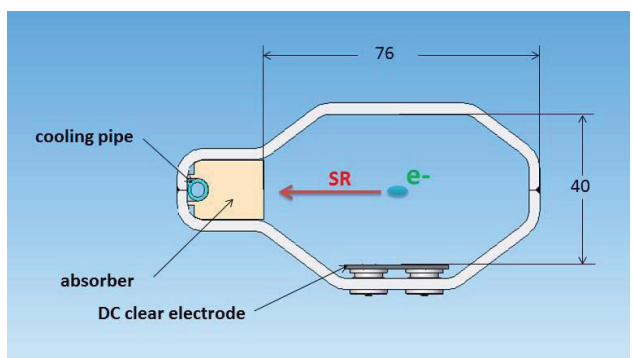


Figure 2: The section of the main vacuum pipe.

* Work supported by Chinese Academy of Sciences
† zhbo@ustc.edu.cn

Content from this work may be used under the terms of the CC BY 3.0 licence (© 2016). Any distribution of this work must maintain attribution to the author(s), title of the work, publisher, and DOI.

ISBN: 978-3-95450-188-5 doi:10.18429/JACoW-MEDSI2016-MOPE29

Because of the low electron energy, the deflection angle of the dipole magnet is relatively large, so the synchrotron light can hardly be absorbed by a lumped photon absorber. To ensure the thermal stability of the vacuum pipes and reduce the photon stimulated desorption, water-cooled absorbers made of oxygen-free copper, which can protect the inner surface of the dipole magnet pipe from being hit by the synchrotron light, are arranged in the pipes along the beam direction and near the light outlet, as shown in Fig.3. The absorbers in the pipes also act as supports and simplify the design of the vacuum pipe.

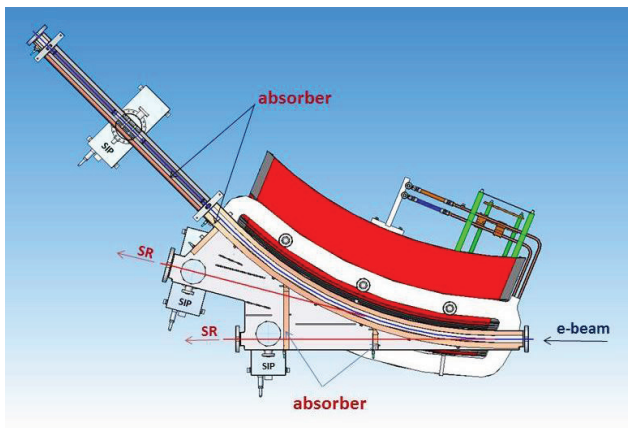


Figure 3: A standard segment of the storage ring.

18 RF-shielded bellows, as shown in Fig. 4, are adopted to eliminate the machining and installing errors, deformation induced by temperature difference, and for smooth transition of chambers with different sections. The bellows are machined by welding with high stability. Considering the smooth transition of the chambers and the high frequency contact resistance, the RF shield is achieved by using shield fingers. Shield fingers (Cu-Be) which bridge the gap between the neighbouring flanges inside the welding bellows. The permissible longitudinal and transverse error are ±10 and 1.5 mm respectively. The design value of the contact stress of shield finger is larger than 25 Kg/cm2.

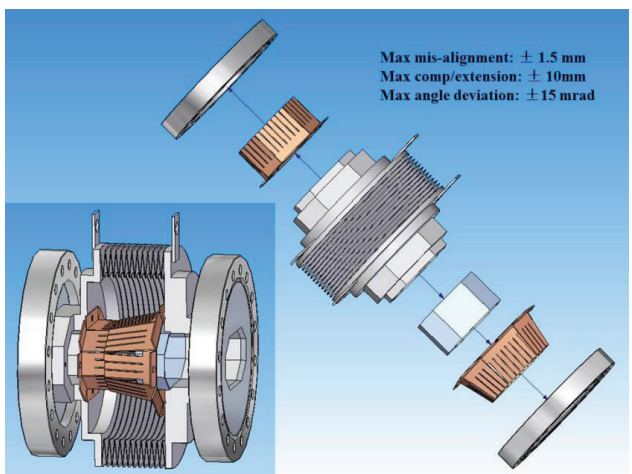


Figure 4: A standard segment of the storage ring.

The pumping system comprises 38 SIPs with the pumping speed of 200 L/s and 3 SIPs with the pumping speed of 400 L/s. NEG strips WP1250 supplied by SAES are added into the SIPs and the pumping speeds are increased by 2-3 times[2]. According to the calculation, the overall degassing of the storage ring after beam scrubbing with 100 Ah dose is approximate 2×10^{-3} Pa·L/s. The pumping system can evacuate this amount of gas load and even higher gas load while the storage is operated at 500 mA.

INSTALLING AND COMMISSIONING

The storage ring of vacuum pipes can't be in situ baked due to the limitation of small aperture of the magnets. Therefore, before the installing of the pipes, the entire ring was divided into 17 subsystem for assembling and vacuum pre-commissioning and each subsystem was baked so that the ultimate vacuum could be better than 5×10^{-8} Pa. After the subsystem was hoisted in place, installed and aligned accurately on the support, high purity nitrogen was introduced and then all the subsystems are connected together. The installing of a subsystem is shown is Fig.5. Only the pipes outside of the magnets and SIPs were baked on 200°C for 48 hours. Two days after the activation of NEG and start of the SIPs, the average pressure is 5×10^{-8} Pa and one week later this value is 2×10^{-8} Pa.

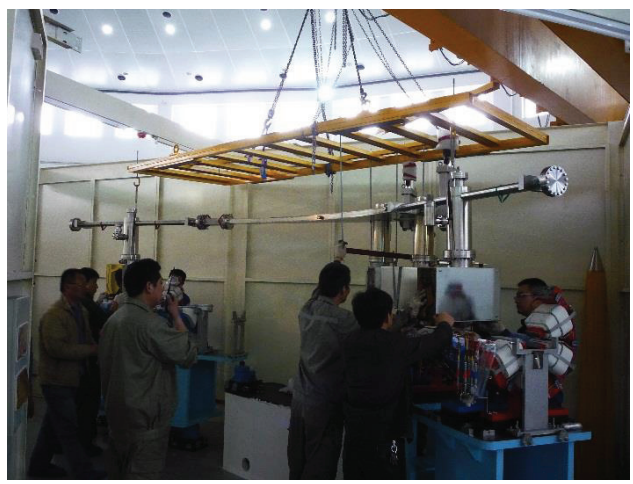


Figure 5: Installing of a subsystem.

Now the HLS-II has been commissioned and operated for more than one year and the total accumulated beam dose is over 1200A·hr. The process of beam scrubbing is shown in Fig.6.

The lifetime with the beam of 300 mA and 800 MeV is more than 300 minutes just after 80 A·hr. In November 2014, the storage ring was exposed to air for replacing of ceramic chambers. After the replacement and baking, the vacuum and beam lifetime restored quickly to the values before exposure to the air, as shown in Fig.6

Content from this work may be used under the terms of the CC BY 3.0 licence (© 2016). Any distribution of this work must maintain attribution to the author(s), title of the work, publisher, and DOI.

ISBN: 978-3-95450-188-5 doi:10.18429/JACoW-MEDSI2016-MOPE29

Content from this work may be used under the terms of the CC BY 3.0 licence (© 2016). Any distribution of this work must maintain attribution to the author(s), title of the work, publisher, and DOI.

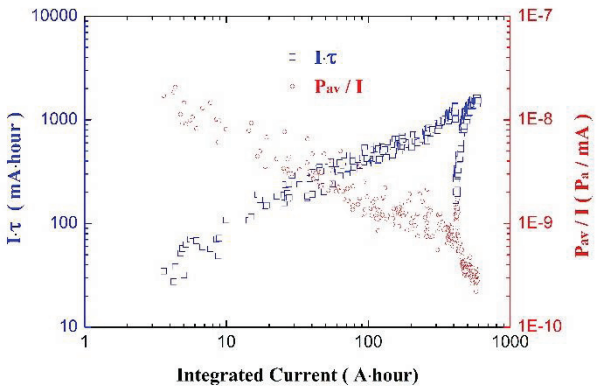


Figure 6: Progress of beam cleaning and growth of beam lifetime.

CONCLUSION

The HLS-II storage ring vacuum system after one year commissioning and operation, the average pressure of static and dynamic vacuum are below 2×10^{-8} Pa and 1.2×10^{-7} Pa respectively and the beam life is more than the design value of 5 hours. All this indicates that the design, installing and commissioning are successful.

ACKNOWLEDGEMENT

Thanks to the people who have given advices and assistance, especially Lixin Yin from Shanghai Synchrotron Radiation Facility, Haiyi Dong from Institute of High Energy Physics, Xiaotian Yang from Institute of Modern Physics and other colleagues of HLS-II.

REFERENCES

[1] W. Li *et al*. "The upgraded scheme of Hefei Light Source", *AIP Conf. Proc*. Vol. 1234, p. 764-767. 2010.

[2] D. Jiang *et al*. "Integration of Commercial Sputtering Ion Pumps with Non-Evaporative Getter", *Vacuum Science and Technology* (China), vol. 24, no. 5, p. 222-224. 2004.

ISBN: 978-3-95450-188-5 doi:10.18429/JACoW-MEDSI2016-MOPE30

THE DEVELOPMENT OF CUCRZR HIGH HEAT LOAD ABSORBER IN TPS

I. C. Sheng†, C.C. Chang, C. K. Chan, C. Shueh, L. H. Wu, National Synchrotron Radiation Research Center, HsinChu, Taiwan,
Sushil Sharma, Brookhaven National Laboratory, Upton, New York, USA

Abstract

Taiwan Photon Source (TPS) project in National Synchrotron Radiation Research Centre (NSRRC) has reached 500mA design goal. Several upgrades and design enhancements are also under development. CuCrZr copper alloy has been selected to examine its UHV compatibility, machinability and high heat load sustainability as one of the upgrade activities. Most importantly, the absorber is made entirely by CuCrZr (including two end flanges) and installed in the mid-section of double minimum of tandem EPU48 undulators to shadow beam miss-steered synchrotron radiation from upstream EPU. Both the result and fabrication time (without brazing) are promising.

INTRODUCTIONS

As to synchrotron accelerator machine, synchrotron radiation is always associated with high density power, and 99% of them are to be shadowed before it reaches beam line users. Due to its high conductivity and ultra-high vacuum (UHV) compatibility, Oxygen free high conductivity (OFHC) copper and GlidCop® are two of the commonly used materials to shadow the unneeded synchrotron power. OFHC is used to absorber lower power density synchrotron radiation whereas GlidCop® can be much higher due to its excellent mechanical material properties.

However GlidCop® is solely fabricated by the company named North American Höganäs, it is much more expensive and it is not readily available when it comes to specific sizes.

In 2013, we have considered other copper material which can replace OFHC and GlidCop®. The reason being is to marry with stainless steel, both them require brazing process, which either is time consuming or has high failure rate. We searched for couple of candidates and found out CuCrZr alloy is the right material to use due to

- It has high yield and tensile strength.
- It is much cheaper than GlidCop® and is available even in our local supply vendors.
- It can be welded with stainless steel.
- It is UHV compatibility.

As shown in Table 1, CuCrZr alloy has comparable mechanical properties with GlidCop®, with a little bit lower thermal conductivity (16% lower than that of OFHC) but its high yield and tensile strength, this alloy is worthwhile to give a try. Other accelerators have used it for undulator chamber [1].

Table 1: Material Properties

Property	**OFHC**	GlidCop®*	**Cu-CrZr**[2]
Conductivity (W/cm°K)	3.83	3.65	3.23
Thermal expansion (m/°K×10^{-6})	16.6	17	18.6
Poisson ratio	0.31	0.35	0.18
Yield strength (Gpa)	0.049-0.078	0.33	0.27-0.44
Tensile strength (Gpa)	0.215-0.254	0.42	0.37-0.47

**GlidCop-15*

In the following sections, we will present how we carry out vacuum and weld tests of CuCrZr copper alloy.

VACUUM TEST

Templates are provided for recommended software and authors are advised to use them. Please consult the individual conference help pages if questions arise.

An outgassing rate test is performed in our vacuum laboratory. The layout is shown in Figure 1.

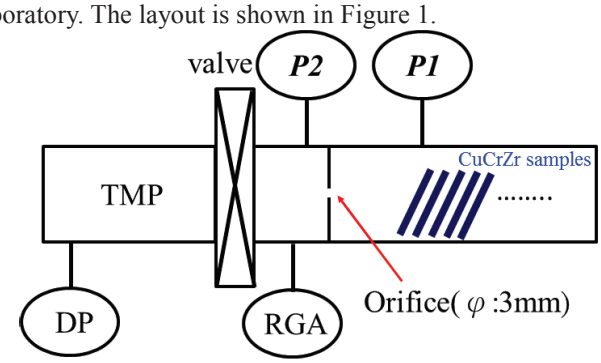


Figure 1: CuCrZr sample outgassing test layout.

The CuCrZr alloy plates has total surface of 4000 cm^2 piled up in the vacuum chamber. They are ultrasonic cleaning in Citranox®, rinsing with de-ionized water for 10 minutes, and dry with 99.9999% nitrogen. Comparing with other materials such as Al and Stainless steel, we list their outgassing rate in Table 2:

The result of outgassing rate comparing with CuCrZr, Aluminum and Stainless steel is illustrated in Figure 2:

† shengic@nsrrc.org.tw

Content from this work may be used under the terms of the CC BY 3.0 licence (© 2016). Any distribution of this work must maintain attribution to the author(s), title of the work, publisher, and DOI.

ISBN: 978-3-95450-188-5 doi:10.18429/JACoW-MEDSI2016-MOPE30

Content from this work may be used under the terms of the CC BY 3.0 licence (© 2016). Any distribution of this work must maintain attribution to the author(s), title of the work, publisher, and DOI.

Table 2: Outgassing rate of CuCrZr, Aluminum and Stainless Steel.

Material	Outgassing rate (Pa m s^{-1})	
	Q_{10}	Q^*_{72}
CuCrZr	1.6×10^{-6}	5.8×10^{-6}
Aluminium	3.3×10^{-6}	1.6×10^{-6}
Stainless Steel	1.8×10^{-6}	1.5×10^{-6}

*Baked out then pumped down.

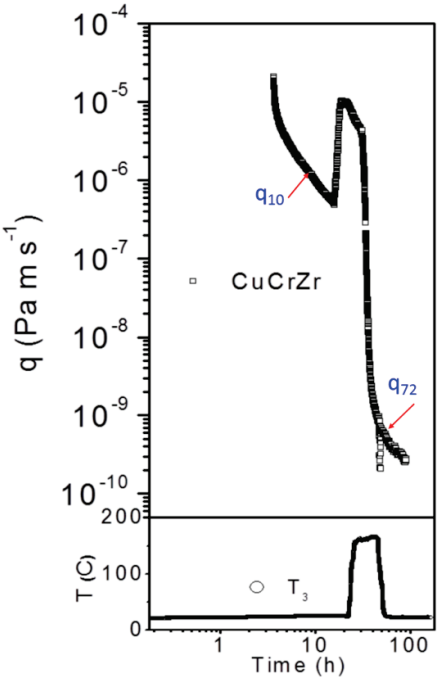


Figure 2: Outgassing rate curve for CuCrZr.

A series of baking out test is also performed in the laboratory. We applied 11N-m torque while bolting CuCrZr-made flange with stainless steel flange. We then baked, pumping down, replace new copper gasket, bolted again. Total of 10 cycles of this process is repeated to the same CuCrZr flange. Each time we recorded its leaked rate. Figure 3 illustrates that even after 10 bake-out cycles, CuCrZr flange still has good leak rate. No visual damages on the knife edges are observed.

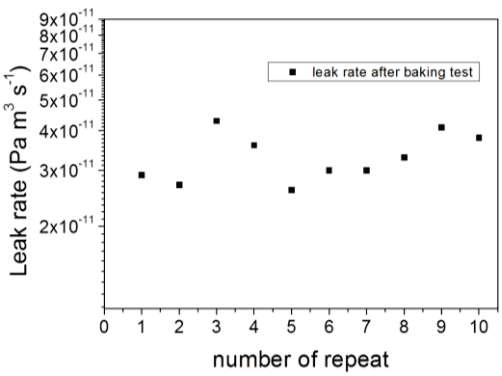


Figure 3: Leak rate of CuCrZr after numbers of flange bolting.

WELDING TEST

Since CuCrZr can be welded with Stainless steel by e-beam weld, it indicates these two dissimilar materials can be jointed together by welding. Even E-beam is able to provide precise, smaller HAZ and deep penetration but it is not readily available among local vendors. Samples of Stainless steel and CuCrZr plates are also prepared and TIG welded together. Due to different thermal conductivities and thermal expansion, extra attention is required during welding. Figure 4 shows post weld result of Stainless steel plate and CuCrZr sample plate.

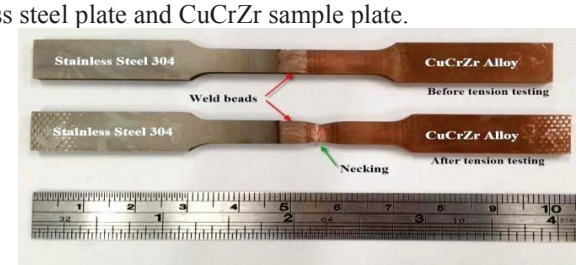


Figure 4: Welded CuCrZr/Stainless steel sample after tensile test.

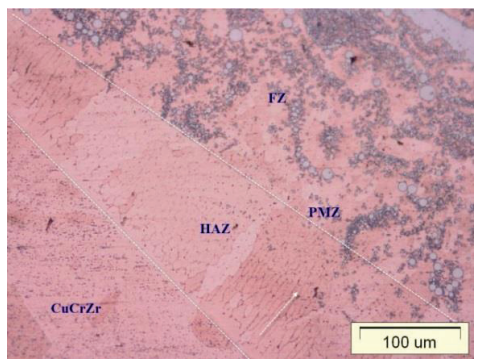


Figure 5: Microscope view of CuCrZr/Stainless steel HAZ area.

The microscope photo in Figure 5 reveals clear Heat affective zone (HAZ) between CuCrZr alloy grain boundary and stainless steel fusion zone (FZ). Stainless steel particles are surrounded by CuCrZr copper matrix. It is believed that stainless steel particles behave as slipping obstacles along the copper grain boundaries to enhance material strength. That's why in Figure 4 the necking appears on the CuCrZr side instead of on the weld bead, this indicates that welded interface is indeed has higher tensile strength that that in CuCrZr itself, as is shown in Figure 6.

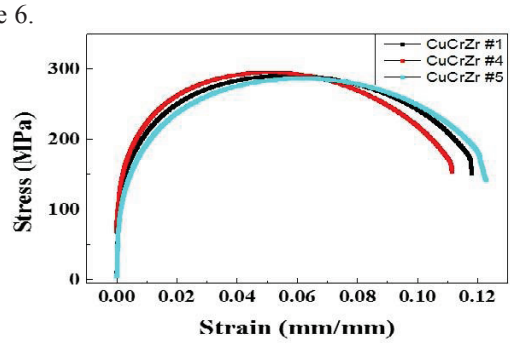


Figure 6: Tensile test result of welded CuCrZr/Stainless steel sample plate.

ISBN: 978-3-95450-188-5 doi:10.18429/JACoW-MEDSI2016-MOPE30

CUCRZR ABSORBERS

In this 2016 July-August shutdown, TPS had experienced several upgrade and maintenance. One of them is to replace middle section of double minimum EPU48. The original chamber height in this section is 8mm, which leads to high radiation dose and high temperature rise on the 8mm height bellow. We upgraded this section by a 20mm height Aluminium chamber. A tapper down absorber (inside aperture is tapered from 20mm back to 8mm downstream EPU48 chamber) is required to absorb synchrotron radiation from its upstream EPU48 during beam miss-steering. A CuCrZr absorber is made and installed for this function, both the flanges, absorber body are fabricated in one piece without any welding or brazing. This largely reduces the cost as well as eliminates the brazing time.

Figure 7 shows the CuCrZr absorber installed in the mid-section of double minimum EPU48 chambers.

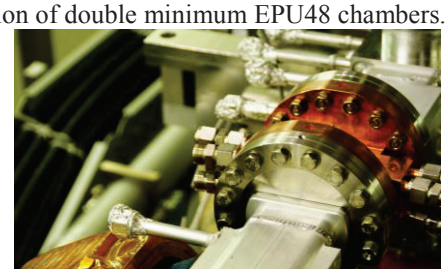


Figure 7: CuCrZr absorber in mid-section of double-minimum EPU48s.

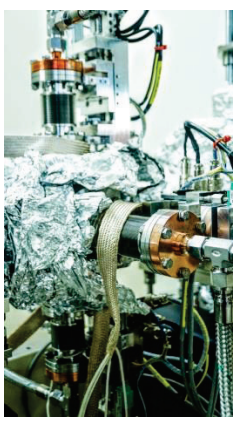


Figure 8: CuCrZr slits in TPS front end 24.

Front end 24 (for TPS phase II beamline) has been installed, as shown in Figure 8, we also designed a four ways slit to confine bending magnet fan for the beam line user. Each slit is made of one piece of CuCrZr alloy, which includes cooling tube, flange and counter flow cooling body.

These two cooling assemblies are first two CuCrZr high heat load components currently installed in TPS storage ring in this year (August, 2016).

NEG COATING

NEG coating on CuCrZr material has also been studied in TPS. The Ti-Zr-V getter films were grown on the CuCrZr alloys. Prior to getter films deposition, the CuCrZr samples were cleaned by the standard cleaning process same as for the TPS vacuum chambers. In our experiments, direct current sputtering method was used. The base pressure of the sputtering chamber was 1.5×10^{-4} Pa. The thickness of the films is in the range of 0.5-1 μm. After a getter film coating was completed, the samples were subjected to a series of analyses and measurement. The surface morphology and the X-ray diffraction pattern of the film were shown in Figure 9 (a), and (b), respectively. The NEG films have a rough surface and circular pores. In addition, the signals marked in Figure 9 (b) come from the Ti-Zr-V getter films and the original substrate. The peak associated with the Ti-Zr-V film occurs at approximately $2\theta = 34^{o}$. The average grain size of Ti-Zr-V films was calculated to be 1.5 nm. It indicates that the Ti-Zr-V films have nanocrystalline structures.

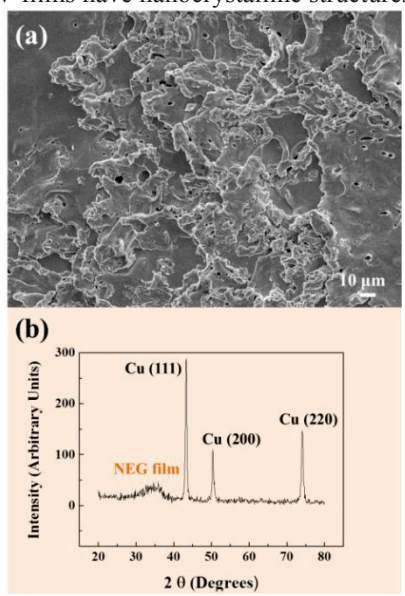


Figure 9: (a) The surface morphology (b) X-ray diffraction pattern of Ti-Zr-V getter films on the CuCrZr alloys.

DISCUSSION AND CONCLUSIONS

CuCrZr alloy has been test and adopted as our new candidate for high heat load components in TPS. Its UHV compatibility has been proved by our outgassing rate test. By carefully controlled welding parameters we are able to TIG weld the alloy with stainless steel. Tensile test has also been carried out to ensure its weldability; primary research on NEG coating on CuCrZr alloy is also studied.

Two high heat load components, TPS double-minimum EPU48 mid-section transition absorber and front end 24 water cooled slits are made in one full CuCrZr piece of material and have been installed in 2016 summer shutdown maintenance. They will be used as first touchstone to verify using this alloy as our next generation high heat load components.

REFERENCES

[1] *Vacuum Science and Technology for Accelerator Vacuum Systems*, CLASSEE, Ithaca, NY, Jan. 2015, pp. 34.

[2] www.conductivity-app.org/download-alloy-pdf/19.

Content from this work may be used under the terms of the CC BY 3.0 licence (© 2016). Any distribution of this work must maintain attribution to the author(s), title of the work, publisher, and DOI.

ISBN: 978-3-95450-188-5 doi:10.18429/JACoW-MEDSI2016-MOPE31

Content from this work may be used under the terms of the CC BY 3.0 licence (© 2016). Any distribution of this work must maintain attribution to the author(s), title of the work, publisher, and DOI.

DYNAMIC PERFORMANCE OF A SUPPORT SYSTEM FOR BBA COMPONENTS IN SXFEL

F. Gao†, Y.X.Dong, R.B. Deng, Y.M.Wen, S. Sun, Z.Q. Jiang, X. Hu, L.Wang,

Shanghai Institute of Applied Physics, CAS, Shanghai, 201204 China

Abstract

The electron beam orbit stability is very important for the Free Electron Laser (FEL) facility. The high beam position stability requirement results in the high position stability for the FEL key components, such as quadruple magnet (Q) and beam position monitor (BPM). This work focus on the research of the dynamic performance of a mechanical support system composed of mechanical supports（including sheets and adjustments）and a granite block mounted on them. It will be applied for the beam based alignment (BBA) Q magnet and BPM for the Soft X-ray FEL project (SXFEL). The Finite-element（FE）calculations of the model characteristics were carried out to guide the subsequent tests. The test results show that the support system can meet the requirement of the SXFEL project.

INTRDUCTION

Shanghai Soft X-ray FEL (SXFEL) and the Dalian Coherent Light Source project (DCLS) are significant national science and technology infrastructure. The electron beam stability is one of the most important factors that influence the properties of FEL. The increasing demands of beam position stability result in the higher position stability requirement for the FEL key parts such as undulator and quadruple magnet. Since the mechanical support system for the FEL provides supporting, location and position adjustment, the high mechanical stability of the supports is indirectly expected.

Soft X-ray Free Electron Laser (FEL) light in the SCSS project developed a new support-stand composed of cordierite body with low thermal expansion rate attached with two flanges at top and bottom used in undulator line [1]. Sand-filled insulated steel support pedestals were used in undulator line of LCLS (Linac Coherent Light Source) [2]. Swiss FEL also developed a new mechanical support with low thermal expansion for BBA [3].

For the DCLS&SXFEL projects, granite blocks with produced from Shandong Province of China have been used as the main component of the support for BBA. In this work, several kinds of mounting method between granite block with mechanical components and Ground were designed and discussed. The first eigenfrequency is an important index for the stability and performance of supports [4].This paper describes an attempt to understand and increase the first eigenfrequency of different kinds of support for BBA to improve its stability, which based on the fact that the ground vibrations at the SXFEL(SSRF site) are larger than at other light sources [5].

This paper presents two different kinds of support prototype for Beam Based Alignment (BBA). Modal hammering experiments and FE analysis of prototypes are discussed in this work. Finally, vibration measurement result about the final support for BBA mounting in the tunnel is shown in this paper.

PROTOTYPES DESIGN

Design of Prototype 1 (See Figure. 1)

- Prototype1 support contains two components of a granite block with a low thermal expansion coefficient and three dimensional adjustments.
- 3 welding bases are fixed on ground with 12 anchor bolts and non-shrinkage cement having high strength.
- 3 direction adjusting can be done by adjustments located on 3 welding bases and M42 Screws.

Design of Prototype 2 (See Figure. 2)

- Prototype2 support contains two components of a granite block with a low thermal expansion coefficient and three layers of steel.
- The bottom steel is fixed on ground with 4 anchor bolts and non-shrinkage cement having high strength.
- 3 direction adjusting can be done by adjusting blocks located on steel and 4 M16 jack screws.

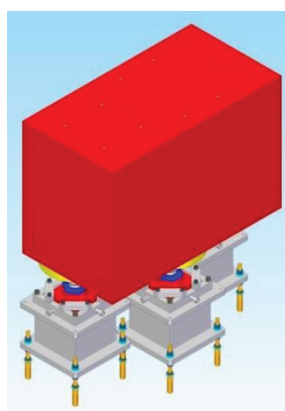


Figure 1: 3-D modal of prototype1.

* Work supported by National Natural Science Fund of China（Grant No.11405255）
† gaofei@sinap.ac.cn

ISBN: 978-3-95450-188-5 doi:10.18429/JACoW-MEDSI2016-MOPE31

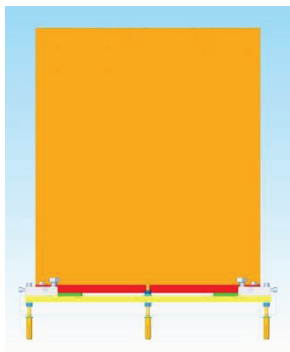


Figure 2: 3-D modal of prototype2.

FE ANALYSIS&MODAL HAMMERING MEASUREMENT OF PROTOTYPES

Table 1: First Eigenfrequency (Hz) of Two Prototypes

Type	Prototype1	Prototype2
FE analysis	29.12	90.32
Modal measurement	28.74	94.28

FE Analysis and Modal Analysis

In order to investigate the dynamic performance and improve the initial mechanical design, FE analysis (ANSYS Workbench14.0) and dynamic measurements (Device:DH5927N Data Collector system，Donghua Testing Technology. Co.,LTD and PCB333B30Acceleration sensors) have been performed on two prototypes.

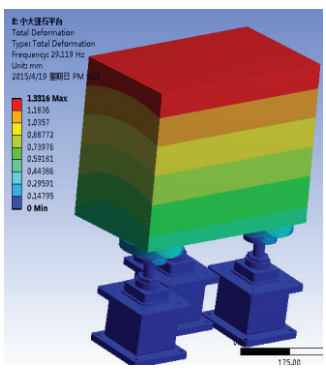


Figure 3: FE analysis of prototype1.

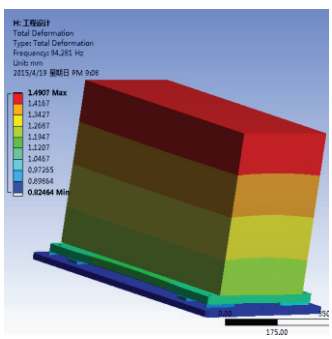


Figure 4: FE analysis of prototype2.

From the results shown in Table 1 we can see that it is very close between FE calculation and modal measurement. Figure3-6 show that the first modal shape of two prototypes is consistent in lateral direction. However, the first eigenfrequency of prototype 2 is much higher than prototype1. Base on the above FE and modal analysis, the structure of prototype2 and connection between a granite block and ground is proposed to improve the first eigenfrequency of the support for BBA.

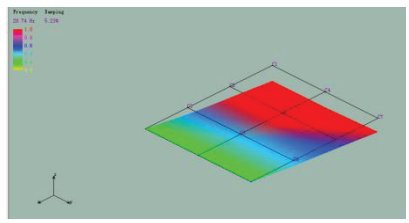


Figure 5: First modal shape of prototype1.

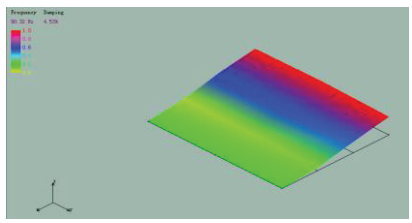


Figure 6: First modal shape of prototype2.

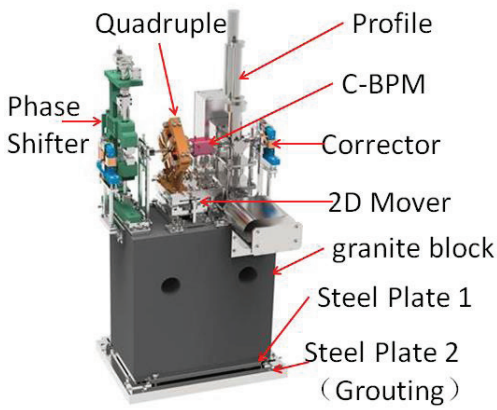


Figure 7: Support system for BBA.

VIBRATION MEASUREMENT OF FINAL SUPPORT INSTALLED IN DCLS

Vibration Measurement

Four measurement points (Top of Q, mover, granite block and ground) were located at the support system (See Figure 7 and 8). The total data taking time in tunnel is approximately 12 hours (quiet time) at night.

Content from this work may be used under the terms of the CC BY 3.0 licence (© 2016). Any distribution of this work must maintain attribution to the author(s), title of the work, publisher, and DOI.

ISBN: 978-3-95450-188-5 doi:10.18429/JACoW-MEDSI2016-MOPE31

Content from this work may be used under the terms of the CC BY 3.0 licence (© 2016). Any distribution of this work must maintain attribution to the author(s), title of the work, publisher, and DOI.

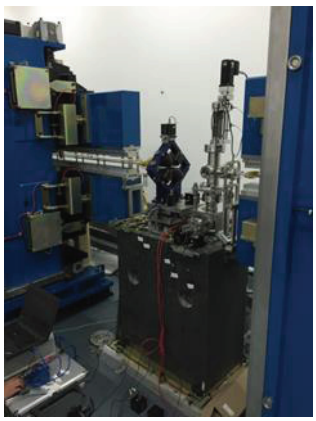


Figure 8: Vibration measurement in DCLS tunnel.

Table 2: Results in Vibration Measurement

	rms(nm)	Ratio(*/ground)
Ground	10.1	1.0
Granite	12.1	1.2
Mover	12.4	1.23
Quadrupole	14.3	1.43

Vibration Analysis

The result of power spectral densities and integrated RMS displacement (*f*: 4-100Hz band) are shown in Figure.9 and Figure.10. The rms average ratio of Quadrupole/ground, Granite/ground and Mover/ground can be seen in table 2. Based on the vibration results, we can see that the most of important average ratio of Quadrupole/ground is 1.43，which is low and can meet the requirement of the SXFEL and DCLS .

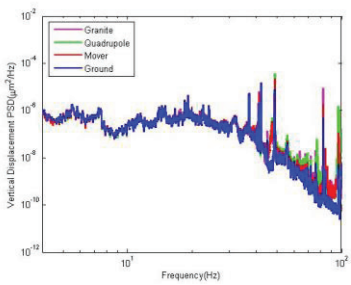


Figure 9: Displacement PSD spectra (vertical direction).

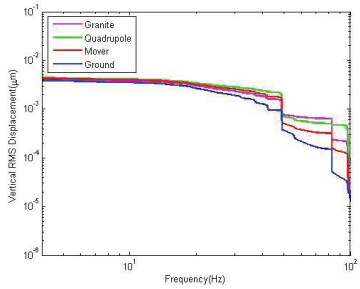


Figure10: RMS Displacement spectra (vertical direction).

CONCLUSIONS

In this paper the dynamic performance of the support for BBA has been studied by FE analysis and modal measurement. Both FE calculations and modal measurement have been performed on two prototypes. The comparison of vibration measurement of support for BBA in DCLS has been also performed. Based on the analysis by FE and modal measurement，the prototype2 is chosen as the final support in DCLS and SXFEL because of its higher first eigenfrequency. In additional, the vibration ratio of Quadrupole/Ground measured in tunnel of DCLS is small，which can meet the requirement of SXFEL and DCLS projects.

ACKNOWLEDGEMENTS

The authors would like to acknowledge financial support from The National Natural Science Fund（Grant No.11405255）.

REFERENCES

[1] T. Saeki, T.S., RIKEN, Mikazuki-chou, Sayou-gun. Development of A New Support-Stand with High Thermal Stability for the SCSS Project

[2] W., M. et al.Performance of Production Support and Motion Systems for the LCLS Undulator System. PAC2009,Vancouver,Canada, WE5RFP063 2009.

[3] Ganter, R. et al. SwissFEL Conceptual Design Report; Paul Scherrer Institute (PSI).Switzerland: PSI, 2011

[4] X., W. et al. Mechanical stability of the magnet girder assembly at the SSRF. J.Synchrotron Rad, (2008).15, 385-391.

[5] B, W. et al. EUROTeV Report 2006-33,http://www.eurotev.org/

ISBN: 978-3-95450-188-5 doi:10.18429/JACoW-MEDSI2016-MOPE32

PRELIMINARY DESIGN AND ANALYSIS OF THE FODO MODULE SUPPORT SYSTEM FOR THE APS-U STORAGE RING *

J. Nudell†, Z. Liu, C. Preissner, J. Collins, H. Cease, Advanced Photon Source, Argonne National Laboratory, Argonne, IL, USA

Abstract

The most technically challenging module of the planned APS Upgrade (APS-U) project is the Focusing-Defocusing (FODO) module. The girder for the FODO must support a ~6m long string of three transverse gradient dipole magnets and four quadrupole magnets. The challenges which emanate from retrofitting the existing APS tunnel with new hardware along with the stringent requirements for alignment and vibrational stability [1] necessitate a unique engineering solution for the magnet support system. FEA is heavily relied upon in order to create an optimized solution and reduce the number of design iterations required to meet specifications. The prototype FODO magnet support design is presented from the ground up, along with FEA justification and the expected vibrational performance of the module.

INTRODUCTION

The APS is planning an upgrade of the storage ring, which will involve replacing all of the existing hardware in a several month time frame. To meet this difficult schedule constraint, magnets, vacuum chambers, and supports will be assembled to a plinth, and installed as a module. After removal of the existing storage ring hardware, modules will be lifted on air casters and brought to their installation location. Technicians will deflate the air casters and rest the module on three outriggers for initial rough alignment. Next, the plinth will be grouted in place, and the outriggers will be removed. Finally, the magnet support and alignment system will be used to precisely align the girder. A three-point semi-kinematic support system has been chosen in order to reduce the time and effort required for alignment.

Given the large combined mass (~9,145 kg) of the seven magnets which comprise the FODO section, design specifications will be most difficult to meet for this module. To work within the available space around the FODO in the storage ring, all installation and maintenance must be performed on the aisle-side. A prototype FODO module has been procured with a string of dummy magnets which will test fabrication methods, mechanical stability with and without water flow, installation logistics, and vacuum performance (Fig. 1).

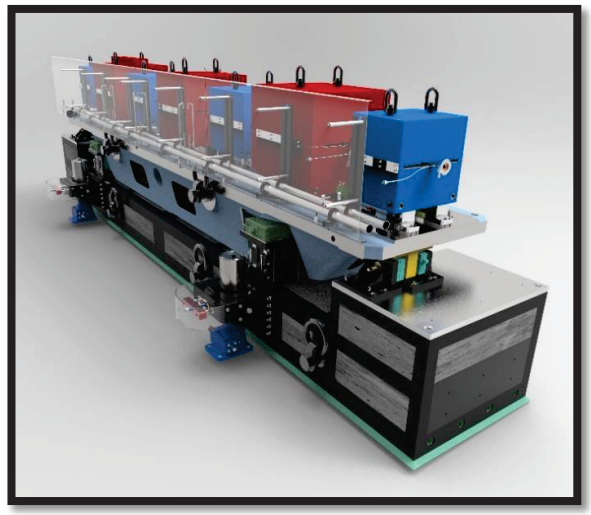


Figure 1: Assembled FODO prototype module.

PLINTH DESIGN

The FODO plinth is a hybrid steel and concrete structure developed through an R&D collaboration with a university, concrete fabricator, steel fabricator, and ANL. Through the use of a proprietary concrete mixture, steel reinforcing bar, and a steel cage which surrounds the concrete, long term shrinkage rates have proven to be acceptably small. The plinth contains all mounting features for the FODO girder support and outriggers, lifting eyes for rigging, and shelves for the two longitudinal gradient dipole magnets, which are positioned directly upstream and downstream of the FODO module. The embedded steel weldments which support the girder have been designed to maximize stiffness while staying within the geometrical boundaries defined by the storage ring walls. The weldments also bring the girder supports as close as possible to beam height in order to reduce the moment of inertia of the girder system and reduce geometric amplification of ground vibrations.

GIRDER DESIGN

The FODO girder has been designed to optimize its stiffness with respect to static deflection and modal response. This was done using a topology optimization software called GTAM [2]. The constraints, an objective function and an initial geometry seed were inputs to the software. An image of the topology optimized geometry is shown in Fig. 2 [3].

* Work supported by: Argonne is managed by UChicago Argonne, LLC, for the U.S. Department of Energy under contract DE-AC02-06CH11357.
† jnudell@aps.anl.gov

Content from this work may be used under the terms of the CC BY 3.0 licence (© 2016). Any distribution of this work must maintain attribution to the author(s), title of the work, publisher, and DOI.

ISBN: 978-3-95450-188-5 doi:10.18429/JACoW-MEDSI2016-MOPE32

Content from this work may be used under the terms of the CC BY 3.0 licence (© 2016). Any distribution of this work must maintain attribution to the author(s), title of the work, publisher, and DOI.

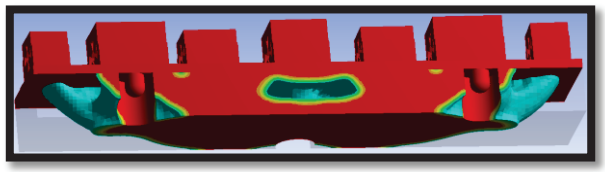


Figure 2: Optimized FODO girder geometry.

Ductile cast iron, A536, GR-60/40/18 was chosen as the girder material because of its design flexibility, low cost, and favorable vibration damping properties. Several design iterations were required with input from a cast iron foundry to transform the ideal geometry into a manufacturable part.

Following the casting process, the girder will be post-machined. Alignment of the magnets on the girder will rely on machining tolerances of the mating parts. Magnet centerlines will be precisely machined relative to fiducial surfaces on the outside of the magnet, and stop-blocks pinned and bolted to the top surface of the casting will be precisely machined after they are assembled to the casting. Pusher-blocks will position the magnets against the stop-blocks with a known force.

Since the design of the support system is semi-kinematic, it is not possible to profile the girder to account for static deflection. The static deflection due to the self-weight of the casting will be negated by grinding the top surface of the casting flat while resting on the three-point support locations. Thus, the static deflection is due to the weight of the magnets alone. The deviation from a best-fit line of in-plane deflection points along the beam path is calculated to be 14 microns.

ALIGNMENT SYSTEM

Airloc-414 KSKC tri-wedge type jacks have been chosen as the vertical alignment device for the FODO support based on the recent success of the ESRF magnet support system [4]. Preload will be achieved prior to alignment with a stack of spring washers which allow the preload to be maintained throughout the adjustment range of the jack. DU Glacier friction reducing plates will be assembled underneath the jacks to allow for lateral adjustment of the girder. A hole through the center of the casting allows for aisle-side adjustment of the wall-side wedge jack with an extension wrench.

ANSYS simulations show that the first mode frequency of the assembly can be significantly raised by using stiff lateral pushers. Therefore, all lateral pushers will use smaller Airloc 2012 wedge jacks rather than conventional pusher screws. A schematic of the pusher locations is shown in Fig. 3.

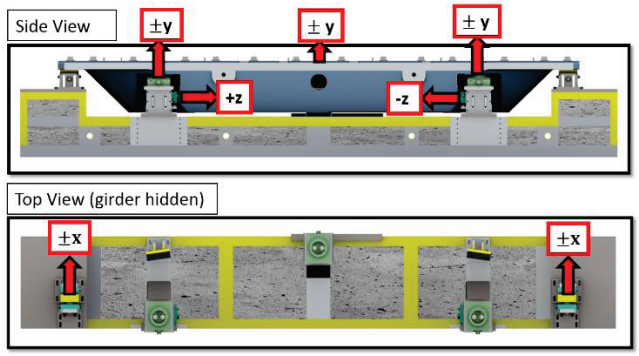


Figure 3: Later pusher locations .

Three outriggers will be procured for the FODO prototype which will be used to rough-align the plinth to within ± 1mm in all degrees of freedom prior to grouting. Since the wall-side outrigger will not be easily reached once installed in the storage ring, the design incorporates push-pull screws so that all lateral adjustments may be made on the aisle-side. The vertical motion is provided with motorized 20-ton NOOK acme screw jacks. A rendering of an outrigger is shown in Fig. 4.

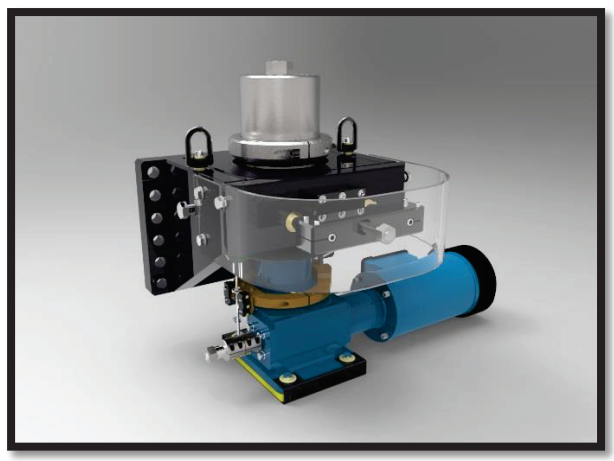


Figure 4: FODO Outrigger.

ANALYSES

Modal Analysis

In order to accurately predict the modal response of the FODO module, dynamic stiffness testing was completed on the vertical and lateral support components. A single wedge jack was placed underneath the center of mass a large granite block, and a modal analysis was conducted while the block was balanced on the jack [5].

Using the equations of motions for this simple dynamic system along with the experimentally determined rigid body modes, the 6x6 diagonal stiffness matrix and damping coefficients of the component were determined.

The experimentally determined stiffness matrix for each vertical and lateral support component was input into an ANSYS modal analysis along with the geometry of the magnets, girder, and plinth. The first mode is a rocking mode at 38.8 Hz, shown in Fig. 5.

ISBN: 978-3-95450-188-5 doi:10.18429/JACoW-MEDSI2016-MOPE32

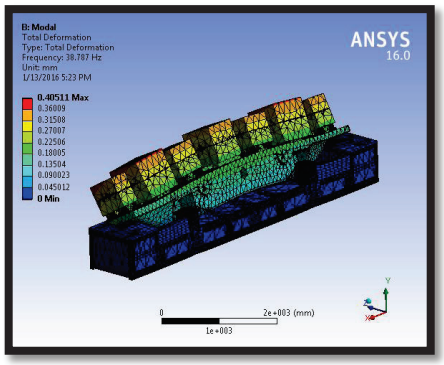


Figure 5: First mode, 38.8 Hz.

Floor Stiffness Analysis

Given the large mass of the assembly, it is possible that the compliance of the storage ring floor will play a significant role in the dynamic performance of the module. Therefore, it is important to include the effect of the floor and underlying aggregate in the modal analysis. Although the approximate stiffness of concrete may be assumed, the aggregate underneath is more difficult to characterize since the stiffness of aggregate varies widely from site to site. Therefore, the floor stiffness was measured as a function of depth for the S28 Experiment Hall floor at the APS by exploiting the frequency dependent properties of shear waves (S-waves) through elastic media, a technique commonly employed by geophysicists [6]. The measured S-wave velocity vs. depth is shown in Fig. 6, from which the Young's modulus of the floor layers may be easily extracted [7].

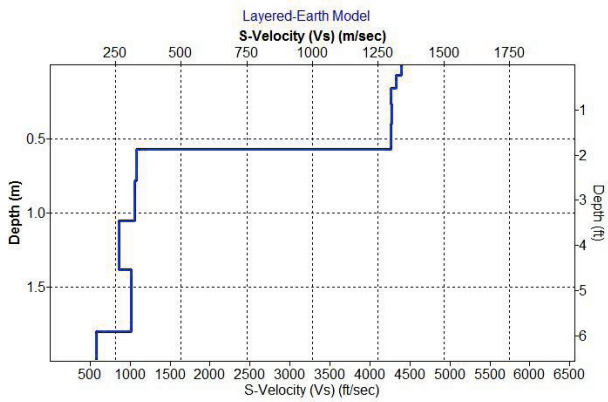


Figure 6: S-wave velocity as a function of depth at APS S28.

By including the floor compliance in the modal analysis, the first mode becomes 35.4 Hz, a reduction of ~10%. In future efforts, similar stiffness measurements for the APS storage ring floor will be obtained.

Random Vibrations Analysis

Ambient floor motion data was taken in 2014 in the APS storage ring at S28 over the frequency range of 1-100 Hz. This floor motion was used as the input to an ANSYS random vibration analysis. The response motion was probed at a point on the upstream quadrupole pole tip. Damping was set to 2% based on an average of the modal damping values found during component testing.

The results are shown in Fig. 7. The RMS vibration response is 13 nm in the X-direction, and 12 nm in the Y-direction. This analysis shows that the dynamics of the system do not play a significant role in amplifying low-frequency motion at the quadrupole pole tip.

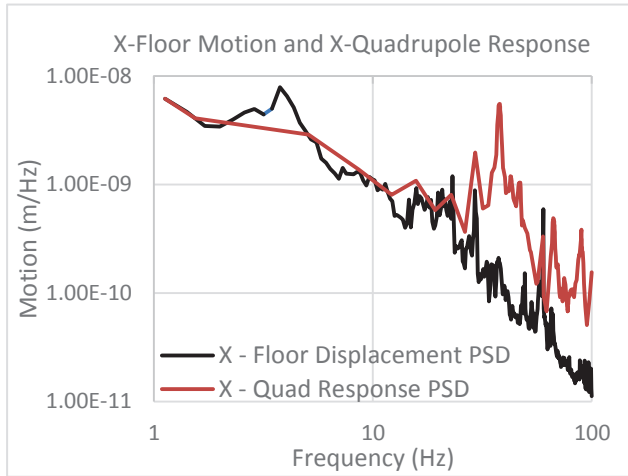


Figure 7: Results of Random Vibration Analysis.

Thermal Analysis

Temperature fluctuations in the storage ring tunnel will be held to ±0.1˚C. The resulting thermal deformations of the girder must be analysed to show that they are negligible compared to the 30-micron RMS magnet-to-magnet alignment tolerance. The z-direction pushers have been placed such that they contact the girder near its neutral axis. This prevents the girder from "bowing" and causing large thermal displacements.

Although a time varying ±0.1˚C temperature change in the tunnel air will not cause the same temperature change in the girder, this analysis assumes a steady state ΔT of 0.1˚C in the entire FODO module. Experimentally determined stiffness values are used for both vertical and lateral supports. The bottom of the grout surface is assumed fixed. The thermal deformation of the girder is shown in Fig. 8.

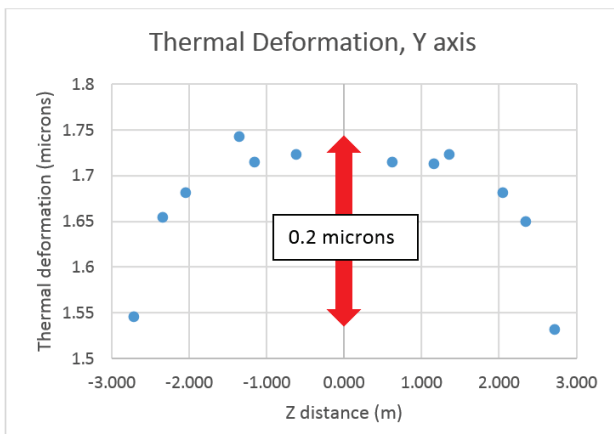


Figure 8: Thermal deformation.

Content from this work may be used under the terms of the CC BY 3.0 licence (© 2016). Any distribution of this work must maintain attribution to the author(s), title of the work, publisher, and DOI.

ISBN: 978-3-95450-188-5 doi:10.18429/JACoW-MEDSI2016-MOPE32

Content from this work may be used under the terms of the CC BY 3.0 licence (© 2016). Any distribution of this work must maintain attribution to the author(s), title of the work, publisher, and DOI.

ACKNOWLEDGEMENTS

Thank you to Bill Turner (Design and Drafting), and Steven Hanuska (Manufacturing) for their help in designing and procuring this assembly. Thank you to Dial Machine (www.dialmachine.com), Corsetti Steel (www.corsettisteel.com), Dukane Precast (www.dukaneprecast.com), Illinois Institute of Technology (http://web.iit.edu/), and ParkSEIS (http://www.parkseismic.com/ParkSeis.html) for their collaborative work with ANL in this R&D effort.

REFERENCES

[1] Glenn Decker (2014) Design Study of an MBA Lattice for the Advanced Photon Source, Synchrotron Radiation News, 27:6, 13-17, DOI: 10.1080/08940886.2014.970932

[2] "GENESIS Structural Optimization for ANSYS Mechanical." *Design Optimization Technologies*. N.p., n.d. Web. 08 Sept. 2016. http://www.vrand.com/GTAM.html.

[3] Liu, Zunping. "Optimization for the APSU Magnet Support Structure." *MEDSI Proceedings* (2016)

[4] Brochard, T. *Design and Characterisation of the Prototype Girder for the ESRF-EBS Storage Ring*. N.p., n.d. Web. 07 Sept. 2016. http://www.esrf.eu/home/UsersAndScience/Publications/Highlights/highlights-2015/enabling-technologies/et08.html.

[5] Preissner, Curt. " Nostradamus and the synchrotron engineer: Key aspects of predicting accelerator structural response." *MEDSI Proceedings* (2016)

[6] Hiesey, J. Scott. Determination of In-Situ Shear Wave Velocities from Spectral Analysis of Surface Waves. Rep. no. FHWA/TX-82/34+256-2.

[7] Park, Choon. "Floor Stiffness at Argonne National Lab." 18 Aug. 2016. E-mail.

ISBN: 978-3-95450-188-5 doi:10.18429/JACoW-MEDSI2016-MOPE34

PRELIMINARY DESIGN OF THE MAGNET SUPPORT AND ALIGNMENT SYSTEMS FOR THE APS-U STORAGE RING*

J. Collins†, Z. Liu, J. Nudell, S. Izzo, C. Preissner, H. Cease
Advance Photon Source, Argonne National Laboratory, Argonne, IL 60439, USA

Abstract

As part of the Advanced Photon Source Upgrade project (APS-U), the storage ring will be upgraded to a multibend achromat (MBA) lattice [1]. This upgrade will provide dramatically enhanced hard x-ray brightness and coherent flux to beamline experiments in comparison to the present machine. The accelerator physics requirements for the upgrade impose very stringent alignment, assembly and installation tolerances and tight vibrational tolerances on the magnet support and alignment system designs. The short installation duration dictates a need for transporting groups of fully assembled magnet modules into the storage ring enclosure while preserving magnet-to-magnet alignment. The current magnet support and alignment systems preliminary design status for the APS-U storage ring will be presented along with an overview of the R&D program required to validate design performance. Magnet module transportation and installation logistics will also be discussed.

INTRODUCTION

The existing APS storage ring will be completely removed and replaced with an MBA lattice as part of the APS-U. The APS-U storage ring will consist of forty repeating arc sectors, each containing nine magnet modules as shown in Figure 1. Each arc sector contains five concrete plinths used to build up groups of magnets that can be installed as a module. The largest magnet module located in the center of the arc sector is the curved Focusing-Defocusing (FODO) module. On either side of the FODO module are straight Multiplet modules followed by Quad Doublet modules. Supported on bridges between the concrete plinths are longitudinal gradient dipole magnets (L-Bend), a total of four per arc sector. The concrete plinths effectively "raise the floor" to help reduce geometric amplification of ground vibrations. The magnet groups on each concrete plinth are mounted to a girder that is supported by a three-point semi-kinematic six degree of freedom (DOF) support and alignment system. The planned installation duration is very short, allowing only one year for removal, installation, testing, commissioning and return to beamline operations. Installing pre-assembled magnet modules will reduce installation time and the three-point semi-kinematic six DOF support and alignment systems will reduce the time and effort required for alignment.

Derived from the APS-U accelerator physics requirements, the survey and alignment assembly and installation tolerances are shown in Table 1. The requirement is that each magnet module girder be aligned to within 100 µm RMS of a neighboring girder at the start of commissioning. The APS-U physics requirements also impose tight vibration tolerances on the magnet support and alignment system designs as shown in Table 2. For instance, a 9 nm RMS vibration tolerance on the vertical magnet-to magnet motion must be satisfied for proper operation. Measurements of the floor vibration spectrum in the APS storage ring indicate that the ground motion will be less than 1 nm above 50 Hz. Therefore, a first mode frequency greater than 50 Hz is chosen as a design goal for the installed magnet modules since it will ensure that vibration tolerances will be met.

Table 1: Survey and Alignment Assembly and Installation Tolerances at Start of Commissioning .

Girder misalignment	100 μm
Elements within girder	30 μm
Initial BPM offset errors	500 μm
Dipole fractional strength error	$1 \cdot 10^{-3}$
Quadrupole fractional strength error	$1 \cdot 10^{-3}$
Dipole tilt	$4 \cdot 10^{-4}$ rad
Quadrupole tilt	$4 \cdot 10^{-4}$ rad
Sextupole tilt	$4 \cdot 10^{-4}$ rad

Table 2: Summary of Vibrational Tolerances

	X (rms)	Y (rms)	X (rms)	Y (rms)
	1-100 Hz		0.1-1000 Hz	
u_{girder}	32 nm	40 nm	320 nm	400 nm
u_{quad}	13 nm	9 nm	130 nm	90 nm

In order to validate design performance, a comprehensive R&D program has been established that addresses major risks. Numerous vibration tests are being conducted on prototype modules that will provide substructure stiffness information and allow finite element model validation [2]. Temperature change-driven misalignment tests are planned that will provide insight into how the alignment of a magnet module reacts to local temperature fluctuations. Since fully assembled magnet modules will be transported and installed into the storage ring, transport tests are being conducted to ensure that magnet alignment is retained through this process. Tests are also being conducted that will inform installation planning and logistics.

* Work supported by the U.S. Department of Energy, Office of Science, under Contract No. DE-AC02-06CH11357
† collins@aps.anl.gov

Content from this work may be used under the terms of the CC BY 3.0 licence (© 2016). Any distribution of this work must maintain attribution to the author(s), title of the work, publisher, and DOI.

ISBN: 978-3-95450-188-5 doi:10.18429/JACoW-MEDSI2016-MOPE34

Content from this work may be used under the terms of the CC BY 3.0 licence (© 2016). Any distribution of this work must maintain attribution to the author(s), title of the work, publisher, and DOI.

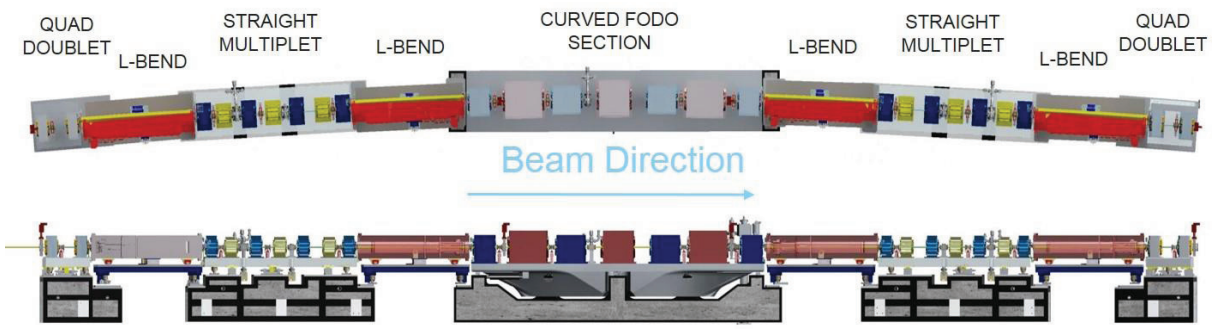


Figure 1: APS-U storage ring arc sector layout.

PRELIMINARY DESIGN

The magnet support and alignment systems design for the APS-U storage ring reflects preliminary design. Future results obtained through R&D and from finite element modelling will further inform the designs and allow for design maturation.

Concrete Plinths

Granite was originally considered for the plinths; however, through an R&D collaboration it was demonstrated that a hybrid steel and concrete plinth design provides excellent dimensional stability at less than half the cost of granite. The concrete plinths use a continuous welded steel frame with internal rebar and large headed anchor studs welded to all channels and plates in order to help minimize shrinkage and distortion. A proprietary low-moisture, low-shrinkage concrete mix was specially developed for the plinths. Several prototype concrete plinths were fabricated and dimensional stability measurements were made over time to monitor shrinkage and distortion. Less than 20 µm of shrinkage was measured during the first two months. For production, after six months of curing each concrete plinth will be painted to seal the concrete in order to prevent dust generation inside of the storage ring.

Girders

All of the magnet support structures, referred to as girders, will be geometrically optimized and fabricated from cast iron. GTAM topology optimization software is used to maximize the first mode frequency response while minimizing strain energy (static deflection) along the beam path through the magnets [3]. Starting with a seed geometry, an objective function and the constraints, the software determines where mass is needed and where it is not. Several initial thicknesses of the girder are chosen for seed geometries and a parametric study is performed to see how the first mode frequency and static deflection vary as a function of girder thickness. The chosen ideal structure may then need to be modified based upon input from the foundry in order to transform the ideal structure into a manufacturable casting design. Figure 2 illustrates this process for the prototype FODO module girder casting [4]. After casting, the girder is heat treated in order to strain relieve the structure prior to machining.

Using ductile cast iron for girders has many advantages over using thick steel plate. Ductile cast iron is more cost effective, can be machined to tighter tolerances, and exhibits higher specific damping capacity. Casting the girders allows material to be used only where it is needed and allows for the fabrication of complicated optimized geometries.

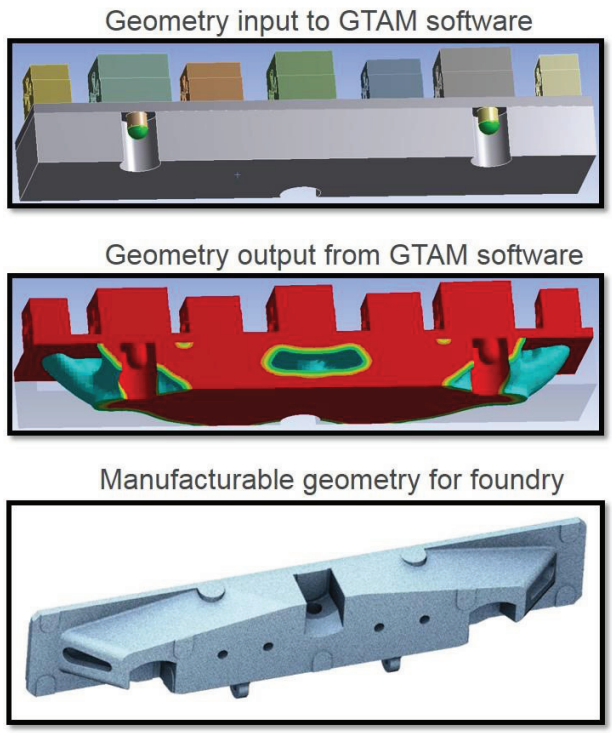


Figure 2: Optimization process for the FODO section girder casting.

Support & Alignment Systems

Each magnet module in the APS-U accelerator is aligned using a three-point semi-kinematic six DOF support and alignment system. Figure 3 shows a typical concrete plinth with the support and alignment systems installed. On the top of the concrete plinth are the components that comprise the support and alignment system for the girder. Three commercially available wedge jacks are used for the vertical supports, and these contain spherical bearings and slip plates to decouple translation and rotation from the vertical motion. The two lateral pushers

ISBN: 978-3-95450-188-5 doi:10.18429/JACoW-MEDSI2016-MOPE34

provide lateral and yaw constraint and alignment, and the longitudinal pusher provides longitudinal constraint and alignment.

In addition, all concrete plinths use a temporary six DOF alignment system, referred to as support outriggers, to align the plinth prior to grouting to the storage ring floor. There are a total of three support outriggers, two on one side of the concrete plinth and one on the other side, and each provides vertical, lateral and longitudinal adjustment. Plinths are moved into location using an air caster system, rough aligned using the support outriggers, grouted in place, and once the grout has cured the support outriggers are removed.

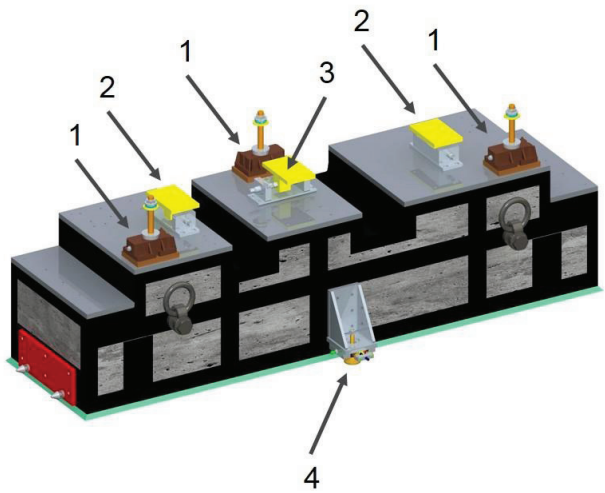


Figure 3: Typical concrete plinth support & alignment systems - (1) three-point vertical wedge jack supports, (2) lateral pushers, (3) longitudinal pusher, (4) support outriggers (3 total).

Magnet Modules

The largest magnet module in the APS-U storage ring is the FODO module with a length of nearly 6.5 m and a total weight around 29,000 kg. Due to space constraints in the storage ring, the FODO module has been designed so that all adjustments can be made on the aisle-side. A prototype FODO module has been procured and extensive R&D on the module is planned. A rendering of what the FODO module will look like in our testing area is provided in Figure 4.

The straight Multiplet module is the next largest magnet module with a length of nearly 3.6 m and a total weight around 11,800 kg. Extensive tests have already been conducted on a demonstration Multiplet module (DMM) we have in our testing area. The smallest magnet module containing a concrete plinth is the Quad Doublet module with a length of only 1.5 m and a total weight around 4,500 kg.

There are a total of 160 L-Bend magnets in the APS-U storage ring, four per arc sector installed on support bridges between the concrete plinths. The L-Bend magnet support bridge contains a manual translation stage that allows removal of the magnet from the vacuum chamber during bake out. Each L-Bend module is around 2 m long and weighs 2,900 kg. Prototypes of the Quad Doublet module and the L-Bend module will be procured and extensive R&D on these modules is planned.



Figure 4: Rendering of the prototype FODO module in the testing area.

CONCLUSION

For the APS-U project, the entire storage ring will be removed and replaced with an MBA lattice consisting of forty repeating arc sectors. There are four types of magnet modules and each arc sector contains nine magnet modules. Due to the short installation duration, pre-assembled magnet modules will be installed in the storage ring and six DOF support and alignment systems will be used to reduce alignment time and effort. Though currently in the early stages of preliminary design, extensive R&D is being conducted on several prototype magnet modules, and results obtained through testing and finite element modelling will further inform the designs.

REFERENCES

[1] G. Decker, "Design Study of an MBA Lattice for the Advanced Photon Source," *Synchrotron Radiation News*, 27:6, 13-17, 2014, DOI: 10.1080/08940886.2014.970932.

[2] C. Preissner *et al.*, "Nostradamus and the Synchrotron Engineer: Key Aspects of Predicting Accelerator Structural Response," in *Proceedings of MEDSI 2016*, 11~16 SEPT, 2016, Barcelona, Spain.

[3] Z. Liu *et al.*, "Optimization for the APS-U Magnet Support Structure," in *Proceedings of MEDSI 2016*, 11~16 SEPT, 2016, Barcelona, Spain.

[4] J. Nudell *et al.*, "Preliminary Design and Analysis of the FODO Module Support System for the APS-U Accelerator," in *Proceedings of MEDSI 2016*, 11~16 SEPT, 2016, Barcelona, Spain.

Content from this work may be used under the terms of the CC BY 3.0 licence (© 2016). Any distribution of this work must maintain attribution to the author(s), title of the work, publisher, and DOI.

ISBN: 978-3-95450-188-5 doi:10.18429/JACoW-MEDSI2016-MOPE37

DIAMOND MULTI-BEND ACHROMATS FOR LOW EMITTANCE AND NEW INSERTION DEVICES

J. Kay†, N. P. Hammond, Diamond Light Source, Didcot, OX11 0DE, UK

Abstract

Diamond Light Source is pioneering the move to a Multi Bend Achromat storage ring lattice for low emittance combined with the creation of new straight sections available for Insertion Devices (ID). Diamond is at an advanced stage of replacing one Double Bend Achromat (DBA) cell of the existing storage ring with a Double Double Bend Achromat (DDBA). The DDBA cell which is to be installed in Autumn 2016 has 4 dipoles and has been designed with a new straight section in the middle. This allows ID radiation to shine down an existing Bending Magnet port in the shield wall for a new micro-focus protein crystallography beamline called VMX-m. This same principle will be applied to the proposed Diamond II project which will be based on a Double Triple Bend Achromat with 6 dipoles per cell achieving even lower emittance whilst providing many more IDs. This paper describes the engineering challenges of these projects.

INTRODUCTION

The move to replace a DBA cell with a DDBA cell is at an advanced stage with 2 girders measuring 7.5 m long nearing completion for installation in an 8 week shutdown between Oct 7th and Dec 5th 2016. The overall geometry is shown in Fig. 1. and a completed girder in Fig. 2. The engineering design was described more fully in [1, 2].

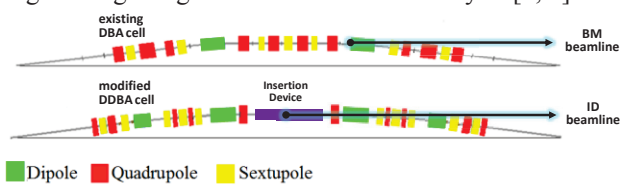


Figure 1: Schematic diagram of the existing DBA and the modified DDBA cell.

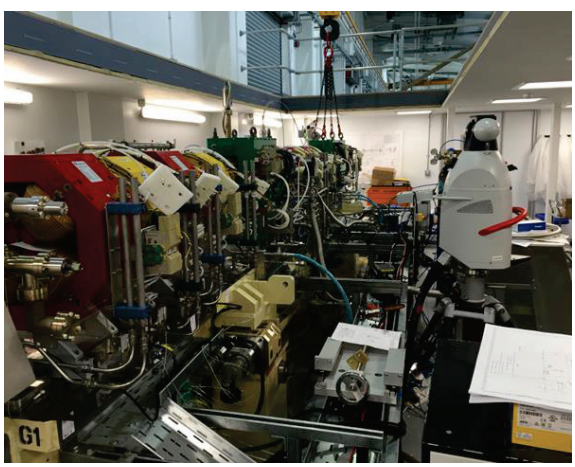


Figure 2: Completed Girder 1 in the assembly room.

† jim.kay@diamond.ac.uk

This paper will give some of the lessons learned from our experience building the DDBA cell as well as point towards a future Diamond II low emittance storage ring.

MAGNETS

A number of issues arose with the magnets to inform future projects. It is essential to keep water connections sufficiently clear of coils and coil terminations to enable pipework and cable connections to be made with good access for hands and tools (see Fig. 3.). Simply identifying 'stay clear' zones in the magnet reference design did not prove sufficient. Another issue on the sextupole magnets which have many terminal connections was the need to space out adjacent terminal blocks to give clear access for different cables to enter the terminal blocks cleanly. Although an overall length for each magnet was specified including coil overhang, the difficulties of achieving the right number of ampere-turns with a real, hollow cross-section conductor meant that this was exceeded which had implications for fitting adjacent components. It is clear that for any significant procurement contract, regular visits are essential to make sure these technical details, overall quality as well as delivery schedule issues are managed. Problems identified during final assembly are just too late and inevitably leave no time for the supplier to put things right and so the client has to compromise.

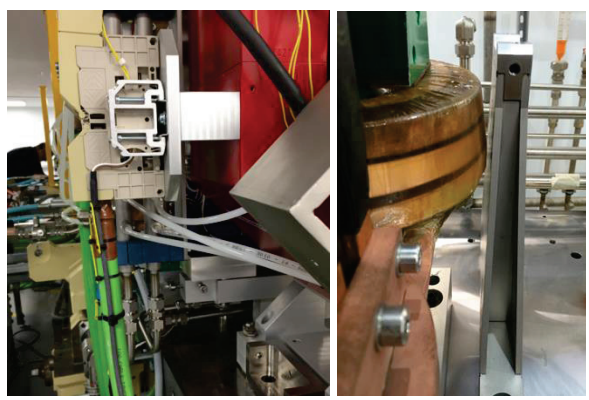


Figure 3: Magnet terminal spacer block added to separate pipes and cables and Dipole coil overhang allowance exceeded.

For more precise alignment of magnets the stretched wire technique was used [3]. This took much longer than was originally estimated by a factor 4 which had a significant impact on programme. The magnets were measured at the manufacturer using the same stretched wire bench and one shim adjustment made per magnet. However this was not checked and in the end all magnets were re-centred and shimmed at Diamond up to 3 times each.

Content from this work may be used under the terms of the CC BY 3.0 licence (© 2016). Any distribution of this work must maintain attribution to the author(s), title of the work, publisher, and DOI.

ISBN: 978-3-95450-188-5 doi:10.18429/JACoW-MEDSI2016-MOPE37

The magnets had to be aligned in groups (see Fig. 4.) which required towers supporting the stretched wire to be re-positioned and aligned for each group. As well as taking more time for the magnet team, this process took a lot of effort for the survey team which had an impact on other alignment tasks in the programme.



Figure 4: Stretched wire measurement of magnet groups.

Because 2 dipoles are mounted on each girder there are 3 intersecting straight line electron trajectories. Figure 5 shows a system of fixed geometry, precision machined 12 mm dowel and fixing holes accurate to 20 µm for magnet and vacuum vessel fixing with a system of shims for fine magnet alignment. This process has worked well.

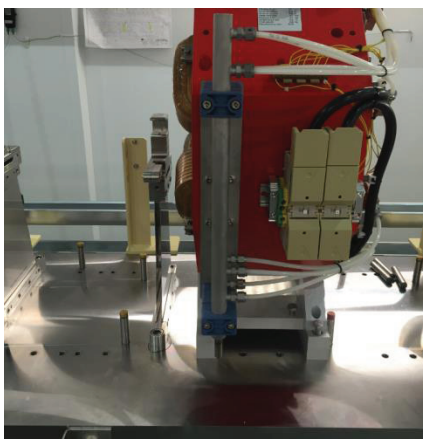


Figure 5: Dowels and shims to position equipment.

VACUUM

Helicoflex© spring reinforced metal seals are used on vacuum vessel joints close to the electron beam to ensure face to face joints with no gaps that might cause RF heating. A problem arose in the DF40 size that a reliable leak tight joint was difficult to achieve. Analysis [4] predicted that during compression of the seal the contact pressure in the middle of the contact zone drops to near zero with relatively low pressures each side. Circular ridges were machined in the contact area to encourage higher pressure 'knife edge' seal regions to be formed (see Fig. 6.).

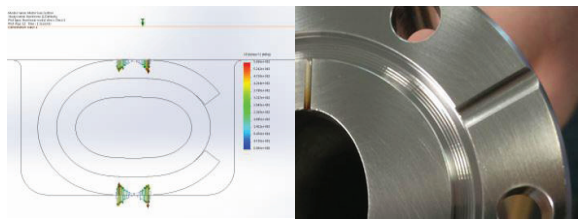


Figure 6: Machined ridges achieve higher pressures.

In reviewing the Helicoflex data tables for HN100, compression forces of 140-150 N/mm are shown for flanges DN40 and DN63 but 200 N/mm for larger sizes. Our view now is a minimum of 200 N/mm for all sizes.

Because the beam tube is oval, it is difficult to guarantee accurate alignment across flange joints minimising steps to <0.1 mm without the use of dowels. Dowels in the flanges require vessel separation so an external dowel arrangement has been developed instead (see Fig. 7.).

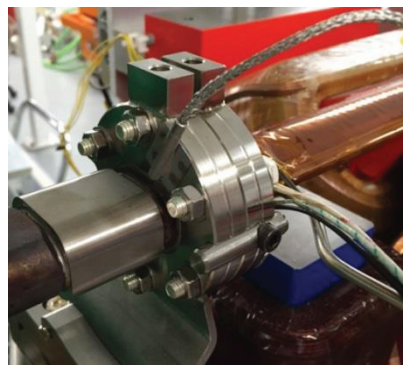


Figure 7: External dowel alignment of flanges.

Developments in electron beam welding of copper have allowed full penetration welds of cooling channels joined to the electron tube to be achieved without voids in the conduction path (see Fig. 8. left) and TIG welding of longitudinal joints in oval vessels with zero projection into the beam space (see Fig. 8. right).



Figure 8: Full penetration welding of copper.

The vessels are baked in-situ and during the assembly we unfortunately had a malfunction of the bake-out controller over a weekend which caused over-temperature damage to a number of vessels. This accident cost a month to programme to recover and repair vessels and valuable lessons have been learned including thermal switches now fitted to the vessels to trip the power.

Content from this work may be used under the terms of the CC BY 3.0 licence (© 2016). Any distribution of this work must maintain attribution to the author(s), title of the work, publisher, and DOI.

ISBN: 978-3-95450-188-5 doi:10.18429/JACoW-MEDSI2016-MOPE37

Content from this work may be used under the terms of the CC BY 3.0 licence (© 2016). Any distribution of this work must maintain attribution to the author(s), title of the work, publisher, and DOI.

GENERAL

A purpose built temperature controlled assembly room was constructed to accommodate both girders. This room is equipped with cooling water, magnet power supply and other services. In order to keep the shutdown to a minimum 8 weeks it was essential to complete off-line tests of magnetic field and cooling flows. Temperature control to 22+/-1 °C is essential for magnetic wire measurement and it was found that removing the roof to the room to enable a component to be delivered upset the stability and required 30 minutes for the air temperature to recover. It also became clear that mechanical, electrical, controls, survey, magnet and vacuum staff all needed competing access to one or both girders at the same time and the assembly room was just too small. For Diamond II a production line is required which respects the 3 different stages of magnet alignment, vacuum assembly and baking followed by cabling, pipework and test. Cables are routed on cable tray fixed to the girder with the cables terminated in a substantial patch panel (see Fig. 9.). This panel is replicated in the tunnel so that on installation the DDBA cell can be quickly connected, powered up and tested. This arrangement though is bulky and time consuming and is not attractive for Diamond II. The vacuum vessels are baked in-situ with the bottom of the magnets in place after alignment but with the magnet tops removed to install the vacuum vessels. The amount of cables involved with baking and temperature measurement is significant and they need to be included in the cabling design and 3D CAD model to route them tidily.

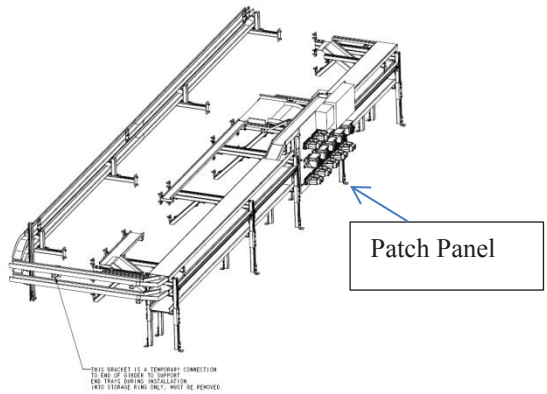


Figure 9: Arrangement of girder cable tray.

DIAMOND II

The DDBA project is proving that we can install a new straight section with an ID providing much more intense light through a previous Bending Magnet (BM) port. This principle can now be applied to the whole 24 cell storage ring effectively creating up to 48 straight sections available for the installation of IDs.

Along with many other light sources, Diamond is busy planning a low emittance upgrade to improve the brightness of the source. Reported in [5] is a proposal to reduce the emittance of Diamond from 2700 pm to 120 pm by building 24 Double Triple Bend Achromat cells (DTBA). A view of one cell of the DTBA lattice is shown in Fig. 10, with one of the new ID straights installed in the middle of the DTBA followed by an existing straight and ID.

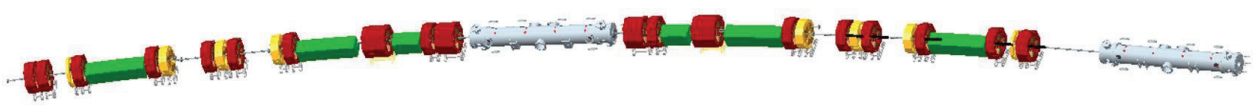


Figure 10: One cell of Diamond DTBA showing new ID position mid-achromat followed by an existing ID.

CONCLUSION

The DDBA project is about to be installed at Diamond creating a new ID straight and source point at a previous BM port. Many lessons have been learned in the practicalities of manufacturing water cooled, small bore, oval vacuum chambers of V22 mm*H29 mm external dimensions in copper and stainless steel, baking them in-situ and achieving face to face flange sealing with the Helicoflex© seal. Lessons have also been learned in the production of small, water-cooled electro-magnets and the essential requirement to achieve magnetic and geometric accuracy at the supplier to avoid delays during final assembly. Any major supply contract requires a dedicated client resource working continuously with the major suppliers.

The challenges on assembly and storage space should also not be underestimated. It is impracticable to manage multi-phase construction of complex girders side by side and a production line should be established with an overall responsible production manager to manage interfaces across many teams on a day-to-day basis.

A low emittance upgrade project is in progress and the lessons learned from DDBA will provide valuable information in planning the delivery of Diamond II.

REFERENCES

[1] J. Kay *et al.,* ''Engineering Solutions for the Diamond Double Double Bend Achromat Project'' in *Proc. MEDSI'14.*

[2] J. Kay *et al., in Proc. IPAC'14,* pp. 328-330.

[3] R.P. Walker *et al., in Proc. IPAC'16,* pp. 2953-2955.

[4] R.J. Smith, ''Evaluation of Hertzian and Finite Element Models of Elastomer and All Metal Spring Energised Seals'', Course Report, University of Central Lancashire, UK, April 2016.

[5] R. Bartolini *et al., in Proc. IPAC'16,* pp. 2943-2946.

ISBN: 978-3-95450-188-5 doi:10.18429/JACoW-MEDSI2016-MOPE38

MILLIPROBE SCANNER STATION*

J. Divitcos†, M. De Jonge, D. Howard, J. McKinlay
Synchrotron Light Source Australia, Australia

Abstract

The research team at the Commonwealth Scientific and Industrial Research Organisation, Clayton (CSIRO) have developed a the high energy dispersive detector referred to as the Maia. The rapid scanning, high resolution detector offers technological advances, including non-invasive technical study of highly valued artwork.

A vital application of the maia detector is scanning x-ray fluorescence microscopy for obtaining the elemental composition of a large number of materials.
The innovative detector allows connection between scientists and arts communities to increase their understanding of historical artworks, broadening the field of authentication and potentially aiding the fight against art forgery as well as historical information.

We have designed a new dedicated milliprobe station that offers improvements in stability, motion control and mounting. The structure is designed to support and scan various samples in size as well as shape powered by X and Y stages. A slide and hold clamping concept has been implemented, incorporating carbon fiber tubes, which provides easy and rapid assembling of samples. This arrangement provides excellent interchangeability, supporting a variety of planar and non-planar samples for scanning [1].

INTRODUCTION

For several years we have used a prototype 'milliprobe' apparatus to successfully scan large objects. Examples include paintings from the National Gallery of Victoria, historical photos and a Melbourne Cup – Australia's most prestigious thoroughbred horse race trophy.

MAIA DETECTOR

Thanks to the highly sensitive CSIRO and Brookhaven National Laboratory (BNL) developed maia detector. The maia system is a high-throughput x-ray fluorescence detector and real-time analysis system that allows samples to be scanned up to 1000 times faster and in much greater detail than previous methods.

When combined with a focused x-ray source, such as the x-ray fluorescence microprobe beamline, it is able to produce high-definition, quantitative element images with microscopic detail in real-time [2].

* Work supported by:
† jim.divitcos@synchrotron.org.au

TECHNICAL SPECIFICATIONS

Ability to adjust beam addressable sample area: X axis: 600 mm, Y axis: 1200 mm travel.
X Stage: Parker 404XR, Motor Sanyo Denki Stepper 56 mm 103H7128.
Y stage: Parker 406XR, Motor Sanyo Denki Stepper 56 mm 103H7128.
Scanning Speed of X stage & Y stage: 20 mm per second.
Maximum sample size: 1250mm Height x 1750 mm wide x 50 mm thick.
Minimum sample size: 100 mm high x 100 mm wide.
Maia Detector minimum scanning distance: 2 mm from sample plane.
Maximum weight of sample: 15 kg.
Weight of structural stand: 276 kg.
Total Assembly Weight: 420 kg

CONCEPTUAL DESIGN

The design envelope included beam addressable regions to cover 1200 mm by 600 mm for large samples limited only by hutch wall constraints. We proposed several conceptual designs to achieve the specifications generated by our scientists, which were finalized during our design review.

The clamps are secured using knobs where feasible, providing quick release concept, reducing the number of tools required during installation and dismantling of sample. High stability and precision was an essential part of the design criteria. Early structural support of small artwork consisted of aluminium extrusions clamped together to help provide the requirements of this size. As the demand grew for larger format artwork, we introduced a large square tubular frame. This reinforced rigidity of the platform assemblies especially during transit mode.

Vertical carbon fiber tubing can also be disassembled to cater for a combination of smaller size samples reducing any vertical congestion within the surroundings of the hutch. The slots in the vertical side clamps are employed to fine tune any vertical misalignment of the artwork during installation.
Wide linear rails/carriages cater for ease of moment loading, increasing rigidity during motion of the upper and lower platforms. The implementation of counter weights on each side provides reduction of motor load on the vertical stage during transit. The design includes standardisation on same size fasteners to ease the assembly procedure and the number of tools required.

Content from this work may be used under the terms of the CC BY 3.0 licence (© 2016). Any distribution of this work must maintain attribution to the author(s), title of the work, publisher, and DOI.

ISBN: 978-3-95450-188-5 doi:10.18429/JACoW-MEDSI2016-MOPE38

Content from this work may be used under the terms of the CC BY 3.0 licence (© 2016). Any distribution of this work must maintain attribution to the author(s), title of the work, publisher, and DOI.

PROTOTYPE CONSTRUCTION

Due to highly interactive and frequently used platforms, we printed 3D prototypes in house using abs plus generated accuracy in line with traditional manufacturing. The construction help prove form, fit, functionality of railing and platforms, confirming the feel, touch, space utilisation & sequence of sample assembly prior to releasing components for manufacture.

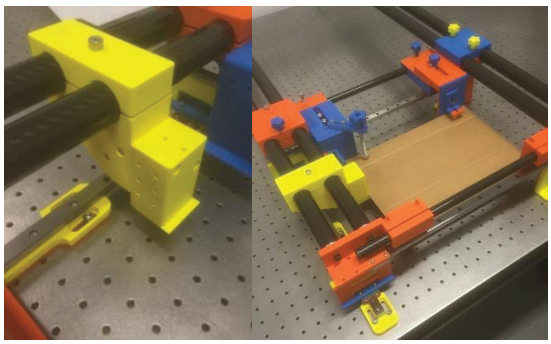


Figure 1: Side clamp assembly. Figure 2: Upper & lower platforms.

The side clamp assembly offers tuning in squareness (horizontal alignment) within a tolerance of ± 20mm of the artwork frame and the option of interchangeable clamps for the support of cylindrical samples. (see Fig.1) The Upper & lower platform assemblies consisted of linking carbon fiber tubing, which help assess the rigidity of structure (see Fig. 2).

TESTING

Using the roll wrap carbon fiber tube provided excellent strength, withstanding twist, torque, compression, tension and deflection without splitting. This is due to the fibers been wound around the diameter of the tube as well as running in length direction.

The tube mandrel is wound with unidirectional carbon fiber around the diameter, and then wrapped with fibers along the length (longitudinally). It is completed with a wrap of 3k twill before it is cured in an autoclave, roll sanded then recoated with epoxy. The assessment below was paramount to our design, clarifying twisting of the horizontal stage in its maximum stroke, securing the complete surface area to the breadboard table.

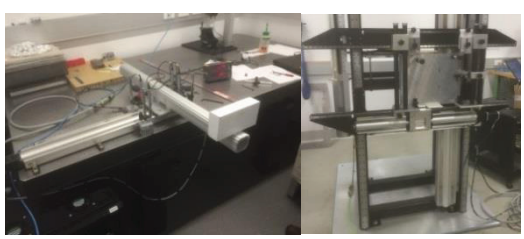


Figure 3: X stage assessment. Figure 4: Small artwork installation.

The X stage extrusion assembly was secured to the breadboard table. Using a 9 kg lead brick at a span of 600 mm, we simulated the equivalent moment in a cantilevered scenario based on our prototype concept which resulted in 0.86 mm in deflection on the stage (see Fig.3).

We simulated the installation of small artwork onto the upper and lower platforms. When assessing the technique, we conducted a work hazard risk analysis with our safety team and independent personnel. (See Fig.4)

MOTION CONTROL

As experienced with the prototype 'milliprobe' stage, the fast scanning axis can introduce vibrations through the linear stage to the large sample frame. We did testing to overcome this problem and plan to switch to a servo motor drive system for smoother scanning.
In the new design, a stepper motor moves the [vertical] scan axis whilst the other stepper motor moves the [horizontal] raster axis. A GeoBrickLV® provides tuning and trajectory planning capabilities required to achieve high trajectory tracking performance scan motion.

MANUFACTURING

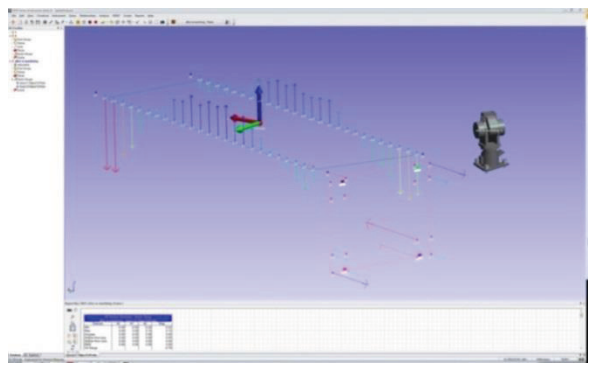


Figure 5: Tubular frame laser scanning.

The test indicated a 0.36 mm variation from right hand bottom to top left hand regions of the frame (Tubular Frame structure orientation: seated in horizontal plane for testing purposes only using a laser tracker) (see Fig. 5).

CONCLUSION

The structure has recently being installed in the x-ray fluorescence microscopy end station (see Fig. 6). It is intented to raster scan at several points to assess the deflection of the assembly at different positions of the moving frame in the
x and y planes. We wish to achieve a result under 100 micron variation from the plane.

In the interim, we assembled the station in our machine assembly room to confirm form, fit & function prior to commissioning. This included assessing the operation of counterbalance weights linked with the lower platform

ISBN: 978-3-95450-188-5 doi:10.18429/JACoW-MEDSI2016-MOPE38

and moving both platforms in the upper & lower positions along the wide rails & bearings. Ultimately confirming parallelism of the linear tracks, with the rigidity of the carbon fiber tubing assembly being paramount.



Figure 6: Milliprobe scanner station recently installed in XFM end station.

ACKNOWLEDGEMENTS

We wish to acknowledge many of our team members involved for contributing their efforts, knowledge and hard work.

REFERENCES

[1] Scientific Reports 6, Article number: 29594, A Hidden Portrait by Edgar Degas. David Thurrowgood1, David Paterson, Martin D. de Jonge, Robin Kirkham, Saul Thurrowgood & Daryl L Howard, December 2015. http://www.nature.com/articles/srep29594

[2] CSIRO Research Minerals Mineral discovery and exploration Resource characterisation Our Research: Maia x-ray imaging: finding hidden 'needles in a haystack' http://www.csiro.au/en/Research/MRF/Areas/Mineral-exploration-and-discovery/Rapid-resource-characterisation/Maia.

Content from this work may be used under the terms of the CC BY 3.0 licence (© 2016). Any distribution of this work must maintain attribution to the author(s), title of the work, publisher, and DOI.

ISBN: 978-3-95450-188-5 doi:10.18429/JACoW-MEDSI2016-MOPE40

Content from this work may be used under the terms of the CC BY 3.0 licence (© 2016). Any distribution of this work must maintain attribution to the author(s), title of the work, publisher, and DOI.

DESIGNING THE FLASH II PHOTON DIAGNOSTIC BEAMLINE AND COMPONENTS

D. Meissner*, M. Brachmanski, M. Hesse, U. F. Jastrow, M. Kuhlmann, H. Mahn,
F. Marutzky, E. Plönjes, M. Röhling, H. Schulte-Schrepping, K. Tiedtke, R. Treusch
Deutsches Elektronen-Synchrotron DESY, 22607 Hamburg, Germany

Abstract

From 2013 to 2016 the free electron laser FLASH at DESY in Hamburg, Germany was upgraded with a second undulator line, photon diagnostic line, beam distribution and experimental hall connected to the same linear accelerator. This paper shows the layout of the photon diagnostic section and an overview of the civil engineering challenges. The mechanical design of selected components, e.g. vacuum components, diagnostic equipment and safety related components is presented.

INTRODUCTION

The x-Ray Free Electron Laser FLASH at DESY has been running as a user facility for XUV and soft x-ray photon experiments since 2005. In 2010 the upgrade project FLASH II was started to increase the number of user end stations by adding a second undulator line to the FLASH accelerator and operating both beamlines simultaneously and independently regarding wavelength [1, 2].

Two largely identical photon diagnostic sections had to be developed to provide beam parameters to accelerator operation and user experiments. The first section is located inside the accelerator tunnel starting at 10 m from the source where the beam is very small and intense, the second section is in the experimental hall and is fully accessible to users. Both provide data on beam intensity, position and wavelength. The complete layout is described in [2].

Since most of the components use various gases at different pressures main focus in designing the vacuum system was on differential pumping, especially the gas attenuator located between tunnel and hall where the beam crosses the PETRA III accelerator tunnel. Additional mechanical component development focused on absorbers and mirror chambers for beam steering and radiation protection.

GAS ATTENUATOR AND DIFFERENTIAL PUMPING

The straight section of 12 m between the end of the FLASH II tunnel and the beginning of the experimental hall is used as an intensity attenuator. For the purpose of reducing beam transmission for selected wavelengths this section can be flooded with gas up to a pressure of 0.5 mbar. Gases available are Xe, N_2, Kr and Ar [2].

To separate the beamline vacuum from the attenuator and minimize gas usage five-stage differential pumping stations with small and long apertures are used on both sides of the section. Pumping apertures are 16 mm diameter in the tunnel and 20 mm in the hall. The aperture lengths for stages 2 to 5 are 287 mm in the tunnel and range from 400 mm to 700 mm in the hall. Stage 1 which is closest to the attenuator features a 1 m (1.2 m in the hall) cantilevered tube that protrudes into the attenuator beam pipe and also into the radiation shielding wall of tunnel and hall (see Fig. 1).

Table 1: Pressure at All Pumping Stages from Attenuator to Following Vacuum Chamber [3]

Stage	Diameter mm	Length cm	Pump type mbar l s^{-1}	Pressure[a] mbar
ATT	100	1300	300, TP[b]	5E-01
1.	16	100	300, TP	9E-03
2.	16	29	300, TP	8E-05
3.	16	28	300, TP	7E-07
4.	16	28	300, TP	7E-09
5.	16	29	300, TP	6E-11
6.[c]	25	7	55, Ion GP	3E-11

[a] Simulated prediction of pressure range
[b] with cooling gas option
[c] Aperture of following UHV section

Stages 2 to 5 use turbomolecular pumps with a volume flow rate of 300 mbar l s^{-1} and additionally ion getter pumps for UHV operation. Stage 1 uses a similar turbomolecular pump which can use cooling gas and can bypass the aperture through a DN100 pipe to allow for rapid pumping of the attenuator down to UHV. Table 1 shows the resulting pressures of the setup.

Due to the long and narrow apertures special care must be taken for supports and alignment. All pumping sections are pre-assembled outside of the accelerator tunnel on granite girders with high precision manufactured steel grooves for alignment of the components. The girder itself sits on two sand-filled supports of thick walled steel tubes and a three-point kinematic mount. Since alignment is done only by adjusting the kinematic girder support the manufacturing tolerances of the girder and the pumping stages have to be very small. Precision steel tubing and special welding equipment were used to achieve the desired concentricity of all apertures. The cantilever tube of the first stage is suspended by three wires to compensate for bending due to its span. By adjusting the tension in the wires while measuring the resulting aperture with an alignment laser the aperture can be maximized.

* daniel.meissner@desy.de

ISBN: 978-3-95450-188-5 doi:10.18429/JACoW-MEDSI2016-MOPE40

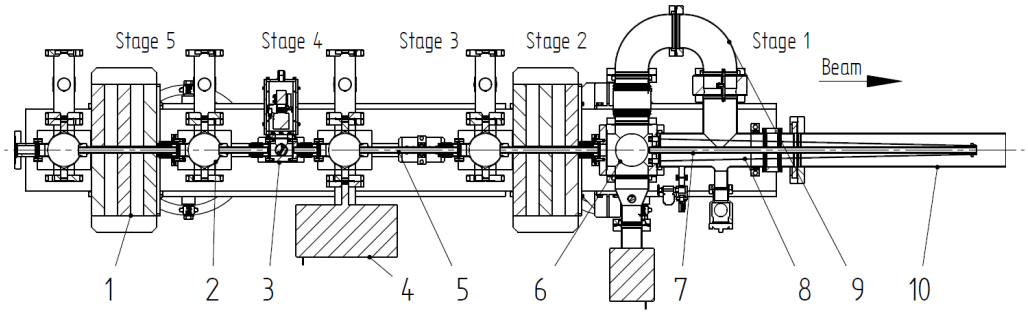


Figure 1: Attenuator Differential Pumping, vertical section. 1: Radiation Collimator, 2: Pumping Chamber, 3: Beam Position Monitor, 4: Ion Getter Pump, 5: Flow Constriction Tube, 6: Stage 1 Pumping Chamber and Support for Cantilever Tube (7), 8: Cantilever Tube Support and Adjusting Wires, 9: Bypass, 10: Attenuator Tube. Turbomolecular pumps not shown.

Each pumping section of stages 2 to 5 consist of a pumping chamber with flanges for turbomolecular pump, ion getter pump and vacuum gauges. The flow constricting tube with an additional bellow is precision welded to the chamber, measured and straightened if necessary.

The attenuator pipe itself connects the FLASH II tunnel and the experimental hall. The beamline has to cross 1.5 m of radiation shielding concrete at the end of the tunnel, 1 m of soil, crosses the PETRA III accelerator (3.5 m), another 6 m of soil until it reaches the wall of the experimental hall. The connection between FLASH II and PETRA III is core drilled with both hole endings not perpendicular to the wall. The hole is fitted with an outer steel tube, an inner steel tube supported in a concrete layer for better alignment and the beamline UHV pipe with aligning supports on either tunnel wall. The other core drilling section features a similar setup. Its slope was measured to pre-align sliding supports of the UHV pipe that rest on the reinforcement tubing. The UHV pipe is welded to one piece on site, outfitted with the pre-aligned sliding supports and installed. Concentricity of the DN100 UHV pipe to the beam axis is inside a few millimeters.

APERTURE AND BEAM DIAGNOSTIC UNIT

For FLASH II the aperture and beam diagnostic units from FLASH I was re-engineered to adjust them to the new requirements and fix long-known mechanical problems with the current design. Furthermore to minimize beamline space the units vacuum chamber should double as differential pumping station. Every chamber can be outfitted with turbomolecular pump, ion getter pump and vacuum gauges. To further minimize space part of the flow constriction tube is also integrated into the chamber wall. The unit features a 3-axis motor driven linear stage setup to adjust diagnostic components or apertures as well as retract them out of the beam. Beam adjustment travel range is ±10 mm and vertical travel range 125 mm from bottom position (paddle in alignment socket) to top position (fully retracted). The reproducibility of position is 0.1 mm [4].

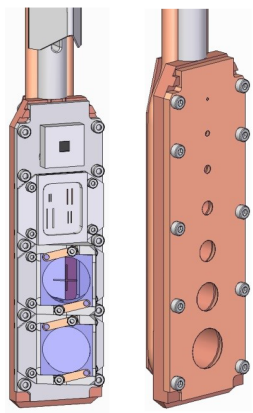


Figure 2: Diagnostic paddle (left) and aperture paddle (right).

Two separate compilations of components can be used alternatively depending on type of the unit. The diagnostic compilation is outfitted with a diode, double slit unit, fluorescent screen and diffusing screen. The aperture compilation has seven apertures from 1 mm to 14 mm in a copper plate. Figure 2 shows both setups. Both compilations can be mounted on the water cooled copper heat sink that sits at the end of the movable aluminum rod. This rod houses the cooling pipes, electric cables and translates the movement from the adjustment drive into the vacuum chamber through an edge welded bellow [4].

Since mechanical stability was one of the main concerns the chamber is milled from a stainless steel block. Its outside dimensions are 230 mm × 170 mm × 195 mm (LxWxH) with a cylindrical pumping chamber of ⌀158 mm × 120 mm. The support structures for the linear stages are precision manufactured from solid aluminum plates to reduce vibrations and deformations due to vacuum forces and bellow reaction forces (see Fig. 3). The total height of the unit including travel is 892 mm [4].

Content from this work may be used under the terms of the CC BY 3.0 licence (© 2016). Any distribution of this work must maintain attribution to the author(s), title of the work, publisher, and DOI.

ISBN: 978-3-95450-188-5 doi:10.18429/JACoW-MEDSI2016-MOPE40

Content from this work may be used under the terms of the CC BY 3.0 licence (© 2016). Any distribution of this work must maintain attribution to the author(s), title of the work, publisher, and DOI.

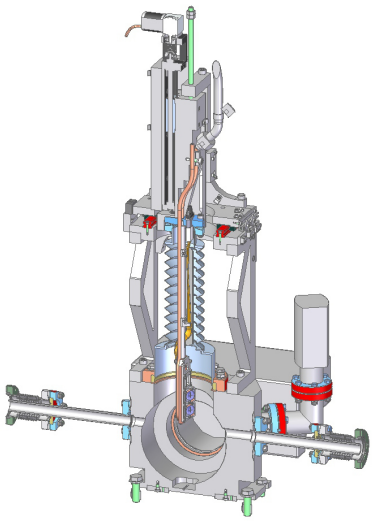


Figure 3: Cross section of aperture and diagnostic unit. Flow constriction tubes attached, diagnostic paddle in fully retracted position. Bellow not detailed.

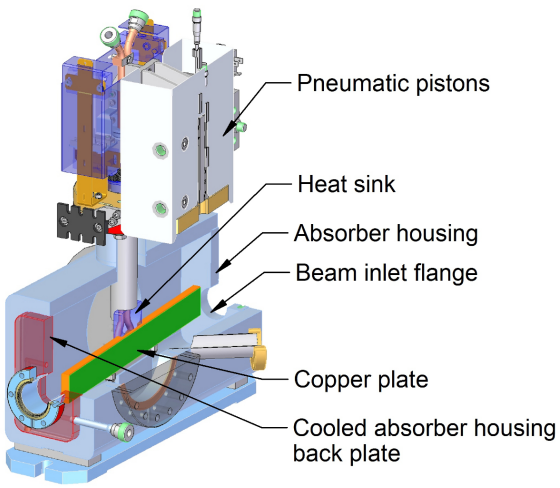


Figure 4: Mechanical concept, absorber housing cut open.

BEAM ABSORBERS

Both photon diagnostic sections feature retractable copper absorbers which were initially placed at 10 m and 45 m along the beamline to allow for machine operation while the photon beamlines are not in use. The thermal load from bunch trains of 3500 bunches with a repetition rate of 10 Hz is 3988 W /mm^2. The mechanical design is a water cooled copper plate at 6 ° that can be retracted upwards by pneumatic pistons. The absorber consists of an EDM[1] machined housing with 40 mm aperture in the open position. For security reasons and to absorb scattered radiation the back plate of the absorber housing is also made of copper and can be cooled externally. Figure 4 shows the mechanical concept with cut-open housing [2, 5].

[1] Electrical discharge machining

FEA calculations at the given values showed peak temperatures in the copper plate of 1041 °C and so variations of geometry and cooling options were considered but none showed significant improvement. Because of the peak temperature the beamline layout, as well as machine operating conditions, had to be changed. The first absorber was moved to 18 m from the source and bunches were limited to 800 per bunch train. This reduced the mean beam power from 1120 W to 256 W and the resulting temperature dropped to 102 °C (see Fig. 5) [5].

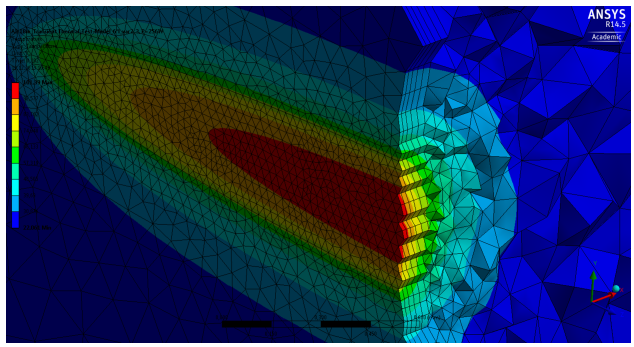


Figure 5: Final FEA result, peak temperature of 102 °C in red in the middle.

CONCLUSION AND OUTLOOK

Manufacturing and installation of all components described went as planned and without problems. The tunnel beamline was commissioned for UHV in August 2013 and received first beam in January 2014. The attenuator and experimental hall saw first light in 2014 and commissioning of the machine started. First user experiments took place in April 2016 on beamline FL24. It is planned to extend FLASH further by adding the FLASH III undulator beamline which will have an identical diagnostic setup in the same tunnel and hall.

REFERENCES

[1] B. Faatz *et al.*, "Simultaneous operation of two soft x-ray free-electron lasers driven by one linear accelerator", *New Journal of Physics*, Volume 18, June 2016.

[2] E. Plönjes *et al.*, "FLASH2 Beamline And Photon Diagnostic Concepts", in *Proc. FEL2013*, New York, NY, USA, Aug. 2013, paper WEPSO50, pp. 614-617.

[3] U. F. Jastrow, "Differential Pumping Stage for Flash2 - Part 7", Presentation at Flash2 Beamlines and Photon Diagnostic Meeting, unpublished.

[4] H. Hahn, "Diagnose-/Apertur-Druckstufe für FLASH II", Poster at KITE - DESY Engineering and Innovation Day 2014, unpublished.

[5] F. Marutzky, "Absorber für FLASH II", Poster at KITE - DESY Engineering and Innovation Day 2014, unpublished.

ISBN: 978-3-95450-188-5 doi:10.18429/JACoW-MEDSI2016-MOPE41

DESIGN AND CONSTRUCTION OF A PW EXPERIMENTAL SYSTEM OF HV CHAMBER ADAPTABLE, MODULAR AND STABLE

A. Carballedo[1†], J. Hernández-Toro[2], C. Colldelram[1], R. Monge[1], L. Nikitina[1], J.R. García[1], L. Roso[2]

[1]ALBA-CELLS Synchrotron, 08290 Cerdanyola del Vallès, Spain
[2]Centro de Láseres Pulsados, CLPU, Parque Científico, 37185 Villamayor, Salamanca, Spain

Abstract

In the recent years, the number of high power lasers devoted to particle acceleration has increased in Europe. Additionally to this, some synchrotrons and accelerators are integrating these lasers in its lines, increasing the scientific synergies. The HP laser must be transported in HV. The use of HV also permits good cleanliness in the optical setup. As addition, is necessary to create an adaptable and modular design where several chambers could be assembled together. One additional constrain is the stability. A new model of HV chambers is presented. These consist in a frame where the walls are exchangeable panels, which make easier the introduction of a new configuration of ports. The system was designed as construction blocks. For a proper connection of the chambers a new interior fixation and pushers system was designed. Thanks to this, coupling new HV chambers, the volume total can be also easily modified. Finally, a third generation decoupled system is integrated inside, consisting of a stable breadboard, this supported by six columns that implement a preloaded kinematical mount, providing both an outstanding stability and a fine regulation (1st RM: 77Hz).

INTRODUCTION

This project is the result of the collaboration between ALBA-CELLS and CLPU in order to promote the Mechanical engineering related with the high power laser. CLPU (Ultra-short Pulsed Laser Center) is a facility specialized in femtosecond laser pulses with peak powers at Gigawatt, Terawatt and Petawatt levels. Previous collaborations have given the 200TW and 1PW laser compressors. The protagonist of this article is the third one, the 1PW Experimental system consisting in a HV modular vacuum chamber and a stable breadboard for the optical equipment.

MAIN CONCEPT

The functionality of this chamber is as interaction chamber, where the target of the laser and the focus system are mounted. Due to the laser is a high power laser, after the laser is compressed, this cannot be transported in air because the laser properties are deteriorated and a complete HV system ($<5 \cdot 10^{-6}$ mbar) is required. Furthermore, this also reduces the presence of hydrocarbon contamination on the system.

REQUIREMENTS

A new paradigm of HV chambers is presented. It is necessary to create an open and adaptable design with the following requirements:

- The vacuum chamber should be modular and allow easily modifications in the ports distribution.
- As different experimental setups might need of different optical equipment distribution, a decoupled system is integrated inside the chamber, based in the experience of the two previous laser compressor chambers.

DESIGN

Vacuum Chamber. Modularity

The Experimental vacuum chamber is designed plate-to-plate in a rectangular configuration. Each plate has rectangular ports for lateral covers. Due to the modularity of its design, faces are identical two by two. It implies that the large lateral covers and the short lateral covers are equal respectively. This fact allows not only using a same design of lateral cover for each experimental chamber but also interconnect different vacuum chambers between each other (Figure 1).

Vacuum chamber is made of AISI 304L stainless steel with the exception of AL 6082 aluminium lateral covers, and can be divided on four main parts: bottom cover, walls, top cover and lateral covers. The global dimensions of the chamber are 3000 mm x 1900 mm x 1500mm.

In order of ensure the tightness a system of double joint with different size was designed. This permits either to fix one lateral cover or another vacuum chamber in the same port.

Furthermore, an internal matrix of holes was added to each port in order to allow the connection between chambers.

Due to the big weight of the chamber a complete system of pushers was added. Low friction intermediate plates are placed between chamber and its support to

† acarballedo@cells.es

Content from this work may be used under the terms of the CC BY 3.0 licence (© 2016). Any distribution of this work must maintain attribution to the author(s), title of the work, publisher, and DOI.

ISBN: 978-3-95450-188-5 doi:10.18429/JACoW-MEDSI2016-MOPE41

Content from this work may be used under the terms of the CC BY 3.0 licence (© 2016). Any distribution of this work must maintain attribution to the author(s), title of the work, publisher, and DOI.

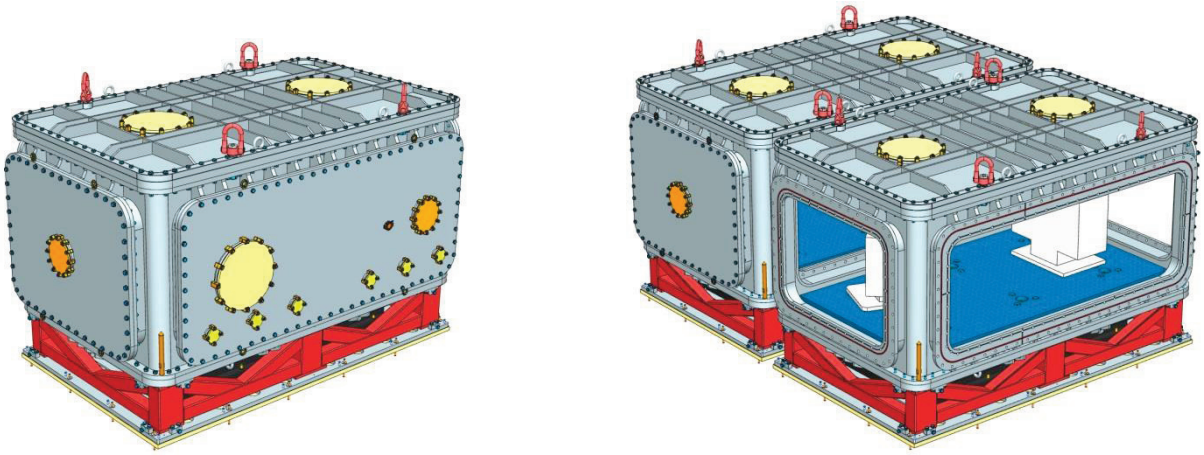


Figure 1: Experimental vacuum chambers. Individual assembly and two chambers connected.

soften the movement the chamber in 2 axis and make the connection easily (Figure 2).

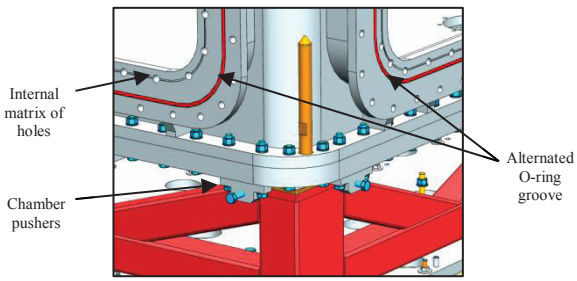
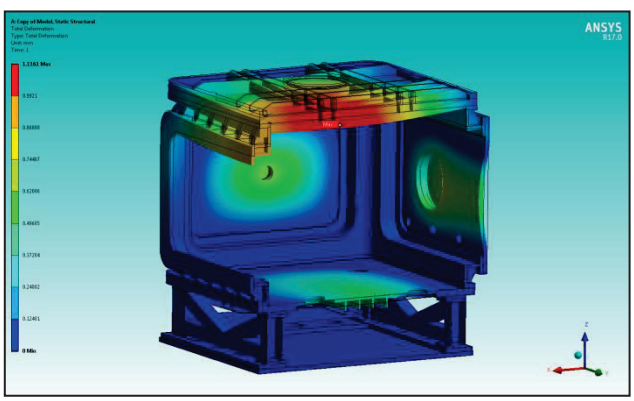


Figure 2: Detail of alternated O-ring grooves, internal matrix of holes and chamber pushers.

Different calculations by means of FEA have been done in order to achieve the standards of safety and technical specifications. The modularity of the design has made necessary to check that in any possible configuration the vacuum chamber would achieve these standards. The resulting maximum deformation and stress for an individual chamber were 0.84 mm and 78.5 MPa respectively. Regarding to two chambers together, deformation and stress was of 1.1 mm and 101 MPa (Figure 3). The values obtained from the modal analyses for both configurations are showed in Table 1.



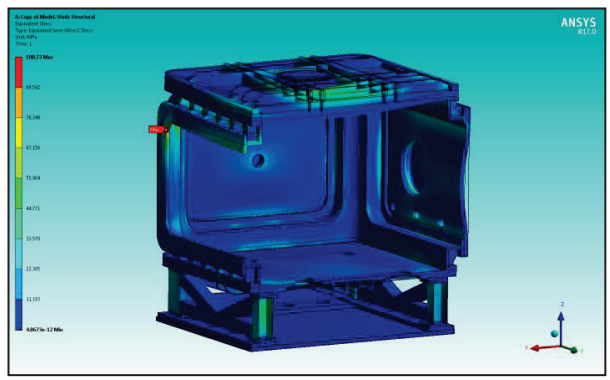


Figure 3: Expected deformation and stress results for two chambers together.

Table 1: Vacuum Chamber Resonance Modes.

Mode	Frequency [Hz]	
	One chamber	Two chamber
1	57.2	61.2
2	80.4	64.9
3	82.5	76
4	105.4	93
5	116.7	101
6	147.8	121.7

Breadboard System: Stability

The Breadboard is a flat, rigid and stable surface (AL 6082) mounted on six pedestals above six blanking flanges (AISI 304 and AISI 420B) and a granite block. The granite rests on a base plate made of conventional steel S-235 and this plate rests on an epoxy layer. Breadboard system is disengaged from the vacuum chamber by means of hydroformed bellows so no vibration is transmitted between both subsystems.

On the six columns, a preloaded kinematical mount is implemented (cone, V slot and four planes). These contacts allow vertical fine regulation (linear resolution of 50 μm) with angular relieving (pitch and roll) thanks to the presence of spherical washers (Figure 4).

ISBN: 978-3-95450-188-5 doi:10.18429/JACoW-MEDSI2016-MOPE41

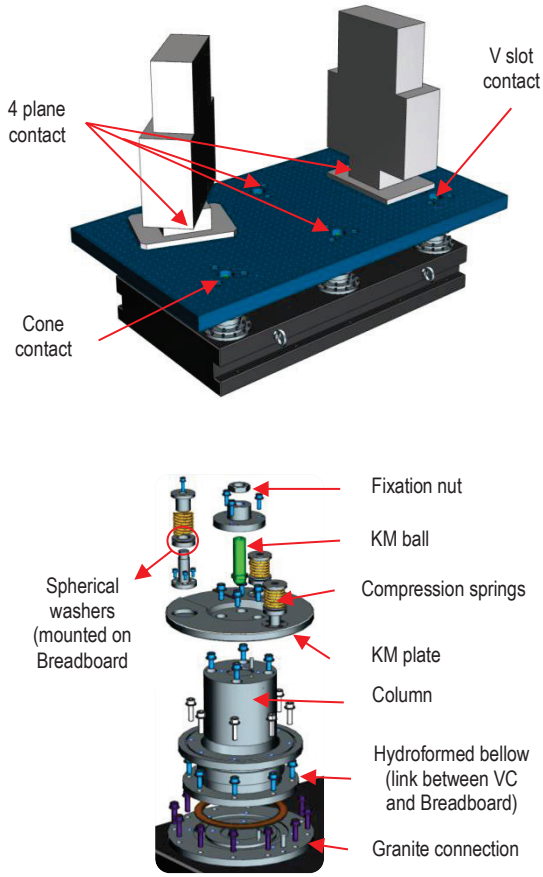
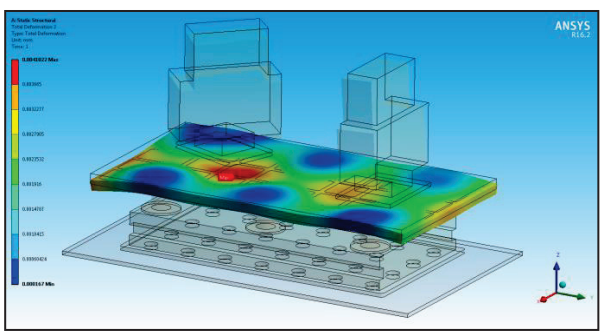


Figure 4: Breadboard assembly and conical KM contact detail.

Different FEA calculations studying the free vibration behaviour were done (Table 2). Figure 5 shows the breadboard deformation and first resonance mode. Maximum expected deformation of 0.004 mm and 1st RM of 76.8 Hz.



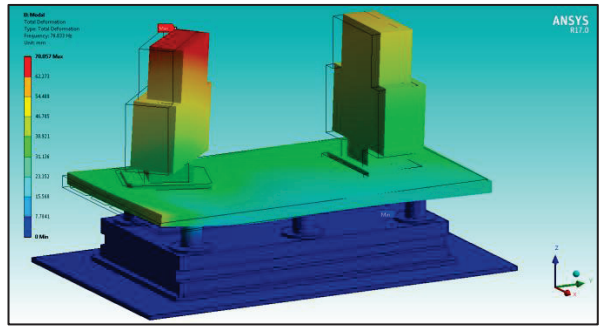


Figure 5: Expected deformation and RM results.

Table 2: Breadboard Resonance Modes.

Mode	Frequency [Hz]
1	76.8
2	115.8
3	126.3
4	141.7
5	143.2
6	168.8

CONCLUSION

As a conclusion, the collaboration between CLPU and ALBA-CELLS has result in a third generation vacuum chamber and breadboard design applied to high power laser plants.

Without refusing to the achievements accomplished of low deformation and stability of the two previous laser compressor chambers (Def.≤1mm and 1st RM>50Hz), the new Experimental vacuum chamber adds the flexibility and modularity needed in any scientific facility who constantly faces new challenges with a limited budget.

The chamber, which is under construction currently, should be tested and installed during this month.

ACKNOWLEDGEMENT

We acknowledge support from the European Union's Horizon 2020 research and innovation programme under grant agreement no 654148 Laserlab-Europe.

Content from this work may be used under the terms of the CC BY 3.0 licence (© 2016). Any distribution of this work must maintain attribution to the author(s), title of the work, publisher, and DOI.

ISBN: 978-3-95450-188-5 doi:10.18429/JACoW-MEDSI2016-MOPE42

Content from this work may be used under the terms of the CC BY 3.0 licence (© 2016). Any distribution of this work must maintain attribution to the author(s), title of the work, publisher, and DOI.

EXPERIMENTAL AND NUMERICAL STUDY OF THE ALBA LINAC COOLING SYSTEM

M. Ferrater†, Universitat Politècnica de Catalunya, Barcelona, Spain
J.J. Casas, C. Colldelram, D. Lanaia, R. Muñoz, F. Perez, M. Quispe*, ALBA – CELLS Synchrotron, Cerdanyola del Vallès, Spain

Abstract

This work investigates experimentally and numerically the performance of the ALBA LINAC cooling system. The main objective is to enhance the hydraulic system in order to significantly improve its thermal and water flow stability. In normal operation some problems have been identified that affect the performance of the LINAC: flowrate below the nominal values and water flow decreasing in time. The cooling subsystems have been experimentally characterized in terms of the pressure drop and flowrate. The measurements were taken using a portable hydraulic unit made at ALBA as well as a set of ultrasonic flowmeters. For the numerical studies the cooling network has been simulated using the software Pipe Flow Expert. The experimental results have shown that a number of components are too restrictive. In some cases the possibility to increase the flowrate is limited. The numerical results show that the velocity magnitude is inadequate in some places, producing air bubble entrapment, high pressure drop at pipes and insufficient flow. Based on this study several modifications are presented in order to raise the nominal flow and to adequate the water flow velocities between 0.5 and 3 m/s.

BACKGROUND

The ALBA facility is composed of a 100 MeV LINAC (see Fig. 1), a Booster that accelerates the beam up to the full energy of 3 GeV, the Storage Ring (SR), and the corresponding transfer lines (LINAC To Booster – LTB, and Booster To Storage – BTS).



Figure 1: The ALBA LINAC.

The LINAC consists of a 90 kV DC thermoionic gun, followed by a bunching system designed to reduce the energy spread and the electron losses. This one comprises a sub-harmonic pre-buncher (500 MHz), a pre-buncher (3 GHz) and 22-cells SW buncher (3 GHz). Two travelling wave constant gradient accelerating sections increase the energy up to 100 MeV. Beam focusing is ensured by shielded solenoids up to the bunching system exit and a triplet of quadrupoles between the two accelerating structures [1, 2].

The LINAC is running reliably since started its operation in 2010. At the early stages of the operation it was experienced that the beam charge is sensitive to variations of more than 0.1 ºC in cooling water temperature of the LINAC bunker and Service Area.

THE LINAC WATER COOLING SYSTEM

Description

The LINAC cooling water system has two different functions. From one side it cools the elements with strong dissipation of power: klystrons, RF cavities, RF loads, RF ceramic windows and magnets. And from the other side the system regulates the water temperature of the RF cavities in order to tune them for working at the nominal RF frequency.

The hydraulic scheme of the cooling water system is illustrated in Fig. 2. The main inlet pipe is connected to the supply ring at the Service Area. The total nominal flowrate is estimated at 100 l/min for a mean increase of temperature of 5.8 ºC. The total power transmitted by the LINAC to the cooling water is 61 kW according with the technical specifications. The inlet pressure of the supply ring is 10.2 bar. However a pressure reducer installed in the supply line set to 8.8 bar protects the downstream piping and components from over–pressurization. The inlet water temperature is 23 +/- 0.1 ºC in nominal conditions.

The main cooling circuit is divided in two subsystems, one for inside and the other for outside the bunker. The resistor load (RL1) and klystron amplifiers (KA1 and KA2) are outside the bunker. Both klystrons dissipate 45 kW.

Inside the bunker the RF cavities are made of copper whose dimensions change with temperature. As the resonant frequency is directly related to the dimensions, any change of temperature will lead to a lower electric field. Calculations of beam dynamics show that a temperature stability of ± 0.2 °C is necessary. The nominal regulation for temperature is around 30 °C.

† marcferrater@gmail.com
* mquispe@cells.es

ISBN: 978-3-95450-188-5 doi:10.18429/JACoW-MEDSI2016-MOPE42

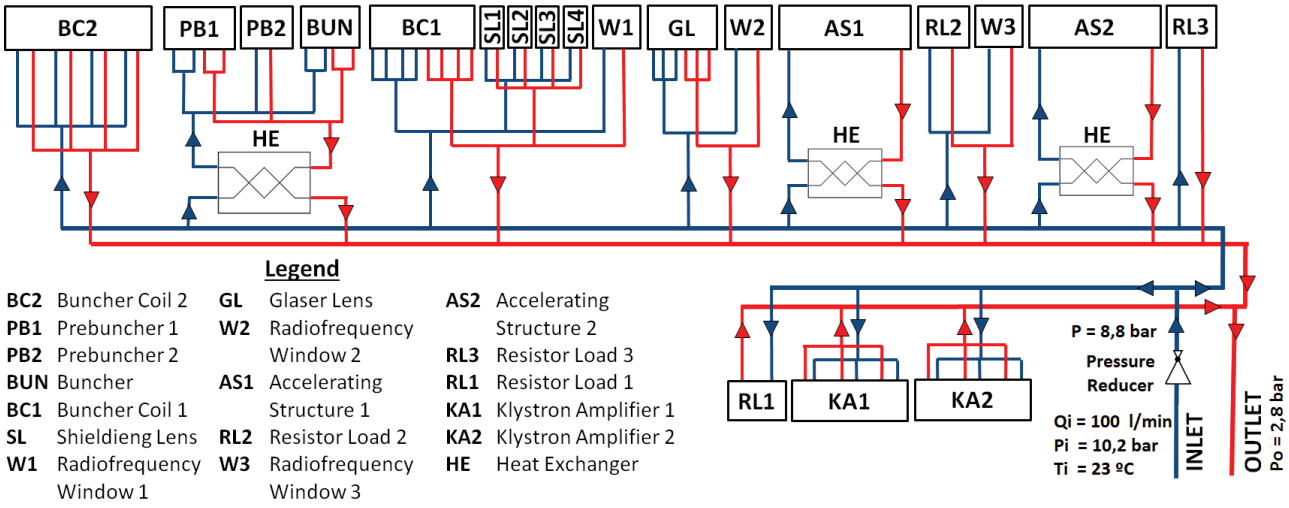


Figure 2: Hydraulic scheme of the LINAC cooling water system.

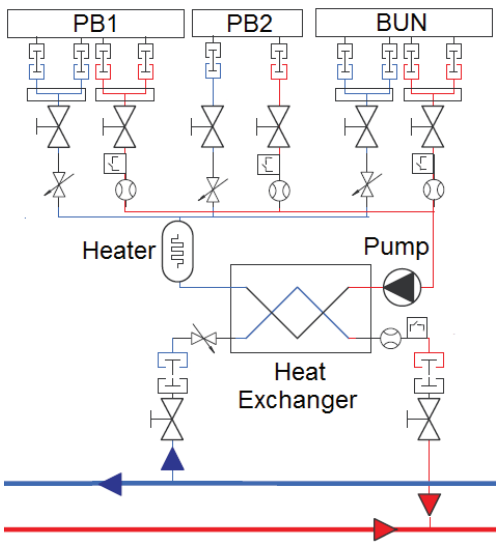


Figure 3: Hydraulic circuit of cooling loop 1 (CL1).

The RF cavities are regulated by three closed circuits, named cooling loops, grouped as follows: CL1 (PB1, PB2 and BUN), CL2 (AS1) and CL3 (AS2). Figure 3 shows the hydraulic scheme of CL1. The main components are a pump, a heat exchanger between the primary and secondary circuits and a heater. The loop operates with 5.5 bar as maximum pressure and 35 l/min. The thermal load is removed from the RF cavities to a secondary circuit across the heat exchanger. The electric heater of 500 W has the function of heating the circuit water and maintain it stable around 30 ºC with an stability of +/-0.1°C. For that, the power drive of the heater is adjusted by a PID.

Hydraulic Problems

In normal operation some problems have been identified that affect the performance of the LINAC:

Flowrate below the nominal values. This problem is affecting some components; as a consequence some points with overheating have been detected in the cooling system.

Flowrate decreasing in time. This phenomenon may be induced for the entrapment of air bubbles inside the system pipes. The problem was solved with an expansion tank installed at the impulsion of pump.

Instrument`s failure. Some flowmeters are not working properly. This fact complicates the study of the cooling system.

Water flow instability in the Service Area return. This problem is associated with an overall instability in the ALBA cooling system [3]. Measurements in the common return confirm that the pressure oscillates with +/- 0.2 bar deviation.

EXPERIMENTAL MEASUREMENTS

All the LINAC sub components have been characterized in terms of the pressure drop versus flowrate. The measurements were taken using a portable hydraulic unit made at ALBA (Fig. 4) as well as a set of ultrasonic flowmeters.

The hydraulic unit consists of a water pump that moves water from a tank to the device to be characterized. The difference of pressure is measured between the inlet and the outlet of the device. The setup is provided with two flowmeters. The readings of differential pressure and water flow are recorded in a central register.

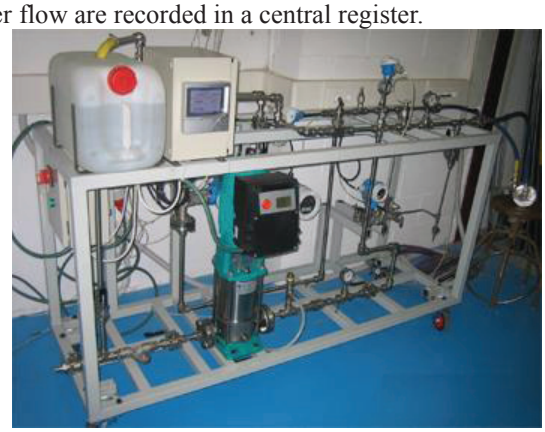


Figure 4: The ALBA experimental hydraulic unit to characterized pressure drop versus flowrate.

Content from this work may be used under the terms of the CC BY 3.0 licence (© 2016). Any distribution of this work must maintain attribution to the author(s), title of the work, publisher, and DOI.

ISBN: 978-3-95450-188-5 doi:10.18429/JACoW-MEDSI2016-MOPE42

Content from this work may be used under the terms of the CC BY 3.0 licence (© 2016). Any distribution of this work must maintain attribution to the author(s), title of the work, publisher, and DOI.

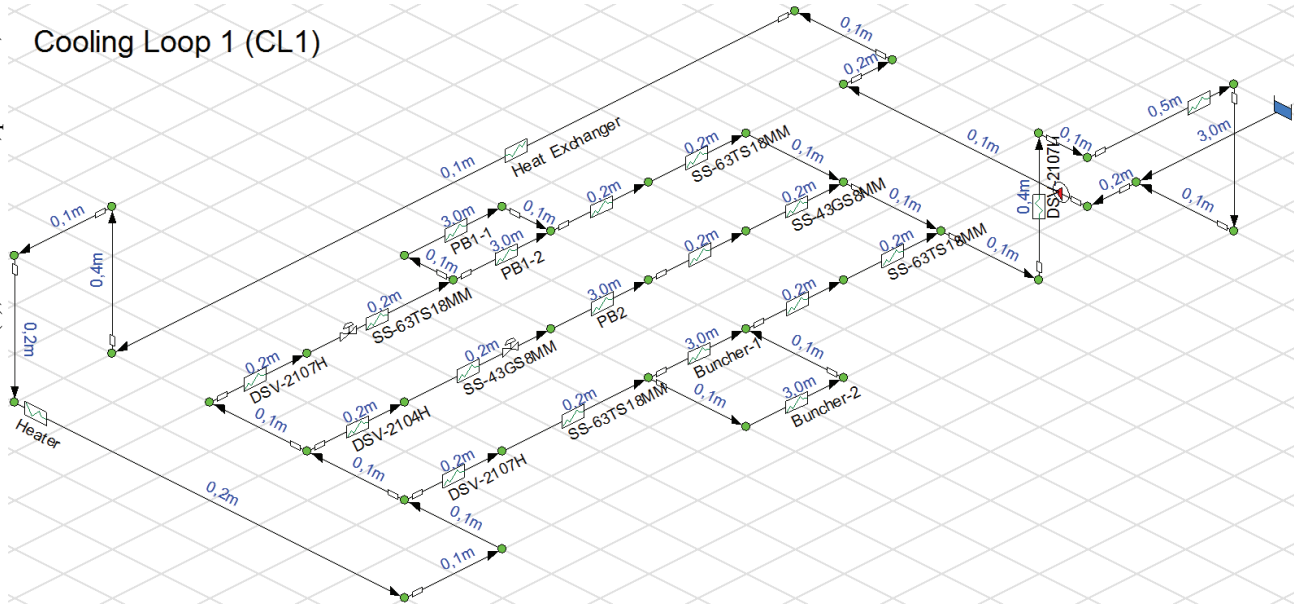


Figure 5: Software Pipe Flow Expert: piping network of the Cooling Loop 1 (CL1).

1D SIMULATION OF THE LINAC COOLING SYSTEM

Based on the software Pipe Flow Expert [4] an accurate 1D model of the LINAC cooling system has been built that permits to evaluate the response of the hydraulic system for the current situation and when it is subjected to possible modifications. The model includes all the net pipes, bends, pipe entrance, changes of section, branding of current, valves (open/close type, regulators), pressure reducer, flowmeters, pumps and local components. A total of 199 pipes and 57 components have been used for the simulation model. The numerical predictions have been compared with experimental data. A good agreement has been found with deviations of the main variables below 11%. Figure 5 shows the model Pipe Flow Expert for CL1.

RESULTS

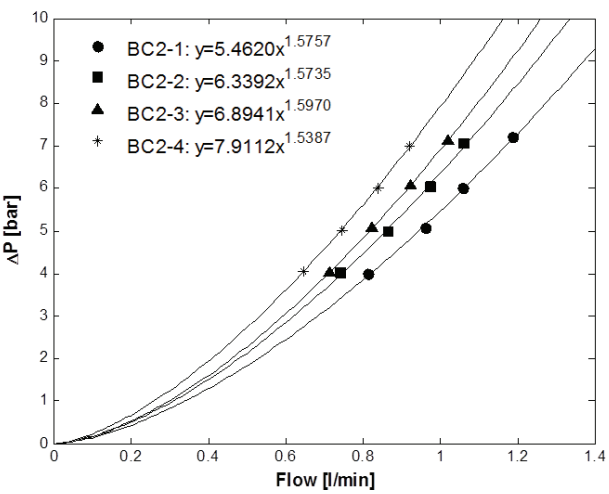


Figure 6: Experimental correlations for BC2.

The 31 subcomponents of the LINAC have been characterized. For each case a mathematical correlation has been developed to describe the pressure drop as a function of the flowrate.

Figure 6 shows the results for BC2 which is the most restrictive case. If the flow had to be increased it would be necessary to increase significantly the gap pressure (which it is limited).

The numerical results show that the velocity magnitude is out of optimum range in some places, producing air bubble entrapment, high pressure drop at pipes and insufficient flow.

Based on the experimental and numerical results a complete modification of the interface of CL1 is proposed. Currently this intervention is in progress.

CONCLUSIONS

The hydraulic characteristics of the LINAC sub components were investigated both experimentally and numerically. By applying mathematical correlations of pressure drop versus flow rate, it has been found that a number of sub components are too restrictive. On the other hand, a detailed description of the velocity magnitude at the interfaces has been obtained. Based on these results, modifications have been implemented in the LINAC cooling system with the aim to improve its performance.

REFERENCES

[1] LINAC, www.cells.es/en/accelerators/linac

[2] *R. Muñoz*, "Operation and improvement of the ALBA LINAC", Proceedings of LINAC2014, Geneva, Switzerland, p. 459 – 461, 2014.

[3] *M. Quispe*, "Cooling System Operation", 21st Meeting of the ALBA Scientific Advisory Committee, Barcelona, Spain, December 2015.

[4] Pipe Flow Expert, http://www.pipeflow.co.uk/

ISBN: 978-3-95450-188-5 doi:10.18429/JACoW-MEDSI2016-MOPE43

HYDRAULIC FAILURE CAUSED BY AIR IN PIPELINES OF THE EXPERIMENTAL AREA RING OF ALBA SYNCHROTRON LIGHT SOURCE: RESEARCH, SIMULATIONS AND SOLUTIONS

Ll. Macià†, Universitat Politècnica de Catalunya, Barcelona, Spain
J.J. Casas, C. Colldelram, M. Quispe*, ALBA – CELLS Synchrotron, Cerdanyola del Vallès, Spain

Abstract

After five years in operation of the ALBA Synchrotron Light Source a hydraulic failure caused a maximum decreasing of water flow about 40% of its nominal value, hampering the refrigeration of the local components. The problem was mainly caused by the air accumulated in pipes due to very low velocities of water flow. A literature review was conducted about the minimum water flow velocity for removing air in pipelines as design criteria. The aim of this work is to develop hydraulic solutions in order to achieve the minimum flow rate in pipelines of the Experimental Area (EA) ring. In the short term it is proposed to install a controlled bypass in the EA. A numerical simulation using the software Pipe Flow Expert has been implemented in order to determine the requirements of the bypass that works under different conditions to assure a minimum flow rate all along the ring. The velocity map in EA ring is simulated for different scenarios: 180 and 360 degrees distribution for both clockwise and anticlockwise rotation. For the long term a design of pipes with variable cross section is proposed which optimizes the flow velocity magnitude in EA ring in agreement with the design criteria.

BACKGROUND

The ALBA cooling system consists of four main rings which feed the local consumption of the Service Area (SA), Booster (BO), Storage Ring (SR) and Experimental Area (EA) (see Fig. 1). The water is heated through all the rings and it is collected in a common return. The pump P11 takes the heated water from the return and feeds a couple of heat exchangers HE that cool it. The cooled water is brought to a storage tank from which a suction line takes water again to the rings' pumps. In order to regulate the water temperature, a series of controlled mixing valves permit to combine the cooled water with the heated water prior to being pumped to the rings. Finally, a pipe line connecting the tank with the common return line permits to compensate the lack/excess of flow to the cooling loop when the total flow rate changes in the rings' loops.

In 2013 a hydraulic failure in the ALBA cooling system caused a maximum decreasing of water flow about 40% of its nominal value, hampering the refrigeration of the local components. The problem was mainly caused by the air accumulated in the four rings due to very low velocities of water flow [1].

This paper analyses the problem and proposes new solutions. The Experimental Area has been selected for this study. The conclusions will be extrapolated to the other rings.

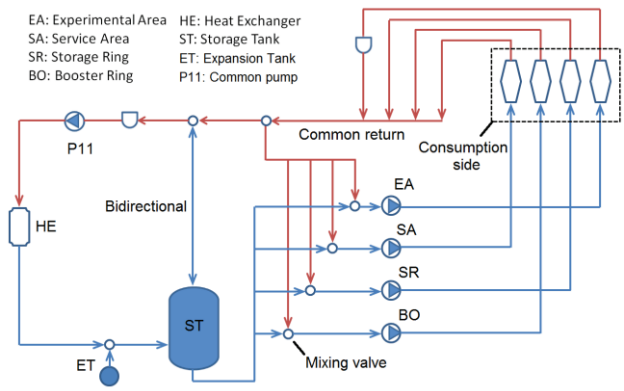


Figure 1: ALBA cooling system scheme.

THE MINIMUM WATER FLOW VELOCITY AS DESIGN CRITERIA

Research studies have shown that a minimum flow velocity is always required to move air pockets in pipelines [2, 3]. Air pockets decrease flow capacity, they induce significant head losses and energy losses, they prompt serious corrosion, and they can trigger and/or enhance pressure surges. Other problems include false flowmeter readings, increased biological activity, vibration and structural damage.

The minimum flow velocity for transporting air pockets depends on the size, shape, and concentration of the bubbles and on the down-slope and diameter of the pipe. The minimum velocity usually increases with increase in bubble size, in down-slope and in pipe diameter. In conditions of low velocity, below the minimum velocity, entrained air bubbles combine to form air pockets at peaks, at the crown of the pipe, at in-line and online fittings and accessories, and at other locations along the pipeline. These entrained air pockets often grow to sizes that even fast-flowing water cannot carry downstream.

Escarameia [3] has studied exhaustibly this issue and analyzes the problem in terms of three variables: diameter of the pipe, angle of inclination and the Froude non-dimensional number. The Froude number, which is proportional to the critical velocity and is inverse proportional to square root diameter, has a range from 0.3 to 0.8 in horizontal pipelines, which is the case of the present paper.

† llorencmaciacid@gmail.com
* mquispe@cells.es

Content from this work may be used under the terms of the CC BY 3.0 licence (© 2016). Any distribution of this work must maintain attribution to the author(s), title of the work, publisher, and DOI.

ISBN: 978-3-95450-188-5 doi:10.18429/JACoW-MEDSI2016-MOPE43

Content from this work may be used under the terms of the CC BY 3.0 licence (© 2016). Any distribution of this work must maintain attribution to the author(s), title of the work, publisher, and DOI.

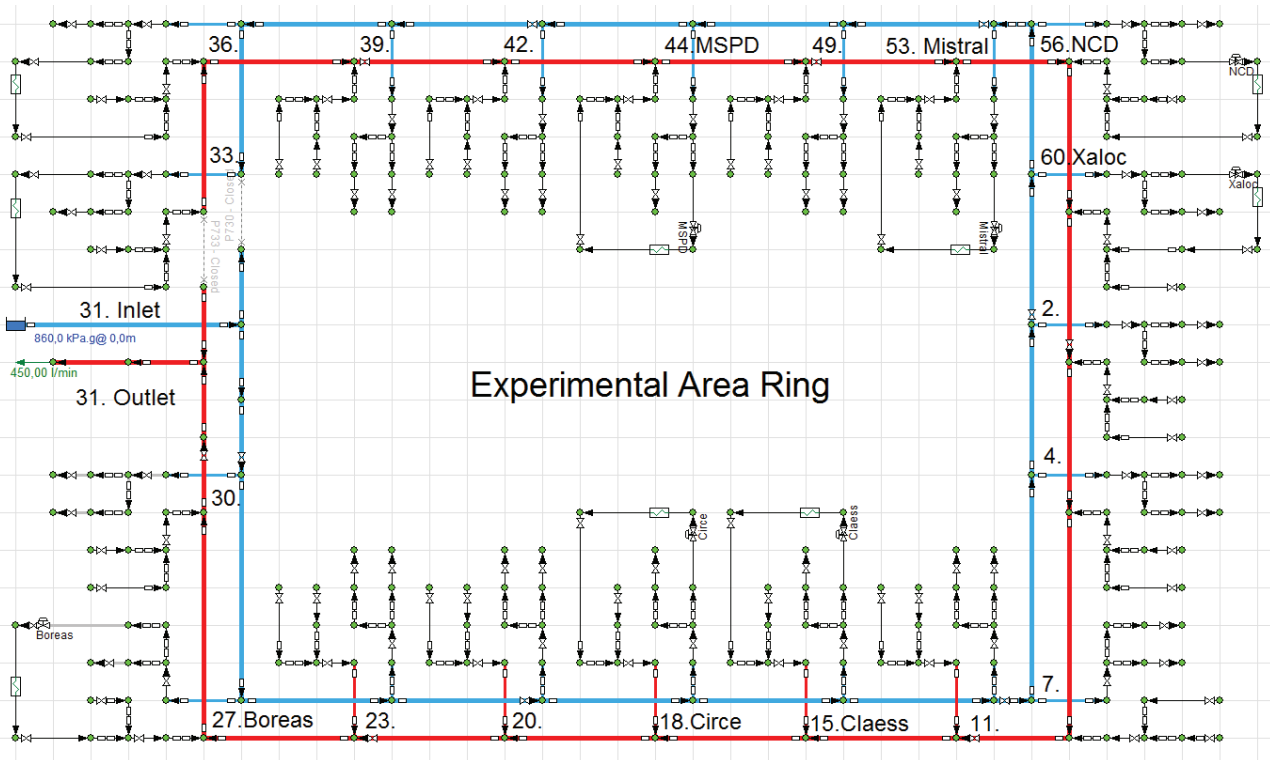


Figure 2: Hydraulic model based on Pipe Flow Expert to simulate the Experimental Area Ring.

EXPERIMENTAL AREA RING

The Experimental Area Ring has been designed to operate with 32 beamlines. In that condition the nominal flowrate capacity is 85 m^3/h. But in the current situation the ring feeds only seven beamlines: BOREAS, CIRCE, CLAESS, XALOC, NCD, MISTRAL and MSPD, which operate with a total consumption of around 27 m^3/h and 8.5 bar at the inlet pressure.

The pipes in Experimental Area (inlet and outlet) have the same cross section along the ring: the type pipe DN100 SCH10S with an internal diameter of 108.20 mm. According to the design criteria [3] the range of minimum velocities in the ring must be in between 0.31 m/s and 0.82 m/s, as gathered in the Table 1.

Table 1: Froude Number, Velocity and Flow per Pipe Ring

Froude number	Internal diameter [mm]	DN	Minimum velocity [m/s]	Flow [m^3/h]
0.3	108.20	DN100 SCH10S	0.31	10.23
0.8	108.20	DN100 SCH10S	0.82	27.28

In the current configuration the water is circulating along the EA ring with 360º rotation, which means the main flow is forced to circulate only in counter clockwise direction at the inlet ring and in the opposite direction at the outlet ring. For this condition the velocity is below 0.3 m/s in around 26 percent of the ring length. Therefore, there is a high risk of air accumulation in this zone.

1D SIMULATION OF THE EXPERIMENTAL AREA RINGS

The experimental area ring has been simulated using the unidimensional software Pipe Flow Expert [4].

To achieve a proper simulation model previously many experimental data have been obtained using non-invasive ultrasonic flowmeters and electronic pressures gauges at three different points.

In this model about 1200 elements have been characterized, not only pipes but singularities, such as dilators, elbows, gate valves, section reducers and pressure reducer valves. Figure 2 shows the simulation model of the Experimental Area Ring.

A good agreement with real measurements has been found with deviations of the main variables below 10%.

As a result the model allows checking the distribution of the flow in the ring in the current conditions and to study all possible configurations for the circulations of the flow in pipes.

PROPOSAL FOR IMPROVEMENTS

The problem of low velocities in the ring is partially solved forcing the flow circulation in the opposite direction periodically. This preventive protocol needs a lot of people and there are many risks [1]. Two solutions are described in order to solve this problem. Both proposals are based on the numerical model described before.

ISBN: 978-3-95450-188-5 doi:10.18429/JACoW-MEDSI2016-MOPE43

Variable Cross Section

Variable cross section is the proper solution for avoiding high or low velocities. For the criteria of minimum flow velocity a range of velocities is suggested based on the Froude number. But this criteria is not practical from the pipe sizing point of view. Based on the 1D simulation model a systematic study has been conducted in order to determine a unique minimum velocity as design criteria. Assuming different future scenarios, considering more beam lines in operation, the present paper proposes 0.6 m/s as the appropriate minimum flow velocity where most scenarios run into the same solution of variable cross section. As result it is proposed to do a modification of the pipes from DN100 to DN40 only in sectors 1, 2, and 3 (see Fig. 3).

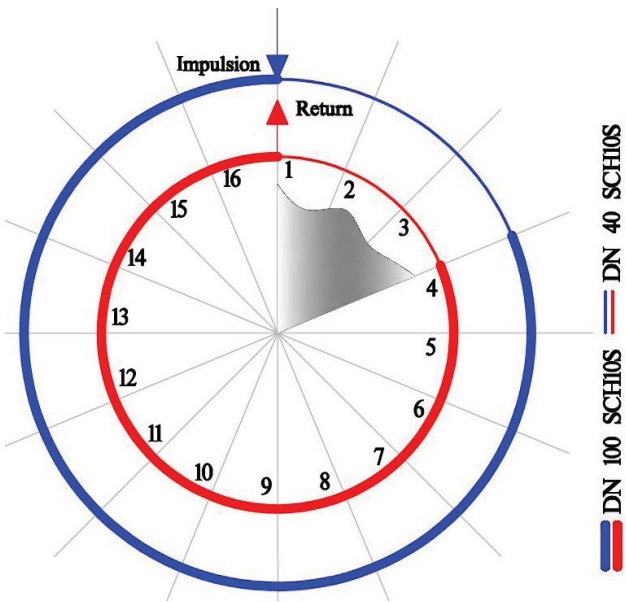


Figure 3: Description of the modification in the pipe ring of EA. Sectors 1, 2 and 3 made of type pipe DN40 SCH10S.

Controlled Bypass

The purpose of a controlled bypass is to regulate the total flowrate in the ring at the last point, in sector 1 (see Fig. 3). This is a practical solution with a minimal intervention in the installation. This solution implies to have a controlled flow that accomplishes the following requirements: (i) increase of the velocity map above of 0.6 m/s for the entire ring, (ii) avoid velocities above of 3 m/s and (iii) working in the range of pump possibilities. This solution has the next advantages: (i) it is not necessary switch off the pumps, (ii) reduced intervention time and (iii) only one person is involved in this operation.

The controlled bypass can operate with the current pipe geometry (all ring at a constant cross section) and also with the previous solution of a variable cross section.

Figure 4 shows a simplified hydraulic scheme with main components and the PID loop to control the flowrate. The controlled bypass has a modulating valve in order to maintain the flow required in the ring that meets the criteria of the minimum velocity. The flowrate in the bypass has been calculated to be 10 m^3/h.

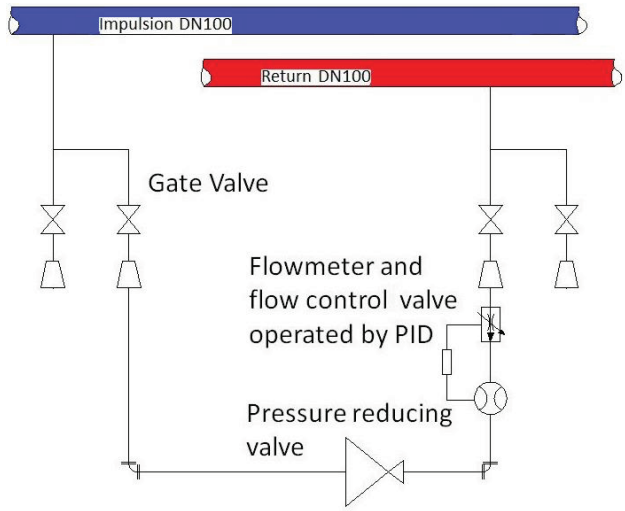


Figure 4: Schematic of the proposed Controlled Bypass.

CONCLUSION

According to the literature review a minimum flow velocity is always required to move air pockets in pipelines.

Based on the software Pipe Flow Expert an accurate 1D model of the Experimental Area Ring has been built that permits to evaluate the hydraulic behaviour of the ring and the response when it is subject to possible modifications.

The two improvements proposed, variable cross section and controlled bypass, solve the problem but have a different scope: the first is dedicated for a final stage of developing of ALBA and causes a great impact on its implementation. The second one is capable to work in the short and middle stage of development. By controlling the flow crossing the bypass it is possible to guarantee the minimum flow that removes the air. In addition, the impact of its implementation is lighter compared to the former one.

REFERENCES

[1] *M. Quispe*, "Cooling System Operation", 21st Meeting of the ALBA Scientific Advisory Committee, Barcelona, Spain, December 2015.

[2] *M.J. Little*, "Air transport in water and effluent pipelines", 2nd. International Conference on Marine Waste Water Discharges, Istanbul, September, 2002.

[3] *M. Escarameia,* "Investigating hydraulic removal of air from water pipelines", Water Management 160 (1), p. 25 – 34, 2007.

[4] Pipe Flow Expert, http://www.pipeflow.co.uk/

Content from this work may be used under the terms of the CC BY 3.0 licence (© 2016). Any distribution of this work must maintain attribution to the author(s), title of the work, publisher, and DOI.

ISBN: 978-3-95450-188-5 doi:10.18429/JACoW-MEDSI2016-TUAA01

PRECISION MECHANICAL DESIGN OF A MINIATURE DYNAMIC MIRROR BENDER FOR THE SSRF BEAMLINE UPGRADE PROJECT

D. Shu[1], A. Li[2], S. P. Kearney[1], C. Mao[2], J. Anton[1,3], and Y. Pan[2]
[1]Advanced Photon Source, Argonne National Laboratory, Argonne, IL 60439, U.S.A.
[2]Shanghai Synchrotron Radiation Facility, Shanghai Institute of Applied Physics, Shanghai 201204, China
[3]University of Illinois at Chicago, Chicago, IL 60607, USA

Abstract

Dynamic mirror benders which enable high precision figuring of planar substrates for x-ray focusing are widely used as conventional optical equipment in various synchrotron radiation beamlines. Especially, in cases for x-ray focusing optics coated with multilayers in a Kirkpatrick-Baez (K-B) configuration [1] as the final focusing elements immediately upstream of the sample, the dynamic mirror benders provide high precision figuring to allow the mirror figure to be tuned to optimize the focusing at different incidence angles to cover a wide energy range [2].

Recently, collaboration between Argonne National Laboratory and Shanghai Institute of Applied Physics has produced designs of a new miniature dynamic mirror bender using Argonne's laminar nanopositioning flexure technique [3-5] for the beamline upgrade project at the Shanghai Synchrotron Radiation Facility (SSRF). The mechanical design and finite element analyses of the miniature dynamic mirror bender are described in this paper.

INTRODUCTION

The SSRF is a 3.5 GeV third generation synchrotron radiation source. Currently, there are sixteen more beamlines under design and construction stage for the SSRF Phase-II beamline construction project. Both SSRF and Advanced Photon Source (APS) have a keen interest in the development of novel K-B mirror mount stages for synchrotron radiation applications. As a part of Argonne Strategic Partnership Project (SPP) (formerly known as work for others or WFO project), collaboration between Argonne National Laboratory and Shanghai Institute of Applied Physics has produced designs of a new miniature dynamic mirror bender using Argonne's laminar nanopositioning flexure technique for the beamline upgrade project at the SSRF. The motivation of the new design is to develop a compact, cost-effective flexure mirror bender with high stability.

TEST MIRROR FOR PROTOTYPE

Figure 1 shows a schematic diagram of a silicon test mirror for the new miniature dynamic bender prototype. The 90 mm long silicon mirror has an effective optical length of 66 mm and thickness of 5.5 mm. The width of the mirror is designed to perform the optical figuring of the mirror under bending [6]. With a dynamic mirror bender, which is capable to provide bent moment tuneable between 0.35 N·m to 0.71 N·m, the elliptical mirror figure radiuses are tuneable between of curvatures of 24 m–88 m to 12 m-44 m.

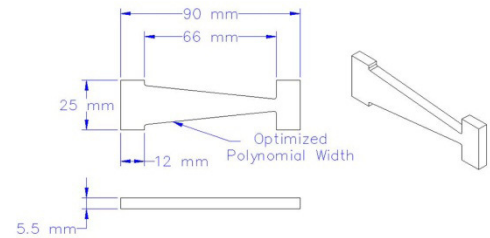


Figure 1: Schematic diagram of a silicon test mirror for the new miniature dynamic bender.

DESIGN OF THE MIRROR BENDER

Based on the type of bending actuators, the miniature dynamic mirror bender is designed with two configurations: the open-loop control configuration with Newportᵀᴹ Picomotorᵀᴹ actuators and the closed-loop control configuration with Newport™ NPM-140 piezo micrometer adapter [7]. Both design configurations use the same flexure bending mechanism module.

Mirror Bender with Newport™ Picomotor™ Actuators

The miniature dynamic mirror bender for open-loop control configuration consists of a base; a pair of laminar flexure mechanism modules; a pair of bending arms; and two Newportᵀᴹ Picomotorᵀᴹ 8301 actuators. The silicon mirror is bonded to a pair of adapters to connect with the bender as shown in Figure 2.

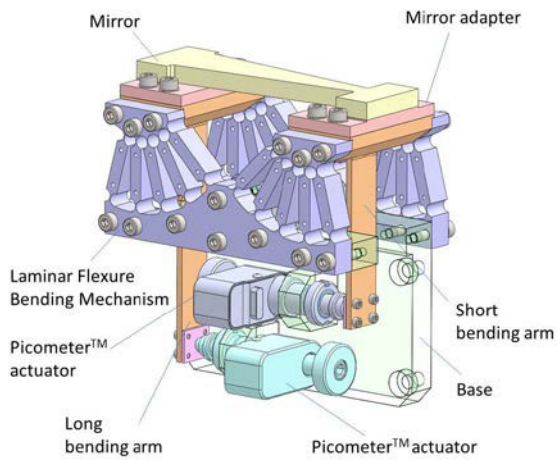


Figure 2: 3-D model of the miniature dynamic mirror bender with Newportᵀᴹ Picomotorᵀᴹ 8301Actuators for open-loop control configuration.

Content from this work may be used under the terms of the CC BY 3.0 licence (© 2016). Any distribution of this work must maintain attribution to the author(s), title of the work, publisher, and DOI.

ISBN: 978-3-95450-188-5 doi:10.18429/JACoW-MEDSI2016-TUAA01

Since the Picomotor™ 8301 piezo linear actuator has a limited 22 N axial load capacity, similar to the ESRF mirror bender design [2], the bender has a longer bending arm to provide the necessary bending moment. The elastic deformation of the bending arm also provides an extended bending resolution.

Mirror Bender with Newport™ NPM-140 Piezo Micrometer Adapter

With Newport™ NPM-140 piezo micrometer adapter's 100 N axial load capacity and nanometer-scale positioning resolution [7], the dynamic mirror bender's closed-loop control configuration also has a more compact design with shorter bending arm. As shown in Figure 3, the closed-loop control configuration consists of a base; a pair of laminar flexure mechanism modules; a pair of bending arms; a Newportᴛᴍ NPM-140 piezo micrometer adapter with 140 micron travel range for the long bending arm, and two manual adjusters for both long and short bending arms. Figure 4 shows a comparison between the two configurations of the dynamic mirror bender design.

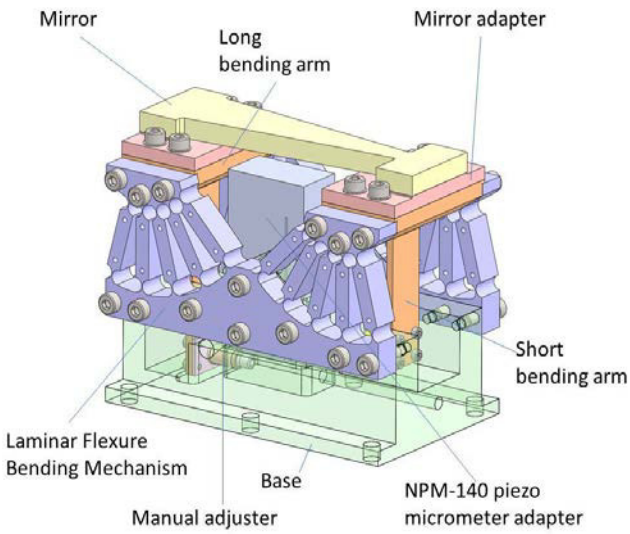


Figure 3: 3-D model of the miniature dynamic mirror bender with Newportᴛᴍ NPM-140 piezo micrometer adapter for closed-loop control configuration.

Design of Laminar Flexure Bending Mechanism

The flexure bending mechanism module is constructed with stacks of thin metal weak-link sheets which are manufactured using photochemical machining processes with lithography techniques [4]. The module is a solid laminar bonded complex structure designed for ultrahigh positioning sensitivity and stability performance.

Figure 5 shows a 3-D model of the laminar flexure bending mechanism module. It is a combination of two individual tip-tilting flexural guiding structures. The 8-mm-thick bonded module consists of forty layers of 200-micron-thick photochemical machined single weak-link sheet. The weak-link sheet material could be 17-7 PH stainless steel (for lager dynamic range) or Invar-36 (for better thermal stability).

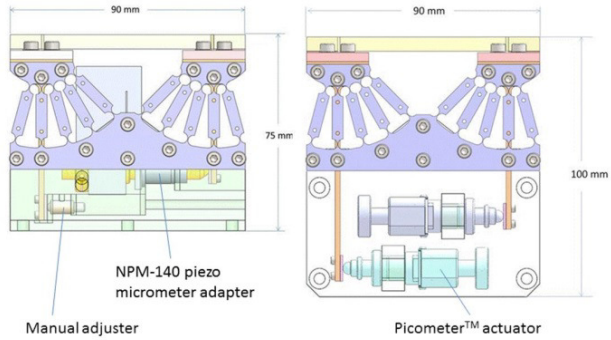


Figure 4: A side view for comparison between the two configurations of the dynamic mirror bender design. The configuration with NewportTM NPM-140 piezo micrometer adapter shows a 25% overall height reduction.

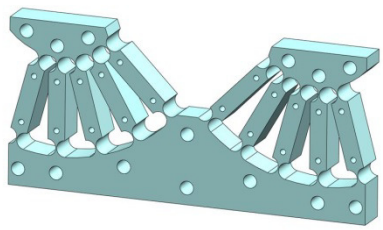


Figure 5: 3-D model of the 8-mm-thick laminar flexure bending mechanism module. It is a combination of two individual tip-tilting flexural guiding structures.

PROTOTYPE FOR FINITE ELEMENT ANALYSIS AND PRELIMINARY TEST

As shown in Figure 6, 7 and 8, finite element analysis (FEA) results for the Z7-5006 dynamic mirror bender prototype with open-loop control configuration show that, with a 15.1 N load applied to the short bending arm and a 11.4 N load applied to the long bending arm (to simulate a bent moment of ~1 N·m), the maximum Von-Mises stress on the 8-mm-thick weak-link modules reaches ~109 MPa, which is only less than 10% of the material yield stress for 17-7-PH stainless steel. The maximum displacement of the long bending arm is ~0.97 mm. The maximum displacement of the short bending arm is ~0.57 mm.

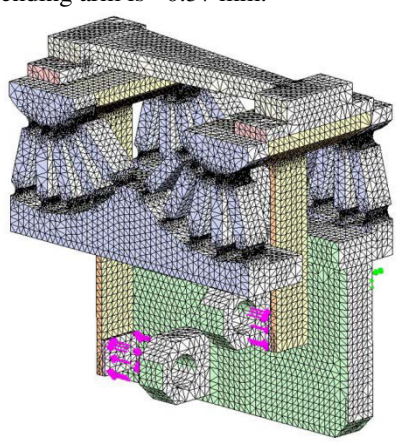


Figure 6: 3-D model of the flexure bending mechanism with solid mesh for FEA.

Content from this work may be used under the terms of the CC BY 3.0 licence (© 2016). Any distribution of this work must maintain attribution to the author(s), title of the work, publisher, and DOI.

ISBN: 978-3-95450-188-5 doi:10.18429/JACoW-MEDSI2016-TUAA01

Content from this work may be used under the terms of the CC BY 3.0 licence (© 2016). Any distribution of this work must maintain attribution to the author(s), title of the work, publisher, and DOI.

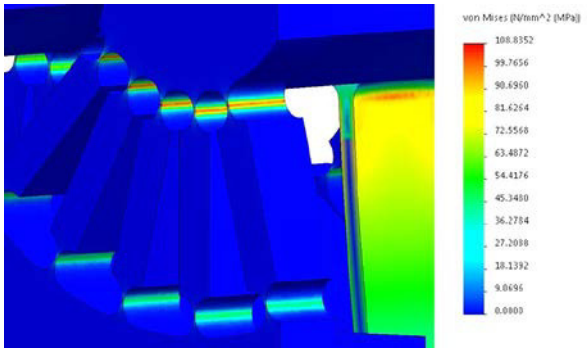


Figure 7: 3-D model of the flexure bending mechanism shows the maximum Von-Mises stress on the 8-mm-thick weak-link modules reaches ~109 MPa.

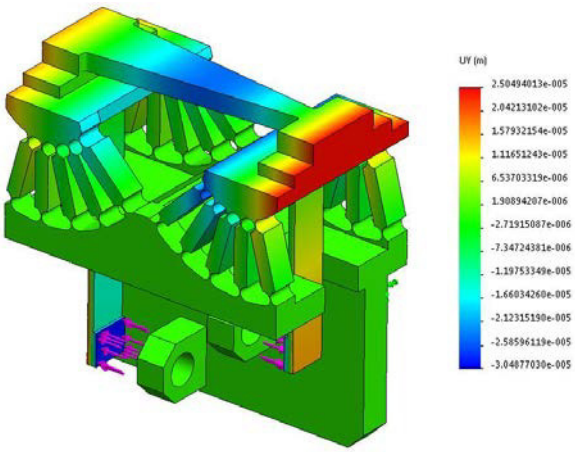


Figure 8: 3-D model of the flexure bending mechanism shows the maximum displacement of the long bending arm is ~0.97 mm, and the maximum displacement of the short bending arm is ~0.57 mm.

A prototype of the miniature dynamic mirror bender Z7-5006 with closed-loop control configuration has been designed and constructed for preliminary mechanical and optical tests. As shown in Figures 9 and 10, an aluminium alloy dummy mirror with mirror adapter is mounted on the dynamic mirror bender for mechanical assembly test. The flexure bending mechanism module is constructed with 17-7 PH stainless steel sheet. The material used for the short and long bending arms is Invar-36. The prototype's base is made from aluminium alloy.

In Figures 9 and 10, the temporary linkages between the two individual tip-tilting flexural guiding structures in the module have not been removed yet.

SUMMARY

The mechanical design of a miniature dynamic mirror bender with open-loop control and closed-loop control configurations for beamline upgrade project at the SSRF are presented in this paper. FEA results have shown that the mechanical design of the Z7-5006 prototype bender is capable of meeting design requirements for the SSRF 90-mm-long test mirror. Table 1 summarizes the design specifications of the Z7-5006 prototype miniature dynamic mirror bender. Mechanical test with laser interferometer is in progress. The results will be presented in a separate paper later.

Table 1: Design Specifications of the Z7-5006 Prototype Miniature Dynamic Mirror Bender

Z7-5006 dynamic mirror bender (open-loop control configuration)	
Overall dimensions (mm)	90 (L) x 62 (W) x 100 (H)
Normal load capacity (kg)	0.1
Driver type	Newport™ Picomotor™ linear actuator
Driver encoder type	N/A
Driver axial load capacity (N)	22
Driver min. incremental (nm)	20
Manual adjustment option	Yes
Tuneable bent moment (N·m)	0.2 - 1
Z7-5006 dynamic mirror bender (closed-loop control configuration)	
Overall dimensions (mm)	90 (L) x 62 (W) x 75 (H)
Normal load capacity (kg)	0.1
Driver type	Newport™ NPM-140 piezo micrometer adapter with closed-loop control option
Driver encoder type	strain-guage
Driver axial load capacity (N)	100
Driver closed-loop travel range (micron)	140
Driver min. incremental (nm)	1
Manual adjustment option	Yes Tuneable bent moment (N·m) 0.2 - 1

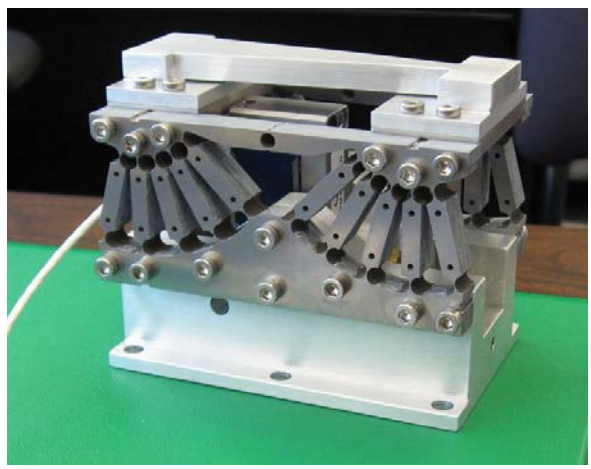


Figure 9: Photograph of the Z7-5006 prototype dynamic mirror bender with closed-loop control configuration.

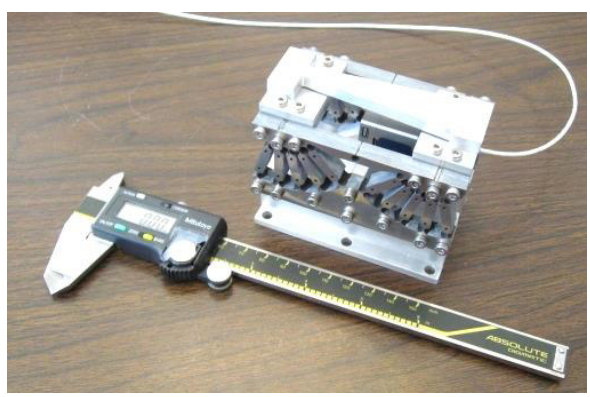


Figure 10: Photograph of the Z7-5006 prototype dynamic mirror bender with closed-loop control configuration.

ISBN: 978-3-95450-188-5 doi:10.18429/JACoW-MEDSI2016-TUAA01

ACKNOWLEDGMENT

Work supported by the U.S. Department of Energy, Office of Science, under Contract No. DE-AC02- 06CH11357 and Argonne SPP project 85E77. Work at SINAP supported by National Natural Science Foundation of China (U1332120).

REFERENCES

[1] P. Kirkpartrick and A. V. Baez, "Formation of Optical Images by X-Rays", *JOSA* 38(9), pp.766-773 (1948).

[2] R. Barrett, J. Härtwig, C. Morawe, *et al.*, *Synchrotron Radiation News*, 23, No.1, 36-42 (2010).

[3] U.S. Patent granted No. 6,607,840, D. Shu, T. S. Toellner, and E. E. Alp (2003).

[4] U.S. Patent granted No. 6,984,335, D. Shu, T. S. Toellner, and E. E. Alp ()2006).

[5] D. Shu, T. S. Toellner, E. E. Alp, J. Maser, J. Ilavsky, S. D. Shastri, P. L. Lee, S. Narayanan, and G. G. Long, *AIP* CP879, 1073-1076 (2007).

[6] A. Li and C. Mao, Private Communications (2016)

[7] http://www.newport.com/Picomotor-Piezo-Linear-Actuators

Content from this work may be used under the terms of the CC BY 3.0 licence (© 2016). Any distribution of this work must maintain attribution to the author(s), title of the work, publisher, and DOI.

ISBN: 978-3-95450-188-5 doi:10.18429/JACoW-MEDSI2016-TUAA02

EARTH, WIND, AND FIRE: THE NEW FAST SCANNING VELOCIPROBE*

C. Preissner†, S. Sullivan, S. T. Mashrafi[1], C. Roehrig, J. Maser, B Lai, C. Jacobsen, J. Deng, F. S. Marin[2], and S. Vogt, Advanced Photon Source, Argonne National Laboratory, Argonne, IL, USA
[1]University of Illinois, Department of Mechanical Science and Engineering, Urbana, IL, USA
[2]DePaul University, Chicago, IL, USA

Abstract

The Advanced Photon Source Upgrade (APS-U) project will include a suite of new beamlines. In preparation for this, a team at the APS is developing an X-ray microscope with a novel granite (Earth), air bearing (Wind) supported stage to take advantage of the two orders of magnitude increased coherent flux (Fire) that will be available with the APS-U. The instrument will be able to operate as a scanning probe for fluorescence microscopy and as a ptychoprobe for the ultimate in spatial resolution. Both are combined with tomography. The goals for the instrument while operating at the current APS are to demonstrate fast scanning of large samples at high resolution and ptychography at the highest resolution (speed and resolution limited by available flux). This presentation will discuss the unique mechanics, interferometry scheme, the advanced scanning control, and some instrument integration.

INTRODUCTION

The dramatic increase in flux (the Fire) from the APS-U will enable reduced measurement times and increase optical resolution [1]. In fact, to make the best use of available photons and minimize sample damage, the X-ray beam will need to be scanned much more rapidly across the sample than is currently done. The high resolution and fast scanning necessitate a stable instrument platform. A new instrument, the Velociprobe, is being built to explore and push these limits. It will use zone plate optics and be able to operate as a scanning probe for fluorescence microscopy and as a ptychoprobe for the ultimate in spatial resolution. The goal is to scan a 1 µm by 1 µm area in less than 10s with the highest spatial resolution (~10 nm or better in fluoro-microscopy mode).

The goal of a highly stable instrument was considered at each point in the design process. The motion system was designed to minimize the positioning degrees of freedom. The fast scanning control is being developed to maximize bandwidth and disturbance rejection. This will be coupled with state-of-the-art laser interferometry to provide the best possible position information to the fast controller and the image collection systems. This paper covers the overall design of the instrument, including mechanics and controls, and the near-term plans as the Velociprobe is brought online.

INSTRUMENT DESIGN

Mechanics

The Velociprobe consists of a set of granite (the Earth) air-bearing supported (the Wind) coarse positioning X, Y, and Z axes stages. On top of these coarse axes sit the sample stack and the optics stack. The granite coarse stages are used to align the optics to the beam. The optics stack is used for the rapid fine scanning of the beam. The sample stack is used to align the tomographic axis to the optics and to select the region of interest on the sample.

The optics stack consists of a fast (bandwidth of hundreds of Hz) parallel kinematic piezo scanner. The order sorting aperture (OSA) stages are also mounted here. The sample stack consists of a coarse sample X axis, sample tomographic rotation axis, and the X, Y, and Z axes for sample centering. In operation, the optics are aligned to the beam, then the tomographic axis is aligned to the optics. The region of interest is brought to the tomographic axes. The fast scanner is then used to image the sample. The sample region of interest is then indexed to tile out larger sample areas. Basic information about all the axes (except those for the OSA) is shown in Table 1.

Table 1: Velociprobe Axes Listing

Axis	Travel	Design Res.	Model
CRSX	± 12.5 mm	5 µm	Custom
CRSY	± 5 mm	.7 µm	Custom
CRSZ	400 mm	5 µm	Custom
ZPXYZ	30, 20, 30 µm	.1 nm	PI 733.DD
OSAXYZ	± 12.5 mm	1 nm	Smaract SLC-17
SAMCX	± 5 mm	3 µm	Custom
SAMθ	360 deg.	.004 deg.	PI DT-380
SAMXYZ	26 mm	6 nm	PI Q-545

Custom Coarse Stage System

The foundation of the instrument, shown in Figure 1, is the granite coarse positioning stages. The design of these stages was driven by the question: How can the most stable microscope platform for an X-ray microscope be constructed? With this in mind, one of the design considerations was to minimize the number of degrees of freedom. This is because each motion degree of freedom also contributes compliance to the system. This can be particularly true for the degrees of freedom that are used to align the instrument, as they typically carry high loads. In addition, these alignment axes are not used frequently.

* Work supported by: Argonne is managed by UChicago Argonne, LLC, for the U.S. Department of Energy under contract DE-AC02-06CH11357.
† preissner@aps.anl.gov

Content from this work may be used under the terms of the CC BY 3.0 licence (© 2016). Any distribution of this work must maintain attribution to the author(s), title of the work, publisher, and DOI.

ISBN: 978-3-95450-188-5 doi:10.18429/JACoW-MEDSI2016-TUAA02

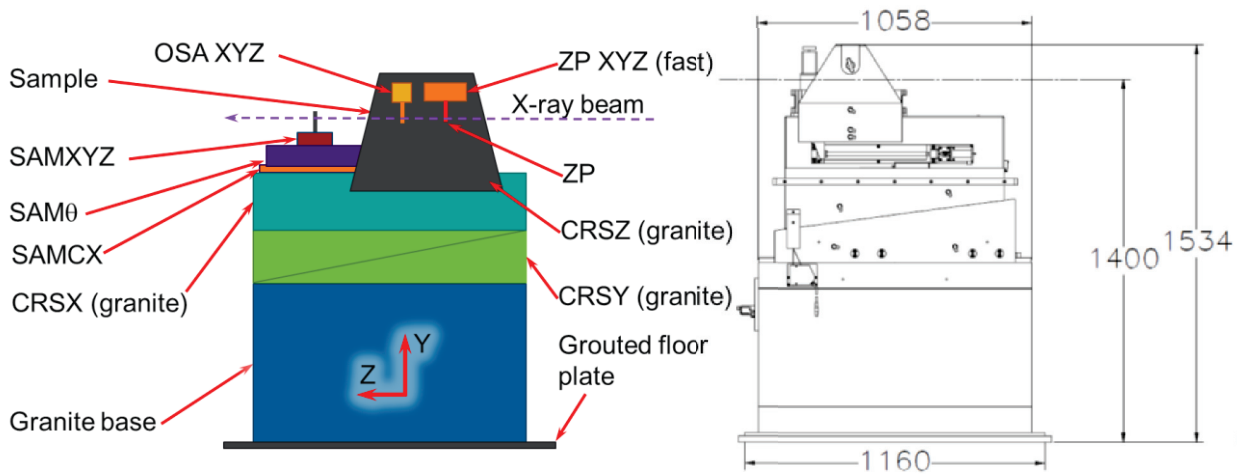


Figure 1: A schematic and line drawing of the velociprobe, showing the various stages. In the schematic on the left, the coarse Z (CRSZ) gantry is shown in the sample-changing position such that the sample stage stack can be seen. The sample, zone plate (ZP), and floor plate are also shown. The mass of the assembly is approximately 3630 kg and it stands about 1.5 m high.

To have motion axes that are not used frequently and reducing the performance potential drove the team to consider alternative. The chosen solution for the coarse positioning axes are granite structures with integrated air-bearing support (and also guiding for Z axis). The implication is that the axes can be moved precisely while moving on the air bearing film, then vented and the structure becomes as rigid as monolithic block of granite. In effect, the coarse positioning stages can be thought of as a shape-changing block of granite—all the advantages of a solid support without the added compliance of motion components. This design enables what the Velociprobe team considers to be the ultimate in stability. In addition, there vertical (Y) axis is novel and bespoke design and for which a patent has been applied [2].

All three coarse axes use the same basic concept, geometry machined directly into the granite to provide integrated air bearings. Typical geometry is shown in Figure 2.

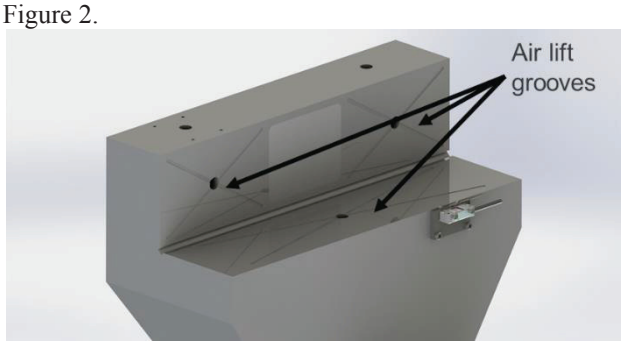


Figure 2: View showing the bottom of the Z axis carriage and the integrated air-lift grooves for the air bearing. Other axes are similar.

The vertical (Y) axis is a friction-locked wedge design. That means that vertical motion is provide through the one wedge being driven against a second wedge. Air bearings enable the motion and when the air bearings are vented, friction prevents the motion of the wedges. Figure 3 shows the force diagram for these wedges.

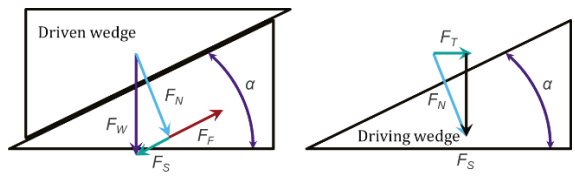


Figure 3: Force diagram of the wedges. F_w is the weight force, F_N is the normal force, F_S is the force along the slope, F_T is the thrust force, and F_F is the friction force. In the case of the Velociprobe, the angle α was chosen to be 7.5 degrees, resulting in approximately 76 mm travel of the driving wedge to move the driven wedge 10mm.

The equations describing the system are:

$$F_W = mg$$
$$F_S = F_W * cos\alpha = mg * cos\alpha \quad (1)$$
$$F_N = F_W * sin\alpha = mg * sin\alpha$$

Figure 4 show the results from an analysis to verify that the design is indeed statically stable for the 7.5 degree angle.

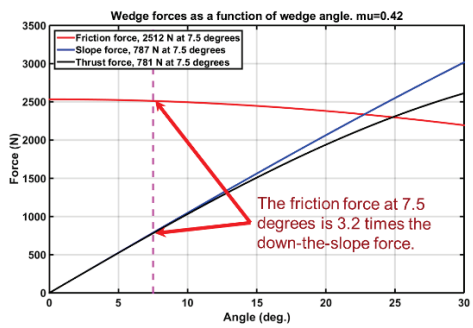


Figure 4: Chart showing that friction is sufficient to ensure stability of the vertical stage.

Each of the wedges have one degree of freedom. The driving wedge (bottom wedge in Figure 5) should be constraint to motion in the horizontal plane, while the

Content from this work may be used under the terms of the CC BY 3.0 licence (© 2016). Any distribution of this work must maintain attribution to the author(s), title of the work, publisher, and DOI.

ISBN: 978-3-95450-188-5 doi:10.18429/JACoW-MEDSI2016-TUAA02

Content from this work may be used under the terms of the CC BY 3.0 licence (© 2016). Any distribution of this work must maintain attribution to the author(s), title of the work, publisher, and DOI.

driven wedge (top wedge in Figure 5) should be constrained to motion in the vertical direction. The driving wedge is guided in the horizontal plane by the air bearing beneath it and a THK LM guide [3]. Decoupling flexures between the THK LM guide and the granite wedge ensure the wedge is not over constrained an allow it to "fly" approximately 5 µm when the air bearing is active. The driven wedge is guided by the air bearing beneath it and by a THK ball spline. Again, a decoupling flexure is used between the wedge and the ball spline to ensure the wedge is not over constrained.

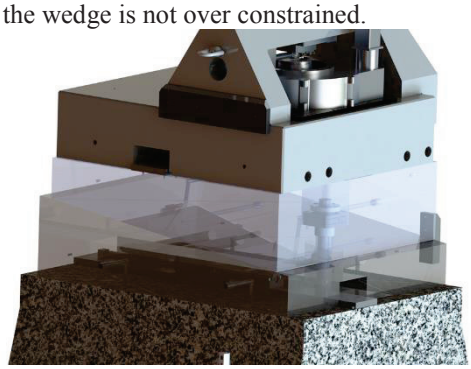


Figure 5: View showing the internal details of the wedge guiding.

The driving wedge is driven with a combination of ball screw and stepper motor. Position is encoded with a Keyence laser displacement sensor. The other coarse motion axes are similar in design, using decoupling flexures to ensure no over constraint and thereby the best stability. The Z carriage has the addition of an air bearing guide in the lateral (X) direction. This decision was made to provide high trajectory accuracy when moving the Z axis to accommodate different optics (change in beam energy).

Fast Scanning Stage

The PI 733.3DD stage is mounted to the coarse Z gantry, upside down. There is no detriment to this configuration and this allowed for a design that did not have the sample or zone plate highly cantilevered. This is shown in Figure 6.

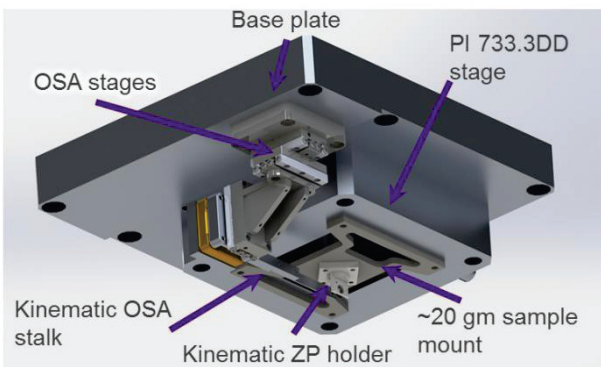


Figure 6: A picture showing the fast scanning assembly, including the PI 733.3DD stage.

Controls and Encoding

The overall control will be handled by a Delta Tau motion controller. This will integrate the coarse motion, fine motion, scanning, and the interferometer signals. The baseline configuration will use the PID controller in the Delta Tau to control the scanning trajectory. In addition, National Instruments (NI) cRIO hardware is being used to develop and implement a set of advanced control strategies. The flexibility of the FPGA in the cRIO chassis allows for a high level of customization. This controller will use an optimized negative feedback architecture and may be combined with model-based feedforward control to increase bandwidth. This technique has been shown to improve performance of similar X-ray microscopes [4]. The Velociprobe team has employed these strategies in other applications, including X-ray microscope hardware [4-6].

A block diagram summarizing the optimal control approach is shown in Figure 7. This approach allows for explicit customization of the dynamics of the closed-loop system by incorporating design objectives of large tracking bandwidth, good positioning resolution, robustness to unmodeled uncertainty, sufficient disturbance rejection and adequate measurement noise attenuation. The trade-off between positioning bandwidth and noise attenuation is addressed in this design. G is a model of the microscope nanopositioning XYZ stages that reflects the dynamics of the whole system, including the sample stage. The nanopositioner performance can be optimized for specific operating regimes. Constraints can be placed on the optimization such that actuator travel range is not exceeded. At the end of the design process, the tracking bandwidth and the tracking error across that bandwidth can be quantified. Additional information on the optimization can be found in [4-6]

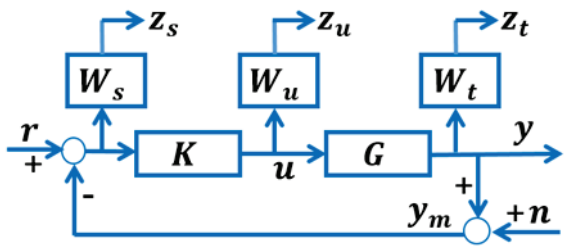


Figure 7: The closed-loop transfer function block diagram for mixed-sensitivity minimization is shown. Here, K is the controller transfer function, G is the model of the microscope dynamics, r the reference signal, u the stage input, and n the measurement noise. W_s, W_u, and W_t are design weighting transfer functions used to shape closed-loop transfer functions to achieve target regulated outputs $z = [z_s \quad z_t \quad z_u]$.

A critical part of the instrument control strategy is accurate position information. The sample and optic positions will be encoded using six axes of Attocube IDS interferometers. In this manner, the error signal used by the advanced control system will be the difference of the sample and optic position. An additional three axes may be included to capture thermal drifts. The IDS sensors have the capability of providing absolute position information. Because the instrument will be operating in

ISBN: 978-3-95450-188-5 doi:10.18429/JACoW-MEDSI2016-TUAA02

atmosphere, the standoff distances of the sensor have been minimized to reduce noise.

The AquadB signals are made available to both the Delta Tau system and the cRIO system. The Delta Tau motion controller will integrate the coarse and fine motions and provide clock signals for image acquisition. For initial operations, the internal PID controller in the Delta Tau will be used to control scanning. When used with the NI hardware driving signals to the PI scanner will be provided from NI analog output modules.

Different data collection strategies will be explored with the Velociprobe. With the advanced control strategy, the scanning bandwidth will be known and the system should track any signal within that bandwidth with a known error (1% is target). This will enable not conventional imaging trajectories [7]. In addition, the close coupling of the interferometry and imaging should provide accurate position information for any image, regardless of the accuracy of the scanning trajectory. Both approaches will be explored.

NEAR-TERM PLANS

Figure 8 shows the coarse motion assembly during manufacture. The coarse motion system will be fully tested and the fine motion systems integrated. The advanced scanning controller will need to be redefined to account for all of the dynamics of the assembled system. High-level control software will also be tested. The intent is to test with beam before the close of 2016.

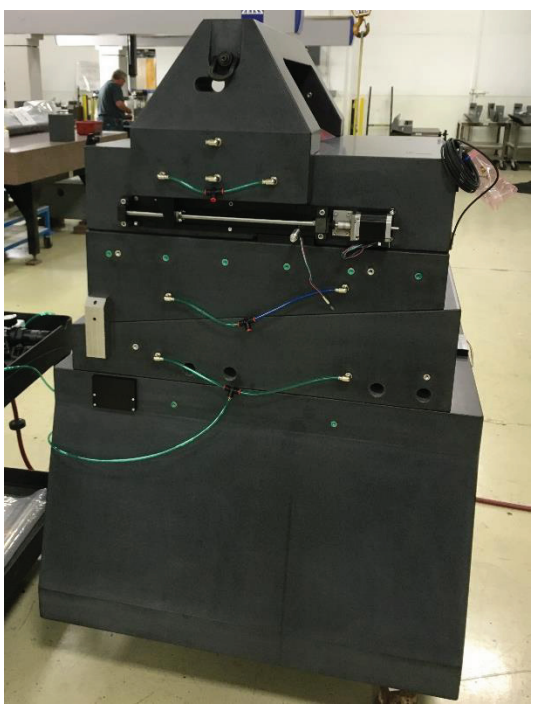


Figure 8: A picture of the Velociprobe granite stage system during final assembly and test.

ACKNOWLEDGMENT

The authors would like to acknowledge Travis Traut and Dennis Ethan of Starrett Tru Stone in Waite Park, MN for their help in the production of the velociprobe.

REFERENCES

[1] J. Maser, B. Lai, T. Buonassisi, Z. H. Cai, S. Chen, L. Finney, S. C. Gleber, C. Jacobsen, C. Preissner, C. Roehrig, V. Rose, D. M. Shu, D. Vine and S. Vogt, Metall. Mater. Trans. A-Phys. Metall. Mater. Sci. 45A (1), 85-97 (2014).

[2] Preissner, C. A., D. Vine, et al. (2016). Method and Apparatus for Implementing ultra-high stability, long-vertical travel stage. U. S. P. a. T. Office. USA, Argonne National Laboratory. Application 15/253,092.

[3] THK America, Inc.

[4] Mashrafi ST, Preissner C, Salapaka SM, Zhao H. Something for (almost) Nothing: X-ray Microscope Performance Enhancement through Control Architecture Change. ASPE 28th Annual Meeting. 2013.

[5] Lee C, Salapaka SM. Robust Broadband Nanopositioning: Fundamental Trade-offs, Analysis, and Design in a Two-Degree-of-Freedom Control Framework. Nanotechnology, Volume 20, Number 3, 2009.

[6] Sebastian A, Salapaka SM. Design Methodologies for Robust Nanopositioning. IEEE Transactions on Control Systems Technology, Volume 13, Number 6, 2005.

[7] Sullivan, S. Optics Express, Vol. 22, Issue 20, pp. 24224-24234 (2014)

Content from this work may be used under the terms of the CC BY 3.0 licence (© 2016). Any distribution of this work must maintain attribution to the author(s), title of the work, publisher, and DOI.

ISBN: 978-3-95450-188-5 doi:10.18429/JACoW-MEDSI2016-TUBA01

Content from this work may be used under the terms of the CC BY 3.0 licence (© 2016). Any distribution of this work must maintain attribution to the author(s), title of the work, publisher, and DOI.

THE DESIGN OF A PRECISION MECHANICAL ASSEMBLY FOR A HARD X-RAY POLARIZER

S. P. Kearney, D. Shu, T. S. Toellner

Advanced Photon Source, Argonne National Laboratory, Argonne, IL 60439, U.S.A.

Abstract

This paper discusses the mechanical design of an x-ray polarizer and the analysis of the design using FEA simulation. In addition, insight was made into the meshing requirements of flexure mechanisms. It was found that the maximum flexure stress will increase in accuracy with a finer mesh, however there is a limit to how well FEA can model stiffness and deflection without incorporating additional advanced FEA analysis techniques such as nonlinear methods. Finally, it was shown that the pitch stages for the polarizer will be capable of a least 80 nrad resolution.

INTRODUCTION

A hard x-ray polarizer is under development for the Advanced Photon Source (APS) at Argonne National Laboratory (ANL). It has been previously shown that polarization of synchrotron radiation can be used to filter a narrow bandwidth of 14.4 keV [1]. This has advantages for Mossbauer spectroscopy (MS) in that it allows for energy spectra to be collected rather than time spectra, which is normal in synchrotron radiation [2].

The paper will first detail and describe the mechanical design of the polarizer device for hard x-rays. Particular attention is paid to the analysis of the flexure mechanism involved in nano-radian level rotations. FEA simulations of a single notch type flexure are conducted followed by simulation of the complete flexure mechanism. Finally, experimental resolution results are shown.

POLARIZER DESIGN

Assembly – Z8-4600

The complete polarizer assembly consists of a total of 7 degrees of freedom (DOF). Three crystals are manipulated using individual actuator stacks, as can be seen in Fig. Figure 1. The left crystal will sit atop two Kohzu™ ST05A-S1T-R tilt stages modified to incorporate Newport™ 8301NF Picomotors™ for controlled positioning in the yaw and roll angles. The middle crystal also has two DOF with the base stage being a custom-designed high precision pitch flexure stage (Z4-4601) and atop that a Kohzu™ ST07A-S1T yaw tilt stage, which also incorporates a slightly larger 8302 Picomotor™ for controlled positioning. Finally, the third crystal has three DOF with the base stage being a more compact version of Z4-4601 designated Z4-4602. Atop this stage is a translation stage Kohzu™ XM05A-C1-R, and another ST05A-S1T-R roll tilt stage with Picomotor™ 8301NF. The detailed design specifications for the assembly can be seen in Table 1.

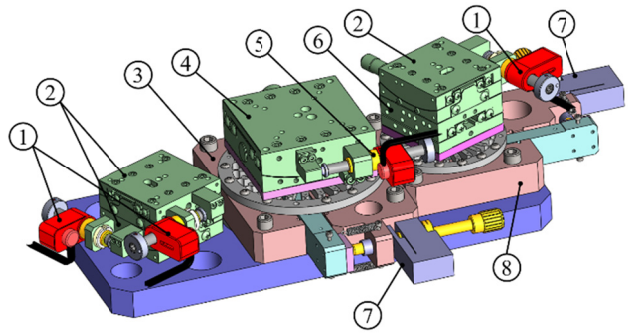


Figure 1: Z8-4600 assembly model view. Numbered items are 1) 3X Picomotor™ 8301NF, 2) 3X Kohzu™ ST05A-S1T-R tilt stage, 3) Z8-4601 pitch stage, 4) Kohzu™ ST07A-S1T tilt stage, 5) Picomotor™ 8302, 6) Kohzu™ XM05A-C1-R translation stage, 7) 2X Newport™ NPM140SG micrometer adapter piezo, and 8) Z8-4602 pitch stage.

Table 1: Design specifications for Z8-4600. The resolutions listed are derived from the published resolutions of the commercial actuators and represent the lower limit.

Specification	Value
Volume (L x W x H) mm^3	(365x214x89)
Mass	4.1 kg
Degrees of Freedom	7
Kohzu™ Tilt Stages Resolution	
ST05A-S1T-R (Open Loop)	0.5 µrad
ST07A-S1T(Open Loop)	0.4 µrad
Kohzu™ Stages Range	
ST05A-S1T-R & ST07A-S1T	±3°
XM05A-C1-R	±3.25 mm
Pitch Flexure Stages Resolution	
Z4-4601 & Z4-4602 (Closed Loop)	15 nrad
Pitch Flexure Stages Range	
Z4-4601 & Z4-4602	±0.7°

Pitch Rotation Stage – Z8-4602

Two laminar weak-link stages have been designed, for fine pitch rotation. For this paper, we will focus on the smaller diameter (73.34 mm vs. 97.78 mm) flexure stage shown in Fig. Figure 2. Pitch rotation is achieved by a Newport™ NPM140SG actuator pushing on an 80 mm sine bar attached to a pair of weak-link flexures. The laminar weak-link structure is comprised of 30 bonded

ISBN: 978-3-95450-188-5 doi:10.18429/JACoW-MEDSI2016-TUBA01

sheets of 17-7 PH stainless steel 0.1524 mm thick each [3-5].

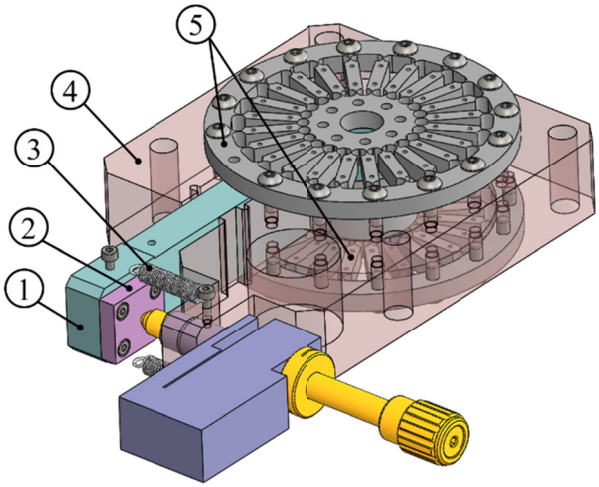


Figure 2: Z8-4602 sub-assembly model view. Numbered items are 1) 80 mm sine bar, 2) 440 hardened SS contact plate, 3) 2X extension springs, 4) base plate (shown transparent for clarity), 5) 2X 73.34 mm diameter weak-link flexure.

As of publication only the Z8-4602 stage has been built and is used as the base prototype for FEA simulation validation and experimentation. The results of these studies have provided insight into the development of Z8-4601 and similar stages based on this design.

DESIGN ANALYSIS

Flexure Modelling

The principal component of the Z4-4602 precision pitch stage is a flexure mechanism. To better understand this larger flexure mechanism, we will first analyze a single notch type flexure.

Figure 3 shows a single notch type flexure on the left with its coordinates and critical dimensions used in analytical models. The critical dimensions are R the notch radius, t flexure thickness, and b flexure depth.

By integrating the beam equation with strip elements of the flexure an approximation of the torsional stiffness about θ_Y is given by

$$K_{\theta_Y} = \frac{M}{\theta_Y} = \frac{2EbR^2}{3f(\beta)}, with \tag{1}$$

$$f(\beta) = \frac{1}{\Delta}\left\{\left(\frac{3+4\beta+2\beta^2}{\gamma\Delta}\right) + \left(\frac{6\gamma}{\Delta^{3/2}}\right)\tan^{-1}\sqrt{\frac{2+\beta}{\beta}}\right\},$$

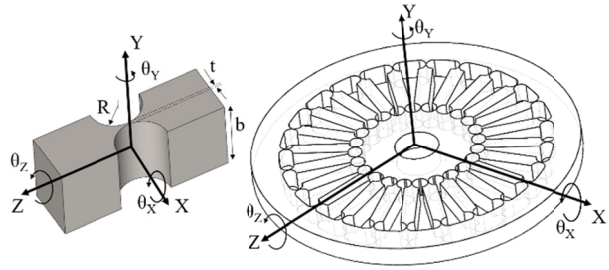


Figure 3: Coordinate frames for the two FEA models used in this study. On the left is a single flexure with dimensions describing b depth, t flexure thickness, and R semi-circular notch radius. On the right is the complete laminar weak-link structure with the coordinate frame now located at the center of the pitch pivot axis, θ_Y.

and with $\beta = t/(2R)$, $\gamma = 1+\beta$, $\Delta = 2\beta+\beta^2$, E the Young's modulus, and M the applied bending moment [6]. Equation (1) is an approximation, and it has a further simplification given by

$$K_{\theta_Y} = \frac{M}{\theta_Y} = \frac{2Ebt^{5/2}}{9\pi R^{1/2}}. \tag{2}$$

The nominal stress can then be determined from the equation

$$\sigma_{nom} = \frac{6M}{t^2 b}. \tag{3}$$

However, it should be noted that this assumes constant cross section and does not account for the concentration of stress that comes from a sudden change in cross-sectional geometry. C. B. Ling [7] derived the exact solution for this stress and it can be determined from the nominal stress using a stress concentration factor K_t

$$\sigma = K_t \sigma_{nom}. \tag{4}$$

The stress concentration factor can be determined graphically using the chart in [8] or from [6] using

$$K_t = (1+\beta)^{9/20} \tag{5}$$

For this paper we will refer to calculations using Eqs. (1), (4), and (5) as Ling's method and Eqs. (2) and (3) as the approximate method.

For the Z4-4602 flexure design stress, angle, and torsional stiffness are calculated using t = 0.115 mm, b = 4.752 mm, R = 1.524 mm, E = 204 GPa, and M = 1 N·mm. These calculations for both analytical methods can be seen in Table 2. The error from using the approximate method is at most 2.7 % for this case. Considering that there is no substantially greater numerical effort required to use Ling's method as compared to the approximate method there is no reason not to use the more com-

Content from this work may be used under the terms of the CC BY 3.0 licence (© 2016). Any distribution of this work must maintain attribution to the author(s), title of the work, publisher, and DOI.

ISBN: 978-3-95450-188-5 doi:10.18429/JACoW-MEDSI2016-TUBA01

Content from this work may be used under the terms of the CC BY 3.0 licence (© 2016). Any distribution of this work must maintain attribution to the author(s), title of the work, publisher, and DOI.

plete Ling method. Therefore, Ling's method is be used in this paper to assess FEA model validity.

Table 2: Comparing theoretical methods for calculation of stress, angle of rotation, and stiffness of the notch flexure.

Method	Stress [Mpa]	Angle [°]	Torsional Stiffness [N·mm/°]
Ling's	100.9	0.25	4.07
Approx.	99.2	0.24	4.18
% Error	-1.65	-2.68	2.70

FEA Flexure Mesh Validation

To ensure that the larger flexure FEA model is meshed with an adequate number of elements so that there can be confidence in the results, we first validate the single notch flexure mesh. We do this using a method described in a previous MEDSI 2014 conference paper [9]. For a single notch flexure, the mesh will be increased in density using SolidWorks Simulation 2016 h-adaptive mesh refining loops. The results are then compared to theoretical calculations.

The FEA mesh and setup can be seen in Figure 4 with the same geometry, material, and moment properties used in the previous section. The mesh shown is that for 5 adaptive mesh loops. At this mesh size there are at least 2 elements across the thinnest part of the flexure. Next to the setup is the von Mises stress results. In the close up of the stress results a sudden spike in stress can be seen only near the surface. This is the stress concentration that needs to be captured for the FEA model to be valid. So, the elements near the surface are much more critical than those within the volume.

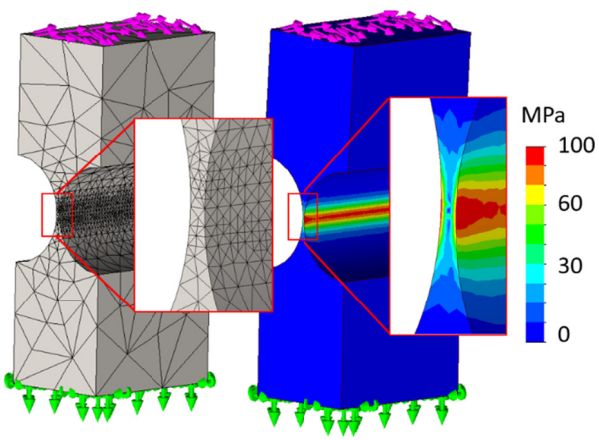


Figure 4: Setup and results of the 5 loops case. On the left is the FEA setup of the single flexure model. The green arrows on the bottom represent the fixed condition and the magenta arrows on the top represent the pure bending moment about the axis θ_Y. On the right is the von Mises stress results with an exaggerated deformation shown.

The results of the setup in Figure 4 are low in error, especially for the max stress criteria, as can be seen in the plot of Figure 5. Here, the error of the FEA results compared to theory is shown as the number of mesh loops is increased. Interestingly, as the mesh density increases (increasing mesh loops) the error in rotation angle and torsional stiffness becomes constant, while the maximum stress error continues to decrease. From the plot we can also see that a mesh using 4 or 5 loops will reduce stiffness and angle errors as far as they will go, and the max stress errors will be around 5%. For the larger flexure model we then used 5 adaptive mesh loops.

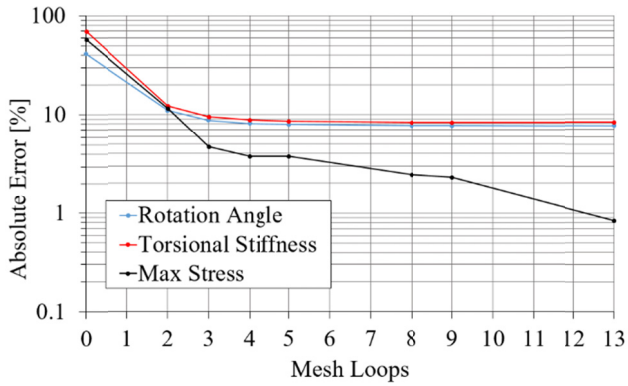


Figure 5: A plot of the relationship between adaptive mesh loops and the absolute error of the FEA model parameters: rotation angle, torsional stiffness, and max stress compared to theoretical predictions.

FEA Weak-Link Model Validation and Simulation

Now using the 5 h-adaptive mesh loops to reduce the stress error to about 5%, as shown in the previous section the full flexure model will be implemented, Figure 6. We first validate the quality of the FEA model by comparing the derived stiffness values to experimentally measured stiffness, and then predict the load capacity of the flexure stage.

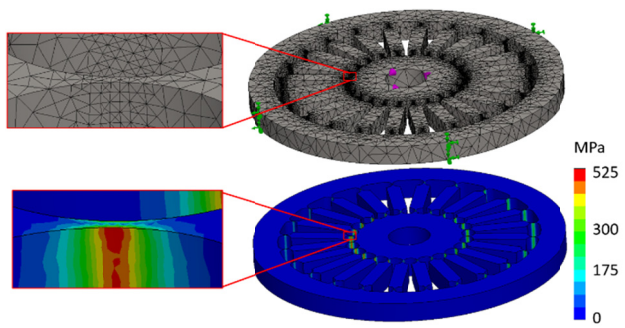


Figure 6: Setup and results using 5 adaptive mesh loops and 0.5 (N·m) of torque applied about the θ_Y axis. On the top is the FEA setup with green arrows on the outside axis representing the fixed condition and the magenta arrows on the inside hole diameter representing the applied torque. On the bottom is the von Mises stress results with about 0.6° rotation about θ_Y.

ISBN: 978-3-95450-188-5 doi:10.18429/JACoW-MEDSI2016-TUBA01

For stiffness validation the flexure model torsional stiffness is measured and then converted to an equivalent linear spring stiffness that is equivalent to the stiffness measured using the setup in Figure 7. Figure 8 shows the results of the stiffness validation. Here we can see that the two force gauge lines overlap, which demonstrates the reliability of the experimentally measured stiffness. Looking at the FEA stiffness results it can be seen that a good match between model and experiment only occurs up to about ~300 µm of equivalent actuator travel. There are many reasons why the FEA model might not be valid past this range; such as the real structure is a bonded stack of 30 laminar sheets of metal, the FEA analysis is linear, and tolerance variations in the real flexure thickness are not accounted for. In future studies these issues will be addressed.

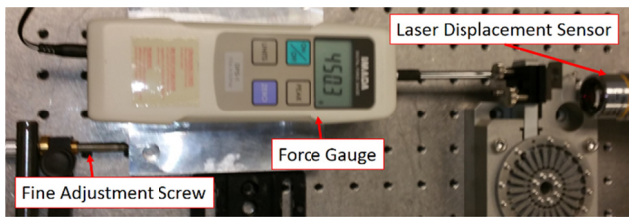


Figure 7: Experimental setup of stiffness measurement for the Z4-4602 sub-assembly.

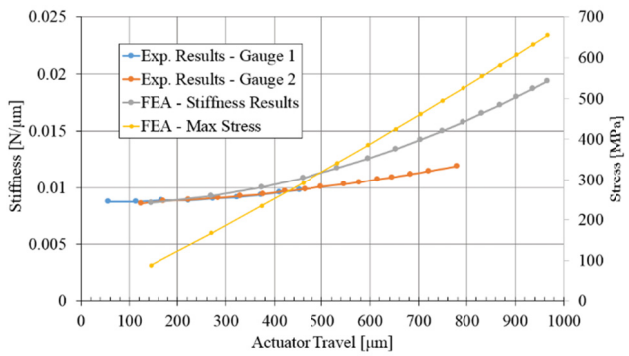


Figure 8: A plot of the stiffness of the Z4-4602 sub-assembly experimentally measured with two force gauges of different precision, gauge 1 being the finer precision of ± 0.001 N and gauge 2 with a precision of ± 0.01 N. Also plotted is the stiffness acquired from the FEA model and the max stress. Note the model can only be validated for use from 0 to ~300 µm of equivalent actuator travel.

Lastly, the model is used inside of the validated region to assess the effect of loading the flexure in the Y direction. An equivalent load of 2 kg was placed on the inside diameter of the flexure and an equivalent moment that would be applied due to a 270 µm actuator displacement. The resulting maximum von Mises stress is 171 MPa and caused 0.63 µm of parasitic motion in the Y direction. This is equivalent to a stiffness in the Y direction of 31.3 N/µm, three orders of magnitude greater than the pitch rotation direction.

Z4-4602 EXPERIMENTAL RESULTS

The fine positioning resolution was tested using a PI™ P840.10 piezo due to unavailability of the NPM140SG actuator. The P840.10 has a stated closed loop resolution of 1 nm. The experimental setup can be seen in Figure 9. Displacement was measured using a Polytec™ OFV 534 vibrometer. Figure 10 shows a set of ~80 nrad steps. The noise floor of the setup looks to be about 20 nrad which is mostly contributed by the P840.10 closed loop control. If we disregard slow drifting, the noise floor of the setup with P840.10 open loop control is about 5 – 10 nrad.

CONCLUSION

Design and development of a mechanism for a hard x-ray polarizer was assessed using FEA simulation and experiment. It was found that the maximum flexure stress will increase in accuracy with a finer mesh, however there is a limit to how well FEA can model stiffness and deflection without incorporating additional advanced model techniques such as nonlinear methods. Finally, it was shown that pitch stages for the polarizer will be capable of a least 80 nrad resolution.

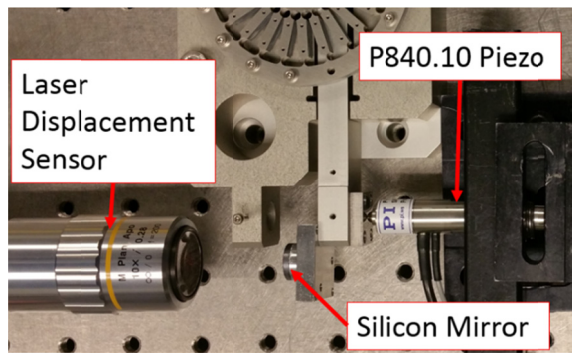


Figure 9: Experimental setup to measure the pitch angle. In this setup an alternative actuator is used to analyze the ultimate capabilities of the stage design.

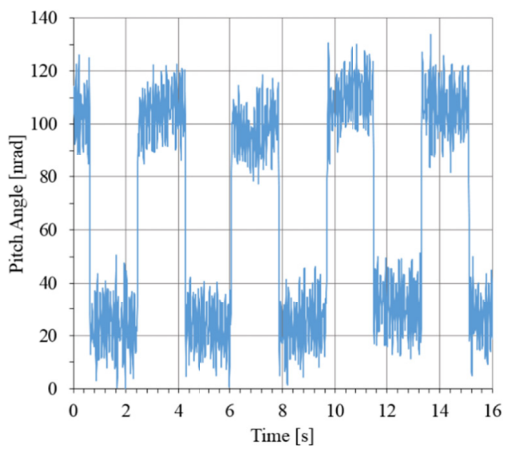


Figure 10: A plot of ~80 nrad steps.

Content from this work may be used under the terms of the CC BY 3.0 licence (© 2016). Any distribution of this work must maintain attribution to the author(s), title of the work, publisher, and DOI.

ISBN: 978-3-95450-188-5 doi:10.18429/JACoW-MEDSI2016-TUBA01

Content from this work may be used under the terms of the CC BY 3.0 licence (© 2016). Any distribution of this work must maintain attribution to the author(s), title of the work, publisher, and DOI.

ACKNOWLEDGMENT

Work supported by the U.S. Department of Energy, Office of Science, under Contract No. DE-AC02-06CH11357.

REFERENCES

[1] T. Toellner *et al.*, "Polarizer/analyzer filter for nuclear resonant scattering of synchrotron radiation," *Applied physics letters,* vol. 67, no. 14, pp. 1993-1995, 1995.

[2] T. S. Toellner, A. Alatas, E. E. Alp, M. Hu, and J. Zhao, "Next-Generation Mossbauer Spectroscopy," Argonne National Laboratory, 2015-164-N0, 2015.

[3] D. Shu, T. S. Toellner, and E. E. Alp, "Redundantly constrained laminar structure as weak-link mechanisms," U.S. Patent granted No. 6,607,840, 2003

[4] D. Shu, T. S. Toellner, and E. E. Alp, "Redundantly constrained laminar structure as weak-link mechanisms," U.S. Patent granted No. 6,984,335, 2006

[5] D. Shu, S. Narayanan, A. Sandy, M. Sprung, C. Preissner, and J. Sullivan, "Precision mechanical design of an UHV-compatible artificial channel-cut x-ray monochromator," AIP CP879, pp. 1073-1076 (2007).

[6] S. T. Smith, V. G. Badami, J. S. Dale, and Y. Xu, "Elliptical flexure hinges," *Review of Scientific Instruments,* vol. 68, no. 3, pp. 1474-1483, 1997.

[7] C.-B. Ling, "On the stresses in a notched strip," *J. of Appl. Mech. Trans. ASME*, vol. 19, no. 2, pp. 141-146, 1952.

[8] R. Peterson, "Stress concentration factors, 1974," *John Willey and Sons*

[9] M. Hillman, "Design of a flexural hinge mechanism for turbo slits," in *Proc. MEDSI '14*, Melbourne, Australia, 2014.

ISBN: 978-3-95450-188-5 doi:10.18429/JACoW-MEDSI2016-TUBA03

THE GENERIC MIRROR CHAMBER FOR THE EUROPEAN XFEL

T. Noll[1,2], H. Sinn[3], A. Trapp[3]

[1]Max-Born-Institut Berlin, Germany, [2]Helmholtz-Zentrum-Berlin, Germany
[3]European XFEL, Schenefeld, Germany

Abstract

For the high demanding requirements of the beamlines of the European XFEL [1] new mirror chambers were developed, designed and tested. A prototype contains the main features of all needed ten units which are tested extensively. The concept of the mirror chamber is a further development of our Cartesian parallel kinematics for X-ray optics in the UHV. The stiffness and vibration behaviour were further improved and the position resolution was increased compared to earlier implementations at HZB – Bessy II and Desy - Flash. For that the drives were redesigned and now feature a stroke of 100 mm with nanometre resolution.

INTRODUCTION

The new mirror chamber contains a mirror of 800 mm in length with adaptive shape compensation and an eutectic cooling. This mirror assembly has a dimension of 1000 mm x 150 mm x 250 mm (L x W x H). That large assembly requires a chamber of 600 mm in diameter and a length of 1800 mm (entry flange to exit flange). Both ends have doors for easy access to all inner components (s. Figure 1).

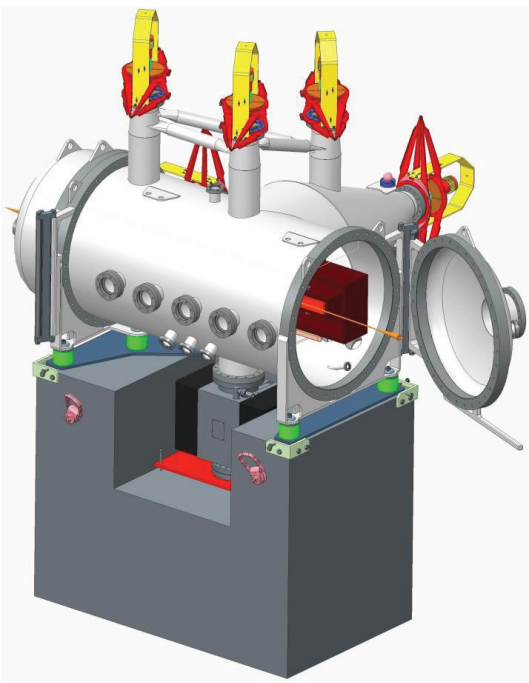


Figure 1: The mirror chamber with one open service flange.

KINEMATIC CONCEPT

The support and alignment mechanics is in principle a six strut parallel kinematics with Cartesian orientation of the movements. This allows the highest possible precision and stability [2], [3], [4] (s. Figure 2).

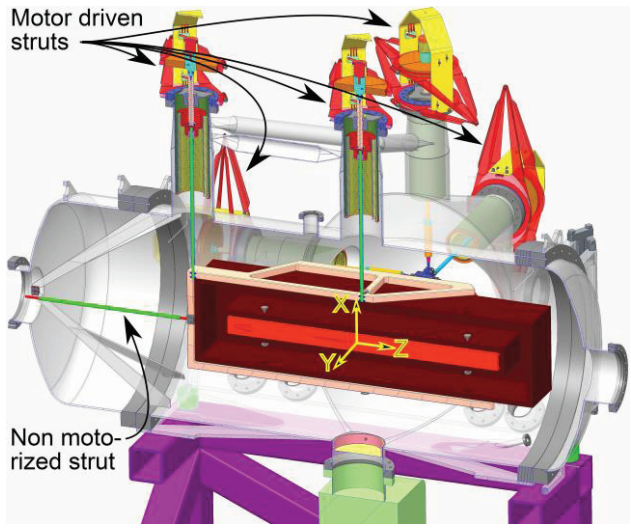


Figure 2: The cross section of the chamber gives a view at the topology of the struts.

The used six struts are the mechanical links between the mirror assembly and the flanges of the UHV-chamber. One of the struts has no motor and is not adjustable because it defines the position of the mirror along the light path which is not of interest for this application. Five of the six struts are motorized with stepper motors and lead screws.

DRIVE DEVELOPMENTS

For the X and Y translations stepper motor driven lead screws are used. For the rotations around X and Z the struts have additional piezo stacks embedded. That allows an even higher resolution and a higher motion dynamic than the stepper motor can deliver. (s. Figure 3).

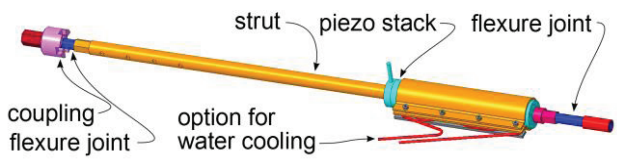


Figure 3: Strut with joints and piezo.

Content from this work may be used under the terms of the CC BY 3.0 licence (© 2016). Any distribution of this work must maintain attribution to the author(s), title of the work, publisher, and DOI.

ISBN: 978-3-95450-188-5 doi:10.18429/JACoW-MEDSI2016-TUBA03

Content from this work may be used under the terms of the CC BY 3.0 licence (© 2016). Any distribution of this work must maintain attribution to the author(s), title of the work, publisher, and DOI.

The struts have flexure ball joints at each end which are made of stainless steel rope segments. They have a good combination of linear stiffness, bending and twisting elasticity, damping behaviour and durability [5], [6]. The struts are screwed into the thrust bearing of the lead screw.

The shaft of the motor gear head is directly attached to the lead screw [7] (s. Figure 4). The torque of the motor is supported by a flexure structure that allows the translation of the motor together with the lead screw while keeping the stator of the motor non-rotating while it translates together with the lead screw.

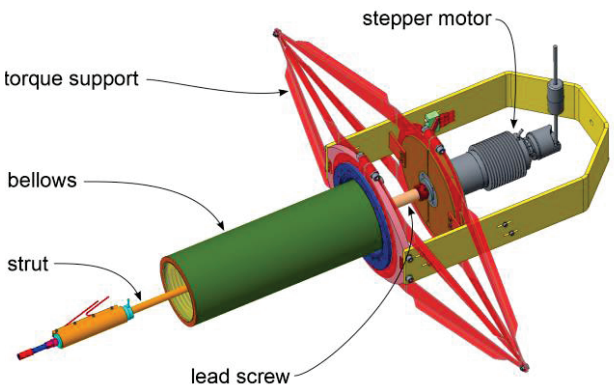


Figure 4: Dedicated feedthrough with strut and piezo.

The design of the lead screw driven linear motion feedthroughs uses a sliding bearing at the bottom of the lead screw (s. Figure 5). This non-rotatable part of the thrust bearing is welded to the bellows which also supports the torque caused by the sliding friction at the bottom of the lead screw.

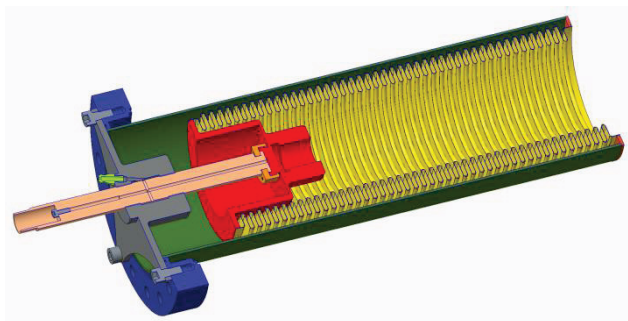


Figure 5: The sliding parts and the UHV-welding assembly.

The nut acts as linear guide way and motion transformer from rotation in to translation at the same time. Thus, we reduce the number of error sources and keep the assembly simple and mass and space saving. The sliding contacts of the thread and the axial bearing have a better reproducibility than the random errors of a ball screw and they are self-locking.

The lead screws have a diameter of 16 mm and a fine pitch of 1 mm. Because the sliding parts are in air they can – and need to be greased. Therefore a channel system was designed which brings the lubricant from the grease nipple to each sliding contact pair without disassembling the unit (s. Figure 6).

The tight tolerances for the fine pitch thread of 1 mm are always a challenge for machining and can nevertheless cause seizing. Maybe for further applications a trapezoid thread combined with a higher transmission rate of the gear head of the stepper motor could make the system more durable.

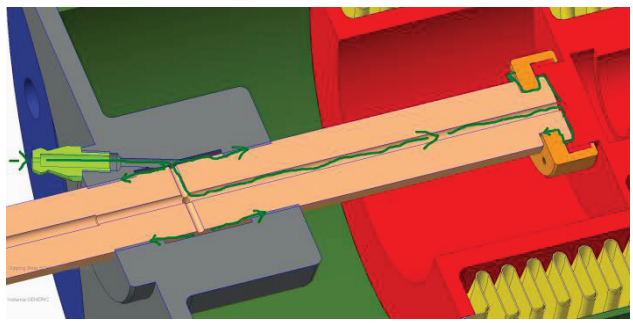


Figure 6: The greasing path for the sliding pairs.

The current setup contains a Phytron stepper motor with 200 steps per revolution and a gear head with a transmission ratio of 72:1. By the fine pitch of 1 mm we have a full step resolution of 70 nm over a distance of ± 50 mm. These simple and light weight assembly allows those ultra high precision linear motions and can be directly attached to the flange of the chamber.

UHV-CHAMBER

The UHV-chamber works as the fixed supporting structure for the drives and gives a rigid link to the base block made of granite and to the concrete floor. Because of its tubular shape and the large diameters the stiffness of the chamber is relatively high. Thereby the position of the flanges where the mirror is attached to is not very sensitive to changes of the air pressure. We calculated a deformation at the flange necks of max. 60 µm while applying air pressure (in the Creo Simulate and Ansys Software) (s. Figure 7).

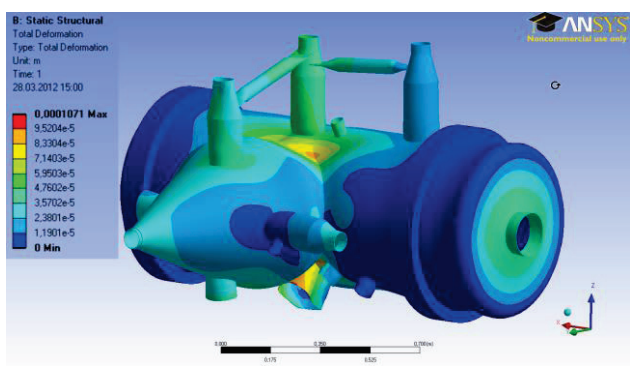


Figure 7: Deformation of the chamber under air pressure.

A second important characteristic of a mirror chamber is its vibrational behaviour. The tubular shape of the

ISBN: 978-3-95450-188-5 doi:10.18429/JACoW-MEDSI2016-TUBA03

chamber is also relatively light weight and stiff. These are the pre-conditions for high eigenfrequencies. Deduced from the CAD-design model a Finite Element Model was created.

The vibrational modes of the chamber could be optimized at a 1st eigenfrequency of 85 Hz. To reach this high stiffness we applied longitudinal connections of the chamber to the granite and cross links between the upper flanges. (s. Figure 8). We decided to have only 5 mm of wall thickness which causes a relatively low weight what increases the eigenfrequencies of the whole chamber on the granite base.

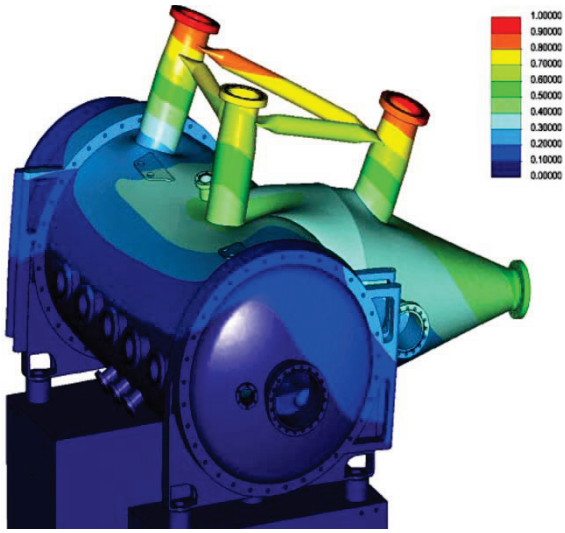


Figure 8: First eigenfrequency at 85 Hz (displacement in m).

At the starting point of the optimization of the vibrations we had low frequencies in a mode of vibrations in beam direction. It was caused by the relatively narrow legs of the chamber at the four corners which showed bending vibrations. This mode could completely eliminated by implementing additional connections to the granite base body (s. Figure 9).

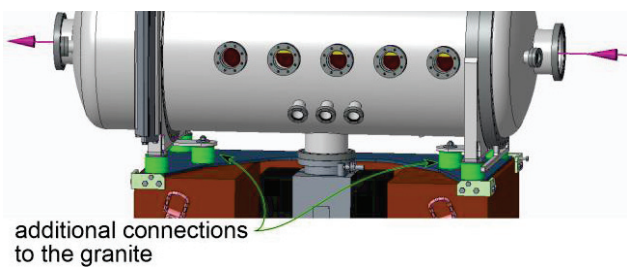


Figure 9: Connection of the chamber to the granite.

For the green pads shown in Figure 9 at the six legs we used the "ball head precision adjusters" from WASI [8]. These alignment screws allow the positioning and rigid fixing of the chamber in a range of about 5 to 10 µm, which is enough for the alignment of the chamber.

CONCLUSION

The generic mirror chamber for the European XFEL is a successful further development of the mirror chambers at Bessy II. The redesigned drives which are supporting and positioning the mirror have a long stroke of 100 mm with nm resolution. This stroke gives the opportunity to switch the mirror in and out of the beam instead of only using the drives for small alignments. There is still space to improve the properties like stroke and durability for further applications.

For the chamber and general set up we found a suitable compromise out of stiffness, weight, manufacturing costs and the functional features. Thus, the generic design can be the base for the required derivatives for each individual installation. The prototype is now for characterisation in the lab (s. Fig. 10).

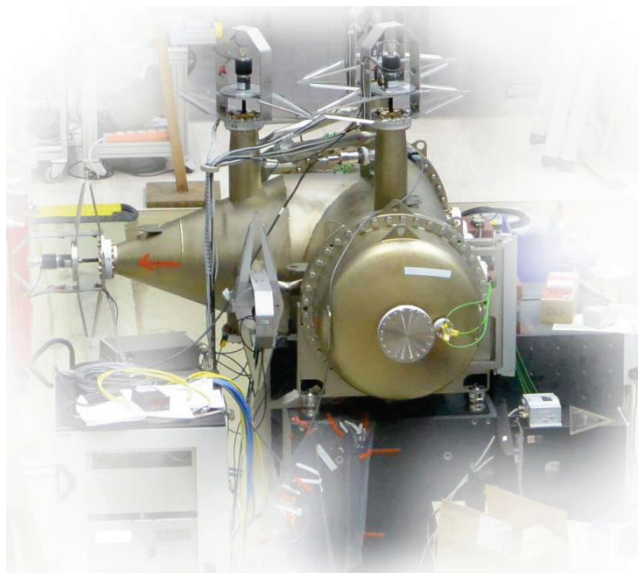


Figure 10: The prototype of the mirror chamber in the test lab.

REFERENCES

[1] H. Sinn, et. al. *„Technical Design Report: X-Ray Optics and Beam Transport"* December 2012, XFEL.EU TR-2012-006, doi:10.3204/XFEL.EU/TR-2012-006.

[2] T. Noll, et al. "*Parallel kinematics for nanoscale Cartesian motions*" Precision Engineering– journal of the international societies for precision engineering and nanotechnology Volume: 33 Issue: 3 Pg. 291-304 Published: JUL (2009).

[3] Patent DE 100 42 801.0 „*Flexibles Gelenk hoher axialer Steifigkeit*", T. Noll, W. Gudat, (2000).

[4] Patent WO 02/16092 A1 *„Device for Multi-Axis fine Adjustable Bearing of a Component"* T. Noll, W. Gudat, H. Lammert, (2001).

[5] T. Noll „*Flexure Joints of High Axial Stiffness*" Precision Engineering 26 (2002) Pg. 460-465.

[6] Patent DE 100 42 801.0 „*Flexibles Gelenk hoher axialer Steifigkeit*", T. Noll, W. Gudat, (2000).

[7] Patent DE 200 15 988.7 „*Spindelantrieb zur hochgenauen Positionierung eines linear zu verschiebenden Bauteils*", T. Noll, H. Lammert, W. Gudat, (2000).

[8] Wasi, www.wasishop.de

Content from this work may be used under the terms of the CC BY 3.0 licence (© 2016). Any distribution of this work must maintain attribution to the author(s), title of the work, publisher, and DOI.

ISBN: 978-3-95450-188-5 doi:10.18429/JACoW-MEDSI2016-TUBA04

Content from this work may be used under the terms of the CC BY 3.0 licence (© 2016). Any distribution of this work must maintain attribution to the author(s), title of the work, publisher, and DOI.

MECHANICAL DESIGN AND DEVELOPMENT OF COMPACT LINEAR NANOPOSITIONING FLEXURE STAGES WITH CENTIMETER-LEVEL TRAVEL RANGE AND NANOMETER-LEVEL RESOLUTION

D. Shu, W. Liu, S. Kearney, J. Anton[1], B. Lai, J. Maser, C. Roehrig, and J. Z. Tischler
Advanced Photon Source, Argonne National Laboratory, Argonne, IL 60439, USA
[1] also at University of Illinois at Chicago, Chicago, IL 60607, USA

Abstract

Nanopositioning techniques present an important capability to support the state-of-the-art synchrotron radiation instrumentation research for the Advanced Photon Source (APS) operations and upgrade project. To overcome the performance limitations of precision ball-bearing-based or roller-bearing-based linear stage systems, two compact linear nanopositiioning flexure stages have been designed and developed at the APS with centimeter-level travel range and nanometer-level resolution for x-ray experimental applications. The APS T8-54 linear flexure stage is designed to perform a precision wire scan as a differential aperture for the 3-D diffraction microscope at the APS sector 34, and the APS T8-56 linear flexure stage is designed for a horizontal sample scanning stage for a hard x-ray microscope at the APS sector 2. Both linear flexure stages are using a similar improved deformation compensated linear guiding mechanism which was developed initially at the APS for the T8-52 flexural linear stage [1,2]. The mechanical design and finite element analyses of the APS T8-54 and T8-56 flexural stages, as well as its initial mechanical test results with laser interferometer are described in this paper.

INTRODUCTION

X-ray Laue Diffraction 3D Microscopy developed at 34-ID beamline in the APS has been a unique and powerful tool for spatially-resolved structural studies at submicron level for materials science [3]. A precision linear stage is needed to perform a wire scan as a differential aperture for the 3-D diffraction microscope [4]. The wire scan motion is usually localized in a very short specific travel range after an initial large travel range alignment. Localized wear of the linear bearing stage, which causes an unrepeatable defect in the linear motion straightness of trajectory is always an issue for the results of the 3-D x-ray diffraction microscope.

To improve the linear motion performance and durability of the wire scan stage, a compact flexural-pivot-based precision linear stage APS T8-54 has been designed and constructed at the APS to replace the existing bearing-based linear stage for wire scan using deformation-compensated flexural pivot mechanisms as shown in Figures 1-3 [5]. Based on the experiences gained from the initial operation of the T8-54 flexure stage at the APS sector 34, a few design enhancements have been made to further improve the performance of the T8-54 stage. These design enhancements have also been implemented in the new compact flexure stage design for scanning sample stages at the APS sector 2. In this paper, we present the design enhancements for the T8-54 linear flexure stage, as well as the design of the new compact linear flexure scanning stage T8-56 for APS sector 2. Preliminary tests for the enhanced flexure linear guiding mechanism with laser confocal displacement meter and laser interferometer are also presented.

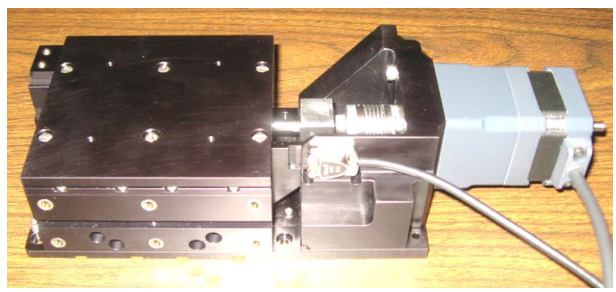


Figure 1: Photograph of the original APS T8-54 linear flexure stage for wire scan as a differential aperture for the 3-D diffraction microscope at the APS sector 34.

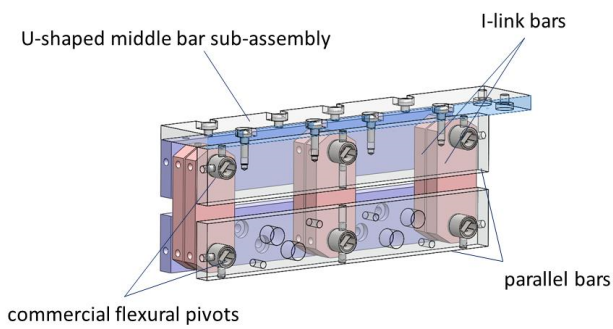


Figure 2: A 3-D model of the basic deformation compensated linear guiding mechanism for T8-54 linear flexural stage.



Figure 3: Photograph of the basic deformation compensated linear guiding mechanism for T8-54 linear flexural stage. A total of 12 C-Flex™ D-20 flexural pivots are applied in the linear guiding mechanism.

ISBN: 978-3-95450-188-5 doi:10.18429/JACoW-MEDSI2016-TUBA04

DESIGN ENHANCEMENT FOR T8-54A

As shown in Figure 4, two major design enhancements have been made for the updated compact linear flexure stage T8-54A:

- A new decoupled driving mechanism with MicroE™ MII6850 encoder replaced the original direct driving mechanism with MicroE™ M3500si encoder to reduce the stage's straightness of trajectory error caused by the ball screw direct driving mechanism and the grating encoder interpreter's error.
- A new middle-Bar relative position control mechanism [6] has been added to the stage's structure to enhance the stiffness of the flexure linear guiding mechanism.

Figure 5 shows a top-view and a side-view of the middle-Bar relative position control mechanism integrated with the T8-54A stage's linear guiding mechanism.

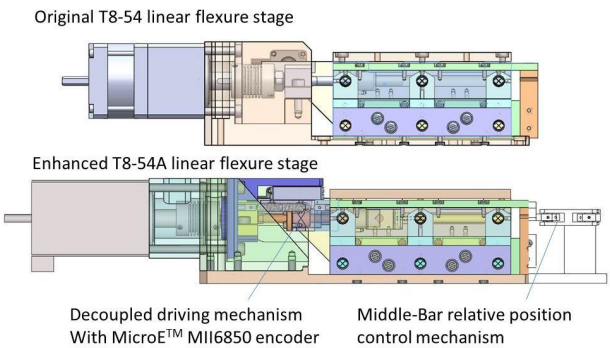


Figure 4: Side views of the 3-D models to compare the original T8-54 linear flexure stage and the enhanced T8-54A stage.

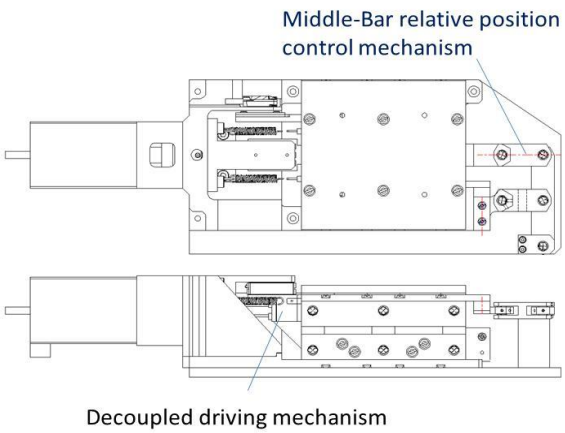


Figure 5: Top-view and side-view of the middle-Bar relative position control mechanism integrated with the T8-54A stage's linear guiding mechanism.

PRELIMINARY ANALYSES AND PROOF-OF-PRINCIPLE TEST FOR THE T8-54A DESIGN ENHANCEMENT

Preliminary finite element analysis (FEA) started with a single flexure linear guiding mechanism to simulate the effectiveness of the middle-Bar relative position control mechanism. A proof-of-principle experiment has also demonstrated a promising result with reasonable agreement with the FEA results. Figure 6 shows a 3-D model for the analysis of displacement of a single flexure linear guiding mechanism with control of the middle-bar relative position. Figure 7 shows a detailed view of the mesh distribution for FEA.

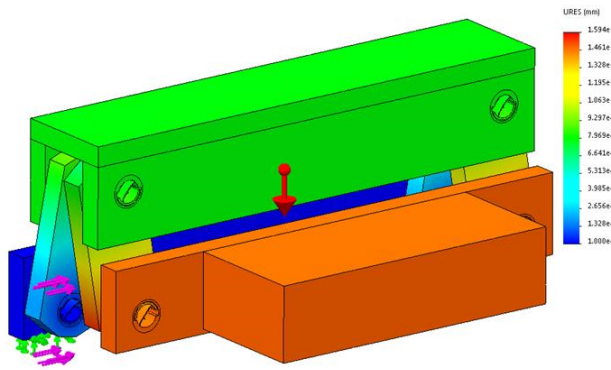


Figure 6: A 3-D model for the analysis of displacement of a single flexure linear guiding mechanism with control of the middle-bar relative position.

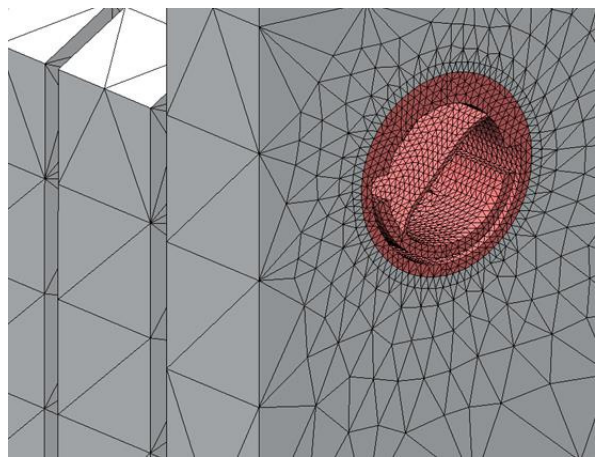


Figure 7: A detailed view of the mesh distribution for FEA 3-D model.

Preliminary test is also started with a single T8-54A flexure linear guiding mechanism with the middle-Bar relative position control. As shown in Figure 8, the relative horizontal positions of the carriage and the middle-bar of the guiding mechanism are positioned by two digital micrometers. A Keyence™ LT-9501 laser confocal displacement meter is used to measure the stage's parasitical vertical displacement. Figure 9 shows the differences between the conditions with a free middle-bar and a middle-bar with relative position control. The results showed that the stage's parasitical vertical motion is reduced to the level of ~1 micron rms over the 8 mm horizontal travel range while the middle-bar's relative horizontal position is controlled at a theoretical 1:2 position with carriage.

Content from this work may be used under the terms of the CC BY 3.0 licence (© 2016). Any distribution of this work must maintain attribution to the author(s), title of the work, publisher, and DOI.

ISBN: 978-3-95450-188-5 doi:10.18429/JACoW-MEDSI2016-TUBA04

Content from this work may be used under the terms of the CC BY 3.0 licence (© 2016). Any distribution of this work must maintain attribution to the author(s), title of the work, publisher, and DOI.

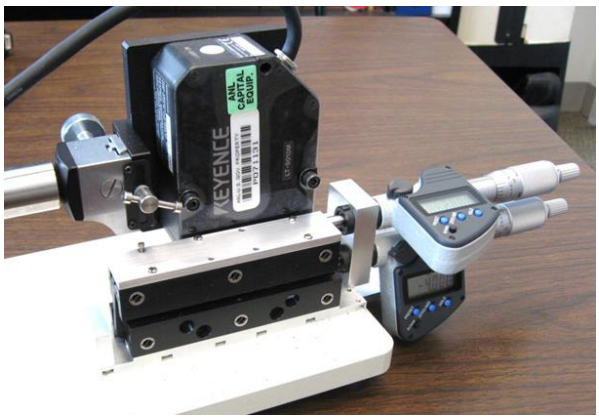


Figure 8: Photograph of the test setup with a single T8-54A flexure linear guiding mechanism with the carriage and middle-Bar relative positions controlled by two digital micrometers. A Keyence™ LT-9501 laser confocal displacement meter is used to measure the stage's parasitical vertical displacement.

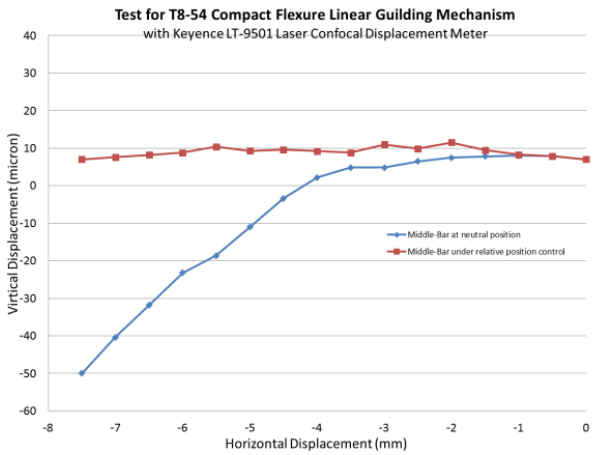


Figure 9: Preliminary test results showed the differences between the conditions with a free middle-bar and a middle-bar with relative position control.

As expected, the flexure linear guiding mechanism has a nanometer-level positioning capability. The flexure stage's positioning sensitivity is limited by its driving mechanism. We have tested the decoupled driving mechanism with 20 nm steps with Attocube™ FPS3010 laser interferometer as shown in Figure 10. Figure 11 is a photograph of the updated compact linear flexure stage T8-54A.

DESIGN OF T8-56 COMPACT LINEAR HORIZONTAL FLEXURE STAGE

The APS T8-56 linear flexure stage is designed for a horizontal sample scanning stage for a hard x-ray microscope at the APS sector 2. The design enhancements for T8-54A have been implemented in this new compact flexure stages design. Figure 12 shows a 3-D model of the APS T8-56 linear flexure stage.

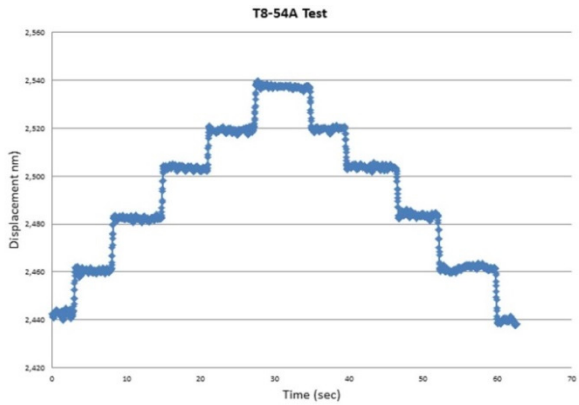


Figure 10: Preliminary test results showed 5-up and 5-down 20 nm steps performed by the decoupled driving mechanism with T8-54 flexure stage.

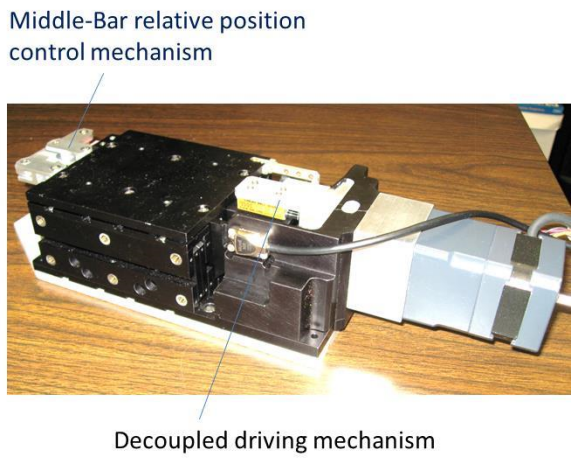


Figure 11: Photograph of the updated compact linear flexure stage T8-54A. The MicroE™ M3500si grating encoder will be replaced by MII6850 grating encoder with reduced interpreter errors.

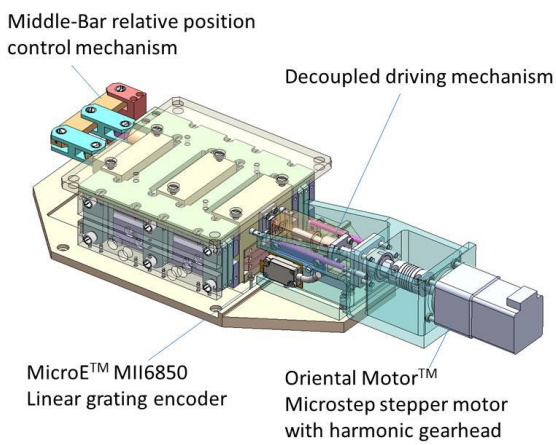


Figure 12: A 3-D model of the APS T8-56 linear flexure stage.

SUMMARY

The mechanical design and finite element analysis of the updated APS T8-54 and T8-56 flexural stages, as well as preliminary mechanical test results are presented in this

ISBN: 978-3-95450-188-5 doi:10.18429/JACoW-MEDSI2016-TUBA04

paper. Comprehensive mechanical tests for T8-54A with laser interferometer system are in progress.

ACKNOWLEDGMENT

The authors would like to acknowledge Patricia Fernandez for her management support. Work supported by the U.S. Department of Energy, Office of Science, under Contract No. DE-AC02-06CH11357.

REFERENCES

[1] U.S. Patent granted No. 8,957,567, D. Shu, S. Kearney, and C. Preissner, 2015.

[2] D. Shu *et al., J. Phys. Conf. Ser*. 425 212011 (2013).

[3] W. Liu and G. Ice, "X-ray Laue Diffraction Microscopy in 3D at the Advanced Photon Source," in *Strain and Dislocation Gradients from Diffraction*, Imperial College Press, 2014, pp. 53-81.

[4] W. Liu *et al.*, *AIP Conf. Proc*. 1365, 108 (2011).

[5] D. Shu, W. Liu, S. Kearney, J. Anton, and J. Z. Tischler, *Proceedings of SPIE-2015*, Optomechanical Engineering conference, 9573-28, San Diego, CA, Aug. 2015.

[6] D. Shu, W. Liu, S. Kearney, J. Anton, B. Lai, J. Maser1, C. Roehrig, and J. Z. Tischler, U.S. Patent application in progress for ANL-IN-16-125, 2016.

Content from this work may be used under the terms of the CC BY 3.0 licence (© 2016). Any distribution of this work must maintain attribution to the author(s), title of the work, publisher, and DOI.

ISBN: 978-3-95450-188-5 doi:10.18429/JACoW-MEDSI2016-TUCA02

STRUCTURAL DYNAMIC MODELLING AND MEASUREMENT OF SWISSFEL BUNCH COMPRESSOR

Xinyu Wang†, Thomas Stapf, Haimo Joehri, Florian Loehl, Marco Pedrozzi

Paul Scherrer Institut, 5232 Villigen PSI, Switzerland

Abstract

Magnetic chicanes are used in accelerator facilities to longitudinally compress the accelerated particle bunches. The second compression chicane of SwissFEL consists of four dipole magnets bending the beam on the horizontal plane along a C-shaped orbit and has a total length of 17 m. The position of the two central dipoles can be continuously adjusted to achieve the required transverse offset in order to realize a wide range of compression schemes. To ensure the requires mechanical stability of the accelerator components sitting on the long and movable steel girder (7.7 m), it is essential to design a stiff support structure with high eigenfrequencies. In the design stage, displacement frequency responses are calculated in a modal based linear dynamic analysis using finite element method to ensure vibration amplitude below 1 micrometer. Special considerations are given to the modelling of linear guide systems, as they introduce nonlinear support conditions and need to be adequately simplified in the calculation. After completing the second bunch compressor (BC2) assembly, vibration measurements were performed. Finally, the validation of the numerical model by measurement results will be presented.

INTRODUCTION

BC2 consists of two welded steel girder structures (Figure 1), which are supported on granite tables. Each granite table is fixed to floor by three or four rigid jacks with built-in commercial levelling wedge elements.

From the middle table girders can be moved together with dipole 2 and 3 transversally 505 mm. With a girder length of 7.7 m (dipole separation), the bending angle is 3.8 degree. Girder is supported on pivot bearing for rotation. A linear stage is used for transversal movement. A second linear stage for longitudinal movement is rotatable against the first stage (Figure 2).

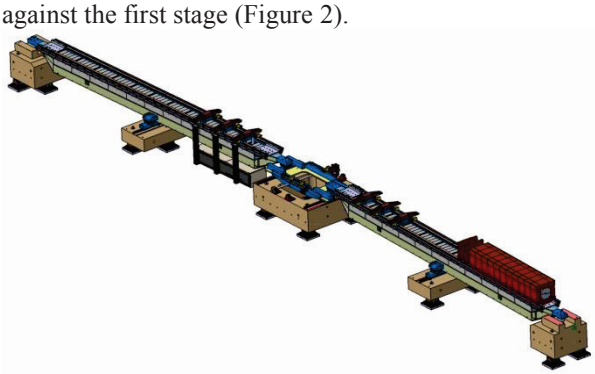


Figure 1: SwissFEL BC2.

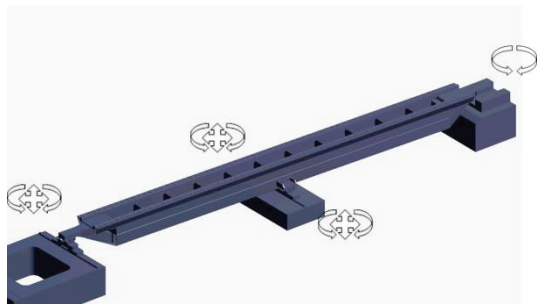


Figure 2: Girder kinematics.

The first steel girder in the beam direction has a total weight of 3'200 kg, including 1'900 kg lead and polyethylene (PE) material for radiation shielding. To ensure the proper operation of accelerator components (BPM and magnets) on the girder, a mechanical vibrational stability below 1 μm is required.

In order to fulfil the stringent design goal of a long and movable steel girder which is in the meantime vibrational stable, finite element (FE) analysis has been performed in the design phase. The modelling is finally verified by vibration measurement.

FINITE ELEMENT MODELLING

The girder structure is welded from rectangular hollow steel sections and steel plates with thickness from 5 mm to 10 mm. Shell elements with 6 degrees of freedom (DOF), three rotational and three translational, have been employed for efficient presentation of in-plane and bending stiffness. Point mass elements have been used to represent shielding masses in 3D space. The voluminous support consoles have been modelled with 3D solid elements (Figure 3). The linear contact connecting shell and solid elements is defined by Multi-Point-Constraint (MPC) formulation with the coupling of rotational DOF to translational DOF.

The FE model has following parameters:

Number of nodes:	329'000
Number of elements:	216'000
Incl. shell elements:	122'000
Degrees of freedom:	1'326'000

Linear static and dynamic calculations have been performed with finite element program ANSYS. FE Modell was prepared from CAD geometry with SpaceClaim Direct modeler.

Content from this work may be used under the terms of the CC BY 3.0 licence (© 2016). Any distribution of this work must maintain attribution to the author(s), title of the work, publisher, and DOI.

† xinyu.wang@psi.ch

ISBN: 978-3-95450-188-5 doi:10.18429/JACoW-MEDSI2016-TUCA02

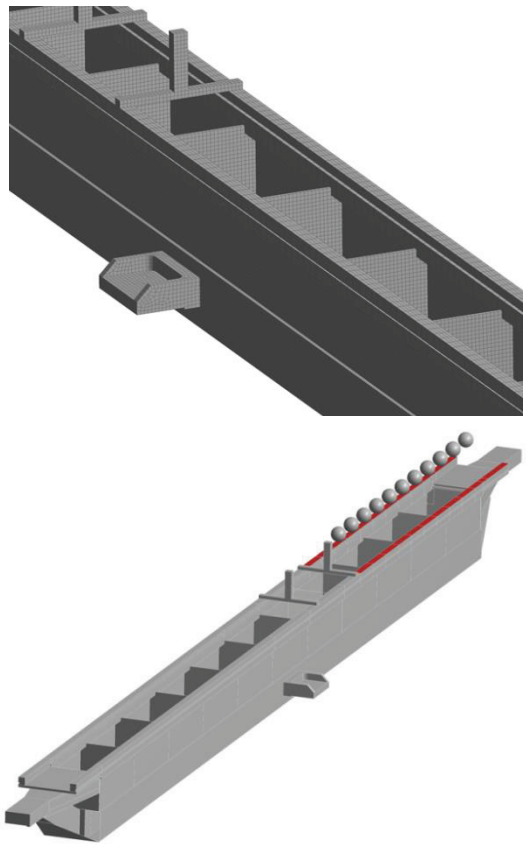


Figure 3: Finite element model.

Support conditions involving linear bearings introduce nonlinearity to the model. In a rigid dynamic analysis dedicated to kinematic simulation, it is simulated to be free a DOF. In a linear steady-state dynamic analysis, the linear guide can be represented by spring elements with equivalent stiffness. The determination of the stiffness requires detailed analysis and measurement [1]. Moreover, the stiffness depending on the preloading on the stage may not be linear. In the early design phase, not all required detail information was available and hence approximation was necessary.

Provided that friction forces in the joint are high enough to withstand excitation forces, joint is well defined and contact is closed. On the other hand, if the excitation force is higher than friction force, the contact becomes open, and we have a non-linearity in the model. We started with the stable situation of closed joint, and finally checked if the condition is fulfilled in a random vibration analysis. It is helpful to model linear bearing constraints with different stiffness and to investigate the sensitivity of structural response. Very stiff constraint stiffness leads to a fixed boundary condition, while extreme soft stiffness leads to a free boundary condition.

STATIC AND MODAL ANALYSIS

We started with a static analysis under gravity load, followed with an undamped modal analysis. Boundary conditions for linear guides are considered as:

1. Free
2. Constraint stiffness k=2e4 N/mm
3. Constraint stiffness k=2e7 N/mm
4. Fixed

Maximum vertical displacements due to gravity load are between 0.152 mm with fixed boundary conditions and 0.157 mm with free boundary conditions (Figure 4). The influence of the linear guide stiffness is small.



Figure 4: Deflection under gravity load

From vertical deformation, bending frequency can be estimated analytically considering relationship between natural frequency f in Hz and maximum static deflection d in mm for pinned-pinned prismatic beam [2]:

$$f = 17.8/\sqrt{d}$$

The first analytical bending frequencies are between 45.7 Hz with fixed boundaries and 45.1 Hz with free boundaries, they are comparable with results from FE analysis in Table 1 between 41.3 and 42 Hz (Figure 6). Except for free boundary conditions, other three models have the same first eigenmode as a transversal torsional mode (Figure 5). The natural frequencies for all three models between 20.3 to 22.8 Hz are quite close to each other.

Table 1: Summary of Natural Frequencies [Hz] with Mode Description

Free Hz	**Soft** Hz	**Stiff** Hz	**Fixed** Hz	**Mode description**
1.6				*Rotational mode*
16.4	20.3	22.7	22.8	*first torsional mode*
31.2	34.6			*first transversal bending*
41.3	41.7	42.0	41.8	*first vertical bending*
47.8	45.5	48.6	49.0	*second torsional mode*
		69.6	70.1	*first transversal bending*

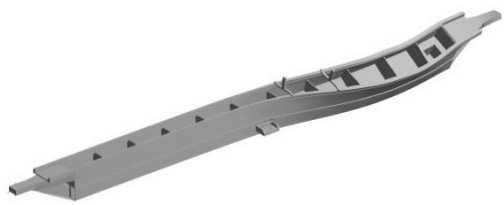


Figure 5: Mode shape of first torsional mode.

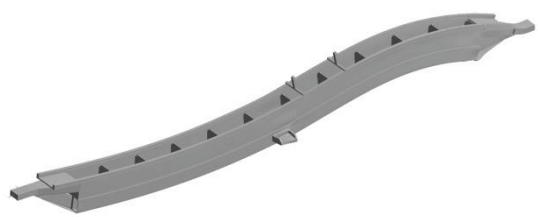


Figure 6: Mode shape of first vertical bending mode.

Content from this work may be used under the terms of the CC BY 3.0 licence (© 2016). Any distribution of this work must maintain attribution to the author(s), title of the work, publisher, and DOI.

ISBN: 978-3-95450-188-5 doi:10.18429/JACoW-MEDSI2016-TUCA02

Content from this work may be used under the terms of the CC BY 3.0 licence (© 2016). Any distribution of this work must maintain attribution to the author(s), title of the work, publisher, and DOI.

HARMONIC RESPONSE ANALYSIS

In a harmonic response analysis, system response to steady-state sinusoidal loading at a given frequency is solved. The general equation of motion is

$$[M]\{\ddot{x}\}+[C]\{\dot{x}\}+[K]\{x\}=\{F\}$$

With mass matrix [M], damping [C], and stiffness [K] Both excitation {F} and response {x} are assumed to be harmonic.

$$\{F\}=\{F_{\max}\}e^{j(\Omega t+\psi)}$$
$$\{x\}=\{x_{\max}\}e^{j(\Omega t+\phi)}$$

Ω: imposed circular frequency, ψ, φ: phase shift. The mode superposition method solves the harmonic equation in modal coordinates, with displacements expressed as a linear combination of mode shapes.

Ground vibration has in general broadband distribution rather than single harmonic. Before facility has been built, and excitation spectrum is not known, harmonic response analysis provides helpful information on critical frequency and on displacement at important locations. Random vibrations measured on ground at different sites at PSI are below 1 mm/s^2. In the harmonic response analysis, a base excitation of 1 mm/s^2 up to 100 Hz is applied in phase in all directions and at all supports in order to give a conservation estimation of structural response. Damping ratio is assumed to be 2%. Frequency responses are evaluated at positions of BPM and magnets. Calculation has been performed with soft and stiff constraint stiffness as well as with fixed boundary conditions. The response in vertical and longitudinal directions is lower than in transversal direction due to the fact that the first mode shape is transversal.

Figure 7 shows transversal displacement response at the position of magnet with fixed boundary conditions. At a frequency of 22.8 Hz, the maximum response was 0.9 μm for both fixed and stiff linear bearings. With soft spring constraints, the maximum response was 1.7 μm. Stiff constraint is important for stable response. To ensure the connection is firm and stable, linear guides are equipped with brakes.

Figure 8 shows transversal acceleration response at the position of magnet with fixed boundary conditions. As the input excitation is defined as 1 mm/s^2, the value of response acceleration in mm/s^2 depicts the transmissibility function. The maximum transmissibility (amplification) for fixed and stiff bearing is 18.8 and 19.1, respectively. And with soft springs it is as high as 28.1. Because the real excitation is rather distributed in a broadband than single harmonic, the amplification will be lower. Stiff support is important to reduce vibration amplitude.

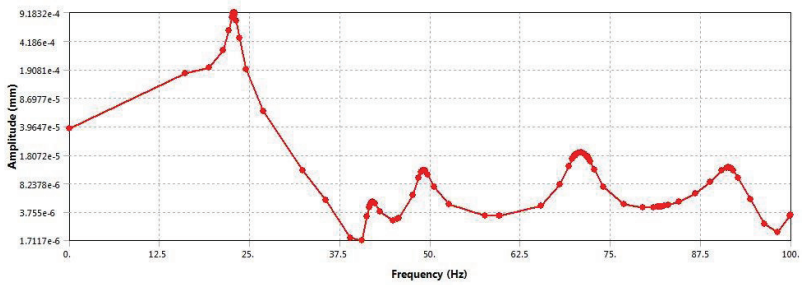


Figure 7: Frequency response of displacement in transversal direction at the position of magnet.

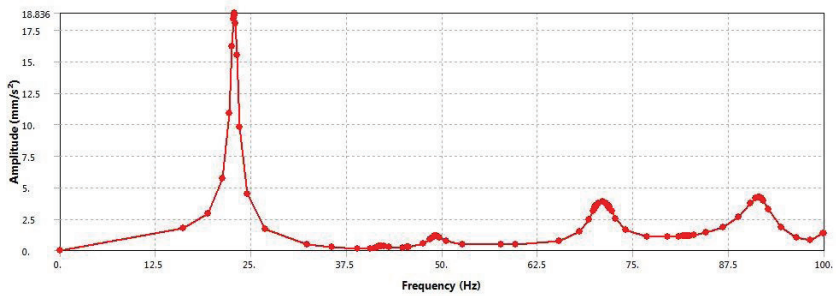


Figure 8: Frequency response of acceleration in transversal direction at the position of magnet.

RANDOM VIBRATION MEASUREMENT

Vibration measurement was performed in May 2016 after BCII is fully equipped and before SwissFEL commissioning. Seismic accelerometers PCB393B31 were placed on the floor, on all three granite tables and on the steel girder both in vertical direction and in horizontal direction transversal to beam. Beam direction is in Figure 9 from right to left. Three measurement positions on the girder, girder1, girder2 and girder3 are placed equal spaced in beam direction between two granite tables. During the measurement brakes were inactive.

A summary of RMS displacement from 5 to 200 Hz is given in Table 2. The amplification ratio girder to ground

ISBN: 978-3-95450-188-5 doi:10.18429/JACoW-MEDSI2016-TUCA02



Figure 9 Vibration measurement on SwissFEL BC2

is below 1.35 in transversal direction, and below 1.14 in vertical direction. BC2 structure shows excellent mechanical stability.

Table 2: RMS Displacement from 5 to 200 Hz

Position	displacement
Floor Transversal	37nm
Floor Vertical	29nm
Table transversal	40 nm
Table vertical	31 nm
Girder1 transversal	41 nm
Girder1 vertical	31 nm
Girder2 transversal	49 nm
Girder2 vertical	33 nm
Girder3 transversal	50 nm
Girder3 vertical	32 nm

Transversal spectral displacements from measurement show peaks at 21.4 Hz and 50 Hz (Figure 10). The first and second torsional modes calculated with fixed boundary conditions are 22.8 Hz and 49 Hz, respectively. The modelling of linear bearing either with fixed conditions or with stiff constraint stiffness yields a good prediction of transversal modes. From the vertical deformation, it is however not clear if there is a mode around 42 Hz, which is predicted to be the first bending mode from FE analysis (Figure 11). Vibration level in vertical direction is very low with amplification ratio girder to floor of only 1.13. It is therefore difficult to detect all eigenmodes in this measurement without external excitation.

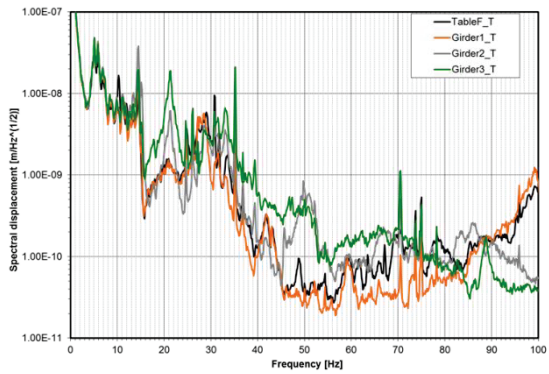


Figure 10: Spectral displacement in horizontal direction transversal to beam.

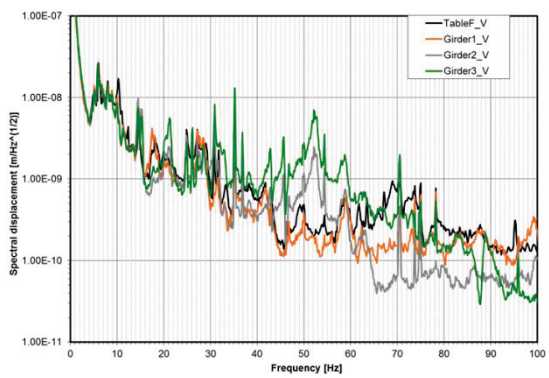


Figure 11: Spectral displacement in vertical direction.

RANDOM VIBRATION ANALYSIS

Random vibration analysis is another spectral method to determine structural response in modal space. The power spectral density (PSD) of acceleration measured on granite table in all three directions is applied as base excitation to all support conditions. For simplicity PSD acceleration from 5 to 100 Hz are applied, a constant damping

Content from this work may be used under the terms of the CC BY 3.0 licence (© 2016). Any distribution of this work must maintain attribution to the author(s), title of the work, publisher, and DOI.

ISBN: 978-3-95450-188-5 doi:10.18429/JACoW-MEDSI2016-TUCA02

Content from this work may be used under the terms of the CC BY 3.0 licence (© 2016). Any distribution of this work must maintain attribution to the author(s), title of the work, publisher, and DOI.

ratio of 2% is assumed. PSD response in the same frequency range is calculated. In Figure 12 response displacement in transversal direction with fixed boundary is depicted. As random vibration analysis considers on time history, both excitation and response are based on statistical representation.

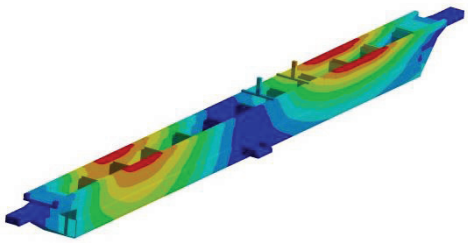


Figure 12: Response PSD displacement in transversal direction on girder.

Table 3: Comparison of RMS Displacement from Measurement and FE Calculation

Position	Measurement	Calculation
Girder1 transversal	41 nm	44 nm
Girder1 vertical	31 nm	31 nm
Girder2 transversal	49 nm	109 nm
Girder2 vertical	33 nm	36 nm
Girder3 transversal	50 nm	44 nm
Girder3 vertical	32 nm	29 nm
Magnet transversal	119 nm	
Magnet vertical	30 nm	

For the girder measurement position 1 and 3 RMS displacements from measurement and from calculation coincide well with each other (Table 3). In the measurement displacement from 100 to 200 Hz is also considered. It makes a contribution of maximum 2 nm. In the middle position between two supports, calculated transversal displacement of 109 nm is twice as much as measured value. A close examination of displacement spectrum depicts high content at high frequency range around 70 Hz. The constant damping ratio of 2% is rather conservative for high frequency vibration.

Reaction forces for all supports have been checked. The maximum reaction force is only 3.3 N in transversal direction and 3.1 N in vertical direction. With a vertical preloading of 9'500 N on the joint estimated from static calculation, a minimum friction coefficient 0.00034 is required. The available friction force is much higher, and the condition for linear modelling for the joint stiffness is fulfilled. In addition, test measurement with brakes also confirms this conclusion.

SUMMARY AND CONCLUSIONS

BCII shows excellent mechanical stability behavior. The amplification ratio girder to floor is below 1.35 in transversal direction, and below 1.14 in vertical direction. A maximum RMS displacement of 50 nm has been measured. The RMS displacement at magnet position is calculated to be 109 nm.

From vibration measurement, the first two transversal modes from finite element analysis can be confirmed. The modelling of linear bearing with fixed conditions or with stiff constraint stiffness provides a good prediction. The vertical bending mode cannot be identified in this measurement as vertical displacement amplification is very low.

For a linear representation of linear guide systems, dynamic excitation forces are required to be very small compared to sliding friction forces. The verification of excitation forces is given in a random vibration analysis. But this procedure is not straight ahead, because PSD analyses is based on modal representation, and finally on correct modelling of boundary conditions. The solution procedure is iterative. The final confirmation of the linear representation of linear guide system is given by vibration measurement.

ACKNOWLEDGEMENT

We want to thank Peter Hottinger for the support in vibration measurement.

REFERENCES

[1] J. Jeong *et al.*, "equivalent stiffness modelling of linear motion guideways for stage systems", in *Intl. J. of Precision Engineering and Manufacturing*, Vol.15, No. 9, pp. 1987-1993, September 2014

[2] C.W. Bert, "Relationship between fundamental natural frequency and maximum static deflection for various linear vibratory systems", *J. of Sound and Vibration* 162(2), 547-557, 1993

ISBN: 978-3-95450-188-5 doi:10.18429/JACoW-MEDSI2016-TUCA03

ESTIMATION OF TEMPERATURE FLUCTUATIONS HARSHNESS REGARDING STABILITY OF STRUCTURES IN THE NANOMETER RANGE

N. Jobert†, F. Alves, S. Kubsky, Synchrotron SOLEIL, Saint Aubin, France

Abstract

Along with mechanical vibrations, thermal-mechanical deformations are the primary contributor to positional and pointing errors. This paper deals with specific analysis and interpretation difficulties encountered when designing and validating ultimate stability systems (i.e. in the range of a few nm). When attempting to design such systems, it is not sufficient to simply reduce overall temperature fluctuations, but it becomes necessary to target efforts at the specific components that are detrimental to the dimensional stability of the system. This calls for an integrated approach where temperature measurements, data analysis and reduction are performed in conjunction with a priori knowledge of the thermal-mechanical system behaviour.

1 INTRODUCTION

When dealing with high-accuracy devices, thermally induced distortions are a key contributor to the overall positional and pointing performance of the system. While it is both correct and obvious that the smaller the temperature fluctuations, the more stable the system will be, there is some hidden complexity in the subject.

Firstly, not all temperature fluctuations will actually distort the structure: very short period (i.e. 'fast') variations will not propagate far into the structure, and will induce very little change in overall dimensions. Nevertheless, they can induce local distortions, hence small positional errors but possibly larger pointing errors. Conversely, very long period (i.e. slow') temperatures fluctuations will result in quasi uniform temperature fields and therefore will efficiently change overall dimensions but possibly induce lower pointing errors.

Secondly, there is always some randomness in temperature fluctuations, which somehow obscures the actual severity of a given environment. This randomness occurs timewise, but also space-wise. For a highly stable environment, the random part of the temperature field has magnitude comparable or even higher to that of the general trend, and simply discarding this part becomes questionable.

Surprisingly, no harshness indicator has been developed that could help quantifying the actual severity of a given realistic thermal environment. It is the objective of this paper to provide some insight on the various phenomena at play. Additionally, we propose a simple yet efficient numerical method allowing the evaluation of actual structural responses to any realistic thermal environment. It is the wish of the authors that such approach should help in making more rational decisions, either at design or commissioning phases.

†nicolas.jobert@synchrotron-soleil.fr

2 ENGINEERING DIFFICULTIES

Thermal Mechanical Susceptibility: Intuition vs Quantitative Analysis

To illustrate the relative efficiency of various thermal fluctuations, it is instructive to start with a simple support structure: the following test-case is nearly academic, and merely aims at providing some feeling for the subject at hand. We assume an L-shaped bracket support structure which is a most desirable shape regarding vibrational stability because of its high stiffness/weight ratio along every axis (Figure 1). The engineering question is: "What about the actual thermal mechanical susceptibility of such a system?"

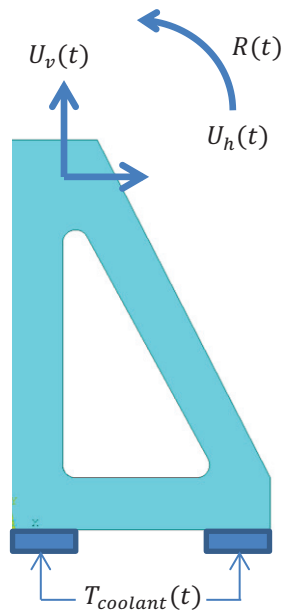


Figure 1: Academic test case.

Clearly, the answer depends on the heat path considered. Generally speaking, this can be either convection through surrounding medium (if any), radiation to the surrounding cavity, or convection to the heat sink. To further simplify the discussion, we will only consider the latter*. Also, we assume a very efficient heat transfer at bottom (which is what we aim for in real life), so that the boundary takes on nearly the same temperature as the coolant fluid.

* Note that, by principle, this is the only heat path that cannot be weakened and therefore ultimate stability will be governed by this disturbance source.

Content from this work may be used under the terms of the CC BY 3.0 licence (© 2016). Any distribution of this work must maintain attribution to the author(s), title of the work, publisher, and DOI.

ISBN: 978-3-95450-188-5 doi:10.18429/JACoW-MEDSI2016-TUCA03

Content from this work may be used under the terms of the CC BY 3.0 licence (© 2016). Any distribution of this work must maintain attribution to the author(s), title of the work, publisher, and DOI.

For very slow fluctuations, the temperature field in the bracket will be uniform and the displacement at support tip may be approximated using beam-type formulas:

$$\Delta U_v \sim \alpha . Height . \Delta T_{coolant} \quad (1)$$

$$\Delta U_v \sim \alpha . Width . \Delta T_{coolant} \quad (2)$$

$$\Delta R_v \sim 3/2 . \alpha . \left(\frac{Width}{Height}\right) . \Delta T_{coolant} \quad (3)$$

Now, how do we estimate what is "fast" and "slow" for such a structure? We may remember that the effective penetration depth for a harmonically time-dependent temperature imposed at the boundary of a 1D system reads:

$$\delta_{effective} \approx \sqrt{thermal\ diffusivity \times T/2\pi} \quad (4)$$

Where:

- Thermal diffusivity is defined by the material thermal conductivity, density and inertia
- T is the temperature fluctuation period

Assuming the effective penetration depth is equal to the characteristic scale of the length of the structure can give a back-of-the-envelope estimation for the boundary between "slow" and "fast" temperature fluctuations. This separation (or corner) period can read:

$$T_{corner} = \frac{2\pi L^2}{thermal\ diffusivity} \quad (5)$$

As an example, for aluminium, thermal diffusivity is about 100 mm²/s. For a 150 mm long structure (typical for optical support), this yields a separation period of about 700 s. This is consistent with engineering judgment that strongly suggests ignoring any temperature variation shorter than 10 minutes or so.

Relative Efficiency of Temperature Components

To confirm this hunch, one can build a numerical model of the structure at hand and run a series of transient thermal mechanical analyses. For each one, a harmonically time-dependent temperature is enforced at the model boundary, and the temperature / displacement in the structure can be estimated and compared to that same quantity as obtained in the static case. That procedure has been applied (using the ANSYS FEM package) to the academic test case, assuming 2D propagation, material aluminium and dimensions typical of support structure (150 mm height, 100 mm width), as shown on Figure 2.

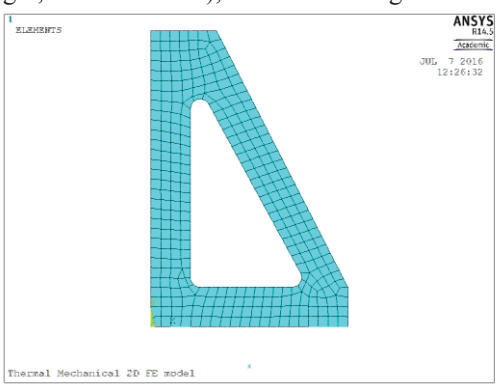


Figure 2: FEM of support structure.

The results are displayed on Figure 3 to 5 and commented hereafter.

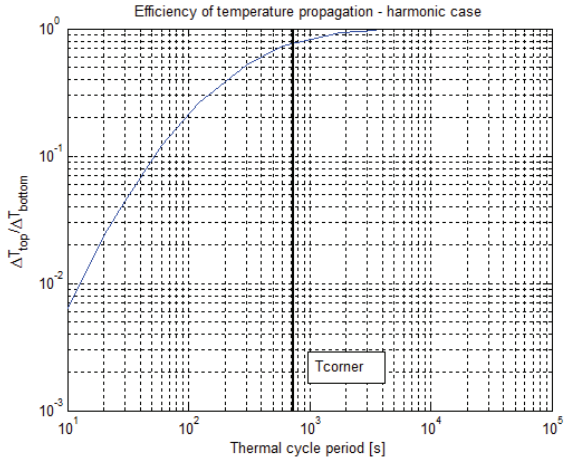


Figure 3: Relative efficiency of temperature propagation.

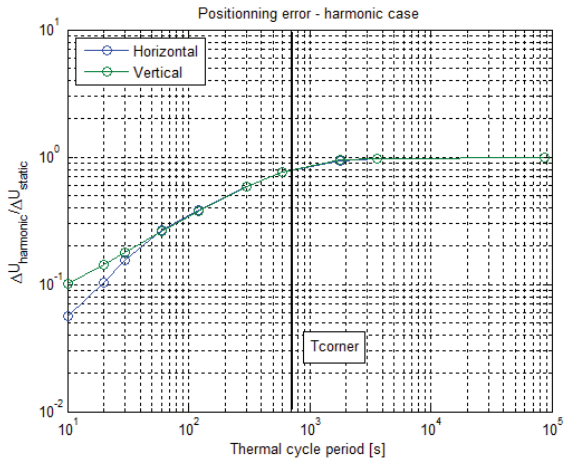


Figure 4: Relative efficiency of position error.

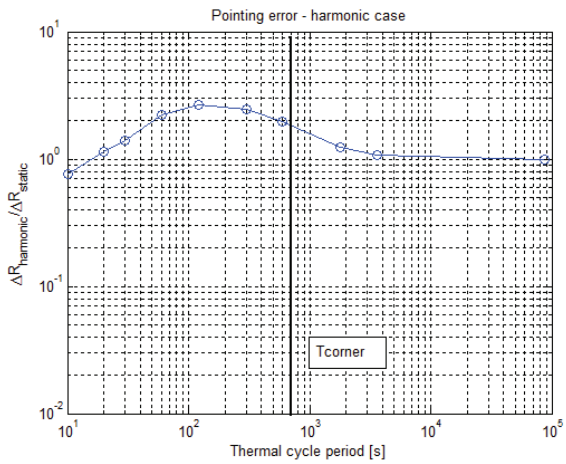


Figure 5: Relative efficiency of pointing error.

From those curves it stems that:

- temperature amplitude at structure tip decreases exponentially with decreasing period.
- positioning errors decrease as the square root of the period.
- pointing errors mildly *increase*, in the period range where the thermal wavelengths are comparable with the structural members dimensions.

ISBN: 978-3-95450-188-5 doi:10.18429/JACoW-MEDSI2016-TUCA03

Those conclusions are expected to be generic and hold true irrespective of the actual structure geometry. A practical conclusion is that, although some filtering (low-pass) effect will exist, its rejection efficiency is generally less than that suggested by intuition. Indeed, regarding dimensional stability, one gets a meagre 3dB/octave filtering effect, far from the exponential decay rate of the temperature propagation. For pointing errors, some amplification (factor 2.5 in our case) is witnessed.

Sadly enough, real-world temperature environments are rarely harmonic[†], but rather random. Therefore, when one wishes to estimate the actual severity of a given environment, an estimator for the spectral content of the temperature disturbance is needed.

3 SPECTRAL ANALYSES

Temperature Spectral Estimator

Now that we have defined the frequency-dependent susceptibility of our structure, we need a way to feed the real world temperature fluctuations into that frequency response function to determine the actual structural response. A very natural approach commonly used in structural dynamics consists in determining the temperature fluctuations Power Spectral Density (PSD).

Mathematically, assuming one has a temperature fluctuation record with sampling period T_s, the Discrete Fourier Transform (DFT) of the temperature signal $T(t)$ can be written:

$$DFT(f) = \frac{2}{n_s}\sum_{ind=1}^{n_s} T(ind.T_s)e^{-2i\pi f.ind.T_s} \quad (6)$$

Assuming this operation has been repeated for a number of n_b time blocks each one having duration T_{block}, the PSD will read:

$$\widehat{\Phi}_{TT}(f) = \frac{1}{n_b T_{block}}\sum_{i=1}^{n}|DFT(f,T_{block})|^2 \quad (7)$$

This seemingly cumbersome formula has a very straightforward physical meaning. The quantity $\widehat{\Phi}_{TT}(f)$ would be the mean square amplitude of the original temperature fluctuation after being processed by a (nearly) ideal band-pass filter, with centre frequency f and unitary bandwidth.

Therefore, the total signal energy can be retrieved by summing up all of its components, i.e.:

$$T^2 = \int_0^{f_{maxi}} \widehat{\Phi}_{TT}(f)df \quad (8)$$

Of course, the uppermost frequency (f_{maxi}) is generally not known beforehand and must be selected based on the thermal mechanical susceptibility of the system at hand.

.

[†] The only cases are when day/night cycles dominate, but this is generally the case for non-stabilized cavities.

Application to Stability Analysis

So far, we have developed:

- a tool to break down the real-world (random) temperature fluctuation signal into harmonic components, the PSD
- another tool that can estimate the relative harshness of all those individual components, the Frequency Response Function (FRF)

What we look for ultimately is an evaluation procedure of the actual harshness of the original fluctuation signal. This can be estimated in a very straightforward manner. For example, knowing the input (coolant) temperature (T_c) fluctuation PSD, and the FRF between coolant temperature and structural temperature (H_{TsTc}), as displayed in Fig 2, the output (structural) temperature PSD can be obtained as:

$$\widehat{\Phi}_{T_sT_s}(f) = |H_{TsTc}(f)|^2\widehat{\Phi}_{T_cT_c}(f) \quad (9)$$

And finally, the mean-squared structural temperature fluctuation can be obtained writing:

$$\langle T_s^2\rangle_t = \int_0^{f_{maxi}} \widehat{\Phi}_{T_sT_s}(f)df \quad (10)$$

This method can naturally be applied to any quantity of interest (displacement, angle). In the following, it will be referred to as the "FRF" method.

Real-world Illustration

The previous procedure has been applied to real-world temperature transient, with duration of 4 days. The temperature of the SOLEIL coolant circuit (17°C nominal value) has been recorded. This was performed using a high-resolution Digital Multimeter (DataTranslation model DT9829), with an original sampling rate of 2Hz. Temperature sensors were miniature thermistors (NTC type), with a temperature coefficient of about 4.5%/degC in the working temperature range. The whole setup (see Figure 6) was double checked and total RMS uncertainty (sensors to sensor deviation) was shown to be less 1millidegreeC. The signal was subsequently filtered and decimated to a 5s sampling period, resulting in the time-history shown on Figure 7.

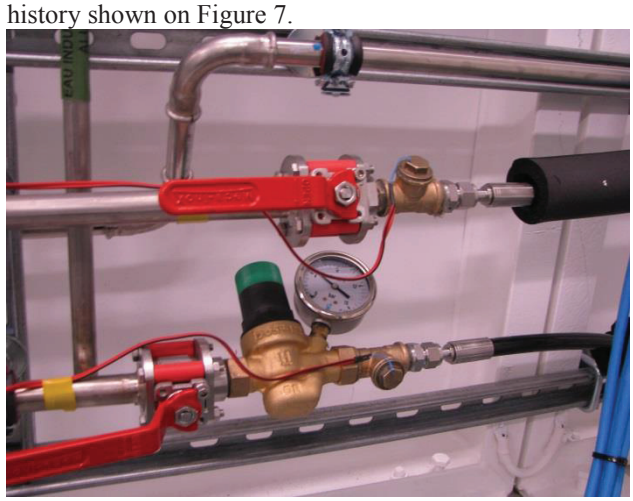


Figure 6 – Coolant water temperature fluctuation measurement (thermal insulation removed).

.

Content from this work may be used under the terms of the CC BY 3.0 licence (© 2016). Any distribution of this work must maintain attribution to the author(s), title of the work, publisher, and DOI.

ISBN: 978-3-95450-188-5 doi:10.18429/JACoW-MEDSI2016-TUCA03

Content from this work may be used under the terms of the CC BY 3.0 licence (© 2016). Any distribution of this work must maintain attribution to the author(s), title of the work, publisher, and DOI.

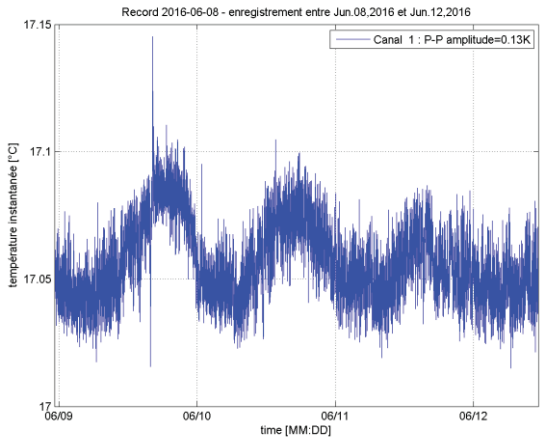


Figure 7: Typical coolant fluid temperature record.

This (purposefully) looks like a well know situation: a dominating quasi-periodic (day/night) component superimposed with a broad band, random noise. This intuition can be consolidated by applying spectral analysis (Figure 8).

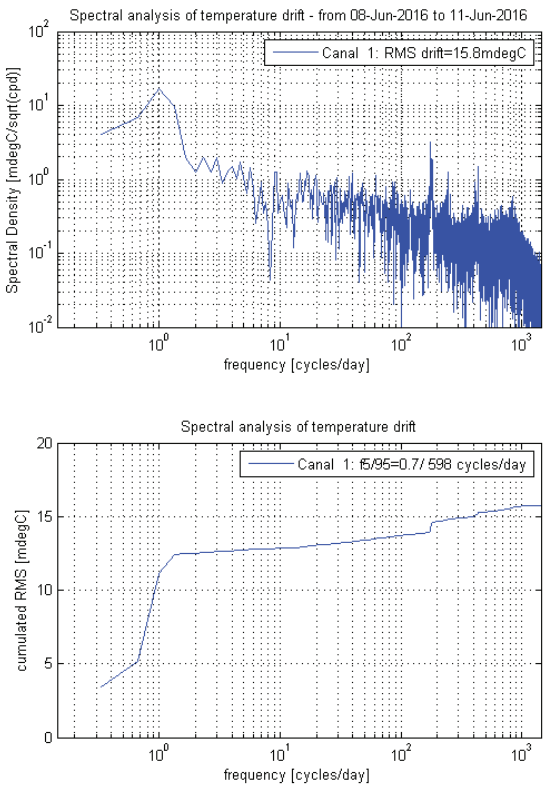


Figure 8: Spectral analysis of coolant fluid temperature.

The uppermost curve represents the square root of the PSD, and has units millidegreeC/sqrt(cycles per day). The lowermost curve is the cumulated RMS level, and provides the RMS amplitude of the signal encompassing all components between 0 (i.e. static) and any frequency. It can be thought of as an indicator of the residual amplitude after applying an ideal low pass filter with variable cut-off frequency *f*.

From the spectral analysis, an interesting fact arises: the cut-off period (700s, equivalent to 123 cycles per day) lies in the far end of the spectrum. The consequence immediately follows: *although we might not expect it, our support structure will statically respond to the coolant temperature fluctuations, with near-zero attenuation due to thermal inertia.*

From an analyst perspective, this is good news, because this means that a simple, quasi static approach is appropriate for the problem at hand.

From a designer perspective, this this is bad news, because this means that one cannot expect any immunity of the structure with respect to coolant-transmitted disturbances.

From an experimentalist point of view, this should also trigger a warning signal, since any extraneous component in the measurements cannot be expected to be efficiently filtered out by the inertia in the thermal mechanical response.

As a means of verification, this simple example was fed into a computer model and a full transient thermal mechanical simulation was executed (Figure 9 and 10). The corresponding spectral contents are compared in Figure 11. This is of course neither practical nor necessary in the engineering practice, but merely aimed at confirming the correctness of our simple approach.

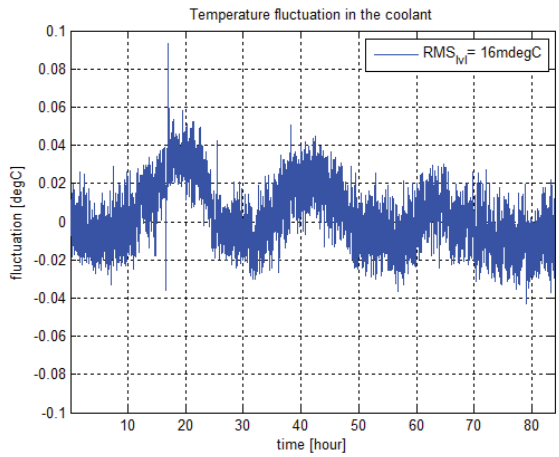


Figure 9: Coolant temperature variations.

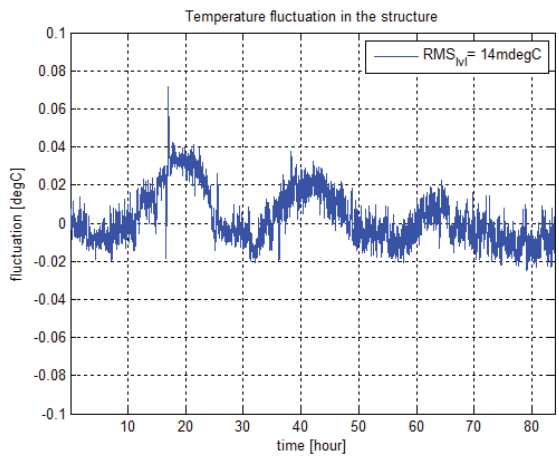


Figure 10: Structural temperature variations.

ISBN: 978-3-95450-188-5 doi:10.18429/JACoW-MEDSI2016-TUCA03

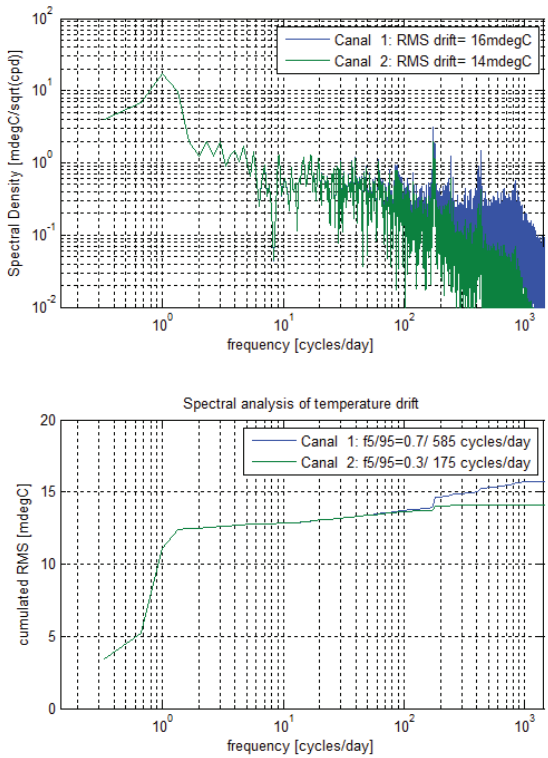


Figure 11: Spectral analysis of coolant/structural temperatures.

We now have confirmation that qualitatively, only minimal temperature attenuation can be expected (14mdegreeC vs 16mdegreeC). The next and more important question is: "does the prediction made using the FRF method also produce reliable estimates regarding position and pointing errors?"

The displacements obtained via detailed FEM analysis are as follows (see Figure 12 and 13).

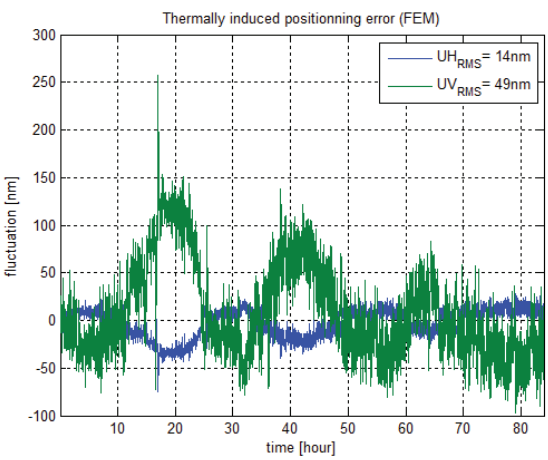


Figure 12: Positioning Error as predicted by FEM transient analysis.

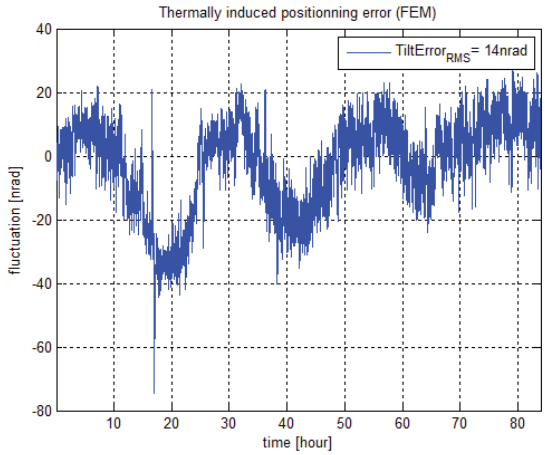


Figure 13: Pointing (Tilt) Error as predicted by FEM transient analysis.

Using the FRF method, very similar results are obtained. The comparison is made in table 1 below:

Table 1: Frequency vs. Time-domain Methods

	Transient	FRF	Ratio
$U_{horizontal}$	15nm	14nm	0.99
$U_{vertical}$	50nm	49nm	0.99
$R_{transverse}$	43nrad	44nrad	1.02

Going a little bit further, we can also compare spectral contents, as shown on Figures 14 to 16:

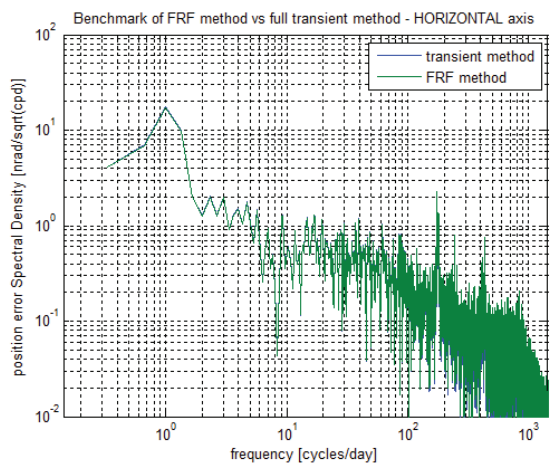


Figure 14: Horizontal Positioning Error as predicted by transient and FRF method.

Content from this work may be used under the terms of the CC BY 3.0 licence (© 2016). Any distribution of this work must maintain attribution to the author(s), title of the work, publisher, and DOI.

ISBN: 978-3-95450-188-5 doi:10.18429/JACoW-MEDSI2016-TUCA03

Content from this work may be used under the terms of the CC BY 3.0 licence (© 2016). Any distribution of this work must maintain attribution to the author(s), title of the work, publisher, and DOI.

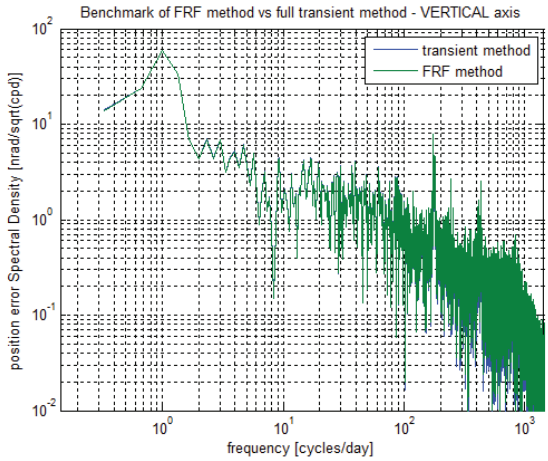


Figure 15: Vertical Positioning Error as predicted by transient and FRF method.

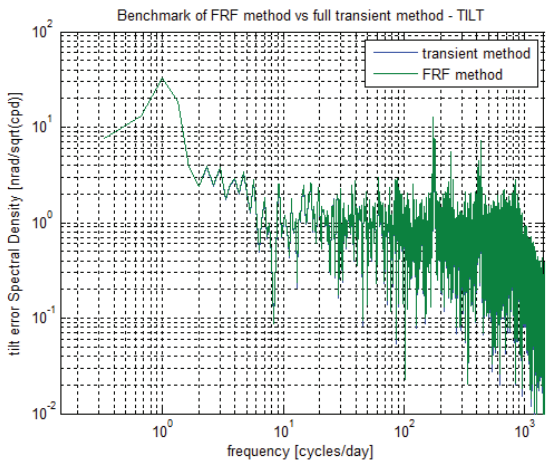


Figure 16: Pointing Error as predicted by transient and FRF method.

As expected, both overall level and the spectra content closely match.

We now have an efficient tool that does provide an accurate estimation of the positioning and pointing errors Root Mean Square (RMS) magnitude and spectral content. This is all very well, but ultimately what is needed from a user's point of view is a probable number of threshold exceedance during an experiment. This will be discussed next.

4 BEAMLINE USER'S PERSPECTIVE: RELIABILITY ANALYSIS

From the user's perspective, the previous considerations are worth listening to, but they lack a fundamental aspect of actual beamline operation that is: time windowing. Since image capturing processes rarely exceed a couple of hours, it is obvious that including the full 24hours drift (for example) in the estimation of the stability clearly induces over-conservatism. Before turning to estimating the stability statistics, we shall therefore take into account the reduction offered by time windowing.

It seems obvious that a simple truncation of the spectra will not do, since low frequency content, albeit attenuated by the finite duration of the observation may still contribute significantly to the total drift. Turning back to the purely harmonic case, it seems obvious that we need to:

- account for the full amplitude of any component whose half period is shorter than the experiment time window
- account for a reduction effect for long term components that capture the worst case scenario, i.e. the experiment takes place at a time (phase) when the drift velocity takes on (and maintains) its peak value.

Assuming a harmonic drifting of amplitude A_{drift} and period T_{drift}, the peak drift rate will read

$$\left(V_{drift}\right)_{peak} = 2\pi \frac{A_{drift}}{T_{drift}}$$

Therefore, the worst-case scenario is that of a steady drift during the whole scanning process, hence effective deviation amplitude reads:

$$A_{effective} = 2\pi \frac{T_{scan}}{T_{drift}} A_{drift}$$

Consequently, we propose to employ the following reduction factor F_{TW} for taking into account the time window effect:

$$F_{TW}\left(\frac{T_d}{T_s}\right) = \frac{2\pi}{Td/Ts + 2\pi}$$

This can be rewritten using frequency instead of period, as illustrated on Figure 17:

$$F_{TW}(f, T_s) = \frac{2\pi}{1/(f \times Ts) + 2\pi}$$

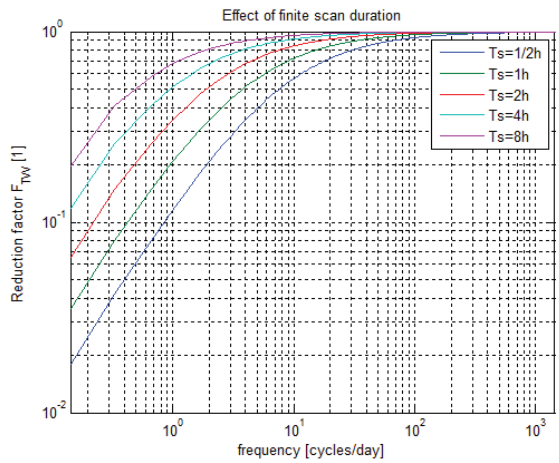


Figure 17: Time Windowing Reduction factors.

Employing this reduction factor yields a substantial reduction in RMS drift amplitude: returning to our test case: we can now estimate the RMS drift amplitudes for various time window durations, as given in Table 2 and graphically displayed in Figure 18 and 19.

ISBN: 978-3-95450-188-5 doi:10.18429/JACoW-MEDSI2016-TUCA03

Table 2: Effect of Time-windowing on RMS Drift

	Ts values [h]					Ref
	1/2	1	2	4	8	inf
U_{hor} [nm]	6	7	8	9	11	15
U_{ver} [nm]	21	24	27	33	37	49
R_{tr} [nrad]	35	36	37	38	40	44

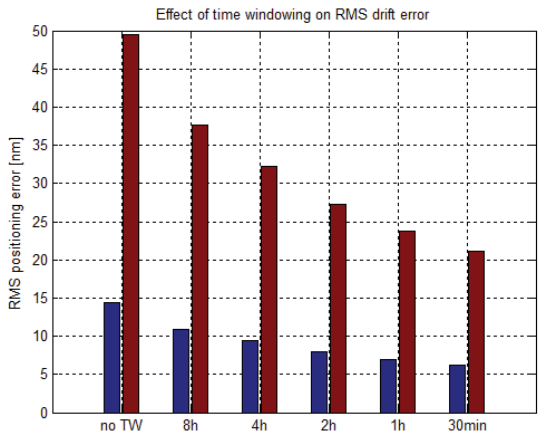


Figure 18: Effect of time windowing on position error.

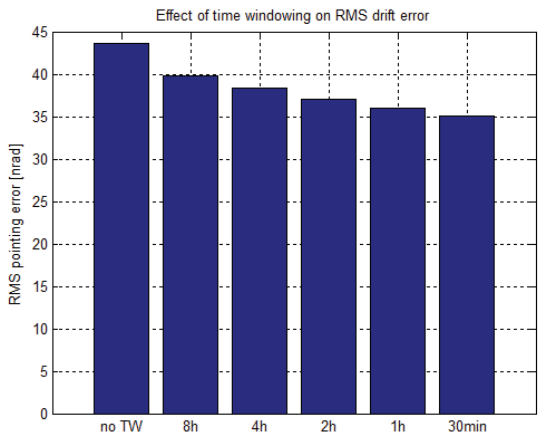


Figure 19: Effect of time windowing on pointing error.

It can be noted that, while the position error is significantly reduced by the time window effect, pointing error almost remains the same. This apparent paradox disappears when examining the frequency content of the pointing error. Pointing errors are dominated by high-frequency components (above 100 cycles/day), hence removing the slow (24h) drift component does not bring much improvement, see Figure 20 to 22:

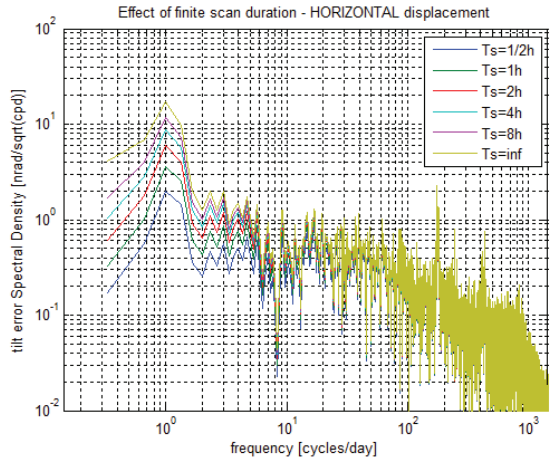


Figure 20: Spectral analysis of VERTICAL drift / Effect of Time Windowing.

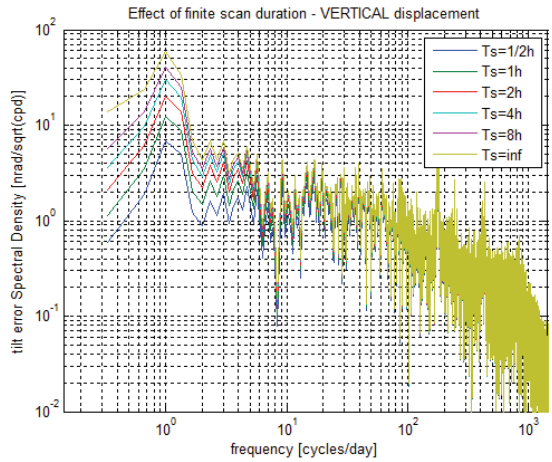


Figure 21: Spectral analysis of VERTICAL drift / Effect of Time Windowing.

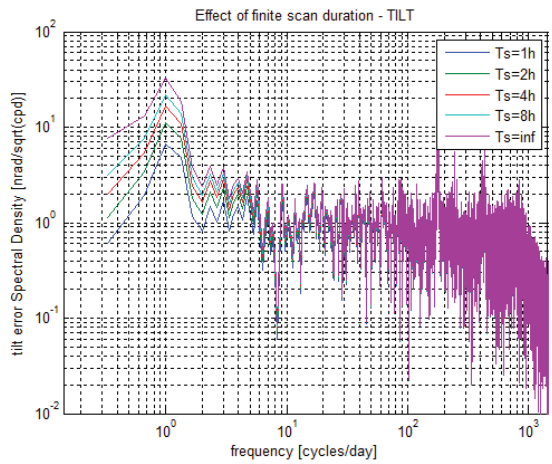


Figure 22: Spectral analysis of TILT drift / Effect of Time Windowing.

Knowing the finite-duration drift RMS levels, we are now in a position to quantify the actual reliability of the mechanical setup. As an example, assuming we have a defined allowable drift threshold *AD* (for example, half a pixel size) that can be used as a boundary between "good" and "faulty" scans. Then, the percentage of faulty scans

Content from this work may be used under the terms of the CC BY 3.0 licence (© 2016). Any distribution of this work must maintain attribution to the author(s), title of the work, publisher, and DOI.

ISBN: 978-3-95450-188-5 doi:10.18429/JACoW-MEDSI2016-TUCA03

Content from this work may be used under the terms of the CC BY 3.0 licence (© 2016). Any distribution of this work must maintain attribution to the author(s), title of the work, publisher, and DOI.

over an observation window of duration T_s can be conveniently estimated using the conventional formulas for broad[‡] band, stationary Gaussian process.

$$P(|Drift(T_s)| > AD) = 1 - \mathrm{erf}\left(\frac{AD}{\sqrt{2}Drift_{RMS}(Ts)}\right)$$

With:

$$Drift_{RMS}(T_s) = \left(\int_0^{f_{maxi}} F_{TW}(f,T_s)^2 . \left|H_{UT_c}(f)\right|^2 . \widehat{\Phi}_{T_cT_c}(f) df\right)^{1/2}$$

In our case, we can easily estimate the percentage of faulty scans, for various $T_s$values. Following is a numerical simulation assuming a 100nm allowable positioning error along both directions: in that (fictitious) case the percentages of faulty scans would read as follows:

Table 3: Effect of Time-windowing on Reliability ([%] of Faulty Scans).

	Ts values [h]					Ref
	1/2	**1**	**2**	**4**	**8**	**inf**
U_{hor} [nm]	0	0	0	0	0	0.1
U_{ver} [nm]	1.8	3.5	6.7	12.1	18.4	31.2

In this particular case, there is a dramatic decrease in the proportion of the faulty scans when reducing the experiment duration. This conclusion holds whenever there are large components with period longer than the experiments duration.

5 CONCLUSIONS

Through the preceding discussion, we have reached a number of practical conclusions, regarding various perspectives:

- designer (1): high-stability structures are generally small and with high thermal conductivity. Consequently, there is little attenuation of short-period temperature fluctuation to be expected, for both positioning and pointing error, some mild amplification may even occur for the latter. Knowing the working frequency range for temperature stability is essential for drawing sound conclusions.
- analyst (1): it is essential to obtain an accurate and comprehensive probing of the thermal environment. Short period components are often wrongly discarded as being spurious or simply not adequately recorded. In both cases, there is a loss of information and loss of quality in the conclusion reached.
- analyst (2) Working in the frequency domain is a convenient approach for long-period phenomena such as temperature transients. It allows for instant calculations and offers insight into the controlling phenomena. It also offers more flexibility in assessing uncertainties and testing design alternatives.
- user (1): Reliability (in a stationary environment) is strongly dependent on the experiment duration. Most often, for evaluating an environment, working with RMS quantities is a relevant indicator.
- user (2) In temperature controlled situations, shortening the scan period can decrease the percentage of faulty scans by more than one order of magnitude.

Hopefully, this article will provide a basis for a common language between designer, experimentalists, computer aided analyst and beamline user regarding thermal mechanical stability. A well balanced and efficient design can only be reached through collaboration, and this begins with the usage of mutually meaningful notions and dependency rules.

ACKNOWLEDGEMENT

The author would like to acknowledge the discussions with Professor André Preumont (Université Libre de Bruxelles), who (quite unintentionally) sparked the inspiration needed to transfer the techniques of random vibrations from the field of structural dynamics to that of thermal mechanical studies.

The support from the JTRC-project MAXIV-SOLEIL "Nanoprobe" which provided the motivation for a comprehensive analysis of thermal sources in support structures stability is also to be heartily acknowledged.

[‡] Remembering that, contrary to structural dynamics, there is not resonance phenomenon that would result in a narrow band situation.

ISBN: 978-3-95450-188-5 doi:10.18429/JACoW-MEDSI2016-TUCA05

THE NEW HIGH DYNAMICS DCM FOR SIRIUS

R. R. Geraldes†, R. M. Caliari, G. B. Z. L. Moreno, L. Sanfelici, M. Saveri Silva,
N. M. Souza Neto, H. C. N. Tolentino, H. Westfahl Jr., LNLS, CNPEM, Campinas, Brazil
T. A. M. Ruijl, R. M. Schneider, MI Partners, Eindhoven, Netherlands

Abstract

The monochromator is known to be one of the most critical optical elements of a synchrotron beamline, since it directly affects the beam quality with respect to energy and position. Naturally, the new 4th generation machines, with emittances in the range of order of 100 pm rad, require even higher stability performances, in spite of the still conflicting factors such as high power loads, power load variation, and vibration sources. A new high-dynamics DCM (Double Crystal Monochromator) is under development at the Brazilian Synchrotron Light Laboratory for the future X-ray undulator and superbend beamlines of Sirius, the new Brazilian 4th generation synchrotron [1]. Aiming at an inter-crystal stability of a few tens of nrad (even during the Bragg angle motion for flyscans) and considering the limitations of the current DCM implementations, several aspects of the DCM engineering are being revisited. In order to achieve a highly repeatable dynamic system, with a servocontrol bandwidth in the range of 200 Hz to 300 Hz, solutions are proposed for a few topics, including: actuators and guides, metrology and feedback, LN2 indirect cooling, crystal clamping, thermal management and shielding. The concept of this high-dynamics DCM will be presented.

INTRODUCTION

In the recent years it has become clear to the synchrotron community that the stability performance of DCMs would turn out to be one of the main bottlenecks in the overall performance of many X-rays beamlines, particularly for the new generation of machines, the so called Diffraction Limit Storage Rings (DLSR). This is because the instabilities in the DCM affect the position and/or the effective size of the virtual source, and, consequently, the spot size and/or the position of the beam at the sample. It is thus imperative that the virtual source instability is kept within a small fraction of the source size. The angular instability between the two crystals is the most critical one because its effects on the virtual source scales with the lever-arm between the monochromator and the source (L_0 in Fig. 1). In the DLSR, the sources are expected to have only a few microns, whereas the typical distances between the source and the monochromator is of tens of meters. Due to that, the stability between crystals is required to be within a few nrad. This scenario has motivated numerous special forums in conferences and even dedicated workshops, as the *ESRF DCM Workshop* in 2014. Since then, an effort has been made by suppliers and the synchrotron engineering community, trying to upgrade the existing systems and come up with new solutions. This work, which is the outcome of such effort at the Brazilian Synchrotron for Sirius beamlines, presents the advanced conceptual design of a DCM with high servo bandwidth closed-loop control. Sirius is in construction phase and the beginning of machine commissioning is planned for mid-2018 [2]. Therefore, a functioning prototype of the DCM has been planned for mid-2017.

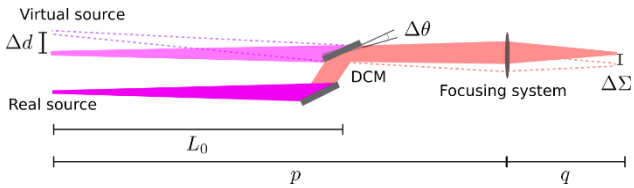


Figure 1: Effects of DCM instabilities in the virtual source.

STATE OF THE ART

Many of the existing DCMs around the world have been recently characterized with respect to stability. Representative cases were shown at the ESRF DCM Workshop, as the one by Ilya Sergeev, in which none of Petra III and ESRF DCMs performed below 100 $nrad_{RMS}$ [3]. Table 1 shows some of the most recent results of one of the state-of-the-art commercial DCMs [4]. The absolute pitch tells the angular instability of the second crystal, whereas the relative pitch shows the instability between the two crystals. The latter not only may affect the monochromatic beam with respect to flux, depending on the energy selection characteristics of the crystals, but, as mentioned, certainly affects the virtual source size and/or position, depending on the acquisition rate and sampling time of the experiments.

Table 1: Pitch Vibrations of State-of-the-Art DCM in the Range between 0 to 2.5 kHz (as reported in [4])

Experimental Condition	RMS (nrad)
Absolute pitch with servoing Bragg	278
Absolute pitch w/ braked Bragg	92
Relative pitch with servoing Bragg	100
Relative pitch w/ braked Bragg	48

From Table 1, it can be seen that this instrument performs around 50 nrad for the braked rotary stage. However, even this lowest value is still too high for the recent and future specs. In addition, given the fast development of detectors and electronics, there has been a lot interest in flyscan experiments, which requires high stability levels to be kept not only with the servoing Bragg, but in actual motion.

SPECIFICATIONS

The project of the DCM at LNLS has started with the case of a beamline with a planar x-ray undulator as the radiation source. Having the DCM at the distance of about 30 m from the source, Fig. 2 shows the variation of the position of the virtual source as a function of the variation of

†renan.geraldes@lnls.br

Content from this work may be used under the terms of the CC BY 3.0 licence (© 2016). Any distribution of this work must maintain attribution to the author(s), title of the work, publisher, and DOI.

ISBN: 978-3-95450-188-5 doi:10.18429/JACoW-MEDSI2016-TUCA05

Content from this work may be used under the terms of the CC BY 3.0 licence (© 2016). Any distribution of this work must maintain attribution to the author(s), title of the work, publisher, and DOI.

the angle between the crystals, and correlates that with 10% of the vertical and horizontal size of the source. It shows that only about 10 nrad instability would be allowed to keep the displacement of the virtual source below 10% of its size. And, of course, this number is further reduced for more conservative targets. Table 2 summarizes the main functional targets of this DCM.

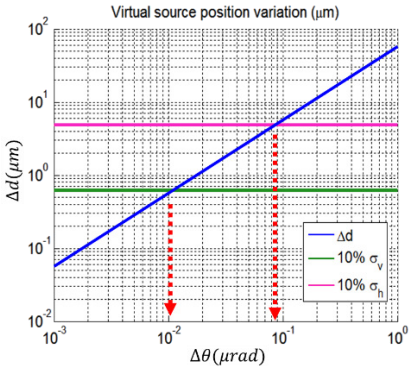


Figure 2: Variation of the position of the virtual source as a function of the variation of the angle between the crystals for the DCM at 30 m from the source.

Table 2: Main Functional Specs for the DCM Prototype

Parameter	Description
Type:	Vertical DCM
Beam offset:	18 mm
Angular range:	3 to 60°
Angular resolution:	0.2 μrad
Pitch/roll stability:	in-position: < **10 nrad** (±3σ) flyscan: < 200 nrad (±3σ)
Crystal sets:	Si(111): 2.3 to 38 keV Si(311): 4.4 to 72 keV
Crystal sizes (*W*x*L*):	1st crystal: 15 x 35 mm^2 2nd crystal: 15 x 190 mm^2
Crystal cooling:	1st crystal: Indirect LN_2 (80 K) 2nd crystal: Copper straps (155 K)
Crystal DoF:	1st crystal: fixed at the rotation axis 2nd crystal: gap, pitch, roll
Beam size:	1.7 x 1.7 mm^2
Input Power:	150 W
Base pressure:	< 5 x 10^{-8} mbar

Concerning in-position stability, the specified level must be improved by a factor between 10 and 100 with respect to existing systems (also note the ±3σ spec as opposed to RMS values in the reference). As for the stability performance during flyscans, similar dedicated evaluation of operating DCMs is unknown to the best of our knowledge. Achieving this large improvement seemed hardly possible by incremental upgrades, thus, a complete revaluation of the DCM as a system has been made. A few concepts have been borrowed from proven technologies in high-end machines of the semiconducting industry and a systematic review of the traditional solutions has been performed.

CONCEPTUAL DESIGN

Guidelines

The first rule in this development was to restrict the number of degrees of freedom (DoF). Therefore, the crystal cage presents only pitch, roll and gap adjustments, and all of them are associated to the 2nd crystal subsystem. The more degrees of freedom, the harder to keep the stiffness and robustness of the system, and the more error sources.

Next, it was believed that the required stability numbers could not be achieved without a high bandwidth closed-loop servo control, through which disturbances can be attenuated to acceptable levels. In this DCM the target is a closed-loop control bandwidth of at least 200 Hz, for which force actuators and a reaction mass are used for pitch, roll and gap adjustments.

This high controllability of the system also imposes strict requirements on the feedback system, particularly on resolution, stability and acquisition rates. With respect to that, some uncertainty lies on what can be available at the beamlines: intensity monitors may not be sensitive enough for nrad variation; beam position monitors (BPMs) may not be sensitive, accurate and/or fast enough (kHz range); due to the high coherence properties of the new machines, some beamlines may not accept any interference of windows or foils in the be beam path. Thus, the DCM has its own internal metrology system for servo feedback to control the gap, pitch and roll between the crystals with the former mentioned high closed-loop bandwidth. High stability and resolution is obtained by using distance measurement interferometers (DMIs) and mechanical components designed to reach high-stability and eigenfrequencies.

Finally, the cooling induced vibrations have been considered as the main risk item, so that alternatives to the cooling technology have been investigated, in order to minimize disturbances and mechanical constrains.

Design

The DCM can be divided in the following parts: support, vacuum vessel, rotary system and core (Fig. 3). The support is responsible for positioning and aligning the system at the beamline and is composed by two thick granite stones stacked upon each other and a few adjustment mechanisms. The bottom granite lays on manual or motorized levellers, that should provide the appropriate level (Rx and Rz) and height (y) to the system. The top granite allows for manual adjustment of the remaining rotation (Ry) and motorized lateral shift (x), which also provides the selection of the crystal set. For this translation, rather than conventional linear guides, customized high-stiffness pads are being designed. The necessity to apply additional damping (with high damping polymer) in the support will be investigated in the next phase. This may elegantly combine non-overconstrained supporting in the low-frequency range (related to mounting and thermal drift) and overconstrained design, with high stiffness, in the high-frequency range (associated with support eigenfrequencies).

The bottom flange of the vacuum vessel is directly glued to the top granite (or bolted from below in a matrix pattern),

ISBN: 978-3-95450-188-5 doi:10.18429/JACoW-MEDSI2016-TUCA05

so that the flange takes advantage of the full stiffness of the granite. Then, the in-vacuum rotary system is directly mounted on the bottom flange. The choice in favour of an in-vacuum solution lies in the attempt to improve the mounting stiffness of the core and prevent it from the vibrations that can be associated with the vessel. Stiffness is improved by means of bearings at both sides of the main rotating frame (GOF). For now, there is an active bearing with a direct-drive actuator at one side and a passive bearing at the other, however, in the future two active bearings may be implemented for superior control. Both bearings have flexural decoupling fixtures in order to prevent over-constrained design, so that each bearing defines a rotation point and the actual rotation axis is defined by the complete set.

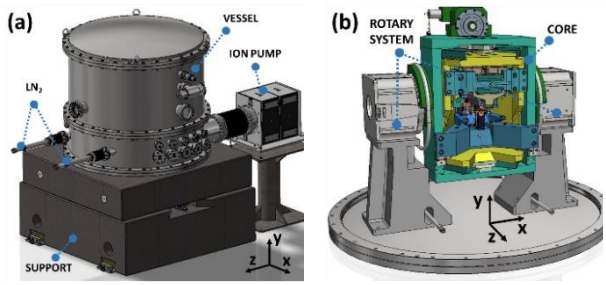


Figure 3: DCM assembly: (a) Overall view. (b) Downstream internal view of the rotary system and the core.

As for the core, the detailed design is shown in Fig. 4. By design the diffracting surface of the 1st crystal (CRYS1) is in the rotation axis of the rotary system, which, being at the beam height, prevents the beam from walking across the first crystal. This maintains the heat extraction as effective and well balanced as possible, and prevents transient effects in the lattice distortion due to the local thermal expansion. CRYS1 is manufactured in T-shape and directly clamped to a metrology frame (MF1) via calibrated pads that can correct coarse miscut errors of the crystals. This correction allows for substantial reduction of the required angular stroke for pitch and roll tuning and also minimizes misalignment metrology errors. In order to limit stress and strain in the crystals due to thermal expansion mismatch with respect to the frame, flexural elements are machined in MF1 around the three fixation points of each crystal. Even so, the eigen modes in the assembly are still made above 1 kHz. These flexures also act as high thermal resistance that help the overall thermal management. The same fixation concept is applied to the 2nd crystals (CRYS2) and their metrology frame (MF2). MF1 holds three mirrors (IFM) and MF2, three heads (IFH) of the DMIs. IFM alignment is guaranteed by machining tolerances, whereas IFH has a submilliradian alignment fixture (IFAM).

MF1 is mounted on an intermediate frame (YFM), which is then mounted to GOF. The LN_2 manifold (CMF), from which the cooling pipes are derived to the copper blocks (CB1), is also fixed to YFM. As commonly done, indium foils are used between CRYS1 and CB1 to improve the lateral cooling thermal contact between and reduce clamping distortions in CRYS1. The pipes are designed so that their stiffness does not compete with the mounting stiffness between CRYS1 and MF1. Inside CB1, channels in a coil profile maintain the dimensions of the tubes, so that the flow can be kept with minimum variation. The small channels also help increasing the effective heat transfer area between the fluid and CB1, allowing for smaller flows, which should lead to smaller vibration levels. They are machined in separate parts that are afterwards brazed together. More details about the dedicated flow-induced vibration studies are found in [5].

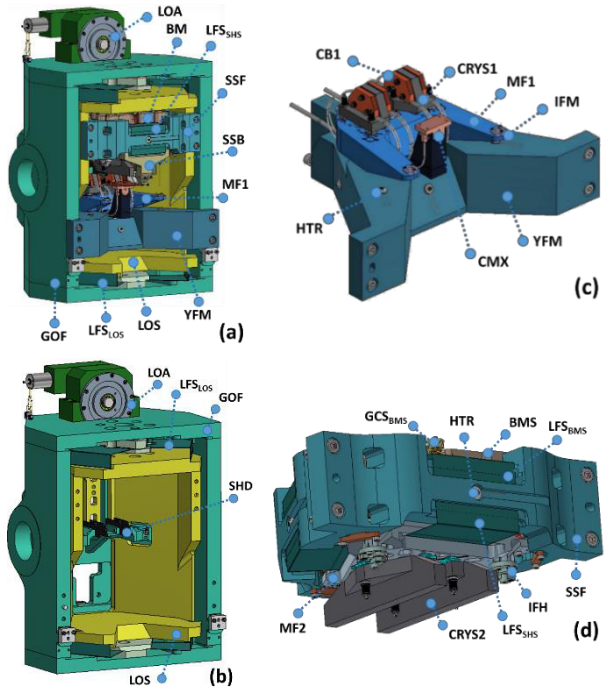


Figure 4: Mechanical design of the core of the DCM: (a) Complete set; (b) Long-stroke module; (c) 1st crystal module; (d) 2nd crystal module. (Acronyms in the text.)

From CMF, an extension is derived (CMX) and serves as the heat sink for CRYS2, so that it can be indirectly cooled through an association of copper straps (HCS and CCS). This indirect cooling solution for CRYS2 prevents flow-induced vibrations and is feasible since they were conveniently specified to work at 155 K. Indeed, as the temperature of the hot spot of the 1st crystal is expected to vary between 77 and 130 K during operation, depending on the total power and power density absorbed (related to the *K*-value of the undulator and the beam footprint, respectively), any attempt to match the lattice parameters of both crystals is quite discouraging. Thus, as it can be seen in Fig. 5, if CRYS2 is stabilized at 155 K, it is half-way the maximum pitch mismatch due to thermal expansion effects, i.e, about 30 µrad at about 130 K with respect to 77 K. In this case, the pitch tuning range that is required to maximize flux can be minimized, only ±15 µrad, as well as the gap adjustment to eventually compensate for beam position variations at any given element downstream the DCM caused by this missteering.

Content from this work may be used under the terms of the CC BY 3.0 licence (© 2016). Any distribution of this work must maintain attribution to the author(s), title of the work, publisher, and DOI.

ISBN: 978-3-95450-188-5 doi:10.18429/JACoW-MEDSI2016-TUCA05

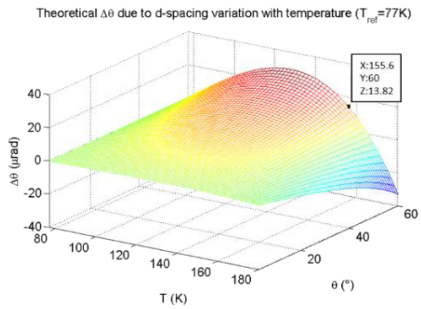


Figure 5: Pitch compensation for perfect energy matching as a function of temperature and angle.

To the best of our knowledge, the main innovation in this project is in the way the DoFs of CRYS2 are guided, actuated and controlled [6]. Firstly, all the guiding is performed by folded leaf-springs. By this choice, lubrication, friction effects and vibrations from recirculating spheres or rollers can be mostly eliminated. These factors allow for more deterministic design, and motions with higher resolution and repeatability and less noise. In addition, all the 3 actively controlled DoFs, namely, gap, pitch and roll, can be implemented for MF2 in a single stage, by the composition of 3 folded leaf-springs (LFS_{SHS}). Yet, since the elastic elements of the guiding have limited working range (and the actuator, limited range/resolution), one complementary translation module, guided by 6 folded leaf springs (LFS_{LOS}), is included. As a matter of fact, 5 folded leaf springs suffices to constrain the necessary DoF for this translation, but the 6th will improve symmetry and stiffness of the assembly.

In regular operation, this long stroke frame LOF may travel over ±2.75 mm with respect to GOF, whereas MF2 may travel over ±1.75 mm and rotate by ±1 mrad in pitch and roll with respect to LOF, so that the 9 mm gap requirement and the angular tuning can be performed. The actuation at the LOS is performed by a servomotor and a cam in a stiff mechanism (LOA), which is fixed to the GOF and has the necessary decoupling design to match with the 6-folded-leaf-spring guide. The actuation of MF2, on the other hand, is provided by three voice-coils actuators (VCA) that act against a reaction mass (or balance mass, BMS), instead of acting against the main structure, as ordinarily done. Just as MF2, BMS is also guided by 3 folded leaf-springs (LFS_{BMS}) and has the same 3 DoF with respect to LOS. Then, as the inherently compliant force actuators allow MF2 and BMS to be decoupled from each other, and both of them decouple from the LOS at about 7 Hz, superior dynamics can be achieved in the system, thanks to filtering effects. Figure 6 shows the schematic drawing of this high-dynamics module, whereas the detailed discussion of the mechatronics concepts is found in [7].

In order to simplify assembly and alignment procedures, MF2 and BMS are not directly mount to LOS via LFS_{SHS} and LFS_{BMS}, but to an auxiliary frame (SSF), which is then stiffly mounted to LOS. Moreover, in order to minimize actuation effort, both MF2 and BMS have the same decoupling frequencies, so that the gravity sag effects are similar to both of them. Additional springs are used as gravity compensators (GCS_{SHS} and GCS_{BMS}), which can be adjusted during assembly to achieve the required positioning alignment. Studies and simulations of stresses in the leaf springs, parasitic motion and alignment have been extensively performed to guarantee that the proposed solution is feasible. Also, several hard end-of-stroke features will assure safe conditions.

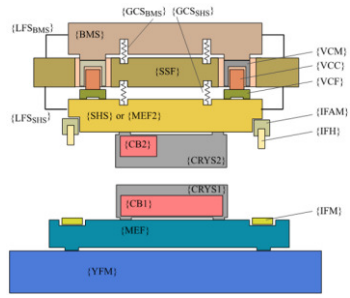


Figure 6: Schematic drawing for the 1st and 2nd crystals submodules in the crystal cage, according to the high-dynamics concepts. (Acronyms in the text.)

VCA is composed of the magnet assembly (VCM) and coil assembly (VCC). The first is directly fixed to BMS and the latter, via an auxiliary fixture (VCF), to MF2. VCF is a thermal barrier between MF2, at -60°C, and VCC, which is required to be above -30°C. This condition should be assured by auxiliary copper straps connecting VCF and SSF, which will have an active temperature control set to room temperature. Besides SSF, CRYS2 and YMF are the two other parts that also have heaters (HTR) for temperature control, at 155 K and room temperature, respectively. More details regarding the thermal management in the DCM are found in [7].

As for shielding, the present design allows the most convenient shielding structure (SHD) to be directly fixed to GOF, so that its negative effect on stability can be virtually eliminated. It is well known that many DCMs suffered from resonances in their shielding structure.

Finally, DMIs seem to be the most suitable option for metrology and feedback in this application, given the working distance constrains, the measurement stroke of several millimeters and nanometric requirements for resolution, accuracy and stability. Fortunately, a few attractive commercial options have been released in the last years, as they are compact and may be specified for vacuum compatibility and radiation hardness. Therefore, the metrology is made by a set of three fiber optics distance measurement interferometers (either Michelson or Fabry-Perot interferometers), having IFM fixed to MF1 and the IFH to MF2, as already mentioned. The 3 measurement axes provide feedback for gap, pitch and roll with a sampling rate of 10 kHz, necessary to achieve 200 to 300 Hz servo bandwidth.

Control

The control system must not only internally manage the DCM system, while maintaining the parallelism between the crystals within the specified 10 nrad stability, but synchronize it with external signals. Internally, there are two very different control level requirements, namely, the energy selection, and the fine gap and parallelism. The first is responsible for controlling GOF (Bragg angle), as well

Content from this work may be used under the terms of the CC BY 3.0 licence (© 2016). Any distribution of this work must maintain attribution to the author(s), title of the work, publisher, and DOI.

ISBN: 978-3-95450-188-5 doi:10.18429/JACoW-MEDSI2016-TUCA05

as the correlated LOS, with respect to their optical encoders and with closed-loop bandwidth of 35 Hz and 20 Hz, respectively; the latter is the main feedback loop, with closed-loop bandwidth above 200 Hz, which controls MF2 with respect to the readings of the interferometers. Concerning external references, the undulator can be used as a master to the energy loop, whereas beam position monitors (BPMs) and/or other instruments at the beamline may be used as auxiliary reference inputs to the high-dynamics loop.

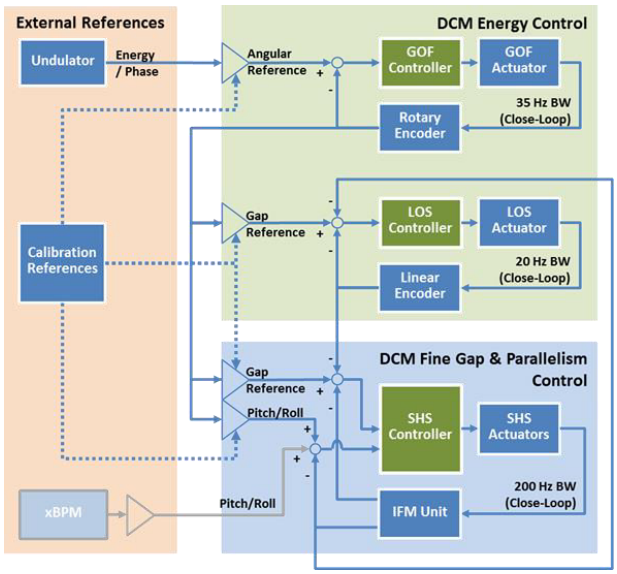


Figure 7: Control system diagram.

Table 3: Main Control Specifications

	GOF	LOS	SHS	Therm.
Actuator Type	Torque Motor	Servo	Voice-Coils	Foil Heaters
Sensor Type	Rotary Encoder	Linear Encoder	IFM	NTC RTDs
Res.	<50nrad	<0.1μm	<0.5nm <5nrad	<10mK
Closed-Loop BW	35 Hz	20 Hz	>200 Hz	0.1 Hz
Feedback Sampling	10 kHz	10 kHz	10 kHz	20 Hz

A diagram of the proposed control system is depicted in Fig. 7. Finally, Table 3 shows some specifications of actuators and sensors, including information regarding the temperature control, in order to minimize alignment and metrology errors.

Calibration and System Characterization

It is known that the parasitic motion of the leaf-springs, particularly the variation that occurs due to the rotation of the system with respect to gravity, and the power load variation, due to the variation of the parameters of the undulator, will require the DCM to be calibrated. Thus, from start the design rule has been to make the system based on high repeatability principles, so that high quality calibration should be possible. We expect that this calibration will be exclusively a function of the Bragg angle. This will be important when additional external feedback is not available during experiments.

Indeed, not all the quantitative data that was desired and/or required in the design phase was available in the literature or by experience. Thus, parallel projects have been carried out, such as the one about flow-induced vibrations [5], and the best efforts have been made in estimating the missing values, such as scattered power in critical components and black-body radiation [8]. Yet, whenever possible, a more conservative design approach has been applied in order to guarantee a functional performance. Nevertheless, the rich sensing architecture and the high controllability of the system should allow for instructive system characterization during commissioning phase.

CONCLUSIONS

The high-dynamics concepts that are applied here are proven technologies in high-end lithography machines, meaning that, although there is some innovation within the synchrotron instrumentation community, it comes under calculated risks, based on extensive and continuously updated analyses and predictive modelling. Thus, based on a consistent approach, the high-stability target has been confidently pursed and a functioning prototype should be ready for commissioning in mid-2017.

Lastly, it is worth mentioning that, regarding motion control and metrology for beamline instrumentation, this project has spawned new engineering concepts for other opto-mechanical devices of 4th generation synchrotron that has reflected in the design of several other mechanisms of the Sirius beamlines, including mirror systems and sample stages.

ACKNOWLEDGEMENT

The authors would like to gratefully acknowledge the funding by the Brazilian Ministry of Science, Technology, Innovation and Communication and the contribution of the LNLS team, the MI-Partners team and those of the synchrotron community who directly or indirectly built the path to this development.

REFERENCES

[1] L. Liu, F. H. de Sá, and X. R. Resende, "A new optics for Sirius," in *Proc. IPAC'2016*, pp. 3413–3415.

[2] A. R. D. Rodrigues *et al.*, "Sirius Status Report", in *Proc. IPAC'16*, Busan, Korea, May 2016, paper WEPOW001, pp. 2811-2814

[3] I. Sergeev and R. Doehrmann, "Vibrations in the DM and their effect on the beam stability and source broadening", presented at ESRF DCM Workshop, Grenoble, France, May 2014.

[4] P. Kristiansen, J. Horbach, R. Doehrmann, J. Heuer *et al.*, "Vibration Measurements of high-heat-load monochromators for DESY PETRA III extension". *J. Synchrotron Rad*, vol. 22, pp. 879-885, Jul. 2015

[5] R. M. Caliari *et al.*, "Studies on flow-induced-vibrations for the new high-dynamics DCM for Sirius", presented at MEDSI 2016, Barcelona, Spain, Sep. 2016.

Content from this work may be used under the terms of the CC BY 3.0 licence (© 2016). Any distribution of this work must maintain attribution to the author(s), title of the work, publisher, and DOI.

ISBN: 978-3-95450-188-5 doi:10.18429/JACoW-MEDSI2016-TUCA05

[6] R. R. Geraldes *et al.*, "Método de controle de grau de liberdade em sistemas mecatrônicos e monocromador de duplo cristal", INPI BR 10 2016 020900 5, Sep. 2016, Patent Pending.

[7] R. R. Geraldes *et al.*, "Mechatronics Concepts for the New High-Dynamics DCM for Sirius", presented at MEDSI 2016, Barcelona, Spain, Sep. 2016.

[8] M. Saveri Silva *et al.*, "Thermal management and crystal clamping concepts for the new high dynamics DCM for Sirius", presented at MEDSI 2016, Barcelona, Spain, Sep. 2016.

Content from this work may be used under the terms of the CC BY 3.0 licence (© 2016). Any distribution of this work must maintain attribution to the author(s), title of the work, publisher, and DOI.

ISBN: 978-3-95450-188-5 doi:10.18429/JACoW-MEDSI2016-TUCA06

THE GIRDER SYSTEM FOR THE NEW ESRF STORAGE RING

Filippo Cianciosi, Thierry Brochard, Philippe Marion, Loys Goirand, Yves Dabin, Marc Lesourd, Lin Zhang
ESRF-European Synchrotron Radiation Facility, 71 Avenue des Martyrs, 38000 Grenoble, France

Abstract

The ESRF is proceeding with the design and procurement of its new low emittance storage ring (Extremely Brilliant Source project).

This completely new storage ring requires a high performance support system, providing high stability (first resonance frequency about 50Hz) and a precise alignment capability (50µm, manual in transverse direction and motorized in the vertical one).

In order to meet these requirements we decided to support the magnets of each of the 32 cells of the synchrotron with four identical girders that was considered the best compromise between cost, complexity and performances. Each of the resulting 128 girders is 5.1m long, carries about seven tons of magnets, and its weight including fixed basement and adjusting system is six tons.

The adjustment system relies on modified commercial wedges; their stiffness was evaluated through laboratory tests. The FEA calculations carried out to optimize the design will be presented, together with the results obtained on a complete prototype girder system which was built and extensively tested and confirmed the modal calculations..

THE NEW LAYOUT

The present machine presents the lattice called Double Bend Achromat, with two bending magnets and 3 groups of optical magnets in each of its 32 cells. Only the groups of optical magnets are supported by adjustable girders. The dipole, less demanding in term of positiong precision, are placed on fixed supports. The lattice of the new machine is a Hybrid Seven Bends Achromat, constituted by 4 dipoles, 3 dipoles-quadrupoles and 24 optical magnets (Figure 1).

This complexity make unpractical the choice of different support for the different magnets, especially considering that the dipoles are relatively small and light. The solution of supporting all the machine on adjustable girders has been taken. The disposition of the magnets in the lattice led us to divide each of the 32 cells in 4 groups of magnets with almost the same weight (6 Tons) and length (5.1m), and support each of them with an adjustable girder.

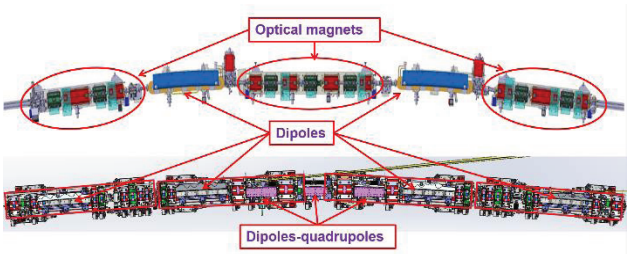


Figure 1: Lattice.

SPECIFICATIONS

The requirement of the girder are summarized in Table *1*.

The positioning precision is due to the physics of the machine and it will not be discussed here.

The re-alignment frequency is linked to the long-term movements and deformations of the ESRF site. During the last years movements of several mm were registered especially in the vertical direction, therefore a fast and convenient alignment method of the machine is required.

The choice of the target value of the first resonance frequency was based upon practical considerations about the behaviour of existing structures and the amplitude of the vibrations present on the site. In theory the important value is the amplification factor of the ground movement as a function of the frequency, but this is nearly impossible to calculate. However this amplification is usually very low for frequency below the 1st resonance. As the amplitude of the ground vibrations is significant mainly for frequency below 30Hz a value of 35Hz was specified for the 1st one.

Table 1: Specifications

Aspect	Value
Length	5.1m
Payload	6-7 Ton
Positioning precision	50µm (Vertical-transv.)
Positioning precision	1mm (Longitudinal)
Alignment freq.	2 times/year
Alignment method	Motorized (Vertical)
Alignment method	Manual (Transv.-long.)
First resonance frequency	35 Hz (minimum)
Planarity of top surface	+/-50 µm

GIRDER DESIGN

Several configurations were considered, with 3 and 4 supports. Three supports permit to not over define statically the girder, but as this solution does not permit to obtain the requested first resonance frequency, we decided to adopt a 4 supports system for this reason. The four supports version hallow holding the load in the vertical direction but not blocking the movements in the horizontal one. Two jacks are used to adjust the transversal position of the girder, while simple pushing screws set the longitudinal one. Figure 2 shows the design of the machine.

Content from this work may be used under the terms of the CC BY 3.0 licence (© 2016). Any distribution of this work must maintain attribution to the author(s), title of the work, publisher, and DOI.

ISBN: 978-3-95450-188-5 doi:10.18429/JACoW-MEDSI2016-TUCA06

Content from this work may be used under the terms of the CC BY 3.0 licence (© 2016). Any distribution of this work must maintain attribution to the author(s), title of the work, publisher, and DOI.

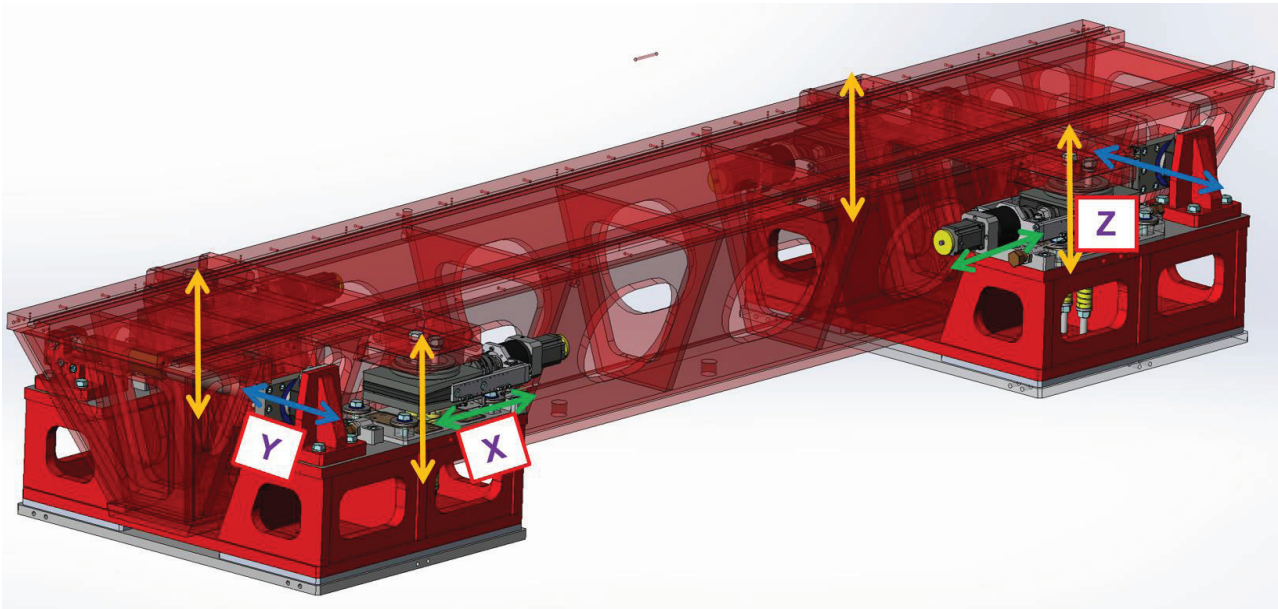


Figure 2: Girder design.

Vertical Supports

The vertical supports are based on the use of commercial wedges produced by Airloc and modified to accept the motorization and the related stress (Figure 3). The nut and some internal washer acting as axial bearing were made in aluminium bronze, the driving shaft for motorization reference and fixation holes added. Two spring were added to add a preload of about 1.4 Tons. Under this component a sliding surface based on Fibro sleds was added to ensure the horizontal motion.

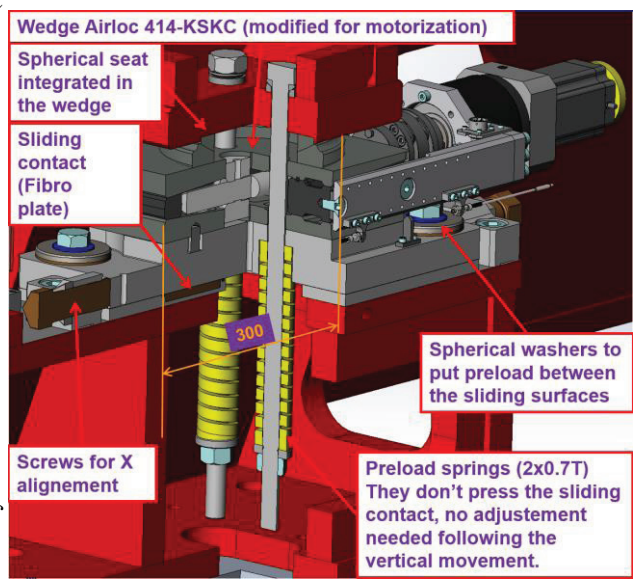


Figure 3: Vertical supports.

Horizontal Jacks

The motion in the transversal direction is ensured by two commercial wedges mounted vertically (Nivell DK2). As these component can only push forward a spring was placed in the other side to permit the reverse movement. These components, as they avoid any translation of the girder in the transversal direction, also ensure the absence of parasitic lateral movement of the girder during the vertical motion (Figure 4).

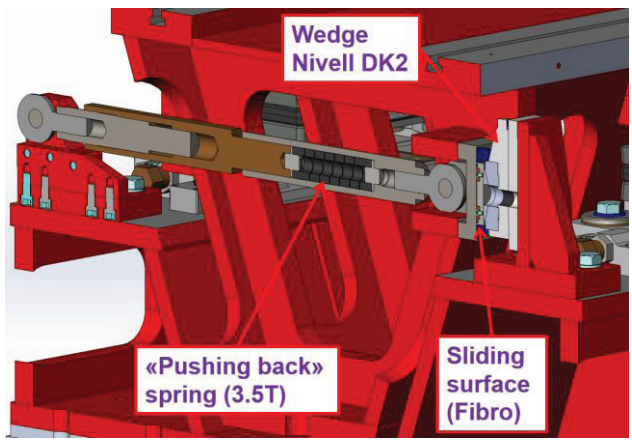


Figure 4: Vertical supports.

STATIC ANALYSIS

Gravity Deformation

To respect the planarity tolerances the deformation due to the own weight of the girder and the one of the magnets has to be taken in consideration, adding it to the machining tolerances. A static FEM analysis using the software Simulation was performed for this purpose. The

ISBN: 978-3-95450-188-5 doi:10.18429/JACoW-MEDSI2016-TUCA06

result shows that the maximum deviation with respect to the medium plane of the upper surface is +/-18µm (36µm height difference between highest and lowest point). The analysis was performed on only ¼ of the structure using the symmetry with respect to the two vertical planes (Figure 5).

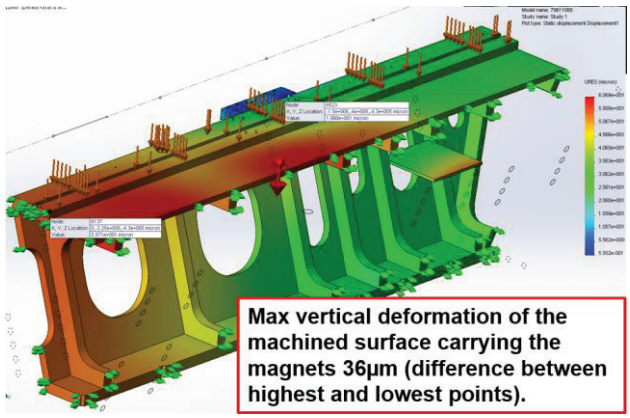


Figure 5: Vertical supports.

Hyperstatic Efforts

As the girder is supported on 4 points it is one time over defined in the vertical direction. This means that if the supports are not in the same plane above a critical value one of them can lose the contact and leave the girder on 3 supports. This condition (like a table on rough floor) is extremely dangerous because then the position of the girder would not be defined anymore and the stability would be compromised. Errors lower than the critical value generate a torsional deformation enabling to keep contact on the four supports. The FEM analysis (Figure 6) made with Simulation indicates that the girder follow a support out of position, twisting, up to about 400µm, which is largely sufficient considering that the motion precision is around 10 µm (see below). Even in this case it was possible to make the analysis only on ½ of the model thanks to a diagonal symmetry plane.

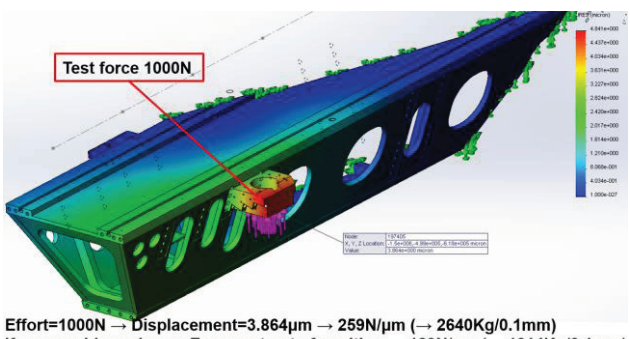


Figure 6: FEM analysis hyperstatic effort.

MODAL ANALYSIS

Boundary Conditions

As the girder system is very stiff the influence of the stiffness of the slab and the ground can't be neglected. A 3D model of these parts including the steel bases of the girder was made (Figure 7) and an elastic analysis was performed to calculate the equivalent stiffness of the supports integrating the floor to be used in the analysis as a virtual "elastic foundation". The stiffness for an optional jack for longitudinal adjustment was also calculated, even if this component was finally suppressed and replaced by simpler pushing screws.

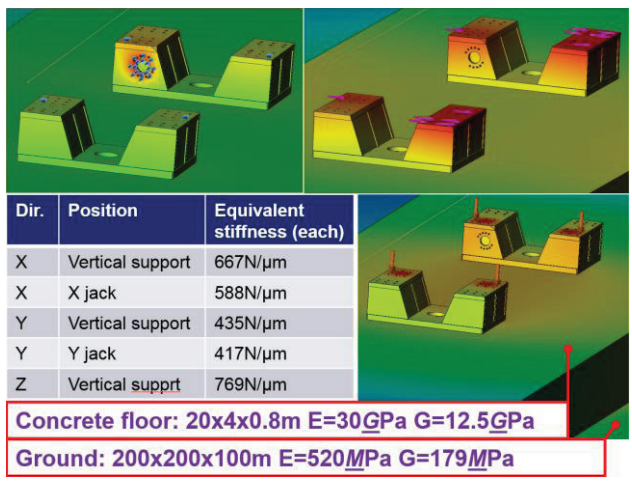


Figure 7: Ground and bases.

Wedges Stiffness

The stiffness of two models of wedges produced by different supplier were tested in our laboratory, using a hydraulic press to apply the real load in the vertical direction and a spring to apply the probing load in the horizontal plane (Figure 8). The one that was retained is the Airloc 414KSKC. This massive component is designed for charges up to 40 Tons, but we chose it for its high rigidity. As the amplitude of the ground vibration is extremely small even the efforts induced in the structure are mini- mal. Hence there is no slipping motion of the sliding surfaces used for the horizontal adjustment. In this way the stiffness of the wedges used for the vertical movement is crucial to avoid vibration in the horizontal direction too.

Content from this work may be used under the terms of the CC BY 3.0 licence (© 2016). Any distribution of this work must maintain attribution to the author(s), title of the work, publisher, and DOI.

ISBN: 978-3-95450-188-5 doi:10.18429/JACoW-MEDSI2016-TUCA06

Content from this work may be used under the terms of the CC BY 3.0 licence (© 2016). Any distribution of this work must maintain attribution to the author(s), title of the work, publisher, and DOI.

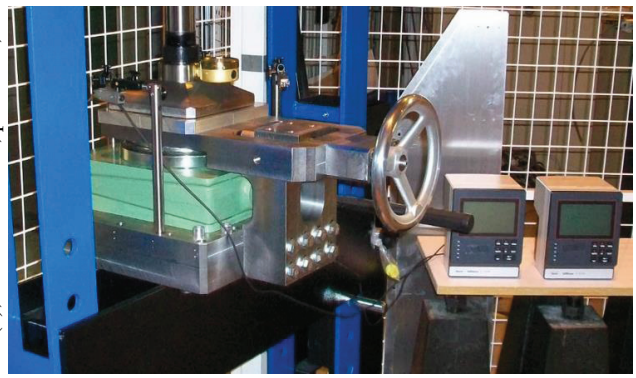


Figure 8: Wedges test.

Complete Analysis

Combining the stiffness of the "ground+slab+bases" and the one of the wedges in the three axis we obtain the values of the equivalent elastic foundation to be used in the girder analysis (Table 2). The Figure 9 shows the first modal shape with the calculated foundation values and an equivalent payload.

Table 2: Equivalent Stiffness for Modal Analysis

Dir.	Position	Ground+ Slab+ bases	Adj. wedge	Global equivalent stiffness
X	Vertical supports	667N/µm	1200N/µm	429N/µm
Y	Vertical supports	435N/µm	1100N/µm	311N/µm
Y	Y jacks	417N/µm	500N/µm	227N/µm
Z	Vertical supports	769N/µm	1600N/µm	519N/µm

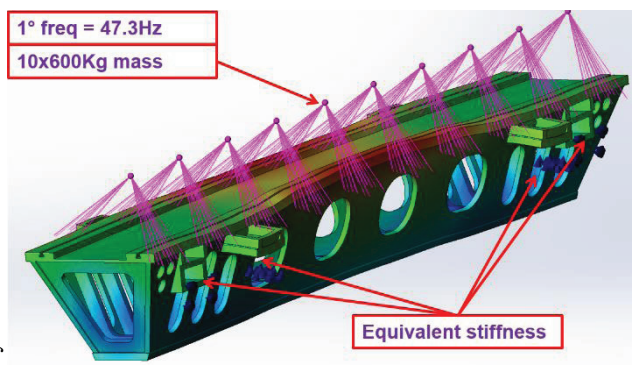


Figure 9: Final Analysis.

PROTOTYPE

Prototype Configuration

A prototype of the whole girder system was made to make a real scale test about the girder's performances, especially regarding vibrations modes and alignment precision. Other purposes of the installation were to check the feasibility of the installation and the interfaces with others sub-system in the limited space of the ESRF storage ring tunnel (Figure 10). The mechanical design of the prototype was more complex than the series, the supports interfaces were screwed and not integrated in the structure in order to have the possibility to make modifications in case of unsatisfactory results.



Figure 10: Prototype installation.

Motion Test

Motion analysis was made to ensure the requested alignment precision, especially in the vertical direction that needs frequent adjustments. Table 3 shows the main results.

Table 3: Motion Test

Performances in +/-2mm motion	Value
Z motion accuracy	10.8 µm
Z motion repeatability	3.3 µm
Z motion increment	0.3 µm
X parasitic movement	11.3 µm
Y parasitic movement	7.8 µm

Vibration Test

Vibration test was performed by Marc Lesourd on the prototype. Dummies magnets with the same shape and weight as the real ones were installed to have a realistic payload. The response of the system to the ground vibration noise is very good, we registered a maximum amplitude of the vertical vibration on the critical magnet (QF6) only marginally bigger than the one of the ground (Figure

ISBN: 978-3-95450-188-5 doi:10.18429/JACoW-MEDSI2016-TUCA06

11). The frequency response of the girder system is in good agreement with the calculated values. The graph of Figure 12 shows that the girder follow perfectly the ground movements up to a frequency around 50Hz. The response to an excitation with hammer indicated that the first vibration mode involving the girder is 51Hz, some lower frequency around 40Hz could interest QF6 only.

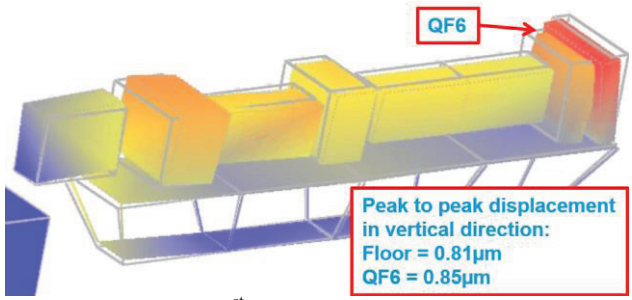


Figure 11: 1st Measured Vibration Mode.

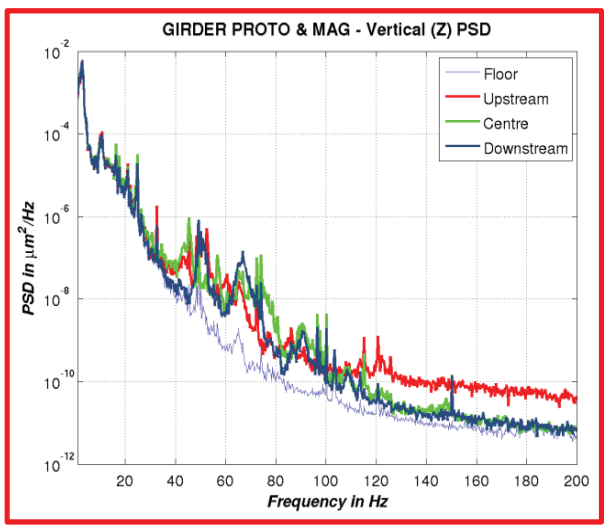


Figure 12: Ground Vibration Response.

CONCLUSION

The results of the test made on the prototype gave the expected results for all the main aspects (both movement precision and modal frequency).

We already started the production of the 128 girders necessary for the new storage ring, two suppliers were selected and they will complete the 2 pre-series before the end of 2016. The delivery of the series ones id foreseen during 2017 and beginning 2018, in order to start the mounting of the components on the girders in 2018 and to do the installation in the tunnel in 2019.

NOTE

This paper is a brief report of a work made internally at ESRF for a specific purpose. The aim of this paper is only to inform about the obtained results. Any reference to existing similar work is not included for mere lack of time before the MEDSI 2016 conference.

Content from this work may be used under the terms of the CC BY 3.0 licence (© 2016). Any distribution of this work must maintain attribution to the author(s), title of the work, publisher, and DOI.

ISBN: 978-3-95450-188-5 doi:10.18429/JACoW-MEDSI2016-TUPE01

DMM THERMAL MECHANICAL DESIGN

J. H. Kelly, Diamond Light Source, UK

Abstract

A Double Multilayer Monochromator (DMM) was designed in-house for the VMXi beamline. Thermal mechanical finite element analysis was performed to design a novel optic geometry, employing In/Ga eutectic cooling. The integration of a DMM into the existing beamline required additional power management components, such as a low energy power filter, a power detector and compact CuCrZr masks. This paper describes the thermal management challenges and their solutions. The DMM has been fully commissioned and is operational within the original I02 beamline.

INTRODUCTION

The in-situ Versatile Macromolecular Crystallography (VMXi) Beamline is effectively a new beamline which has been built through the original Diamond Phase one beamline I02. The new fully automated endstation has been built downstream of the original within a novel mini-hutch. A new experimental cabin was built to allow I02 operation during the majority of the VMXi build. The insertion device (ID) is planned to be upgraded from a U23 to a Cryo-cooled permanent magnet undulator (CPMU) giving a factor of 3 useful flux increase. The DMM was designed and installed to give an additional 60 fold increase in flux as compared to a Si(111) DCM [1]. The dramatic increase in flux necessitated a detailed evaluation of the power management within the beamline. This paper details the new power management components designed and procured for the VMXi upgrade.

MULTILAYER EUTECTIC COOLING

The DMM was designed to operate over the energy range of 10 – 25 keV using two multilayer stripes 2.0 nm and a 2.4 nm (See Figure 1). The worst case was assumed to be at 12 keV as the ID is optimised for flux at this energy. This is also a larger angle of incidence and hence small foot print. The absorbed power with the future CPMU K2.04, 500mA would be ~ 480W over a 97.5 x 3.4 mm foot print. This flux density would not be challenging for a cryocooled silicon optic; however concerns over the stability of the deposited layer under thermal contraction lead to a water cooled solution. To minimise turbulence induced vibration, a eutectic bath method was chosen. Numerous geometries were investigated using ANSYS but only the chosen one is presented here.

Two eutectic troughs were machined through the top surface of the bounce down first optic. The original aim of separating the cooling channels by slotting the silicon, was to mimic the ESRF mirror cooling model, of side cooling near the optical surface [2]. The troughs also act as temperature stabilised stiffening ribs to the optical surface. When the heatload is not central, which is always the case for the two stripe design a variation of tangential radius across the foot print is introduced but the effect is small enough to be neglected.

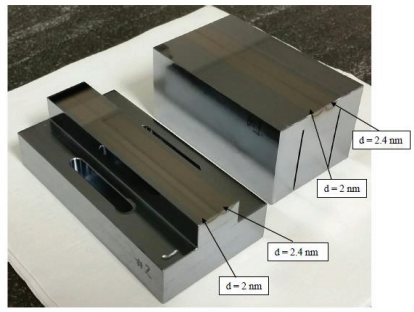


Figure 1: VMXi DMM Multilayer Optics procured from Rigaku, 1st multilayer on the right shown upside-down.

The use of an average young's modulus and poison ratio has been shown to give a good approximation to anisotropic material properties for modelling silicon Zhang [3]; however the non-standard nature of this design may make this finding invalid. The final optimisation was done using the anisotropic material properties. An FEA check was performed see the effect of aligning the X direction with the ML normal and the Y direction normal to the front, side and at ~30º. As expected from the cubic symmetry and Zhang [3], the results are identical for the Y axis aligned with the sides but differ at other angles. The Si(100) surface plane, Si(010) side plane, was found to give the best results and so was used throughout this study.

The eutectic trough was originally designed to come down to within 5 mm of the optical surface; however after manufacturing issues this was increased to 10 mm. This compromised the tangential slope error (fitted parabola radius 50 km to 22 km, 152W absorbed power) but made the optic significantly more robust.

A eutectic wetted area heat transfer coefficient (HTC) of 10,000 W/m^{2}K was chosen after performing a literature review [4-8]. Prandtl, Nusselt and Reynolds numbers extracted from these sources were used to calculate a range of HTCs. This appears to be a reasonable value for natural convection, which has also been used during the design of other instruments for DLS. The optic tangential slope error was relatively insensitive to HTC i.e. double HTC reduced the deformation by 15%. The eutectic troughs were filled to a depth of ~ 10mm. This was deep enough to ensure that the cooling fins remained immersed over the angular range; while shallow enough to minimise the possibility of splashing upon pump-down. After filling the troughs and inserting the Ni plated Cu fins the water chiller was run with a set-point of 50ºC for a few hours. It has been found that this reduces the eutectic viscosity and improves wetting.

Content from this work may be used under the terms of the CC BY 3.0 licence (© 2016). Any distribution of this work must maintain attribution to the author(s), title of the work, publisher, and DOI.

ISBN: 978-3-95450-188-5 doi:10.18429/JACoW-MEDSI2016-TUPE01

FEA Setup

A bulk fine mesh was defined with a 0.5 mm mesh control applied to the illuminated face and to the bottom faces of the trough isolation cuts (See Figure 2). The illuminated area split faces were used to constrain the model about the centre of the optical area. No support structures were modelled. The calculated heat load profile was projected onto the optic taking care to scale the imported heat flux to give the correct absorbed heat load as measured by a reaction probe on the wetted areas. The models were exported from ProEngineer as a step file with a co-ordinate system defined to match the angle of incidence. The projected heat load imported into ANSYS using an External Data block was then aligned horizontally. A section view through the meshed model is given below.

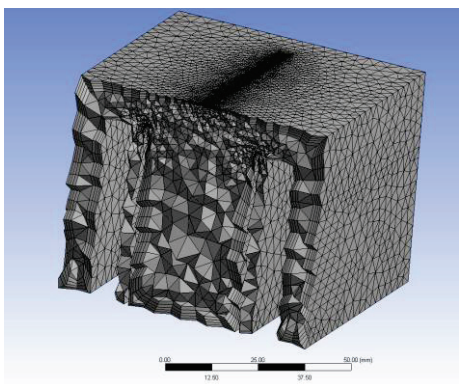


Figure 2: Section view of the meshed multilayer substraight.

FEA Results

It was found that the lower the wetted depth the lower the thermal distortion because the substraight above the wetted area is at the same temperature and hence not distorted.

DLS currently operate with a nominal 300 mA ring current but there are future plans to increase this to 500 mA. The data plots presented below in Figure 3 & 4 are for a CPMU, 500mA 480 W absorbed.

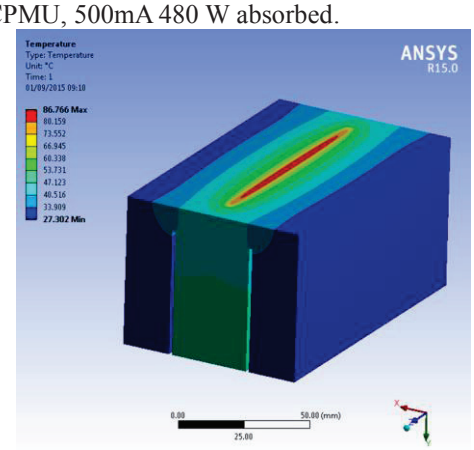


Figure 3: Temperature distribution of the DMM 1st multilayer with an absorbed power of 480W.

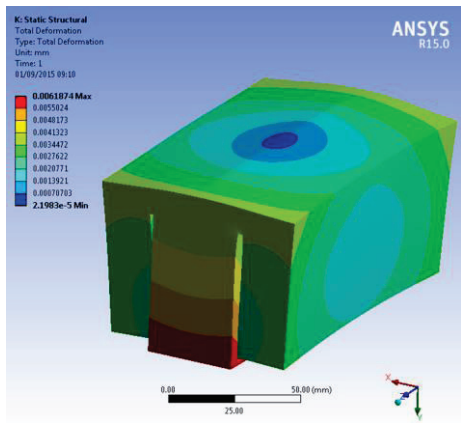


Figure 4: Mechanical Deformation of the DMM 1st multilayer with an absorbed power of 480W.

The FEA study acceptance criteria for the highest foreseeable power load were:

- Eutectic Temperature 34°C (480 W) << 100°C
- Silicon Stress 41 MPa (480 W) << 7 GPa
- Beam collimation effect within compensation range of the KB mirrors – Optics Group Define As Pass

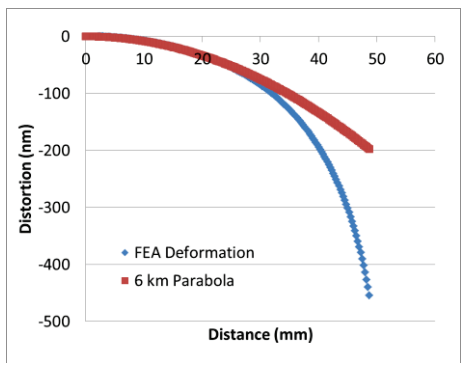


Figure 5: Tangential slope error & 6 km radius parabola plot the DMM 1st multilayer with an absorbed power of 480W. Distortion vs. Distance from spot centre.

The radius reduces to 6 km under the absolute maximum absorbed power condition; however the beamline will not operate with a CPMU with a 500 mA ring current within the next five years if at all (See Figure 5). The optic is deliberately over filled so that only light diffracted from the low slope error central third is accepted into the Endstation.

With Beam DMM Data

No specific tests have been performed to measure the optic slope error; however the DMM has been used to solve structures in diffraction experiments operating with an absorbed heat load of 91 W. The flux at the sample was measured to be 7.8 x10^{13} ph/s, using a calibrated diode. The beam stability was measured at the sample position using an X-ray camera running at 700 Hz. With all the other optics removed from the beam, an X-ray pitch stability of 34 nrads RMS integrated from 1- 350 Hz was measured. This was the best data taken during the day. Sporadic local construction activity clearly had a detrimental effect increasing the stability up to 50 nrads

Content from this work may be used under the terms of the CC BY 3.0 licence (© 2016). Any distribution of this work must maintain attribution to the author(s), title of the work, publisher, and DOI.

ISBN: 978-3-95450-188-5 doi:10.18429/JACoW-MEDSI2016-TUPE01

Content from this work may be used under the terms of the CC BY 3.0 licence (© 2016). Any distribution of this work must maintain attribution to the author(s), title of the work, publisher, and DOI.

RMS. This X-ray camera data was confirmed with a separate single crystal diamond beam position monitor running at 20 kHz.

POWER FILTERS

The DMM delivers a wide band pass monochromated beam at shallow Bragg angles (0.7º – 1.5º, 21 - 9.9 keV for 2.4 nm stripe). The shallow angular range means that the optics also act as mirrors reflecting the low energy harmonics. As DLS is a 3GeV ring the low energy 1st harmonic holds ~ 100W, which would cause unnecessary heating, distortion and damage to downstream components. The low energy harmonics would also corrupt the diffraction data. So the low energy fraction is filtered out by a diamond filter, with the thickness optimised for a specific beamline energy range. The design of a 50 µm thick diamond filter which could absorb 110 W of power over a 3.4 x 2.1 mm spot, indefinitely, is non-trivial. A commercial solution was procured from Diamond Materials GmbH, although the full performance will only be tested when the ID is upgraded. The thin diamond filter is bonded to a thicker diamond support ring, which is in turn bonded to a Cu tube. This provides cooling without over constraining the diamond. An FEA study was performed to validate the design. An elasti-plastic analysis was required as high differential thermal expansion stresses are created. The design requires the annealed Cu to yield to alleviate the stress. Ferrous and titanium alloys have a fatigue endurance limit so a spring may be designed to work for ever; however non-ferrous metals such as Cu do not. The Number of cycles to fracture depend upon numerous factors including composition, grain size and temperature [9]. A "rule of thumb" is that fatigue strength equals 1/3rd the tensile strength [10]. It is difficult to say what the life expectancy of the diamond filters will be, but the total number of temperature cycles in operation will be relatively small. An FEA result is given below in Figure 6.

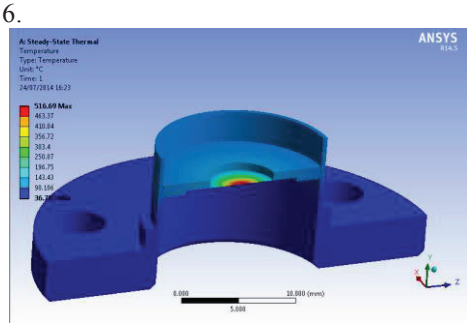


Figure 6: Thermal FEA result for 50 µm diamond filter thickness absorbing 110 W.

POWER DETECTOR

A power detector has been engineered to provide a measurement that the pre-DMM filters are in place and undamaged; while also protecting the detector from the power in case of a failure. The assembly mounted just upstream of the Endstation, employs a 20 µm thick diamond filter with a 100 nm Ti coating to attenuate the visible light and nitrogen doping to give a uniform fluorescence. Downstream of the filter a camera gives a beam position and a diode gives a machine protection signal.

WATER COOLED MASKS

A detailed raytrace was created to identify all the locations down the beamline where significant power might be deposited. The Gas Bremsstrahlung Stop (GBS) and the transfer pipes were clearly vulnerable. Zero length water cooled masks were designed which were thin enough to be inserted between existing components by compressing the bellows (See Figure 7). These masks were machined from CuCrZr alloy removing any requirements for brazing or welding [11]. Prior to installation the knife edge robustness was investigated. No visible damage was caused by repeated bolting and baking cycles as long as the alloy material had been heat treated i.e. using Ampcoloy 972. The photon shutter was also upgraded to a water cooled design.

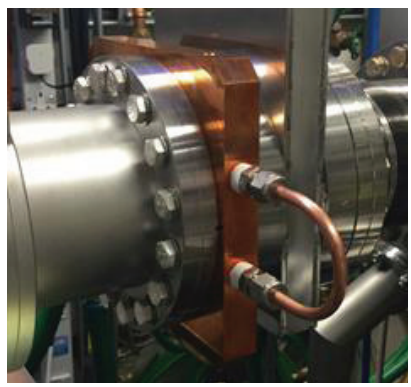


Figure 7: Cu alloy water cooled mask.

Three fixed masks and one moving mask/diamond fluorescent screen were integrated into the DMM design. These masks limit the solid angle of the exiting rays and allow an aperture to either block the deflected, undeflected or both beams. This was required because the VMXi beamline may be operated with either a DCM or DMM. The DMM high power nitrogen doped diamond fluorescent screen was designed with a 10 x 30 mm usable area to allow both the undeflected and 25 mm bounce down monochromated beams to be seen, along with all the alignment steps in between.

CONCLUSION

An in-house designed DMM with power filters and power detector have been built, installed and are operational on the beamline. They have been successfully tested with the existing source and ring current.

REFERENCES

[1] L. Alianelli, "Double Multilayer Monochromator for VMXi", Diamond Light Source, Harwell, UK, Rep. SCI-OPT-REP-0097, April 2014.

[2] L. Zhang et al., "Thermal distortion minimization by gometry optimization for water-cooled white beam mirror or multilayer optics", in Journal of Physics

ISBN: 978-3-95450-188-5 doi:10.18429/JACoW-MEDSI2016-TUPE01

Conf (SRI 12), Lyon, France, July 2012, paper 425 (2013) 052029.
[3] L. Zhang et al., "Anisotropic elasticity of silicon and its application to the modelling of X-ray optics", J. of Sync. Rad. Vol 21, Part 3, p 507-517, May 2014.
[4] A. Miner and U. Ghoshal, "Cooling of high-power-density microdevices using liquid metal coolants", App. Phys Let. Vol 85, No. 3, p 506-508, July 2004.
[5] H. Steiner, J. Konys, "Heat and mass transfer calculations in heavy liquid metal loops under forced convection flow conditions", J. Nuc. Mat. Vol 348, p 18-25, 2006.
[6] Indium Corp, http://www.indium.com/technical-documents/product-data-sheets/.
[7] A. M. Vaidya et al., "Liquid Metal Natural Convection Heat Transfer over a Horizontal Cylinder", Proc. of the 37th National & 4th International Conference Fluid Mechanics and Fluid Power, Madras, India, Dec 2010.
[8] F. Wolff et al., "Natural Convection of Liquid Metals in Vertical Cavities", Exp. J. of Therm. Fluid Sci.. Vol 1, p 83-91, 1988.
[9] S. Heikkinen, "Fatigue of Metals, Copper Alloys", presented CERN CLIC Meeting Jun. 2003, unpublished.
[10] Copper Development Association, https://www.copper.org/.
[11] S. Sharma et al., "A Novel Design of High Power Masks and Slits", presented at Mechanical Engineering Design of Synchrotron Radiation Equipment and instrumentation conf.(MEDSI 2014), Melbourne, Australia, Sept. 2014, unpublished

Content from this work may be used under the terms of the CC BY 3.0 licence (© 2016). Any distribution of this work must maintain attribution to the author(s), title of the work, publisher, and DOI.

ISBN: 978-3-95450-188-5 doi:10.18429/JACoW-MEDSI2016-TUPE02

Content from this work may be used under the terms of the CC BY 3.0 licence (© 2016). Any distribution of this work must maintain attribution to the author(s), title of the work, publisher, and DOI.

EXPERIMENTAL VALIDATED CFD ANALYSIS ON HELIUM DISCHARGE

J.C. Chang, Y.C. Chang, F.Z. Hsiao, S.P. Kao, H.C. Li, W.R. Liao, C.Y. Liu
National Synchrotron Radiation Research Center, Hsinchu, Taiwan

Abstract

National Synchrotron Radiation Research Center in Taiwan (NSRRC) had set up three cryogenic systems to provide liquid helium to superconducting radio-frequency (SRF) cavities, insertion devices, and highly brilliant hard X-ray. The first one could produce liquid helium 134 LPH, with maximum cooling capacity of 469 W at 4.5 K. The second one could produce liquid helium 138 LPH, with maximum cooling capacity of 475 W at 4.5 K. The third one could produce liquid helium 239 LPH, with maximum cooling capacity of 890 W at 4.5 K. However, large liquid helium discharge in a closed space will cause personnel danger of lack of oxygen. We performed Computational Fluid Dynamic (CFD) simulation to analyse helium discharge through a SRF cavity in the Taiwan Light Source (TPS) tunnel. We simulated cases of helium discharge flow rates from 0.1 kg/s to 4.2 kg/s with and without fresh air supplied from the air conditioning system. We also set up both physical and numerical models within a space of 2.4m in length, 1.2m in width and 0.8m in height with nitrogen discharge inside to validate the CFD simulation.

INTRODUCTION

Liquid helium for transferring cooling power from the cryogenic plant to the magnets and SRF cavities had been widely applied on the advanced large superconducting particle accelerators. Those superconducting particle accelerators are typically designed in elongated structures and require wide distributed cryogenic system. For requirements of high stable and reliable operation, many efforts have been put into the improvement and modification of the cryogenic system.

One cryogen distribution system has been installed and commissioned to transfer liquid nitrogen and LHe from storage dewars to superconducting radio-frequency (SRF) cavities at TPS. [1] The cryogenic system has maximum cooling capacity 890 W with associated compressors, an oil-removal system, four helium buffer tanks, one 7000-L Dewar, gaseous helium piping at room temperature, transfer lines to distribute helium, and a transfer system for liquid nitrogen. Currently, there are two SRF cavities are located one upstream and one downstream of the distribution valve box.

Personnel safety is another critical issue of the cryogenic system. Once large liquid helium (LHe) was released on the atmospheric tunnel, the volume of helium will expand several hundred times in short time due to sudden change of its density. Therefore, cold helium discharge test in the LHC tunnel at CERN had been experimentally conducted. [2] Numerical simulation of cold helium safety discharges had also been performed at European Spallation Source (ESS). [3] In this study, we applied numerical simulation to analyse helium discharge through a SRF cavity in the TPS tunnel. We also set up a small experiment to validate the numerical simulation.

NUMERICAL SIMULATION

CFD began from the early 30s of the 20th century to solve the linearized potential equations with 2D methods (1972). As rapid development of numerical analysis and computer science, CFD has more advantage of well adaptation than traditional theoretical analysis and experimental measurements. Nowadays, CFD has been widely applied in many fields. Detailed 3D numerical simulation was performed using a commercial general purpose CFD code ANASYS Fluent.

Governing Equation

We set our simulated model as a 3D turbulent flow in this study. The basic governing equations include the continuity equation, the momentum equation and the energy equation.

We apply the k-ε turbulence model and SIMPLEC to solve the velocity and pressure problem.

Mass conservation equation (continuity equation)

$$\frac{\partial \rho}{\partial t} + \nabla \cdot (\rho \mathbf{u}) = 0 \quad (1)$$

where ρ is density of fluid, t is time and $\mathbf{u}$ refers to fluid velocity vector.

Momentum conservation equation

$$\frac{\partial (\rho \mathbf{u})}{\partial t} + \nabla \cdot (\rho \mathbf{u}\mathbf{u}) = -\nabla p + \rho \mathbf{g} + \nabla \cdot (\mu \nabla \mathbf{u}) - \nabla \cdot \tau_t \quad (2)$$

where p is pressure, $\mathbf{g}$ is vector of gravitational acceleration, μ is dynamic viscosity of fluid, and τ_t is divergence of the turbulent stresses which accounts for auxiliary stress due to velocity fluctuations.

Energy conservation equation

$$\frac{\partial (\rho e)}{\partial t} + \nabla \cdot ((\rho e + p)\mathbf{u}) = \nabla \cdot \left(k \nabla T - \sum_j h_j \mathbf{j}_j \right) \quad (3)$$

where e is the specific internal energy, T is fluid temperature, k is heat conductivity, h is the specific enthalpy of fluid, $\mathbf{j}_j$ is the mass flux. In this study, RNG (Re-Normalisation Group) κ - ε turbulent model was used.

Geometry and Grid Generation

A detailed 3D model of 2 of 24 sections of the TPS tunnel, where a SRF cavity is located, was built for the numerical simulation. The space of the simulation zone is about 860.5 m^3. The geometry was built according to the dimensions of the tunnel, as shown in Fig.1. We also take

ISBN: 978-3-95450-188-5 doi:10.18429/JACoW-MEDSI2016-TUPE02

the effects of the air conditioning system into simulation. Supplied air exits and two air exhausts are distributed on overhead of the inner wall. There is one exhaust blower installed on the inner wall near the helium discharge exit.

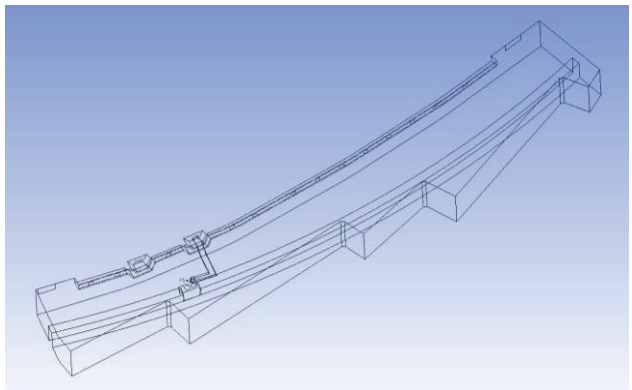


Figure 1: Numerical model of 2 sections of TPS.

According to the geometry of the model, we applied hybrid grid to discretize the model. The total number of the grid elements was about 3.34 million. To more accurately analyse the flow fields and greater control over sizing function, we applied the Advanced Size Function. The size of relevance center was fine. The minimum grid element size is 0.00177m near the helium discharge exit. Figure 2 shows the generated grids of the numerical simulation.

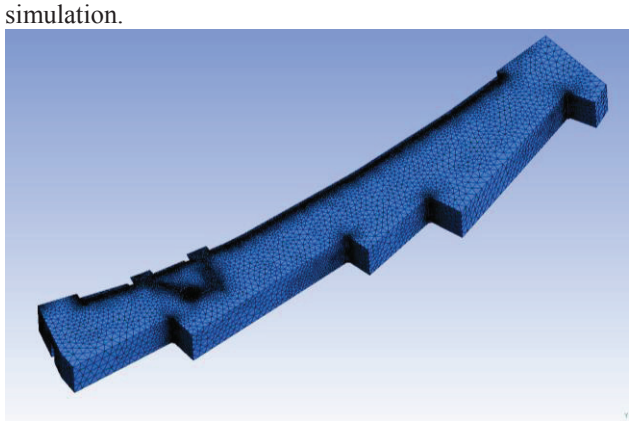


Figure 2: Generated grids of the numerical model.

Initial and Boundary Conditions

The flowrate of helium discharge was given the worst case of 4.2 kg/s by our SRF people. Time of helium discharge is 10 s. There are two simulation cases A and B in this study. Case A: Discharge helium flows vertically upward. Case B: Discharge helium flowing toward the exhaust blower on inner wall. Other initial and boundary conditions are list as follow.

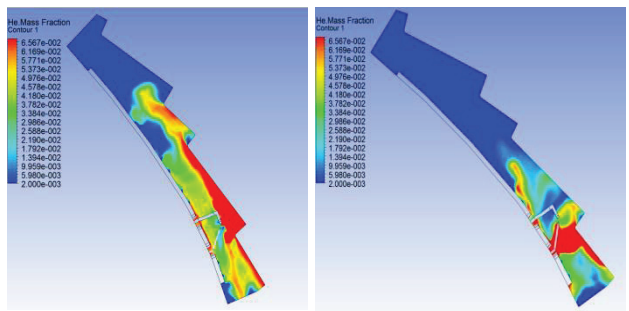
1. Air temperature in the tunnel is 25 °C at t = 0s.
2. Discharged helium temperature is 4 K.
3. Wall and floor are adiabatic.
4. Both sides are opened to atmosphere (1atm).
5. Supplied air flow velocity is 2 m/s from air exits.
6. Back pressure of the air exhaust is 1000pa.

RESULTS AND DISCUSSION

We select a monitor plane at the z= 1.5 m. Figure 3 shows the simulation results of helium mass fraction of cases A and B on the plane z =1.5 m at t = 10s.

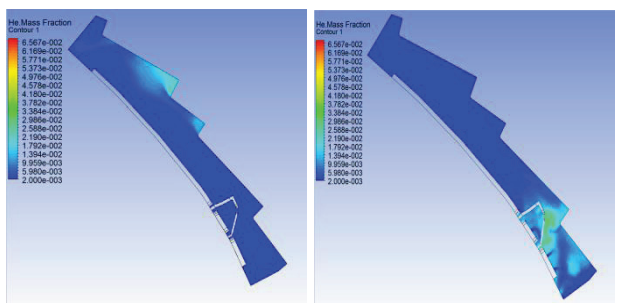
The simulated helium mass fraction is distributed from 6.567% to 0.2%. It can be observed that the helium mass fraction of case B is lower than that of case A due to the effect of the exhaust blower. High helium mass fraction is shown on the wedge area near the outer wall in case A because that a circulation forms in that area. On the other hand, the helium mass fraction is higher in the area between the helium discharge exit and the exhaust blower in case B.

Figure 4 shows the simulation results of helium mass fraction of cases A and B on the plane z =1.5 m at t = 30s. The helium mass fractions of both cases at t = 30s are clearly lower than that at t =10s. However, some residual helium still remains on the wedge area near the outer wall in case A and in the area between the helium discharge exit and the exhaust blower in case B.



(A) (B)

Figure 3: Simulation results of helium mass fraction of cases A and B on the plane z =1.5 m at t = 10s.



(A) (B)

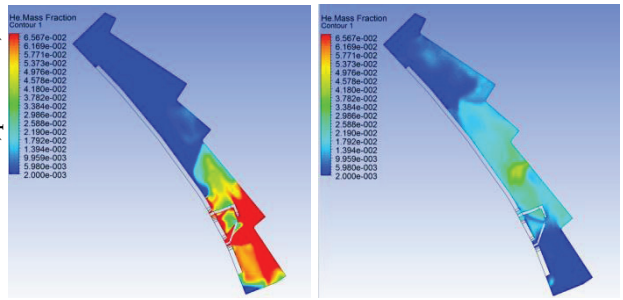
Figure 4: Simulation results of helium mass fraction of cases A and B on the plane z =1.5 m at t = 30s.

We also simulate the case without fresh air supplied by the air conditioning system. Figure 5 shows the simulation results of helium mass fraction of cases without supplied air on the plane z =1.5 m at t = 10s (A) and t = 30s (B). Higher helium mass fraction simulation results are shown in Fig. 5 (A) and (B) than the cases with supplied air shown in Figs. 3 and 4.

Content from this work may be used under the terms of the CC BY 3.0 licence (© 2016). Any distribution of this work must maintain attribution to the author(s), title of the work, publisher, and DOI.

ISBN: 978-3-95450-188-5 doi:10.18429/JACoW-MEDSI2016-TUPE02

Content from this work may be used under the terms of the CC BY 3.0 licence (© 2016). Any distribution of this work must maintain attribution to the author(s), title of the work, publisher, and DOI.



(A) (B)

Figure 5: Simulation results of helium mass fraction of cases without supplied air on the plane z =1.5 m at t = 10s (A) and t = 30s (B).

EXPERIMENTAL VALIDATION

We also set up a small experiment to validate our numerical simulation. A cubical space of 2.4m in length, 1.2m in width and 0.8m in height with nitrogen discharge inside. To clearly observe the nitrogen discharge inside the space, the cubical cover was made of transparent acrylic. Another small cubic box of 1.2m in length, 0.2m in width and 0.4m in height was installed inside. The nitrogen discharge exit is located on the top of the small cubic box. An air exhaust hole was located on the upper area of the wall, as shown in Fig. 6, the geometry of the experiment.

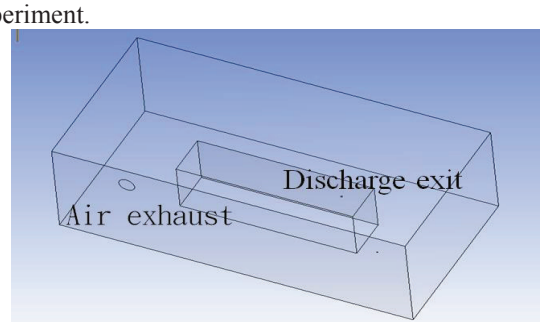


Figure 6: Geometry of the experiment.

Two oxygen sensors were put on the small cubic box. The range and resolution of the sensor are 0-30% and 0.1%, respectively. Three T-type thermocouples are installed at the nitrogen inlet, air exhaust and on the box. A flowrate multi-meter is installed at the nitrogen inlet. Figure 7 shows the experiment with nitrogen discharge in the cubic space.



Figure 7: Experiment with nitrogen discharge.

We also set up a 3D numerical model to simulate the experiment case. The total number of the grid elements was about 180,000. Figure 8 shows the simulation results of O_2 mass fraction. Low O_2 mass fraction is shown near the nitrogen exit. The profile of low O_2 mass fraction is similar to that of experimental result shown in Fig. 7.

Figure 9 shows experimental and simulation results of oxygen concentration. Although the experimental data is lower than the simulated ones, slopes of curves are close.

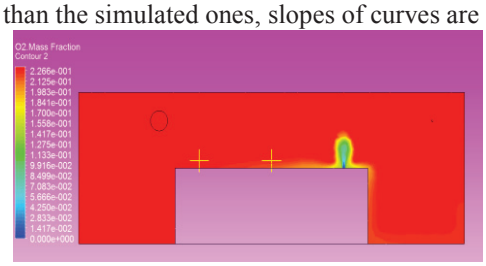


Figure 8: Simulation results of oxygen mass fraction.

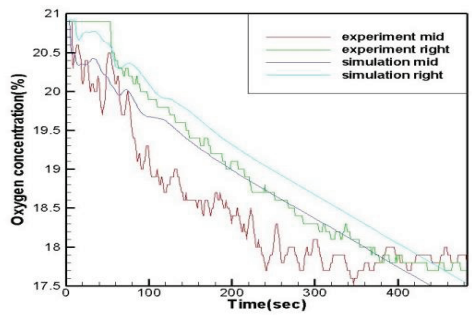


Figure 9: Experimental and simulation results of oxygen concentration.

CONCLUSION AND FUTURE WORKS

We performed CFD simulation to analyse the worst case of helium discharge through a SRF cavity in the TPS tunnel. It shows that the oxygen concentration will recover to safety level within 30 s after the worst case of helium discharge through a SRF cavity into TPS. We also conducted a small experiment to validate our simulation.

ACKNOWLEDGEMENT

Authors would like to thank colleagues in the utility and civil, RF, Cryogenic group and Safety division of NSRRC for their assistance.

REFERENCES

[1] H.H. Tsai et al., "Installation and commissioning of a cryogen distribution system for the TPS project", Cryogenics, Volume 77, July 2016, Pages 59–64.

[2] L Dufay-Chanat et al., “Final report on the Controlled Cold Helium Spill Test in the LHC tunnel at CERN”, IOP Conf. Series: Materials Science and Engineering 101, 2015.

[3] R. Andersson et al., “Numerical simulation of cold helium safety discharge into a long relief line”, 25th International Cryogenic Engineering Conference and the International Cryogenic Materials Conference, University of Twente, Enschede, Netherlands, 2014.

ISBN: 978-3-95450-188-5 doi:10.18429/JACoW-MEDSI2016-TUPE04

COHERENT SOFT X-RAY EPU VACUUM CHAMBER THERMAL ANALYSIS FOR SYNCHROTRON RADIATION PROTECTION*

Huston Fernandes, Charles Kitegi, David Harder, Dean Hidas, Jim Rank, Marco Musardo, Peter Cappadoro and Toshi Tanabe. Brookhaven National Laboratory, Upton, NY 11973 U.S.A.

Abstract

The purpose of this study was to determine the effect of beam mis-steering, on the temperature of the vacuum chamber. The chamber used for this study was for the Coherent Soft X-Ray (CSX) Elliptically Polarizing Undulator (EPU). Finite Element Analysis was conducted on the vacuum chamber to determine the temperature distribution on the chamber for set values of beam mis-steer, for NSLS-II. These results were then compared with on-site temperature measurements taken using RTD's, as well as thermal sensitive cameras. The accuracy of these results was analyzed and further FEA studies were proposed for steeper beam mis-steers and beam offsets.

INTRODUCTION

The Coherent Soft X-Ray (CSX) Elliptical Polar Undulator (EPU) beam line has two EPU's at a canted angle of 0.16 mrad. The effect of synchrotron radiation of the upstream device was studied on the vacuum chamber downstream. A single vacuum chamber made of Aluminum, as indicated in Fig. 1, covers the entire length of both the EPU's. The maximum aperture of the vacuum chamber is 8 mm as indicated in Figure 2.

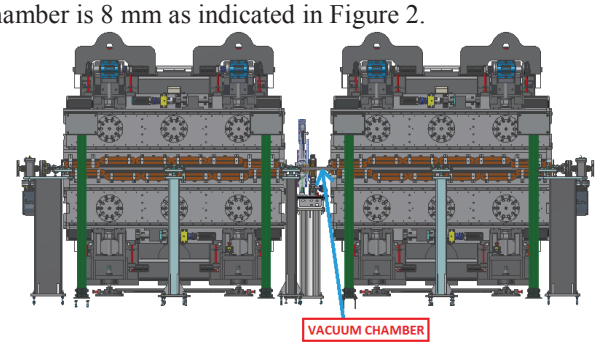


Figure 1: CSX EPU Vacuum Chamber.

The total on axis power of both the devices is around 10.1 KW [2].

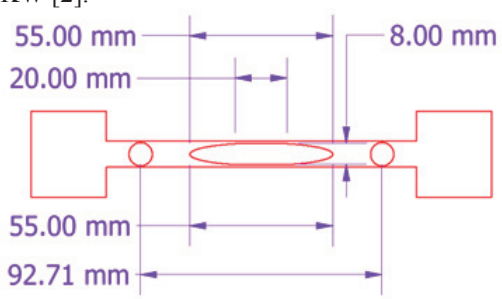


Figure 2: CSX EPU Vacuum Chamber Cross Section.

Since the effect of beam mis-steer of the upstream device is studied on the vacuum chamber, heat fluxes for 0.05 mm beam offset and 0.2 mrad angle beam mis-steer were studied. These offset and mis-steer limits were obtained from the maximum allowable active interlock limits set. After determining the close correlation of the FEA results to the actual measurements, FEA analysis of larger beam mis-steer angles were determined. The maximum beam mis-steer studied was 0.7 mrad.

HEAT LOAD CALCULATIONS

SRW code was used to compute the heat load on the wall of the vacuum chamber. Figure 3 shows the magnetic structure of the CSX EPU.

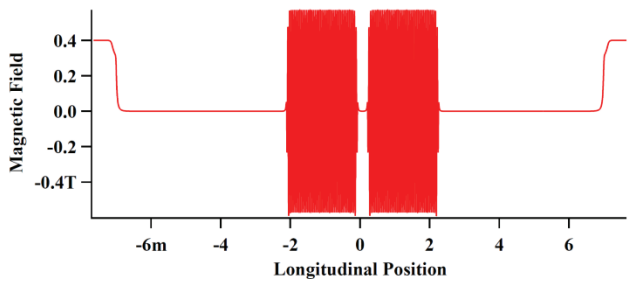


Figure 3: Magnetic Structure of CSX EPU.

The straight section has two EPU's of magnetic length 2 meters placed next to each other with a canting magnet in-between.

Table 1: CSX EPU Parameters Used for Heat Load Calculations

CSX EPU Properties	
Length	2x2 meters
Canted Angle	0.16 mrad
K_{eff}	4.34
Power Total	10.1 KW
Straight	Low Beta
Fan angle (V)	0.79 mrad
Fan angle (H)	0.76 mrad

Table 1 indicates the characteristics of CSX EPU [1]. Figure 4 indicates the power density (heat flux) in SRW code (using Igor-Pro) for synchrotron radiation, on the wall of the vacuum chamber, using a 0.2 mrad mis-steer.

Content from this work may be used under the terms of the CC BY 3.0 licence (© 2016). Any distribution of this work must maintain attribution to the author(s), title of the work, publisher, and DOI.

ISBN: 978-3-95450-188-5 doi:10.18429/JACoW-MEDSI2016-TUPE04

Content from this work may be used under the terms of the CC BY 3.0 licence (© 2016). Any distribution of this work must maintain attribution to the author(s), title of the work, publisher, and DOI.

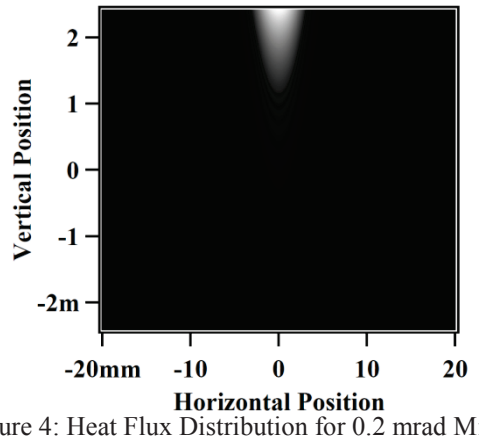


Figure 4: Heat Flux Distribution for 0.2 mrad Mis-steer.

This was the maximum allowable beam-mis-steer angle proposed, before active interlock gets activated and dumps the beam. Figure 5 indicates the heat flux distribution for the 0.2 mrad beam mis-steer [1].

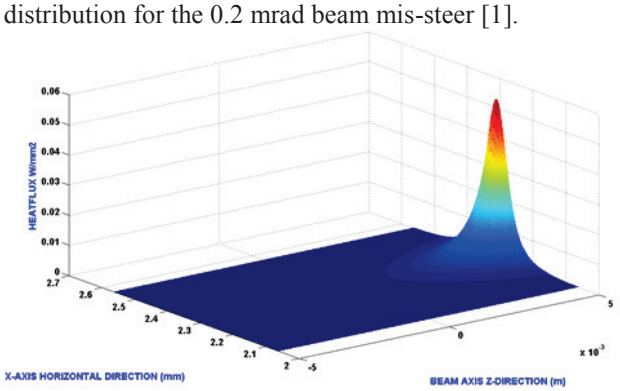


Figure 5: CSX EPU Heat Load for 0.2 mrad beam mis-steer.

After measuring the temperature on the vacuum chamber and correlating it to the FEA analysis, the SRW code was run for a mis-steer angle of 0.25 mrad and beam offset of 1.5 mm. In order to run this case, the active interlocks installed in the NSLS-II ring at the CSX EPU straight section would have to be de-activated.

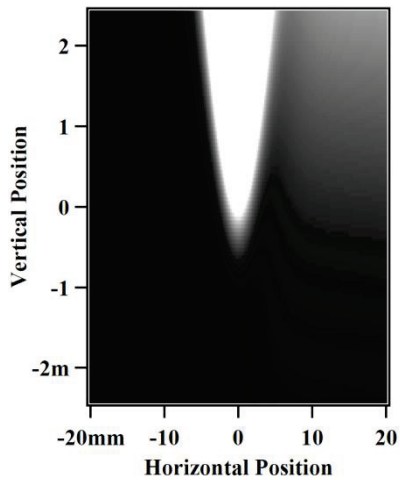


Figure 6: Heat Flux Distribution for 0.25 mrad Mis-steer and 1.5 mm Offset.

FEA ANALYSIS

The chamber was defeatured to improve the mesh quality. The devices are not centered at the center of the straight section. The upstream device is 1.125 meters upstream of the center of the straight and downstream devices is 1.2 meters downstream of the center of straight. Using SRW the heat flux distribution on the walls of the vacuum chamber was calculated. As indicated in Figure 2, the chamber minimum aperture is 8 mm, with the wall thickness of 0.95 mm. FEA was conducted using Ansys 16.2. Figure 7 indicates the temperature distribution on the Aluminum vacuum chamber for this case. The Ring temperature is 25.56 degree C. As indicated in figure 7, the maximum temperature on the walls was 25.8 degree C. A rise of approximately 0.4 degree was determined on the vacuum chamber as per FEA analysis.

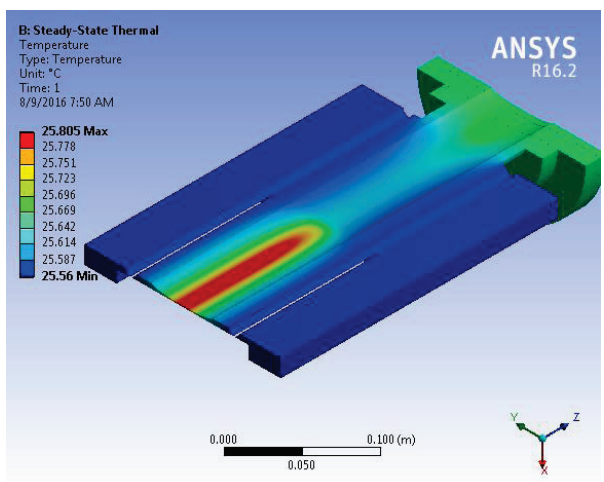


Figure 7: Thermal Analysis of the vacuum chamber for 0.2 mrad mis-steer.

ISBN: 978-3-95450-188-5 doi:10.18429/JACoW-MEDSI2016-TUPE04

For a 0.25 mrad beam mis-steer, along with a 1.5 mm offset, the temperature distribution, calculated as per FEA analysis was 128 degree C., as indicated in figure 8.

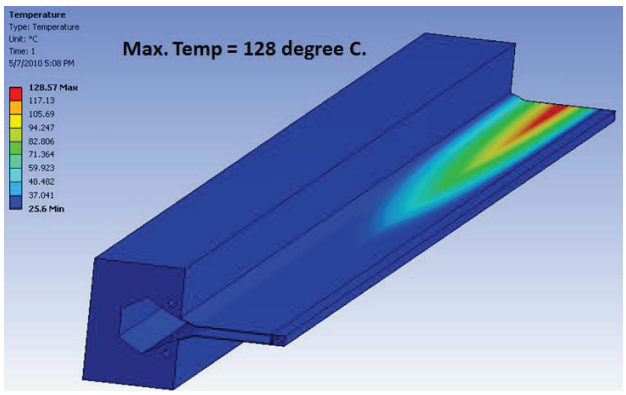


Figure 8: Temperature Distribution for 0.25 mrad Mis-steer and 1.5 mm offset.

MEASUREMENTS

RTD's and thermal sensitive cameras were set to determine the correlation of the FEA results with the vacuum chamber temperature measurements. There was a spike of about 0.125 degree C in the measured value. Since the RTD's were attached on the vacuum chamber wall away from the actual hot spot, the peak temperatures were not captured. In future we intend to conduct physical measurements on the CSX EPU vacuum chamber for the 0.25 mrad beam mis-steer and 1.5 mm beam offset. The heat flux distribution for a 0.25 mrad beam mis-steer and 1.5 mm offset is indicated in figure 6. We intend to attach RTD's at the locations where the hot spots were indicated in the FEA analysis as indicated in Figure 8 and compare analytical and practical results.

ACKNOWLEDGEMENTS

The authors would like to thank S. Sharma, F. DePaola, Mark Breitfeller, for their help and insight.

REFERENCES

[1] C. Kitegi, et al, "Progress of the coherent soft xray straight section layout at NSLS-II", IPAC'11.
[2] J. Skaritka, et al, "The Design and Construction of the NSLS II Magnets", MO6PFP008, PAC '09.

Content from this work may be used under the terms of the CC BY 3.0 licence (© 2016). Any distribution of this work must maintain attribution to the author(s), title of the work, publisher, and DOI.

ISBN: 978-3-95450-188-5 doi:10.18429/JACoW-MEDSI2016-TUPE05

Content from this work may be used under the terms of the CC BY 3.0 licence (© 2016). Any distribution of this work must maintain attribution to the author(s), title of the work, publisher, and DOI.

NUMERICAL SIMULATION OF THE ALBA SYNCHROTRON LIGHT SOURCE COOLING SYSTEM RESPONSE FOR FAILURE PREVENTION

X. Escaler*, Universitat Politècnica de Catalunya, Barcelona, Spain
J.J. Casas†, C. Colldelram‡, M. Quispe§, M. Prieto#, ALBA Synchrotron Light Source, Cerdanyola del Vallés, Spain

Abstract

The ALBA Synchrotron Light Source cooling system is designed with a common return pipe that interconnects the four consumption rings. Such configuration is believed to compromise its optimal operation. To understand its thermo-fluid dynamic behaviour, a detailed 1D model has been built comprising all the components such as the pipes, fittings, bends, valves, pumping stations, heat exchangers and so on, and the various regulation mechanisms. Preliminarily, the model results in steady state operating conditions have been compared with experimental measurements and the maximum deviations have been found below 13%. Then, a series of transient numerical simulations have been carried out to determine the system response. Specifically, effects of the blockage and leakage of a consumption line as well as the increase and decrease of heat duty for the tunnel rings have been investigated. As a result, the stability of the system has been evaluated and the operational limits have been estimated in front of hydraulic and thermal load variations. Moreover, particular behaviours have been identified which can be used to design monitoring and control strategies to prevent unexpected failures.

INTRODUCTION

The ALBA Synchrotron Light Source cooling system presents a common return pipe that interconnects the four consumption rings as outlined in Fig. 1. This design configuration introduces complexity to the system behaviour because strong interdependency among them exists.

As clearly exposed by Swetin [1], it is imperative that water flow and temperature are both maintained with a high degree of reliability because most accelerator components are interlocked. In particular, it is necessary to understand the system behaviour when facing typical piping problems like blockages or leakages to prevent failures. Moreover, the capacity of the system to respond against temporary changes in the required thermal loads must be checked out.

The motivation of such knowledge is to develop and apply correct monitoring and maintenance strategies to optimise system operation and reliability. It is also necessary in order to allow upgrades that improve reliability and integrate new operating parameters.

* escaler@mf.upc.edu
† jcasas@cells.es
‡ ccolldelram@cells.es
§ mquispe@cell.es
# mprieto@cells.es

Consequently, a numerical simulation appears as an economic and reliable procedure if a preliminary adjustment is carried out to guarantee the accuracy. For that purpose, the Flowmaster® software has been chosen because it has been successfully used to simulate complex fluid networks and advanced control systems as demonstrated in the work of Sprengel [2].

NUMERICAL MODEL

A complete model of the generation side of the cooling system has been built up with typical elements such as pipes, junctions, bends, transitions and valves. More particular elements are the pumps, the heat exchangers, the storage tank and the expansion tank. The consumption side, comprising the four rings, has been simplified due to its complexity to a heat exchanger component with the corresponding total heat duty. The properties of each component have been defined from information provided by the manufacturer as well as from data obtained by visual inspections and measurements in-situ. Details and images of the current model can be found in [3].

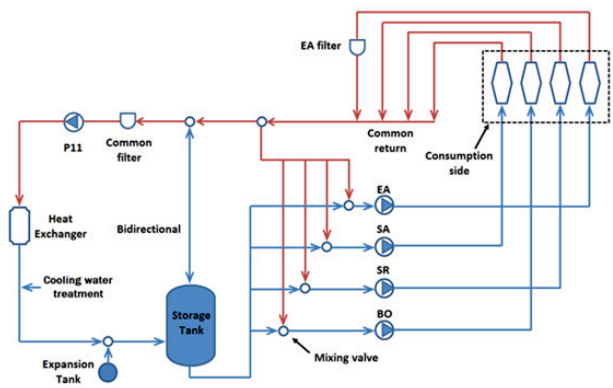


Figure 1: Outline of the ALBA cooling system.

The main regulation systems which correspond to the three-way valves (V3V's) for mixed water temperature at 23 °C, the heat exchangers (EX07) for cooling at 21 °C and the pump engine frequency converters for limiting the delivery pressures have been modelled with PID elements. The four pumping stations have been named P07, P08, P09 and P10 for the Experimental Area (EA), the Storage (SR), the Booster (BO) and the Service Area (SA) consumption rings, respectively.

In order to certify the accuracy of the model, the simulated results under steady state conditions were compared with on-site measured data indicated in Table 1. The hydraulic variables showed maximum deviations around 6 % and the thermal variables around 13%.

ISBN: 978-3-95450-188-5 doi:10.18429/JACoW-MEDSI2016-TUPE05

Table 1: Nominal Delivery Pressures, Flow Rates, Outlet Temperatures and Head Duties

Ring	P [bar]	Q [m^3/h]	To [°C]	$\dot{Q}$ [W]
BO	10.2	28.5	23.6	16559
SR	11.0	271.1	25.6	684116
SA	10.2	200.2	25.3	486354
EA	7.5	16.2	22.2	3752

SIMULATED RESPONSE

Thermal Load Shut-down

The outlet temperature of the SR has been reduced from its nominal level of 25.6 °C until 23.4 °C as if no heat duty demand existed. The evolution of the V3V's water temperatures takes 540 s to stabilize as observed in Fig. 2.

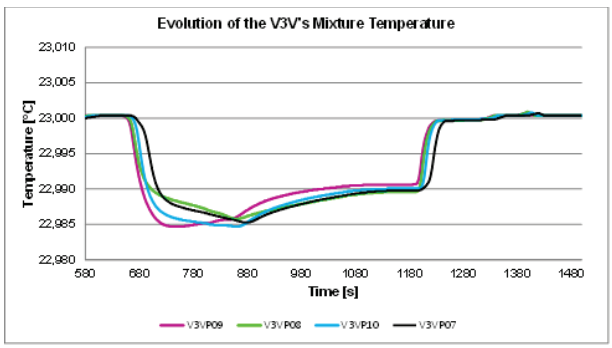


Figure 2: Temperature evolution due to the SR's thermal load shut-down.

Initially, the outlet temperature reduction takes around 80 s to affect progressively the mixed flow temperatures from the closest pumping station until the furthest one to the common return pipe. The regulation system reacts reducing the cold flow from the tank and simultaneously increasing the hotter flow from the common return. At the same time, the increased demand of water from the common return by the V3V's provokes a reduction of the suction flow rate of the pumping station P11. Such reduction is automatically compensated by an equivalent increase of flow from the storage tank to the P11 suction pipe through the bidirectional connection. As shown in Fig. 3, all the pumping stations suffer a reduction of the suction pressure.

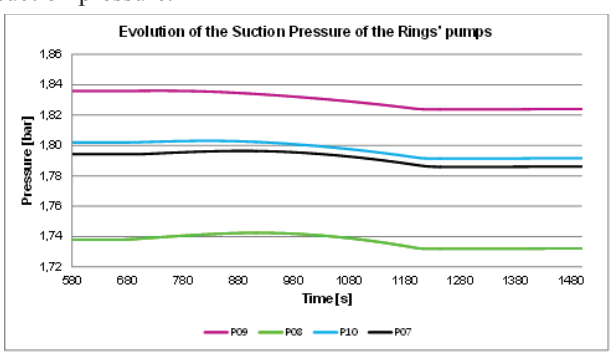


Figure 3: Pumps' suction pressures evolution during the SR's thermal load shut-down.

Thermal Load Start-up

The SR's outlet temperature has been increased progressively during 540 s from 23.4 °C at around 600 s to 25.5 °C. This transient is initially felt at around 680 s by the V3V's. As a response, the suction of cold water from the tank is increased and the one from the return flow is decreased. Consequently, the common return flow rate increases again and the flow through the bidirectional line is reduced. Regarding the suction pressures, initially they increase again but later on they show a slight decrease. At the end of the process, all of the pumping stations' suction pressures have increased significantly as shown in Fig. 4.

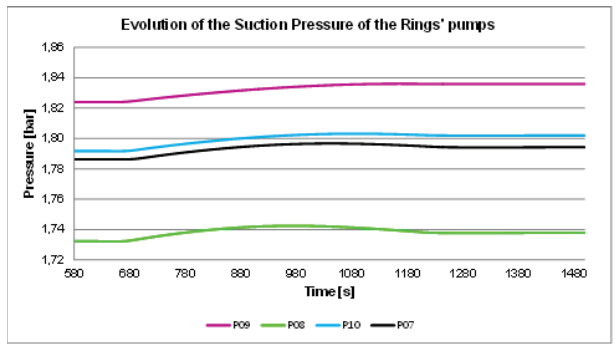


Figure 4: Pumps' suction pressures evolution during the SR's thermal load start-up.

Pipe Blockage

At constant heat duty, the SR valve has been progressively closed and thus provoking a flow rate reduction from its nominal value of 271.1 m^3/h until a 20 % reduction in approximately 190 s. As shown in Fig. 5, this procedure has been forced with two different closure laws, first fast and second slow, owing to the fact that the flow rate is not significantly reduced until the valve ratio is below 0.2.

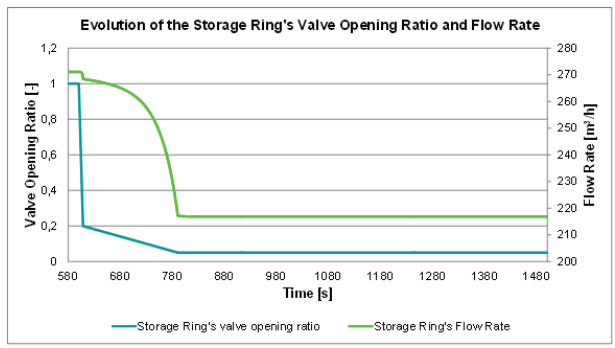


Figure 5: Evolution of the closure of the SR's outlet valve and of the resulting flow rate reduction.

The initial change of valve position provokes an immediate effect on the hydraulic parameters but the system thermal response is delayed because the consequent increase of the SR's outlet temperature takes 80 s to reach the V3V's.

Regarding the hydraulic response, a significant increase of the P08 suction pressure is provoked that is also observed in the rest of pumps but with lower amplitudes as shown in Fig. 6. Simultaneously, the temperature of the

Content from this work may be used under the terms of the CC BY 3.0 licence (© 2016). Any distribution of this work must maintain attribution to the author(s), title of the work, publisher, and DOI.

ISBN: 978-3-95450-188-5 doi:10.18429/JACoW-MEDSI2016-TUPE05

Content from this work may be used under the terms of the CC BY 3.0 licence (© 2016). Any distribution of this work must maintain attribution to the author(s), title of the work, publisher, and DOI.

mixed flow decreases because less flow arrives from the common return. As a result, the regulation starts to close the tank flow at the V3V's. At the same time, the flow from the tank towards P11 also increases to compensate the flow rate reduction at the common return pipe.

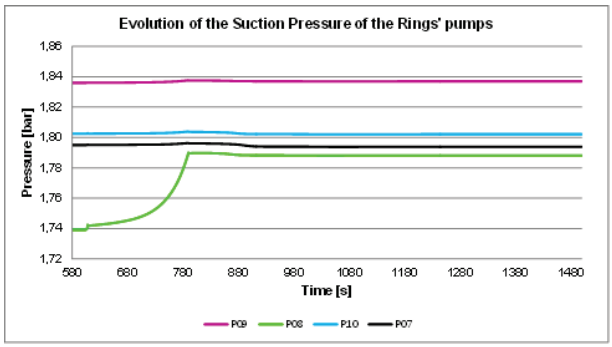


Figure 6: Pumps' suction pressures evolution during the SR's pipe blockage.

Due to the delayed thermal response, the pump suction pressures and the flow rate at the bidirectional connection decrease slighty, although they stabilize with a higher level than the initial one. Therefore, only the P08's suction pressure has increased significantly than the rest at the end.

Pipe Leakage

A leakage at the inlet of the SR that increases steadily during 400 s to reach a continuous flow rate loss of 0.8 m^3/h has been forced. Previous simulations have been carried out to determine the minimum leakage that decreases the return pressure until 1.6 bar which is the minimum admissible return pressure.

In general terms, the suction pressures at the pumping stations also decrease provoking an increase of the pumps' rotational speed as well as the rings' flowrate as shown in Fig. 7. It is observed that the P08 supplies the leaked flow which is almost entirely provided by the expansion tank. The remainder as well as the increase of the ring's flowrate is supplied by the storage tank through the mixing valves.

In addition, the ascending flow rate through the bidirectional connection decreases to compensate the increase of the ring's flow rate, which does not provoke any significant thermal transient.

Finally, when the return's pressure reaches the value of 1.6 bar the expansion tank is unable to supply the leakage flow. At this point, an external pump (P21) would start injecting water stored in an emergency reservoir.

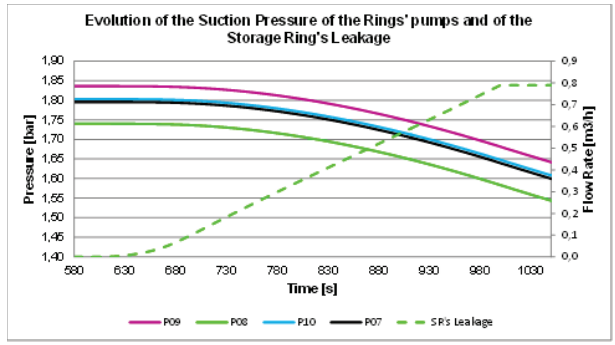


Figure 7: Pumps' suction pressures evolution during the SR's pipe leakage.

CONCLUSION

An accurate 1D model of the ALBA Synchrotron Light Source cooling system has been built that permits to evaluate the response to hydraulic or thermal transients.

The system response to a thermal load shut-down and start-up, to a ring blockage and to a ring leakage have been simulated and investigated in the SR. It has been predicted that the hydraulic transients propagate immediately through the entire network. Meanwhile, the thermal transients travel with the flow and they require a certain time to reach other zones. The common return design enhances the interaction between rings so that the transients affecting large flow rates propagate their effects to the rest of rings.

The current results indicate that thermal stability is guaranteed during thermal start-up and shut down. For hydraulic stability, it is required that the expansion tank copes with the pressure fluctuations provoked by the transients. The existence of a flow blockage or leakage at any ring can be identified from the behaviour of the pumps' suction pressure. Therefore, their monitoring and control should be used for detection and prevention of unexpected operating changes or failures in the pipes.

ACKNOWLEDGEMENT

The authors would like to acknowledge the support of the ALBA Cooling System Upgrade Team.

REFERENCES

[1] E. Swetin, M. Kirshenbaum, and C. Putnam, "Cooling Water Systems for Accelerator Components at the Advanced Photon Source", in Proc. *2nd International Workshop on Mechanical Engineering Design of Synchrotron Radiation Equipment and Instrumentation (MEDSI02)*, Argonne, Illinois, USA, 2002.

[2] J. Sprengel, "Flowmaster for Dynamic Water Network Simulations Down Under", *Engineering Edge*, vol. 3, no. 2, pp. 36-39, 2014, *http://s3.mentor.com/mechanical/engineering-edge/vol3-issue2/volume3-issue2.pdf*

[3] M. Quispe *et al.*, "ALBA cooling system upgrade: thermal hydraulic numerical simulations", in *Proc. MEDSI 2014 Conference*, Melbourne, Australia, October 2014, pp. 1-14.

ISBN: 978-3-95450-188-5 doi:10.18429/JACoW-MEDSI2016-TUPE06

THERMO-FLUID NUMERICAL SIMULATION OF THE CROTCH ABSORBERS' COOLING PINHOLES FOR ALBA STORAGE RING

X. Escaler*, V. Arbó†, Universitat Politècnica de Catalunya, Barcelona, Spain
J.J. Casas‡, C. Colldelram§, M. Quispe#, M. Prieto$, ALBA Synchrotron Light Source, Cerdanyola del Vallés, Spain

Abstract

The ALBA Synchrotron Light Facility crotch absorbers, that remove the unused storage ring radiation, incorporate an internal cooling system composed by a number of parallel pinholes and by the corresponding stainless steel inner tubes inserted into each of them. Water flows in the resulting annular sections to evacuate the total heat power. Around each inner tube, a spiral wire is fixed along the whole length with a given pitch height in order to enhance the convection heat transfer. The influence of several design parameters on the absorber thermo-fluid behaviour has been evaluated by means of the CFD software ANSYS CFX®. In particular, the wall heat transfer coefficients and the pressure losses through a single pinhole have been evaluated for a range of different flow rates and pitch heights. Moreover, some modifications of the end wall geometry have been simulated as well as the effect of reversing the flow direction inside the channels. Finally, the critical crotch absorber type 3 has also been simulated and the limiting pitch height-flow rate combinations have been found based on the available driving pressure of the cooling system.

INTRODUCTION

Most of the synchrotron radiation generated by the bending magnets in the Storage Ring (around 95%) is absorbed in the crotch absorbers. An important challenge in the engineering of the crotch absorbers is the ability to withstand the temperature and thermal stress induced by the high heat load in the component materials within the accepted safety limits. For the critical crotch absorbers the peak linear and surface power densities at normal incidence are about 64.4 W/mm and 246.2 W/mm^2 respectively, and the maximum total power is about 6.78 kW as presented in [1].

Due to this thermal load, the crotch absorber must be carefully designed to guarantee longevity and good performance. A flow of water at 23 °C circulates inside the absorber through a series of pinholes to cool it. Hence extensive Computational Fluid Dynamics (CFD) work has been conducted on various aspects of a single pinhole design such as the spiral wire pitch height, the flow rate, the direction of the flow and the end wall geometry. This work is of interest since few information is available for design, only the empirical correlations from [2] provide the wall heat transfer coefficients for a couple of pitch heights in a similar pinhole design but with different dimensions. Based on the previous results, several pinholes connected in series have also been simulated.

The current design of ALBA crotch absorbers is shown in Fig. 1. A detail of the spiral wire at the end wall and the two possible flow directions, forward and reverse, are indicated in Fig. 2.

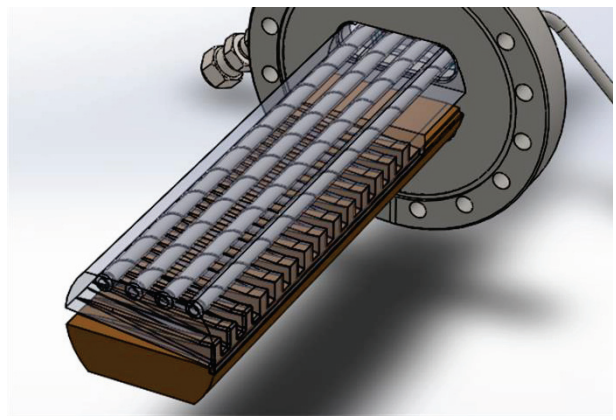


Figure 1: Transparent view of a crotch absorber to visualize the internal cooling pinholes with the spiral wire.

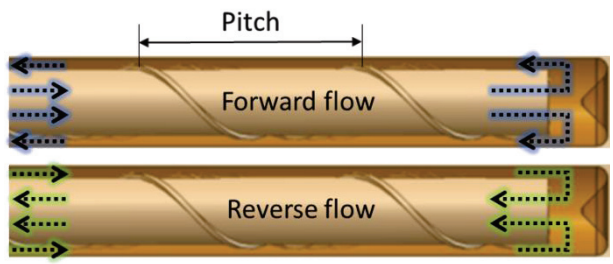


Figure 2: Pitch height of the spiral wire. Forward and reverse flow rate directions inside the pinholes.

CFD MODEL

A mesh sensitivity analysis has been carried out to identify the optimal mesh for the model. As a result, a final mesh of about 1.5 M elements with good quality has been used for a single pinhole. The total thermal load has been uniformly distributed along the contact wall surface with the fluid. At the inlet, the mass flow rate has been imposed ranging from 0.03 to 0.09 kg/s. At the outlet, the boundary condition has been set constant to a relative

* escaler@mf.upc.edu
† victorarbo@gmail.com
‡ jcasas@cells.es
§ ccolldelram@cells.es
# mquispe@cell.es
$ mprieto@cells.es

Content from this work may be used under the terms of the CC BY 3.0 licence (© 2016). Any distribution of this work must maintain attribution to the author(s), title of the work, publisher, and DOI.

ISBN: 978-3-95450-188-5 doi:10.18429/JACoW-MEDSI2016-TUPE06

Content from this work may be used under the terms of the CC BY 3.0 licence (© 2016). Any distribution of this work must maintain attribution to the author(s), title of the work, publisher, and DOI.

pressure of 0 Pa. The Shear Stress Transport (SST) turbulence model has been used.

SINGLE PINHOLE

Effect of Pitch and Flow Direction

For a fixed mass flow rate of 0.06 kg/s, the effect of increasing the pitch height from 0.005 to 0.05 m on the pressures loss and the average wall heat transfer coefficient is shown in Fig. 3 and Fig. 4, respectively. Both parameters tend to decrease as the pitch is increased. The maximum heat transfer coefficient and pressure loss are found for the minimum pitch height. For pitch heights above 0.03 m, the effects are insignificant.

In relation to the flow direction, a slightly higher heat transfer coefficient is achieved in the whole range of flow rates with the reverse sense. Moreover, the pressure losses are significantly reduced. Therefore, the global performance of the reverse flow is clearly superior to the forward flow.

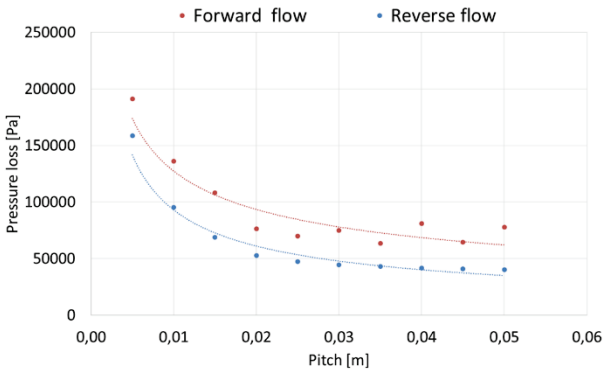


Figure 3: Pressure loss as a function of pitch height for forward and reverse flow.

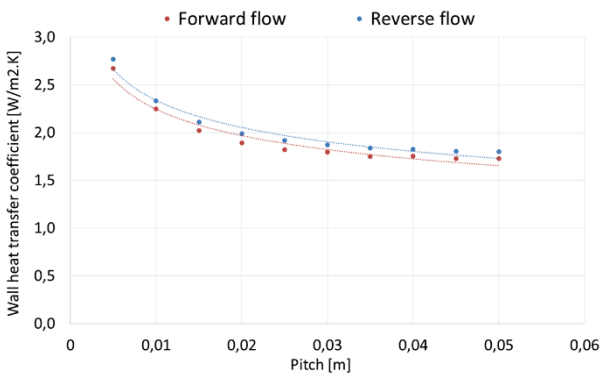


Figure 4: Wall heat transfer coefficient as a function of pitch height for forward and reverse flow.

The flow streamlines inside the pinhole for a reverse flow rate of 0.06 kg/s and a pitch height of 0.03 m are plotted in Fig. 5. The guiding effect of the spiral wire on the flow orientation is clearly observed within the annular section.

Effect of Pitch and Mass Flow Rate

The effect of increasing the forward flow rate is observed in Fig. 6 and Fig. 7 for the pressure loss and the average wall heat transfer coefficient, respectively. For the reverse flow, analogous results are obtained.

The pressure losses increase following a power law as the flow rate increases. Meanwhile, the heat transfer coefficients appear to increase linearly with the flow rate. The results obviously indicate that the maximum heat transfer coefficient is found for the highest flow rate and the minimum pitch height. For this condition, the maximum pressure loss is also found.

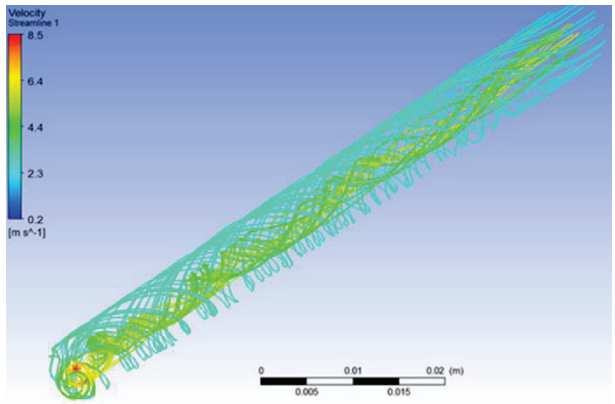


Figure 5: Flow streamlines indicating velocity magnitude.

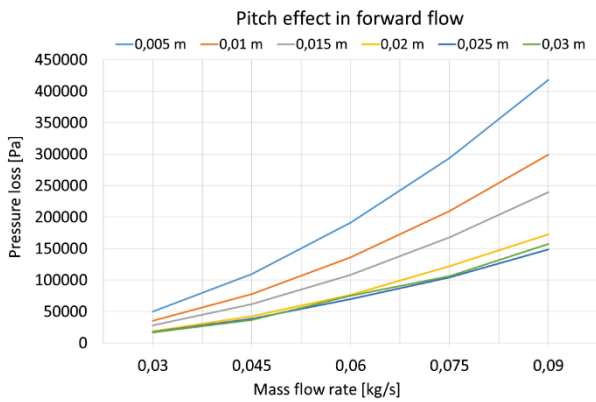


Figure 6: Pressure loss as a function of forward mass flow rate for different pitch heights.

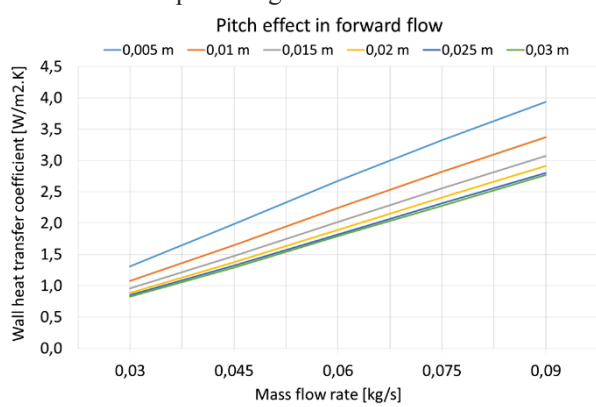


Figure 7: Wall heat transfer coefficient as a function of forward mass flow rate for different pitch heights.

ISBN: 978-3-95450-188-5 doi:10.18429/JACoW-MEDSI2016-TUPE06

Effect of end Wall Geometry and Mass Flow Rate

As it can be seen in Fig. 5, the strongest flow perturbations and maximum velocities are found at the end of the pinhole. In this location also the maximum temperatures are found as shown in Fig. 11. Consequently, a verification of the already predicted influence of the end wall geometry [1] has been carried out. The current flat wall and two cone-type configurations (inward and outward) have been simulated to determine the optimal one.

The pressure losses and the average wall heat transfer coefficients have been compared in Fig. 8 and Fig. 9, respectively, for the three geometries in the case of reverse flow and a pitch height of 0.015 m. It can be observed that the geometry change has an insignificant effect on the average heat transfer but a significant effect on the total pressure loss. The inward cone presents the minimum pressure losses for all the mass flow rates. Therefore, this wall geometry optimizes the flow 180° turnaround at the end of the pinhole.

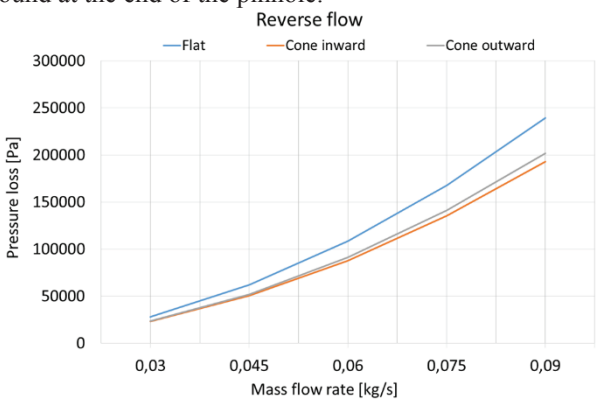


Figure 8: Pressures loss as a function of reverse mass flow rate for different end wall geometries.

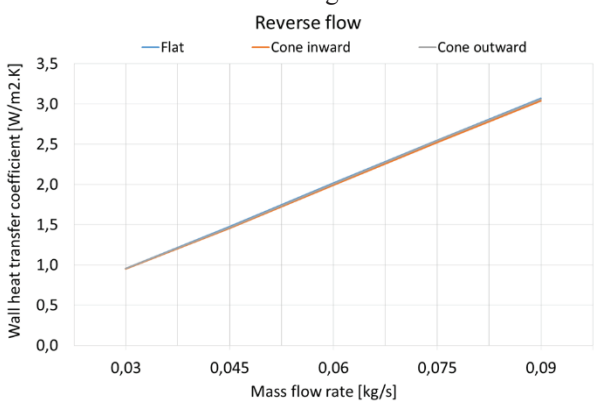


Figure 9: Wall heat transfer coefficient as a function of reverse mass flow rate for different end wall geometries.

MULTIPLE PINHOLES

To finish, the complete cooling system of a type 3 crotch absorber composed of two independent circuits with 4 pinholes each has been simulated. Given the symmetrical design of the piece, only the performance of one circuit has been considered and the results of pressure loss have been presented in Fig. 10.

The current cooling system of the Storage Ring can provide a maximum pressure level at the entrance of the crotch absorbers of about $6{\cdot}10^5$ Pa (6 bar). As a result, the unfeasible combinations of flow rate and pitch height have been shaded in Fig. 10 with red colour. Thus, only the remaining values are the possible ones to design an adequate system from the hydraulic point of view.

In Fig. 11, the wall temperature distribution indicates that maximum levels are found at the end walls of two pinholes located on the left.

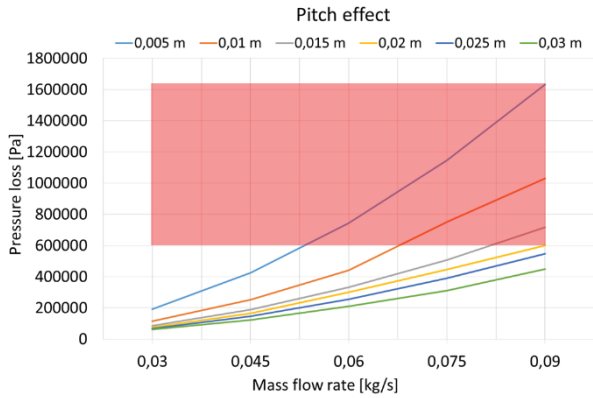


Figure 10: Pressure loss as a function of mass flow rate for different pitch heights in crotch absorber type 3. Red area conditions are not possible due to insufficient driving pressure.

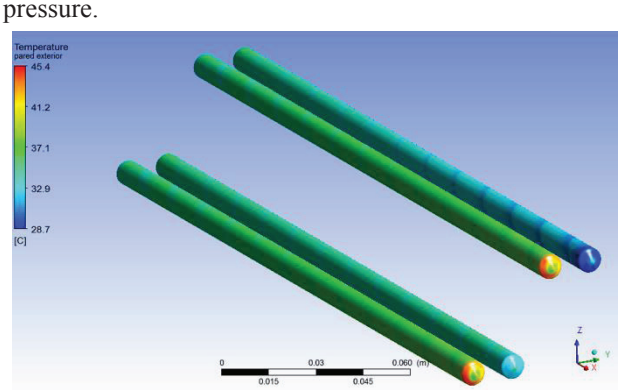


Figure 11: Wall temperature distribution on a set of 4 connected pinholes of the crotch absorber type 3.

CONCLUSION

The CFD simulation of the thermo-hydraulic behaviour of the crotch absorber's cooling pinholes has leaded to the following conclusions:

- Minimum pitch height and maximum flow rate maximizes the convective heat transfer but also requires the highest driving pressure.
- Reverse flow performance is better than forward one.
- Optimal end wall geometry is outward cone type.
- SR available driving pressure limits the choice of design parameters.

Content from this work may be used under the terms of the CC BY 3.0 licence (© 2016). Any distribution of this work must maintain attribution to the author(s), title of the work, publisher, and DOI.

ISBN: 978-3-95450-188-5 doi:10.18429/JACoW-MEDSI2016-TUPE06

Content from this work may be used under the terms of the CC BY 3.0 licence (© 2016). Any distribution of this work must maintain attribution to the author(s), title of the work, publisher, and DOI.

REFERENCES

[1] M. Quispe *et al.*, "Development of the crotch absorbers for ALBA storage ring", in *Proc. MEDSI 2008 Conference*, Saskatoon, Saskatchewan, Canada, June 2008, pp. 1-15.

[2] G. Heidenreich and L. Schulz (PSI), private communication.

ISBN: 978-3-95450-188-5 doi:10.18429/JACoW-MEDSI2016-TUPE08

FINITE ELEMENT ANALYSIS OF A PHOTON ABSORBER BASED ON VOLUMETRIC ABSORPTION OF THE PHOTON BEAM

K. J. Suthar* and P. Den Hartog, Advanced Photon Source Engineering Support Division, Argonne National Laboratory, Lemont, USA

Abstract

A photon absorber is a device used to protect vacuum chambers and other hardware from synchrotron radiation by intercepting unwanted radiation, converting its energy to heat, and then removing that heat. Design of a photon absorber requires careful consideration of the high temperatures and steep thermal gradients that are possible with highly localized absorption of these photons. For next-generation machines, like the multi-bend achromat envisioned for the APS Upgrade (APS-U), a designer is likely to be simultaneously faced with more intense synchrotron radiation beams, more limited available space, and closer proximity to the particle beam than have been designed for in the past. Volumetric absorption of synchrotron radiation, which makes use of materials that are semi-transparent to x-rays, is an attractive option which gives the designer greater freedom by spreading the heat load due to the absorbed photons. Volumetric absorption may also help to reduce residual gas pressures in a vacuum system by reducing the photon-stimulated desorption that results from photons reflected by the incident absorber surface. This paper describes simulations which were performed to evaluate the benefit of utilizing volumetric absorption for a conceptual "crotch" photon absorber for the APS Upgrade (APS-U), so-called because of its location in the vacuum system where the chamber is forked to permit x-ray extraction. Results of these simulations show clear benefits of volumetric photon absorption and suggest that such an approach may help to substantially relax constraints on the size, shape, and materials used for such absorbers.

VOLUMETRIC ABSORPTION

Two crotch absorbers are planned for each APS-U storage ring sector. These are expected to intercept roughly 1-3 kW each with power densities, as would be intercepted on a normally-intercepting surface, that approach 100 watts/mm^2. Conventionally, photon absorbers are made using high opacity and high thermal conductivity materials such as copper and GlidCop™ which cause the heat load to be concentrated on the absorber surfaces. A designer typically struggles with reducing the incident angle of those surfaces and increasing the efficiency of cooling to those surfaces as much as possible to manage the thermal stresses that result. In addition, the high reflectivity of these materials to x-rays, coupled with the grazing angles, causes scattering of a considerable fraction of incident photons which can then be a significant driver of photon-stimulated gas desorption. Finally, the high water flow rates required to maintain surface temperatures at safe levels can introduce vibration that may upset critical, precisely-aligned hardware in the accelerator.

A potential solution is the use of an absorber which is semi-transparent to incident x-rays. Such an arrangement allows the heat load into the absorber to be gradually deposited in the body of the component, reducing the associated thermal stresses. In doing so, a designer can find a solution which is more compact than would otherwise be possible. Another approach is to combine an opaque absorbing body with a more transparent, but thermally conductive, material. Doing so similarly limits the resulting temperature rise of absorber materials by allowing the heat generated on the opaque body to be more effectively conducted away.

Such approaches have three distinct advantages over a conventional, surface-absorbing design:

1. The material temperatures and the thermal gradients may be reduced, reducing potentially-damaging thermal stresses, fatigue, and structural softening.
2. Reflection of photons may be reduced, thus reducing the outgassing associated with photon-stimulated desorption.
3. Heat transfer may be more efficient due to overall greater proximity of cooling to the heat load, relaxing water flow requirements.

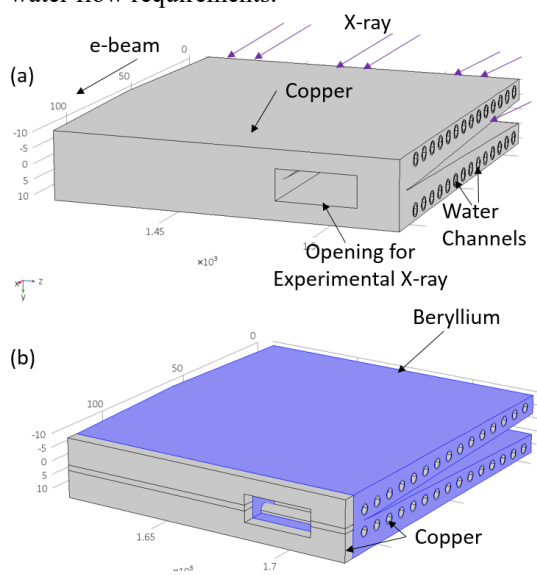


Figure 1: Conceptual APS-U crotch absorber options (a) copper body design (b) beryllium and copper design.

* Corresponding author's email: suthar@anl.gov

Content from this work may be used under the terms of the CC BY 3.0 licence (© 2016). Any distribution of this work must maintain attribution to the author(s), title of the work, publisher, and DOI.

ISBN: 978-3-95450-188-5 doi:10.18429/JACoW-MEDSI2016-TUPE08

Content from this work may be used under the terms of the CC BY 3.0 licence (© 2016). Any distribution of this work must maintain attribution to the author(s), title of the work, publisher, and DOI.

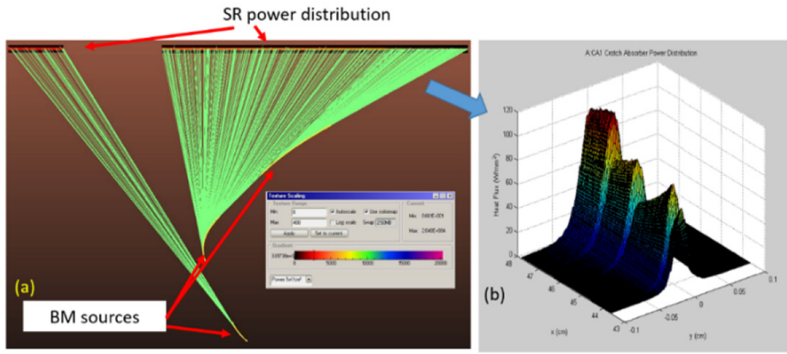


Figure 2: Power profile distribution (a) SynRad trajectories and power profile for B crotch absorber for APS-U project (b) power distribution and profile.

THEORY

The physics of the absorption of energetic photons in solids is fairly straightforward and is primarily associated with the number of electrons that can accept the required exchange of energy from the photons. The electrons that are free or easily dislocated from the orbit most readily satisfy this criterion. The electron concentration in two materials can be estimated from the atomic number. Precise tabulated data for different materials is also available over a wide range of photon energies.

The incident photon beam loses energy when interacting with material. The change in the incident beam's energy can be estimated using the following relation:

$$dI(x,y,z) = -I(y,z) \cdot n \cdot \sigma \cdot dx \text{ [1]}$$

Where, dI(x, y, z) = the change in absorbed intensity
I(y, z) = the initial intensity, SynRad output
n = the number of atoms/cm^3
σ = a proportionality constant
dz = the incremental thickness of material from surface into the body of the absorber
Here x, and y are transverse direction while z is direction along the beam path.

The combination of the number of atoms per cubic centimetre and the proportionality constant is the linear attenuation coefficient (μ). Therefore, the equation becomes:

$$I(x,y,z) = I_0(y,z) \cdot e^{-\mu \cdot x}$$

The linear attenuation coefficient (μ) describes the fraction of a photon beam that is absorbed or scattered within the thickness of the absorber.

SIMULATION MODEL

As shown in Fig. 1 (a), the crotch absorber envisioned for the APS-U consists of two distinct features: an opening to allow synchrotron radiation passage to the experimental beamline and a central V-shape opening which captures the unwanted radiation on the absorber. Figure 2 shows the expected power distribution profile as computed with SynRad, a computer program developed at CERN [2]. The total power deposited on the crotch absorber is approximately 3 kW.

Dissipation of power in the absorber was determined using the theory described above. A thermal mechanical simulation was then performed using COMSOL Multiphysics [3]. Figure 3 shows the analysis process.

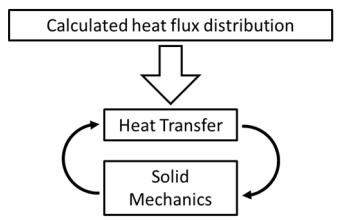


Figure 3: Flow chart of solution strategy.

For the baseline study, copper was used as the body material. The water channel is assumed to be simply machined into the body. For the volumetric absorber design beryllium was assumed for the body material and copper for lining of the water channels. In addition, a 5 mm thick copper plate was modelled on the back side of this photon absorber to capture any x-rays not absorbed by the beryllium body and copper water channels. A list of the thermal and mechanical properties assumed in the simulations are shown in Table 1.

Table 1: Assumed Material Properties for FEA

Material	**Attenuation Length @10keV**[4]	**Thermal Conductivity** [5]
Be	10,000 μm	216 W/m/K
Cu	5-30 μm	385 W/m/K

RESULTS AND DISCUSSION

Calculations of the dissipated power were as expected. The attenuation length of copper is 5- 30 microns at relevant photon energies. As a consequence, photon absorption in copper was found to occur primarily at the surface. Beryllium has a much longer attenuation length at these photon energies, roughly 10 mm, so what absorption occurs in beryllium was found to be much more distributed though the bulk of the material.

ISBN: 978-3-95450-188-5 doi:10.18429/JACoW-MEDSI2016-TUPE08

In the baseline design option, roughly 1.2 kW of power was found to be absorbed at the junction of the two halves of the V-shaped notch, while the rest was absorbed on the intercepting surface. Similarly, 1.2 kW of power was found to be absorbed in the copper back plate assumed in the volumetric absorber design.

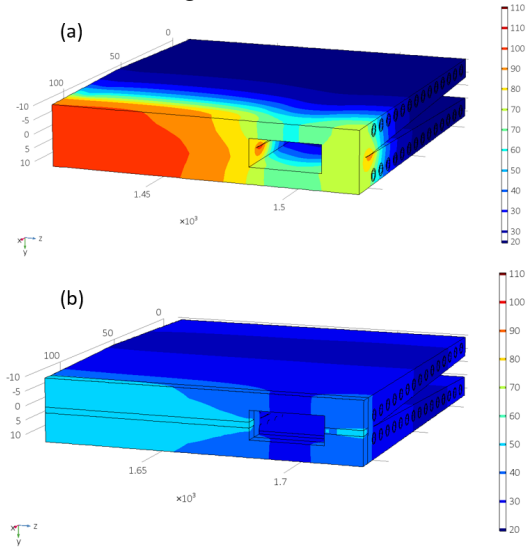


Figure 4: Temperature distribution on exterior surfaces (˚C) for (a) simple copper body design (b) beryllium and copper body design.

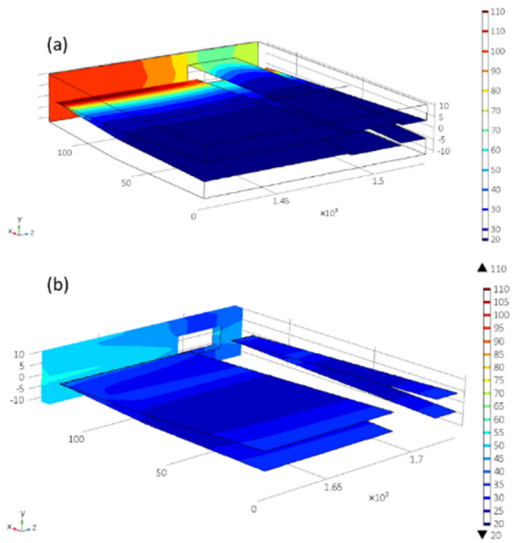


Figure 5: Temperature profile (˚C) on surface where x-rays enter the absorber for (a) simple copper body design (b) beryllium and copper body design.

The maximum temperature observed in the baseline (all-copper) design occurred at the intercepting surface where the incident photon intensity was maximum. The maximum temperature indicated was 110 ˚C. Figure 4 shows a comparison of the temperature profiles predicted for each of the cases. In the case of the volumetric absorber design, the maximum temperature occurs at the interface of the copper surface in the copper backing plate where photon intensity was maximum (see Fig. 5). The maximum temperature in case of volumetric absorber design was found to be 56 ˚C.

One sees from these results that the basic difference between the baseline design and the volumetric absorber design is the proximity of the water mass flow to the areas where heat input is the greatest. In the baseline design absorption of radiation primarily occurs at a distance of roughly 5 mm from the cooling water. In the case of the volumetric absorber design, the distance is approximately 2 mm. Structural deformation was also found to be much lower in the volumetric absorber relative to the baseline design (Fig. 6).

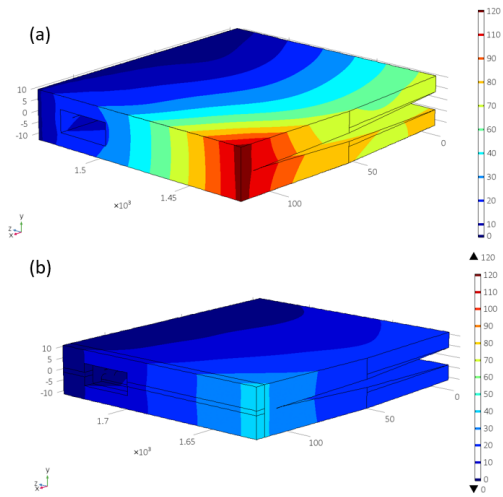


Figure 6: Deformation (µm) of (a) simple copper body design (b) beryllium and copper body design.

CONCLUSION

A simulation of a conceptual volumetric crotch absorber for the APS-U showed substantial reduction in developed material temperatures compared with a simple, all-copper baseline design. Temperature rise in the volumetric absorber was found to be 56 ˚C, which is 50 ˚C less than what was found for the baseline design. Moreover, the thermal gradient found for the volumetric absorber was much less steep, indicating substantially reduced thermal stresses. These improvements clearly suggest that employing volumetric photon absorbers can help to relax design constraints associated with the size, shape, and materials these critical components for next generation accelerators.

ACKNOWLEDGMENT

This research used resources of the Advanced Photon Source, a U.S. Department of Energy (DOE) Office of Science User Facility operated for the DOE Office of Science by Argonne National Laboratory under Contract No. DE-AC02-06CH11357. The authors would like to thank Dr. John Noonan, Benjamin Stillwell, and Dr. Branislav Brajuskovic for valuable discussions and Jason Carter for providing SynRad-calculated radiation profiles.

Content from this work may be used under the terms of the CC BY 3.0 licence (© 2016). Any distribution of this work must maintain attribution to the author(s), title of the work, publisher, and DOI.

ISBN: 978-3-95450-188-5 doi:10.18429/JACoW-MEDSI2016-TUPE08

Content from this work may be used under the terms of the CC BY 3.0 licence (© 2016). Any distribution of this work must maintain attribution to the author(s), title of the work, publisher, and DOI.

REFERENCES

[1]. G.V. Pavlinsky, "Fundamentals of X-ray Physics". 2008: *Cambridge International Science Pub*.
[2]. R. Kersevan, "A Monte-Carlo Simulator package developed at CERN", CERN 2015.
[3]. COMSOL, *COMSOL Multiphysics,* http://www.comsol.com/. 2015.
[4]. CXRO. *Optical constants*. 2016 [cited 2016 9/6/2016]; calculator]. Available from: http://henke.lbl.gov/optical_constants/.
[5]. Matweb_LLC. *Material property database*. 2016 [cited 2016 9/6/2016]; Available from: http://www.matweb.com/

ISBN: 978-3-95450-188-5 doi:10.18429/JACoW-MEDSI2016-TUPE09

THERMO-FLUID STUDY OF THE UPC RACE-TRACK MICROTRON COOLING SYSTEM*

X. Escaler†, Departament de Mecànica de Fluids, UPC, Barcelona, Spain
Yu.A. Kubyshin, V. Blasco, J.A. Romero, A. Sánchez, Institut de Tècniques Energètiques, UPC, Barcelona, Spain,
M. Prieto, ALBA Synchrotron Light Source, Cerdanyola del Vallès, Barcelona, Spain
V.I. Shvedunov, Skobeltsyn, Institute of Nuclear Physics, Moscow State University, Moscow, Russia

Abstract

The cooling system of the race-track microtron (RTM), which is under construction at the Universitat Politècnica de Catalunya (UPC), has been simulated by means of a computational fluid dynamics (CFD) software. The hydraulic and thermal performance of the system for various operation conditions has been studied. Firstly, the hydraulic model has been validated by comparison with experimental measurements at different flow rates. Then, the cooling fluid temperatures and the pressure losses of the system have been determined and the capacity of the current design to remove the generated heat at nominal power has been confirmed. Finally, the maximum and average wall temperatures and heat transfer coefficients inside the accelerating structure have been calculated. These results have allowed us to localize sections of the cooling system with a low convection due to detached flows where, therefore, a risk of zones of high temperatures exists. An optimization of the cooling circuit with the aim to reduce such high temperature zones has been proposed.

12 MEV RACE-TRACK MICROTRON AND ITS COOLING SYSTEM

The UPC in collaboration with the Skobeltsyn Institute of Nuclear Physics of the Moscow State University and CIEMAT (Madrid) is building a compact electron accelerator of race-track microtron (RTM) type with the maximal beam energy 12 MeV. Its main envisaged application is Intraoperative Radiation Therapy. Modification of this low power consumption machine can be used also for cargo inspection and industrial radiography. The design of the accelerator is described in [1], the course of its systems development was reported in a number of papers, see for example [2-4]. Currently the RTM is at the final phase of its construction.

The UPC 12 MeV RTM is a pulsed accelerator with the output beam energies 6, 8, 10 and 12 MeV, energy gain per turn equal to 2 MeV approximately and low average current, of the order of 10-100 nA. The electron beam is produced in a module called accelerator head, its 3D view is given in Fig. 1 where main elements, like 180º bending magnets, usually called end magnets, and the accelerating structure (linac) are shown. All magnets are permanent magnets and therefore do not consume power. These elements are fixed on a rigid platform placed inside a vacuum chamber.

The cooling of the RTM is provided by a chiller that comprises a positive displacement pump with a discharge pressure limited to around $6.8 \cdot 10^5$ Pa (6.8 bar) that can be regulated to reach a maximum flow rate of $2.83 \cdot 10^{-4}$ m^3/s if necessary. The main function of the RTM cooling system is to provide a safe and stable operation of all accelerator systems, in particular guarantee a temperature stability of ±1°C in the end magnets and linac. In addition, at the stationary regime of RTM operation the temperature differences between different parts of the end magnets and linac must not exceed the same limit of ±1°C.

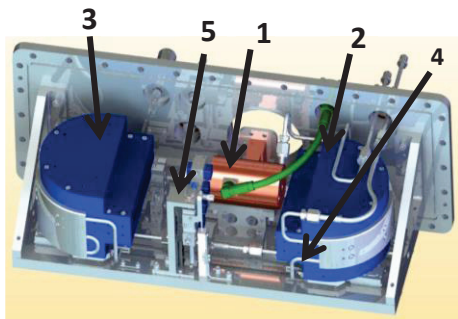


Figure 1: 3D view of the accelerator head of the 12 MeV RTM. The numbered elements are: 1- accelerating structure (linac), 2 and 3 – end magnets M1 and M2, respectively, 4 – cooling tube, 5 – extraction dipoles.

In the present paper we study the performance of the cooling system of the RTM accelerator head. Chilled distilled water is sent through the inlet collector and inlet feedthrough to the vacuum box. Firstly, the cooling circuit, which is a tube of 4 mm internal diameter, passes along the rear walls of the two end magnets, M1 and M2, as one can see in Fig. 1. The tube is partially covered with jackets in order to achieve a good thermal contact with the magnet bodies. After the M2 magnet the cooling tube is connected to the inlet of the linac which has four 4 mm diameter longitudinal cooling channels connected in series. Finally, the outlet of the linac is connected to the output feedthrough and then to the output collector. The connecting tubes are made of stainless steel and also have the 4 mm internal diameter. The total length of the cooling channels and connecting tubes inside the vacuum chamber is about 2 m.

* Work supported by the 2014 SGR846 of AGAUR (Generalitat de Catalunya)
† escaler@mf.upc.edu

Content from this work may be used under the terms of the CC BY 3.0 licence (© 2016). Any distribution of this work must maintain attribution to the author(s), title of the work, publisher, and DOI.

ISBN: 978-3-95450-188-5 doi:10.18429/JACoW-MEDSI2016-TUPE09

Content from this work may be used under the terms of the CC BY 3.0 licence (© 2016). Any distribution of this work must maintain attribution to the author(s), title of the work, publisher, and DOI.

According to the RTM Technical Design Report [5] the maximum total power which must be removed by the cooling system from all RTM systems is about 4 kW, in particular approximately 1 kW is dissipated in the linac and 0.01 kW in the end magnets. The nominal water flow rate was fixed at $\dot{m} = 0.05$ kg/s. The accelerating structure is normal conducting, thus the dissipated heat power is due to the currents which are induced in its copper walls by the magnetic component of the RF electromagnetic wave. The magnets are permanent and the dissipated power is due to beam losses only.

The accelerating structure consists of four accelerating and three coupling resonance cavities. According to calculations of the detailed distribution of the RF power losses in the cavity walls carried out in Ref. [6] the RF power dissipated in the 1st, 2nd, 3rd and 4th linac segments is equal to 189.5 W, 273.7 W, 273.7 W and 263.1 W, respectively. Each segment comprises the corresponding resonant cavity, in addition the 1st and 4th segments contain annular passages from one cooling channel to another.

As a part of preliminary tests of RTM systems, measurements of the pressure loss in the cooling system of the RTM accelerator head without RF power dissipation in the linac were carried out. For this the inlet and outlet feedthroughs were connected to the chiller and two pressure sensors (model PT5404 from ifm®) and a flowmeter (model PF3W520-F03-1-R from SCM®) between the chiller and the vacuum chamber were mounted. During the measurements the data from the pressure sensors was read and processed with a 10 bits Arduino® Ethernet board. The measured values of the pressure loss for different flow rates are given in Fig. 2.

CFD MODEL AND HYDRAULIC PERFORMANCE

The CFD model of the RTM cooling system that comprises the fluid domain (see Fig. 3) has been developed using the ANSYS CFX® version 14.5 [7]. The annular passages connecting the cooling channels in the 1st and 4th segments are clearly seen in Fig. 3. All no slip pipe walls were considered as adiabatic with the exception of those which are in contact with the end magnets or represent the linac cooling channels. In solving the energy transport equation the viscous dissipation was not taken into account because the friction effect is negligible in comparison with the temperature increase due to heat transfer from the solid surface towards the moving fluid. In the simulations the inlet flow condition was set as a function of the distilled water flow rate at $T_{inlet} = 10°C$ and the outlet flow condition was set to the average static pressure $p_{out} = 0$ Pa in relative terms. The Shear Stress Transport (SST) turbulence model was used [8]. After a preliminary model sensitivity analysis it was decided to limit the size of the mesh by about 6.2M elements.

Using this model we performed simulations of the total pressure loss Δp in the system in the range from a minimal mass flow rate of $\dot{m} = 0.042$ kg/s until a maximum one of $\dot{m} = 0.075$ kg/s. For the considered average flow velocities (from V=3.3 m/s to V=6.0 m/s), the Reynolds number varies from Re=10137 to Re=18247, so that the water flow is always turbulent.

The obtained results indicate that Δp increases with the flow rate, as it is shown on the plot in Fig. 2, in very good accordance with the experimental results. For the maximal flow rate, the pressure loss is $\Delta p = 6.4 \cdot 10^5$ Pa. Since the location of the pressure sensors was not exactly at the inlet and outlet of the cooling system the measured values have been corrected correspondingly. The error bars correspond to the ± 10% interval around the corrected measured values.

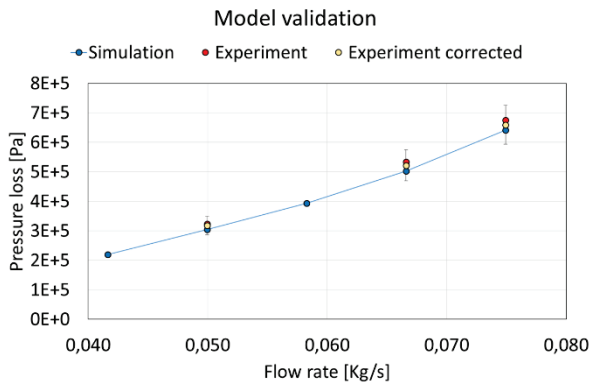


Figure 2: Pressure loss in the cooling system as a function of the flow rate. The continuous curve fits the simulation results indicated with blue dots. Red dots are measured values and yellow dots are corrected measured values.

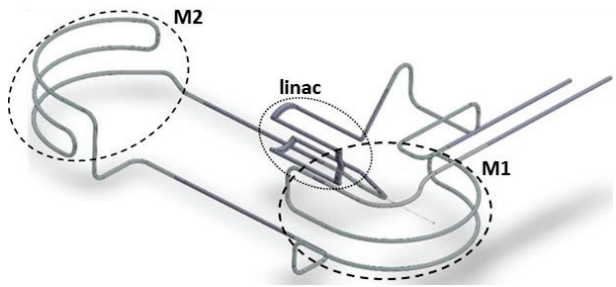


Figure 3: Fluid domain representing the internal diameter of the water piping.

THERMAL PERFORMANCE

In the thermo-fluid analysis of the cooling system the distribution of the heat power transfer specified in above was used. We performed numerical simulations of the following charcteristics:

- Flow temperature increase along the cooling circuit, $\Delta T = T_{outlet} - T_{inlet}$.
- Pipe wall temperature distributions, in particular the average and maximum values, T_{av} and T_{max}, at each linac segment.
- Pipe wall heat transfer coefficients, in particular the average and maximum values, h_{av} and h_{max}.
- Flow velocity distributions.
- Streamlines of the water flow inside the linac channels.

ISBN: 978-3-95450-188-5 doi:10.18429/JACoW-MEDSI2016-TUPE09

Some of these results are given in Table 1. The maximum wall temperatures T_{max} are always in the 1st segment, in the rest of the segments the temperatures are very close between them and are considerably lower than in the 1st segment. As far as the average wall temperature T_{av} is concerned, for any flow rate its maximum value is in the 3rd segment and the minimum value is in the 1st one. The interval of values of the average temperatures in the linac segments is approximately 1.5° C at the minimum mass flow rate $\dot{m} = 0.042$ kg/s and is about 0.7° C at the maximum flow rate $\dot{m} = 0.075$ kg/s .

Table 1: Flow Temperature Increase ΔT, Maximum Wall Temperatures T_{max}, and Average Heat Transfer Coefficients h_{av} for Different Water Flow Rates

$\dot{m}$ [kg/s]	ΔT_{sim} [°C]	T_{max} [°C]	h_{av} [W/(m^{2}K)]
0.042	5.78	26.1	5832
0.050	4.82	22.3	6711
0.058	4.15	20.1	7556
0.067	3.64	19.8	8392
0.075	3.25	18.4	9129

The explanation of the fact that the maximum wall temperatures are in the 1st linac segment, even though the heat power generated there is considerably lower than in the rest of the segments, can be deduced from the plots in Fig. 4 where water streamlines through the conduits are plotted being colored as a function of the flow velocity in Fig. 4a and the flow temperature in Fig. 4b. Due to the abrupt change of direction, the flow experiences a boundary layer detachment in the 1st segment entering from the circular conduit into the annular passage and making a 90° turn. Thus, a region with stagnant water and very low velocity in the region close to the wall is created and, consequently, the local convective heat transfer reduces significantly. Such behavior takes place in the two annular connections in the 1st segment and also in the connection path in the 4th segment. As a result, regions with defective flow velocities below 4 m/s appear in these segments.

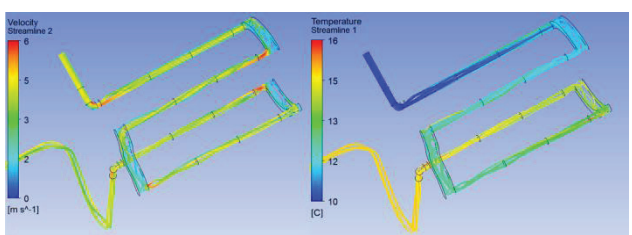


Figure 4: Streamlines of the water flow inside the linac conduits colored as a function of the velocity (a) and the temperature (b).

DISCUSSION OF THE RESULTS AND CONCLUSIONS

We studied the hydraulic and thermal performance of the cooling system of the accelerator head of the UPC 12 MeV RTM. Numerical simulations of the cooling system with the CFD code were performed. For this a 3D model representing the fluid domain with a mesh with 6.2M elements was developed. The accuracy of the model was checked for a few values of the mass flow rate by comparison of the pressure loss simulation results with the measured ones, and quite a good agreement was found.

The results of the simulations validate the cooling system design. We obtained that the difference of the average temperatures between the linac segments is below 1° C at the maximum flow rate $\dot{m} = 0.075$ kg/s. Thus, the RTM design requirement, that the temperature difference between different segments of the linac does not exceed the limit of ±1° C, is met for the maximal flow rate only.

The study of the water streamlines showed that the appearance of regions with high temperatures in the 1st linac segment is due to boundary layer detachments of the flow and low flow velocities there. These effects are caused by 90° abrupt bending of the conduits inside the linac in this segment. The temperature in this region can be reduced by modifying the cooling channel geometry at the transition between the circular pipes and the annular arms, in particular by filleting the two surfaces at their contact edges in order to create a rounded smooth transition that would help the flow to turn without detaching from the surfaces. This improvement of the cooling pipes geometry can be implemented in a future upgrade of the RTM design.

REFERENCES

[1] A.P. Poseryaev, M.F. Ballester, Yu.A. Kubyshin, V.I. Shvedunov, "Design of 12 MEV RTM for Multiple Applications", in *Proc. EPAC'06*, Edinburgh, UK, June 2006, paper WEPCH175, pp. 2340-2342.

[2] Yu.A. Kubyshin et al., "Current status of the 12 MeV UPC race-track microtron", in: *Proc. PAC'09*, Vancouver, Canada, May 2009, paper WE6PFP112, pp. 2775--2779.

[3] I.Y. Vladimirov,N.I.Pakhomov, V.I. Shvedunov, Y.A.Kubyshin, J.P.Rigla and V.V. Zakharov, "End magnets with rare earth permanent magnet material for a compact race-track microtron", *Eur. Phys. J. Plus*, 129: 271, 2014.

[4] Yu.A. Kubyshin, V. Blasco, J.A.Romero, A. Sanchez, G. Montoro, and V. I. Shvedunov, ·Control system of a miniature 12 MeV race-track microtron", in: *Proc. IPAC'14*, Dresden, Germany, June 2014, pp. 3165--3167.

[5] V.I. Shvedunov, Yu.A. Kubyshin, "Intraoperative radiation therapy dedicated race-track microtron design", INTE, UPC, Rep. T-07-01, 2007.

[6] D. Carrillo, "C-band linac for a race-track microtron", PhD thesis, CIEMAT, Universidad Complutense de Madrid, Spain, 2010.

[7] ANSYS, http://www.ansys.com/Products/Fluids/ANSYS-CFX

[8] F. R. Menter, "Review of the shear-stress transport turbulence model experience from an industrial perspective", *Intern. J. Comp. Fluid Dynamics*, Vol 23, Issue 4, 2009, pp. 305-316.

Content from this work may be used under the terms of the CC BY 3.0 licence (© 2016). Any distribution of this work must maintain attribution to the author(s), title of the work, publisher, and DOI.

ISBN: 978-3-95450-188-5 doi:10.18429/JACoW-MEDSI2016-TUPE10

Content from this work may be used under the terms of the CC BY 3.0 licence (© 2016). Any distribution of this work must maintain attribution to the author(s), title of the work, publisher, and DOI.

A THERMAL EXPLORATION OF DIFFERENT MONOCHROMATOR CRYSTAL DESIGNS

J. S. Stimson†, M. Ward, Birmingham City University, Birmingham, United Kingdom
S. Diaz-Moreno, P. Docker, J. Kay, J. Sutter, Diamond Light Source, Didcot, United Kingdom

Abstract

Eight potential monochromator crystal designs were subjected to a combination of three different beam powers on two different footprints. The temperature and thermal deformation were determined for each. It was found that thermal deformation of the lattice is negligible compared to the surface curvature, and that while the thinnest crystal wafer showed the smallest temperature increase, crystals cooled from the bottom alone demonstrated a far more uniform thermal deformation and a larger radius of curvature.

INTRODUCTION

In this work we have explored various monochromator crystal designs. Monochromator crystals are used to select a single wavelength of x-rays from the broad spectrum produced in a synchrotron device [1-2]. The high energies these crystals are subjected to causes them to heat up significantly, leading to thermal deformations that distort the uniform surface of the crystal, leading to multiple wavelengths being selected [3-4]. This is problematic as it is not always obvious whether the change in wavelength at the detector is due to thermal distortion of the monochromator or interaction with the sample being tested.

In order to attempt to reduce or even eliminate this thermal deformation it must be understood how different variables affect the system. To this end we have modelled several different designs of monochromator crystal to see what effect changing the geometry has on the thermal deformation.

As we are concerned primarily with thermal behaviours, we have made a number of approximations. The cooled surfaces remain at 80 K throughout to approximate the flow of liquid nitrogen with an ideal thermal contact [5]. This is a very non-physical boundary condition, which means the results are not directly comparable to real world systems. However, for the purpose of this work it has been used to create a directly comparable baseline between the different models.

It is also assumed that each crystal has thermalized prior to exposure to the beam, and therefore is initially at a uniform temperature of 80 K.

Three beam powers were considered; 110 Watts, 550 Watts and 1100 Watts. This was to simulate exposure to low power, high power and future high power beams as used at the Diamond Light Source. Each of these powers had to be applied using the Beer-Lambert law of beam transmission [6], as shown in Eq. (1) below.

$$I = I_0\, e^{-\mu x} \tag{1}$$

In Eq. (1) I is the intensity of the beam, I_0 is the intensity of the beam at the surface, μ is the absorption coefficient and x is the distance into the material.

As the beam produced by the I20 beamline is broad spectrum, this calculation was done for each energy and then integrated across all energies as shown in Eq. (2).

$$I = \int I_0(E) e^{-\mu(E)x}\, dE \tag{2}$$

In Eq. (2) I_0 (E) is the intensity of the beam at the surface for x-rays of a given energy and μ(E) is the absorption coefficient for x-rays of the given energy in silicon.

This was done for the measured intensities of each wavelength at the I20 beamline for the given power values. The intensity penetrates the surface, decreasing as it propagates.

Two major factors were considered; the deformation of the diffracting surface could change both the spacing of the lattice layers and change the angle of incidence, both of which can damage the Bragg diffraction desired by modifying lattice layer structure [1].

These are only an issue if they are non-uniform across the diffracting surface, as a uniform change can be allowed for when angling the monochromator crystal. As such the radius of curvature of the diffracting surface has been calculated at the centre of the surface for each design.

The curvature, k, can be calculated by mapping some function y to the deformation of the surface, then applying Eq. 3 [7].

$$k = \frac{\left(\frac{d^2y}{dx^2}\right)^{\frac{3}{2}}}{1+\left(\frac{dy}{dx}\right)^2} \tag{3}$$

The radius of curvature is simply the reciprocal of the modulus of curvature [7], as shown in Eq. 4.

$$R = \frac{1}{|k|} \tag{4}$$

A larger radius of curvature relates to a flatter crystal surface, i.e. the larger the radius of curvature the better.

The lattice spacing as a function of temperature was also calculated, to see if a non-uniform temperature gave rise to a non-uniform lattice that would have affected the Bragg diffraction. However, calculations showed that between 150 K and 80 K the lattice spacing varied only by 5.5e-15 m, a statistically negligible change given the lattice spacing is only of the order of Angstroms. This shows that the variance of the lattice spacing directly due to temperature is unlikely to impact the Bragg diffraction.

Despite varying designs between the different crystals, the mechanical boundary conditions used stay the same; each crystal is anchored by a single fixed point in the centre of its base, with a line extending from this point to

ISBN: 978-3-95450-188-5 doi:10.18429/JACoW-MEDSI2016-TUPE10

the diffracting surface prescribed movement in the x- and y-directions. The entire crystal is also mounted to a spring foundation of ten Newtons per metre. This combination of boundary conditions enables us to model free thermal expansion, giving an accurate image of how each crystal would behave.

METHOD

Eight monochromator crystal designs were considered, varying structure and/or cooling method: the current monochromator design for Diamond's I20 beamline, a number of modifications to that crystal and then a silicon wafer. These designs are subjected to each of the incident powers in both the minimum and maximum angles of the beam footprint, i.e. at a footprint of 36 mm x 25 mm representing an incident beam angle of 30° to the crystal and at a footprint of 5 mm x 25 mm representing an incident beam angle of 6° to the crystal.

The first design modelled was the crystal currently used in Diamond Light Source's I20 beamline as shown in Fig. 1. The crystal is based on a rectangle with the top edges removed; this is to allow the beam to pass, as the I20 beamline features very little space between the monochromator crystals. The entire crystal is thermalized at 80 K, to represent liquid nitrogen cooling reaching an equilibrium.

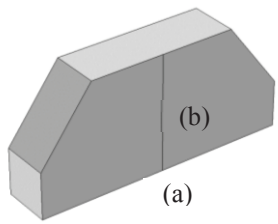


Figure 1: a cutaway view of the existing I20 monochromator crystal design. Point (a) is held fixed while line (b) is restrained in the x- and y-directions.

The next model simulated was using the same crystal design as shown in Fig. 1, but this time cooling only the bottom surface. This was to allow the heat to dissipate more evenly through the crystal, and was anticipated to produce less overall cooling and a higher peak temperature but a more uniform deformation across the diffracting region.

In order to explore alternate designs we next simulated a five-hundred-micron silicon wafer as shown in Fig. 2. Theoretically by reducing the thickness of the crystal we should allow more of the waste X-ray to pass through, reducing the thermal load on the crystal and therefore the peak temperature.

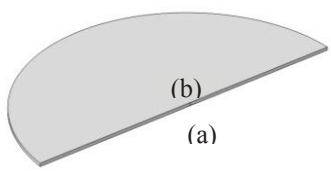


Figure 2: a cutaway view of the silicon wafer monochromator crystal design. Point (a) is held fixed while line (b) is restrained in the x- and y-directions.

RESULTS

Although eight crystal structures were modelled, in the interest of brevity we have chosen the existing crystal and the two most interesting results to explore here in depth. Figures 3, 4 and 5 show the temperature distribution and resulting deformation caused by the 1100 W power in the 30° configuration.

In the current I20 crystal with both sides cooled as well as the base, the temperature profile is drastic as shown in Fig. 3; the centre of the diffracting surface is somewhat hotter than the edges, resulting in stresses in the diffracting surface. There is high stress particularly in the centre of the diffracting region; this could cause a stress dislocation, where the lattice misaligns as a result of the stress on it. The crystal surface distorts by fifty-five picometres over a width of twenty-five millimetres, giving rise to a radius of curvature of 688,000 m (3s. f) at the centre of the diffracting surface.

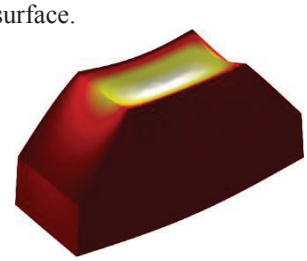


Figure 3: The current I20 monochromator after thirty second exposure to the 1100 W beam at a 30o angle of incidence.

With only the bottom cooled, we see a far more uniform temperature profile in the diffracting region as shown in Fig. 4. There is very little stress in the diffracting region; what stress is found is on the edges of the crystal and is formed by the surface contracting; in essence the crystal is attempting to curl up. Although the crystal as a whole deforms more, it is worth noting that the relative deformation of the diffracting region is largely constant due to the lack of cooling on the sides. The diffracting surface deforms by forty picometres over a width of 25 mm, giving a radius of curvature of 917,000 m (3s.f.) at the centre.

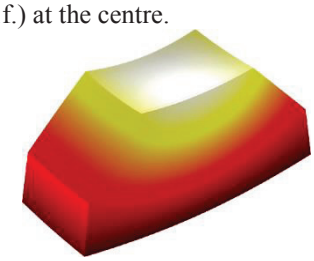


Figure 4: The current I20 monochromator cooled from the bottom only after thirty second exposure to the 1100 W beam at a 30° angle of incidence.

As theorised the thinner crystal does accomplish a slightly lower temperature than that of the current crystal design. However, due to the thinness of the crystal it bows very easily under the lower temperature as shown in Fig. 5; the diffracting surface deforms by six hundred picometres, resulting in a radius of curvature of 103,000 m (3s.f.) at the centre.

Content from this work may be used under the terms of the CC BY 3.0 licence (© 2016). Any distribution of this work must maintain attribution to the author(s), title of the work, publisher, and DOI.

ISBN: 978-3-95450-188-5 doi:10.18429/JACoW-MEDSI2016-TUPE10

Content from this work may be used under the terms of the CC BY 3.0 licence (© 2016). Any distribution of this work must maintain attribution to the author(s), title of the work, publisher, and DOI.

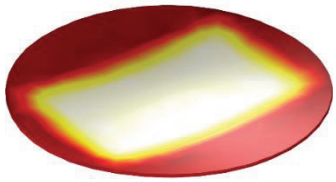


Figure 5: The silicon wafer monochromator after thirty second exposure to the 1100 W beam at a 30° angle of incidence.

CONCLUSION

To help analyse the performance of the crystals the radius of curvature of each design at each power has been plotted on Figs. 6 & 7 for the 30° and 6° angle of incidence respectively.

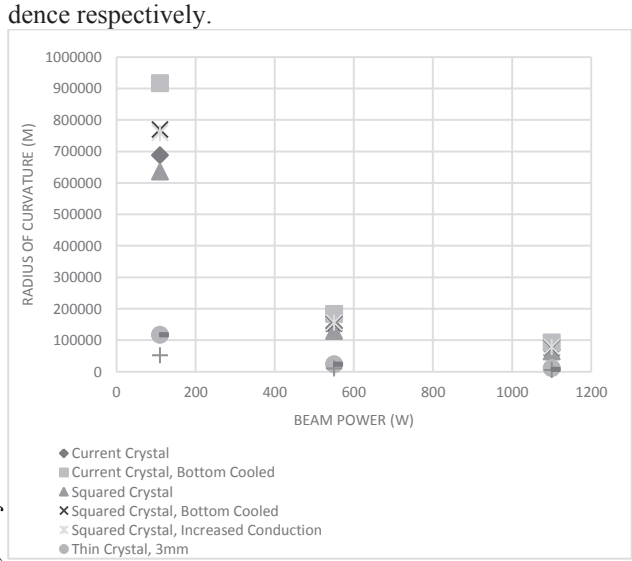


Figure 6: Radius of curvature as a function of beam power deposited in a 36 mm footprint.

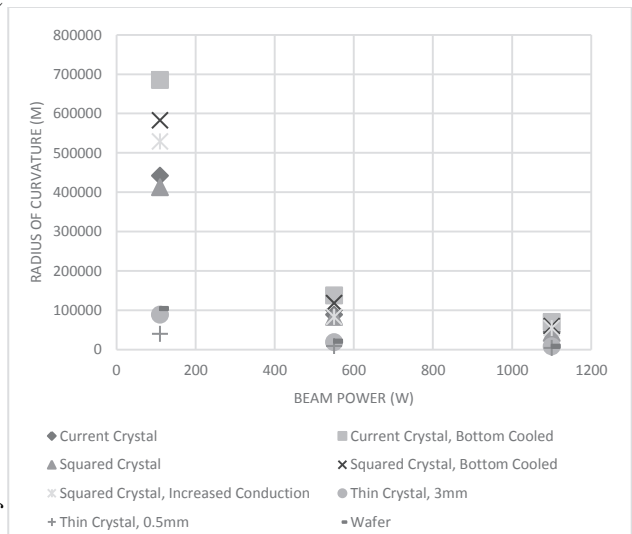


Figure 7: Radius of curvature as a function of beam power deposited in a 5mm footprint.

A common feature of all the models tested is that the thinner the crystal, the lower the maximum temperature. This is due to the heat conducting to the cooled surface in less time when the crystal is thinner. However, due to their flexibility these designs also show significant bowing with a lower radius of curvature.

The models with consistently the highest radius of curvature, and therefore the least bowing, are thicker crystals cooled from the bottom alone. This design allows the heat to dissipate more evenly, though more slowly, throughout the crystal, resulting in less variation in the deformation and a higher radius of curvature.

The next step is to explore the mechanical side of these designs; how would they be held in good thermal contact with the heat exchangers and what steps can be taken to minimise mechanical stresses upon them. Many synchrotron facilities clamp their monochromator crystals between heat exchangers to hold them in the beam path; this design is not compatible with the concept of cooling the crystal from the base alone. However, bolting directly down to a heat exchanger or cooling the bolting plate itself could cause stresses to develop in the diffracting surface as the crystal contracts from the surface. Further work is needed to ascertain the feasibility of this approach.

REFERENCES

[1] W. H. Bragg and W. L. Bragg, "The Reflexion of X-rays by Crystals," in *Proceedings of the Royal Society of London*, 1913, pp. 428–438.

[2] J. A. Golovchenko, "X-ray monochromator system for use with synchrotron radiation sources," *Rev. Sci. Instrum.*, vol. 52, no. 4, p. 509, Apr. 1981.

[3] P. Carpentier, M. Rossat, P. Charrault, J. Joly, M. Pirocchi, J. L. Ferrer, O. Kaïkati, and M. Roth, "Synchrotron monochromator heating problem, cryogenic cooling solution," *Nucl. Instruments Methods Phys. Res. Sect. A Accel. Spectrometers, Detect. Assoc. Equip.*, vol. 456, no. 3, pp. 163–176, 2001.

[4] L. Zhang, M. Sánchez Del Río, G. Monaco, C. Detlefs, T. Roth, A. I. Chumakov, and P. Glatzel, "Thermal deformation of cryogenically cooled silicon crystals under intense X-ray beams: Measurement and finite-element predictions of the surface shape," *J. Synchrotron Radiat.*, vol. 20, pp. 567–580, 2013.

[5] D. H. Bilderback, a K. Freund, G. S. Knapp, and D. M. Mills, "The historical development of cryogenically cooled monochromators for third-generation synchrotron radiation sources.," *J. Synchrotron Radiat.*, vol. 7, no. Pt 2, pp. 53–60, 2000.

[6] A. Beer, "Bestimmung der Absorption des rothen Lichts in farbigen Flüssigkeiten," *Ann. Phys.*, vol. 162, no. 5, pp. 78–88, 1852.

[7] A. Borovik and M. G. Katz, "Who Gave you the Cauchy-Weierstrass Tale? The Dual History of Rigorous Calculus." 2011.

ISBN: 978-3-95450-188-5 doi:10.18429/JACoW-MEDSI2016-TUPE11

STUDY ON THERMAL MECHANICAL DESIGN AND OPTIMIZATION ANALYSIS FOR THE ALBA INFRARED MICROSPECTROSCOPY BEAMLINE (MIRAS) EXTRACTION MIRROR BASED ON FINITE ELEMENT ANALYSIS

M. Quispe†, A. Carballedo, J.J. Casas, C. Colldelram, A. Crisol, G. Peña, Ll. Ribó, I. Sics, I. Yousef, ALBA – CELLS Synchrotron, Cerdanyola del Vallès, Spain

Abstract

This paper reports design, modelling, simulation and optimization results for the ALBA MIRAS infrared radiation extraction mirror. Finite element analysis (FEA) was used to simulate the thermal mechanical behaviour of the device. With the aim to ensure a good thermal performance, conservative assumptions were applied: all of the incident Bending Magnet (BM) radiation is absorbed at the mirror surface, constant bending magnetic field and low thermal contact between the mirror Al 6061 and the OFHC copper arm. A novel solution has been implemented in order to provide an effective cooling by a natural convection on the in-air part of extraction mirror assembly. This has voided the necessity for a water cooling that often causes problems due to the associated vibrations. The power conditions were calculated by using SynRad+. The main ALBA Storage Ring design parameters are: 3 GeV, 400 mA and 1.42 T. According to these conditions, the mirror absorbs 15 W with a peak power density of 0.51 W/mm^2. The peak temperature calculated was 63.2 ºC. The real measurements reported during the commissioning stage showed a good thermal performance, in agreement with the results predicted by FEA.

BACKGROUND

MIRAS is one of phase II beamlines, currently under commissioning stage at the ALBA synchrotron light source. It will go into operation with official users in October 2016 and will be dedicated to Fourier Transform Infrared spectroscopy and microscopy [1].

The MIRAS engineering (conceptual design and production drawings), assembly and qualification metrology tests have been performed at ALBA. One of the key elements is the infrared extraction mirror that will collect the infrared radiation and reflect it back to the storage ring tunnel in order to be transported to the experimental hall.

The ALBA infrared extraction mirror is based on the slotted, non-cooled, type. The concept of the slotted mirror not only avoids interaction with the central high energy core of the dipole emissions, but also allows to realize a simple design that functions reliably without additional water cooling that often causes problems due to the associated vibrations [2, 3]. A novel solution has been implemented in order to provide an effective air cooling system by natural convection on the in-air part of extraction mirror assembly.

THE ALBA INFRARED EXTRACTION MIRROR

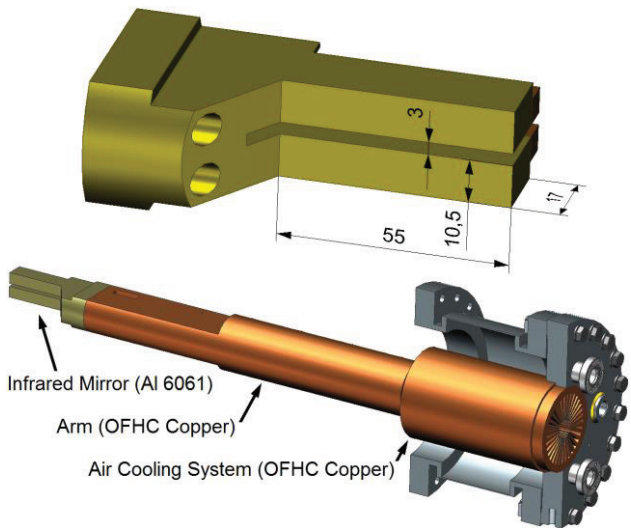


Figure 1: The ALBA infrared extraction mirror. Top: mirror Al 6061, dimensions in mm. Bottom: overall view of the device.

The main parts of the infrared extraction mirror are shown in Fig. 1: the mirror Al 6061, a copper arm and the cylindrical air cooling system made of copper.

The mirror is a rectangular bar 17x24x55 mm with the reflective face at an angle of 63.7º to the electron beam trajectory in the upstream vacuum chamber (see Fig. 2). A 3 mm slot in the mirror allows the high-energy radiation to pass through it. The much wider vertical divergence of the infrared radiation is collected on both sides above and below the slot and redirected towards the emission port. The mirror is attached to the copper arm using screws; indium foil is placed at the interface to improve the heat transfer to the copper arm.

The air cooling system consists of a cylinder made of copper, 65 mm internal diameter, 10 mm thickness and 131 mm long which is provided with 32 longitudinal, straight fins of 1 mm thick and 22.5 mm height. The copper cooling system is brazed into the stainless steel flange providing a perfect contact for the heat transfer.

† mquispe@cells.es

Content from this work may be used under the terms of the CC BY 3.0 licence (© 2016). Any distribution of this work must maintain attribution to the author(s), title of the work, publisher, and DOI.

ISBN: 978-3-95450-188-5 doi:10.18429/JACoW-MEDSI2016-TUPE11

Content from this work may be used under the terms of the CC BY 3.0 licence (© 2016). Any distribution of this work must maintain attribution to the author(s), title of the work, publisher, and DOI.

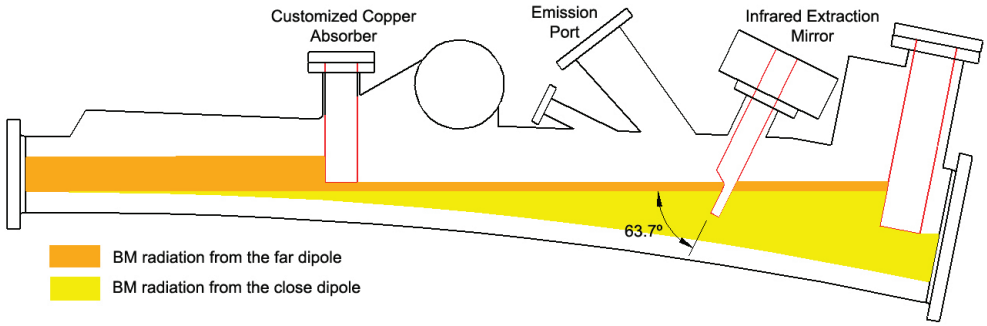


Figure 2: Ray tracing for MIRAS dipole chamber. The orange fan is the BM radiation coming from the far dipole chamber and the yellow zone is the radiation from the close dipole.

FEA STUDIES

Air Cooling Geometries

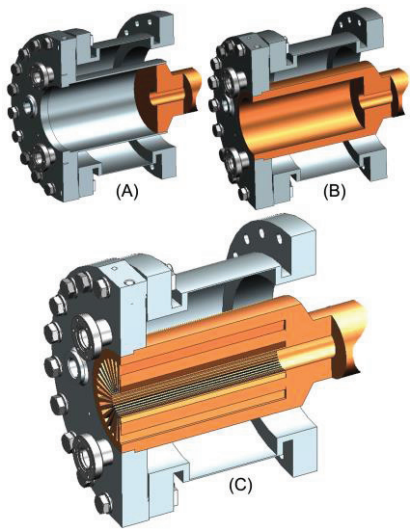


Figure 3: The three types of air cooling system: (A) Stainless steel cylinder, 2 mm wall thickness, (B) Copper cylinder, 10 mm wall thickness, and (C) Case B with internal fins attached.

Numerical simulations (FEA) were used to optimize the cooling performance of the infrared extraction mirror. In order to enhance the heat dissipation on the air cooling system, three geometries are studied:

- Case A: the original prototype, it consists of a simple cylinder made of stainless steel, 85 mm internal diameter, 2 mm thickness and 157.6 mm long.
- Case B: the optimized model after a first modification of case A, a cylinder made of copper, 65 mm internal diameter, 10 mm thickness and 131 mm long.
- Case C: the optimized model after adding rectangular copper fins to the cylinder of case B, as described in previous section.

Figure 3 shows the cross-sectional shapes of the infrared extraction mirror of the three cases mentioned before.

Boundary Conditions

The heat deposited on the mirror is transfer by conduction from the mirror to the copper arm across the indium foil interface. Next it goes by conduction up to the cylinder cooling system and finally it is transported by free convection to the environment.

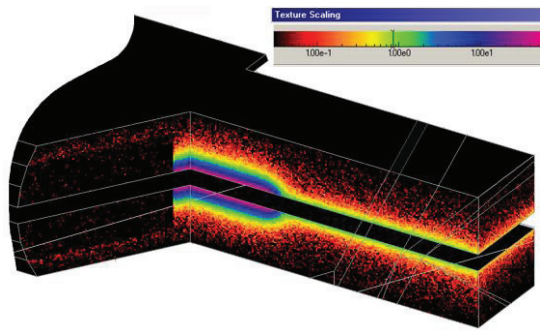


Figure 4: Surface power density distribution using the SynRad+ computer code. The units are in W/cm^2.

Table 1: Main Parameters for ALBA Storage Ring

Parameter	Magnitude
Beam energy, E	3 GeV
Design current, I	400 mA
Dipole magnetic field, B	1.42 T

The mirror is subject to BM radiation coming from the far and close dipoles. A big amount of heat from the far dipole is deposited on a customized absorber placed upstream the mirror (See Fig. 2). Under these conditions, considering the parameters of Table 1, the power deposited on the mirror is estimated using the SynRad+ computer code (See Fig. 4). The total power calculated is 15 W and the peak power density is 0.51 W/mm^2. The non–reflection condition has been established as conservative criteria for the mirror surface.

The conservative air convective heat transfer coefficient was chosen to be 5 W/m^{2}K at 23ºC (quiet air).

The thermal conductivities of Al 6061, OFHC copper and stainless steel are 167, 391 and 15 W/mK, respectively.

At the interface mirror – copper arm the thermal contact conductance of 2000 W/m^{2}K is selected as conservative design criteria (dry contact).

Results

Comparing numerical results of air cooling geometries in Table 2, it can be seen that the case B exhibits a significant decrease in peak temperature compared to case A

ISBN: 978-3-95450-188-5 doi:10.18429/JACoW-MEDSI2016-TUPE11

(from 125.6 ºC to 76.6 ºC). For case C the peak temperature is reduced to 63.2 ºC. It can be clearly concluded that geometries B and C improve the heat dissipation from the air cooling side. Among all cases, case C has been found the most appropriate geometry in terms of maximum heat dissipation.

For all cases the maximum normal deformation calculated for the mirror surfaces is below of 2 um.

Table 2: Peak Temperature (T_{MAX}) on the Mirror for the Three Types of Cooling Systems

Type	T_{MAX} (ºC)
Case A	125.6
Case B	76.6
Case C	63.2

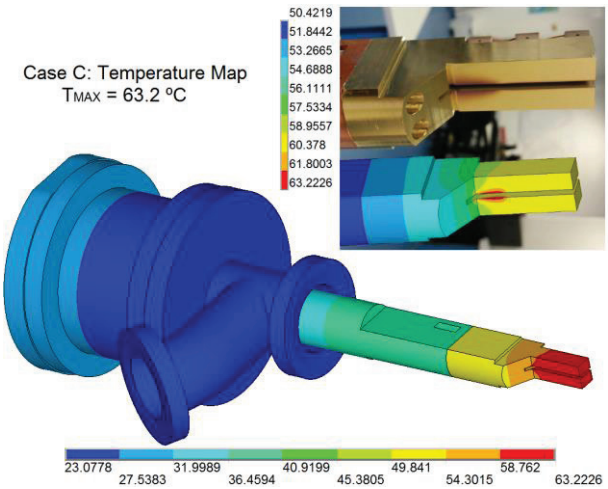


Figure 5: Temperature distribution for case C: isolated mirror with a real photo (top) and overall view of the extraction mirror (bottom).

Figure 5 depicts the calculated temperature map on the mirror for case C. The peak temperature reached is 63.2 ºC. The top right shows the temperature distribution for the isolated mirror together with a real photo captured during the commissioning stage. The carbonized zone in the mirror matches the observed BM power deposition calculated by SynRad+ (Fig. 4). The bottom shows the temperature distribution for the complete infrared extraction mirror.

Effect of fin surface on the temperature This effect is studied by means of the variable F_A: ratio between the total fin surface and the case without fins (Fig. 6). Table 3 shows the results. The peak temperature for F_A = 1 (case B) was reduced by 17.5 percent when F_A = 8.1 (case C).

Table 3: Peak Temperatures (T_{MAX}) as a Function of F_A.

F_A	T_{MAX} (ºC)
1.0	76.6
3.0	70.1
5.0	66.5
8.1	63.2

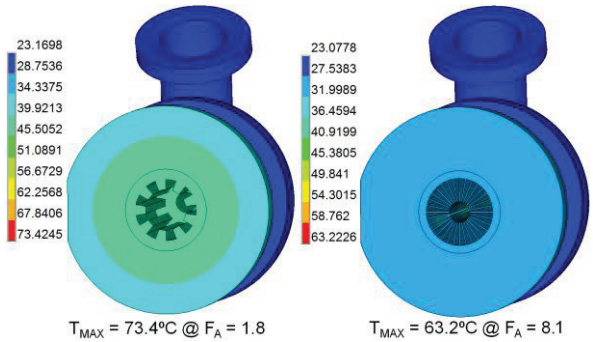


Figure 6: Temperature results for F_A = 1.8 and 8.1.

Effect of Thermal Contact Conductance (TCC) on the temperature TCC is one of the important parameters in the thermal design. It depends on various factors, for example surface roughness, the contact pressure and the hardness of the material. Therefore, quantitative evaluation is difficult, and a little information can be obtained for every case. In order to be conservative for FEA studies we used a coefficient of 2000 W/m^{2}K. According to the literature we can expect TCC > 10000 W/m^{2}C, in that condition the peak temperature in the mirror should be < 55.1 ºC (see Table 4).

Table 4: Peak Temperatures (T_{MAX}) as a Function of TCC.

TCC (W/m^{2}K)	T_{MAX} (ºC)
2000	63.2
5000	57.1
10000	55.1
1.0e5	53.2
1.0e6	53.0

CONCLUSIONS

During the commissioning run held in January 2016 temperatures in the mirror have been reported. Eight K-type thermocouples are installed on mirror. Two sensors are imbedded into the body and six sensors are mounted on the back side of the mirror (downstream) with the heads being exposed to the photon beam.

The local temperature measured in the body above the slot was 25.5 ºC with 130 mA. The FEA model predicts T < 32 ºC for TCC > 10000 W/m^{2}K.

The measurements reported during the commissioning stage showed a good thermal performance of the mirror, and the results are in agreement with the conservative results predicted by FEA.

Content from this work may be used under the terms of the CC BY 3.0 licence (© 2016). Any distribution of this work must maintain attribution to the author(s), title of the work, publisher, and DOI.

ISBN: 978-3-95450-188-5 doi:10.18429/JACoW-MEDSI2016-TUPE11

Content from this work may be used under the terms of the CC BY 3.0 licence (© 2016). Any distribution of this work must maintain attribution to the author(s), title of the work, publisher, and DOI.

REFERENCES

[1] MIRAS, www.albasynchrotron.es/en/beamlines/bl01-miras.

[2] *D. Creagh et al.*, "The design of the infrared beamline at the Australian synchrotron", *Vibrational Spectroscopy*, 41, p. 213–220, 2006.

[3] *I. Yousef et al*, "Simulation and design of an infrared beamline for SESAME (Synchrotron-Light for Experimental Science and Applications in the Middle East)", *Nuclear Instruments and Methods in Physics Research A*, vol. 673, p. 73–81, May 2012.

ISBN: 978-3-95450-188-5 doi:10.18429/JACoW-MEDSI2016-TUPE12

DEVELOPING WHITE BEAM COMPONENTS OF TPS BEAMLINE 24A

Ming-Han Lee†, Chien-Hung Chang, Shih-Hung Chang, Din-Goa Liu, Yi-Jr Su, Liang-Jen Huang, Cheng-Chi Chen, Chao-Chih Chiu, Longlife Lee, Hong-Yi Yan, Chao-Yu Chang, Lee-Jene Lai
National Synchrotron Radiation Research Center,
101 Hsin-Ann Road, Hsinchu Science Park, Hsinchu 30076, Taiwan

Abstract

The TPS 24A, Soft X-ray Tomography (SXT) beamline, is one of the beamlines in the second construction phase at the Taiwan Photon Source (TPS). This bending magnet (BM) beamline has high flux in the range between 260 eV and 2600 eV. It is designed for transmission full-field imaging of frozen-hydrated biological samples. At the exit slit, the beam flux optimized in 520 eV is 2.82×10^{11} photons/second with resolving power 2000, the beam size is 50×60 μm^2 (V×H, FWHM) and the beam divergence is 1.73×1.57 mrad^2 (V×H, FWHM). By contributions of the generic beamline components project in recent years, modular mechanisms would be used in this beamline such as mask, X-ray beam position monitor (XBPM), photon absorber (PAB), and screens. However, these beamline components were designed for ID beamlines, so they should be redesigned for BM beamlines. This paper generally introduce these beamline components decided and redesigned for the TPS 24A. They will play important roles at the BM beamlines in the future.

BEAMLINE LAYOUT

Figure 1 shows the layout of the SXT beamline.

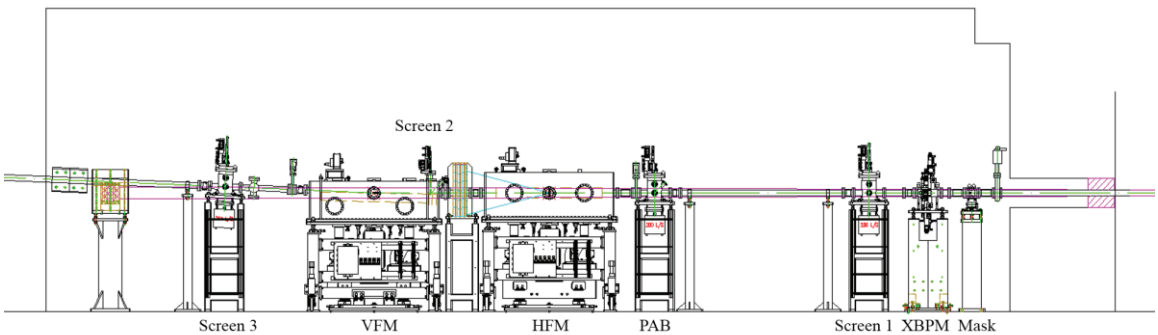


Figure 1: White beam components layout of the SXT beamline.

MASK

The mask as shown in Figure 2 is used to confine the beam size of 21 mm (H) × 20 mm (V) with small range adjustment. Due to the much larger beam size and lower heat load of BM beamlines, we cancelled the tungsten blades used in ID beamlines and simplified the route of cooling water in the chamber of the mask. The entrance and exit ports were also changed from 2.75 inch to 4.5 inch CF flanges. Furthermore, a local shielding which contains of lead and Polyethylene (PE) was added to the mask to prevent the bremsstrahlung radiation.

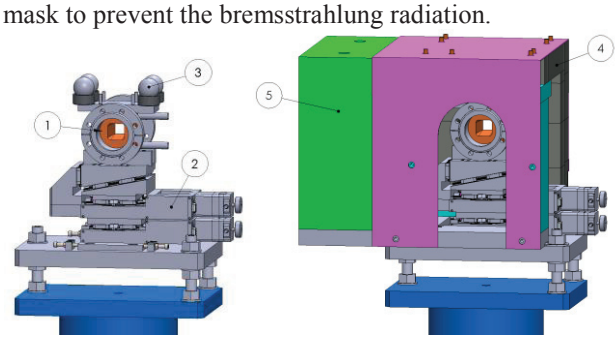


Figure 2: The schematic drawing of the mask and local shielding.
1. UHV water-cooling chamber, 2. Motorized XZ stage, 3. Laser tracker target, 4. Lead, 5. PE.

XBPM

The XBPM with high precision and current detecting function is used to confine the beam size and observe the beam fluctuation. Four tungsten blades moved by linear stages are used to confine the beam size. The stroke of the linear stages and bellows was changed from 10 mm to 30 mm to make sure that the blades travel longer than the beam size. The beam could fully pass through when the blades are opened, and would be cut off when the blades are closed. Optionally, eight M16 × 2.0 screw holes made on the granite stand could be used if a bremsstrahlung stopper is needed. Figure 3 shows the schematic drawing of the XBPM.

† lee.mh@nsrrc.org.tw

Content from this work may be used under the terms of the CC BY 3.0 licence (© 2016). Any distribution of this work must maintain attribution to the author(s), title of the work, publisher, and DOI.

ISBN: 978-3-95450-188-5 doi:10.18429/JACoW-MEDSI2016-TUPE12

Content from this work may be used under the terms of the CC BY 3.0 licence (© 2016). Any distribution of this work must maintain attribution to the author(s), title of the work, publisher, and DOI.

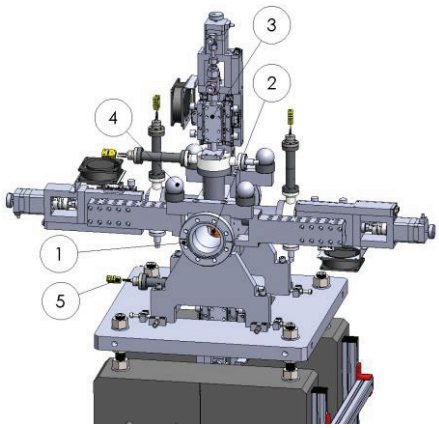


Figure 3: The schematic drawing of the XBPM. 1. UHV chamber, 2. Blades with cooling unit, 3. Motorized linear stage, 4. Laser tracker target, 5. Thermocouple.

WHITE BEAM SCREEN

The screen as shown in Figure 4 is designed to observe the beam size and position. There are five screens in the TPS 24A and three of them were used for white beam. In the generic beamline components project, a small type of chamber and liner stage module is used for the screen while a large one is used for the PAB. Modules of the screen 1 and 3 in the TPS 24A were changed to the PAB type because of the much larger beam size of BM beamlines. Linear stage of the screen 2 is still the typical small type so it could be put into a narrow space in the VFM chamber. Finally, the stroke of the three linear stages and bellows was changed to 30 mm, too.

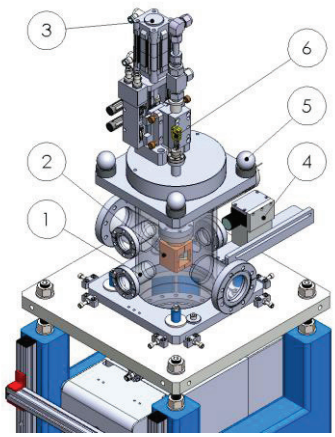


Figure 4: The schematic drawing of the screen 1. 1. UHV chamber, 2. Screen with cooling unit, 3. Linear stage, 4. CCD, 5. Laser tracker target, 6. Thermocouple.

PAB

The PAB as shown in Figure 5 is used to block the beam temporarily when user need. Reticules were made on an oxygen-free high thermal conductivity copper (OFHC) which was coated with fluorescent material to observe the beam position roughly. The stroke of the linear stages and bellows was also changed to 30 mm. A tungsten local shielding could be added into the chamber if it is needed.

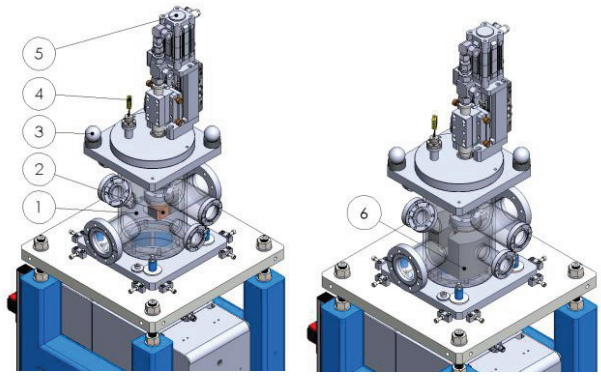


Figure 5: The schematic drawing of the PAB and local shielding.
1. UHV chamber, 2. OFHC with cooling unit, 3. Laser tracker target, 4. Thermocouple, 5. Linear stage, 6. Tungsten shielding.

FLOW RATE OF COOLING WATER

For flow in a pipe or tube, the Reynolds number is generally defined as: [1]

$$\mathrm{Re} = \frac{\rho v D_H}{\mu} = \frac{v D_H}{\upsilon} \quad (1)$$

where:
D_H = hydraulic diameter of the pipe (m)
v = mean velocity of the fluid (m/s)
μ = dynamic viscosity of the fluid (Pa·s)
ν (nu) = kinematic viscosity (m^2/s)
ρ = density of the fluid (kg/m^3)

If Re is under 2300, the behavior of the fluid is laminar; turbulent flow occurs when Re is over 2300 and gets fully developed after Re is over 4000. Turbulent flow takes more heat away than laminar but brings vibration, so the minimum flow rate of cooling water was determined by Re = 4000 in generally condition. Minimum flow rate of the beamline components which got less concern about vibration than heat issue was determined to Re = 2300. A table of minimum flow rate of the generic beamline components is listed in Table 1:

Table 1: Minimum Flow Rate of Cooling Water.

	Mask	PAB/Screen	XBPM
D_H (m)	0.0075	0.0053	0.0027
Re	4000	4000	2300
Flow Rate (L/min)	5.2	5.2	1.9

THERMAL SIMULATION

Thermal Simulations were done to calculate the temperature and thermal stress of the white beam components by SOLIDWORKS Simulation. Since the beam is Gaussian distribution in vertical direction, the power load used in simulation was divided to five area according to the proportion of Gaussian distribution. The power loads and

ISBN: 978-3-95450-188-5 doi:10.18429/JACoW-MEDSI2016-TUPE12

simulation results are listed in Table 2 and the simulation results are shown in Figure 6 to 9:

Table 2: Power Load of White Beam Components.

	Mask	PAB	Screen	XBPM
Power Load (W)	23.8	100	67.1	100

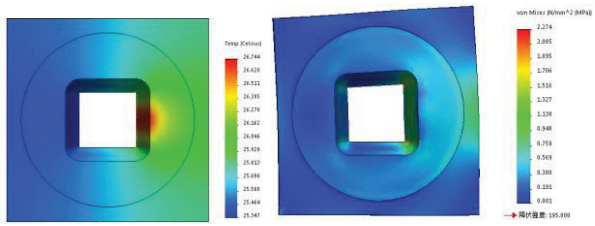


Figure 6: Temperature and thermal stress of the mask.

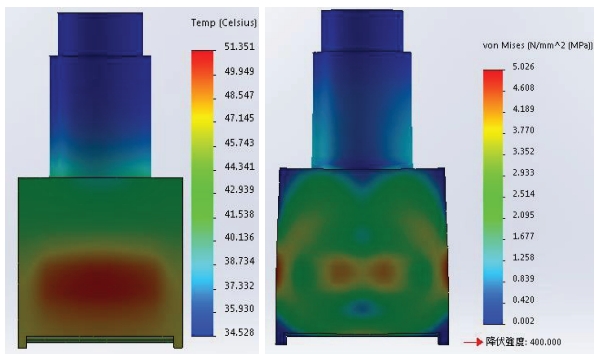


Figure 7: Temperature and thermal stress of the XBPM.

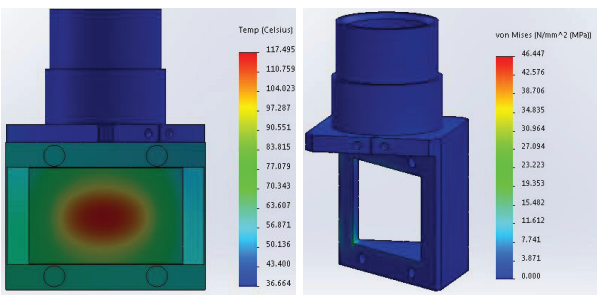


Figure 8: Temperature and thermal stress of the screen.

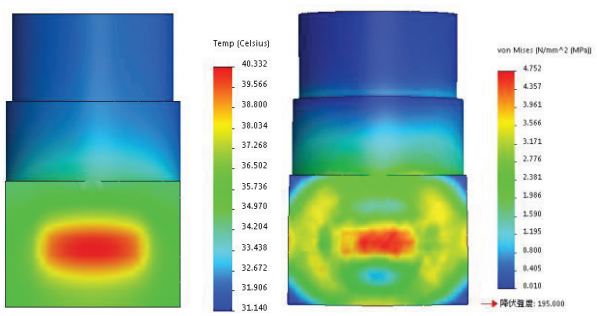


Figure 9: Temperature and thermal stress of the PAB.

CONCLUSION

- All these white beam components have not been tested online and the test is scheduled in October, 2016.
- The bremsstrahlung radiation of the mask and the PAB is needed to be observed continuously.
- 30 mm is the maximum beam size due to the chamber inner space of generic beamline components, bigger chambers should be designed for larger beam size.
- We would keep developing the design for getting more accurate beam size and position.
- To determine the flow rate of cooling water needs more experiments and data, especially the pressure loss of long pipe.

ACKNOWLEDGEMENT

The authors would like to thank all colleagues of the NSRRC beamline group for funding this project.

REFERENCES

[1] The Engineering Toolbox, http://goo.gl/ByO7Wj

Content from this work may be used under the terms of the CC BY 3.0 licence (© 2016). Any distribution of this work must maintain attribution to the author(s), title of the work, publisher, and DOI.

ISBN: 978-3-95450-188-5 doi:10.18429/JACoW-MEDSI2016-TUPE12

Content from this work may be used under the terms of the CC BY 3.0 licence (© 2016). Any distribution of this work must maintain attribution to the author(s), title of the work, publisher, and DOI.

ISBN: 978-3-95450-188-5 doi:10.18429/JACoW-MEDSI2016-TUPE13

NUMERICAL SIMULATION OF THE ALBA SYNCHROTRON LIGHT SOURCE COOLING SYSTEM RESPONSE TO PUMP START-UP AND SHUT-DOWN

X. Escaler*, D. Juan†, Universitat Politècnica de Catalunya, Barcelona, Spain
J.J. Casas‡, C. Colldelram§, M. Quispe#, M. Prieto$, ALBA Synchrotron Light Source, Cerdanyola del Vallès, Spain

Abstract

The ALBA Synchrotron Light Source cooling system is submitted to regular pump start-ups and shut-downs. Moreover, pumps can trip due to motor power failures. As a result, the piping system can be subjected to surges and pressure oscillations. The 1D thermo-fluid simulation software Flowmaster® has been used to predict these transient conditions taking into account the fluid compressibility, the pipe elasticity, the characteristic time response of the check valves and the pump/motors moments of inertia. During pump start-ups, significant pressure rises are detected that can be reduced by readjusting the PID controller parameters. Unexpected pump shut-downs do not appear to provoke significant water hammer conditions. However, pressure fluctuations are generated mainly in the same pumping line but also in the rest of the system due to the particular common return configuration. In all the cases the pressure regulation mechanisms acting on the pump rotating speeds serve to attenuate the consequences of these transients. Finally, the feasibility of the model to simulate the effect on the system response of trapped air inside the pipes has also been evaluated.

INTRODUCTION

The Consortium for the Exploitation of the Synchrotron Light Laboratory (CELLS) is in implementation state of a transversal project whose objective is to develop and improve the ALBA's synchrotron cooling system. It is aimed at improving the system reliability and stability faced to flow changes induced during normal operation and occasional failures.

One particular activity consists of understanding the cooling system response to start-up and shut-down of any pump device in the cooling system and detecting if pressure variations created in transient events may lead to failures and/or piping components' deterioration.

It is well known that transient flow conditions in piping systems with large flow rates can cause unwanted water hammer problems. Water hammer creates high amplitude pressure waves that travel back and forth inside the pipe network until they are dissipated by friction [1-2]. Excessive high pressures can lead to damage or rupture of pumps and valves. Excessive low pressures can lead to air entrance, cavitation and release of large amounts of dissolved air.

Faced with the difficulty and risk of carrying out experimental tests on the actual pipe network, it has been decided to use the existing Flowmaster® model [3] to simulate numerically the system response. For that, the model has been modified to take into account the inertial and compressibility effects in pumps and pipes by replacing and adding the adequate components. In addition, it has also been necessary to program new scripts and to make changes in the PID controllers in order to simulate the real pumping system start-up/shut-down procedures.

NUMERICAL MODEL

A key parameter to calculate water hammer phenomenon in pipes is the pressure wave propagation speed, a, that can be estimated with Eq. (1) where B is the bulk modulus of elasticity of the liquid, ρ is the fluid density, D is pipe diameter, e is the pipe wall thickness and E is the modulus of elasticity of the pipe wall material.

$$a = \sqrt{\frac{B/\rho}{1+\frac{DB}{eE}}} \quad (1)$$

For example, the wave speed a is around 1200 m/s for water at 23 °C flowing inside a stainless steel pipe of size DN 150 Sch 10. Accordingly, the adequate wave speed for all the different pipe sizes of the network have been calculated and used in the model.

Most common causes of transient problems in pipe systems are the pump start-up and pump shut-down due to a power failure (pump trip). To correctly simulate these effects the pump and the motor moments of inertia must be included in the model. For that, the Thorley empirical equations have been used [4]. The motor inertia, I_m, and the pump inertia, I_p, have been calculated with Eq. 2 and Eq. 3, respectively, where P is the brake horsepower in kW and N is the rotational speed in rpm.

$$I_m = 118\left(\frac{P}{N}\right)^{1,48} \quad (2)$$

$$I_p = 1{,}5 \cdot 10^7\left(\frac{P}{N}\right)^{0,9556} \quad (3)$$

The generation side of the cooling system is comprised of four pumping stations named P07, P08, P09 and P10 for the Experimental Area (EA), the Storage (SR), the Booster (BO) and the Service Area (SA) consumption rings, respectively. In P08 and P10 two pumps operate simultaneously in parallel, meanwhile in P07 and P09 only one pump is working. Another pump, P11, is in

* escaler@mf.upc.edu
† david_78jg@hotmail.com
‡ jcasas@cells.es
§ ccolldelram@cells.es
# mquispe@cell.es
$ mprieto@cells.es

Content from this work may be used under the terms of the CC BY 3.0 licence (© 2016). Any distribution of this work must maintain attribution to the author(s), title of the work, publisher, and DOI.

ISBN: 978-3-95450-188-5 doi:10.18429/JACoW-MEDSI2016-TUPE13

Content from this work may be used under the terms of the CC BY 3.0 licence (© 2016). Any distribution of this work must maintain attribution to the author(s), title of the work, publisher, and DOI.

charge of delivering the hot water to the chillers that cool it down again. Accordingly, the adequate moments of inertia for all the different pump sizes have been calculated and used in the model.

Finally, the non-return valves mounted at the discharge pipe lines have also been modelled. They are tilting disk check valves that only allow the passage of the fluid in a single direction shown in Fig. 1. If the flow tries to return, the valve will prevent this by shutting under its' own weigh. To model them, a characteristic operating time of 1 s and a minimum flow velocity of 0.6 m/s were assumed.

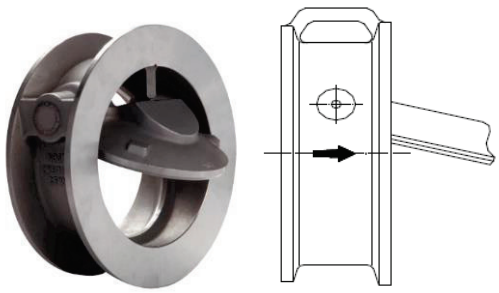


Figure 1: Tilting disc check valve mounted at pump discharge pipeline (arrow indicates permitted flow sense).

It must be noted that the cooling system presents several regulation mechanisms that are automatically applied to guarantee hydraulic and thermal stability. All of them have been considered in the current model. In terms of pump pressures, a series of proportional–integral–derivative controllers (PID's) try to maintain the maximum values below a fixed set-point by regulating the pump's rotational speed. In terms of water temperature, a series of mixing valves and chillers ensure a temperature of 23 °C at the consumption rings also by means of PID's controllers acting on three-way valves and heat exchangers.

SIMULATED RESPONSE

Normal Pumping System Start-Up

The typical start-up procedure is carried out sequentially starting from pump P11 and finishing with the two pumps in P10 as indicated in Fig. 2. The total time takes around 100 s.

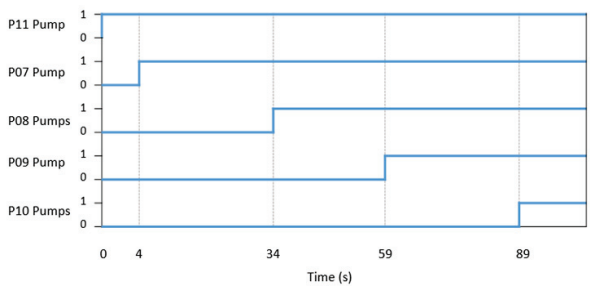


Figure 2: Selected instants of time for each pumping station start-up based on current practice by ALBA operators.

As it can be seen in Fig. 3, for each pump start-up the corresponding delivery pressure rises above the pressure set-point during a certain period of time. The highest pressure increase is found in P09, reaching the 54% of its set point value, which is $1.02 \cdot 10^7$ Pa. Meanwhile, the lowest overpressure is produced by pump P11. The reason for that is the observed delay time between PID controller and pump.

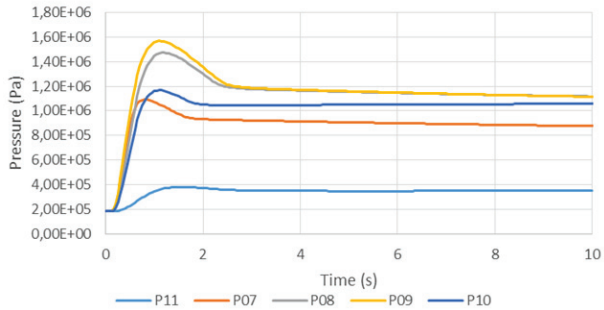


Figure 3: Pump delivery pressures during the initial seconds of sequential start-up.

In order to reduce such overpressures that might damage the system components, an adequate modification of the PID controller's characteristic values has been preliminary investigated with the model. Some results are shown in Fig. 4 for P09. It has been found that adjusting the proportional constant, K_p, around a value of 1, the pressure increase can be reduced to 32% of the set point. Regarding the integral and derivative constants, the simulations did not show any significant improvement in overpressure levels.

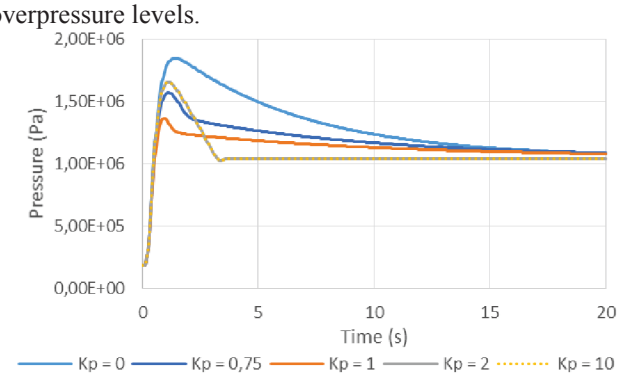


Figure 4: Effect of adjusting the Kp PID parameter on the pressure evolution during P09 start-up.

Pump Trip Without Thermal Load

The effects of the unexpected shut-down of only one of the pumps in P08 station have been simulated without thermal demand and the mixing valves at 50% opening ratio. As it can be observed in Fig. 5, the closure of the check valve happens around 0.8 s after the pump trip. As a result, there is a reverse flow during 0.3 s until the valve closes completely. At this point, a typical water hammer disturbance is generated through all the pumping lines. Fortunately the pressure wave is of low amplitude and short duration.

It must be noted that the expansion wave at the pump inlet seems to reach the vapour pressure, which could induce cavitation. After the water hammer, a low frequency fluctuation is generated in the system that disappears after 20 s.

ISBN: 978-3-95450-188-5 doi:10.18429/JACoW-MEDSI2016-TUPE13

Another point of interest is the significant effect observed in P11 rotational speed and the common return pipe during the transient.

At the end, the second pump is capable of compensating the lack of flow from the tipped pump and the original pressure set-point is achieved. However, this is not the case in P10 pumping line and at the end of the transient the system cannot maintain the nominal flow rate and delivery pressure.

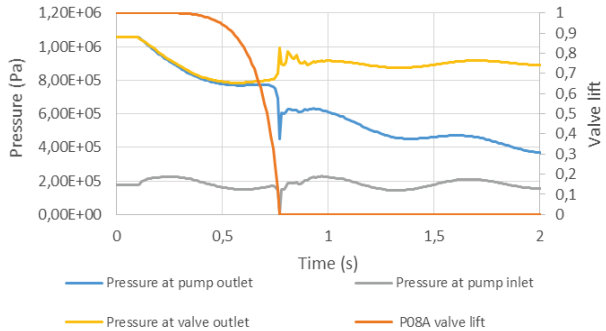


Figure 5: Evolutions in P08A pumping line of the pressures and the check valve position after a pump trip.

Pump Trip with Thermal Load

In the case that the synchrotron light source is at full operation, the most critical case corresponds to a pump trip effecting P11 which is responsible of feeding the chillers to reduce the temperature of the cooling system water.

The simulated evolution of the mixed water temperature at each of the consumption rings after a P11 trip is shown in Fig. 6. It is significant to note that, due to the length of the pipe network, the consequences take around 600 s to reach the rings. At this end point, the system is obviously unable to cool the water anymore if P11 is not started again.

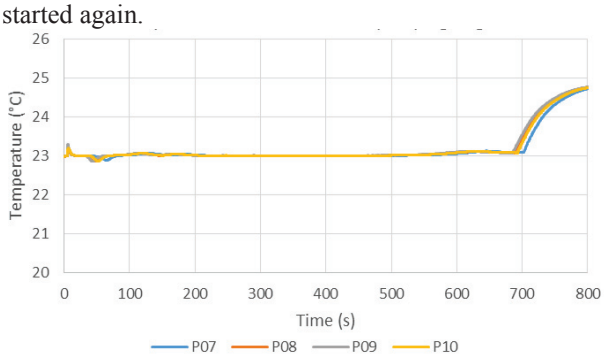


Figure 6: Temperature evolution at ring's inlets after a P11 pump trip occurring at time 0 s.

Normal Pumping System Shut-Down

The system pressure response to a simultaneous stoppage of all the pumps once the thermal demand is already closed is presented in Fig. 7. Some oscillations are detected in all the pumping lines but they are rapidly attenuated. This procedure is not currently being applied in ALBA, which is actually a sequential shut-down of the pumping lines what makes the consequences even softer.

Effect of Trapped Air

In Fig. 8 it can be seen that the presence of an accumulator of air at the exit of the ring when the flow in this ring is stopped due to a pump shut-down damps the amplitude of the pressure oscillations and increases the period.

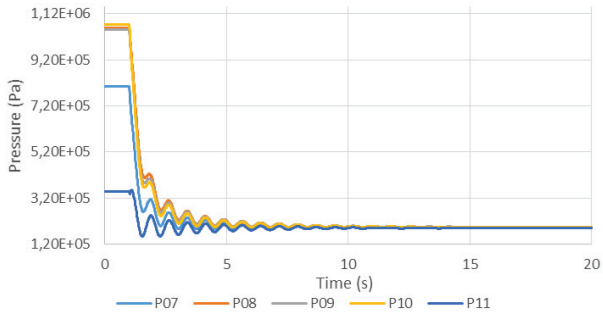


Figure 7: Pressure evolution at pump outputs during a simultaneous pump shut-down.

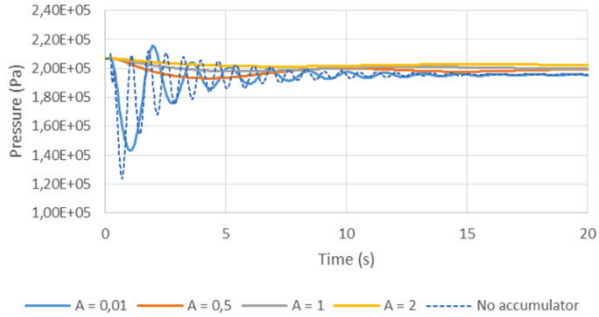


Figure 8: Effect on pressure oscillation due to P08 pumping station shut-down for different air volumes.

CONCLUSION

The normal start-up manoeuvre of the pumping system has been simulated and the fluid dynamic response has been analysed. The results indicate the generation of significant pressure rises. To mitigate them, changes in the PID controller parameters have been proposed, improving the transient behaviour reducing such peaks.

The simulation and analysis of sudden pumps' shut-downs due to system unexpected failures has served to identify the consequences on the system behaviour. The calculations have been carried out without and with simultaneous thermal regulation. The results serve to identify the most dangerous situations and the time spans of the transient events. This information can be used to predict undesired behaviours.

Finally, the effect of air in the pipes has been analysed during the pump shut-down and it has been confirmed that the transient pressure fluctuations predicted in the system are modified.

REFERENCES

[1] B. E. Larock, R. W. Jeppson, and G. Z. Watters, *Hydraulics of pipeline systems.* CRC Press, 1999.

[2] M. S. Ghidaoui *et al.*, "A Review of Water Hammer Theory and Practice", *Applied Mechanics Reviews, Transactions of the ASME*, vol. 58, pp. 49-76, Jan. 2005.

Content from this work may be used under the terms of the CC BY 3.0 licence (© 2016). Any distribution of this work must maintain attribution to the author(s), title of the work, publisher, and DOI.

ISBN: 978-3-95450-188-5 doi:10.18429/JACoW-MEDSI2016-TUPE13

[3] M. Quispe *et al.*, "ALBA cooling system upgrade: thermal hydraulic numerical simulations", in *Proc. MEDSI 2014 Conference*, Melbourne, Australia, October 2014, pp. 1-14.

[4] A.R.D. Thorley, *Fluid Transients in Pipeline Systems*. D&L George Ltd, U.K., 1991

Content from this work may be used under the terms of the CC BY 3.0 licence (© 2016). Any distribution of this work must maintain attribution to the author(s), title of the work, publisher, and DOI.

ISBN: 978-3-95450-188-5 doi:10.18429/JACoW-MEDSI2016-TUPE14

STUDY, DESIGN AND OPTIMIZATION ANALYSIS OF THE ALBA LOREA DIPOLE VACUUM CHAMBER AND CROTCH ABSORBERS BASED ON FINITE ELEMENT ANALYSIS

M. Quispe†, J. Campmany, J.J. Casas, C. Colldelram, A. Crisol, J. Marcos, G. Peña, M. Tallarida,
ALBA – CELLS Synchrotron, Cerdanyola del Vallès, Spain

Abstract

This work deals with the FEA study, design and optimization of the LOREA dipole vacuum chamber and Glidcop Al-15 crotch absorbers. At present LOREA is the ninth beamline being designed at ALBA with an Insertion Device (ID) consisting of an Apple II-type helical undulator. For the standard dipole chamber the vertical polarized light hits the walls because of the very narrow vertical aperture between the cooling channels. In vertical mode the ID vertical divergence equals +/- 2.2 mrad and the peak power density and total power are 5.6 kW/mrad² and 5.5 kW, respectively. Due to the high power a temperature as high as more than 600 ºC is calculated. In consequence the dipole chamber has to be modified and the absorbers have to withstand the Bending Magnet (BM) and ID radiation. The new absorbers have to be thicker and its cooling channels are farer from BM power deposition than the standard absorbers. The thermal mechanical simulations show good results, the new absorbers are in a safe range, the maximum temperature, stress and strain are 309.2 ºC, 164.2 MPa and 0.14%, respectively. The main ALBA Storage Ring design parameters used in the simulations are: 3 GeV, 400 mA and 1.42 T (BM).

BACKGROUND

LOREA is the ninth beamline being designed at ALBA synchrotron light source. It will deliver photons with high resolution and high photon flux for Spin and Angle Resolved Photoemission Spectroscopy. Its Insertion Device (ID) consists of an Apple II-type helical undulator (EU125) [1]. This type of EPU can produce horizontal, circular and vertical modes of polarization of the magnetic field.

The radiation emitted by the ID at low photon energies has a very large angular divergence. Although the large divergence is not a problem in case of horizontal and circular polarization, it is instead a problem, considering the "V profile" of the dipole vacuum chamber. Here, the "V profile" necessary to allow the cooling channels produces a very narrow aperture, and the vertical polarized light hits the chamber. This problem is described in Fig. 1: the green fan depicts the ID radiation in a vertical plane at the middle of the cone radiation. The schematic fan is calculated for vertical mode polarization which vertical opening is +/- 2.2 mrad. Because of this large angular divergence there is an interference with the cooling channel and a big amount of heat is deposited on the dipole vacuum chamber.

† mquispe@cells.es

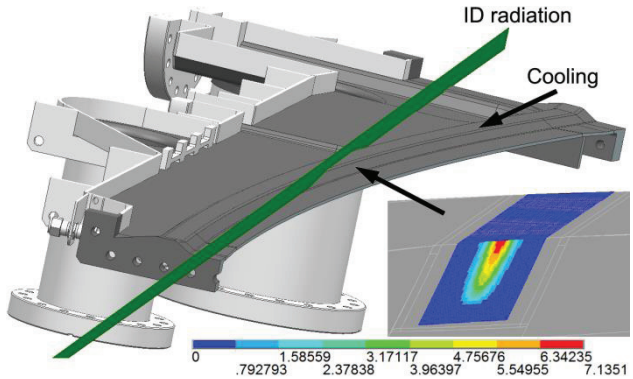


Figure 1: Schematic cross-sectional view of standard dipole vacuum chamber, displaying the lower longitudinal cooling channel and ID radiation interference for vertical mode polarization. The footprint is in W/mm².

THERMAL STUDIES OF THE STANDARD DIPOLE CHAMBER SUBJECT TO ID RADIATION

Thermal Boundary Condition

Thermal simulations (FEA) were used to study the effect of the ID radiation (vertical mode) on the standard stainless steel dipole chamber.

The power deposited on the chamber is calculated with the parameters of Table 1. It is imposed a nominal trajectory of the beam. The power calculated for each cooling channel is 693 W and the peak power density is 7.1 W/mm². Figure 1 shows the footprint for the lower cooling channel.

Table 1: Main Parameters of Insertion Device for LOREA (vertical mode). The Emitted Power and Power Density are Computed for an Electron Beam Current of 400 mA.

Parameter	Magnitude
Maximum magnetic field	1.06 T
K	12.37
Power density	5.6 kW/mrad²
Total power	5.5 kW

Fluid Boundary Conditions

The cooling channels have originally been designed to dissipate the reflected heat radiation from the crotch absorbers. Under this condition the amount of power is very low, the heat is spread uniformly on the chamber and a laminar regime of water flow is sufficient for heat dissipation.

Content from this work may be used under the terms of the CC BY 3.0 licence (© 2016). Any distribution of this work must maintain attribution to the author(s), title of the work, publisher, and DOI.

ISBN: 978-3-95450-188-5 doi:10.18429/JACoW-MEDSI2016-TUPE14

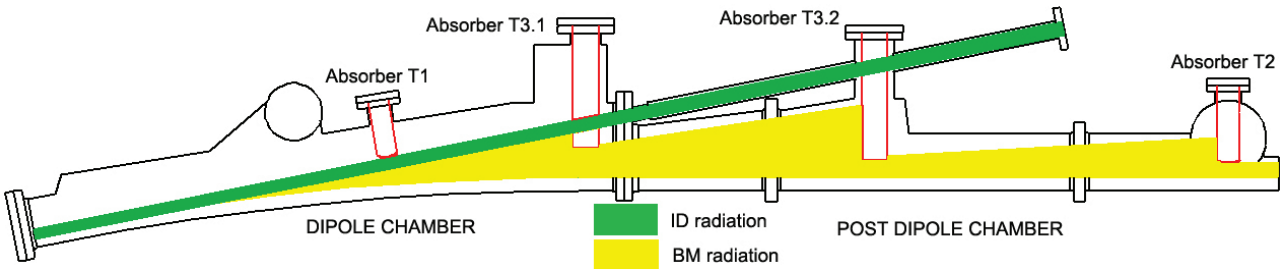


Figure 2: Ray tracing for LOREA dipole chamber. The green fan is the ID radiation and the yellow zone is the Bending Magnet (BM) radiation from the close dipole.

In order to study the thermal behavior of the dipole chamber, three water flow conditions have been imposed: laminar regime, which is the current flow condition (case A), and turbulent regimes (cases B and C). The cases are defined in terms of the convective heat transfer coefficient "h" (see Table 2).

Results

Table 2 shows the results. Even for turbulent conditions the maximum temperature is non – acceptable. Due to the very high power a temperature as high as more than 637 ºC is calculated. Figure 3 shows the temperature distribution in the dipole chamber for the worst case.

Table 2: Peak Temperature (T_{MAX}) in the Dipole Chamber for Different Water Flow Conditions.

Case	h (W/m^{2}K)	T_{MAX} (ºC)
A	1500	961.2
B	5500	717.2
C	13000	637.1

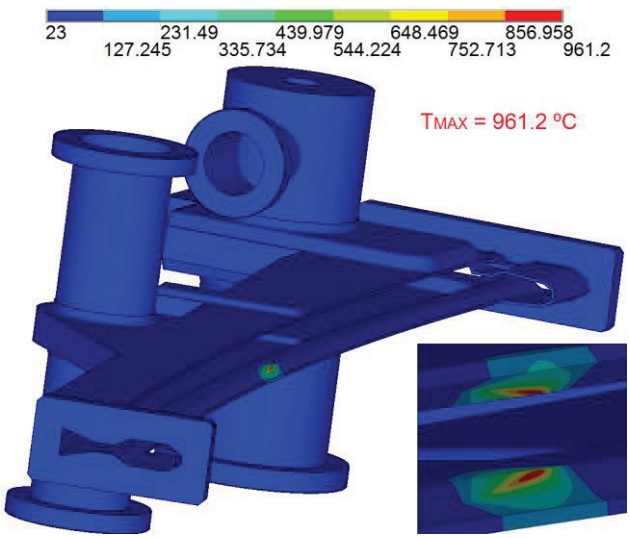


Figure 3: Temperature reached on the dipole chamber (upper and lower cooling channels) due to interference of ID radiation in vertical mode. The maximum temperature is 961.2 ºC (case A).

Because of the thermal results two main modifications have to be introduced on the chamber as follows:

- The longitudinal cooling channels have to be removed to increase the vertical aperture. This modification allows the cone radiation going toward the first Glidcop Al–15 crotch absorber T3.1 (see Fig. 2), which also has to be redesigned.
- The biggest rectangular port has to be modified to accommodate the new crotch absorber T3.1.

THE NEW GLIDCOP AL–15 CROTCH ABSORBER IN THE DIPOLE CHAMBER

The new crotch absorber follows the standard design done at ALBA. Some modifications to the design have been implemented in order to improve its thermal and mechanical performance.

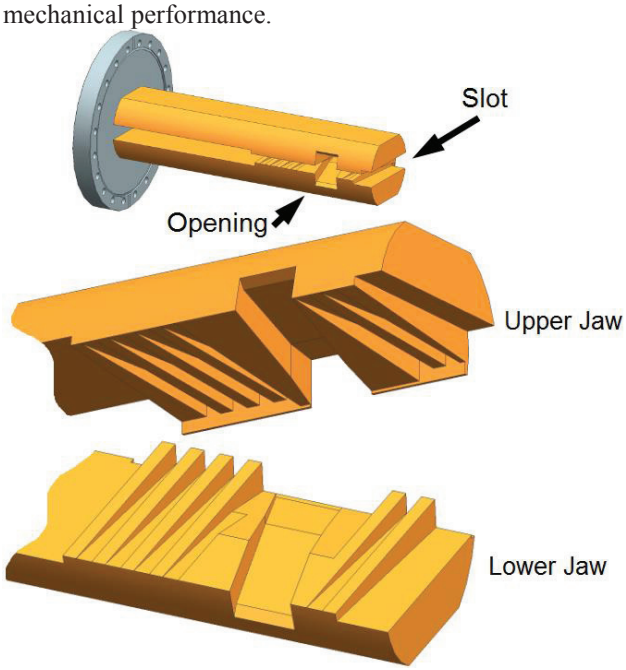


Figure 4: The assembly and two jaws of new Glidcop Al–15 crotch absorber for LOREA dipole chamber.

The proposed geometry is shown in Fig. 4. The main characteristics are as follows:

- An opening is provided through the two jaws to allow ID radiation passing to the front end. Part of the radiation will be collected on the upper and lower jaws. The sizing opening has to avoid interference between the ID radiation and the post dipole chamber.
- The new absorber has to stand ID and BM radiation at the same time, so the inclination of surfaces on the opening has to be optimized in order to reduce the power density of the ID radiation.

Content from this work may be used under the terms of the CC BY 3.0 licence (© 2016). Any distribution of this work must maintain attribution to the author(s), title of the work, publisher, and DOI.

ISBN: 978-3-95450-188-5 doi:10.18429/JACoW-MEDSI2016-TUPE14

- A slot is provided at the end of the absorber. This aperture avoids radiation impinging at the end of the absorber, since the cooling in that region is not efficient. With this modification the radiation passes through the absorber T3.1 and is deposited on the downstream absorber T3.2, but in a region with a better cooling (see ray tracing in Fig. 2).
- The cooling efficiency will be also optimized with a different design of the cooling channels.

Figure 5 shows a comparative description of the geometries for the standard and new crotch absorber. The main differences are as follows:

- In the new absorber the vertical distance (L) between the footprint (BM radiation) and the cooling channels (22.5 mm for the worst case), is longer than the standard absorber (11.6 mm). This constraint affects the thermal mechanical performance of the new absorber.
- The height (H) of the new absorber is longer than the standard case: 71 and 49 mm, respectively. This modification affects the design of the dipole chamber,
- The cooling channels are aligned in a horizontal (standard absorber) and in an inclined straight line (new absorber).

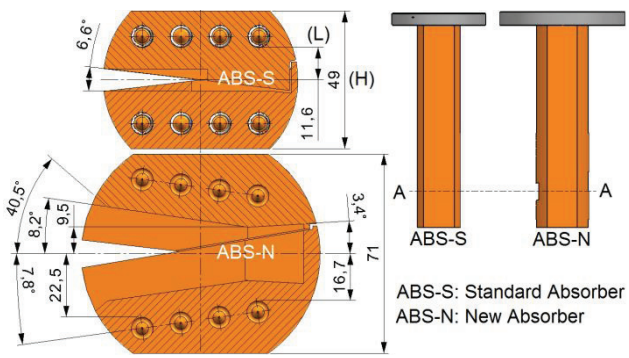


Figure 5: Comparative study between the dimensions of standard (ABS-S) and new crotch absorber (ABS-N). View for the cross section A–A. Dimensions are in mm.

FEA STUDIES OF THE NEW ABSORBER

Boundary Conditions

The main parameters which characterize the LOREA ID (vertical mode) and BM power on the absorber are shown in Tables 1 and 3.

For all the FEA studies only the upper jaw is simulated. This jaw is subject to the maximum power load conditions, in comparison with the lower jaw.

For the ID power deposition the vertical misalignments, angular (+/- 0.11 mrad) and displacement (+/- 0.16 mm), have been imposed. For these conditions the ID power on the upper and lower jaws are 610.7 and 296.2 W, respectively, and the ID peak power density is 19.8 W/mm^2.

The total power (ID and BM) on the upper jaw is 2729 W and the maximum power density is because of BM radiation: 43 W/mm^2.

Table 3: Main Parameters for ALBA Storage Ring

Parameter	Magnitude
Beam energy, E	3 GeV
Design current, I	400 mA
Dipole magnetic field, B	1.42 T

The crotch absorber is cooled by water at 23 ºC inlet temperature. The velocity in the cooling channels is kept in 3 m/s and the imposed convective heat transfer coefficient is 15000 W/m^{2}K.

Results

The temperature, stress and strain distribution have been calculated based on linear elastic analysis. The thermal mechanical simulations show good results, the new absorber is in a safe range according to the design criteria [2]. The maximum temperature, stress and strain are 309.2 ºC, 164.2 MPa and 0.14%, respectively (Fig. 6).

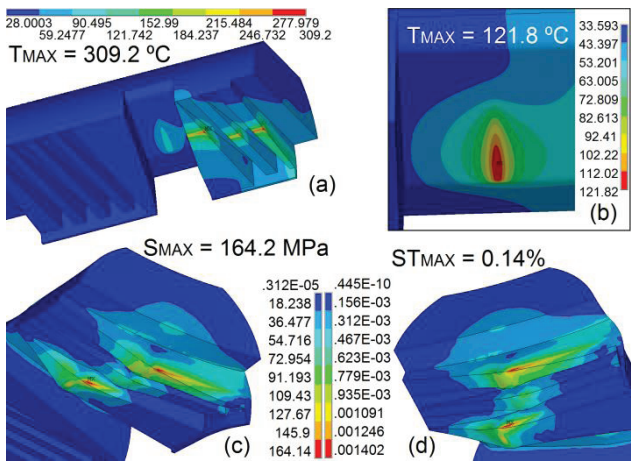


Figure 6: FEA results for the new Glidcop Al–15 crotch absorber in the dipole chamber: (a) Temperature map, (b) Local detail of the temperature distribution at the ID power deposition, (c) Stress map, and (d) Strain map.

CONCLUSIONS

The study confirms the necessity to do a modification of the dipole vacuum chamber. From the ray tracing it resulted that the post-dipole vacuum chamber should not be modified, but the two Glidcop Al-15 crotch absorbers (T3.1 and T3.2) should be designed anew. The new absorber T3.2 has to be modified following the same design criteria for absorber T3.1. The FEA results of the new crotch absorber show a good performance according with the limits of the design criteria.

REFERENCES

[1] LOREA, www.cells.es/en/beamlines/en/beamlines/lorea-beamline-proposal

[2] *E. Al-Dmour et al*, "The conceptual design and thermal analysis of ALBA crotch absorbers", *PAC07*, MOPAN065, p. 299–301, 2007.

Content from this work may be used under the terms of the CC BY 3.0 licence (© 2016). Any distribution of this work must maintain attribution to the author(s), title of the work, publisher, and DOI.

ISBN: 978-3-95450-188-5 doi:10.18429/JACoW-MEDSI2016-TUPE15

THERMAL MANAGEMENT AND CRYSTAL CLAMPING CONCEPTS FOR THE NEW HIGH-DYNAMICS DCM FOR SIRIUS

M. Saveri Silva*, R. R. Geraldes, A. Gilmour, LNLS, Campinas, Brazil
T. A. M. Ruijl, R. M. Schneider, MI Partners, Eindhoven, Netherlands

Abstract

The monochromator is known to be one of the most critical optical elements of a synchrotron beamline, since it directly affects the beam quality with respect to energy and position. Naturally, the new 4th generation machines, with emittances in the range of order of 100 pm rad, require even higher stability performances, in spite of the still conflicting factors such as high power loads, power load variation, and vibration sources. A new high-dynamics DCM (Double Crystal Monochromator) is under development at the Brazilian Synchrotron Light Laboratory for the future X-ray undulator and superbend beamlines of Sirius, the new Brazilian 4th generation synchrotron [1, 2]. In order to achieve high-bandwidth control and stability of a few nrad, as well as to prevent unpredicted mounting and clamping distortions, new solutions are proposed for crystal fixation and thermal management. The design is based on flexural elements, aiming for a highly predictable performance, like support stiffness, crystal distortion and thermal insulation. It was optimised by using mechanical and thermal FEA, including CFD. Efforts were made to predict thermal boundaries associated with the synchrotron beam, including incident, diffracted and scattered power, for which the undulator spectrum was employed in the Monte Carlo simulation package – FLUKA.

INTRODUCTION

The goal of this work is to present the thermal management and the mechanical clamping concepts for the new high stability DCM for Sirius. Details about the full system and its specifications can be found in [3].

THERMAL MANAGEMENT

The first step towards modelling the thermal behaviour of the system was collecting power loads and boundary conditions.

Incident Power

Taking 19 mm period undulator as the source (with 105 periods and at 350 mA current), its spectrum was simulated using SPECTRA [4] and post-processed in MATLAB [5] in order to find both the total incident power and the power variation for energy scans as a function of energy. The results are presented in Fig. 1 and it can be seen that the power load does not exceed 150 W. However, the DCM has to deal with a variation of more than 100 W over the full range, and as much as 38 W for 1 keV scans.

From the total incident power, most of it is absorbed by the 1st crystal (CRYS1), whereas a small fraction of it is diffracted and the remaining of it is scattered. These quantities have been estimated for a better comprehension of each contribution to the system.

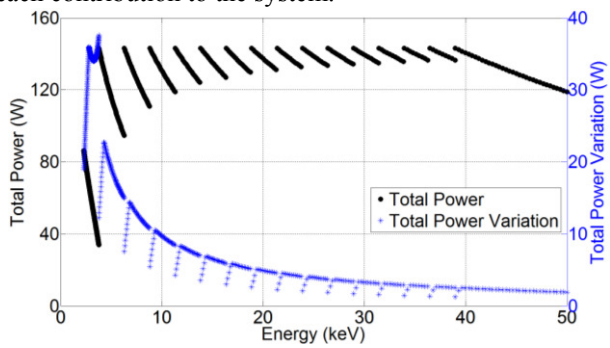


Figure 1: Incident power and power variation in ±0.5 keV scans as a function of energy for Si (111) with an acceptance of 60x60 μrad^2.

Absorption and Scattering

A user routine was implemented into the Monte Carlo package FLUKA [6, 7] in order to guide the design of the shielding structure, to estimate the radiation doses in sensitive elements and to evaluate the deposited energy in the main components after scattering and absorption. Both the Bremsstrahlung flux, generated inside FLUKA from the electron beam, and the synchrotron flux, imported from SRW [8], have been evaluated. The first was found to be several orders of magnitude smaller than latter, so that its contribution could be neglected regarding power levels. Super MC [9, 10] was used to convert CAD drawings in FLUKA geometries. Figure 2 shows the original simplified CAD model and its conversion inside FLUKA, as well as some results of the photon track length density for different shielding designs.

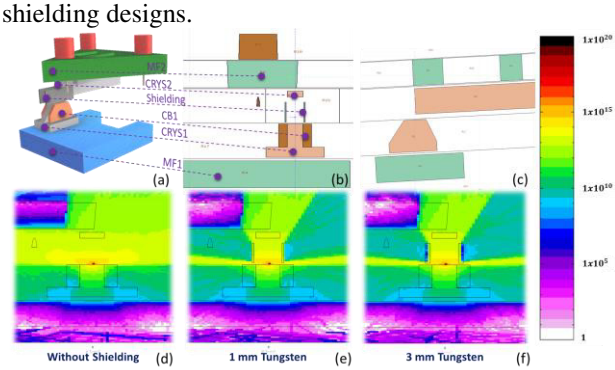


Figure 2: FLUKA simulations: (a) original CAD model; (b) upstream view of the model in FLUKA; (c) side view of the model in FLUKA; (d) to (f) upstream view of photon track length density (Particles/cm²/s) for three shielding designs.

* marlon.saveri@lnls.br

Content from this work may be used under the terms of the CC BY 3.0 licence (© 2016). Any distribution of this work must maintain attribution to the author(s), title of the work, publisher, and DOI.

ISBN: 978-3-95450-188-5 doi:10.18429/JACoW-MEDSI2016-TUPE15

As expected, the simulations have shown that the scattering profiles strongly depend on photon energy and incidence angle. Therefore, the power distribution over the components also strongly depends on the Bragg angle (θ) and *K*-value of the undulator. Table 1 resumes the percentage of power that is absorbed by the 1st and 2nd crystals (CRYS1 and CRYS2, respectively) with respect to the incident power in four representative scenarios.

Table 1: Power Absorption in Crystals

Scenario	CRYS1 (%)	CRYS2 (%)
3º, K=2.27	95.54	1.02
3º, K=0.62	99.00	0.07
60º, K=2.27	98.38	0.15
60°, K=0.62	99.57	0.02

Diffracted Power

The diffracted power was estimated by applying the energy selection of each crystal to the flux spectra weighted by the photon energy. The highest levels of diffracted power occur for low energies and with the Si (111) crystal, when compared to Si(311). This is not only because at low energies the flux is higher and the Darwin Width (DW) of both crystals is larger, but also because the DW of Si(111) is larger than that of Si(311). As expected, the magnitude of the diffracted beam is very small when compared to the incident one, but it is already in the same order of magnitude of scattered power, reaching 0.7 W. Fortunately, most of this power should also be diffracted by CRYS2 and leave the DCM.

Black Body Radiation

Since a few key elements in the crystal cage work at low temperatures, the irradiation power contribution has also been investigated. A simple model was built in ANSYS [11] with roughly similar geometry to that of the crystal cage of the DCM. The main interest was the evaluation for CRYS1 and CRYS2, and their metrology frames, MF1 and MF2. As an approximation, a general emissivity of 0.1 has been considered. Table 2 shows the designed temperature target and the resulting power absorption for each element. Since the resulting numbers are non-negligible, they have become part of the thermal management strategy.

Table 2: Black Body Radiation FEA Estimate

Element	Temperature (K)	FEA Result (W)
CRYS1	80	0.4
MF1	150	3.8
CRYS2	155	0.9
MF2	213	2.7

Thermal Model

In order to define a consistent thermal management strategy, a lumped-mass thermal model has been developed for the DCM core, as depicted in Fig. 3. In order to control the temperature of the second crystal and prevent cooling down of surrounding parts, several local heaters with temperature sensors are applied, so that the temperature at YFM, SSF and CRYS2 are controlled at 22ºC, 22°C and 155 K, respectively. The approximated heat input by the local heaters is also depicted in the figure (arrows). Finally, each link between two nodes defines the thermal conductance (g_i) between them, as seen in Table 3. The conductance values were evaluated by hand calculation and FEA, also taking into account references from literature [12].

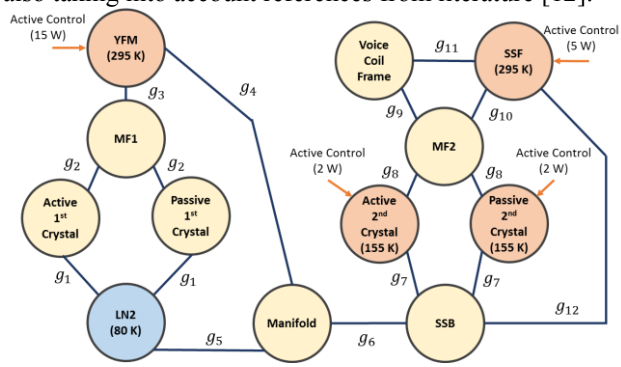


Figure 3 – Thermal Model.

Table 3: Thermal Conductances

Link	Description	g (W/K)
g1	LN2 HTC (block) + Cu + In + Si	36
g2	CRYS1 mount on MF1	0.081
g3	MF1 mount on YFM	0.057
g4	Manifold mount on YFM	0.025
g5	LN2 HTC (manifold)	10
g6	High-conductivity copper strap	0.750
g7	CRYS2 compliant copper strap	0.100
g8	CRYS2 mount on MF2	0.055
g9	Voice Coil mount on MF2	0.048
g10	Leaf springs	0.018
g11	Voice Coil copper straps	0.030
g12	SSB mount on SSF	0.020

No water cooling is considered in this project in order to prevent the need of a thermal bath and more sophisticated cooling design, as vacuum guards, for instance. Instead, most of the power load is taken by the LN_2 system, whereas the chamber and the environment work as an auxiliary heat sink.

Cooling Design

CRYS1 will be indirectly cryogenically cooled by copper blocks (CB1), which are clamped at both sides of the crystal via three fasteners and disc washers, to guarantee the clamping pressure over thermal expansion. The fastener that is close to the diffraction plane should deliver 50 N, whereas the two others are allowed to be stronger, with 125 N each. Each cooling block is a brazed structure made of three separate parts, creating two circular channels, through which LN_2 flows in opposite directions in order to better balance disturbances. Ideally, a laminar flow should be chosen for minimum vibration levels, however,

Content from this work may be used under the terms of the CC BY 3.0 licence (© 2016). Any distribution of this work must maintain attribution to the author(s), title of the work, publisher, and DOI.

ISBN: 978-3-95450-188-5 doi:10.18429/JACoW-MEDSI2016-TUPE15

Content from this work may be used under the terms of the CC BY 3.0 licence (© 2016). Any distribution of this work must maintain attribution to the author(s), title of the work, publisher, and DOI.

this condition was insufficient to keep the hotspot temperature below 130 K, as specified. Thus, turbulent flow (Re ≈ 40000) was chosen to achieve a higher heat transfer coefficient (HTC). Analytical estimates and CFD were used to simulate the performance of several cooling layouts, aiming for high HTC and minimum velocity change, which is considered to be correlated with vibrations levels [13]. The best solution found so far is outlined in Fig. 4, but 3D-printed options are also under evaluation. The small internal diameter, only 2 mm, matches that of the low-stiffness pipes and allows for an increased effective contact area between the fluid and the block.

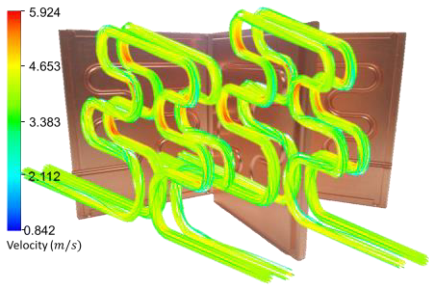


Figure 4 - Cooling channels prototype and velocity distribution obtained by CFD analysis.

An indium layer is used for increasing the heat exchange between CRYS1 and CB1, as well as the deformation of CRYS1 due to clamping and thermal expansion effects. Indeed, the difference in thermal expansion in the cooling processes from room temperature to cryogenic temperatures may cause non-negligible stresses and strains. As for CRYS2, it will be cooled by copper straps (HCS and CCS) linked to an extension of the manifold (CMX), as displayed in Fig. 5.

CLAMPING CONCEPTS

Strict stability performance and positioning tolerances for metrology require not only well designed structures, but also adequate contact interface and coupling between elements, so that high stiffness and high eigenfrequencies can be achieved. Nevertheless, as already mentioned, different thermal expansions might result in unacceptable stresses and deformations, not only in the crystals but also in the metrology frames. Furthermore, the thermal model requires low thermal conductance of some of these connections in order to limit active heating power and manage thermal sensitivity. Thus, there should be an appropriate compromise between stiffness and thermal conductance in fixing the crystals and metrology frames.

Kinematic mounts (as spheres in V-grooves) have been considered for crystal mounting. However, the static friction stiffness is something difficult to be precisely predicted, so that it might lead to uncertain accommodation of the thermal expansion and deformations. Thus, this solution was replaced by fixing each crystal on three wire-eroded flexures in MF1 and MF2 (inset in Fig. 5), which can be more deterministically designed. An optimization process was applied to design them in order to minimize the thermal conductivity, while maximizing stiffness in the principle supporting degrees of freedom and minimizing it in the principle compliant degrees of freedom, so that the crystals may relatively freely expand. Table 4 shows FEA results for CRYS2 assembly on MF2, including stresses and deformation (slope error) due to the cooling down process.

Table 4:Results Using Flexures for CRYS2 Clamping

Property	Value
1st Eigen Frequency	1.7 kHz
Stiffness in stiff direction (x3)	$1x10^{8}$ Nm^{-1}
Stiffness in compliant direction	$1x10^{5}$ Nm^{-1}
Maximum principal stress in CRYS2	1.4 MPa
Slope error on footprint (θ=3°)	0.19 µrad

The preload applied in each fastener has to be high enough to overcome the resulting forces from actuators, gravity effects, disturbances and assembly misalignments, but must not cause large deformations on the diffraction plane nor exceed the stress limits in the crystals. Taking these effects into account and considering that the fastening system should as well guarantee the clamping forces over thermal expansion, a suitable composition of disc washers is used to deliver 320 N per fastener.

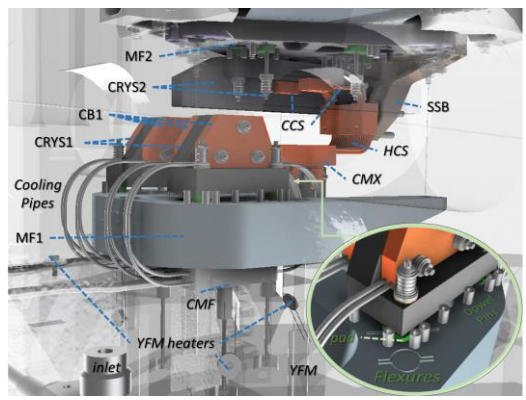


Figure 5 – Main elements related to the solutions proposed for cooling and clamping of crystals.

CONCLUSION

This work briefly described the thermal and clamping solutions for the new high-dynamics DCM for Sirius, which are important to guarantee the integrity and optimum performance of the crystals. Several analytical and numerical tools have been used in order to design them with specific targets regarding slope errors, thermal response, mechanical stiffness and manufacturability. This work will continue during the Detailed Design Phase and, after validation, may be extended to different systems, such as mirrors and other monochromators.

ACKNOWLEDGEMENT

The authors would like to gratefully acknowledge the funding by the Brazilian Ministry of Science, Technology, Innovation and Communication and the contributions of the LNLS team, notably Materials and Optics groups, and the MI-Partners team.

ISBN: 978-3-95450-188-5 doi:10.18429/JACoW-MEDSI2016-TUPE15

REFERENCES

[1] L. Liu, F. H. de Sá, and X. R. Resende, "A new optics for Sirius," in *Proc. IPAC'2016*, pp. 3413–3415.

[2] A. Rodrigues *et al.*, "Sirius Status Report", in *Proc. IPAC'16*, Busan, Korea, May 2016, paper WEPOW001, pp. 2811-2814.

[3] R. Geraldes *et al.*, "The new high dynamics DCM for Sirius", presented at MEDSI 2016, Barcelona, Spain, Sep. 2016, this conference.

[4] T. Tanaka and H. Kitamura, "Spectra: a synchrotron radiation calculation code", *Journal of Synchrotron Radiation*, vol. 8, pp. 1221-1228, Nov. 2001.

[5] MATLAB Release 2011b, The MathWorks, Inc., Natick, MA, USA.

[6] T. Böhlen *et al.*, "The FLUKA code: developments and challenges for high energy and medical applications". *Nuclear Data Sheets*, vol. 120, pp. 211-214, 2014.

[7] A. Ferrari *et al.*, "FLUKA: a multi-particle transport code". CERN-2005-10, INFN/TC_05/11, SLAC-R-773, 2005.

[8] O. Chubar, P. Elleaume, "Accurate and efficient computation of synchrotron radiation in the near field region", in *Proc. of the EPAC98 Conference*, Jun 1998, pp. 1177-1179.

[9] Y. Wu, "CAD-based interface programs for fusion neutron transport simulation", *Fusion Engineering and Design*, vol. 84, pp. 1987-1992, Feb. 2009.

[10] Y. Wu, J. Song, H. Zheng *et al.*, "CAD-Based Monte Carlo program for integrated simulation of nuclear system Super MC", *Ann. Nuel*, vol. 82 pp. 161-168, Aug. 2015.

[11] ANSYS® Academic Research, Release 17.1.

[12] P. Marion, L. Zhang, L. Goirand, M. Rossat, and K. Martel, "Cryogenic cooling of monochromator crystals: indirect or direct cooling?" in *Proc. MEDSI 2006*, Hyogo, Japan, May 2006.

[13] R. Caliari *et al.*, "Studies on flow-induced-vibrations for the new high-dynamics DCM for Sirius", presented at MEDSI 2016, Barcelona, Spain, Sep. 2016, this conference.

Content from this work may be used under the terms of the CC BY 3.0 licence (© 2016). Any distribution of this work must maintain attribution to the author(s), title of the work, publisher, and DOI.

ISBN: 978-3-95450-188-5 doi:10.18429/JACoW-MEDSI2016-TUPE16

DESIGN OF A LEAF SPRING BENDER FOR DOUBLE LAUE CRYSTAL MONOCHROMATOR AT SSRF *

H. Qin†, H. Zhang[1,2], L. Jin[1], W. Zhu[1], K. Yang[1]
[1]Shanghai Institute of Applied Physics, Shanghai 201800, P. R. China
[2] University of Chinese Academy of Sciences, Beijing 100049, P. R. China

Abstract

A leaf spring bender geometry for water-cooled double Laue crystal monochromator (DLM) is presented. The DLM will be employed to acquire high energy monochromatic X-ray (60keV to 120keV) on the ultra-hard applications beamline at SSRF. A compact bending mechanism is designed in order to get horizontally focused high energy monochromatic X-ray as small as 0.5mm. The bender applies a piece of thin asymmetric crystal and a pair of leaf springs which push the crystal to a sagittally bent radius as small as 1 meter by a pair of symmetry moments. An optimized crystal geometry is achieved by taking into account the meridional and sagittal bendings coupled and defined by the anisotropic elasticity of the asymmetric crystal. Furthermore, thermal slope error and structural stress of the bent crystal are analyzed by finite element method (FEA).

INTRODUCTION

Ultra-hard applications beamline will be constructed during phase II project at Shanghai Synchrotron Radiation Facility (SSRF). High energy focused monochromatic X-ray (60 to 120keV) will be chosen for materials science experiments on ultra-hard applications beamline which is derived from a superconductive wiggler light source whose horizontal divergence is as large as 6 mrad. It is critical how to utilize the light source effectively. The sagittally bent double Laue crystal monochromator (DLM) is a desirable optics for hard X-ray beamline and it's very attractive at high energies for its flux, energy resolution and tunability properties [1,2].

In bent Laue-Laue configuration, as illustrated in Figure 1, the first crystal is arranged in inverse-Cauchois geometry, with the source on its Rowland circle at a distance of F_1 from it. Consequently, a virtual-image point is formed on its Rowland circle at a distance of $R_{m1}\cos(\chi-\theta_B)$ from the crystal. The second crystal is bent so that the virtual image point of the first crystal is on its Rowland circle at a distance of $R_{m2}\cos(\chi+\theta_B)$ from it, while its focus point is at a distance of F_2 from it, where R_{m1} and R_{m2} are the meridional bending radius of the first and second crystal, respectively. Both crystals focus the X-rays sagittally and are in the inverse-Cauchois geometry in the meridional plane. The overall focal length of the DLM is:

$$f_s = R_s/(4\sin\theta_B \sin\chi)$$

when both crystals are bent to radius R_s. θ_B and χ are the Bragg angle and asymmetry angle respectively.

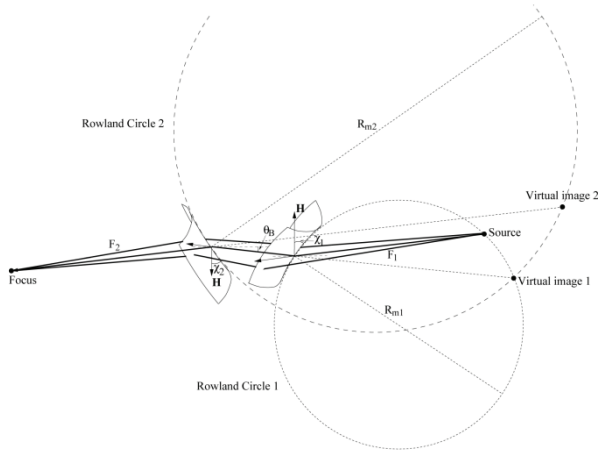


Figure 1: Principle of DLM.

DESIGN AND OPTIMIZATION

Specifications for DLM

The DLM is located at 97 meter from the light source and adopts a pair of thin rectangle crystals with an asymmetric angle of 64.76°. (100) and (311) are the silicon crystal surface and diffraction plane respectively. It will focus the beam horizontally from 30 millimeter to about 500 microns. Main specifications for the DLM is shown in table 1.

Table 1: Specifications for DLM

Parameter	Value
Energy range	60-120 keV
Energy resolution	10^{-3}
Minimum energy step	1eV
Sagittal radius	1-3m
Incident beam size (H×V)	30mm×2.5mm
Beam vertical offset	50mm
Thickness of crystal	1mm
Sagittal residual slope error (RMS)	<6μrad
Meridional residual slope error (RMS)	<10μrad
Vacuum pressure	< 10^{-5} Pa

Optimization for Crystal Dimension

In order to keep the energy resolution at the order of 10^{-3} and obtain a flux of 10^{12} photons/s within the energy range, we set the sample spot at 15 meter (F_2) from the second crystal, due to the limitation for the layout of beamline, whereafter the diffraction plane and asymmetry

† qinhongliang@sinap.ac.cn

Content from this work may be used under the terms of the CC BY 3.0 licence (© 2016). Any distribution of this work must maintain attribution to the author(s), title of the work, publisher, and DOI.

ISBN: 978-3-95450-188-5 doi:10.18429/JACoW-MEDSI2016-TUPE16

angle are chosen by calculation. Sagittal and meridional curvatures change along with crystal dimensions. The ratio of R_s/R_m depends significantly on the aspect ratio (l/w) of the crystal [3], where l and w are the length and width of the Laue crystal, respectively.

Considering meridional radii are not uniform at different positions of crystal laterally, R_m on the crystal surface at a distance of 7.5mm from center as the optimization. It is optimized by changing the aspect ratio with a constant sagittal radius of 1.78 meter at 100keV.

Poisson ratio is another factor of affect the ratio of R_s/R_m. As asymmetry-cut silicon crystal is anisotropic, the Poisson ratio is fixed for a given crystal orientation [4,5]. The length and width of the crystal cutting boundaries are in the [011] and [0-11] direction respectively. The Poisson ratio for the silicon (100) crystal bent around the [011] direction is -0.0642.

An optimized crystal geometry is achieved by taking into account the meridional and sagittal bendings coupled and defined by the anisotropic elasticity of the asymmetric crystal. Figure 2 shows that the bending curvatures depend significantly on the aspect ratio of the crystal. The crystal dimension is 90mm×40mm×1mm (l×w×t). There is 10mm at both sides clamped by each arm.

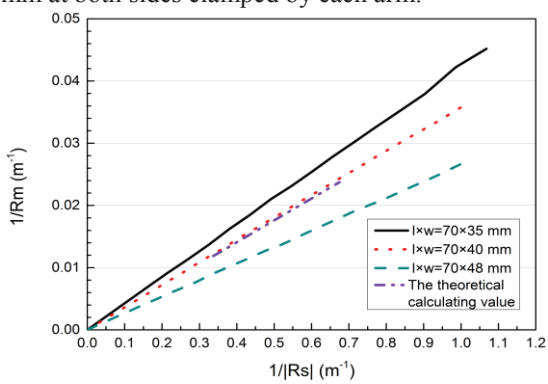


Figure 2: Bending Curvatures Depend on Aspect Ratio.

Leaf Spring Bender

The DLM bender, illustrated in Figure 3, is designed based on a leaf spring bender which was operated on X7B beamline at the National Synchrotron Light Source (NSLS). There are three actions integrated with the bender, which are bending, twist and roll adjustments. Crystal is clamped by a oxygen-free high-conductivity copper spacer inside the groove of each arm which is tightened by screws. The sagittal radius is obtained by pushing one of the two stainless steel leaf springs attached to the clamping blocks while fixing the other one. The bending actuator is a UHV picomotor, which has a desired resolution as small as 30 nm and works with the close-loop control of a DVRT gauge. The flexible springs reduce the local strain and preserve the natural cylindrical bending. There is a twist adjustment on one side of the crystal clamp to ensure that it is parallel to the other side. This adjustment was performed by revolving around the lateral axis of crystal, which is actually a flexible hinge made of QBe2, through a picomotor driven. To correct the downstream beam position laterally when energy is changed, it is essential to set a roll adjustment. Crystal will be rotated around the longitudinal axis, a pair of stainless steel pivots, which are clamped on each sides of the L-shaped plate under the crystal. Specifications for the bender adjustments are listed in table 2.

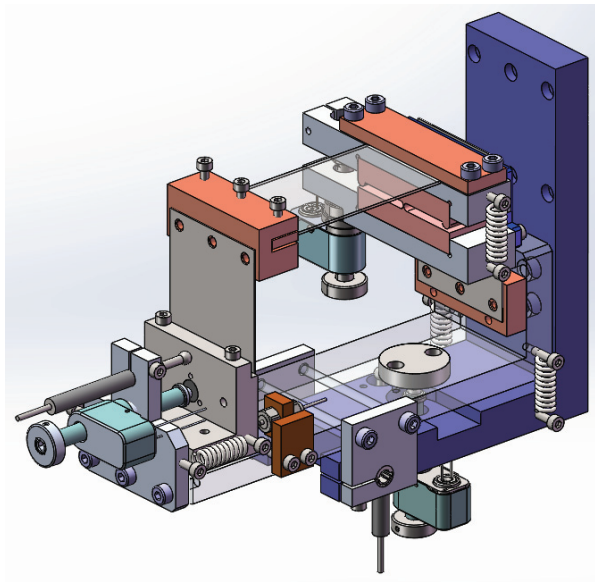


Figure 3: Mechanism of The Leaf Spring Bender.

Table 2: Specifications for The Bender Adjustments

Adjustment	Range	Resolution	Repeatability
Bender	1-3m	0.001m	0.005m
Twist	±1°	0.14arcsec	4.7arcsec
Roll	±2°	0.155arcsec	5arcsec

Residual Slope Error Analysis

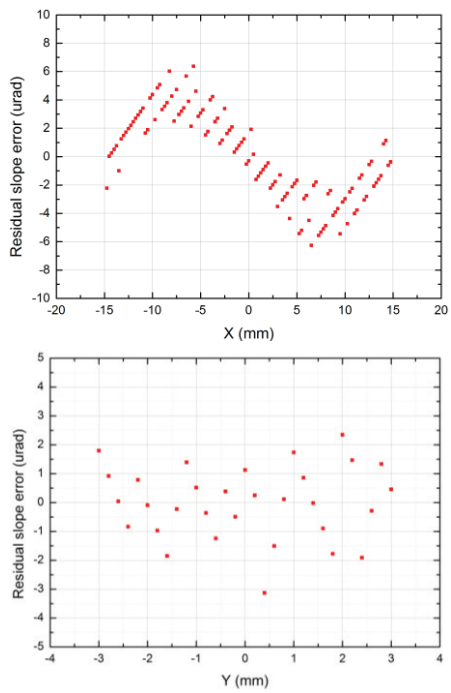


Figure 4: Residual slope error of crystal .

Because of transmission mode, the total heat load absorbed by the first crystal is about 15W with a couple of

Content from this work may be used under the terms of the CC BY 3.0 licence (© 2016). Any distribution of this work must maintain attribution to the author(s), title of the work, publisher, and DOI.

ISBN: 978-3-95450-188-5 doi:10.18429/JACoW-MEDSI2016-TUPE16

Content from this work may be used under the terms of the CC BY 3.0 licence (© 2016). Any distribution of this work must maintain attribution to the author(s), title of the work, publisher, and DOI.

diamond (2.2mm) and SiC (4mm) filters upstream. The maximum thermal density is 0.15 W/mm^2. Crystal holders are water-cooled indirectly by two copper braids which connected with each leaf spring bottom clamps plate. In this way, the maximum temperature and thermal stress of the crystal are 177 centigrade degree and 66.6 MPa.

Large slope error of the crystal will result in lower flux and beam drift on focus point. To keep a reasonable residual slope error sagittally and meridionally for Laue crystal, they are obtained by nonlinear curve fit respectively which take into account the affect of crystal stress, calculated by FEA model, both from bending and heat load.

As illustrated in Figure 4, the sagittal and meridional residual slope error are 3.02μrad (RMS) and 1.25μrad (RMS) respectively.

Tolerance

We have considered and calculated some tolerance situations during manufacturing and installation, which would result in a nonuniform on sagittal radius. Such results are listed in Table 3. The thickness of leaf springs is sensitive to the sagittal radius. It is credible to regard 5 ‰ variation of R_s caused by each parameter as the tolerance limit.

Table 3: Tolerances for The Bender Assembly

Parameter	Dimension	Tolerance
Length of leaf springs	63mm	1mm
Thickness of leaf springs	0.5mm	0.01mm
Angle between bending actuator and leaf spring	90°	±0.015°

SUMMARY

We presented the design and optimization of the leaf spring bender for DLM on ultra-hard applications beamline at SSRF. The surface bending curvatures ($1/R_s$ and $1/R_m$) of an asymmetry-cut crystal were calculated numerically using FEA under the small-deformation theory [6]. And analysis and assignment of tolerances are carried out based on installation. Further optical metrology measurements and x-ray tests for the bending curvatures will be planned and carried out.

ACKNOWLEDGEMENT

The authors would like to thank Dr. Zhong Zhong from NSLS, Brookhaven National Laboratory for his warm help with the DLM development.

REFERENCES

[1] Zhong, Z., Kao, C. C., Siddons, D. P. & Hastings, J. B., " Sagittal focusing of high-energy synchrotron X-rays with asymmetric Laue crystals. I. Theoretical considerations" , J. Appl. Cryst. 34, 504–509, 2001.

[2] Zhong, Z., Kao, C. C., Siddons, D. P. & Hastings, J. B., " Sagittal focusing of high-energy synchrotron X-rays with asymmetric Laue crystals. II. Experimental studies", J. Appl. Cryst. 34, 646–653, 2001.

[3] Shi X., Ghose S., Zhong Z., et al. "Surface Curvatures and Diffraction Profiles of Sagittaly Bent Laue Crystals", Journal of Applied Crystallography, 44(4):665-671, 2011.

[4] Lin Z., Barrett R., Cloetens P., et al. "Anisotropic elasticity of silicon and its application to the modelling of X-ray optics", J. Syn. Rad., 21(3):507–517, 2001.

[5] Lin Z., "Anisotropy and crystal orientation of silicon-application to the modeling of a bent mirror", Aip Conference Proceedings, 2010, 1234(1):797-800.

[6] Krisch M., "Study of dynamically bent crystals for X-ray focusing optics", Nuclear Instruments & Methods in Physics Research, 305(1):378–381, 1991.

ISBN: 978-3-95450-188-5 doi:10.18429/JACoW-MEDSI2016-TUPE18

DESIGN AND FEA OF A 3D PRINTED DETECTOR WINDOW FRAME

W. Tizzano*, Diamond Light Source, Didcot, United Kingdom

Abstract

The purpose of the project was to design and simulate a window assembly to be used in GISAX/GIWAX[1] experiments. The window lies between the sample and the WAXS[2] detector, a modified, in-vacuum detector, with modules removed to allow scattered radiation to pass through to a SAXS[3] detector positioned downstream. The window uses 75 µm thick Kapton® HN film and given the size, pressure and the short distance to the sensors, it was necessary to support it on a frame.

To avoid any information loss from shadowing of the detector, a frame was designed so that shadows will be projected into the gaps between the detector modules. The geometry was such that DMLS[4] was an effective way of producing the item. Given the slenderness of the structure and the forces it supports, the material approaches or exceeds its yield point, so a bilinear, isotropic, hardening material model was chosen; moreover, large deflections were enabled. Also, the contacts were modelled with augmented Lagrange frictional formulation. All these assumptions made the analysis strongly non-linear.

INTRODUCTION

I22 is a non-crystalline diffraction beamline for physical and life sciences that records simultaneously both SAXS and WAXS [1]. A recent upgrade project made GISAX/GIWAX experiments possible.

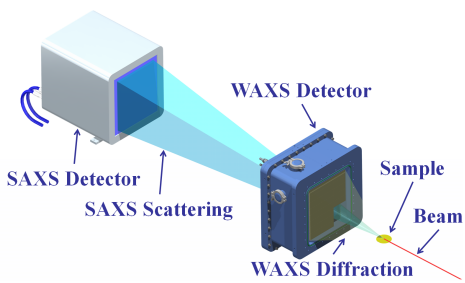


Figure 1: I22 Layout.

I22 is structured as follows (Fig.1): the beam coming from the BCO[5] hits the sample, and the diffracted light goes through a nosecone and is recorded by a 2D in vacuum WAXS detector; the above mentioned detector has some missing modules on the bottom right (Fig.2), allowing part of the radiation to pass through a snout and a camera tube, so the SAXS scattering can be recorded as well, by a detector at a distance that can vary up to 10 m [2] from the sample; three beamstops prevent the direct and reflected beam, and the glare from hitting the detector damaging it.

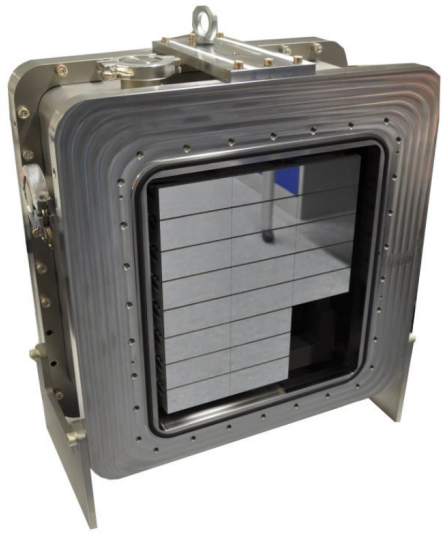


Figure 2: PILATUS3 2M-DLS-L [3].

WINDOW DESIGN

The PILATUS3 2M-DLS-L is an in-vacuum detector, so it was needed to design a window to isolate it from the atmosphere. A 75 µm thick Kapton® HN film was used, because of its transparency to X-ray and low scattering [4]. However, given the area of the window ($\approx 5.8 \times 10^4$ mm^2), the force generated by the differential pressure between the two sides of the film was considerable (≈5.8 kN); for this reason it was necessary to support the Kapton film, or it would have deformed too much, and eventually would have broken.

Nonetheless, any support frame would project a shadow on the detector, and some information would be lost. However, the detector is made up of multiple modules, with gaps between them; the horizontal gaps are 17 pixels tall, and the vertical ones are 7 pixels wide. Since the pixels are square, and have a size of 172 µm^2, the gaps sizes are 2.9 mm and 1.2 mm, respectively. Hence, it was decided to design a support frame consisting in different ribs positioned and angled in such a way that, given a specific relative position between the sample and the detector, the shadow would be projected into the gaps (Fig. 3); in this way no information would be lost.

A rib section was drawn in PTC Creo, and all the necessary constraints were chosen so that in the software the ribs would adapt to the sample position, until this was fixed and the design finalised.

* walter.tizzano@diamond.ac.uk
[1] Grazing Incidence Small/Wide Angle X-ray scattering
[2] Wide Angle X-ray Scattering
[3] Small Angle X-ray Scattering
[4] Digital Metal Laser Sintering
[5] Beam Conditioning Optics

Content from this work may be used under the terms of the CC BY 3.0 licence (© 2016). Any distribution of this work must maintain attribution to the author(s), title of the work, publisher, and DOI.

ISBN: 978-3-95450-188-5 doi:10.18429/JACoW-MEDSI2016-TUPE18

Content from this work may be used under the terms of the CC BY 3.0 licence (© 2016). Any distribution of this work must maintain attribution to the author(s), title of the work, publisher, and DOI.

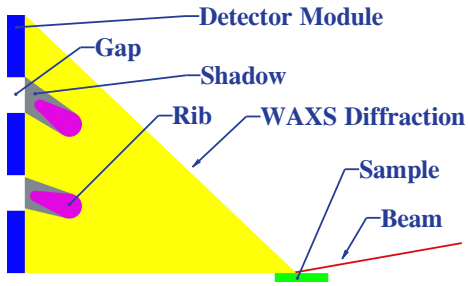


Figure 3: Ribs generation.

Since the resulting geometry was quite complex, and the volume of material was very small compared to the total volume of the part, traditional machining techniques would have been very expensive, so we decided to use an additive manufacturing technique (DMLS).

Among the ones available for this particular manufacturing technique, the material selected was stainless steel 1.4542, due to its mechanical properties (Table 1), and its behaviour in vacuum.

Table 1: SS 1.4542 Mechanical Properties [5]

Property	Unit	Heat Treated
Tensile strength	MPa	1040 ± 60
Yield point (Rp 0.2%)	MPa	430 ± 30
Elongation at break	%	15
E modulus	GPa	170 ± 30

FINITE ELEMENTS ANALYSIS

Given the slenderness of the structure, and the big loads applied to it, it was decided to run an FEA to check before manufacturing that the design was adequate.

Setup

Since the thickness of the Kapton film was very small compared to the other two dimensions, this element was modelled with shell elements and the mechanical properties used are summarised in Table 2:

Table 2: Kapton® HN Mechanical Properties [6]

Property	Unit	Heat Treated
Tensile strength	MPa	231
Yield point at 3%	MPa	69
Elongation at break	%	72
E modulus	GPa	2.5

The contact between the window and the support frame was modelled with an Augmented Lagrange frictional formulation, which reduces the sensitivity of the result to the choice of the contact stiffness, compared to a pure penalty method; in this way, the converged solution will have less penetration, hence being more accurate, at a cost of more iterations to reach convergence [7].

The Kapton film would deform a lot, and the displacements would be large compared to its thickness, so that the force generated by the pressure differential would change direction; for this reason it was necessary to enable the Ansys large deflections option [8].

A preliminary analysis confirmed that both the Kapton film would go beyond the yield point and the steel frame would approach it, so to model these materials as linear elastic was not considered appropriate. To take into account the plastic deformation without increasing too much the complexity of the simulation, a bilinear isotropic hardening model was chosen (Fig. 4).

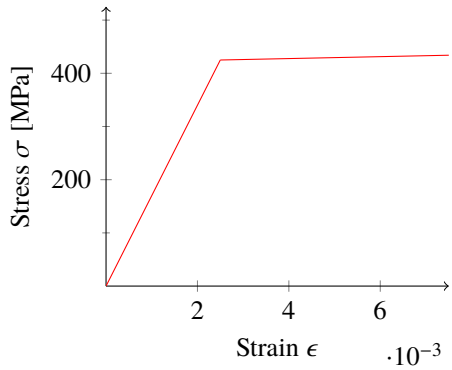


Figure 4: Bilinear Isotropic Hardening.

The Kapton film was meshed using quadrilaters, and the steel structure using tets (Fig. 5). The mesh quality was adequate (Fig. 6). Frictionless supports were used to constrain the Kapton film and the steel structure, and the load was a pressure evenly distributed on the Kapton film.

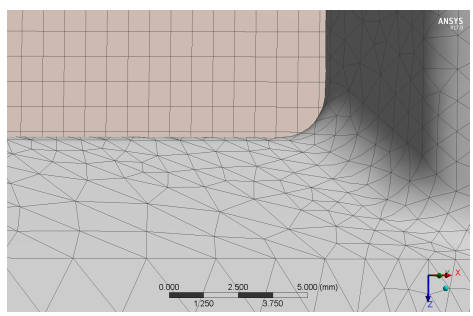


Figure 5: Mesh detail.

Results

The shape of the ribs and the non-linear contact required a fine mesh to reach convergence (minimum size of the elements 1.5 mm), and this was refined even more to 1 mm and then 0.8 mm to check that the solution was not sensitive to the mesh size; neither the stress nor the displacements sensibly changed by modifying the mesh.

The results showed that the support frame would not deform sensibly (Fig. 7); there is a point in the structure where

ISBN: 978-3-95450-188-5 doi:10.18429/JACoW-MEDSI2016-TUPE18

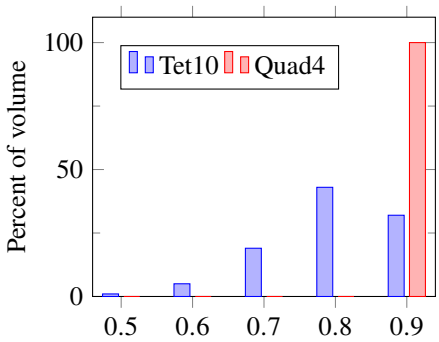


Figure 6: Element quality.

the stress is beyond the yield point, but it is a constrained sharp corner under compressive load, so this is a numerical singularity [9]; other than that, the most stressed point is below the yield point (Fig. 8). The displacements were not excessive for the intended use, as the structure and the Kapton window are far from the detector modules, and the structure does not deform enough to affect the shape of the shadows and make them fall outside the gaps between the modules.

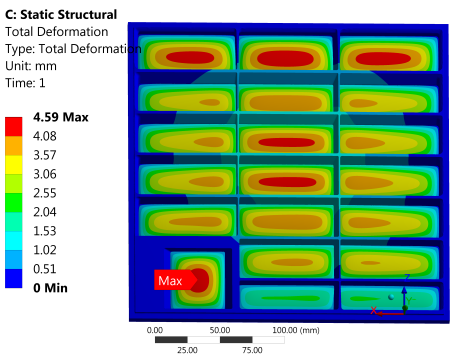


Figure 7: Displacements.

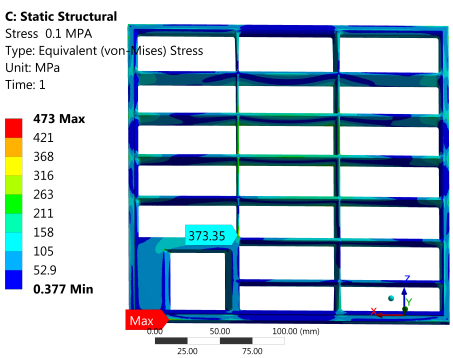


Figure 8: Stress.

FUTURE WORK

The parts were manufactured and assembled (Fig. 9), and they went through a pressure test to check that there were no leaks or visible damage.

A visual examination did not highlight any noticeable permanent deformation so the window is now operative (Fig. 10); a test is planned to measure stress and strain, so the results can be compared to the simulated ones, to validate them.

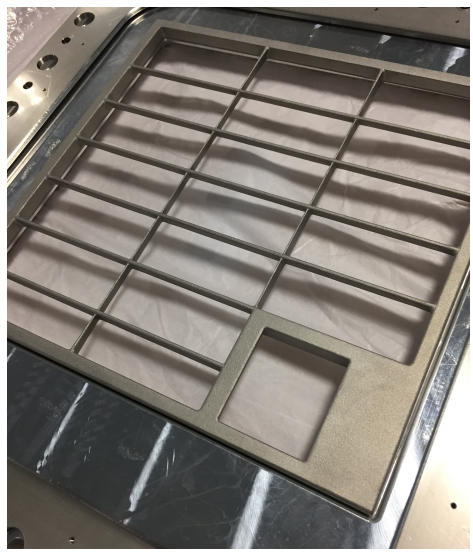


Figure 9: Assembled window (without Kapton film).



Figure 10: Window in operation.

CONCLUSION

A window frame was designed for use in GISAX/GIWAX and manufactured with an additive manufacturing process, only after an FEA confirmed the ability of the design to cope with the loads. It is now in use on the beamline.

REFERENCES

[1] Diamond Light Source, http://www.diamond.ac.uk/Beamlines

Content from this work may be used under the terms of the CC BY 3.0 licence (© 2016). Any distribution of this work must maintain attribution to the author(s), title of the work, publisher, and DOI.

ISBN: 978-3-95450-188-5 doi:10.18429/JACoW-MEDSI2016-TUPE18

Content from this work may be used under the terms of the CC BY 3.0 licence (© 2016). Any distribution of this work must maintain attribution to the author(s), title of the work, publisher, and DOI.

[2] A. Marshall, "Upgrading a Transmission SAX/WAX Beamline to Allow High Quality GISAX/GIWAX Experiments for Soft Matter Thin Films", presented at MEDSI'16, Barcelona, Spain, Sep. 2016, paper THAA04.

[3] DECTRIS PILATUS3 2M-DLS-L Detector System, Technical Specification and Operating Procedure, Version V1.0.

[4] M. Antimonov *et al.*, "Large-area kapton X-ray windows", in *Proc. of SPIE - The International Society for Optical Engineering.*, vol. 9588, 95880F, SPIE, Advances in X-Ray/EUV Optics and Components X, San Diego, United States, 11-12 Aug. DOI: 10.1117/12.2193680.

[5] 3D Alchemy, https://www.3d-alchemy.co.uk/assets/datasheets/3d-Alchemy-Stainless%20Steel%201-4542%20-%2001_13.pdf

[6] Dupont, http://www.dupont.com/products-and-services/membranes-films/polyimide-films/brands/kapton-polyimide-film/products/kapton-hn.html

[7] Ansys Blog, http://www.ansys-blog.com/what-are-the-differences-between-the-contact-formulations

[8] E. Madenci and I. Guven, "Nonlinearity", in *The Finite Element Method and Applications in Engineering Using ANSYS®*, Springer US, 2015, pp. 18–19.

[9] J. Dundurs and M. S. Lee, "Stress concentration at a sharp edge in contact problems", *Elasticity*, vol. 2, Issue 2, pp. 109-112, Jun. 1972.

ISBN: 978-3-95450-188-5 doi:10.18429/JACoW-MEDSI2016-TUPE19

APLICATION OF A NEG COATED CHAMBER AT THE CANADIAN LIGHT SOURCE

S.Y. Chen, D. Bertwistle, M. Kei, C. Murray, T. Pedersen Canadian Light Source Inc., Saskatoon, Canada

Abstract

In the Fall of 2015 a 4800 mm long NEG coated chamber was installed in the Canadian Light Source in cell 9 straight section. The chamber will occupy to majority of the straight length. The chambers vacuum has been monitored for +1 year and no obvious issues has been found.

The chamber body is 10 mm thick and the aperture is an ellipse with an 8 mm height and a 65 mm width. A design feature of the chamber is a lack of support in-between the ends of the chamber. This is due to the double elliptically polarizing undulator (54 mm, and 180 mm period). This proceeding details the following: Structure design and Deflection and strength Finite Element Analysis (FEA); Heat loads and cooling calculation; Supports design and deflection correction; Current strips installation and activation.

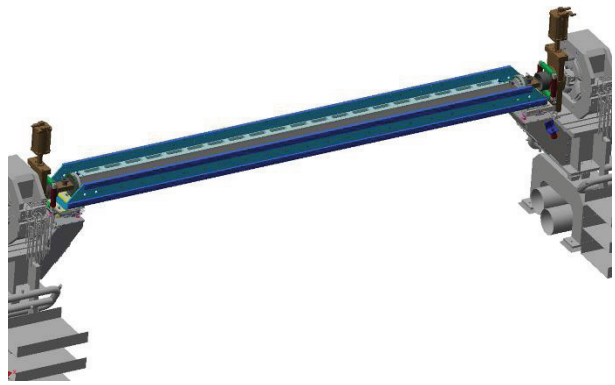


Figure 1: QMSC NEG Coated chamber.

INTRODUCTION

The Canadian Light Source (CLS) is constructing a new phase III Beamline – the Quantum Material Spectroscopy Centre (QMSC). QMSC is designed to cover the energy from EUV radiation to soft X-ray (15 - 1000 eV) with arbitrary polarized light. Two APPLE II type undulators are designed to fulfil this energy range. The 180 mm period Low Energy Elliptically Polarizing Undulator (LE-EPU) covers the photon energy ~15-200 eV while the 55 mm period High Energy EPU (HE-EPU) covers the energy range of ~200-1000 eV. Each of the EPUs are 4 meters in length. The minimum gap for the high energy EPU is 14.5 mm. This double-EPU design required considerable engineering and analysis for the support structure and straight section vacuum chamber.

1. There was no possibility of a middle absorber so the vacuum chamber needed to be capable of absorbing roughly 900 Watts of bend magnet power deposited and an additional 700 Watts heat load from the EPU along the length of the chamber.
2. The chamber could not have a support in-between the two ends, due to the requirement of being able to switch between the HE- and LE-EPU's.
3. The chamber thickness between the magnets was limited to 10 mm, with an aperture of 8 mm. The chamber sag was limited to 0.3 mm. A regular chamber and ion pumps would not be able to be accommodated with the above restrictions.

FMB Berlin supplied a non-evaporable getter (NEG) coated chamber and CLSI designed the two ends supports and put the current strips on the chamber surfaces. Figure 1 shows the chamber assembly.

STRUCTURE, STRENGTH, AND DEFLECTION

Due to the limited space, an H-style structure was required. Both the H-beam width and height were strictly limited by the double-EPU. To ensure the maximum sag was less than 0.3 mm, stiffening bars were attached to the side flanges. The end supports were also designed in such a way that the unti-sag torque could be applied to the chamber. Figure 2 shows the chamber structure. A series of FEA analyses were performed with positive results. Figure 3 and 4 (a), (b) and (c) show the FEA results at different conditions.

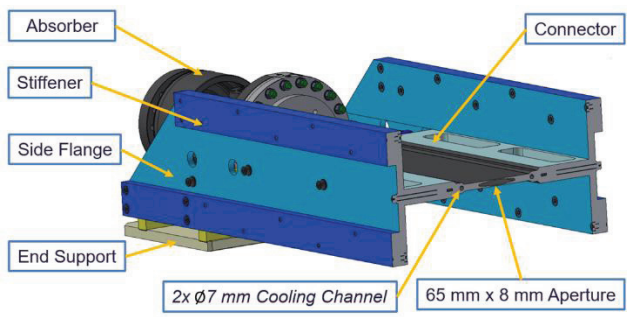


Figure 2: The chamber structure.

Content from this work may be used under the terms of the CC BY 3.0 licence (© 2016). Any distribution of this work must maintain attribution to the author(s), title of the work, publisher, and DOI.

ISBN: 978-3-95450-188-5 doi:10.18429/JACoW-MEDSI2016-TUPE19

Content from this work may be used under the terms of the CC BY 3.0 licence (© 2016). Any distribution of this work must maintain attribution to the author(s), title of the work, publisher, and DOI.

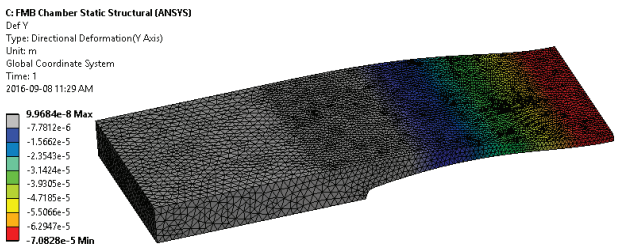
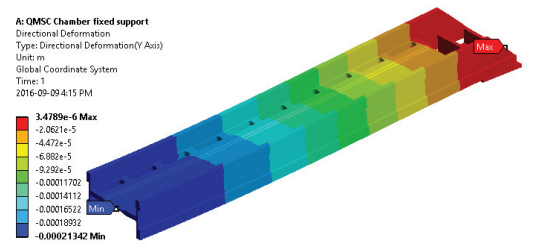
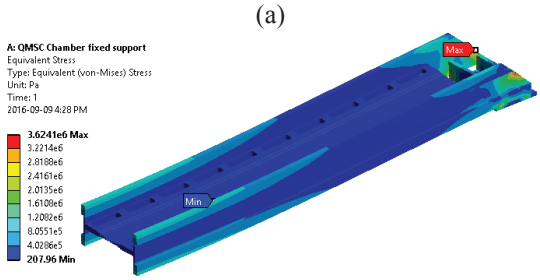


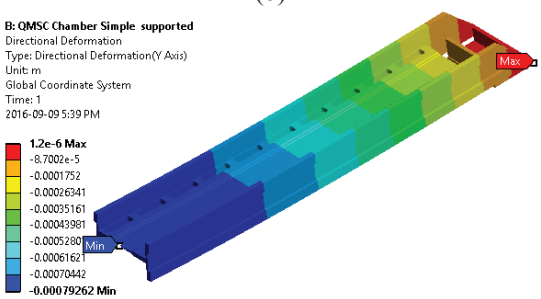
Figure 3: The chamber thin wall deflection and Von-Mises stress results at vacuum pressure.



(a)



(b)



(c)

Figure 4: (a) Chamber deflexion at the gravity force and end fixed supported condition. (b) Chamber Von-Mises stresses at the gravity force and end fixed supported condition. (c) Chamber deflection at the gravity force and end simply supported condition.

SUPPORT DESIGN AND SAG COMPENSATION

The two end support pieces were designed to be attached to two quadrupole magnet girders, with connections for water cooling channels near the ends. For NEG coating activation the chamber needs to be heated to 180 °C. The aluminium chamber length will extend 16.38 mm. For the chamber position stability, one end support was designed to be fixed along the beam direction, while the other end has a custom designed M/V rail stage. This stage allows this end free movement in the beam direction, while a unti-sag correction torque can be transfer to the chamber. Each support has full 6-degree adjustment during chamber installation. Figure 5 shows the two end supports.

Unfortunately, when the real chamber was installed, the chamber sag due to gravity was more than 2 times of the calculated value. The maximum surveyed sag was 0.88 mm. At each end three adjusting jacks were used to compensate for this chamber sag. Figure 6 (a) shows the surveyed chamber sag along the length. Figure 6 (b) shows the chamber's top surface flatness after installation and be adjusted in the Storage Ring.

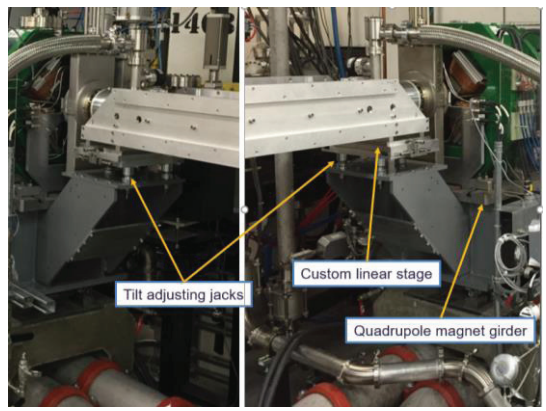
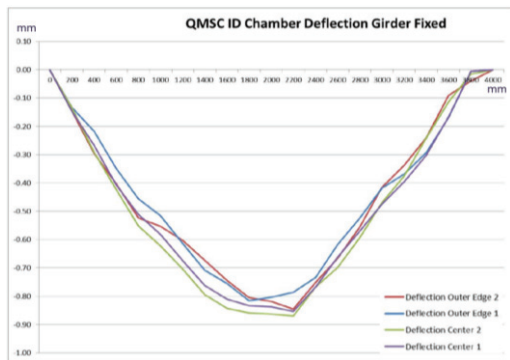
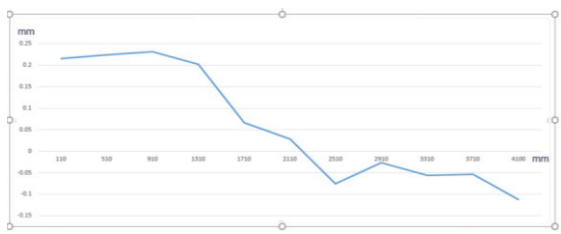


Figure 5: The chamber two end supports.



(a)



(b)

Figure 6: (a) Chamber tested deflexion. (b) Chamber top face flatness after correction.

ISBN: 978-3-95450-188-5 doi:10.18429/JACoW-MEDSI2016-TUPE19

HEAT LOADS & COOLING CALCULATIONS

The chamber takes the upstream bend magnets heat load and also the heat load from the EPU in the straight section.

The bend magnet heat load was calculated using the following CLS storage ring parameters: electron beam current of 500 mA; beam energy of 2.9 GeV; magnetic field 1.354 T, and a bending angle of 15°. The calculated normal linear power density is 69.76 W/mrad and the normal peak power density is 259.6 W/mrad^2. The total bend magnet heat load on the chamber is 900 W. This heat load is primarily distributed on the upstream half of the chamber. See Figure 7 for details.

At the worst case scenario, with the low energy EPU at a minimum gap of 15 mm, and the electron beam is offset from the chamber centre (1.25 mm, 1.25 mm) in the X and Z (out-board, upper) directions. The downstream chamber receives 700 W of heat from the EPU. 603 W impinges evenly on the upper half inner channel surface. The remaining 97 W hits the bottom half of the inner surface evenly. The heat loads are shown in Figure 7, 8.

The heat transfer coefficient 'h' is calculated to be 12003 W/m^2·°C. This is using both of the available Ø7 mm cooling channels, with a flow rate of 2.5 m/s for the cooling water. The pressure drop is 58 Pa, and the cooling water temperature rises 2 °C.

Figures 9 and 10 show the temperature profile on the upstream and downstream chamber halves. Further calculations show that increasing the water flow rate does not reduce the chamber temperature significantly.

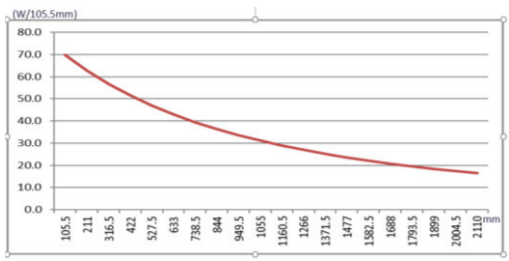


Figure 7: Heat load on upstream half chamber.

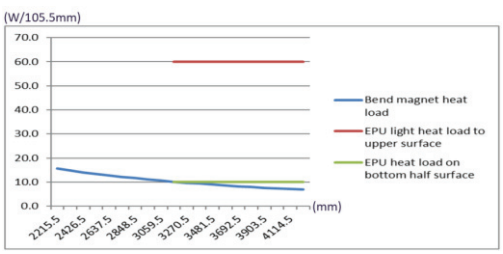


Figure 8: Heat load on downstream half chamber.

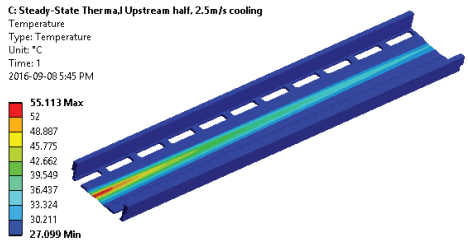


Figure 9: Upstream half chamber temperature.

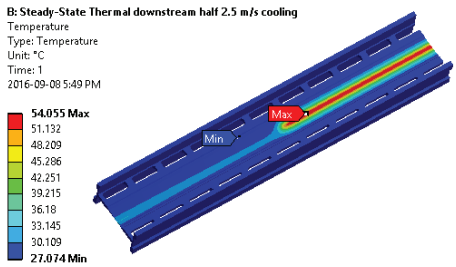


Figure 10: Downstream half chamber temperature.

CURRENT STRIPS INSTALLATION

The current strip array was adopted from the approach BESSY took for one of their insertion devices (ID). It makes use of two regular 12-strip arrays of conductors mounted flush with the EPU vacuum chamber. The independently powered current strips allow for compensation of dynamic multipoles during the EPU's operation.

The challenge was to find appropriate current strips and attach them on the chamber with a position tolerance of 0.1 mm. Several different engineering approaches were considered and tested. The end result was adapted from the NSLS-II solution for their ID. Two 4-metere flexible printed circuit boards were glued on the chamber surfaces. The accurately placed pin holes on the circuit board can be used for positioning the current strips. A jig for gluing the pins and aligning them on the chamber was designed. Figure 11 shows the alignment process.



Figure 11: Alignment jig.

Content from this work may be used under the terms of the CC BY 3.0 licence (© 2016). Any distribution of this work must maintain attribution to the author(s), title of the work, publisher, and DOI.

ISBN: 978-3-95450-188-5 doi:10.18429/JACoW-MEDSI2016-TUPE19

Content from this work may be used under the terms of the CC BY 3.0 licence (© 2016). Any distribution of this work must maintain attribution to the author(s), title of the work, publisher, and DOI.

ACTIVATION

Due to the severe space limitations, the straight section has no ion pumps installed. There is a roughing port and a vacuum gauge on the absorber at each end of the chamber. During the activation process, both ends are pumped on. The activation procedure was supplied by FMB Berlin and Figure 12 illustrates the activating process and pressure results.

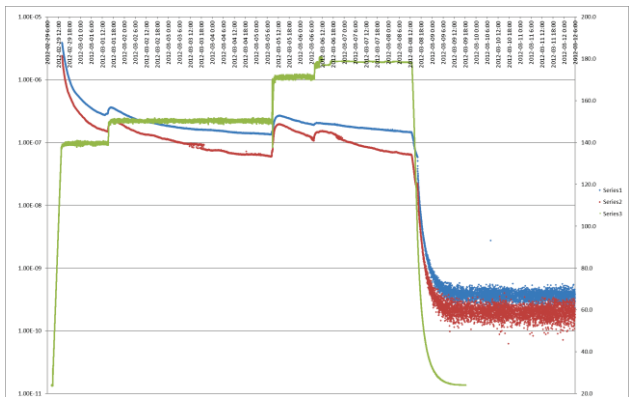


Figure 12: Activating temperature & vacuum levels versus time

CONCLUSION

The QMSC vacuum chamber is the second NEG-coated chamber in use at the CLS. It also has the longest span and uses the thinnest walls out of any chamber at the CLS. The current strips are the first to be installed and used at the CLS. The chamber has been installed in the storage Ring for over 1 year, with no vacuum or cooling issues to date.

ACKNOWLEDGEMENTS

A special thanks goes to Charles Hetzel at NSLS-II for sharing their current strip installation knowledge.

ISBN: 978-3-95450-188-5 doi:10.18429/JACoW-MEDSI2016-TUPE21

CLSI BMIT'S SUPER-CONDUCTING WIGGLER CRYOGENIC SAFETY IMPROVEMENTS*

L. Lin †, T.W. Wysokinski, Canadian Light Source (CLS), Saskatoon, Canada

Abstract

4.1 T superconducting (SC) wiggler on CLS Biomedical Imaging and Therapy (BMIT) beamline [1-4] developed a critical problem in the cryogenic safety relief and refill paths. Ice blockage formed and prevented helium gas from relieving during liquid helium (LHe) refill. This resulted in an internal pressure built up, which caused expelling of the LHe and cold gas helium (GHe) from the wiggler cryostat. Several improvements were performed over the years including replacement of the original rupture disk, the pressure relief valves and installation of metal O-ring seals at external ports. Following these improvements, a major upgrade on the wiggler safety relief path was implemented by adding a new vent pipe directly connected to the cryostat for safety exhaust. The LHe refill path was also modified to eliminate possibility of ice blockage. During initial tests after the upgrades, we experienced significant heat load increase which was linked to the thermal acoustic oscillations in the LHe transfer line. The problem was resolved by improving the insulation vacuum in the transfer line and adding a super insulation assembly into the direct vent pipe along with a plug at the refill path.

BACKGROUND

BMIT's 05ID-2 beamline 4.1-Tesla, 25+2 pole wiggler was designed and constructed by Budker Institute of Nuclear Physics (BINP) [3]. The wiggler is equipped with Sumitomo cryo-coolers. During normal operation, the wiggler runs at sub-atmospheric pressure ~50 mbar below zero gauge-pressure with temperature range of 3.1-3.5 K at the second stage of the top cryo-coolers. The minimal no-load pressure recorder during the SR shutdown was –162 mbar. In case of the single quench, the boil-off gas is usually contained within the cryostat with a pressure rise to below 300-400 mbar activation pressure of the two pressure relief valves. There is a rupture disk with activating pressure of 1.7 bar (gauge) in case of further pressure rise for machine safety protection.

During LHe refilling procedure it was observed that the LHe transfer was blocked. Pressure was building up inside the cryostat with no sings and indications from the external pressure gauges. A large amount of cold helium gas was expelled from the cryostat through the refill port when the refill tube was removed.

The ice blockage was experienced several times over the 2-3 years of operation. The wiggler had to be warmed up to about 100 K in order to enable a LHe refill.

INVESTIGATIONS

The following areas were investigated for the refill and pressure built up problems:

1. Air leaks.
2. Vent path
3. LHe refill path

Air Leak Problems

Air leaks were discovered at the followings:

- Air leaked through the pressure relief valves which were not able to seal-back tight after gas release during quench, especially when a large amount of cold helium gas was passing through the seal surface.
- Air also leaked through the mechanical and electrical connection ports that had Buna O-ring seals.
- There was a small leak through the pinhole in the rupture disk.

Vent Path Problem

The air leaking into the cold space eventually froze at the wiggler's vent path – see Figure 1, separating the cold space from the room temperature gas space. The vent path was made of a spiral channel cut in a foam insulation installed in wiggler's central throat. The vent path/channel was about 15 mm wide and 10 mm deep, connecting dewar with the top casing where the vent outlet was located. The pressure relief valves and the rupture disk were both connected to this vent outlet. As a result of the blockage, the helium gas was not able to relief through this vent path during liquid helium refilling procedure, at the same time the pressure gauges were not showing properly the cold space pressure - a safety concern was raised.



Figure 1 Spiral vent path cut in the insulation foam.

*Work supported by Budker Institute of Nuclear Physics under contract No. C60109-029
† Linda.Lin@lightsource.ca

Content from this work may be used under the terms of the CC BY 3.0 licence (© 2016). Any distribution of this work must maintain attribution to the author(s), title of the work, publisher, and DOI.

ISBN: 978-3-95450-188-5 doi:10.18429/JACoW-MEDSI2016-TUPE21

Content from this work may be used under the terms of the CC BY 3.0 licence (© 2016). Any distribution of this work must maintain attribution to the author(s), title of the work, publisher, and DOI.

LHe Refill Path Problem

The wiggler refill path is constructed with three-sections: external LHe transfer line is inserted into the wiggler through the top section and sits on the first funnel. The middle section is made of an internal LHe transfer tube that leads LHe to the second funnel located on the top of the magnets. The bottom section is a bended LHe transfer tube built around the magnets that discharges the LHe to the bottom of the cryostat (see Figure 2). Ice has formed at all three refilling path sections. A heated copper pipe was used to successfully remove the ice at the top and the middle sections. However, if ice-block formed at the second funnel or the bottom section it was not removable without the warmup. When attempting to refill with vent path blocked, LHe would boil-off at the transfer line sections and at the top section of the cryostat. Pressure therefore would build up until refill tube was removed. A large amount of cold helium gas came out from the cryostat at high pressure at this point, cryogenic hazard occurred.

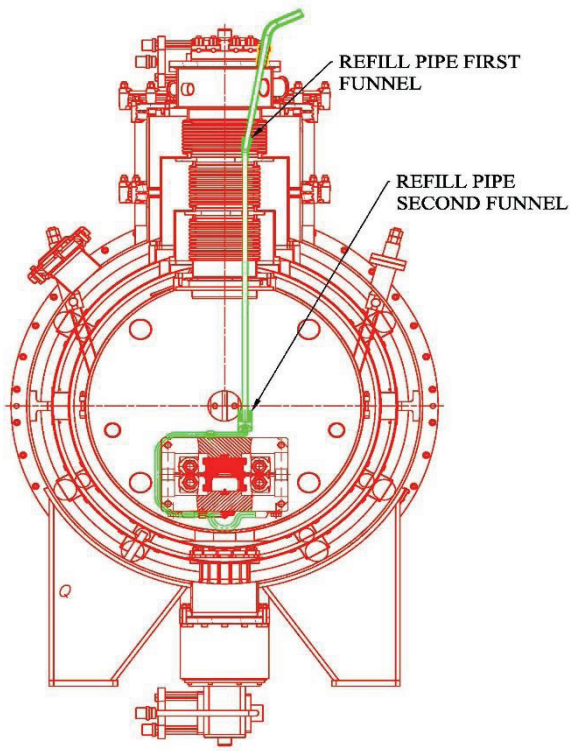


Figure 2 BMIT's wiggler initial refill path.

SOLUTIONS

1. Fix the leaks – the source of the ice blockage

- Pressure relief valves were replaced with the type equipped with zero leak seals at reset pressure. Valves were piped about 450 mm away from the vent outlet port and connected with a 300 mm straight pipe downstream to prevent from ice and condensations forming at valve seal surface.
- All Buna O-ring seals were replaced with aluminium O-rings providing leak free operation.
- Rupture disk was replaced with the new one and equipped with rupture indication signal.

2. Major modifications at the wiggler vent path and refill path – made by BINP group.

- A separate and direct vent path was added - 1.5" DIA pipe connected the wiggler cryostat cold and warm space through the central throat. This hollow pipe runs from the top of the cryostat to the new rapture disk located on the top of the wiggler and provides a barrier free direct exhaust for emergency pressure relief.
- The vent path for the pressure relief valves uses improved spiral channel at the foam insulation.

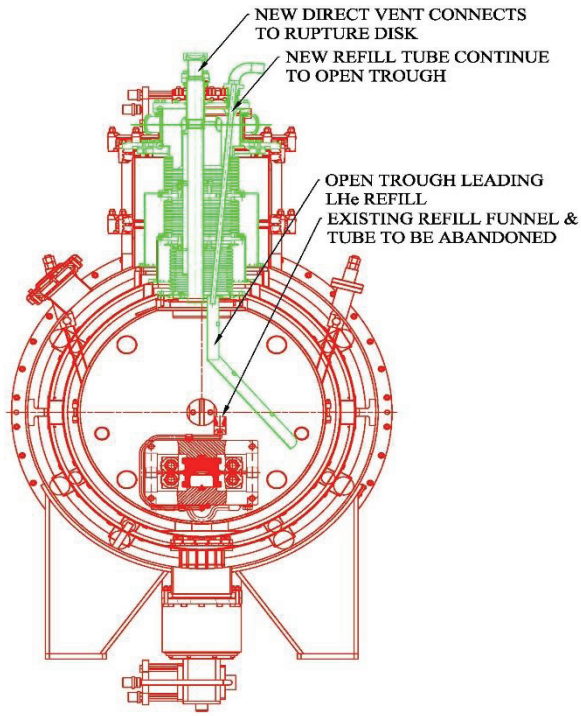


Figure 3 A new vent path & refill path.

- Two heaters were added into the pressure relief vent path to the two narrow points of the central throat - at the two copper flange plates (20 K & 60 K) to mitigate potential ice built up.
- A new LHe refill path was constructed to replace the existing one with two sections. The top section is a single tube runs straight into the bottom section - an open trough that leads the LHe to the lower side of the wiggler cryostat (Figure 3). This change is to eliminate potential ice blockage at the bends.
- Liquid helium transfer line was permanently connected to the wiggler – This became a huge problem as discovered later.

OUTCOMES

1. The wiggler experienced thermal acoustic oscillation problems at refill after the upgrades [4]

- The problem was discovered at the first refill: pressure at the cryostat built up to 350 mbar two hours after the refill was completed and stabilised for about 5

ISBN: 978-3-95450-188-5 doi:10.18429/JACoW-MEDSI2016-TUPE21

hours then started oscillated. The LHe started evaporating right after and the LHe level in the cryostat dropped from 43% to 0 in less than 2 hours (see Figure 4).

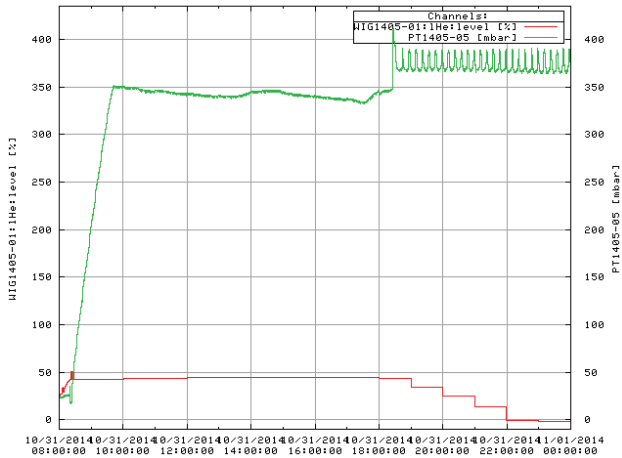


Figure 4 Pressure & level changes at oscillation.

- The second refill repeated and confirmed the same problem: 7 hours after the refill, pressure built up to 350 mbar and stabilised for about 4 hours then started oscillations again.
- BINP indicated that the thermal acoustic oscillation was most likely caused from the long, warm, LHe transfer line that was connected to the cryostat.

2. Several steps performed to fix the thermal acoustic oscillation problem

- LHe transfer line was removed. Pressure at cryostat built up to below pressure relief pressure (350 mbar) and was able to drop and stabilized. Small osculation was still shown (see Figure 5). The above atmosphere pressure at no load condition indicated that heat load increased at this new configuration.

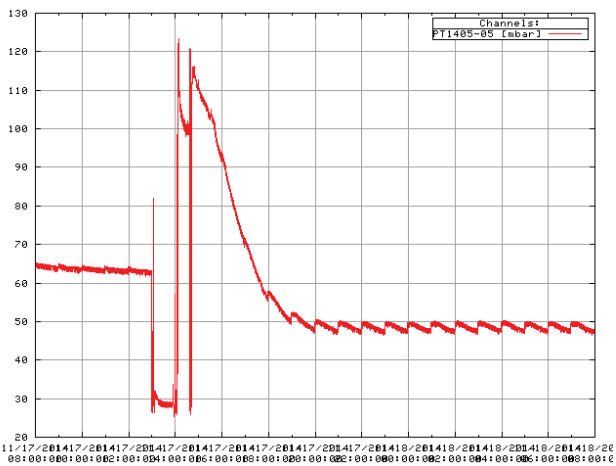


Figure 5 pressure change at LHe transfer line removed.

- A dummy plug made of G-10 FR4 (epoxy the surface) installed at the LHe refill tube to close the opening in the central throat insulation.
- Supper insulation disks designed and installed inside of the 1.5" DIA exhaust pipe using multilayer insulation to reduce radiative and convention heat-loads.

3. End results

- The secondary vent path provides a barrier free safety relief to the wiggler cryostat with super-insulation disks to reduce the heat leaks.
- Pressure at the wiggler cryostat is able to run back to sub-atmosphere to about -160 mbar after the upgrades with no SR heat-load.

CONCLUSIONS

BMIT SC wiggler has performed very well since from the initial installation in 2007. However due to air leaks, ice blockages have formed both at vent and refill path which prevented the refilling process and also isolated the cold space from the safety relief system. Pressure was building up within the cryostat causing cold GHe expelled from the top sections of the refill path when LHe transfer line was removed.

Several improvements were performed over the years trying to resolve this cryogenic safety problem. All air leak sources were removed via replacing the original rupture disk, pressure relief valves and installing metal O-ring seals at external ports. A major upgrade on the wiggler was performed by BINP group in 2014. A new barrier free safety vent pipe that is directly connected to the cryostat was added along with a significant change on LHe refill path to eliminate possibility of ice blockage. Serious heat load increase which was linked to the thermal acoustic oscillations in the LHe transfer line and direct vent path was observed through LHe refill after the upgrade. This heat load was minimised when the LHe transfer line was disconnected, a super-insulation assembly installed within the direct vent pipe and a plug installed at the refill path.

ACKNOWLEDGMENTS

The authors would like to acknowledge helps from the CLS engineering staff and BMIT scientific staff.

Work described in this paper was performed at the BMIT facility at the Canadian Light Source, which is supported by the Canada Foundation for Innovation, Natural Sciences and Engineering Research Council of Canada, the University of Saskatchewan, the Government of Saskatchewan, Western Economic Diversification Canada, the National Research Council Canada, and the Canadian Institutes of Health Research.

REFERENCES

[1] A. Sitnikov, (2005) CLSI Doc. No. 5.8.25.5 Rev. 0.
[2] L.D. Chapman, (2007) CLSI Doc. No. 26.2.1.1 Rev. 0.A.
[3] S.V. Khrushchev, V.K. Lev, N.A. Mezentsev, E.G. Miginsky, V.A. Shkaruba, V.M. Syrovatin, V.M. Tsukanov, "27-Pole 4.2 T wiggler for biomedical imaging and therapy beamline at the Canadian light

Content from this work may be used under the terms of the CC BY 3.0 licence (© 2016). Any distribution of this work must maintain attribution to the author(s), title of the work, publisher, and DOI.

ISBN: 978-3-95450-188-5 doi:10.18429/JACoW-MEDSI2016-TUPE21

source",
http://dx.doi.org/10.1016/j.nima.2008.12.112.

[4] Wysokinski, Tomasz W. and Chapman, L. Dean and Miller, Denise and Belev, George and Lin, Linda and Adam, Madison and Wurtz, Ward and Dallin, Les, "25+2 poles, 4.3 T wiggler at BMIT – 7 years operational experience ", AIP Conference Proceedings, 1741, 020026 (2016), DOI:http://dx.doi.org/10.1063/1.4952805.

Content from this work may be used under the terms of the CC BY 3.0 licence (© 2016). Any distribution of this work must maintain attribution to the author(s), title of the work, publisher, and DOI.

ISBN: 978-3-95450-188-5 doi:10.18429/JACoW-MEDSI2016-TUPE22

LOW-ORDER ABERRATIONS CORRECTION OF EXTREME ULTRAVIOLET IMAGING OBJECTIVE WITH DEFORMABLE MULTILAYER MIRRORS*

Mitsunori Toyoda†, Ryo Sunayama, Mihiro Yanagihara
IMRAM, Tohoku Univ, 2-1-1 Katahira, Sendai, Miyagi, 980-8577 Japan

Abstract

To realize high spatial resolution of an extreme ultraviolet (EUV) microscope, the key technical challenge would be reducing wave aberrations of an imaging objective. Astigmatism arising from figure error of a mirror substrate is the primary aberration which spoils spatial resolution. In this study, we develop a deformable multilayer mirror which is capable of correcting astigmatism on the Schwarzschild objective for EUV microscopy. The deformable mirror is consisting of a concave mirror with a Mo/Si multilayer coating, and a mirror holder with a three-points holding mechanism. This novel device acts as a stigmator, since radii of curvature in mutually orthogonal directions on the concave mirror can be precisely controlled by applying bending forces on the holding points. We report detail of optical and mechanical design of the deformable mirror, which can correct relatively large astigmatism with amplitude of 4 nm rms.

INTRODUCTION

When we apply extreme ultraviolet (EUV) with a wavelength between 3 to 30 nm to optical microscopy, high spatial resolution of a few tens of nanometers can be expected in diffraction-limited imaging. Recently, we have proposed the three-multilayer mirror objective for a full-field EUV microscope [1, 2]. The primary advantage of this novel design would be large numerical aperture (NA). The objective can provide large NA of 0.25, which is at least ten times larger than that for conventional zoneplate optics in EUV and soft X-ray region. The large NA design yields good Rayleigh resolution as well as high image illuminance, which is proportional to the square of NA.

Besides, the objective can bring high magnification, which is essential for fast video observation with an EUV CCD camera with moderate pixel size. To realize a high magnification of 1500, we employ a two-stage imaging configuration by combining the Schwarzschild mirror as primary objective (magnification: x30) and an additional magnifier with a single concave mirror (magnification: x50). To confirm an imaging performance of the objective, we have developed the full-field microscope for at-wavelength observation of an EUV lithography mask [3], and we successfully demonstrated that the microscope can resolve fine line and space patterns with half pitch of 30 nm, at an operating wavelength of 13.5 nm [4].

* Work supported by
JSPS KAKENHI: Grant Numbers. 16H03877, and 16K13693,
Shimadzu Science Foundation.
† toyoda@tagen.tohoku.ac.jp

To provide diffraction-limited resolution on the novel objective, the key engineering challenge would be reduction of wave aberrations, where we should eliminate aberrations below 1/14 of an operating wavelength, so as to satisfy the Maréchal criterion [5]. In case of the EUV microscope, allowable aberrations fall within an extremely small value, i.e., 1 nm rms. Wave aberrations does not only originate from an intrinsic effect of optical design, but also from misalignments and figure errors of multilayer mirrors. Especially, astigmatism resulting from figure error of mirror substrates would be a common issue to spoil resolution of the high magnification objective. We often observe astigmatism on the objective, since a small holding forces or gravity applied to mirrors yield considerable figure error, even if we apply well-polished substrates. This fact motivates us to develop a stigmator which can modify surface figure to reduce astigmatism in real time. In this paper, we report detail of a deformable multilayer mirror which can act as a stigmator for stable operation of the EUV microscope.

MECHANICAL DESIGN OF DEFORMABLE MULTILAYER MIRROR

As shown in Fig. 1, the Schwarzschild objective, which is employed as a primary optics for the EUV microscope, is consisting of the two concave (M1) and convex (M2) mirrors.

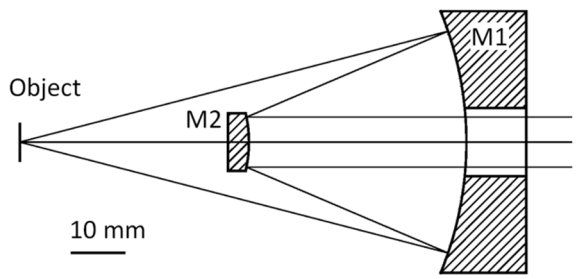


Figure 1: Schematics for the Schwarzschild objective configuration see Table 1.

Table 1: Optical Configuration for the Objective

Magnification	30
Numerical aperture	0.25
Radius of curvature r_1 (mm)	65.935
r_2 (mm)	24.286
Mirror separation d (mm)	41.65
Effective diameter ϕ_1(mm)	42.8
ϕ_2(mm)	9.6

Content from this work may be used under the terms of the CC BY 3.0 licence (© 2016). Any distribution of this work must maintain attribution to the author(s), title of the work, publisher, and DOI.

ISBN: 978-3-95450-188-5 doi:10.18429/JACoW-MEDSI2016-TUPE22

Content from this work may be used under the terms of the CC BY 3.0 licence (© 2016). Any distribution of this work must maintain attribution to the author(s), title of the work, publisher, and DOI.

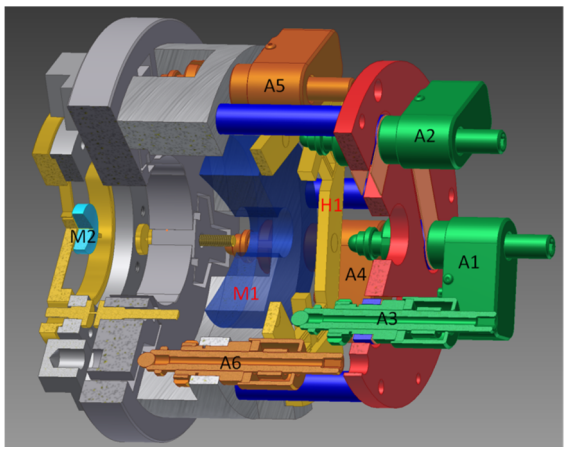


Figure 2: Mechanical drawing of a mirror holder with the substrate bending mechanism.

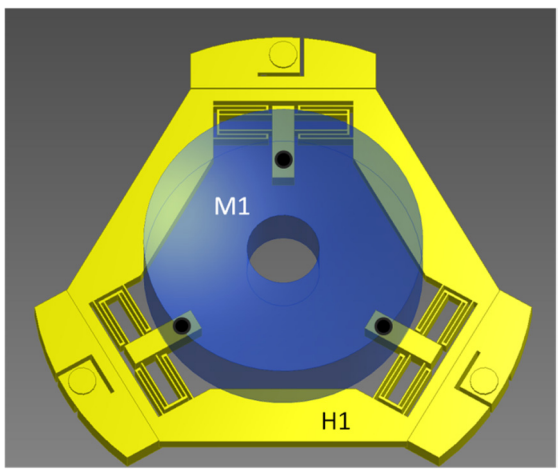


Figure 3: Schematics for the mirror holding plate (H1). The concave mirror (M1) is glued to edge of the holding arm (black circle).

The system in a concentric configuration is capable of correcting first three Seidel aberrations, i.e., spherical aberration, coma, and astigmatism, and thus it can provide blur-free imaging over a large field of view. Optical design has been detailed in Ref. [2]. Figure 2 represents a mechanical drawing for the objective. To realize the concentric configuration, the convex mirror, M2, can be precisely aligned by using the three-axis flexure stage with the piezoelectric motors, A4 to A6.

The both mirror substrates were glued to the holding plates shown in yellow. As shown in Fig. 3, the plate has three holding arms with a flexure spring, and the bottom of the mirror substrate was glued to the edge of the arm. The flexure spring was employed so as to absorb difference of thermal expansion between the mirror substrate and holding plate, which are made of different materials, i.e., fused silica and duralumin, respectively. Basic concept for a stigmator is shown in Fig. 3. Radii of curvature in mutually orthogonal directions of the mirror can be controlled by applying two torsional moments in the opposite direction to the holding arms, which are shown

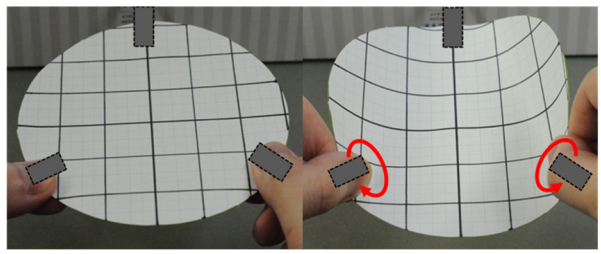


Figure 3: Basic concept of a stigmator.

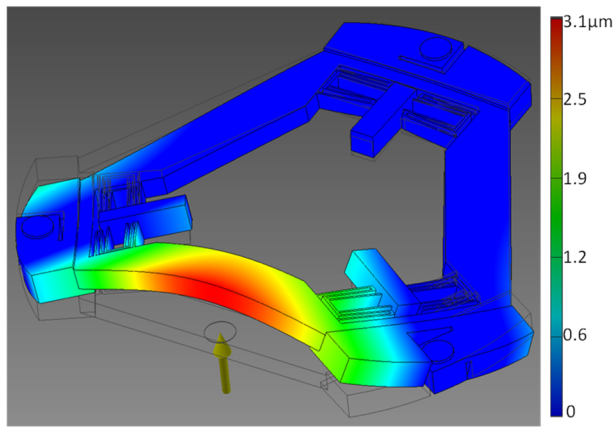


Figure 4: Torsional moments generation on the holding plate. Force along the optical axis (yellow allow: 10 N) is loaded on the plate. The mirror substrate was excluded in the calculation. Color bar shows deformation along the optical axis.

with the red allows. To correct astigmatism with sub-nm accuracy, the torsional moments were precisely controlled by loading forces along an optical axis on the holding plate. The piezoelectric motors, i.e., A1 to A3 in Fig. 2, and flexure springs were equipped to press the middle points between the holding arms with the maximum load of 20 N. Figure 4 illustrates torsional moment generation on the holding plate, which was given with numerical calculation based on a finite element method (FEM). For the numerical analysis, we applied the two software, i.e., Inventor (Autodesk Inc., CA, USA) for 3d modeling, and ANSYS Multiphysics (ANSYS, Inc., PA, USA) for FEM calculation. As shown in Fig. 4, the two holding arms next to the load point are rotated in the opposite direction, when we apply the force on the holding plate. We also see that the edges of the two arms move along the optical axis. This result indicates that applied force should bring a small tilt of the concave mirror.

Wave aberrations generated on the stigmator was numerically analyzed. For quantitative analysis, firstly, surface figure of the concave mirror was calculated with a FEM. Figure 5 shows a FEM result in which we apply 10 N load on the middle point. Then, the surface figure was represented by using annular Zernike polynomials [6]. Amplitudes for the polynomials with obstruction ratio of 0.26 were computed with Mathematica software (Wolfram, IL, USA). Table 2 summarize the amplitudes for the low-order terms, i.e., z_1 to z_6, when we apply a 10-N load

ISBN: 978-3-95450-188-5 doi:10.18429/JACoW-MEDSI2016-TUPE22

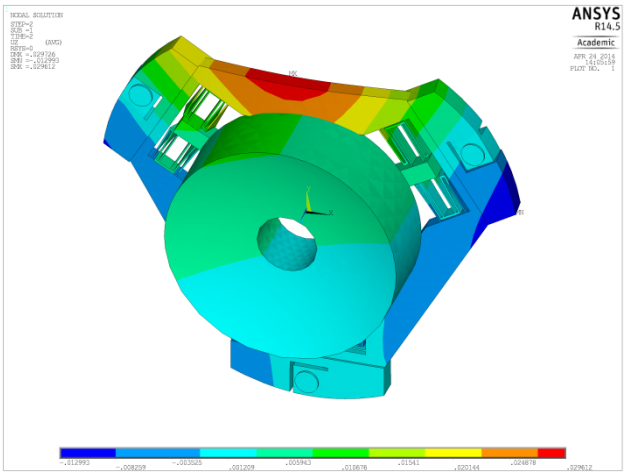


Figure 5: FEM result in which we apply 10-N load on the middle point. Color bar shows deformation along the optical axis.

Table 2: Low-Order Aberration Arising from Figure Deformation of Concave Mirror

Piston z_1 (μm)	7.82
Tilt x z_2 (μm)	-1.52
Tilt y z_3 (μm)	3.91
Power z_4 (nm)	0.09
Astigmatism x z_5 (nm)	-3.96
Astigmatism y z_6 (nm)	-0.69

on the middle point. The data clearly show that astigmatism with an amplitude of 4 nm was generated by the figure deformation, which is large enough value for the stigmator on an EUV imaging system. We also see that the terms representing the piston and tilts i.e., z_1 to z_3, are also raised. These effects yield misalignments of the mirror, where the sphere center moves 4 μm along the optical axis, and 12 μm in the vertical direction to the axis. These misalignments can be easily corrected with the three-axis stage on the convex mirror to be the concentric configuration. Higher-order effects were also estimated. Figure 3 represents amplitudes for the higher-order terms, i.e., z_7 to z_{32}. According to the computation, we confirmed that the amplitudes were below 0.15 nm rms., which indicates the higher-order terms are negligibly small for diffraction-limited imaging in a 13-nm wavelength region.

CONCLUSION

Astigmatism arising from figure error of a mirror substrate is the primary effect which spoils spatial resolution on an EUV microscope. To realize diffraction-limited resolution, the novel stigmator correcting astigmatism on the Schwarzschild objective for EUV microscopy is proposed. The stigmator is consisting of a concave mirror with a Mo/Si multilayer coating, and a mirror holder with a surface bending mechanism. We successfully demonstrate via FEM calculations that the stigmator can correct relatively large astigmatism with an amplitude of 4 nm rms., without introducing higher-order aberrations. In the next step, we experimentally confirm validness of the stigmator proposed by applying an interferometer to measure a wavefront of the EUV imaging objective.

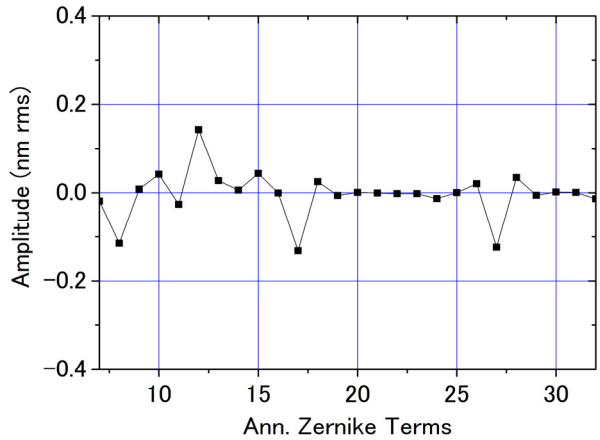


Figure 6: Amplitude for higher-order terms (z_7 to z_{32}). In the calculation, the diameter of unit circle and obstruction ratio was 50 mm and 0.26, respectively.

ACKNOWLEDGMENT

This work was partially supported by JSPS KAKENHI (Grant Numbers. 16H03877, and 16K13693), and Shimadzu Science Foundation. The authors thank E. Sasaki of Tohoku Univ. for a fruitful discussion about mechanical design.

REFERENCES

[1] M. Toyoda, Japan Patent, No. P5489034, Mar. 7, 2014.

[2] M. Toyoda, "Flat-field anastigmatic mirror objective for high-magnification extreme ultraviolet microscopy", *Adv. Opt. Techn.*, vol. 4, no. 4, pp. 339-346, 2015.

[3] M. Toyoda *et al.*, "At-wavelength extreme ultraviolet lithography mask observation using a high-magnification objective with three multilayer mirrors", *Appl. Phys. Express*, vol. 5, p. 112501, 2012.

[4] M. Toyoda *et al.*, "Demonstrating 30-nm spatial resolution of three-multilayer-mirror objective for extreme ultraviolet microscopy: Imaging test by observing lithography mask", *Appl. Phys. Express*, vol. 7, p. 102502, 2014.

[5] M. Born and E. Wolf, "Principles of Optics", Oxford, UK: Pergamon Press, 1980.

[6] V. N. Mahajan, "Zernike annular polynomials for imaging systems with annular pupils" *J. Opt. Soc. Am.* vol. 71, pp. 1408-1408, 1981.

Content from this work may be used under the terms of the CC BY 3.0 licence (© 2016). Any distribution of this work must maintain attribution to the author(s), title of the work, publisher, and DOI.

ISBN: 978-3-95450-188-5 doi:10.18429/JACoW-MEDSI2016-TUPE23

GLIDCOP BRAZING IN SIRIUS' HIGH HEAT LOAD FRONT-END COMPONENTS

G. V. Claudiano, O. R. Bagnato, P. T. Fonseca, F. R. Francisco, R. L. Parise, L. M. Volpe
LNLS, Campinas, Brazil

Abstract

Sirius is a 4th generation synchrotron light source in project. Some of Sirius' beamlines will have a very high power density, more than 50 kW/mrad², to be dissipated in components that have a limited space condition. Thus, the refrigeration of these components is complex when one has in mind that the coolant flow cannot be too turbulent in order to not induce much vibration in the components.

Oxygen Free Copper (C10200) has been replaced by the Glidcop on high heat load synchrotron applications due to its good thermal conductivity and preservation of mechanical properties after heating cycles. However, this material is not very workable in terms of union with other materials. It leads to the necessity of development of a brazing process for Glidcop and stainless steel union.

Glidcop samples were submitted to a Cu-electroplating process and a silver base alloy (BVAg-8) was used to join the parts in a high vacuum furnace. Electroplating was used to improve the filler metal wettability. The results were very satisfactory, ensuring water and vacuum tightness. A desirable characteristic not yet proved is the virtual leak property. This paper will discourse about this brazing method.

INTRODUCTION

Currently under construction, Sirius is a 3 GeV, fourth generation synchrotron light source [1]. Sirius is designed to have up to 37 beamlines with ultra-low emittance and high brightness, which will allow high-level research and development on a large range of areas as structural biology, materials science and nanoscience. Development of high-quality technologies is an important point as well (as the Sirius' monochromators and metrology equipment [2]). Figure 1 shows the construction status of the Sirius' project.



Figure 1: Sirius' construction status in August, 2016.

Given its high quality, its components rely on fine requirements on size, safety and cooling capability, having their design on the state of the art. Taking Front-End power absorbers as example: the refrigeration of these components is complex due to their reduced size allied to the high thermal load that is irradiated on them [3]. To solve this problem, engineered materials must be used.

The Glidcop is a good choice due to its good thermal conductivity and preservation of mechanical properties after heating cycles. The difficulty of this project lies on the fact that dissimilar metal components (*i.e.* Glidcop and stainless steel) must be joined and it is needed to isolate both the vacuum and the water chambers. Thus, the joint must be resistant to hold the pressure in the water chamber and must be tight to not allow the transport of small atmosphere molecules to the vacuum chamber. As a trial to manufacture these components, given its specific features, the brazing was chosen as a joining process.

The brazing is a chemical bonding process that consists in heating regions of interest on a set of components in order to reach temperatures at which the filler metal will melt [4]. The liquid filler metal will flow across the gaps by capillary action, covering the mating surfaces and then alloy and create a permanent chemical bond between them. It can join dissimilar metals and porous metal components.

Also, brazing allows the bonding of complex set of components in one operation, saving time and materials that otherwise could be consumed. It is important to emphasize that if the components and the process are properly designed, the brazed joint will be as strong as the base materials and the dimensional stability of the assembly will be maintained. That fact happens because the temperatures reached on a brazing process are much lower in comparison to other processes, as welding.

In addition, if the brazing is done in furnaces the heat is broadly distributed in the whole body volume, reducing the temperature difference between regions. When allied to the smaller heating rates, it results on less stress during the process.

Some other important points are the limitations of the process: stress raisers must be avoided in order to do not result in a fragile brazing joint; and the combination of materials is restricted by the fact that the filler alloy must have its melting temperature below the melting temperature of the base materials.

Brazing is a technique usually applied when there are high demands on strength, fatigue, corrosion and oxidation resistance. Apart from synchrotron technologies, brazing is found on areas such as automotive, aerospace and toll industries.

Content from this work may be used under the terms of the CC BY 3.0 licence (© 2016). Any distribution of this work must maintain attribution to the author(s), title of the work, publisher, and DOI.

ISBN: 978-3-95450-188-5 doi:10.18429/JACoW-MEDSI2016-TUPE23

MATERIALS AND METHODS

The materials used on the process were Glidcop Al15 (a copper alloy strengthened with a dispersion of ultrafine particles of aluminium oxide) and stainless steel 304L. They were chosen because they have already been successfully applied on other synchrotron light sources around the world due to great properties as thermal conductivity and mechanical resistance.

The Glidcop is required as a resistant alloy to receive and dissipate the heat load, and the stainless steel is important to give mechanical resistance to the component structure during its whole lifetime.

Considering the whole manufacture chain, the brazing stages are: machining of the Glidcop component; Glidcop coating; machining of the stainless steel components; stainless steel coating; cleaning; assembly; and in-vacuum heating. It is needed two machining steps once the internal diameter dimensions of the stainless steel components will depend on the dimension of the external diameter dimension of the after-coating Glidcop parts. If the coating process is well known, the growth rate will be specified and then it can be done until the component reaches a desired dimension. That fact allows all the machining steps to be done at the beginning of the manufacture chain.

Related to the preparation of the components, the mechanical adjustment was designed to reduce as much as possible the gap between the components, but without resulting on the necessity to apply force while assembling them. In addition, the volume of the filler metal was calculated to be at least the double of the volume of the gap between the components. It was done on the intent to guarantee that all the space on the mating region would be filled.

Later, the coatings used on the base materials were: the nickel strike (which is more aggressive to the surface material in order to allow the deposition and bonding of the first thin nickel layer); the nickel Watt (effectively grows the nickel coating); and copper (which is applied only to the Glidcop parts). There are studies on the literature that shows the applicability of these electroplating coatings [5].

Those coatings were applied to improve the capability of the filler metal to wet the surfaces and to create a barrier to do not let the filler metal to reach the base materials by diffusion. It should be emphasized that the parts were cleaned (including ultrasonic cleaning) just before each new step – being the most critical the one before the assembling and heating stages.

The filler metal chosen was the Cusil (an eutectic copper-silver alloy, trademark from Morgan Advanced Materials) because of its combination of mechanical resistance and melting temperature.

The tests done up to now were on specimen rather than on real components in order to reduce machining time. The Photon Shutter, a power absorber that will be brazed by this technique, is shown on Figure 2. Its brazing points are four: one on each very last point of contact between the Glidcop body and the stainless steel tube (*i.e.* on both tube endings); and two more on the ending diameters of the Glidcop body, where it mates the flanges.

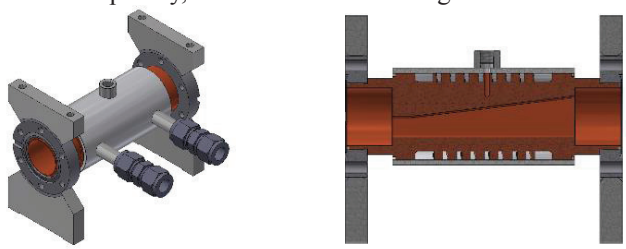


Figure 2: The photon shutter (isometric view on the left and half section view on the right side).

This manufacture chain will build two more components: the Fixed Mask and the High Power Slits (both having the same external dimensions as the Photon Shutter, varying mostly on length). The external dimensions of the specimen are equal to the ones of the real component.

The major simplifications done were on the shape of the longitudinal whole and on the water-chamber helical channels. As the materials are the same, the brazing steps and brazing cycle that will be applied to the manufacture of the real components will be the same as well. The brazing step is described on Table 1.

Table 1 - Description of the Brazing Process

Stage	Heating Rate [°C/min]	Temperatures [°C]	Time [min]
SP1.1	4	25 - 675	-
SP1.2	-	675	15
SP2.1	3	675 - 740	-
SP2.2	-	740	5
SP3.1	1	740 - 795	-
SP3.2	-	795	4

The brazing was done positioning the centre whole on the vertical direction (i.e. the brazing channels to support the fillers were in the vertical). It was chosen once it is easier to avoid greater misalignments of the components with themselves during the assemble and brazing phases.

It is important to notice that when the filler melts, by capillary action, it flows across the gap between the components, independently of the gap orientation, filling it before starting to flow to other directions. That effect had its efficiency proven later by analysing the metallography samples and by approving the specimen on the leak test.

The step after the heating cycle of the component was an inertial cooling inside the furnace.

RESULTS AND DISCUSSION

Figure 3 presents the microstructure analysis of the Glidcop and stainless steel joint. Frame a) shows that the coatings wet efficiently both surfaces (*i.e.* there are no empty spaces between a coating and the base material). In addition, the filler alloy is well bonded to the coatings over the whole surfaces and it filled the whole gap, as desired.

Content from this work may be used under the terms of the CC BY 3.0 licence (© 2016). Any distribution of this work must maintain attribution to the author(s), title of the work, publisher, and DOI.

ISBN: 978-3-95450-188-5 doi:10.18429/JACoW-MEDSI2016-TUPE23

Content from this work may be used under the terms of the CC BY 3.0 licence (© 2016). Any distribution of this work must maintain attribution to the author(s), title of the work, publisher, and DOI.

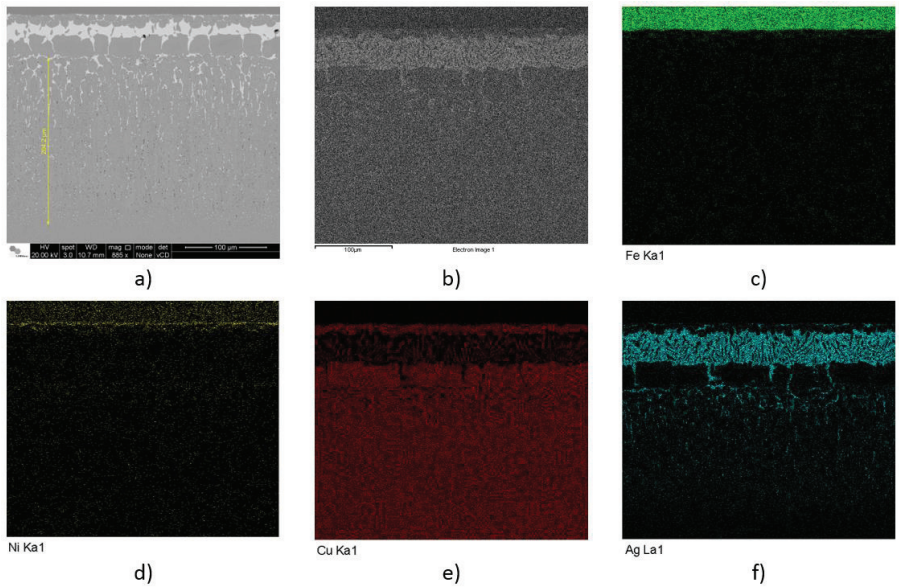


Figure 3: Glidcop and stainless steel brazing section. Frame a) shows the first section and d) the second one. An EDS analysis is show for the elements: Fe on frame b); Ni on c); Cu on e); and Ag on f).

Frame b) shows a brazing section where the EDS (Energy-dispersive X-ray spectroscopy) analysis was done. The stainless steel is on the upper side and the Glidcop on the lower.

On frames c), d), e) and f), the EDS elemental analysis are shown. Frame c) shows that only the stainless steel contains iron (Fe).

Frame d) presents the elemental analysis for the nickel (Ni). It is present in the stainless steel 304L alloy in small quantities and more concentrated on its coatings. The Glidcop's nickel coating suffered diffusion to the base material during the brazing process.

Copper concentrations are shown on frame e), which are high: on the Glidcop (base material and coating) and on the filler metal.

Finally, on frame f) it is show distribution of the silver (Ag) contained on the filler alloy. Also, it is possible to notice some diffusion of silver on the Glidcop matrix.

Some improvements on the coatings used on the Glidcop parts resulted on a reduction of this diffusion. Observing the behaviour of the filler alloy it is possible to notice that it distributed homogeneously across the gap, illustrating the uniformity of the process.

Considering the filler metal microstructure, there are two noticeable phases in it: the first rich in copper with silver in solid solution; and the second rich in silver containing copper in solid solution.

Related to the mechanical adjusts, the coatings could cover the whole part surface, accompanying the surfaces irregularities and keeping almost constant the deposition rate (apart from the corners, where there was always a concentration of coating material). The fillers alloys could also bear some minor irregularities on the base material's surface while filling the gaps between them.

Another point of analysis was the comparison between the upper and lower regions of brazing. Once the brazing was done with the specimen's longitudinal axis on the vertical direction allied to its upper half being symmetric to the lower one, it could be studied if the capillary action resulted on symmetrical joints on both sides.

Metallography analysis and leak testes were done to check both regions and it was proven that their behaviour under operational conditions were similarly acceptable.

Leak tests were conducted on the two regions of each specimen: the water chamber and the vacuum. All those regions were approved on the test with no leak detected up to 10^{-10} mbar.l/s, full scale and minimum leak rate of the equipment.

Afterwards, hydrostatic pressure tests were done. The operational water pressure of the components on the beamline will be eight bar. It was established that tests must be conducted on pressures 50% higher than the operational pressure to ensure the safety of the component. Hydrostatic pressure tests were conducted using pressures above 12 bar for 24 hours. In addition, a pressure of 34 bar was applied to the brazed component for a few 5 minutes to test it under super-critical conditions. It supported the test without any problems.

CONCLUSIONS

The objective of the current study was to obtain a brazing process that could be integrated to the manufacture chain of the Sirius' power absorbers. Also, the joint needed to bond dissimilar metals and result on a leak-tight and mechanical-resistant structure. It is possible to conclude after microstructure analysis, leak tests and hydrostatic pressure tests that the developed process (based on nickel and copper coating and the Cusil filler alloy) attends the requisites imposed for its application. The components made of the combination of Glidcop and stainless steel presented satisfactory performance on the tests.

ISBN: 978-3-95450-188-5 doi:10.18429/JACoW-MEDSI2016-TUPE23

REFERENCES

[1] A. R. D. Rodrigues *et al.*, "Sirius Status Report," in *Proceedings of IPAC2016*, 2016, pp. 2811–2814.

[2] R. R. Geraldes *et al*, "The New High Dynamics DCM for Sirius", presented at MEDSI'16, Barcelona, Spain, September 2016, this conference.

[3] L. M. Volpe *et al*, "High Heat Load Front-end for Sirius", presented at MEDSI'16, Barcelona, Spain, September 2016, this conference.

[4] Bagnato, O. R. ; FRANCISCO, F. R. ; Gabos, C. B. ; Pardine, C. . Brasagem Metal/Metal E Metal/Cerâmica Para Fabricação dos Guias de Onda e Monitores de Potência do Linac do Anel no Laboratório Nacional de Luz Síncrotron - LNLS. In: XXVII Congresso Brasileiro de Aplicações de Vácuo na Industria e Na Ciência, 2006, Itatiba. XXVII Congresso Brasileiro de Aplicações de Vácuo na Industria e Na Ciência, 2006. v. 1.

[5] Yadav, D., Kaul, R., Sankar, P., Kak, A., Ganesh, P., Shiroman, R., Singh, R., Singh, A., Tiwari, P., Abhinandan, L., Kukreja, L. and Shukla, S. (2012). A study on brazing of Glidcop ® to OFE Cu for application in Photon Absorbers of Indus-2. *J. Phys.: Conf. Ser.*, 390, p.012019.

Content from this work may be used under the terms of the CC BY 3.0 licence (© 2016). Any distribution of this work must maintain attribution to the author(s), title of the work, publisher, and DOI.

ISBN: 978-3-95450-188-5 doi:10.18429/JACoW-MEDSI2016-TUPE25

Content from this work may be used under the terms of the CC BY 3.0 licence (© 2016). Any distribution of this work must maintain attribution to the author(s), title of the work, publisher, and DOI.

METALLURGICAL EVALUATION OF DISSIMILAR METAL JOINTS FOR ACCELERATOR VACUUM CHAMBER CONSTRUCTION AT THE ADVANCED PHOTON SOURCE UPGRADE PROJECT *

G. Navrotski† and B. Brajuskovic, Advanced Photon Source,
Argonne National Laboratory, Argonne, Illinois, 60439 USA

Abstract

Tubular vacuum chamber assemblies made of aluminum, copper and stainless steel alloys will be used in the new Multi Bend Achromat (MBA) storage ring that is being developed at Advanced Photon Source (APS). Details of the new lattice magnet system design and ring impedance considerations continue to drive these vacuum chambers to smaller dimensions and thinner walls with tighter geometric tolerances under higher thermal loads. It is important to carefully evaluate the methods used to join these dissimilar metal components looking for compromise in primary strength, permeability, electrical and thermal properties while still creating structures that are ultra-high vacuum compatible and leak-tight. This paper visually details the underlying metallurgical changes that occur when joining various combinations of aluminum, OFE copper, GlidCop® and stainless steel using brazing, bonding and welding techniques. Each of the techniques has its advantages and disadvantages with engineering and economic consequences.

VACUUM BRAZING

To support the accelerator systems development program, a series of vacuum test coupons of a style shown in Fig. 1 were prepared and evaluated. The exact sample shown below includes a 316L stainless steel (UNS S31603) CF flange to GlidCop-Al15® (UNS C15715) vacuum braze (left end), a GlidCop® to OFE copper (UNS C10100) TIG weld (left center) and a stainless to OFE copper braze (right).

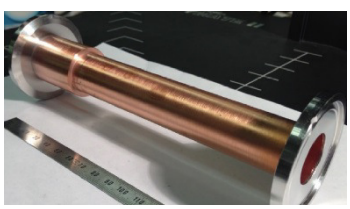


Figure 1: Typical dissimilar metal test coupon.

Joining two different materials using a third intermediate substance that bonds well to both is a highly developed and mature technology. For ultra-high vacuum (UHV) component fabrication using dissimilar metals, vacuum brazing is the 'gold standard' by which other techniques are measured.

A magnified cross-section of a OFE copper to 316L stainless steel vacuum joint is shown in Fig. 2. Both metals are well wet and fused by the gold braze alloy. Excess braze both inside and outside of the joint has a clean well-

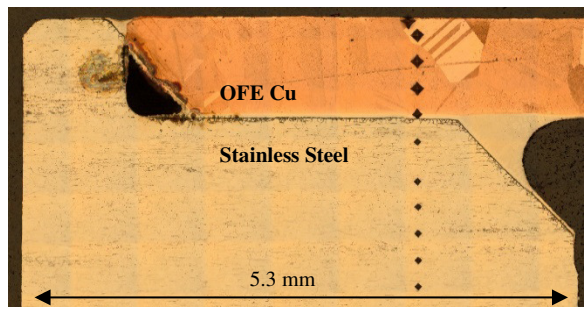


Figure 2: Vacuum braze of stainless to OFE copper.

formed meniscus without voids. The joint design, specifically the chamfer on the OFE copper, creates an unintended trapped volume and potential virtual leak in the component. There has been tremendous grain growth in the copper during processing. Microhardness tests (small diamond indents) show that, as expected, the copper has become fully annealed from its original work-hardened condition.

A similar braze of GlidCop-Al15® to 316L stainless steel is shown in Fig. 3. The reader should carefully consult the literature for the exacting conditions required for GlidCop® brazing [1, 2]. Both metals are nicely wetted and well bonded. There are a few insignificant voids present in the braze metal layer. Microhardness tests confirm that both the stainless and GlidCop® retain their full base metal strength properties, unaltered by the brazing process.

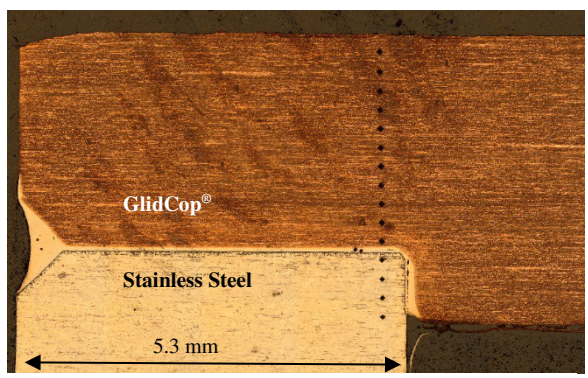


Figure 3: Stainless steel to GlidCop® vacuum braze.

* Funding provided by the Advanced Photon Source, U.S. Department of Energy, Office of Science, Argonne National Laboratory under Contract No. DE-AC02-06CH11357
† email address: Navrotski@anl.gov

ISBN: 978-3-95450-188-5 doi:10.18429/JACoW-MEDSI2016-TUPE25

E-BEAM WELDING

Electron beam welding in vacuum is an alternative dissimilar metal joining technique. Figure 4 shows a cross-section of a full penetration e-beam weld joining OFE copper to 316L stainless steel. The two metals are linked by a complex intermetallic mixture and are well fused. Microhardness and grain size measurements confirm that the heat affected zone does not extend through the full 4 mm of copper. The vacuum (top) surface of the copper tube maintains 85% of its as-received, work hardened strength transitioning to a fully annealed condition at the mid-line position.

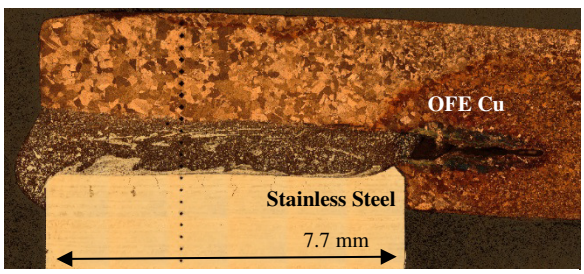


Figure 4: E-beam weld of stainless to OFE copper.

There are two negative consequences to imparting the high energy densities needed for this 8 mm deep weld. First, the process creates a three-millimetre-deep weld-root void in the copper. This should not be a factor for vacuum integrity nor for impedance but, as an internal stress concentration source, the void could be a factor in structural considerations. Secondly, the stainless steel has a very high level of induced and retained residual stress. Symptoms of this residual stress state can be seen in the series of small, almost equidistant 500 µm deep stress cracks in the stainless steel flange metal.

Very similar observations are made on the full penetration e-beam weld of GlidCop® to 316L stainless steel shown in Fig. 5. That is to say; the metals are well fused by a complex intermixture, there is a large weld-root void and there are high levels of residual stress in the stainless steel.

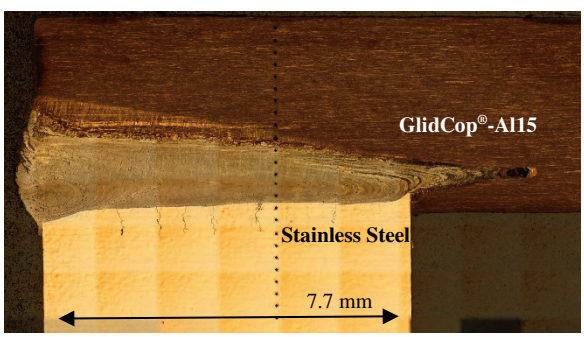


Figure 5: E-beam weld of stainless to GlidCop®.

Unlike the previous case with OFE copper, the GlidCop® strength is unaffected by the welding process except for a narrow band of recrystallized material (light copper band), especially near the weld face and weld toe. In this region the GlidCop® has lost half of its strength.

Figure 6 shows a typical microstructure for an electron beam weld joining OFE copper (left) to GlidCop® (right). Microstructural regions in this sample are more complex. Reviewing the image from left to right, note the cold-worked base metal OFE grain structure (A), a recrystallized copper zone (B), a region copper grain growth (C), the e-beam weld bead (D) with conspicuous grain flow pattern, a thin region of GlidCop® recrystallization (E) and GlidCop®-Al15 base metal (F). The reader is advised to ignore the surface cracks on the under-bead side (top surface this view) of the weld as a preparation artifact. Microhardness measurements across the weld confirm a highly asymmetric heat affected zone. The region between

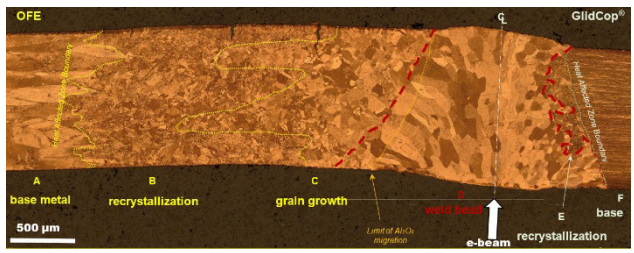


Figure 6: E-beam weld of OFE to GlidCop®.

the two base metals (A) and (F) has been highly annealed. To the left of the approximately 1 mm wide weld bead centerline, the OFE copper has been annealed to a distance of 4 mm. To the right of the centerline, the GlidCop® has only annealed within a thin < 500 µm recrystallized region.

A word of caution is necessary. On numerous other occasions, e-beam welds of GlidCop® have shown a chronic tendency to form both gas voids at the weld-bead center and interface voids at the weld-bead to recrystallized GlidCop® interface as shown in Fig.7. If this were another type of welding, gas entrainment from the atmosphere (N_2 or O_2) or gas generation by wet surfaces (H_2) would normally be blamed. In the vacuum electron-beam process there are no such sources. It is conjectured, without proof, that the e-beam welding process itself could be disassociating the Al_2O_3 dispersoids present in the GlidCop® creating Al, which readily dissolves into the copper matrix, and O_2, which coalesces into the observed gas pockets.

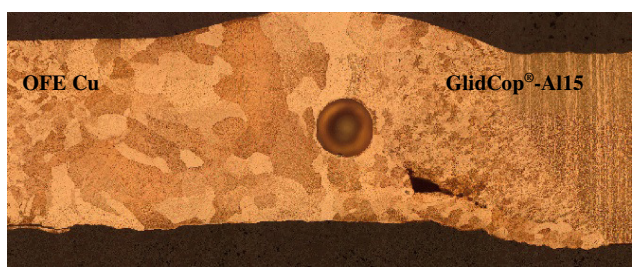


Figure 7: Problems in OFE to GlidCop® e-beam welds.

Overall, electron beam welding shows great promise for dissimilar metal joining needed in accelerator vacuum chamber construction. As with all welding methods, careful quality control over surface preparation, beam power, penetration depth and post-weld inspection are needed for each different configuration.

Content from this work may be used under the terms of the CC BY 3.0 licence (© 2016). Any distribution of this work must maintain attribution to the author(s), title of the work, publisher, and DOI.

ISBN: 978-3-95450-188-5 doi:10.18429/JACoW-MEDSI2016-TUPE25

Content from this work may be used under the terms of the CC BY 3.0 licence (© 2016). Any distribution of this work must maintain attribution to the author(s), title of the work, publisher, and DOI.

TIG WELDING

Tungsten inert gas (TIG) welding of OFE copper to GlidCop® and its extremely wide heat affected zone is shown in contrast to the e-beam case above. Figure 8 shows the central 5 mm of a typical TIG weld. To the left of the TIG centreline is the OFE side of the weld bead with large fully annealed grain structure. To the right is the weld bead and 1.33 mm of recrystallized GlidCop®. A single large and numerous small interface voids are seen at the weld bead to recrystallized GlidCop® interface.

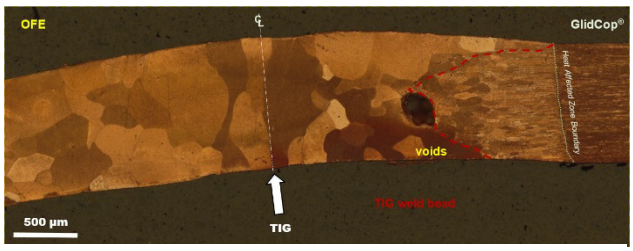


Figure 8: TIG weld of OFE to GlidCop®.

The heat affected zone on the OFE side of the weld extends to 33 mm from the weld bead centerline. The corresponding heat affected zone on the GlidCop® side is limited to the 1.3 mm region recrystallized material delimited by the white dashed line. The welds are vacuum tight but design must account for low mechanical strength over many cm of annealed material and potential midline voids.

LASER WELDING

Industrial lasers provide another source of welding power. With focusing, they have an advantage of being used either in vacuum or in a controlled atmosphere. Figure 9 shows a 50% penetration, capping weld of a 316L stainless steel to a thin wall OFE copper tubing. The input power is sufficient to fully anneal the copper for the full 8 mm length of the weld preparation. Copper recrystallization and large grain growth near the weld bead can be seen.

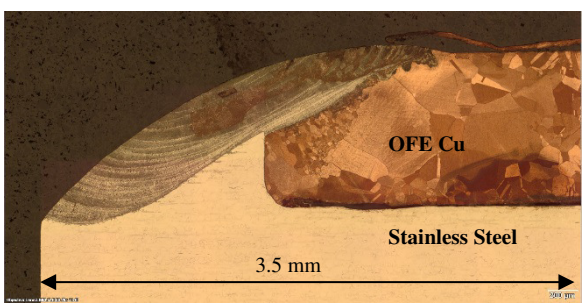


Figure 9: Laser weld of stainless to OFE copper.

Scalloped layering from consecutive laser pulses can be seen in the weld bead. Pockets of intermixed copper are also visible. The two metals are well fused and vacuum tight but the specific design of this joint provides only ~450 µm of brittle intermetallic weld material between the UHV conditions inside the accelerator chamber (top in this photo) and the continuous crevice leak to atmosphere along the OFE / stainless interface. With an improved weld design and further power controls, laser welding is a viable option, both technically and economically, for fusing dissimilar metal components for synchrotron applications.

FRICTION WELDING

Spin friction welding of an aluminum alloy tube to a 316L stainless steel tube is shown in Fig. 10. The interface is sharp and vacuum tight. On the aluminum (left) side, a 600 µm band the metallurgical structure has been highly modified to a fine grain condition with a 20% decrease of strength. The stainless steel (right) remains unaltered. Although the interface is extremely sharp and continuous with no noticeable melting, the reader will note a uniform 4 µm wide region between the two 'forged' surfaces. This band contains altered material that was preferentially removed during the metallographic electropolishing. Further investigation is warranted but the technique shows great promise for accelerator vacuum chamber fabrication.

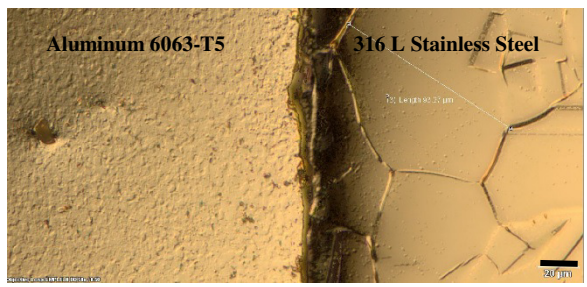


Figure 10: Friction weld of aluminum to stainless.

EXPLOSION BONDING

Explosion bonding is also a reliable but somewhat expensive option for dissimilar metal joining. A compatible dissimilar metal couple is created as seen in Fig. 11 by the explosion bonding process and fabricated into a coupling component. Only traditional similar-to-similar metal welding is then required fabricate the assembly. Careful materials design considered is required to choose an appropriate stack of explosion-bonded coupling materials.

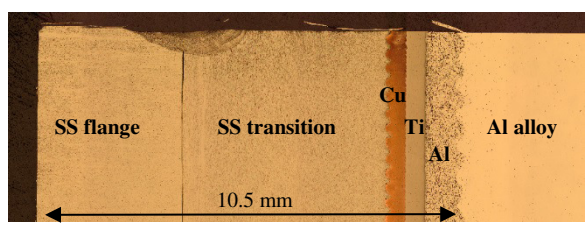


Figure 11: Explosion bonding interface.

REFERENCES

[1] P.K. Samal, *"Brazing and Diffusion Bonding of Glidcop® Dispersion Strengthened Copper,"* The Metal Science of Joining, edited by M.J. Cieslak et al., Minerals, Metals & Materials Society, 1992.

[2] W. Toter and S. Sharma, *"Analysis of Gold-Copper Braze Joints in Glidcop® for UHV Components at the Advanced Photon Source"* MEDSI (2004)

ISBN: 978-3-95450-188-5 doi:10.18429/JACoW-MEDSI2016-TUPE26

CARBON-STEEL/POLIETHYLENE RADIATION ENCLOSURES FOR THE SIRIUS BEAMLINES*

L. Sanfelici†, F. H. Cardoso, H. F. Canova, R. Madacki, M. A. Pereira, M. L. R. Santo, J. E. Santos, M. Saveri Silva, L. G. Silva, LNLS, Campinas, Brazil
M. H. A. Costa#, L. Bucianti, E. Palombarini, C. Prudente, Biotec Solução Ambiental, São José dos Campos, Brazil

Abstract

Lead enclosures have been used over the past decades for radiation protection at mid and high-energy synchrotron light-sources, requiring nearly 10% of the investment needed to set up a new beamline. Due to the increasing concern about neutron levels, in part due to the reduction of the photon radiation levels with the increased thickness of the hutch walls, the existing constructive models were revisited and a new constructive approach based on Carbon-Steel (CS) and High-Density Polyethylene (HDPE) is proposed for the SIRIUS beamlines, leading to increased overall radiation protection and potentially lower cost. This work is going to show preliminary simulation results, cost-comparison, as well as a few mechanical design details and prototyping initiatives.

INTRODUCTION

With the progress of the beamlines design for Sirius [1], and driven by the strong bias to foment the national industry motivated by the project sponsors, in 2015 a review of existing constructive options for optical hutches began. In that way the LNLS partnered to Biotec [2], a local company specialized in the design and construction of animal holding houses and clean rooms, not only to develop a solution for optical hutches that meet the radiological requirements but also to explore other companies in the region capable of manufacturing beamline hutches.

As part of an initial survey and assessment of existing solutions, a cost projection was carried out for the main constructive options identified, such as the traditional Pb hutches [3], Barite concrete [4] and CS/HDPE versions. Table 1 presents a simple functional comparison. The price is normalized by reference values obtained from traditional suppliers in the field.

Table 1- Constructive Options for Optical Hutches: Comparing Basic Features and Projected Costs

	Lead	CS/HDPE	Barite Concrete
Wall Thickness	30 mm	50 mm/50 mm	300 mm
Bremsstrahlung	Best	Best	Best
Neutrons	Bad	Best	Best
Synchrotron	Best	Best	Best
Thermal Insul.	Bad	Best	Good
N. Price [0..1]	~1	~0.7	~0.6

The projected costs showed the potential advantage of working with Barite concrete or CS/HDPE combined in comparison to conventional Pb hutches, not to mention the occupational benefits brought by avoiding handling a toxic material such as Lead. The selected option to mechanical-design was the double-walled CS/HDPE due to their dust-free and easy-machining characteristics.

It is not the aim of this work to present deep details regarding radiation protection of the Sirius beamlines or the mechanical design attained but offer a panorama and perspectives of the whole study and development process.

FIRST SIMULATION RESULTS

Table 2: Main Simulation Parameters for Sirius

Simulation Parameters	Value	
Straight section (SS) length	10.34	m
Pressure in the SS	5.10^{-8}	mbar
Distance to hatchet wall	24	m
Electrons energy	3	GeV
Fill current	500	mA
Max. dose rate ($\gamma + n^0$)	0.5	µSv/h

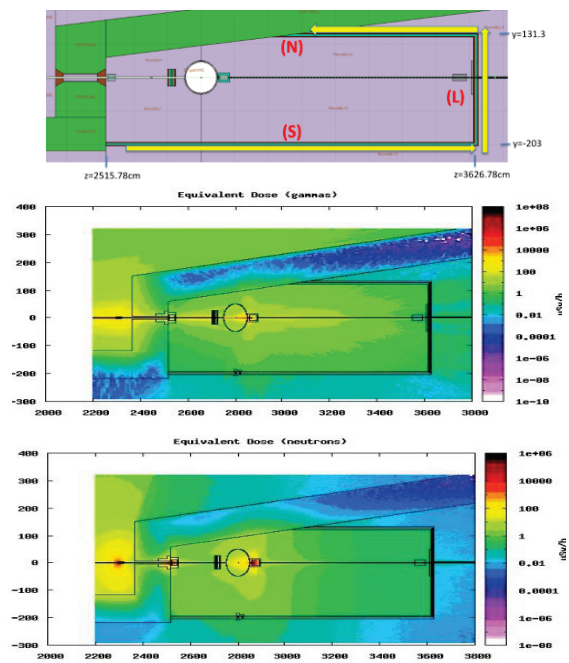


Figure 1: Results for a double-wall hutch composed of 50mm CS followed by 50mm HDPE at Sirius. Top: geometric model. Middle: effective dose distribution for photons. Bottom: effective dose distribution for neutrons.

* Work supported by the Brazilian Ministry of Science, Technology, Innovation and Communication
† lucas.sanfelici@lnls.br
# mhc064@gmail.com

Content from this work may be used under the terms of the CC BY 3.0 licence (© 2016). Any distribution of this work must maintain attribution to the author(s), title of the work, publisher, and DOI.

ISBN: 978-3-95450-188-5 doi:10.18429/JACoW-MEDSI2016-TUPE26

Content from this work may be used under the terms of the CC BY 3.0 licence (© 2016). Any distribution of this work must maintain attribution to the author(s), title of the work, publisher, and DOI.

Table 3: Comparison of Effective Doses for Different Constructive Scenarios at Sirius and The Shielding Thicknesses

Shielding Material	Photons/Neutrons Doses (μSv/h) and Thickness (mm)			
	South	East	North	Roof
Barite Concrete	0.10/0.26	0.28/0.02	0.01/0.02	0.16/0.35
	200	300	200	150
Fe/Pb/Fe	0.24/1.11	0.37/0.09	0.02/0.17	0.43/0.99
	3+30+3	3+60+3	3+30+3	3+10+3
Fe/HDPE	0.20/0.23	0.38/0.04	0.08/0.05	0.14/0.15
	50+50	70+50	50+50	48+50

Table 2 shows the main parameters adopted for the simulation runs with FLUKA [5]. Figure 1 presents the resulting dose distribution for a hutch employing CS/HDPE as shielding materials in the dimensions of Sirius, whereas Table 3 summarizes the results for all cases under investigation. The masks at the front end were not considered in this scenario. Because of the forward peaking nature of the high energy bremsstrahlung scattering the CS shielding thickness required at small angles along the beam direction is large. Considering a uniform downstream wall (East wall) thickness of ~7 cm, additional shielding of 5 cm of Pb will be required for scattering angles < 6 degrees. It was also considered 6 mm of Pb shielding against ground shine effect.

PROTOTYPE AT THE UVX RING

Table 4: Specification of The Optical Hutch Prototype

Enclosure Description		Prototype White Beam Enclosure
Shielding Material		CS/HDPE
Outer Dimensions	Height max	2.5 m
	Width max	5.3 m
	Length max	6.5 m
Shielding Panels	Side	50 mm/50 mm
	Roof	40 mm/50 mm
	Downstream	50 mm/50 mm
	Guillotine	Not required
	Alignment Window	Not required
Roof Static Load		500 kg/m^2
Internal Crane		Not required
Door	Position	Outboard side
	Size (m)	2.2 H x 2.45 W
	Type	Sliding double
	Floor groove	No
	Window	Not required
Labyrinths	Fluids labyrinth	1
	Gases labyrinth	1
	Electrical labyrinth	3
	Air inlet labyrinth	1 (on roof)
	Air outlet labyrinth	1 (on roof)
	Users' labyrinth	2
	LN_2 labyrinth	1 (on roof)
Air Conditioning	Temperature	24±0.1°C
	Thermal Load	3 kW

The table below summarizes the main features of the optical hutch prototype currently entering the manufacturing tests phase.

Figure 2 depicts the prototype hutch developed in the past months implanted in the UVX ring [6]. It is going to be installed at the exit of a free straight section to allow the highest gas-bremsstrahlung levels that the LNLS can provide at the moment for radiological tests. The hutch follows similar specifications planned for the Sirius' optical hutches, except for the height, 1m lower due to conflicts with the pipe rack.

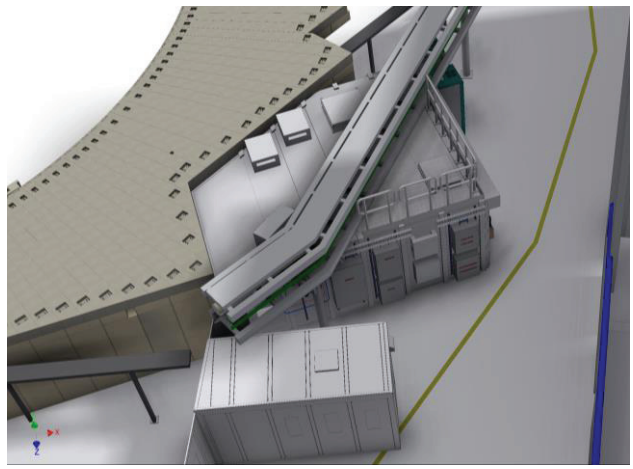


Figure 2: Optical hutch prototype – implantation to be installed in the UVX storage ring.

MECHANICAL DESIGN

The mechanical design encompassed all main hutches components: wall and roof modules, chicanes, doors, joints and supports to general infrastructure. The development took place based on a set of premises:

1. The prototype follows strictly the specifications of an optical hutch for Sirius;
2. Any ray leaving the hutch must cross at least the specified radiation protection thickness;
3. The radiation tightness of joints must not rely on strict fabrication or assembly tolerances, overlaps and chicanes must be pursued throughout the design;
4. The design must allow the use of both CS/HDPE modules as CS alone;
5. Modular design seeking standardization of dimensions and easy assembly;
6. The structural design must allow the eventual removal of roof and wall modules for survey and equipment transportation;
7. The assembly process shall be possible without cranes, and at height-restricted places;
8. The roof must be capable of supporting human traffic, instrumentation cabinets and air handling units;
9. The final price shall be comparable to the offered by Chinese suppliers of Fe/Pb hutches.

Figure 3 shows the main cuts of the hutch. They exhibit the closing design employing a double shielding layer composed of thick Carbon-Steel and HDPE plates.

ISBN: 978-3-95450-188-5 doi:10.18429/JACoW-MEDSI2016-TUPE26

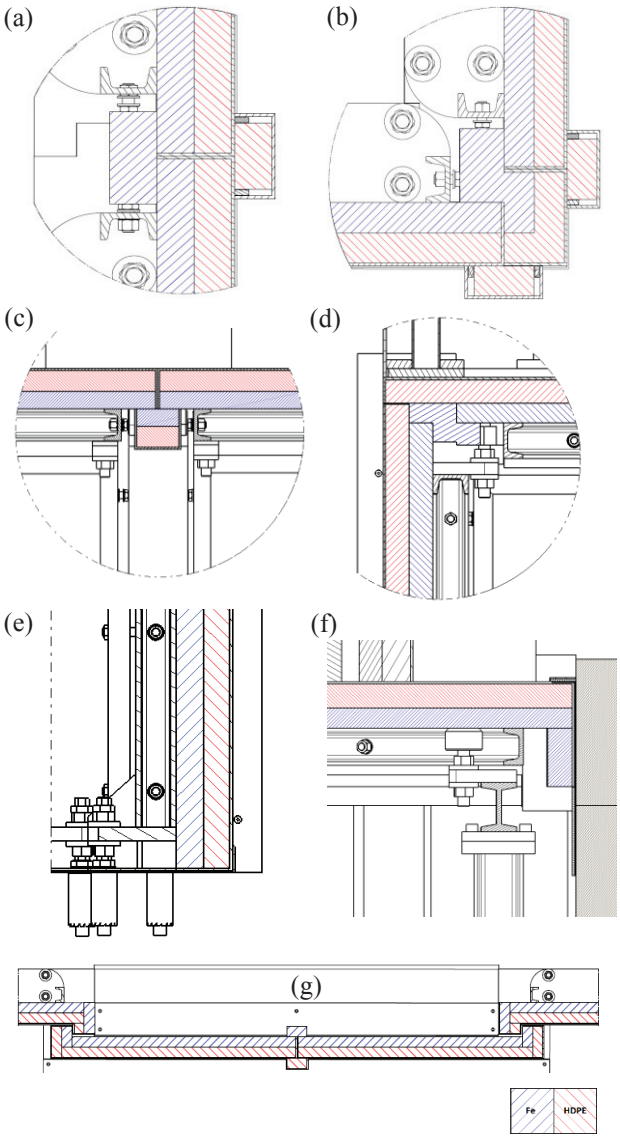


Figure 3: (a) Joint of 2 wall modules, (b) Corner of 2 wall modules, (c) Joint of roof modules, (d) Joint of wall and roof modules, (e) Floor fixation of wall module, (f) Roof interface to hatchet wall, (g) Double-sliding door.

UTILITIES, SAFETY SYSTEMS AND HVAC

The underway prototyping effort at the LNLS spams from utilities to sophisticated optical components responsible for delivering ultra-stable beams to the new Beamlines [7, 8]. This sort of initiative is of uppermost importance to the engineering teams in charge of the design and construction of the beamlines to validate and improve the design patterns being created, before widely replicate them to the Sirius' phase-1 beamlines.

The teams have as a premise to design highly monitored facilities, integrated to the beamline and building management system, which supports the maintenance teams work by employing alarms and historical data, enabling real-time monitoring of the whole facility, not to mention the advantages this integration brings during the commissioning phase.

The prototype hutch is equipped with a typical set of mechanical and electrical utilities, equipment and personal protection systems, as well as a precise air conditioning system.

STATUS AND PERSPECTIVES

Given the innovative nature of the project, a small set of wall, roof, and chicanes modules are about to be prototyped and heavily inspected in order to validate the production process before the complete manufacturing of the hutch. The full installation (hutch, utilities, HVAC and protection systems) in the UVX ring is planned to take place until February/2017 when extensive radiological and functional tests begin.

In parallel, the production process is going to be reviewed and optimized in costs, risks and overall quality.

The hutches of the first set of Sirius beamlines shall be installed in the new building by July/2018. The completion of the bid process is expected for Q2/2017.

We look forward that the current prototyping stage assists to improve the design of this new type of hutch, ending up with a safer optical hutch in the radiation protection perspective, especially during the early operational stage of the new accelerator. Also that this partnership model proves successful in fostering the local industry.

ACKNOWLEDGEMENT

The authors would like to thank many colleagues across the globe who contributed to valuable discussions and received our delegations for visits in the past few years.

REFERENCES

[1] A. R. D. Rodrigues *et al.*, "Sirius Status Report," in *Proceedingsof IPAC2016*, 2016, pp. 2811–2814.

[2] G. Foianesi, "Biotec Webpage" [Online]. Available: http://www.grupofoianesi.com.br/. [Accessed: 01-May-2016].

[3] F. N. P. Berkvens, P. Colomp, J. P. Magnien, P. Mackrill, D. Salieti, "Radiation Safety around the ESRF Beamlines," in *Proceedings of the Fifth EPAC*, 1996, pp. 1–3.

[4] J. Knabe, S. Lessmann-Bassen, A. Wefer, T. Wroblewski, "Presentation: Radiation Protection at the PETRA III Photon Beamlines," in *Radsynch*, 2009, pp. 1–33.

[5] T. T. Böhlen *et al.*, "The FLUKA Code: Developments and Challenges for High Energy and Medical Applications," *Nucl. Data Sheets*, vol. 120, pp. 211–214, 2014.

[6] "UVX - Accelerator Parameters", *LNLS Website*. [Online]. Available: http://lnls.cnpem.br/accelerators/accelerator-parameters/. [Accessed: 09-Nov-2016].

[7] L. M. Volpe *et al.*, "High Heat Load Front-end for Sirius", presented at MEDSI'16, Barcelona, Spain, September 2016, this conference.

[8] R. R. Geraldes *et al.*, "The New High Dynamics DCM for Sirius", presented at MEDSI'16, Barcelona, Spain, September 2016, this conference.

Content from this work may be used under the terms of the CC BY 3.0 licence (© 2016). Any distribution of this work must maintain attribution to the author(s), title of the work, publisher, and DOI.

ISBN: 978-3-95450-188-5 doi:10.18429/JACoW-MEDSI2016-TUPE28

Content from this work may be used under the terms of the CC BY 3.0 licence (© 2016). Any distribution of this work must maintain attribution to the author(s), title of the work, publisher, and DOI.

CHARACTERIZATION OF THE ACOUSTIC FIELD GENERATED BY THE SINGLE-AXIS ACOUSTIC LEVITATOR

A. H. Chavan[1], B. Hu[2], A. D. Dichiara[2], P. Den Hartog[1], K. J. Suthar[1*]
[1]Engineering Support Division, Advanced Photon Source, Argonne National Laboratory, USA
[2]X-ray Science Division, Advanced Photon Source, Argonne National Laboratory, USA

Abstract

The acoustic levitator utilizes two vertically-aligned, face to face, transducers that emit identical acoustic waves. A standing wave is generated between the two transducers that allows the levitation of liquid droplets at the nodes. These levitated droplets experience an instability. In order to aid in the process of solving this instability, the acoustic field created by one of the transducers was characterized in this experiment and simulated using numerical methods. This characterization and simulation helps to understand the intensity and shape of the acoustic field at different points throughout the region and how the acoustic wave diverges as it travels away from the transducer.

INTRODUCTION

X-ray characterization of the liquid sample usually needs to be held in a container. While x-ray passes through liquid sample, it also passes through the glass capillary. [1, 2] Thus, resulting spectra will have background information with the capillary material. In order to provide container less and contamination free environment, acoustic levitator is utilized for x-ray characterization of material.

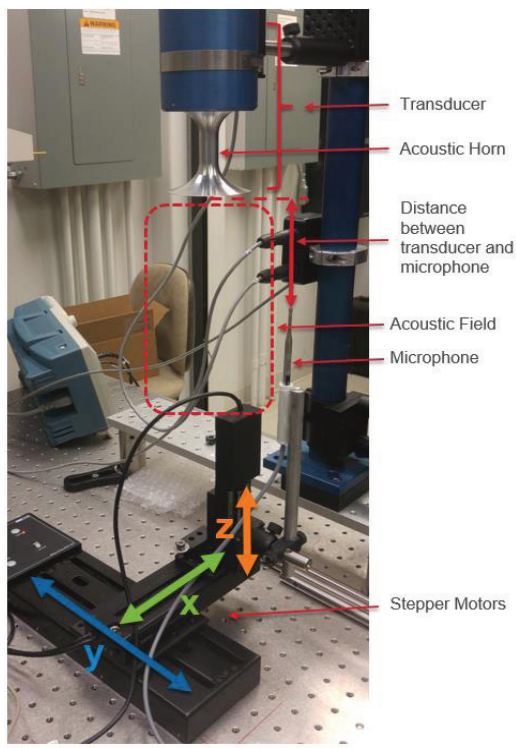
When using the acoustic levitator in experiments, levitated particles experience an instability in the acoustic field. This instability can steer the levitating sample away from the X-ray beam. The acoustic field that is generated by the levitator is affected by various components, such as the driving voltage, the frequency and amplitude of the acoustic wave, and the distance between the two transducers that emit the acoustic waves. [3] This paper presents our efforts to understand the instability by characterization and finite element analysis of the acoustic field. We simulated the acoustic field generated by a single transducer using finite element analysis. The simulation results of a sound level profile were compared to the experimental results. The results are discussed in the following sections.

EXPERIMENTAL SET-UP

The characterization of the acoustic field was performed using a high precision microphone (B and K, 4138 - 1/8-inch pressure-field microphone, 6.5 Hz to 140 kHz, 168 dB, 200 V polarization). [4] The position of the microphone was controlled using three stepper motors in Cartesian geometry. The goal was to manipulate the motors to have them move the microphone incrementally throughout a three-dimensional region.

The microphone received the acoustic signal transmitted by the transducer of the acoustic levitator. We placed microphone body away from the measuring point to avoid any interference. The microphone signal was sent to an oscilloscope that digitized the acoustic signal and passed it to a computer for processing. In order to complete accurate and detailed characterization of the acoustic field, a step size of 1 mm was used in the X-Y plane and a step size of 7.5 mm was used on the Z-axis. The wavelength of the acoustic wave is 15 mm; half of this wavelength, 7.5 mm, was chosen as the step size for the Z-axis so as to achieve characterization at key points throughout the acoustic field.

The motion of the motors, control of the microphone, data acquisition, and post processing was performed using LabVIEW. [5] Fig. 1, as seen below, depicts the experimental set-up of the motors along with the microphone and how they are positioned with respect to the transducer.



* Corresponding Author : Suthar@anl.gov +1(630)-252-2000

ISBN: 978-3-95450-188-5 doi:10.18429/JACoW-MEDSI2016-TUPE28

Figure 1: The experimental set-up, involving the stepper motors, microphone, and single transducer.

The data analysis was done with MATLAB. Using MATLAB, the data recorded by LabVIEW was processed and plotted. The analysis of the data is being done using the X, Y, Z position data and the data for the amplitude of the acoustic field. Although this MATLAB code can also be used to analyse the relative phase of the acoustic field, the focus of this experiment was to analyze the amplitude of the acoustic field.

The numerical simulation was performed using COMSOL® Multiphysics software version 5.2a. [6] The geometry of the air volume and transducer were modelled as shown in Fig. 2. 2D axisymmetric modeling was used to simplify the analysis. The pressure acoustic, solid mechanics, and electrostatic modules were used for this simulation. The numerical calculation was performed in the frequency domain with a frequency of 22.3 kHz. The acoustic field intensity is obtained at various planes located at 1.5, 3, 6 and 10.5 cm away from transducer surface.

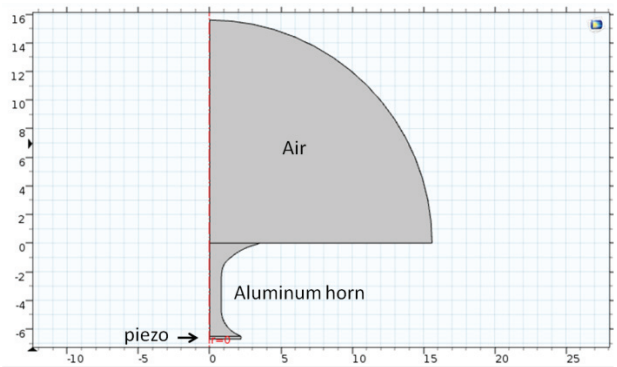


Figure 2: The geometry of one transducer in air.

RESULTS & DISCUSSION

Numerous experiments were required to achieve proper characterization of the acoustic field. A major factor that defined the quality of the characterization was the step size used in moving the X, Y and Z motors. The results of these measurements can be seen in Fig. 3.

The plots show how the peak intensity of the waveform in the center increases until the measurements are past the near-field region. Since the acoustic levitator utilizes a circular transducer, the wave-front looks like a peak with several pressure rings surrounding the peak. The pressure is always higher at the center of the acoustic wave. The pressure is 3200 Pa at 1.5cm from the transducer. In this acoustic field, the near-field region extend to about 3 cm and the maximum pressure reaches about 5000 Pa. After that point, it is clear that the peak intensity gradually starts to decrease. It can be inferred that as the distance between the transducer and waveform increases, the acoustic wave diverges, Fig. 5 & 6. Specifically, the size of the center wave and outer rings increases. The data representing the peak intensities at all the measured distances from the transducer were compiled and plotted in Fig. 5.

The numerical simulation results of the acoustic-pressure intensity profiles are compared with the experimental data and shown in Fig. 4. This comparison was completed at the same distances as the 2D profiles shown in Fig. 3.

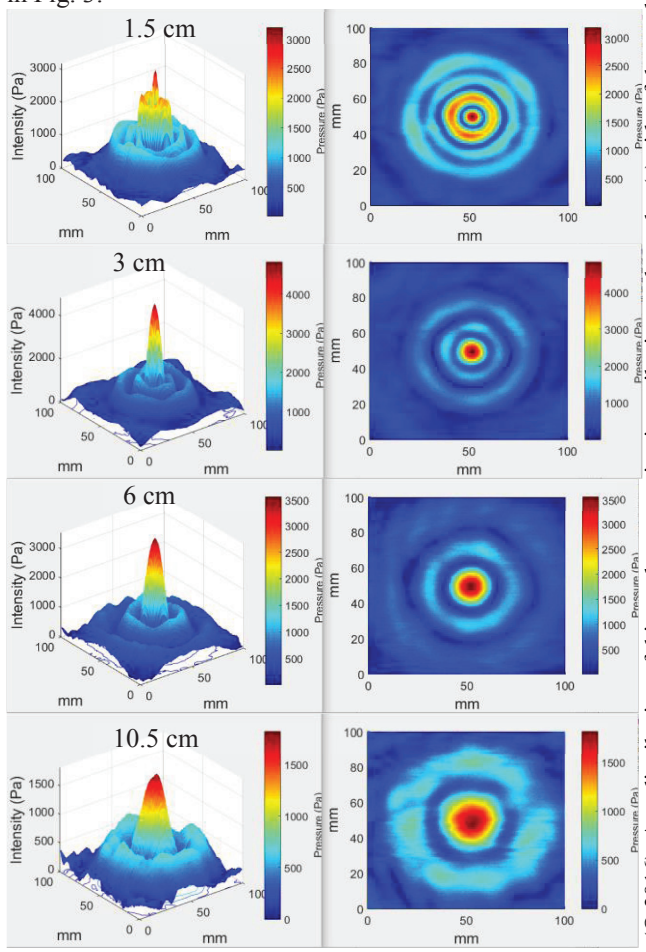


Figure 3: Intensity plots 1.5cm, 3cm, 6cm, and 10.5cm away from the transducer. Left column show pressure (Pa) as height with respect to x and y coordinates and right side column show intensity in 2D.

At all distances, the simulation results are in agreement with the experimental results both in pressure distribution and sound intensity. At 1.5 cm, the simulation results differ the most from the experimental data, but that can be attributed to the background noise or discrepancy in material properties. A small difference between the piezoelectric material properties and modelled material properties could also cause a slight deviation in results.

Fig. 5 & 6 shows the acoustic wave divergence obtained through FEA and experimental data. The diameter of the wave front has a bell shape distribution and it is obtained by measuring the full width half maximum of the distribution. This process was done along the X- and Y-axes, and the average value was used as the final diameter the bell shape distribution in the central region. The outer ring diameter was measured from peak-to-peak of the fist ring around central peak. The average value was used as the final outer ring diameter. The plots of this data are shown in Fig. 5 & 6. The simulation of peak intensity

Content from this work may be used under the terms of the CC BY 3.0 licence (© 2016). Any distribution of this work must maintain attribution to the author(s), title of the work, publisher, and DOI.

ISBN: 978-3-95450-188-5 doi:10.18429/JACoW-MEDSI2016-TUPE28

Content from this work may be used under the terms of the CC BY 3.0 licence (© 2016). Any distribution of this work must maintain attribution to the author(s), title of the work, publisher, and DOI.

and wave-front divergence are also plotted for comparison. The simulation results are in good agreement with the experimental test data on both peak pressure-intensity and acoustic wave divergence.

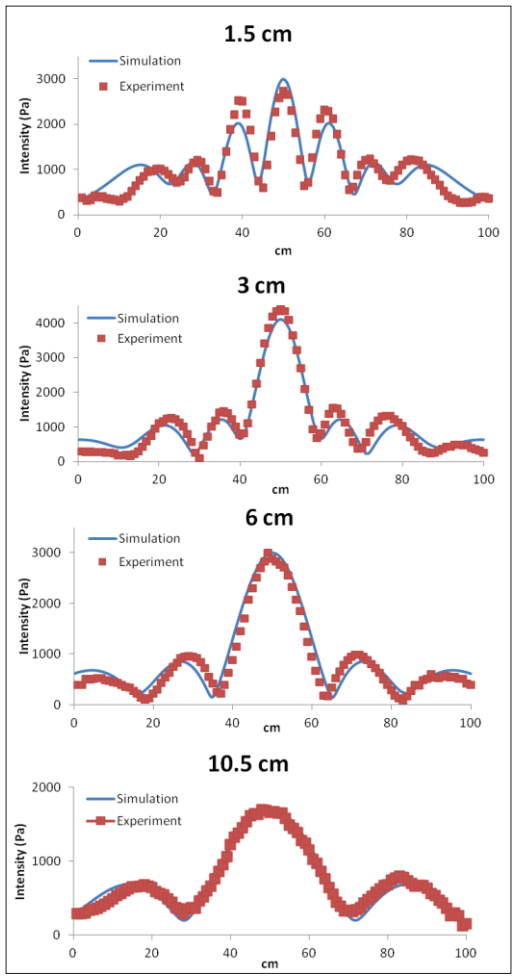


Figure 4: Comparison of acoustic sound profile between experiments and numerical simulation.

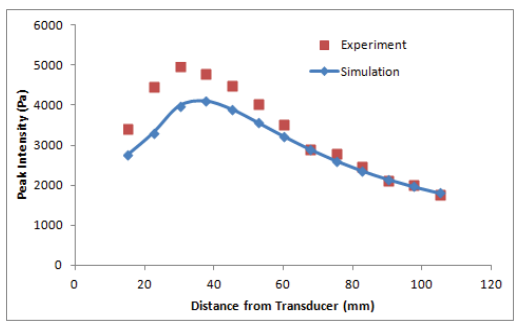


Figure 5: Comparison of experiment and simulation of peak intensities.

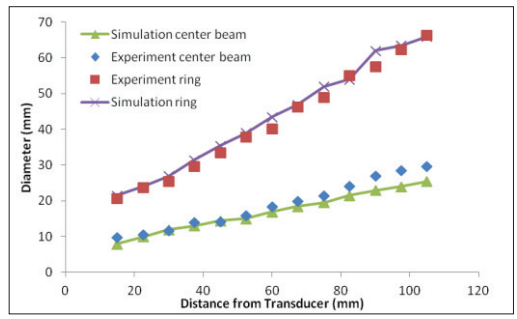


Figure 6: Comparison of experiment and simulation of beam and outer ring divergence.

CONCLUSION

The presented investigation was conducted on the acoustic field produced by a single transducer. The experimental characterization and numerical simulation of the acoustic field and acoustic wave divergence are in agreement with each other. Thus, the numerical simulation strategy was also validated. A closer look at the 2D pressure intensity graph (Fig. 3 right column) shows variations in intensity in second ring. This variation could be due to mix mode harmonics. This variation in pressure intensity could be a source of instability, however this can not be inferred from the single transducer analysis. To understand the instability in acoustic levitation, the entire acoustic field should be analysed using FEA, with some perturbation, in order to understand the variation in pressure intensity in annular area of the acoustic wave. Knowing the divergence of the acoustic wave is vital information when attempting to focus the wave for more stable levitation. Additionally, characterization of the outer rings in the acoustic field will aid in understanding where the instability in levitated particles is coming from. Overall, this experiment provides a greater understanding of how the acoustic levitator works, hence allowing for a more adept application of a more stable trapping in the acoustic field.

ACKNOWLEDGMENT

This research used resources of the Advanced Photon Source, a U.S. Department of Energy (DOE) Office of Science User Facility operated for the DOE Office of Science by Argonne National Laboratory under Contract No. DE-AC02-06CH11357. Authors would like to thank Jason Lerch for his help with simulation.

REFERENCES

[1]. Suthar, K., C.J. Benmore, P.D. Hartog, A. Tamalonis, and R. Weber. *Levitating water droplets formed by mist particles in an acoustic field*. in *2014 IEEE International Ultrasonics Symposium*. 2014. 10.1109/ULTSYM.2014.0116

[2]. Weber, J.K., C.J. Benmore, K.J. Suthar, A.J. Tamalonis, O.L. Alderman, S. Sendelbach, V. Kondev, J. Yarger, C.A. Rey, and S.R. Byrn, *Using containerless methods to develop amorphous pharmaceuticals*. Biochim Biophys Acta, 2016. 10.1016/j.bbagen.2016.03.037

ISBN: 978-3-95450-188-5 doi:10.18429/JACoW-MEDSI2016-TUPE28

[3]. Settnes, M. and H. Bruus, *Forces acting on a small particle in an acoustical field in a viscous fluid.* Phys Rev E Stat Nonlin Soft Matter Phys, 2012. **85**(1 Pt 2): p. 016327. 10.1103/PhysRevE.85.016327

[4]. B&K. *pressure-field microphone, 6.5 Hz to 140 kHz, 200V polarization - 4138*. 2015 [cited 2016 9/7/2016]; Available from: http://www.bksv.com/Products/transducers/acoustic/microphones/microphone-cartridges/4138 .

[5]. NationalInstruments, *LabVIEW,* http://www.ni.com/. 2016.

[6]. COMSOL, *COMSOL Multiphysics,* http://www.comsol.com/. 2015.

Content from this work may be used under the terms of the CC BY 3.0 licence (© 2016). Any distribution of this work must maintain attribution to the author(s), title of the work, publisher, and DOI.

ISBN: 978-3-95450-188-5 doi:10.18429/JACoW-MEDSI2016-TUPE29

INTEGRATION OF A STRIPLINE KICKER PROTOTYPE FOR CLIC PROJECT INTO ALBA STORAGE RING

R. Monge†, J. C. Giraldo, J. Ladrera, M. Llonch, L. Nikitina, M. Pont, M. Quispe
ALBA – CELLS Synchrotron, Cerdanyola del Vallès, Spain

Abstract

The Compact Linear Collider (CLIC) project is an international collaboration working on the development of a high-energy and high-luminosity machine which will accelerate and collide electrons and positrons at energies between 0.5 and 5 TeV. The extraction system for the Damping Rings of CLIC shall follow very tight requirements in order to maintain the ultra-low emittance of the extracted bunches. A first prototype of the extraction kicker based on stripline technologies has been built and characterized at CERN without beam. The stripline will be shortly installed in the ALBA Synchrotron to be tested under beam. In situ measurements of the impedance, transversal field homogeneity and flat-top ripple aims to complete its characterization. This contribution presents the design of the set up for the integration of the stripline in one of the medium straight sections of ALBA storage ring.

INTRODUCTION

The CLIC project is an international collaboration working on the development of a high-energy and high-luminosity machine which will accelerate and collide electrons and positrons at energies between 0.5 and 5 TeV. The Pre-Damping Rings (PDR) and Damping Rings (DR) are required for reducing the emittance of the beams before being injected into the main linac. The injection and extraction from the PDR and DR are performed by kicker systems based on stripline technologies which allow to maintain a low beam coupling impedance and acceptable broadband impedance matching to the electrical circuit [1].

A first prototype of the extraction kicker for the CLIC DR has been designed, built and studied without beam in previous works from C. Belver-Aguilar et al. [1, 2, 3]. In order to complete its characterization, the stripline kicker will be shortly installed in the ALBA Synchrotron to be tested under beam. The results of the in situ tests and measurements of the beam coupling impedance, transversal field homogeneity and flat-top ripple will be compared to the simulations to validate the final design.

This contribution presents the design of the measurement set up for the integration of the stripline kicker into the ALBA storage ring.

LAYOUT INTEGRATION

ALBA Synchrotron was elected for the kicker testing under beam due to the similarity of characteristics in terms of beam energy and low emittance. Figure 1 and Table 1 shows the accelerator layout and main parameters of ALBA machine respectively.

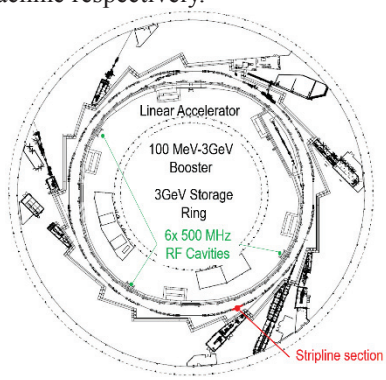


Figure 1: Location of the stripline installation.

Table 1: ALBA Machine Main Parameters

Energy	3 GeV
Design Current	400 mA
Circumference	268.8 m
Horizontal Emittance	4.58 nm·rad

The kicker chamber will be installed in a medium straight section of 3200 mm length, between Sector 07 and Sector 08 of ALBA storage ring. The adjacent vacuum chambers and absorbers have been designed in order to not disturb the beam performance and to protect the stripline from the synchrotron radiation. Figure 2 shows the general layout of the final assembly.

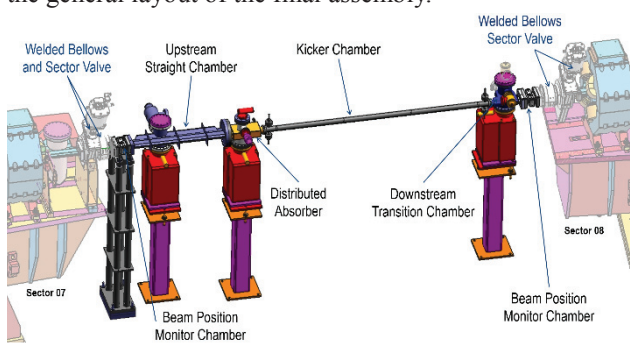


Figure 2: General assembly of stripline section.

Ray Tracing Study

To avoid the incidence of synchrotron radiation over the new elements of the section, ray tracing calculations have been performed. A safety margin of 1 mm has been considered between the inner part of the kicker chamber's ring supports and the x-ray fan. The position and dimensions of the distributed absorber were optimized taking into account the available space of the section, the dis-

† rmonge@cells.es

Content from this work may be used under the terms of the CC BY 3.0 licence (© 2016). Any distribution of this work must maintain attribution to the author(s), title of the work, publisher, and DOI.

ISBN: 978-3-95450-188-5 doi:10.18429/JACoW-MEDSI2016-TUPE29

tance to the electron beam and ensuring that the last ray coming from the edge of the absorbing surface ends up in the next crotch absorber installed in Sector 08. Figure 3 shows the fan radiation coming from the previous bending magnet till the edge of the distributed absorber.

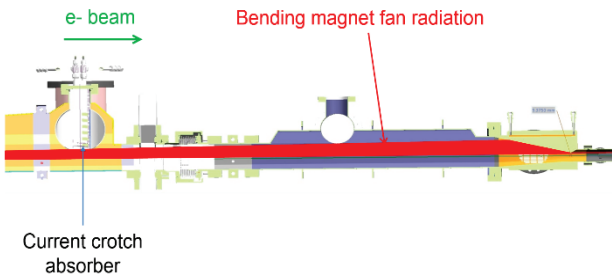


Figure 3: Ray tracing of the first section of the assembly.

CHAMBERS DESIGN

Stripline Kicker

The stripline kicker consists of two half-moon shaped electrodes enclosured along a cylinder vacuum chamber as shown in Fig. 4. Each of the electrodes is driven by an equal but opposite polarity pulse. Its geometry has been optimized to achieve an excellent field homogeneity, good power transmission and very low beam coupling impedance [1].

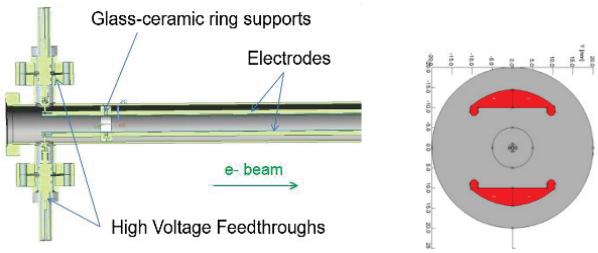


Figure 4: Kicker chamber cross section.

The kicker will be installed 90° rotated to avoid the synchrotron radiation incidence over the electrodes.

Beam Position Monitor (BPM)

Two BPMs will be installed at the beginning and end of the assembly. The downstream BPM will be fixed in a bracket and referenced to the girder as the rest of the BPM net. On the other hand, the upstream BPM will be installed in a fixed position acting as a global reference respect to the floor. For this purpose, a standalone FeNi36 support has been designed for keeping a beam orbit stability of 10% of the beam size and restricting the vertical deformation to a submicron level. Figure 5 shows the results for the vibrational analysis with a first resonance mode of 65 Hz and a deformation of 3.8 calculated for the vertical Z direction.

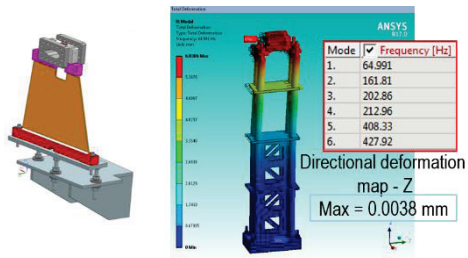


Figure 5: Downstream BPM bracket and upstream BPM support static and vibrational analysis.

Upstream Straight Chamber

The upstream straight chamber showed in Fig. 6 connects the first BPM with the distributed absorber. As the rest of storage ring standard chambers, it is designed in AISI 316 LN stainless steel with a "key-hole" cross section. The electron beam circulates through the main chamber and the photon beam channel, as antechamber, allows the synchrotron radiation to be delivered to the front ends or to be stopped in the absorbers. Static calculations were performed to validate the design ensuring that no stress due to the vacuum forces exceeds 100 MPa.

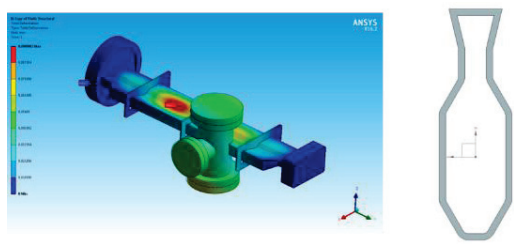


Figure 6: Straight chamber calculations and cross section

Distributed Absorber

The distributed absorber is installed before the stripline kicker and protects the rest of the assembly elements from the photon radiation. Figure 7 shows the cross section, which is tapered from the standard profile of ALBA storage ring to a circular opening of 40 mm diameter. The main block is made of oxygen free high conductivity (OFHC) copper brazed to the stainless steel flanges and auxiliary ports.

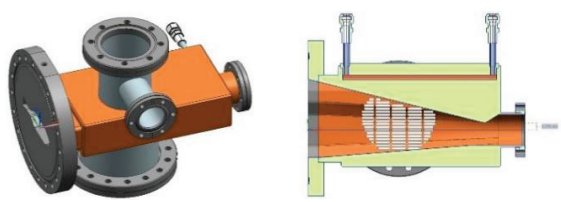


Figure 7: OFHC distributed absorber and cross section.

Static calculations were performed to validate the design ensuring that no stress due to the vacuum forces exceeds 100 MPa. Below Fig. 8 shows part of the

Content from this work may be used under the terms of the CC BY 3.0 licence (© 2016). Any distribution of this work must maintain attribution to the author(s), title of the work, publisher, and DOI.

ISBN: 978-3-95450-188-5 doi:10.18429/JACoW-MEDSI2016-TUPE29

Content from this work may be used under the terms of the CC BY 3.0 licence (© 2016). Any distribution of this work must maintain attribution to the author(s), title of the work, publisher, and DOI.

thermal-mechanical studies carried out in order to optimize the inner dimensions of the absorbing surface and the cooling channel.

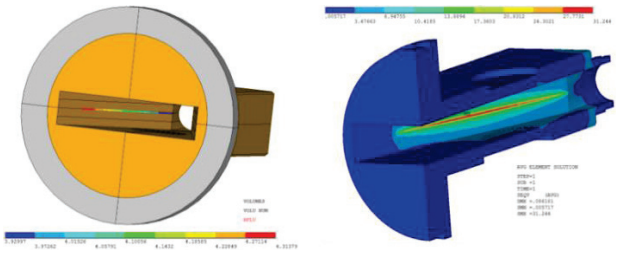


Figure 8: Power density and stress distribution of absorber

Table 2 shows the results of the analysis for the power density distribution, stress and strain distribution, water convective heat transfer coefficient and temperature distribution along the absorbing surface.

Table 2: Thermal-Mechanical Results of Absorber

Power density distribution (Beam current=400 mA)	$P_{a,max}$=4.3 W/mm^2
Stress	S_{max}=31.2 MPa
Strain	Smax=0.027 %
Water convective heat transfer coefficient	h=13625 W/m^2 T_{water}=24 °C
Temperature distribution	T_{max}=58.5 °C

Downstream Transition Chamber

Figure 9 shows the downstream transition chamber, which is made in AISI 316 LN stainless steel and connects the stripline kicker with the downstream BPM. In the same way as the distributed absorber, it has a transitional cross section with a smooth tapering from the ALBA standard profile to a circular opening. A pattern of holes is placed over the pumping ports to prevent any disturbance of the electron beam and to ease the evacuation of the chamber.

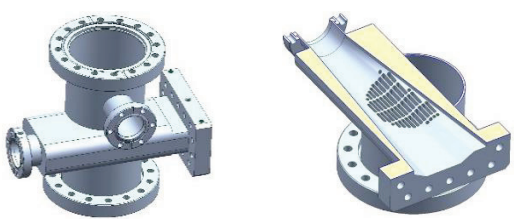


Figure 9: The downstream chamber and cross section.

Static calculations were performed to validate the design ensuring that no stress due to the vacuum forces exceeds 100 MPa.

INSTALLATION AND COMMISSIONING

Before being installed into ALBA machine, the complete assembly of the vacuum chambers will be mounted and baked in a dedicated clean area.

The mechanical supports will be placed in its final position to allow the installation and connection of the assembly. All the chambers, excepting the stripline kicker, have fiducial holes to ease the subsequent alignment of the components. After instrumentation and cabling installation, the logic of the Equipment Protection System (EPS) for the vacuum and temperature signals will be checked.

The commissioning will be finished with the functional tests of the kicker and BPM tests with beam.

The final testing with beam will include measurements for the beam coupling impedance, transversal field homogeneity and flat-top ripple.

CONCLUSION

In summary, the integration of a stripline kicker prototype for CLIC DR into ALBA storage ring is presented. The layout, design and result of calculations of the assembly chambers is described. Finally, it is outlined a list of the installation and commissioning tasks prior to the final tests with beam.

REFERENCES

[1] C. Belver-Aguilar et al., Design and Manufacturing Description of the Prototype Striplines for the Extraction Kicker of the CLIC Damping Rings, IPAC'13, Shangai, China, May 2013.

[2] C. Belver-Aguilar et al., Final Cross-section Design of the Stripline Kicker for the CLIC Damping Rings, IPAC'12, Louisiana, USA, May 2012.

[3] C. Belver-Aguilar et al., Beam Impedance Study of the Stripline Kicker for the CLIC Damping Ring, IPAC'12, Louisiana, USA, May 2012.

ISBN: 978-3-95450-188-5 doi:10.18429/JACoW-MEDSI2016-TUPE31

MANUFACTURING OF PHOTON BEAM-INTERCEPTING COMPONENTS FROM CuCrZr

F. DePaola, C. Amundsen, S. Sharma, NSLS-II, Brookhaven National Laboratory, New York, USA

Abstract

Photon beam-intercepting components in synchrotron light sources have usually been made as water-cooled Glidcop® bodies brazed to stainless steel Conflat type flanges. This fabrication method involves many manufacturing steps which result in increased cost, long procurement time and lower manufacturing reliability. A new design approach was recently proposed which simplifies fabrication by eliminating brazing and utilizes a readily available copper alloy, CuCrZr. This paper describes the manufacturing experience gained at NSLS-II from fabricating many components of this new design. Results of an investigation of various techniques for joining CuCrZr to itself, to SS304, and to AL-6061 are also presented.

INTRODUCTION

For over 20 years synchrotron facilities have used Glidcop® material to make photon beam-intercepting components. Glidcop® was chosen because of its good thermal conductivity and because it retains its strength at high temperature. These Glidcop® components require advanced procurement planning because of their high cost, long lead time to produce, and the high risk associated with manufacturing them. Brazing Glidcop® can be challenging due to the tendency of the braze alloy to diffuse into the Glidcop®. Braze repairs are often required to produce vacuum leak-tight joints. This paper is based on the new design approach that was proposed at MEDSI 2014 [1] which eliminates brazing and substitutes Glidcop® with a less expensive and readily available copper alloy, CuCrZr.

NSLS-II CuCrZr COMPONENTS

NSLS-II has installed (1) bending magnet (BM) and (2) 3-pole wiggler (3-PW) frontends to date with total of (24) components made from CuCrZr (Installed components include: Absorbers, Masks, Slits, and Photon Shutters). There are (24) new components currently being manufactured from CuCrZr for future installation of three additional 3-PW frontends. A typical BM/3-PW slit body and fixed mask are illustrated in Fig. 1 and 2, respectively.

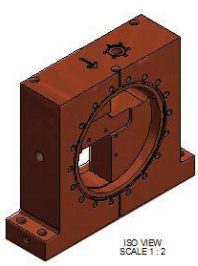


Figure 1: Typical BM/3-PW frontend slit body.

Prototype development of absorbers, masks, slits, and photon shutters based on the new design is ongoing for the insertion device (ID) frontends. The current Glidcop® design for an ID frontend fixed mask is illustrated in Fig. 3 and the proposed CuCrZr design is shown in Fig. 4.

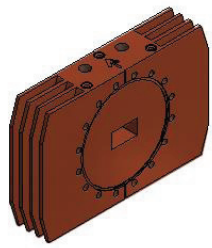


Figure 2: Typical BM/3-PW frontend fixed mask.

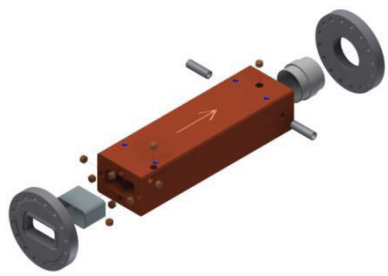


Figure 3: Current design of ID frontend components.

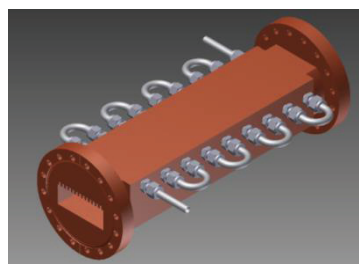


Figure 4: Proposed design of ID frontend components.

EXPERIENCE GAINED AT NSLS-II

General Machining and EDM of CuCrZr

The machinability of CuCrZr was found to be about the same as that for GlidCop® but significantly better than that of oxygen-free copper. Wire EDM of CuCrZr was also straight forward although cutting an aperture into a component 16" long is a slow process as would be expected of a high conductivity copper alloy.

Conflat Flange Knife Edge

The original design incorporated the standard 70° knife edge which is typically machined in stainless steel Conflat flanges. During incoming inspection a number of

Content from this work may be used under the terms of the CC BY 3.0 licence (© 2016). Any distribution of this work must maintain attribution to the author(s), title of the work, publisher, and DOI.

ISBN: 978-3-95450-188-5 doi:10.18429/JACoW-MEDSI2016-TUPE31

Content from this work may be used under the terms of the CC BY 3.0 licence (© 2016). Any distribution of this work must maintain attribution to the author(s), title of the work, publisher, and DOI.

BM/3-PW fixed masks made from CuCrZr were found to have vacuum leaks. After a detailed investigation it was determined that the vacuum leaks were caused by small burrs left on the knife edges from the machining operation. The knife edge design was changed from 70° to 90° and a knife edge tip radius of 0.006" [2] was added (see Fig. 5). The machining process was also refined which now utilizes profile machining on a CNC lathe and a new cutting tool with carbide inserts [3].

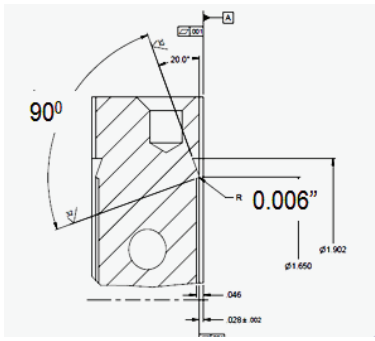


Figure 5: Knife edge angle and tip radius in CuCrZr flanges.

EDM Wire Gap in Fixed Mask

During ½-scale prototyping of the ID fixed mask from CuCrZr the EDM wire gap was measured at 0.032". This gap would allow an unacceptable amount of beam power to escape through the mask. EDM programming changes were made that reduced the number of passes of the EDM wire to two (one for each of the top and bottom surfaces of the aperture). Based on the EDM machine manufacturer recommendation, a 0.010" diameter zinc-coated brass wire was used for cutting the aperture. These changes reduced the EDM wire gap to 0.020" but the escaped power was still too high and other design options based on the weldability of CuCrZr are under investigation [4].

Welding of Conflat Flanges

During prototyping it was also realized that making integral flanges would require excessive machining in some cases depending on geometry of the mask and its aperture. In addition, long masks for high power IDs would require too many cooling channels and fittings. It was then decided to investigate the weldability of CuCrZr so that the conflat flanges could be made separately and then joined to the main body by welding. As discussed in the Section of "Joining Techniques", CuCrZr was found to be easily welded.

MANUFACTURING COMPARISON

Because the new design eliminates brazing, the manufacturing reliability of producing the frontend components is greatly improved. In the current GlidCop® design of an NSLS-II ID frontend fixed mask assembly there are (13) brazed joints (2 vacuum and 11 water joints). If any one of these joints is not leak tight the assembly has to be re-brazed. Re-brazing is a high risk as it can open up a leak in another joint. Even suppliers with many years of experience of brazing Glidcop® have to re-braze assemblies, often multiple times, before all joints are vacuum or water leak tight. Table 1 shows a manufacturing comparison between the current GlidCop® and new CuCrZr designs for a typical NSLS-II ID frontend component assembly. Actual cost and time data were used for this compari- son although only a limited amount of data is currently available for CuCrZr.

Table 1: Manufacturing Comparison

	Glidcop®	CuCrZr	Note
# of Assembly Components	16	1 - 4	
Material Price (per pound)	$40.45	$8.99	1
Material Delivery Lead Time	16 weeks	1 week	1
Material Selection (shape & size)	Limited	Large Variety	2
Manufacturing Cost Factor	1.35 (X)	1.00 (X)	3
Production Lead Time (average)	6 months	3.5 months	4
Design Options	Note #5	Note #6	
Note #1 – Based on actual quotes received in August of 2016.			
Note #2 – Glidcop® is available in a limited number of standard sizes, custom sizes can be ordered at a higher cost and extended delivery lead time.			
Note #3 – Based on actual costs which include both material and labor to produce the parts.			
Note #4 – By eliminating brazing and reducing the number of components required for the newly designed CuCrZr assembly, production time is reduced by 2.5 months.			
Note #5 – In the future, front end components manufactured at NSLS-II will only use Glidcop® when brazing cannot be eliminated from the design such as in a beryllium window assembly.			
Note #6 – New CuCrZr designs offers design flexibility; components can be made with all features machined into a single piece or a multiple piece welded construction.			

JOINING TECNIQUES

Processes Used for Joining CuCrZr

Samples were machined and welded to determine the weldability of CuCrZr material [5]. The sample welded joints were evaluated for heat affected zone (HAZ) and base metal hardness, weld size, vacuum leak tightness using a Mass Spectrometer Leak Detector (MSLD), and metallographic analysis. Samples were welded using Electron Beam Welding (EBW) and Gas Tungsten Arc Welding (GTAW). Welding was performed in a manner that would minimize the heat input and still achieve a vacuum tight joint. Weld sample test results are shown in Table 2. It was concluded that joints in CuCrZr are easily fused and reproducible with minimal effect on the base metal. Small vacuum leak tight joints were achievable with both EBW and GTAW processes with very narrow heat affected zones. A picture of the GTAW CuCrZr weld sample is shown in Fig. 6 (top) and micrographs of

ISBN: 978-3-95450-188-5 doi:10.18429/JACoW-MEDSI2016-TUPE31

the excellent quality of the GTAW and E-beam welded joints are shown in Fig. 6 (bottom).

Table 2: CuCrZr Weld Sample Test Results

Criteria	EBW	GTAW
	Vickers Micro Hardness	
HAZ/Weld/Base Metal	87/104/143	88/98/138
	Weld Size (Inches)	
Weld Width / Weld Depth	0.070/0.020	0.071/0.020
HAZ (beyond fusion line)	0.035	0.025
MSLD Results	No response at $1x10^{-9}$ CC/SEC (He)	
Metallurgical Structure	Good fusion, No defects	

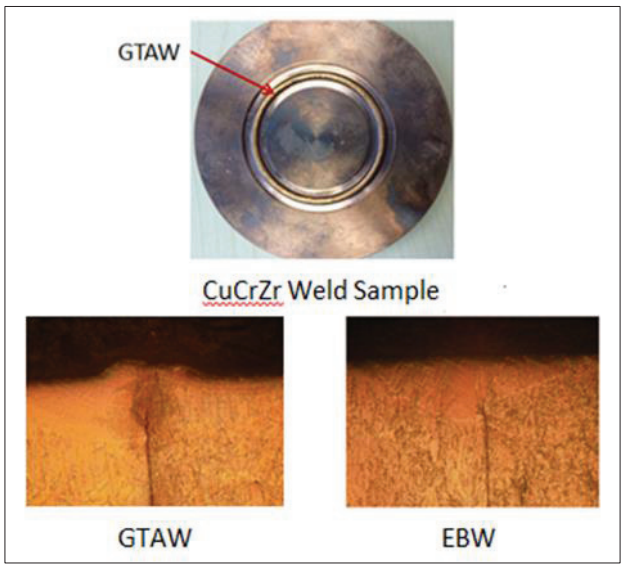


Figure 6: A GTAW CuCrZr weld sample (top). Micrographs of the GTAW and E-beam welds are shown below.

Explosion Bonding

Two types of explosion bonded bimetallic plates (4 pieces of each type) were produced and evaluated. One type with 304L stainless steel bonded to CuCrZr and the other with 6061 T-6 aluminum bonded to CuCrZr, each bonded plate is 12" square x 1.0" thick (each material type is 0.5" thick) . Ultrasonic and dye-penetration testing was performed on each bonded plate by the supplier (High Energy Metals, Inc., Sequim, WA, USA). There were no un-bonded indications found on the 304L/CuCrZr plates and one non-bonded area (1.0" long) was found along one edge on one of the four 6061 T-6/CuCrZr plates.

Additional evaluations including metallographic analysis and tensile testing of the bonded joints are being performed by an independent outside testing laboratory (Dayton T. Brown, Inc., Bohemia, NY, USA). Testing has not been completed so the final results are not available for presentation in this paper. A picture of the 304L/CuCrZr explosion bonded plate is shown in Fig. 7.

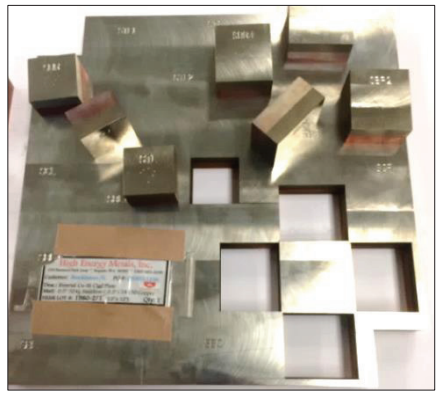


Figure 7: Explosion bonded plate with samples removed.

Summary and Conclusion

CuCrZr material is readily available in a large variety of shapes and sizes and significantly lower in price then Glidcop®. Conflat flanges can be machined directly into the main body or joined to it by welding. By eliminating brazing and reducing the number of components necessary for the CuCrZr assembly, production costs are reduced by approximately 35% and production time is reduced by 2.5 months. Eliminating brazing also improves the manufacturing reliability of the components.

These new CuCrZr designs allow component assemblies to be manufactured in advance with all features except the final aperture. Once the final aperture size is specified it can be added quickly in a simple machining operation. The lead time for manufacturing can thus be reduced from several months to a few days.

Another significant advantage of the CuCrZr designs is that they facilitate standardization of components, for example the number of spares required to support operations is minimized since mask assemblies without apertures can be available as a universal spare to be completed as needed.

CuCrZr offers many benefits as shown throughout this paper without the high cost, long lead time to manufacture, and high risk associated with manufacturing components made from Glidcop®.

REFERENCES

[1] S. Sharma et al., "A novel design of high power masks and slits," in *Proc. MEDSI 2014*, Melbourne, Australia, Sep. 2014

[2] S. Kurokouchi, et al., "Dependence of the seal property of Conflat type flanges on the fine dimensions of the knife edge," Vacuum Science Technology, Mar./Apr. 2003.

[3] E. Clauss, Javcon Machine, Inc., Deer Park, New York, USA, Private Communication, Jul. 2016

[4] S. Sharma et al., "Recent progress on the new design of high-heat-load components," in *Proc. MEDSI 2016*, Barcelona, Spain, Sep. 2016

[5] W. Toter, Internal test report on the weldability of CuCrZr, Performed at Argonne National Laboratory, Argonne, Illinois, USA, May 2015.

Content from this work may be used under the terms of the CC BY 3.0 licence (© 2016). Any distribution of this work must maintain attribution to the author(s), title of the work, publisher, and DOI.

ISBN: 978-3-95450-188-5 doi:10.18429/JACoW-MEDSI2016-TUPE32

A GIRDER-FREE MAGNET SUPPORT SYSTEM DESIGN

S. Sharma, NSLS-II, Brookhaven National Laboratory, NY, USA

Abstract

Magnet support systems for the new light sources are required to satisfy several rigorous performance specifications. The support system must be rigid so that its static deflection under its own weight and the combined weight of the magnets is small and repeatable. For vibration stability the lowest natural frequency of the magnet-support assembly should be greater than 50 Hz. To meet thermal stability requirements it is desirable to minimize bending deformations of the support system when subjected to temperature changes. In addition, the magnet support system should be easy to transport, easy to align, and cost effective. Altogether these requirements are difficult to satisfy, especially if the main structural component of the support system is a girder of length greater than 3 meters.

In this paper we propose a magnet support system design consisting of column-type supports joined by removable C-channel beams. The column-type supports provide a superior stability performance without compromising the alignment capability. Analysis results are presented to characterize the performance of this support system.

INTRODUCTION

The storage ring (SR) magnets of new high-brightness light sources have stringent mechanical alignment and stability requirements. The magnets are usually grouped together for assembly on girders in such a way that the stricter specifications apply to magnets on the same girder whereas the specifications for the girders are substantially relaxed. Table 1 shows the alignment and stability specifications for the NSLS-II storage ring magnets [1].

Table 1: NSLS-II Alignment and Stability Specifications in X (horizontal) and Y (vertical) Directions.

Specifications	Alignment (μm)		Stability (nm)	
	Δ X	ΔY	Δ X	ΔY
Magnets	30	30	150	25
Girders	100	100	600	70

Magnets are usually assembled on long girders (in 3–7 m range) outside the SR tunnel. This allows advanced preparation of magnet-girder assemblies as well as use of better techniques for magnet alignment such as the vibrating wire method. Long girders support the weight of the magnets primarily by bending (flexural) deformations which are not conducive to magnet alignment. Bending vibration modes and thermal bending deformations also work against meeting the magnet stability specifications. This is illustrated below for a simple box-beam girder.

A BOX-BEAM GIRDER

A steel box-beam girder of 0.5 m height, 0.5 m width and 0.04 m wall thickness (inset of Figure 1) is analysed for deflection under its self-weight and the weight of the magnets. The weight of the magnets is approximated by doubling the weight density of steel. The deflection for simply-supported boundary conditions is calculated both by a flexural beam equation and by 3-D Ansys analysis that includes shear and compression deformations. As shown in Fig. 1, the gravity loads are resisted primarily by shear and compression deformations for span-to-height ratio R of < 3. For R > 7, the loads are resisted mainly by bending deformations which increase as R^4. As a comparison, the measured gravity deflection of a 5 m long (R = ~ 10) NSLS-II girder was 117 μm, and had a scatter of ~ 15 μm (half of the alignment tolerance) because of friction at the support points.

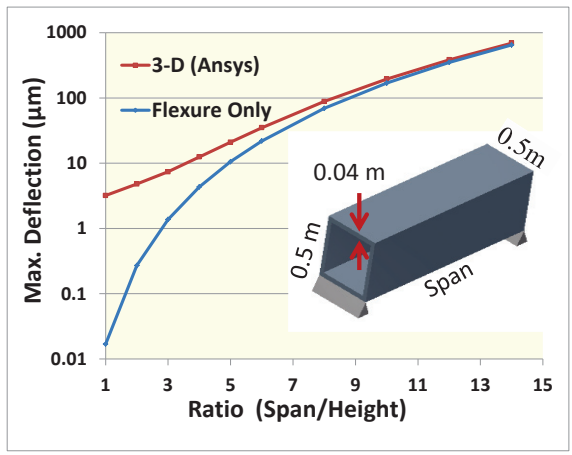


Figure 1: Gravity deflection of a box-beam girder under its self-weight and weight of the magnets versus R (Span/Height).

The box-beam girder can also be used for an insight into its mechanical stability. A natural frequency of > 50 Hz in bending (or torsion) mode is commonly used for the magnet-girder assembly to ensure that the vibration stability specifications are met for the ambient ground motion. Thermal bending deformations are induced in the girder when the girder's expansion or contraction due to change in the tunnel-air temperature is constrained. Because of thermal inertia, a girder typically experiences only a fraction (~ 10%) of the change in the tunnel air temperature. Thermal bending also occurs due to diurnal expansion/contraction of the floor.

The first natural frequency in bending mode and thermal bending (for 1° C change in girder temperature) of the box-beam girder are plotted in Fig. 2. The weight of the magnets is again included approximately by doubling the weight density of steel. As can be seen the natural frequency decreases as $1/R^2$ whereas the thermal bending deformation increases as R^2. A natural frequency of > 50 Hz is obtained for R < 9. Assuming that the stability

Content from this work may be used under the terms of the CC BY 3.0 licence (© 2016). Any distribution of this work must maintain attribution to the author(s), title of the work, publisher, and DOI.

ISBN: 978-3-95450-188-5 doi:10.18429/JACoW-MEDSI2016-TUPE32

specifications of Table 1 also apply to thermal stability (effectively 2.5 μm/ °C), R for this beam needs to be ~ 1.

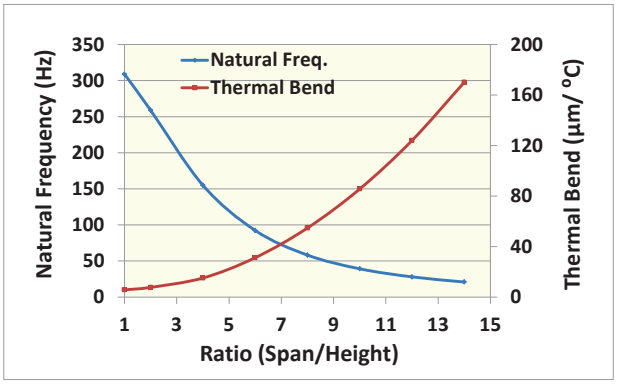
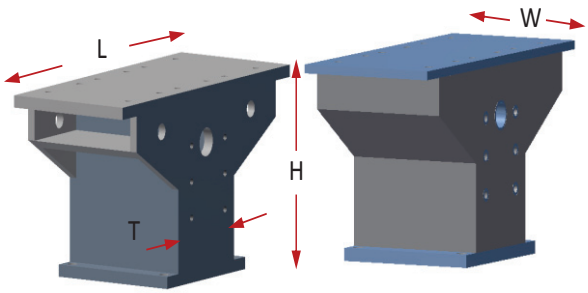


Figure 2: Natural frequencies and thermal bending deformation of a box-beam girder versus R (Span/Height).

GIRDER-FREE SUPPORT SYSTEM

From the example above it is clear that bending deformations of the girder make it difficult to meet the alignment and stability specifications. Special measures, such as profiling, damping pads [1] and locking system [2], are often introduced to meet the specifications. We propose a magnet support system based on hammerhead columns (Fig. 3) which minimize bending deformations. A hammerhead column can be constructed either as a welded steel structure (Fig. 3-a) or as a solid reinforced concrete (RC) structure (Fig. 3-b). RC hammerhead piers are commonly used for bridge construction where they are designed to carry a large fraction of loads in shear and compression.

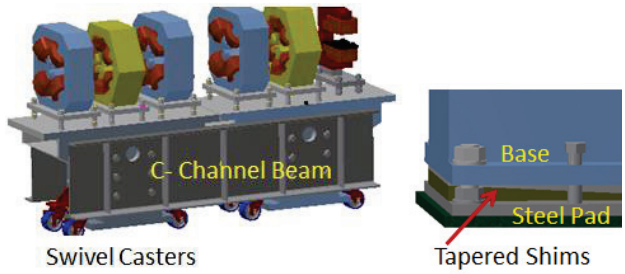


(a) (b)

Figure 3: Hammerhead support columns – (a) welded steel construction, (b) from reinforced concrete with steel plates. Dimensions used in analyses are H = 0.8 m, L = 1.5 m, W = 0.65 m, and T = 0.5 m.

Basic dimensions of the hammerhead columns, used for analyses in the following sections, are shown in Fig. 3. Both the steel and RC hammerhead columns weigh in the range of 1400–1500 kg. For the RC hammerhead a combined density of 2500 kg/m^3 and Young's modulus of 30 GPa are used in the analyses. The length L of the top plate can be increased if the T dimension is increased proportionately to achieve the same performance. Because of their simple construction and manageable dimensions these hammerhead columns are cost-effective and easy to fabricate.

ASSEMBLY, TRANSPORTATION AND ALIGNMENT



(a) (b)

Figure 4: (a) An assembly with two hammerhead columns, removable c-channel beams and spring- loaded swivel casters, (b) tapered shims between the hammerhead base and grouted steel pad.

Two or more hammerhead columns can be used to replace a girder of the same length for the assembly and alignment of magnets, vacuum chamber and other ancillary components. The hammerheads columns are joined by removable C-channel beams (Fig. 4-a). Spring-loaded swivel casters are attached for transportation and load sharing. After transportation into the SR tunnel a precise alignment over pre-grouted steel pads is performed either for the entire assembly or for each hammerhead assembly. In the latter case simple pusher-type alignment mechanisms can be used since the weight of the entire hammerhead assembly is comparatively small (~ 3000 kg) and there is no cross-talk between the two assemblies. Tapered shims (Fig. 4-b) can be used between the base and the grouted pad for better mechanical stability and to help automate the alignment process. For subsequent global alignment of the SR, the use of a smoothing technique [3] can be used to reduce the number of hammerhead assemblies to be aligned.

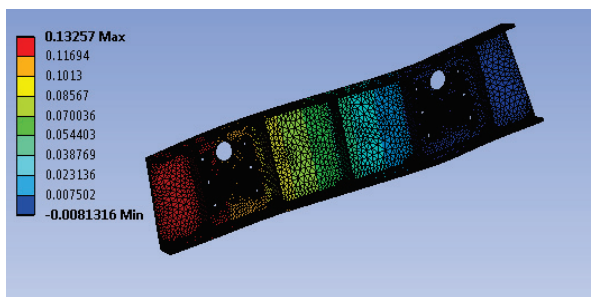


Figure 5: Deflection of C-channel beams subjected to the weight of a hammerhead assembly is 0.14 mm.

The C-channel beams are approximately 0.13 m in width and 0.6 m in height, weighing approximately 270 kg. These dimensions for the C-channel beams ensure that the relative displacement between the two hammerhead assemblies is a small fraction of 1 mm even if they are accidentally subjected to the full load of one hammerhead assembly (see Fig. 5). The maximum effective stress in the beams is less than 50 MPa as compared to 200 MPa yield strength of structural steel.

Content from this work may be used under the terms of the CC BY 3.0 licence (© 2016). Any distribution of this work must maintain attribution to the author(s), title of the work, publisher, and DOI.

ISBN: 978-3-95450-188-5 doi:10.18429/JACoW-MEDSI2016-TUPE32

Content from this work may be used under the terms of the CC BY 3.0 licence (© 2016). Any distribution of this work must maintain attribution to the author(s), title of the work, publisher, and DOI.

ANALYSIS OF PERFORMANCE

Ansys finite element analyses were carried out for magnet assemblies on both steel and RC hammerheads. The results for gravity deflection, modal analysis and thermal stability are described below.

Gravity Deflection

Gravity deflection of a steel hammerhead column under its self-weight and weight of the magnets is depicted in Fig. 6. The maximum and minimum deflections of the magnets on a steel hammerhead column are 5 µm and 4 µm, respectively, resulting in a misalignment of only 1 µm. A similar misalignment (0.7 µm) was obtained for an RC hammerhead column. These values are more than an order of magnitude smaller than those measured for NSLS-II steel girders. High-precision alignment of the magnets is simpler when the effect of gravity deflection is negligible.

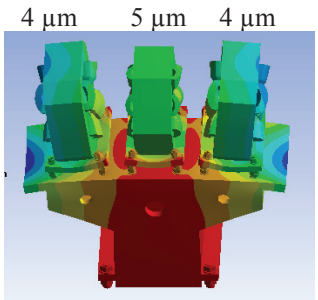
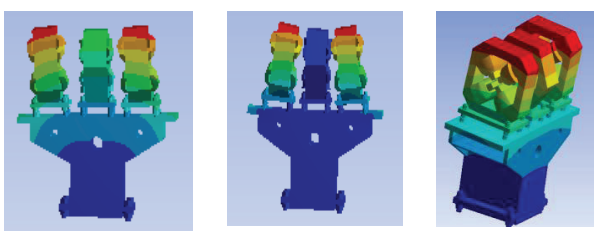


Figure 6: Gravity deflections for a steel hammerhead – magnets assembly.

Modal Analysis

Natural frequencies for the first four lowest modes of a steel hammerhead - magnets assembly were calculated as 70.3 Hz, 94.3 Hz, 100.8 Hz and 102.7 Hz. In the 1st, 2nd and 4th modes all motions are along the beam direction. In the 1st mode (Fig, 7) the hammerhead column itself bends at the base whereas in the 2nd and 4th modes the magnets move with respect to the column. These modes are not relevant for the stability of the magnets. In only the 3rd mode at 100.8 Hz, the column bends in the transverse-to-beam direction and is subject to the mechanical stability criterion of natural frequency > 50 Hz.



1st Mode 2nd Mode 3rd Mode

Figure 7: First three modes of a steel hammerhead - magnets assembly (natural frequencies of 70.3 Hz, 94.3 Hz and 100.8 Hz).

For the RC hammerhead assembly the first four natural frequencies are 59.3 Hz, 77.5 Hz, 97.87 Hz and 102.0 Hz. The transverse motion of the column occurs in the 2nd mode at 77.5 Hz. This is expected to be close to the actual natural frequency because of a single-unit construction of the column and because the stiffness uncertainty of bolted connections is mitigated by tightening the bolts against tapered shims.

Thermal Stability

A transient analysis was performed for a tunnel air temperature change of ± 0.1° C at 1 hour cycle. As expected, the temperature change in the steel hammerhead column and the magnets is only 10% of the change in air temperature because of thermal inertia. Thermal deformation of the hammerhead-magnets assembly under the induced thermal gradients, which are maximum at time = 1,260 seconds, is shown in Fig. 8. Magnet misalignment due to the thermal gradient is only 9 nm which is a fraction of the stability specification of 25 nm. The corresponding misalignment in the RC hammerhead – magnets assembly is 10 nm. It should be noted that the thermal stability of hammerhead columns is immune to SR floor's diurnal expansion/contraction and counter-measures such as viscoelastic pads [1] are not required.

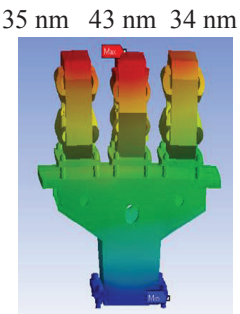


Figure 8: Thermal deformations in a steel hammerhead – magnets assembly due to tunnel air temperature change.

CONCLUSIONS

Bending deformations in girder-based magnet support system are detrimental to meeting the stringent mechanical alignment and stability specifications of the magnets of new storage rings. Such deformations are minimized in a support system based on hammerhead columns. These columns are joined with removable C-channel beams only during assembly and transportation. High-precision alignment is simplified in the proposed design because gravity deflections are reduced by more than an order of magnitude. This support system meets all vibration and thermal stability specifications by a substantial margin.

REFERENCES

[1] S. Sharma, et al, "Optimization of magnet stability and alignment for NSLS-II", *in Proc. PAC11, NY, USA.*

[2] P-L Sung, et al, "Vibration measurements for the Girders with Multi-Stage Adjustable Dampers in TPS Storage Ring, *in Proc. MEDSI2012*, Oxford, UK.

[3] C-Y Yu et al, "The Application of Smoothing in NSLS-II", *paper to be presented at IWAA2016,* Grenoble, France.

ISBN: 978-3-95450-188-5 doi:10.18429/JACoW-MEDSI2016-TUPE33

NSLS-II BEAM APERTURE SLIT VIBRATION STUDIES

C. Spataro, C. Amundsen, H. Bassan, S. Sharma
Brookhaven National Laboratory, Upton, NY 11973 USA

Abstract

Beam aperture slits mounted on stepper-motor driven X-Y stages are used in NSLS-II frontends to define the beam size and to limit thermal loads on downstream optical components. The X-Y stages have positional and resolution requirements of 1 µm and 0.1 µm, respectively. This is achieved by micro-stepping the stepper motor by a Delta-Tau GeoBrick-LV-NSLS-II controller. During the initial operation of the X-Y stages unacceptable levels of vibration when the stages were in motion, and an intermittent sharp squealing when they were at rest, were discovered. In this paper we present the studies that were undertaken to investigate these issues and the solutions that were implemented.

INTRODUCTION

The NSLS-II frontend slit assembly consists of an invar stand, a baseplate, X-Y stages, and water cooled Glidcop slit (Fig. 1).

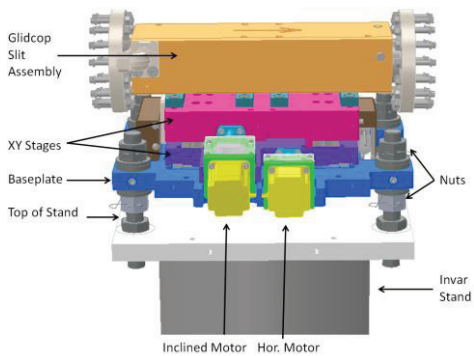


Figure 1: NSLS-II Frontend Slit Assembly.

A pair of slit assemblies is used for the adjustment of the beam size exiting the front end. The L-shape aperture of the upstream slit trims the lower and left edge of the beam while a similar aperture of the downstream slit trims the upper and right edge of the beam. X-Y stages provide the required motion in the horizontal and vertical directions taking into account the coupling of the two motions by the inclined stage. In canted beamlines one pair of slits is used (total of 4 slits) to trim each beam independently. The slit assembly is mounted on a thermally stable invar stand to meet the long term positional stability requirements of 1 um.

XY STAGE MOTOR CONTROLLER

The X-Y stages have position and resolution requirements of 1 µm and 0.1 µm, respectively.

A stepper motor system incorporating a Delta Tau GeoBrick-LV-NSLS-II controller with relative encoders are used for precise positioning of the slits. The horizontal and inclined axis motors are identical. The horizontal position is controlled by the horizontal axis motor. The vertical position is controlled by the horizontal axis motor and the inclined axis motor which is at a 14 degree angle to the horizontal plane. This design was implemented to minimize the vertical size of the slit assembly, thus improving its mechanical and thermal stability. The motors have a micro-step resolution of 160 nm. Both stages are equipped with Renshaw optical encoders with a resolution of 40 nm.

PRE-INSTALLATION TESTING

The motors were installed and configured on the X-Y stage assembly before installation. Extensive tests were performed on the X-Y stages to verify their performance, vibration characteristics, and number of cycles to failure. A slit was mounted on the stages during these tests but the water lines and bellows were not connected. The tests were deemed successful as all performance specifications were met.

RUNAWAY VIBRATION

After the slit assemblies were installed in the SR tunnel, initial testing and calibration revealed that there was a vibration problem which did not occur during the laboratory tests. A homing test routine was used for calibration in which the stages were exercised in both horizontal and vertical directions. During execution of the homing routine, the stages often experienced runaway vibrations, causing the controller to quit the routine. With two slit assemblies side by side, the excessive vibrations from one stage in motion caused the other to move as well. The large vibrations between the stages were being transmitted through the vacuum and water connections.

One of the potential sources of this vibration was identified as the electrical noise picked by long instrumentation wiring. At NSLS-II, the controllers are located on top of the storage ring tunnel about 20 meters away from the motors. However, electrical noise was ruled out as a source when the same vibration problem occurred even when the motors were run locally by an identical controller brought in a close proximity to the motors.

A closer mechanical inspection of the slit assembly revealed some twist in the baseplate. This occurred because the final set-screw adjustments for alignment were performed after the nuts were already torqued, causing distortions in the baseplate. The alignment procedure was modified so that most of the torque was applied after final adjustments. The vibration levels were reduced but not sufficiently to eliminate the runaway incidences.

An experiment was then performed in which a viscoelastic pad was added to the top of the slit to help dampen

Content from this work may be used under the terms of the CC BY 3.0 licence (© 2016). Any distribution of this work must maintain attribution to the author(s), title of the work, publisher, and DOI.

ISBN: 978-3-95450-188-5 doi:10.18429/JACoW-MEDSI2016-TUPE33

Content from this work may be used under the terms of the CC BY 3.0 licence (© 2016). Any distribution of this work must maintain attribution to the author(s), title of the work, publisher, and DOI.

out the vibrations (Fig. 2). This reduced the peak vibration levels but at the expense of broadening the bandwidth. The runaway vibration problem was still not resolved.

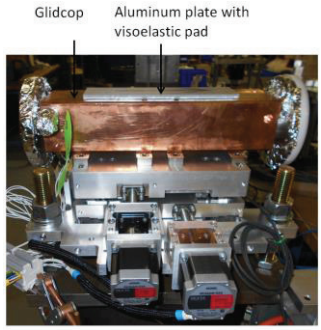


Figure 2: Slit assembly with viscoelastic pad.

A detailed inspection of the slit assembly revealed gaps between the slit body and the outside stainless steel (SS) bars. The solution was to add 2 set screws and tapped-holes to the two outside bars (Fig. 3). By turning the set screws, the SS bars were pushed tightly against the slit body. This reduced the vibration levels considerably and eliminated the runaway vibration occurrences.



Figure 3: Set screws for raising the outside SS bars.

VIBRATION MITIGATION

Numerous tests were done both in the storage ring tunnel and in the laboratory to further mitigate the vibration levels. It was discovered that the motor current tuning and the PID loop tuning in the laboratory did not provide the best response in the tunnel due to the added forces from the vacuum and water connections.

Current tuning of the motors followed by the PID loop tuning was done to get a better response. It was found that when moving the motor by a small number of encoder counts (for instance, 25 counts, which is equivalent 1 micron in position) the motor actually moved up and down over one thousand counts (±40 microns) before arriving to the desired position (Fig. 4).

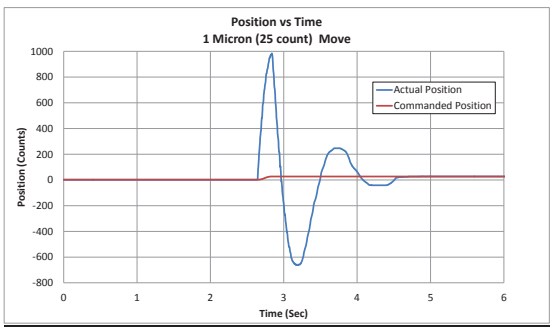


Figure 4: Actual and Commanded Position vs Time.

The motors were re-tuned and this reduced the unwanted excursion to 14 microns, which is still large but much better than the original tuning.

A large factor in the vibration was the default motor velocity. Tests were performed at various velocities. It was found that there was a linear correlation between vibration levels and the default motor velocity. After numerous rounds of tests, a reduced velocity of 1/3 of the default velocity was deemed to be a good compromise which reduced the vibration levels by a factor of three (Fig. 5 and 6).

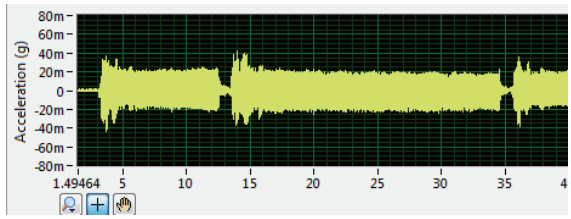


Figure 5: Acceleration vs Time - Default Velocity.

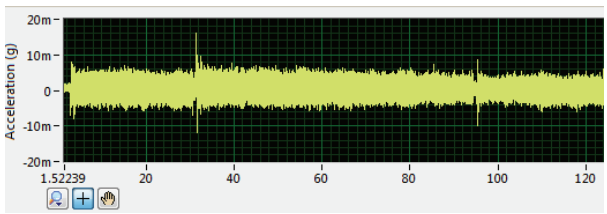


Figure 6: Acceleration vs Time - 1/3 Default velocity.

INTERMITTENT SQUEALING

The motors in the tunnel were often found to be squealing with a high frequency pitch (like a jet engine revving up for take-off). The squealing could be stopped by opening and closing the feedback loop. This was only a temporary solution, as the problem surfaced again and again over time.

Tests were performed in the laboratory to try to duplicate the squealing condition. It was surmised that the squealing could be duplicated by changing the micro-stepping or the holding current because this would affect the holding torque. After some testing, it was discovered that the squealing could be duplicated by lowering the holding current. A PLC runs in the background of the motion program. After a move is completed, the holding current is reduced to 50% of the nominal current for motion (2A). By dropping the holding current to 5%, the squealing could be duplicated every time.

When the holding currents for both motors are dropped to 5%, the high frequency noise starts within 15 seconds. When the holding current is first dropped to 5% and then immediately brought back up to 50%, no noise was produced. It was also found that it was the inclined-axis motor that was the cause of the squealing. When the holding current on only the horizontal-axis motor was dropped, no squealing occurred.

A holding current vs temperature test was performed. The holding currents for both motors were set to 99% of the nominal and monitored for over 4 hours (Fig. 7).

ISBN: 978-3-95450-188-5 doi:10.18429/JACoW-MEDSI2016-TUPE33

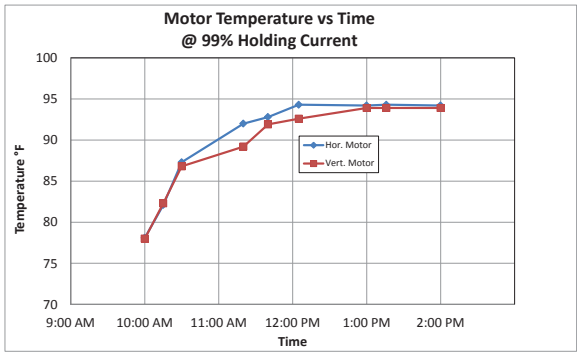


Figure 7: Motor Temperature vs Time.

Temperatures reached equilibrium within two hours and were within specifications. This meant that the holding current could be increased without overheating the motors.

The intermittent nature of the problem is likely to be caused by the reduction in the motor torque when microstepping is used. At the 32 usteps/step setting of the motor, the torque drops to 5% of its rated value (Fig. 8).

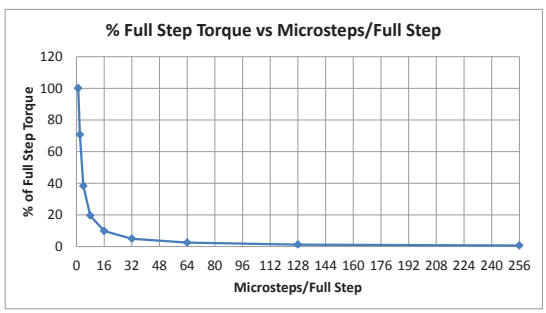


Figure 8: % Full Step Torque vs Microsteps/Step.

Depending on the exact position in relation to the motor steps, the torque will vary, so in some micro-stepping positions the torque is higher and the motor does not squeal, where as in other positions, the torque is lower and the motor starts to squeal. While reduced torque has been established as the cause of motor squealing, the sequence of events in terms of motor current, pulse counts, and position, is still under investigation.

It is now planned to increase the holding current and reduce the number of micro-steps for the inclined-axis motor. If the motor squealing persists then 90^0 worm-gear reducers will be used to increase applied torque to the stages.

CONCLUSIONS

Although the NSLS-II slit assemblies with the X-Y stages met all performance specifications in laboratory tests, their implementation in the SR tunnel revealed three vibration-induced problems. First, there were incidences of runaway vibrations that caused the Delta Tau controller to exit calibration routine. This problem was resolved by stiffening the ends of the slits using set screws that raised the SS support bars.

Secondly, high levels of slit vibrations were observed when the X-Y stages were in motion. These were traced to incorrect current and PID-loop tuning of the motors as well as to their higher than optimal velocity. Once the motors' tuning was optimized and their velocity was reduced by a factor of three, the vibration levels were reduced substantially.

A third problem was frequent squealing of the inclined-axis motor due to a low holding torque in certain microstepping positions. This problem will be resolved shortly by a combination of measures, namely, increasing the holding current, reducing the number of microstepping, and using a 90^0 worm-gear reducer.

ACKNOWLEDGMENT

The authors would like to thank M. Brietfeller, L. Doom, J. Duff, J. Escallier, A. Jain, F. Lincoln, and A. Munoz for their help and insight.

Content from this work may be used under the terms of the CC BY 3.0 licence (© 2016). Any distribution of this work must maintain attribution to the author(s), title of the work, publisher, and DOI.

ISBN: 978-3-95450-188-5 doi:10.18429/JACoW-MEDSI2016-TUPE36

GROUND VIBRATION MONITORING FOR SXFEL CONSTRUCTION AT SSRF*

R. B. Deng†, F. Gao, L. X. Yin
Shanghai Institute of Applied Physics (SINAP), Shanghai 201204, P. R. China

Abstract

Shanghai X-ray Free Electron Laser test facility (SXFEL) began construction on Dec.30 2014. It is quite important to monitor the ground vibration influenced by the construction at Shanghai Synchrotron Radiation Facility (SSRF), because the SXFEL is just in the north of SSRF and the nearest distance is only 20m. In this paper, the results of ground vibration measurement during the construction period at SSRF experimental hall, tunnel and experimental room near the SXFEL site are shown. Vibrations at different hours, frequency bands and directions are discussed to provide more detailed information on the influence of SXFEL construction to SSRF.

INTRODUCTION

Shanghai X-ray Free Electron Laser test facility (SXFEL) with total length about 300 meters is being built at Zhangjiang campus of Shanghai Institute of Applied Physics (SINAP), where Shanghai Synchrotron Radiation Facility (SSRF) is situated [1]. SXFEL began construction on Dec.30, 2014. It is quite important to monitor the ground vibration influenced by the construction at Shanghai Synchrotron Radiation Facility (SSRF), because the SXFEL is just in the north of SSRF and the nearest distance is only 20m.

METHODOLOGY AND EQUIPMENT

Large-scale pile foundation construction of SXFEL started on Mar. 9, 2015, so a series of vibration measurements were carried out at the SSRF Experimental Hall, Tunnel and Experimental Room since Mar. 2015. The measurement points of A, B, C at SSRF are shown in Fig. 1. Point A locates on the floor of Experimental Hall, with B on the floor of Room 1049 and C in the tunnel. We used a DHDAS5927 data acquisition system and DH610 seismometers from Donghua Testing Technology Co., LTD, China. The test site of A is shown in Fig. 2.

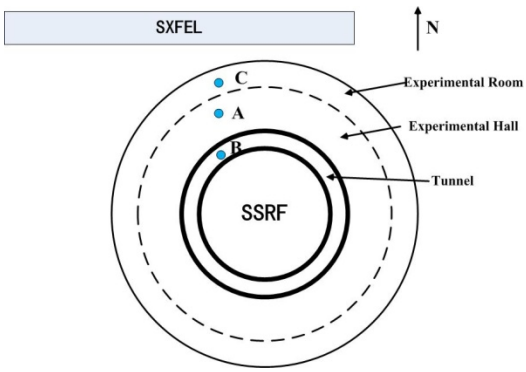


Figure 1: Measurement points at SSRF.



Figure 2: Test site on the floor of Experimental Hall.

The displacement power spectrum density (PSD) and integrated root-mean-square (RMS) displacement are derived based on the data analysis techniques [2].The range of the RMS displacement is between 1 Hz to 100 Hz, which is within the effective frequency band of the DH610 seismometer.

MEASUREMENT RESULTS

Contrast of Vibration with and without Pile Foundation Construction

The contrast of continuous RMS displacements of the measurement point A at SSRF Experimental Hall in vertical direction, west-east (W-E) direction and north-south (N-S) direction every Friday in Mar. 2015 before and after large scale pile foundation construction are shown individually in Figs. 3–5. It can be seen that large scale pile foundation construction affects greatly on ground vibration in the vertical direction while affects less on vibration both in the W-E and N-S directions.

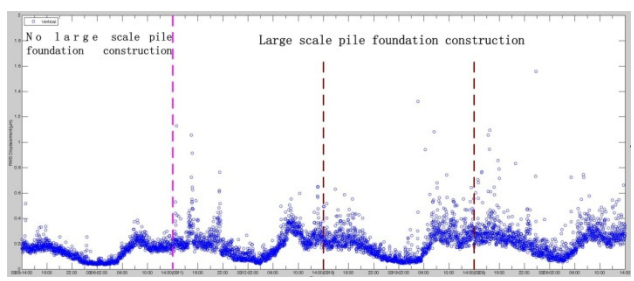


Figure 3: RMS displacement of the point A at SSRF Experimental Hall in vertical direction every Friday in March, 2015.

* Work supported by the National Natural Science Foundation of China (Grant No. 11405255)
† dengrongbing@sinap.ac.cn

Content from this work may be used under the terms of the CC BY 3.0 licence (© 2016). Any distribution of this work must maintain attribution to the author(s), title of the work, publisher, and DOI.

ISBN: 978-3-95450-188-5 doi:10.18429/JACoW-MEDSI2016-TUPE36

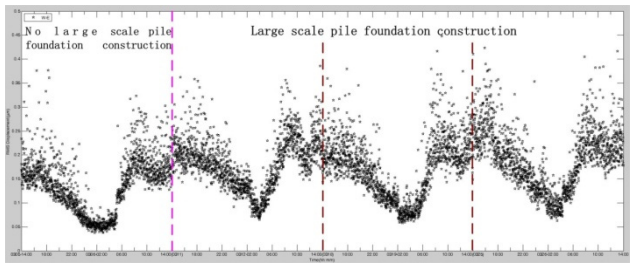


Figure 4: RMS displacements of the point A at SSRF Experimental Hall in west-east direction every Friday in March, 2015.

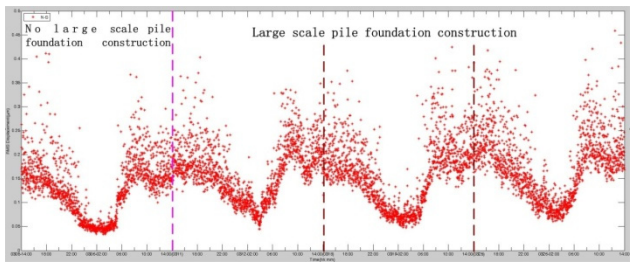


Figure 5: RMS displacements of the point A at SSRF Experimental Hall in north-south direction every Friday in March, 2015.

Contrast of Vibration with and without Surface Construction

Surface foundation construction began on May 6, 2015 and then we studied the effect of surface construction on ground vibration. The contrast of continuous RMS displacements of the point A at SSRF Experimental Hall in vertical direction and N-S direction every Friday in May, 2015 with and without surface construction are shown individually in Figs. 6 and 7.

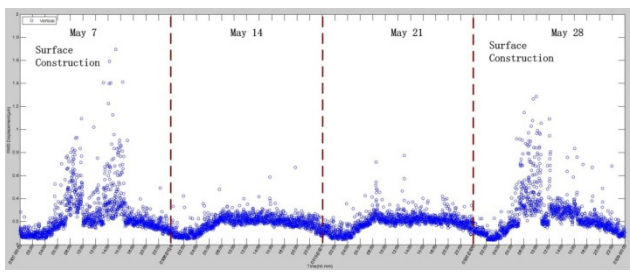


Figure 6: RMS displacement of the point A at SSRF Experimental Hall in vertical direction every Friday in May, 2015.

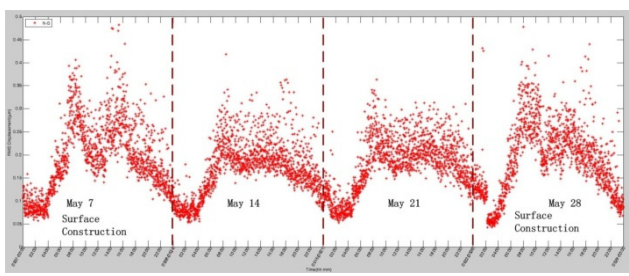


Figure 7: RMS displacements of the point A at SSRF Experimental Hall in N-S direction every Friday in May, 2015.

It can be seen that vibration of Hall floor in the vertical direction increased greatly on May 7 and May 28 because of the vibration of on-site construction vehicles such as excavator, crane, etc. In contrast, vibration of Hall floor in the vertical direction dropped greatly on May 14 and May 21 because the two days are during concrete curing and there was rarely vehicles working on site. The real scenes of SXFEL construction at 9:00 A.M. on May 14 and May 28 are shown individually in Figs. 8 and 9.

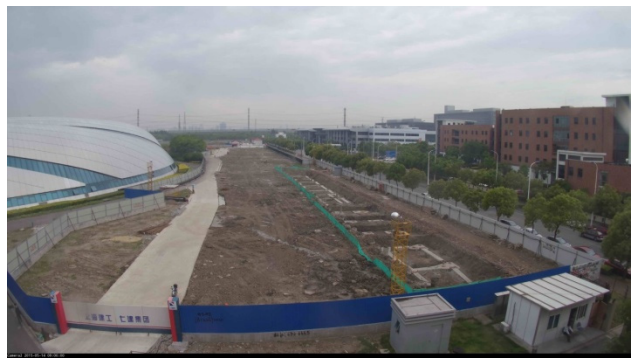


Figure 8: SXFEL construction site at 9:00 A.M. on May 14, 2015.



Figure 9: SXFEL construction site at 9:00 A.M. on May 28, 2015.

Contrast of Vibration on Different Floor

In order to study the ground vibration of SXFEL construction on different floor, we placed 3 typical measurement points shown in Fig. 10: Point A located on the floor of Experimental Hall, Point B located on the Tunnel floor, Point C located on the floor of 1049 Room (Experimental Room). Floor of Point A and floor of Point B are the same floor with 1m thickness and 48m-height pile underground, while the floor of Point C is only 0.12 m thick with no pile underground and there is no connection with floor of Point A or Point B.

Content from this work may be used under the terms of the CC BY 3.0 licence (© 2016). Any distribution of this work must maintain attribution to the author(s), title of the work, publisher, and DOI.

ISBN: 978-3-95450-188-5 doi:10.18429/JACoW-MEDSI2016-TUPE36

Content from this work may be used under the terms of the CC BY 3.0 licence (© 2016). Any distribution of this work must maintain attribution to the author(s), title of the work, publisher, and DOI.

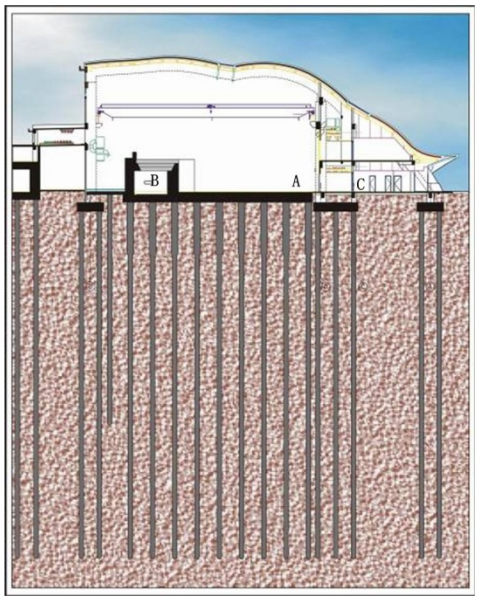


Figure 10: Measurement points at SSRF.

PSD and RMS curves of vibration of Point A (Hall), Point B (C14) and Point C (Room 1049) during noisy and quiet time in vertical direction are shown in Figs. 11-14.

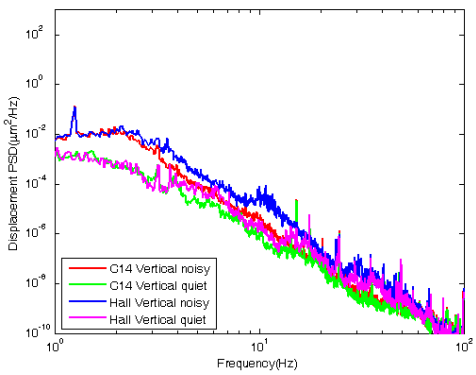


Figure 11: PSD curves of ground vibration of Point A (Hall) and Point B (C14) in noisy and quiet time at SSRF in vertical direction.

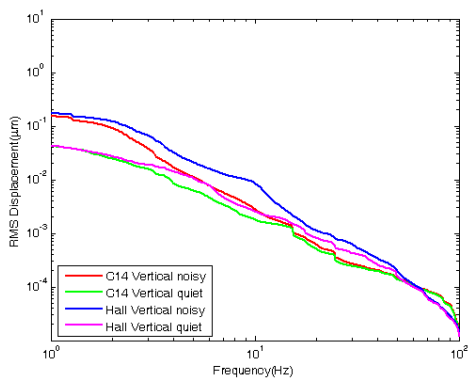


Figure 12: RMS curves of ground vibration of Point A (Hall) and Point B (C14) in noisy and quiet time at SSRF in vertical direction.

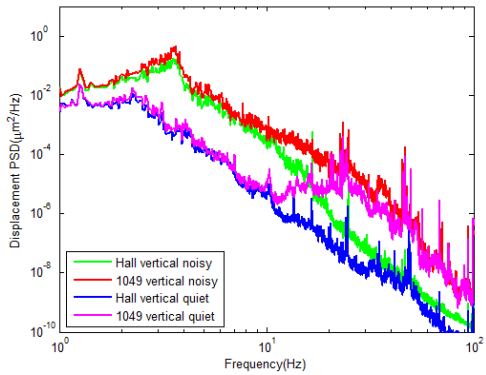


Figure 13: PSD curves of ground vibration of Point A (Hall) and Point C(Room 1049) in noisy and quiet time at SSRF in vertical direction.

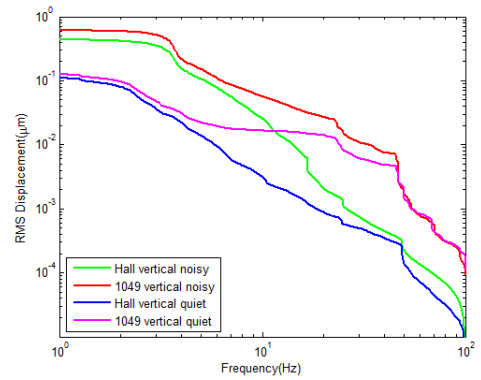


Figure 14: RMS curves of ground vibration of Point A (Hall) and Point C(Room 1049) in noisy and quiet time at SSRF in vertical direction.

RMS values of ground vibration in Tunnel, Experimental Hall and Room 1049 in noisy and quiet time are listed in Table 1 and Table 2.

Table 1: RMS Values of Ground Vibration in Noisy Time

Noisy	Tunnel	Hall	Room 1049
Vertical	420.4 nm	441.8 nm	612.6 nm
N-S	231.2 nm	234.7 nm	239 nm

Table 2: RMS Values of Ground Vibration in Quiet Time

Quiet	Tunnel	Hall	Room 1049
Vertical	107.3 nm	110.9 nm	126 nm
N-S	102.7 nm	105.8 nm	109.7 nm

It can be seen that RMS value of vibration of tunnel between 1 to 100 Hz is a little less than that of Hall. PSD curves of vibration of tunnel and Hall differ little because the floor of tunnel is just the same with the floor of Hall.

The vibration of Hall floor is less than that of floor of Room 1049. What's more, the vibration above 10 Hz on Hall floor is much less than of floor of Room 1049. The floor of Tunnel and Hall has a better damping effect to vibration above 10 Hz.

ISBN: 978-3-95450-188-5 doi:10.18429/JACoW-MEDSI2016-TUPE36

Difference between noisy time and quiet time is relatively large whether in the vibration of Tunnel, Hall floor or floor of Room 1049, especially between 1 and 10 Hz.

CONCLUSIONS

SXFEL finished construction of main structure and decoration engineering by Mar. 2016. Ground vibration caused by SXFEL construction at SSRF has been studied in this paper. Continuous tests are performed both during pile foundation construction and surface construction. Conclusions to be drawn are as follows.

(1) SXFEL construction affects greatly on ground vibration in the vertical direction while affects less on vibration in the N-S and W-E direction.

(2) The floor of Tunnel and Hall has a better damping effect to vibration above 10 Hz than that of Experimental room due to different floor structure.

(3) Ground vibration between noisy time and quiet time is relatively large whether on the floor of Tunnel, Hall floor or Room 1049, especially between 1 and 10 Hz.

REFERENCES

[1] Shanghai X-ray FEL Concept Design Report, Shanghai, 2015.

[2] D.B. Li and Q.H. Lu, “Analysis of Experiments in Engineering Vibration”, Beijing, China: Tsinghua University Press, 2011.

Content from this work may be used under the terms of the CC BY 3.0 licence (© 2016). Any distribution of this work must maintain attribution to the author(s), title of the work, publisher, and DOI.

ISBN: 978-3-95450-188-5 doi:10.18429/JACoW-MEDSI2016-TUPE38

PROGRESS AND MECHANICAL ENGINEERING OF FEL PROJECTS AT SINAP

L. Yin†, L. Wang, S. Sun, W. Zhang, X. Hu, L. Yu, W. Fang
Shanghai Institute of Applied Physics, Shanghai, P. R. China

Abstract

Free electron laser (FEL) technology is the next focus at Shanghai Institute of Applied Physics (SINAP). Shanghai Deep Ultraviolet Free-Electron Laser (SDUV-FEL), a test facility for new FEL principles, was operated for 5 years and got a series of important results. Dalian Coherent Light Source (DCLS), a 50~150nm wavelength FEL user facility based on a 300MeV linac located at Dalian Institute of Chemical Physics, started beam commissioning in August. Shanghai X-ray Free-Electron Laser (SXFEL), a soft X-ray FEL test facility based on an 840MeV linac, will be installed in this month and the commissioning is scheduled at the beginning of 2017. The Progress of the FEL projects and the mechanical engineering in the design and construction are presented.

INTRODUCTION

Shanghai Synchrotron Radiation Facility (SSRF) is a 3.5 GeV light source opened to users from 2009. There are 15 beamlines in operation and the SSRF Phase-II Project, including 16 new beamlines, will be started at the end of 2016. In the meantime, the free-electron laser (FEL) projects are also performed at Shanghai Institute of Applied Physics (SINAP). The Shanghai Deep Ultraviolet Free-Electron Laser (SDUV-FEL) source is a test facility for new FEL principles and techniques. A series of experiments have been successfully carried out in it. It will be closed when SXFEL starts operation in 2017. Dalian Coherent Light Source (DCLS) is developed jointly by Dalian Institute of Chemical Physics (DICP) and SINAP. It is a EUV coherent light source based on ultrafast lasers and electron accelerator techniques. The installation was just completed at DCIP campus and the first light is hoped to be obtained in this autumn. It will be the first user FEL user facility in China. Shanghai X-rays Free-Electron Laser (SXFEL) project, approved by the central government at the beginning of 2015, is under construction. It is located at the north of Zhangjiang campus, just adjacent to the SSRF facility. Fig. 1 shows the view of the SXFEL building. Installation of the facility was started in August and will be completed by the end of 2016. The FEL commissioning is scheduled in early 2017.



Figure 1: The SXFEL building adjacent to SSRF.

† yinlixin@sinap.ac.cn

SDUV-FEL

SDUV-FEL is an integrated multi-purpose test platform for FEL principles and techniques. The linac is mainly composed of a low emittance photocathode injector, five 3 m long S-band accelerating structures and one bunch compressor. The undulator line includes six 1.5 m long planar undulators with period length of 25 mm and fixed gap of 10 mm. Fig. 2 shows the undulators of SDUV-FEL. The FEL experiments were began in 2009. Some major milestones are achieved. In the end of 2009, SASE experiments were carried out and the SASE light at the end of the 9 m long undulator were obtained. Seeded FEL experiments were began in May 2010. The HGHG saturation was achieved at the end of 2010. The FEL with an EEHG scheme was obtained at the 10th harmonic of the seed in 2013 (shown in Fig. 3). Besides these, a widely-tuneable HGHG, cascaded HGHG and the polarization control via crossed-planar undulators are demonstrated in the following years [1- 3].



Figure 2: Undulators of the SDUV-FEL.

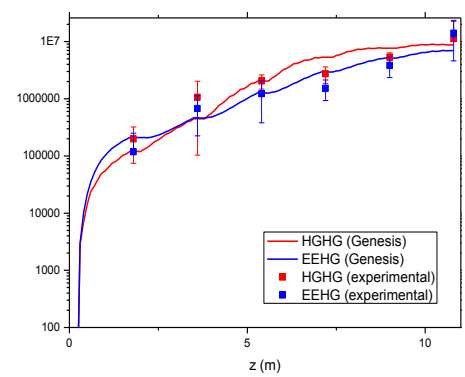


Figure 3: Gain curves of HGHG and EEHG.

Content from this work may be used under the terms of the CC BY 3.0 licence (© 2016). Any distribution of this work must maintain attribution to the author(s), title of the work, publisher, and DOI.

ISBN: 978-3-95450-188-5 doi:10.18429/JACoW-MEDSI2016-TUPE38

DCLS

DCLS is based on the HGHG technique and will provide the highly bright and ultrafast laser light pulses. Electron pulses of 500 pC with normalized emittance below 1 mm·mrad are generated using a photo-injector. The linac consists of 6 S-band accelerating structures and an adjustable chicane. Fig. 4 shows the injector and the linac. The electrons are accelerated to 300MeV before entering the HGHG amplifier. In the amplifier, six undulators are used to generate 50~500 nm FEL with pulse energy of >5.2 uJ @ 130 fs. In the beamline, the FEL radiation will be delivered to four end stations.



Figure 4: DCLS injector and linac.

Six 3 m long planar undulators with period length of 30 mm, minimum gap of 8.75 mm and maximum adjustable taper of 0.5 mm are developed. Fig. 5 shows the undulators installed in DCLS tunnel. The requirement of undulator phase error is less than 5 degrees rms and the beam orbit straightness in the undulator is less than 5 μm rms. Measurements have been performed and the results show that the performance satisfies DCLS's requirements, as shown in Fig. 6.

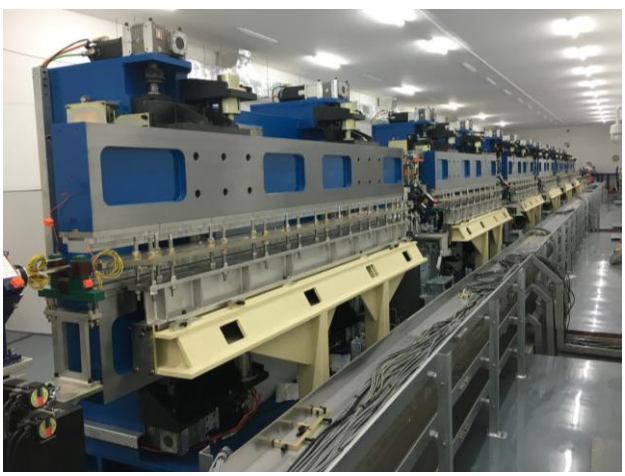


Figure 5: Undulators installed in DCLS tunnel.

In the gap of undulator, an aluminium extrusion vacuum chamber with elliptical beam channel of 15mm(H) × 6mm(V) and minimum wall thickness of 0.75 mm is set with flatness of 0.2 mm. Two Φ4 mm channels are designed at each side of the beam channel for horizontal correction coil and optical fibre of beam loss monitor. Two pairs of grooves on top and bottom side of the

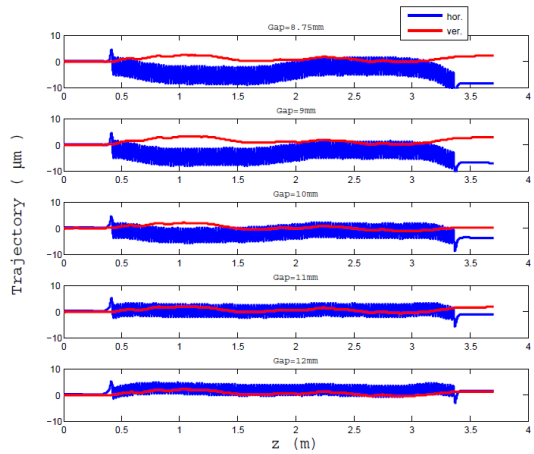


Figure 6: Trajectory of the beam in undulator.

chamber are arranged to set the vertical correction coils. Fig. 7 shows the cross section of the chamber. A roughness of about 200 nm in the inner surface of the beam channel was achieved by a precision extrusion. A pressure of less than 10^{-6} Pa is achieved at each end of the chamber after 90 ℃ bakeout for the chamber and pump.

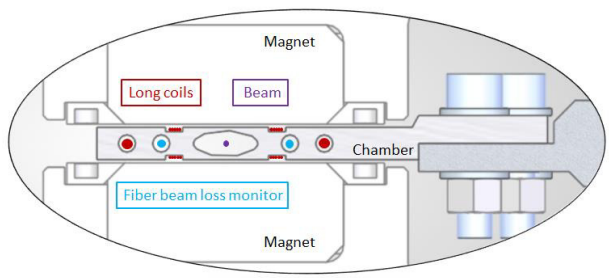


Figure 7: Cross section of the vacuum chamber.

Better than 1μm beam position measurement resolution is necessary for FEL. To achieve this resolution, a cavity type BPM (CBPM) system was developed at SINAP, consisting of a cavity pick-up, a RF frontend and a signal processing unit. The cavity pickup is comprised of a reference cavity working at 4693 MHz and a position cavity at 4680(H) and 4688(V) MHz. Precision machining and vacuum brazing are adopted to fabricate the pick-up from OFHC. Fig. 8 shows the parts fabrication of the pick-up. A beam test at SDUV-FEL for the prototypes shows that the resolution is better than 1μm @ 0.5 nC.

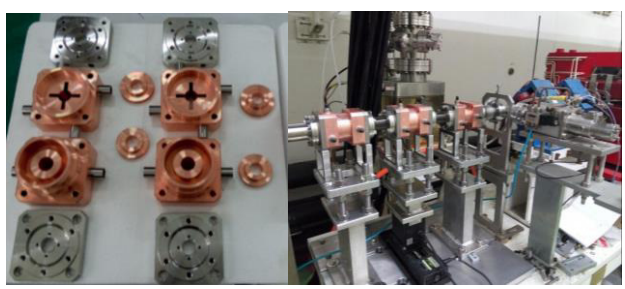


Figure 8: CBPM fabrication and beam test.

Content from this work may be used under the terms of the CC BY 3.0 licence (© 2016). Any distribution of this work must maintain attribution to the author(s), title of the work, publisher, and DOI.

ISBN: 978-3-95450-188-5 doi:10.18429/JACoW-MEDSI2016-TUPE38

Content from this work may be used under the terms of the CC BY 3.0 licence (© 2016). Any distribution of this work must maintain attribution to the author(s), title of the work, publisher, and DOI.

SXFEL

The main purpose of the SXFEL test facility is to promote the development of FEL science, which includes exploring the possibility of seeded X-ray FEL by using two-stage cascaded HGHG-HGHG and EEHG-HGHG schemes, and conducting R&D on X-ray FEL related key techniques. The SXFEL test facility consists of a 130 MeV photo-cathode injector, an 840 MeV main linac, an undulator system and a diagnostic beamline. The layout of SXFEL is schematically shown in Fig. 9.

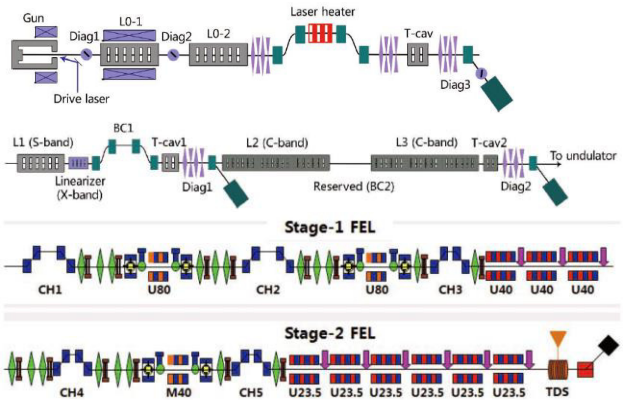


Figure 9: Layout of SXFEL.

The accelerator is based on S-band and C-band linac techniques, and it is designed toward a compact linac with the high performance photo-cathode RF gun and C-band high gradient RF accelerating structures. The C-band accelerating structure is optimized to work at a $4\pi/5$ mode with a round cell shape for obtaining high shunt impedance and low short-range wakefields [4]. The structure design of a 1.8 m C-band accelerating structure is shown in Fig. 10. Prototype has been developed successfully. High power tests show that the average accelerating gradient of the prototype structure reaches 47 MV/m, and the breakdown rate is about 0.01% on average in over 24 hours at 42.7 MV/m gradient. The beam tests have also been successfully performed in SDUV-FEL, as shown in Fig. 11.

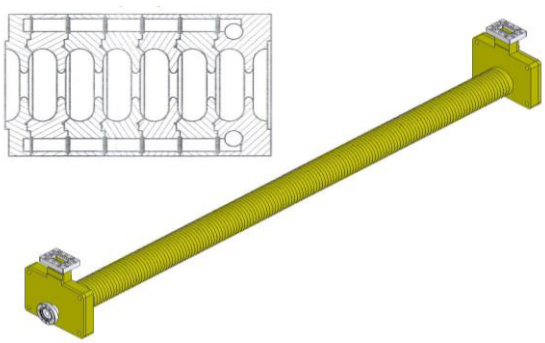


Figure 10: Design of the C-band structure.

The final FEL output from SXFEL will be at 8.8 nm with peak power greater than 100 MW. The two-stage undulator line is comprised of a seed laser system, stage-1 modulators and radiators, stage-2 modulator and radiators, as well as a couple of chicanes. The 8.8 nm radiation will be generated by the fresh bunch in the radiators of the second stage. The total harmonic conversion number of the two stages is 6×5 (264nm→44nm, 44nm→8.8nm).

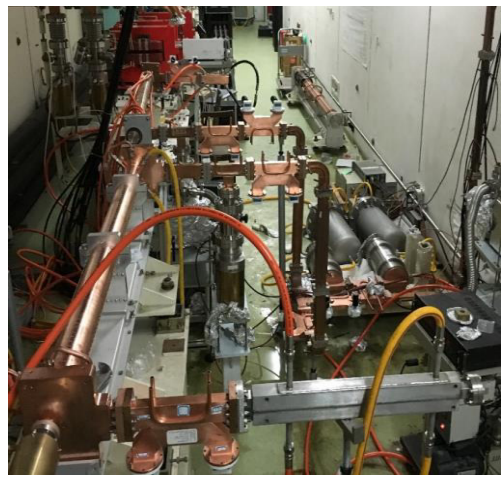


Figure 11: C-band structure beam test.

A proposal about upgrading the SXFEL test facility to a user facility was approved in 2016. This would be accomplished by having the radiation wavelength extended to cover the "water window" region by boosting the electron beam energy to 1.6 GeV with more C-band accelerating structures and by making the FEL output saturation with more undulators in the second stage.

SUMMARY

A series of achievements on new FEL principles and techniques have been obtained based on the SDUV-FEL source. The DCLS user facility is under commissioning and will have wide applications in the frontier researches of molecular photochemistry, combustion chemistry, etc. The SXFEL test facility with the output of 8.8 nm radiation is under construction and will be commissioned at the beginning of 2017. By adding more accelerating structures and undulators, the machine will be upgraded to a user facility with saturated 3 nm output wavelength in the future.

REFERENCES

[1] Z. T. Zhao, et al., Nat. Photonics 6 (2012) 360

[2] B. Liu, et al.: Phys. Rev. ST Accel. Beams 16 (2013) 020704

[3] H. X. Deng, et al.: Phys. Rev. ST Accel. Beams 17 (2014) 120702

[4] W. Fang, et al.: IPAC2011, San Sebastian, Spain, (2011) MOPC030

ISBN: 978-3-95450-188-5 doi:10.18429/JACoW-MEDSI2016-TUPE40

CRYO-READY UNDULATOR U15: PASSING SOLEIL'S 2 METER THRESHOLD IN USEFUL MAGNETIC LENGTH

M. Tilmont, F. Briquez, N. Bechu, L. Chapuis, K. Tavakoli, C. De Oliviera, J. P. Duval, M. Sebdaoui, M.E. Couprie, J.L. Marlats, J.M. Dubuisson, C. Herbeaux, A. Lestrade
Synchrotron SOLEIL, Saint-Aubin, France

Abstract

The U15 is an in-vacuumundulator designed to operate at room temperature and at 70K. It is the first in-vacuum undulator designed, assembled and which will be used in SOLEIL's storage ring that have support beams for magnets longer than 2 meters.A clear gap is felt in the technologies used for manufacturing and assembling compared to our standard 2m length in-vacuum undulators. This is due, in part, to the tolerances imposed by the maximum phase error admissible in SOLEIL's storage ring. The poster will shine lights on those difficulties from a design and manufacturing point of view.

INTRODUCTION

The SOLEIL Synchrotron is in operation since May 2006. 18 of its beamlines use undulators as sources. The first undulators were electromagnet-built (such as HU 640[1]) and Apple-IIs followed since a few years by in-vaccum (cryogenic or not) undulators.

The U15 undulator will be first used in the frame of the LUNEX5 (free electron Laser Using a New accelerator for the Exploitation of X-ray radiation of 5th generation) project of advanced and compact Free Electron Laser (FEL). It will be used for a test experiment of FEL with a laser wakefield accelerator under preparation in the frame of the COXINEL ERC Advanced Grant project[2]. It has been designed as the longest possible magnetic field that can be used for this experiment: 3 meters.

In the design and building phases of the U15, there was a clear threshold that complicated nearly every step of the project compared to the U18s even if the basis of both instruments are very close to one another.

CONTEXT

The in-vaccum in used at the moment are U20s, functioning at room temperature and one cryogenic U18 (a second one is being built). Both are two meters long (with a magnetic period of 20 and 18 mm respectively). The Apple-IIs are typically 2m long when electromagnet-based undulator can reach 6 meters. In the past, HU640 was so long and heavy, that it has been partially reassembled directly in SOLEIL storage ring. This process is not compatible with in-vaccumundulators considering the level of cleanliness required for a storage ring.

The phase error disturbs the electron dynamics in the storage ring, and causes a reduction in the intensity of synchrotronradiation in an undulator as well as impacting the lifetime of the electron beam. In a facility of SOLEIL's size, the beam is very sensitive to the phase error compared to larger storage rings. The definition of the magnetic fields in each undulator (as well as any potentially magnetic instrument affecting the beam) is critical in its impact on the electron beamline.

CHARACTERISTICS OF THE UNDULATOR

- The magnetic useful length of the undulator being 3 meters, its overall length has been designed as 3,4 meters. Its height (2,2m) and depth (1,52m) are closer to U18s and U20s
- It is designed to functions both at room temperature and 70K. The compatibility for both temperatures is a difficulty in itself: the difference in temperature between max and min imply a 12mm shortening of the in-vacuum beams.
- The magnetic forces between the beams are of 10 tonnesfor a 2,6mm gap. The undulator will serve to test the effects of tapering on the electron beam.

PRE-DESIGN AND BUDGETING PHASE

The study of the buildings where the undulator will transit and will be assembled before starting the design is crucial. The most significative element that can be examined beforehand is the assembly of the vessel: adding 1meter to the magnetic length of the undulator adds 2meter at the minimum to the length needed during this stage.

Study of the existing assembly process is then a point to investigate. The beams supporting the magnets are made of aluminium in our IVUs and are light enough to be handled by hand by only two persons. Investigating the efforts needed during manutention and calculating the impacts of adding 50% of length shows that the handling is not possible at all without lifting tools.Are those lifting tools available near the assembly space? Are those lifting tools as long as needed for the new design?

When investigating this second point for example, we saw that our tools and buildings restrained the positions possible for the assembly process to only two options. One of theserequiresto move and recalibrate several instruments in the assembly hall. These questions have several effects on the final budget and the manpower needed for the project and may impact the decision of starting the design or greatly change the time table of the project.

Content from this work may be used under the terms of the CC BY 3.0 licence (© 2016). Any distribution of this work must maintain attribution to the author(s), title of the work, publisher, and DOI.

ISBN: 978-3-95450-188-5 doi:10.18429/JACoW-MEDSI2016-TUPE40

Content from this work may be used under the terms of the CC BY 3.0 licence (© 2016). Any distribution of this work must maintain attribution to the author(s), title of the work, publisher, and DOI.

Finally, it is important to study the industrial partners of the lab. When changing one parameter, you can eliminate an experiencedpartner and have to rely only on companies more expensive than first expected. The Western-European industrial network seems to be separated between the companies that use mills and turning mills up to 2.5mx2.5m milling capacity and the companies that use machines with a capacity of 6m to 12m. It is difficult to find companies in between and to evaluate their level of expertise if you do not already work with them.

The second parameter that separate these companies are the markets which they target. Bigger capacities companies often work for big budget clients and are not interested in the risks they would have to take to comply with our demands. Those that do understand our needs, usually work in the nuclear field of expertise and have very high structural costs.

These two parameters hugely impact the budget. The next table will show our experience. The price for 50% longer beams is not 50% higher. This one example can be used several times in the design portion of the project.

DESIGN PHASE

Augmenting the length DOES NOT augments linearly other parameters. We decided early in the pre designing phase to not take anything for granted even if the base of the U18s and U20s is strong and efficient.

Firstly, more precision is needed to keep a low phase error on a longer distance which demanded a new module designand more a controlled assembly process. The final characteristics needed for the U15 brought us into the micro-mechanic field. When it was possible to differentiate the standard modules and the modules that would fix sensors and probes on a 2m beam, it is no longer the case for a longer beam that cannot be machined as precisely, and thus, that needs more precisely tuned modules on the entirety of the useful magnetic length.

The second point is that assembling 200 modules is way more than twice easier than assembling 400. Even with a final precision being the same in both cases. Labs are rarely equipped for chain work and the precision of assembly will decline during the time needed to assemble all modules without the help of tools during the whole process.

Lastly, as seen before, tools and process are to be rethought (or reevaluated) when the proper design is at an advanced stage. Longer beams augment the maximum deformation even with the same value of linear efforts. For instance, the tool used to attach the two magnetic beams together for the assembly in the vessel had to be redesigned to avoid contact between the two rows of magnets.

REFERENCES

[1] Marcouillé, O ;Brunelle, P ; Chubar, O ; Marteau, F ; Massal, M ; Nahon, L ; Tavakoli, K ; Vétéran, J ; Filhol, J M " Design, Construction and Magnetic Measurements of the HU640 (OPHELIE2) Undulator dedicated to the DESIRS VUV Beamline at SOLEIL", *in Proc. 9th International Conference On Synchrotron Radiation Instrumentation, Daegu, Korea, 28 May - 2 Jun 2006, pp.311-314, https://cds.cern.ch/record/1066737?ln=fr*

[2] M.-E. Couprie, C. Benabderrahmane, P. Berteaud, S. Bielawski, C. Bourassin-Bouchet, F. Bouvet, et al., "Advances on the LUNEX5 and COXINEL Projects", *in Proc. 37th International Free Electron Laser Conference(FEL2015*, Daejeon, Republic of Korea, August 2015,paper WEP078, pp. 730–734, ISBN: 978-3-95450-134-2,http://accelconf.web.cern.ch/AccelConf/FEL2015/papers/wep078.pdf, doi:10.18429/JACoW-FEL2015-WEP078, 2015

Table 1: Relative Prices For Similar Beams

Company	2m beams (mean price for 2 projects – 2014 and 2015)	3m beams (Price for 1 project – 2016)
1	98	154
2	52	Machine capacity to small
3	100	195
base 100 for the highest price offered in 2015		

ISBN: 978-3-95450-188-5 doi:10.18429/JACoW-MEDSI2016-TUPE41

DESIGN AND DEVELOPMENT OF A SYSTEM OF HYBRID TYPE TO MEASURE THE MAGNETIC FIELD OF A CRYOGENIC UNDULATOR

Cheng-Hsing Chang†, C. K. Yang, S. D. Chen, J. C. Huang, C. S. Hwang
National Synchrotron Radiation Research Center, Hsinchu Science Park, Hsinchu 30076, Taiwan

Abstract

Cryogenic permanent-magnet undulators (CU) have currently become the most important scheme serving as sources of hard X-rays in medium-energy facilities worldwide. One such set (length 2 m, period length 15 mm) is under development for Taiwan Photon Source (TPS). To obtain a magnetic-field distribution of the cryogenic undulator after it is cooled to an operating target temperature below 80 K, a device of hybrid type combining a Hall probe and stretched-wire method has been designed and developed, to perform the field measurement at low temperature and in an ultra-high vacuum environment. The Hall probe is used to measure the field on axis in the transverse and vertical directions; the stretched wire is utilized to measure the field integral in the vertical and horizontal directions in the horizontal plane. Unlike a conventional field-measurement system in air, this innovative system must be located in an ultra-high vacuum environment with limited clearance. This paper describes mainly the entire system, including kernel components, control systems and preliminary test results in detail.

INTRODUCTION

To obtain great brilliance within the hard X-ray region from an accelerator facility of medium beam energy, approximately 3 GeV, an approach with a cryogenic permanent-magnet undulator (CU) places magnet arrays of short period inside a vacuum chamber [1], which enhances the peak magnetic field strength around 20% compared with an in-vacuum undulator (IU). The deflection parameter (K) is thus kept consistent with an undulator of type out of vacuum. After the entire machine was assembled with the vacuum chamber, the scheme resulted in a difficulty of taking data through a conventional device for field measurement. Many solutions have thus been proposed to solve this problem: BNL designed a customized rectangular vacuum chamber or rectangular port of which one side can be used for access [2, 3]; ESRF adopted a specific dedicated chamber for field measurement [4]; SPring8 has a SAFALI system, and so on [5, 6]. Considering not taking off the main vacuum chamber and using standard vacuum components, NSRRC developed a set of field-measurement system in situ for an undulator in vacuum. It was applied to verify the magnetic field on axis of several undulators in vacuum, but had facilitated only an atmospheric environment [7]. To fulfill a further requirement for the measurement of a cryogenic permanent-magnet undulator in the near future, the device must be able to accommodate to an ultra-high vacuum surrounding without contamination and interference. This paper presents the current efforts of a new design and development of a CU field-measurement system.

† cschang@nsrrc.org.tw

SYSTEM REQUIREMENTS

To characterize the magnetic performance of CU15 in operating conditions at low temperature, the field-measurement devices must be placed in a narrow clearance space of the ultra-high vacuum environment around a vacuum chamber, magnet array and a nearby cooling system. Adjacent components in the vicinity of the magnets and the field-measurement device must neither interfere with each other nor perturb the signal source. As stated above, a compact design is a crucial and essential element of the system development. The movement requirements of the measurement system are listed in Table 1. To avoid an accidental collision due to loss of control resulting in component damage or system failure, interlock protection devices must also be taken into account.

Table 1: Movement Requirements of Each Method

Method	Stretch Wire	Hall Probe
Stroke range		
Vertical	±1 mm	±5 mm
Transverse	±22 mm	±1 mm
Longitudinal	-	2.4 m
Scanning Speed	10 mm/s	3 mm/s

System Composition - Hardware

Figure 1 displays the overall construction of the system to measure a magnetic field. The free space between vacuum chambers is used to accommodate the measured undulator. According to the functions of the system, the field-measurement equipment of hybrid type can be divided into two portions, a Hall probe and a stretched wire.

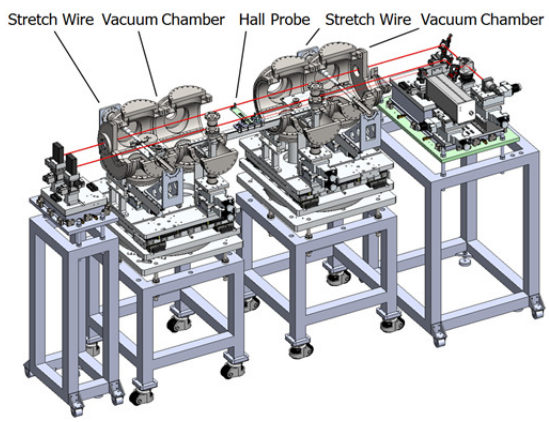


Figure 1: Overview of the measurement system.

Content from this work may be used under the terms of the CC BY 3.0 licence (© 2016). Any distribution of this work must maintain attribution to the author(s), title of the work, publisher, and DOI.

ISBN: 978-3-95450-188-5 doi:10.18429/JACoW-MEDSI2016-TUPE41

Content from this work may be used under the terms of the CC BY 3.0 licence (© 2016). Any distribution of this work must maintain attribution to the author(s), title of the work, publisher, and DOI.

Hall-probe field-measurement equipment The carriage of the optical components and the Hall probe is dragged with a circulating loop of stainless-steel wire and driven with a rotary stepping motor. The rotational motion of the stepping motor is transferred from air into the vacuum with a magnetic rotary feed-through. During the sliding actuation, the carriage is guided with a Y-shaped rail and moves in the longitudinal direction. Figure 2 shows that the configuration arrangement of the wheels of the carriage is distributed to fit three surfaces -- the upper side and both inclined sides of the Y-shaped rail. One inclined side of the wheel assembly is equipped with a flat spring; its purpose is to constrain the freedom of the carriage in the vertical and transverse directions, but it could also prevent the carriage from skipping due to wire dragging. To obtain a highly accurate position of the probe sensor within a long travel stroke, a He-Ne laser scale (Agilent 5517C laser head, beam splitter, corner-cube reflector and photon detector, resolution 0.01 μm) is built in; the reflector is mounted on the carriage inside the vacuum chamber.

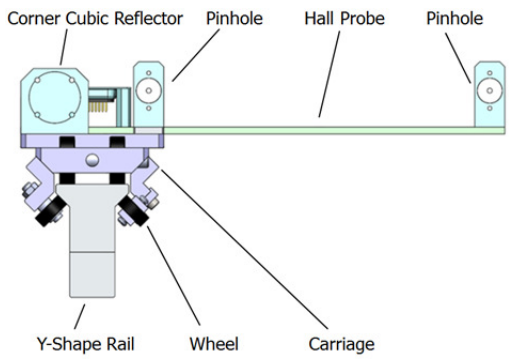


Figure 2: Hall probe carrier.

Because of an excessive slenderness ratio of the geometric profile of the guiding rail, fabrication with high precision of this part was difficult. Moreover, considering the self-weight of the rail and only two or three supporting locations for the rail (length 2.5 m) and carriage, deformation of the rail will result in wander from its course during a field measurement. To diminish the deviation and to improve the centering accuracy in both vertical (Y) and transverse (X) directions, a position-measurement technique would be introduced to monitor the extent off-axis of the probe sensor and to correct the error in real time. A solid-state laser spot of light becomes expanded to a beam of diameter 3 mm with a beam expander before the light travels to a beam splitter. Of the light intensity, half would be directly reflected toward the pinhole near the rail; the other half would penetrate the beam splitter to the next reflector and thus be reflected to the pinhole far from the rail. These two pinholes are mounted on both sides of the probe sensor, as shown in Fig. 2. The position of the Hall probe sensor is related to the distribution configuration of these pinholes. After the light travels to the pinhole, a portion of the light becomes intercepted by the pinhole; the residual light would be allowed to pass through the pinhole (1.5 mm). The actual bi-directional position of the holes of the pinhole is altered on following the carriage moving along the guiding rail. Two beams of penetrating light would eventually be received by two sets of quadrant detectors settled on two axes of a moving stage individually; the real position coordinate of the probe sensor could be determined immediately. Furthermore, it could simultaneously be used to compensate for the deviation through each of two axes of the moving stage to support the rail located at both ends and, or, the middle position.

To solve the storage of the signal wire and for usage in a vacuum condition with no influence on the accuracy of the carriage movement, the method of a reel drum that deploys a constant torque spring is proposed. One end of the signal cable is fixed on the carriage and connected to sensors; the other end is stored on winding around the reel drum. During a field measurement, the signal wire accompanying a restoring force would be smoothly relaxed or retracted through the mechanism of the reel drum.

Stretched-wire field-measurement equipment A Litz wire made on twisting eight wires and a series connection of all taking advantage of increasing the ratio of signal to noise would be adopted to measure the integral field measurement. The cable passes a horizontal central plane across a pair of magnet arrays and is then fixed on the cable fixture at both ends. The pre-tension mechanism of the cable shown in Fig. 3 is proved to tighten the cable and to decrease the sag of the cable to lessen systematic deviation. The cable scanning within a desired range in vertical and horizontal directions must be performed with both ends of the two axes of the moving stage.

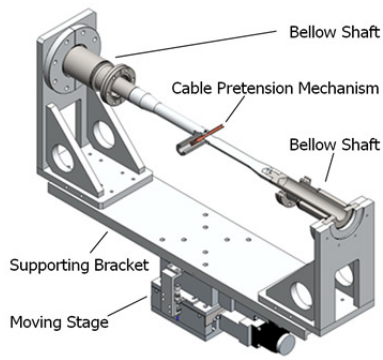


Figure 3: Section view of stretched-wire mechanism.

Control and Data Acquisition System

Figure 4 shows an architectural diagram of the entire control and data acquisition system. The laser scale generates “A quad B” signals. The controller (Galil) uses these signals to determine the longitudinal positions of the Hall probe and triggers a voltmeter at particular intervals. As the core of the control system, a computer monitors the x-y positions of the Hall probe through two quad-cell PSD and corrects them with two rail-supported x-y stages. It also controls the movements of the x-y stages of the stretched-wire movement and the Hall probe rotary stepping motor. After measurement, this computer reads data of a voltmeter and a digital integrator and plots the measurement results.

ISBN: 978-3-95450-188-5 doi:10.18429/JACoW-MEDSI2016-TUPE41

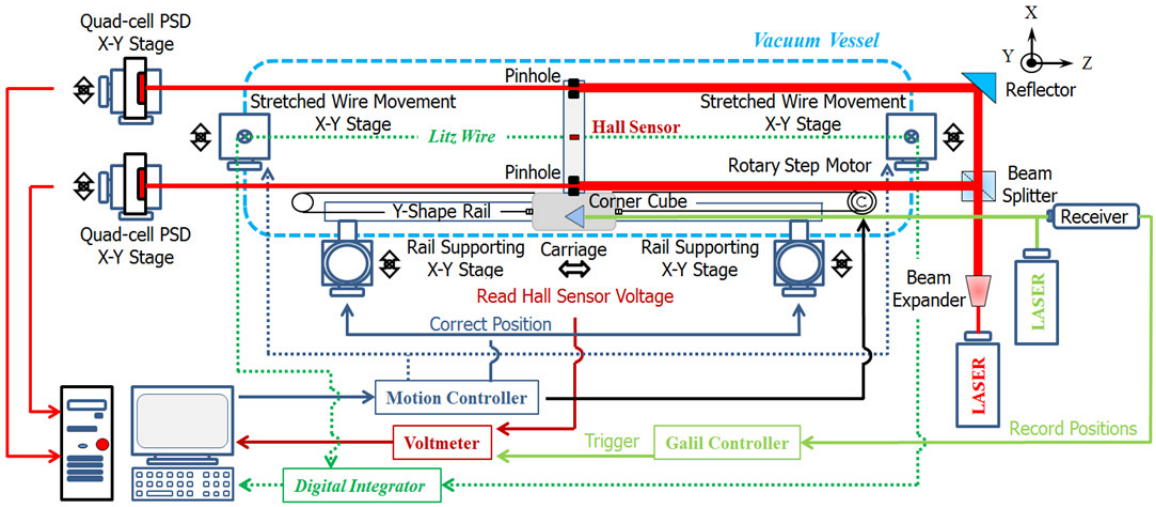


Figure 4: Diagram of the control and data acquisition system.

VERIFICATION OF RESULTS

To verify the function and performance of the system under the vacuum-sealed condition at 10^{-4} Pa, a couple of magnet arrays (length 0.2 m) of period length 22 mm and a gap fixed at 7 mm would be dedicated to testing, as shown in Fig. 5. Figure 6 shows that the reproducibility of Hall probe system is better than 0.2° in RMS phase error, which indicates that this system is reliable to examine an undulator in a vacuum environment.

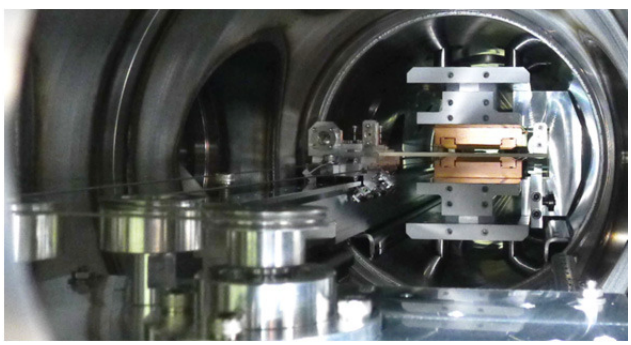


Figure 5: Magnetic-field measurement of IU22 with 0.2 m long.

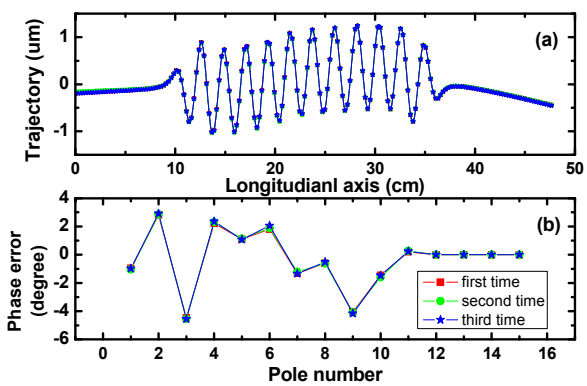


Figure 6: Result of measurement of the magnetic field.

CONCLUSION

The design of a system of hybrid type to measure the magnetic field of a cryogenic permanent-magnet undulator is proposed. The fabrication of Hall-probe components has been accomplished; some significant experiments of the system have been performed at room temperature and in a vacuum environment. The test results confirm that the engineering architecture enables collection of information about the magnetic field. Calibration of the Hall probe at varied temperature and testing of the reliability at cryogenic temperature are required. The stretched-wire parts are under fabrication and will also be tested.

REFERENCES

[1] T. Hara *et al.*, "Cryogenic permanent magnet undulators," *Phys. Rev. ST Accel. Beams*, vol. 7, p. 050702, 2004.

[2] James Rank, D. Harder, G. Rakowsky, and T. Tanabe, "Design concept for a modular in-vacuum undulator Hall probe mapper for use with CPMU convertible in-vacuum undulators of varying magnetic length", in *Proc. 2011 Particle Accelerator Conf.*, New York, NY, USA, paper THP218, pp. 2534-2536.

[3] Jih-Perng Hu, Conrad L. Foerster, John R. Skaritka, and David Waterman, "Novel chamber design of an in-vacuum cryo-cooler mini-gap undulator", in *4th Int. Workshop on MEDSI,* Egret Himeji, Japan, 2006.

[4] J. Chavanne *et al.,* "Construction of a cryogenic permanent magnet undulator at the ESRF," in *Proc. of EPAC08*, Genoa, Italy, paper WEPC105, pp. 2243-2245.

[5] T. Tanaka *et al.*, "In situ correction of field errors induced by temperature gradient in cryogenic undulators," *Phys. Rev. ST Accel. Beams*, vol. 12, p. 120702, 2009.

[6] T. Tanaka, T. Seike, and H. Kitamura, "Measurement of SPring-8 XFEL undulator prototype with the SAFALI system," in *Proc. 30th Int. Free-Electron Laser Conf. (FEL'08)*, Gyeongju, Korea, paper TUPPH053, pp. 371-373.

[7] C. K. Yang *et al.*, "A measurement system in situ to measure the magnetic field of an in-vacuum undulator," *IEEE Trans. Appl. Supercond.*, vol. 24, issue 3, p. 9001205, 2014.

Content from this work may be used under the terms of the CC BY 3.0 licence (© 2016). Any distribution of this work must maintain attribution to the author(s), title of the work, publisher, and DOI.

ISBN: 978-3-95450-188-5 doi:10.18429/JACoW-MEDSI2016-TUPE44

OPTIMIZATION FOR THE APS-U MAGNET SUPPORT STRUCTURE *

Zunping Liu †, Jeremy Nudell, Curt Preissner, Jeff Collins, and Herman Cease
Advance Photon Source, Argonne National Laboratory, Argonne, IL 60439, USA

Abstract

The Advanced Photon Source Upgrade (APS-U) is to replace the existing storage ring with a multi-bend achromat (MBA) accelerator lattice [1]. For the APS-U removal and installation, current planning calls for a 12-month shutdown and testing period, prior to resumption of operations. It calls for quick installation of the magnet support system within assembly and installation alignment tolerances. A three-point semi-kinematic vertical mount for the magnet modules is the approach to reduce time for alignment. The longest section is the curved Focusing-Defocusing (FODO) section (four quads with three Q-bends interleaved, and a three-pole wiggler). All magnets of the FODO module sit on a single piece of support structure in order to have good control over the magnet-to-magnet alignment tolerance. It brings challenge to minimize the top surface deflection and maximize the first mode frequency of the magnet support structure that is supported at three points. These constraints require optimizing the magnet support structures. Details of the optimization, including three-point positioning, material selection, and topology optimization, are reported in this study.

INTRODUCTION

Optimization is subjected to constraints. For example, the APS-U removal and installation is planned for a 12-month shutdown and testing period prior to resumption of operations, and the assembly and installation alignment tolerance is specified as 100 microns RMS for girder-to-girder alignment [1]. To meet such specifications within a one-year period, a three-point semi-kinematic vertical mount for the magnet modules is considered as the best approach, in comparison with four-point and/or non-kinematic vertical mount. The conceptual design is based on the three-point semi-kinematic vertical mount, and the goal of optimization is to meet the technique specifications.

The APS-U specifies 9 nm RMS as magnet-to-magnet vibration tolerance and 30 microns RMS as magnet-to-magnet static tolerance within a girder [1], a common term for the magnet support structure. Spacing of the three-point support can be optimized, which helps to minimize the magnet-to-magnet static tolerance due to surface deflection of the support structure. The vibration tolerance is related to the ground vibration spectrum. The floor vibration spectrum in the APS storage ring has 1 nm absolute value at 50 Hz [2,3]. It indicates that the first mode frequency around 50 Hz of an assembled module is guaranteed to meet the magnet-to-magnet vibration tolerance. It leads to a goal, 50 Hz as the lower bound of mode frequency, for optimization. A parametric study of girder height is performed during optimization.

For conceptual design and optimization, topology optimization is an ideal tool. It allows selecting the best elements in a given design space that maximizes the use of material. Research on numerical topology optimization started three decades ago [4] and Genesis® incorporated the discipline nearly two decades ago [5]. It's available for statics, eigenvalue, buckling, frequency response and random response load cases. Among a bunch number of commercially available topology optimization software, the Genesis Topology for Ansys Mechancial (GTAM) [6] is utilized in this study. Two major constraints, minimizing strain energy and maximizing frequency response, are applied during the optimization process.

For a given structure, material of higher elastic modulus produces a higher natural frequency. Fabrication capacity by vendors constrains in material selection because of the structure size and complexity. Fabrication constraints are available in GTAM but not applied for the conceptual design and optimization. A cast iron design was chosen because of its design flexibility, low cost, and favorable vibration damping properties.

The FODO girder, the longest of the APS-U girders at approximating 5.6 meters long, is studied as a representative. All magnets of a FODO module sits on the girder, a single piece of support structure. The girder is then supported on a concrete plinth through a three-point semi-kinematic mount together with horizontal pushers. The plinth sits on a nominal 1-inch thick epoxy grout on floor. The pushers are ignored during optimization. This study focuses on the girder.

SPACING OPTIMIZATION OF VERTICAL SUPPORTS

The FODO girder has a top surface 5.568-meter long and 1.1-meter wide. As an initial step of the conceptual design, a 160mm thick plate is assumed as the girder. Because the length-to-width ratio is as large as 5 times, the three points are arranged with one point at center and the other two symmetrically toward two ends along the long side, as shown in Fig.1. The point at the center along the long side is set at one end along the short side and the other two points at the other end. The support span along the short side is maximized, which is preferred from the point view of stability and the rolling mode of vibration. In such a scheme, the spacing optimization is to find an optimized span between the two symmetrically arranged points along the long side. In the calculation the structure is supported by three bars, each 100mm in diameter and 200mm long. Figure 1 shows the total displacement when the span is set at 4 meters. When the span varies, the maximum value of

* Work supported by the U.S. Department of Energy, Office of Science, under Contract No. DE-AC02-06CH11357
† zpliu@anl.gov

Content from this work may be used under the terms of the CC BY 3.0 licence (© 2016). Any distribution of this work must maintain attribution to the author(s), title of the work, publisher, and DOI.

ISBN: 978-3-95450-188-5 doi:10.18429/JACoW-MEDSI2016-TUPE44

the displacements at the top and bottom surfaces changes as shown in Fig.2. The displacement along the vertical direction is at the nanometer level. Horizontal displacements make major contributions to the total displacement. When the span is 4 or 2.6 meters, the minimum values of displacement occur.

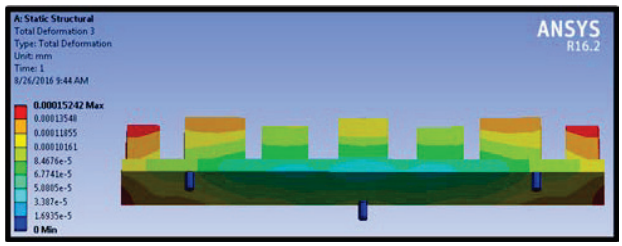


Figure 1: Deformation of girder supported by three bars.

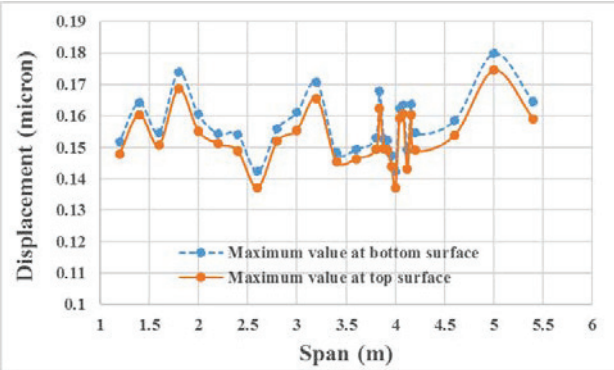


Figure 2: Maximum value of displacement at top and bottom surfaces of FODO girder.

1ST TOPOLOGY OPTIMIZATION

Topology optimization of the girder used software GTAM and ANSYS. The low bound of the 1st mode frequency is set to 60Hz. Minimizing the strain energy is another goal. The latter ensures that the static deflection along the beam path is minimized. The optimized geometry is then analyzed as a structure with the static structure and modal modules of ANSYS Workshop.

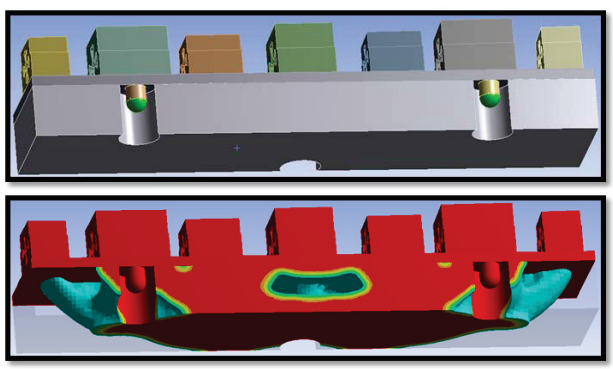


Figure 3: Topology optimization. Top, initial geometry seed. Bottom, optimized geometry.

Figure 3 shows the seed geometry used as an input (top) and the optimized one (bottom). The girder is assumed as a cast iron block of 5.568 m long and 1.1 m wide. Its height varies and is split into two parts. The top plate is excluded from topology optimization, but its thickness varies from 20 mm to 100 mm as part of the parametric study. The bottom part is the region for topology optimization, and its thickness varies from zero to 800mm also as part of the parametric study. Three vertical supports are simulated as ball-in-socket joints, allowing each socket freely rotating on a fixed ball. The vertical support has a diameter 200mm. The span is chosen as 3.5m with a smaller value preferred.

The parametric study showed that a top plate thickness of 50 mm gives the maximum value of the 1st mode frequency when the total thickness of girder is 850 mm. Figure 4 shows the corresponding static deflections due to gravity before and after topology optimization. The dots are in-plane deflection of points along the beam path. The dashed line is a best-fit of deflection before topology optimization, while the solid line is a best fit of deflection after optimization. A figure of error is derived from the deviation from the best fit line. The maximum figure of error decreases from 10 to 2 microns after optimization in this calculation.

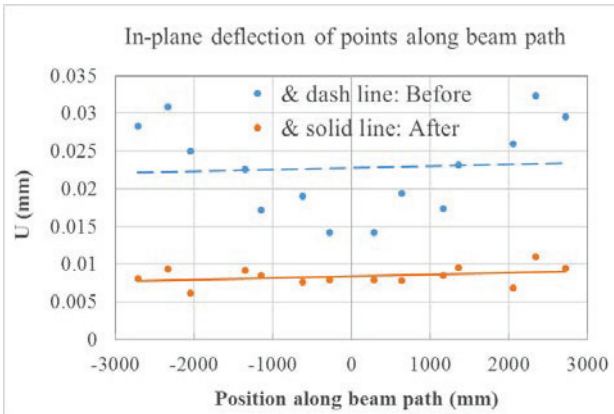


Figure 4: Static deflection before and after topology optimization

Figure 5 shows trends of the 1st mode frequency and the maximum figure of error when girder thickness increases and the top part of the girder stays at 50 mm thick. The 1st mode frequency increases monotonically before the girder thickness reaches 700mm. The trend is the same for both seed and optimized geometries. The maximum figure of error drops for seed geometry when its thickness increases. While for optimized geometry the decrease stops at a thickness of 600mm and stays at about 6.6 microns. When the girder thickness increases from 600 to 700 mm, the 1st mode frequency increases from 50.5 to 52.6 Hz, and the girder volume increases from 2.13 to 2.27 m^3. Less weight of the girder and more space for the plinth are preferred so that a girder thickness of 600 mm was chosen for preliminary design. As a result, contacts of the vertical support and girder are in a plane near the center of mass of magnets and girder assembly. This reduces the moment of inertia of the girder system.

Content from this work may be used under the terms of the CC BY 3.0 licence (© 2016). Any distribution of this work must maintain attribution to the author(s), title of the work, publisher, and DOI.

ISBN: 978-3-95450-188-5 doi:10.18429/JACoW-MEDSI2016-TUPE44

Content from this work may be used under the terms of the CC BY 3.0 licence (© 2016). Any distribution of this work must maintain attribution to the author(s), title of the work, publisher, and DOI.

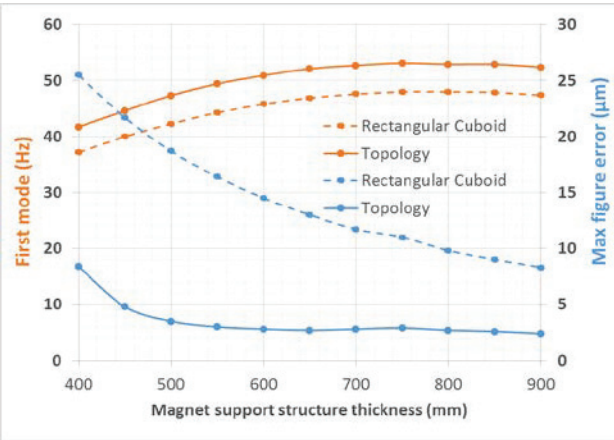


Figure 5: Max figure of error and the 1st mode frequency vs. girder thickness.

2ND TOPOLOGY OPTIMIZATION

The preliminary design of the girder is based on the optimized girder thickness of 600mm thick. The FODO module is shown in Fig.6, and the assembled FODO prototype module can be found in [2]. The span of vertical supports is changed to 3 m long. The thickness of top part of the girder is changed to 150 mm, and the contact surface of vertical support is 200 mm underneath the girder top surface. The girder material is ductile cast iron, A536, GR-60/40/18. The three-point vertical mount is realized with Airloc 414-KSKC wedge jacks. The maximum figure of error is 14 microns and the 1st mode frequency is 39 Hz [2]. The preliminary prototype is under test.

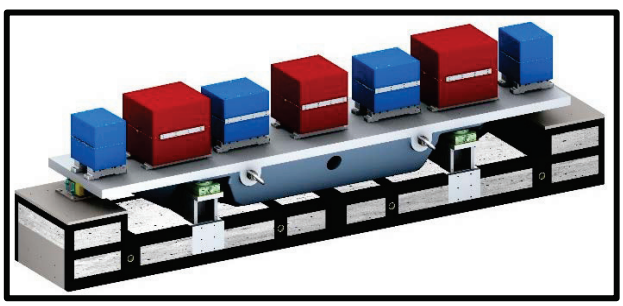


Figure 6: FODO module of preliminary design.

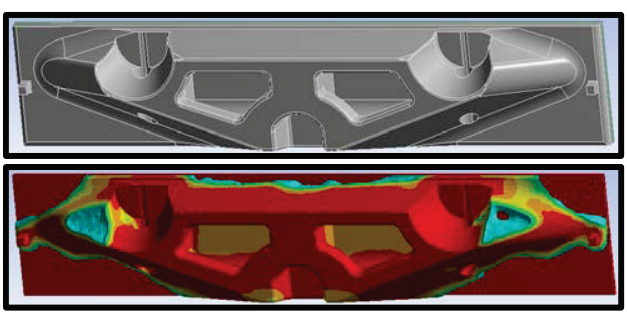


Figure 7: FODO girder 2ND topology optimization. Top, preliminary design as seed. Bottom, optimized geometry.

In case that the current prototype does not meet the specifications during test, the girder geometry is fed back into the model for further optimization. The stiffness of the Airloc 414-KSKC wedge jack is applied in this calculation. The resultant girder geometry is shown in Fig.7. The volume decreases from 1.83 m^3 to 1.57 m^3. This optimized geometry is not realized yet.

CONCLUSION

Structure optimization plays an important role in the conceptual design phase. It leads to the right direction for preliminary design in terms of mass reduction and sound performance. By using the FODO girder, the longest of the APS-U girders, as a representative, structure optimization gives an optimized structure in two steps. It first leads to the optimized spacing range for the three-point semi-kinematic vertical support. Static structure analysis is applied in this step. In the second step topology optimization is applied for a parametric study with goal of minimizing strain energy and maximizing the mode frequency response of the girder. It then leads to the optimized girder thickness and geometry. The material utilization is maximized in preliminary design of the girder, which meets the design specifications of 9 nm RMS as magnet-to-magnet vibration tolerance and 30 microns RMS as magnet-to-magnet static tolerance within a girder.

ACKNOWLEDGEMENT

Thank you to Patrick Den Hartog (leader of the Mechanical Engineering and Design group in the APS) for his help in editing this paper.

REFERENCES

[1] G. Decker, "Design Study of an MBA Lattice for the Advanced Photon Source," *Synchrotron Radiation News*, 27:6, 13-17, 2014, DOI: 10.1080/08940886.2014.970932.

[2] J. Nudell *et al.*, "Preliminary Design and Analysis of the FODO Module Support System for the APS-U Accelerator," in *Proceedings of MEDSI 2016*, 11~16 SEPT, 2016, Barcelona, Spain.

[3] C. Preissner *et al.*, "Nostradamus and the Synchrotron Engineer: Key Aspects of Predicting Accelerator Structural Response," in *Proceedings of MEDSI 2016*, 11~16 SEPT, 2016, Barcelona, Spain.

[4] M.P. Bendsoe and N. Kikuchi, "Generating Optimal Topologies in Structural Design Using a Homogenization Method," Comp. Meth. Appl. Mech. Eng., Vol.71, 1988, pp.197-224.

[5] J.P. Leiva and et al., "Modern Structural Optimization Concepts Applied to Topology Optimization," Proceedings of the 40th AIAA/ASME/ASCE/AHS/ASC Structures, Structural Dynamics, and Material Conference. St. Louis, MO, April 12-15, 1999, pp.1589-1596.

[6] http://www.vrand.com/GTAM.html

ISBN: 978-3-95450-188-5 doi:10.18429/JACoW-MEDSI2016-WEAA02

X-RAY ABSORBER DESIGN AND CALCULATIONS FOR THE EBS STORAGE RING

F. Thomas[1], J.C. Biasci, D. Coulon, Y. Dabin, T. Ducoing, F. Ewald, E. Gagliardini, P. Marion
European Synchrotron Radiation Facility (ESRF), Grenoble, France
[1] also at Institut Laue-Langevin (ILL), Grenoble, France

Abstract

The Extremely Brilliant Source (EBS) of the ESRF will hold new type of X-Ray absorbers: a new material will be used (CuCr1Zr suggested by [1]) together with a novel design integrating:

- Conflat (CF) flange machined in the absorber body. No weld, no braze.
- Optimized toothed surface profile, reducing the induced thermal stresses.
- Fluorescence Compton and Rayleigh scattering integrated blocking shapes.
- Concentric cooling channels.

A brief overview of the new design and concepts for toothed absorbers will be given.

The presentation will then focus on thermal-mechanical absorber calculations, combining both Computational Fluid Mechanics (CFD) and Finite Elements Analysis (FEA). The calculations were made using the ANSYS packages [2, 3].

The calculations and calculation process will be discussed as well as the design criteria chosen by the team.

The CFD calculations will show that an effective heat transfer coefficient between the water and the copper part can be estimated for concentric cooling channels as well as the pressure drop through the absorber.

Finally, the stress analysis will be emphasized. The type of stresses (tensile, compressive or shear) and their nature (primary or secondary) will be linked to the choice of design criteria.

INTRODUCTION

The ESRF took the strategic decision to make most if not all the X-Ray absorbers of the new EBS storage ring in CuCr1Zr copper alloy instead of classical Cu OFE [4] or Glidcop® AL-15 [5]. In order to reduce the risk of using a new material, we designed absorbers in a way that they work always in the purely elastic regime.

The first paragraph will be a brief overview of the new design and concepts used for toothed absorbers – machined CF flange, toothed scattering blocking shape and concentric cooling channels.

In the second paragraph, we will discuss the CFD model used to determine an effective heat transfer coefficient of 15 kW/m^2/K per cooling channel for a flow rate of 4.24 l/min together with an estimated pressure drop of $\Delta p \sim$ 0.3 bar.

The third paragraph will show thermal and mechanical calculation results of one of the new absorbers: the 2 cooling channels, single jaw, ABS-CH9-1-2 horizontal absorber. The stress analysis will be detailed and linked to stress design criteria.

BRIEF OVERVIEW

In the EBS, the toothed absorbers will have to absorb normal power incident densities up to 110 W/mm^2. In order to spread out the heat load on larger surfaces, one can make triangular toothed surfaces, reducing the power density by $\sin(\beta).\tan(\alpha)$, 2β being the top angle of the triangular tooth and α the tilt angle of the teeth base relative to the beam, i.e. the grazing angle if they were no teeth – see fig. 1. In our case, optimization between large spreading surfaces, implementation in the vacuum chamber, standardization and machinability leads to a 2β angle of 45° and an α angle around 10° (absorber dependent due to geometrical constraints), reducing the power density deposited by ~ 90-95% (theoretically).

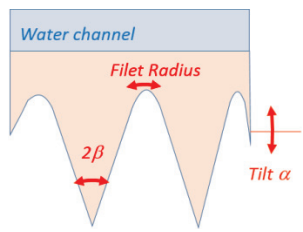


Figure 1: Relevant parameters for an absorber's jaw

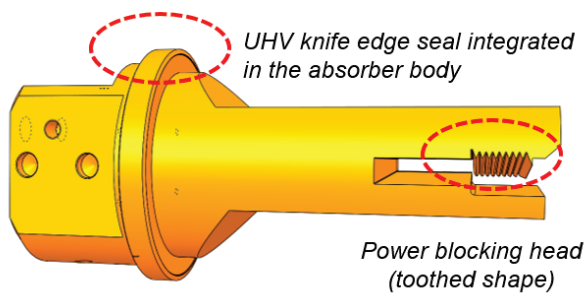


Figure 2: Toothed horizontal absorber overview

Figure 2 emphasizes the innovating design choices made for the EBS absorbers: CF knife edge machined in the absorber body, single jaw absorbers with a longer tooth at the right end of the jaw.

We made the calculations assuming that the angular misalignment was 1.5°, 0.5° from the angular divergence of the X-ray beam and keeping 1° safety margin.

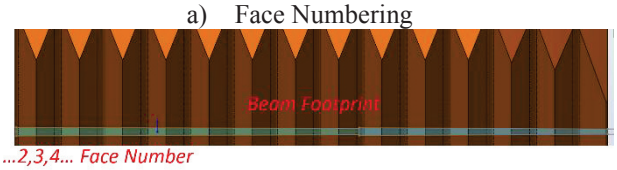
Content from this work may be used under the terms of the CC BY 3.0 licence (© 2016). Any distribution of this work must maintain attribution to the author(s), title of the work, publisher, and DOI.

ISBN: 978-3-95450-188-5 doi:10.18429/JACoW-MEDSI2016-WEAA02

Content from this work may be used under the terms of the CC BY 3.0 licence (© 2016). Any distribution of this work must maintain attribution to the author(s), title of the work, publisher, and DOI.

A majority of the absorber's calculations were made 3 times with the beam centered on the jaw and with a beam offset by ± 2 mm in height. Shifting the beam by ± 2 mm is a second order modification compared to rotating the absorber by 1.5°.

a) Face Numbering



b) Heat Load

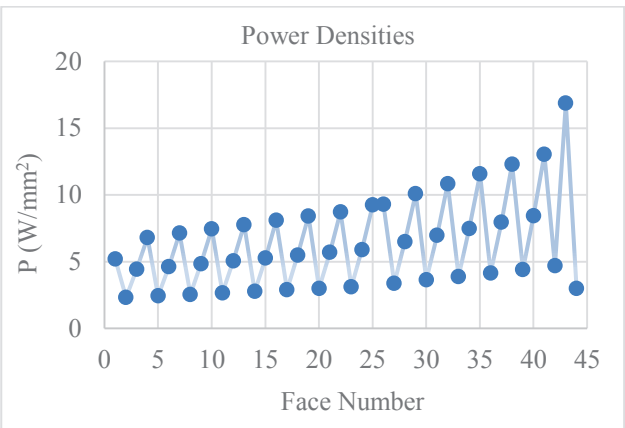


Figure 3: Heat load per face ABS-CH9-2-2

Figure 3 shows surface numbering (a) and heat load per face (b) for one of the toothed absorber: ABS-CH9-2-2, the vertical absorber of the vacuum chamber 9. Faces 1,4,7...38,41 are 0.32 mm in radius connecting filets between the teeth, the other faces being the teeth faces: 2,5,8… are the left faces viewed by the beam and 3,6,9… the right faces. The 1.5° misalignment induces large left right asymmetry (a factor of 2) in the heat load between the 2 faces of each tooth. Nevertheless, the power density is still smaller (but close) on flat faces that on connecting filets. In other words, we optimized the pair tooth angle – connecting filet radius to handle roughly the same maximum power density on both objects.

Last tooth is made longer (and named the super tooth, see fig.2). A flat face is put below the jaw. Both objects are fluorescence, Compton and Rayleigh scattering blockers and their efficiency has been estimated at ~ 90%. Even if they make the design and machining more complicated, they avoid the cooling of vacuum chambers with water.

Complementary details about the design of theCuCr1Zr EBS absorbers are given in [6]. One of the main advantages is that the material is hard enough – Brinell hardness larger than 125 HB – and isotropic enough to machine the CF flange directly on the CuCr1Zr part, making an absorber with no weld and no braze therefore no assembling problem.

CFD MODEL

Surprisingly, CFD has not been widely used in the past for absorber heat transfer calculations. Even in recent literature (see for example [1, 7, 8]), authors refer to a heat transfer film coefficient value that varies from 10 to 20 kW/m^2/K with no or little precisions concerning the cooling channel dimensions and the flow rate.

For the EBS absorbers, we decided to study a generic case of concentric cooling channels with a water flow rate (2.5 m/s ~ 4.24 l/min) that will be eventually used, in order to extract both the average heat transfer coefficient per channel and the total pressure drop.

All CFD calculations were made using the k-ε turbulence model with automatic wall functions [9]. A sensitivity study has been performed for the turbulence model.

Hydraulic Model

Each concentric cooling channel consists in a Φ6x8 mm stainless steel 316L tube inserted Φ10 mm hole in the bulk of the absorber. The channel cross section is roughly the same inside the tube than between the tube and the copper alloy hole (~ 28 mm^2). The extremity of the tube is in contact with the bottom of the hole and machined with two apertures of sections 2x14 mm^2 for the water to pass between the inside of the tube and the annular channel. The tube is centered in the hole by small spacers. The geometry was chosen for its simplicity and for its compactness.

Calculations are performed on ½ of the model, due to symmetry.

Figure 4 shows the pressure drop across two consecutive cooling channels. The water enters the model at the inner of the top left hand side stainless steel tube, going down, then the flow reverses at the bottom of the tube and goes up in the gap between the tube and the bulk of the absorber. The water flows horizontally in the green part and then flows down in the gap between the right hand side tube and the bulk. At the bottom of the hole, there is a second flow reversal and the water exits through the inner of the right hand side stainless steel tube, going up.

Gravity is oriented in the –y direction (downward).

ISBN: 978-3-95450-188-5 doi:10.18429/JACoW-MEDSI2016-WEAA02

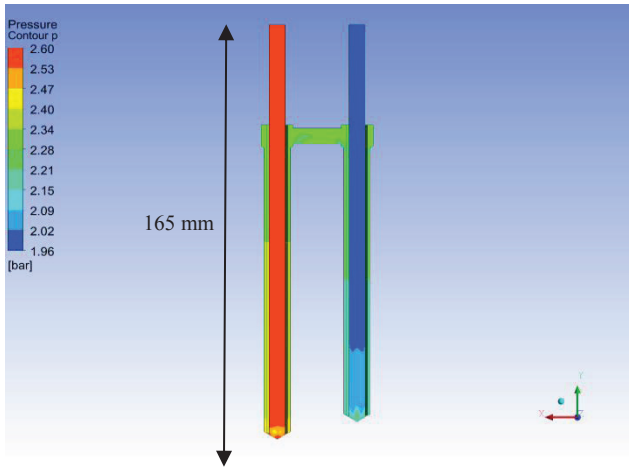


Figure 4: Pressure drop across two consecutive coaxial cooling channels.

Pressure drop is found to be $\Delta p \sim 0.6$ bar for two channels - see fig. 4. As the cross section is kept the same along all the cooling path, the specific pressure loss is due to changes on the flow direction and friction along tubes. One sees also on the contour plot that the total pressure drop is dominated by specific pressure losses. A rough estimate per channel would give:

- Frictional loss coefficient: $\xi = 0.04 \times 350/6 = 2.3$.
- Specific loss coefficient: $\xi > 5$ [10].
- Gravity: no.

The total loss coefficient is found to be $\xi_{tot} > 7.3$ with the rough estimate and $\xi_{tot} = 10$ with the CFD result.

From this study (and from other studies too) we decided to keep the $\Delta p \sim 0.3$ bar per cooling channel at 4.24 l/min ($\xi_{tot} = 10$) as the design value for all concentric cooling absorbers. Note that as the flow is turbulent, the pressure drop varies essentially with the square of the flow rate.

Thermal Hydraulic Model

The thermal-hydraulic model is a simplified absorber with a single cooling channel (see fig. 4). Calculations are performed on ¼th of the model, due to symmetries. In this model, the extremity of the tube has four apertures of sections 4x7 mm^2 to be consistent with the symmetry.

Figure 5 shows the calculated heat transfer coefficient. The coefficient varies in the range 6-46 $kW/m^2/K$ for an average value of 18 $kW/m^2/K$.

In addition to the generic absorber, thermal-hydraulic calculations have been performed on two more absorbers, giving comparable results. We decided to take a conservative design value of 15 $kW/m^2/K$ for calculations for which there was no time to make a complete fluid-structure model. The design value is conservative because:

- Its value is lower than the calculated value.
- Using an average value is conservative: the heat transfer coefficient is bigger than its average in the region where the heat flux is large, i.e. close to the region where the beam is absorbed.

In other words: the flow reversal induces a significant pressure drop, but at the same time, increases the heat transfer coefficient significantly.

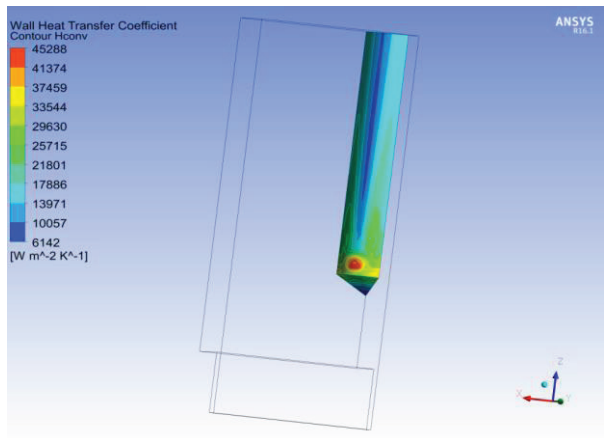


Figure 5: Heat Transfer Coefficient of a Cooling Channel.

Finally, we verified with a parametric calculation that the average heat transfer coefficient h varies linearly with flow velocity v (or flow rate), in the range 0-5 m/s. This result is not trivial: using the Dittus and Boelter correlation [11] would have led to $h \propto v^{0.8}$. But again, the space saving concentric cooling geometry is somehow exotic to address a heat transfer problem.

THERMAL-MECHANICAL MODELS

Specified Mechanical Properties

Using off-the-shelf CuCr1Zr would be risky as the thermal and mechanical properties may vary significantly from one batch to another, as well as purity, grain size, inclusions, etc... In other words, the EN standard CW106C was too permissive to guaranty the supplying of material with high enough thermal, mechanical and chemical properties.

The ESRF took the decision to write a full specification [12] to focus on material definition for the call for tender (CFT), making the CFT more challenging for suppliers. In particular, at 250°C, the material should have a yield strength value larger than 280 MPa, an elongation at break larger than 8%, a Brinell hardness larger than 125 HB and a thermal conductivity larger than 300 W/m/K.

Elastic Analysis Stress Criteria

During the past 10 years, several different criteria have been proposed for the dimensioning of X-Ray absorbers and the acceptable maximum stress for Copper and Glidcop® submitted to thermal stresses and to a large number of fatigue cycles [13-17]. Completing and updating the survey made by [13], we have built the table 1. In the table, S_y refers to the yield strength,

Content from this work may be used under the terms of the CC BY 3.0 licence (© 2016). Any distribution of this work must maintain attribution to the author(s), title of the work, publisher, and DOI.

ISBN: 978-3-95450-188-5 doi:10.18429/JACoW-MEDSI2016-WEAA02

Content from this work may be used under the terms of the CC BY 3.0 licence (© 2016). Any distribution of this work must maintain attribution to the author(s), title of the work, publisher, and DOI.

S_F to the fatigue strength, σ_{VM} to the Von-Mises equivalent stress, σ_1 and σ_3 to the maximum and minimum principal stress respectively and τ_{Max} to the maximum shear stress.

Table 1: Thermal and Stress Analysis Criteria

Accelerator	Maximum Temperature	Maximum Stress / Strain
ALBA	400° (Glidcop®)	0.2% strain (10^5 cycles)
ANKA, SLS	(Copper)	0.2% strain (10^4 cycles)
APS	541° (Copper) 405° (Glidcop®)	$2.S_y$, S_F (10^5 cycles) Fatigue Model
DIAMOND	(Copper)	0.5% peak strain 0.1% bulk strain
ESRF	$T_{Melt}/2$ (All Materials)	$\sigma_{VM} < S_y$
ESRF, EBS	250° (CuCr1Zr)	$\sigma_1 < S_y = 280MPa$ $\sigma_3 > -S_y$ $\tau_{Max} < S_y/2$
SOLEIL	(All Materials)	$\sigma_{VM} < 0.75.S_y$
SPRING-8	(All Materials)	Fatigue Model

Many authors propose acceptable stresses higher than the material yield strength. In comparison, the ESRF-EBS criteria look conservatives, but we had to manage the fact that:

- Around 400 absorbers will be mounted in the storage ring for 20 years.
- We should be conservative as we deal with a new material.

Toothed absorbers are often different in the nature of the stress. Due to the teeth, the maximum principal (tensile) and maximum shear stress reach high values as in flat face absorbers, the stress is dominated by the minimum principal (compressive) stress. Those tensile and shear stresses impact more the robustness – in case of cracks in the absorber for example - than a pure compressive stress.

Most if not all the stresses in absorbers are secondary stresses as they are due to shape adaptation of the part and not to an external force and/or pressure.

If one wants to use ASME like criteria for elastic analysis and secondary stresses, the criterion would be in this case $\tau_{Max} < S_y$ [18]. In other words, in the ASME frame, for secondary stresses, we have a safety factor of 2 in the elastic analysis stress criteria.

ABS-CH9-1-2 Horizontal Absorber

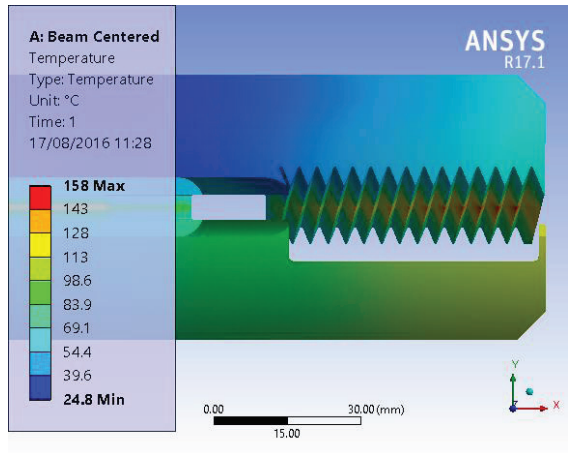


Figure 6: Temperature Plot CH9-1-2 Absorber.

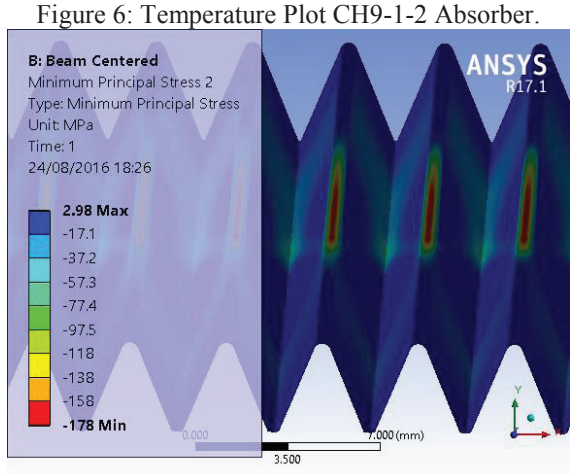


Figure 7: Minimum Principal Stress CH9-1-2 Absorber.

The ABS-CH9-1-2 is a 51 faces, 16 teeth crotch absorber with a total heat load of 3373.3 W.

The thermal load per face is similar to the one shown in figure 2. The calculations where made with a 1.5° misalignment and a heat transfer coefficient of 15 $kW/m^2/K$, those choices being explained in paragraph 1 and 2.

The maximum temperature is found to be 158° C at the tooth n°15 as shown in figure 6. According to our criteria, the dimensioning stress (together with the maximum shear stress) is the minimum principal stress shown in figure 7. Its minimum value is -178 MPa in the filet connecting tooth n°8 and tooth n°9. We found a maximum principal stress peak value of 116 MPa and a maximum shear stress peak value of 89 MPa.

This example shows what we observed on roughly every absorber: the connecting filet cannot be optimized independently from the teeth:

- Using a smaller filet radius would increase the tensile and shear stresses on adjacent teeth; the teeth needs loose connections one to each other in order to expand with no stress when warming.

ISBN: 978-3-95450-188-5 doi:10.18429/JACoW-MEDSI2016-WEAA02

- Using a larger filet radius would increase furthermore the compressive stress in the filet as the "average" grazing angle in the filet would increase.

Again, we decided to have all the EBS storage ring toothed absorbers with 45° tooth angle and 0.32 mm connecting filet radius.

Finally, this example points out a very fundamental difference between frontal and toothed absorbers:

- Frontal absorbers are large bulky parts with very localized heat loads, their thermal-mechanical behavior is plane ***strain*** driven.
- At the other end of the spectrum, focusing lenses, for example, are light thin parts, their thermal-mechanical behavior is plane ***stress*** driven.

Toothed absorbers with small teeth and loosed teeth connections are transition objects in between, plane strain dominated close to the beam and plain strain dominated in the rest of the jaw. Depending on the design, the plain stress or the plain stress may be the dimensioning factor, or, as in ABS-CH9-1-2, both play a role.

CONCLUSION

The ESRF decided to use a new material (CuCr1Zr) for most of its EBS storage ring absorbers. To turn this decision into a success, we decided to be conservative in term of design and calculation criteria:

- The position and angle tolerances are loose: ± 2 mm in height and ± 1° in angle.
- The maximum temperature for the absorber should be less than 250°C.
- The maximum principal stress peak value should be less than 280 MPa, and the maximum shear stress peak value less than 140 MPa.
- The minimum principal stress peak value should be more than -280 MPa.

All CuCr1Zr storage ring absorbers have been calculated so far and they all comply to the design and calculation criteria.

In addition to that, we studied extensively the efficiency of a new type of cooling channel, with a concentric design. We found that the effective heat transfer coefficient for such a channel is larger than 15 $kW/m^2/K$ for a water velocity of 2.5 m/s and varies linearly with the water velocity. The cooling channel geometry leads to a specific pressure loss coefficient of 10.

Finally, the hardness of the material and prototypes of CF flanges in CuCr1Zr [6] validate the fact that one can design a storage ring absorber as a single mechanical part with no braze and no weld, thus reducing the risk of failure/leaks and the complexity of manufacturing them.

REFERENCES

[1] S. Sharma, "A Novel Design of High Power Masks and Slits", Proc. of MEDSI2014, Australia (2014).

[2] ANSYS CFX, http://www.ansys.com/Products/Fluids/ANSYS-CFX

[3] ANSYS Mechanical Enterprise, http://www.ansys.com/Products/Structures/ANSYS-Mechanical-Enterprise

[4] Oxygen-free copper Wikipedia, https://en.wikipedia.org/wiki/Oxygen-free_copper

[5] Wikipedia Glidcop, https://en.wikipedia.org/wiki/Glidcop

[6] E. Gagliardini *et al.*, "A new generation of X-ray absorbers for the EBS storage ring", poster session, MEDSI2016, Barcelona, Spain, this conference.

[7] L. Zhang, J.C. Biasci and B. Plan, "ESRF Thermal Absorbers: Temperature, Stress and Material Criteria", Proc. of MEDSI2002, U.S.A. (2002).

[8] C.K. Kuan *et al.*, "Thermal Analysis of Absorbers for the 3 GeV TPS", Proc. of MEDSI2006, Japan (2006).

[9] CFD Online, http://www.cfd-online.com/Wiki/Two_equation_turbulence_models

[10] I.E. Idelchick, "Handbook of Hydraulic Resistance", 4th Revised and Augmented Edition, Ed. Begell House, Inc., 2007, p 469, ISBN: 978-1-56700-251-5.

[11] R.H.S. Winterton, "Where did the Dittus and Boelter equation come from?", Int. J. Heat Mass Transfer, Vol. 41, Nos 4-5, pp.809-810, 1998.

[12] ESRF / ENG / 15-09

[13] M. Quispe *et al.*, "Development of the Crotch Absorber for ALBA storage ring", Proc. of MEDSI2008, Canada (2008).

[14] S. Takahashi *et al.*, "Prediction of fatigue life of high-heat load components made of oxygen-free copper comparing with Glidcop", J. Synchrotron Radiat., 20 (Pt 1), pp.67-73, Jan. 2013.

[15] S. Takahashi *et al.*, "Reconsideration of Design Criteria for High-Heat-load Components at Spring-8 Front Ends", Proc. of MEDSI2006, Japan (2006).

[16] J. Colins *et al.*, "Results from Studies of Thermomechanically- Induced Fatigue in Glidcop®", Proc. of MEDSI2014, Australia (2014).

[17] L. Zhang, "Absorber Conceptual design and optimisation", ESRF Technical Report (2014).

[18] M.H. Jawad and J.R. Farr, "Structural Analysis and Design of Process Equipment", Ed. John Wiler & Sons, 1984, p 20 and p 32, ISBN: 0-471-09207-X.

Content from this work may be used under the terms of the CC BY 3.0 licence (© 2016). Any distribution of this work must maintain attribution to the author(s), title of the work, publisher, and DOI.

ISBN: 978-3-95450-188-5 doi:10.18429/JACoW-MEDSI2016-WEAA03

THERMAL STABILITY OF THE NEW ESRF EXTREMELY BRILLIANT SOURCE

B.Tampigny, Y. Dabin, F. Thomas[1], J.F. Bouteille, L. Favacque, T. Marchial, F. Favier, P. Roux-Buisson, J.C. Biasci, P. Raimondi, D.Martin, M.Diot, A.Flaven Bois,
European Synchrotron Radiation Facility (ESRF), Grenoble, France
[1]also at Institut Laue-Langevin (ILL), Grenoble, France

Abstract

In the frame of the Extremely Brilliant Source project (EBS), studies dedicated to disturbances have been more intensively investigated. Engineering instabilities have two origins: mechanical and thermal.

Major thermal issues are:

- air conditioning presents a temperature ramp up of 2°C along the sector, in the tunnel
- storage ring requires a warm up period of 4 days for reaching stable orbit

These effects have been observed and corrected for 20 years.

With EBS requirements, we need to identify these thermal effects in order to reduce disturbances, thus improving more systematically source stability. The study is led by the comparison between present and new thermal system.

To do so, it is necessary to evaluate the heat balance in this system, as well as to identify the thermal time constant for each component.

Finite Element Analysis (FEA) models have been performed to explore the sensitivity of these thermal issues. A full scale mock-up cell equipped with a prototype girder was implemented aimed at revealing power cables influence inside. A FEA model was also developed for the present storage ring to analyze the air stream cooling process.

Although investigations have already been developed, some others remain to be achieved by the end of 2016.

OVERVIEW

This is the domain of instability. Light source storage rings errors have been investigated for a long time, however the new EBS project is faced to set new questions within the facility. The present storage ring has been operated for 25 years, and of course, it is highly compensated in many error aspects.

Instabilities We proposed to consider the closed-orbit errors, in the following breakdown:

1. Permanent static errors from the origin
2. Permanent variable errors (quick effects)
3. Errors triggered by the beam operating conditions
4. Long period errors

While the two first have mechanical origins effects (alignments, fiducialisation, vibrations, etc.), the last two have thermal origins effects. The present storage ring has two major thermal issues:

- A longitudinal gradient of 2°C between the air ventilation inlet and outlet along a tunnel quarter
- A transient warm-up period of 4 days before reaching a stable orbit

Resolving these thermal errors requires having a very fine understanding of the storage ring thermal behaviour. We have in fact to deal with a thermal system, which we need to define.

Thermal system Such a thermal system is very complex. It contains many components coupled all together. We proposed to consider the following system:

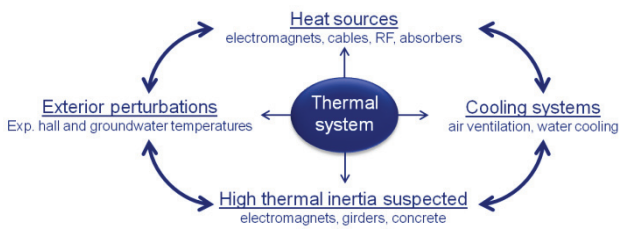


Figure 1: Thermal system of the ESRF storage ring.

As we can see in Figure 1, the thermal system is composed by four main components:

- Components heat sources: electromagnets, cables, Radio Frequency (RF), absorbers
- Two cooling systems of the storage ring: the air ventilation and the water cooling system
- High thermal inertia items: electromagnets, girders, concrete walls and slabs
- External disturbances: experimental hall and groundwater temperatures

Like any usual system vision, most of these components are coupled together.

This paper will not cover all aspects of this system; we will focus mainly on electromagnets as main heat source and thermal capacity. We will discuss also about the air ventilation of the storage ring, girders, external disturbances (experimental hall temperature), power cables and concrete slab.

Our approach is led by some parallel exploration with FEA, as well as full scale mock-ups measurements.

EXPLORATING WORKS

In order to characterize the thermal system of the ESRF storage ring, several components of the lattice were calcu-

Content from this work may be used under the terms of the CC BY 3.0 licence (© 2016). Any distribution of this work must maintain attribution to the author(s), title of the work, publisher, and DOI.

ISBN: 978-3-95450-188-5 doi:10.18429/JACoW-MEDSI2016-WEAA03

lated with FEA. Numerical models were performed using Comsol Multiphysics package, combining Computational Fluid Dynamics (CFD), thermal and thermomechanical calculations.

CFD

Tunnel ventilation A very first 3D model was performed to study the air velocity inside the tunnel. The storage ring is divided in four sectors. At each end of the sector, air enters the tunnel at ~10m/s. It exits the tunnel at the other side. Total length of air path in each section is around 210m.

This model represents magnets and girders by cubes, which is aimed at being simplified. It gives, however, an estimation of air velocity: ~1.4m/s in the internal area of the tunnel (freeway) and ~0.7m/s in the external area (front-end side).

By reinserting this velocity field in a smaller and finer model, we noted that the air velocity was very low inside electromagnets, which behave as obstacles limiting by the way the air flow. By comparing forced convection with natural convection, we noticed that natural convection was dominating heat transfers. For that reason, we decided to only consider natural convection in the next calculations.

EBS Quadrupole Modelling directly the air flow due to natural convection around a full 3D quadrupole is very CPU and time expensive. For that reason, we chose to consider a 2D quadrupole model where inner air could flow in a cavity.

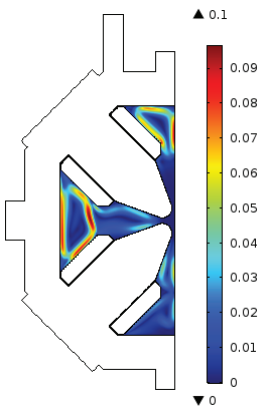


Figure 2: Air velocity (m/s) for half 2D quadrupole heated by coils.

Figure 2 shows the velocity field in the inner air volume of the quadrupole. By effect of gravity and density change, air heated by coils goes up, transfers its heat to the yoke and then goes down; it looks like a Benard roll. We note that the velocity field is almost null in the gap between coils and yoke: heat transfer in this area is mainly air-conduction driven.

Thermal Calculations

EBS Quadrupole 2D models are quick to set up, but do not represent truly the reality. We decided to exploit 2D models by computing local convective coefficients, and to introduce them into a 3D model without CFD.

The 3D quadrupole model includes the quadrupole yoke and its poles, coils, its support, and a part of the girder. The only heat source is potentially due to the coils.

Coils are directly in contact with the yoke via rubber spacers, and with poles via holders, as shown in Figure 3.

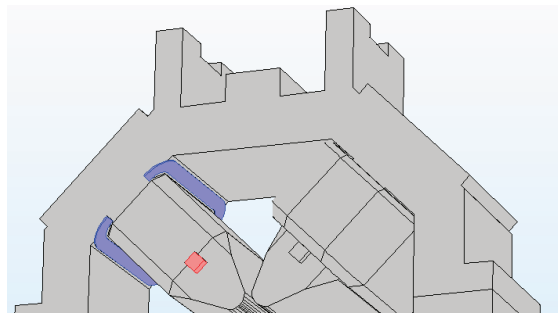


Figure 3: Rubber spacer (blue) and holder (red) of quadrupole coils.

2000W are dissipated in coils (500W each), which are cooled with water (~0.45L/min) at 24°C. Outlet water temperature is then ~40°C. We assumed that coils surfaces in front of the poles were at 24°C while those facing air at 40°C. We also assumed that the ambient air were constant at 24°C, as well as the ground temperature.

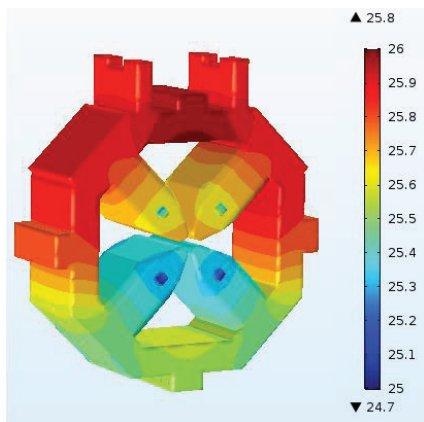


Figure 4: Temperature field (°C) in a 3D quadrupole heated by coils.

Initially at 24°C, the quadrupole reaches an average temperature of 25.4°C (+1.4°C) in ~1.5 days (99% of final state and time constant of 0.3 day).

Figure 4 shows that the upper part of the quadrupole is warmer than the lower part. On one hand, this is due to the air convection: since heated air goes up, it transfers more heat to the upper part. On the other hand, this can be explained by the fact that the lower part of the quadrupole is in contact with its support and the girder, which both behave as heat sink. We also note that holders tend to be cooler, because of their contact with coils surfaces which are at a temperature close to 24°C.

Heat balance At this state, it is necessary to determinate the thermal coupling between these different components by post-processing a heat balance.

Content from this work may be used under the terms of the CC BY 3.0 licence (© 2016). Any distribution of this work must maintain attribution to the author(s), title of the work, publisher, and DOI.

ISBN: 978-3-95450-188-5 doi:10.18429/JACoW-MEDSI2016-WEAA03

Content from this work may be used under the terms of the CC BY 3.0 licence (© 2016). Any distribution of this work must maintain attribution to the author(s), title of the work, publisher, and DOI.

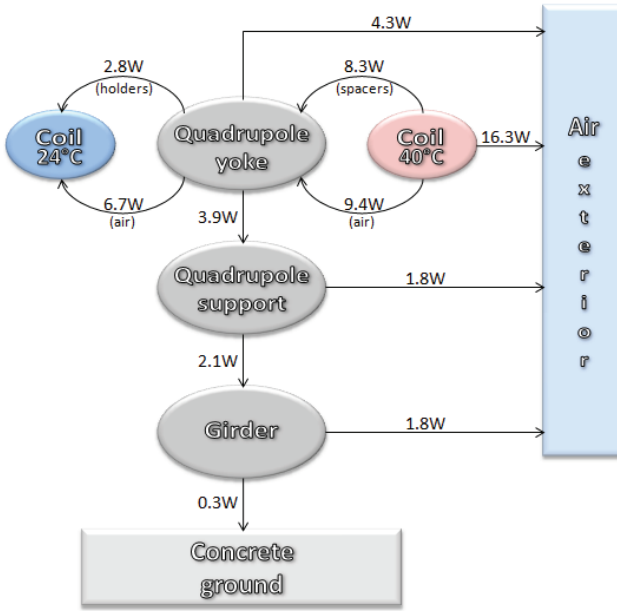


Figure 5: Heat balance of a quadrupole coupled with the girder and ambient air.

Figure 5 shows that coils both contribute to add and remove heat: 34W is added to the system and 9.5W is removed due to the coils. They globally add more heat (+24.5W).

There is a total of 24.2W of heat (1.2% of the total heat dissipated in coils) which goes in air. This amount, cumulated with other electromagnets and heat sources in the tunnel, will tend to increase the average temperature of the air flow and to create a temperature gradient between air inlet and outlet.

As previously mentioned, only natural convection is taken into consideration. If we noted that forced convection had less impact than natural convection inside the quadrupoles, this is not necessarily true for the outside of it. In the previous model, outside convective coefficients h were in the range of 2-4W/m^2/K. But it could be higher (magnitude of 10W/m^2/K) due to forced convection. In the same way, the ambient and ground temperature both set in the previous calculation at 24°C require a finer estimation.

Only 0.3W goes in the concrete slab. This value is optimist since we considered the ground temperature at 24°C (the water table temperature varies from 12 to 16°C at 2.2m from the slab surface). It could be lower in reality, modifying also the heat balance. Further investigations are then required.

Thermomechanical Calculations

The deformation of a 3D quadrupole due to the temperature was calculated. This model includes yoke, poles, quadrupole support, and contacts conditions between different parts of these components.

The initial temperature of the quadrupole is assumed to be at 24°C. The temperature field used for this calculation is the one from Figure 4.

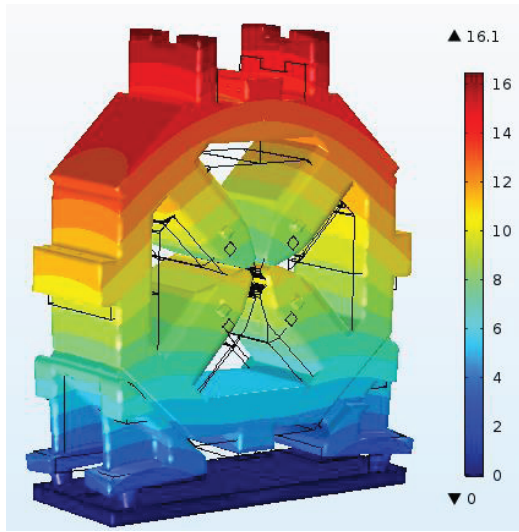


Figure 6: Total displacements (µm) in a 3D quadrupole heated by coils.

Figure 6 shows the total displacements of the quadrupole. We noticed that a temperature average increase of 1.4°C to the quadrupole would lead to a maximum deformation of 16.1µm. Poles move from 8 to 10 µm.

MOCK-UP MEASUREMENTS

Two mock-ups were operated. The first one is to study electromagnets while powered, whereas the second is to study a prototype girder with power cables running inside the central channel.

Electromagnets

An EBS quadrupole is placed on a table. It is alimented by current and its coils dissipate a total heat of 2730W of heat. Coils are water-cooled. Both inlet water and outlet temperature are measured with probes, as well as the water flow. Air cooling is run by natural convection. The quadrupole is probed with several PT100, and is also measured with thermal camera, as shown in Figure 7.

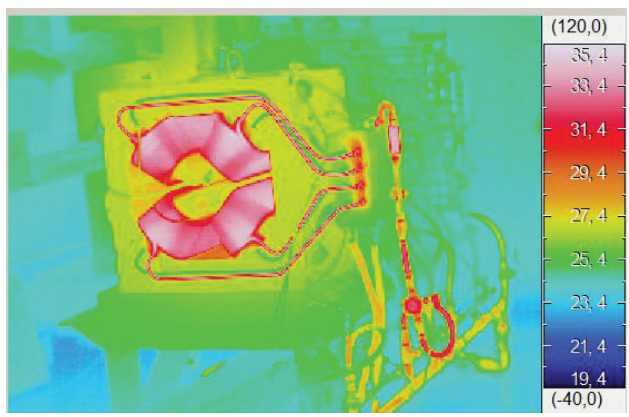


Figure 7: EBS quadrupole measured with a thermal camera.

Quadrupole yoke temperature increases from 23.9°C to 26.7°C (+2.8°C) within ~1.5 days. Through a heat balance on water, we found that 4.5% of the total heat generated in coils goes in air.

ISBN: 978-3-95450-188-5 doi:10.18429/JACoW-MEDSI2016-WEAA03

The time constant of this quadrupole is the same than the one studied with FEA. However, both temperature increase and % amount of heat in air are higher. This is due to different reasons:

First, the total heat in the coils are higher with the mock-up (2730W) than in the FEA model (2000W).

Then, in the FEA model, power cables were not modelled, whereas they were put under the table that supports the quadrupole. Cables add additional heat to the quadrupole.

Finally, the quadrupole studied experimentally is more than twice as long as the one studied in FEA, which mean that surface exchange with coils / spacers and coils / inner volume of air are higher (refer to Figure 3. For a geometrical view). Thus more heat is extracted from coils, hence a higher % of heat goes in air.

Prototype Girder

A short-time issue was led by the project manager to put electromagnets cables inside the girder, in order to save space in the freeway. This relevant idea, however, may be dangerous: the girder may indeed get deformed by the heat generated by cables. Hence we developed a full scale mock-up of a prototype girder. 32 cables (30 with 120mm^2 diameter, 2 with 70mm^2) are put in a custom tray inside the girder. Cables are powered with 90A.

The girder is confined with walls and a ceiling in order to reproduce a cell of the storage ring. A fan is added to create an air flow and enabling to measure the coupling between air and girder. In Figure 8, we can note that the fan is located in such a way that the stream is more important near a side of the girder (referring to internal zone) rather the other side (referring to external zone), similarly with the storage ring ventilation.

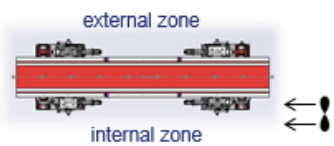


Figure 8: Location of the fan in regards to the girder.

Several probes (PT100) are put at different places of the girder (foot, up and down sides, extremities, internal and external zones). Two probes are also put on the concrete ground: one near a feet, another one far from the girder but still into the cell.

We did two series of transient tests:

1. No power in cables. Ventilation on. After a while, ventilation is switched off, still without power.
2. Ventilation off. We switched on power in cables. After a while, we switched the ventilation to 25% of its nominal flow (840m^3/h) and then to 100% (3360m^3/h)

With the first test, we noted that with ventilation, all girder temperatures were fluctuant (±0.05°C) with a period of 24h. These fluctuations are due to the variation of the surrounding experimental hall temperature during the day. Then, when with switched the ventilation off, we noted a decrease of all temperatures. This is due to the fact that the concrete slab is cooler than the ambient air. By switching the ventilation off, we reduced the coupling air/girder, hence the coupling concrete/girder is more important. In any case, we need further investigations on the concrete slab because its coupling with the girder cannot be neglected.

We the second test, we noted an increase in temperature of the girder of ~1.7°C within ~3days (time constant of 0.6day). We noted that by switching the ventilation on, temperatures were decreasing by ~25% when the ventilation is at 25% of its nominal flow, and by ~50% when ventilation is at 100% of nominal flow. We also note that the higher the air flow is, the more temperatures fluctuate (±0.15°C when 100% nominal flow), because of the increasing coupling between air and girder. We also note that concrete temperatures keep increasing slowly even after 20days, due to its high thermal inertia.

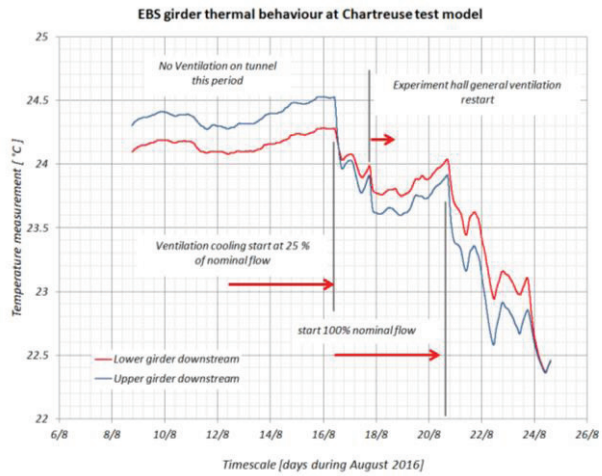


Figure 9: Temperature in the middle of the girder, up and down sides.

Figure 9 also shows interesting phenomena. When there is no ventilation while cables are powered, because the only convective regime is natural: the heat from cables goes upward due to Buoyancy forces, hence the upside of the girder (blue line) is warmer than the downside (red line). But these two curves crross and reverse when ventilation is switched on: air as heat carrier in natural convective regime is then pushed away by the forced air flow, as a consequence the upside of the girder becomes less heated.

We must also notice that the girder deformation has also been measured during these experiences. The girder tends to take a “banana” shape. Results are, however, not available yet. But the deformation is such that we abandoned the idea to place power cables inside the girder.

CONCLUSION

Thermal stability exploration requires considering it as a system: every components are coupled together. It mobilizes many experts from different domains, it is by nature a multi-physics approach. This exploration needs:

Content from this work may be used under the terms of the CC BY 3.0 licence (© 2016). Any distribution of this work must maintain attribution to the author(s), title of the work, publisher, and DOI.

ISBN: 978-3-95450-188-5 doi:10.18429/JACoW-MEDSI2016-WEAA03

Content from this work may be used under the terms of the CC BY 3.0 licence (© 2016). Any distribution of this work must maintain attribution to the author(s), title of the work, publisher, and DOI.

- More experimental mock-ups with many probes, which is not a common use
- More thermal simulations in order to estimate transfer functions or to implement a "thermatronic" domain.

The EBS is a new installation on an already existing facility; its thermal optimization is consequently difficult. Investigations are not completed yet. Some subjects are still under investigations. At the end, coupling coefficient will be better determined. The period of 4 days before reaching stable orbit seems to be very complex and difficult to solve, because it is probably connected with many causes. The +2°C ramp-up into a tunnel sector could be improved with extra cooling systems that we are currently studying.

A better approach would consist in considering the thermal stability at the beginning of a project.

ISBN: 978-3-95450-188-5 doi:10.18429/JACoW-MEDSI2016-WEAA04

NOVEL NUMERICAL METHOD FOR CALCULATING THE SHADOW PROJECTION AND COLLISIONS OF A MULTI-AXIS GONIOMETER AT DIAMOND

V. Grama†, A. Wagner, Diamond Light Source, Didcot, UK

Abstract

Beamline I23 is a long-wavelength macromolecular crystallography beamline at Diamond Light Source. The end station is a unique instrument with a bespoke cryogenically cooled multi-axis goniometer and a large curved Pilatus 12M detector in a high vacuum environment. As experiments become limited by radiation damage to the crystals, optimised strategies are needed to orient crystals in the most efficient way to obtain a complete dataset with a minimal X-ray dose.

Two key factors affect the optimisation strategies. Firstly, shadowing on the detector by the goniometer resulting in data loss in this region and secondly, collisions between the goniometer and other components in the end station restricting the available angular range for sample centering and data collection. This paper discusses the numerical methods for calculating the shadowing of a multi-axis goniometer on a semi-cylindrical detector and the calculation of the allowable angles for various conditions to prevent collisions with neighbouring components.

INTRODUCTION

The long-wavelength macromolecular crystallography (MX) beamline I23 at Diamond Light Source is a unique instrument currently being commissioned. Its main use is to solve complicated protein or nucleic acid structures without additional labelling directly from the naturally occurring sulphur or phosphorus atoms in these macromolecules. To eliminate air absorption at longer wavelengths, the complete end station including the goniometer and detector is in vacuum. As diffraction angles increase at long wavelengths, dedicated solutions for the detector and a multi-axis goniometer have been developed. The detector is a large semi-cylindrical Pilatus 12M area detector developed by Dectris. The multi-axis goniometer in inverse-kappa geometry has been built by the UK Astronomy Technology Centre. It has an $\propto_{\kappa}$ angle of 50° which allows the alignment of crystals along any given crystallographic axis [1].

The samples can be exposed to only a certain amount of radiation dose for data collection before they are damaged. Hence, it is vital to predetermine the most efficient way of orienting the crystal to obtain a complete dataset with minimal X-ray dose.

In order to generate strategies for data collection it is important to know two key factors which affect the optimisation in advance. Firstly, the goniometer kappa head assembly has a fairly large footprint. Because of this, at certain kappa and omega angle combinations the kappa assembly interferes with the projected diffraction leading to shadowing on the detector. This results in a data loss in this region. The shape and location of the shadow is dependent on the orientation of the kappa and omega axes. Secondly, it is important to know what angles are accessible for crystal centering and orienting for data collection. There is a restricted angular range which varies due to potential collisions with other moving components, such as the beamstop, backlight and sample viewing system. These share a common space envelope with the goniometer. Also, it is necessary to generate a collision model to ensure safety during operation since all critical systems operate inside a large vacuum vessel with limited visibility.

SHADOW PROJECTION MODEL

There are six main factors which affect the location and shape of the shadow on the detector –

1. The 3D geometry of the goniometer kappa axis assembly
2. The 3D geometry of the detector
3. The omega angle
4. The kappa angle
5. The XYZ offset on the centering stage
6. The sample position

The global coordinate system for the model is in accordance with the Diamond beamline axis orientation standard. The origin of each axis is at the sample position with the axis arrangement following the right had rule.

- The X axis is horizontal and perpendicular to the beam with the positive direction towards the goniometer.
- The Y axis is vertical with the positive direction being upward.
- The Z axis is horizontal and parallel with the beam with the positive direction being in the direction of propagation of the X-ray beam.

The global coordinate system is shown in Fig. 1.

Goniometer Geometry

The multi-axis goniometer is in inverse-kappa geometry. The main rotational axis or omega (ω) axis has an angular range of ±270°, the secondary kappa (κ) axis

Diamond Light Source, UK
† vinay.grama@diamond.ac.uk

Content from this work may be used under the terms of the CC BY 3.0 licence (© 2016). Any distribution of this work must maintain attribution to the author(s), title of the work, publisher, and DOI.

ISBN: 978-3-95450-188-5 doi:10.18429/JACoW-MEDSI2016-WEAA04

Content from this work may be used under the terms of the CC BY 3.0 licence (© 2016). Any distribution of this work must maintain attribution to the author(s), title of the work, publisher, and DOI.

has a range of +10° to -190° and the tertiary phi (φ) axis has a range of ± 180°. The kappa and phi axis assembly is mounted on an XYZ stage providing a ±2.5 mm translation in all three axes for centering samples. The XYZ stage is in turn mounted on the omega axis. The angle between the kappa axis and the omega axis is 50° which is defined as the $\propto_\kappa$ angle.

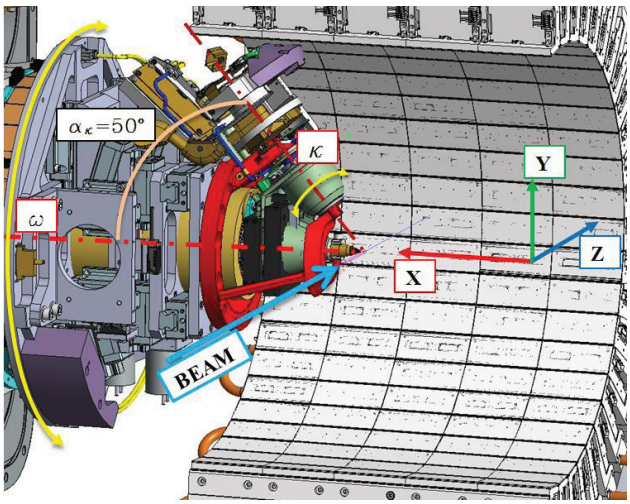


Figure 1: Goniometer coordinate system.

Detector Geometry

The Pilatus 12M detector comprises of 120 modules with 24 banks of 5 modules each arranged in a semi-cylindrical array with the sensor surfaces tangential to a 250 mm diameter cylinder as shown in Fig. 2. The total width of 5 modules on the detector is 424.6 mm. During data collection, the axis of the cylinder is collinear with the omega axis on the goniometer.

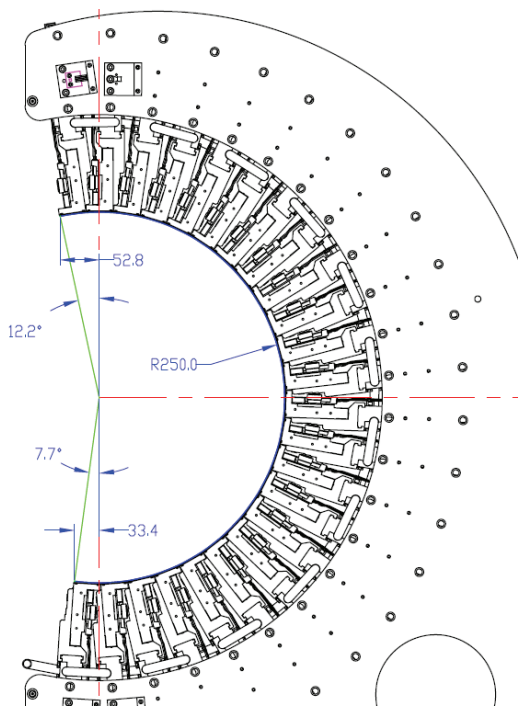


Figure 2: Detector geometry.

Sample Position

There are three possible sample positions along the X-axis direction. These three positions are defined by the combination of the Focussing mirror and Harmonic rejection mirror systems. The goniometer is repositioned in order to align the sample with the beam which results in a shift of the shadowing coordinates in the X direction.

Sample position-1 (default) is considered to have coordinates (0, 0, 0) and is at a distance of 192.3 mm from the outboard end of the detector (goniometer side). Sample position-2 is at (6.4, 0, 0) with reference to Sample position 1 and Sample position-3 is at (-6.4, 0, 0) as shown in Fig. 3.

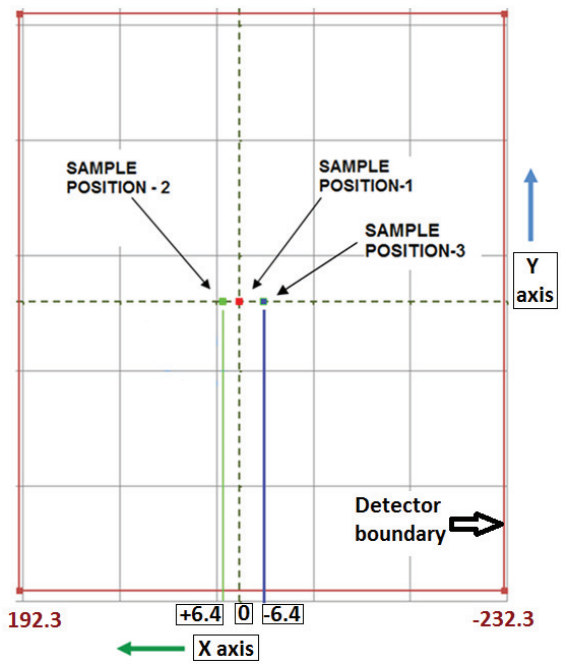


Figure 3: Sample positions (detector shown as red rectangle).

The kappa head assembly was analysed and it was deduced that the shadow on the detector would mainly be due to the outer edge of the kappa assembly. The 3-dimensional coordinates of the outer edge were measured on the CAD model and a 3D profile was generated as shown in Fig. 4.

The coordinate matrix of the profile is given by -

$$C_G = \begin{bmatrix} X_1 & Y_1 & Z_1 \\ \vdots & \ddots & \vdots \\ X_n & Y_n & Z_n \end{bmatrix} \quad (1)$$

These coordinates were then rotated by a defined angle about the kappa axis to obtain a second set of coordinates. The rotation matrix about the kappa axis is expressed as [2] -

$$R_K = \begin{bmatrix} u^2 + v^2 \cos\kappa & uv(1-\cos\kappa) & -v\sin\kappa \\ uv(1-\cos\kappa) & v^2 + u^2\cos\kappa & +u\sin\kappa \\ +v\sin\kappa & -u\sin\kappa & (u^2+v^2)\cos\kappa \end{bmatrix} \quad (2)$$

ISBN: 978-3-95450-188-5 doi:10.18429/JACoW-MEDSI2016-WEAA04

Where,

- κ is the angle about which the 3D profile coordinates are rotated about the kappa axis,
- |u v| is a unit vector of the kappa axis where -

$$u = \cos\ (50^0) \tag{3}$$

$$v = \sin\ (50^0) \tag{4}$$

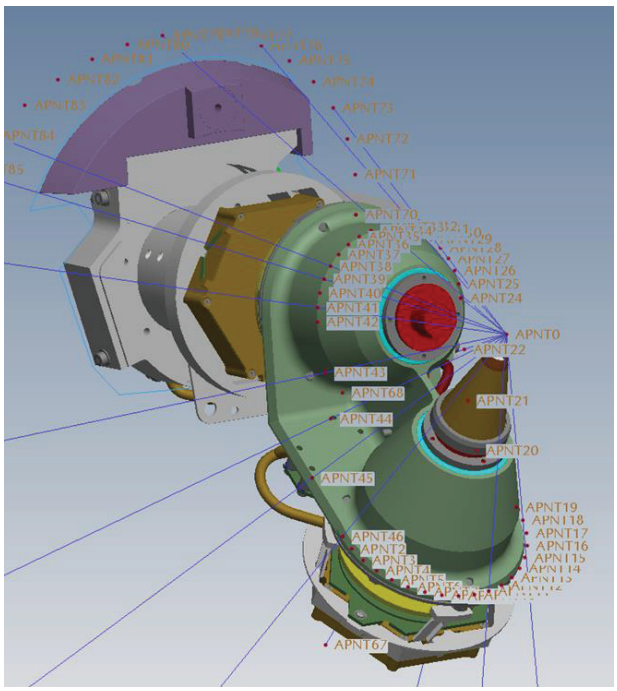


Figure 4: CAD model profile coordinates.

The resulting coordinate matrix is given by:-

$$[C_{KG}] = [C_G] \times [R_K] \tag{5}$$

The coordinates are then offset as a set in the X, Y and Z planes based on the offset from the omega axis for sample centering. This new coordinate matrix $[C_{KO}]$ is then rotated about the Omega axis or global X-axis. The rotation matrix is given by -

$$R_\omega = \begin{bmatrix} 1 & 0 & 0 \\ 0 & \cos\omega & \sin\omega \\ 0 & -\sin\omega & \cos\omega \end{bmatrix} \tag{6}$$

The resulting coordinate matrix is given by -

$$[C_{\omega G}] = [C_{KO}] \times [R_\omega] \tag{7}$$

The coordinates of matrix $[C_{\omega G}]$ are then projected as a ray on to a cylinder of infinite length having a radius equal to 250 mm which is collinear with the Omega axis (X-axis). The rays are defined by the origin (0, 0, 0) and an offset vector given by each set of coordinates (x_i, y_i, z_i) in the matrix $[C_{\omega G}]$. The equation for the projected coordinates is given by [3] -

$$\begin{aligned} x(t) &= t.x_i \\ y(t) &= t.y_i \\ z(t) &= t.z_i \end{aligned} \tag{8}$$

The ray-cylinder or ray-detector intersection is the point with the lowest non-negative value of *t*. The cylinder aligned along the X-axis is defined by -

$$z^2 + y^2 = 250^2 \tag{9}$$

To intersect the ray with the cylinder, equation (8) is substituted in equation (9) to solve for *t* -

$$t = \frac{\pm\sqrt{[-(4(z_i^2 + y_i^2)(-(250^2))]}}{2(z_i^2 + y_i^2)} \tag{10}$$

Since the detector is a partial-cylinder of finite length, the X and Z coordinates are valid if –

- For sample position – 1: -232.3 mm < x < 192.3 mm and z > -52.8 mm (i.e., $-12^0 < \omega < 190^0$)
- For sample position – 2: -238.7 mm < x < 185.9 mm and z > -52.8 mm (i.e., $-12^0 < \omega < 190^0$)
- For sample position – 3: -225.9 mm < x < 198.7 mm and z > -52.8 mm (i.e., $-12^0 < \omega < 190^0$)

The model can be refined for the lower half of the detector geometry by considering the coordinate to be valid for all values of Z greater than -33.4 mm if the Y coordinate of that point is less than zero.

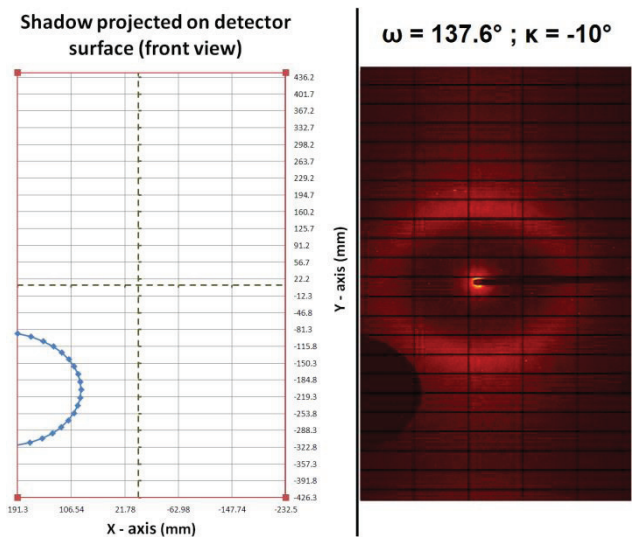


Figure 5: Calculated shadow on detector (left) and recorded shadow (right).

Figure 5 shows a plot of the calculated shadow boundary at ω = 137.6° and κ = -10° against an image recorded on the detector. The calculated profile has been visually compared against the recorded shadow. Detailed analysis is yet to be performed.

Content from this work may be used under the terms of the CC BY 3.0 licence (© 2016). Any distribution of this work must maintain attribution to the author(s), title of the work, publisher, and DOI.

ISBN: 978-3-95450-188-5 doi:10.18429/JACoW-MEDSI2016-WEAA04

Content from this work may be used under the terms of the CC BY 3.0 licence (© 2016). Any distribution of this work must maintain attribution to the author(s), title of the work, publisher, and DOI.

COLLISION MODEL

The collisions mainly occur between the goniometer kappa assembly and the beam stop, backlight and objective lens during the following two scenarios –

a) During sample centering: collisions between the goniometer kappa axis assembly and the objective lens and backlight.
b) During data collection: collisions between the goniometer kappa axis assembly and the beam stop.

The collision angles are dependent on the following factors –

a) The kappa angle
b) The omega angle
c) The XYZ centering offsets on the goniometer centering stage.
d) The distance of the objective lens from the sample position in the Z direction.
e) The distance of the backlight from the sample position in the Z direction.
f) The distance of the beam stop from the sample position in the Z direction.
g) The geometry of the colliding parts.

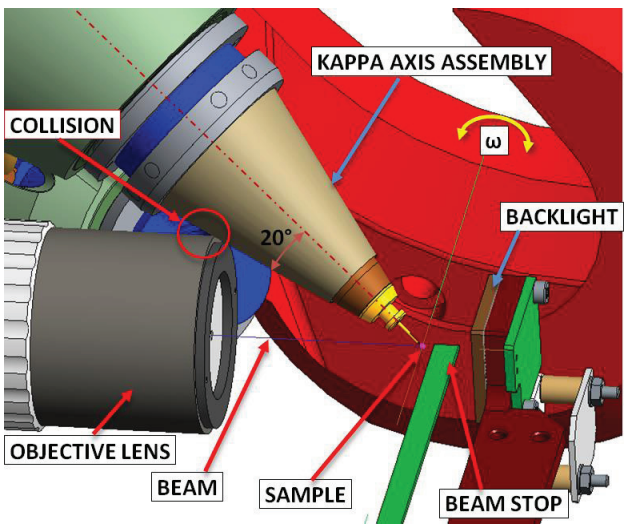


Figure 6: CAD image showing collision between the kappa assembly and objective lens.

Collisions: Kappa Assembly - Objective Lens

The on-axis viewing system allows the visualisation of the sample from the point of view of the beam. The objective lens on the on-axis viewing system has a hole machined through its centre allowing the beam to pass through. During sample centering, the goniometer omega axis is aligned and perpendicular to the beam axis. Also, the objective lens has a diameter of 34 mm with its axis collinear with the beam axis and positioned at a distance equal to its working distance from the sample position. The objective lens can be moved along the Z-axis for into a position which clears all collisions when not being used for sample centering.

The part of the kappa assembly which collides with the objective lens is a cone with a half cone angle of 20° as shown in Fig. 6. The axis of the cone is collinear with the phi axis. In order to predict the collision angles, the problem was simplified to a cone-circle interaction with the apex of the cone at the origin and the circle (front of the objective lens) at a distance of 34 mm from the origin. Theoretically, the vertex of the cone (or sample position) stays at the origin for all kappa and omega angles.

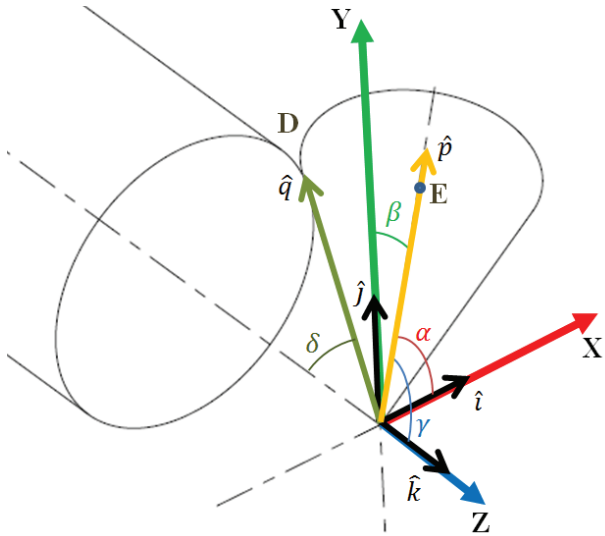


Figure 7: Cone-circle vectors.

Let $\hat{\imath}$, $\hat{\jmath}$ and $\hat{k}$ be unit vectors in the direction of the X, Y and Z axes respectively (Fig. 7). Consider a unit vector $\hat{p}$ directed along the phi axis and the angles between $\hat{p}$ and vectors $\hat{\imath}$, $\hat{\jmath}$ and $\hat{k}$ to be α, β and γ respectively. Let unit vector $\hat{q}$ be directed from the origin to a point D on the circle lying in the $\hat{k} - \hat{p}$ plane and the angle between $\hat{p}$ and $-\hat{k}$ be δ.

In order to calculate the omega angles at which the collisions occur, consider a point E on $\hat{p}$. The centreline of the kappa-cone can be represented as a line joining the origin and point E –

$$A_C = \begin{bmatrix} 0 & 0 & 0 \\ x_E & y_E & z_E \end{bmatrix} \tag{11}$$

The coordinates of point E when rotated about kappa is given by –

$$[A_{KC}] = [A_C] \times [R_K] \tag{12}$$

This new coordinate matrix $[A_{KC}]$ is then rotated about the Omega axis to get the final orientation of the kappa axis cone. The resulting coordinate matrix is given by –

$$[A_{\omega C}] = [A_{KC}] \times [R_\omega] = \begin{bmatrix} 0 & 0 & 0 \\ x_{E1} & y_{E1} & z_{E1} \end{bmatrix} \tag{13}$$

ISBN: 978-3-95450-188-5 doi:10.18429/JACoW-MEDSI2016-WEAA04

Let $\gamma_{\omega C}$ be the angle between the rotated centreline and the unit vector $-\hat{k}$ in the negative direction of the Z-axis. It can be calculate as –

$$\gamma_{\omega C} = \pi - \left(\cos^{-1}\left(\frac{z_{E1}}{\sqrt{(x_{E1}^2 + y_{E1}^2 + z_{E1}^2)}}\right)\right) \quad (14)$$

It can be seen that the kappa assembly collides with the objective lens if $\gamma_{\omega C}$ (in degrees) is less than or equal to δ + 20°. For a given kappa angle, there are two possible omega angles at which the kappa assembly can collide with the objective lens; one at the top of the lens and the other at the bottom. Figure 8 shows the calculated collision between the kappa assembly and objective lens at the same ω & κ angle as shown in Fig. 6.

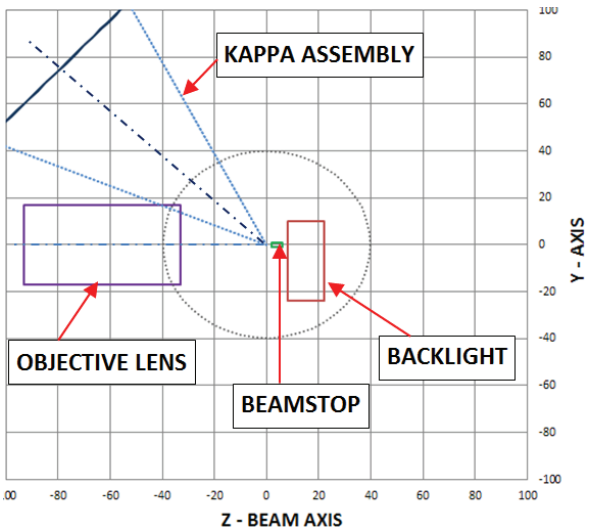


Figure 8: Collision model plotted in 2D.

Collisions: Kappa Assembly - Beam Stop / Backlight

The collisions between the beam stop / backlight and the kappa assembly were simplified and considered to be collisions between a cone and a rectangle.

Let ε be the angle between the Z-axis and the left vertical edge of the beam stop in the horizontal or Y-plane. Also, let ζ be the angle between the Z-axis and the top horizontal edge of the beam stop in the X-plane as shown in Fig. 9.

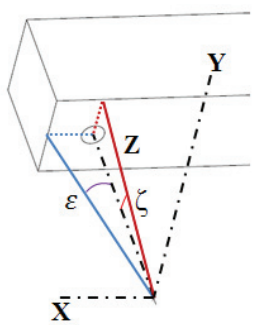


Figure 9: Beam stop: collision angles.

For a given kappa angle, the angle between the kappa cone axis and the X-plane (or α) remains constant for all values of omega. Let $\widehat{p_x}$ be the projection of vector $\hat{p}$ in the X-plane and θ_k be the angle between the projected vector and the Y-axis which is collinear with omega 0°. The omega angles at which the kappa assembly collides with the top edge of the beam stop is, ω_{Bt} = - (ζ + θ_k + 20°) and to the bottom edge is, ω_{Bb} = (ζ - θ_k + 20°). It can said that the kappa assembly collides with the beam stop if both the following conditions are true –

a) If α + 20° is greater than or equal to 90° - ε
b) If omega is between ω_{Bt} and ω_{Bb}

The beam stop is mounted on a linear stage; hence its distance from the sample position varies in Z. However, the collision angles can be easily updated since any change in Z results in a change in angles ε and ζ.

SUMMARY

The shadow model has been visually compared against a set of recorded images and found to be similar. The beamline is still in the early stages of commissioning and detailed analysis of the shadowing data is yet to be performed. This model will be the basis of the crystallographic strategy software currently being developed by Global Phasing Limited, which will take both collisions and shadowing into account.

The collision model was initially verified by manually rotating the kappa and omega axes to different angles in the CAD assembly. Thorough tests have been later performed on the installed system and the model has been found to be accurate. A safety margin of 6 mm has been added to the outer boundary or profile of the objective lens, beam stop and backlight to accommodate for the centering offsets and minor misalignments.

The model has been easily adapted for calculating the shadowing of other goniometers such as the SmarGon on standard detectors with flat surfaces at Diamond.

ACKNOWLEDGEMENT

We would like to thank the team of engineers, scientists and technicians mainly Ramona Duman, Dave Butler, Kamel El Omari and Vitaliy Mykhaylyk for their extensive support during collision testing.

REFERENCES

[1] A. Wagner, R. Duman, K. Henderson and V. Mykhaylyk, "In-vacuum long-wavelength macromolecular crystallography", *Acta Cryst.*, D72, p. 430-439, Jan. 2016.

[2] Rotation About an Arbitrary Axis in 3 Dimensions, http://inside.mines.edu/fs_home/gmurray/ArbitraryAxisRotation

[3] Ray tracing primitives, http://www.cl.cam.ac.uk/teaching/1999/AGraphHCI/SMAG/node2.html

Content from this work may be used under the terms of the CC BY 3.0 licence (© 2016). Any distribution of this work must maintain attribution to the author(s), title of the work, publisher, and DOI.

ISBN: 978-3-95450-188-5 doi:10.18429/JACoW-MEDSI2016-WEBA01

Content from this work may be used under the terms of the CC BY 3.0 licence (© 2016). Any distribution of this work must maintain attribution to the author(s), title of the work, publisher, and DOI.

NOSTRADAMUS AND THE SYNCHROTRON ENGINEER: KEY ASPECTS OF PREDICTING ACCELERATOR STRUCTURAL RESPONSE*

C. Preissner†, H. Cease, J Collins, Z. Liu, J. Nudell,
Advanced Photon Source, Argonne National Laboratory, Argonne, IL, USA
B. N. Jensen, MAX IV Laboratory, Lund University, Lund, Sweden

Abstract

Multibend Achromat (MBA) synchrotron designs are placing stringent mechanical tolerances on the magnet support systems. At the APS-U the magnet-to-magnet vibration tolerances are about 10 nm. [1]. Timelines, installation requirements, and budgets constrain the resources available for prototyping and physical testing. Reliance on FEA to predict dynamic response is paramount in insuring the tolerances are met. However, obtaining accurate results from a magnet support structure FEA is not as simple as analysing the CAD model of the structure.

The 16th century author Nostradamus published a collection of prophecies that since his time, have been held up as predictions of various world events. While it is attractive to think his collection of short poems can be used to foretell the future, in reality it is only the vagueness and absence of any dates that make them easy to apply in a posthoc basis. Arguably, a similar statement can be made about the use of FEA in predicting accelerator support response. In this paper the important contributors to FEA dynamic modelling will be discussed along with techniques that can be used to generate necessary data for models that can accurately predict response.

INTRODUCTION

Background

Numerous multi-bend achromat (MBA) synchrotrons are either under construction or planned [2, 3]. At the Advanced Photon Source (APS) a major upgrade is in the planning stages. The electron beam in this machine will have much smaller transverse dimensions, and consequently more stringent beam stability requirements than the current APS. In addition, the X-ray beams will be focused to ever smaller dimensions, placing more stringent stability requirements on the X-ray source point [4]. Both of these requirements result in magnet-to-magnet vibration tolerances on the order of 10 nm and magnet group-to-magnet group (girder) requirements of a few tens of nanometers.

Along with challenging physics requirements, facility, budget, and logistic constraints cause significant pressure on the design process. For example, the APS-Upgrade (APS-U) project spans multiple years, though the installation and commissioning phase is to take place over a single 12-month dark period. Critical engineering choices need to be made very early in the process. The combination of the physics and project planning constraints push engineering designs in new directions for which limited performance data are available. In the context of magnet support structures, predicting the modal and vibration response before construction are viewed by the APS-U engineering team as essential to completing the magnet support structure designs [5-7] and meeting the machine requirements in and economical and timely manner.

The goal is to have a validated process and set of models, by which the important magnet support system structural response characteristics such as natural frequency, vibration response, static deflection, and thermally-induced distortion can be predicted for each of the magnet support systems. Ideally, the testing of physical prototypes is reduced to an exercise of design verification rather than one of discovery, as shown in the workflow in Figure 1. This level of simulation is commonly referred to as *virtual prototyping* [8]. It is already being done in the automotive sector [9].

While the motivation for virtual prototyping in the automotive or aerospace sectors may be primarily one of reducing the cost of testing and of serial production products, there is certainly significant desire to produce products that have higher levels of out-of-the-box performance than ever before. This is the similarity to the synchrotron world—to engineer and build magnet support structures that have higher levels of mechanical stability than previous generations of synchrotrons.

Analytical and computational simulation have been used extensively in the design of synchrotron components, primarily in the area of absorbers and optics. Thermal finite element analysis (FEA) models for synchrotron radiation absorbers or optics depend on five important aspects: component geometry, boundary condition definition, material properties, thermal load profile and cooling fluid conditions/properties. These have all been characterized sufficiently such that performance can be well predicted from computational models. In fact, recent work has continued to refine the failure criteria through a better understanding of absorber failure mechanisms. The same level of a priori computational confidence is not currently possible in the arena of synchrotron structural dynamics.

* Work supported by: Argonne is managed by UChicago Argonne, LLC, for the U.S. Department of Energy under contract DE-AC02-06CH11357.
† email address: preissner@aps.anl.gov

ISBN: 978-3-95450-188-5 doi:10.18429/JACoW-MEDSI2016-WEBA01

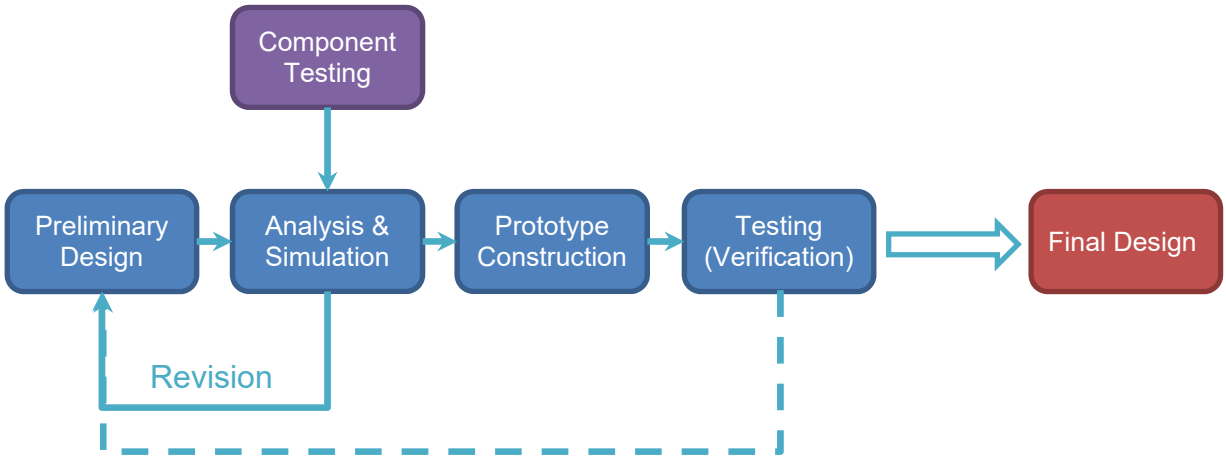


Figure 1: An example of the design workflow. If the loop can be reliably closed between simulation and design (solid arrow), then reliance on feedback from testing to design (dashed arrow) can be reduced. The enabler for this to happen is strategic component testing and correct use of the identified properties in the analysis and simulation step.

The use of analytical and computational simulation in the structural dynamics area for synchrotron components differs from the thermal area. While in a typical optic or absorber thermal analysis the important area of the model does not extend beyond the boundaries of a single part, in a structural dynamics analysis, the model involves multiple parts and interconnections. Component geometry, mass, stiffness, and damping all play a role in the system behavior.

The Problem: Nostradamus We Are Not…

Simply using a CAD model of a complete magnet support structure for the starting point of either a modal or vibration response analysis will result in over predictions that are far from the measured result. For instance, a test article for the APS-U magnet support structures is shown in Figure 2. The geometry, mass, and material properties are well known for the girder, magnets and plinth. In fact, if a modal analysis were conducted using the CAD model for the girder and magnet assembly (*not including the support and alignment mechanism*), the results would be quite reasonable.

In contrast, if the same type of modal analysis were run for the whole test article, the results could over predict the natural frequencies by as much as 100%. A random vibration analysis would be even more erroneous. This is because the modal response of the assembly is highly dependent upon the stiffness of the support mechanism and the vibration response is highly dependent on both the stiffness and damping of the support mechanism. Using a CAD model of the support mechanism as the FE analysis model (just geometry, no accounting for interfaces) significantly over estimates the stiffness of the support and has no true relation to the damping present in the support. These properties are dependent not only on the component geometry but friction, loads, and all the minute interfaces.

A modal FEA model based on the CAD data can be tuned in a posthoc basis to match the experiment. One way this could be done is that the Young's modulus of the support mechanisms might be altered such that simulation and experiment modal results can be more closely matched. Drawbacks include difficulty in determining the appropriate changes in modulus and material damping and difficulty in incorporating directional and load dependency. Most importantly, the results obtained with model tuning are obtained only after testing a complete structure, and are then only good for a specific case. Due to the posthoc nature of this method, it is difficult to generalize this process to other designs, much as it is difficult to generalize Nostrodamus' predictions to future events. Virtual design iteration as described in Figure 1 cannot be done.

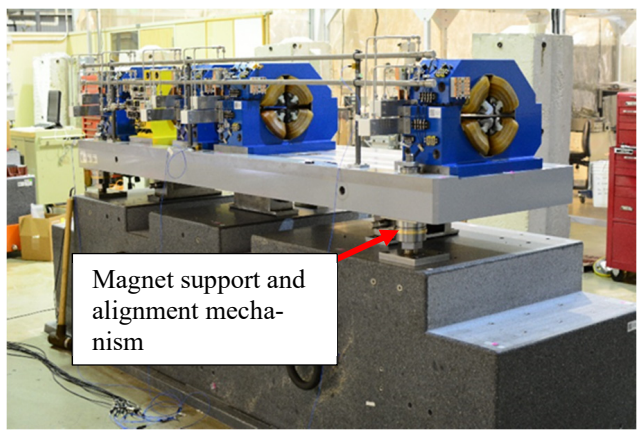


Figure 2: APS-U magnet support test article. The arrow points to one of the supports. Below the support and alignment mechanism is the plinth and above the support and alignment mechanism are the girder and magnets. A thin epoxy grout layer couples the assembly to the floor.

A general methodology is needed that can a) provide stiffness and damping properties of any support mechanism, and b) incorporate those properties into an analysis model of the complete magnet support system. This paper outlines a method by which the stiffness and damping of

Content from this work may be used under the terms of the CC BY 3.0 licence (© 2016). Any distribution of this work must maintain attribution to the author(s), title of the work, publisher, and DOI.

ISBN: 978-3-95450-188-5 doi:10.18429/JACoW-MEDSI2016-WEBA01

Content from this work may be used under the terms of the CC BY 3.0 licence (© 2016). Any distribution of this work must maintain attribution to the author(s), title of the work, publisher, and DOI.

any support mechanism can be quantified in a phenomenological manner and these data subsequently incorporated into analysis models. Model validation is also discussed.

METHODS OF PROPERTY ESTIMATION

In the most general sense the support system can be considered as in Figure 3. The support and alignment mechanism can be represented by stiffness and damping matrices.

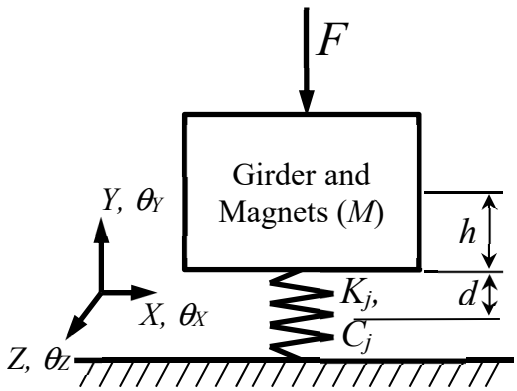


Figure 3: A generalized view of a magnet support mechanism. The support alignment mechanism is represented by the stiffness K_J and the damping C_J. F are the applied forces. h is the height of the center of mass above the support and d is the half-height of the support mechanism.

The equations of motion describing the system are:

$$F = \mathrm{M}\ddot{\mathrm{x}} + \mathrm{C}\dot{\mathrm{x}} + \mathrm{K}\mathrm{x}. \quad (1)$$

Where the coordinates are described by:

$$x = [X \quad Y \quad Z \quad \theta_X \quad \theta_Y \quad \theta_Z]. \quad (2)$$

In the equations of motion, the mass matrix is diagonal (mass centered coordinate system). The stiffness and damping matrices are symmetric. The most general form of the *support* stiffness and damping matrices (K_J and C_J) are of the form:

$$K_J = \begin{bmatrix} K_{XX} & K_{XY} & K_{XZ} & K_{X\theta x} & K_{X\theta y} & K_{X\theta z} \\ & K_{YY} & K_{YX} & K_{Y\theta x} & K_{Y\theta y} & K_{Y\theta z} \\ \vdots & & K_{ZZ} & K_{Z\theta x} & K_{Z\theta y} & K_{Z\theta z} \\ & & & K_{\theta X} & K_{\theta x\theta y} & K_{\theta x\theta z} \\ \vdots & \iddots & & & K_{\theta y} & K_{\theta y\theta z} \\ & \cdots & & \cdots & & K_{\theta Z} \end{bmatrix}_{sym} \quad (3)$$

Notice the off-diagonal coupling terms, relating translation-translation, rotation-rotation, and translation-rotation. It is reasonable in the case of the magnet support system to neglect the coupling terms, resulting in a diagonal stiffness matrix. In the case of a diagonal K_J, the stiffness matrix K becomes:

$$K = \begin{bmatrix} K_{XX} & 0 & 0 & 0 & 0 & (h+d)K_{XX} \\ 0 & K_{YY} & 0 & 0 & 0 & 0 \\ 0 & 0 & K_{ZZ} & -(h+d)K_{ZZ} & 0 & 0 \\ 0 & 0 & -(h+d)K_{ZZ} & K_{\theta X} + (h+d)^2 K_{ZZ} & 0 & 0 \\ 0 & 0 & 0 & 0 & K_{\theta y} & 0 \\ (h+d)K_{XX} & 0 & 0 & 0 & 0 & K_{\theta Z} + (h+d)^2 \end{bmatrix} \quad (4)$$

Three methods were considered for determining the stiffness and damping of the support mechanism, that is K_J and C_J. The methods, merits, and results for each are discussed below.

"Constitutive" FE Modeling

Virtual single-axis testing can be used in FE modeling to estimate the support stiffness. This sub-modeling approach is "constitutive" in the sense that all parts and interfaces are modeled. allows all of the interfaces to be captured, including the threads and the spherical washer geometry. An example of a support post similar to those used in the MAX IV design [10] and one of designs considered for the APS-U is shown is shown in Figure 4.

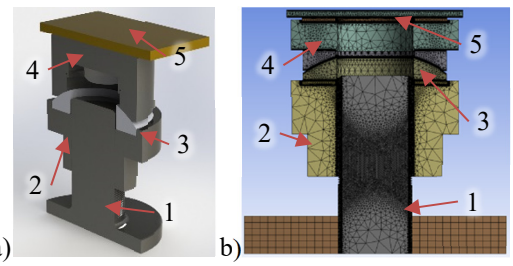


Figure 4: Views showing a) a cutaway of the MAX IV support post, and b) the FEM of the same part. The parts are: 1-post, 2-adjusting nut, 3-sperical washer set, 4-spacer, and 5-sliding plate. The dark areas in view b) are the interfaces and have high mesh density.

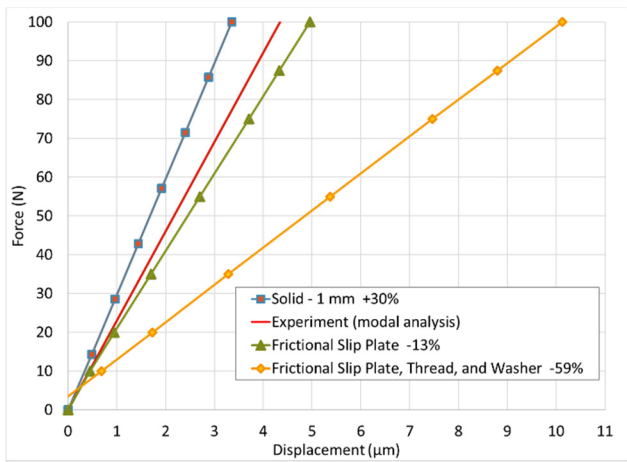


Figure 5: Chart showing the results from three different virtual stiffness tests compared the stiffness value determined from an experiment. Squares – solid model 1mm elements, Triangles – friction only at slip plate, Diamonds – friction at all interfaces, No marker – experiment.

Three of these posts are used to support and align the magnets. In order to estimate the stiffness of this support unidirectional virtual testing was carried out with the FE model shown in Figure 4b. The vertical and transverse stiffness (K_{XX}, K_{YY}, and K_{ZZ}) were to be determined by first applying a vertical load equal to the magnet weight. Then, a vertical or transverse load were applied and the

ISBN: 978-3-95450-188-5 doi:10.18429/JACoW-MEDSI2016-WEBA01

displacement probed. Results for the lateral stiffness are shown in Figure 5. The experimental measurement is considered to be the target stiffness. It can be seen that the solid model, one where the interfaces are not modelled, over predicts the stiffness (steeper slope). Whereas it can be seen that in the frictional model the stiffness is dependent on the number of frictional interfaces. Not shown here are the dependence of the stiffness upon element size for the solid model and upon friction coefficient and preload for the frictional model. In short, this result confirms the over-prediction of a solid model (regardless of element size). The constitutive model presents the opposite problem of under prediction. Other than a negative correlation to the number of frictional interfaces and a positive correlation to friction level, this under prediction is not readily understood. The conclusion is that while convenient to implement, it would not be possible to use this method to estimate support stiffness without prior measurement for calibration.

Static Testing

Conventional static stiffness testing was investigated. Figure 6. Fixturing was designed to allow axial and lateral stiffness measurements. For each type of measurement, preload equal to the weight force from the magnet assembly was applied. Then, an Instron machine was used to apply the load and record the displacements.



Figure 6: A post-type support installed in an Instron testing machine for lateral stiffness testing.

This type if testing is typically limited to linear measurements. It was not possible to measure torsional stiffnessses in this manner. The vertical and transverse stiffness (K_{XX}, K_{YY}, and K_{ZZ}) obtained appeared reasonable in form. However, when used in a FE model and the resulting system dynamics did not match the experiment

Dynamic Testing

The dynamic test method involves constructing a test setup similar to that shown in Figure 3. The practical realization of this is shown in Figure 7. In the dynamic testing a single support is used and a test mass is installed on top of the support. Equation (1) describes the system and the stiffness matrix is as in equation (4). Both large (~2900 kg) and small (~120 kg) test masses were used. The test mass is symmetric and the support is known to be centered under the mass because it was balanced. A hammer with integral force transducer is used to impact the assembly and the response is measured at multiple points with a set of triaxial accelerometers.

Dynamic testing has a few advantages over the constitutive FE and static testing approaches. First, the whole stiffness matrix can be determined if desired. Whereas the FE and static approaches require distinct test for each stiffness value. The dynamic approach can use one set of measurements to extract all of the stiffnessses. There are two basic ways in doing dynamic testing, a modal approach and a frequency response function-based (FRF) approach [11].

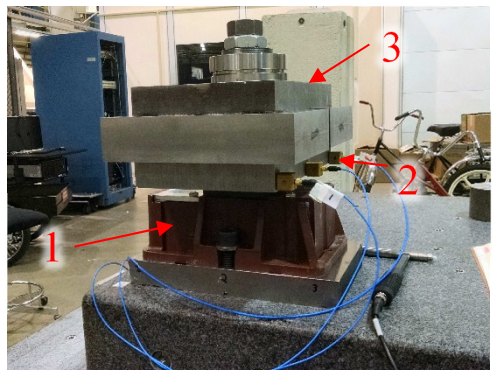


Figure 7: Dynamic testing setup for wedge jack-type support (Unisorb RK-IV is shown). 1-jack and base, 2-accelerometers (hammer on table), and 3-test mass.

The modal approach was used for this work. It is important to choose the test mass such that it is rigid in the frequency range of interest. Another important consideration is that the base of the isolator is “fixed”. Alternatively, this test could be performed with free boundary conditions. In the modal approach an experimental modal analysis (EMA) was conducted and the six rigid body modes were identified. The natural frequencies, mode shapes, and damping were then used along with the equations of motions (1), with diagonal stiffness matrix (4), in a Matlab script to solve for the support stiffnesses. As a check for self-consistency, a FE model of the test was built using the identified stiffness data and a modal analysis was run. The model was found to be in agreement with the experiment.

APPLICATION OF PROPERTY DATA

Property Usage

Regardless of how the support properties are obtained these data need to be incorporated into models of the complete support system to be useful. This overall model could be analytical, or as in this paper, a FE model. In the case of the FE model, each type of FE software typically has discrete stiffness elements. Through the use of discrete stiffness elements, the stiffness matrix can be entered directly. In this manner, a simple testing method can be used to generate data that can then be used in a variety of magnet support structures to investigate and predict performance. It is important to note that this same analysis mode cound not

Content from this work may be used under the terms of the CC BY 3.0 licence (© 2016). Any distribution of this work must maintain attribution to the author(s), title of the work, publisher, and DOI.

ISBN: 978-3-95450-188-5 doi:10.18429/JACoW-MEDSI2016-WEBA01

Content from this work may be used under the terms of the CC BY 3.0 licence (© 2016). Any distribution of this work must maintain attribution to the author(s), title of the work, publisher, and DOI.

Model Validation

The method and data were validated by comparing the results from a free boundary condition, experimental modal analysis conducted on a prototype magnet support system, shown in Figure 8. Free boundary conditions are the easiest to create.

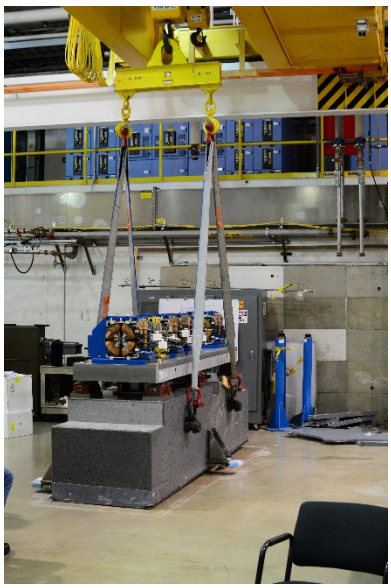


Figure 8: Setup for the free boundary condition, EMA conducted on the ~10000 kg APS-U magnet support prototype. The whole assembly was hung from an overhead crane. The support dynamics were sufficiently lower in frequency than the structural dynamics such that they did not confound the identification of these dynamics.

The test was conducted in a manner similar to the single-support test. A large instrumented hammer was used to excite the structure and the response was measured in multiple locations on the structure. Commercial modal analysis software was used to identify and visualize the natural frequencies and mode shapes.

A FE model of the test setup was also constructed in ANSYS. Discrete stiffness elements were used to incorporate the support stiffness identified in the single-support test. A modal analysis was run with free boundary conditions. The resulting natural frequencies and modeshapes were then compared to the natural frequencies and modeshapes from the EMA as shown in Table 1.

Table 1: Comparison of EMA and FEA Obtained Natural Frequencies

	Mode			
	1	**2**	**3**	**4**
EMA	64 Hz	91 Hz	130 Hz	137 Hz
FEA	67 Hz	90 Hz	122 Hz	137 Hz
% diff.	5	1	6	0

It can be seen that the results from the experiment and finite element model compare well. The jack stiffnesses can also be incorporated in other support structure models for which tests have not been done or are not planned.

CONCLUSION

We have developed a testing and modeling process that "closes the loop" on the design-analysis-testing workflow as shown in Figure 1. Establishing this process provides confidence in simulation results and enables the exploration of many different designs using the same components.

ACKNOWLEDGMENT

The authors would like to acknowledge the assistance of Josh Abraham and the Argonne riggers and Bruce Hoster and the APS machine shop In addition we thank Dr. Sheldon Mustovoy at the Illinois Institute of Technology for his assistance with static testing.

REFERENCES

[1] G. Decker, "Design Study of an MBA Lattice for the Advanced Photon Source," *Synchrotron Radiation News*, 27(6), 13-17. doi:10.1080/08940886.2014.970932 (2014).

[2] E. S. Reich, "Ultimate upgrade for US synchrotron." *Nature*, 501(7466), pp.148-149 (2013).

[3] M. Borland, "Ultra-Low-Emittance Light Sources," *Synchrotron Radiation News*, 27(6), 2-2. doi:10.1080/08940886.2014.970927 (2014).

[4] J. Maser *et al.*, "A Next-Generation Hard X-Ray Nanoprobe Beamline for In Situ Studies of Energy Materials and Devices," *Metallurgical and Materials Transactions* A, 45A(1), 85-97, doi:10.1007/s11661-013-1901-x (2014).

[5]-J. Collins *et al.,* "Preliminary Design of the Magnet Support and Alignment Systems for the APS-U Storage Ring," presented at MEDSI2016, 11-16 Sept. 2016, Barcelona Spain, paper MOPE34.

[6] Z. Liu *et al.*, "Optimization for the APS-U Magnet Support Structure," presented at MEDSI2016, 11-16 Sept. 2016, Barcelona Spain, paper TUPE44.

[7] J. Nudell *et al.*, "Preliminary Design and Analysis of the FODO Module Support System for the APS-U Accelerator," presented at MEDSI2016, 11-16 Sept. 2016, Barcelona Spain, paper MOPE32.

[8] D. LaCourse, "Virtual Prototyping Pays Off", Retrieved from `http://www.cadalyst.com/manufacturing/virtual-prototyping-pays-9774` , (2003).

[9] S. Birch and B. Visnic, "Jaguar, Exa say simulation to eliminate prototypes by 2020", *Automotive Engineering, SAE International* 3: 3 (2016).

[10] M. Johansson, B. Anderberg, and L.-J. Lindgren, "Magnet design for a low-emittance storage ring", *Journal of Synchrotron Radiation*, 21(5), 884-903. doi:10.1107/S160057751401666X (2014).

[11] P. J. Wyatt Becker, R. H. Wynn, Jr., E. J. Berger, and J. R. Blough, "Using Rigid-Body Dynamics to Measure Joint Stiffness," *Mechanical Systems and Signal Processing,* 13(5), pp. 789-801, doi:10.1006/mssp.1999.1232 (1999).

ISBN: 978-3-95450-188-5 doi:10.18429/JACoW-MEDSI2016-WEBA03

RECENT PROGRESS ON THE DESIGN OF HIGH-HEAT-LOAD COMPONENTS

S. Sharma†, C. Amundsen, F. DePaola, F. Lincoln, J. Tuozzolo, NSLS-II, Brookhaven National Laboratory, NY, USA

Abstract

A new design was recently proposed for the high power masks and slits of the frontends at the 2014 MEDSI Conference. The main features of the new design are integrated knife edges in high conductivity copper alloys, interception of the photon beam only on horizontal surfaces, replacing Glidcop with readily available CuCrZr, and thermal optimization with internal fins. Numerous components based on this design have been built for NSLS-II frontends and some of the design features have been incorporated into other high-heat-load components such as beamline masks and crotch absorbers. In this paper we describe recent progress at NSLS-II in further advancing this design approach by FE analysis, fabrication and testing.

INTRODUCTION

High-heat-load (HHL) components in light sources have usually been made from GlidCop brazed to stainless steel (SS) flanges. GlidCop has high thermal conductivity comparable to that of OFHC copper, but it can also retain a large fraction of its yield strength after brazing. A new design approach was recently presented [1] that allows a wide flexibility in the design of HHL components. The new designs are cost-effective and eliminate long lead-time for procurement [2]. The main features of the new design and their advantages are as follows:

1. **Integral Conflat Flanges**: Conflat flanges are made directly in high strength copper alloys (such as GlidCop and CuCrZr). This eliminates the expensive and time consuming process of brazing the main body of the HHL components to SS Conflat flanges.
2. **Alternate Copper Alloys**: The elimination of brazing allows the use of other hard copper alloys besides GlidCop (specifically, CuCrZr) which are less expensive and are readily available.
3. **Vertical Beam Interception**: Photon beams are intercepted only vertically (on horizontal surfaces). This leads to a common design for all HHL components because the vertical beam size is usually the same. In addition, the design of these components for canted beamlines is considerably simplified since there is no beam interception horizontally.
4. **Internal Fins**: Fins are machined on the inside (beam intercepting) surfaces which significantly improve the thermal efficiency of the components while trapping the scattered beam.

This new design approach is already under implementation not only at NSLS-II but also at other light source facilities [3, 4]. The progress made at NSLS-II is described in the following sections.

† sharma@bnl.gov

BM/3-PW FE COMPONENTS

One bending magnet (BM) and two 3-pole wiggler (3-PW frontends (FEs) at NSLS-II saw the first full scale implementation of the new design. Approximately 25 components consisting of masks, slits and photon shutters were installed in these frontends in May 2016. They have all been performing well as per specifications. Although intercepting comparatively low beam power, they provided the proof of principle of using CuCrZr components with built-in Conflat flanges.

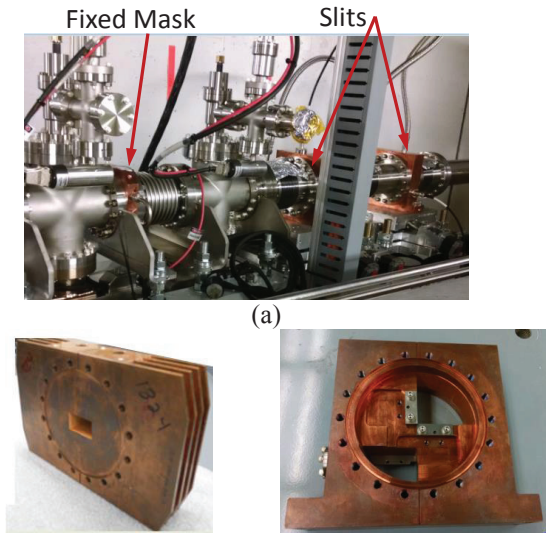


Figure 1: A 3-PW partial FE at NSLS-II, (a) a fixed mask and a pair of slits, (b) air-cooled fixed mask, (c) water-cooled slit.

A partial 3-PW FE is shown in Fig. 1-a consisting of a fixed mask and a pair of slits. Details of the fixed mask and the slit are depicted in Fig. 1-b and Fig. 1-c, respectively. Because of low beam power the fixed mask uses fins for natural convection (air) cooling eliminating the need for flow meters and associated controls. The slits are water cooled for thermal stabilization of the beam aperture. Photon shutters are designed as vertically movable masks. During the pre-installation vacuum processing some of the components were found to have vacuum leaks. This was traced to manufacturing errors resulting in burrs at the knife edges [2].

ID FE AND BEAMLINE COMPONENTS

FE Photon Shutters and Slits

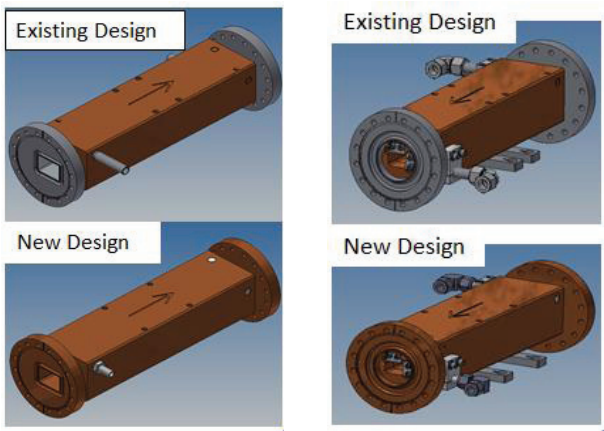
Existing designs of the ID FE photon shutters and slits can be easily replaced with the new designs of very similar overall dimensions. During the prototyping of the new design it was realized that a single piece construction, in which the flanges are machined directly into the main

Content from this work may be used under the terms of the CC BY 3.0 licence (© 2016). Any distribution of this work must maintain attribution to the author(s), title of the work, publisher, and DOI.

ISBN: 978-3-95450-188-5 doi:10.18429/JACoW-MEDSI2016-WEBA03

Content from this work may be used under the terms of the CC BY 3.0 licence (© 2016). Any distribution of this work must maintain attribution to the author(s), title of the work, publisher, and DOI.

body, would in some cases require excessive amount of machining. It was also found that weld joints in CuCrZr could be easily made [2] either by gas tungsten arc welding (GTAW) or by e-beam welding. This allowed CuCrZr flanges to be machined separately and then welded to the main body. Before welding the flanges water-cooling channels could also be gun-drilled in the main body parallel to the beam path as in the existing GlidCop designs. The two designs are compared in Fig. 2 for photon shutters and slits. As can be seen the main difference is that the flanges in the GlidCop designs, which require both brazing and welding, are replaced with welded-only flanges in the CuCrZr designs.

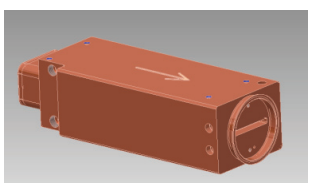


(a) (b)

Figure 2: A comparison of the existing GlidCop designs and new CuCrZr designs, (a) photon shutters, (b) slits.

Fixed Masks

The proposed alternate design for fixed masks in Ref. [1] encountered a challenging problem. The wire EDM process, in which sine waves are created on the top and bottom beam-intercepting surfaces, leaves a wire gap at the downstream end of the fixed mask (see Fig. 3). This gap was at least 0.5 mm with an optimum wire diameter of 0.3 mm. Normally the central part of the photon beam will exit through the nominal aperture, but if the beam is offset then a substantial amount of power (about 1 kW for NSLS-II IDs) can exit through this wire gap. The exiting power will melt even water-cooled copper at normal incidence.



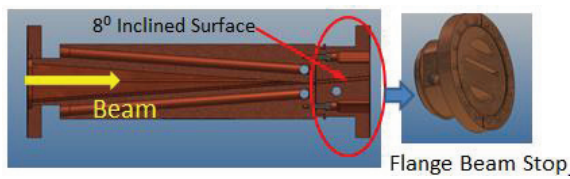
Fixed Mask Body



Upstream End Downstream End

Figure 3: The main body of the fixed mask and views from upstream and downstream ends.

In a ½-length prototype of the fixed mask shown in Fig. 3, the wire gap could not be closed even when a large force (~ 100,000 kgf) was applied. Three different options are being pursued as potential solutions of this problem. In the first option, that is already under implementation for one of the ID frontends, the downstream flange of the fixed mask (Fig. 4-a) is modified to act as a beam stop. It provides a beam intercepting surface at an 8° angle of incidence and has its own water-cooling channel. This flange beam stop is welded to the main body after sine-wave surfaces have been created by wire EDM but before the nominal aperture is machined. The nominal aperture is created in both the main body and the flange beam stop at the same time as the last manufacturing step. A full scale prototype of this design is shown in Fig 4-b.



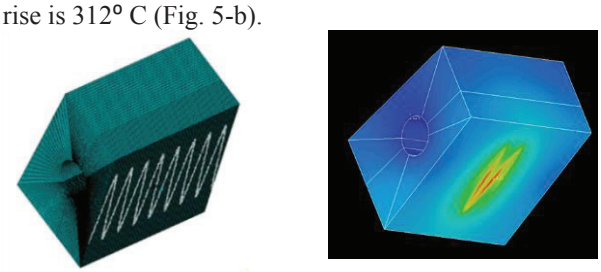
(a)



(b)

Figure 4: Fixed mask – Option 1, (a) model showing downstream flange beam stop, (b) full scale prototype.

An Ansys finite element analysis was performed to determine the temperature rise in the flange beam stop subjected to the beam power exiting through the sine wave gap. The ID beam has a peak power density of 100 kW/mrad^2 and the fixed mask is located at 17.7 m from the center of the ID. Only the central portion of the inclined surface and the water channel are modelled. Figure 5-a shows the Ansys model and the beam footprint. The sine-wave footprint becomes extended in the vertical direction because of 8° angle of inclination. The beam power has a Gaussian distribution with 68% of the power contained in ± 1σ. The resulting maximum temperature rise is 312° C (Fig. 5-b).

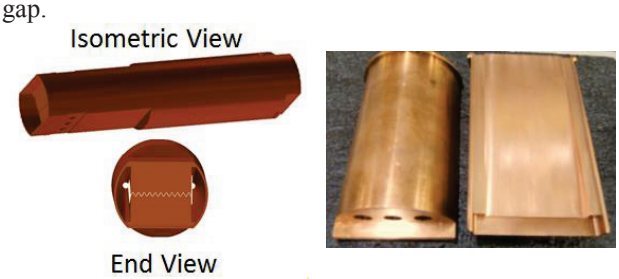


(a) (b)

Figure 5: Ansys finite element analysis of the flange beam stop, (a) Ansys model with beam footprint, (b) temperature contours; maximum T = 312° C.

ISBN: 978-3-95450-188-5 doi:10.18429/JACoW-MEDSI2016-WEBA03

In the second option, the side walls of the fixed mask are hollowed out (Fig. 6-a) by wire EDM at the same time as when the beam aperture is created. The thin side walls bend when a force is applied at the downstream end causing the wire gap to close. From an Ansys FE analysis a force of 2,200 kgf was found to be sufficient to close the gap.



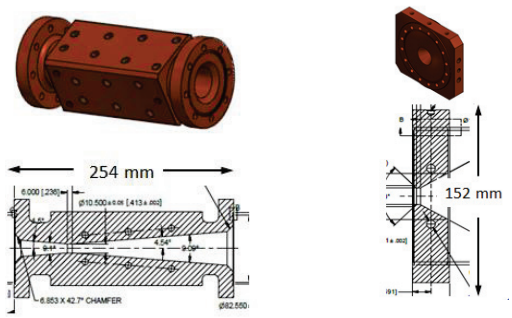
(a) (b)

Figure 6: (a) Option 2 – mask with thin side walls, (b) Option 3 – mask with top and bottom halves.

The third option takes advantage of the weldability of CuCrZr. The top and bottom halves of the masks (without the flanges) are first machined with the required features (see Fig. 6-b). The two halves are then joined by welding the two sides at the mid-plane. Finally, the upstream and downstream flanges are welded to complete the mask. All machining in this design can be done without using EDM process, making it possible to build long masks with arbitrary internal fin geometry.

Beamline Masks and Photon Shutters

The new designs are also applicable to beamline masks and photon shutters. Recently (in June 2016) one of the NSLS-II ID beamline had an urgent situation when one white beam mask and two pink beam masks were not received in time for beam commissioning because the supplier had GlidCop brazing problems. The designs were quickly revised based on the integral Conflat flange concept (see Fig. 7) and the parts were made within 10 days in an NSLS-II small machine shop.

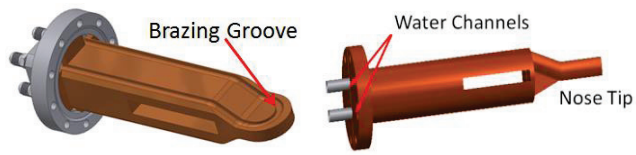


(a) (b)

Figure 7: Components of an NSLS-II ID beamline, (a) white beam mask, (b) pink beam mask.

SR ABSORBERS

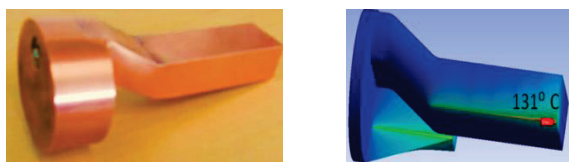
SR absorbers including crotch absorbers have been made at ESRF and TPS based on the new design [3, 4]. At NSLS-II temporary absorbers were installed in most of the dipole chambers because of difficulties in brazing bent copper tubes in semi-circular grooves of the GlidCop crotch absorbers (Fig. 8-a). In a new design, currently in prototyping phase, the crotch absorber is made as a single piece machined from a round bar of CuCrZr (Fig. 8–b). Two water channels, in which SS tubes with wrapped springs are inserted, provide counter-flow water cooling. The nose tip is bent after the insertion of tube with spring in the top channel.



(a) (b)

Figure 8: NSLS-II crotch absorber, (a) existing brazed - GlidCop design, (b) new single piece CuCrZr design.

In a partial prototype of the absorber, the nose tip with a spring-wrapped SS tube in the water channel was successfully bent (Fig. 9-a). Results of an Ansys thermal analysis for a dipole linear power density of 22 W/mrad at the nose tip (total intercepted power = 1.18 kW) are shown in Fig. 9-b. The maximum temperature at the nose tip is 131° C.



(a) (b)

Figure 9: Prototype evaluation of a new NSLS-II crotch absorber, (a) test bending of the nose tip, (b) temperature contours under the dipole beam power.

CONCLUSIONS

Recent progress at NSLS-II in the implementation, testing, and extension of the new design concept for HHL components have been described in this paper. The closing of EDM wire gap in FE masks has been discussed in detail. Ansys analyses have been performed to validate the new designs. FE and beamline components based on the new design have already proven to be cost-effective, reliable and easier for production. The design has been extended to SR absorbers at NSLS-II and other light source facilities.

ACKNOWLEDGMENT

The authors thank I-C Sheng (TPS), P. Marion (ESRF), and L. Volpe (SIRIUS) for many useful discussions.

REFERENCES

[1] Sharma et al., "A Novel Design of High Power Masks and Slits", *MEDSI2014*, Melbourne, Australia.

[2] F. DePaola et al., "Manufacturing of Photon Beam-Intercepting Components from CuCrZr", *this conference (MEDSI2016),* Barcelona, Spain.

[3] P. Raimondi, "ESRF EBS Accelerator Upgrade", *IPAC2016,* Busan, Korea.

[4] Private communication, I-C Sheng (TPS) and P. Marion (ESRF), 2016.

Content from this work may be used under the terms of the CC BY 3.0 licence (© 2016). Any distribution of this work must maintain attribution to the author(s), title of the work, publisher, and DOI.

ISBN: 978-3-95450-188-5 doi:10.18429/JACoW-MEDSI2016-WEBA04

Content from this work may be used under the terms of the CC BY 3.0 licence (© 2016). Any distribution of this work must maintain attribution to the author(s), title of the work, publisher, and DOI.

A DISCUSSION ON UTILIZATION OF HEAT PIPE AND VAPOUR CHAMBER TECHNOLOGY AS A PRIMARY DEVICE FOR HEAT EXTRACTION FROM PHOTON ABSORBER SURFACES

K. J. Suthar*, A. Lurie, P. Den Hartog, Argonne National Laboratory, Advanced Photon Source, USA

Abstract

Heat pipes and vapour chambers work on heat exchange phenomena of two-phase flow and are widely used for industrial and commercial applications. These devices offer very high effective thermal conductivities (5,000-200,000 W/m/K) and are adaptable to various sizes, shapes, and orientations. Although they have been found to be an excellent thermal management solution for laptops, satellites, and many things in-between, heat pipes and vapour chambers have yet to be adopted for use at particle accelerator facilities where they offer the possibility of more compact and more efficient means to remove heat from unwanted synchrotron radiation. As with all technologies, there are inherent limitations. Foremost, they are limited by practicality to serve as local heat transfer devices; heat transfer over long distances is likely best provided by other means. Heat pipes also introduce unique failure modes which must be considered.

INTRODUCTION

The heat pipe or, more-generally, a vapour chamber, is a device used to facilitate rapid heat transfer via phase-change. The process requires only a moderate temperature gradient and requires no additional power input. Typically, the heat pipe is used to move energy short distances from heat sources to heat sinks. [1,2] Because of the large transfer of heat associated with a phase change and rapid fluid flow that generally develops in these devices, heat exchange can be well beyond the limits seen in simple conduction or convection-based approaches. The operating principle is simple: A fluid in its liquid state enters the evaporative section of the pipe where it is heated, causing it to evaporate. The vapour then travels to the condensation section where it is liquefied and releases the heat it absorbed in the evaporative section.

Present designs for the APS Upgrade call for photon absorbers which are cooled strictly by convective water flow, as it has conventionally been done. However, consideration of the thermal stresses that will result from intercepting the concentrated beams of synchrotron radiation that are expected with the upgrade suggests that absorber design options, particularly material and geometry choices, will be severely limited. Particularly it is critical as there is a little space afforded by the new, higher-performing MBA lattices that are being evaluated. Another issue of concern is vibration. For required beam performance, exceptionally low levels of vibration are needed to ensure that the particle beam can be precisely steered though lattice magnets. Heat pipes would likely help to reduce vibration as they would reduce the amount of cooling water flow needed to maintain absorber surface temperatures to an acceptable level.

Presently, alternatives like heat pipes are being explored for manufacturing feasibility, economic operation, and ease of fabrication. To help answer these questions, analysis of a conceptual absorber utilizing heat pipes was performed. MATLAB was used to calculate heat pipe performance characteristics based on geometry and other factors and ANSYS was used to perform finite element thermal simulations. The results show that heat pipes can meaningfully improve thermal performance. There are, however, lingering concerns about the reliability of heat pipes for *accelerator applications* which cannot be addressed with such analysis.

Heat Pipe Limiting Factors

A number of design options should be considered when choosing to implement a heat pipe. One such option is the *chamber design*. Thin walls and conductive materials may help to enhance thermal transfer but such choices also may mean that the heat pipe is less mechanically robust. Another option is the *fluid type*. Fluids should be selected which optimize the heat transfer process but which also should not cause corrosion or other degradation of the wick and chamber materials. A number of experiments have established a commonly used list of compatible metal and fluid combinations. [3] There is considerable flexibility in the *wick design* as well. Wicks may consist of a mesh that liquids are squeezed through, they may consist of fibers that guide liquid along, or they may even consist simply of grooves built into the heat pipe wall. Each option offers a different set of advantages and disadvantages which should be weighed relative to the needs of the specific application.

There are a number of physical limitations which impact the transport capabilities in a heat pipe. These include: *capillary pressure difference* - which must exceed the limits introduced by the fluid flow in order to properly move and sustain the motion of the liquid and vapour [1]; s*onic limitations*, or *bottlenecking of fluid* at state change regions, which must be avoided [2]; *entrainment*, or the tendency for droplets of liquid to get caught up in the vapour flow can disrupt flow [2]; *boiling and bubble formation* in the liquid filled wick can also limit the heat capacity [1]. Many of these phenomena will be the result of excess heat capacity. Which limiting factor will limit

* Corresponding author: Suthar@anl.gov, +1(630) 252-4256

ISBN: 978-3-95450-188-5 doi:10.18429/JACoW-MEDSI2016-WEBA04

the performance of a heat pipe at a given temperature and that will depend on the heat pipe design. Often, graph as shown in Fig. 1 can be plotted for any given heat pipe to visualize the trends of the limitations. (MatLab program developed based on theory presented in [4-11]).
Moreover, there is a chemical compatibility issue with presence photon radiation and interaction with operating fluid, construction material at an operating temperature, [3] which is not discussed here.

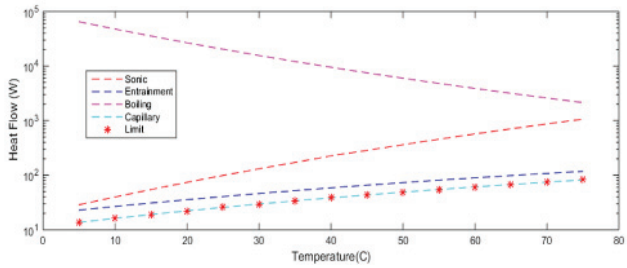


Figure 1: Example of a heat pipe limitations graph for approximately 6 mm diameter heat pipe containing water as working fluid.

FINITE ELEMENT ANALYSIS

In regards to the application, the simulated absorber has a V-shaped surface to intercept unwanted radiation and a rectangular hole to allow passage of useful radiation. Any heat pipe assembly would be used to move heat developed in the body of the absorber to a water-cooled heat sink. Fig. 2 shows the conceptual absorber geometry, computed power profile, and results from an ANSYS thermal simulation.

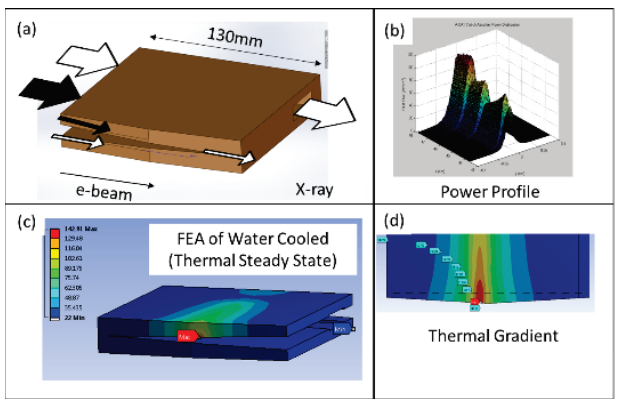


Figure 2: (a) conceptual absorber design for the APS-U (b) computed power profile, (c) FEA result, and (d) thermal gradient.

The four theoretical models were employed to assess performance improvement due to the heat pipe. In order to set establish conductivity values, custom materials were created and assigned to different parts of the assembly for each model.

(1) Pipe is modelled as a hyper conductive rod allowing identify other resistances to be quantified and an equivalent thermal conductivity for the heat pipe to be established.
(2) Multiple layers of the heat pipe are modelled using rule of thumb conductivity values to understand "worst case scenarios."
(3) Variations on the hyper-conductive rod and multiple layer model simulations are performed which treat temperature as a constant 2-5°C difference and alter the conductivities to achieve this.
(4) Treat the heat pipe's temperature difference as a few degrees constant. Set the contact thermal conductance to rule of thumb values and change the thermal conductivity of the heat pipe to achieve desired temperature change.

Generally, it was found that, regardless of the method used, a heat pipe reduces the temperature gradient on the absorber surface (Fig. 3). Some of the worst-cases scenarios showed only a marginal improvement in performance relative to the baseline design while others indicated a larger benefit is achievable, but all cases suggested that the heat pipe is a reasonable option in this application.

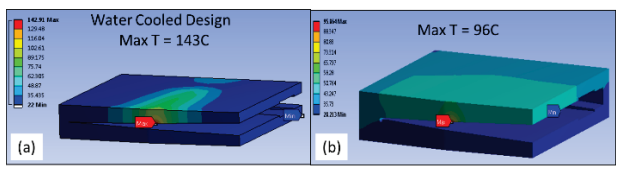


Figure 3: Comparison between water cooled design and heat pipe design.

Modelling Method Variation

In regards to the variations examined in each method, it is clear that the greatest focus on improving the system's thermal performance is creating large heat sink surface area around the high heat flux regions. This can be done via methods like increasing diameter and creating a greater density of heat pipes towards it. While other factors like the number of heat pipes and length are important, the effects can be small in comparison. It is also important to look at the design of the heat pipe itself, as the temperature performance is highly dependent on the thickness of the layers of wall, wick, and vapour.

RELIABILITY ISSUES

Start-up Conditions

Over time, of course, a heat pipe will gravitate towards a stable operating thermal gradient. However, during start up the temperature gradient may vary considerably. Conditions in the heat pipe leading to these variations include uniform distributions of the fluid, frontal distributions associated with a loss of the uniformity as the fluid reaches the condenser, and frontal distributions which lack condensable gases resulting in a sudden drop off in temperature. Initial temperature and the rate of start-up can be large factors in the development of such conditions. [7]

Failure is a legitimate concern under such conditions. Possibilities include: capillary pumping failure, boiling, dry-out from a frozen fluids restricting the self-replenishing nature, and entrainment of the liquid flow. In

Content from this work may be used under the terms of the CC BY 3.0 licence (© 2016). Any distribution of this work must maintain attribution to the author(s), title of the work, publisher, and DOI.

ISBN: 978-3-95450-188-5 doi:10.18429/JACoW-MEDSI2016-WEBA04

Content from this work may be used under the terms of the CC BY 3.0 licence (© 2016). Any distribution of this work must maintain attribution to the author(s), title of the work, publisher, and DOI.

addition, low thermal resistance at the condenser can overwhelm the system and enhance the probability that such failures will occur. There are ways to avoid some of these failure modes, for example utilizing an entrainment limit which exceeds sonic limit. However, solutions to such problems, and the degree to which they may be avoided are strongly dependent on the specific application.

Structural Stability

It is important to note that heat pipes may be required to withstand vibrations, shock, and severe temperatures. Copper and, to a greater extent, GlidCop™, may be used to construct a heat pipe with very thin walls owing to the strengths of those materials. The minimum thickness may be found using equation given below and it is assumed to be effective at the same bonding temperature as assumed in the base problem. [1]

$$t=(P\cdot r)/\sigma_r$$

In this case, σ_r is a tenth of the wall's ultimate tensile strength, P is the vapour pressure at the temperature, and r is the internal radius of the pipe walls.

Material Compatibility for Operation

One major aspect of designing the heat pipe system is material compatibility. Some fluid and solid combinations will result in chemical reactions that develop gas pockets which hamper or cease operation of the heat pipe [3]. Water is known to be generally compatible with copper however compatibility between water and GlidCop™-another common absorber material, is less established. The Acetone or some refrigerants would be some potential alternatives by being compatible with both [1]. However, these would offer notable downgrades in performance capabilities.

Contact Variance

Another major concern is the thermal interaction between the heat pipe and the absorber.

Manufacturing Concerns

Manufacturing heat pipes requires the development of a shell, the insertion of a wick, and filling the pipe with fluid as it is sealed off at one of the ends. Afterwards, some experimentation is need on any given heat pipe to ensure it performs as intended. At the same time, to achieve the design needed, the evaporative section needs to be built into the absorber itself for all the heat pipes. This also solves the question of how to connect the heat pipes to the absorber. The issue that arises with this is, considering the reliability of manufacturing one heat pipe is in doubt enough to call for basic tests on all of them, would see an assembly with dozens of heat pipes become a potential manufacturing difficulties to a considerable degree.

The precise precision of manufacturing methods can also generate heat pipe with different pressure in each product and it does offer enough to concerns to clarify and gauge how extensive potential complexities that arise from manufacturing process.

CONCLUSION

Heat pipes offer an attractive solution for efficient and compact transport of heat in photon absorber applications. Simulations show that heat pipes offer tangible improvements over conventional water cooling. However, a number of potential disadvantages should be weighed against the performance improvements. These include potentially more complex and costly fabrication, limited performance predictability, and reliability. Continued investigation is warranted, particularly as the requirements for next generation accelerators continue to become more challenging.

ACKNOWLEDGMENT

This work was supported in part by the U.S. Department of Energy, Office of Science, Office of Workforce Development for Teachers and Scientists (WDTS) and the Science Undergraduate Laboratory Internship Program (SULI). This research used resources of the Advanced Photon Source, a U.S. Department of Energy (DOE) Office of Science User Facility operated for the DOE Office of Science by Argonne National Laboratory under Contract No. DE-AC02-06CH11357.

REFERENCES

[1]. H. S. Lee, "Heat Pipes." *Advanced Thermal Design: Heat Sinks, Thermoelectrics, and Heat Pipes*. N.p.: Western Michigan University, n.d. 110-171. Print.

[2]. P. D. Dunn and D. A. Reay, *Heat Pipes*, 4th ed. Tarrytown, New York: Elsevier Science Inc, 1994.

[3]. D. Chisholm, *The Heat Pipe*. London, Great Britain: Mills & Boon Limited, 1971.

[4]. Jeremy Nudell, "MBA Vacuum System – Conceptual Design of Absorbers", Argonne National Laboratory, 2015. (available upon request)

[5]. C. C. Silverstein, *Design and Technology of Heat Pipes for Cooling and Heat Exchange*. Philadelphia: Hemisphere Publishing Corporation, 1992

[6]. A. Faghiri, *Heat Pipe Science and Technology*. Washington DC: Taylor & Francis, 1995

[7]. M.N. Ivanovskii, V.P. Sorokin, and I.V. Yagodkin, *The Physical Principles of Heat Pipes*, New York: Oxford University Press, 1982.

[8]. Z. Lu and B. Ma, "Equivalent Thermal Conductivity of Heat Pipes," *Frontiers of Mechanical Engineering in China*, vol. 3, Dec. 2008.

[9]. "When to Use Heat Pipes, HiK™ Plates, Vapour Chambers, and Conduction Cooling." *ACT Advanced Cooling Technologies*. Advanced Cooling Technologies, n.d. Web. 1 July 2015.

[10]. J. H. Rosenfeld and M. T. North, "Porous Media Heat Exchangers for Cooling of High-Power Optical Components", vol. 34, *Optical Engineering* (1995).

[11]. Y. A. Cengel and M. A. Boles, *Thermodynamics: An Engineering Approach*, 7th ed. New York: McGraw-Hill, 2011.

ISBN: 978-3-95450-188-5 doi:10.18429/JACoW-MEDSI2016-WECA03

EXPERIENCE WITH THE COMMISSIONING OF THE U15-UNDULATOR FOR SWISSFEL-ARAMIS BEAMLINE AND NEW DEVELOPMENTS FOR THE ATHOS BEAMLINE

P.Boehler†, H. Joehri, A.Keller, M.Locher, M.Bruegger, T.Schmidt, M.Calvi, L.Schulz
Paul Scherrer Institut, Villigen, Switzerland

Abstract

The development of the U15 undulator was presented at the Medsi conference 2012 in Shanghai. Meanwhile the undulatorline is finished. The presentation will explain the experience with the production, the assembling and the commissioning of the undulators. We succeeded to implement a robotic system, that did the final adjustment of all the magnets automatically. Therefore, we were able to reduce the time for the adjustment of the magnets dramatically. A whole loop with measuring, adjustment of the columns and final adjustment with the robotic system for the magnets takes 3 days. The presentation will explain these steps.

For the next beamline, we will profit from the experience of the U15 undulator development, but there are new requirements, because it will be a polarized undulator with a period of 38mm. We are developing a new arrangement of the drives, a further development of the magnet keepers and a vacuum pipe with only 0.20mm of wall thickness.

SWISSFEL PROJECT OVERVIEW

SwissFEL with electron energies of 5.8 GeV will have two undulator lines for hard- and soft X-rays. The first beamline is Aramis that will produce hard X-ray (7 – 1) Å

The second beamline will be Athos for soft X-rays.

ARAMIS UNDULATOR U15

Overview

Figure 3 shows the overview with the following main parts:

- Main frame in mineral cast
- Outer beam
- Wedge drive system
- Cam shaft mover
- Vacuum chamber
- I-beam with block keeper, magnets and poles
- Gap measuring system
- Columns
- Power and controls

† Pirmin.boehler@psi.ch

Main Parameters of U15 Undulator

- Magnetic length 3990mm
- Period 15mm
- Gap workspace 3 to 20mm
- K-values 1.0 to 1.8
- Vertical forces max. 27.4kN
- Magnet material Nd2Fe14Br + Diffused Dy

Changes

After the design, manufacturing and measuring the pre-prototype we had to change and add several things:

- Design and thickness of magnets/poles considering existing block-keeper design (Figure 1)
- Design of columns (Figure 2)
- Monitoring system of wedge drive
- Motor cooling
- Temperature stabilised assembling area
- FEM based column adjustment

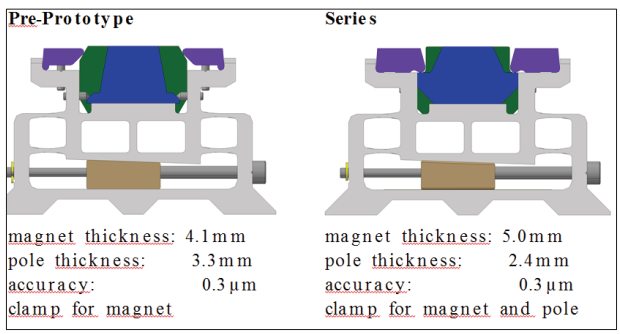


Figure 1: Keeper design changes.

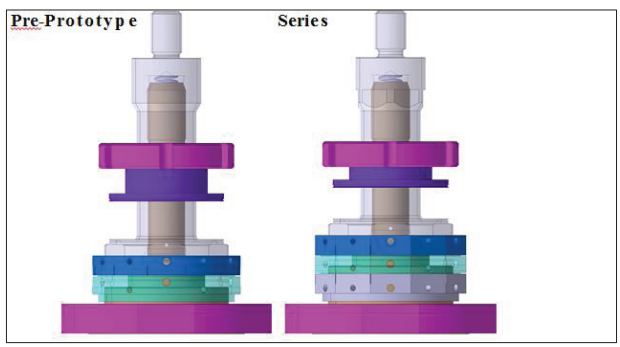


Figure 2: 2nd lock nut to stabilize the fix position. Adjustable range: ± 0.5mm. Accuracy: 1µm

Content from this work may be used under the terms of the CC BY 3.0 licence (© 2016). Any distribution of this work must maintain attribution to the author(s), title of the work, publisher, and DOI.

ISBN: 978-3-95450-188-5 doi:10.18429/JACoW-MEDSI2016-WECA03

Content from this work may be used under the terms of the CC BY 3.0 licence (© 2016). Any distribution of this work must maintain attribution to the author(s), title of the work, publisher, and DOI.

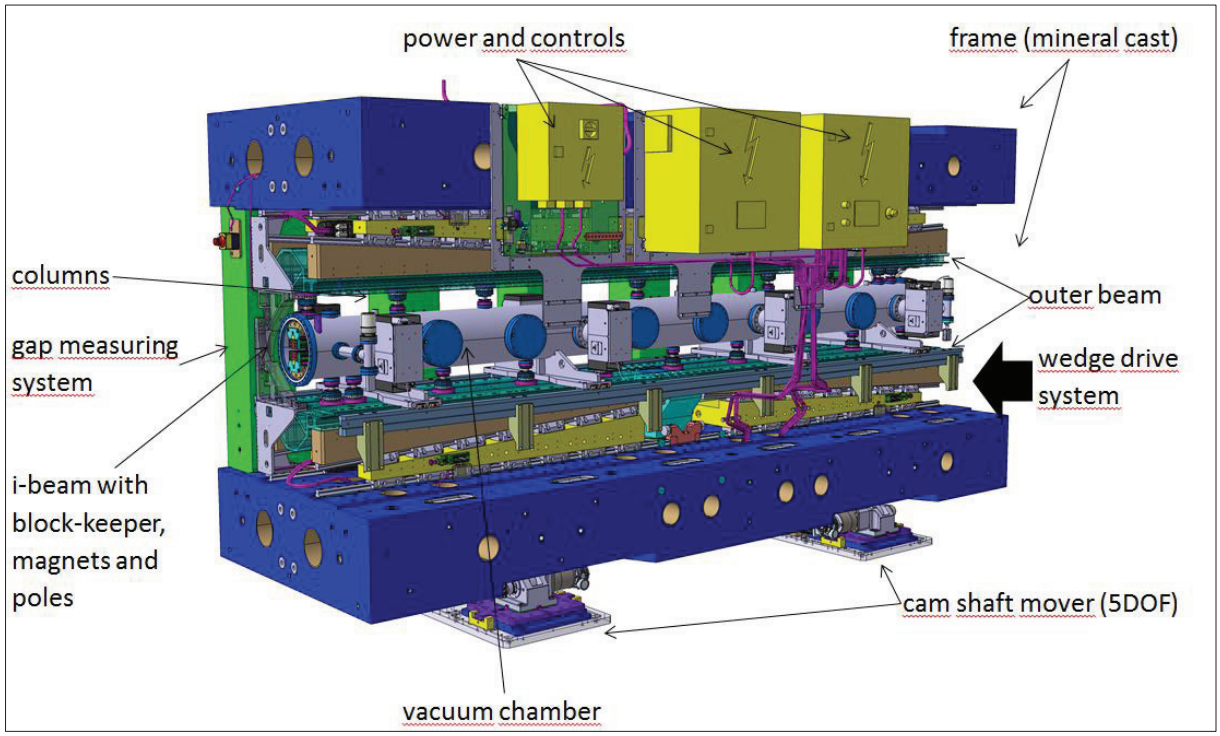


Figure 3: Overview of U15.

Measurements Benches

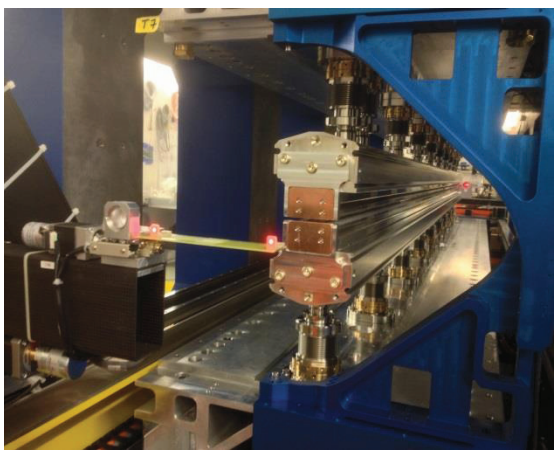


Figure 4: Measurement without vacuum tank.

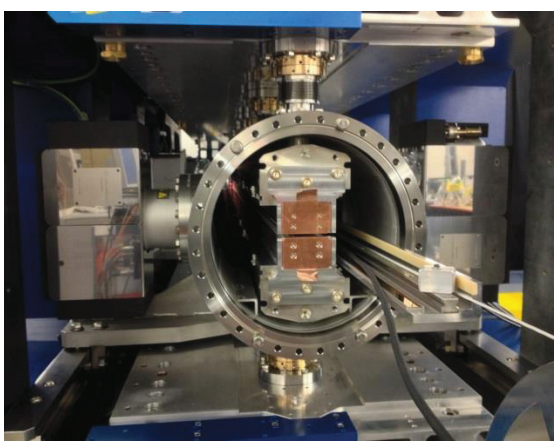


Figure 5: Measurement inside the vacuum tank.

The magnetic fields are measured with hall probes. They are driven from a linear motor and stabilized with a laser based control system. Trajectory and phase are measured and optimized without vacuum chamber (Figure 4). With a second system, that measures inside the vacuum tank, phase and calibration field are checked with different gaps (Figure 5).

Column Adjustment

FEM calculations are made for every column with the influence to the I-beam. These results were included in the algorithm for the optimization. The first step in the optimization adjustment of the columns (Figure 6 -8)



Figure 6: Adjustment of the columns.

ISBN: 978-3-95450-188-5 doi:10.18429/JACoW-MEDSI2016-WECA03

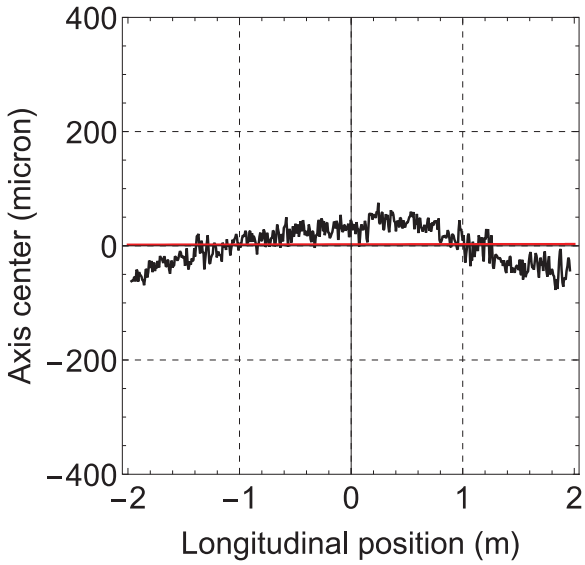


Figure 7: Magnetic field before the optimization.

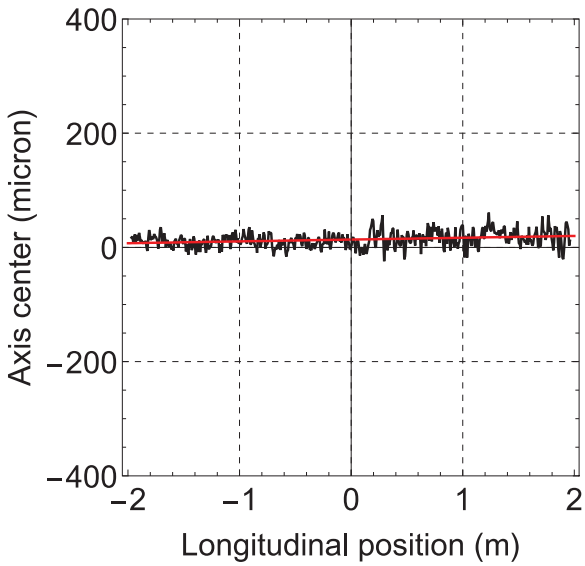


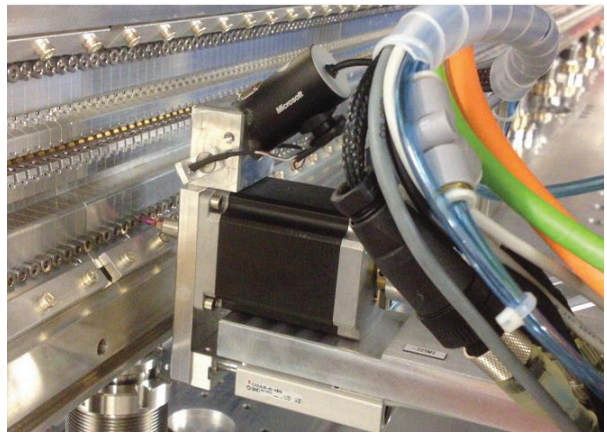
Figure 8: Magnetic field after the first optimization.

Automated Pole Height Adjustment

The pole heights are optimized with a robot system. With that system a complete optimization run takes between one and two hours.

It is a stepper motor that works as a screw driver. It sits on a pneumatic drive. With the pneumatic drive, the system checks when the screwdriver fits the screw.

With that system, every individual height of the magnets is adjusted (Figure 9).


Figure 9: Robot system for adjustment.

Optimization

The whole optimization is done in 3 steps without the vacuum chamber.

1. Optimization of the columns to straighten the axis (Figure 11: After first step)
2. First automated pole height adjustment (Figure 12 after 2nd step)
3. Second automated pole height adjustment (Figure 13 after 3rd step)

These steps are done in 3 days, instead of 1 or 2 month, which we needed in the past.

The phase error is different for different gaps. We optimize at a gap of 4mm (Figure 10)

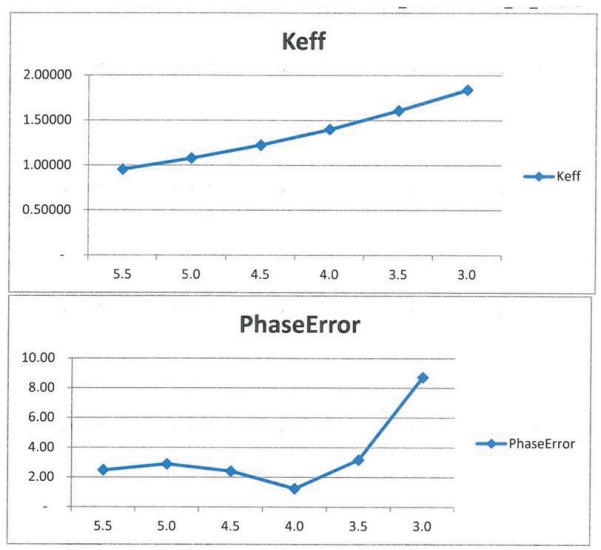


Figure 10: Keff and PhaseError for different gaps.

Content from this work may be used under the terms of the CC BY 3.0 licence (© 2016). Any distribution of this work must maintain attribution to the author(s), title of the work, publisher, and DOI.

ISBN: 978-3-95450-188-5 doi:10.18429/JACoW-MEDSI2016-WECA03

Content from this work may be used under the terms of the CC BY 3.0 licence (© 2016). Any distribution of this work must maintain attribution to the author(s), title of the work, publisher, and DOI.

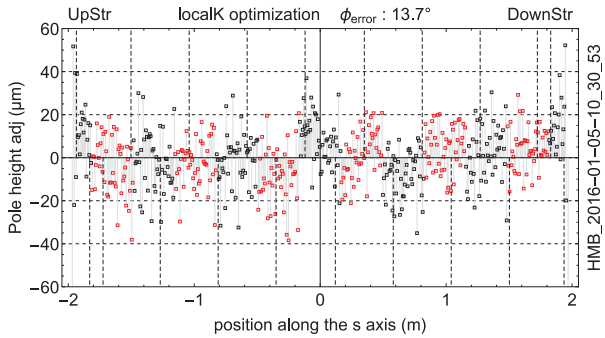


Figure 11: Measurement after first optimization.

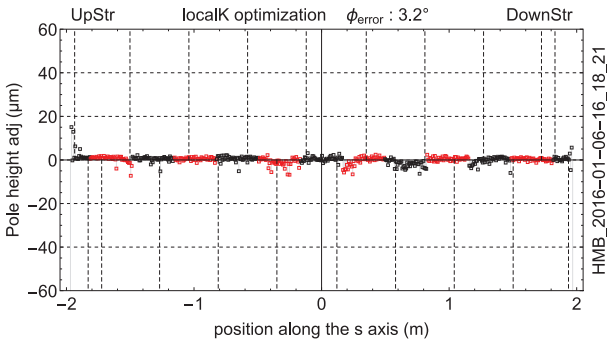


Figure 12: Measurement after second optimization.

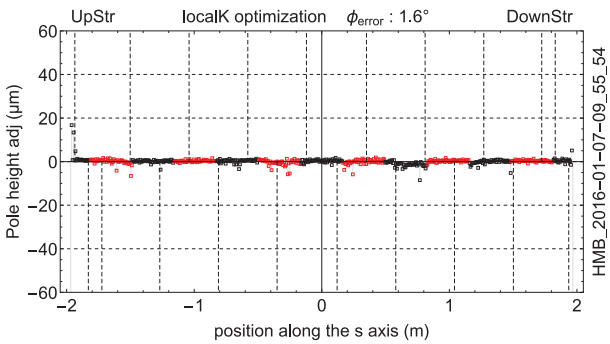


Figure 13: Measurement after third optimization.

Summary of Time Schedule

- Design from October 2008 – April 2014
- Pre-prototype from November 2010 – October 2013
- Series from July 2013 – September 2015
- Optimisation in the ID-laboratory from September 2015 - September 2016
- Installation in the tunnel starts in January 2016

ATHOS UNDULATOR UE38

The undulator for the Athos beamline will have e period of 38mm and an APPLE-X configuration (Figure 14)

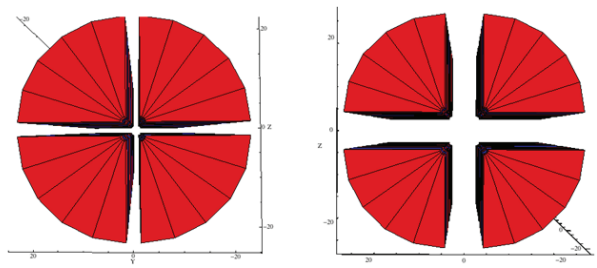


Figure 14: APPLE-X configuration.

Each of the 4 Magnetic bars has its individual drive. This gives the highest flexibility for different modes (Figure 15)

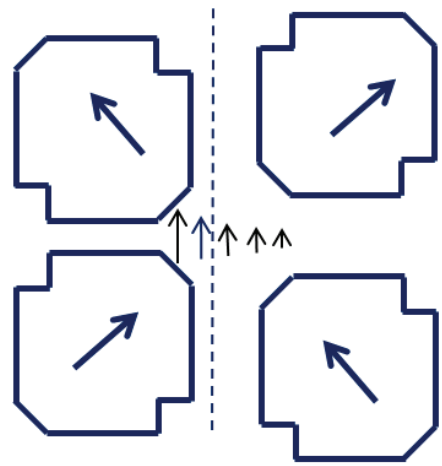


Figure 15: Highest flexibility.

The length of each module is 2m. The mechanism is mounted in a closed frame, which is made from cast iron. It is designed for maximum stiffness in all directions.

The drives for gap and shift are arranged orthogonal. This gives the advantage, that no combined movements of drives are needed. Also the measurement systems for gap and shift can measure directly the relevant movement. Figure 16 shows the general arrangement.

ISBN: 978-3-95450-188-5 doi:10.18429/JACoW-MEDSI2016-WECA03

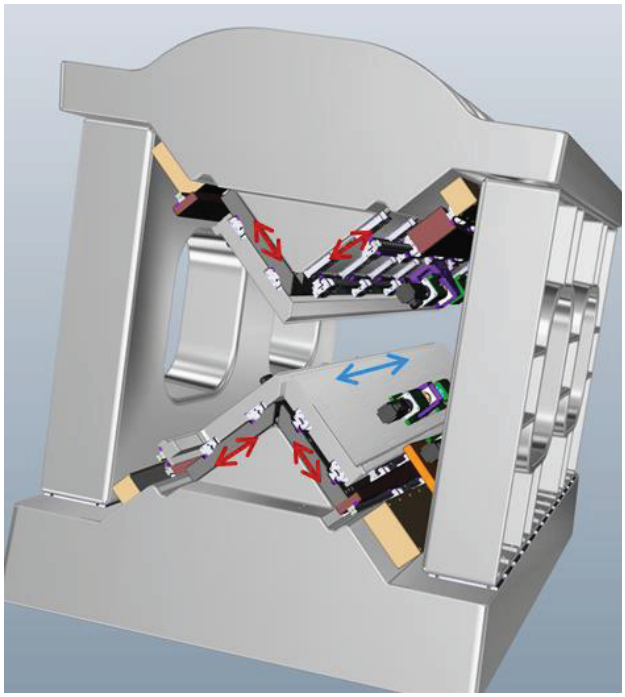


Figure 16: Frame and arrangement of the drives.

The keeper design is a flexor system like in the U15 with the following optimizations (Figure 17):

- The flexors are drawn to the wedge with a spring
- The fine adjustment is done with a differential screw

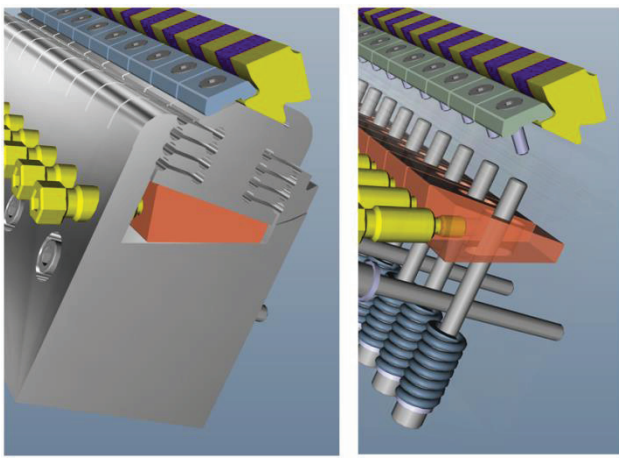


Figure 17: Keeper design.

For the vacuum chamber, we will use a tube made of copper with a very thin wall of 0.2mm (Figure 18)

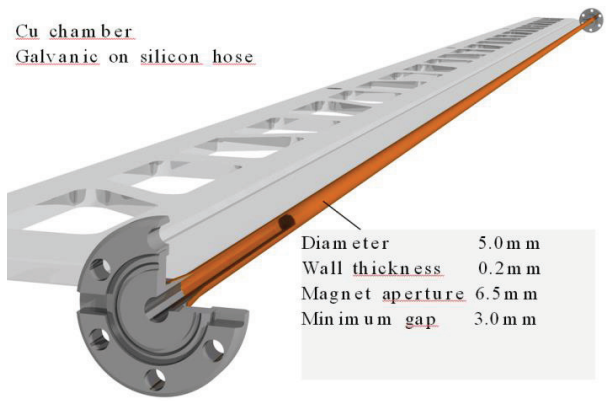


Figure 18: Vacuum Chamber.

CONCLUSION

With the new keeper system of the U15 Undulator, we can adjust the 2000 Magnets of a 4m long module with an automated robot system within 3 days.

For the new Athos beamline, we will develop a new arrangement of the magnets (APPLE-X) with orthogonal movements and a vacuum chamber in copper with a wall thickness of only 0.2mm.

ACKNOWLEDGMENT

We want to thank the whole ID-Group, the Vacuum Group, the Engineers from the department of mechanical engineering and the external partners, specially the company MDC Max Daetwyler AG.

Content from this work may be used under the terms of the CC BY 3.0 licence (© 2016). Any distribution of this work must maintain attribution to the author(s), title of the work, publisher, and DOI.

ISBN: 978-3-95450-188-5 doi:10.18429/JACoW-MEDSI2016-WECA04

HORIZONTAL-GAP VERTICALLY-POLARIZING UNDULATOR (HGVPU) DESIGN CHALLENGES AND RESOLUTIONS*

O. Schmidt[1], J. Xu[1], I. Vasserman[1], E. Trakhtenberg[1], K. Suthar[1], N. Strelnikov[1,2], G. Pile[1], D. Jensen[1], E. Gluskin[1]
[1]Argonne National Laboratory, Lemont, IL 60439, USA
[2] Budker Institute of Nuclear Physics, Novosibirsk 630090, Russia

Abstract

The Horizontal-Gap Vertically-Polarizing Undulator (HGVPU) is a compact, innovative, variable-gap insertion device developed by Argonne National Laboratory for the LCLS-II HXR beamline at SLAC. A full sized 3.4-meter-long prototype has been built and fully tested meeting all LCLS-II undulator specifications. An array of conical springs compensates the attractive magnetic forces of the undulator jaws. These springs are designed to exhibit non-linear spring characteristics that can be closely tuned to match the force curve exerted by the magnetic field, thereby minimizing the overall deflection of the strong-backs. The HGVPU also utilizes the existing LCLS-I support and motion system along with other existing equipment and infrastructure, thus lowering overall cost and installation downtime.

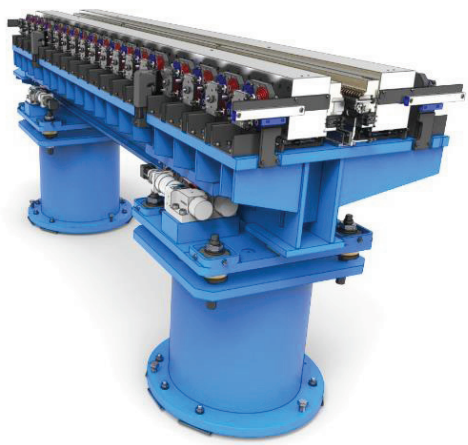


Figure 1: Rendering of final 3.4m HGVPU prototype.

INTRODUCTION

The 3.4-meter-long prototype HGVPU, shown in Figure 1, was successfully developed and built but not without its own unique challenges [1,2]. Very stringent straightness requirements of the strongbacks, temperamental properties of the spring compensation mechanism, mechanical stability over a large temperature range, installation and handling logistics, and unique control system demands all contributed to the development process of this device. Some of the more significant of these challenges will be examined as well as their final resolutions.

* Work supported by the U.S. Department of Energy, Office of Science, Basic Energy Sciences, under contract #DE-AC02-06CH11357.

DESIGN OVERVIEW

The HGVPU is a variable gap undulator that uses an array of springs to compensate for the large attractive magnetic forces between the horizontally opposed undulator jaws. In order to minimize deflection of the strongbacks and to reduce the forces on the actuators, the conical springs are designed with non-linear spring characteristics that approximate the exponential-like force curve induced by the magnetic attractive forces over the variable gap range. Figure 2 shows the cross-sectional view of a single undulator jaw. The magnets and poles are mounted to the magnet/pole mounts which are bolted to the undulator strongback from the back side. Each jaw rests on and is guided by two linear slides that are bolted to the girder surface.

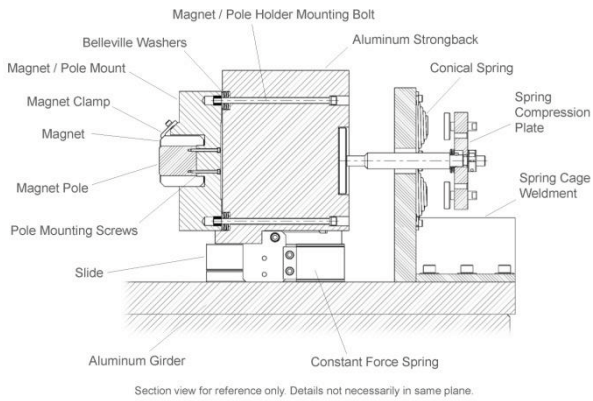


Figure 2: Cross-Section View of Undulator Jaw.

Two actuators, which are not shown in this view, position each undulator jaw at fixed engagement points along the length of the strongback to provide accurate positioning and allow for tapering capability. The springs are affixed to stationary spring cage brackets where they are engaged by the spring compression plates which are directly coupled to the strongbacks. For gaps >21mm, the attractive magnetic forces are negligible and spring compensation is unnecessary. At 21mm, the springs are engaged and increasingly compressed as the gap is decreased to a minimum gap of 7mm.

STRONGBACK STRAIGHTNESS AND ACTUATOR POSITION

Minimizing deflection of the strongbacks was the single greatest design challenge to overcome. The physics requirement for this particular undulator is that the strongbacks deflect less than 19 microns over the full gap range of 200mm to 7mm [3]. The attractive magnetic

Content from this work may be used under the terms of the CC BY 3.0 licence (© 2016). Any distribution of this work must maintain attribution to the author(s), title of the work, publisher, and DOI.

ISBN: 978-3-95450-188-5 doi:10.18429/JACoW-MEDSI2016-WECA04

force of the two opposing undulator jaws exceeds 6000lbs at minimum gap. Without an extremely rigid strongback the magnetic arrays would deflect under these forces rendering the undulator ineffective. Typically, this would be resolved by utilizing a very wide beam with a high moment of inertia.

As this is a horizontal gap device, the overall width was limited to one meter in order to fit within the undulator hall while still allowing the proper egress. A very wide cross-sectioned beam, was not a viable option, therefore the idea of using springs to compensate for the magnetic forces was conceived.

In a perfectly balanced system, the spring forces would have the same force curve as the magnetic forces and would be equally spread across the length of the undulator. The beam would have zero deflection, and the actuators could, in theory, be mounted anywhere along the length of the strongback.

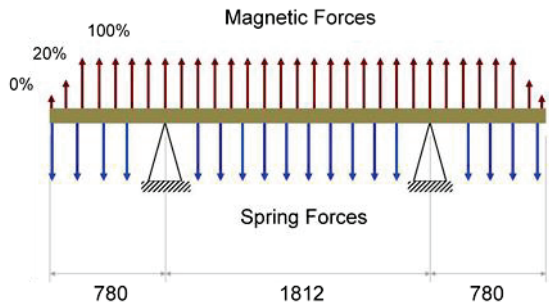


Figure 3: Free-Body Diagram of Strongback.

In reality, the magnetic force is evenly distributed across 260 poles with slightly lower field strength at the end poles. The corresponding spring cage units themselves take up a finite amount of space limiting the number of force compensation points to 18. Position and space to accommodate the actuators had to be considered also.

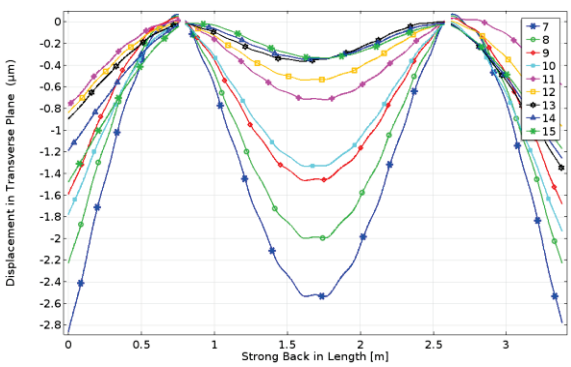


Figure 4: Simulated strongback deflections at gaps of 7mm to 15mm.

For a perfectly evenly distributed force, the ideal position for the actuator engagement points, to minimize deflection of a beam, would be close to the Airy points ($L/\sqrt{3}$). Due to the non-ideal factors of the system, and after some iteration and compromises where made, the final arrangement, shown in Figure 3, was chosen. A slightly tighter spacing of the spring cages between the actuators as opposed to those at the ends was necessary due to the space constraints of the components.

Figure 4 shows simulated deflections of the strongback over its length for gaps of 7mm to 15mm. Finite element analysis of the system showed the maximum deflection of the strongback would be less than 6µm per side in its worst case scenario with a gap of 7mm, which is well within the straightness requirements of the system. The simulation results were later confirmed by magnetic measurement.

SPRING CAGE CALIBRATION AND INSTALLATION

The attractive magnetic field strength drops off exponentially over distance. Unlike standard springs which exhibit a linear force change with displacement, conical springs can be designed to mimic the exponential force curve of a magnetic field. Working with a spring manufacturer, two separate types of conical springs were designed. One set of springs with slightly higher forces and the other with slightly lower forces than the ideal calculated magnetic force curve.

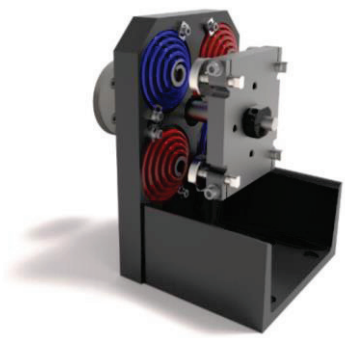


Figure 5: Individual Spring Cage Assembly.

The springs were initially numbered, measured, and sorted in pairs for both the strong and weak type. A special calibration fixture was designed to measure both the spring curves of the individual springs and also the full spring cage assemblies. Each spring cage is comprised of opposing strong and weak pairs, identified as red and blue in figure 5, that were previously sorted in order to achieve an ideal spring rate. Each spring cage is then individually calibrated over the full gap range on the calibration fixture, then moved to a specific gap of 30mm where a transfer clamp is installed to lock the position of the spring compression plate for final transfer to the undulator.

Figure 6 shows the force vs. compression plot of the four springs in a typical spring cage assembly. It is evident that any slight misalignment of the spring cages at the smallest gaps can significantly affect the forces at that gap. Displacements of 10µm, corresponding to forces of 2lbs or more were deemed enough to induce unacceptable

Content from this work may be used under the terms of the CC BY 3.0 licence (© 2016). Any distribution of this work must maintain attribution to the author(s), title of the work, publisher, and DOI.

ISBN: 978-3-95450-188-5 doi:10.18429/JACoW-MEDSI2016-WECA04

Content from this work may be used under the terms of the CC BY 3.0 licence (© 2016). Any distribution of this work must maintain attribution to the author(s), title of the work, publisher, and DOI.

deformations in the strongback. Transferring the calibrated spring cage to the undulator at final assembly therefore requires that the position of the spring compression plate be in the exact same position relative to the mounting surface of the strongback as its corresponding position in the calibration fixture. Installation of each spring cage is done individually while the encoder readouts are monitored to ensure that the gap of the undulator is the same as that of the spring cage calibration and that there are no binding forces. Even tightening the bolts that fasten the spring cage to the girder surface can create positional errors so this step is critical to the performance of the HGVPU.

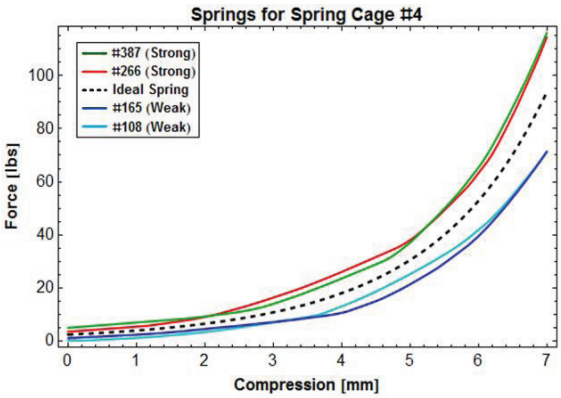


Figure 6: Spring Cage Load Curves.

GIRDER OPTIMIZATION & DESIGN

Initially, the prototype HGVPU utilized the original LCLS steel girder, however the steel girder was less than ideal for a number of reasons.

- The elevation of the girder top surface was around 3.5 inches too short and therefore required an array of spacers to make up for the difference (Figure 7).

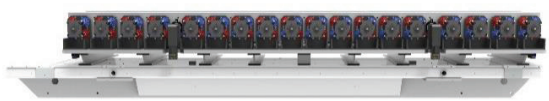


Figure 7: HGVPU Prototype on Steel Girder.

- Because of the offset loading condition of the girder, the spacers had to cantilever off of the girder on one side yet provide enough rigidity to resist the magnetic loads. This required the spacers to be very thick and heavy.
- The combined weight of the new gap-separation mechanism, base plate, and spacers increased the overall weight of the undulator by roughly 1500lbs. to a total of 6500lbs which is more than the capacity of the crane in the LCLS magnetic measurement facility.
- The dissimilar thermal expansion coefficients of the steel girder and aluminium strongbacks and magnet structures could potentially cause issues when undergoing temperature variations.

To meet the vigorous installation schedule of LCLS-II, it was decided early on that rather than reuse the old girders, new girders would be fabricated so that the undulator could be preassembled and ready for installation. This provided the opportunity to design new girders that would be optimized for the unique requirements of the HGVPU. Four initial concepts were presented;

- Option 0; Keep the existing steel girder design using the spacers.
- Option 1; A one-piece integrated undulator/girder assembly requiring the girder, undulator, and vacuum chamber to be moved as a single unit.
- Option 2; A girder with a rigid undulator support plate that can be separated from the girder, allowing the girder to remain in place, but still required that the vacuum chamber would have to be removed and re-aligned.
- Option 3; A two-piece gap separation mechanism with separate right and left side undulator jaws/spring compensation units, that could be removed leaving the vacuum chamber installed so that chamber realignment and breaking vacuum would not be necessary. The jaws would be tuned as a matched pair on a separate fixture, and then reassembled onto the girder in the undulator hall. This third option, although unique from a maintenance perspective, would have been much too difficult to align with the precision necessary to meet the magnetic requirements.

Ultimately, Option 1 was chosen as it was the most robust and stable design, the most cost effective, and any minor shortcomings in maintenance were deemed negligible.



Figure 8: Optimized Aluminum Girder Design.

The new girder is a welded aluminum structure that is much lighter than the steel girder and has the same thermal expansion characteristics as the undulator jaws. It is taller to make up for the height of the spacers, which also adds to its stiffness, and has identical interfaces for the LCLS pedestal supports. As shown in figure 8, the girder structure underneath the top plate is designed so that a rib is centered on each spring cage in order to stiffen the structure directly where the forces are concentrated.

Figure 9 shows the simulated surface profile plot of deflection for the force-bearing components of the undulator. The maximum deflection of the girder baseplate is around 12µm, which occurs a little bit off-center in the central region towards the aisle side. A deflection of around 80µm is seen at the highest point of the vertical

ISBN: 978-3-95450-188-5 doi:10.18429/JACoW-MEDSI2016-WECA04

plate of the spring cages, and although the spring cage deflection is much greater than the maximum allowable deflection of the girder, this deflection is already compensated for in the individual spring cage calibration. The linear bending of the cage itself could also conceivably help to smooth out the approximated exponential force curve of the springs.

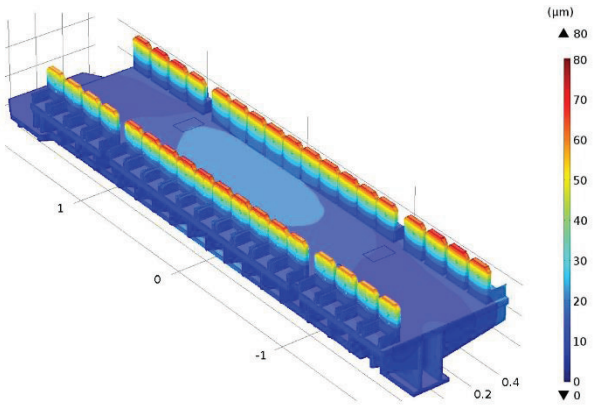


Figure 9: Simulation results of deformation.

MECHANICAL TUNING

Mechanical tuning is essentially levelling of the pole tips as measured with a very precise gap measurement probe. Typically, at the APS, undulator magnetic arrays are mechanically tuned by shimming in between the magnet/pole holders and the strongback. For the very stringent requirements of this undulator, this process became more difficult as minor adjustments lead to adjacent shims losing contact or falling out entirely. The idea of using Belleville washers in place of shims was born. Inserted at each of the hold down bolts, the washers allow continuous alignment of the strongbacks as they are designed hold position rather than having to loosen, shim, and re-tighten the bolts. The cross-section view of Figure 2 shows the position of the three spring washers. Stacked in series, they provided roughly 950lbs of force at each bolt. As these springs act in the same direction as the magnetic force, their deflection does not vary due to a change in gap. Initially, the assembly started with a 100μm gap so that tuning could be done in both directions. Later it became easier to measure and identify the highest pole tip as the nominal position and correspondingly adjust all of the others out to this point. This seemed like a sound idea however we later discovered that with changing gap, the points where the magnet base and strongbacks were in contact behaved differently due to the tensile forces within the bolts. The original plan with the 100μm gap would likely eliminate this. Since the mechanical specifications had been met and due to the tight delivery schedule, we did not have time to investigate the issue as we would have had to recalibrate all of the spring cages to compensate for the 100μm shift.

SUPPORT COMPATIBILITY

To ensure compatibility with the existing LCLS pedestal supports and cam movers, the HGVPU was fully evaluated for both overall gross weight and seismic performance. The original fixed-gap LCLS undulator girder was centered on the undulator strongbacks rather than the beam centerline. The HGVPU gap-separation mechanism is however centered around the electron beam which requires a non-symmetric girder. The unique off-center loading condition of the undulator was investigated and since the gap changes symmetrically, and the center of gravity stays within the footprint of the cam movers, it was determined to be a non-issue. The new girder design also gave us the opportunity to optimize for this condition as shown in figure 10.

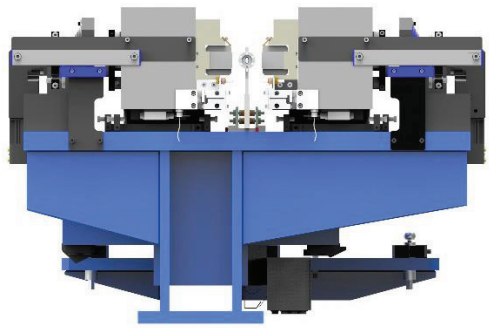


Figure 10: Upstream End View of HGVPU.

ENVIRONMENTAL TESTING

The goal for mechanical stability of the HGVPU was that it be able to remain tuned after undergoing a temperature variation of 20°C +/- 15°C (5°C-35°C). The concern was that the dissimilar thermal expansion coefficients of the steel girder relative to the aluminum strongbacks and magnet arrays would cause stresses in the system as it underwent temperature variations during transport and storage.

For temperature cycling of the undulator, a temperature controlled heating enclosure was purchased from Hemi Heating in Sweden. The heating enclosure has an operating range of up to 240°C. Six heating units, controlled by 12 thermocouples, regulate an even temperature distribution inside the tent. The temperature profile can also be programmed for ramp-up and cool-down times. The direct temperature of the HGVPU was measured separately via six thermocouples attached directly to the device itself. Readings from these sensors were recorded in LabView over the duration of the test. To cool the undulator below ambient temperature, the enclosure was specified with two slots to install standard residential A/C window units. Two 15,000 Btu, 115V units were purchased. The units have an operating range down to 16°C. In order to reach temperatures below 16°C, two line-voltage thermostats were purchased and wired in-line with the 120V power input of the units. We tested that the A/C unit came back on with its previous settings when we interrupted the

Content from this work may be used under the terms of the CC BY 3.0 licence (© 2016). Any distribution of this work must maintain attribution to the author(s), title of the work, publisher, and DOI.

ISBN: 978-3-95450-188-5 doi:10.18429/JACoW-MEDSI2016-WECA04

Content from this work may be used under the terms of the CC BY 3.0 licence (© 2016). Any distribution of this work must maintain attribution to the author(s), title of the work, publisher, and DOI.

power by unplugging the device from the wall. The thermocouple internal to the A/C unit was then re-routed to remain outside of the enclosure, therefore making the unit think that the temperature was higher, and in-turn tricking the unit into staying on indefinitely. The inline thermostats then regulated the temperature inside the tent by cycling the power to the unit. This worked very well.

At the time of testing, the HGVPU was still assembled on the original LCLS steel girder. Although it was assumed that the dissimilar thermal expansion coefficient of the steel girder relative to the aluminum magnet structures could cause stresses and mechanical tuning issues, this appears not to be the case. Furthermore, the final design of the optimized girder is aluminum so this is no longer an issue. Ultimately, the HGVPU was shipped to SLAC and measurements showed that it remained tuned.

GAP SYMMETRY

As much as possible of the existing LCLS control system was reused and/or modified. The cam mover controls remained the same, and a few motors, limit switches and their respective control chassis were added for the new variable gap design. The gap symmetry of the HGVPU is critical. If left uncompensated, the extremely high internal forces could severely damage the device. In one possible scenario where the undulator is at minimum gap and one of the jaws were allowed to open, the remaining jaw would be subjected to the full spring compensation force without the balancing magnetic force. In this scenario, the strongback would surely deform and the motors and drive components would likely undergo significant damage. Symmetry monitoring is therefore incorporated into the control logic.

CONCLUSION

As with any project, typical time constraints, cost constraints, and space constrains all had to be balanced and compromises were made. The end result however produced a very robust device that lead to the HGVPU being chosen as the baseline for the LCLS-II project hard x-ray undulator line shown in Figure 11.

ACKNOWLEDGMENT

The success of this project was the culmination of work of many talented individuals that I had the great pleasure of working with. As the project manager, and integration engineer for the 3.4-meter prototype, I became involved with the project after much of the initial concepts had been ironed out and two smaller scale prototypes had previously been built and tested. In addition to this paper's co-authors, Rich Voogd and Marty Smith did exceptional work developing the control system for the device, Jie Liu and Vic Guarino provided additional finite element analysis, Greg Wiemerslage and Jason Lerch developed the integrated vacuum chamber, Bill Jansma, Kristine Mietsner, Keith Knight and Rolando Gwekoh, provided survey and alignment support, John Terrhar, Joe Gagliano, Eric McCarthy and Mike Merritt provided technician support, and Pat Den Hartog, Marian White, and Patricia Mast were instrumental in costing and scheduling. We also appreciate all of the correspondence with our peers at SLAC National Accelerator Laboratory and Lawrence Berkeley National Laboratory.

REFERENCES

[1] N. Strelnikov, E. Trakhtenberg, I. Vasserman, J. Xu, E. Gluskin, "Performance of The Full-Length Vertical Polarizing Undulator Prototype for LCLS-II" NAPAC 2016.

[2] N. Strelnikov, E. Trakhtenberg, I. Vasserman, J. Xu, E. Gluskin, "Vertically Polarizing Undulator with the dynamic compensation of magnetic forces for the next generation of light sources," Rev. Sci. Instrum. 85, 113303 (2014).

[3] Physics Requirements Document. LCLSII-3.2-PR-0038-R1.

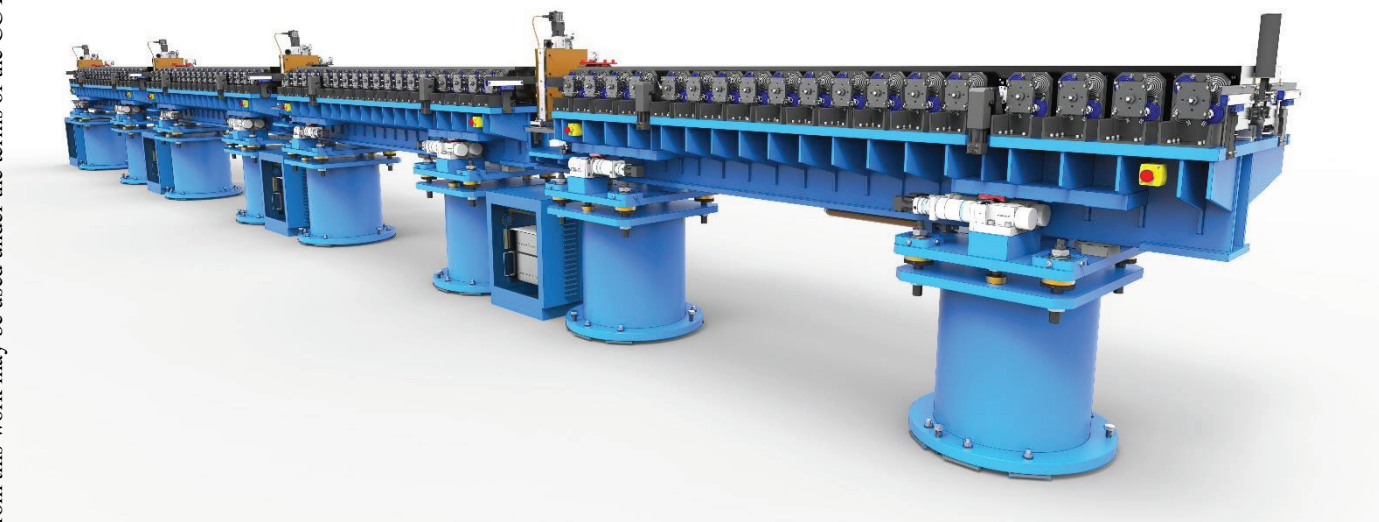


Figure 11: Rendered Image of Hard X-ray Undulator Beamline.

ISBN: 978-3-95450-188-5 doi:10.18429/JACoW-MEDSI2016-WECA05

SUPERCONDUCTING RF SYSTEM PLANS AT CLS

C. N. Regier†, Canadian Light Source Inc., Saskatoon, Canada

Abstract

Canadian Light Source (CLS) in Saskatoon, Canada has several cryogenic systems. One of the most critical is a 4.4 K liquid helium system for a superconducting RF cavity. This system consists of a Linde TCF-50 liquid helium plant coupled to a Cornell-designed CESR-B 500 MHz cavity and cryomodule via a 52 metre multi-channel transfer line. Over the years CLS has evaluated failures on the system as well as risks for downtime, and has come up with plans for a major upgrade to the superconducting RF system to improve reliability. An overview of performance and issues to date is presented. Some of the specifics of the risk analysis and upgrade plan will be examined, and details of the process flow discussed.

INTRODUCTION

The Canadian Light Source (CLS) uses a superconducting radio-frequency (SRF) cavity to replace energy lost by the electron beam due to synchrotron radiation. The SRF system operated by CLS consists of a 500 MHz Cornell-designed Cornell Electron Storage Ring B-factory (CESR-B) cryomodule [1] [2] connected via a 52 metre multi-channel transfer line (MCTL) to a Linde TCF-50 liquid helium cryogenic plant. Along with Taiwan Light Source, CLS was one of the first synchrotrons to use SRF for storage ring applications, with the system initially commissioned in 2003. Since then, several other synchrotrons including Diamond Light Source, SSRF, PLS, and NSLS-II have chosen to use the CESR-B design for storage ring radio-frequency (RF) [3] [4] [5]. SIRIUS in Brazil is also planning to use the CESR-B as its storage ring SRF platform.

As with most other synchrotron facilities CLS is a user facility, meaning that operational consistency and reliability are of critical importance. While the SRF system has generally been reliable, over the last 13 years of operation CLS has experienced some problems. Cryogenic transfer line ruptures, cryoplant and compressor issues, and SRF cryomodule vacuum leaks have all occurred at CLS between 2007 and 2013. Based on these experiences, CLS has undertaken several avenues to increase system reliability. Two major projects are planned: The purchase of a third CESR-B cryomodule and a "Cryo Upgrade" project that will see a second cryomodule installed in the storage ring and an additional compressor installed at the plant.

THE CLS SRF SYSTEM

The SRF system at CLS comprises of a single CESR-B cryomodule in Straight 12 of the storage ring, coupled via a cold valve box and a 52 metre multi-channel transfer line (MCTL) to a Linde TCF-50 liquid helium cryoplant. The arrangement of this system is shown in Fig. 1, and a schematic of the system is shown in Fig. 2.

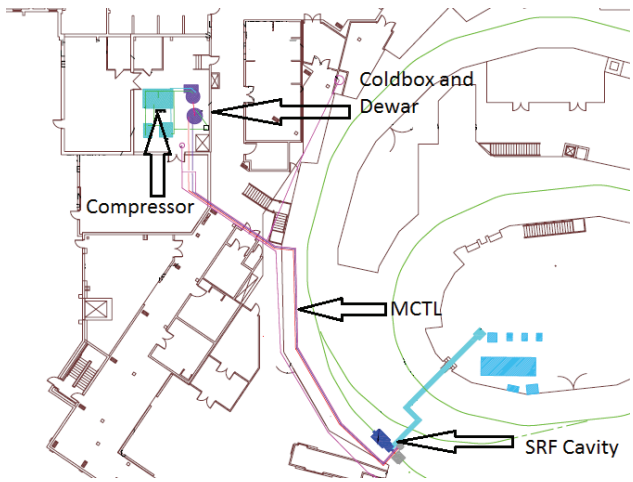


Figure 1: The layout of the CLS SRF system.

The cryoplant is located off of the experimental floor to prevent vibrational interference with ongoing experiments. A 200 kW compressor feeds oil through an oil recovery system (ORS) and gas management panel (GMP) to the coldbox, which deposits liquid into a 2000 L dewar. Pressure head drives liquid down the MCTL to the valve box on top of the storage ring concrete shielding, where a control valve regulates the level in the cryomodule below. Boil-off is returned to the valve box, where a second control valve meters flow back to the plant to regulate the cryomodule helium pressure. Both the liquid supply from the plant and the cold gas return to the plant are piped through the MCTL, along with a liquid nitrogen supply line for the cryostat. The liquid nitrogen is used to cool a thermal shield for the helium along the MCTL and in the cryomodule. A complete spare cryomodule is kept at CLS so that in the event of a cryomodule failure CLS is not required to wait for repair before continuing service. The cryomodules are identified as Cavity 1 and Cavity 2, with Cavity 1 being the first one delivered to CLS.

Figure 3 shows a simple cut-away of the CESR-B cryomodule. Radio-frequency (RF) energy is supplied to the cryomodule via waveguide. The RF passes through a ceramic window located under the cryomodule to transition from the air-filled waveguide into the ultra-high vacuum (UHV) required for the cavity. From there, the RF passes through a pump-out box, which is the point at which turbomolecular pumps can be attached to the UHV, and travels into the waveguide elbow. The elbow curves

† chris.regier@lightsource.ca

Content from this work may be used under the terms of the CC BY 3.0 licence (© 2016). Any distribution of this work must maintain attribution to the author(s), title of the work, publisher, and DOI.

ISBN: 978-3-95450-188-5 doi:10.18429/JACoW-MEDSI2016-WECA05

Content from this work may be used under the terms of the CC BY 3.0 licence (© 2016). Any distribution of this work must maintain attribution to the author(s), title of the work, publisher, and DOI.

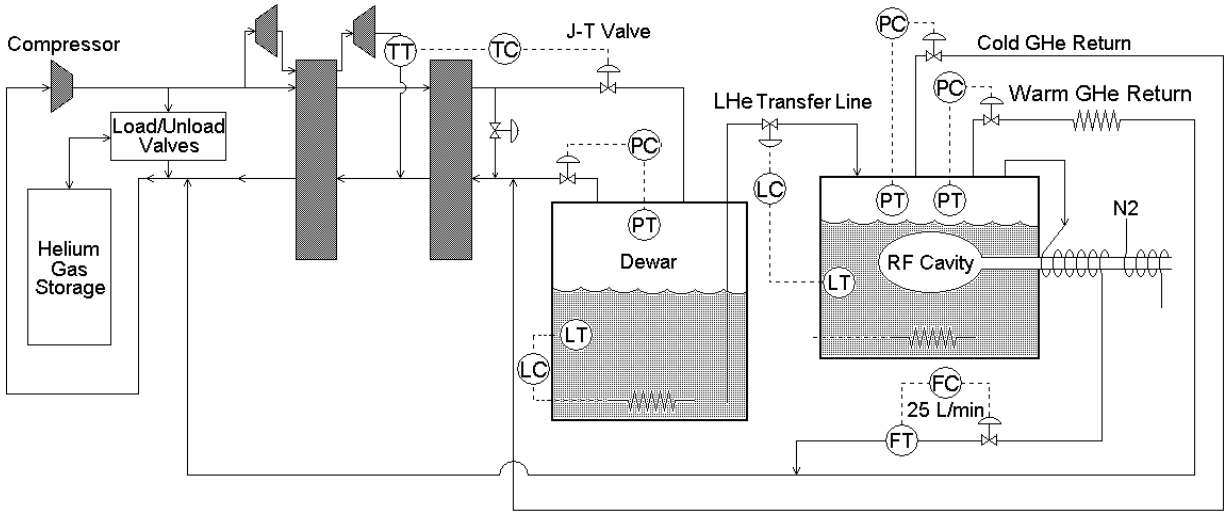


Figure 2: Schematic of the CLS SRF system.

upward and then backward, steering the RF through 180 degrees. The vertical section of the waveguide elbow is also wrapped in a coil through which the liquid nitrogen flow passes before exiting the cryomodule. This provides a thermal transition for the waveguide, going from near room temperature to liquid nitrogen temperature.

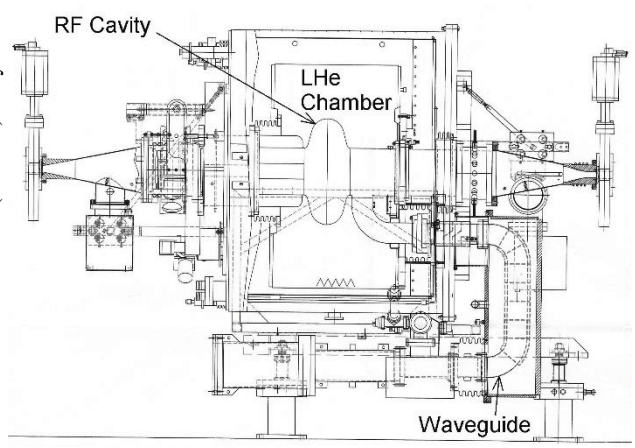


Figure 3: Cut-away view of the CESR-B cryomodule.

A short helium heat exchange (HEX) section connects the top of the elbow to the wall of the helium vessel. This section is similar to the liquid nitrogen section, but uses boil-off helium gas for cooling to provide a thermal transition from liquid nitrogen temperatures to liquid helium temperatures. Inside the helium vessel, the waveguide is niobium and is part of the cavity.

At CLS the SRF cavity is typically operated at an accelerating voltage of 2.05 MV and at RF power inputs of 260 to 270 kW or more. To consistently achieve these high voltages and power inputs, the cavity must be well-conditioned and be kept free of contaminants. This is made more difficult by the fact that the cold cavity will cryo-pump any storage ring vacuum contaminants. Build-up of these contaminants on the cavity inner walls will cause increased liquid helium consumption due to an increase in the electrical resistance seen by the RF, and can create emitters. An emitter is the equivalent of a steel tower in a thunderstorm – it provides a path of reduced resistance for current flow, and can cause arcing across the cavity. If this happens then a quench occurs and the entire cavity quickly becomes normal-conducting, causing cryogenic system oscillations and tripping the RF off.

Two methods are used to prevent this increased helium use and quenching: pulse conditioning and partial warm-ups. Pulse conditioning is done by pushing high-power pulses of RF into the cavity to burn off any potential emitters. Partial warm-ups are more effective, and involve removal of the liquid helium from the cryostat and warming the cavity to roughly 50 K. This allows cryo-pumped gases, largely hydrogen and air, to sublime off of the inner wall of the cavity and into the vacuum space, from which they can then be removed by vacuum pumping with a turbomolecular pump.

CLS CESR-B HISTORY

Cavity 1 was delivered to CLS in May 2003 and commissioned in August 2003 in the storage ring. While Cavity 1 was commissioned in the CLS storage ring, it was used to commission the storage ring as well. After conditioning a cavity voltage of 2.4 MV was achieved.

Cavity 2 was delivered in mid-2004. During the fall maintenance outage in 2004 Cavity 1 was removed from the storage ring and Cavity 2 was installed. Cavity 2 was also successfully commissioned, however a leak into the insulation vacuum of Cavity 2 was noted. While the leak was small and was controlled by continuous pumping, it was decided that Cavity 2 should be removed and Cavity

ISBN: 978-3-95450-188-5 doi:10.18429/JACoW-MEDSI2016-WECA05

1 reinstalled. This was done in the fall maintenance outage in 2005.

While Cavity 2 was being commissioned, Cavity 1 was stored with dry nitrogen gas in the UHV space. This was done to avoid any potential issues that could arise with vacuum maintenance during storage. When Cavity 1 was reinstalled in the storage ring in late 2005 it took only four hours after cool-down to achieve 2.2 MV across the cavity. Because of this Cavity 2 was also stored with dry nitrogen in the UHV space when it was removed in late 2005.

In January 2013 a problem with Cavity 1 forced CLS to remove it from the storage ring and bring Cavity 2 out of storage. Cavity 2 was installed in the storage ring and Cavity 1 was shipped to Research Instruments in Germany for repair. While Cavity 1 had quickly come back to normal operating conditions after storage, Cavity 2 required six months of regular conditioning and partial warm-ups to achieve full operation again. During this period CLS was forced to operate with reduced beam current, slowly working up from 150 mA to 250 mA over the six-month period.

When Cavity 1 was disassembled it was found that there were vacuum leaks at two small RF pickup flanges on the cavity. While the repair of these seals was a relatively minor job in itself, it required complete disassembly of the cryomodule to complete, which is quite time-consuming. Because of this, it was roughly 27 months from the time the failure occurred until Cavity 1 was returned to CLS.

Since 2013 CLS has operated with Cavity 2, and while there have been a few minor issues that have caused some concern, operation has been reliable over the last 3 ½ years.

PAST PROBLEMS

In 2007 the CLS experienced a failure of the MCTL. A helium leak into the insulation vacuum formed on the cold gas return line. This was found to be due to a manufacturing issue with the transfer line: a bellows was used in place of a solid piece of pipe as an elbow. A slight overpressure resulted in deformation of this bellows, causing several pinhole leaks. A second bellows developed a leak one year later, but this bellows was installed correctly and the leak is thought to be a delayed result of the first problem.

In 2012 there were several issues with the airend in the compressor. After several airend changes in a short period of time, it was determined that a misprint in the compressor maintenance manual had caused CLS to underfill the compressor with oil. Once this misprint was discovered, the airend issues ceased.

Soon after the compressor issues it was discovered that there was oil in the coldbox. This was unusual in that the oil was in the return, or low-pressure side of the coldbox. With assistance from Linde, an acetone flush was performed on the low-pressure side of the coldbox and the system was placed back into operation. The supply side was found to be completely clean and dry. This oil was forced into the coldbox during the compressor airend issues, and once removed the plant was restored to normal operation. Roughly 15 L of oil was removed from the coldbox, and plant performance is now slightly better than it was before any issues were noticed.

Finally, in early 2013 Cavity 1 developed the leak from the helium vessel into the cavity UHV space as mentioned in the previous section. The leak was slow, but enough to keep the system from operating. Cavity 2 was installed in the storage ring, and the damaged unit was removed and sent back to the manufacturer for repair. The removal of a cryomodule can be completed in roughly three days, but the installation of a new cryomodule requires almost two weeks. This is due to the quantity of instrumentation connections, and the time taken to properly ring-out these connections to establish that all instrumentation is functioning properly.

These failures have cost the CLS roughly 12 weeks of downtime. Figure 4 shows a breakout of the SRF cryogenic system failures and the percentage of the overall system downtime for which each is responsible. Included is the "Cryostat Reduced Ops" category. This describes the period after the spare cryomodule had been installed in 2013 during which much conditioning and many partial warm-ups were required before a full 250 mA of beam current could be consistently run in the storage ring. While users had beam during this time, the flux was substantially reduced and there was significant impact on both experimentation and operations.

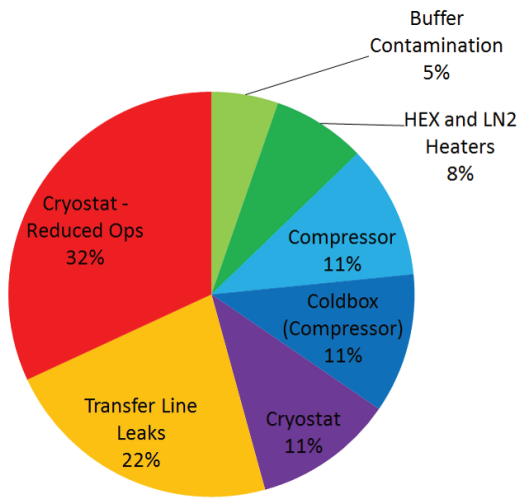


Figure 4: Downtime contributions for CLS SRF cryogenic system problems.

While the system has been repaired and has operated very reliably for the last 3 ½ years, many of the weaknesses in the system still exist. For this reason, current risk mitigation strategies for the SRF cryogenic system at CLS are focused both on reducing the chance of occurrence of the issues shown in Fig. 4 and in reducing the risk of having a double cryomodule failure.

Content from this work may be used under the terms of the CC BY 3.0 licence (© 2016). Any distribution of this work must maintain attribution to the author(s), title of the work, publisher, and DOI.

ISBN: 978-3-95450-188-5 doi:10.18429/JACoW-MEDSI2016-WECA05

Content from this work may be used under the terms of the CC BY 3.0 licence (© 2016). Any distribution of this work must maintain attribution to the author(s), title of the work, publisher, and DOI.

THE CRYO UPGRADE

CLS has planned an upgrade to the SRF cryogenic system that would eliminate many of the system weaknesses that could cause downtime. The upgrade consists of putting the spare SRF cryomodule into the storage ring in another straight section (Straight 2), and installing a second compressor and ORS/GMP system. Space for the second compressor would be gained by moving the coldbox and dewar onto the top of the storage ring shielding bunker to a central location between the two cryomodules. Figure 5 shows the proposed layout for this upgrade.

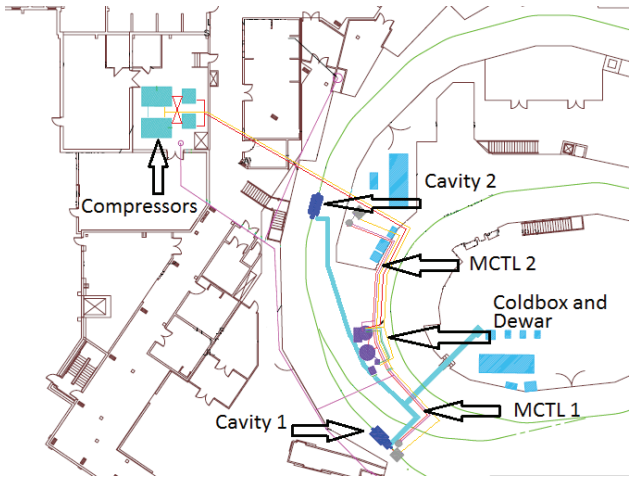


Figure 5: The layout for the proposed upgrade for the CLS SRF cryogenic system.

Several benefits are realized from the cryo upgrade proposal. First, a second compressor is in-line and available in event of a compressor failure, or if maintenance is required on a compressor. This would reduce cryoplant downtime to roughly 3 hours from multiple days in event of a problem. The same principle is valid for the second ORS/GMP unit. The proposal calls for cross-piping the compressors and ORS/GMP skids, so that either ORS/GMP can be used with either compressor. This provides further redundancy.

Second, the coldbox and dewar will be on top of the storage ring enclosure. This elevates the coldbox relative to the compressors, making it much more difficult for oil to transfer into the coldbox from the compressor circuits. The coldbox and dewar are also elevated relative to the SRF cryomodules, meaning additional pressure head is available via this elevation to supply liquid helium to the cryomodules. This will help with system stability.

Third, the distance from the dewar to each cryomodule will be far less than the current setup, meaning the length of each MCTL will be smaller. This will help reduce chances of an MCTL failure, and will also reduce heat leak into the liquid helium. It is better to use a longer pipe run for the room-temperature gas and a shorter pipe run for the cold fluids, as room-temperature piping is simpler, cheaper, and easier to construct and maintain.

Fourth, the second cryomodule in the storage ring will reduce downtime in event of a cryomodule problem. While a cryomodule must be removed from the storage ring if it cannot be kept cold, removal is much faster than the current removal and replacement required if there is a problem with the single cryomodule. As an added benefit, the second cryomodule will reduce the load on the first. The power being put into the beam can be spread over two cavities instead of all going into one. This will decrease the chance of an RF window fracture on the cryomodules, increasing their reliability, and will also allow CLS to pursue higher beam current operation in the range of 350 to 500 mA in the future.

CLS began preliminary work on the cryo upgrade in 2013, but because of other priorities the project did not make as much progress as desired. In mid-2015 the project was put on hold while CLS analysed the possibility of spending the money and effort installing a normal-conducting RF cavity system instead. While the decision has been made to proceed with the cryo upgrade, the project has not progressed since mid-2015 because resources have been diverted to other higher-priority work.

SUPERCONDUCTING VERSUS NORMAL CONDUCTING

In mid-2015 CLS considered the possibility of removing the superconducting RF system and installing normal-conducting cavities instead. Normal-conducting cavities have some advantages in that they do not require a complex liquid helium system, they don't require time-consuming warm-up and cool-down procedures to repair problems, and they don't have quenching or arcing issues because normal-conducting cavities operate at lower accelerating voltages than superconducting cavities do. Also, the Euro cavities considered take up less space because they do not require vacuum insulation, magnetic shielding, or liquid nitrogen shielding.

Disadvantages of normal-conducting cavities are that they are more susceptible to beam interference from higher-order modes (HOMs) in the cavity, they are much less efficient and create large amounts of heat that must be removed, and they are only capable of accelerating voltages in the 0.6 to 0.8 MV range for 500 MHz cavities, whereas the CESR-B is capable of 2.4 MV. Because of the HOMs CLS would need to implement longitudinal feedback for the beam to compensate. The heat generation would add a significant load to the CLS cooling water systems, requiring additional fluid cooler capacity and increased cooling water supply to the storage ring. In addition, the inefficiency of normal-conducting cavities would necessitate an increase in RF power input from 300 kW to 600 kW to compensate. The lower accelerating voltages mean three to four times as many normal-conducting cavities would be required as compared to SRF cavities, negating the benefits in size.

Several facilities have done analyses comparing superconducting and normal-conducting storage ring cavity options. These analyses typically come out very close, with the increase in cost and complexity for supercon-

ISBN: 978-3-95450-188-5 doi:10.18429/JACoW-MEDSI2016-WECA05

ducting equipment and the helium plant being offset by the reduced HOM effects on the beam, the smaller required investment in RF system capital due to lower RF power requirements, and the reduction in operating costs due to greater efficiency. In the case of CLS, the increases in size and capacity that would be required to the cooling water and storage ring RF systems to implement normal-conducting cavities are significant and expensive. In the end this fact along with the longitudinal feedback system requirement resulted in the CLS decision to remain with SRF.

ANOTHER SRF CRYOMODULE

When cryomodule 1 failed in early 2013, CLS installed the spare cryomodule in the storage ring. At that point there was not a spare cryomodule at CLS, meaning another failure would result in loss of beam. Total time between the failure and the return of the repaired cryomodule to CLS was 27 months. This length of time meant that the possibility of another failure during this period, while low, was significant. In fact, of total of 30 new or refurbished CESR-B modules that have been installed, five have failed upon initial cool-down or shortly thereafter.

Roughly two months before the return of cryomodule 1 to CLS, the insulation vacuum space on cryomodule 2 began to show signs of problems. Additional turbo pumping was added to attempt to combat this problem, but there were concerns at CLS that cryomodule 2 would become inoperable before cryomodule 1 was returned. Because of this concern, along with the extended repair times required for cryomodules, CLS has decided that another cryomodule is necessary to ensure continued operation in event of a double cryomodule failure. While a chance of a triple failure still would exist, this chance is statistically small enough that it is an acceptable risk.

While CLS was the first synchrotron to use SRF for normal storage ring operations, several others have chosen the CESR-B for their storage ring RF cavity system since. Each of these iterations of the CESR-B has seen improvements and design variations, particularly in the cryomodule, cryogenic connections, tuner, and heater systems. This complicates the process of specifying the new CLS CESR-B, as writing the technical specification becomes a balance between ensuring the new module will work with existing CLS infrastructure and taking advantage of improvements and lessons learned over the 12 years since the CESR-B was first delivered to CLS.

CLS is just in the process of releasing a request for expressions of interest in providing a new CESR-B cryomodule. Once potential vendors have been established CLS plans to go forward with a request for proposals this fall.

THE COLD RF TEST

After Cavity 1 was repaired in Germany, high power RF testing was done on it before it was returned to CLS. This testing was done at the Diamond Light Source RF test facility. An interface was constructed to allow connection of the CLS CESR-B to Diamond's RF test infrastructure, and the cryomodule was tested in January and February of 2015. During testing the cavity achieved 2.1 MV at 80 kW of RF. After testing, the Cavity 1 was returned to Germany before shipping to CLS.

The integrity of both the insulation vacuum and the UHV was tested in Germany before shipping, and again at CLS after being received. However, accelerometers mounted on the frame during shipping indicated some significant bumps and jarring during the unloading from the aircraft and during the 600 km truck trip from the airport to CLS. This has caused some concern that, while there are currently no leaks in the vacuum spaces, leaks may develop on cool-down. Even a small leak can easily stop operation of the cryomodule.

While a third cryomodule will reduce the risk to CLS in the event of a double cryomodule failure, to order and receive a new CESR-B takes roughly 24 to 30 months. Because of this CLS is planning a cold test of Cavity 1 during an upcoming maintenance outage in February, March, and April. Cavity 1 will be moved into the storage ring shielding and connected to the cryogenic system with instrumentation cable and cryogenic flex line connections. This will permit testing without moving the installed cryomodule, which could cause potential cavity contamination issues.

CONCLUSIONS

CLS has successfully and reliably operated a storage ring SRF system for over 12 years. While operation has proven reliable, there have been some issues over the 12 year operating period. The system is complex, and repair times for cryomodules are long, meaning that there are risks of significant downtime periods of multiple weeks in event of equipment failure, and a risk of extended downtime of months or even years in the event of a double cryomodule failure.

To reduce these risks, CLS has focused on four main areas. First, an assessment was completed examining whether a normal-conducting storage ring RF option was feasible and realistic. It was found that it was too complicated and expensive to switch from SRF to normal-conducting RF. Second, a cryogenic system upgrade has been proposed and conceptually designed. This would increase redundancy and reduce downtimes in the event of equipment failures. Third, a third cryomodule is being ordered. This will reduce the likelihood of extended downtime due to the chance of a double cryomodule failure. Fourth, a cold test is planned for the recently repaired Cavity 1 to ensure vacuum spaces will remain leak-free upon cool-down.

REFERENCES

[1] D. Moffat, P. Barnes, J. Kirchgessner, H. Padamsee, and J. Sears, "Preparation and Testing of a Superconducting Cavity for CESR-B," in *Proc. 1993 Particle Accelerator Conf.*, Washington D.C., USA, May 1993, pp. 763-765.

[2] S. Belomestnykh *et al.*, "Commissioning of the Superconducting RF Cavities for the CESR Luminosity Upgrade," in

Content from this work may be used under the terms of the CC BY 3.0 licence (© 2016). Any distribution of this work must maintain attribution to the author(s), title of the work, publisher, and DOI.

ISBN: 978-3-95450-188-5 doi:10.18429/JACoW-MEDSI2016-WECA05

Proc. 1999 Particle Accelerator Conf., New York City, USA, Mar-Apr 1999, pp. 980-982.

[3] M. R. F. Jensen, "Operational Experience with SRF Cavities for Light Sources," in *Proc. SRF2011 Conf.*, Chicago, USA, Jul 2011, pp. 27-31.

[4] S. Belomestnykh, "Superconducting RF in Storage-Ring-Based Light Sources," *13th Annual Workshop on RF Superconductivity*, Bejing, China, Oct 2007, pp. 19-23.

[5] F. Gao *et al*., "Commissioning and Early Operation Experience of the NSLS-II Storage Ring RF System," in *Proc. Int. Particle Accelerator Conf. (IPAC'15)*, Richmond, USA, May 2015, pp. 3606-3608.

Content from this work may be used under the terms of the CC BY 3.0 licence (© 2016). Any distribution of this work must maintain attribution to the author(s), title of the work, publisher, and DOI.

ISBN: 978-3-95450-188-5 doi:10.18429/JACoW-MEDSI2016-WECA06

MECHANICAL ENGINEERING SOLUTIONS FOR COXINEL PROJECT*

K. Tavakoli†, T. André, I. Andriyash, C. Basset, C. Benabderrahmane, P. Berteaud, S. Bobault, S. Bonnin, F. Bouvet, F. Briquez, L. Chapuis, M. E. Couprie, Y. Dietrich, D. Dennetière, C. De Oliviera, J. P. Duval, M. El Ajjouri, T. El Ajjouri, C. Herbeaux, N. Hubert, M. Khojoyan, M. Labat, N. Leclercq, A. Lestrade, A. Loulergue, O. Marcouillé, A.Mary, F. Marteau, P. Ngotta, F. Polack, P. Rommmeluère, M. Sebdaoui, F. Thiam, M. Valléau, J. Vétéran, D. Zerbib, Synchrotron SOLEIL, Gif-sur-Yvette, France
J. Gauthier, K. Ta Phuoc, G. Lambert, V. Malka, A. Rousse, C. Thaury, Laboratoire d'Optique Appliquée, Palaiseau, France
E. Roussel, Elettra-Sincrotrone Trieste, Basovizza, Italy

Abstract

COXINEL (COherent Xray source INferred from Electrons accelerated by Laser) is a European Research Council (ERC) advanced grant aiming at the demonstration of Free Electron Laser amplification using electrons generated by laser plasma acceleration. A special electron beam transfer line with adequate diagnostics has been designed for this project. Strong-focusing variable-field permanent magnet quadrupoles, energy de-mixing chicane and a set of conventional quadrupoles condition the electron beam before its entrance in an in-vacuum U20 undulator. This article describes some of the features incorporated into the design of the magnets, girders, vacuum chambers and diagnostic equipment for this experimental machine. Progress on the equipment preparation and installation is presented as well.

INTRODUCTION

When a short multi-TW laser pulse propagates through a gaseous medium, it drives strong plasma waves in its wake. The electric field generated by these plasma waves can exceed by few orders of magnitude those technically achievable with conventional linear accelerators. This accelerating technic is called Laser Wakefield Accelerator (LWFA) [1, 2].

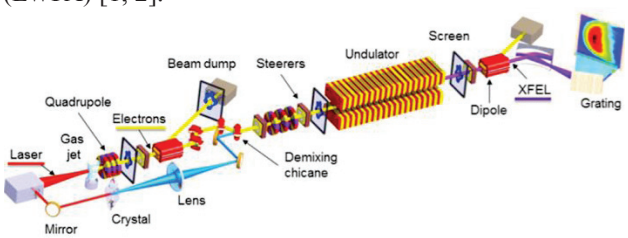


Figure 1: COXINEL's schematic layout.

Using LWFA to operate a Free Electron Laser (FEL) remains very challenging. Among others projects [3, 4] COXINEL aims at using a LWFA to drive an FEL, taking advantage of a specific design of the transfer line to handle divergence and energy spread [5]. The key concept relies on an electron beam longitudinal and transverse manipulation in the transport towards an undulator: a set of strong quadrupoles handles the large divergence of the electron beam and then a "demixing" chicane sorts the electrons in energy and reduces the slice energy spread [6, 7] (see Figure 1).

EXPERIMENT HALL

The experiment hall, called "Salle jaune", is located in "Laboratoire d'Optique Appliquée (LOA)" in Palaiseau, 10 km far from SOLEIL synchrotron site.

The hall is partially covered by a one-tonne crane, which is not sufficient for transportation of the main girders. Some architectural modifications have been performed in the hall in order to free more space for COXINEL installation. Although, there is only 11 meter available between the electron source and the hall's wall. This limited space imposed some trade-off in the choice of installed devices as well as the assembly and alignment sequences. Each different device has been characterized independently and installed on its girder prior to shipping and installation on the LOA site.

GENERAL LAYOUT AND INSTALLATION

Furthermore, all the main components will be presented starting from the electron source down to the final detector following the electron beam direction. A 3D view of COXINEL installation generated by CATIA is presented in Figure 2.

Electrons are produced by one of the two powerful 60 TW laser beam of the LOA "salle jaune laser". The laser beam is focused in a gas jet located in a dedicated chamber called LWFA vacuum chamber. Three permanent magnet variable-gradient (up to 200 T/m) quadrupoles, so called QUAPEVA, placed near to the source inside the LWFA chamber focus strongly the beam. Each QUAPEVA has its independent motorized adjustment table in Z and X directions.

* Work supported by European Research Council
† Keihan.tavakoli@synchrotron-soleil.fr

Content from this work may be used under the terms of the CC BY 3.0 licence (© 2016). Any distribution of this work must maintain attribution to the author(s), title of the work, publisher, and DOI.

ISBN: 978-3-95450-188-5 doi:10.18429/JACoW-MEDSI2016-WECA06

Content from this work may be used under the terms of the CC BY 3.0 licence (© 2016). Any distribution of this work must maintain attribution to the author(s), title of the work, publisher, and DOI.

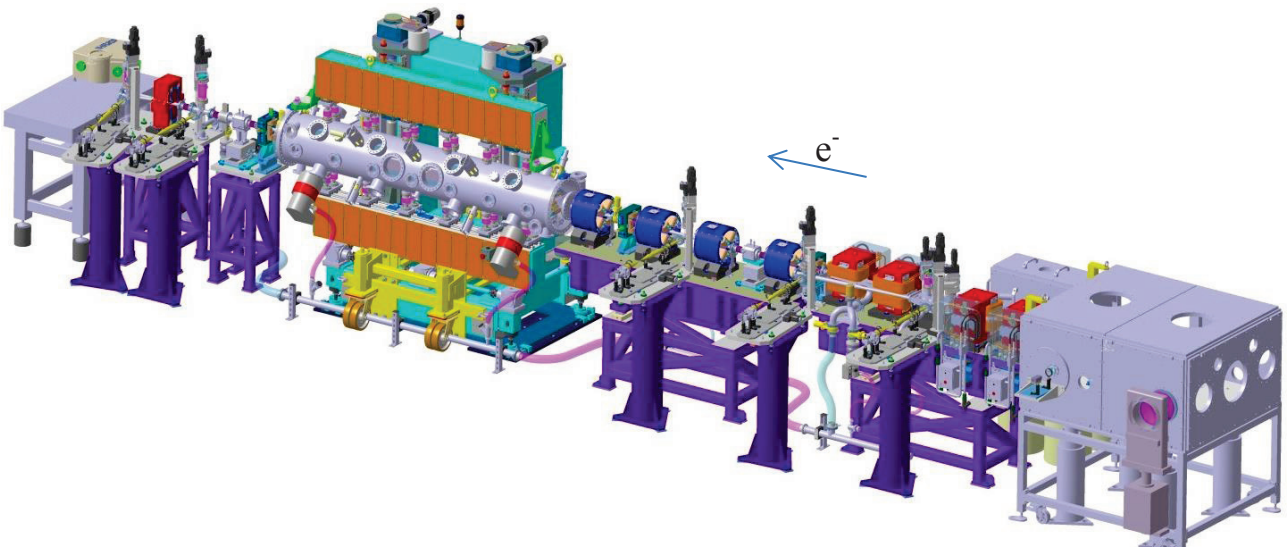


Figure 2: From right to left following the electron beam: LWFA vacuum chamber, magnetic chicane dipoles (in red), quadruplet of quadrupoles (in blue), U20 undulator, beam dump dipole (red) and the spectrometer.

An integrating current transformer (ICT) from BERGOZ is located after the QUAPEVAs inside the LWFA chamber for electron beam charge measurements. The electrons pass then through the first steerer. In order to keep the transport line as compact as possible, the exit panel on the LWFA vacuum chamber has been modified creating an hollow cylinder in which the steerer as well as a gate valve have been installed (see Figure 3).

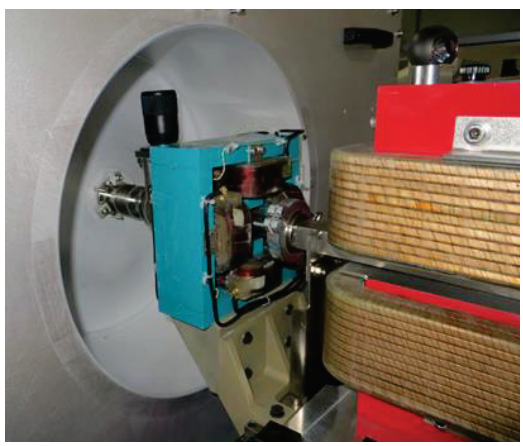


Figure 3: The first steerer and vacuum separation gate valve installed inside the LWFA hollow panel.

The magnetic chicane is composed of four water-cooled and variable field dipoles. Key parameters of chicane dipoles are presented in Table 1.

Table 1: Chicane Dipole Parameters

Parameter	Unit	Value
Gap	mm	25
Yoke length	mm	200
Magnetic field @ 150 A	T	0.55
Technology		Water cooled

A first design of air cooled dipole led to excessive coil heating. The design was then renewed to a water-cooled version, enabling also to get more compact components (see Figure 4). The dipoles are mounted on the top of the girder with calibrated shims, allowing magnets to be fixed in position, height and roll to meet the specifications. This girder has been fabricated by ALSYOM. The positioning precision of each dipole with respect to the beam axis shall not exceed 25 microns.

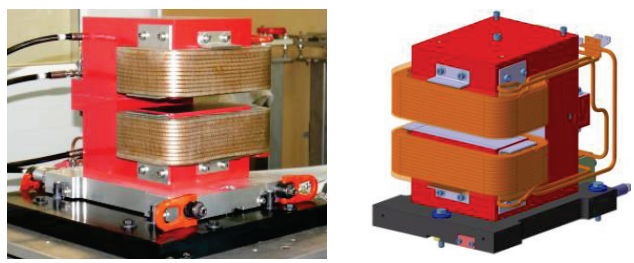


Figure 4: 3D model (right) and fabricated chicane dipole (left).

In total, five imagers are actually installed on the COXINEL transfer line, a sixth one will be added in a near future for the next run. Imager 2 and 3 are placed in the middle of the chicane off-axis for energy and energy spread measurement (see Figure 5). Different screens of 1" size, mounted on a motorized arm at 45◦, intercept the beam. The extracted light through a window is imaged via lenses onto a CCD camera.

The second and third dipoles are shifted laterally by 16 mm with respect to the beam axis. This permits the use of the most uniform part of dipolar magnetic field for the deviated electron beam. The first and second dipole pairs are installed in a face to face configuration in order to ease the access to diagnostic elements installed in the

ISBN: 978-3-95450-188-5 doi:10.18429/JACoW-MEDSI2016-WECA06

middle of the chicane. A second steerer is installed on the same girder as the magnetic chicane at the exit side (see Figure 6).

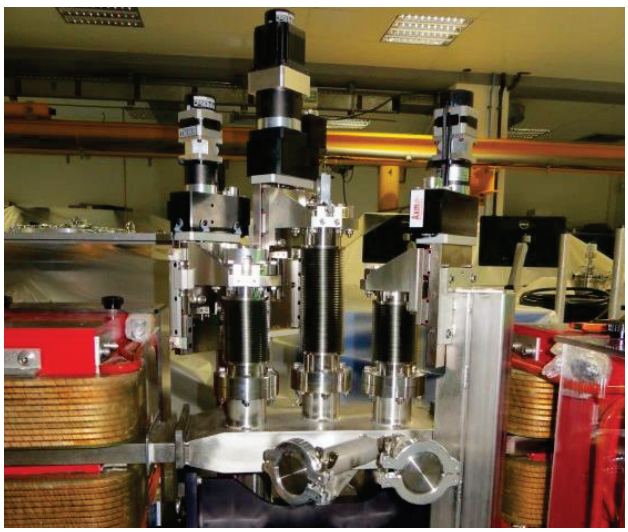


Figure 5: Diagnostic equipment in the middle of magnetic chicane.

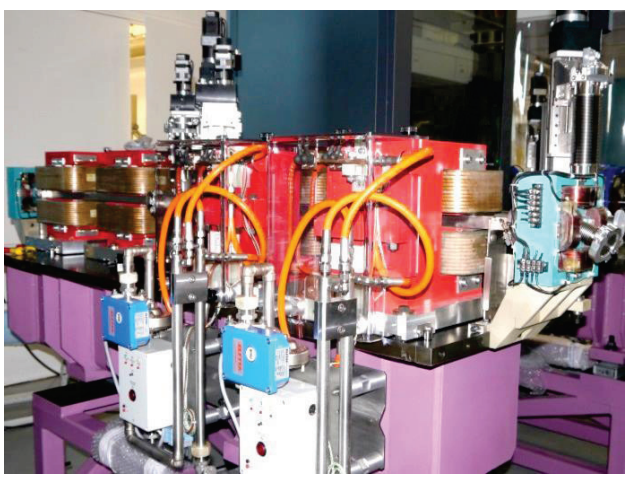


Figure 6: Magnetic chicane and steerers.

After the magnetic chicane and the second steerer, a set of 4 quadrupoles is installed on an independent girder, also manufactured by ALSYOM. These electromagnetic and air-cooled quadrupoles have been measured by SOLEIL's stretched wire bench in the magnetic measurement Lab (Table 2).

Table 2: Quadrupole Parameters

Parameter	Unit	Value
Bore diameter	mm	24
Yoke length	mm	200
Maximum gradient	T/m	20
Technology		Water cooled

Dimensions for the height and thickness of shim packs used to position the magnet on the girder are defined at this stage. The general view of the quadrupole is shown in Figure 7. The quadrupoles are aligned with respect to the beam axis with a precision of 20 microns. The reference axis has been defined using a laser tracker and some fiducial references were taken for all magnetic elements on the magnetic measurement benches and reported on the LOA site.

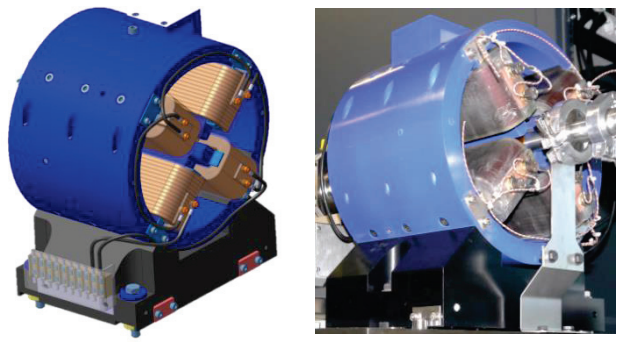


Figure 7: 3D model (left) and produced quadrupole (right).

The space between the quadrupoles has been used optimally in order to keep the installation as compact as possible. Thus, the cavity BPM (cBPM), the Imager 4 as well as the pre-undulator steerer are placed in between the quadrupoles on the same girder (see Figure 8).

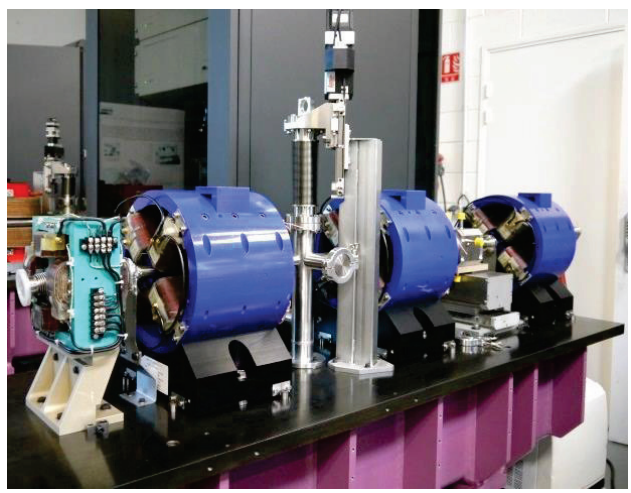


Figure 8: Quadrupole girder including the cBPM, Imager 4 and pre-undulator steerer.

For the first phase of COXINEL experiment, a SOLEIL's spare in-vacuum U20 undulator has been used. Table 3 presents the parameters of this undulator.

Working usually under storage ring vacuum conditions (~10^{-9} mbar), the pumping system has been modified for COXINEL needs. All ion pumps as well as Titanium Sublimation pumps (TSP) have been disassembled and replaced by two 300 l/s PFEIFFER turbomolecular pumps with magnetic levitation rotors in order to reduce as much

Content from this work may be used under the terms of the CC BY 3.0 licence (© 2016). Any distribution of this work must maintain attribution to the author(s), title of the work, publisher, and DOI.

ISBN: 978-3-95450-188-5 doi:10.18429/JACoW-MEDSI2016-WECA06

Content from this work may be used under the terms of the CC BY 3.0 licence (© 2016). Any distribution of this work must maintain attribution to the author(s), title of the work, publisher, and DOI.

as possible the impact of pump vibration on the stability of the undulator (see Figure 9).

Table 3: U20 In-vacuum Undulator Parameters

Parameter	Unit	Value
Magnetic period	mm	20
Magnetic length	mm	1950
Minimum gap	mm	5.5
Peak field	T	1.5
Magnet technology	-	$Nd_2Fe_{14}B$

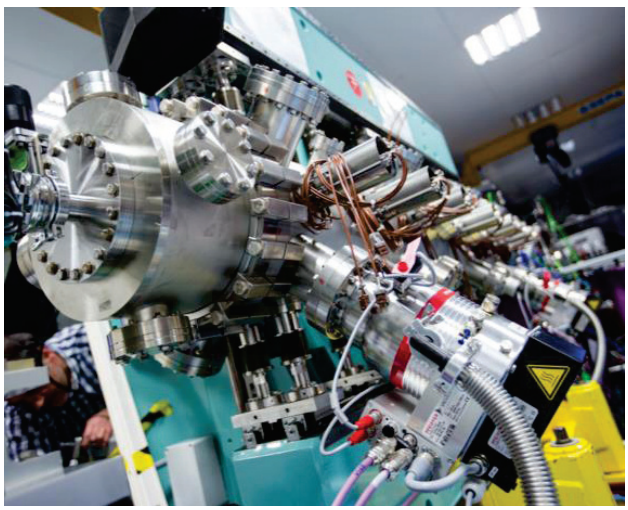


Figure 9: SOLEIL U20 in-vacuum undulator equipped with turbomolecular pumps.

An U20 in-vacuum undulator weights around 4 tonnes. Special transport tooling with retractable wheels has been developed in order to run the whole carriage on the floor without using the crane (see Figure 10). BOVIS Company had in charge the undulator transportation between SOLEIL and LOA experiment hall.

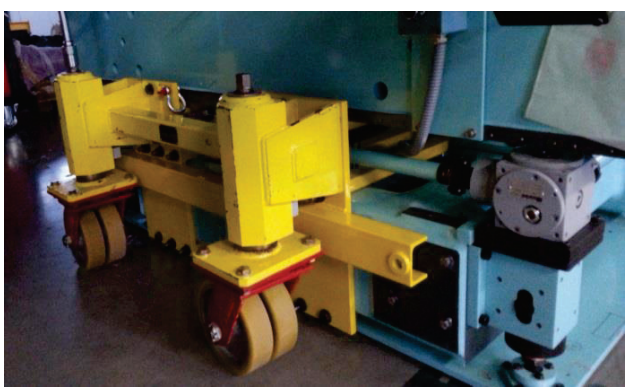


Figure 10: Special transport tooling for in-vacuum undulator.

An R&D program on the construction of a cryo-ready undulator is under way in the frame of a French-Swedish collaboration agreement. The choice of the period has been studied regarding its use on both LUNEX5 and SOLEIL 2.75 GeV storage ring. The use of a specific grade of $Pr_2Fe_{14}B$ with poles in Vanadium-Permendur enables operation both at room temperature and at 77 K. (Table 4). This U15 undulator will replace the U20 on the COXINEL layout in medium term.

A Stripline is also under study and it will be installed at the exit of the U20 undulator even if it will have to be removed when the 3m cryo-ready U15 undulator is ready because of a lack of space.

The following devices are placed directly after the undulator: 4th steerer, ICT-2, cavity BPM-2 and Imager 5 (see Figure 11 and Figure 12). A spectrometer for the spontaneous emission and Free Electron Radiation characterization is also installed at the exit of the undulator [8, 9].

Table 4: U15 Cryo-ready Undulator Parameters

Parameter	Unit	Value
Magnetic period	mm	15
Magnetic length	mm	3000
Minimum gap (COXINEL)	mm	3
Magnet technology	-	$Pr_2Fe_{14}B$
Peak field @ 239K	T	1.53
Peak field @ 80 K	T	1.67

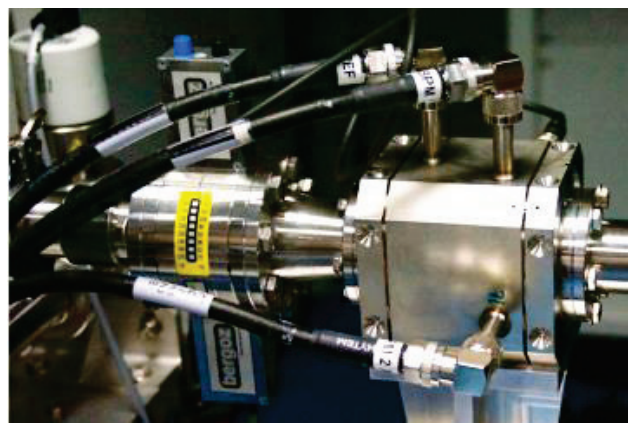


Figure 11: ICT-2 and cavity BPM-2 at the exit of the undulator.

A permanent magnet dipole enabling a 1 T field for deflecting the electrons towards the dump is under measurement at SOLEIL's magnetic lab for the next phase of the installation. An overview of all installed devices is shown in Figure 12.

COXINEL's general vacuum system is composed by a primary circuit all along the line and four PFEIFFER turbomolecular pumps at different locations: two (80 l/s) on the chicane girder, one (80 l/s) on the quadrupoles girder and one (80 l/s) at the end of the line. The vacuum level in the transfer line is about 10^{-5} mbar whereas in the

ISBN: 978-3-95450-188-5 doi:10.18429/JACoW-MEDSI2016-WECA06

LWFA chamber, it is a few 10^{-3} mbar. The U20 undulator has its own independent pumping system.

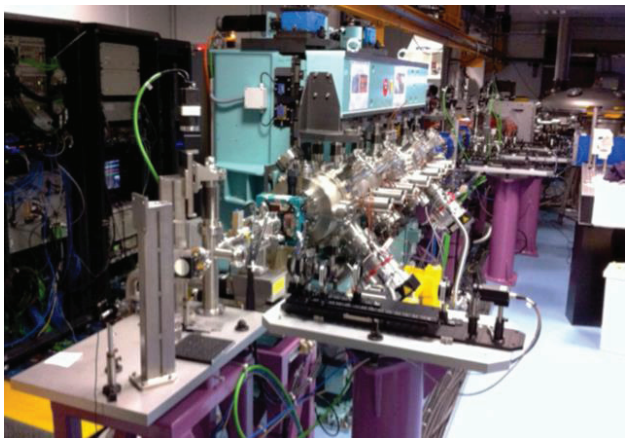


Figure 12: COXINEL installed in LOA's "Salle jaune".

CONCLUSION

The COXINEL LWFA-FEL line is assembled in LOA experiment hall and is operational since February 2016. Since all the equipment had already been tested and pre-aligned at SOLEIL before shipping to LOA, the installation has been done only in few days.

Because of some parallel experiments in the LOA's experiment hall, only few weeks of data collection could be performed since the installation. The LWFA electron beam has been successfully transported through the line. The preliminary results are encouraging for the pursuit of this experiment. Next series of tests and data collection will be performed before the end of this year [5].

ACKNOWLEDGEMENT

The authors are grateful to the support from the European Research Council for COXINEL (340015) and X-Five advanced grants (339128), the French-Swedish collaboration for the support on the U15 cryo-ready undulator, the "Triangle de la Physique" for the QUAPEVA valorisation contract and to J. L. Lancelot, F. Forest and O. Cosson from Sigmaphi for their involvement in the project.

REFERENCES

[1] E. Esarey, C. Schroeder, and W. Leemans, "*Physics of laser driven plasma-based electron accelerators*" Reviews of Modern Physics, vol. 81, no. 3, p. 1229, 2009.

[2] V. Malka, "*Laser- plasma accelerators"* Physics of Plasmas, vol. 19, 055501, p. 056703, 2012.

[3] M. P. Anania, D. Clark, R. Issac, A. Reitsma, G. Welsh, S. Wiggins, D. Jaroszynski, S. van der Geer, M. de Loos, M. Poole, et al., "*The ALPHA-X beam line: toward a compact FEL*", Proceedings of IPAC, vol. 5, pp. 2263–2265, 2010.

[4] CFEL, *https://www.cfel.de.*

[5] T.André, M.E.Couprie et al., "*First electron beam measurements on COXINEL*", IPAC2016, Busan, Korea.

[6] A. Loulerge, M.E.Couprie et al., "*Experiment preparation towards a demonstration of laser plasma based free electron laser amplification*", Advances in X-ray Free-Electron Lasers Instrumentation III, 95121G (12 May 2015).

[7] A. Loulergue et al., "*Longitudinal and transverse beam manipulation for compact laser wakefield accelerator based free-electron lasers*", Physics and applications of High Brightness Beams : towards a fifth generation light source, Puerto-Rico, March 25-28, 2013; A. Loulergue, "*Beam Manipulation for Plasma Accelerator Based Free Electron Lasers*", THPO01, these proceedings, FEL'14, Basel, Switzerland (2014).

[8] A. Loulergue, M. Labat, C. Evain, C. Benabderrahmane, V. Malka, and M. Couprie, "*Beam manipulation for compact laser wakefield accelerator based free-electron lasers*", New Journal of Physics, vol. 17, no. 2, p. 023028, 2015.

[9] M. Labat et al., "*Electron beam diagnostics for COXINEL*", FEL'14, Basel, Switzerland (2014).

Content from this work may be used under the terms of the CC BY 3.0 licence (© 2016). Any distribution of this work must maintain attribution to the author(s), title of the work, publisher, and DOI.

ISBN: 978-3-95450-188-5 doi:10.18429/JACoW-MEDSI2016-WECA07

Content from this work may be used under the terms of the CC BY 3.0 licence (© 2016). Any distribution of this work must maintain attribution to the author(s), title of the work, publisher, and DOI.

ENGINEERING CHALLENGES OF THE VMXi BEAMLINE

J. H. Kelly, Diamond Light Source, UK

Abstract

The in-situ Versatile Macromolecular Crystallography (VMXi) Beamline delivers a high flux density, taking data directly from crystallisation experiments within the plate, using a fully automated endstation. A double multilayer monochromator (DMM) was designed in-house to deliver a 60 fold increase in flux. Two robots and an automated load-lock pass the plates from the crystallisation storage units to the goniometer. A compact endstation was designed to accept the high flux and take data with acquisition times down to a millisecond. This paper gives an overview of the beamline layout and the interesting pieces of engineering design. The beamline is planned to take first user at the end of 2016.

INTRODUCTION

The in-situ Versatile Macromolecular Crystallography (VMXi) Beamline is effectively a new beamline which has been built through the original Diamond Phase one beamline I02. The new fully automated endstation has been designed to obviate the manipulation of individual crystals, preserving crystal integrity and giving diffraction feedback during as well as at the end of growth. A number of new custom components have been designed in-house for this unique beamline. This paper outlines some of the components engineered for the endstation.

The DMM has not been described here as it is the topic of other papers[1][2][3].

VMXI HUTCH

The VMXi hutch is a 4 mm thick fabricated steel construction. The structure is split into four parts. The chicanes are all at floor level. The upper shielding is split in to three rolling sections which may be manually pulled back for access. There are 24 leaded glass windows providing a very good view of the interior. A CAD image of the hutch next to the two plate storage units and external robot is given below (see Figs. 1 and 2).

SAMPLE LOADING AUTOMATION

When either a 20 or 4°C crystallisation plate is deemed ready for either screening or diffraction data capture, it will be ejected from the rear of the Formulatrix crystallisation storage units through a hatch. An industrial six axis robot mounted on a horizontal rail will then take the plate to the Endstation loadlock rotating it to the correct orientation on the way. The loadlock is a pneumatic device with a linear stage mounted upon a 180° rotation. The plate is retracted into the loadlock cylinder, rotated by 180° and driven out, presenting it to the internal gantry robot (See Fig. 3). The loadlock is radiation fail safe so it is not possible to break the radiation containment with a driven axis. It incorporates a bar code reader, a plate in-position switch and stage limit switches to give feedback to the control system.

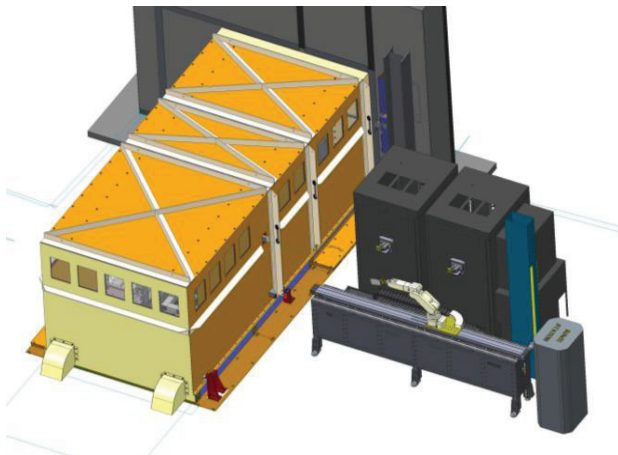


Figure 1: VMXi Hutch with the crystallisation units.

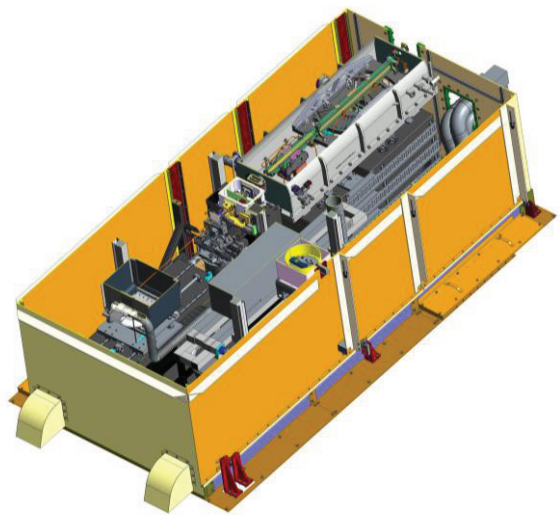


Figure 2: Section view of VMXi Hutch just above the beam path.

The plate will then be transferred into the internal storage buffer, sliding into the goniometer sample mount assembly. The journey from the temperature controlled crystallisation units to the temperature controlled internal storage will take less than 10s. For 4°C plates a thermal stability sleeve will be placed over the plate prior to being transferred onto the goniometer for data collection. The sleeve is designed to slow down the temperature rise of the 4°C plate in the 20°C environment. It was decided that active cooling on the goniometer would be likely to have a detrimental effect on the goniometer motion errors and thermal stability. The passive sleeve has been de-

ISBN: 978-3-95450-188-5 doi:10.18429/JACoW-MEDSI2016-WECA07

signed to both insulate from the ambient air and provide a large heat capacity per unit mass. The sleeve body contains a phase change chemical which absorbs latent heat as it melts.

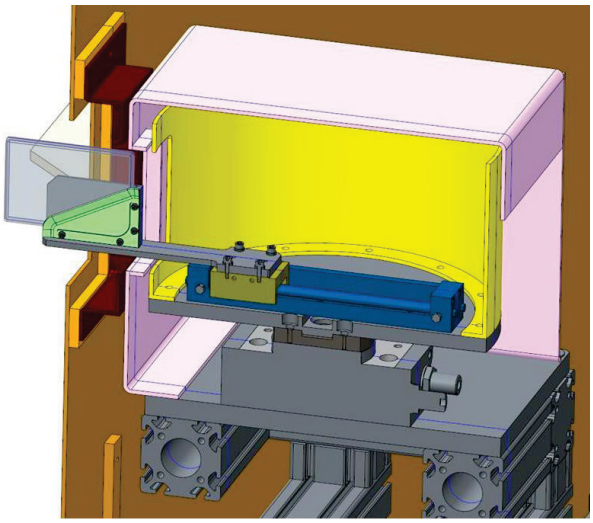


Figure 3: Hutch Loadlock; the plate is pulled into the yellow drum, which rotates within the pink shielding. The red & orange door may be rolled back to access the hutch.

The hutch gantry robot pneumatic gripper has two sets of fingers to hold either a plate or a sleeve with feedback to indicate which is held.

SAMPLE VIEWING SYSTEM

The on-axis vision system has been designed to give the optimum optical resolution without compromising flux. Either a high resolution objective, low resolution drilled lens or a He filled beam pipe can be driven in to position. The camera assembly will remain static with a three Vee kinematic mount providing the position repeatability rather than relying on the servo motion stages. The lens position repeatability will be key to the beamline performance because the visible and X-ray optics must remain coaxial. The samples will be automatically positioned using image pattern recognition. This compares the online image with the offline image used by the user to select the type and location of scan. An image of the mechanical assembly is given in Figure 4.

BEAM CONDITIONING ASSEMBLY

The beam conditioning assembly will be housed within a water cooled helium enclosure with a transparent lid. It will consist of attenuators, an X-BPM, a shutter/chopper and an I1 detector. The use of a He environment will provide convective cooling which is required for the motors and also the attenuators because the absorbed power could be > 2 W.

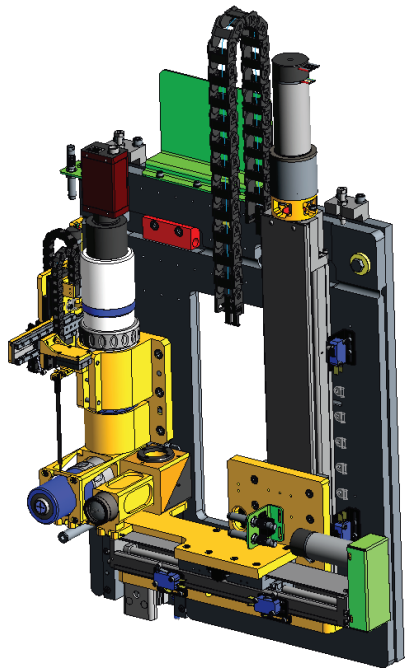


Figure 4: VMXi on-axis viewing and aperture assembly.

The three attenuator wheels will be mounted directly on stepper motor shafts. Absolute magnetic shaft encoders will be used for position feedback. The foils will be held in place by monolithic 3D printed flexure disks with numbers printed on the edge to give a visual position check through the lid. The Cividec single crystal diamond beam position monitor (BPM) will be mounted on an invar shaft directly through to the granite support for optimum stability. Cividec were chosen after a thorough diagnostics group performance study, for their good stability and linearity [4]. An image of the mechanical assembly is given in Figure 5.

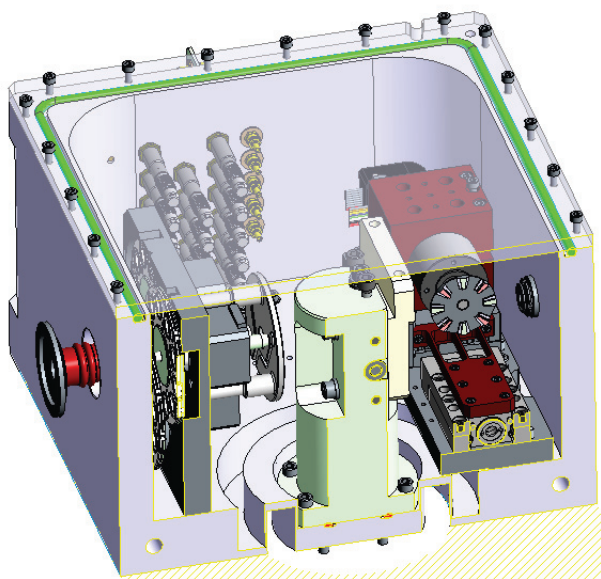


Figure 5: A section view of the beam conditioning assembly.

Content from this work may be used under the terms of the CC BY 3.0 licence (© 2016). Any distribution of this work must maintain attribution to the author(s), title of the work, publisher, and DOI.

ISBN: 978-3-95450-188-5 doi:10.18429/JACoW-MEDSI2016-WECA07

Content from this work may be used under the terms of the CC BY 3.0 licence (© 2016). Any distribution of this work must maintain attribution to the author(s), title of the work, publisher, and DOI.

A combined chopper/shutter was designed to provide shutter transit times < 20 µs and the ability to chop the beam synchronised to the detector readout, minimising the sample dose. A low inertia chop disk with a three step pattern is mounted directly on the shaft of a servo motor. This has been tuned to perform a 22° step in less than 6 ms to open/close the shutter. The whole servo motor is mounted on a horizontal slide to drive it into the beam and select the chopper pattern. The balanced design creates negligible vibration and should provide long term reliability.

The I1 detector is a boron doped CVD diamond to give a similar fluorescence yield to YAG but with the transparency and thermal conductivity of diamond. A diode detects the fluorescence signal through the edge of the diamond so the whole assembly is contained within the wall of the Al box.

SAMPLE GONIOMETER

The sample goniometer has been designed in-house to position the crystallisation plates for data collection. The design consists of a very stiff (11.5 Nm/µrad) air bearing to provide the omega rotation mounted with the rotary axis vertical. The axis of rotation will be driven coaxial with the X-ray using a custom crossed roller, harmonic drive horizontal X/Z table. On top of the airbearing will be a crossed roller horizontal Z stage, supporting a parallel kinematic X/Y stage. There is also a pneumatic tilt stage to rotate the plate by 20°. The main challenges for the design were that a large range of motion (120 x 80 x 50 mm) is required to position any part of the sample area in the beam, combined with the local accuracy requirement of < 0.5 µm over a sample volume of 2 mm^3. A high beamline throughput required a high speed, whereas a sphere of confusion goal of 0.5 µm required high resolution and accuracy. The space envelope was severely restricted by the neighbouring components. The data capture will be both dynamic and static. The final goniometer design is currently being finalised and will be commissioned by the end of the year.

Goniometer Prototype Design

A prototype of the parallel kinematic stage was built to refine the design. A full prototype goniometer will be assembled onto the endstation to allow the other systems to be commissioned while the final goniometer is built and calibrated. The prototype shown below used a number of plastic 3D printed parts. This was chosen because of the fast turn around and the amplified deflection as compared to the final metallic parts. It is possible to see or feel the stiffness of the nylon structures and quickly iterate the design accordingly. This is more rapid than a detailed ANSYS structural study and gives a tangible impression of performance.

The design required a ball joint angular range beyond that available from commercial products (±35°). Novel leg joints were created by sitting a 440C stainless steel ball in a nest of three ceramic balls. High flux magnets were positioned between the balls to preload the joint. This design provides a machine protection feature of disassembly rather than damage from a collision.

The leg supports were guided by two preloaded carriages and driven by a preloaded ball screw coupled directly to a servo motor. The stages separate use Renishaw™ readheads viewing the same central encoder scale.

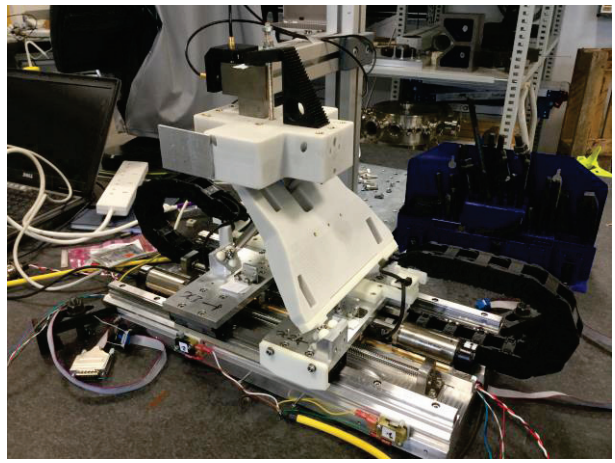


Figure 6: Prototype goniometer X/Y axes under test.

Goniometer Prototype Testing

The parallel kinematic assembly was tested in the lab as shown above in Figure 6, with orthogonal capacitance sensors. To drive right, both slides move right. To drive up, the slides move together. A number of automated scans were performed with varying motion parameters. An example plot of a 3 cycle scan is given below in Figure 7 with a zoomed-in view given in Figure 8. This data demonstrates position repeatability and cross talk between the virtual axes.

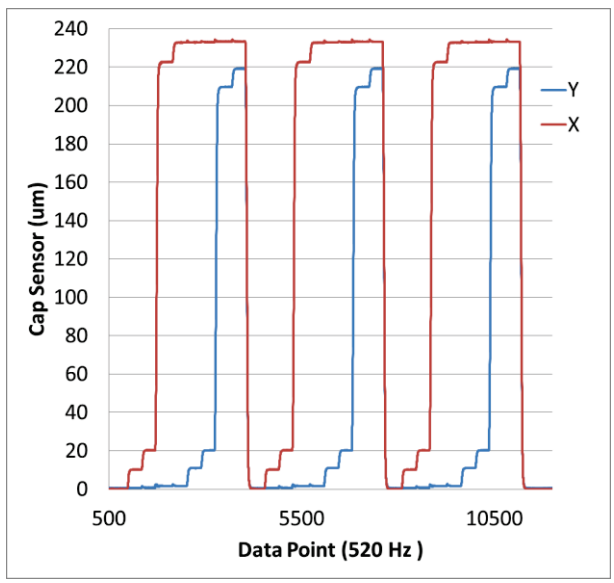


Figure 7: Prototype motion test data set full range,

ISBN: 978-3-95450-188-5 doi:10.18429/JACoW-MEDSI2016-WECA07

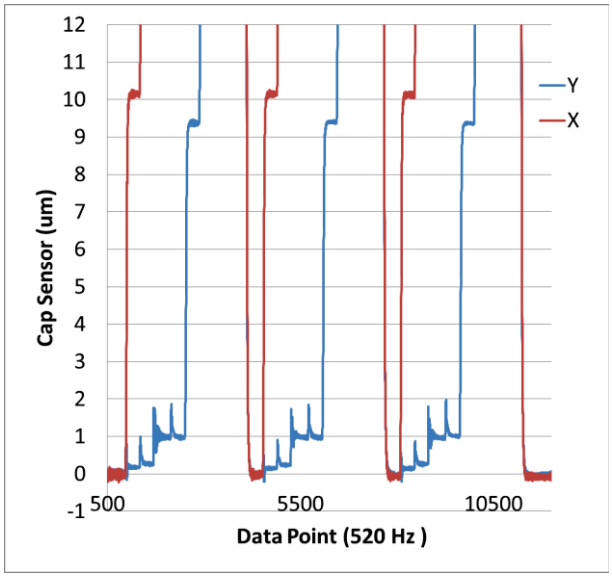


Figure 8: Prototype motion test data set zoom Y axis.

The stage exhibited < 200 nm bidirectional position repeatability even with repeated test moves of 20 mm. There were motion errors of ~ 1 µm as the stage accelerated and there were significant parasitic motions of ~ 0.5%. The parasitic motions were expected because of the geometry errors. Alignment and length of the legs was set by the 3D printed parts. Interferometers have been integrated into the final design mounted as close to the sample as possible to minimise the parasitic motions and hence improve accuracy.

AIR CONDITIONING

A custom air conditioning system has been designed for the hutch using computational fluid dynamics (CFD). The two dominant criteria were that the sample plate temperature should be maintained ± 1°C and that the mechanics should be stable to << 0.5 µm. The mechanical stability of the sample and the vision system is dictated by both air temperature and velocity. This is significantly complicated by the use of both 20°C and 4°C plates. The nominal hutch temperature will be 20 ± 0.1°C but within the hutch envelope is the internal storage with a 4°C section. The CFD was used to optimise duct locations with the aim of preventing the chilled air from moving past the sample viewing system.

CFD Results

A simplified model of the Endstation was created with a number of possible duct locations to allow easy reconfiguration. Heat load power and location approximations were made. An integrated Al heat exchanger with fan product was chosen to be used with water cooled Peltier units. The reason for selection was to minimise design effort and to define the size and the flow parameters. The AC units will be located in the neighbouring hutch with the air ducted through where required. This will allow the use of the existing dehumidified air supply and will place the fans outside the sensitive area. The AC control racks and raw cooling water droppers are also located in the upstream hutch. Numerous configurations were run with the following conclusions:

- The air extract should be located close to the 4°C on the other side from the sample position to draw the cool air out of the hutch as shown in Figure 9.
- The use of a roof mounted air sock would require an unrealistic flow rate to disrupt the thermal stratification.
- The heat input to the hutch should be minimised. This will be achieved by ducting away the warm air from the 6M area detector and the fluorescence detector and by water cooling all the motors. An example image of thermal data is given in Figure 10.
- The addition of sealed volumes within the hutch envelope could both direct flow where required and reduce the volume of air to be actively cooled. An example of flow into the extract duct is presented in Figure 11.
- Any almost enclosed regions form a reservoir of stagnant warm air which could periodically flow giving detrimental effects.
- The use of an extra separate heat exchanger system to provide could provide a gentle flow of thermal stabilised air across the sample position creating a well-defined temperature.
- Significant air leaks to ambient can disrupt the desired flow.

The final design and some example CFD results are given below.

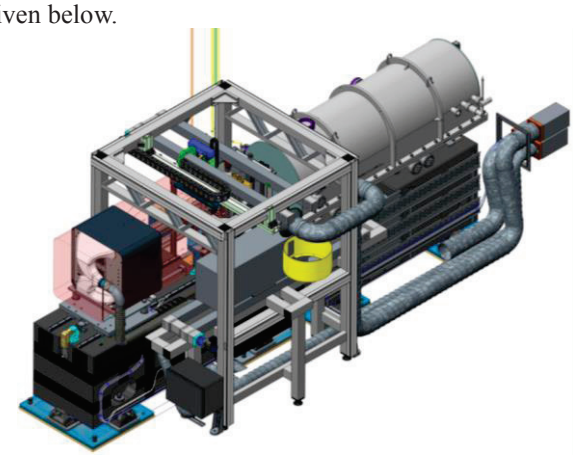


Figure 9: VMXi air conditioning design showing the detector extract and the ducting.

CONCLUSION

The VMXi beamline is currently being assembled and commissioned with first user planned for the end of 2016.

Content from this work may be used under the terms of the CC BY 3.0 licence (© 2016). Any distribution of this work must maintain attribution to the author(s), title of the work, publisher, and DOI.

ISBN: 978-3-95450-188-5 doi:10.18429/JACoW-MEDSI2016-WECA07

Content from this work may be used under the terms of the CC BY 3.0 licence (© 2016). Any distribution of this work must maintain attribution to the author(s), title of the work, publisher, and DOI.

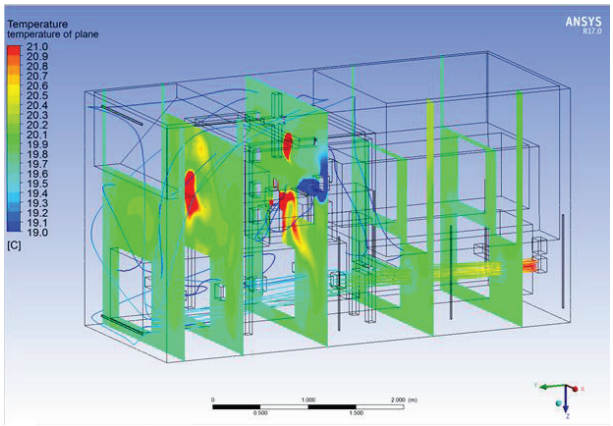


Figure 10: CFD data; the planes show temperature slices and flow streamline source is the main hutch AC inlet.

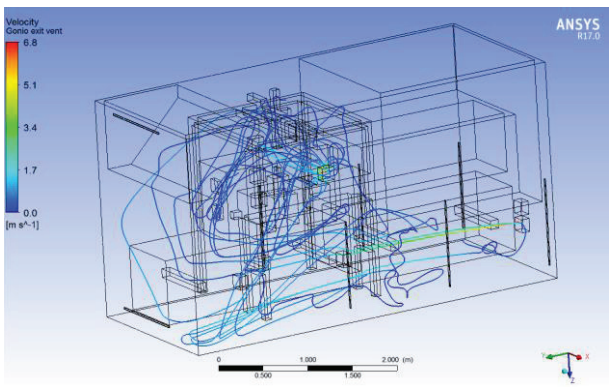


Figure 11: CFD data; flow streamlines show the paths to the main hutch AC outlet. The velocity is represented by the colour.

REFERENCES

[1] D. Butler and J. Kelly, "Design of the Diamond Light Source DMM for the VMXi Beamline", presented at MEDSI'16, Barcelona, Spain, September 2016, paper FRBA03, this conference.

[2] J. Kelly, "DMM Thermal Mechanical Design", presented at MEDSI'16, Barcelona, Spain, September 2016, paper TUPE01, this conference.

[3] L. Alianelli, "Double Multilayer Monochromator for VMXi", Diamond Light Source, Harwell, UK, Rep. SCI-OPT-REP-0097, April 2014.

[4] C. Bloomer et al., "An Experimental Evaluation of Monochromatic X-ray Beam Position Monitors at Diamond Light Source", presented at SRI Conf. (SRI 2015), New York, US, July 2015, paper WED-P-077, unpublished.

ISBN: 978-3-95450-188-5 doi:10.18429/JACoW-MEDSI2016-WEPE01

COMBINED FIXED MASK, PHOTON SHUTTER, SAFETY SHUTTER, AND COLLIMATOR DESIGN FOR BXDS IVU AT THE CLS

M. J. P. Adam *, C. Bodnarchuk, Canadian Light Source Inc., Saskatoon, Canada

Abstract

The first shutter assembly outside of the Front End (FE) for Brockhouse X-Ray Diffraction and Scattering Sector (BXDS) beamline required a unique design solution to accommodate all components into the safety shutter position.

Located between the IVW high energy wiggler monochromator and POE1 wall, the total envelope size approximated 1 m x 0.660 m (LxW). Accommodating this smaller space required an alternative shutter design than traditionally used implemented at the CLS.

The alternative design combined the collimator (CLM), safety shutter (SSH), photon shutter (PSH) and Fixed Mask (FM) into one chamber. Finite Element Analysis (FEA) was conducted on the FM and PSH assembly to verify that geometric designs were adequate for reasonable operation in the beamline. FEA was used to determine the steady-state thermal and static-structural response in both operating positions. Missteer was analyzed for both operating positions to a maximum of 2.5 mm (commonly accepted missteer used at the CLS) from center. Finally, two extreme position (partially closed/open) analyses were completed for determination of potential, but unlikely operating conditions.

INTRODUCTION

The first In Vacuum Undulator (IVU) shutter assembly outside of the Front End (FE) for Brockhouse X-Ray Diffraction and Scattering Sector (BXDS) beamline required a unique design solution to accommodate radiation protection of the In Vacuum Wiggler (IVW) IVU secondary optical enclosures.

Located between the IVW high energy wiggler monochromator and the end of POE1, the total envelope size approximated 1 m in length and 0.660 m width. This space required the design and installation of a FM to protect and shield all downstream components, a PSH to absorb incoming beam, a SSH to close and isolate radiation for entrance into the downstream hutches, and a CLM to remove Bremsstrahlung radiation from escaping the IVU beamline. Accommodating a smaller space required an alternative shutter design than traditionally implemented at the CLS (Fig. 1). IVU shutter is located between 27 890 mm and 29 015 mm from the center of straight Cell 04. SPECTRA [1] was used to calculate the heat source data from parameters for the CLS Storage Ring (SR1) (with ring current 500 mA and field energy of 1 T).

The shutter precedes SOE2, POE2, and finally SOE3 along the beamline and has a total power absorption requirement of 1100 W (at 500 mA). The beam spot as seen by the combined shutter is directly apertured by Fixed Mask 3 from the FE.

* madison.adam@lightsource.ca

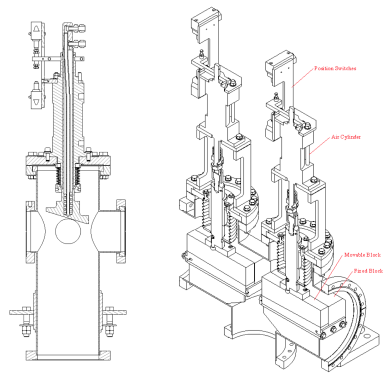


Figure 1: Typical CLS shutter designs. PSH (left) used most commonly in the FE is 300 mm in chamber length. SSH (right) used most commonly within the FE and POE of beamlines ranges between 500 mm–1200 mm in chamber length. And CLM (not shown) 400 mm in chamber length. Total length of a basic arrangement of these components exceeds the allowable space for the BXDS shutter location.

Design Objectives

The key design considerations for the shutter design, in addition the requirements stipulated within CLS Technical Specifications, are:

- The FM and PSH are combined into one component that will act as a photon absorbing surface as well as protection for the CLM/SSH.
- The SSH and CLM have been combined so that as one they block Bremsstrahlung radiation. The SSH must have a movable tungsten block directly in front of the collimator to prevent unintended Bremsstrahlung to pass by when in the closed position.

The FM-PSH must satisfy two operating positions:

- Open – allowing beam to pass through with clearance, while shielding IVW SOE2.
- Closed – stopping all beam energy produced from the IVU and missteered IVW rays. Stopping all associated radiation from the SOE2, POE2, and SOE3 enclosures.

PSH/SSH Requirements at the CLS

The below requirements are particularly important to the safety shutter set (PSH & SSH). The final design needed to ensure that both sets of requirements for the photon and radiation absorbing materials meet facility design expectations.

From "CLS Photon & Safety Shutter Design Specification 8.4.41.1 – Rev. 0" [2]:

Content from this work may be used under the terms of the CC BY 3.0 licence (© 2016). Any distribution of this work must maintain attribution to the author(s), title of the work, publisher, and DOI.

ISBN: 978-3-95450-188-5 doi:10.18429/JACoW-MEDSI2016-WEPE01

Content from this work may be used under the terms of the CC BY 3.0 licence (© 2016). Any distribution of this work must maintain attribution to the author(s), title of the work, publisher, and DOI.

- Transition from the open to the close position of either SSH or PSH must occur within 1 second.
- The PSH and SSH must be designed as 'fail safe'; loss of air pressure, electrical power, and/or external forces (atmospheric) must result in the absorber moving to the closed position

From "CLS Guideline for Analysis of Synchrotron and Electron Beam Absorbing Components 8.1.69.1 – Rev. 0" [3] Specific CLS facility cooling water properties are:

- Density: 971 kg m^{-3}
- Specific Heat: 4179 J kg^{-1} °C]

CLSI Facility Limits:

- Velocity: <=5 m/s
- T <= 10 °C (using bulk temp rise equations)

Heat load of the IVU beam was estimated using SPECTRA resulting in a power load of 1.1 kW. The allowable thermal film coefficient found from the cooling calculations is 10.475 W^2 m^{-1} W/m2 with water supply velocity of 2.1m/s as per the CLS expected design requirements.

DESIGN SOLUTION

Combination of FM-PSH, SSH, & CLM

The design combined the CLM, SSH, PSH and FM into one chamber (Fig. 2). The total length of the chamber assembly is 680 mm with 6" CF flanges for entrance and exit ports. The chamber includes the basic regiment of CCG/TCG and rouging ports. The Ion Pump port (8" CF flange) accommodates a 300 l s^{-1} Varian Starcell, mounted from the bottom of the chamber.

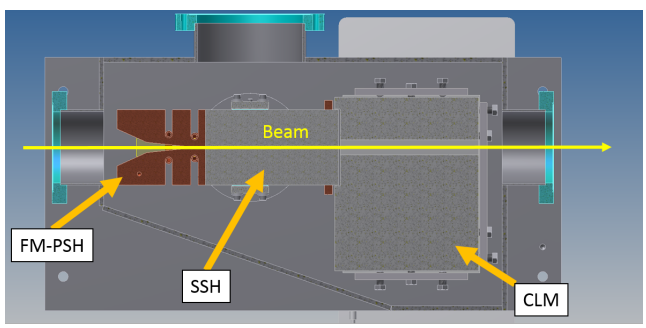


Figure 2: Plane view showing internal layout of the combined shutter. Beam passes left to right through the chamber.

The open position allows for all desirable IVU beam to pass through the combined shutter. The beam proceeds through the white beam transport, into the POE2 enclosure and finally into the SOE3 endstation. The closed position stops the beam and radiation from leaving POE1, while not hindering IVW operation.

To accommodate access to the chambers internal components, the lid is removed from above (Fig. 3). This arrangement was required after the shielding calculations for the IVW High Energy monochromator were complete. The interface between the location of the shielding and the required IVU CLM width was extremely snug. The required configuration allows access to the chamber without removing lead shielding, that would affect operation for the IVW high energy beamline.

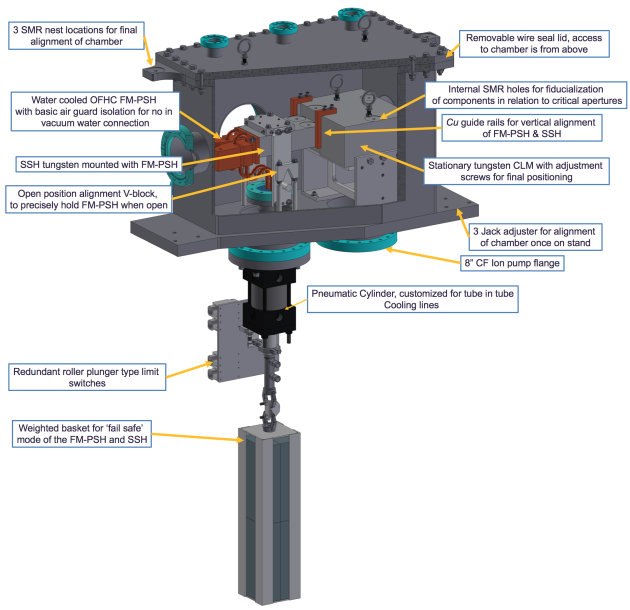


Figure 3: Illustration showing combined shutter design. Details are listed for unique design features.

The combined shutter includes a vacuum air guarded interface for the cooling water supply channels, preventing an in vacuum water connection.

An RTD is located on the surface of the FM-PSH for use in assessing the amount of heat absorbed on the FM-PSH during normal operation.

The combined shutter procurement was awarded to RMD Engineering (Saskatoon, Saskatchewan). Fabrication is estimated to complete Nov. 2016. Installation and testing to be completed during the CLS Winter shutdown.

FEA VERIFICATION

Methodology

Finite Element Analysis (FEA) using ANSYS 17.0 was conducted on the FM-PSH assembly to verify that geometric designs were adequate for reasonable operation in the beamline. FEA was used to determine the steady-state thermal and static-structural response in both operating positions. Missteer was analyzed for both operating positions to a maximum of 2.5mm (commonly accepted missteer used at the CLS [2] from center. Finally, two extreme positions (5 mm open and closed) analysis were completed for determination of potential, but unlikely operating conditions.

ISBN: 978-3-95450-188-5 doi:10.18429/JACoW-MEDSI2016-WEPE01

Analysis for the FM-PSH was performed on the full part and cooling water lines. With case by case specified target surfaces for imported heat flux. Heat flux data was calculated from SPECTRA, using beamline parameters for the IVU, and projected onto the FM-PSH model.

Grazing angle scaling was completed using APDL scripts to more accurately represent actual heat absorption. The main grazing surface (sides) is 6.04° from the sagittal (YZ-plane). The secondary grazing surface is 24.23° from the sagittal plane. The tertiary grazing surface is 3.01° from the sagittal plane. The root of the absorber is semi-cylinder in shape and was estimated to approximate the secondary surface angle. Heat flux was imported into workbench from SPECTRA derived files. Realistic heat source dimensions as defined by the FE FM3 are approximately 9.84 mm x 3.48 mm at the combined shutter location (28 524 mm from ID source).

Results

Fully closed the beam absorption resulted in acceptable values (Fig. 4) as described by the CLS Technical Specifications [2].

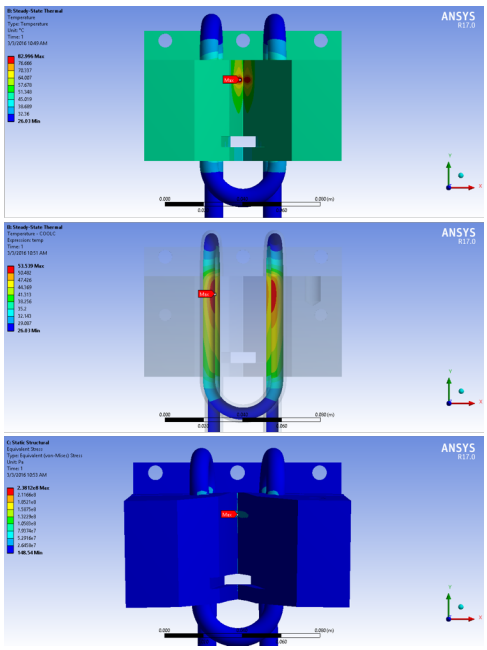


Figure 4: Fully closed results with maximum temperature (top) found to be 83 °C, cooling channel maximum temp of sidewall 54 °C, and maximum vonMises Stress 240 MPa of the OFHC FM root.

Missteer scenario, the beam is only partially absorbed resulting (Fig. 5) in heating along the edge aperture of the FM-PSH, still within acceptable CLS specifications [2]. Beam

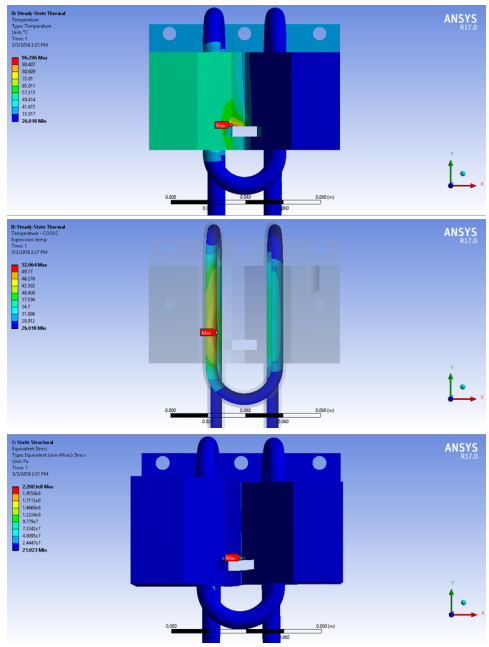


Figure 5: Partially open with missteer results with maximum temperature (top) found to be 97 °C, cooling channel maximum temp of sidewall 52 °C, and maximum vonMises Stress 220 MPa of the OFHC FM root.

projections were rigidly transformed within ANSYS to apply heat flux load.

CONCLUSION

The combined shutter design offers beam and radiation absorption in a considerably smaller space when compared to conventional CLS designs. The design and FEA provided verification of heat mitigation when the shutter experiences closed, open and missteer conditions.

ACKNOWLEDGMENT

Special acknowledgment to Shawn Carriere and Siyue Chen. *Thank You* to the CLS Engineering group and the participants of the combined shutter design review.

REFERENCES

[1] SPECTRA (version 10.0.7 64bit) http://radiant.harima.riken.go.jp/spectra/

[2] "CLS Photon & Safety Shutter Design Specification 8.4.41.1 – Rev. 0", Canadian Light Source Inc., Saskatoon, Saskatchewan, Canada

[3] "CLS Guideline for Analysis of Synchrotron & Electron Beam Absorbing Components 8.1.69.1 – Rev. 0", Canadian Light Source Inc., Saskatoon, Saskatchewan, Canada

Content from this work may be used under the terms of the CC BY 3.0 licence (© 2016). Any distribution of this work must maintain attribution to the author(s), title of the work, publisher, and DOI.

ISBN: 978-3-95450-188-5 doi:10.18429/JACoW-MEDSI2016-WEPE02

PERFORMANCE EVALUATION OF FAST CLOSING SHUTTER SYSTEM AT THE SPring-8 FRONT-END

S. Takahashi*, M. Sano, A. Watanabe
JASRI, Hyogo, 679-5198, Japan

Abstract

The fast closing shutter (FCS) system plays an important role in protecting the ultra-high vacuum in the SPring-8 storage ring from an accidental vacuum hazard in the beamlines. In order to predict the transit time of the shock wave and the following pressure increase, a shock tube system with an inner diameter of 35 mm and a total length of 10 m was prepared to measure the shock Mach number. Experiments have been conducted that simulated an inrush of the atmosphere into the high-vacuum (~10^{-3} Pa) pipe by using a trigger system that combines a thin cellophane diaphragm with a plunger. Special ionization gauges with a high-speed amplifier were distributed about every 1 m to detect the transit time of the shock wave and to measure the pressure in the low-pressure chamber (LPC) after the actuation of the FCS system. By inserting larger pipes (inner diameter=390 mm) with various lengths into the shock tube, the attenuation in the shock wave was systematically investigated. The results of the experiment confirmed that the pressure increase in the LPC exhibits a close relationship with the total internal volume of the shock tube.

INTRODUCTION

More than 55 beamlines, which are arranged radially from the SPring-8 storage ring (circumference: ~1.5 km), are now in operation for various experiments. Maintaining the ultra-high vacuum (UHV; 10^{-8}–10^{-9} Pa) in the storage ring is indispensable for avoiding any decrease in beam lifetime and the generation of Bremsstrahlung radiation. Therefore, when a severe vacuum accident occurs in a beamline, it becomes possible for the UHV of the storage ring to break due to an air inrush, which would be followed by the long-term suspension of the user experiments. To prevent such a situation from occurring, a commercially available fast closing shutter (FCS) system (VAT Series 773 linear actuator type) was prepared in each front-end. This system works to detect rapid vacuum deteriorations and is capable of immediately closing the shutter main body, which is installed at the most upstream side of the beamline front end. The shutter does not have an airtight, UHV-compatible vacuum at the seat; that is because typical sealing materials, such as VITON (a type of fluorocarbon rubber), cannot be used because of the severe radiation environment in the 8 GeV ring tunnel. In this way, the FCS system primarily aims to prevent the inrush of a shock wave into the storage ring without delay. Accordingly, a general all-metal gate valve (GV) that is radiation resistant and interlocked with the FCS must also be installed at the upstream side of the FCS in order to prevent further vacuum deterioration.

EXPERIMENTAL SETUP

As shown in Fig. 1, the shock tube system, which has a total length of about 10 m, is mainly composed of vacuum pipes with electro-polishing treatment on the inner surface, a window part with a thin diaphragm made of moisture-proof cellophane and an HV sensor for the trigger, low-pressure and high-pressure chambers at both ends of the pipe, and miniature ionization gauges (MIGs) with a sampling time of 0.1 ms. We defined the low-pressure chamber (LPC) and high-pressure chamber (HPC) as the upstream side and downstream side, respectively. The inner diameter of the vacuum pipe is 35 mm. This corresponds to the standard 2.75-inch ConFlat flange, which has the same nominal aperture size of actual front-end components for the SPring-8 standard undulator beamline. Both the FCS and GV, which are installed just downstream from the LPC, are used with the 2.75-inch ConFlat flange. The window part can simulate momentary fracture of the beryllium window by breaking the cellophane diaphragm using a plunger connected to a pneumatic driving cylinder. The aperture size of the window is 10 mm (diameter), in accordance with the actual component. The MIG measurement spans three orders of magnitude in the range from 10^{-4} to 10 Pa (typically 10^{-3}–1 Pa) by fixing the emission current. Fast pressure measurement with a sampling time of 0.1 ms can be achieved by combining a high-speed amplifier with a generic vacuum controller.

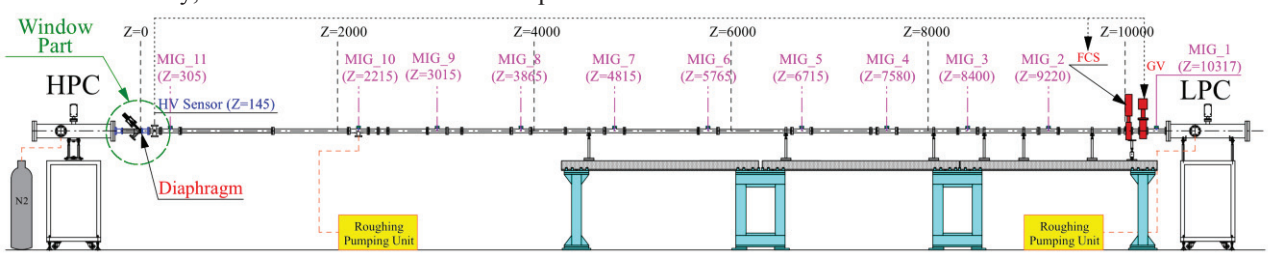


Figure 1: Schematic layout of the shock tube basic system with a total length of 10 m.

* takahasi@spring8.or.jp

Content from this work may be used under the terms of the CC BY 3.0 licence (© 2016). Any distribution of this work must maintain attribution to the author(s), title of the work, publisher, and DOI.

ISBN: 978-3-95450-188-5 doi:10.18429/JACoW-MEDSI2016-WEPE02

The MIGs were mounted at ~1 m intervals to detect rapid increases in pressure, and the transit time of the shock wave at each MIG is represented by the time when the rapid increase in pressure is detected at each MIG. In addition to analog output from the MIGs, the following signals were recorded with a high-speed data logger synchronized with the operating command of the plunger as a trigger: "HV sensor" (output INRUSH), "FCS closed" (close output external), and "GV closed".

ADVANCED PREPARERATION

Measuring Rupture Time of Diaphragm

To determine the exact time when the diaphragm was broken, we prepared a high-speed video camera system. By synchronizing the starting time of the photographing with the triggering of the operating command of the plunger, the delay time between the moment of the diaphragm fracture and the rapid increase in pressure at MIG_11 in Fig. 1 (the closest MIG to the diaphragm) was estimated to be 0.2 ms on average.

Measuring Closing Time of FCS

The signal of "FCS closed" is output at the moment when the latch is just released – namely, the starting time of the closing operation. An off-line experimental setup, which consisted of the FCS, a pin photodiode, and a laser system, was prepared to measure the actual driving time of the FCS. The laser emitted inside the FCS aperture through view glass windows was detected by the pin photodiode, which was located on the opposite side of the FCS from the laser. We monitored the temporal relationship between the output of the "FCS closed" signal and the signal of the pin photodiode being interrupted. By varying the height level of the laser, the driving speed from the open position to the close position was estimated to be 8.32 mm/ms. As the result, the actual driving time of the FCS with an aperture size of 35 mm was calculated to be 4.2 ms.

EXPERIMENTS

The LPC and vacuum pipes were evacuated to a pressure on the order of 10^{-3} Pa by two roughing pump units. A nitrogen gas container was connected to the HPC to maintain atmospheric pressure, resulting in a pressure differential that spanned eight orders of magnitude. Then, we actuated the plunger to break the diaphragm immediately after isolating the pumping units by valves. Besides the basic configuration shown in Fig. 1, (which was constituted only by 35 mm inner-diameter plain pipe (35PP)), experiments were carried out for some configurations with 16" plain pipe (16"PP) inserted into the tube. Three kinds of the 16"PP (inner diameter=390 mm) with lengths of 0.25 m, 0.5 m, and 1 m were prepared. For each configuration, measurements were carried out four times in the cases of both FCS/ACT and FCS/NON-ACT; the mean value was used in the evaluation. FCS/NON-ACT means that only the GV was actuated by a signal of the HV sensor.

RESULTS AND DISCUSSIONS

The blue-circled closed symbols (Basic_35PP) in Fig. 2 show the transit times of the shock wave as a function of the distance from the diaphragm in the case where only 35PP is present. The shock wave velocity gradually decreased with the propagation of the wave owing to the pipe friction. The transit time when the shock wave reached MIG_1, which was located about 10.32 m from the diaphragm, was 15.7 ms. Figure 3 shows a flow chart for the series of events accompanying the FCS action with actual values measured in the case of 35PP as an example. Immediately after the diaphragm was broken, the HV sensor detected the abnormality and sent a command to close the FCS in 3.4 ms, which was followed by the start of the FCS closing action after 21.6 ms has elapsed, which is thought to depend on the cable length between the controller and the FCS body. We utilized a 50 m long cable in this experiment that is identical to that actually used in SPring-8. The FCS completely closed in 25.8 ms, which was derived by adding the FCS driving time of 4.2 ms to 21.6 ms. On the other hand, the shock wave propagation reached MIG_1 in 15.7 ms, so that in this configuration the FCS could not prevent the inrush of the shock wave into the LPC. After that, the vacuum leak continued through the FCS to the LPC until the GV closed after 619 ms had elapsed.

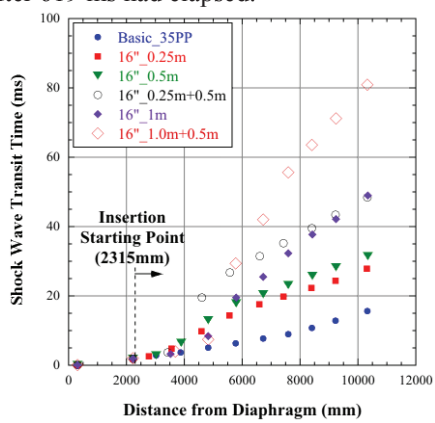


Figure 2: Transit times of the shock wave as a function of the distance from the diaphragm in the case of plain pipe (Basic_35PP) and in the case of inserting various 16"PPs.

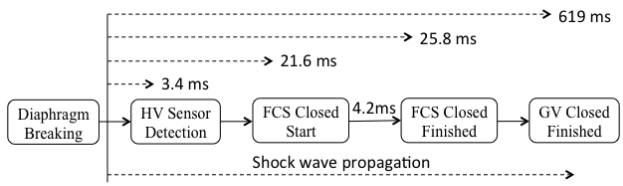


Figure 3: Flow chart for a series of event accompanying the FCS action, along with typical actual values in the case of basic configuration (35PP only) as an example.

The transit times of the shock wave in the case of inserting various 16"PPs into the tube are also shown in Fig. 2. In all cases, the 16"PP was inserted from the same starting point, which was located 2315 mm from the diaphragm. The case of "0.25 m + 0.5 m" implies that a 0.25 m long 16"PP and a 0.5 m long 16"PP were installed in

Content from this work may be used under the terms of the CC BY 3.0 licence (© 2016). Any distribution of this work must maintain attribution to the author(s), title of the work, publisher, and DOI.

ISBN: 978-3-95450-188-5 doi:10.18429/JACoW-MEDSI2016-WEPE02

Content from this work may be used under the terms of the CC BY 3.0 licence (© 2016). Any distribution of this work must maintain attribution to the author(s), title of the work, publisher, and DOI.

tandem. The velocity of the shock wave began to drop sharply after exiting from the inserted pipe; this means that the insertion of an expanding pipe delays the shock wave propagation. To evaluate this effect quantitatively, we organized the data by using the Mach number (M_a), which indicates the intensity of the shock wave, and can be represented by the following equation:

$$M_a = \frac{(Z_i/t_i)}{c}. \quad (1)$$

where Z_i is the distance from the diaphragm at the measuring point (i), t_i is the transit time of the shock wave at the measuring point (i), and c is the speed of sound. As shown in Fig. 4, which depicts the relationship between the M_a and the distance from the diaphragm, the value of M_a in the case of only 35PP decreased gradually from 3 to 2. On the other hand, in the case of inserting the 16"PP, M_a dropped sharply after exiting the insertion component and became almost constant at 0.6–1.1 when the distance from the diaphragm exceeded about 8 m. This means that the transit time should be proportional to the distance after 8 m. Moreover, the larger pipe (16"PP) should be installed within at least 4 m of the diaphragm so that the sufficient delay time could be gained.

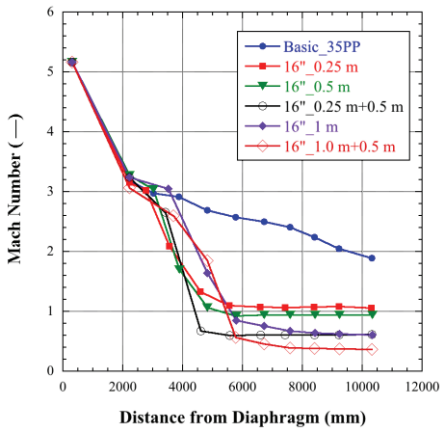


Figure 4: Relationship between the Mach number and the distance from the diaphragm in the case of inserting various 16"PP.

Figure 5 shows M_{ave} as a function of the total internal volume of the shock tube. Here, M_{ave} represents the value of M_a averaged over three points at locations further than 8 m. With an increase in the total internal volume, the attenuation effect of the shock wave increased, which resulted in a decrease in M_{ave}. It was found that M_{ave} became subsonic when the total internal volume exceeded 0.05 m^3. Figure 6 shows the final pressure in the LPC for FCS/ACT (right Y-axis with open symbols) and FCS/NON-ACT (left Y-axis with closed symbols) as a function of the total internal volume. Roughly speaking, the former is about four orders of magnitude lower than the latter for every configuration, which is a direct consequence of the FCS system. It should also be noted that the final pressures exhibited an almost linear relationship with the total internal volume.

CONCLUSIONS

The performance of the FCS system was successfully evaluated by using a shock tube system with a total length of about 10 m, which was able to simulate an air inrush into the rarefied gas dynamics region. The experiments were carried out for not only the plain pipe configuration but also for many configurations with larger pipes having various lengths into the shock tube. In the case of only plain pipe with an inner diameter of 35 mm, which corresponded to the standard 2.75-inch ConFlat flange, the shock wave propagation would reach a distance of 10.32 m in 15.7 ms. The insertion of the larger pipe resulting in the rapid cross-sectional change is effective for delaying the transit time of the shock wave, and the total internal volume of the shock tube is the primary factor in the delay time and the following pressure increase. The FCS system could suppress the pressure increase by about four orders of magnitude compared with the case of only the GV.

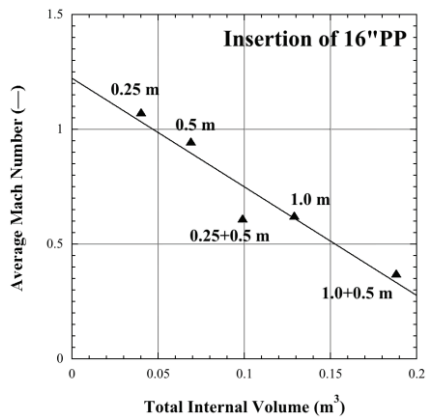


Figure 5: Average Mach number as a function of the total internal volume in the shock tube in the case of inserting various 16"PPs.

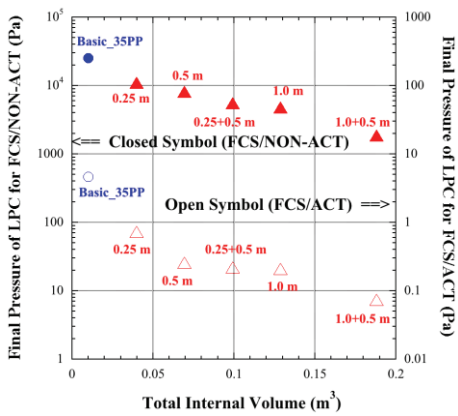


Figure 6: Final pressures in the LPC after closing the GV as a function of the total internal volume. The right Y-axis with open symbols and the left Y-axis with closed symbols correspond to FCS/ACT and FCS/NON-ACT, respectively.

ACKNOWLEDGEMENT

The authors would like to thank Dr Ohkuma of SPring-8 for valuable discussions and comments.

ISBN: 978-3-95450-188-5 doi:10.18429/JACoW-MEDSI2016-WEPE03

BEAMLINE FRONT ENDS AT THE 2.5-GeV PHOTON FACTORY STORAGE RING

H. Miyauchi†, S. Asaoka, T. Tahara, Accelerator Laboratory, High Energy Accelerator Research Organization (KEK), Tsukuba, Ibaraki, Japan

INTRODUCTION

Since the first commissioning in 1982, the 2.5-GeV Photon Factory (PF) storage ring has been upgraded third times in 1986, 1997 and 2005, in order to reduce the beam emittance and to produce new short-straight sections for in-vacuum short period undulaters.

In order to adopt the PF storage ring upgrades, the beamline front ends were necessary to be modified. We look back the old and new components of the PF beamline front ends.

MANUAL GATE VALVES

Manual gate valves separate the beamline front ends from the storage ring. We used to use the Viton O-ring seal manual gate valves, but the Viton O-ring seal could not bear the radiation damage. So we replaced the Viton O-ring seal manual gate valves into the all metal manual gate valves (Figs.1 and 2).

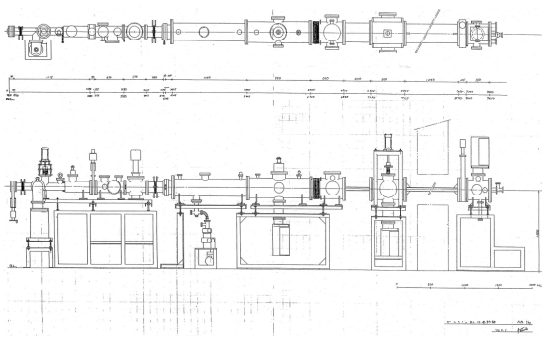


Figure 1: Old BL-15 Front End Layout.

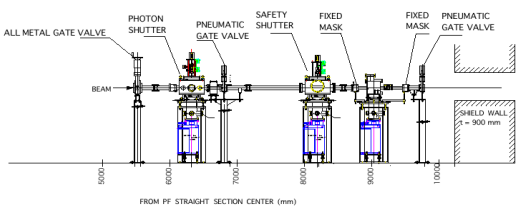


Figure 2: New BL-15 Front End Layout.

PHOTON SHUTTERS

At the first commissioning in 1982, the PF storage ring had only 4 bending beamlines and no insersion devices, the structure of the water cooling Cu absorber inside the photon shutter was very simple (Fig. 3). After installing undulators, we developed the rod type of photon shutter (Fig. 4). And after installing multi-pole wigglers, in order to reduce the loading power density on the surface of shutter, the water cooling Cu absorber inside the photon shutter was made triangle-shaped at the multi-pole wiggler beamline front ends (Fig. 5).



Figure 3: Photon Shutter for Bending BL Front End (Old Type).

† hiroshi.miyauchi@kek.jp

Content from this work may be used under the terms of the CC BY 3.0 licence (© 2016). Any distribution of this work must maintain attribution to the author(s), title of the work, publisher, and DOI.

ISBN: 978-3-95450-188-5 doi:10.18429/JACoW-MEDSI2016-WEPE03

Content from this work may be used under the terms of the CC BY 3.0 licence (© 2016). Any distribution of this work must maintain attribution to the author(s), title of the work, publisher, and DOI.

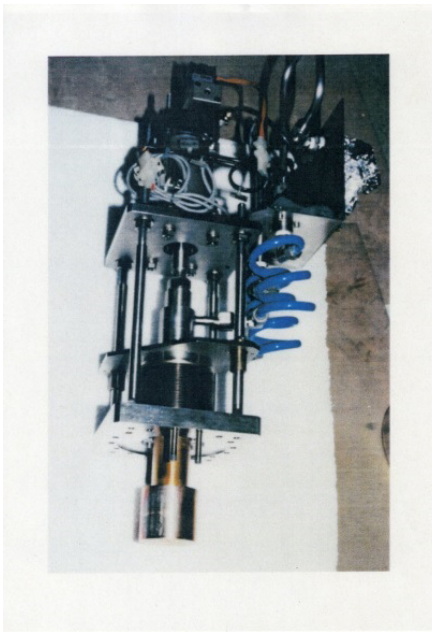


Figure 4: Photon Shutter for Undulator BL Front End (Old Type).

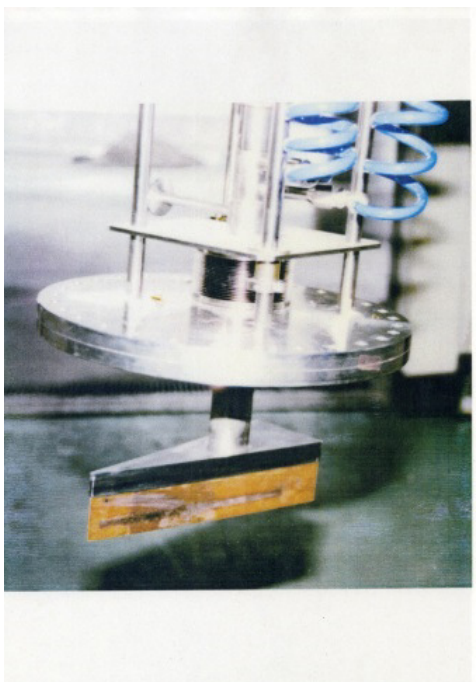


Figure 5: Photon Shutter for Multi-Pole Wiggler BL Front End (Old Type).

At the time of the upgrade in 1997, we designed the photon shutter with 86 degrees-inclination-angle for the insertion-device sources, that was able to adopt the plan of the PF high current operation (2.5-GeV, 1000 mA) (Fig. 6). We have to take measure of the multi-reflection between the shutter block surface and the water cooling Cu cover, because the grazing angle incidence promotes the photon reflectivity. At the time of upgrade in 2005, we developed the com-pact design "V" shaped water cooling Cu absorber (V-absorber) inside the photon shutter for in-vacuum short period undulator (Fig. 7). The V-absorber is designed for universal use of photon shutters for compact SR facilities.

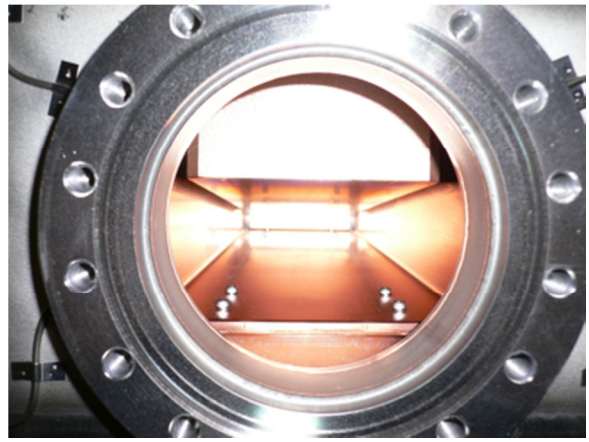


Figure 6: Photon Shutter for Multi-Pole Wiggler and Long Undulator BL Front End (New Type).

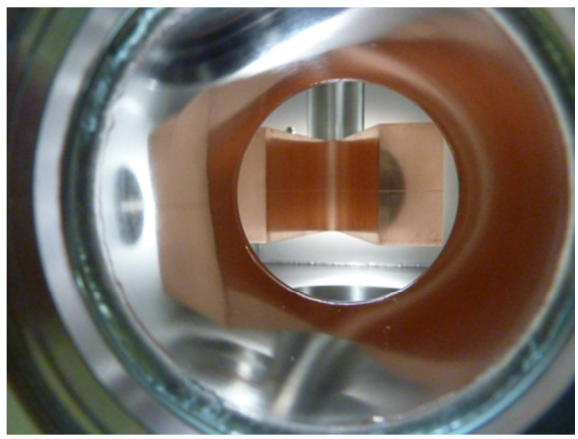


Figure 7: Photon Shutter for Multi-Pole Wiggler and Long Undulator BL Front End (New Type).

SAFETY SHUTTERS

The material of the safety shutter block was replaced from 400-mm thick stainless steel with oil-hydraulic cylinder (Figs. 8 and 9) by 250-mm thick tungsten with pneumatic cylinder (Figs.10 and 11).

ISBN: 978-3-95450-188-5 doi:10.18429/JACoW-MEDSI2016-WEPE03



Figure 8: Old Safety Shutter: 400-mm Thick Stainless Steel Block.



Figure 9: Old Safety Shutter: Oil-Hydraulic Cylinder.

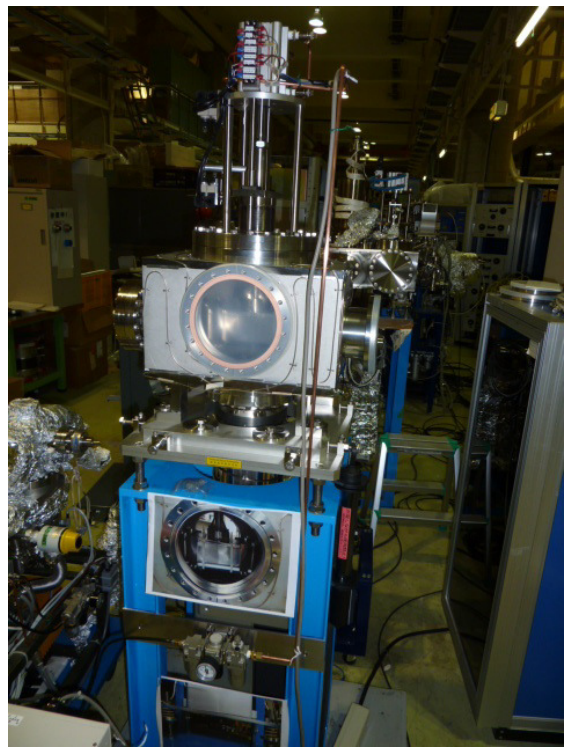


Figure 10: New Safety Shutter: 250-mm Thick Tungsten Block with Pneumatic Cylinder.

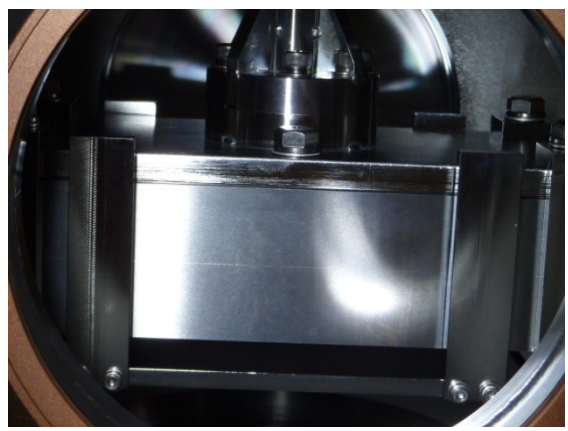


Figure 11: New Safety Shutter: 250-mm Thick Tungsten Block.

Content from this work may be used under the terms of the CC BY 3.0 licence (© 2016). Any distribution of this work must maintain attribution to the author(s), title of the work, publisher, and DOI.

ISBN: 978-3-95450-188-5 doi:10.18429/JACoW-MEDSI2016-WEPE04

DESIGN OF X-RAY BEAM POSITION MONITOR FOR HIGH HEAT LOAD FRONT ENDS OF THE ADVANCED PHOTON SOURCE UPGRADE*

S.H. Lee†, B.X. Yang, J. Mulvey, M. Ramathan
Advance Photon Source, Argonne National Laboratory, Argonne, IL 60439, USA

Abstract

Accurate and stable x-ray beam position monitors (XBPMs) are key elements in obtaining the desired user beam stability in the Advanced Photon Source (APS). Currently, the APS is upgrading its facility to increase productivity and to provide far more highly coherent and brilliant hard x-rays to beamline experiments with a new storage ring magnet lattice based on a multi-bend achromat (MBA) lattice. To improve the beam stability, one of the proposed beam diagnostics is the grazing-incidence insertion device x-ray beam position monitor (GRID-XBPM) for high heat load (HHL) front ends (FEs) at the APS. In this paper, final design of the GRID-XBPM and the high-power beam test results at beamline 27-ID-FE will be addressed.

INTRODUCTION

The APS at Argonne National Laboratory is the largest synchrotron radiation facility in the western hemisphere, providing the highest-brightness high-energy x-rays to users. To provide far more highly coherent and brilliant hard x-rays to beamline experiments, the APS upgrade (APS-U) project team is currently developing a new storage ring magnet lattice based on a multi-bend achromat (MBA) lattice, which offers small electron beam emittance, increases brightness several orders of magnitude, and approaches diffraction limits at higher photon energies. The APS-U project will put the APS on the path to continued world leadership in hard-x-ray science. To fully support the APS-U, the FEs located inside the storage ring tunnel need to be upgraded. Also, because the storage beam size will be down to several microns from one hundred micron in the horizontal plane, a major improvement in beam stability is required in order to realize the benefits of this upgrade [1]. To deliver a high degree of x-ray beam position stability to the users and to achieve the APS-U beam stability goal, the x-ray beam position tolerance and XBPM resolution requirements at 20 m from the source are listed in Table 1. To meet these values, the APS has been conducting research in developing a hard x-ray BPM that uses the 8-keV Cu K-edge x-ray fluorescence (XRF). To implement the XRF-based XBPM in place of the present photoemission-based XBPM, a grazing-incidence insertion device x-ray beam position monitor (GRID-XBPM) has been developed and its first articles were installed for tests at 27-ID and 35-ID FEs in May 2014, as seen in Fig. 1 An experimental test result with two inline undulators showed that the XBPM has approximately 30-fold improvement in rejection of bend magnet radiation background and a gap-independent calibration in one of the two dimensions as shown in Fig. 2.

Table 1: APS–U XBPM Tolerance and XBPM Resolution Requirements (Z=20 m from the Source Point)

XBPM	Plane	RMS AC motion (0.01~1000Hz)	RMS Long-term Drift (7 days)
Position tolerance	Horizon.	5.3 μm	12.0 μm
	Vertical	3.4 μm	10.0 μm
Resolution	Horizon.	3.7 μm	8.5 μm
	Vertical	2.4 μm	7.1 μm



Figure 1: Installed GRID-XBPM at 27-ID FE (Looking upstream) [2].

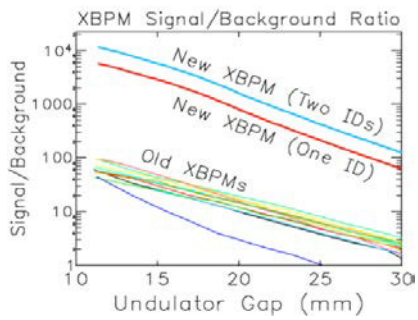


Figure 2: Ratio of undulator signal over BM background for the GRID-XBPM [2].

GRID-XBPM DESIGN

The design has been further value-engineered to make it compact. To reduce the cost, the vertical adjustment capability will be removed because the undulator gap changes are not correlated to the vertical motion of the mask. Fig. 3 shows the final design of the GRID-XBPM which is composed of two masks and two detector assembles mounted on two separate granite block for structural and temperature stability with a translation motion stage. This stage can translate the mask and detector assembly horizontally during machine study. For detecting the XRF signals, both Si-

* Work supported by the U.S. Department of Energy, Office of Science, under Contract No. DE-AC02-06CH11357
† shlee@aps.anl.gov

Content from this work may be used under the terms of the CC BY 3.0 licence (© 2016). Any distribution of this work must maintain attribution to the author(s), title of the work, publisher, and DOI.

ISBN: 978-3-95450-188-5 doi:10.18429/JACoW-MEDSI2016-WEPE04

PIN diode and CVD diamond can be utilized. There is a Be-window between the mask and the detector to protect the synchrotron ring vacuum during periodic maintenance of detector system. So, the detector has its own vacuum pump and will be operated under a high vacuum. To decouple the detector signal readout from the main mask's deformation due to transient thermal loads, a bellows will be integrated into the detector chamber assembly. Also, to monitor the vertical and horizontal motions of the GRID-XBPM relative to the floor, the capacitive detection system and hydraulic levelling system will be equipped to provide accurate and reliable beam position information.

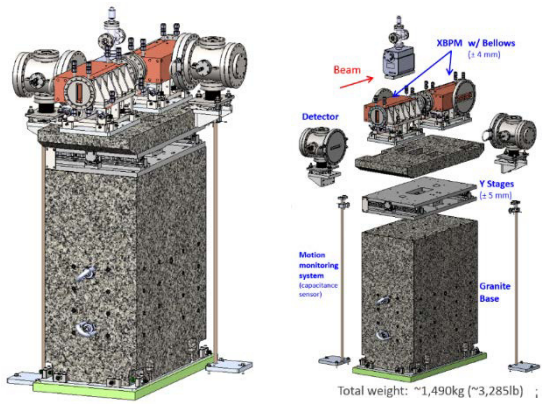


Figure 3: Final design of the GRID-XBPM and its exploded view.

Masks

The maximum total power and the maximum power density of the HHL FE for the APS-U will be limited to 19.45 kW and 453.3 kW/mrad^2 based on the operation of two in-line 2.75-cm-period, 2.4-m-long undulators at k=2.44, 200 mA, 6 GeV. Based on heat load estimation [3], the angle of incidence on the active surface of the mask was determined at 1.0º (17.5 mrad) to increase the beam footprint. For the calculation of the minimum length with a grazing incidence angle of 1.0º, the dynamic range, tolerance of misalignment (±0.15 mm), and an additional 0.1 mm overlap section into the shadow at the far downstream end are considered. As shown in Fig. 4, a pre-mask is mounted on the main mask weldment with a Pyrolytic Graphite Sheet (PGS) foil for better heat transfer [4].

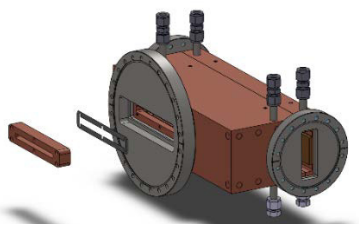


Figure 4: Recommended design of mask with PGS foil and pre-mask.

Be Windows

5.25″ x 1.0″ x 2 mm thick Beryllium sheet will be brazed to the zero-length stainless steel reducer flange of 10″ x 8″. Detector side of Be-window will be in the high vacuum (HV) and the other side will be in the ultra-high vacuum (UHV) during operation. For periodic maintenance, the detector side of Be-window will be exposed to the air.

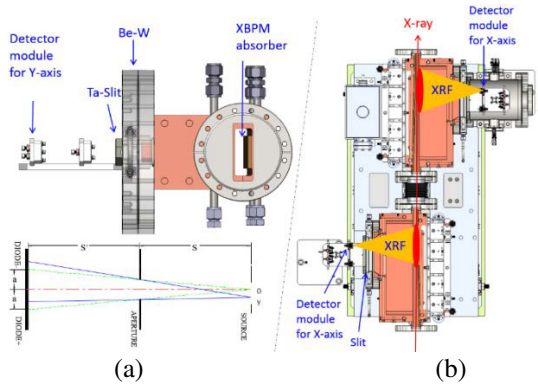


Figure 5: (a) Vertical position measurement principle (pinhole camera), (b) Horizontal position measurement principle (Integral sampling).

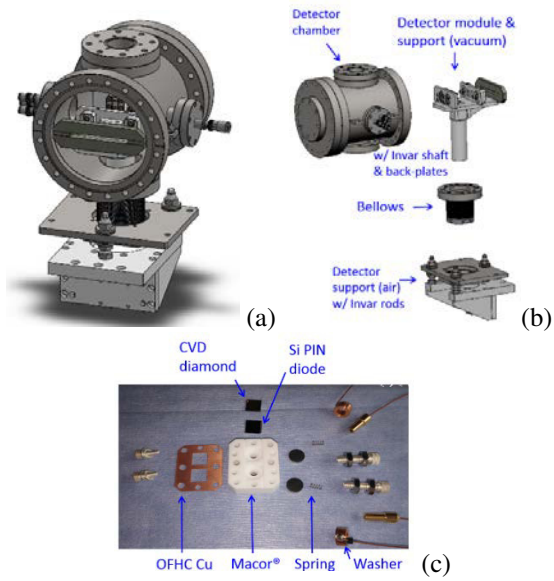


Figure 6: (a) Detector assembly, (b) its exploded view, (c) detector module with a plunger spring.

Detectors

Fig. 5 shows the XBPM position measurement principles. For the vertical position as shown in Fig. 5(a), it is possible to perform center-of-mass measurements by adding an aperture (pinhole) optics before the segment detectors. As a pinhole optics, a high Z (Tantalum) shielding material will be used to collimate the sensor's field of view to only the desired signal source footprint. For the horizontal position as shown in Fig. 5(b), it is possible to integrate the signal from each mask and compare signal intensities from two masks. Since the detector sensors will be potentially exposed to a high radiation environment to either cause drift in their response or outright failure, CVD diamond is a preferred material for reading out the intensity signals than Si-PIN diode, but the cost will be more. Detector assembly consists of detector module, its support structure with a bellows module, and vacuum chamber as

Content from this work may be used under the terms of the CC BY 3.0 licence (© 2016). Any distribution of this work must maintain attribution to the author(s), title of the work, publisher, and DOI.

ISBN: 978-3-95450-188-5 doi:10.18429/JACoW-MEDSI2016-WEPE04

Content from this work may be used under the terms of the CC BY 3.0 licence (© 2016). Any distribution of this work must maintain attribution to the author(s), title of the work, publisher, and DOI.

shown in Fig. 6. To reduce radiation or thermal damage to the detector sensors, they will be kept in a holder made of Macor® machinable glass ceramics, sandwiched by a OFHC copper sheet, then pressed by a spring-loaded SST disk with an Ag-coated #10 SHC Screw.

Support Structures

Masks and detector assemblies will be mounted on the manually adjustable support structures, top and base granites with a translation stage as shown in Fig. 7.

Manual adjustment support structure Mask will be mounted on the manually adjustable support structure. G-11 thermal insulation materials are used to reduce heat transfer from the mask to the support structure. Heat transfer can be further minimized by water-cooling for better thermal stability of the structure. For alignment of the mask during assembly and installation, the support structure has the following adjustment range of motions to manually adjust the position of mask during alignment and installation.

- X-Y linear translation: ± 6 0 mm
- Rotation around x, y, z axis: ± 1.0°

Bellows To decouple the signal readout at the detector from the deformation of the mask due to transient thermal loads, a bellows module will be integrated into the detector chamber assembly. One side of the module is blocked and the other side has 4.5″ CF flange with thru holes. To meet the specification below, the bellows core should have O.D. ϕ2.75″ x I.D. ϕ2.125″ x 39 convolutions with 0.004″ ply made of AM350 SS.

- Axial stroke bellows core:
  - Extended: 2.18″
  - Compressed: 1.68″
  - Operating stroke: 0.50″
- Lateral offset bellows core:
  - Operating @ Extended: 0.25″
  - Operating @ Compressed: 0.25″
- Angular offset bellows core:
  - Operating @ Extended: 5.0°
  - Operating @ Compressed: 5.0°

Fully assembled, the bellows shall survive 10,000 cycles of maximum lateral offset at room temperature of 77°F while set at full angular offset and ±50% axial offset. The maximum axial offset will not be used as this condition but will only be present at assembly.

Translation motion stages A horizontal motion will be provided to the GRID-XBPM, which can move the mask and detector together in the horizontal direction. Most important requirement of the translation stage is of a yaw angle error for better beam position monitoring. Typical specifications are as follows;

- Yaw angle error < 3.5 arc sec (10µm/580mm ≅ 17µrad)
- Running straightness < 3.0 µm
- Step resolution (full step) 0.1 µm (2mm/2,000)
- Repeatability (open loop) < 3.0 µm
- Load capacity > 880lb (400kg)
- Designed Speed = 0.14 mm/sec
- Travel = +/-2.0 mm w/hard stop, +/-1.6 mm w/soft stop
- Total weight (design) = 360 lb (162kg)
- Size = 762 mm (L) x 457 mm (W) x 107 mm (H)

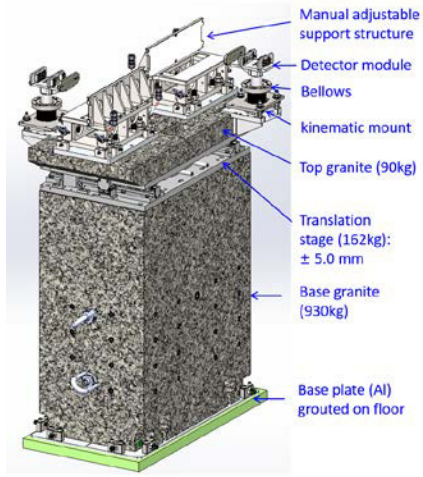


Figure 7: Support Structures.

CONCLUSION

The GRID-XBPM is one of the important components in the beam stabilization system for the APS-U. For the HHL FEs with single beam, the GRID-XBPM using XRF will be the baseline design for the APS-U FEs. With an incidence angle of 1.0 deg., it is expected that the XBPM masks will be thermally well-performed and its function will be better than the first articles installed at 27-ID and 35-ID FEs. The detector motion will be decoupled from thermal deformation of the main body and the detector vacuum will be isolated from the ring vacuum by Be-windows. The motion stage has been simplified to eliminate the vertical adjustment capability because the undulator gap changes are not correlated to the vertical motion of the mask. Thus, a compact and value-engineered design of the GRID-XBPM has been achieved for APS-U MBA FEs.

REFERENCES

[1] B.X. Yang *et al.*, "Design and development for the next generation x-ray beam position monitor system at the APS," in *Proceedings of IPAC2015*, Richmond, VA, USA, paper MOPWI014.

[2] S.H. Lee *et al.*, "Progress on the Development of the Next Generation X-ray Beam Position Monitors at the Advanced Photon Source," in *Proceedings of SRI 2015*, 6~10 JULY, 2015, New York, NY, USA.

[3] S.H. Lee *et al.*, "Design of the Grazing-incidence Insertion Device X-ray Beam Position Monitor for APS Upgrade," in *Proceedings of MEDSI 2012*, 15~19 OCT., 2012, Shanghai, China.

[4] T. Takeuchi *et al.*, "Investigation of high thermal-contact-conductance at low contact pressure for high-heat-load optical elements of synchrotron radiation," in *Proceedings of SPIE 8848*, Advances in X-Ray/EUV Optics and Components VIII, 884813 (September 27, 2013).

ISBN: 978-3-95450-188-5 doi:10.18429/JACoW-MEDSI2016-WEPE05

INNOVATIVE DESIGN OF RADIATION SHIELDING FOR SYNCHROTRON LIGHT SOURCES

M. G. Breitfeller, Brookhaven National Laboratory, Upton, N.Y., USA
S. L. Kramer, Operations and Accelerator Design Consulting, Ridge, N.Y., USA

Abstract

Over the course of decades, the shape of the bulk shielding walls for synchrotron light sources has developed into a standard configuration, including a ratchet shape of the outer storage ring wall, to accommodate the clearance needs for front end and first optical enclosure assemblies. New state of the art light sources will have low emittance, high energy beams, which will give potential for higher beam losses. These losses will yield higher radiation dose rates at the downstream wall and stricter safety requirements in the first optical enclosure. Throughout the installation of local shields at NSLS-II, verification dose rate studies of various shielding configurations were performed. Analysis of these studies revealed that a circular outer bulk shield wall could greatly reduce the dose rate to the users who work near the front end optical components. This presentation discusses the benefits of this circular bulk shield wall verses the challenges of component installation near the wall and ways to mitigate them.

INTRODUCTION

The bulk shield wall is the first line of defense from harmful radiation for human health safety, which is the highest of all priorities. A well designed outer storage ring wall attenuates the radiation field to acceptably low level dose rates for people near the wall. A wall with circular geometry presents a large arcing radius, relative to the beam path, that naturally maximizes wall thickness and attenuation. The challenge for engineers is to adapt new methods for interfacing the front ends to the beamline components through the much thicker concrete wall and it's curved outer surfaces.

BENEFITS AND PLANNING FOR THE CIRCULAR WALL

The safety benefits of the circular wall are numerous. The bulk wall shield is the first line of defense for radiation safety, a passive system, and once it is built it requires no additional attention. Other than the penetrations themselves, costly radiation analysis of complex wall geometry is simplified, and fewer local shields are required for hot spots. Next generation light sources will require thicker downstream walls, because higher dose rates will exist in the First Optical Enclosures (F.O.E.) resulting from abnormal losses caused by mis-steering. These higher dose rates can occur even when the safety shutters are actuated to block the X-ray beam path. More details on the advantages of the circular shield wall are given in Ref [1]. Also, cost savings may be significant. The circular wall will require less labor to build forms, less cement to pour, and less lead, needed for strengthening an inferior ratchet shield design.

At NSLS-II, the shape of the existing ratchet wall makes it convenient to connect the front end's gate valve to the first component of the F.O.E. The outer ratchet wall's orthogonal shape allows F.O.E. girders to position close to wall, and their hutches use the bulk wall as the backbone for its boxed shape (see Fig. 1). The downstream wall thickness is 1.5 m, so relatively little layout space is lost by feeding a drift tube through the wall to connect the two systems. To accommodate the new circular wall design, engineering methods must be considered to create penetrations in the thick wall that will gain access to components where needed.

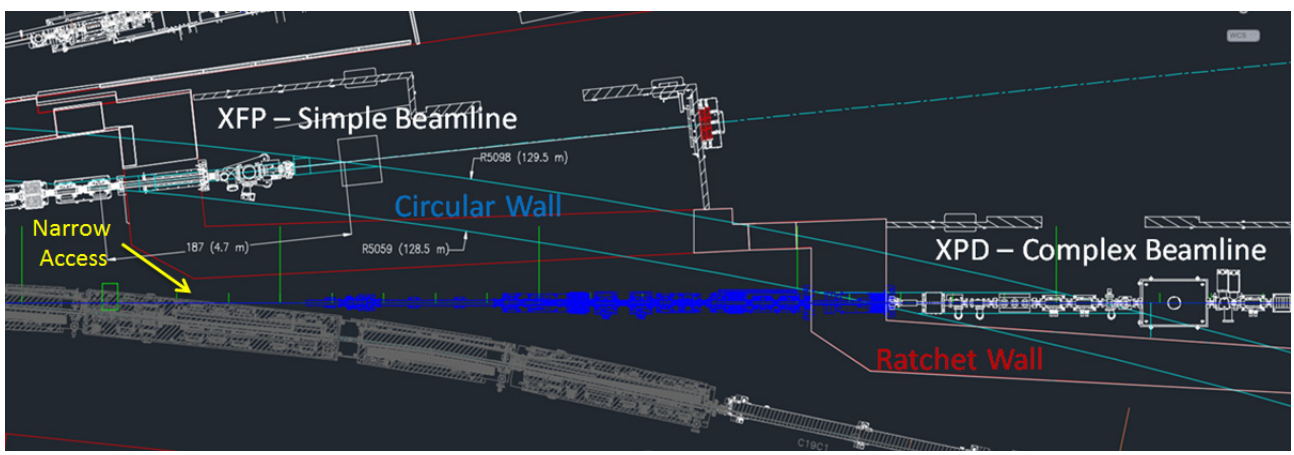


Figure 1: Existing adjacent beamlines at NSLS-II, with ideal circular wall outline overlay.

Content from this work may be used under the terms of the CC BY 3.0 licence (© 2016). Any distribution of this work must maintain attribution to the author(s), title of the work, publisher, and DOI.

ISBN: 978-3-95450-188-5 doi:10.18429/JACoW-MEDSI2016-WEPE05

Content from this work may be used under the terms of the CC BY 3.0 licence (© 2016). Any distribution of this work must maintain attribution to the author(s), title of the work, publisher, and DOI.

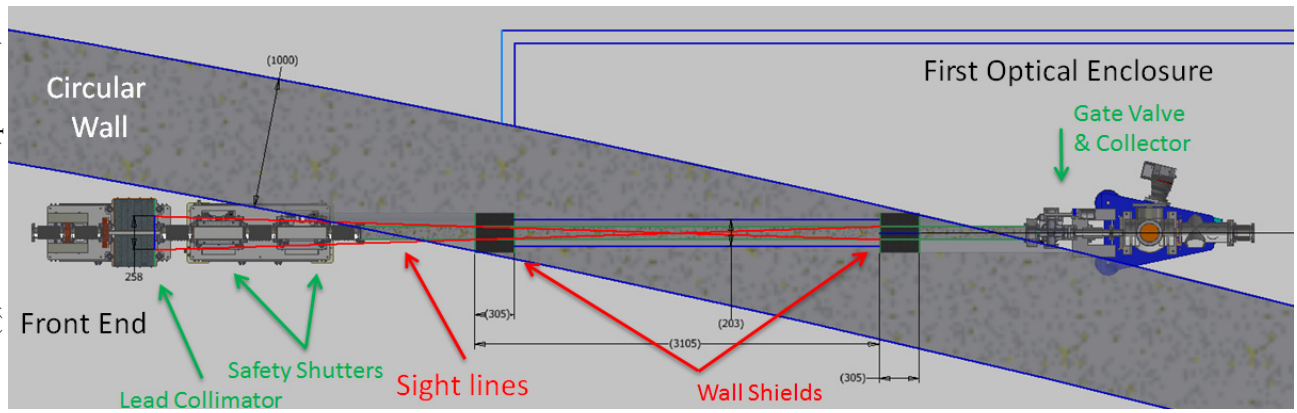


Figure 2: Simple beam line cut wall view from top.

MITIGATION

Two example adaptations, that detail engineering requirements to create penetrations through thick circular walls, will be compared. The details are illustrated by referring to two adjacent NSLS-II beamlines and are described in Fig. 1. The first is X-Ray Footprinting (XFP), a simple beamline, typical for BM sources, with few components and plenty of floor space in the F.O.E. hutch. The second is X-ray Powder Diffraction (XPD), a complex beamline, typical for ID sources, with many tightly spaced components and limited floor space.

A simple beamline adaptation is illustrated in Fig. 2. A long drift tube is the only component that would need to be installed. The example beamline included a toroidal mirror in the front end, which gives the synchrotron fan a rising pitch of .007 radians. Given the existing lattice geometry, the centerline hole length through the circular wall is 4.7 m, and projecting the rising pitch through the wall, the ends of the penetration would have a height difference of 40 mm. At NSLS-II, many simple beamlines were designed after the ratchet wall penetrations were formed with sleeves, and with mirrors causing beam path variations, it seems the practical approach to facilitate installation of the long drift tube would be to core drill, rather than pre-install a sleeve.

The actual breakout core cutting distance would be 5.7 m, but this should not be a problem as companies specializing in core drilling are equipped with a large supply of long tube core bits, as well as a host of drill motors and mast configurations to accommodate concrete thicknesses in excess of 18 m. In preparation for core drilling, the wall's penetration area should be free of rebar. Unreinforced concrete is easier and faster to drill. To minimize the effect of angular error of drilling, it would be ideal to drill from each side.

Rectangular tube lengths are available up to 7.3 m long, so a seamless 100 mm x 50 mm tube, with standard 150 mm welded Conflat flanges can be manufactured and would slide completely through a 200 mm diameter core. The cored hole should be counter bored to 300 mm diameter at each end, to allow for the shielding material to install and overlap the full length thru-wall seams. When installed, the tube would sag under its own weight, so length long ribs could be welded to the tube and shimmed supports could be installed in the middle to minimize deflection. After the tube flanges are surveyed, machined steel rounds are inserted in the counter bore, around the tube, and become the wall collimating shields.

As can be seen in the illustration, an added benefit is that the extended distance between the wall shields is more than double that of the ratchet wall configuration. With the line of sight through the wall shields narrowed, size of the Front End's collimator shield can be reduced to ½ of its existing size, and the need for additional front end scatter shields is eliminated.

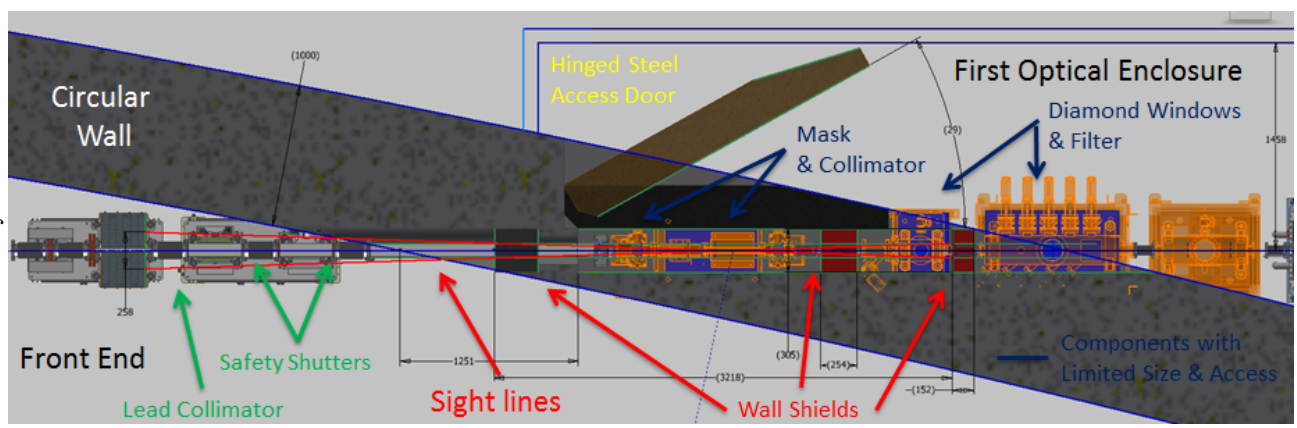


Figure 3: Complex beam line cut wall view from top.

ISBN: 978-3-95450-188-5 doi:10.18429/JACoW-MEDSI2016-WEPE05

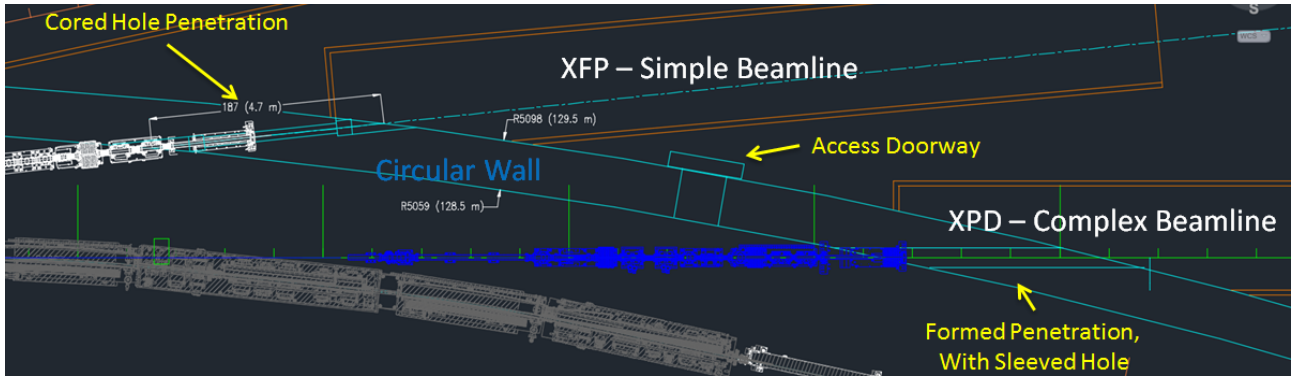


Figure 4: View of access with new circular wall layout.

A complex beamline adaptation is illustrated in Fig. 3. At NSLS-II, complex beamlines do not include mirrors in the front end, so designed penetration sleeves can be located in forms and surveyed to position. With the concrete properly formed, their surfaces can act as supporting structures for components. For the front end side of the wall, the cored-hole method, with a small diameter hole, would leave the circular surface of the shielding wall intact, for a depth of 1.25 m, enabling it to absorb the forward radiation shower. To minimize voids and maintain the ideal wall thickness of 1 meter, the upstream, near wall, beamline components would be mounted in a section of the circular wall that would be shaped with a steel sleeve. The steel sleeve would form a rectangular access window on the FOE side of the wall. The window would provide access to components, such as gate valves, masks and collimators, and allow enough room for installation, survey and service. An additional step in the forming sleeve would create a pocket that would house a steel plate shield. The steel plate would fit in the sleeve pocket, so the steel can overlap the full length thru-wall seams. The steel to concrete attenuation ratio is 4:1, so a 30 cm thick plate would adequately substitute for the concrete removed from the circular wall shape and would serve as an access door. The proposed access door would weigh close to 4 tons, but mounted on a frame with pins and thrust bearings, it could easily swing open. A 30 cm wide x 50 cm high mounting area would be large enough to facilitate most of the upstream beamline components. Larger beamline components, such as monochromatic mirrors must be located clear and downstream of the wall. Some planning would be needed for beamline layouts, to ensure that components in the wall would be size limited and facilitated for full supply and service. Additional blind sleeves could be installed in the wall to provide utilities to the components. After the components are installed, lead stacks would be assembled in between the components to shield any forward radiation through the penetration to the F.O.E.

FINAL LAYOUT

With the circular wall beamline penetrations defined, adjustments to the F.O.E. hutches and access doors can be made. Although existing ratchet wall F.O.E. hutches typically use the orthogonal wall as a backbone, hutches located out on the experimental floor are free standing. The new F.O.E. hutches would be similar to these designs, only needing supports to fasten the hutch wall ends to the circular wall. The hutches would be aligned parallel to the beamline to maximize floor space (see Fig. 4).

As seen in the illustration, and comparing to Fig. 1, much floor space has been gained on the storage ring side of the wall. The narrow access area between front ends has expanded to 1.5 meters. By eliminating the narrow access area, half of the access doorways can be removed from the circular wall, as one doorway can adequately service adjacent front ends. With limited time available for building after storage ring commissioning and ongoing construction of new front ends and insertion devices only during shutdowns, the open space is a great resource which enables movement of pre-assembled girders and gives easy access to all areas.

CONCLUSION

The need for the circular wall from a radiation perspective is compelling and additional benefits have been discovered while finding ways to mitigate the challenges of adapting to the proposed wall. Although detailed preparation and planning is required to ensure that all beamlines can be installed in a timely and cost effective manner, these efforts are balanced by the many cost and time saving benefits discussed.

ACKNOWLEDGEMENT

Sushil Sharma contributed insightful knowledge and guidance towards ideas for this paper from his vast experiences from working on Synchrotron Accelerators for many years.

REFERENCES

[1] S. L. Kramer *et al.*, “Shielding Synchrotron Light Sources: Advantages of Circular Shield Walls Tunnels”, *Nuclear Instruments and Methods in Physics Research*, **A827** (2016) p.24–31.

Content from this work may be used under the terms of the CC BY 3.0 licence (© 2016). Any distribution of this work must maintain attribution to the author(s), title of the work, publisher, and DOI.

ISBN: 978-3-95450-188-5 doi:10.18429/JACoW-MEDSI2016-WEPE06

HIGH HEAT LOAD FRONT ENDS FOR SIRIUS*

L. M. Volpe†, P. T. Fonseca, H. F. Canova, P. P. S. Freitas, A. Gilmour, H. G. P. Oliveira, A. S. Rocha, G. L. M. P. Rodrigues, L. Sanfelici, M. Saveri Silva, H. Westfahl Jr., LNLS, Campinas, Brazil

Abstract

Currently under construction on Brazilian Synchrotron Light Laboratory Campus, Campinas/SP, Sirius is a 3GeV, 4th Generation Synchrotron Light Source. In this paper we describe the Front End that has been designed to transmit the intense synchrotron radiation generated by the insertion devices that will generate the most critical thermal stress, with a peak power density of 55.7 kW/mrad² and a total power of 9.3kW at 500mA in the storage ring.

The functions of the main components and their location in the layout are described. Computational fluid dynamics (CFD) and structural simulations, that have been carried out to verify the performance under the high heat loads generated by Sirius, are also detailed along with the limits of temperature and stress that have been employed in the design.

INTRODUCTION

Sirius storage ring uses the multi-bend-achromatic design approach (5BA in this case) to achieve a very low beam emittance of 0.25 nm·rad. The 518 m circumference contains 20 straight sections of alternating 6.5 and 7.5 meters in length, to be used for insertion devices as well as injection and RF systems. The central dipole of the 5BA cells is a permanent magnet with transverse and longitudinal field gradients to reduce the emittance and provide a hard X-ray radiation source. The 3.2 T narrow high field section in its center provides radiation with critical energy of 19 keV. The other low field dipoles (0.58 T), responsible for the main beam deflection, will be electromagnets [1].

A Front End is a group of components connecting the storage ring to the beamline. They are responsible for defining the final aperture, absorbing exceeding beam power, radiation protection, storage ring vacuum protection and photon-beam diagnostics [2]. The first 5 Sirius' beamlines are planned to use in-vacuum and elliptically polarized undulators. An IVU19 front-end was first designed since it is the Insertion Device (ID) that will generate the most critical thermal stress, with a peak power density of 55.7 kW/mrad² and a total power of 9.3kW at 500mA. This paper will present the requirements, design and prototyping details.

FRONT END LAYOUT

The Front End functions are fulfilled by a proposed set of interlocked components, whose locations are shown in Fig. 1. Ion Pumps provide ultra-high vacuum to the Beamline, Front End and Storage Ring, whose level ($\leq 10^{-9}$ mbar) is monitored by vacuum readers placed at strategic locations.

Since for most of the Sirius' Front Ends there is no physical vacuum insulation (such as windows), preserving the pressure levels in the Storage Ring in the case of any event on the Beamline side becomes critical. If a sudden pressure rise is detected, the electron-beam is dumped and the Fast Valve shut to partially seal the vacuum path and stop the pressure wave. It is followed by the Slow Valve, which completely seals the path between Storage Ring and Beamline, preventing a significant pressure rise occurrence in the Storage Ring [3].

Pre-Masks upstream the Front End will be designed restricting the photon beam generated by B1 and protecting the vacuum tubes. Also, a Machine Photon Shutter upstream the Front End will be designed to block the photon beam in maintenance cases.

Table 1 resumes the Front End project, showing the components position, apertures, and the incident/absorbed power. Power values were calculated using Spectra v10.

FRONT END COMPONENTS

Power Absorbers

They are components that absorb the beam power, shape its size and form to the first optical components. The IVU Front End will have a Fixed Mask, a Photon Shutter, and High Power Slits as components responsible for these functions.

There are two materials that are being studied to be used to dissipate the thermal power, Glidcop and Copper Chromium Zirconium (CuCrZr) [4]. The major difference between the two materials is that Glidcop can be brazed and CuCrZr cannot, but CuCrZr can be purchased in the local market and is available in a vast number of suppliers. As CuCrZr is hard enough to be used in flanges, the idea is to make the components without the need of brazing the flanges.

Table 2 presents the design parameters to which the power absorbers are submitted.

Fixed Mask The Fixed Mask (FM) is a static and water-cooled block of high thermal conductivity alloy. It absorbs unwanted or misteered beam, preventing components downstream to suffer from high thermal load effects. It presents an hourglass form orifice, which provides grazing incidence to the beam in order to reduce the power density on its surface, and, at the same time, define the Front End's entrance acceptance. It has four helical water channels for cooling. Figure 2 shows the internal design of the Fixed Mask.

* Work supported by Brazilian Ministry of Science, Technology, Innovation and Communication (MCTIC)
† lucas.volpe@lnsl.br

Content from this work may be used under the terms of the CC BY 3.0 licence (© 2016). Any distribution of this work must maintain attribution to the author(s), title of the work, publisher, and DOI.

ISBN: 978-3-95450-188-5 doi:10.18429/JACoW-MEDSI2016-WEPE06

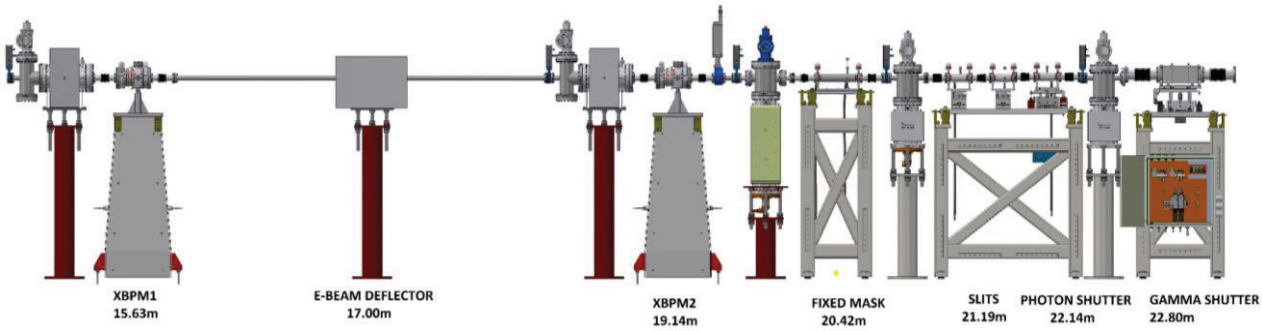


Figure 1: General Front End (FE) layout.

Table 1: IVU19 Front End Aperture Table

Component	Distance from ID source [mm]	Beam Size HxV [mrad]	Beam Size HxV [mm]	Aperture Size [mrad]	Aperture Size [mm]	Incident Power [kW]	Absorbed Power [kW]
XBPM1	15,626	2.00x1.00	31.2x15.6	1.01x0.94	15.8x14.6	9.25	0.18
EBD	17,000	1.01x0.94	17.2x16.0	ø2.35	ø40	-	-
XBPM2	19,143	1.01x0.94	19.3x18.0	1.10x1.02	21x19.6	-	-
FV	19,429	1.01x0.94	19.6x18.3	ø2.06	ø40	-	-
FM	20,417	1.01x0.94	20.6x19.2	ø0.152	ø3.1	9.07	8.11
HPS-1*	21,190	ø0.152	ø3.22	0.38x0.38	8x8	0.96	0.96 max
HPS-2*	21,516	ø0.152	ø3.27	0.37x0.37	8x8	0.96	0.96 max
PS	22,136	ø0.152	ø3.36	0.68x0.68	15x15	0.96	0/0.96
GS	22,803	ø0.152	ø3.47	ø0.44	ø10	-	-

** The set of HPSs will be limited to an aperture of 66x66 µrad^2 (1.42x1.42 mm^2@21.5m), resulting in a maximum of 247W (500mA) exiting the FE.*

Table 2: Design Parameters/Boundary Conditions for the Power Absorbers

Maximum Values	
σ_{VM}	σ_{yield} (370 MPa)
ε	0.2%
T_{max}	300°C
$T_{max\ wc}$	100°C
v_{water}	3 m/s

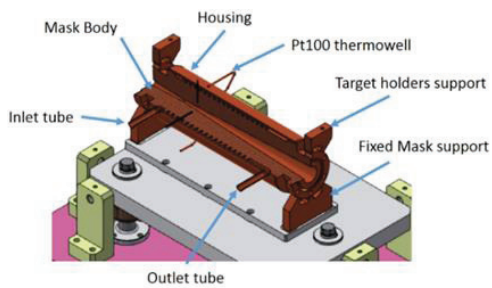


Figure 2: Fixed Mask Design.

High Power Slits A set of High Power Slits (HPS) is placed downstream the Fixed Mask to define the photon beam size exiting the Front End. It is going to be limited for a maximum aperture of 66x66 µrad, which is 110% of the maximum beam size expected by downstream components in the First Optical Enclosure.

The HPS are composed by two L-shaped components that will move by X-Z linear stages in a way to define the exit aperture size, as shown in Fig. 3. The design is similar to the Fixed Mask's, but having only one helical channel and reduced length. The stages specified for this application have an accuracy of 10µm, which results in a movement accuracy, in relation to the beam source, of 0.5 µrad.

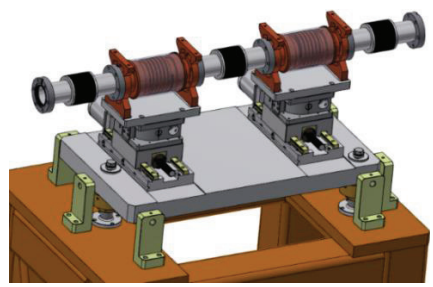


Figure 3: High Power Slits.

Photon Shutter The Photon Shutter (PS) function is to close the photon beam to downstream Front End components and beamline itself.

Its design is the same as the HPS, but having only one helical channel and reduced length. It has a grazing incidence surface with 9° angle that will intercept the photon beam when closed, resulting in a maximum power density of 17.4 W/mm^2. It has an aperture of 15x15 mm^2. One

Content from this work may be used under the terms of the CC BY 3.0 licence (© 2016). Any distribution of this work must maintain attribution to the author(s), title of the work, publisher, and DOI.

ISBN: 978-3-95450-188-5 doi:10.18429/JACoW-MEDSI2016-WEPE06

Content from this work may be used under the terms of the CC BY 3.0 licence (© 2016). Any distribution of this work must maintain attribution to the author(s), title of the work, publisher, and DOI.

thermocouple is placed inside the Photon Shutter to acquire its temperature for the interlock system.

Gamma Shutter

The Gamma Shutter (Fig. 4) uses a block of Tungsten for radiation personal protection. Radiological Safety Group stated that the minimum material thickness to block Bremsstrahlung radiation to a safe level is 244 mm. To close the Gamma Shutter, the block is moved down in 2 seconds with a stroke of 30 mm. There is a hole of 10 mm diameter to permit the photon beam to pass when the Gamma Shutter is open, therefore it also has the functionality of a Collimator [5].

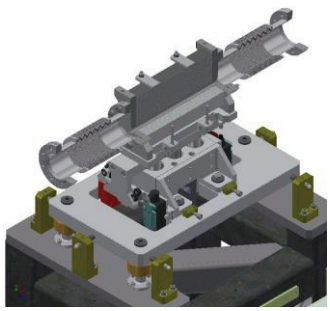


Figure 4: Section view of Gamma Shutter.

E-Beam Deflector

The installation of an e-Beam Deflector (EBD), a permanent magnet dipole, allows directing occasional escaping electron-beam towards the shielding wall.

A 280 mm length 0.6 T magnetic field e-Beam Deflector was specified. Positioned 6.65 m from the shielding wall it can deviate the electron beam down by 50 mm.

XBPM

The X-Ray Beam Position Monitors detect the photon-beam position with micrometric resolution. Two Tungsten-blades XBPMs are foreseen in order to provide both position and steering angle information. The device depicted in Fig. 5 is an improvement of the XBPM used at Soleil and developed in a collaboration to the LNLS [6], it is further addressed in [7].

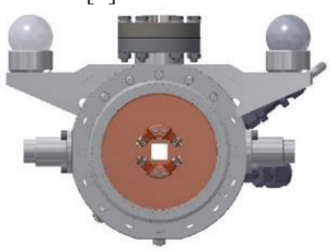


Figure 5: XBPM front-view.

MECHANICAL SUPPORTS

Four key points were attended in the design of the mechanical supports: damping and non-amplification of ground vibration; reduction of displacement due to temperature fluctuations; ease and accuracy of positioning systems; and ease of transport and assembly [8].

Measurements were performed at LNLS indicating 60 Hz as the frequency to avoid. In this direction, having in mind that the special floor already isolates the system from the ground, 75 Hz was adopted as minimum first eigenfrequency for all supports except for the XBPMs. The target sought for the later was at least 100 Hz, regarding future applications relative to diagnostics.

CURRENT STATUS

A first fully equipped Front End prototype is under construction and shall be ready by the end of this year, including all mechanical, vacuum, interlock, controls and diagnostic systems.

Most of the components are being manufactured at local companies and only specialized tasks such as brazing, assembly and vacuum conditioning are executed internally by the LNLS team.

ACKNOWLEDGEMENTS

The design and construction of Front Ends is a collective work that involves the entire LNLS Engineering team. We would like to acknowledge everyone who has been contributing to the development of this project. Finally, we would like to thank J.C. Biasci (ESRF), N. Béchu (Soleil), S. Forcat (MAX IV) and H. Schulte-Schrepping (DESY).

REFERENCES

[1] L. Liu, F. H. de Sá and X. R. Resende, “A new optics for Sirius”, in *Proc. IPAC'16*, Busan, Korea, May 2016, paper THPMR013, pp. 3413-3415.

[2] C. Benson, *et al*. "Mechanical design of a front end for canted undulators at the advanced photon source", *Synchrotron Radiation Instrumentation*, vol. 705, p. 466-469, May 2004.

[3] “PDR In-Vacuum Undulator Front-ends”, LNLS Internal Documentation, 2016.

[4] S. Sharma, “A Novel Design of High Power Masks and Slits,” in *Proc. MEDSI'14*, Melbourne, Australia, 2014.

[5] W. R. Job, P.K., Casey, “Bremsstrahlung Ray Tracing Guidelines for NSLS II Beamlines and Front Ends,” BNL, Brookhaven, USA, 2006.

[6] N. Hubert *et al*., “Design of a new blade type X-BPM” in *Proc. IBIC'14*, Monterey, CA, USA, Sep. 2014, paper WEPD22, pp. 687-690.

[7] L. M. Volpe *et al*., “Blade XBPM Optimization for Sirius”, presented at MEDSI’16, Barcelona, Spain, 2016, paper WEPE08, this conference.

[8] B. N. Jensen, "Managing Vibrations, go to the Source(s)," in *Proc. MEDSI'14*, Melbourne, Australia, 2014.

ISBN: 978-3-95450-188-5 doi:10.18429/JACoW-MEDSI2016-WEPE07

A HIGH HEAT LOAD FRONT-END FOR THE SUPERCONDUCTING WIGGLER BEAMLINE AT SSRF*

Y. Li†, M. Zhang, D. Jia, S. Xue, W. Zhu, Shanghai Institute of Applied Physics, Chinese Academy of Sciences, Shanghai, P. R. China

Abstract

A superconducting wiggler (SCW) will be first employed to generate high energy X-rays for ultra-hard X-ray applications beamline at Shanghai synchrotron radiation facility (SSRF). The front-end will handle a heat load of 44.7 kW with a peak power density of 45 kW/mrad², which is much higher than the commissioned ones at SSRF. Overall design of the high heat load front-end has been completed, including one short absorber with a length of 300 mm and three long absorbers longer than 500 mm. Long absorbers have been designed to be made by medium speed wire-cut electrical discharge machining (WEDM-MS) or electron beam welding (EBW). Thermal analyses of all absorbers have also been done to comply with the failure criteria of SSRF.

INTRODUCTION

Shanghai synchrotron radiation facility (SSRF) is an advanced third generation synchrotron light source with a 3.5 GeV electron storage ring and a designed beam current of 300 mA. A superconducting wiggler (SCW), as source of the ultra-hard X-ray applications beamline BL12SW at SSRF, will be able to generate high-energy X-rays up to 150 keV. Meanwhile, the SCW has an intensive power of over 43.3 kW with a peak power density of 45 W/mrad^2. Overlapping the radiations from upstream and downstream bending magnets, the total power will reach 44.7 kW, which are about 4 to 64 times compared with the commissioned front-ends. This is also the highest heat load for a front-end in SSRF phase-II beamline project.

Overall design of the high heat load front-end, abbreviated as BL12SW front-end, was introduced in this study. Thermal analyses of all absorbers were done to comply with the failure criteria of SSRF. Three long absorbers with lengths bigger than 500 mm were designed to be made by medium speed wire-cut electrical discharge machining (WEDM-MS) or electron beam welding (EBW).

OVERALL DESIGN

Power of SCW

Table 1 is the major parameters of SSRF storage ring and SCW. Power distribution is shown in Figure 1.

Table 1: Parameters of SSRF Storage Ring and SCW

E_e (GeV)	I (A)	B_0 (T)	N	L (m)	K
3.5	0.3	4.2	22	1.08	18.824

Where: E_e is beam energy of the storage ring, I is the maximum circulating current; B_0 is the maximum magnetic field, N is period, L is total length and K is deflecting parameter of SCW.

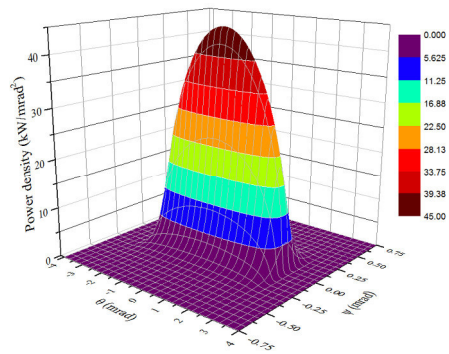


Figure 1: Power distribution of SCW.

Layout of the Front-end

Figure 2 shows the layout of BL12SW front-end with a total length of about 8.9 m. Three fixed masks (FM) confine the photon beam and protect the downstream components from a mis-steered beam. Two photon shutters (PS) intercept the photon beam and protect downstream safety shutter and valves.

Therefore, power from SCW, together with part of the bending magnet, will be absorbed by three FMs and PS2. Technical specifications of these four high heat load photon absorbers are given in Table 2.

THERMAL ANALYSIS

Failure Criteria

Absorbers of FMs and PS2 are all made of Glidcop Al-15. Conservative failure criteria [1] are used as:

- The maximum equivalent stress σ_{max} should be less than 420 MPa.
- The maximum temperature on the Glidcop body T_{max_body} should be less than 300 °C.
- The maximum temperature on the water cooling channel walls T_{max_wall} should be less than water boiling temperature at channel pressure.

Thermal Analysis Results

Direct water cooling and grazing incidence structures are applied to improve heat-absorbing ability for front-end photon absorbers. The temperature and thermal stress distributions of all beam striking components, including pre-mask, FM, PS, fluorescence monitor and XBPM, were simulated carefully and optimized by thermal analysis with ANSYS.

* Work supported by SSRF phase-II beamline project
† email address: liyongjun@sinap.ac.cn

Content from this work may be used under the terms of the CC BY 3.0 licence (© 2016). Any distribution of this work must maintain attribution to the author(s), title of the work, publisher, and DOI.

ISBN: 978-3-95450-188-5 doi:10.18429/JACoW-MEDSI2016-WEPE07

Content from this work may be used under the terms of the CC BY 3.0 licence (© 2016). Any distribution of this work must maintain attribution to the author(s), title of the work, publisher, and DOI.

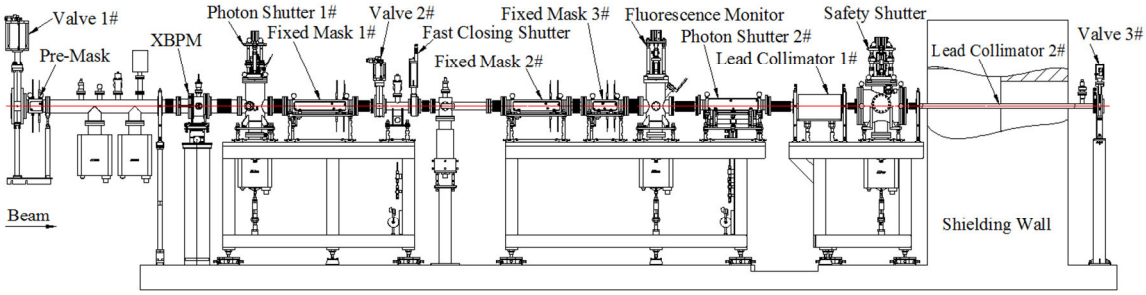


Figure 2: Layout of BL12SW front-end.

Table 2: Technical Specifications of Photon Absorbers

	Distance to SCW (m)	Total Absorbed Power (kW)	Beam Size (H×V, mrad×mrad)		Aperture (H×V, mm×mm)	
			Inlet	Outlet	Inlet	Outlet
FM1	11.404	14.1	5.6×1	3.3×0.5	70×28	39.2×6
FM2	13.191	14	3.3×0.5	1.7×0.4	54×20	23.2×5.4
FM3	13.846	5.7	1.7×0.4	1.2×0.3	34×14	17×4.2
PS2	14.781	10.2	1.2×0.3	0	26×12	0

The optimized parameters for photon absorbers are [2]: diameter of cooling channels is 6 mm, distance of absorbing surfaces to cooling channel walls is 9 mm, corner radiuses of two adjacent absorbing surfaces are bigger than 2 mm, roughness of absorbing surfaces is better than 6.3 μm and directions of cooling channels should be parallel to the beam approximately.

Table 3 shows thermal analysis results of three FMs and PS2 with mis-steered beam, which fairly comply with SSRF failure criteria. Equivalent stress and temperature distribution maps for FM2 are shown as examples in Figure 3 - Figure 5.

Table 3: Thermal Analysis Results

	σ_{max} (MPa)	T_{max_body} (°C)	T_{max_wall} (°C)
FM1	154.1	111	52.2
FM2	182.1	103.2	58.3
FM3	242.1	104.6	63.8
PS2	228.3	144.5	70.9

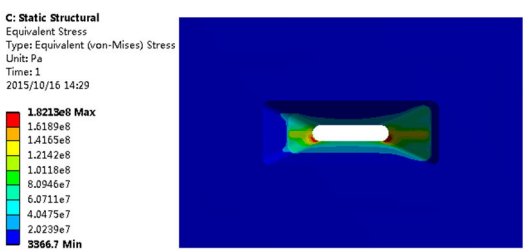


Figure 3: Equivalent stress distribution for FM2.

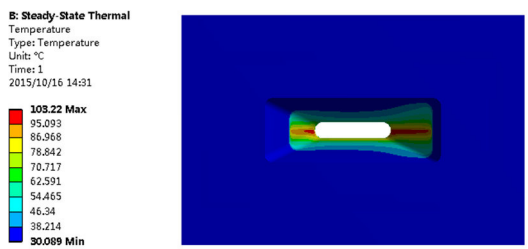


Figure 4: Temperature distribution for FM2.

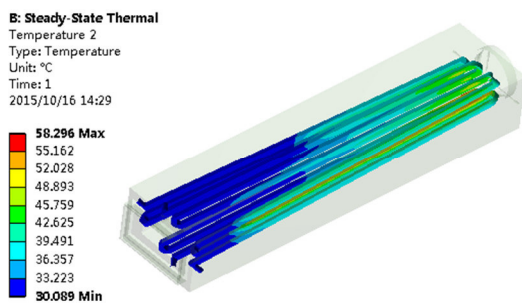


Figure 5: Temperature distribution of the cooling channel walls for FM2.

TECHNOLOGY OF MANUFACTURING

As seen in Table 2, the total power on the exit mask FM3 is 5.7 kW, and FM3 has a short absorber with a length of 300 mm, which is the maximum available length of low speed wire-cut electrical discharge machining (WEDM-LS) in China. While, the total power on

ISBN: 978-3-95450-188-5 doi:10.18429/JACoW-MEDSI2016-WEPE07

FM1, FM2 or PS2 is higher than 10 kW. These three long absorbers will be longer than 500 mm to minimize the grazing angles. Therefore, technology of manufacturing long photon absorbers becomes a big issue for BL12SW front-end.

WEDM-MS

WEDM-MS is one way to make long absorbers. Unlike WEDM-LS, WEDM-MS is a reciprocating multi-cutting high-speed WEDM to manufacture larger workpieces with less time and a little worse precision [3]. After repeatedly adjusting of process parameters of WEDM-MS, PS2 has been successfully manufactured, as shown in Figure 6. The accuracies of apertures are 0.6 mm and the vacuum degree after baking out is 2.2×10^{-10} Torr, which satisfy the specifications of photon shutters.



Figure 6: PS2 (WEDM-MS).

EBW

EBW is another way to make long absorbers. Figure 7 is a proposal design of FMs made by EBW. Two sub-absorbers will be made by WEDM-LS and then be welded to each other by EBW, thus the accuracies of apertures will be better than 0.1 mm.

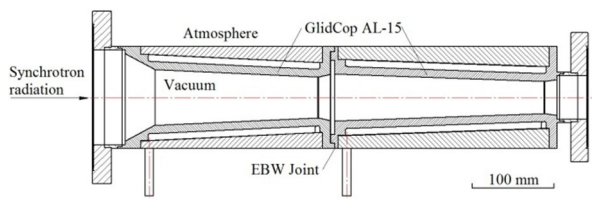


Figure 7: FM (EBW).

Some tests, including vacuum sealing tests and tensile tests, have been done for EBW joints and brazed joints of two Glidcop Al-15 workpieces. Vacuum sealing tests results indicated that both the EBW joints and brazed joints satisfy the ultrahigh vacuum requirements of SSRF front-end.

Tensile tests were done at 20 °C, 100 °C and 200 °C based on GB/T 228.1-2010 specifications (ISO 6892-1: 2009, MOD) and GB/T 4338-2006 specifications (ISO 783: 1999, MOD). Testing results show that mechanical properties of both joints are lower than that of Glidcop Al-15, as shown in Figure 8. Tensile strength of brazed joints is below half that of the base metal and about 70% for EBW joints. Elongation of brazed joints approaches to 0, while that of EBW joints is approximately 15% that of Glidcop Al-15. The trends with changing temperature of mechanical properties of EBW joints are consistent with that of the base metal. Compared to brazed joints, EBW joints have higher tensile strength, better ductility and more stable performance.

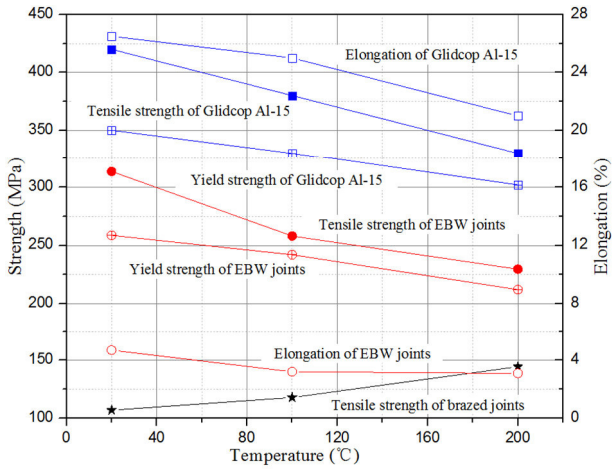


Figure 8: Tensile testing results of joints versus the Glidcop Al-15 base metal.

In practical engineering applications, joints are subjected to low stress and strain as being kept out of direct high power radiation. Therefore, EBW joints of Glidcop Al-15 entirely satisfy the severe thermo-mechanical requirements.

CONCLUSION

Overall design of BL12SW front-end, which is the highest heat load one in SSRF phase-II beamline project, has been completed. Thermal analysis results show all absorbers will comply with the failure criteria of SSRF.

PS2 has been successfully made by WEDM-MS. Vacuum sealing and tensile tests indicate that EBW joints satisfy the vacuum and mechanical requirements; thereby EBW will also be applied to make long absorbers in SSRF phase-II beamline project.

REFERENCES

[1] G. Wu, "Engineering design report for SSRF front-end", Shanghai, China, 2006.

[2] Y. Li, M. Zhang, *et al.*, "Structure design and optimization of high heat load absorbers in SSRF front-end", *Optics and Precision Engineering*, vol. 24, no. 7, pp.1640-1646, Jul. 2016.

[3] M. Li, Z. Yang, and W. Jiang, "Characteristics and Development of Medium-Speed Wire Cut Electro Discharge Machine", *Aeronautical Manufacturing Technology*, vol. 8, pp.32-35, 2011.

Content from this work may be used under the terms of the CC BY 3.0 licence (© 2016). Any distribution of this work must maintain attribution to the author(s), title of the work, publisher, and DOI.

ISBN: 978-3-95450-188-5 doi:10.18429/JACoW-MEDSI2016-WEPE09

Content from this work may be used under the terms of the CC BY 3.0 licence (© 2016). Any distribution of this work must maintain attribution to the author(s), title of the work, publisher, and DOI.

DESIGNING THE PHOTON BEAMLINE FRONTENDS IN THE PETRAIII EXTENSION PROJECT

Hilmar Krüger*, W.A. Caliebe, M. Degenhardt, M. Hesse, F. Marutzky,
H.B. Peters, R. Peters, M. Röhling, H. Schulte-Schrepping, B. Steffen
Deutsches Elektronen-Synchrotron DESY, 22607 Hamburg, Germany

Abstract

The new insertion device beamlines in the PETRAIII extension project are arranged in three new sector types. The following will present the designs of the photon beamlines frontends for these sectors. The designs are based on the original design concept developed for the photon beamline frontends at PETRAIII. The aim of this generic approach was to minimize the number of specialized components for all beamlines. The existing girder concept allows a fast and reliable installation phase. The newly designed frontends aimed at using the same proven components and minimizing of the number of girder variations.

There will be 4 new sectors with two undulator IDs in each sector. The canting angle between the undulators was increased from 5 mrad to 20 mrad in difference to the generic beamlines. Additionally, two of the straight sections are modified. One straight section will be transformed in a side station sector with a 1 mrad canting angle. The other straight section with a 40 m long damping wiggler section will be used as a single beamline with a hard X-ray source. The modifications of the original frontend design, the components and the deviations between the sector types are being presented.

INTRODUCTION

For the next step in the development of PETRAIII as a synchrotron radiation source the PETRAIII extension project added up to 10 further insertion device beamlines located in two new additional buildings [1]. The beamlines are arranged in three new sectors types with different layouts to the PETRAIII in the Max von Laue experimental hall. This includes the layout of the frontends of the beamlines in the new tunnel. One of the three sector types contains two beamlines with one new generic frontend for the PETRAIII extension project with an increased canting angle from 5 mrad (PETRAIII) to 20 mrad. Additionally, two of the straight sections are modified. One straight section will be transformed in a side station sector with a 1mrad canting angle (P21) [2]. The other straight section with the 40 m long damping wiggler will be used as a single beamline with a hard X-ray source (P61) [3].

The reasons for the new layout are a different topology of the machine, the space available in the tunnel and the crane system for the transport of the components. This leads to an increased distance between the source of the beamline and the beginning of the girder frontend from at average 4.5 m to more than 35 m. In this section the photon beam is guided only in a UHV tube with vacuum pumps and a mask system. The distance between the beamline source and the optic hutches in the new halls are 50 m for the new generic beamline, 77 m for the side station beamline and 90 m for the the damping wiggler beamline.

GENERIC PHOTON BEAMLINE FRONTEND FOR PETRAIII EXTENSION PROJECT

The aim of the design concept of the old generic frontend as well as the new generic frontend was to minimize the number of specialized components for all beamlines [4, 5]. Additionally a second objective was to use the existing girder concept for PETRAIII with only small adjustments. The already existing girder concept allows a fast and reliable installation phase and is robust and versatile during commissioning and user operation [6].

The major difference of the new generic approach is the change of the canting angle between the two beamlines of one sector. The sector exist 4 times with two undulator IDs in each sector (P22-P23, P24-P25, P62-P63 and P64-P65). The large horizontal gap between the two beamlines in the girder frontend allows the use of a seperate girder system for each beamline per sector (see Fig. 1 at the bottom). The classic generic approach required components for both beamlines per sector on one girder and therefore complex girders. In the new approach the use of only single beamline girder was possible. The only difference in the new generic designs was one additional tube in one beamline to align the girders for a better accessibility during installation and maintenance in the tunnel.

Due to some minor adjustments to some components and the integration of additional components (e.g. water cooled CVD diamond screen) it was necessary to change the arrangement of the components on the girders. Thereby only one girder design of the generic approach for PETRAIII could be re-used. In the the new generic design only four different girders types are used instead of eleven different girder types.

Common to all frontend designs and new in contrast to PETRAIII is the use of the water cooled CVD-diamond flourescent screen with an attached CCD camera system. It is installed on the first girder in front of any other component. This new component allows to image the footprint of the white beam. Also new and common to all beamlines is the modified filter chamber. Now a CCD camera system is attached as well. Right behind the vacuum diagnostic

* hilmar.krueger@desy.de

ISBN: 978-3-95450-188-5 doi:10.18429/JACoW-MEDSI2016-WEPE09

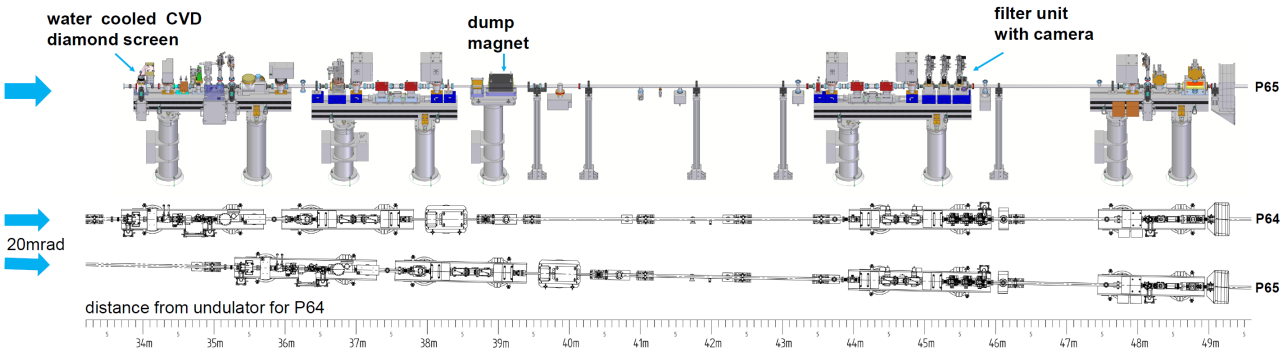


Figure 1: Generic girder frontend photon beamline frontend for PETRAIII extension project.

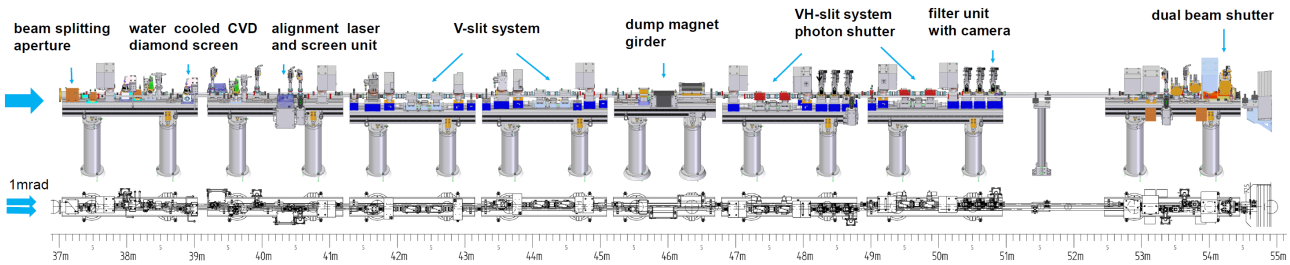


Figure 2: Side station photon beamline girder frontend P21.

unit in the optic hutch a CVD-diamond window is installed. Even at the highest beam current in the machine the camera readouts of these three screens allows an alignment of each white photon beam [6].

SIDE STATION BEAMLINE FRONTEND P21

The source of the two photon beams of the side station beamline are an 4 m in-vacuum undulator and a canted 2 m insertion device [2]. The two beams are guided to the beginning of the girder frontend in a common vacuum system with a rectangular tube. On the first girder the two beams are seperated in different tubes. The distance at this point between both beams is 63 mm. The separation is performed by a new beam splitting aperture followed by a modified aperture in each beamline. From this point on the components used are mostly standards. Because of the small distance between the two beams modifications of the housing are necessary. At the end of the frontend just before the 1.5 m thick storage ring shielding wall the beamlines have a distance of 77.5 mm. Just as in the generic approach a collimator and a beam shutter for each beamline is required at this point for the personal interlok. Because of the small distance a new dual beam shutter with integrated collimator is designed (see Fig. 3). The absorbers are moveable independently for each beam. Because of this dual beam shutter the beamlines share a common vacuum system. At the mostly generic components the vacuum system pumped individually the single beamlines. At several points a large pumping vessel connected the vacuum systems. This allows for fewer vacuum pumps and a shorter frontend (see Fig. 2). Right behind the concrete shielding wall a dual diagnostic unit seperates the vacuum system for each beamline. Nevertheless eight specialized girders for the side station frontend are necessary because of the small distance and the high density of components.

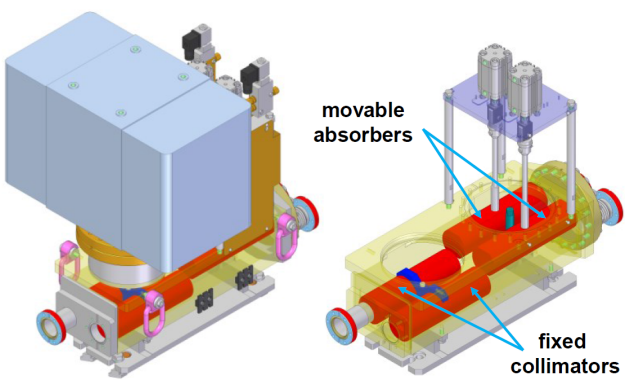


Figure 3: Dual beam shutter with integrated collimator for the side station frontend.

DAMPING WIGGLER BEAMLINE FRONTEND P61

The generic approach for the frontend design allows the reuse of three generic girders for the damping wiggler frontend (see Fig. 4). Only for the first girder a new arrangement is necessary. Because of the fixed gap operations of the 40 m long damping wiggler section a new setup of the mask system had to be designed. This system contains a new 3 mm x 2 mm rectangular aperture (see Fig. 5) followed by a new

Content from this work may be used under the terms of the CC BY 3.0 licence (© 2016). Any distribution of this work must maintain attribution to the author(s), title of the work, publisher, and DOI.

ISBN: 978-3-95450-188-5 doi:10.18429/JACoW-MEDSI2016-WEPE09

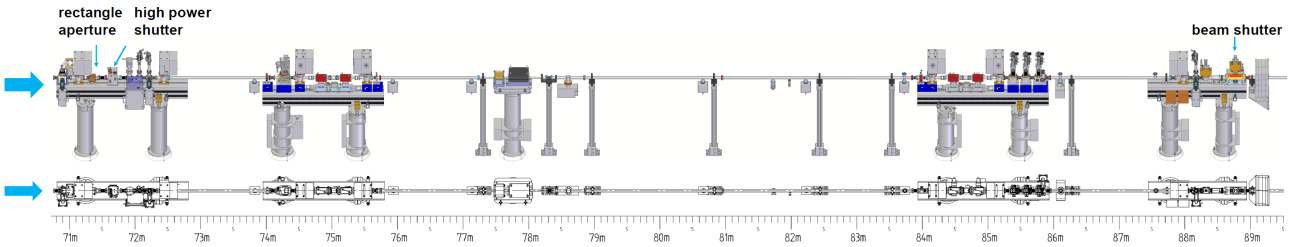


Figure 4: Damping wiggler beamline girder frontend P61.

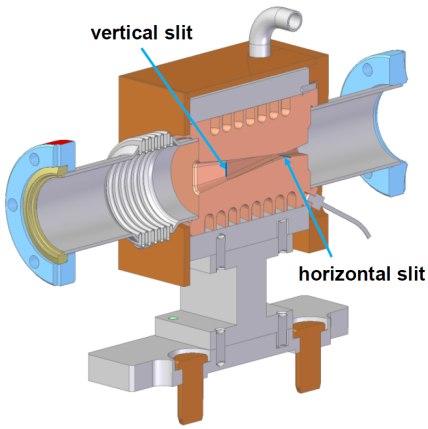


Figure 5: 3 mm x 2 mm rectangular aperture for the damping wiggler frontend with two slits in a row.

high power shutter which is based on a modified "slit blade" of the high power slit system. The effective 3 mm x 2 mm rectangular opening in the aperture is realized by Electrical discharge machining a vertical opening transitioning into a horizontal opening into a copper alloy[1] body.

CONCLUSION

The buildings and the tunnel sections with the concrete shielding are completed. PETRAIII resumed user operation in the Max von Laue experimental hall for the other 14 photon beamlines in April 2015. Most of the new generic 20 mrad extension frontends are installed and commissioned for UHV, but not in use for photon beam. The modified straight sections will be installed at the end of 2016 and in 2017 and are currently in manufacturing. The work in the optic hutches and experimental hutches is continuing.

[1] Glidcop

REFERENCES

[1] W. Drube, M. Bieler, W.A. Caliebe, H. Schulte-Schrepping, J. Spengler, M. Tischer, R. Wanzenberg, "The PETRAIII extension", *AIP Conf. Proc.* 1741, 020035 (2016), doi:10.1063/1.4952814

[2] A. Schöps, P. Vagin, M. Tischer "Properties of the insertion devices for PETRA III and its extension", *AIP Conf. Proc.* 1741, 020019 (2016); doi:10.1063/1.4952798.

[3] M. Tischer, K. Balewski, A. Batrakov, I. Ilyin, D. Shichkov, A. Utkin, P. Vagin, P. Vobly, "Damping Wigglers at the PETRAIII light source", *Proceedings of EPAC08*, Genoa, Italy, pp. 2317-2319.

[4] U. Hahn, H.B. Peters, R. Röhlsberger, H. Schulte-Schrepping, "The generic beamline concept of the PETRAIII undulator beamlines", *AIP Conf. Proc.* 879, (2006), pp. 539-542.

[5] M. Degenhardt, H.B. Peters, U. Hahn, J. Heuer, M. Hesse, H. Schulte-Schrepping, "Status of PETRAIII photon beamline frontends and optical systems", *J.Phys.:Conf. Ser.* 425 0042005.

[6] H. Schulte-Schrepping *et al.*, "Photon beamline frontends for the PETRA III extension project", *AIP Conf. Proc.* 1741, 020041 (2016), doi:10.1063/1.4952820.

Content from this work may be used under the terms of the CC BY 3.0 licence (© 2016). Any distribution of this work must maintain attribution to the author(s), title of the work, publisher, and DOI.

ISBN: 978-3-95450-188-5 doi:10.18429/JACoW-MEDSI2016-WEPE10

MECHANICAL DESIGN OF PULSE-BY-PULSE X-RAY BEAM POSITION MONITOR USING DIAMOND HEAT SINK*

Hideki Aoyagi†, Sunao Takahashi,
Japan Synchrotron Radiation Research Institute (JASRI), Hyogo, Japan

Abstract

It is indispensable to diagnose dynamics of synchrotron radiation beam for stable supply of the beam in synchrotron radiation facilities. We are developing a pulse-by-pulse X-ray beam position monitor using diamond heat sinks for an undulator beamline. We have designed the monitor aiming at improving heat-resistance property without degradation of high frequency property, and manufactured a prototype to evaluate a feasibility of the design. Thermal finite element analysis was carried out to design an effective structure of a detector head and a holder. Time-domain reflectometry was utilized to evaluate high frequency property of the prototype.

INTRODUCTION

A conventional X-ray beam position monitor (XBPM) is photoemission type, and blade-shaped tungsten is used as detector heads to secure heat resistance. Stabilization of pulse-by-pulse electron beam position has been realized at a high level in the SPring-8 storage ring [1,2]. The conventional XBPM, however, cannot measure pulse-by-pulse beam position, because the time constant of the detector head is long due to the stray capacitance and the impedance is not matched to 50 Ω of cables. To overcome this problem, a pulse-by-pulse XBPM equipped with microstripline structure (stripline-XBPM), which also works as a photocathode, had been developed for the SPring-8 bending magnet (BM) beamlines [3,4]. This monitor has potential to function as (1) a pulse intensity monitor, (2) a pulse-by-pulse XBPM, and (3) a pulse timing monitor [5]. For the undulator beamlines, further improvement of heat-resistance is required. Therefore, we are developing a pulse-by-pulse XBPM for undulator beamlines by introducing heat resistance structure that employed a diamond heat sink.

STRUCTURE OF PROTOTYPE

We started a design work for realization of the pulse-by-pulse XBPM from the following points of view. We decided to suppress an increase in time constant (t = RC) by lowering the stray capacitance as much as possible with securing an effective area of a photocathode, while accepting impedance mismatch around the photocathode [6]. As shown in Fig. 1, the photocathode is mounted on a diamond heat sink as a detector head. We adopted heat-resistant structure to reduce an effective irradiation cross section by aligning four detector heads parallel to a beam axis. A heat sink holder is attached to a cooling base welded to a DN40CF (ICF70) flange. A signal transfer line having microstripline structure is mounted on another ICF70 flange [7]. By separating signal transfer line from cooling mechanism, although high frequency property is degraded compared with the stripline-XBPM mentioned above, the heat-resistant property is expected to be improved. Figure 2 shows a prototype with a 6-way cross chamber. A couple of ICF70 flanges equipped with the detector heads (the signal transfer lines) are mounted on the top/bottom (left/right) ports. Two beam ports are faced using DN63CF (ICF114) flanges with a face-to-face dimension of 120 mm.

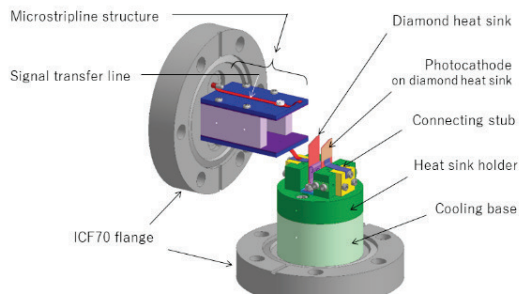


Figure 1: 3D image of the cooling structure (bottom) and the microstripline structure (left).

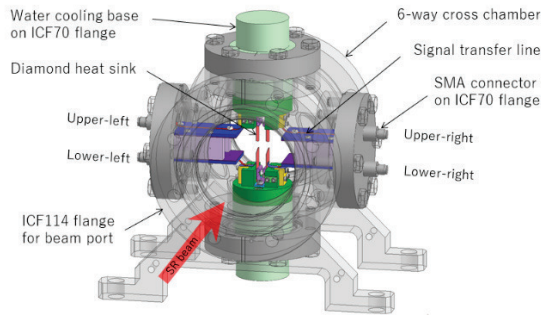


Figure 2: 3D image of the prototype.

THERMAL FINITE ELEMENT ANALYSIS

The thermal finite element analysis (FEA, ANSYS® Release 17.0) was carried out on the diamond heat sink (20 mm × 8 mm × 0.3 mm), the heat sink holder and the cooling base. A quarter model was used for the analysis, and the heat sink holder and the cooling base are treated as an integrated object for simplification. Figure 3 shows an analysis result of the typical case in the normal operation of the SPring-8 standard undulator beamlines. The thermal conductance (TC) of diamond and copper are set to 1,500 and 400 W/(m·K), respectively. Thermal contact conductance (TCC) between the diamond heat sink and the heat sink holder made of copper is assumed to be 10,000W/(m^2·K) in this calculation. The total power of 10W is input with uniform heat flax on the tip (1 mm × 8 mm × 0.3 mm) of the heat sink. This input power is equivalent to the maximum value assumed in the normal operation. The homoiothermal condition (30°C) is put to the bottom of the cooling

* This work was partly supported by Japan Society for the Promotion of Science through a Grant-in-Aid for Scientific Research (c), No. 20416374.
† aoyagi @spring8.or.jp

Content from this work may be used under the terms of the CC BY 3.0 licence (© 2016). Any distribution of this work must maintain attribution to the author(s), title of the work, publisher, and DOI.

ISBN: 978-3-95450-188-5 doi:10.18429/JACoW-MEDSI2016-WEPE10

Content from this work may be used under the terms of the CC BY 3.0 licence (© 2016). Any distribution of this work must maintain attribution to the author(s), title of the work, publisher, and DOI.

base. If the tolerance of the temperature rise is set as Δt = 100 K for a realistic value, the analysis result of this representative model is within the tolerance.

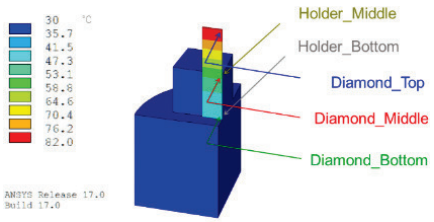


Figure 3: Quarter model for the FEA and the results. Arrows indicate locations of measuring points.

The temperature at each point on condition that the TC of the diamond is 1,500 W/(m·K) is plotted as a function of the TCC between the diamond sink and the copper, as shown in Fig. 4. This result suggests that the TCC is not so effective for heat-resistance property if the TCC exceeds 10,000 W/(m^2·K), and that, on the other hand, the temperature rise exceeds the tolerance of 100 K if the TCC below 2,000 W/(m^2·K).

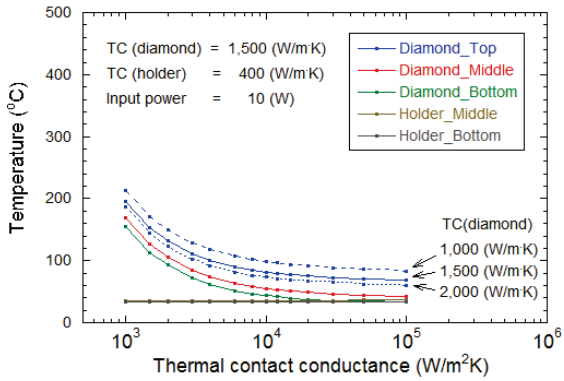


Figure 4: Thermal contact conductance (TCC) dependence of temperature.

Figure 5 shows the temperature variations by the difference in the TC of blade material used for the heat sink on condition that the TCC is 10,000 W/(m^2·K). If the TC of diamond is higher than 1,500 W/(m·K), the temperature rise is suppressed reasonably, and it is not required to know the exact number of the TC of diamond. If copper or tungsten plates are used for the heat sink, the temperature rise would exceed the tolerance level.

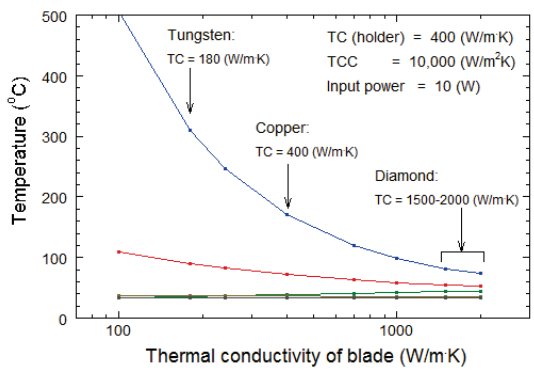


Figure 5: Thermal conductivity (TC) dependence of temperature.

The maximum input power reaches around 25W during commissioning/tuning of beamlines. Figure 6 shows the expected temperature of each point as a function of the input power, when the TCC is assumed to be 10,000 W/(m^2·K). The calculation shows that the current design is practicable.

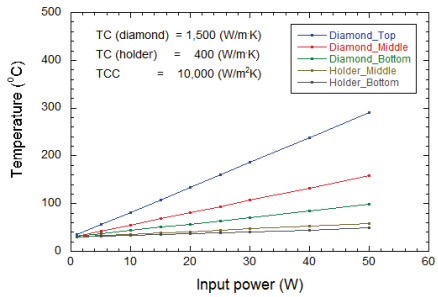


Figure 6: Input power dependence of temperature.

TIME-DOMAIN REFLECTOMETRY

A time-domain reflectometry (TDR) by using a single input pulse was utilized to evaluate high frequency property of this monitor. Although either a rising or a falling edge of rectangular wave is usually used for TDR, we used the isolated single pulse with unipolar (140 ps FWHM) for an input signal because of easiness of the interpretation.

The actual role of this monitor is to propagate an impulse from a tip of the detector head to the measuring instrument through the signal transfer line. Therefore, it is possible to predict a time structure of an actual output signal by observing the isolated single pulse that is input directly from the detector head through a probe, namely, a time-domain transmissometry (TDT). We discuss about the results using TDR here, because it has been already confirmed that the results from TDR resembles those from TDT [8].

As shown in Fig. 7, the input pulse from a pulse generator branches into an oscilloscope (4 GHz, 20 GS/s) and measured objects with a divider. The reflected signal makes a round trip along the cable (1m), and about 10ns later it is observed with the oscilloscope.

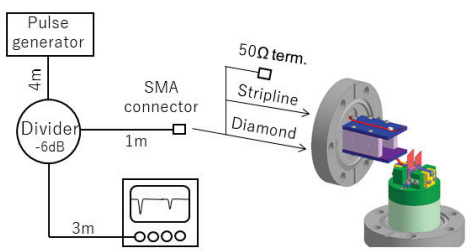


Figure 7: Experimental setup for the time-domain reflectometry.

As shown in Fig. 8, the peaks at t = 0 ns is the input pulse observed directly. The pulse shapes observed at t = 9 ~ 10 ns are the reflected pulse as follows: (1) SMA connector with 50 Ω termination (light green), (2) SMA connector with open end (green), (3) with microstripline structure (blue), (4) with microstripline structure and a connecting stub (purple), (5) with microstripline structure, a connecting stub and a diamond heat sink (red). There is delay of

ISBN: 978-3-95450-188-5 doi:10.18429/JACoW-MEDSI2016-WEPE10

0.7 ns, which corresponds to the length of microstripline structure, in the reflected signal with microstripline structure (blue), compared with the reflected signal from the SMA with open end (green). The time structure is almost maintained. The double peak was observed in the reflected signal from the diamond heat sink (red), which has an electrode as the photocathode. This is the result of impedance mismatching of the section between the microstripline structure and the electrode on the diamond heat sink.

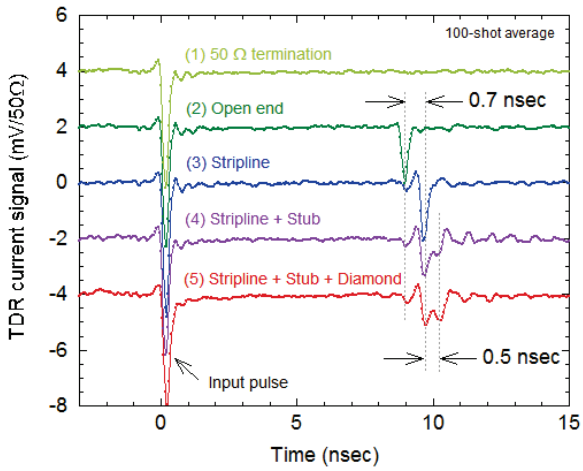


Figure 8: Experimental results of Time-domain reflectometry.

To consider the relation between the results obtained by TDR and the waveform generated actually from a monitor, three kinds of diamond device, as shown in Fig. 9, were compared: (a) the diamond heat sink with an electrode introduced this time, (b) a dummy diamond plate prepared for a preliminary study, and (c) a diamond semiconductor detector developed as an electron beam halo monitor [9].

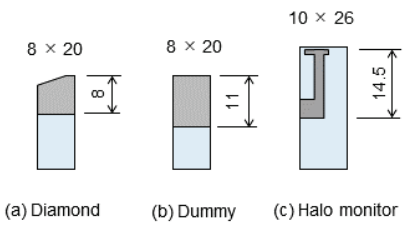


Figure 9: Structure of heat sinks and a diamond detector. Shaded areas are electrodes. The thickness is 0.3mm.

As shown in Fig. 10, (5), (6) and (7) are reflected pulses in TDR from the diamond devices of (a), (b) and (c), respectively. The waveform generated from the diamond detector of the halo monitor actually (blue) is also indicated by shifting a time axis. The pulse length of the actual pulse (blue) is 0.4 ns FWHM, while the width of the double peak (black) seen in TDR of (c) is 0.5 ns. The width of the double peak of the diamond heat sink (5) is narrower than that of the dummy plate (6), because the diamond heat sink is designed to have a smaller electrode. These results suggest that this monitor generates the unipolar pulse signal with the pulse length of sub-nanosecond.

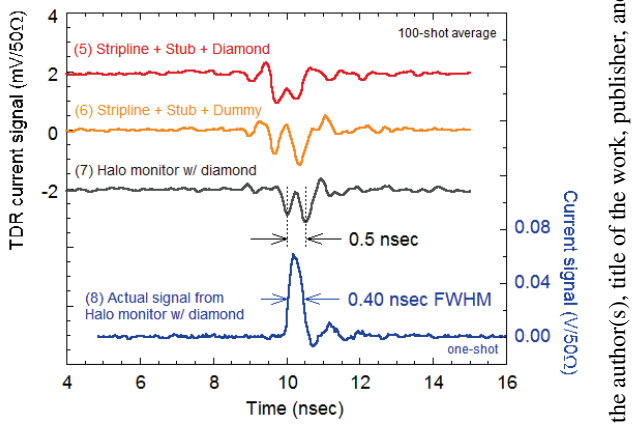


Figure 10: Comparison of the results of time-domain reflectometry with an actual pulse shape of the halo monitor.

SUMMARY

We have designed the pulse-by-pulse X-ray beam position monitor using the diamond heat sink, and manufactured the prototype to evaluate the thermal and high frequency properties. The results of thermal finite element analyses suggest that the diamond heat sink mounted on the holder described here is practicable from the heat-resistant point of view, if the TCC between diamond and copper is assumed to be 10,000 W/(m^2·K). The evaluation tests of the prototype on high frequency property using TDR suggest that the single isolation pulse of the sub-nanosecond can be provided.

It's necessary to estimate experimentally the thermal contact conductance between the diamond heat sink and the heat sink holder made of copper in the next step. Furthermore, we are planning to manufacture a real component, to install it into the beam line, and to carry out overall performance tests.

ACKNOWLEDGEMENT

The authors would like to thank T. Nakamura, K. Kobayashi, S. Kimura and H. Osawa of Japan Synchrotron Radiation Research Institute (JASRI) for the useful advice regarding high frequency analysis. The design and fabrication of the prototype of the pulse-by-pulse XBPM has been achieved by getting cooperation of Vacuum and Optical Instruments (Shinku-Kogaku, Inc, Tokyo, Japan).

REFERENCES

[1] T. Nakamura et al., Proc. EPAC 2004, 2646.
[2] T. Nakamura, K. Kobayashi, Proc. ICALEPCS 2005, PO2.022-2.
[3] H. Aoyagi et al., Proc. PASJ2006, TO25, 159-162.
[4] H. Aoyagi et al., AIP Conf. Proc. 879, 1018 (2007).
[5] H. Aoyagi et al., Proc. DIPAC2011, MOPD91, 260-262.
[6] H. Aoyagi et al., Proc. PASJ2015, THP085, 1224-1226.
[7] H. Aoyagi et al., Phys. Rev. ST Accel. Beams 16, 032802.
[8] H. Aoyagi et al., Proc. PASJ2016, TUP086.
[9] H. Aoyagi et al., Phys. Rev. ST Accel. Beams 15, 022801.

Content from this work may be used under the terms of the CC BY 3.0 licence (© 2016). Any distribution of this work must maintain attribution to the author(s), title of the work, publisher, and DOI.

ISBN: 978-3-95450-188-5 doi:10.18429/JACoW-MEDSI2016-WEPE14

MINIMIZING GRATING SLOPE ERRORS IN THE IEX MONOCHROMATOR AT THE ADVANCED PHOTON SOURCE

M. V. Fisher†, L. Assoufid, J. McChesney, J. Qian, R. Reininger, F. Rodolakis
Advanced Photon Source, Argonne National Laboratory, Argonne, IL, USA

Abstract

The IEX beamline at the APS is currently in the commissioning phase. The energy resolution of the beamline was not meeting original specifications by several orders of magnitude. The monochromator, an in-focus VLS-PGM, is currently configured with a high and a medium-line-density grating. Experimental results indicated that both gratings were contributing to the poor energy resolution and this led to venting the monochromator to investigate. The initial suspicion was that a systematic error had occurred in the ruling process on the VLS gratings, but that proved to not be the case. Instead the problem was isolated to mechanical constraints used to mount the gratings into their respective side-cooled holders. Modifications were made to the holders to eliminate problematic constraints without compromising the rest of the design. Metrology performed on the gratings in the original and modified holders demonstrated a 20-fold improvement in the surface profile error which was consistent with finite element analysis performed in support of the modifications. Two gratings were successfully reinstalled and subsequent measurements with beam show a dramatic improvement in energy resolution.

BEAMLINE

The Intermediate-Energy X-ray (IEX) beamline at the Advanced Photon Source (APS) at Argonne National Laboratory was designed with two separate branches, each with a dedicated endstation: one dedicated to angle-resolved photoemission spectroscopy (ARPES) and the other to resonant soft X-ray scattering (RSXS) [1]. The high energy resolution required by the ARPES endstation is achieved using an in-focus variable line spacing plane grating monochromator (VLS-PGM) [2]. To meet the demands of the two experimental techniques the monochromator is designed to house up to four water side-cooled gratings. It is currently configured with a high-line-density grating (HEG) with a nominal 2400 l/mm and a medium-line-density grating (MEG) with a nominal 1200 l/mm. The HEG is primarily for use with the ARPES branch when conducting higher resolution experiments. The MEG offers higher flux with moderate resolution that can be used by both the ARPES and RSXS branches. Future plans include a low-line-density grating (LEG) with a nominal 400 l/mm that is optimized for photon hungry RSXS experiments.

The diffracted beam downstream of the exit slit was observed to shift in energy depending on the size and position of either the synchrotron beam or the clean-up aperture located just downstream of the monochromator. As a result, the energy resolution was very poor except for the smallest aperture sizes.

GRATINGS

The cause of the poor energy resolution was eventually isolated to the gratings using photoemission measurements at the ARPES endstation. A systematic scanning of a vertical aperture just downstream of the monochromator (before the beam significantly disperses) revealed that the energy of the diffracted beam shifted at the exit slit as one selected different sections of the dispersing beam. This technique essentially allowed one to scan along the length of the grating. Both the HEG and the MEG showed similar energy shifts.

Ruling Line-Density

In order to fully investigate the gratings, the monochromator needed to be vented. The initial suspicion was that a systematic error had occurred in the ruling process on both gratings which had been holographically ruled by the same vendor. No metrology had been performed to verify the variable ruling line density on either grating.

In anticipation of the ruling density being the problem, a new mechanically ruled MEG was acquired. In parallel, plans were made to remove the existing MEG and measure its ruling density. Unfortunately, the long trace profilometer (LTP) at the APS was undergoing an upgrade; as a result, arrangements were made with the optics metrology group at the SOLEIL Synchrotron to measure the ruling density of the original MEG on their LTP. The measurements confirmed that the original MEG was properly ruled. In the meantime, the real problem with the gratings had been isolated to the grating holder itself.

Grating Substrate

The mechanical details of the grating holder were reviewed in preparation for mounting the new MEG. The grating substrate design adopted for the IEX monochromator has three horizontal through-holes to facilitate clamping of side cooling blocks and three vertical holes to facilitate bolting the grating to a support from below as illustrated in Figure 1. The grating substrates were originally specified and fabricated with extremely good surface profiles of better than 1nm RMS. Surface profile measurements were not made after the original MEG and HEG were ruled or after they were installed into their respective

* Work at the Advanced Photon Source is supported by the U. S. Department of Energy, Office of Science, Office of Basic Energy Sciences, under Contract No. DE-AC02-06CH11357.
† mfisher@aps.anl.gov

Content from this work may be used under the terms of the CC BY 3.0 licence (© 2016). Any distribution of this work must maintain attribution to the author(s), title of the work, publisher, and DOI.

ISBN: 978-3-95450-188-5 doi:10.18429/JACoW-MEDSI2016-WEPE14

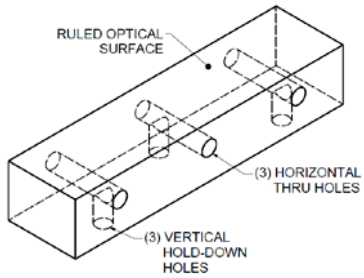


Figure 1: Grating Substrate Mounting Details.

holders. This is a lesson learned. Others have demonstrated the value in performing metrology at each step along the way to verify surface profile integrity [3, 4].

Original Grating Holder Design

A drawing of the original grating holder design is shown in Figure 2. The cooling blocks are clamped to the sides of the gratings with three custom bolts that pass through the gratings and are secured "finger tight" with a nut. These three custom bolts have tapped holes through their shanks that allow three vertical screws to pull the grating down against three steady rests. Each of the vertical screws are also torqued "finger tight". A review of this design revealed that the gratings were being subjected to bending moments as a result of the lever arms between the vertical hold-down screws and the steady rests. In addition, the use of screws that were torqued "finger tight" without any compliance were easy to overload. All of this had the potential to cause surface profile errors and led to a decision to modify the original grating holder.

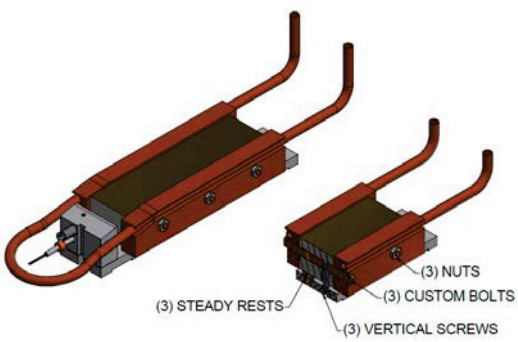


Figure 2: Original Grating Holder.

Modified Grating Holder Design

A drawing of the modified holder design is shown in Figure 3. The cooling blocks are still clamped to the sides of the grating with the same custom bolts, but a Belleville washer now resides beneath each of the nuts. The three steady rests have been eliminated and replaced with three spherical washers of the same height. The three spherical washers are located coaxial to the three vertical hold-down screws. A larger and deeper counterbored hole in the holder base plate allowed for the introduction of a stack of three Belleville washers at the head of a new low profile

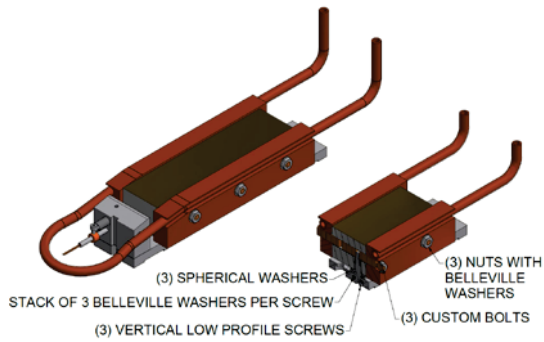


Figure 3: Modified Grating Holder.

vertical hold-down screw. The Belleville washers allow for the application of a repeatable, small clamping force that is thermally compliant.

FEA Modelling of Grating

Finite element analysis (FEA) was conducted on a model of the grating to verify that the proposed changes to the holder would be beneficial. Figure 4 compares the mechanical distortion of the grating by imposing constraints associated with the original and modified holders. A loading of 10N was assumed at each vertical screw on the original holder design. Contours of the resulting vertical displacement are displayed in mms. In order to achieve a similar distortion scale in the modified holder, it was required to apply a 1000N force to each of the corresponding screws. One can clearly see that potential surface profile errors are reduced significantly in the modified holder design.

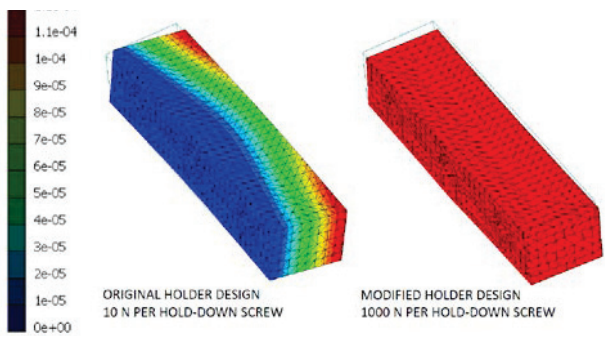


Figure 4: FEA Comparison of Grating Distortions.

Metrology

The plan was to perform surface profile measurements on the gratings in their original holders and to repeat these measurements with each grating unmounted and then remounted in the modified holder. With the LTP in the midst of an upgrade, another means of making such measurements was needed. An appropriate methodology was eventually developed using a Wyko 6000 Interferometer.

Surface profile measurements are much easier to make on a mirror than a grating, therefore a series of measurements were made by using a spare grating substrate. Measurements were made with the substrate unmounted,

Content from this work may be used under the terms of the CC BY 3.0 licence (© 2016). Any distribution of this work must maintain attribution to the author(s), title of the work, publisher, and DOI.

ISBN: 978-3-95450-188-5 doi:10.18429/JACoW-MEDSI2016-WEPE14

Content from this work may be used under the terms of the CC BY 3.0 licence (© 2016). Any distribution of this work must maintain attribution to the author(s), title of the work, publisher, and DOI.

in the original holder and in the grating holder after it had been modified. The results of these measurements along the longitudinal centerline of the grating substrate are plotted in the upper and lower graphs of Figure 5. These results were consistent with the earlier FEA and confirmed that the original holder was inducing a significant surface error.

Similar measurements were also made with the Wyko on the actual gratings once the methodology had been perfected. Measurements on the MEG in its original holder before it was removed and sent to SOLEIL confirmed the presence of a large surface profile error which is also plotted in the upper graph of Figure 5. The original HEG and the new MEG were measured mounted in the modified holders before installing into the monochromator. The results of those measurements are summarized in the lower graph of Figure 5.

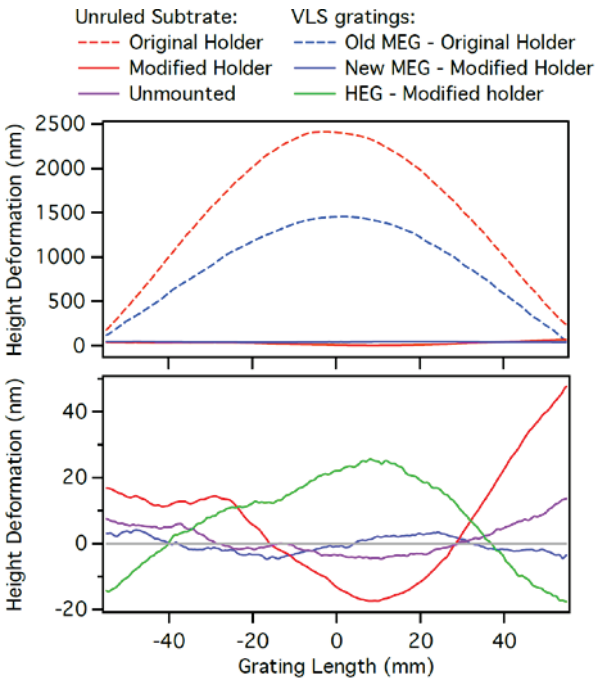


Figure 5: Surface Profile Measurements.

IMPROVED PERFORMANCE

With the original HEG and a new MEG mounted in modified holders and installed in the monochromator, commissioning of the monochromator resumed. The position of the horizontally deflecting M1 Mirror upstream of the monochromator was adjusted in roll to better center vertically the incoming beam on the monochromator. This was adjusted in response to another suspicious issue that had been corroborated during the removal of the gratings. The original MEG had developed a carbon contamination stripe that was only visible on the downstream half of the grating. This was consistent with the asymmetric plots that had been obtained when scanning a vertical aperture downstream of the monochromator to evaluate the shifts in energy before the monochromator was vented. The "before" plots in Figure 6 were made with the original MEG in the original holder and the "after" plots were made with the new MEG in the modified holder. They show a dramatic improvement in energy shift as one measures the energy of the Au 4f photoemission peaks and scans the vertical aperture downstream of the monochromator [5]. Similar results were also obtained for the HEG.

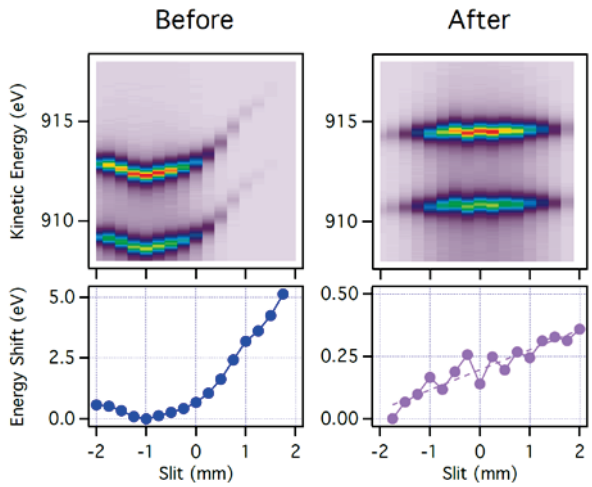


Figure 6: Photoemission Measurement Demonstrating Improved Energy Resolution.

CONCLUSIONS

Modifications to the grating holders in the monochromator at the IEX beamline significantly reduced surface profile errors in the grating thereby providing a dramatic improvement in the energy resolution of the beamline. Proper metrology of beamline optics at all stages of assembly cannot be over emphasized.

REFERENCES

[1] J. McChesney *et al.*, The Intermediate Energy X-ray beamline at the APS, Nuclear Instruments and Methods in Physics Research A 746 (2014) 98.

[2] R. Reininger, "The in-focus variable line spacing plane grating monochromator", Nuclear Instruments and Methods in Physics Research A 649 (2011) 139.

[3] F. Siewert *et al.*, "Inspection of a Spherical Triple VLS-grating for Self Seeding of FLASH at DESY, AIP Conf. Proc. 879 (2007) 667.

[4] J. Viefhaus *et al.*, "The Variable Polarization XUV beamline P04 at PETRA III: Optics, mechanics and their performance", Nuclear Instruments and Methods in Physics Research A 710 (2013) 151.

[5] F. Rodolakis *et al.*, "In-situ characterization of monochromators by energy-resolved imaging of both the incident and diffracted beam for a soft x-ray monochromator", unpublished.

ISBN: 978-3-95450-188-5 doi:10.18429/JACoW-MEDSI2016-WEPE15

HIGH FREQUENCY UHV MECHANICAL X-RAY BEAM CHOPPER

Nahikari González, Carles Colldelram, Salvador Ferrer, Carlos Escudero
CELLS-ALBA, 08290 Cerdanyola del Vallés, Spain

Abstract

An in vacuum mechanical chopper has been designed and built to perform X-ray Absorption Spectroscopy (XAS) experiments with operating liquid electrochemical cells at the Near Ambient Pressure Photoemission (NAPP) end station of ALBA Synchrotron (BL24, CIRCE Beamline). While operating the liquid electrochemical cell, in order to separate the weak currents induced by the X-ray absorption process at the working electrode in contact with the liquid electrolyte (total electron yield signal or TEY) from the faradaic current stablished between the electrodes when applying a bias, the incoming beam must be chopped at a certain frequency (ω) and then, by means of a lock in amplifier, the signal at this frequency ω can be extracted and measured. The in vacuum chopper developed at ALBA can operate at variable frequencies and when inserted in the X-ray beam path, produces pulses with a certain frequency ω, therefore modulating the TEY signal. This new chopper design, improves previous designs which used piezo-actuated choppers constrained to work at fixed oscillating frequencies [1].

The design consists of a slotted disk that spins around an axis by means of an UHV stepper motor. A LED and photodiode based UHV sensor ensures that frequency drifts do not affect the measurements. The motor is hold by an internally water cooled oxygen-free high thermal conductivity copper (OFHC) support, which allows long duration experiments at high speeds without stopping.

INTRODUCTION

In some soft X-ray absorption experiments, when performing electrochemical characterization of electrode-electrolytes systems under operando conditions, the big currents prevent from effectively collecting the tiny total electron yield currents (TEY) that shape the XAS spectra that contain the information that one wishes to extract from the operating electrode.

In order to separate these weak currents induced by the X-ray absorption process from the dominant faradaic currents (typically 10^6 times bigger), the incoming X-ray is chopped at certain frequency ω and then, by means of a lock in amplifier, the Fourier component of the signal corresponding to the ω frequency is extracted and measured. To modulate the TEY current, ALBA has developed an in vacuum mechanical chopper with variable frequency that, if inserted in the X-ray incoming beam, modulates the TEY signal whose amplitude is measured with a lock in amplifier

This technique has been typically performed using piezo actuated choppers with a fixed oscillating frequency, however, in this paper the viability of using a stepper motor driven chopper and the required surrounding elements is described.

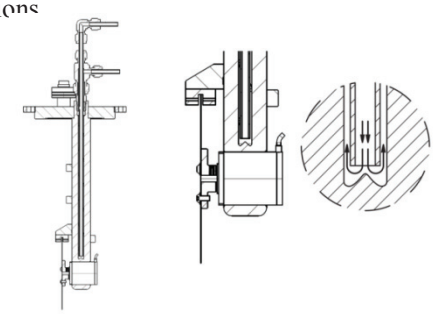
SYSTEM DESCRIPTION

The chopper consists of a slotted spinning disk driven by an UHV stepper motor. The main requirements of the mechanical chopper are the following:

- Sustain a high and stable rotation speed up to 1 kHz continuously for hours.
- Have a controlled and variable frequency.
- Be fully UHV compatible (10^{-9} – 10^{-10} mbar).
- Enable in-out motion in order to remove it from the beam path, if necessary.
- Allow the synchronization with the chopped electron yield current by means of a lock-in amplifier.

The selection of a stepper motor is the key issue of the design since a speed around 2.000 rpm was required. This velocity is beyond the normal working speed for standard stepper motors, which are capable to work at up to 6.000 rpm in air. However, due to the fact that the motor is placed in UHV and therefore, without air cooling at all, the working speed is limited -according to the manufacturer catalogue [2] - to 600 rpm. Because of the negligible cooling capacity in vacuum environments, the motor may overheat, stop and even be damaged in just a few seconds.

The proposed solution to the above mentioned issue is to support the motor with an internally water cooled clamp made of massive oxygen-free high thermal conductivity copper (OFHC). The gap between the motor and the water recirculation path is reduced to its minimum, 2mm. In this way the water arrives as close as possible to the motor's body and hence, the heat exchange between the motor and the water is maximized. A thermocouple connected to the motor's body controls the operating temperature continuously. Fig. 1 shows the basic cooling solution with the motor at the bottom, the holding clamp column with internal concentric water cooling and the brazed CF flange with the corresponding water and electrical connections



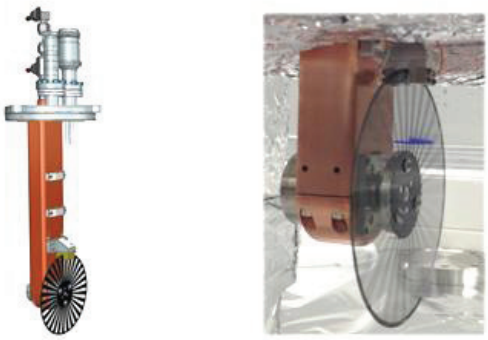
(a) (b)

Figure 1: a) Cross section of the motor cooling elements. (b) Detailed view of the water recirculation.

Content from this work may be used under the terms of the CC BY 3.0 licence (© 2016). Any distribution of this work must maintain attribution to the author(s), title of the work, publisher, and DOI.

ISBN: 978-3-95450-188-5 doi:10.18429/JACoW-MEDSI2016-WEPE15

Content from this work may be used under the terms of the CC BY 3.0 licence (© 2016). Any distribution of this work must maintain attribution to the author(s), title of the work, publisher, and DOI.



(a) (b)

Figure 2: (a) Basic components of the device. (b) Chopper disk, motor and support.

A Thorlabs´ slotted disk of 0,25mm thickness and Ø101,6mm was chosen for chopping the beam. The disk was tested in UHV and the RGA showed no evidence of any compatibility issues under UHV. The blade is available with different numbers of slots. The more slots, the higher the frequency but the smaller the beam size that can be chopped. A ray tracing calculation was performed to estimate the beam size at the chopper position and a 30 slots disk was chosen for the first experiments.

A thin aluminium support holds the disk directly coupled to the motor axis to both reduce the mass inertia and to avoid introducing possible frictions in the motion system.

At the top part of the spinning disk, a fully UHV compatible speed sensor, based on a LED transmitter and a photodiode, is installed in order to generate a periodic signal with the frequency of rotation of the disk. The photodiode output feeds into the lock in reference input. This ensures that frequency drifts do not affect the measurements since the X-ray beam is chopped at the same precise frequency that the one of the sensor current. All the components of the device are shown in Fig. 2.



Figure 3: Complete chopper unit.

A UHV linear manipulator allows inserting or removing the chopper unit from the beam path. Both the cooling and electrical connections are located on the top CF63 flange to prevent relative movements of the cables. The system is mounted in a vacuum chamber over a rigid and stable structure, which includes levelling elements in order to adjust chopper disk position, as shown at Fig. 3. The whole chopper unit is installed in a vacuum chamber after the M3 mirror of the CIRCE beamline, just upstream a fluorescence screen unit of the NAPP branch.

SIMULATIONS

Thermal Calculations

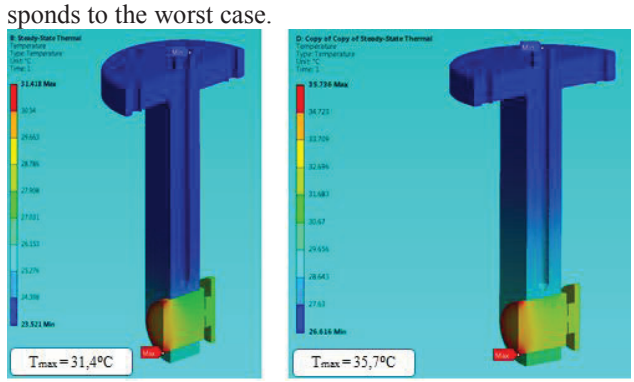
In order to study the thermal behaviour of the in-vacuum components with the water cooling system, a steady state thermal calculation was performed in Ansys, assuming the following boundary conditions:

- Electrical power given to the motor and therefore, approximate power to be dissipated [Eq.1]

$$\left.\begin{array}{l} \textit{Serial Bipolar Connection} \\ I = 0{,}6A \\ V = 25V \end{array}\right\} \quad P = V.I = 15W \qquad (1)$$

- Cooling water temperature: 23,5ºC

The most significant temperature maps for two different subcases are shown in Fig. 4, both of them assuming a non-perfect contact between the components with a thermal conductance value of k= 2000W/ m^2.ºC, which corresponds to the worst case.



(a) (b)

Figure 4: (a) Temperature map with V_{water} = 3m/s. (b) Temperature map with V_{water} = 0,5m/s (minimum flow).

As seen in Fig. 4 above, the maximum temperature of the motor is below 40ºC, which is completely acceptable.

Static Analysis and Vibrational Behaviour

In order to check the vibrational stability and static behaviour of the whole system, both the static and vibrational analysis simulations were performed in Ansys. The results show a maximum deformation of 3µm at the chopper disk and the 1st vibration mode at 66,6Hz, validating the system' stability.

ISBN: 978-3-95450-188-5 doi:10.18429/JACoW-MEDSI2016-WEPE15

TEST & RESULTS

First Results

After mounting the whole system and before baking it out, the chopper commissioning was done under vacuum. The motor was moved at 13.500 halfsteps/s (2.000 rpm), corresponding to a chopping frequency of 1kHz for a 30 slots´ disk, with a water flow of 2l/min at 23ºC. As shown in Fig. 5 a steady state temperature of 30,2ºC was achieved, which was in the range of the calculated values.

After performing a bake out for 1 week at 120ºC, the temperature of the motor stabilized at about 60ºC, as shown in Fig. 5. This difference might be explained because of the contact loose between the clamp and the motor due to thermal deformation drifts during the bakeout, causing a loss of heat exchange capacity.

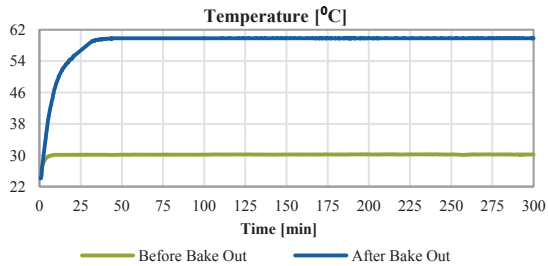


Figure 5: Temperatures in vacuum at 2.000 rpm with a water flow of 2l/min at 23ºC before the bake out and after the bake out.

Results After Intervention

In order to improve the contact between the motor and the cooled support, and therefore, to enhance the cooling capacity, a 50µm thick indium foil was installed between the motor and the support. After the intervention, and before doing a bake out, the steady state temperature was stabilized at 48ºC, with same flow and speed conditions as the ones tested before the intervention. After doing a bake out at 120ºC during 8 days, the temperature stabilized at 51ºC, which means that the cooling capacity had improved with the indium foil but also, that the contact had been loosen a bit again during the bake out. The two temperature graphs are shown in the Fig. 6.

The chopper was used continuously for more than 10 hours in different shifts during one week, without temperature readings above the ones shown in Fig. 6.

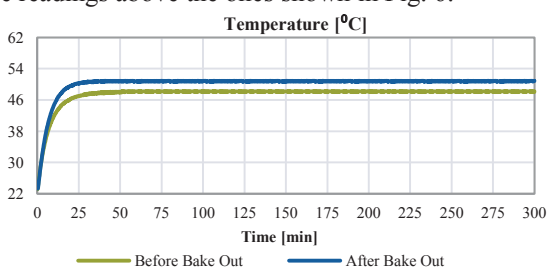


Figure 6: Temperatures in vacuum at 2.000 rpm with a water flow of 2l/min at 23ºC after the foil installation before the bake out and after the bake out.

CONCLUSIONS

Even if the steady state temperature of the motor is higher than calculated, the feasibility of using a stepper motor in UHV at rotation speeds above 600 rpm with the cooling system developed in-house has been validated.

The variable frequency operation is an important quality of this device since the operating frequency in a real experiment has to be determined to be different from the eigen frequencies of the mechanical vibrations induced by fluids, vacuum pumps or other stimuli and of the electrical noise.

In general terms, the chopper could be used to filter low frequency electrical noise whose origin are mechanical vibrations, network noise or accelerator feedback (150 Hz). Operating at higher frequencies than noise sources (2 or 3 times), noise could be filtered thanks to a lock in amplifier so as to have cleaner signals with a better signal/noise ratio. This is useful when measuring weak signals or in general where signal's intensity is comparable to the noise level.

Furthermore, the chopper disk is interchangeable, allowing maximum flexibility regarding the frequency working range, up to 3,3kHz for a disk with 100 slots. This is at variance with other choppers used in most laboratories that consist of resonant vibrating metal foils excited by piezoelectric resonators and are limited to work at a certain fixed frequency. Besides, in these cases, due to the inertia of the vibrating foils, the achievable frequencies are below ca. 200 Hz. In our case, the operating frequency was determined experimentally by looking to the quality of the spectra. The results obtained in the first experiment showed spectra of good quality..

This design was registered as utility model at the Spanish patent and trademark office the 1st of August 2016 [3].

ACKNOWLEDGEMENTS

The authors wish to acknowledge all the ALBA staff involved in the design and construction of the beam chopper, in particular, Marta Llonch and Jon Ladrera (alignment group); Jose Ferrer, Karim Maimouni, Oscar Borrego and Francisco Trujillo (mechanical workshop); Josep Nicolás (optics group); Abel Fontserè, Bern Saló and Fulvio Becheri (electronics and controls group) and all the BL24, CIRCE beamline staff.

REFERENCES

[1] Velasco-Velez et al, *Science* 2014, *346*, 831–834.

[2] Phytron Vacuum Stepper Motors VSS Catalogue.

[3] Utility Model registration no. U201630988.

Content from this work may be used under the terms of the CC BY 3.0 licence (© 2016). Any distribution of this work must maintain attribution to the author(s), title of the work, publisher, and DOI.

ISBN: 978-3-95450-188-5 doi:10.18429/JACoW-MEDSI2016-WEPE18

APS 2-ID BEAMLINE, UPGRADE TO CANTED CONFIGURATION *

D. Capatina†, M. Beno, M. Fisher, J. Knopp, B. Lai, E. Moog, C. Roehrig, S. Vogt,
Advanced Photon Source, Argonne National Laboratory, Lemont, USA

Abstract

To provide independent operation of the two 2-ID beamline experimental stations, a new canted beamline design is being developed. The constraint of keeping the existing front end limits the canting angle. The optimal canting angle was determined to be 400 µrad and is achieved by using a permanent magnet. A coil is added to the canting magnet to provide a steering adjustment of maximum 40 to 50 µrad. In order to increase the beam separation as well as to provide power filtering and higher harmonics rejection for the downstream optics, a dual mirror system with focusing capability is used as the first optic at approximately 28 m from the center of the straight section. The inboard mirror (2.6 mrad) reflects the inboard beam outboard while the outboard mirror (4.1 mrad) reflects the outboard beam inboard. The beam presented to the dual mirror system is defined by two 1 mm x 1 mm apertures. The maximum power absorbed by each mirror is 200 W. Two vertically deflecting monochromators with minimum offset of 17 mm are located in the First Optical Enclosure on the outboard branch. The monochromator for the inboard branch is located in the corresponding experimental station.

BEAMLINE LAYOUT

The 2-ID beamline infrastructure consists of three existing shielded enclosures, three mini-hutches and shielded transport. The mini-hutches are existing as well and are relocated as needed. The shielded transport is a new design. The schematic layout of the major optical and shielding components is shown in Fig. 1.

SOURCE

The X-ray source for the beamline consists of two 2.4-m-long undulators with a period length of 3.3 cm (U33), one for each branch, located symmetrically about the center of the straight section. The period may be further optimized in the future.

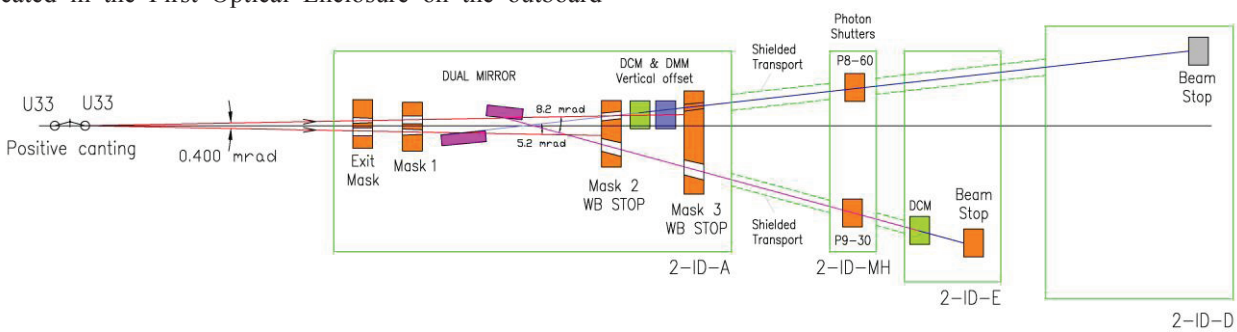


Figure 1: Schematic layout of the major optical and shielding components.

CANTING MAGNET

The design of the canting magnet for 2-ID is based on the permanent-magnet canting magnet planned for Sector 4-ID that introduces a bend of 400 µrad with a magnetic gap of 8.5 mm. Modifications are made to accommodate the larger vacuum chamber and larger magnetic gap in Sector 2. In addition, the ability to adjust the bend by a small amount is desired so the electron beam can be steered independently through the two undulators. A coil is added to the canting magnet to provide a steering adjustment of 40 to 50 µrad, maximum. That limitation on the steering adjustment avoids potential issues with power level increases on downstream masks. The cant centerline is offset 0.61 mm outboard of the traditional centerline (positive canting).

FRONT END

For cost reasons, the existing front end (FE), designed for inline operation, is kept in place, with a new exit mask and collimator. This constraint required that the canting angle be smaller than the typical APS canting angle of 1 mrad. The optimal angle for 2-ID was determined to be 400 µrad. In order for the FE masks and beam stops to remain within the design limits, the undulators cannot be set to their minimum gaps simultaneously. The output power of the undulators is limited to 6553 W. However, in designing the exit mask and the beamline heat absorbers, credit was not taken for the FE power limitation.

DUAL CANTING MIRROR

In order to increase the beam separation as well as to provide power filtering and higher-harmonics rejection for the downstream optics, a dual mirror system with focusing capability is used as the first optic at approximately 28 m from the center of the straight section.

Design Concept

The mirrors are mounted in a vacuum chamber, facing each other, in a staggered configuration, see Fig. 2. The mirror motions are completely independent of each other.

Content from this work may be used under the terms of the CC BY 3.0 licence (© 2016). Any distribution of this work must maintain attribution to the author(s), title of the work, publisher, and DOI.

ISBN: 978-3-95450-188-5 doi:10.18429/JACoW-MEDSI2016-WEPE18

The inboard mirror (IM) with a nominal incident angle of 2.6 mrad reflects the inboard beam outboard while the outboard mirror (OM) with a nominal incident angle of 4.1 mrad reflects the outboard beam inboard. With the upgrade of the APS storage ring (APSU), all canting angles will be 1 mrad. To be able to continue using the Dual Canting Mirror, the system is provided with a one-time-change of the relative distance between the mirrors from 11.1 mm, for the current beamline configuration, to 28.0 mm after the APSU. This way the lateral translation is maintained to a small range of ± 6 mm for stability.

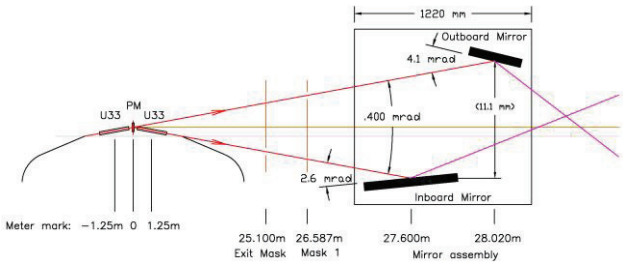


Figure 2: Schematic of the staggered mirror system.

The optical layout allows the beam separation to be between 38 mm and 56 mm at the monochromators.

To reduce the total power incident on the OM, the Exit Mask, located at 25.1 m, has a defining aperture of 1 mm x 1 mm, centered on the outboard white beam (WB). The inboard WB passes the Exit Mask through an aperture of 4 mm x 2 mm (HxV). Similarly, Mask 1 located at 26.5 m, has a defining aperture of 1 mm x 1 mm centered on the inboard WB, while the outboard WB passes through an aperture of 4 mm x 2 mm (HxV). Having the defining apertures in two separate masks assures the ease of manufacturing and alignment at installation.

Mirror Specifications

Each mirror has three reflecting surfaces: bare silicon substrate, rhodium, and platinum. Each mirror is provided with three motorized motions: X, Y, and pitch. The bending mechanism produces a surface figure that can be varied from flat to elliptical with minimal aberrations. The IM focuses horizontally onto a beam-defining aperture 6.25 m downstream, and the OM focuses horizontally onto a beam-defining aperture 6.43 m downstream. OM minimum bending radius is 2.6 km. IM minimum bending radius is 3.9 km. The white beam reaching each mirror is slightly over 1 mm^2 and the maximum power absorbed in each mirror is 208 W. The OM active length is 270 mm and the IM active length is 400 mm so that each mirror accepts the entire beam passing through the defining apertures.

Both mirrors are indirectly cooled to reduce vibrations via a typical "cooling slot and fin" design located at the top and bottom of the substrate. The Indium/Gallium eutectic is used as interface layer to enhance heat transfer. The meridional RMS slope error is expected to be ≤ 0.3 µrad and the RMS micro-roughness after coating ≤ 2.5 Å.

Compton scattering is a significant source of heat. When scattered radiation strikes a mirror support, the component could drift, resulting in a change of the mirror angle. The mirror supports therefore are designed to minimize exposure to scattered radiation, and are protected by shields. In addition, a shield is installed between the two mirrors to prevent Compton scattering produced by the IM from reaching the OM.

BEAMLINE SHIELDING COMPONENTS

The beamline shielding components consist of the masks, primary and secondary bremsstrahlung collimators located in the First Optics Enclosure (FOE), the photon shutters in the mini-hutch and the end station beam stops.

Collimators Specifications

Besides power filtering and suppression of high-order undulator harmonics, the dual canted mirror allows the separation of the bremsstrahlung radiation from the synchrotron radiation. The primary bremsstrahlung radiation is stopped at the end of the FOE by using the FE collimators and three beamline collimators, each one protected from the synchrotron beam by a mask. The task would have been achieved using two beamline collimators. By using an additional collimator, the minimum vertical offset of the monochromators located at the downstream end of the FOE has been reduced from 25 mm to 17 mm. In designing the secondary bremsstrahlung collimators (SBC), the OM was considered the worst scattering target in the FOE and the design follows the internal guidelines.

Masks Specifications

There are four masks in the beamline layout, all located in the FOE.

The **Exit Mask** intercepts the two canted WBs at full size in the horizontal (about 12 mm) and 7.2 mm in the vertical direction. In the worst case scenario, the canting angle is 350 µrad and the beams are overlapping at the Exit Mask by 3.2 mm and are 8.8 mm center to center. The beams cannot overlap at **Mask 1**, and the outboard beam passes through the outboard aperture in all mistering scenarios. Table 1 shows the total power and peak power density incident on each mask in the worst case scenario and the predicted maximum temperature (T_{max}) developed on the mask bodies. The Exit Mask is made of GlidCop, while Mask 1 is made of OFHC Copper. The power density distribution was calculated using SRUFF [1].

Table 1: WB Masks Key Parameters and T_{max}

Mask name	**Power** (W)	**Peak power density** (W/mm^2)	**Incident angle**	**T_{max}** (°C)
Exit M	9928	278	1.5°	259
Mask 1	977	248	2.0°	98

Mask 2, with an incident angle of 4°, is the first mask after the dual canting mirror. It intercepts the mistering cone of both focused pink beams (PBs), and stops the inboard WB and partially intercepts the outboard WB if either or both mirrors are retracted. Given the sources

Content from this work may be used under the terms of the CC BY 3.0 licence (© 2016). Any distribution of this work must maintain attribution to the author(s), title of the work, publisher, and DOI.

ISBN: 978-3-95450-188-5 doi:10.18429/JACoW-MEDSI2016-WEPE18

Content from this work may be used under the terms of the CC BY 3.0 licence (© 2016). Any distribution of this work must maintain attribution to the author(s), title of the work, publisher, and DOI.

listed above, the total PB power and size incident on the mask depends upon the mirror reflective stripe, incidence angle, total length and bend radius. Neither the limit switches, nor the possible hard stops of the mirrors' pitch are interlocked in the Personal Safety System and therefore Mask 2 was designed to handle the entire angular range [2]. For certain mirror angles the PB of one branch can overlap the WB of the other branch. Also, the PBs can overlap each other. The power calculation was conservative because it did not take into account the roughness of the mirrors, which could be below the specified value of 2.5 Å. The focused beam size was estimated as an ideal focal spot size with the Eq. (1):

$$F_{Ideal} = 2.35 \times \Sigma_{RMS} \times M \quad (1)$$

In Eq. (1) Σ_{RMS} is the RMS radiative source size and M is the demagnification. M = q/p, where q is the distance from mirror to image and p is the distance from source to mirror. Unlike Graber's calculations [3], the spherical aberration was neglected in this calculation because the mirror figure is expected to be very close to an elliptical shape. The fabrication slope error was neglected as well because the slope error of the actual mirrors might be smaller than the specified value of 0.3 µrad and the contribution of this error is very small. The OM and IM can focus onto Mask 2 for angles smaller than 1.8 mrad and 1.4 mrad, respectively. For larger incident angles and minimum bend radius, the mirrors will focus the beam downstream of Mask 2. In this case the beam size at Mask 2 was calculated using simple geometry. The relationship between the mirror bend radius (r), incidence angle (θ), p and q is defined by Eq. (2):

$$r = \frac{2}{(\frac{1}{p}+\frac{1}{q})\times\theta} \quad (2)$$

Several scenarios have been analysed and the maximum temperature (T_{max}) and von Mises stress (σ_{max}) were obtained when the smallest outboard PB was overlapping the outboard WB center. The IM incident angle was 1.9 mrad in this case. Table 2 shows beam size, power and peak power density of each beam for the worst loading case scenario.

Table 2: Mask 2 Worst Loading Case Scenario

Beam	Beam size		Power (W)	Peak power density (W/mm^2)
	H (mm)	V (mm)		
Outb WB	1.21	1.21	215.6	156.2
Outb PB	.399	1.16	109.7	237.0
Total			325.3	393.2

For OFHC Copper and a minimum water flow rate of 0.5 GPM, T_{max} was 126.9°C and σ_{max} was 111.1 MPa. The mask design is very simple and suitable for CuCrZr single-piece construction as described by Sharma [4]. For CuCrZr and the same flow rate, T_{max} was 146.3°C and σ_{max} was 142.8 MPa, which are well under the typical maximum values. The power of the PB striking outside of the mask body is very low (under 12.5 W) and doesn't present a safety issue.

Mask 3, with an incident angle of 7°, is the second mask after the dual mirror system and the first mask after the monochromators. It intercepts the mistering cone of the inboard PB, and stops the outboard WB and the outboard PB. Unlike Mask 2, the beams cannot overlap on Mask 3. The OM and IM incident angles of 3.6 mrad and 2.1 mrad, respectively, are the minimum angles for which the PBs pass downstream through the Mask 2 apertures. The mirrors can focus onto Mask 3 at these angles. The worst loading case is when Mask 3 intercepts the outboard WB and outboard PB. The beam parameters are in the same range as those in Table 2 with the main difference being the horizontal PB size of 0.166 mm. The T_{max} and σ_{max} are also well below the typical values and the mask is suitable for CuCrZr single-piece construction.

Photon Shutters and Beam Stops Specifications

The PB Photon Shutter absorber as well as the PB End Station Beam Stop have normal incidence to the beam. There is no significant demagnification of the beam in the horizontal direction at these devices and therefore the peak power density is relatively low (49 W/mm^2 at the Photon Shutter). The T_{max} and σ_{max} are well below the typical values. The Monochromatic Beam Photon Shutter and the End Station Beam Stop consist of Tungsten and Lead, respectively. The heat load output of the DMM is under 1 W.

CONCLUSION

The productivity of the 2-ID beamline will increase significantly with the canted configuration. The final design is ongoing. The installation of the 2-ID canted beamline will take place during the January 2018 shutdown followed by commissioning in March 2018.

REFERENCES

[1] Mati Meron, CARS_CAT, "SRUFF: A Comprehensive Package for Synchrotron Radiation Spectral and Optics Calculations", unpublished, 2001.

[2] D. Capatina *et al.*, "DCS - A High Flux Beamline for Time Resolved Dynamic Compression Science – Design Highlights", Proceedings SRI Conf. (SRI2015), New York, USA, July 2015.

[3] T. Graber *et al.*, "BioCARS: a synchrotron resource for time-resolved X-ray science", *Journal of Synchrotron Radiation,* 18, 658-670, 2011.

[4] S. Sharma *et al.*, "A Novel Design of High Power Masks and Slits", Proceedings MEDSI Conf. (MEDSI2014), Melbourne, Australia, October 2014.

* Work at the Advanced Photon Source is supported by the U. S. Department of Energy, Office of Science, Office of Basic Energy Sciences, under Contract No. DE-AC02-06CH11357.
† capatina@aps.anl.gov

ISBN: 978-3-95450-188-5 doi:10.18429/JACoW-MEDSI2016-WEPE22

F-SWITCH: NOVEL 'RANDOM ACCESS' MANIPULATOR FOR LARGE NUMBERS OF COMPOUND REFRACTIVE LENSES

G.M.A.Duller†, A.Stallwood, D. R. Hall, Diamond Light Source, Didcot, UK

Abstract

The F-Switch is a new concept of device for the manipulation of large arrays of 2D CRLs or similar disc-shaped optical elements (12mm dia, 2mm thick) under high vacuum. Unlike the well-known transfocator devices the optical elements are randomly selectable. This enables a number of potential modes of operation, including the fine adjustment of focal length by adjusting the effective lens centre position when using CRLs or the use of some positions within the array to implement filters or reference foils. Actuation and guidance is achieved within the thickness of the element, so that the overall length of the device is minimised.

The device has been in user operation on the I04 MX beamline at Diamond Light Source (DLS) since 2015. Another device is being assembled for use on the I11 beamline at DLS. It is also hoped to install another device on the I03 beamline.

We present details of the mechanical design of the F-Switch and some examples of its operation.

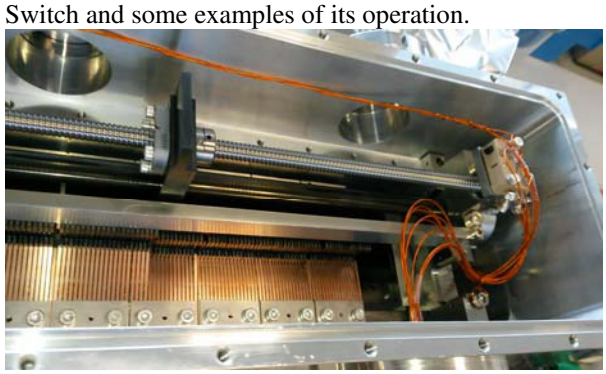


Figure 1: A general view of the F-Switch from above. The leadscrew and claw actuator shaft are visible along with a number of the bistable springs. The lenses are all hidden below this view.

THE RATIONALE

The I04 end-station upgrade [1] created an adaptable and stable platform for the final beam-conditioning elements of the beamline. In order to further enhance its capabilities a specification was developed to add to this platform a transfocator [2, 3] style device. However, it was quickly appreciated that with the short focal length required the limitations of the binary basis of the transfocator would limit the system performance. To illustrate this problem consider a transfocator with a total of 63 lenses. This would consist of six individual moving parts holding 1, 2, 4, 8, 16 and 32 lenses each. To insert 31 lenses the first five holders have to be inserted into the beam. To change to 32 lenses all five of these parts have to be withdrawn and the sixth lens holder has to be inserted. However, the effective centre of the lens has now been translated along the beam direction and so the resulting spot size at a fixed distance from the assembly may be very different from what is predicted if this effect is ignored.

The concept of the f-switch is that each of 120 lenses can be uniquely manipulated in and out of the beam. The benefit of this is obvious when the example above is considered, but it also allows for the number of lenses to be kept constant whilst the effective lens centre may be translated, thus allowing very fine control of the focal spot.

THE BISTABLE SPRING AND ACTUATION BLADE

The lenses used in the F-Switch are now a well-proven technology [4, 5] and are 2-D devices (rotational symmetry) mounted in a disk 2mm thick with a diameter of 12mm. The challenge was to design an actuation system within 2mm measured along the beam direction. The final design implemented a travelling actuator capable of operating on any one of the lenses, which implied that each lens then had to be securely retained in either of two states (in or out of beam) in the absence of an individual actuator. To allow beam to pass a lens which is nominally 'out of beam' the lens holder must be translated by a minimum of 6mm plus half the beam size. The acceptance of the lenses is 900µm, so the total motion required is a minimum of approximately 6.5mm.

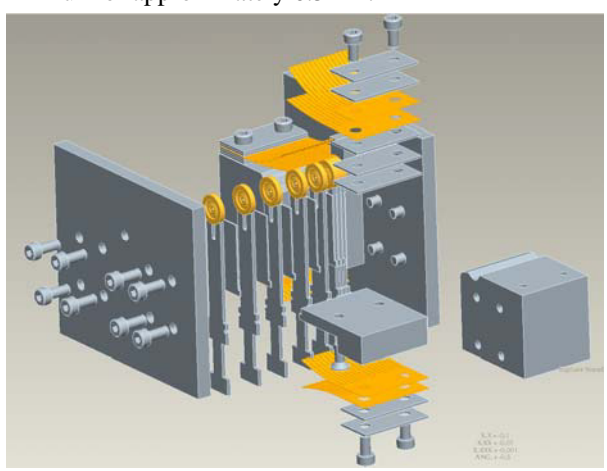


Figure 2: An exploded view of a prototype assembly. In this view the system is inverted wrt the final implementation, with the lenses shown at the top, acted on by a pair of leaf springs. Below this are the fixed spacers and the actuator blades with their bistable springs. The view of each spring is duplicated showing both the in-beam and out-of-beam condition.

†graham.duller@diamond.ac.uk

Content from this work may be used under the terms of the CC BY 3.0 licence (© 2016). Any distribution of this work must maintain attribution to the author(s), title of the work, publisher, and DOI.

ISBN: 978-3-95450-188-5 doi:10.18429/JACoW-MEDSI2016-WEPE22

Content from this work may be used under the terms of the CC BY 3.0 licence (© 2016). Any distribution of this work must maintain attribution to the author(s), title of the work, publisher, and DOI.

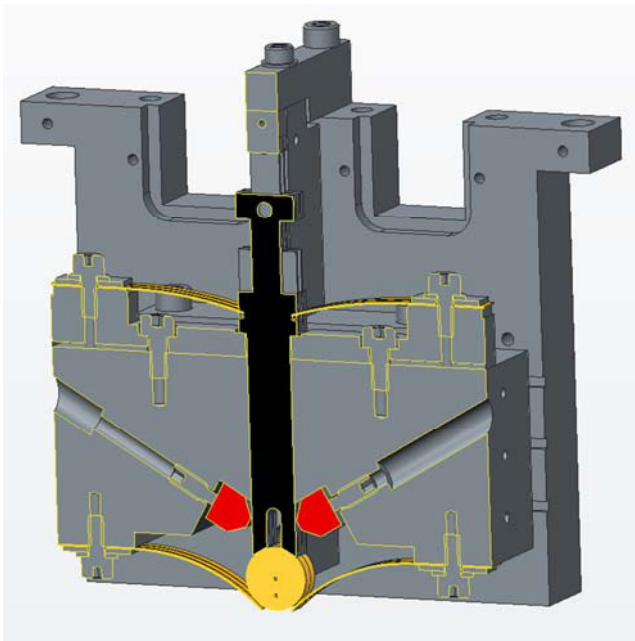


Figure 3: A section through the device showing the lenses (orange disks at the bottom of the view) held off the alignment vee (red) by the actuator blades (black). The beam passes through the slot in the actuator blade. The pair of bistable springs is seen at the centre of the image acting on the actuator blade.

When in beam the lens is held against a vee by a pair of CuBe leaf springs (Fig. 2, 3, 4). This ensures that the alignment of the lenses is repeatable.

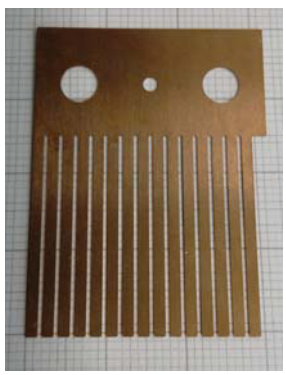


Figure 4: Atypical CuBe leaf spring. These are fabricated by chemical etching and each serves a bank of 15 lenses.

To remove the lens from the beam a narrow blade 1.2mm thick (Fig. 3, 5) is used to push the lens away from the vee and allow the beam to pass. This actuation blade is the key item allowing the operation in such a short space. The blade is supported from the sides by another pair of CuBe leaf springs, but in this case they are configured to give a bistable operation. When the blade is actuated (in either direction) the leaf springs are buckled. This is an intrinsically unstable condition so that in the event of incomplete operation the springs will always tend to return the lens to either the in or out positions. In the in and out positions the blade leaf springs return to a simplex curved shape which ensures that they are stiff (and, therefore, stable).

For both types of spring it is important to apply the correct heat treatment. Half-hard was used for both sets of parts. Initial tests showed that the bistable springs would crack due to fatigue after about 5000 operations. This was solved by slightly lengthening the springs for the final design.



Figure 5: An actuator blade alongside a fixed spacer. Wire EDM was found to be the most cost-effective method of production for these parts. These examples are not yet DLC coated.

Finally, a 0.5mm fixed spacer blade separates each of the actuation blades to ensure no crosstalk between adjacent lenses (Fig. 2, 5).

ACTUATION

Actuation requires just two stepper motors, working in air. These drive a translation mechanism and a switching claw (Fig. 1, 6). The switching claw engages with tabs at the sides of the actuation blades to either pull them up to allow the lens to return to the in-beam position or to push them down, in which case the lens is then supported by the end of the actuation blade approximately 7.5mm away from the vee.



Figure 6: The actuation claw. The single blade actuation claw is to bottom left, while the three blade option is to top right. This item is DLC coated.

Full actuation requires less than 90° of rotation, so the claw has been manufactured with single-blade and triple-

ISBN: 978-3-95450-188-5 doi:10.18429/JACoW-MEDSI2016-WEPE22

blade options on opposite sides of its disk. To switch between single and triple blade actuation requires that the claw is translated to the end of travel, where it can be safely rotated through 180°.

The vacuum vessel and internals have all been designed to allow the implementation of a second actuation system (motors, feedthroughs, translation leadscrew and claw operating shaft) if required. This has not yet been implemented, but it is intended to install this soon during the next upgrade to the system.

DRIVETRAIN

The drivetrain has been designed to allow continuous operation by removing the stepper motors from the vacuum space. Currently, the motors drive toothed belts through a torque-limiting device. The torque-limit ensures that if a hard limit is struck (which is quite likely in the operation of the claw) then no damage is caused to the in-vac parts or to the drivetrain. At the driven end of the belt drive a ferrofluidic seal takes the rotary motions through the upstream vessel wall. The outer end of each of the ferrofluidic seal shafts is fitted with a compact magnetic rotary encoder. In order to make the unit even more compact the next upgrade will delete the belt drives and replace them with bevel gear drives.

The in-vacuum end of the ferrofluidic seal shaft is fitted with an Oldham coupling to allow easy assembly and setup. The leadscrew and claw-operating shafts are suspended between ball bearings, with one of the bearings being spring-energised to compensate for any expansion in the shafts due to operation.

THE PROBLEM OF SLIDING COMPONENTS

With such a compact space in which to implement the manipulation of each lens there are a great number of sliding surfaces in vacuum. The majority of the parts sliding against one another are stainless steel for vacuum compatibility and ease of manufacture. Because of concern that this could cause variable friction coefficients and/or the generation of particulate debris all sliding parts were initially Dicronite coated. Unfortunately, this was not found to be a good solution in this environment as a lot of particulate debris was formed. Following this, the Dicronite was stripped and all parts were Diamond-like-carbon (DLC) coated. This has provided a very hard, low friction coating which has not generated any noticeable debris to date.

TOLERANCES

The unit was designed to accept 128 lens elements initially. Early testing identified that tolerance build-up through such a long stack of components was excessive and could allow the actuation blades to develop excessive motion or to stick. A fixed divider was then introduced in seven positions to divide the lenses into eight blocks of fifteen lenses each, thus reducing the total number of lenses available to 120. The length of a block of fifteen lenses is, essentially, defined by the thickness of the lenses themselves. Actuation blades were made in three different thicknesses to allow their selection during assembly to ensure that the stack of actuating blades matched the stack of lenses.

FEEDBACK

The unit is fitted with encoders on each of the two rotating shafts and microswitches to identify ends-of-travel. A pair of microswitches is also included which identify that the claw is in a safe position to translate along the unit. This was felt essential to ensure that a simple error of positioning could not cause significant damage to the rather delicate moving parts of the assembly. The encoders allow the speed of operation to be optimised, although the speed is still an aspect we would like to improve. Currently, a typical user-requested lens re-configuration takes about 30s (a single lens change is 1-2s), which should be halved when we install the second actuator drive. This, however, is still outside our original specification of 10s for a typical change. Further enhancement of the controls algorithms may allow us to increase performance to our desired level.

PERFORMANCE

The F-Switch has been operational for more than a year at the time of writing. Counters record the number of times lenses are operated, and in this time many of the lenses have been operated between 2000 and 2500 times with no issues.

The user is able to select beam sizes to match the size of crystal to be analysed over a wide range of sizes (5-100µm) and to work with focussed beam over a wide range of energies (6-18keV).

Speed of operation remains an issue, but the device can already make typical lens changes within ~30s. The addition of a second actuation system shortly should halve (or better) this figure.

REFERENCES

[1] Hall, D. R. et al "Bringing microfocus beam and improved sample environment to MX users at Diamond" *Acta Cryst.* (2011). A67, C483-C484

[2] Snigirev, A. *et al* (2009). "High energy X-ray transfocator based on Al parabolic refractive lenses for focusing and collimation" *J. Phys. Conf. Ser.* 186, 012073.

[3] Vaughan, G. B. M. *et al* (2011). "X-ray transfocators: focusing devices based on compound refractive lenses" *J. Synchrotron Rad.* 18, 125-133

[4] Lengeler, B *et al* "Imaging by parabolic refractive lenses in the hard x-ray range," *J. Synchrotron Rad.* 6(6), 1153–1167 (1999).

[5] Lengeler, B. *et al* "Refractive x-ray lenses," *J. Phys. D Appl. Phys.* 38(10A), A218–A222 (2005).

Content from this work may be used under the terms of the CC BY 3.0 licence (© 2016). Any distribution of this work must maintain attribution to the author(s), title of the work, publisher, and DOI.

ISBN: 978-3-95450-188-5 doi:10.18429/JACoW-MEDSI2016-WEPE24

LIVE ANIMAL IMAGING PROGRAM AT BIO-MEDICAL IMAGING AND THERAPY FACILITY AT THE CANADIAN LIGHT SOURCE

M. A. Webb, G. Belev, D. Miller, T. W. Wysokinski, Z. Zhu, Canadian Light Source, Saskatoon, Canada
M. Gibbons, University of Saskatchewan, Saskatoon, Canada

Abstract

The live animal imaging program at the Bio-Medical Imaging and Therapy (BMIT) facility at the Canadian Light Source has been developing for the last 5 years and continues to grow. It is expected to become a large portion of the user activity as numerous groups work towards the goal of live animal studies. Synchrotron-based imaging of live animals is an opportunity for great science that also brings challenges and specific requirements for the experimental end-station. The beamline currently provides basic support and has been improving the facilities available. For example, there have been changes to the lab to allow for longer rodent housing and improved housing during measurements. Remote control of heat lamps and of flow rate for gas anaesthesia allow a veterinarian or animal care worker to make adjustments without interrupting the imaging. Integration of user equipment such as heart/breathing monitoring and ultrasound equipment with the beamline systems can be used for gating control of imaging. Future improvements will be done with consultation with university veterinarians and the user groups.

INTRODUCTION

The Bio-Medical Imaging and Therapy (BMIT) facility at the Canadian Light Source (CLS) provides a world class facility with unique synchrotron specific imaging and therapy capabilities [1 – 3]. BMIT is used to study diverse problems in human medicine, veterinary medicine, micro-beam radiation therapy, dosimetry, agriculture, and other biomedical areas. The facility is comprised of 05ID-2 and 05B1-1 beamlines and supporting laboratories. This paper will first look at the background and requirements involved with working with live animals and then describe some of the engineering solutions which were developed in a collaboration of all those involved.

LIVE ANIMAL PROGRAM AT THE CLS

The live animal imaging program at the BMIT facility at the Canadian Light Source has been developing for several years and continues to grow. It is expected to become a large portion of the user activity as numerous groups work towards the goal of live animal studies. Key goals of the beamline include assuring best practices in animal anaesthesia monitoring and producing the best images and scientific results possible with minimal dose delivered. Figure 1 shows statistics for live animals brought to BMIT. Usage varies considerably depending on the research groups. Note that recent groups have begun to image larger animals such as rabbits and dogs.

There are a number of considerations for the design of the end-station for the imaging of live animals and university veterinarians are consulted closely. The key requirement centres on animal care. In brief, animals arrive at the facility and are under the care of a veterinarian or other animal care personnel. When ready, an animal is placed under anaesthesia and taken into the hutch to be imaged and/or treated. Treatments may include radiation or medical procedures. Imaging may be used to evaluate results. The animal is monitored throughout the process. Once the measurements are finished the animal is removed from the hutch for recovery in the lab. Other requirements are from external bodies. The CLS is regulated by the Public Health Agency and follows the Canadian Biosafety Standards and Guidelines[4, 5]. The CLS is also a member of the Canadian Council on Animal Care (CCAC) [6, 7] and a participant of the University Animal Care Committee [8].

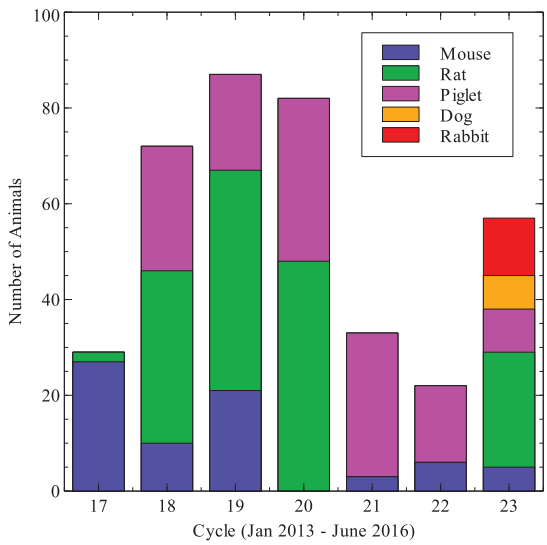


Figure 1: Animal usage statistics. Cycles correspond to 6 month periods.

LABORATORY FACILITIES

The CLS provides basic laboratory facilities and a change-room. There are two labs adjacent to the end-stations, as well as a life science lab nearby. These labs provide equipment for the users and areas for sample preparation. The labs include biosafety level 2 areas.

The BMIT labs also provide a place for the temporary housing of animals, medical procedures and for recovery after experiments. For example rodents may be kept in micro-environment cages up to 72 hours. The lab has red film on the windows and red lights to simulate a day/night

Content from this work may be used under the terms of the CC BY 3.0 licence (© 2016). Any distribution of this work must maintain attribution to the author(s), title of the work, publisher, and DOI.

ISBN: 978-3-95450-188-5 doi:10.18429/JACoW-MEDSI2016-WEPE24

cycle for rodents. Other animals may be kept, if properly housed, for up to 24 hours. The hutches have a separate air intake from the rest of the experimental hall and can have up to 10 air exchanges per hour. There is a controllable air pressure differential with the hall and limited temperature control. Records of hutch conditions including temperature, humidity, and air flow data are available for audit purpose when requested.

END-STATION EQUIPMENT

The end-station is where the measurements are made and so is the nexus of all experiments. All the equipment is arranged around the holder where the animal will be placed for imaging or therapy. The goal is to be able to do as much as possible from outside the hutch as during the measurement no one can be inside. It is important to have coordination between the safe operation of the equipment which may not always be able to stop quickly and the animal care worker who may need rapid access to the animal to administer care. To facilitate this quick access and fast exit, a Zone Bypass Button (ZBB) feature has been implemented as an extension to the Access Security and Interlock System (ACIS)[9] used at the CLS.

Figure 2 and Figure 3 show experimental set-up at BMIT on the two currently used end-stations. These are meant as illustrative examples as there are many possibilities. Cameras are (security, web-cam) are arranged such that various aspects of the experiment can be monitored from outside (Figure 4). The breathing of the animal can be closely monitored as well as vital signs and temperature. The heat lamp is controlled from outside. A prototype has been made to control the anaesthesia gas levels. In Figure 2, the equipment is placed around the table. The animal (not shown) is on a motorized stage which is controlled remotely.

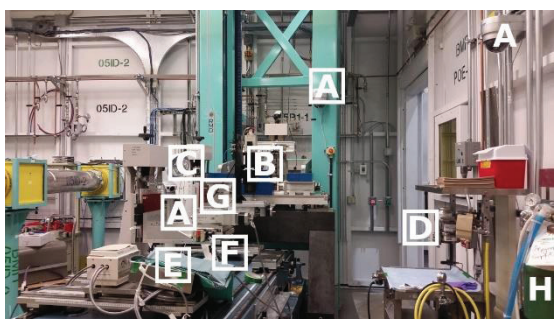


Figure 2: Experimental setup on 05B1-1 showing some of the equipment needed for an imaging session. A. cameras, B. detector, C. heat lamp, D. anaesthesia machine, E. heating pad, F. vital signs monitor, G. Sample location on stage, H. Oxygen tank.

Figure 3 shows a somewhat different configuration using a micro-beam therapy (MRT) lift. In this case, the animal (not shown) is on a medium size positioning device. Some of the equipment is arranged on the stage with the animal. This means that during a CT scan all of the equipment will rotate in addition to the animal. Consequently, all tubes, cables, wires, etc. need to be able to rotate without becoming entangled or pulled off. Wireless communication is necessary in order to record vital signs or to control equipment such as a ventilator, remotely.

The synchrotron beam is a stationary beam unlike in conventional imaging equipment. This means that it is the sample that must rotate and move in order to image which introduces a dimension of difficulty in the design. The sample must be held in place while preventing any motions that would distort the images. Naturally this includes the animal and the support apparatus. Samples may also have to be held vertically rather than in the more natural horizontal position used in clinical devices. The users and the facility have designed and built a plethora of mounting plates, adaptors, simple and complex animal holders, a universal sample holder and more in order to address this deceptively simple issue.

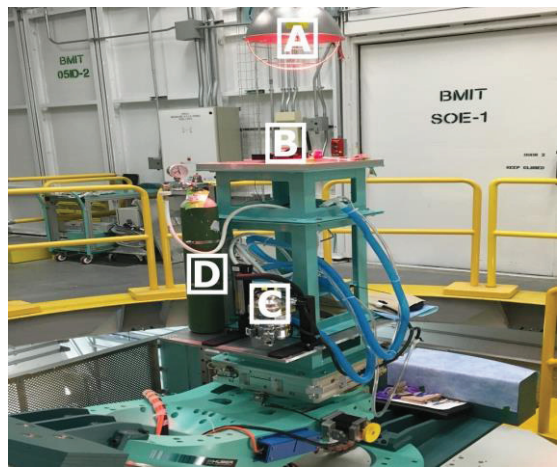


Figure 3: Experiment set-up for micro-beam therapy on 05ID-2 on MRT lift. A. heat lamp, B stage for sample, C. anaesthesia machine, D. oxygen tank.

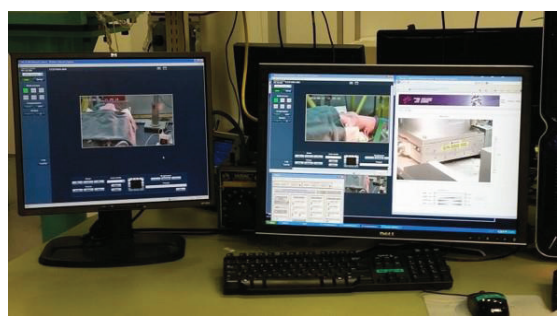


Figure 4: Conditions in the hutch are monitored from the control room. Multiple cameras, vital signs monitors and user equipment can be watched and controlled remotely.

A helpful tool for creating sample is the 3D printer. It can be time consuming and expensive to design, draw and machine a new sample holder or a part. The rapid drop in prices and ever expanding capabilities of 3D printers has meant that rapid prototyping and testing is quite affordable. One project went through multiple versions (~8) of a holder for a mouse for doing a CT of the lungs [10].

Content from this work may be used under the terms of the CC BY 3.0 licence (© 2016). Any distribution of this work must maintain attribution to the author(s), title of the work, publisher, and DOI.

ISBN: 978-3-95450-188-5 doi:10.18429/JACoW-MEDSI2016-WEPE24

Content from this work may be used under the terms of the CC BY 3.0 licence (© 2016). Any distribution of this work must maintain attribution to the author(s), title of the work, publisher, and DOI.

Through the use of 3D printing they were able to design, test and determine problems quickly. 3D printing was used to create a plastic holder for cartilage samples that could be used for both phase-contrast computed tomography and magnetic resonance imaging [11]. Figure 5 shows a drawing for a cell irradiation holder that was 3D printed. This holder is intended for cells but relates to dosimetry and cell work which is needed for micro-beam radiation therapy, an area of interest at various synchrotron facilities. The simplicity of using 3D printing means that student projects can go from concept to design to a final project in a matter of days to weeks and if successful can then immediately be used in a research setting.

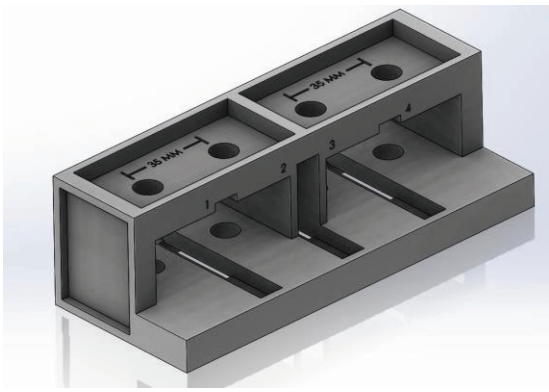


Figure 5: Drawing of cell irradiation holder. This holder has four holes for sample tubes and slots for tungsten plates for shielding between samples.

Software is an important component of beamline operation and it is important to be flexible as user needs can change rapidly. User groups are unlikely to have dedicated computer staff so it often falls to the beamline to provide technical assistance. A number of programs have been written using LabVIEW [12]. LabVIEW is an easy language for creating graphical interfaces. It is important to have fairly easy to use interfaces for users as they may little to no experience with the system. The main benefit for the staff is that rapid prototyping and custom programs are relatively easy to produce. This improves the ability of the beamline to alter measurements, match experimental requirements and to solve issues as they arise.

CONCLUSION

Live animal experiments are challenging but also present great opportunities for high-impact science. The engineering challenges include holding and remotely manipulating the animals in order to do the imaging. Each experiment can create specific engineering challenges. Multiple modalities must be supported and simultaneously it is necessary to ensure the health and safety of a living animal to the satisfaction of the attending veterinarian. It is the collaborative efforts of the users, animal care, and the beamline and engineering staff that allow for such rewarding work to progress and to advance the important science of a live animal imaging program.

ACKNOWLEDGMENT

The authors would like to also acknowledge the work of the CLS engineering staff and summer students that worked at BMIT such as Karandeep Kalsy and Graham Kerr.

Work described in this paper was performed at the BMIT facility at the Canadian Light Source, which is supported by the Canada Foundation for Innovation, Natural Sciences and Engineering Research Council of Canada, the University of Saskatchewan, the Government of Saskatchewan, Western Economic Diversification Canada, the National Research Council Canada, and the Canadian Institutes of Health Research.

REFERENCES

[1] T. W. Wysokinski, D. Chapman, G. Adams, M. Renier, P. Suortti, and W. Thomlinson, "Beamlines of the biomedical imaging and therapy facility at the Canadian light source—Part 1," *Nucl. Instrum. Methods Phys. Res. Sect. Accel. Spectrometers Detect. Assoc. Equip.*, vol. 582, no. 1, pp. 73–76, 2007.

[2] T. W. Wysokinski, D. Chapman, G. Adams, M. Renier, P. Suortti, and W. Thomlinson, "Beamlines of the Biomedical Imaging and Therapy Facility at the Canadian Light Source - Part 2," *J. Phys. Conf. Ser.*, vol. 425, no. 7, p. 72013, 2013.

[3] T. W. Wysokinski, D. Chapman, G. Adams, M. Renier, P. Suortti, and W. Thomlinson, "Beamlines of the biomedical imaging and therapy facility at the Canadian light source – part 3," *Nucl. Instrum. Methods Phys. Res. Sect. Accel. Spectrometers Detect. Assoc. Equip.*, vol. 775, no. 0, pp. 1–4, 2015.

[4] HSE - Biosafety. ,http://hse.clsi.ca/hse-groups/biosafety/.

[5] P. H. A. of C. Government of Canada, "Canadian Biosafety Standard (CBS), Second Edition - Canadian Biosafety Standards and Guidelines," 11-Mar-2015, http://canadianbiosafetystandards.collaboration.gc.ca/cbs-ncb/index-eng.php.

[6] CCAC - Canadian Council on Animal Care: Standards and Policies, http://www.ccac.ca/en_/standards.

[7] CCAC - Canadian Council on Animal Care: CCAC Certification., http://www.ccac.ca/en_/assessment/certification.

[8] Ethics - University of Saskatchewan., http://research.usask.ca/for-researchers/ethics/index.php.

[9] C. D. Miller, T. W. Wysokinski, G. Belev, and L. D. Chapman, "Human factors design for the BMIT biomedical beamlines," *J. Phys. Conf. Ser.*, vol. 425, no. 2, p. 22005, 2013.

[10] K. B. Gagnon, S. Caine, N. Samadi, M. Martinson, M. van der Loop, J. Alcorn, L. D. Chapman, G. Belev, and H. Nichol, "Design of a mouse restraint for synchrotron-based computed tomography imaging," *J. Synchrotron Radiat.*, vol. 22, no. 5, pp. 1297–1300, Sep. 2015.

[11] S. Bairagi, G. Belev, D. Chapman, D. Cooper, W. Dust, A. Webb, N. Zhu, and B. F. Eames, "Is phase-contrast computed tomography more sensitive than magnetic resonance imaging in quantifying cartilage damage in osteoarthritis?," *Abstr. 2015 World Congr. 2015 World Congr.*, vol. 23, Supplement 2, p. A258, Apr. 2015.

[12] M. Dierick, D. Van Loo, B. Masschaele, M. Boone, and L. Van Hoorebeke, "A LabVIEW® based generic CT scanner control software platform," *J. X-Ray Sci. Technol.*, vol. 18, no. 4, pp. 451–461, 2010.

ISBN: 978-3-95450-188-5 doi:10.18429/JACoW-MEDSI2016-WEPE26

UPGRADE THE BEAMLINE PF-AR NW14A FOR THE HIGH-REPETITION-RATE X-RAY PUMP-PROBE EXPERIMENTS

S. Nozawa† , High Energy Accelerator Research Organization, Tsukuba, Japan

Abstract

The time-resolved X-ray measurements at storage ring has achieved successfully in investigating the structural dynamics of excited states, however the most of its experimental repetition rate has been limited to about ~1 kHz . The low repetition rate decided by the frequency of the pump laser system leads to a lack of photon in the time-resolved experiments. In this study, the high-repetition-rate time-resolved X-ray experimental system is reconstructed at PF-AR, NW14A. To use full of the x-ray flux without the x-ray isolation, the precise transient structure could be visualized. This study demonstrated the high-repetition-rate time-resolved X-ray measurements offer an opportunity to understand of the detailed photoreaction process and can be available as a fundamental observation technology for the development of new photo-functional materials.

INTRODUCTION

Time-resolved X-ray measurement is a powerful tool for the investigation of ultrafast science in various research fields ranging from local photochemical or photobiological processes, such as photocatalyzed reaction and photodissociation to photo-induced phase transitions in crystals[1]. Time-resolved X-ray experiments that have been developed with the rapid progress of synchrotron sources have made it possible to study photo-induced ultrafast transformations by synchronizing X-ray pulses with ultrashort laser pulses. This pump–probe synchronization can be combined with established X-ray techniques, such as absorption, diffraction, and scattering experiments [2]. Especially, time-resolved X-ray absorption fine structure (XAFS) is important for studying the molecular dynamics.

The Photon Factory Advanced Ring (PF-AR) is a full-time single-bunch synchrotron radiation source operated for time-resolved X-ray studies with pulsed X-rays. Electrons with a ring current of 60 mA (75.5 nC per bunch) are stored in a single bucket with a lifetime of about 20 h. The radio frequency (RF) for cavities and harmonic number of the PF-AR are 508.58 MHz and 640, respectively. Therefore, the X-ray pulses are delivered at a frequency of ~800 kHz with a pulse duration of about 100 ps.

Previously, the typical laser system, installed in the beam line for time-resolved experiments is a fs Ti:sapphire regenerative amplifier laser system. The Ti:sapphire laser system, which is operated at 800 nm fundamental wavelength, is capable of reaching up to 1 mJ pulse with a repetition rate of ~1 kHz. At that time, the experimental frequency of the laser pump and x-ray probe experiment was limited to ~ 1 kHz to excite samples with an ideal pulse energy. The low-flux condition, attributed to the about one thousandth isolated x-ray, sometimes prevents advanced researches for the dynamic structural analysis [3].

In recent years, the developments of high-repetition laser systems and x-ray focusing technologies has provided the pump-prove experiments without the x-ray isolation. Also at PF-AR, NW14A, the high-repetition-rate time-resolved X-ray experimental system was reconstructed. The improvement of measurement efficiency is described in this paper with an example from time-resolved XAFS.

X-RAY FOCUSIG OPTICS

The X-ray focusing optics are a bent cylindrical focusing mirror and a poly-capillary focusing optics (XOS, USA). In regard to the bent cylindrical mirror, the mirror is coated with rhodium (100 nm thick). The mirror can be bent at a range of bending radii between -2000 m and +2000 m by a mechanical bender. The glancing angle is adjusted by tilting the mirror at the mirror's center. A bending mechanism directly applies the bending momentum to the mirror. By the bent cylindrical mirror, the beam is focused at the sample position with 464 μm (H) ×236 μm (V). In this focusing condition, to add the poly-capillary focusing optics with the 5mm working distance, the beam size at the sample position with 60 μm (H) × 60 μm (V) is achieved.

HIGH REPETITION LASER SYSTEM

For the pump laser with the high repetition rate, a 350 fs Yb fiber laser system (Tangerine, Amplitude Systèmes) was installed. The Yb fiber laser system is operated at 1030 nm fundamental wavelength. The fundamental wavelength can be converted to second (515 nm), third (343 nm), and forth (257 nm) harmonics by a higher harmonics generator for the Tangerine. The fiber laser is capable of reaching up to 30 μJ with a repetition rate of the 794 kHz. The fiber laser is installed at near the sample in the experimental hutch.

TIME RESOLVED XAFS WITH HIGH REPETITION RATE

The time-resolved Ru K-edge X-ray absorption fine structure (XAFS) were measured with the 400 kHz repetition rate by using a scintillation counter, a gated integrator and the fiber laser system. Through the metal filter and the solar slit, the fluorescence signal was detected by the fast scintillation counter, which has a 50 mm diameter of acceptance surface. The experimental condition, where the frequency of laser pulses is a half of the 800 kHz x-ray frequency, removes the low frequency noise components from the laser on/off difference of XAFS spectrum.

† noz@post.kek.jp

Content from this work may be used under the terms of the CC BY 3.0 licence (© 2016). Any distribution of this work must maintain attribution to the author(s), title of the work, publisher, and DOI.

ISBN: 978-3-95450-188-5 doi:10.18429/JACoW-MEDSI2016-WEPE26

Content from this work may be used under the terms of the CC BY 3.0 licence (© 2016). Any distribution of this work must maintain attribution to the author(s), title of the work, publisher, and DOI.

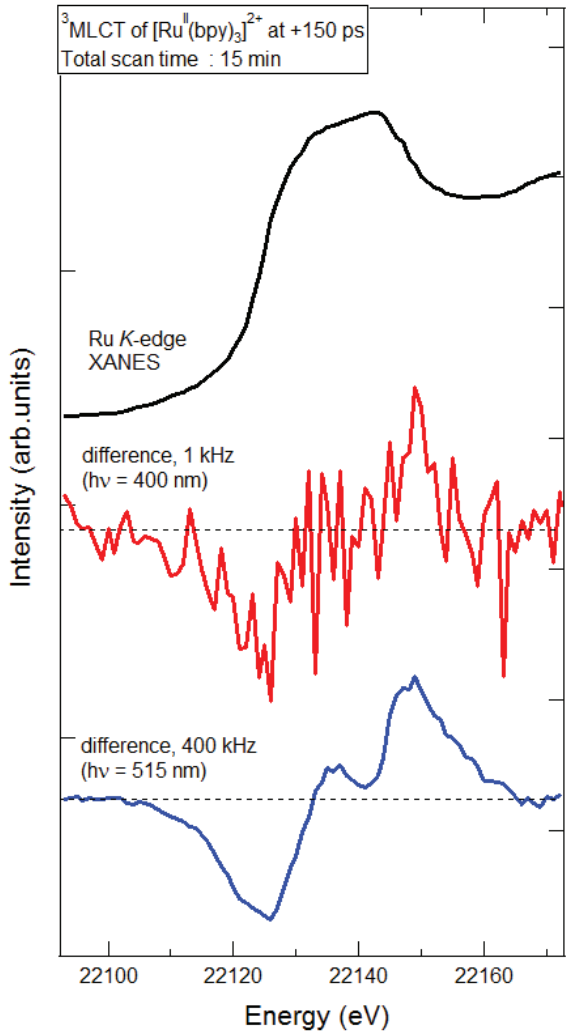


Figure 1: The Ru K-edge XANES spectrum of $[Ru^{II}(bpy)_3]^{2+}$ and its transient differences measured with 1 kHz and 400 kHz repetition rates.

The ground state of Ru K-edge XANES spectrum and its transient differences measured with 1 kHz and 400 kHz repetition rates are shown in Fig. 1. The metal to ligand charge transfer (LMCT) band of the 10 mM aqueous solution of Ruthenium(II)-tris-2,2'-bipyridine ($[Ru^{II}(bpy)_3]^{2+}$) was excited with the 100 mJ/cm^2 laser pulse density. By the LMCT excitation, the edge shifts were shown in both XANES transient differences due to the change of the Ru oxidation state from Ru(II) to Ru(III). The both transient differences were measured for 15 min, which is the typical measurement time for the conventional static XANES measurement. According to the increase of ~ 400 times in the repetition rate, the improvement of ~20 = √400 times in the S/N ratio was obtained in the transient difference.

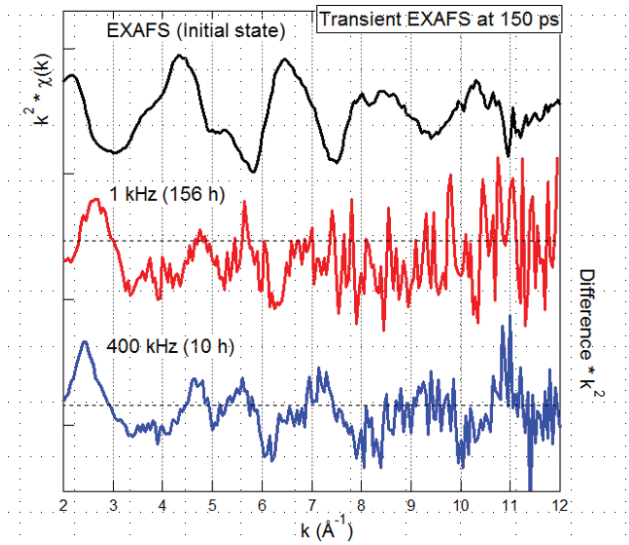


Figure 2: The Ru K-edge EXAFS oscillation of $[Ru^{II}(bpy)_3]^{2+}$ and its transient EXAFS differences measured with 1 kHz and 400 kHz repetition rates.

Also, to analyze the transient structure in detail, it is necessary to measure the wide range of EXAFS oscillation. The Ru K-edge EXAFS oscillation of $[Ru^{II}(bpy)_3]^{2+}$ and its transient EXAFS differences measured with 1 kHz and 400 kHz repetition rates are shown in Fig. 2. In the 1 kHz repetition rate, it is hard to measure transient EXAFS difference above k ~ 7 even the spectrum was accumulated in 156 hours. On the other hand, in the 400 kHz repetition rate, the transient EXAFS difference around k ~ 12 was observed by only the 10 hours scan. The improvement of the transient EXAFS detection capability makes it possible to visualize a precise transient structure.

CONCLUSION

In the x-ray pump-probe experiment, the great improvement of measurement efficiency was achieved by the installation of the high-repetition-rate experimental system. The improvement of experimental efficiency make it possible to visualize the detailed transient structures. In future dynamic studies, the ultra-low emittance ring allows us to obtain the inhomogeneous information in photochemical reactions.

REFERENCES

[1] S. Nozawa, T. Sato et al., *J. Am. Chem. Soc.*, 132, (2010) pp. 61-63.

[2] S. Nozawa, S. Adachi et al., *J. Synchrotron. Rad.*, 14, (2007) pp. 313-319.

[3] T. Sato, S. Nozawa et al., *J. Phys. Chem. C*, 116, (2012) pp. 14232–14236.

ISBN: 978-3-95450-188-5 doi:10.18429/JACoW-MEDSI2016-WEPE28

MINIMIZING EXPERIMENTAL SETUP TIME AND EFFORT AT APS BEAMLINE 1-ID THROUGH INSTRUMENTATION DESIGN

Erika Benda*, Jonathan D. Almer, Peter Kenesei, Ali Mashayekhi, John Okasinski, Jun-Sang Park, Rogelio Ranay, Sarvjit Shastri

Advanced Photon Source, Argonne National Laboratory,
9700 S. Cass Av, Argonne, IL, USA

Abstract

Sector 1-ID at the APS accommodates a number of different experimental techniques in the same spatial envelope of the E-hutch end station. These include high-energy small and wide angle X-ray scattering (SAXS and WAXS), high-energy diffraction microscopy (HEDM, both near and far field modes) and high-energy X-ray tomography. These techniques are frequently combined to allow the users to obtain multimodal data, often attaining 1 μm spatial resolution and <0.05° angular resolution. Furthermore, these techniques are utilized while the sample is thermo-mechanically loaded to mimic real operating conditions. The instrumentation required for each of these techniques and environments has been designed and configured in a modular way with a focus on stability and repeatability between changeovers. This approach allows the end station to be more versatile, capable of collecting multi-modal data in-situ while reducing time and effort typically required for set up and alignment, resulting in more efficient beam time use. Key instrumentation design features and layout of the end station are presented.

BEAMLINE 1-ID

Focus

The 1-ID beamline at the APS delivers high brilliance, monochromatic ($\Delta E/E \approx 10^{-3}$) high-energy X-rays (>40 keV) resulting in exceptional penetrating power and spatial-angular resolution. The Materials Physics and Engineering (MPE) group operates the beamline and takes advantage of this combination to investigate a wide variety of polycrystalline material systems *in situ* / *in operando*, such as structural alloys, chemical compounds used in batteries, and bones to name a few.

Techniques

User experiments are typically performed at the 1-ID-E end station. Three primary techniques are supported at the 1-ID-E end station:

Small and wide angle X-ray scattering (SAXS/WAXS) While these two techniques are typically supported individually, the unique WAXS detector array at the 1-ID-E end station allows the combination of the two techniques. WAXS provides information such as phase volume fraction, preferred crystallographic orientation, and aggregate-average strain. SAXS provides information such as precipitate or void size distribution. The combined technique is capable of interrogating a wide range of length scales and is particularly useful in investigating polycrystalline materials with small grains (1 μm or less) and/or large prior deformations.

High-energy diffraction microscopy (HEDM) This novel technique is capable of non-destructively characterizing an individual constituent grain in a polycrystalline aggregate. Several variants of this technique exist; depending on the location of the detector, the morphologies and intragranular crystallographic orientation information of the grains (near-field) or the average crystallographic orientations, positions, and stress tensors associated with the individual grains (far-field) can be obtained.

Tomography While tomography is a widely available technique, the ability to combine SAXS/WAXS or HEDM with high resolution (1 μm) phase or absorption contrast tomography is quite unique and allows the users to gain a more complete picture of material behavior at these length scales.

Users

The user groups supported by the 1-ID beamline are diverse, ranging from university research groups investigating the micromechanics of materials at a more fundamental level to large corporate users interested in process optimization. Large polycrystalline aggregates with a variety of applications are investigated.

Examples of research performed at beamline 1-ID:

- Understanding the micromechanics associated with microcrack nucleation in nickel based superalloys used for turbine blades. [1]
- Strain development in bovine bone under uniaxial compression. [2]
- Investigating the effects of irradiation on materials used in nuclear engineering. [3]

* benda@aps.anl.gov

Content from this work may be used under the terms of the CC BY 3.0 licence (© 2016). Any distribution of this work must maintain attribution to the author(s), title of the work, publisher, and DOI.

ISBN: 978-3-95450-188-5 doi:10.18429/JACoW-MEDSI2016-WEPE28

Content from this work may be used under the terms of the CC BY 3.0 licence (© 2016). Any distribution of this work must maintain attribution to the author(s), title of the work, publisher, and DOI.

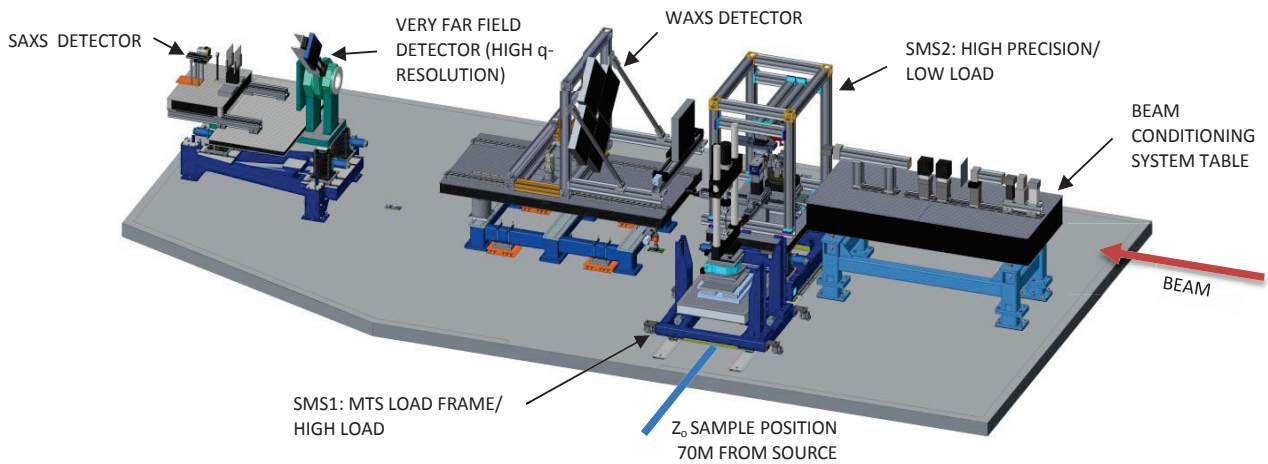


Figure 1: Standard configuration of instrumentation at beamline 1-ID E-hutch.

E-HUTCH INSTRUMENTATION

Layout

The configuration of the hutch has been largely driven by user requirements. In addition to utilizing the existing instrumentation, many users want to bring their own experimental components such as custom load frames, environmental chambers or heaters. The modular configuration and organization of the hutch are critical to accommodating these custom components and handling frequent setup changeovers with the least amount of time and effort (see Figure 1).

Beam Conditioning System (BCS) Table

The BCS table is located at the upstream end of the endstation. It is equipped with ion chambers capable of monitoring the flux and beam position, slits, horizontal and vertical focussing sawtooth refractive lenses and a fast shutter. The lenses are equipped with full degrees of motion necessary to provide 1 μm (vertically) and 15 μm focussed beam (horizontally) on demand. The table is also equipped such that new high energy optics can be deployed and tested without disturbing the existing optics. The individual optical elements can be utilized flexibly according to the actual experimental needs for the given technique.

Sample Location and Manipulation Systems

Immediately downstream from the BCS table is the sample support which is located at a fixed APS-Z position of approximately 70 m from the source. Samples are typically mounted in one of two independent sample manipulation systems (SMS) which can be brought into and out of the beam position. An SMS is essentially a predefined experimental setup for different demands which can be used as a baseline configuration for a sample environment combined with a combination of techniques.

The available SMS at Sector 1 are listed below:

1. **Large vertical translation and high load capacity table with an MTS load frame** (permanent) – An optical table capable of large Y motion range is equipped with an appropriate stage stack to rotate and translate a 15 kN uniaxial tension/compression MTS load frame. An infrared furnace can be added to the setup. The MTS load frame can be removed to utilize the table and stage stack for other large size sample environments (e.g. furnace, welder, or microwave chamber). While predominantly used for SAXS/WAXS types of experiments, a series of successful HEDM measurements has been performed using this setup.
2. **High precision and low load capacity sample manipulation table** (permanent) – A standard APS optical table is equipped with a set of high-end translation and arc stages and an air bearing rotation stage (see Figure 2). Optionally a compact size load frame or a furnace can be deployed on the top of the stage stack. This table is to routinely deliver the stability and motion necessary for HEDM.

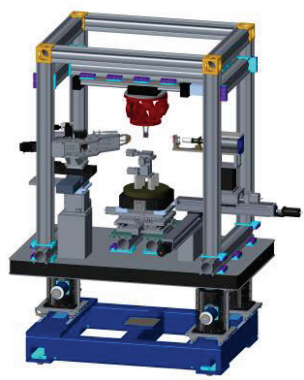


Figure 2: High precision SMS with near field and tomography detectors and overhead rail system supporting the conical slit cell.

ISBN: 978-3-95450-188-5 doi:10.18429/JACoW-MEDSI2016-WEPE28

3. **Open spot for custom user instrumentation** - The clearance required for the two permanent SMS to be positioned into the beam also serves as space for custom instrumentation to be installed.

Floor Rails

A set of two parallel linear profile rails have been installed in recessed pockets in the concrete floor. Each SMS is permanently mounted to the rail system and can translate transverse to beam direction into or out of position. The motion is manual and can be easily be done by one person. Manually moving the SMSs, reduces the risk for collision between auxiliary equipment which changes continually. The rails allow multiple SMS to occupy the same spatial area maintain their alignment in APS-Z and Y.

In the case that custom equipment which does not use the rails must be brought in, a set of low profile trough covers are put into position to cover the rail system. Equipment can then be wheeled over the rails and people can safely walk over the troughs as well.

The floor rail system, however, is flexible and a new SMS can be adapted through the use of locating components on the support base bottom (see Figure 3). The locating scheme utilizes custom made case hardened steel conical locators which also serve as feet for the SMS which can be removed from the rails if needed. The receivers, similar to a kinematic mount, include two flats, one vee and one cone (see Figure 4).

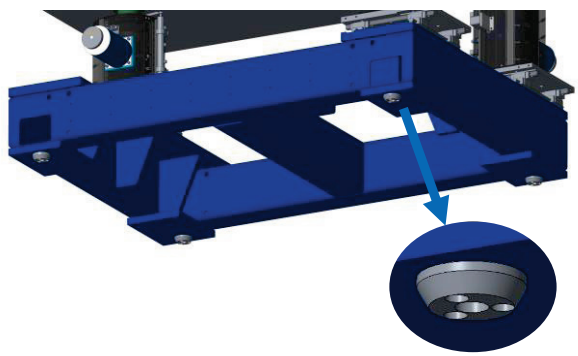


Figure 3: Locators on the bottom of a SMS support table.

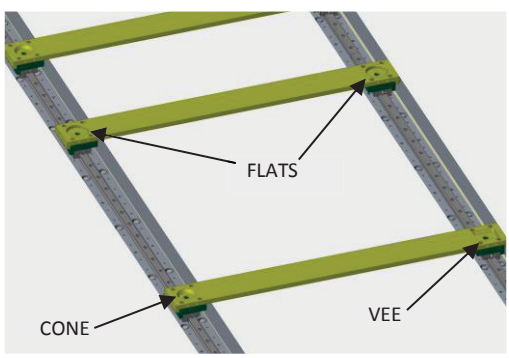


Figure 4: A set of receivers on "straps" mounted to the floor linear rails.

Overhead Rail

The high-precision SMS is equipped with an extruded aluminium structural rail frame mounted to the support base for the SMS. The cube shaped structure is used for mounting auxiliary components around the sample including:

- Digital imaging correlation camera (DIC)
- Conical Slit cell and manipulator
- Heater
- Keyence laser system
- Shielding

This framework was constructed relatively quickly and was intended to be temporary. A larger more permanent version of this system is currently under design.

WAXS Detector Array

A four panel GE detector array used for WAXS fills the central portion of the hutch area. It was initially designed for a static installation with a panel adjustment of 2m in Z obtained through the support table's rack and pinion system. Since the initial installation, the detector's support table has been retrofitted with air pads and upstream and downstream locators to increase its range and coverage. The alignment scheme consists of one vee on the downstream end of the table and one cone on the upstream end of the table. Two sets of receivers installed into the concrete floor are in line with the beam and allow the table to gain an additional 1m in panel throw (see Figure 5).

The air pads and locating system are also used to position the detector panel array asymmetrically from the beam to increase or change coverage or to be moved out of the way completely for use of the VFF detector setup.

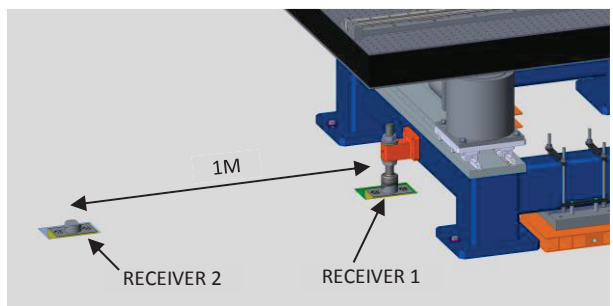


Figure 5: A locator on the support frame and receivers in the concrete floor allow for quick alignment of the WAXS detector.

FUTURE PLANS

Permanent Overhead Rail System

Although the temporary overhead rail system has achieved expectations for the high-precision SMS over the short term, a more permanent structure made out of structural steel tubing is currently in design. The new structure will span the width of the hutch and provide a universal framework with additional motions incorporated (both manual and motorized) which can allow these

Content from this work may be used under the terms of the CC BY 3.0 licence (© 2016). Any distribution of this work must maintain attribution to the author(s), title of the work, publisher, and DOI.

ISBN: 978-3-95450-188-5 doi:10.18429/JACoW-MEDSI2016-WEPE28

components to be moved into position as needed without repeated mounting and alignment. The near field and tomography detectors may join the group of components which will be suspended from the structure. Currently these two detectors, mounted from below, must be relocated and aligned based on the experiment.

SUMMARY

Beamline 1-ID accommodates a number of complimentary techniques and sample environments in the same spatial envelope. The configuration of the hutch has evolved to minimize the time and effort required for changeovers between techniques. Instrumentation design features have been incorporated to achieve maximum stability and repeatability of both the instruments and sample.

In addition, flexibility exists for users to install their own custom sample environments. New instrumentation can be designed or modified to adapt for installation to the floor rail system. The configuration of the end station will continue to evolve with the needs of users.

REFERENCES

[1] Jay C. Schuren, Paul A. Shade, Joel V. Bernier, Shiu Fai Li, Basil Blank, Jonathan Lind, Peter Kenesei, Ulrich Lienert, Robert M. Suter, Todd J. Turner, Dennis M. Dimiduk, Jonathan Almer. New opportunities for quantitative tracking of polycrystal responses in three dimensions, *Current Opinion in Solid State and Materials Science* 19(4) (2014) pp. 235-244

[2] Singhal, F. Yuan, S.R. Stock, J.D. Almer, L.C. Brinson, D.C. Dunand. Evolution of phase strains during tensile loading of bovine cortical bone, *Adv. Eng. Mater.*, 15 (2013), pp. 238–249.

[3] Park, J.-S., Zhang, X., Sharma, H., Kenesei, P., Hoelzer, D., Li, M. and Almer, J. High-energy synchrotron x-ray techniques for studying irradiated materials, *Journal of Materials Research*, 30(9) (2015) pp. 1380–1391

Content from this work may be used under the terms of the CC BY 3.0 licence (© 2016). Any distribution of this work must maintain attribution to the author(s), title of the work, publisher, and DOI.

ISBN: 978-3-95450-188-5 doi:10.18429/JACoW-MEDSI2016-WEPE29

A NOVEL FILTER AUTO-MOUNTER FOR THE BIOXAS BEAMLINES AT THE CLS

S. Carriere *, D. Beauregard, B. Schneider, G. Steel, D. Taylor,
Canadian Light Source Inc., Saskatoon, Canada

Abstract

The BioXAS beam-lines are a recently completed group of beam-lines at the Canadian Light Source (CLS). The Biological X-ray Absorption Spectroscopy (BioXAS) – Extended X-ray Absorption Fine Structure (EXAFS) beamlines host three 32-element germanium detectors. There was a need to introduce an exchangeable filter between the soller slits and the 32-element germanium detectors. It was further required to have an automated filter exchange system so that users could quickly vary filter thicknesses and types to determine the effect on the signal. An auto-mounting filter system was created to meet these requirements and allows users to quickly exchange filters without breaking experimental hutch lockup. The auto-mounter cartridge can hold up to ten slides that measure 100 mm X 55 mm in cross-section. The device inserts slides in an extremely small envelope between the soller slits and the liquid helium cryostat. The auto-mounter assembly also houses the stages required to actuate the soller slits laterally and vertically. During device commissioning we performed 800 consecutive successful filter exchanges as part of a stress test. The spatial constraints, mechanics, and fabrication of the device will be presented. Software development will also be discussed.

INTRODUCTION

The BioXAS beamlines are a recently completed group of three beamlines at the CLS. The two EXAFS beamlines are sourced from a single "flat top" hybrid wiggler and were designed to be capable of extremely high resolution EXAFS measurements. They are capable of measuring biologically relevant concentrations of metals in dilute samples.

The SIDE EXAFS beamline hosts one 32-element germanium detector mounted at 90° to a liquid helium sample cryostat.

The MAIN EXAFS beamline hosts two 32-element germanium detectors mounted at 90° to a liquid helium sample cryostat (mounted inboard and outboard of the cryostat).

Part of the beamline scope is to allow users to quickly vary filters between the sample and the detector so that they can determine the effect on the signal. Individual users will decide on the type and thickness of filter material. It was decided that the filter exchange would be automated so users could change filters without breaking experimental hutch lock-up.

A Filter Auto-Mounter (FAM) (Fig. 1) was designed to meet these requirements.



Figure 1: Main Beamline Endstation with 2 FAM units.

Constraints/ Requirements

The following were determined to be the FAM design constraints and requirements:

- The design of the FAM has to work for both EXAFS beamlines.
- Users need to be able to pre-load a set of filters according to their needs.
- Two FAM systems are required on the MAIN beamline.
- The system needs to also house the Soller slits and provide them XZ translation.
- Distance from 32-el detector snout and sample is 81mm.
- 1 mm of space between Soller slit and detector snout.
- The sample cryostat is motorized in XYZ, +/- 10 mm in all directions.
- Filters to be placed immediately in front of Soller slits. The available thickness for the filter insert mechanism is 13 mm after accounting for Soller slit thickness, detector position, and cryostat travel.
- The only available route for filters to enter is to be lowered in from above the 32-el detector snout.
- FAM system to be fully automated with the ability to keep track of filter position in order to prevent collisions.
- FAM units to be removable for service without detaching other endstation critical hardware.

DESIGN FEATURES

The overall FAM assembly (Fig. 2).

* shawn.carriere@lightsource.ca

Content from this work may be used under the terms of the CC BY 3.0 licence (© 2016). Any distribution of this work must maintain attribution to the author(s), title of the work, publisher, and DOI.

ISBN: 978-3-95450-188-5 doi:10.18429/JACoW-MEDSI2016-WEPE29

Content from this work may be used under the terms of the CC BY 3.0 licence (© 2016). Any distribution of this work must maintain attribution to the author(s), title of the work, publisher, and DOI.

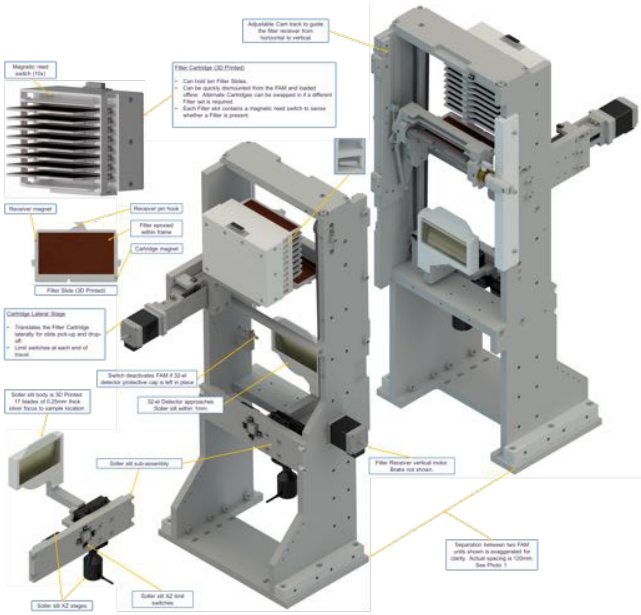


Figure 2: General overview of the FAM setup.

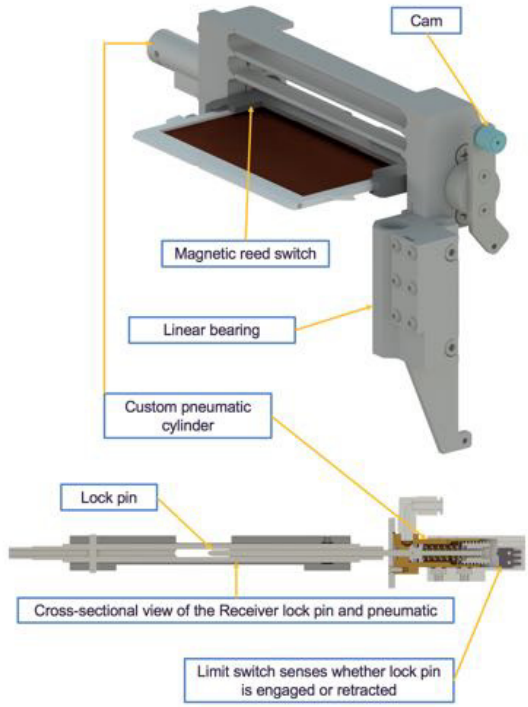


Figure 3: Detail illustration of the Filter Receiver Assembly.

Filter Receiver Assembly

Transfers Filter Slides from the Cartridge (Fig. 3) to the installed position (installed position is between the Soller slits and sample cryostat). A linear bearing slides along a precision shaft to provide smooth vertical motion. As the Filter Receiver Assembly travels vertically, a cam rotates the Filter Slide from horizontal (for cartridge engagement) to vertical (for installed position). A motor, timing belt, and timing pulleys move the assembly vertically. A custom pneumatic cylinder engages a lock pin to lock the filter in place so it is restrained when the filter leaves the cartridge. A magnetic reed switch in the receiver body senses the presence of a Filter Slide. Limit switches are placed at the top and bottom of receiver stroke. Before placing or removing a slide in the cartridge, the receiver calibrates position from the top limit switch.

Filters

The Receiver inserts a Filter into the top of a Cartridge slot (Fig. 4). The Filter is then lowered to the bottom of the Cartridge slot. As the Filter is lowered, it engages hook features within the Cartridge. The Receiver lock pin is retracted. As the Receiver is withdrawn, the Filter remains with the Cartridge. The reverse process occurs for removing Filters from the Cartridge.

PLC Control

The FAM software is built on EPICS 3.14.12 and makes use of SNL (State Notation Language) as the state engine. There are two state machines. One keeps track of all the Filters to make sure that all of them are accounted for, and simply displays a message to the user. The second state machine does all the actual control of the FAM. Each step in the process of changing Filters is a state in the state machine.

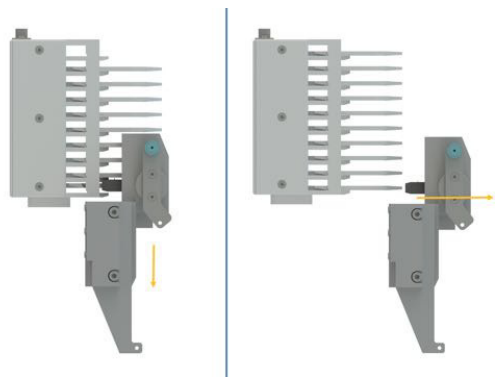


Figure 4: Illustration showing the cartridge & slide installation. Inserted (left) orientation. Receiver withdrawing (right) after depositing a slide.

There is only one path through all of the states, and all conditions must be met within the expected amount of time or the state machine goes into an error condition. There is also a simple state machine in the machine protection PLC Fig. 5) which determines when motors are allowed to move based on limit signals and location of the Filters. Since there are no encoders, each motor is calibrated to a limit switch on every Filter change. The position of the top limit is used as the calibration point for the vertical motor. All subsequent moves are calculated based on the measured position of the first Filter. The program knows the position of the first Filter, the distance between Filters, the lift distance to unseat a Filter, and the drop distance to seat a Filter. All calculations are based on this simple information. For testing purposes,

ISBN: 978-3-95450-188-5 doi:10.18429/JACoW-MEDSI2016-WEPE29

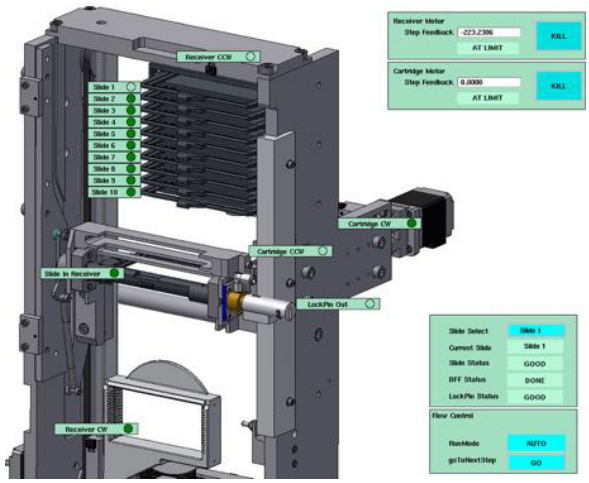


Figure 5: Screenshot of the commissioning screen.

the software can be made interactive and it can wait at the transition of each state so that the user has to allow the state machine to proceed.

CONCLUSION

Three identical Filter Auto-Mounters were successfully built for use on the two BioXAS EXAFS beamlines. All spatial constraints were met without sacrificing device performance. All three units have been tested and commissioned. During device commissioning we performed 800 consecutive successful filter exchanges as part of a stress test. Mounting of various filter types within the 3D printed Filter frames is still ongoing. Software recently enhanced to shorten slide change interval. Beamline staff and users are now able to remotely switch filters without breaking experimental hutch lock-up.

Content from this work may be used under the terms of the CC BY 3.0 licence (© 2016). Any distribution of this work must maintain attribution to the author(s), title of the work, publisher, and DOI.

ISBN: 978-3-95450-188-5 doi:10.18429/JACoW-MEDSI2016-WEPE30

INTRODUCTION TO NEUTRON SCATTERING INSTRUMENTS – HOW ARE THEY DIFFERENT?*

R. Connatser, Canadian Light Source, Saskatoon, Canada

Abstract

Neutron scattering is a complementary technique to x-ray scattering scientifically, but while there are similarities, there are some unique challenges in the design, construction, and operations. This poster will provide a brief description of neutron scattering, describe the technical components of spallation neutron scattering instruments, and discuss the engineering challenges found in the design and construction of these instruments.

KEY DIFFERENCES

Neutrons interact with matter via the strong nuclear force (nuclei) and the dipole-dipole interaction between magnetic moments (unpaired electrons). Neutrons penetrate deeply into samples in comparison to x rays, which interact with electrons.

Key differences:

- Weak interaction with matter
- Sources/Generation
- Induced Radioactivity and secondary particle generation
- Time of Flight methodology

SHIELDING

Significant shielding is needed around the energetic production of neutrons and the incidental high energy photons (and associated hadron showers). Where most intense, this shielding will be very thick (meters). This shielding is not just for the protection of humans, but to prevent background radiation from interfering with the experiments (see Fig. 1).

Shielding Composition

To shield against a range of particles and photons involves using multiple materials to account for the varying ways in which they interact with matter. For high energy neutrons and photons, high Z materials are needed, generally steel. For lower energy neutrons, materials containing a high concentration of hydrogen is best, such as concrete (with water) or high density polyethylene.

Complicated Shapes

Similarly to synchrotron beamlines, the technical components of neutron instruments have varying shapes and need utilities supplies to them. Slow neutrons also have a peculiar scattering property in which they almost appear to be a gas. Thus cracks or edges through the shielding must have multiple bends in them. Given the sheer volume of shielding needed on an instrument, the shapes needed meet all the varying needs often more resemble Tetris blocks than Lego.

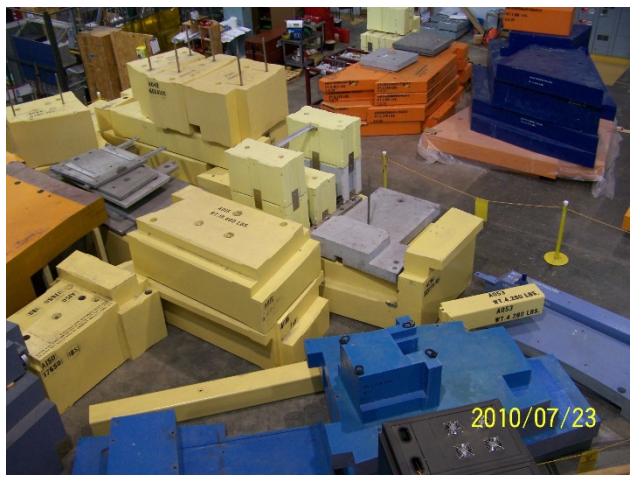


Figure 1: Neutron shielding from the Spallation Neutron Source, Oak Ridge National Laboratory, USA.

Time of Flight Methodology

Unlike photons traveling at the speed of light, neutrons of different energies travel at different speeds – the more energetic, the faster. Neutron instruments must take into account the time of travel from the source to the sample, sample to detector. There must also be methods of removing the prompt pulse and other unwanted neutrons from the beam.

Chopping the Beam

The premise is to physically disrupt the neutron beam with a rotating device. Three examples are:

T0 – to remove the prompt pulse of high energy neutrons with a heavy rotating mass.

Bandwidth – often a cascade of rotating disks that are timed with the pulse to only allow particular energy/wavelengths to pass through to the sample.

Fermi – used to select particular energy/wavelength neutrons.

Sample to Detector

A spectrometer measures an energy change in the neutrons created by the interaction with the sample. The energy change is seen at the detector by measuring the difference in the flight time of the neutrons – e.g. we know when the neutrons of x energy interacted with the sample, we know the precise distance from the sample to the detector and the speed of neutrons of that energy. Neutrons that gain energy will arrive sooner, those that lose energy will arrive later. By having appropriate distances between sample and detector, measurement of these time differentials is possible.

Content from this work may be used under the terms of the CC BY 3.0 licence (© 2016). Any distribution of this work must maintain attribution to the author(s), title of the work, publisher, and DOI.

ISBN: 978-3-95450-188-5 doi:10.18429/JACoW-MEDSI2016-WEPE30

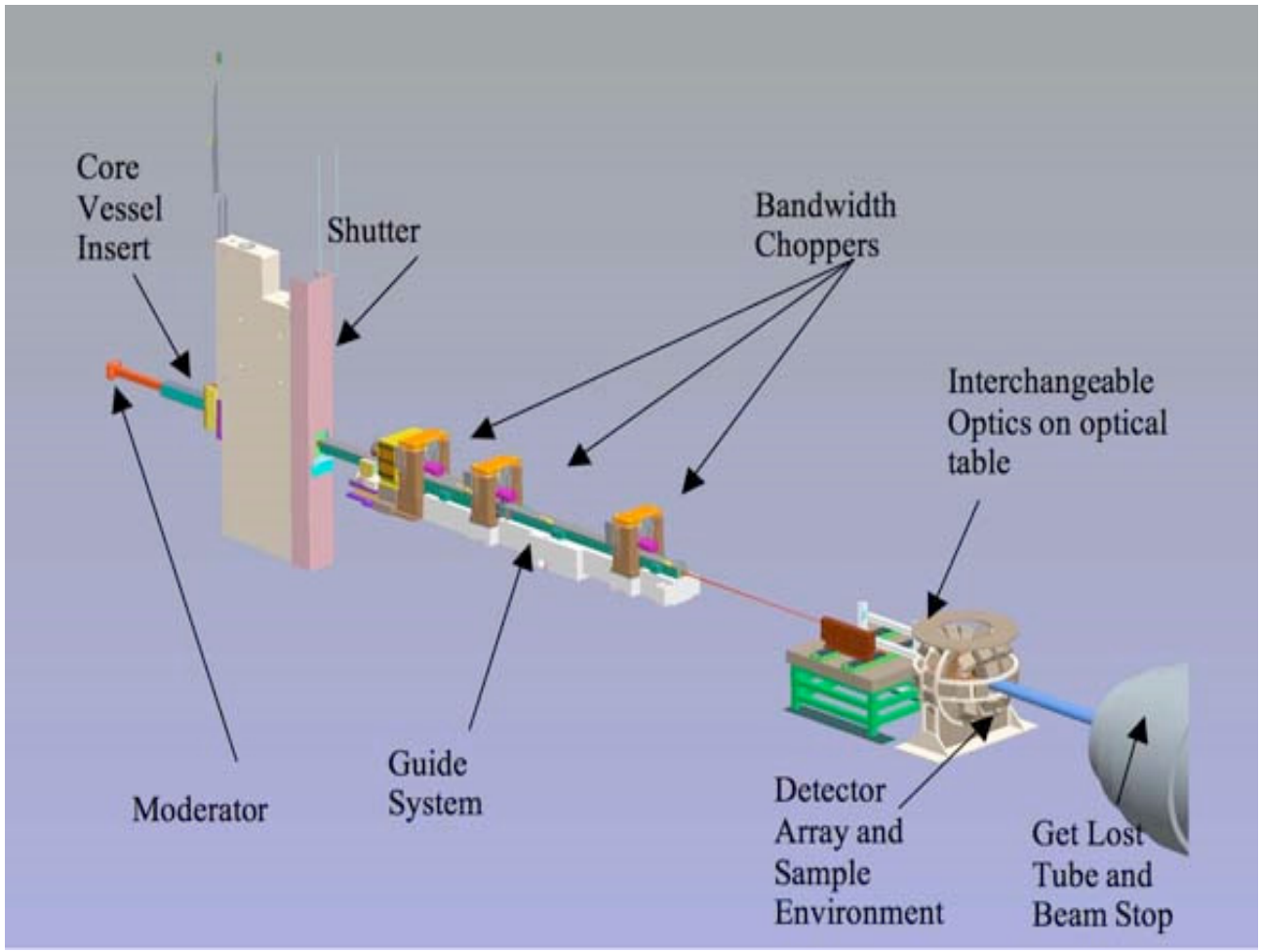


Figure 2: The MaNDi instrument at the Spallation Neutron Source at Oak Ridge National Laboratory. Image courtesy of S. Keener.

Vacuum

Given the limited interaction with matter, neutron instruments do not typically require particularly good vacuum. Turbo and roughing pumps are the common equipment used to evacuate choppers, beam transport systems, and scattering chambers.

Source/Generation of Neutrons

Production of neutrons is either by fission or by spallation. Fission yields 2 MeV neutrons, while spallation 0.5 – 3 GeV, depending on the accelerator.

Neutron scattering experiments typically utilize thermal (~25 meV) or colder neutrons. Conversion happens via moderation (multiple energy loss scattering events in a material (C, Be, H2O, Methane, LH2, LD2). These moderators are the sources for neutrons, compared to insertion devices. However, they are typically designed to have one output spectrum and serve multiple instruments.

Transmission of Neutrons

Depending on the needs of the instrument, modern neutron instruments often utilize super mirror guides of carefully designed shapes to focus and "guide" the neutrons towards the sample. Guides are generally composed of multiple layers of vacuum deposited coatings of Ni (or similar metals) on top of a glass substrate. These glass housings are installed inside metal vacuum chambers. These guides allow the neutrons to "bounce" or very shallowly reflect off the sides of the guides, increasing the number of neutrons that can reach the sample.

Neutron guides also allow instrument designers to move the neutron beam in space and can be one of the tools used to help discriminate against unwanted neutrons or provide a particular beam shape or profile to the sample. High energy neutrons do not interact with guides and travel in straight lines from the source. By curving the beam of desired neutrons out of line of sight, the unwanted high energy neutrons can allowed to spill into localized shielding, where they are absorbed. The radius of curvature on these types of instruments is often a kilometre or more.

Get Lost Tubes and Beam Stops

Neutron scattering experiments may only scatter a small portion of the total beam – for really hard experiments the sample could be designed to interact with little as 0.1% of the flux. The remaining neutrons are unwanted and must be "disposed of" in a fashion that prevents them from being

Content from this work may be used under the terms of the CC BY 3.0 licence (© 2016). Any distribution of this work must maintain attribution to the author(s), title of the work, publisher, and DOI.

ISBN: 978-3-95450-188-5 doi:10.18429/JACoW-MEDSI2016-WEPE30

Content from this work may be used under the terms of the CC BY 3.0 licence (© 2016). Any distribution of this work must maintain attribution to the author(s), title of the work, publisher, and DOI.

noise in the measurement or being a radiological hazard. A "Get Lost Tube" provides an evacuated space for the neutrons to travel to the beam stop. As with all neutron shielding, this will be composed of multiple materials, much of which is heavy. Beam stops on higher energy instruments at high intensity sources can weigh in excess of 15 tons, consisting of a steel core with polyethylene and boron carbide inside a high density concrete shield. Figure 2 shows the MaNDi instrument at the Spallation Neutron Source at Oak Ridge National Laboratory.

CONCLUSION

Design and engineering of neutron instrumentation utilize many of the same skills as x-ray beamlines. However, due to the physical differences in the base particle, there are significant differences. The source term for neutron production has a different size, shape, as well as directional components compared to the much more directed synchrotron beam generated by insertion devices. Transmission and movement of neutron beams has its own challenges compared to utilization of mirrors and monochromators.

There is significantly more effort in the physics and engineering design of the shielding for neutron instruments. Absorption of neutron beams induces radioactivity in the shielding materials, but does not generate significant heat loads. The time of flight methodology is an inherent part of the design of the neutron instrument and causes instruments to need meters of space between components, specifically from the sample to the detector in most neutron spectrometers.

ACKNOWLEDGMENT

Special thanks to Scott Keener of the Spallation Neutron Source at Oak Ridge National Laboratory. A good source of basic information on neutron scattering is "Neutron Scattering, A Primer" [1].

REFERENCES

[1] R. Pym, "Neutron Scattering, A Primer", produced by the Los Alamos National Laboratory https://www.ncnr.nist.gov/summerschool/ss16/pdf/NeutronScatteringPrimer.pdf

ISBN: 978-3-95450-188-5 doi:10.18429/JACoW-MEDSI2016-WEPE36

DESIGN, CONSTRUCTION AND COMMISSIONING OF TWO HIGHLY INTEGRATED EXPERIMENTAL STATIONS FOR MICRO-FOCUSING MACROMOLECULAR CRYSTALLOGRAPHY BEAMLINES AT NSLS-II

D. K. Bhogadi*, B. Andi, L. E. Berman, M. Carlucci-Dayton, M. R. Fuchs†, J. Jakoncic, T. Langdon, J. Lara, B. Martins, S. Myers, D. K. Schneider, S. McSweeney, R. M. Sweet
National Synchrotron Light Source II, Brookhaven National Laboratory, Upton, NY 11973, USA

Abstract

We present the final engineering design and first commissioning results of two highly integrated experimental stations for macromolecular crystallography (MX) at the National Synchrotron Light Source II (NSLS-II). One of the beamlines will provide micro-focusing (FMX) and the other high automation (AMX). These beamlines will support a broad range of biological and biomedical structure determination methods from serial crystallography on micron-sized crystals, to structure determination of complexes in large unit cells. The experimental stations were designed and fabricated largely in-house to obtain highly flexible and modular units that meet the challenging stability and integration requirements required by the small beam sizes and the limited work envelopes. Key components to meet these criteria are a highly compact beam conditioning unit and exchangeable main and secondary goniometers (sample rotation axes) integrated in a granite support structure.

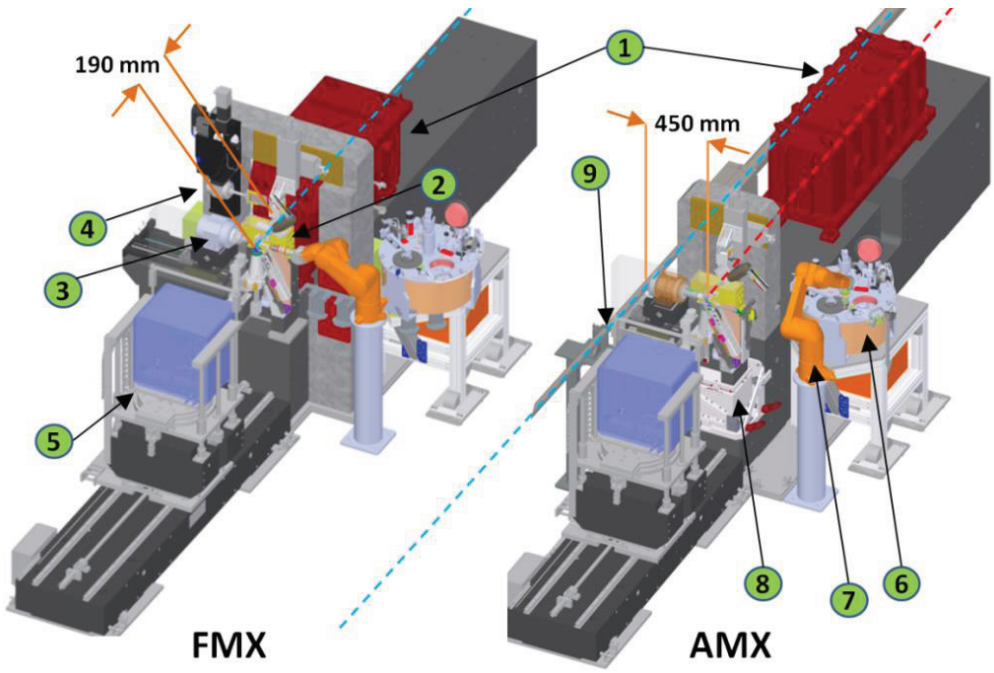


Figure 1: The FMX (left) and AMX (right) experimental stations. The beams come from the top right (FMX cyan dashed line, AMX red dashed line). Devices (identical at both endstation if not indicated otherwise): (1) KB focusing mirror tanks, (2) beam conditioning unit, (3) main goniometer, (4) FMX secondary goniometer, (5) detector support, (6) LN2 sample Dewar (7) Stäubli 6-axis sample mounter (8) AMX XY lift stage (9) FMX beam pipe passing the AMX endstation.

INTRODUCTION

The FMX and AMX beamlines were designed and constructed as part of a suite of Advanced Beamlines for Biological Investigations with X-rays – the ABBIX project [1–3]. The beamlines' layout and scientific mission greatly influence the endstation design: beam sizes of down to 1 and 4 µm respectively require high vibrational stability. The two beamlines share sector 17 of the storage ring in a canted undulator arrangement. Combined with the Kirkpatrick-Baez (KB) focusing mirrors' short focal distances, this layout poses great spatial constraints for the experimental stations and beam conditioning units. To support different measurement

* dbhogadi@bnl.gov
† mfuchs@bnl.gov

Content from this work may be used under the terms of the CC BY 3.0 licence (© 2016). Any distribution of this work must maintain attribution to the author(s), title of the work, publisher, and DOI.

ISBN: 978-3-95450-188-5 doi:10.18429/JACoW-MEDSI2016-WEPE36

Content from this work may be used under the terms of the CC BY 3.0 licence (© 2016). Any distribution of this work must maintain attribution to the author(s), title of the work, publisher, and DOI.

modes such as serial micro-crystallography or crystallization plate screening, and to open the possibility to accommodate novel experiments that have not been specified at the time of design, the design needs to be modular and flexible.

The experimental stations comprise a beam conditioning unit, an on-axis microscope, a specimen goniometer, an array of auxiliary devices, and a sample changing robot (Figure **1**). Each of these major components can be aligned independently into the beam. The specimen goniometers consist of a high precision air bearing main goniometer with horizontal spindle axis, interchangeable with a secondary goniometer at FMX for specialized experiments. The on-axis microscopes are reflective optics telescopes (Questar QM100 [4], with customized housing) complete with front and back illumination. The auxiliary apparatus includes collimation and diagnostic units, a beamstop, and a nitrogen gas cryo cooler. The endstations are highly integrated in a compact space on a granite support structure with high modularity for future upgrades and extensions.

This article highlights the construction of the self-contained beam conditioning unit and the collimating and diagnostic system, as well as the main goniometer.

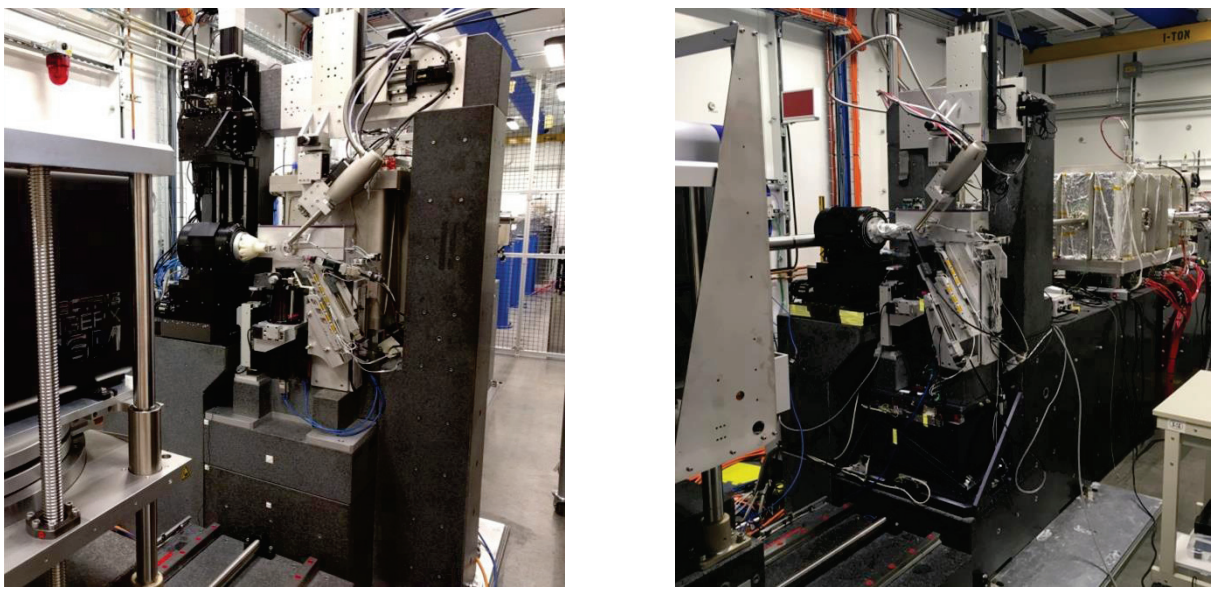


Figure 2: Current status of the experimental stations of FMX (left) and AMX (right). Both endstation core modules are mounted on the main granite block supporting the focusing mirrors. The CryoStream sample coolers and the FMX secondary goniometer are mounted on granite arches.

END STATION DESIGN, INTEGRATION AND ENGINEERING

In the design of the experimental stations (Figure 2), two main spatial restrictions had to be overcome which result from the beamlines' optical layouts. The so-called experimental station core module aligns these components along the beam path from upstream to downstream: the compact beam conditioning unit, the on-axis microscope, an x-ray fluorescence detector, the beam collimator, a diode and scintillator unit, the beamstop, and the backlight. At FMX, due to the KB focusing mirrors' short focal length, the distance from the mirror tank's downstream face to the sample is only 190 mm along the beam (Figure 1). This extreme restriction led us to design and develop a highly compact beam conditioning unit that contains, within 140 mm, a **B**eam position monitor, **A**ttenuator, **S**lits, **I**ntensity monitor, sub-millisecond **S**hutter, and secondary **S**lits – the BASISS unit (Figure 3). The remaining 50 mm to the sample position fit the on-axis microscope and the beam collimation unit. At AMX, there is ample space along the beam, but here the lateral distance between the adjacent FMX beam pipe and AMX focal spot is just ~450 mm (Figure **1**), which greatly restricts the space for the main goniometer. In each case, the more restrictive environment sets the boundary conditions to keep the design identical for the two endstations wherever possible.

Both beamlines' focusing KB mirrors can be retracted from the beam to provide a more parallel beam for large unit cell crystals – at the expense of dose rate. At FMX, this leads to a beam movement of 5 mm vertically and 2.5 mm horizontally, accommodated within the BASISS unit. At AMX, the corresponding beam movements are 19 mm and 14 mm respectively. To accommodate this large beam shift, a wedge-based XY lift and translation stage carries the endstation core module.

BASISS Beam Conditioning Unit

Several constructional details are the key to fitting all six components of the beam conditioning unit into a 140 mm long space. Instead of the commonly used vacuum

ISBN: 978-3-95450-188-5 doi:10.18429/JACoW-MEDSI2016-WEPE36

tank, a helium-filled aluminum enclosure was built with lower requirements on wall thickness. Compact stick-slip piezo positioners with nm resolution (SmarAct SLC-17XX) and integrated encoders were used not only to achieve high positioning repeatability and speeds (up to 20 mm/s) but also to minimize component dimensions. Additionally, the thickness along the beam of each device was carefully minimized: The *X-ray beam position monitor* (Sydor Instruments SI-DBPM-M405, [5]) is driven by two SmarAct SLC1740-D positioners that have a repeatability of 25 nm and provide holding power against its 5 coaxial signal cables. The *attenuator* was constructed as a slim stack of 4 sliders with 8 attenuator slots each. In order to provide attenuation with sufficient dynamic range over FMX's energy range of 5-30 keV, an octal system of layered thin Al and Sn foils was implemented [3]. Both *four-blade slits* and the *intensity monitor* inherit their compactness from the careful arrangement of SmarAct SLC1720 and SLC1740-D positioners, respectively. The design of the fast *shutter* is derived from a highly compact unit developed at the APS [6] which uses a galvanometer motor (Cambridge Technologies 6220H) with ±20° opening angle to rotate two tungsten blades bracketing a channel to pass the beam. Depending on the local beam size, this shutter provides opening times of a few 100 µs, which is required to limit the sample exposure before the actual data collection in high-flux experiments.

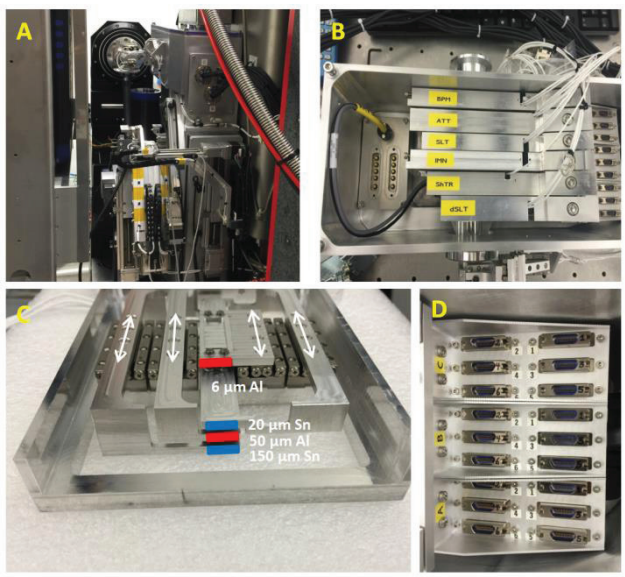


Figure 3: (A) Closeup view of the BASISS beam conditioning unit integrated in the endstation. (B) All devices aligned inside the unit, (C) attenuator module, (D) Patch panel: Omnetics micro-D latch connectors for 17 nano-positioners (1 spare).

An important design goal for this unit was for it to be highly modular and enable rapid exchange of modules to reduce service times. All devices are mounted on a specially designed rail with 2D kinematic mounting brackets for easy and reproducible access to each device. A central patch panel and short cable loops allow for quick exchange of components.

Beam Collimator and Diagnostics

A molybdenum collimator tube (OD 0.51 mm, ID 0.35 mm) acts as a guard aperture for radiation scattered from upstream BASISS components and suppresses air scatter from the beam path between the drilled microscope deflection mirror and the cold stream used to cool the sample (Figure 4, left). The collimator is aligned along the beam by a compact retractable mechanism with a motorized XYZ stack and manual flex pivot-based pitch and yaw adjustments. A wire-eroded 0.5 mm thin holder minimizes the shadowing of the on-axis microscope. On a second retractable positioner, a diode and scintillator provide beam shape, position and intensity at the focal spot (Figure 4, right).

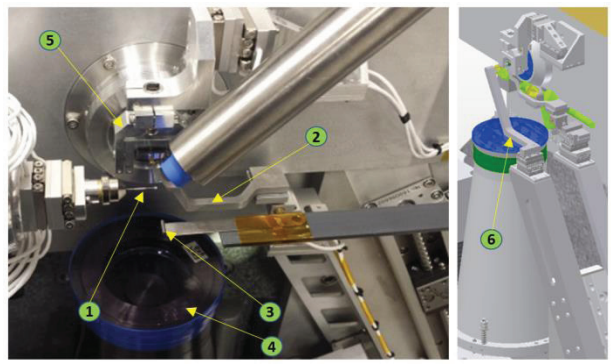


Figure 4: *Above*: FMX sample environment. (1) sample pin, (2) collimator tube holder, (3) beam stop, (4) microscope objective, (5) microscope on-axis deflection mirror. *Right*: Same region viewed from right, showing collimator positioner and (6) scintillator / diode positioner.

Both collimator and scintillator fingers are supported by magnetic kinematic mounts for rapid exchange and protection against accidental touching. Due to the mounts' high reproducibility, after an initial collimator alignment the collimator's pitch and yaw does not require re-adjustment even after repeated dismount/mount operations, only a minimal translational realignment in X and Y direction was required; this can be automated.

Main Goniometer

The main sample goniometers employ a Nelson Air SP150 rotary air bearing for the horizontal rotation axis. Its total spindle runout 50 mm above the rotation table has been determined to ±20 nm. The spindle is carried by an XYZ translation stack with a linear air bearing stage in the X-direction for sample scanning and positioning (Aerotech ABL15050) and Y and Z stages to align the rotation axis into the beam (Aerotech ANT180 and custom AVS lift stages). For sample centering, a stick-slip piezo XY centering stage (SmarAct SLC-1720) is mounted on a light weight extension arm, with a

Content from this work may be used under the terms of the CC BY 3.0 licence (© 2016). Any distribution of this work must maintain attribution to the author(s), title of the work, publisher, and DOI.

ISBN: 978-3-95450-188-5 doi:10.18429/JACoW-MEDSI2016-WEPE36

customized base plate containing the positioner's sensor modules. The final mounting arm (Figure 5) is just coming out of fabrication.

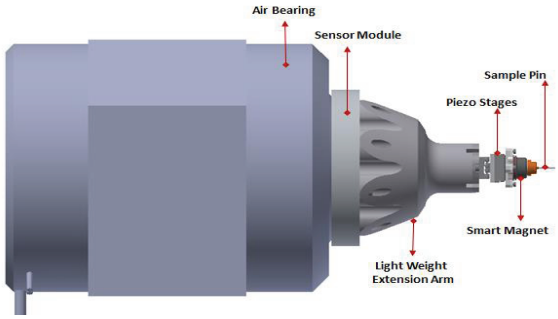


Figure 5: Main goniometer arm assembly on air bearing spindle.

In first metrology tests with a prototype arm, a sphere of confusion of 860 nm peak-peak at the sample position was obtained. The main contribution to this error is reproducible, so these first tests and previous measurements on an identical SmarAct centering stage setup [7] suggest that using active correction and the final centering arm, a target sphere of confusion on 100 nm can be achieved. At FMX, the main goniometer can be retracted laterally and replaced by a secondary goniometer for specialized experiments such as crystallization plate screening. This goniometer would be lowered from above and is currently being commissioned.

CONCLUSION

Two highly compact experimental stations for macromolecular micro-crystallography have been developed at the FMX and AMX beamlines. After the beamlines' first light on March 8, 2016, the first diffraction images were recorded in June, and the first user groups collected their first datasets in August.

ACKNOWLEDGEMENT

This work is supported by US Department of Energy BER contract DE-SC0012704 and by an US National Institutes of Health NIGMS grant P41GM111244. NSLS-II is operated under DOE BES contract DE-AC02-98CH10886.

REFERENCES

[1] Schneider D K, Berman L E, Chubar O, Hendrickson W A, Hulbert S L, Lucas M, Sweet R M and Yang L 2013 Three Biomedical Beamlines at NSLS-II for Macromolecular Crystallography and Small-Angle Scattering *J. Phys. Conf. Ser.* 425 12003.

[2] Fuchs M R, Sweet R M, Berman L E, Hendrickson W A, Chubar O, Canestrari N, Idir M, Yang L and Schneider D K 2014 NSLS-II Biomedical Beamlines for Macromolecular Crystallography, FMX and AMX, and for X-ray Scattering, LIX: Current Developments *J. Phys. Conf. Ser.* 493 12021.

[3] Fuchs M R, Bhogadi D K, Jakoncic J, Myers S, Sweet R M, Berman L E, Skinner J, Idir M, Chubar O, McSweeney S and Schneider D K 2016 NSLS-II biomedical beamlines for micro-crystallography, FMX, and for highly automated crystallography, AMX: New opportunities for advanced data collection *AIP Conf. Proc. SRI2015* 1741 30006.

[4] Gofron K J, Molitsky M, Alkire R W and Joachimiak A 2011 On-axis viewing: Sample visualization along the synchrotron X-ray beam *Nucl. Instr. and Meth. A* 649 109–11.

[5] Keister J W, Smedley J, Muller E M, Bohon J and Héroux A 2011 Diamond X-ray photodiode for white and monochromatic SR beams *Nucl. Instr. and Meth. A* 649 91–3.

[6] Goetze K and Lienert U 2009 A Galvanometer Based Fast Shutter - presented at the SRI2009.

[7] Fuchs M R, Pradervand C, Thominet V, Schneider R, Panepucci E, Grunder M, Gabadinho J, Dworkowski F S N, Tomizaki T, Schneider J, Mayer A, Curtin A, Olieric V, Frommherz U, Kotrle G, Welte J, Wang X, Maag S, Schulze-Briese C and Wang M 2014 D3, the new diffractometer for the macromolecular crystallography beamlines of the Swiss Light Source *J. Synchrotron Rad.* 21.

Content from this work may be used under the terms of the CC BY 3.0 licence (© 2016). Any distribution of this work must maintain attribution to the author(s), title of the work, publisher, and DOI.

ISBN: 978-3-95450-188-5 doi:10.18429/JACoW-MEDSI2016-WEPE37

UPGRADE OF THE SUPER ADVANCED X-RAY SPECTROMETER (SAX-ES) OF THE RIXS ENDSTATION FOR BETTER RESOLUTION AND LARGER DETECTOR SIZE

St. Maag†, P. Hirschi[1], L. Nue, X. Wang, T. Schmitt,
Paul Scherrer Institut (PSI), 5232 Villigen PSI, Switzerland
[1]also at HELVETING Engineering AG, 6331 Hünenberg, Switzerland

Abstract

The RIXS endstation of ADRESS beamline at Swiss Light Source (SLS) is equipped with an ultrahigh resolution X-ray spectrometer as described in [1]. In the scope of a CCD camera upgrade, the modification of the vertical alignment of the guiding structure and ultra-high vacuum tanks became necessary. The new camera with a higher resolution and larger detector size weights around 25 kg. It is required to have a vibration-amplitude well below 2 microns. We will present the critical design parameters of the upgrade, and the effort to increase bending stiffness of vacuum guide structure while keeping major geometry parameters. In addition, kinematic over determinacy was removed. After the upgrade we performed vibration measurements verifying that the dynamic stability of the camera is improved, and the design goal is reached. The site acceptance test confirmed the proper operation of the new mechanism. The redesigned spectrometer is shown in Fig. 1 with the welded bellows only connected on one side.

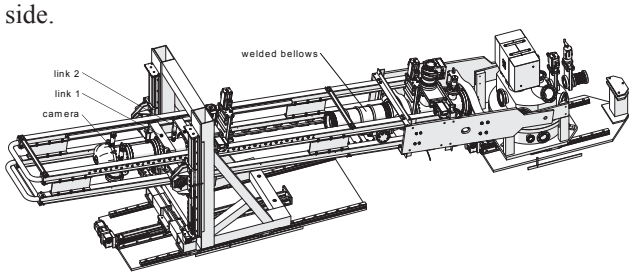


Figure 1: The redesigned spectrometer.

INTRODUCTION

The spectrometer with a length of 5 m is installed on a rotating girder platform and allows varying scattering angles from 30° to 130°. The position of the CCD detector is longitudinally adjustable on the girder and vertically adjustable on a moving frame to allow an angle between 2° to 15° in the vertical plane. For the new and much bigger detector system with 3 inches in width, the whole vacuum section and beam guiding chambers had to be enlarged to get use of a wider beam. The bigger ultra-high vacuum chambers and the new welded bellows were made of stainless steel 316LN.

The retrofit also included a new and larger turbo and ion getter pump as well as an automated vacuum valve on both ends of the bellow. The three separate vacuum compartments allow individual ventilation without ventilating the bellows. The retrofit was performed while aiming at the minimum number of changed parts.

† stephan.maag@psi.ch

The enlargement together with the new vacuum pumps would cause a substantial increase in weight. This could decrease stability of the instrument and it could require changes in the air movers or the girder. To increase the stability and to make sure the instruments weight and centre of gravity could be maintained, the whole supporting structure was built in aluminium with more efficient beam cross-sections. Therefore, the carrier structure is now built with 4 aluminium I-shaped beams with a higher stiffness than the old steel L-shaped beams but with lower weight. The same concept was adapted to the new camera support, which is now made of two big aluminium cross links about 50% lighter than the old design but much stiffer. The revolute joint of the camera support consists of much bigger self-aligning ball bearings, which allows compensation of inaccuracy in all required directions. Thus, the two linear drives at the mainframe are no longer fixed together by an overdetermined structure, they move simultaneous driven by the same motor. The linear bearing, which supports the connection of the carrier structure, also allows this compensation by using cam followers at the floating bearing side. The cam follower is a compact bearing with a high-rigidity shaft and a built-in needle bearing. Contrary to the normal installation case these rollers run on a hardened shaft guideway.



Figure 2: The spectrometer after the upgrade.

For the fixed bearing side normal linear ball bearings were used, running on the same type of shaft guideways. To support the new and bigger vacuum chambers, the carrier structure had to be redesigned and a new bellow guiding system was required. The vacuum chambers are carried by two big aluminium cross links, which allows linear displacement compensation in case of higher temperatures, such as a high bake out temperature of min.

Content from this work may be used under the terms of the CC BY 3.0 licence (© 2016). Any distribution of this work must maintain attribution to the author(s), title of the work, publisher, and DOI.

ISBN: 978-3-95450-188-5 doi:10.18429/JACoW-MEDSI2016-WEPE37

Content from this work may be used under the terms of the CC BY 3.0 licence (© 2016). Any distribution of this work must maintain attribution to the author(s), title of the work, publisher, and DOI.

150 °C. Therefore another fixed and floating bearing concept was applied to cope with thermal elongation during bake out.

The new bellow has a diameter of 150 mm (DN150) and enables an elongation of 1700 mm. Therefore a new guiding system was designed, made of two linear ball bearing tracks fixed at the carrier structure. For the coupling between the bellow and the tracks there are special between rings welded directly in the bellow. This new system allows a save and smooth operation of the bellow within its whole elongation. The final spectrometer after the upgrade can be seen in Fig. 2.

KINEMATICS

According to the requirements, the Instrument parameters, the range and the drive elements shouldn't change. Only the rotation axis of the camera support had to be moved closer to the vertical guiding structure, to improve stability and the natural frequency of the supporting structure. The given kinematics was highly over determined, which lead to a poor regularity in operation. A new bearing concept was indispensable.

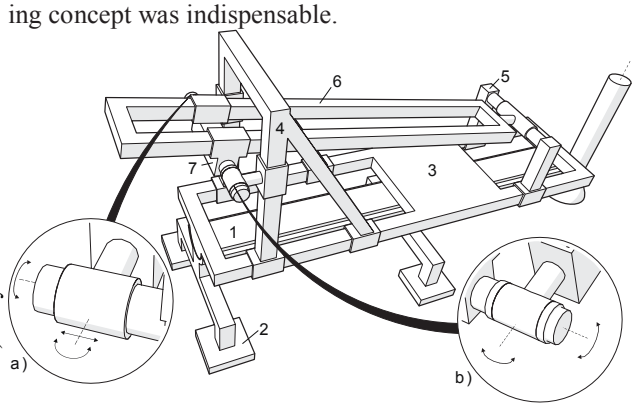


Figure 3: Kinematics of the spectrometer.

The kinematics of the spectrometer are shown in Fig. 3. The main platform (1) is carried by multiple air movers (2) to adjust the horizontal scattering angle from 30° up to 130°. On this platform there is an adjustable girder (3) to make sure that the instrument is aligned horizontally and independent form the inaccuracy of the air movers. On top of the girder the instrument is separated in two individual moveable parts. One is the mainframe support (4) and the other is the scattering grid chamber (5). Both of them are moveable along the longitudinal axis of the instrument to adjust the distance from the grating to the detector. These two parts are connected by a carrier structure (6) which carries the vacuum sections and guides the beam in an UHV environment of 10^{-9} mbar to the camera. To adjust the vertical angle of the carrier there is a joint at the scattering grid chamber and the carrier is moveable up and down along the mainframe support. The camera is mounted at the detector support (7) which connects the mainframe with the carrier structure. Thus, the detector support is movable in height and distance and is automatically aligned with the vertical angle of the carrier structure.

The new bearing concept enables the kinematics as described above, without being overdetermined but is on the other hand very stiff and stable. The bearings of the camera support were replaced with self-aligning ball bearings and linear ball bearings. Furthermore, one side has been designed as a floating bearing (a) and the other as a fixed bearing (b).

STABILITY AND PERFORMANCE

The design of spectrometer guide structures, and also the vertical alignment, has been modified as described above. The girder itself and the movers as well as the longitudinal positioning remain unchanged. Vibration measurements were performed before the upgrade on the original spectrometer in January 2015 and after the upgrade in June 2016 to verify the success of the project.

Initial Measurements

During the measurement period, ground vibration is instable and the calculated PSD displacements are all chosen to be in the quiet periods and are therefore not completely representative for the user operation. The girder itself shows low frequencies and a relatively high amplification ratio. Since the girder was beyond the scope of this project, its vibration remains determinative for the overall stability behaviour of the system.

Table 1: Displacement Amplification Ratio from Girder to Camera

Direction	Before Upgrade	After Upgrade
Vertical	4	3.2
Horizontal	4	2.5

Final Measurement

For the final measurement after the upgrade, the detector was driven to the upmost longitudinal position. Also the camera position is slightly higher than in the first measurement, to make sure that the new measurement is conservative. For the comparison of the two situations, the amplification ratio between the camera and the girder has been evaluated as shown in Table 1. The amplification ratio from the camera to the girder, especially in transversal direction, is much lower after the upgrade, manifesting the stiff structure and improved stability of the new camera support.

Ground vibration spectrum is not fully comparable with the measurements before the upgrade, with a higher vibration around 48 Hz in the second measurement. The displacement behaviour on the camera and articulation can be seen in Fig. 4. The measuring positions are indicated in Fig. 1. The eigenmodes of the structure are barely visible due to the low amplification.

The RMS displacement vertical to the beam from 5 to 200 Hz is below 100 nm and around 100 nm in horizontal direction. The specified camera movement of 2 microns is therefore fulfilled.

ISBN: 978-3-95450-188-5 doi:10.18429/JACoW-MEDSI2016-WEPE37

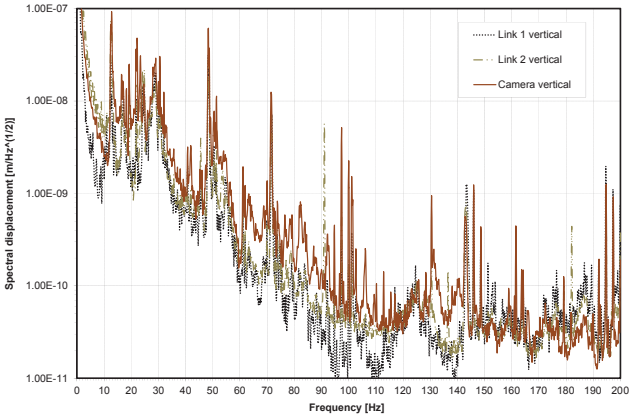


Figure 4: Displacement behaviour on the articulation.

CONCLUSION

The spectrometer features a new and stiffer aluminium guide structure and the vacuum tubing diameter is larger, to make full use of the broader CCD detector. The new bearing concept leads to improvements in use and the spectrometer works well.

Since the girder mover support was out of the scope of this upgrade, it remains a weak point when considering vibrations. However, the specified camera stability below 2 microns is easily surpassed with RMS displacement amplitudes around 100 nm. Furthermore, the amplification ratio from camera to girder, especially in transversal direction, is much lower than before the upgrade, manifesting the stiff structure and improved stability of the new camera support.

The improvements in the spectrometer prove effective and could well be used as base for a longer spectrometer arm in future development.

ACKNOWLEDGEMENT

We want to thank Markus Kropf, the workshop and the controls systems crew for their support.

REFERENCES

[1] G. Ghiringhelli *et al.*, "SAXES, a high resolution spectrometer for resonant x-ray emission in the 400 – 1600 eV energy range", *Rev. Sci. Instrum.*, vol. 77, no. 11, p. 113108, Oct. 2006.

Content from this work may be used under the terms of the CC BY 3.0 licence (© 2016). Any distribution of this work must maintain attribution to the author(s), title of the work, publisher, and DOI.

ISBN: 978-3-95450-188-5 doi:10.18429/JACoW-MEDSI2016-WEPE38

THE MECHANICS OF THE VEKMAG EXPERIMENT

T. Noll[1,2], F. Radu[2]

[1]Max-Born-Institut Berlin, Max-Born-Straße 2 A
12489 Berlin, Germany

[2]Helmholtz-Zentrum Berlin, Albert-Einstein-Str 16, 12489 Germany

Abstract

For the experiments at the synchrotron radiation source BESSY II synchrotron of the Helmholtz-Zentrum Berlin a new end station and a new beamline were developed and are now in user operation. The end station contains a 9-2-1 Tesla vectorial magnet and a cryostat with manipulator for the sample cooling and positioning, a deposition chamber, and a UHV detector chamber. We report here mainly on the technical design of the detector chamber which is placed below the magnet chamber and it is also connected to the deposition chamber. Because of various constrains including the limited available space between the bottom flange of the magnet chamber and the floor level, a sophisticated mechanics had to be developed to provide integrated functionality for both the detector holder and the sample transfer units. The detector unit consists of a tubular holder of 5 cm diameter which travels more than 60 cm vertically and exhibits an unlimited rotation degree of freedom of 360 degrees within the magnet bore. The sample transfer unit consists of a telescopic movement mechanism allowing for the sample holder vertical travel within the detector tubular holder. The functionality challenges and their resolve were addressed in an innovative mechanical design at HZB which was financed and build by the VEKMAG consortium.

INTRODUCTION

Soft x-rays are establishing as the most successful probe for a wide range of disciplines seeking answers of fundamental questions at the nanoscale and for different timescales down to femtosecond resolution[1,2]. In particular the magnetism community has benefited greatly from the element specific sensitivity which allows to disentangle the spin and orbital moments through the theoretical prediction and experimental observation of the XMCD effect [3,4,5,6]. Since then, the instrumentation is being continuously developed for advanced methods providing opportunities for magnetic imaging, spectroscopy, and scattering. To this end the VEKMAG consortium [7] has developed, build and comissioned an endstation installed at a newly build beamline located at segment 7.1 in the BESSY II experimental hall of the Helmholtz Zentrum Berlin.

The VEKMAG endstation includes a magnet chamber which includes a superconducting vector magnet and a cryostat, a detector system mounted below the magnet and a deposition chamber connected to the detector chamber which allows for in-situ growth and transfer of the samples. The magnet provides 9T in the beam direction, 2T perpendicular to the beam direction and in the horizontal plane, and 1T in the vertical direction. The available temperature on the sample ranges between 2.5 K and up to 500 K. A more detailed description of the system and the methods (spectroscopy, scattering and X-FMR) will be described elsewhere. Here we describe the technical design of the mechanics for the detector system and for the magnet chamber support frame.

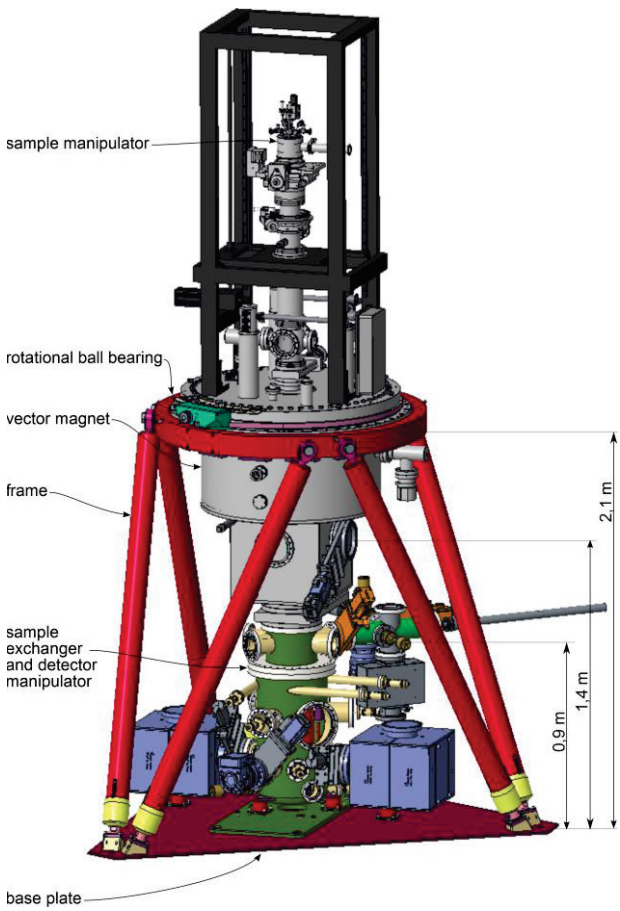


Figure 1: The VEKMAG end-station (the deposition chamber is not shown).

The superconducting vector magnet is accommodated in an individual UHV-chamber which is attached via its upper circular flange of 1 m in diameter to a rotating platform on top of a hexapod frame (s. Figure 1). This

Content from this work may be used under the terms of the CC BY 3.0 licence (© 2016). Any distribution of this work must maintain attribution to the author(s), title of the work, publisher, and DOI.

ISBN: 978-3-95450-188-5 doi:10.18429/JACoW-MEDSI2016-WEPE38

rotation is manually driven via a worm gear and a spur belt.

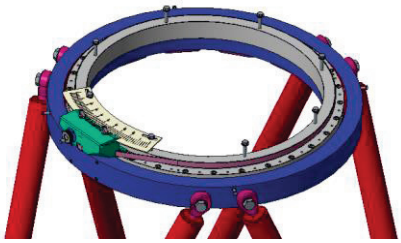


Figure 2: The rotational platform.

The outer frame bears this large ball bearing using six struts in the topology of a W-shape hexapod (Figure 2). The struts have a diameter of 115 mm, a wall thickness of 13.5 mm and are more than 2 m in length. They are attached to a 10 mm thick base plate made of aluminium using ball joints at both ends of the struts. The hexapod frame fulfils best the demanding specifications for highest stability, low vibration amplitudes and precise adjustment of the whole system. It is a result of an optimization process to obtain the stiffest structure combined with a suitable accessibility to the detector chamber. It is actually quite comfortable to work on the experiment chamber. The large top ring of the frame is on an altitude of over 2 m and on the floor it is placed only on a sheet of metal plate. So the scientist can stand direct in front of the chamber and access the rotation unit.

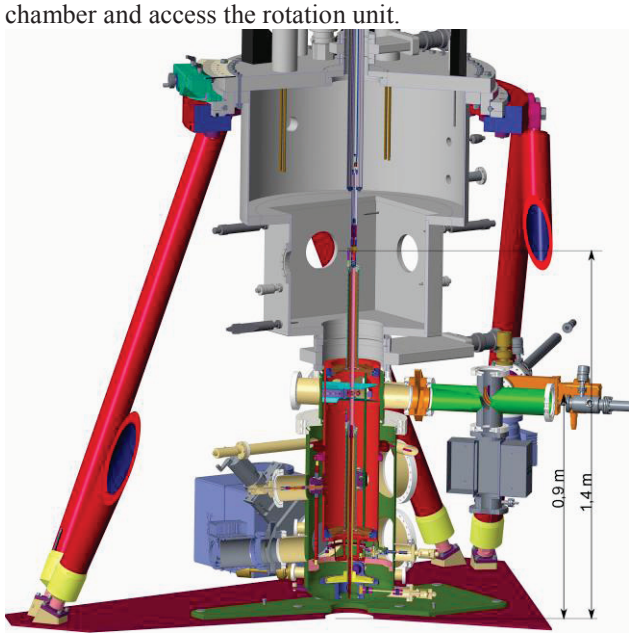


Figure 3: Section view of the end station.

A cryostat is attached to a manipulator on top of the magnet and reaches in to the centre of the magnet at 1.4 m altitude over the floor, at the beam focus location (see Figure 3). The sample exchange level is on an altitude of 0.9 m. The detector chamber is attached to the lower flange of the magnet chamber. It provides mainly two functionalities: vertical sample transfer unit and detector lift which allows for the diode detectors to rotate and translate around the sample within the magnet bore of 60 mm. The samples are brought in to the UHV chamber via a load lock and a magazine which carries nine sample supports were the samples are mounted on (see Figure 4). It is attached rigidly to a long magnetic transfer rod which translates and rotates the magazine manually. The magazine has long blades on the outside, like on Nordic ice skates to allow to slip over the openings of the chamber.

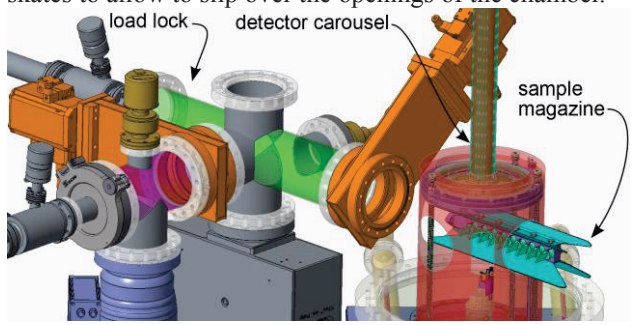


Figure 4: The sample magazine and the transfer system.

Because of the space limitations below the magnet chamber and down to the concrete floor a telescopic mechanism for lifting and screwing the sample in to the cryostat was developed (see Figure 5).

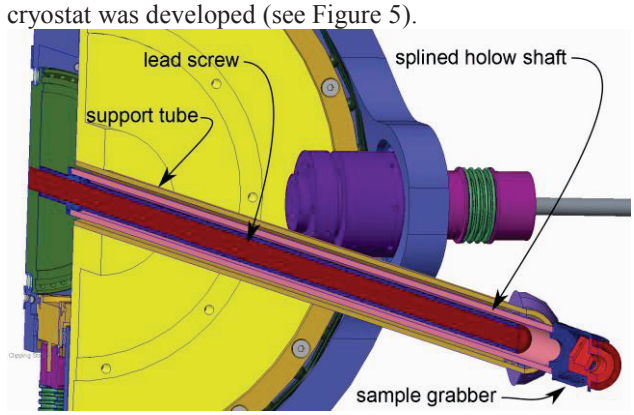


Figure 5: The sample lift.

A trapezoid lead screw made of stainless steel with a nut made of PEEK moves the sample from the magazine up to the cryostat. The rotational definition is featured by a splined shaft made of aluminium on which a hub made of PEEK slides in.

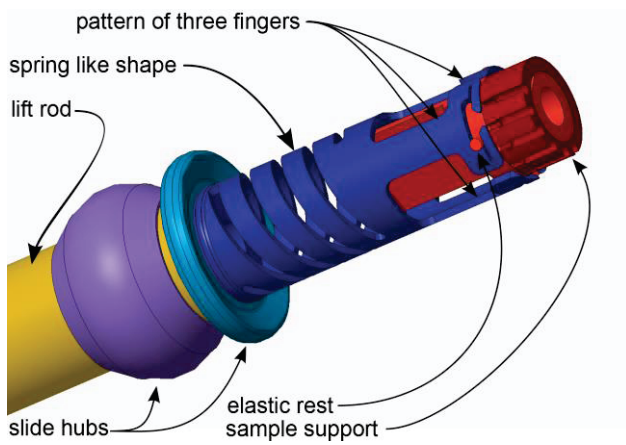


Figure 6: The grabber with a sample holder.

The sample grabber has three holding fingers with elastic clamps to keep the sample holder fixed after it is

Content from this work may be used under the terms of the CC BY 3.0 licence (© 2016). Any distribution of this work must maintain attribution to the author(s), title of the work, publisher, and DOI.

ISBN: 978-3-95450-188-5 doi:10.18429/JACoW-MEDSI2016-WEPE38

Content from this work may be used under the terms of the CC BY 3.0 licence (© 2016). Any distribution of this work must maintain attribution to the author(s), title of the work, publisher, and DOI.

screwed out of the magazine or of the cryostat head (Fig. 6). The clamping works in both left and right direction. This grabber holds the sample support while it is screwed into the threads. Because there is no axial play for the lead screw or for the cryostat, the grabber has an elastic zone consisting of a compression spring which compensates the axial deviations in the pitch of both screws (Fig. 7).

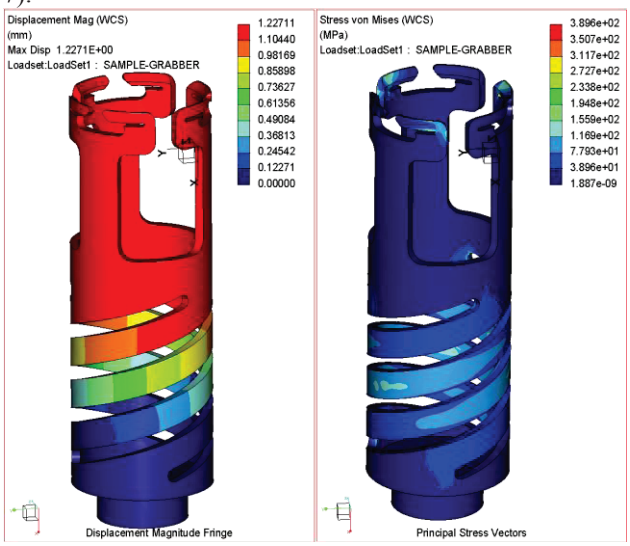


Figure 7: Sample grabber with stress representation in MPa and displacement in mm.

The detector lift and manipulation system are arranged concentric to the sample lift (see Fig. 8). Up to six detector holders can be plugged in to the detector carousel with two electrical contacts for each. A detector holder contains the detector mounted in an electrically isolated slot

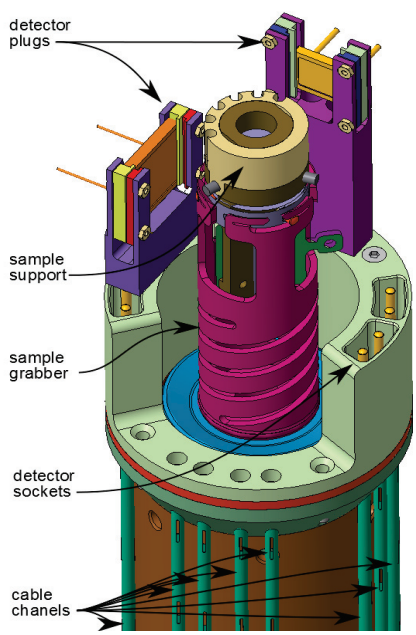


Figure 8: The detector carousel and the sample grabber holding the sample support.

where it can be fixed with screws. In front of the detector a second slot contains an aperture (a pin hole or a slit) and the third slot is used for mounting an electron filter. All three parts can be assembled in the lab and consequently just plugged into the sample carousel.

The top part of the carousel with the sockets is made of PEEK. From there the cables of the contact pins are guided through capillary tubes downwards. At the lower end of the detector lift a spiral shaped tube starts and guides the cables to a fix point from where they connect to the electrical feedthrough.

The lowest four rotational motion feedthroughs are for driving the sample grabber up and down and rotate them, and to move the detector carousel up and down and rotate them (see Figure 9).

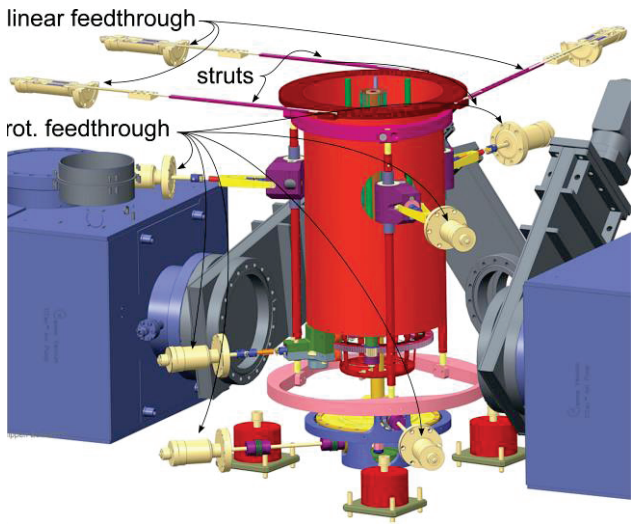


Figure 9: Kinematic structure of the detector carousel.

For the alignment of the detector carousel axis with respect to the sample and to the magnet, a dedicated Cartesian parallel kinematic platform was designed (see Fig. 9) [8], [9]. There are three vertical parallel struts with flexure fibre joints at both ends for supporting the weight of the detector unit and give a guide mechanism for the X and Y translations [10], [11]. This alignment movements are driven by three horizontal arranged linear motion feedthroughs. For one Cartesian direction the two parallel struts are working like a parallelogram and are driven by one single strut through its linear motion feedthrough. For the second translation in the transverse plane two parallel struts have to be actuated through their linear motion feedthroughs by the same travel distance.

The struts are made of aluminium hollow tubes with crimped pieces of stainless steel ropes at both ends. The stainless steel rope is a 7 x 7 cross section design of 6 mm in diameter. These short pieces of steel rope can not only bear strain load. They can also bear axial thrust load without buckling. It is very stiff in axial direction and flexible for bending and twisting in the orthogonal directions. Furthermore, it exhibits high endurance. This design of struts with flexure joints is extensively used for opto-mechanics in different facilities.

The length of the vertical struts can be modified by the three rotational feedthroughs which are attached to these struts (see Fig. 10). There is a worm gear which drives a

ISBN: 978-3-95450-188-5 doi:10.18429/JACoW-MEDSI2016-WEPE38

ferrule with left and right handed thread in a turnbuckle fashion.

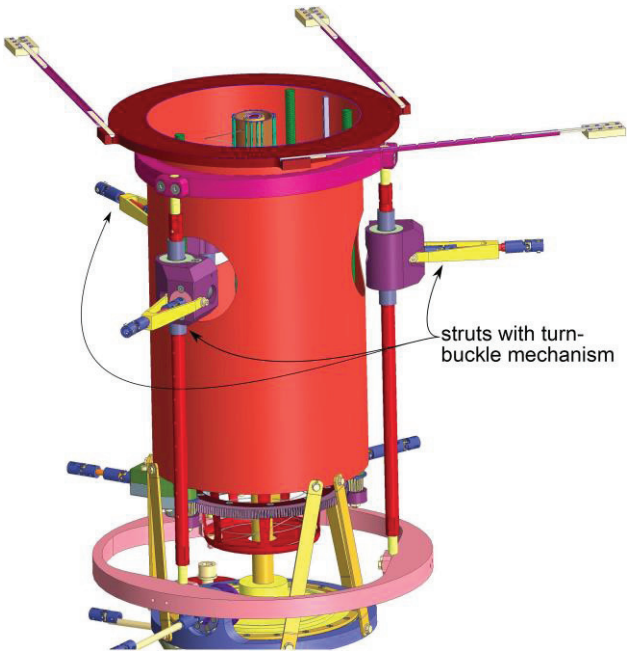


Figure10: Detector lift unit, supported by struts with flexure joints in a Cartesian parallel kinematic topology.

In conclusion, we have described the technical design of the holding frame and of the detector system which is part of the VEKMAG end station installed at the PM2 beamline (BESSY II, HZB). The hexapod frame holding the magnet and the detector chamber provides a large rotational degree of freedom, high vibrational stability through optimised stiffness, and precise adjustment capability within the X-ray beam focus. The detector system was developed to provide two functionalities, telescopic sample transfer and detector motion within a highly constrained geometrical space. The fabrication of these units where accomplished partly at the Ruhr University Bochum and at the University of Regensburg and are now in full operation.

ACKNOWLEDGEMENTS

We acknowledge discussions and help during the design, fabrication and commissioning phases with Radu Abrudan (RUB), Hartmut Zabel (RUB), Markus Hollnberger (UR), Chen Luo (UR), Christian Back (UR), Hanyo Ryll (HZB), Thorsten Wagner (HZB), Steffen Rudorff (HZB) and the whole team of the VEKMAG consortium. The financial support was provided by HZB and BMBF (05K10PC2, 05K10WR1).

REFERENCES

[1] D. Attwood and A. Sakdinawat, *X-Rays and Extreme Ultraviolet Radiation: Principles and Applications* (Cambridge University Press, October 2016)

[2] J. Stöhr and H. C. Siegmann, *Magnetism: from fundamentals to nanoscale dynamics*, Springer Series in Solid-State Sciences 152, Springer (Heidelberg, 2006).

[3] B. T. Thole, G. van der Laan, and G. A. Sawatzky, "*Strong magnetic dichroism predicted in the M4,5 X-ray absorption spectra of magnetic rare-earth materials"*, *Phys. Rev. Lett.* **55**, 2086–2088, 1985.

[4] G. van der Laan, B. T. Thole, G. A. Sawatzky, J. B. Goedkoop, J. C. Fuggle, J. M. Esteva, R. Karnatak, J. P. Remeika, and H. A. Dabkowska, "*Experimental proof of magnetic X-ray dichroism,*" Phys. Rev. B **34**, 6529–6531, 1986.

[5] G. Schütz, W. Wagner, W. Wilhelm, P. Kienle, R. Zeller, R. Frahm, and G. Materlik, "*Absorption of circularly polarized x rays in iro,*", Phys. Rev. Lett. 58, 737–740, 1987.

[6] C. T. Chen, F. Sette, Y. Ma, and S. Modesti, "Soft-X-ray magnetic circular dichroism at the _ edges of Nickel," Phys. Rev. B **42**, 7262–7265, 1990.

[7] The VEKMAG consortium includes University of Regensburg (Prof. Christian Back), Free University Berlin (Prof. Wolfgang Kuch), Ruhr University Bochum (Prof. Hartmut Zabel), and Helmholtz Zentrum Berlin (Dr. Florin Radu)

[8] T. Noll, et al. "*Parallel kinematics for nanoscale Cartesian motions*" Precision Engineering – journal of the international societies for precision engineering and nanotechnology Volume: 33 Issue: 3 Pg. 291-304 Published: JUL (2009)

[9] Patent WO 02/16092 A1 *„Device for Multi-Axis fine Adjustable Bearing of a Component"* T. Noll, W. Gudat, H. Lammert, (2001)

[10] Patent DE 100 42 801.0 *„Flexibles Gelenk hoher axialer Steifigkeit*", T. Noll, W. Gudat, (2000)

[11] T. Noll *„Flexure Joints of High Axial Stiffness* "Precision Engineering 26 (2002) Pg. 460-465

Content from this work may be used under the terms of the CC BY 3.0 licence (© 2016). Any distribution of this work must maintain attribution to the author(s), title of the work, publisher, and DOI.

ISBN: 978-3-95450-188-5 doi:10.18429/JACoW-MEDSI2016-WEPE39

FABRICATION, ASSEMBLY, AND METROLOGY METHODS TO OPTIMIZE AN ADJUSTABLE EXIT SLIT FOR A SOFT X-RAY BEAMLINE

J. Takakuwa, C. Hernikl, T. Lipton, T. Stevens, T. Warwick, LBNL, Berkeley, USA

Abstract

Exit slit edge geometry and paired edge parallelism can directly impact performance of a synchrotron beamline. At the same time, maximizing the performance of an existing design is often a financial and logistical necessity. The construction project for beamline 7.0.1 (BL7.0.1, Coherent Scattering and MICroscopy (COSMIC)) at the Advanced Light Source (ALS) facility located at Lawrence Berkeley National Laboratory (LBNL) consists of two branch lines, each of which has vertical and horizontal slit assemblies. These assemblies were fabricated from a pre-existing design, positively impacting project schedule and budget. Apart from orientation, the slit assemblies are identical. The goal for parallelism is +/- 2 microns over the full 25 mm length. Each Slit blade edge can travel +/- 5mm about the beam center with the resolution of a micron; slits can scan over that range with a nominal size of about 10 microns. A variety of fabrication and metrology techniques were implemented to maximize the performance of the current design and feature areas of improvement in fabrication, metrology, and design were identified.

INTRODUCTION

At the ALS, recently constructed beamlines 7.0.2 and 7.0.1 use eight sets of the exit slits described herein. Additionally, beamline 6.0 has five sets of similar design. In constructing new beamlines, existing designs are leveraged for the cost and schedule benefits they provide. Increasingly demanding specifications associated with new beamlines poses a challenge when leveraging these reused designs. After the construction of beamline 7.0.2, efforts were made to improve the performance of the exit slits on beamline 7.0.1 without resorting to a redesign of the assemblies themselves. These efforts resulted in varying degrees of success.

The COSMIC beamline, 7.0.1, has two branchlines and associated end stations. Each branchline uses two exit slit sets where one set confines the beam vertically and one set confines the beam horizontally. The goal was to have an exit slit parallelism of +/- 2 µm over the 25 mm length of the slit. Perpendicularity between the vertical and horizontal sets was not adjustable and resulted from the flange orientations on the welded chamber.

The blades themselves were made from OFHC copper, C10100 alloy, were paddle style blades, electrically isolated (and wired to measure current), and were water cooled for temperature stability. The blades were mounted to the end of actuators for insertion/retraction of the blades into/out of the beam to form a rectangular exit slit with adjustable dimensions and locations. Each blade signal was used in a feedback loop to steer the beam so that the position on the exit slit was consistent. The motion of the exit slit blades was not part of this feedback loop.

BLADE FABRICATION AND EDGE STRAIGHTNESS

The GD&T tolerance for the blade edge was a profile with a 1 µm tolerance zone. The initial fabrication used a fine wire EDM and were considered to be a "best effort". After cleaning, the edge was measured.

First Measurement

Metrology was performed on an Optical Gaging Products, SmartScope Quest 800 machine. Metrology software used was MeasureMind 3D v15.1

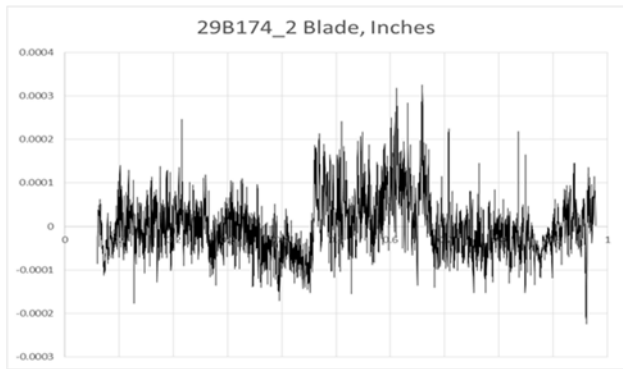


Figure 1: Typical first measurement.

Typical results (see Fig. 1) yielded a variation of the exit slit blade of +/- 2.5 µm to +/- 7.5 µm. As a result a lapping process was chosen for a secondary fabrication operation with the goal of improving the edge geometry of the blades.

Lapping Process

Simple blade fixturing maintained a consistent orientation relative to a surface plate. The blade edges were lapped using a series of graded abrasives (see Table 1). Lapping pressure and motion was done by hand by a journeyman machinist.

Table 1: Graded Abrasives

Abrasive	Grade
Roughing	1200 grit wet/dry silicon carbide
Semi-finish	3 µm (1500 grit), aluminum oxide
Finish	1 µm (2000 grit), aluminum oxide
Final Polishing	.1 µm (2500 grit), diamond

The lapping with grit paper was done by stroking repeatedly in sets of four, in one direction, at ~150 mm per second, along the direction of the blade length. Between sets, the lapped blade surface was visually inspected with a 10 X jeweler's loupe. A new area of abrasive was used after 3-4 sets of strokes. The blades were rinsed with ethanol and dried with compressed air at the time the new area of

Content from this work may be used under the terms of the CC BY 3.0 licence (© 2016). Any distribution of this work must maintain attribution to the author(s), title of the work, publisher, and DOI.

ISBN: 978-3-95450-188-5 doi:10.18429/JACoW-MEDSI2016-WEPE39

abrasive was introduced. Progressively finer grits were introduced when no change in the lapped surface was observed through the jeweler's loupe.

Cleaning Process

After lapping the blades were cleaned in the LBNL plating shop with the following sequence:

1. 909 Cleaner wash
2. Electro-polish at 130 F for < 1 minute*
3. Dip in nitric acid
4. Rinse in deionized water at 180 F

Second Measurement

The second metrology methodology was identical to the first.

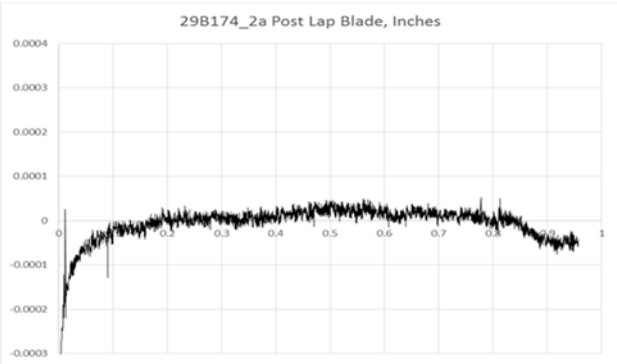


Figure 2: Typical second measurement.

The data (see Fig. 2) from 0 mm – 2.5 mm exhibited a consistent "fall-off" in the blades, indicating a greater degree of material removal from the lapping process. This was attributed to the manual lapping process as well as the asymmetric geometry of the lapped surface.

A single data point at 2.29 mm along the edge of -2.5 µm was observed in all the measurements. This point was interpreted as a digital artifact and not representative of an actual geometry and was removed in all subsequent data analysis. Other points were left in as their origin was unknown and they could have represented actual geometries of the blade edge.

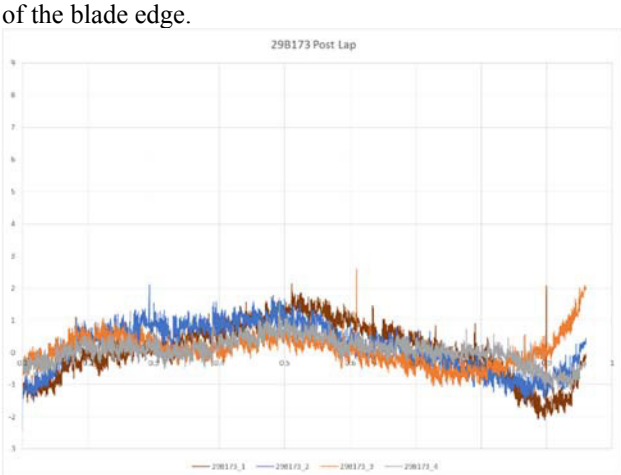


Figure 3: Second measurements for 29B173.

* The bath time ends when bubble formation is observed.

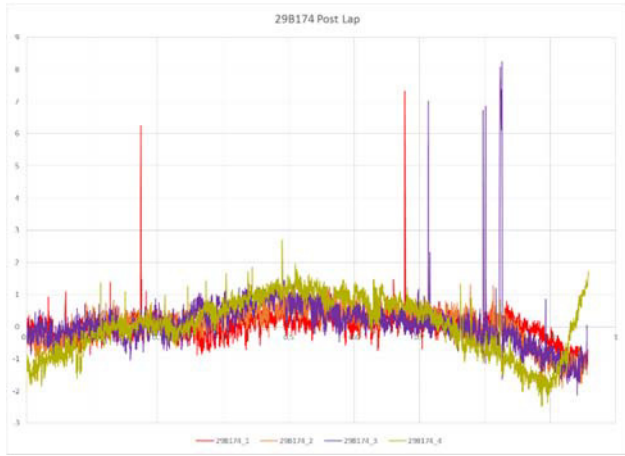


Figure 4: Second measurements for 29B174.

Excluding the "fall-off" region, the straightness measurement data for the eight blade edges had an RMS from .4 µm to 3.0 µm (see Figs. 3 and 4). It is unclear what of this was due to physical features and what was due to limits of the metrology methodology.

Edge Straightness Acceptance

The reworked edges of the blades did not fall within the specified 1 µm tolerance zone. The results of the rework were considered to be acceptable for the 7.0.1 beamline, particularly over the anticipated "short" 10 µm scan lengths.

SLIT PARALLELISM

The assembly of the slit sets were first done with conventional tools and measuring devices. The results were then measured with an optical measurement device (identical to the blade edge metrology). Iterations of adjustments were performed with feedback from metrology results.

Initial Assembly

Blade parallelism was adjusted using dial indicators. So as not to damage the blade edges themselves, indicator stylus contact was to the side opposite the blade chamfer (edge) side. This assumed parallelism between the edge and opposite side.

First Parallelism Measurements

The optical metrology device used was the same one used for the edge measurements. At 33.8 X power (optical) the parallelism of the blade edges was measured. The ends of ~2.5 mm were excluded to eliminate edge effects and limit the area of correction to the anticipated nominal working area. This left ~19.7 mm of slit length which is what is considered in all the following parallelism data. Best fit lines were created for each blade edge and these lines were adjusted for parallelism. Note, this method excluded any straightness issues with the blades.

First parallelism measurements of the conventionally assembled slit sets resulted in a range of 3 µm to 34 µm over the 19.7 mm slit lengths, compared to a specification of +/- 2 µm over 25 mm.

Content from this work may be used under the terms of the CC BY 3.0 licence (© 2016). Any distribution of this work must maintain attribution to the author(s), title of the work, publisher, and DOI.

ISBN: 978-3-95450-188-5 doi:10.18429/JACoW-MEDSI2016-WEPE39

Content from this work may be used under the terms of the CC BY 3.0 licence (© 2016). Any distribution of this work must maintain attribution to the author(s), title of the work, publisher, and DOI.

Parallelism Adjustment

Each of the four sets were adjusted on the optical metrology machine, using measurement feedback for each adjustment iteration. Due to the stick-slip inherent in the mounting of the blades, the adjustment was to a best effort. The resultant parallelism was individually assessed. Adjustment iterations were generally less than five per slit set.

Parallelism Adjustment Results

Over the ~19.7 mm slit length, the parallelism results ranged from 10 µm to 0 µm. Slit set #3 was measured to be 3 µm after the initial assembly and was not adjusted. The results were considered acceptable over the 10 µm scan length and the assemblies were installed on the beamline as is.

FUTURE DESIGN CONSIDERATIONS

Possible improvements were documented during and after the fabrication, assembly, and installation efforts of the exit slit assemblies:

1. Add symmetric "lands" about the blade at the lapping surface to eliminate the lapping "fall-off".
2. Add lapping fixture specific mounting points, symmetric about the blade for even pressure application during lapping.
3. Add flexures for parallelism adjustment, possibly from outside the vacuum envelope.
4. Find or fabricate an edge standard of known straightness and finish to use as a point of comparison for the optical metrology, particularly over the smaller scale measurements.
5. Improve measuring edge straightness and parallelism over the 10 µm scan length.
6. Include metrology after installation and vacuum loading.
7. Replace linear ball screw translation stage with a flexure for consistent blade edge insertion and retraction.
8. Add physical anti-clash hard stops.

CONCLUSIONS

It was not possible to claim that the specification of +/- 2 µm parallelism over 25 mm was achieved. However, the results of the rework were a significant improvement over the original effort. Financial and schedule impacts of a redesign were avoided. Within the constraints of a beamline construction project, this fabrication was a success. The exit slit assemblies are expected to function for the beamline 7.0.1 and were installed. Performance will be gauged during/after commissioning in early 2017.

ACKNOWLEDGEMENTS

The Advanced Light Source and this work are supported by the Director, Office of Science, Office of Basic Energy Sciences, Division of Materials Sciences and the Division of Chemical Sciences, Geosciences, and Biosciences of the U.S. Department of Energy at Lawrence Berkeley National Laboratory under Contract No. DE-AC03-76SF00098.

ISBN: 978-3-95450-188-5 doi:10.18429/JACoW-MEDSI2016-WEPE39

APPENDIX

The following Figures 5-11 show the before and after parallelism measurements for each of the four sets of slits. Units are in mm.

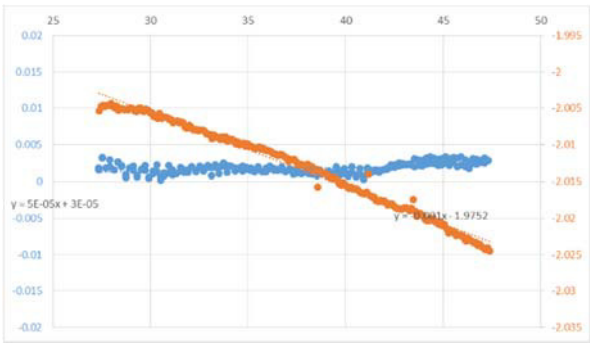


Figure 5: First measurements for Set #1.

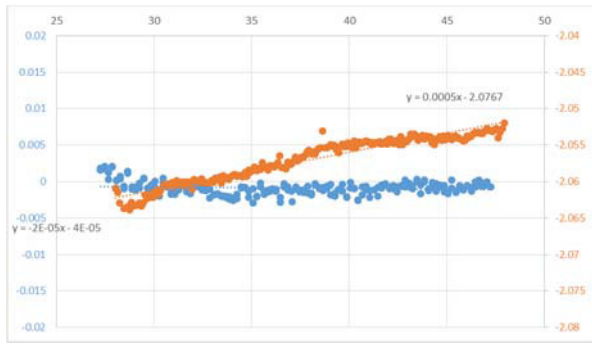


Figure 6: Second measurements for set #1.

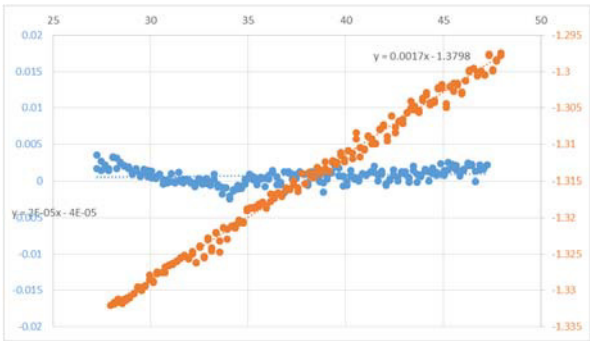


Figure 7: First measurements for Set #2.

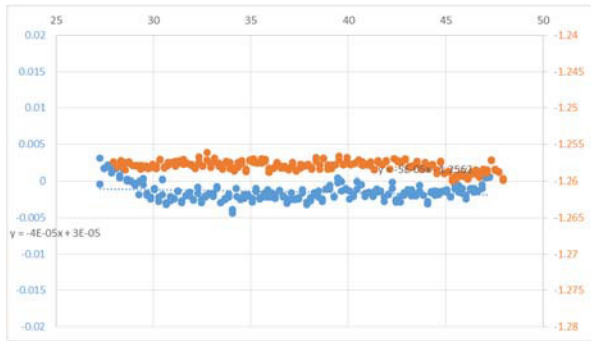


Figure 8: Second measurements for set #2.

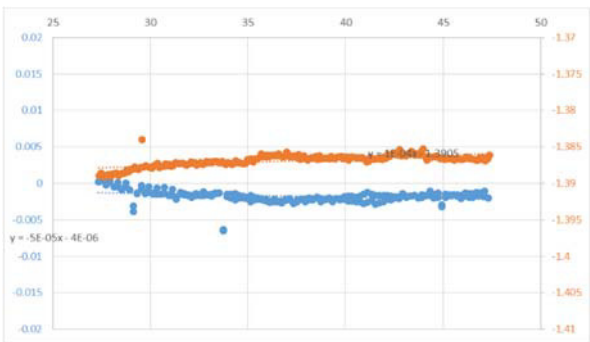


Figure 9: Only measurements for Set #3.

Set #3 was identified as having an acceptable parallelism and was not adjusted. See Table 2 for the tabular results.

Table 2: Parallelism Adjustment Results

(mm)	Preadjustment	Postadjustment
Slit# 1	0.021	**0.010**
Slit# 2	0.034	**0.000**
Slit# 3*	0.003	**0.003**
Slit# 4	0.026	**0.000**

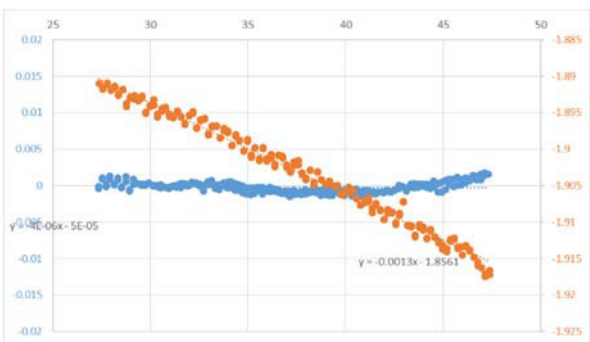


Figure 10: First measurements for Set #4.

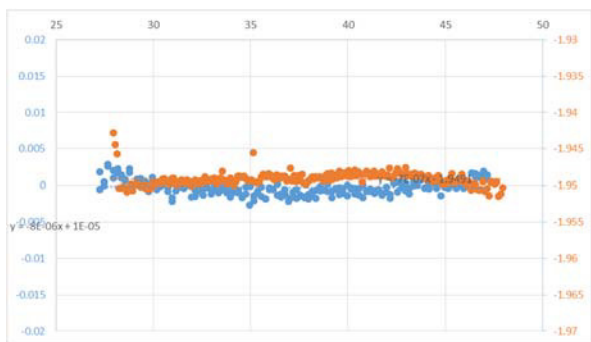


Figure 11: Second measurements for Set #4.

Content from this work may be used under the terms of the CC BY 3.0 licence (© 2016). Any distribution of this work must maintain attribution to the author(s), title of the work, publisher, and DOI.

ISBN: 978-3-95450-188-5 doi:10.18429/JACoW-MEDSI2016-WEPE40

TWO-ROTATION MECHANISM FOR AN IN VACUUM BEAMSTOP

J.B. González, C. Colldelram, A. Fontserè, G. Jover, J. Ladrera, M. Malfois, J.C. Martínez
ALBA-CELLS Synchrotron, Cerdanyola del Valles, Spain

Abstract

At Small-angle X-ray Scattering beamlines (SAXS), beamstops are needed to block the intense primary beam that has not been scattered by the sample in order to protect the detector from any damage. Beamstops are usually confined inside a vacuum tube minimizing air space between the sample and the detector. For certain experiments, a motorized beamstop is required to achieve a precise positioning in different regions of the detector active area. ALBA has developed a new motorized beamstop consisting of a two-rotation mechanism inside vacuum that composes a movement able to cover all range of the active area of the detector. The presented solution involves a main rotation reached by a gear and a worm drive actuated by a stepper motor and a second rotation relative to the main one produced by a piezo rotation stage. For each position appears two different solutions. This characteristic permits take two equivalent images in the detector with the same beamstop position but different orientation in the beamstop support; thus permitting the compensation of the support shadow on the active area of the detector.

INTRODUCTION

At SAXS beamlines, beamstops are needed to block the intense primary beam that has not been scattered by the sample in order to protect the detector from any damaged. Beamstops are usually confined inside a vacuum tube minimizing air space between the sample and the detector. For certain experiments (for example SAXS/WAXS or GSAXS), a motorized beamstop is required to achieve a precise positioning in different regions of the detector active area.

ALBA has developed a new motorized beamstop consisting of a two-rotation mechanism inside vacuum that composes a movement able to cover all range of the active area of the detector (Fig. 1), permitting for each position appears two different solutions.

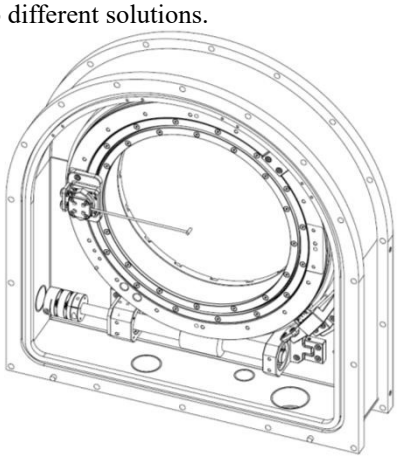


Figure 1: Beamstop main view.

TECHNICAL SPECIFICATIONS

The motorized beamstop must comply with the following specifications:

- Cover all range of the active area of the SAXS detector (210x210mm).
- Obtain two solutions for each position demanded.
- In vacuum motorized movements.
- 5µm resolution.
- 1 rpm speed.
- Compact and integrated in the current Flight Tube of the End Station.
- Mounting interface DN320 ISO-K.
- Vacuum compatible (10^{-2}mbar).

DESIGN

The complete mechanism is confined in a vacuum chamber that belongs to the vacuum flight tube between the sample and the detector. The mechanism involves a main rotation reached by a gear and a worm drive actuated by a stepper motor and a second rotation relative to the main one produced by a piezo rotation stage (Fig. 2). The vacuum chamber contains fixed supports for appropriate bearings which permit the main rotation of the axis. The relative rotation holds the beamstop support that consists of a rod usually made of a material partially transparent to the beam. Finally, the beamstop itself is mounted in the extreme of this support and consists of a cylindrical block of an opaque material to the beam.

This motorized beamstop is more compact and shows a better stability than other conventional alternatives such as linear stages due to a shorter and stiffer beamstop rod and a more packed mechanism.

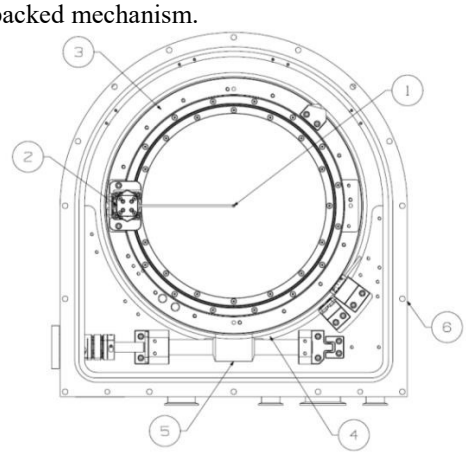


Figure 2: Parts breakdown. (1) Beamstop, (2) second rotation, (3) main rotation, (4) gear, (5) worm drive, (6) vacuum chamber.

Content from this work may be used under the terms of the CC BY 3.0 licence (© 2016). Any distribution of this work must maintain attribution to the author(s), title of the work, publisher, and DOI.

ISBN: 978-3-95450-188-5 doi:10.18429/JACoW-MEDSI2016-WEPE40

MOVEMENTS DESCRIPTION

The beamstop is moved with the relative rotation and in turn, the latter is driven by the main rotation (Fig. 3). Moving each rotation a certain angle, the mechanism covers the full active area of the detector and permits the positioning of the beamstop at any point.

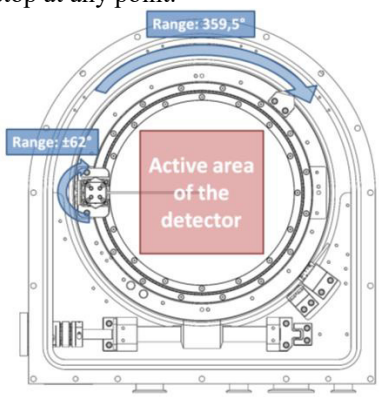


Figure 3: Movements description.

For a position of the beamstop given by the coordinates (a,b), the solutions of a system of polynomial equations of two circumferences, one with the centre in the main rotation (0,0) and the other with the centre in the beamstop position (a,b), are the two points of intersection between them. With these two intersection points it is possible to resolve the two angles for each of the two solutions (Fig. 4).

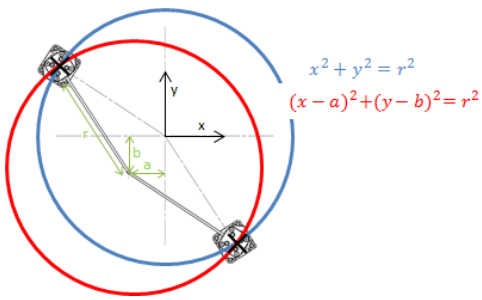


Figure 4: Polynomial equations.

At the same time, these two solutions allow to take two identical images in the detector with the same beamstop position but different orientation in the beamstop support (see example in Fig. 5).

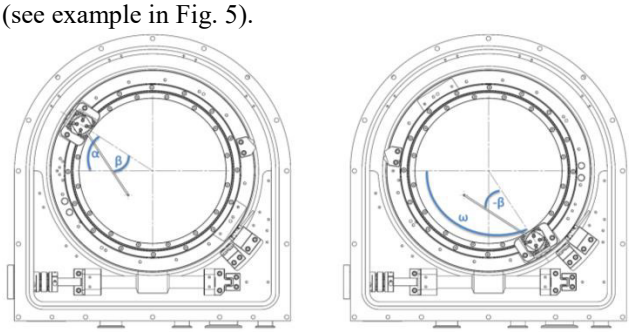


Figure 5: Two solutions for the same position.

ASSEMBLY, TESTS & INSTALLATION

The manufacturing of the parts and their assembly have been performed following high vacuum cleaning procedures (Fig. 6).



Figure 6: Vacuum cleaning procedures during assembly.

In order to test the pseudo motors (x-y movements based in the two rotation movements), a laser tracker and a prism attached to a beamstop dummy has been used. The laser tracker provided several positions of the beamstop dummy and these measurements were correlated with the theoretical position given by the equations in order to validate the control system.

Finally, the beamstop was installed in the Flight Tube section in the End Station of NCD beamline.

RESULTS

Figure 7 shows an example of two equivalent scattering patterns of the same collagen fiber with the same beamstop position but with different orientation of the beamstop support.

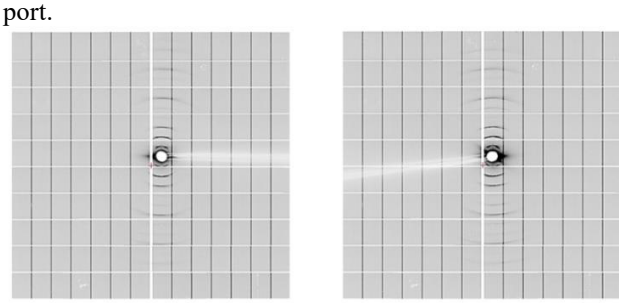


Figure 7: Two equivalent scattering patterns of the same collagen fiber.

CONCLUSION

In summary, a design of an in-vacuum motorized beamstop based in a two-rotation mechanism that composes a movement able to cover all range of the active area of the detector and permits two solutions for each position has been presented. This design has been patented under the Spanish Patent and Trademark Office and No. P201631058 [1].

ACKNOWLEDGEMENT

Authors wish to acknowledge all mostly involved in the design, construction and test: NCD Beamline Staff, Francesc Farré, Christina Kamma-Lorger and Eva Crosas; Mechanical Workshop Staff, José Ferrer, Jordi Navarro, Manuel Murcia and Oscar Borrego; Electronics Section, Bern

Content from this work may be used under the terms of the CC BY 3.0 licence (© 2016). Any distribution of this work must maintain attribution to the author(s), title of the work, publisher, and DOI.

ISBN: 978-3-95450-188-5 doi:10.18429/JACoW-MEDSI2016-WEPE40

Content from this work may be used under the terms of the CC BY 3.0 licence (© 2016). Any distribution of this work must maintain attribution to the author(s), title of the work, publisher, and DOI.

Saló; Engineering Alignment Group, Marta Llonch; Vacuum Group, David Calderón, and Lluis Ginés.

REFERENCES

[1] J.B. González & C. Colldelram, "Dispositivo de tope para haces de radiación", Spanish Patent and Trademark Office and No. P201631058, Aug. 1, 2016.

ISBN: 978-3-95450-188-5 doi:10.18429/JACoW-MEDSI2016-THAA02

MECHANICAL ENGINEERING OF A CRYO STXM AT CLS*

C. N. Regier†, A. F. G. Leontowich, D. M. Taylor, Canadian Light Source, Saskatoon, Canada

Abstract

A Scanning Transmission X-ray Microscope (STXM) is a useful imaging tool, but its application to certain types of samples is limited by significant rates of x-ray damage to the sample. Cooling samples to liquid nitrogen temperatures can delay radiation damage, but must be done in a vacuum environment to prevent rapid formation of ice on the sample. The Canadian Light Source (CLS) has constructed a Cryo-STXM, which can maintain sample temperatures at 100 K in an ultra-high vacuum environment and rotate the samples in the beam to collect tomographic data sets. This presentation will discuss the mechanical engineering aspects of the development of this Cryo-STXM including the finite element analysis (FEA) for stresses and vibrations, and present the performance parameters being achieved by the instrument.

INTRODUCTION

The Canadian Light Source (CLS) is a third-generation synchrotron located in Saskatoon, Canada. One of the Phase 2 beamlines constructed at CLS was the spectromicroscopy (SM) beamline [1], an insertion device (ID) beamline with an ID in straight 10 of the CLS storage ring. The SM beamline has been operational since 2005, however, the EPU was not installed until May 2006. Before this the beamline used upstream bend magnet radiation to operate. Two end-stations were originally included on the SM beamline: a photon emission electron microscope (PEEM) and a scanning transmission x-ray microscope (STXM) which started operation in 2007.

The SM beamline is currently undergoing an upgrade. The first phase of this upgrade is the construction and installation of a cryo-STXM. The goal is to have a STXM with sub-30 nm resolution that is capable of cryogenically cooling the sample to near liquid nitrogen temperatures, and perform tomography measurements on the sample. There are currently very few cryo-STXMs in the world, and the one at CLS is the first soft x-ray STXM capable of tomography through a 90 degree rotation in both directions. As of August 2016 the cryo-STXM is just completing its final benchmark experiments, and is now operating at the CLS SM beamline.

* Work supported by CFI, the governments of Saskatchewan, Alberta, and Ontario, and the Automotive Fuel Cell Corporation.
† chris.regier@lightsource.ca

The mechanical design phase of the cryo-STXM project presented CLS with some interesting problems. This paper will briefly discuss the SM beamline, and will present an overview of the cryo-STXM. A few specific mechanical engineering issues related to the development of the instrument are examined, and finally the performance of the cryo-STXM to date is reviewed.

THE CLS SM BEAMLINE

Figure 1 shows the layout of the SM beamline at CLS. The SM beamline uses an elliptically-polarizing undulator to supply synchrotron radiation. Downstream of the M1 mirror, a plane-grating monochromator (PGM) filters the desired energy out of the supplied spectrum. The range of energy that the SM beamline is designed to make use of is from a low end of roughly 130 eV to a high end of up to 2500 eV, placing it in the soft x-ray range.

From the PGM the beam proceeds through two further mirrors, M3PEEM and M3STXM, which split the beam and direct it down one of the branch lines. One ray proceeds through another mirror before reaching the PEEM, while the other goes directly into the existing STXM.

Table 1 shows specifications of the CLS SM beamline.

Table 1: CLS SM Beamline Specifications

Spot size (STXM)	30 nm
Spot size (PEEM)	50 nm
Energy Resolution (E/ΔE)	3000-10000
Energy Range	130-2500 eV
Wavelength	95-4.5 Å
Photon Flux (STXM)	~10^8 ph/sec in 30 nm spot
Photon Flux (PEEM)	~10^{12} ph/sec in 50 nm spot

The regular STXM is capable of several techniques, including near-edge x-ray absorption fine structure (NEXAFS) in transmission mode, total electron yield (TEY) mode, and x-ray fluorescence (XRF) mode, soft x-ray tomography, x-ray linear dichroism (XLD), x-ray magnetic circular dichroism (XCMD), and ptychography. The goal of the new cryo-STXM would be to use some of these techniques, specifically TEY and ptychography, on a sample that can be kept at cryogenic temperatures to delay radiation damage and can be rotated +/- 70 degrees in the beam for tomography.

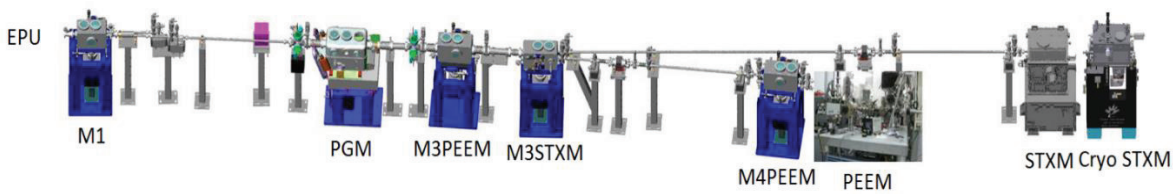


Figure 1: The layout of the SM beamline at CLS.

Content from this work may be used under the terms of the CC BY 3.0 licence (© 2016). Any distribution of this work must maintain attribution to the author(s), title of the work, publisher, and DOI.

ISBN: 978-3-95450-188-5 doi:10.18429/JACoW-MEDSI2016-THAA02

Content from this work may be used under the terms of the CC BY 3.0 licence (© 2016). Any distribution of this work must maintain attribution to the author(s), title of the work, publisher, and DOI.

STXM BASICS

There are three basic components to a STXM: the zone plate, the sample and associated sample holder, and detector. These components are shown in Fig. 2.

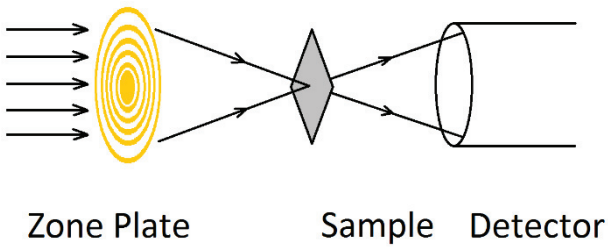


Figure 2: Fundamental components of a STXM.

The zone plate is a focusing device made of circular slits, using diffraction to create a focal point where, ideally, the sample is located. Zone plates at CLS are etched into a thin layer of gold coating a silicon nitride window, and the beam spot size is limited by the size of the etching on the zone plate. Several different types of detectors may be used. Photo-multiplier tubes (PMTs) are typically located behind the sample, while devices such silicon-drift detectors (SDDs) for x-ray fluorescence must be located to the side of the sample. The arrangement at CLS also uses an order-sorting aperture (OSA) [2] between the zone plate and sample to block zero- or higher-order radiation.

In order to place the sample in the focal point of the beam, the zone plate, OSA, sample, and detector can all be moved independently. Typically three of these components can be moved in x,y and z, while the fourth will only move in x and y, but in some cases all four can move in x,y and z. The motion of these components necessitates a significantly complex base of motion stages which, when considering that both coarse and very fine motions are desired, requires 3-axis coarse stages and 3-axis fine stages for each component.

The precision of the zone plate and the < 30 nm beam spot size means that the sample and/or zone plate must be positioned accurately. This requires feedback measurement of the sample position on the order of 3 nm or less. These types of measurements require a laser interferometer along with mirrors mounted on the sample or zone plate stage to reflect the laser signal.

The CLS STXM beam spot size of < 30 nm requires extreme stability to achieve. Vibrations with an amplitude of 15 nm will effectively move the beam spot to a completely new area of the sample between vibrational peaks and valleys. Any motion results in a "blurring" of the image or a distortion of the data collected. Vibration damping techniques are critical to realizing a clear image at small spot sizes.

THE CRYO-STXM

The design of the cryo-STXM had several design requirements. These included:

- STXM with < 30 nm resolution
- Sample cooling to near liquid nitrogen temperatures
- Ability to introduce a cold sample through a load-lock
- Sample tomography (rotation) to +/- 70 degrees or more
- Near ultra-high vacuum (UHV) or full UHV chamber to prevent ice formation on the sample
- Can also function as a conventional STXM and at atmospheric pressure.

It should be noted that this combination of requirements is unique for any device in the world [3].

From these goals a set of engineering parameters were generated. The mechanical parameters of the cryo-STXM are listed in Table 2.

Table 2: Cryo-STXM Mechanical Design Specifications

Vacuum Level	$\leq 10^{-8}$ Torr
Sample Temperature	≤ -175 C (98 K)
Vibration at Sample	≤ 5 nm RMS from 0 to 200 Hz
Zone Plate Scanning Resolution (X,Y)	≤ 1 nm
Conventional Sample Scanning Resolution (X,Y)	≤ 5 nm
Detector Stage Resolution (X,Y)	≤ 50 µm
Sample Rotation	≥ +/- 70 deg

THE CRYO-TOMO UNIT

While UHV and motion requirements are typical for modern STXM units, the unique part of the CLS cryo-STXM is the cryo-tomography capability. In a general sense, tomography is imaging using data taken from some type of penetrating wave or mechanical method. In the case of the CLS cryo-STXM, cryo-tomography is the process of rotating a cryogenically-cooled sample to various angles in the beam, taking images at these angles, and then constructing a 3-D model of the sample based on this imaging.

Cryo-tomography work has been done in the field of electron microscopy, and options exist in this field for equipment capable of both rotating a sample and keeping it cooled to cryogenic temperatures. Through contacts in the field, CLS became aware of a JEOL goniometer available from Dr. Chris Jacobson at Northwestern University. The goniometer was not in use, but had previously been part of a successful imaging end station at the Advanced Light Source. Dr. Jacobson was contacted, and graciously agreed to allow CLS to use this goniometer in the cryo-STXM. Figure 3 [4] shows a model of this goniometer.

The JEOL goniometer is capable of 2.25 mm motion in the x-direction (inboard-outboard), and 0.8 mm and 1.0 mm travel in the y- (up and down) and z- (along the beam) directions respectively. This is sufficient for fine travel scanning, however, scanning can also be done with

ISBN: 978-3-95450-188-5 doi:10.18429/JACoW-MEDSI2016-THAA02

the zone plate, meaning the goniometer would only be required to rotate or to do coarse sample moves if required. This is the standard method that will be used for cryo-tomography in the cryo-STXM. Rotational motion was tested to be +/- 90 degrees, exceeding the CLS specification.

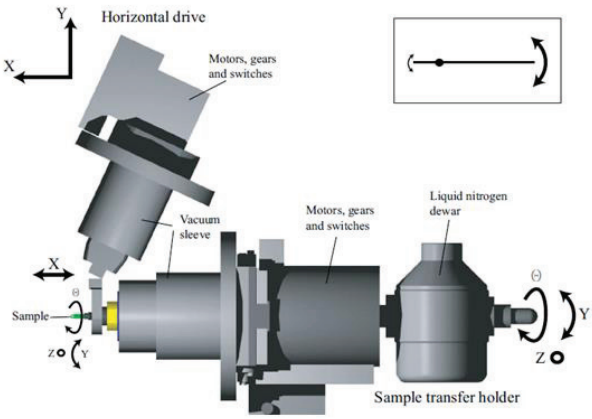


Figure 3: JEOL cryogenic goniometer.

The goniometer also contains a load-lock device, allowing introduction of cold samples into the STXM vacuum. This is done via a vacuum valve, differential pumping, and o-ring seals.

The size and shape of the JEOL goniometer dictated much about the size and shape of the vacuum chamber required. The chamber needed to accommodate the angular two-section goniometer design, and to have the appropriate space for the required stages, detectors and peripheral equipment and connections.

While the goniometer was complete, work was required to repair and upgrade the motion control. CLS undertook work to replace the motors, cables and drivers for the device before testing the motion.

DESIGN PROBLEMS AND SOLUTIONS

Positioning

The zone plate and sample motion resolutions are extremely fine, and require piezo flexure-based motion stages and laser interferometry feedback for accurate positioning. The Renishaw RLE20 was selected as the laser interferometer for sample and zone plate positioning. The RLE20 has a resolution as low as 0.39 nm, but the laser head is not vacuum-compatible so it was necessary to mount the head on the outside of the cryo-STXM vacuum chamber.

The mounting location outside of vacuum chamber makes laser pitch and yaw adjustments simple, since vacuum does not need to be broken to do these. However, there were design concerns regarding the flex of the chamber walls under vacuum relative to their positions at atmospheric pressure. This required careful analysis of the deflections of the vacuum chamber walls at vacuum pressures, and design of the chamber to ensure these deflections were not excessive. Geometric calculations showed that a deflection of 90 µm would be enough to cause problems with the interferometers, but it was agreed that a smaller deflection of less than 35 µm would be specified.

Also important were deflections of the chamber floor, to which all of the motion stages are mounted, and of the goniometer mounting locations. Large deflections here could result in alignment issues with the sample, and because the goniometer has two separate vacuum penetration points that connect inside the vacuum space misalignments could cause motion control issues and binding.

A basic ANSYS finite element analysis (FEA) was performed on the chamber to determine wall deflections. Initial results showed larger than tolerable deflections even with significant wall thicknesses, so ribbing was added to the outside of the chamber. After three or four ribbing design iterations a design was found that reduced deflections to less than 35 µm at the critical points: goniometer and interferometer mounting locations.

The ANSYS images for the cryo-STXM vacuum chamber deflection are shown in Fig. 4. Note that the red colour represents 50.6 µm of deflection, which is the maximum for the structure. Yellow-green represents deflections between 28 and 33 µm, and green represents deflections between 22 and 28 µm.

Once the cryo-STXM was constructed it was pumped down with dial-gauges in place as shown in Fig. 5 to measure deflections at the interferometer heads. The deflection at the x-head was measured at 29 µm, as compared to an ANSYS-predicted value of 28 µm, and at the y-head deflection was measured at 25 µm as compared to an ANSYS-predicted value of 15 µm. While the y-head deflection was 60% higher than predicted, this is a good demonstration of the design accuracy that can be achieved using FEA software. Both measured values are well below the required maximum, and to this point the interferometers have performed flawlessly.

Vacuum

To prevent rapid ice formation on a cryogenically-cooled sample it is important to have the sample in a good vacuum. At liquid nitrogen temperatures carbon dioxide and water will freeze out of the air onto the sample, and even gases like oxygen will liquefy on the sample. These deposits will interfere with STXM measurements.

There are several ports on the vacuum chamber, and it was important to ensure a proper seal at each one. However, the importance of the seal had to be balanced with the necessity for ease of access to the chamber interior to change samples, adjust internal settings, or perform minor repairs. For this reason, o-rings were used for the majority of the seals on the chamber ports.

To facilitate access to the stages, it was decided that an o-ring would also be used to provide the vacuum seal between the chamber and the baseplate. However, because of the length of this seal it was decided to design it as a double o-ring with differential pumping between the o-rings. Some of the larger access ports were also de-

Content from this work may be used under the terms of the CC BY 3.0 licence (© 2016). Any distribution of this work must maintain attribution to the author(s), title of the work, publisher, and DOI.

ISBN: 978-3-95450-188-5 doi:10.18429/JACoW-MEDSI2016-THAA02

Content from this work may be used under the terms of the CC BY 3.0 licence (© 2016). Any distribution of this work must maintain attribution to the author(s), title of the work, publisher, and DOI.

signed in this fashion. Conflat® flanges were used wherever regular access was not required.

After baking at 60°C for eight days, vacuum levels in the chamber have been measured to be as low as 7.7×10^{-9} Torr, better than the design goal of 2×10^{-8} Torr.

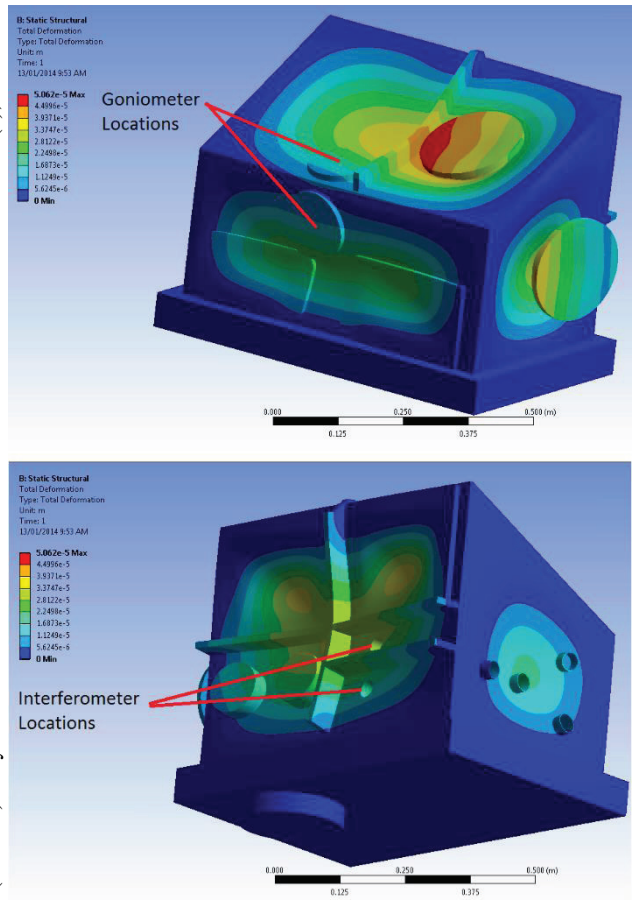


Figure 4: ANSYS results for cryo-STXM vacuum chamber deflections. The goniometer and interferometer mounting locations are indicated.

Vibration

Analyzing vibration is, at the best of times, very difficult. The specification required vibrational amplitudes of less than 5 nm root-mean-square (RMS), but during the design phase calculation of these values is complicated by the complex shape of the model and the unknowns in, or changes to the input frequency spectrum. For this reason, the design focused more on minimizing calculated vibrations rather than achieving the parameter of < 5 nm RMS.

Analysis of vibrational spectra shows that almost all of the power in a vibrational signal is realized in the low frequencies, less than 100 Hz. Standard design practices for instruments that require high vibration isolation include mounting the instrument on a concrete or zanite (polymer concrete) block. Examining the unit as a dynamic system, we can say that the block and instrument will move according to Eq. (1).

$$m\ddot{x} + b\dot{x} + kx = F \tag{1}$$

In Eq. (1), m is the mass of the block-instrument combination, b is the natural vibrational damping provided by the block-instrument system, k is the natural spring constant for the block-instrument system, F represents the applied force, and x represents the position in space of the sample point.

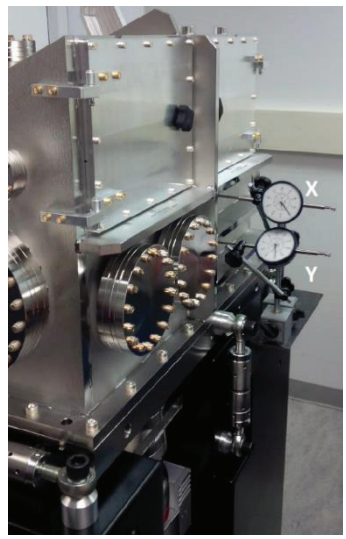


Figure 5: Dial gauges for measuring chamber deflection at the interferometer head locations.

The variables $\dot{x}$ and $\ddot{x}$ represent the velocity and acceleration of the sample point respectively. Basic dynamic analysis shows that Eq. (1) can be represented as

$$\ddot{x} + \frac{b}{m}\dot{x} + \frac{k}{m} = \ddot{x} + 2\xi\omega_n\dot{x} + \omega_n^2 \tag{2}$$

where ξ is the damping constant for the block-instrument system and ω_n is the natural frequency of the block-instrument system. It can be inferred from Eq. (2) that

$$\omega_n = \sqrt{\frac{k}{m}} \tag{3}$$

meaning the natural frequency increases with and increase spring stiffness and decreases with an increase in mass.

A dynamic system will maximize its vibrational amplitude at its natural frequency, meaning that in order to prevent vibrations at low frequencies of 0-200 Hz it is desirable to design the block-instrument system's natural frequency to be as high as possible. From Eq. (3) it can be seen that to do this, the block should be very stiff but have relatively low mass. Zanite and concrete fit this description well, since these substances are extremely hard and therefore stiff, and at densities in the neighbourhood of 2600 kg/m^3 are relatively light compared to metals. Note that Styrofoam is another material that has a relatively high stiffness to weight ratio, largely due to its extremely low weight. Styrofoam feet are used on the

ISBN: 978-3-95450-188-5 doi:10.18429/JACoW-MEDSI2016-THAA02

cryo-STXM to support the Zanite block and provide some additional cushion.

The cryo-STXM itself requires its materials to be selected for properties other than high stiffness and low mass, so in order to avoid potential areas of lower frequency resonance a modal analysis of the unit was done with ANSYS. The purpose of this modal analysis was not to calculate exact resonance frequencies but rather to look for areas with generally lower frequency resonance characteristics and determine how to design these to avoid vibration. Only one mode was found, on the DN160 vacuum valve separating the turbo-molecular pump from the main chamber that was at any frequency close to 100 Hz. Figure 6 shows this mode. The natural frequency of this mode was increased by designing a clamp to hold the valve body firmly.

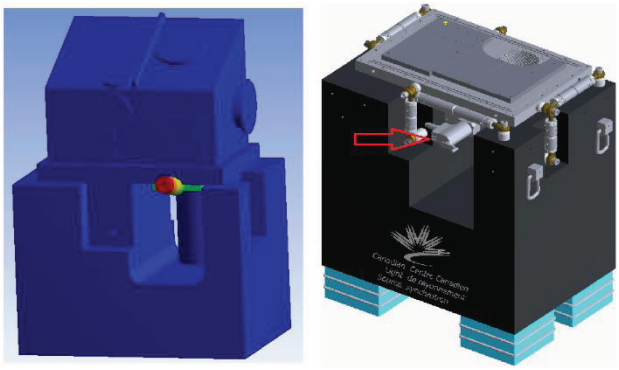


Figure 6: Lowest vibration mode on the cryo-STXM on the left. On the right is a picture of the Zanite block and STXM baseplate, with the offending valve body indicated by a red arrow.

Another aspect of vibrational design is to reduce or eliminate possible sources of vibration on the device itself. For the cryo-STXM the main sources of potential vibrations are the vacuum pumps. For scroll pumping vacuum conductance is generally not a concern, so the scroll pump was simply located at some distance from the cryo-STXM and placed off of the experimental floor. The turbo-molecular pump selected was a Pfeiffer HiPace 700M, which is a 700 L/s turbo that is magnetically levitated on five axes.

With all of these vibration considerations implemented, the Renishaw laser interferometers were used to measure the vibration of the sample stage. With the cryo-STXM on the experimental floor at CLS, the vacuum pumping in operation, and using active vibration damping via the stages, the interferometers measured a RMS vibration amplitude at the sample of less than 1 nm. This was better than the design goal of 5 nm by a significant margin.

PERFORMANCE

Figure 7 shows a picture of the cryo-STXM at CLS.

As described, the steps taken to analyse vibration and chamber deflection resulted in a design that met its goals in these parameters. However, the true test of the cryo-STXM is the imaging that it is capable of performing. Initial tests have provided images with resolutions down to 30 nm, which is the design goal and near the limit of the zone plate.

CONCLUSION

CLS has constructed a cryo-STXM capable of performing tomography on a cryogenically-cooled sample. This device is the first STXM in the world with this capability. During the design phase, careful consideration was paid to chamber wall deflections and vibration in the unit. This work resulted in a high-performance cryo-tomo-STXM that met or exceeded design goals.



Figure 7: CLS cryo-STXM on the SM beamline.

ACKNOWLEDGMENT

CLS would like to acknowledge Dr. Chris Jacobson for his help with this project, as well as our funding partners, the Canadian Foundation for Innovation, the governments of Alberta, Ontario, and Saskatchewan, and the Automotive Fuel Cell Corporation.

REFERENCES

[1] K. V. Kaznatcheev et al., "Soft X-ray Spectromicroscopy Beamline at the CLS: Commissioning Results," *Nucl. Instr. Meth.*, vol. 582, pp. 96-99, 2007.

[2] T. Warwick et al., "Development of Scanning X-ray Microscopes for Material Science Spectromicroscopy at the Advanced Light Source," *J. Synch. Rad.*, vol. 5, pp. 1090-1092, 1998.

Content from this work may be used under the terms of the CC BY 3.0 licence (© 2016). Any distribution of this work must maintain attribution to the author(s), title of the work, publisher, and DOI.

ISBN: 978-3-95450-188-5 doi:10.18429/JACoW-MEDSI2016-THAA02

[3] A. P. Hitchcock, "Soft X-ray Imaging and Spectromicroscopy," in Handbook of Nanoscopy, G. van Tendaloo, D. van Dyck, S. J. Pennycook, Eds. Weinheim, Germany: Wiley, 2012, vol. 2, pp. 745-792.

[4] T. Beetz, "Soft X-Ray Diffraction Imaging With and Without Lenses and Radiation Damage Studies," Ph.D. thesis, Phys. Dept., Stony Brook University, Stony Brook, NY, U.S.A., 2004.

Content from this work may be used under the terms of the CC BY 3.0 licence (© 2016). Any distribution of this work must maintain attribution to the author(s), title of the work, publisher, and DOI.

ISBN: 978-3-95450-188-5 doi:10.18429/JACoW-MEDSI2016-THAA03

MECHANICAL DESIGN OF NEW DUAL PINHOLE MINI-BEAM COLLIMATOR WITH MOTORIZED PITCH AND YAW ADJUSTER PROVIDES LOWER BACKGROUND FOR X-RAY CRYSTALLOGRAPHY AT GMCA@APS *

Shenglan Xu, Nagarajan Venugopalan, Oleg Makarov, Sergey Stepanov and Robert F. Fischetti
GM/CA and XSD, Advanced Photon Source,

Argonne National Laboratory, Argonne, IL60439 USA

Abstract

The GM/CA-developed, quad-mini-beam collimator [1, 2, 3], advanced rastering and vector data-collection software tools [4], have enabled successful data collection on some of the most challenging problems in structural biology. This is especially true for membrane-protein crystals grown in lipidic cubic phase, where crystals are typically small, fragile, and "invisible" when cryo-cooled. There are two main sources of X-ray scattering (besides the sample) that reach the detector, contribute to background and limit data resolution. These are scattering within the collimator that escapes the exit aperture and air-scattering of the direct beam before it terminates in the beam-stop. Scattering from the collimator can be reduced by decreasing the exit aperture size. A quad mini-beam collimator was built consisting of 5-, 10-, 20- and 150 µm beam defining apertures with 50-, 70-, 100- and 300 µm exit apertures, respectively. Previous collimators were positioned in the X-ray beam by two motorized translational motions and two manual angular adjustments via a kinematic mount. The individual beams were selected by recalling stored translational positions. The pitch and yaw angular adjustments were manually pre-adjusted to one optimal position for all four apertures. Due to reduced tolerance in the new design, aligning each of the pin-hole combinations to high-precision required motorizing both translational and angular motions. The novelty of the new mechanical design is the compactness and positional stability of the structure. The new collimator positioning system consists of three frames, four C-flex bearings, two actuators and two high precision stages. The two pairs of commercial flex bearings function as a universal joint.

INTRODUCTION

Since 2007, GM/CA has provided micro-diffraction capabilities at both 23-IDD and 23-IDB beamlines through versatile collimator systems. A robust, monolithic quad-collimator provided user-selectable beam sizes of 5, 10, 20 µm or "full beam" (~25 x ~75 µm FWHM). These quad collimators were positioned in the X-ray beam by two motorized translational motions and two manual angular adjustments via a kinematic mount. The individual beams were selected by recalling stored translational positions. The pitch and yaw angular adjustments were manually pre-adjusted to one optimal position for all four apertures (Figure 1). An active beam stop of 1.0 mm diameter is typically positioned about 35 mm downstream of the sample. A prototype collimator with 5 µm beam defining and 150 µm exit aperture was developed for scanning X-ray micro diffraction studies of tissue architecture. This collimator in combination with a 0.5 mm beam stop resulted in a 30% background reduction, prompting us to develop dual pin-hole collimators for reduced background.

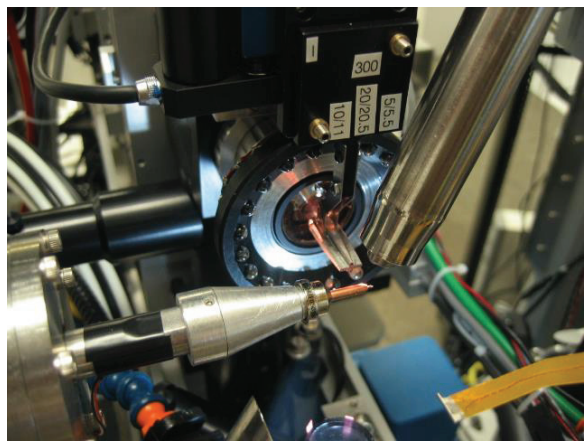


Figure 1: Close up of the Quad collimating system installed at the beamline end station. Two high resolution micro translation stages are combined to form an XY system for the collimators alignment. The travel range is 15 mm for both horizontal and vertical. The design resolution is 0.007 µm and the repeatability is 0.1 µm. The whole system stability is +/- 0.1 µm.

DUAL PIN-HOLE COLLIMATOR

Design of Dual Pinhole Collimator

The dual pinhole collimator design significantly reduces the X-ray scattering that escapes the collimator, Figure 2. The collimator assembly has a steel scatter guard body that hosts an entrance and exit sub-assembly. Both sub-assemblies consist of a steel cap and a Platinum pinhole

Content from this work may be used under the terms of the CC BY 3.0 licence (© 2016). Any distribution of this work must maintain attribution to the author(s), title of the work, publisher, and DOI.

ISBN: 978-3-95450-188-5 doi:10.18429/JACoW-MEDSI2016-THAA03

Content from this work may be used under the terms of the CC BY 3.0 licence (© 2016). Any distribution of this work must maintain attribution to the author(s), title of the work, publisher, and DOI.

aperture. The pinhole of the entrance sub-assembly acts as the X-ray beam defining aperture while the pinhole of the exit sub-assembly captures the scatter from the beam defining aperture and air scatter within the collimator body. The steel cap upstream of the beam defining aperture prevents back scatter from escaping the collimator body, while the steel cap down-stream of the exit aperture further reduces the scatter escaping the collimator.

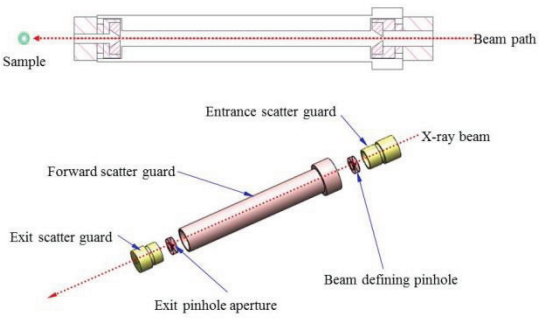


Figure 2: GMCA dual- pinhole mini-beam collimator assembly.

Quad Mini-beam Collimator with Dual Pinhole

The dual pinhole concept was incorporated into a quad, uni-body collimator, Figure 3. The collimator includes four sets of pinholes. Three sets are for mini-beams and one trims the full beam in the horizontal direction to allow a 0.5 mm diameter beamstop to be used. The history of the development of the GMCA quad collimator is illustrated in Figure 4.

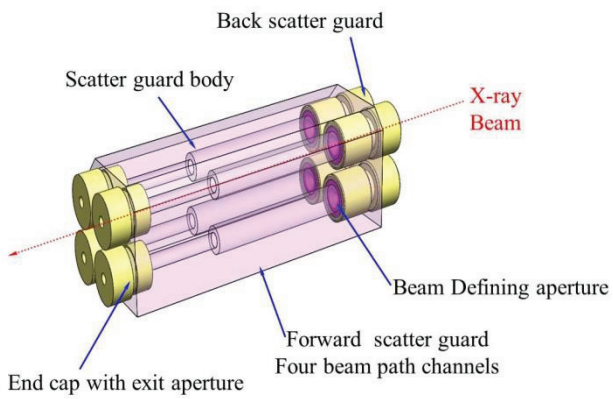


Figure 3: GMCA Quad - dual- pinhole Mini-beam Collimator Assembly.

Table 1: Dual Collimator Pinholes

Collimator	Beam Defining Aperture (μm)	Exit-pinhole Aperture (μm)
1	5	50
2	10	70
3	20	100
4	150	300

Development of the Design of Quad Collimator on GMCA Beamlines

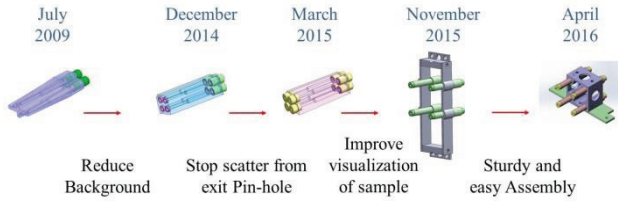


Figure 4: Development history of GMCA quad mini-beam collimator.

COLLIMATOR POSITIONING WITH MOTORIZED PITCH AND YAW ADJUSTER

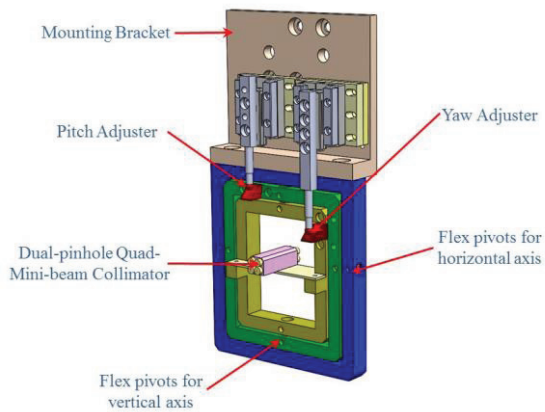


Figure 5: Schematic diagram of the assembled new dual pinhole mini-beam collimator with motorized pitch and yaw adjuster. Backscatter guards with pinholes are inserted in the square-shaped scatter guard. The exit holes are smaller for mini beams. The pinhole selects the central part of the focused beam.

Collimators with small exit apertures require not only X and Y translations to select a particular beam size, but also adjustment of the pitch and yaw angles to center the exit aperture. This necessitated developing a new collimator positioning system with motorized pitch and yaw adjustments, a 3-D model of the collimator positioning system is shown in Figure 5 and two prototype quad collimator assemblies have been built and installed (Figure 6) It consists of: three frames, four C-flex bearings, two actuators and two high precision stages. The two pairs of commercial flex bearings function as a universal joint. The motions of this universal joint are manipulated about the vertical and horizontal axes by two high precision SmarAct actuator stages. Four dual- pinhole collimators are mounted on a block that in turn is mounted on the internal frame. The block's center coincides with the intersection of the two rotation axis resulting in pitch and Yaw motions. The novelty of the new mechanical design is the compactness and positional stability of the structure.

ISBN: 978-3-95450-188-5 doi:10.18429/JACoW-MEDSI2016-THAA03

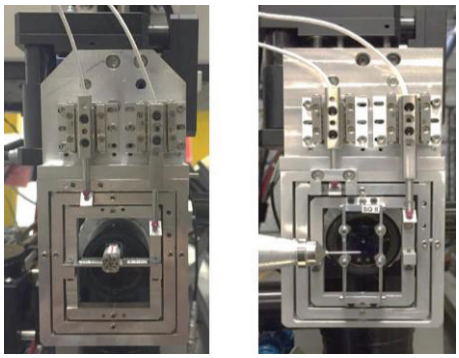


Figure 6: New quad mini-beam collimators installed on the GMCA ID stations. The one on the left is on the ID-B station and the other is on the ID-D station.

MINI-BEAM COLLIMATOR WITH SMALL EXIT APERTURES PROVIDES LOWER BACKGROUND

A quad mini-beam collimator was built consisting of 5-, 10-, 20- and 150 µm beam defining apertures with 50-, 70-, 100- and 300 µm exit apertures, respectively. Background diffraction patterns (no sample) were systematically recorded for various aperture combinations, and the scattered intensity was radially integrated from the origin to the edge of the pattern, and normalized by the number of pixels.

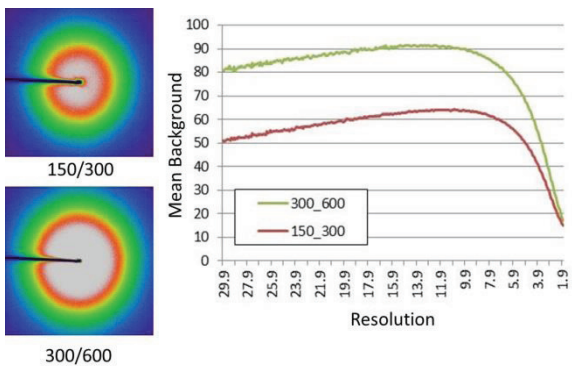


Figure 7: Full beam with different beam defining/exit aperture combination.

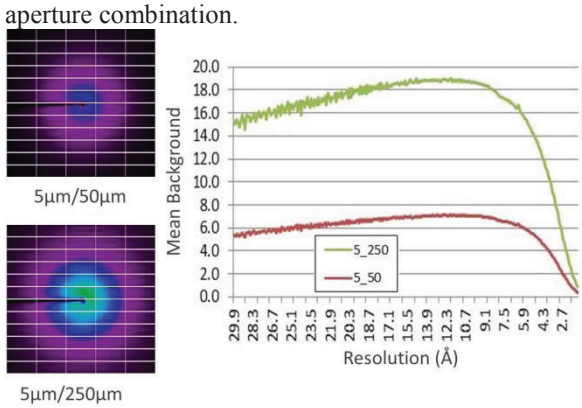


Figure 8: Background scatter for 5µm beam defining aperture.

The 150/300 (beam defining/Exit pinhole aperture) collimator had 27% less background compared to the 300/600 collimator (Figure 7), while the 5/50 collimator had 60% less background compared to 5/250 collimator (Figure 8).

A prototype collimator system consisting of 5µm beam defining apertures with varying exit apertures was constructed to estimate the extent of background reduction; the result is graphically represented in Figure 9. The graphs show a systematic reduction in background across all resolution as the size of the exit aperture was reduced for a 5µm beam defining aperture.

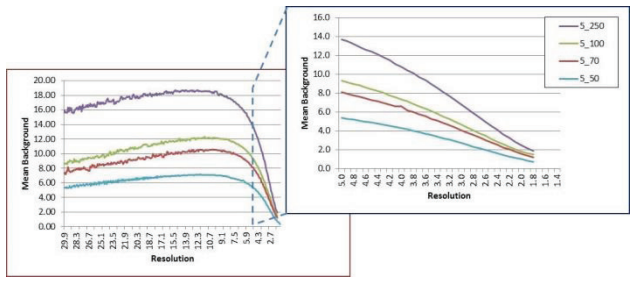


Figure 9: Graphical representation of background scatter for 5µm beam with varying exit apertures.

ACKNOWLEDGMENT

GM/CA@APS has been funded in whole or in part with Federal funds from the National Cancer Institute (ACB-12002) and the National Institute of General Medical Sciences (AGM-12006). This research used resources of the Advanced Photon Source, a U.S. Department of Energy (DOE) Office of Science User Facility operated for the DOE Office of Science by Argonne National Laboratory under Contract No. DE-AC02-06CH11357

REFERENCES

[1] Fischetti, R.F., Xu, S., Yoder, D.W., Becker, M., Nagarajan V., Sanishvili, R., Hilgart, M.C., Stepanov, S., Makarov, O. and Smith, J.L. (2009) Mini-beam collimator enables micro-crystallography experiments on standard beamlines. JSR 16, 217-225 PMCID 2725011.

[2] Shenglan Xu, Oleg Makarov, Richard Benn, Derek W. Yoder, Sergey Stepanov, Michael Becker, Stephen Corcoran, Mark Hilgart, Venugopalan Nagarajan, Craig M. Ogata, Sudhir Pothineni, Ruslan Sanishvili, Janet L. Smith, and Robert F. Fischetti;" Micro-Crystallography Developments at GM/CA-CAT at the APS" AIP Conference Proceedings 1234, 897 - 900 (2010).

[3] Shenglan Xu, Venugopalan Nagarajan and Robert. F. Fischetti "Design and manufacturing of mini beam Collimators for Macromolecular Crystallography at the GMCA CAT at APS" Diamond Light Source Proceedings, Vol 1, e27, page 1 of 4 (Nov.01, 2010).

[4] Hilgart MC1, Sanishvili R, Ogata CM, Becker M, Venugopalan N, Stepanov S, Makarov O, Smith JL, Fischetti RF. "Automated sample-scanning methods for radiation damage mitigation and diffraction-based centering of macromolecular crystals J Synchrotron Radiat. 2011 Sep;18(Pt 5):717-22. doi: 10.1107/S0909049511029918. Epub 2011 Jul 29.

Content from this work may be used under the terms of the CC BY 3.0 licence (© 2016). Any distribution of this work must maintain attribution to the author(s), title of the work, publisher, and DOI.

ISBN: 978-3-95450-188-5 doi:10.18429/JACoW-MEDSI2016-THAA04

Content from this work may be used under the terms of the CC BY 3.0 licence (© 2016). Any distribution of this work must maintain attribution to the author(s), title of the work, publisher, and DOI.

UPGRADING A TRANSMISSION SAX/WAX BEAMLINE TO ALLOW HIGH QUALITY GISAX/GIWAX EXPERIMENTS FOR SOFT MATTER THIN FILM

A. R. Marshall*, Diamond Light Source, Didcot, UK

Abstract

The project required a sample environment to deliver experiments in vacuum or helium, with high humidity, including capacity to use aggressive solvents. The compact, transportable system incorporates a high precision in-vacuum manipulator/ positioning stage (with repeatability better than 1 µm/ 1 mdeg) allowing for multiple sample configurations. Current sample mounts include in-situ film formation (Doctor Blade), thermal annealing/drying heater stage, sample cooling and multiple sample stages; the system has been designed to accommodate many sample substrate formats. The existing end station camera system has been upgraded to include two, in-vacuum, WAXS and SAXS area detectors, which are custom builds based on the Pilatus 6M. The SAX detector module includes three in vacuum, independent ,configurable SAXS beam stop manipulators to block GISAXS transmitted, reflected and specular flare as well as isotropic and anisotropic SAX, a photon sensitive detector shutter plate is included. The 4 mm diameter tungsten beam stops each include a miniature photodiode to measure beam intensity and can be positioned to within 10 µm precision in X and Y over 300 mm x 250 mm motion range.

I22 EXISTING CAPABILITIES

I22 [1] is an insertion device beamline operating at diamond since 2007. The beamline (see Fig.1) is dedicated to Non Crystalline Diffraction including small angle and wide angle x-ray scattering. The beam transmitted through samples in bulk form. Small angle X-ray scattering (SAXS) is a technique that is used to probe the internal structure of condensed matter systems at the micron and nanometre length scales. The Wide Angle X-ray scattering (WAXS) technique measures length scales on the order of Angstroms, and is typically dominated by diffraction processes, suited to study the close chain packing of semi-crystalline polymer chains within polymer blend films. The end station consisted of a 1D WAX camera and a 2D SAX camera of variable length from 800 mm up to 10 m. A single fixed beam stop, with built-in diode, measures beam intensity and blocks the transmitted beam. This paper discusses the changes made and features added to add high quality GISAXS functionality to this beamline.

THE GISAXS UPGRADE

The scope of the project was to replace hardware and reuse existing infrastructure. This limited the work to a GISAXS sample environment and positioning system, and a new SAXS detector module to deliver the greater motion ranges required by GISAXS, with a new motorized beam stop module. The upgrade was combined with replacing the ageing 1D WAX detector with a 2D in vacuum WAX detector.

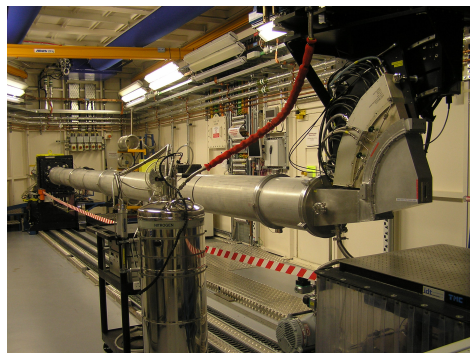


Figure 1: Original camera.

GISAXS Functionality

In transmission Small Angle X-ray Scattering (SAXS) the data is based around the axis of the transmitted beam with the elastic scattering pattern perpendicular to, and centred, on the axis of the primary beam. The technique is used to measure bulk samples where the interaction of the beam with the sample is determined by the size of the beam (≈300 µm × 100 µm) and the sample thickness which range from hundreds of microns to several millimetres. Grazing Incidence

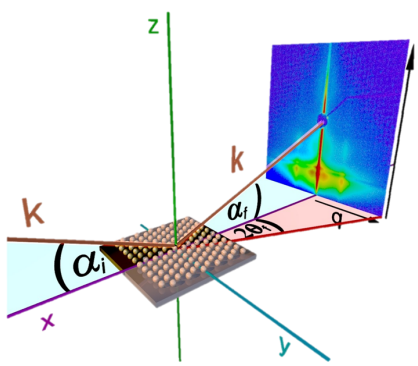


Figure 2: GISAXS theory,GISAXS Image courtesy of Dr Andreas Meyer [7].

Small Angle X-ray Scattering (GISAXS) is based on reflection geometry with the scattering pattern based around the reflected beam axis. It is intended to measure thin films cast on flat substrates. Typical film thicknesses are in the nanometer range and operating at the grazing incidence angles allows

* andrew.marshall@diamond.ac.uk

ISBN: 978-3-95450-188-5 doi:10.18429/JACoW-MEDSI2016-THAA04

for increased length scales of beam/sample interaction, additionally other signals are generated that provide information about sample surface to environment and sample surface to substrate interfaces.

Sample System Design

It was chosen to design a specific, self-contained, GISAXS sample system. This has the capability of positioning GISAXS sample surfaces, oriented vertically (horizontal plane reflection) or horizontally (vertical plane reflection). The vertical orientation allows for in-situ dip cast films, the horizontal allows for ex-situ cast films and in-situ spread and spin coated samples. Sample environment is designed to allow for medium vacuum (1×10^{-4} mbar), a helium atmosphere or helium with humidity and helium with solvent vapour, the helium and vacuum being necessary to reduce parasitic scatter of the beam. To accommodate the vacuum function with such flexible sample arrangements it was felt necessary to enclose the entire system in a vacuum vessel. To prevent cross contamination between the sample manipulator stack and the sample volume the vessel was split into two chambers with a flexible motion feedthrough linking the two. The differential pressure between the two chambers is controlled to within 2 mbar by the pumping system, with pressure relief valves that vent the chambers if higher pressures (0.4 bar) occur. Note that system sat on the existing sample table, limiting the maximum mass of the system to 150 kg.

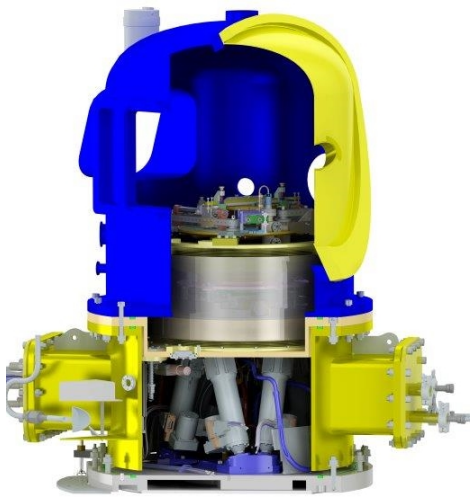


Figure 3: Sample System concept.

Motion Stack

For GISAXS measurement the sample must be positioned very precisely to the beam; once aligned, the sample has to be rotated about a point on its surface. The motion requirements are shown in table 1.

The entire sample manipulator stack is based on a custom built medium vacuum compatible (1×10^{-4} mbar) hexapod which is topped with a linear lateral stage which moves the sample surface across the beam to scan the surface in case of beam damage. The motion is transferred into the upper vessel via a support post. The flexibility for the six degrees of motion is provided by a pair of bellows mounted on bearings with rotary seals. At the top there is an interface for mounting various sample holder arrangements, including a breadboard.

Table 1: Motion Specifications

Translation	**range**	**resolution**	**repeatability**
Height	±20 mm	1.0 µm	0.5 µm
Lateral	±2.5 mm	1.0 µm	1.0 µm
Longitude	±2.5 mm	1.0 µm	1.0 µm
Lat.scan	±20 mm	1.0 µm	1.0 µm
Rotation	**range**	**resolution**	**repeatability**
Pitch	±140 mrad	17.4 µrad	17.4 µrad
Roll	±140 mrad	17.4 µrad	17.4 µrad
Yaw	±140 mrad	17.4 µrad	17.4 µrad

Hexapod was designed and built by Symetrie [4] delivering sub-micron and millidegree precision at the sample position. The control system has two fixed machine coordinate systems plus two programmable coordinate systems, this allows the sample surface to align precisely to the beam and users to control the position and orientation at the sample surface relative to the beam. The additional linear stage placed on the moving table of the hexapod allows the sample surface to move laterally without losing alignment and maintaining the programmed coordinate systems.

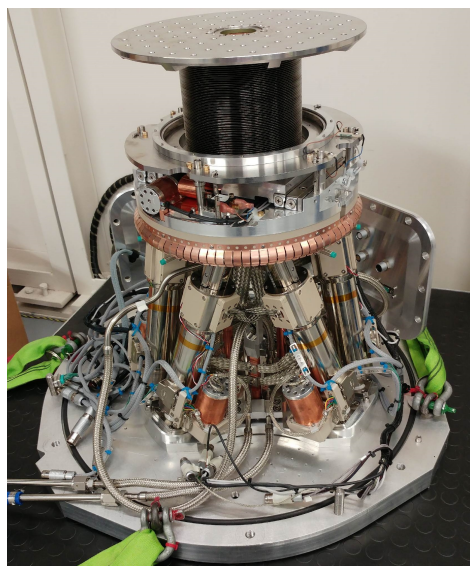


Figure 4: GISAXS ManipulatorStack.

Motion Stack Cooling

Temperature stability was addressed using invar for the hexapod legs and the sample support pillar, the hexapod drive motors are thermally isolated from the legs internal water cooling circuit, all seven motors and encoders plus

Content from this work may be used under the terms of the CC BY 3.0 licence (© 2016). Any distribution of this work must maintain attribution to the author(s), title of the work, publisher, and DOI.

ISBN: 978-3-95450-188-5 doi:10.18429/JACoW-MEDSI2016-THAA04

Content from this work may be used under the terms of the CC BY 3.0 licence (© 2016). Any distribution of this work must maintain attribution to the author(s), title of the work, publisher, and DOI.

each part of the support structure above the hexapod are thermally linked to the cooling system using copper braids or copper foil laminations. The cooling system goes on to a heat exchanger at the top of the sample manipulator stack in the upper vessel. Enabling a thermal anchor for the different sample mounts. Additionally the vessel baseplate

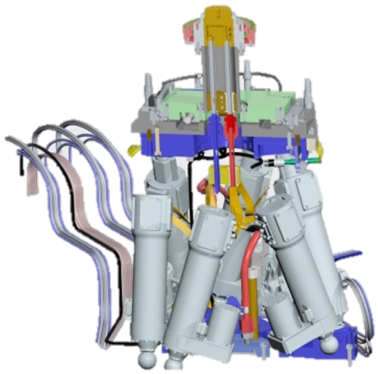


Figure 5: Manipulator Stack Cooling.

was designed carefully to avoid passing on vacuum forces to the manipulator stack by having a thin membrane to distort freely without disturbing the hexapod mountings

Sample Substrates

The sample substrate defines the sample quality; surface roughness causes diffuse scattering which affects the signal data significantly and inadequate flatness causes serious problems with alignment and contamination of data
Silicon wafers were specified for standard substrates as they are easily available with good flatness and surface roughness. Various formats are accommodated in the design, ranging from 25 mm rounds and squares, up to 100 mm rounds, with thickness ranging from 0.5 mm to 5.0 mm (some surface film coating techniques such as spin coating can lead to a thin substrate distorting as the film contracts). Additionally other materials are possible such as glass, although the critical angle of the material should be greater than that of the sample. In each case the substrate mounting must be designed to accurately locate the substrate without distorting it, and be simple to operate. Typically all the samples sit on flat surfaces with lateral position defined by two points of contact and a very light spring load. As well as substrates a sample alignment tool has been made to assist with initial beam alignment, it uses the same location features as the samples.

Sample Holder – Doctor Blade, Annealing Stage

The doctor blade annealing stage was designed to position the sample substrates in the beam and allow for fresh films to be applied in situ. The system uses spreader bar to cast the film onto the substrate, and can heating the substrate up to 250 °C to anneal or dry the sample. Substrates sit on an 85/15

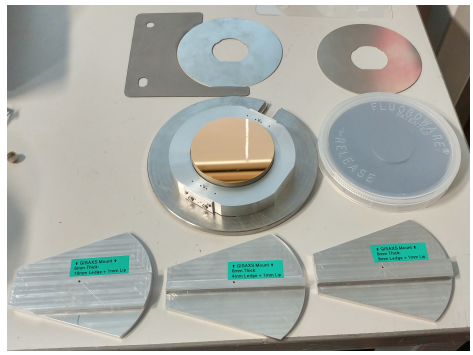


Figure 6: Sample holders and alignment tool.

tungsten copper plate, which combines high conductivity with stiffness, hardness and stability. The substrate mounting surface is lapped flat to 1 micron and Nickel plated. Beneath is clamped a 1.8 kW silicon nitride ceramic heater with a gas cooling matrix [5], the heater has excellent temperature uniformity and is larger than the maximum substrate size in order to keep the sample temperature uniform. The whole assembly sits on three height adjustable pillars topped with drilled Zirconia balls resting in Vee grooves, the interface point is located to neutralise heater plate expansion. The heater plate is very well insulated from baseplate by the balls (small contact area and low conductivity) this reduces the heat load to the internal cooling, and keeps the heat change in the support structure to a minimum. The baseplate assembly is thermally linked to manipulator stack cooling circuit. The Doctor Blade is a wire wound bar which spreads liquids into a uniform film across the substrate in a single stroke; a ramp lifts it clear of substrate at the end of stroke. The bar sits on a self-aligning carriage which runs along two stainless steel shafts using Iglide X bearing bushes. The Carriage is driven via a continuous stainless steel belt drive running around pulleys. A motor drive is encased in vacuum vessel to protect it from solvents and humidity and to prevent contamination of the sample volume.

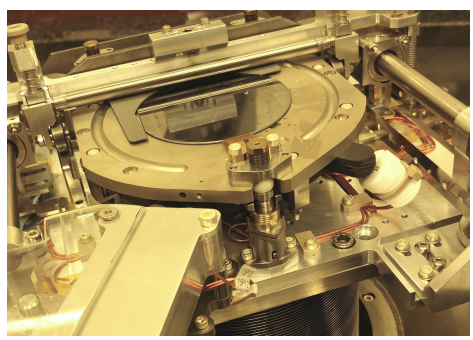


Figure 7: Dr Blade System.

IN-VACUUM AREA WAXS DETECTOR

The new WAX detector provides 2D WAX data, it is based on the Pilatus 2M [6] modified for use in vacuum (modules moved into a vacuum vessel, electronics remain in air). Ad-

ISBN: 978-3-95450-188-5 doi:10.18429/JACoW-MEDSI2016-THAA04

ditionally the detector has three modules removed to allow the SAXS data to pass through to the SAXS detector further downstream. The system is mounted to the original gantry

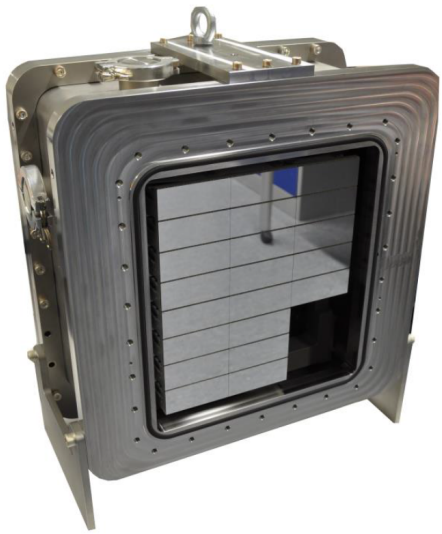


Figure 8: WAXS Detector [3].

system but has X and Y motions to position the detector in the appropriate position relative the data being collected. The rear of the detector interfaces to the SAX camera tube via a large gate valve (essential to maintain vacuum during camera length changes) and the bellows support by a gimbal which allows independent SAXS camera articulation. For GISAXS the detector is fitted with a large reinforced Kapton window [2] – otherwise there are various nosecone adapters for transmission SAXS/WAXS experiments.

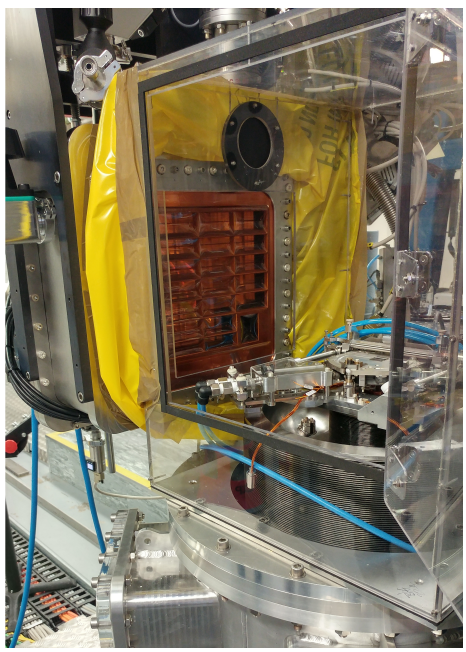


Figure 9: WAXS Detector in He.Trials.

GISAXS BEAMSTOPS

For the GISAX detector up to three beam stops are required to block transmitted beam and overspill , the reflected beam and specular flare, which would otherwise damage the detector. Each beam stop is required to be positioned at any point over the SAX detector area. The stops can have a silicon PIN diode fitted, or are isolated, shielded and connected to current amplifiers, so that photon/drain current can be measured. This generates useful transmitted beam intensity information that can be useful in data analysis and greatly assists beam stop alignment. the specular flare stop comprises a tungsten rod mounted on a rotary stage which allows for angular adjustment. The beam stop must be big enough to stop the transmitted beam and small enough to maximise the observed scattering intensity at very low angle, in this case the beam stops are 4 mm diameter10. Each tungsten beam stop is suspended by a combination of polyamide filaments and thin Kapton foils that are near-invisible on the detector and giving 360° of data collection. A pair of gold conductors connects the diode to the instrumentation.

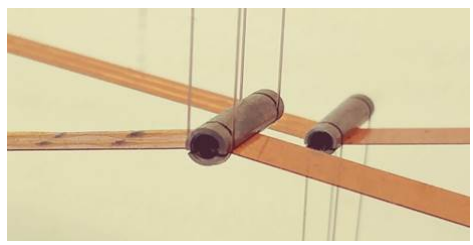


Figure 10: Beam Stops.

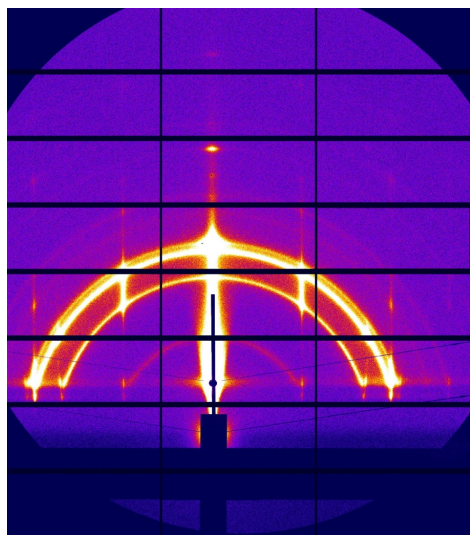


Figure 11: GISAXS image showing beam stop shadows.

Beamstop Vessel Assembly

The beam stops are mounted in module frames that locate inside a vacuum vessel (1×10^{-4} mbar) which is located in front of the SAX detector. There are three independent X Y stages inside the vessel that accommodate a module

Content from this work may be used under the terms of the CC BY 3.0 licence (© 2016). Any distribution of this work must maintain attribution to the author(s), title of the work, publisher, and DOI.

ISBN: 978-3-95450-188-5 doi:10.18429/JACoW-MEDSI2016-THAA04

Content from this work may be used under the terms of the CC BY 3.0 licence (© 2016). Any distribution of this work must maintain attribution to the author(s), title of the work, publisher, and DOI.

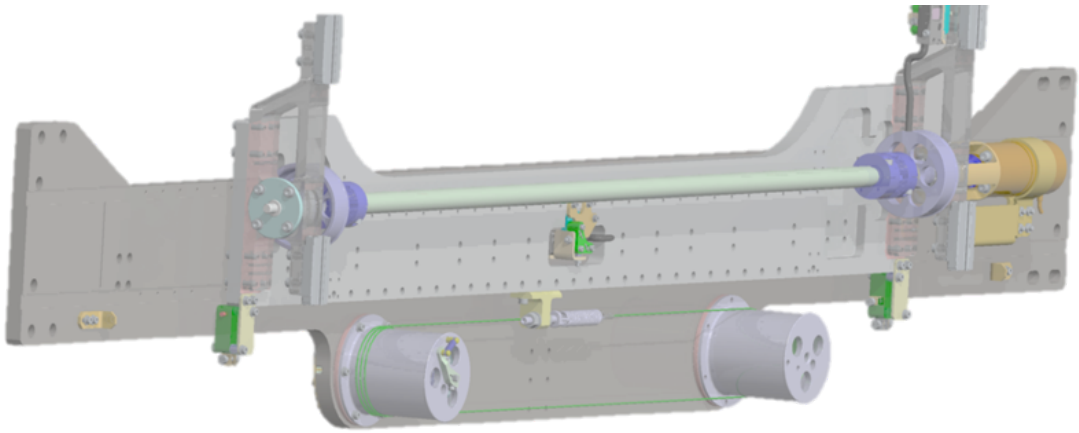


Figure 12: Beamstop actuator.

each. Each beam stop module can be loaded from outside the vessel through a rectangular flange. For GISAXS the beam stops include a large transmitted beam stop, a small reflected beam stop and rod specular reflection stop, for transmission SAXS only one beam stop is necessary. Also mounted on the vessel back plate is a photon shutter plate designed to isolate the SAXS detector face until the beam stops have been aligned. The plate is also configured to collect drain current, this signal is interlocked to prevent the shutter opening when the SAXS detector is in danger of damage. The shutter motion uses a crank slider mechanism actuated from outside the vessel using a pneumatic actuator via a magnetic rotary feed through.

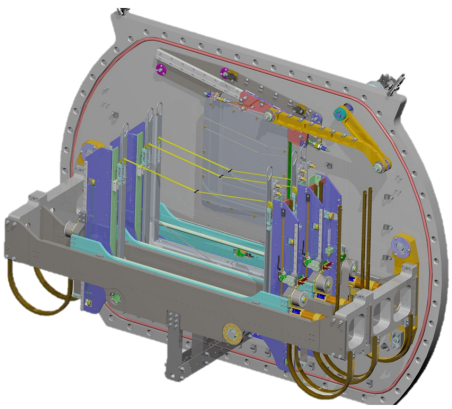


Figure 13: Internal mechanisms on vessel baseplate.

Beamstop Drives

The X Y drives have a range of 300 mm vertical by 252 mm horizontal to enable a beam stop to be positioned anywhere in front of the detector active area. The motions are actuated by capstan driven cable drives, where a preloaded drive cable is wound around a motorised cylindrical drum. The friction of the cable around a cylindrical drum T_2 is calculated using the capstan equation $T_2 = T_1 e^{\mu\beta}$ where T_1 is the tension in the cable, μ is the coefficient of friction and β is the total angle of cable contact.

For the X drive (horizontal) the cable attaches to the driven stage, runs 2.5 times around a driven drum then back around an idler drum before attached to the driven stage via a preload spring. For the Y drive (vertical) uses twin cable drive to prevent crabbing, the cables attach at the top and bottom of driven stage, with a spring preload and run 2.5 times around driven drums mounted on a shaft. See Figure 12 for arrangement. Each drive is equipped with linear encoders and a static low speed positioning accuracy of 0.01mm. However the low actuator stiffness limits the dynamic precision to around 0.1mm. These drives are low cost, light weight and compact and vacuum compatible.

SAXS DETECTOR TABLE

The beam stop vessel and Pilatus 2M SAX detector are all carried on a mobile support table. The table weighing 2600 kg runs along the floor under the power of a single driven wheel with very simple guidance this allows a SAX camera length (sample to detector distance) adjustment from 1.6 m minimum up to 10 m. The SAX table also allows 300 mm horizontal and 1000 mm vertical adjustment of the camera axis to align with the reflected beam from the sample. Additionally there are 3 linear motions to adjust the detector and added to the beam stops this amounts to 14 axes on this table. Instrumentation including photo diode amplifiers and remote I/O plus power cabling, compressed air and cooling water make for a complex and substantial cable management system.

CONCLUSION

The design project is complete and built with some beamline commissioning work to be done;

- GISAX sample environment assembled and tested for use in air and under helium, full vacuum operation function not completed.
- WAX Detector and system installed and fully commissioned and operational.
- SAX table installed and fully commissioned and operational.

ISBN: 978-3-95450-188-5 doi:10.18429/JACoW-MEDSI2016-THAA04

REFERENCES

[1] I22 Non Crystalline Diffraction, http://www.diamond.ac.uk/Beamlines/Soft-Condensed-Matter/small-angle/I22.html

[2] W. Tizzano, “Design and FEA of a 3D Printed Detector Window Frame", presented at MEDSI’16, Barcelona, Spain, September 2016, paper TUPE18.

[3] DECTRIS PILATUS3 2M-DLS-L Detector System, Technical Specification and Operating Procedure, Version V1.0.

[4] Symetrie, http://www.symetrie.fr/en/.

[5] Bach rc, http://www.bachrc.de/index.html?language=en

[6] Dectris, https://www.dectris.com/.

[7] GISAX Website, http://www.gisaxs.de/index.html

Content from this work may be used under the terms of the CC BY 3.0 licence (© 2016). Any distribution of this work must maintain attribution to the author(s), title of the work, publisher, and DOI.

ISBN: 978-3-95450-188-5 doi:10.18429/JACoW-MEDSI2016-THBA01

AN ENDSTATION WITH CRYOGENIC COILS CONTRIBUTING TO A 0.5 TESLA FIELD AND 30-400K SAMPLE THERMAL CONTROL*

G. A. Scharfstein, D. Arbelaez, J. Jung
Advanced Light Source at Lawrence Berkeley National Laboratory, Berkeley, USA

Abstract

The Engineering Division of Lawrence Berkeley National Laboratory presents a design for an Endstation to enable X-ray Photon Correlation Spectroscopy (XPCS), which is a method to study temperature-induced fluctuation in hard and soft condensed matter systems. XPCS, when applied to a magnetic system, can yield information about how domains fluctuate as the system goes through a phase transition; these phase transitions can occur at low temperatures (less than 100K) and at an applied magnetic field. Therefore, requirements for the Endstation include a 0.5 Tesla (T) field at the sample and temperature control of the sample from 30K to 400K.

INTRODUCTION

Our beamline delivers a 10 micron diameter beam of coherent light and the Endstation can hold and manipulate a maximum sample size of about 7 square mm. Coherent x-ray scattering gives rise to speckles; these speckles can be imaged using a CCD detector. Resonantly tuned coherent x-rays that scatter off a magnetic sample generate magnetic speckles which are representative of the exact lateral magnetic heterogeneity (i.e domains). With the addition of low temperature control, the sample can experience a phase transition. During phase transition the sample morphology will change and causes a subsequent change in the speckle pattern. By monitoring the speckle pattern over time at a particular temperature with magnetic and/or electric fields, it is possible to determine the temporal evolution of the surface features.

The magnetic and thermal systems required to produce the above-mentioned environment present a challenge to the engineering team due to the strength of the field, range and stability of the temperature control for the sample and relatively small volume in which to accomplish this. When the motion control of the sample and pinhole are included, the endstation quickly becomes an extremely complex and tightly integrated system.

*The Advanced Light Source and this work are supported by the Director, Office of Science, Office of Basic Energy Sciences, Division of Materials Sciences and the Division of Chemical Sciences, Geosciences, and Biosciences of the U.S. Department of Energy at Lawrence Berkeley National Laboratory under Contract No. DE-AC03-76SF00098.

MAGNETIC SYSTEM

The magnetic system is based on a three-dimensional Opera Vector Field magnet design with vanadium permendur as the pole material and a 5000 ampere-turn coil as the magnetic source. To obtain the proper field strength and meet the thermal requirements, a cryogenic solution was implemented to keep the energized coils from heating the sample. Liquid nitrogen floods a stainless steel can encasing the coil and the resulting thermal balance exhausts gaseous nitrogen via a vacuum chamber feed through. The geometry of the poles is influenced by the proximity of the pole tip to the sample and its translation normal to beam; 5mm is the vertical range (along gravity vector) and 7mm is the horizontal range of motion, along with about 190 degrees of rotation along the horizontal axis. The tapered shape is required to control the flux as the coils are relatively far from the pole tips and magnetic field target. Overall, the magnet system is optimized for field along the beam axis and it can be rotated along the beam-horizontal-to-gravity plane by controlling the power of opposing coils (see Figure 1).

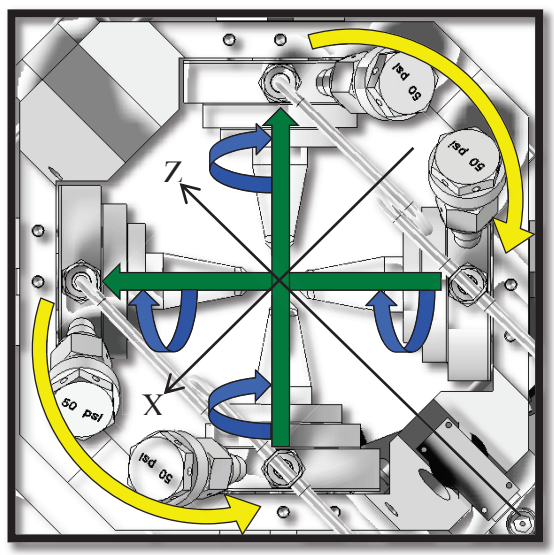


Figure 1: A diagram of the magnet system showing the current direction for each coil (blue arrows), the field vectors (green arrows) and the flux return through the yoke (yellow arrows).

Content from this work may be used under the terms of the CC BY 3.0 licence (© 2016). Any distribution of this work must maintain attribution to the author(s), title of the work, publisher, and DOI.

ISBN: 978-3-95450-188-5 doi:10.18429/JACoW-MEDSI2016-THBA01

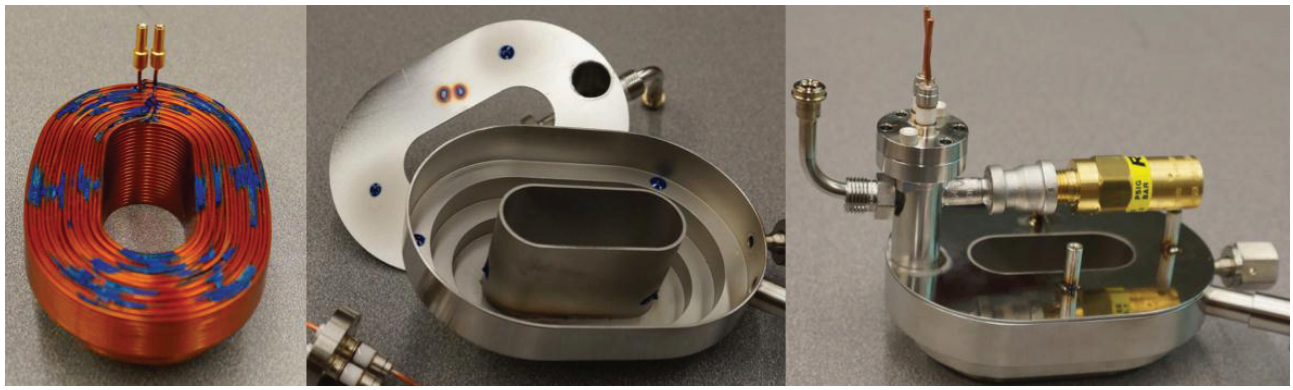


Figure 2: Our prototype wound coil (left), stainless steel coil can prior to final assembly (center), and the final assembled prototype coil-can assembly (right).

We have completed analysis of the magnet using Opera Vector Field and performed a cold test of one prototype coil-can assembly (see Figure 2). The results of the cold test yielded a maximum power of 18A at 2.85V.

The top-level magnetic assembly has a repeatable, three-point mount at the vacuum chamber base with flexlines connecting the LN2 and two independently-controlled power connections. For serviceability, the system is removable after full integration. With its sub-mm proximity to the sample hardware, a precision lifting fixture will be designed to facilitate this task.

SAMPLE THERMAL CONTROL

Sample cooling is enabled by a coaxial flow cryostat that is attached to a trunnion that rotates the sample. The rotary axis is electrically isolated from the experiment, as the Endstation User would like to apply up to 200V to the sample. The yoke of the trunnion sits atop two translation stages at six degrees to produce motion normal to the beam. The system requirements called for a short cryostat design, which is accomplished with a serpentine path for the exhaust (see Figure 3). The unique helium exhaust transition employs automatic thermal control to ensure an ice-free feed through.

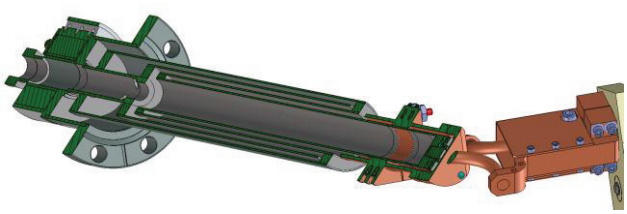


Figure 3: A cross section of the cryostat exhibiting the serpentine design.

The scattering requirements put strict demands on the stability of the sample. While the cryostat is cantilevered off the chamber wall, the cold finger reaches the sample via copper braid to the trunnion through the center of the sample axis. The goal is that the trunnion with provide dimensional stability as the system maintains thermal equilibrium. Active and passive shielding will be added as testing continues and the system is better understood from a thermal standpoint.

Preliminary thermal tests of the cryostat-trunnion sub-assembly reveal a cold-finger temperature of about 5K with the sample holder getting to 13.9K after two hours of cooling. Figure 4 shows the test apparatus used for this test; the cold fingers connect to the trunnion via copper braids and the sample holder is made of glidcop. These results are promising for the final sample temperature, which will be determined after the complete Endstation is assembled and tested.

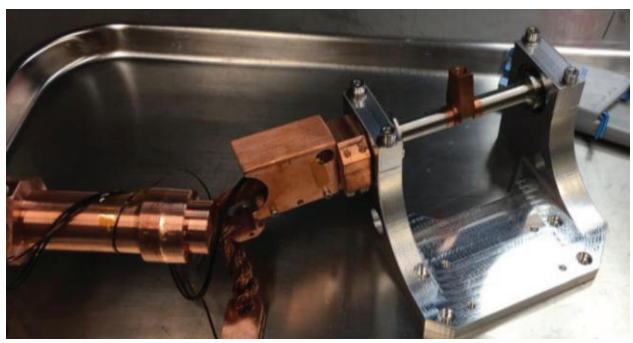


Figure 4: Apparatus used for the preliminary thermal tests. The copper hardware on the left connects to the cryostat (not shown) and an aluminium yoke holds the stainless steel-glidcop sample holder to complete the trunnion assembly.

CONCLUSION

The Endstation is in the final stages of design with preliminary tests and analysis forecasting a 0.5 T field while meeting the required field stability within the sample volume. The thermal system is also showing promise with early tests revealing excellent helium vaporization at the cold tip. We have enhanced the shielding and thermal connections to provide an efficient thermal path to the sample. Near term activities include further testing of both systems to correlate analysis and early tests with the final hardware. The system is scheduled to be commissioned by mid-2017 with final tests wrapping up in early 2017.

Content from this work may be used under the terms of the CC BY 3.0 licence (© 2016). Any distribution of this work must maintain attribution to the author(s), title of the work, publisher, and DOI.

ISBN: 978-3-95450-188-5 doi:10.18429/JACoW-MEDSI2016-FRAA01

ENGINEERING CHALLENGES ON THE I14 NANOPROBE BEAMLINE

A. Peach, Diamond Light Source, Oxford, UK
F. Cacho-Nerin, J. Parker, P. Quinn, Diamond Light Source, Oxford, UK

Abstract

An overview of the double branch 185m I14 Nanoprobe beam-line under construction at DLS will be presented together with the end-station design in further detail. The end station consists of a split vacuum vessel containing a KB mirror configuration (at UHV) and the sample environment (at HV) which is just 50mm from the end of the final KB optic. An in-vacuum detector is mounted between the KB and the sample whilst two externally mounted detectors will operate between 0.25m & 3m from the sample. Four cryogenic samples can be brought into the vessel at a time and transferred remotely to the sample position with cooling provided by a Helium pulse tube cooler. With an initial 50nm size beam, stability is absolutely critical and careful attention has been paid in the design to mitigate any thermal and structural sources of vibration. An array of interferometers reference the KB mirrors and sample position and will be used to actively correct for any drifts. The very tight space constraints involved have greatly increased the complexity and duration of the design but testing of prototypes is now underway. The system is scheduled for build and test through the Autumn 2016.

INTRODUCTION

The long Nanoprobe Beamline currently under construction and commissioning at Diamond Light Source features both a Nanoprobe & Mesoprobe branch. The Nanoprobe branch will be accepting first users in Spring 2017 whilst the Mesoprobe branch will be completed later in a 2nd build phase.

Each branch has a separate experiments hutch within the newly constructed external building, which also features a suite of Electron Microscopes laboratories.

Due to the arrangement of the Mirrors and Double Crystal Monochromator (DCM) it will be possible to deliver pink or mono beam to the end station of either branch.

BEAMLINE CHALLENGES

The goal of the beamline is to provide a sub-50nm X-ray beam through which samples can be scanned in 2D and 3D under various conditions whilst collecting data from several detectors. In particular a nano-KB system was selected to achieve nano-focussing with a cryogenic system able to handle frozen hydrated samples for biological imaging. To achieve this we need:-

- Beam stability of < 50 nrad RMS before the nano-focus endstation and stability at the sample of <3 nm
- A KB mirror and sample stage system designed for flexible sample conditions in air or vacuum whilst maintaining the KB system under UHV at all times.
- Long term thermal stability to minimize thermal drift.
- A detector layout for multi-modal experiments.
- An interferometry system capable of sample rotation.
- Cryogenic cooling for 2D and 3D scanning with associated sample handling and sample staging for frozen hydrated samples.

BEAMLINE LAYOUT

The beamline is 185m long to improve demagnification of the beam at the sample, whilst maintaining a reasonable working distance. This also provides a coherent beam for diffraction limited focussing and coherent imaging applications.

The beamline was designed for a cryogenic in-vacuum undulator, with the main optics installed inside two hutches within the main synchrotron building. The beam propagates through a long vacuum pipe to an external building some 90 m away from the main synchrotron which houses a third Optics Hutch together with the Nanoprobe and Mesoprobe Experiments concrete hutches.

Hutch 1&2 Key Components

Optics Hutch 1 contains the primary optics including the mirrors and DCM.

Nano-focussing and coherence experiments require high stability and the beamline targeted < 50 nrad rms beam movement in both the vertical and horizontal direction from 1-100 Hz.

With the demands for vertical beam stability at the sample ultimately to within a few nanometres, the optical arrangement was carefully considered and an all horizontally deflecting geometry was used.

The Mirrors M1 (with bender) & M2 (flat) use stripes of Si, Rh and Pt to provide harmonic rejection and horizontal beam shaping with respect to the secondary source.

The horizontally deflecting monochromator is a fixed exit system using a pair of Si(111) crystals to provide continuous energies from 4.5 to 26 keV with much attention paid to the mechanism stiffness and arrangement of the cryogenic cooling pipework which has been proven to provide vibration free performance below 100 Hz and less than 50 nrad RMS up to 200 Hz.

A fast feedback system operating at 500Hz will be used to actively control the pitch and roll and suppress low frequency vibrations based on beam position measurements. As nano-probe experiments are flux hungry, a filtered pink beam option was considered by using mirror M3 (to be installed at a later date) with space also available to consider a multilayer monochromator.

Content from this work may be used under the terms of the CC BY 3.0 licence (© 2016). Any distribution of this work must maintain attribution to the author(s), title of the work, publisher, and DOI.

ISBN: 978-3-95450-188-5 doi:10.18429/JACoW-MEDSI2016-FRAA01

As I14 is on a short straight at Diamond, only a single undulator can be used. However, swapping between end-stations for the nano-probe or meso-probe will be achieved with the further future addition of M4 & M5 switching mirrors which would allow either mono or pink beam to be delivered to the Mesoprobe branch.

Whilst the DCM is cryo-cooled, the mirrors employ a gravity fed water cooling system to minimise vibration.

In Optics Hutch 2 at around 50 m from the source a double set of precision slits (S3) define a secondary source for each branch. Beyond this point each branch occupies its own vacuum space through to the external building.

At the end of Optics Hutch 2 each branch has its own independent photon shutter allowing beam to be maintained on the upstream optics, whilst the external hutches are accessed thus assisting thermal stability.

Beam Duct

The Ø100 mm beam pipes to the external building are housed in a concrete beam duct which passes under two roads.

Due to the harsh environment and maintenance access difficulties there are no pumps in the duct although there are vacuum gauges to monitor pressure. Despite a distance of around 113 m between the pumped ends of we have achieved vacuum pressures in the region of $1x10^{-8}$ mBar at the midpoint.

External Building

The 1500 m^2 footprint external building is a purpose built facility for the I14 Nanoprobe beamline and the complimentary Electron Bio-Imaging Centre (eBIC) and Electron Physical Sciences Imaging centre (ePSIC)

The beamline and electron microscopy (EM) laboratory floors are constructed on 800 mm thick concrete supported on 14 m concrete piles for stability in the same manner as the main Diamond synchrotron hall floor.

Excellent thermal management is essential to maintain stability of the sample. Consequently where forced air conditioned ventilation is traditionally used, we have opted for radiant panels mounted on the ceilings and walls to remove short term thermal oscillations and limit air pressure fluctuations.

Further to aid thermal stability, each experimental hutch is constructed from 300 mm thick concrete and is accessed via a vestibule with self-closing door to minimise the volume of air exchange when opening the hutch door.

Optics Hutch 3

Optics hutch 3 serves to provide pumping at the external end of the beam duct and also the first external diagnostics. Sufficient space is provided for future installation of optics (such as Compound Refractive Lenses) on the Mesoprobe branch.

Experiments Hutch 1 (Mesoprobe)

The Nanoprobe beam pipe is brought through the Mesoprobe Experiment Hutch inside a lead shielded box thus allowing access to the room whilst the Nanoprobe branch is taking beam. The Mesoprobe endstation is yet to be designed. The switching mirrors in Optics Hutch 1 together with the length of the beamline means that a 12 mrad deflection of the beam results in over 1.5 m separation of the beam pipes at this position.

Experiments Hutch 2 (Nanoprobe)

A series of components on the "Pre Table" include an XBPM and a set of precision slits to finally define the beam before the endstation and control beam position onto the KB. These are mounted on a common granite block.

The rest of the hutch contains the KB mirror system, sample station and detector table.

KB MIRRORS / NANOSTAGE

The KB/Nanoprobe endstation is shown in Fig.1. It will be used for 2D scanning and 3D tomography both at cryogenic and room temperatures. With experiment times ranging up to 24 hours and a beam size of 50nm (reducing by more than a factor of 2 in the future), much effort has been made to achieve the best possible thermal and mechanical stability within the space available.

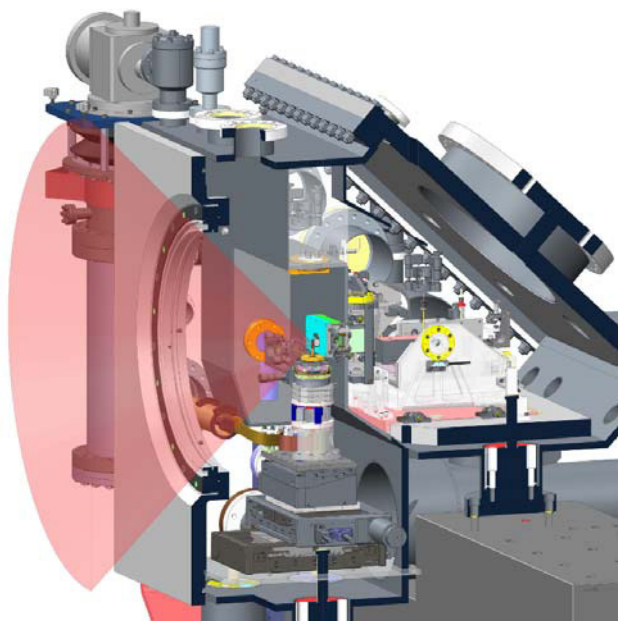


Figure 1: KB/Nanoprobe endstation.

With the sample point only 50 mm away from the end of the last KB mirror optic and an XRF detector required in the space between them, it has proved a considerable challenge to arrange and best support each mechanism within separate vacuum environments.

With no space for separate vessels they are mounted in a common vessel separated by a thin dividing wall housing a diamond window for passage of the beam on

Content from this work may be used under the terms of the CC BY 3.0 licence (© 2016). Any distribution of this work must maintain attribution to the author(s), title of the work, publisher, and DOI.

ISBN: 978-3-95450-188-5 doi:10.18429/JACoW-MEDSI2016-FRAA01

Content from this work may be used under the terms of the CC BY 3.0 licence (© 2016). Any distribution of this work must maintain attribution to the author(s), title of the work, publisher, and DOI.

through the XRF detector to the sample. The KB mechanism will operate at UHV whilst the sample side will either be at HV or used in air. This is to protect the KB mirrors from contamination and allow greater flexibility with the sample environment.

The vessel and internal mechanisms will be supported initially by a granite block directly fixed to the floor during commissioning and first use. However the intention is to upgrade this in the near future with an air bearing slide arrangement designed to easily swap the end station for other alternative setups.

The design can be broken down into the following key areas:-

- KB mechanisms
- Nanoprobe sample stage
- Interferometry for active corrections
- Sample mount and cooling
- Sample docking and transfer
- On axis sample viewing camera
- Vessel and support structures

KB Mirror Mechanism

The fixed focus KB mirrors consist of the Vertical Focussing Mirror (VFM) first followed by the Horizontal Focussing Mirror (HFM) mounted onto a common base plate which is directly supported by the granite block through the vessel.

Flexure mechanisms provide pitch and roll (VFM roll only) adjustment with a motorised coarse adjustment provided for initial setup and fine piezo adjustment with <50 nrad resolution when in use. Each axis is directly encoded with a resolution of around 35 nrad to assist initial setup and commissioning. This could be improved further to <5 nrad using a different encoder if deemed useful to use as part of the position monitoring system.

The mirror optics are of an extremely high specification and have been measured and verified by the Diamond NOM facility to have slope errors <50 nrad with a figure error of <0.2 nm.

The mechanisms have been designed and built for some time. Whilst metrology tests have not been able to reveal any weakness in the design, limitations in the stability of the test set up has not allowed us to measure down to the levels of stability we will actually need at the endstation.

Nanoprobe Sample Stage

The sample stage stack features coarse stepper motor driven XYZ stages at the base with piezo XYZ, rotation and tip tilt stages mounted above. With a target of < 5 nm linear repeatability and a radial error < 30nm required at the sample we have bought the best commercial stages we can source to fit within the space envelope. The repeatable and non-repeatable system motion error imposes a limitation on performance which will need to be addressed by active corrections using look up tables and feedback from the interferometers.

The stage assembly is mounted on a base plate directly supported through the vessel to the granite support block below.

Working upwards from the base, the stepper motor XY stages offer 50mm travel range whilst the vertical stage offers 13mm total range. These large translations are needed for experiments at positions other than just the focal point of the KB mirrors to allow for variations in sample mounts as well as reaching all areas on a sample TEM grid.

The custom piezo driven combination tip/tilt/height stage provides +/- 2 mrad tip/tilt and up to 200 µm vertical fine adjustment along with a combination Piezo XY stage offering a 200 µm range.

The piezo driven sample rotation stage mounted at the top provides up to +/- 180° rotation with a resolution of around 5 µrad.

The fine piezo stages are needed to correct wobble / runout arising from the rotation stage and also to fine scan the sample.

Interferometry for Active Corrections

In order to maintain the position of the beam and the sample to < 3 nm we need to actively correct the mirrors and sample stages to account for drifts and other sources of error and instability.

The arrangement has been the source of considerable iteration during the design process made all the more challenging by the space constraints involved. The final concept is shown in Fig. 2.

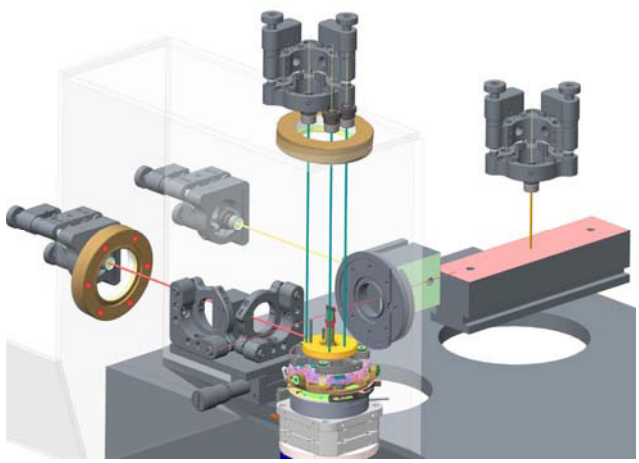


Figure 2: Interferometry arrangement.

All interferometers are mounted inside the KB vacuum space and supported from the mechanism base plate which should provide a good support and common reference of the sample stage relative to the KB optics themselves. Nonetheless it will be a challenge to finalise a structure which will provide sufficient stability within the space allowable. An interferometer references each KB optic whilst the others reference the sample stage through viewports in the chamber wall.

A gold coated Be Cu disk mounted below the sample has a highly polished top surface and edge which acts as a 3D mirror for the interferometers. It was designed to

ISBN: 978-3-95450-188-5 doi:10.18429/JACoW-MEDSI2016-FRAA01

reach cryogenic temperatures to maintain alignment with the sample mount.

Up to three interferometers will point vertically down at the surface of the disk to monitor pitch, roll and height variations whilst one pointing at the side of the disk monitors XY variations. The horizontal interferometer will also be mounted on motorised XY stages in order to maintain a perpendicular reference to the radius of the disk for maximum signal. To assist with this a beam splitter and diode will also be mounted in the path of the laser beam to indicate intensity as the interferometer falls off the peak reflection of the disk.

The disk allows for around 25 mm stage movement along the beam before the interferometers referencing the surface of the disk start to fall off the edge.

Although not allowing for the full movement of the nano-stage the aim is to provide active interferometry at positions other than the nominal sample position.

Sample Mount & Cooling

Whilst the power in the beam is only around 0.01 mW the small beam size gives rise to a significant power density. With the need to keep cryo samples to <100 K with the beam on, FEA confirmed that LN_2 cooling would not be sufficient. Therefore we opted for a closed circuit gaseous Helium two stage pulse tube cooler system capable of achieving 4 K on the primary stage. The chosen unit is specifically an ultra-low vibration design.

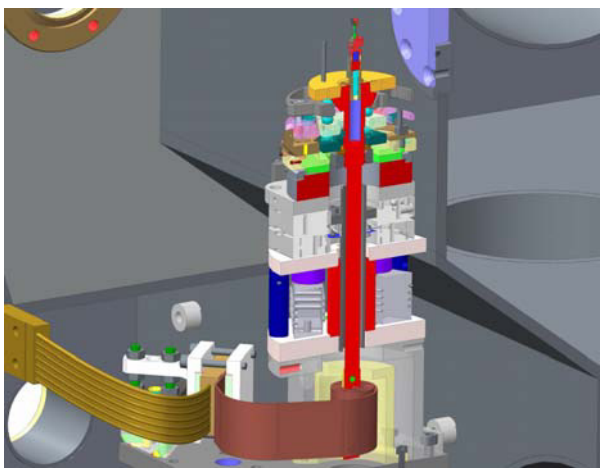


Figure 3: Cooling to sample.

In order to minimise radiation losses, the thermal link to the cooler primary stage is kept as short as possible whilst still allowing sufficient flexibility for the motions of the stage. Various arrangements were considered to transfer the cooling to the sample mounts allowing for the movement ranges of the stages whilst minimising potential strain on the piezo stages.

The final design shown in Fig. 3 brings the cooling to an anchor point on the stepper stages and then on axis through the stage stack via a Be Cu shaft which is attached to the sample mount tip.

To allow for virtually strain free movement of the sample rotation, the bottom of the shaft is thermally linked to the anchor point via a laminated soft copper coil "clock spring" design.

The sample mount tip is centred on axis by adjusting its mounting plate relative to the stage stack with 3 levels of thermal separation provided via zirconia balls in a kinematic arrangement. This minimises cold leakage into the stage stack which would give rise to thermal instability.

Tests on an earlier prototype setup revealed an 80 K gradient between the cooler at around 4 K and the sample tip. The goal is to achieve a temperature of around 20 K at the sample tip which is a considerable challenge. Minimising losses at such low temperatures is extremely difficult however we anticipate a significant improvement with the final design which contains some major enhancements including better clamping of the cooling at the base of the shaft, thermal isolation and less joints in the thermal link to the cooler. An array of PT 111 temperature sensors will be fitted around the structure to monitor temperatures and losses.

As well as the cooling aspects, the mass and height of the parts making up the overall stack above the stepper stages were minimised as far as possible to arrive at a stiff and light structure to facilitate the best dynamic performance from the piezo stages.

Sample Docking & Transfer

We have adapted a commercially available sample transfer arm system to manually place loaded cryo samples into the vacuum chamber via a load-lock. Up to four sample mounts can be loaded at once on copper docking block (with cryogenic radiation shield) using magnets to retain them in place. There is also a magnet in the cooled sample stage tip which helps to positively locate the transferred sample mount and provide some preload to aid thermal transfer between them.

The transfer arm itself is a source of thermal gain for the cryogenic samples and is the subject of a separate Diamond project to improve its performance.

Once inside the chamber the sample loading block shown in Fig. 4 is docked on a rotation stage to allow full access for the internal XYZ piezo driven sample transfer shuttle.

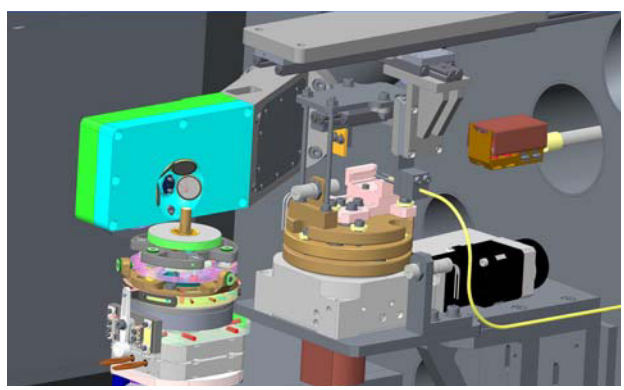


Figure 4: In vacuum sample transfer.

Content from this work may be used under the terms of the CC BY 3.0 licence (© 2016). Any distribution of this work must maintain attribution to the author(s), title of the work, publisher, and DOI.

ISBN: 978-3-95450-188-5 doi:10.18429/JACoW-MEDSI2016-FRAA01

Content from this work may be used under the terms of the CC BY 3.0 licence (© 2016). Any distribution of this work must maintain attribution to the author(s), title of the work, publisher, and DOI.

The docking block is maintained cold in a similar way to the sample stage but made off the cooler's second stage at around 20 K.

The design of the internal sample transfer mechanism along with variations of cryogenic sample mount is currently being refined further but a prototype arrangement has proved the principle works.

Alternative types of sample mount for non-cryogenic use are also being developed. A feature of the design allows the sample mount tip on the sample stages to be removed without disruptive dis-assembly to allow the fitment of different styles and sizes of samples.

On Axis Sample Viewing Camera

An on axis sample viewing camera is currently being developed which will work around the limited space available in the vessel.

Vessel and Support Structures

The vacuum vessel to house the KB and sample stage mechanics along with their associated sub systems and space constraints is complex. It has undergone many iterations arriving at the final design. The vessel is mounted on a granite block with internal posts supporting the mechanisms also grounded to the support block.

The lid on the UHV side has an aluminium wire seal whilst the sample side at HV is sealed via a hinged door and Viton™ O-ring. This door will allow the passage of a full 90° cone signal from the sample through to the air-side detectors via a large laminated carbon fibre reinforced sheet window. This window minimises deflection under vacuum which would otherwise infringe upon the working envelope of the vessel. An ion pump is fitted on the HV side to achieve the best vacuum possible when in cryogenic operation.

In the dividing wall between the two vacuum spaces a 50 µm thick single crystal diamond window has a clear diameter of 4mm for the passage of beam. It will be sealed using a Helicoflex® seal to maintain UHV on the KB side.

Initially the whole assembly will be mounted on a granite block for commissioning and first users. Once all aspects the system have been fully proved in use we will develop the air bearing slide system as an upgrade for rapid exchange of alternative setups whilst maintaining high stability support.

DETECTOR TABLE

As well as the in vacuum XRF detector there is an air side Excalibur detector and an X-Ray Eye camera set up mounted on a common granite base block. Each one can be placed between 3 m and 250 mm from the sample using independent motorised drives. Each detector also has a vertical lift stage whilst the X-Ray Eye has an additional fine lateral stage. The general arrangement is shown in Fig. 5.

The key to getting the arrangement to work was how to provide a very stable 200 mm range vertical lift for the Excalibur detector in a very compact space envelope. An "aggressive" wedge angle stage design was chosen. Tests proved the stage was very stable even at the extreme positions and could still achieve full range in 45 seconds.

A motorised beam stop is mounted before the Excalibur detector and travels with it.

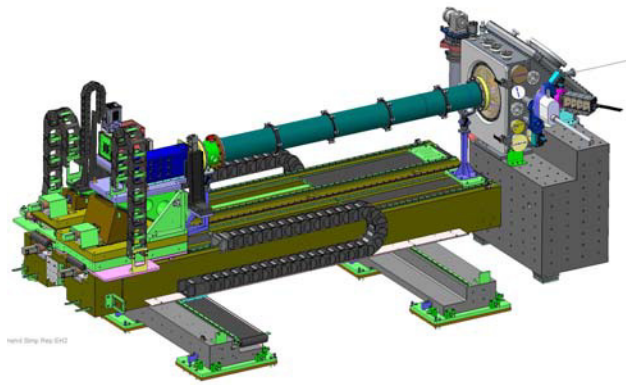


Figure 5: Detector Table.

A Ø200 mm vacuum pipe can be fitted between the endstation and the Excalibur detector which can be extended as required to the detector position.

Motorised lateral motion of the base block is provided to swap between either detector systems in less than a minute.

The detector table is currently being assembled in the hutch.

CONCLUSION

I14 will be taking first light into the external building during September 2016.

A temporary setup in air for this milestone will utilise the KB mechanism and the upper piezo sample stages along with a representative interferometry set up to gain an understanding of the initial conditions and learn lessons for the final design.

Alongside this we will continue to test and refine elements of the cooling and sample transfer systems as well as the sample viewing camera design.

The vacuum vessel is due to be delivered in September 2016, when assembly of the final system will commence. Commissioning and extensive testing will follow in readiness for first users in Spring '17.

ISBN: 978-3-95450-188-5 doi:10.18429/JACoW-MEDSI2016-FRAA03

MECHANICAL DESIGN OF MIRAS, INFRARED MICROSPECTROSCOPY BEAM LINE AT ALBA SYNCHROTRON

Llibert Ribó†, Igors Šics, Artur Gevoryan, Josep Nicolas, Alejandro Crisol, Carles Colldelram, Liudmila Nikitina, Raquel Monge, Marcos Quispe, Ibraheem Yousef
ALBA Synchrotron Light Source, Cerdanyola del Vallés, Catalonia, Spain
Paul Dumas, SOLEIL, Gif-sur-Yvette, France
Gary Ellis, ITP CSIC, Madrid, Spain

Abstract

The infrared (IR) micro spectroscopy beam line MIRAS has been an in-house project fully developed at ALBA as a result of a collaboration of different teams during the period of 2014 when the design started to 2016 It is composed of a horizontally retractile mirror to extract the IR light from the bending magnet radiation and a system of 8 transport mirrors located by positioning systems designed for a high stability performance, to transport the extracted IR light outside the tunnel until the first End Station.

LAYOUT

The layout was defined by the scientific and the optical teams, in close collaboration with Dr. Paul Duma's team (SOLEIL, France) and Dr. Gary Ellis (IPT CSIC, Spain), who contributed a lot during the design phase.

The extraction mirror M1 is located inside a bending magnet vacuum chamber. At the beginning of its bending radius, starts the optical layout: This is named the source point. M1 reflects the infrared fan of the synchrotron radiation of the bending magnet where M1 is located as well as a fraction of emission fan of the upstream bending magnet (in addition to the "edge radiation"). The infrared beam is transported through a layout of 4 transport mirrors with a toroidal mirror used to focus the beam at the focal point F1 just outside the tunnel wall. Subsequently, 3 additional mirrors direct the beam to the focal point F2 located inside the 1st End station. The beam line is prepared to be upgraded up to 3 End stations (See Fig. 1) as the beam splitter mirrors (MBSP1 and MBSP2) are retractile and allow part of the beam to pass through the other possible end stations (F3 and F4). At present, MIRAS is completed up to MBSP1 and F2 with 1st End station being operational.

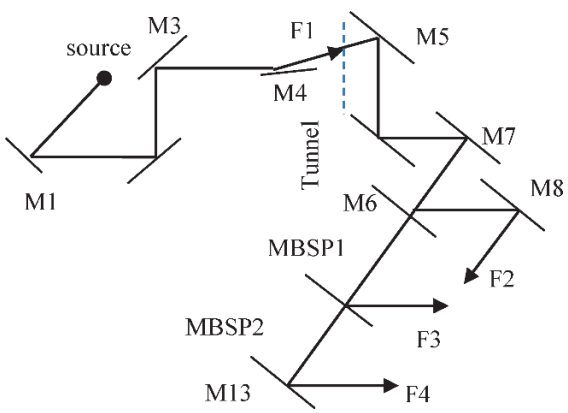


Figure 1: Schematic Layout of MIRAS.

SYSTEMS DESCRIPTION

Extraction Mirror M1

The slotted extraction mirror M1 is inserted inside the Dipole vacuum chamber in a certain angle, facing a portion of the synchrotron radiation coming from the last bending magnet, passing through a 3 mm slot (see Fig. 2a). In order to maximize the optical performance of the mirror the clearances with the inner face of the dipole chamber are very tight, 2 mm nominally with the inner wall and 1.8 mm with the slot end (see Fig. 2b).

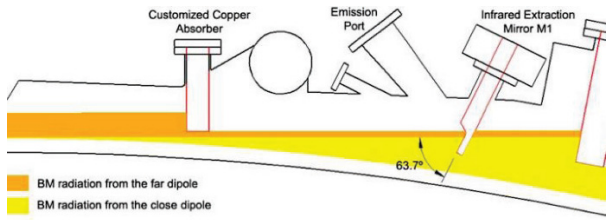


Figure 2a: Schematic of IR emissions collected by M1.

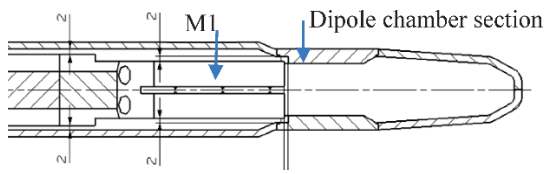


Figure 2b: M1 nominal clearance.

The mirror has been manufactured from polished aluminium 6061, and optical surface is gold plated (unprotected) (Fig. 3). An array of 6 thermocouples is positioned on the back side of the mirror protruding by 0.5 mm into the slot space. With their reading, the vertical position of the extraction mirror in respect to the beam can be fine-tuned. Apart from those, another pair of thermocouples are embedded into the non-reflective surface for temperature measurement of the body of M1.

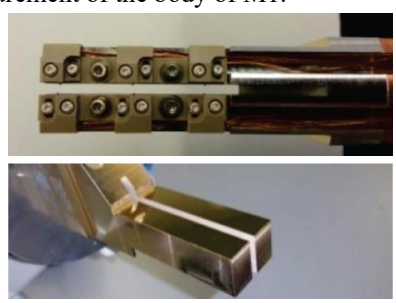


Figure 3: Top: back side of the mirror and portion of the cooper arm. Down: reflective surface.

Content from this work may be used under the terms of the CC BY 3.0 licence (© 2016). Any distribution of this work must maintain attribution to the author(s), title of the work, publisher, and DOI.

ISBN: 978-3-95450-188-5 doi:10.18429/JACoW-MEDSI2016-FRAA03

Content from this work may be used under the terms of the CC BY 3.0 licence (© 2016). Any distribution of this work must maintain attribution to the author(s), title of the work, publisher, and DOI.

The mirror is mounted on the extreme of a cooper arm which links the mirror body with its positioning system. The copper arm also acts as a cooler for the mirror and evacuating generated heat. For this reason, it has been designed as a hollow cylinder on its air-side part, optimized with brazed ribs on the inner part (see Fig. 4). It functions as a heat sink, cooling by natural convection and maintaining the temperature of the body of M1 around 63ºC, with no need for extra cooling system. The FEA analysis has been done considering the main ALBA Storage Ring design parameters: 3 GeV, 400 mA and 1.42 T, which means 15 W of power absorption. Other simulations were done for operation at 200 mA

A temperature of 25ºC was observed during the commissioning phase on the body of M1, (operating at 130 mA current in Storage Ring). This corresponded to the previous simulation. More details can be found in a specific report [2] where those simulations are developed.

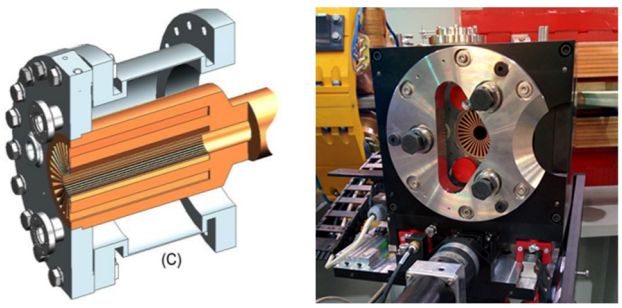


Figure 4: Left: section of the mirror cooper arm. Right: photo of the rear side of the cooper arm showing heatsink.

M1 needs to be retracted and inserted into the dipole chamber. Apart from that, the mirror has to be moved in certain small vertical range of ±1 mm in order to adjust it in respect to the electron beam inside the chamber. Both movements have to be motorized. The cooper arm is mounted on a mechanical system composed by a spindle actuator to position the linear horizontal movement, and wedge mount mechanism which will be used as a high resolution positioner, making stiff and stable mechanics.

A modal analysis has been performed in order to establish the Eigen modes on the mechanical assembly, where the maximum deformation of the M1 edge was estimated around 0.15 mm due to the self-weight, and first mode of vibration appears represented in Fig. 5, which correspond to a roll at 58.5 Hz.

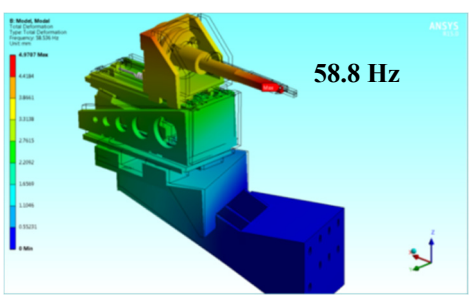


Figure 5: First mode of vibration.

All the assembly is mounted on a support fixed to the girder in order to link M1 to the same support as the bending magnet and the dipole chamber. Figure 6 shows the M1 mechanics assembly mounted on a spare girder mock-up which was used to make stability and performance tests before the final installation in the accelerator tunnel.

The tests showed that a good resolution can be guaranteed after 4 full steps of the motor. According to the displacement per step calculations it corresponds to 1.56 µm/step. Accuracy of the real position of the mirror on the linear movement is 15 µm in respect to its theoretical given position in open loop. First significant mode is observed at 61 Hz, after hammer-shock on the girder. The significant results are shown in Fig. 7.



Figure 6: Top: Mechanics assembly mounted on mock-up girder. Down: Extraction mirror retracted mounted inside accelerator's tunnel.

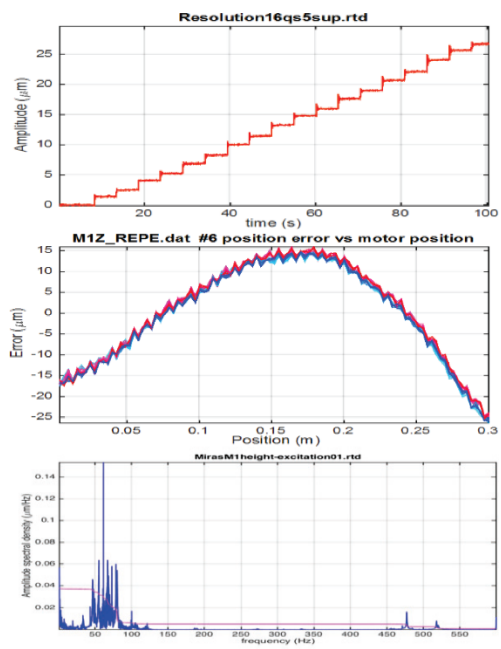


Figure 7: Performance results.

ISBN: 978-3-95450-188-5 doi:10.18429/JACoW-MEDSI2016-FRAA03

Transport Mirrors M2 to M8

MIRAS is constituted by an array of mirrors of different shapes that make the infrared beam to be focused in two focal points: F1 and F2 (see Fig. 1). To achieve this, all 8 mirrors are positioned in the space, and have to be adjusted for the pitch and roll according to the following specs (see Table 1). The same positioning mechanism design is used for all of 8 mirrors.

Table 1: Specifications

Specification	mrad	deg
Range	± 9.07 mrad	± 0.5º
Resolution	15 µrad	$9 \cdot 10^{-4}$ º
Accuracy	0.25 mrad	0.014º
Repeatability	32 µrad	$2 \cdot 10^{-4}$ º

The transport mirror positioning mechanism has been designed as a 2 angle goniometer system, where both angular movements are guided by circular rails. See the scheme at Fig. 8. The movement on the rails are generated by motorized spindle actuators connected through an elastic articulation (flexure).

Mirror support has to be very rigid and light to have a high stability mechanical system. The mirror itself is inside a vacuum, and the angular movement is transmitted by a bellow.

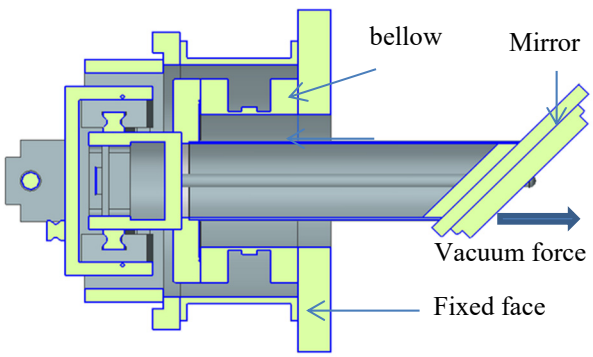


Figure 8: Conceptual design of the transport mirror system.

FEA calculations were performed in order to check the stability of the system and to optimize the shape of the flexure when moving the full range (see Fig. 9).

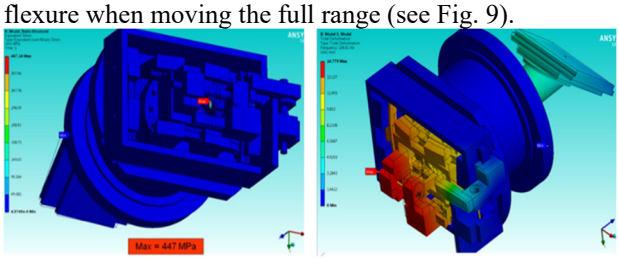


Figure 9: FEA analysis.

According to the FEA, the flexure of the actuator was loaded with 447 MPa when the mirror was at one extreme position (±1º). Flexures were manufactured using high modulus steel. The first Eigen mode is estimated at 135 Hz.

After mounting, one of the transport mirrors was tested to measure the pitch and roll resolution, accuracy and vibration behaviour. The results are presented in the following Fig. 10 and Fig. 11.

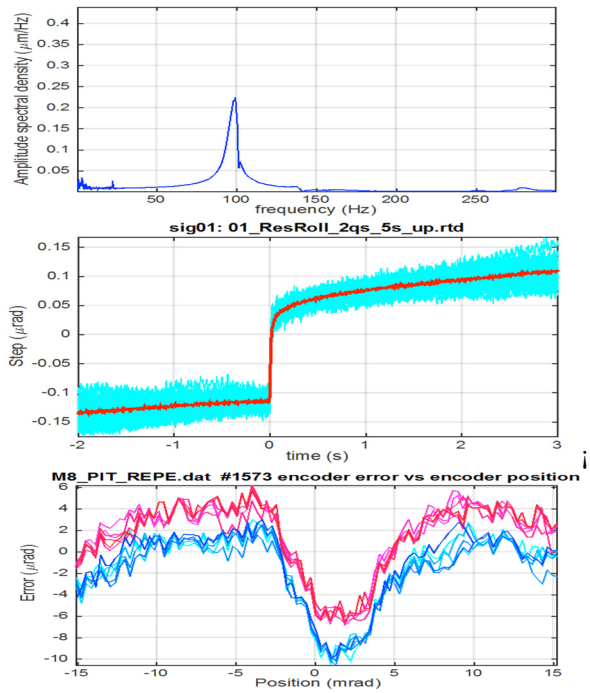


Figure 10: Top: Significant resonance peak. Middle and down: Measurements of the resolution and linearity of the movement in the open loop.

The lowest angular resolution has been measured for the pitch movement of 0.16 µrad for half step, with a window of 2 quarter steps for each 5 seconds. Repeatability with open loop was measured of 1.6 µrad. The worst accuracy error was 57.2 µrad measured in open loop for the pitch, but was significantly improved to 10 µrad with the use of the encoder in a closed loop. Peak resonance is at 98 Hz (see Fig. 10 above).

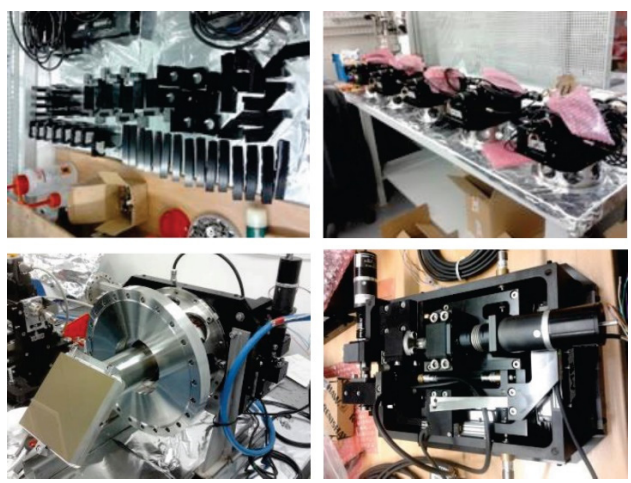


Figure 11: Top: series assembling in ALBA Workshop. Down: detail of the goniometer and mechanical test.

Content from this work may be used under the terms of the CC BY 3.0 licence (© 2016). Any distribution of this work must maintain attribution to the author(s), title of the work, publisher, and DOI.

ISBN: 978-3-95450-188-5 doi:10.18429/JACoW-MEDSI2016-FRAA03

Content from this work may be used under the terms of the CC BY 3.0 licence (© 2016). Any distribution of this work must maintain attribution to the author(s), title of the work, publisher, and DOI.

BEAM LINE ARCHITECTURE

Supports and Other Subsystems

The transport mirrors are mounted in the vacuum chamber which is supported by a granite block and positioned in respect to the orbit of e-beam in storage ring. All the vacuum layout of up to the focal point F1 maintains 10^{-9} mbar which is common with storage ring vacuum. Just before F1 a brazed CVD diamond window separates the vacuum section of the front end inside the tunnel to the rest of the beam line at the experimental area.

Granite supports have been chosen as a main solution for the full beam line for the stability performance. The alternative of steel supports was evaluated and found complicated. All of them would be thin and high structures to be fitted inside the crowded tunnel area, between the girders and 2 other front ends and cooling pipes. A model of the beam line in tunnel area is presented at Fig. 12 with the most significant parts.

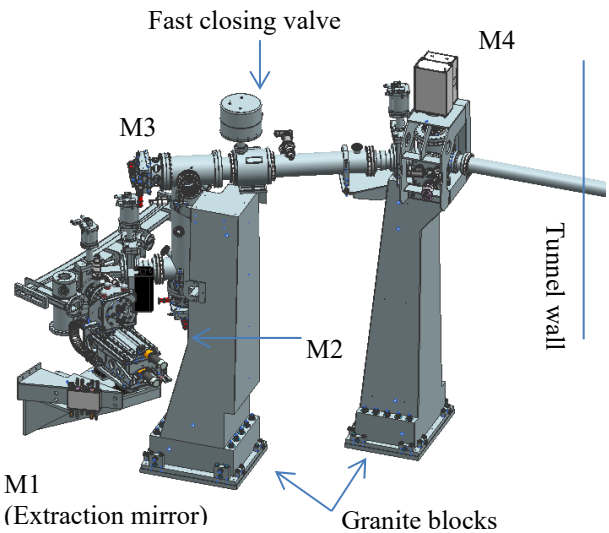


Figure 12: Model of MIRAS inside the tunnel. The significant components highlighted.

Downstream the tunnel wall and the CVD window, the IR beam is transported up to the first end station. (See details in Fig. 13). This area is a complete assembly with a defined vacuum section. A diagnostic setup consisting of a mirror and a camera are introduced after the focal point F1 to assess the shape and size of the infrared beam. Mirrors M5 and M6 are mounted on the same granite pedestal (see Fig. 13a). Top part containing M5, CVD window and diagnostics setup is located in front of tunnel wall penetration and are covered by a small lead hutch to protect the experimental area from possible radiation leaks. The tight architecture obliged to fit M6 inside the granite bock (Fig. 13).

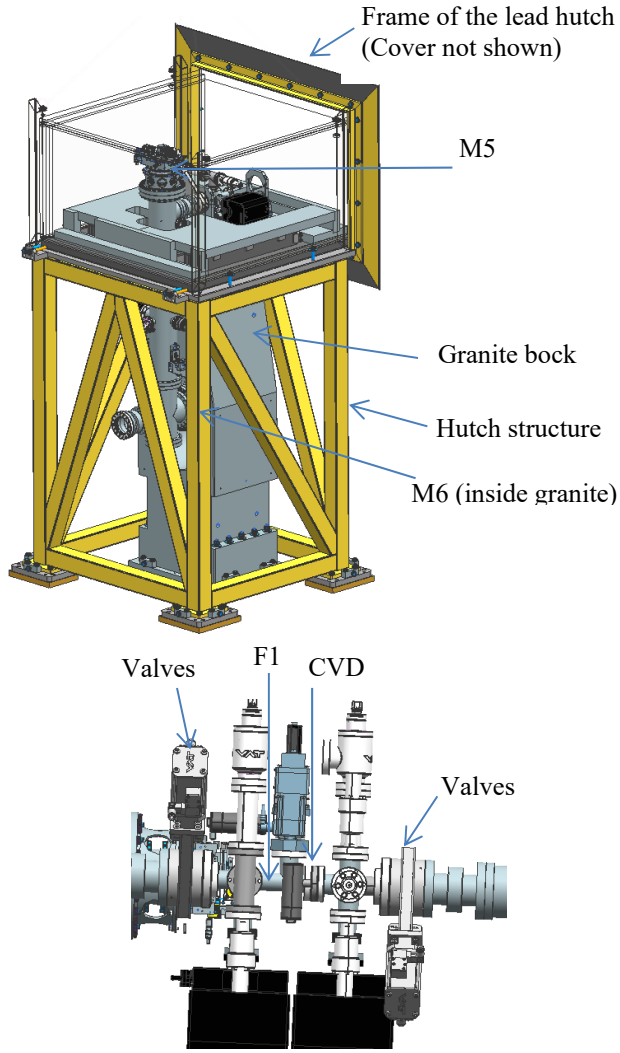


Figure 13: Top: M5, M6 support architecture. Down: Detail of the CVD vacuum section, top view.

The beam is transported to the end station inside the experimental hutch by mirror M7. A flat mirror in its goniometric assembly is mounted on top of a linear translation mechanism (see Fig. 14) which intercepts the incoming IR beam (or a part of it) and deflects towards mirror M8 and to the micro spectroscopy End station. The other fraction of IR beam propagates towards 2nd and 3rd End station to be developed in the future (see Fig. 15).

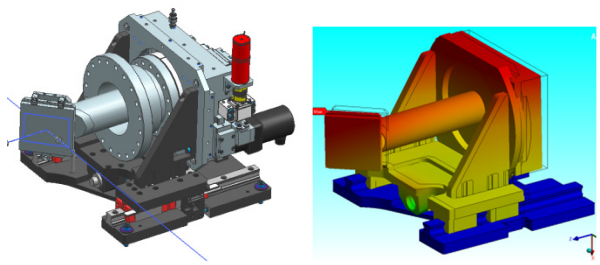


Figure 14: The beam splitter consists on a high resolution actuator that positions the transport mirror in a way that reflects only part of the IR beam.

ISBN: 978-3-95450-188-5 doi:10.18429/JACoW-MEDSI2016-FRAA03

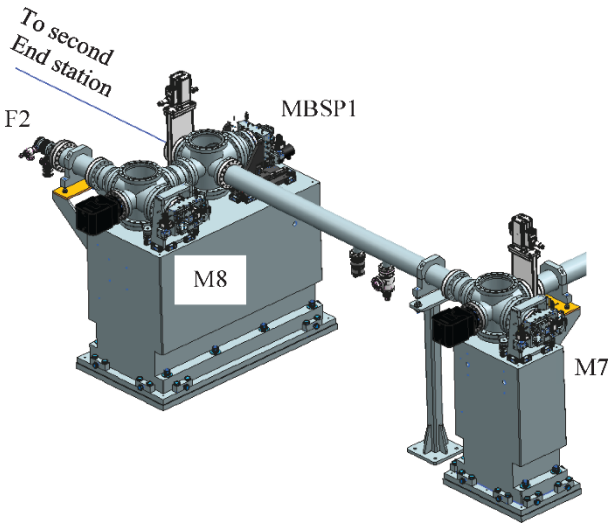


Figure 15: Focal point F2, MBSP1, M7 and M8.

VACUUM PRESSURE PROFILE

From the point of view of vacuum system design the operation of MIRAS requires a moderately high vacuum, except for beam extraction [3] section. In order to eliminate problems due to water vapour and carbon dioxide, pressures of about 100 mbar are sufficient. Vacuum calculation as a part of the comprehensive vacuum system design has been performed by Monte-Carlo simulation code using Molflow+ program, developed by R. Kersevan [4].

A simplified CAD model of the beam line vacuum chambers and transport mirrors were created based on fully developed 3D model. These models were exported to `.stl` format providing the geometry for simulations. The outgassing rate of materials varies by several orders of magnitude depending on the surface treatment and properties.

The transport mirrors and chambers of MIRAS are made of aluminium grade of 6061 and stainless-steel grade of 304L respectively. Thus, thermal outgassing rates of above mentioned materials have been selected for simulations. We consider an outgassing rate for non-baked aluminium because we assume that the heat will be poorly transferred to the mirrors from the chamber walls during the bake out cycle and the mirrors will not be well-baked.

The outgassing rate is $1x10^{-10}$ mbar·l/s·cm^2 for aluminium is, while for the stainless steel: $2x10^{-12}$ mbar·l/s·cm^2. The main gas source in the beam line is the thermal desorption which is distributed all over the system. Several simulations have been performed for the residual gases considering highest desorption rate and taking into account the molar masses as well as, pumping speeds of each corresponding gas type. Finally calculated partial pressures of each individual gas were summed.

Figure 15 shows simulation results considering 25 l/s pumps throughout the layout except for the first pump after the diamond window (45 L/s). The optimal pumping speed of 25 L/s was selected. The pumps were defined taking into account the lifetime during the operation and the achievable vacuum level for the beam line. Ion pumps were selected for the ease of maintenance and pressure below 10^{-6} mbar targeted for the pump's lifetime extension.

Comparing the gauge readings with the simulation result which is shown in the Fig. 16 (red dots), we can estimate the reasonable agreement of real gauge measurements against simulation result.

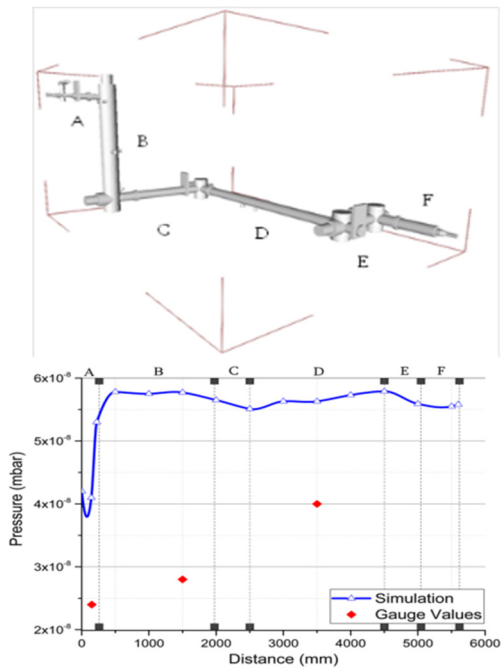


Figure 16: Pressure profile distribution along the beam path.

COMMISSIONING

After the first commissioning of M1 at 130 mA, temperature readings on the thermocouples along the slot did not exceed was 32ºC and 25ºC on the mirror's body respectively. This value agrees well with one produced by the simulation at 130mA, where the maximum temperature of the body of the mirror will not exceed 34ºC.

Fig 16 shows the camera image of M1 during operation where the visible light fraction of the radiation emission can be observed illuminating edges of the slot. The thermocouples protruding into the slot can be appreciated.

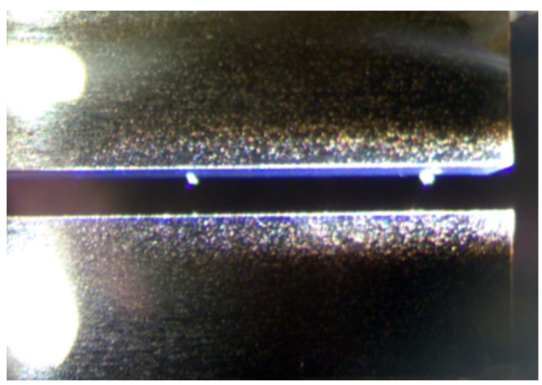


Figure 16: IR beam on M1 surface.

Content from this work may be used under the terms of the CC BY 3.0 licence (© 2016). Any distribution of this work must maintain attribution to the author(s), title of the work, publisher, and DOI.

ISBN: 978-3-95450-188-5 doi:10.18429/JACoW-MEDSI2016-FRAA03

Content from this work may be used under the terms of the CC BY 3.0 licence (© 2016). Any distribution of this work must maintain attribution to the author(s), title of the work, publisher, and DOI.

ACKNOWLEDGEMENTS

We would like to acknowledge the technical and scientific assistance by SOLEIL (France) SMIS beamline team, Dr. Paul Dumas and Stephane Lefrancoise as well as contribution by Dr. Gary Ellis (ITP CSIC, Spain).

REFERENCES

[1] MIRAS, www.albasynchrotron.es/en/beamlines/bl01-miras

[2] M. Quispe†, A. Carballedo, J.J. Casas, C. Colldelram, A. Crisol, G. Peña, Ll. Ribó, I. Sics, and I. Yousef, "Study on Thermal Mechanical Design and Optimization Analysis for the ALBA Infra-Red Microspectroscopy Beamline (Miras) Extraction Mirror Based on Finite Element Analysis", in *Proc. MEDSI'16*, Barcelona, Spain, Sep. 2016, pp. 179-182. doi:10.18429/JACoW-MEDSI2016-TUPE11

[3] A. Carballedo, M. Quispe, C. Colldelram, Ll. Ribó, and A. Crisol, "Vacuum and Optical Design of the ALBA Infrared Beam Line MIRAS", in *Proc. MEDSI'14,* Melbourne, Australia, Oct. 2014.

[4] http://test-molflow.web.cern.ch/

ISBN: 978-3-95450-188-5 doi:10.18429/JACoW-MEDSI2016-FRBA01

A NEW CRYSTAL BENDER FOR THE ID31 LAUE-LAUE MONOCHROMATOR

M.Magnin-Mattenet[1], P. Got[1], A. Vivo[1], V. Honkimäki[1]
[1]ESRF, 71 avenue des Martyrs, 38043 Grenoble, France.

Abstract

The ID31 beamline is able to provide X-Ray energies ranging from 20 to 150keV. The energy range 50-150keV is covered by a Laue-Laue monochromator located at 105.2 meters from the source. Two asymmetrically cut Si crystals equipped with benders, based on a new concept, provide an energy resolution ranging from few hundreds of eV down to the Darwin width of few eV.

The bender principle, design, manufacture and first commissioning will be described. The virtual source, produced with a white beam transfocator, can be before or after the monochromator. Therefore the bending mechanism must allow both concave and convex configuration with bending radius from 20m to infinite. Each bender is equipped with two home made piezo-jacks controlled in close loop with capacitive sensors. The system is liquid Nitrogen cooled. The thermal behaviour will be described in detail and thermo-mechanical finite element analysis will be presented.

INTRODUCTION

The X-ray source of ID31 is an in-vacuum cryo-cooled undulator with 14.5mm period and the aim of the optical design of the ID31 beamline is to provide the highest possible X-ray beam intensity over the energy range of 20 to 150 keV. The X-ray techniques available at ID31 are tomography, reflectivity, SAXS and WAXS techniques which are used to study fuel cells, solar cells, rechargeable batteries, catalytic materials and various "dirty" interfaces. The beamline is equipped with three focusing devices used in combination with the ID31 Laue-Laue monochromator which is located at 105.2 meters from the source and covers the energy range from 50 to 150keV.

THE LAUE-LAUE MONOCHROMATOR

The Laue-Laue monochromator consists of two bent Si(111) crystals in non-dispersive geometry with an asymmetric cut of −36°. The crystals can be rotated so that other reflections in the (110) and (001) plane can be used, e.g. the Si(113) reflection with an asymmetric cut of −6.5°. The crystals thickness is 5 mm and they are LN2-cooled. Since the virtual source given by the compound refractive lens can be before or after the monochromator the bending mechanism allows both concave and convex bending. The beam offset can vary between 7 and 25mm. To allow the full energy range with 20 mm offset, the second crystal has a translation along the incident beam from 250 to 750mm relative to the first crystal.

THE BENDER

Various benders for mirrors or crystals have been developed in the past at ESRF [1-2], but none of them fully answer the specifications for the ID31 beam line.

Specification

The beam bandwidth is proportional to the inverse of the bending radius of the crystal determined by the virtual source to crystal distance. Therefore a convex and a concave bending with cylindrical shape is needed from ∞ to 20m. A coarse rotation of the crystals (±40°) is used to select reflections from (110) and (001) plane.The liquid nitrogen cooling is mandatory due to the high heat load generated by X-rays. Furthermore, the cooling scheme has to be optimized for both crystals to minimize thermal bump caused by the incident X-ray beam. Moreover, the absorbed power is tuned with the absorbers located in the first optical hutch. The crystals and bending mechanism has to be high vacuum compatible (10^{-8}mbar). The resolution in energy has to be 1ev. All this constraints led to a new principle for the bender.

Principle and Concept

The main difficulty is to fix the cryo-cooled crystal so that it is not sensitive to the vibrations induced by the cooling or other sources. Furthermore, the crystal should be mounted without torsion. Due to these constraints the concepts based on four-bar-bender or cantilever are not suitable. The new concept consists in finding a clever dimensioning of the bender relatively to the crystal so that the fixing points are placed where no significant aberration of the bender and crystal from the cylinder occurs [e.g, Fig.1a]. The new bender described here is very well adapted to provide at the same time a cylindrical shape of the crystal, a very high stiffness with a very good thermal contact for the cooling [e.g, Fig.1b]. The bender has a rigid middle part which is strongly attached to the support. On each side, one flexure is used as a rotating point to allow the motion controlled by the piezojacks. Two piezo-jacks attached on both side provide the push/pull forces. The piezo jacks are controlled in close loop with capacitive sensors located on both sides.

Content from this work may be used under the terms of the CC BY 3.0 licence (© 2016). Any distribution of this work must maintain attribution to the author(s), title of the work, publisher, and DOI.

ISBN: 978-3-95450-188-5 doi:10.18429/JACoW-MEDSI2016-FRBA01

Content from this work may be used under the terms of the CC BY 3.0 licence (© 2016). Any distribution of this work must maintain attribution to the author(s), title of the work, publisher, and DOI.

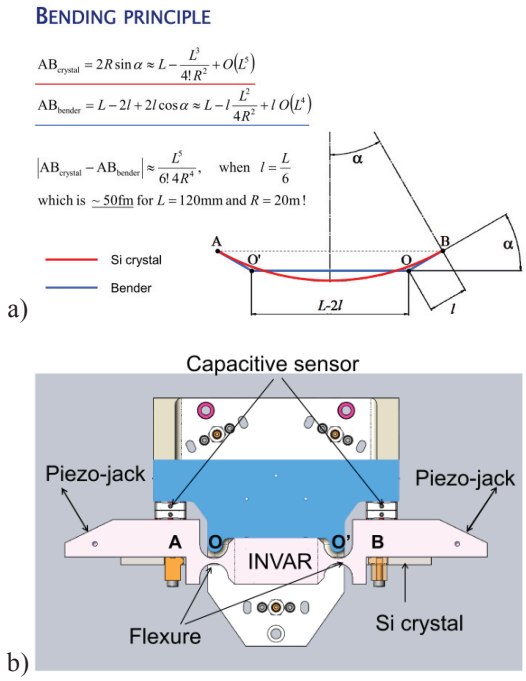


Figure 1: a) The bender is represented in blue line. The crystal is in red. Flexure points are on O and O'. No significant aberration from the cylinder occurs at the fixing point A and B, when the lengths of the lever arms AO' and BO are one sixth of the length of the crystal. b) The concept of the bender. The flexure points O and O' of the bender made from Invar are like in Fig. 1a. The crystal is clamped on the lever arms which are pushed or pulled by the piezo-jacks. The capacitive sensors measure the displacement of the lever arms at the opposite side of the clamps.

Analytical Approach

The deformation of the crystal $u(x)$ is analytically defined starting from the mechanical beam theory approximation [e.g, eq.1].

$$\frac{\partial^2 u}{\partial x^2} = \frac{M(x)}{EI} \quad (1)$$

where E is the Young modulus of Si, I is the inertia of the beam which equals $bh^3/12$, b is the width of the crystal, h is the thickness, and $M(x)$ the local bending moment.

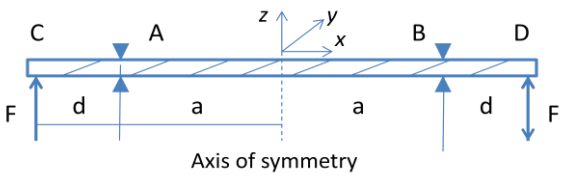


Figure 2: The crystal is attached to the bender on points A and B. F is the pulling/pushing force delivered by the piezo-jacks at C and D. Note the similarity with the four-bar-bender.

The crystal is bent in the horizontal plane and therefore the weight of the crystal can be neglected. The forces applied on both sides on points C and D [e.g, Fig. 2] by the piezo-jacks are equal. The anticlastic effect is neglected and the origin of the referential is taken in the middle of the crystal [e.g, Fig. 2]. The deflection is zero at the origin to simplify the equations. The deflection of the crystal between the fixing point A and B follows a pure cylinder as expressed in the following equation:

$$u_1(x) = \frac{d.F}{EI} * x^2 \quad (2)$$

The deflection of the crystal between the fixing points A and B and the pushing/pulling points C and D, respectively, follows the motion of the bender which can be considered rigid in this region, rotating around the flexures located in O and O'[e.g, eq 3].

$$u_2(x) = \frac{2d.Fa^2}{EI} x - \frac{dFa^2}{EI} \quad (3)$$

A matlab program developed by the authors calculates the deformation along the crystal and determines the displacement of the the piezo jacks for a specified bending radius. Figure 3 shows the deflection curve of the crystal for a requested radius of 20m. As an example the analytical model indicates that a radius of curvature of 20m is obtained with a displacement of 283.7 microns of the jacks. A displacement of zero of the piezo-jacks corresponds to an ∞ radius, i.e. a flat crystal.

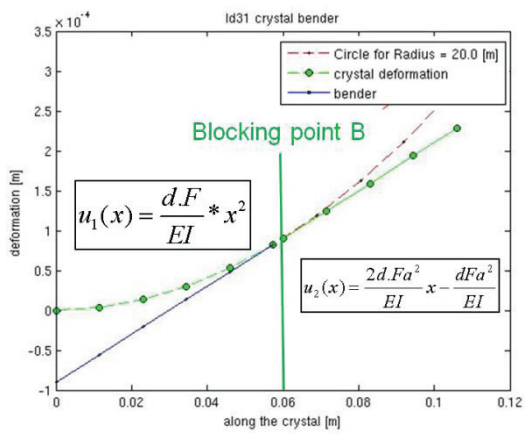


Figure 3: The deformation of the crystal follows the green curve. It is composed of a cylindrical shape between the fixing points AB and a linear slope given by the bender beyond these points.

Finite Element Analysis

The material of the bender has been determined taking into account the behaviour in a cryo environment. The

ISBN: 978-3-95450-188-5 doi:10.18429/JACoW-MEDSI2016-FRBA01

relative motions between the bender and crystal must be small enough to reduce the stresses during the cooling down of the assembly from room temperature to 88K. Furthermore, the final stresses should be as low as possible to avoid any torsion of the crystal. Invar was a natural candidate despite of its very low thermal conductivity. Two studies were made with finite element analysis with "Solidworks Simulation". The first model is a mechanical study of the bending of the crystal and the bender [e.g, Fig 4]. As expected, the maximum stress is registered in the flexure.

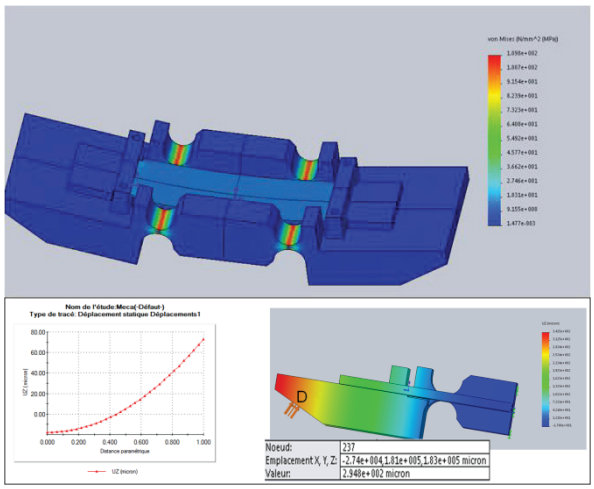


Figure 4: FEA for a radius of curvature of 20m. Top: the maximum stress is 110MPa. It remains much lower than the invar limit of 450MPa. Bottom left: deformation along the crystal . Bottom right: the jack motion is 295microns.

The second model is a non-linear thermo-mechanical model which takes into account the variations of the expansion coefficient and thermal conductivity as a function of the temperature [3-6]. The variation of the Young modulus as a function of the temperature has been estimated as a second order effect in the calculations and has not been taken into account. This model simulates the behaviour of the system during the cooling from room temperature to LN2 cryogenic temperature (88K).The stresses between the crystal and the bender are very close to the limit. This point has been solved by adding a layer of Indium between the crystal and the bender. Furthermore, it serves as well as an excellent thermal contact. The final stresses at 88K temperature due to the different thermal expansion of the Invar and the Si predicts a slight bending of the crystal.

Design and Prototype

Taking into consideration the different results from analytical and FEA analysis, the bender was designed as shown in the Figure 5. The bender with 3mm thick flexures and the clamps are in Invar. The crystals are 5mm thick. Copper cooling parts (not shown in the Fig. 5) are strongly attached on both sides of the bender and are also in contact with the end parts of the crystal with indium foil that insures a good thermal contact and a reduction of stresses. The thermal stability of the assembly is guaranteed by a thermal regulation made with resistive heaters on the interface plate between the bender and the rest of the mechanics below the bender. The crystal is stiffly maintained on to the bender. All the mechanics are high vacuum compatible (10^{-8}mbar). The resolution is insured by the piezo- jack in close loop with the capacitive sensors located at the opposite side of the crystal clamps. The piezo-jacks specially designed for this application have a very high resolution: 20nm.

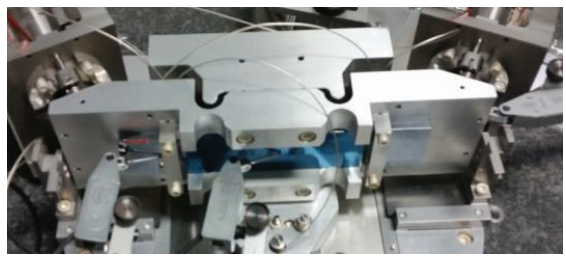


Figure 5: A prototype of the bender with its crystal. Two piezo-jacks behind are pulling/pushing on both sides. The path is free in the middle for the X-ray beam.

Commissioning

Preliminary measurements have been made in optics laboratory with a Fiseau interferometer. The first measurement is made when the crystal is free, i.e. before the mounting. This gives the zero reference radius of the crystal planes. Figure 6 shows the curvature of the surface of the crystal when bent to 20m radius. One can observe the anticlastic effect in the middle of the crystal. When the initial topography of free crystal was subtracted the slope errors from the cylinder are less than 1nm at the middle part of the crystal. At the vicinity of the clamps the errors are close to 100nm due to the clamping which prevents the anticlastic bending.

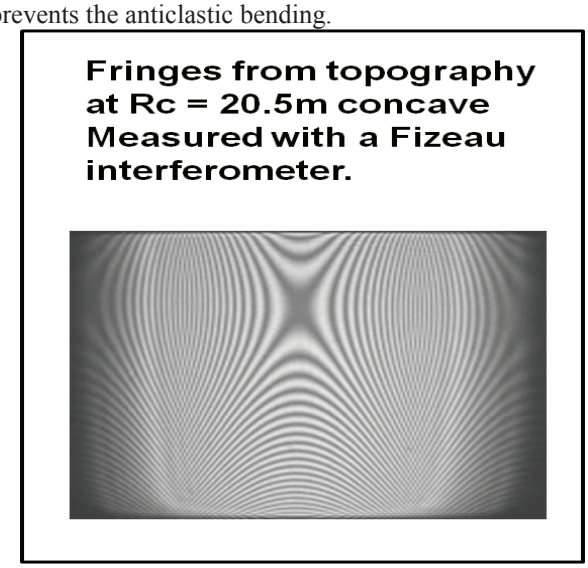


Figure 6: Optical franges showing the deformation of a crystal bend at radius 20.5m from zero lattice plane reference.

The ID31 Laue-Laue is now installed at ID31 with its two crystals and two benders inside. The first X-ray

Content from this work may be used under the terms of the CC BY 3.0 licence (© 2016). Any distribution of this work must maintain attribution to the author(s), title of the work, publisher, and DOI.

ISBN: 978-3-95450-188-5 doi:10.18429/JACoW-MEDSI2016-FRBA01

Content from this work may be used under the terms of the CC BY 3.0 licence (© 2016). Any distribution of this work must maintain attribution to the author(s), title of the work, publisher, and DOI.

measurements were done to determine the initial radius of curvature. Results shown in the Fig. 7 are in good agreement with the FEA analysis.

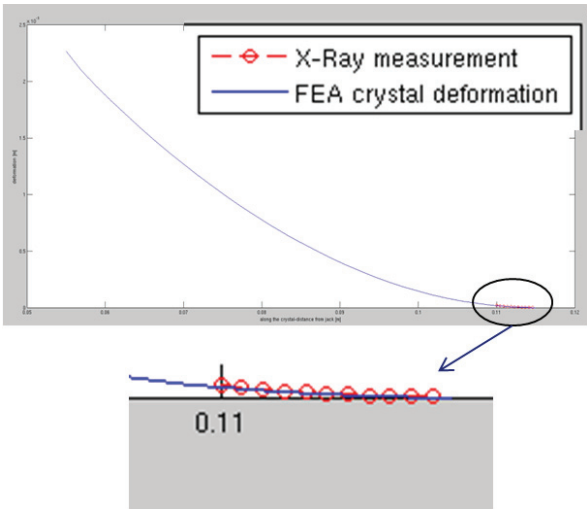


Figure 7: Behavior of the bender and its crystal when cooling down to 88K. The blue curve is the result of the deformation of the crystal as a result of the FEA analysis. The red circles represent the deformation as measured at the beam line with X-rays.

CONCLUSION

As described above the analytical analysis, the FEA analysis, the optical results and the first X-ray commissioning converge to give similar values for the behaviour of the system. As a resume we can say that the strong point of this system is its stiffness which makes the system insensible cryo cooling or other vibration sources. The cylindrical bending is reached in the region of interest and the resolution is given by the piezo-jacks, specifically developed for this application, in close loop with capactive sensors.

AKNOWLEDGEMENTS

We would like to thank the different groups from ESRF who participate in the mounting, cabling, testing, alignment, handling and installation of the system. Particular thanks will go to G.Malandrino for mounting, K. Amroui for cabling, H.P Van Der Kleij, L. Rousset, B.Lantelme for testing, H.Witsch, A.Homs for control and B. Picot for the manufacturing of the cystal.

REFERENCES

[1] Rossetti D. , Lienert U. , Pradervand C. , Schneider R. , Shi M. , Zelenika S. , Rossat M. , Hignette O. , Rommeveaux A. , Schulze-Briese C. – Design and performance of the flexural hinge-based mirror bender at the SLS protein crystallography beamline X06SA Proceedings SPIE 4782, 86-93 (2002).

[2] Barrett R. , Baker R. , Cloetens P. , Dabin Y. , Morawe C. , Suhonen H. , Tucoulou R. , Vivo A. , Zhang L. - Dynamically-figured mirror system for high-energy nanofocusing at the ESRF Proceedings SPIE 8139, 813904-1-813904-12 (2011)

[3] Watson, T.W. and Robinson, H.E., ASME J. Heat Transfer, v83(4), 403-8 (1961) and NIST, Physical and Chemical Properties Division, Cryogenics Technologies Group at http://cryogenics.nist.gov

[4] "The JPL cryogenic dilatometer: measuring the thermal expansion coefficient of aerospace materials" P.G. Halverson and al,Jet Propulsion Laboratory, California Institute of Technology, Pasadena, California 91109

[5] C.Y. Ho, R.W. Powell and P.E. Liley, J. Phys. Chem. Ref. Data, v1, p279 (1972)

[6] C.A. Swenson, J. Phys. Chem. Ref. Data, vo. 12(2), p179 (1983)

ISBN: 978-3-95450-188-5 doi:10.18429/JACoW-MEDSI2016-FRBA02

THE NANOBENDER: A NEW X-RAY MIRROR BENDER WITH NANOMETER FIGURE CORRECTION

Carles Colldelram[1*], Josep Nicolas[2], Claude Ruget[1], Pablo Pedreira[1], Igors Sics[1], Llibert Ribó[1], Albert Tomas[3], Joan-Manel Casalta[3], Carlos-Martín Nuño[3], David Úbeda[3]
1 CELLS, Cerdanyola del Vallès, Spain
2 SLAC, Stanford, California, United States
3 Sener Ingeniería y sistemas, Cerdanyola del Vallès, Spain

Abstract

Over time X-Ray mirrors are demanded for better focusing, closer to sample refocusing, spot size as well as better beam uniformity at sample position. Based on the experience of ALBA Phase I beam lines a new alternative design of a mirror bender is proposed [1]. The system includes two main functionalities: the mirror bender mechanism and mirror figure error correction. Both mechanisms are based on the introduction of a force constrain on the mirror surface instead of a geometrical one. As being based on a force mechanism they could reach high resolution and especially for the correctors which can achieve nanometre resolution. The correctors are designed to provide high force stability in the mirror side, eliminating the crosstalk between bending and figure correction, and minimizing the sensitivity to drifts. With such controlled deformation of the mirror substrate it is possible to obtain the desired surface figure not only to correct mirror figure errors but also to adapt it to the incident wavefront, thus becoming adaptive system. The mechanical solutions are presented which are able to correct mirror surfaces with a resolution of 1 nm reaching slope errors below 100 nrad.

INTRODUCTION

This new X-Ray mirror bender system has been conceived in the ALBA Beam Lines Phase I framework. The protein crystallography beam line at ALBA, BL13 XALOC [2], has a quite simplified optical lay-out with a channel-cut crystal monochromator and a couple of focusing mirrors placed in a Kirkpatrick-Baez (KB) configuration [3]. The mirror system allows reaching a focus spot of 50×5.5 μm^2 FWHM (H×V). This both mirror system were outsourced. The spot quality at sample position is mainly depending of the optical surface quality of this vertical focusing mirror (VFM), of its slope error, and in order to minimize the striation in the beam it was requested to the manufacturer to include a number of gravity sag compensators to have the possibility to use them not only to correct gravity flexion but also for mirror optics figure corrections.

Already with these correctors [4], thought to compensate gravity sag errors, the system has already an initial rough but enough force resolution allowing the mirror figure correction based on the Elastic Beam Theory [5] and a high-accuracy profile metrology, the ALBA NOM optical metrology system (see Fig. 1).

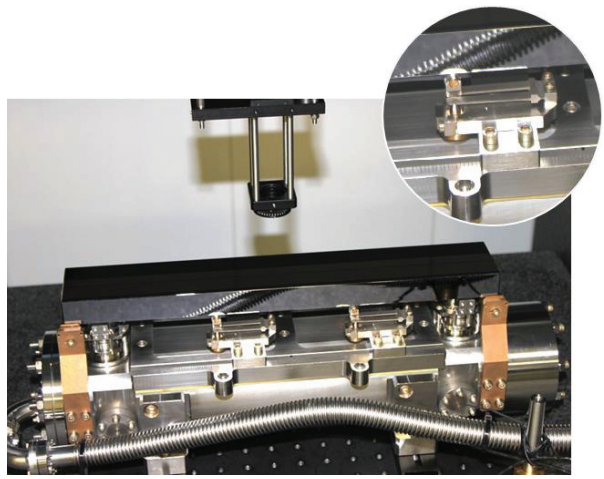


Figure 1: BL13 Xaloc VFM at ALBA NOM.

By means this analytical calculation, the actual surface error and an optimization algorithm we were able to calculate the number of correctors, setting force and position along the mirror to improve the mirror figure. Although these corrector were manual and not made to deal with this function the 300mm mirror was corrected from its initial slope error of 0,242µrad up to 0,055 µrad (see Fig. 2) by mean two of these gravity sag compensators and both pushing from below.

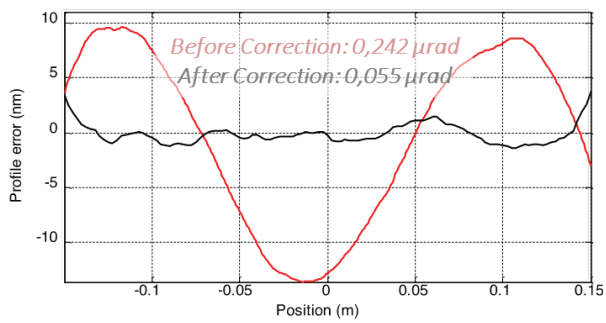


Figure 2: VFM optical surface height.

A ray tracing simulation of the mirror before and after the correction give a picture of the beam quality at sample position and its undesired striations improvement (see Fig. 3).

* ccolldelram@cells.es

Content from this work may be used under the terms of the CC BY 3.0 licence (© 2016). Any distribution of this work must maintain attribution to the author(s), title of the work, publisher, and DOI.

ISBN: 978-3-95450-188-5 doi:10.18429/JACoW-MEDSI2016-FRBA02

Content from this work may be used under the terms of the CC BY 3.0 licence (© 2016). Any distribution of this work must maintain attribution to the author(s), title of the work, publisher, and DOI.

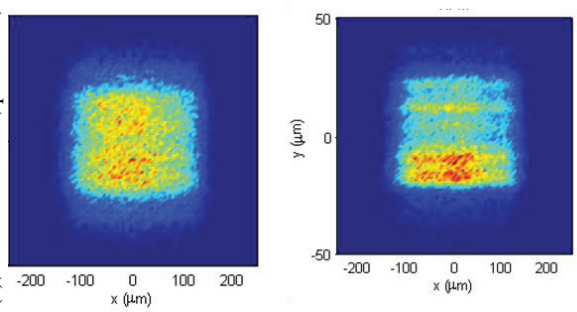


Figure 3: Beam spot ray tracing simulation at sample position.

Moreover beam line in-situ measurement (see Fig. 4) was possible to be performed by means pencil beam technics after 2 years of its installation at the beam line. These measurements show a very good agreement between the optics laboratory optimization and the in-situ test demonstrating the performance of this method and its high stability which motivates the design if a new bender concept developed in following chapters.

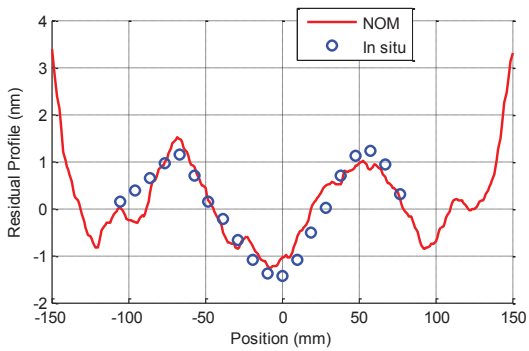


Figure 4: Laboratory measurement vs in-situ test after two years.

NEW CONCEPTS

Geometrical vs Force constrains

From the experience acquired with the optimization of this initial mirror new concepts were applied to a new bender design. A mirror substrate could be deformed in order to optimize its optical surface by means high resolution force actuators (see Fig. 5).

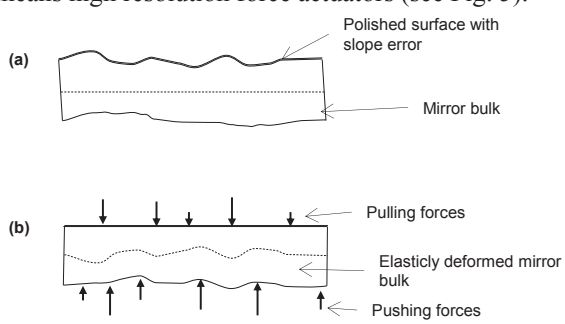


Figure 5: Illustration of surface correction by elastic deformation of the substrate. (a) Original mirror with surface errors. (b) mirror deformed compensating surface errors.

This optimization could be done by means two type of mechanisms. One could be based on rigid mechanics which introduce the desired deformation. Second option is the soft way by low rigidity mechanism as stable-force actuators which allow the introduction of a force with high resolution and much more insensitive to drift thus much more stable (see Fig. 6).

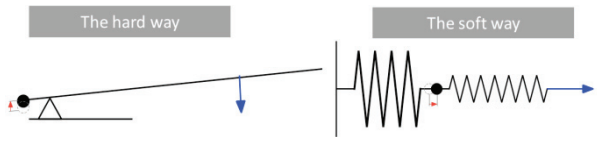


Figure 6: Possible mechanism concepts to bend a mirror.

The second concept it has been applied for the design of this new bender mechanisms in both mirror bender and mirror figure correctors mechanics.

BENDER DESIGN

Lay-Out

In this project, this novel concept of mirror bender is proposed (see Fig7). A bender mechanism that introduce a force constrain close to the support ends introducing the flexion torque which deforms the mirror in a way that can be predicted by the above mentioned theory which can be resolved by a third degree polynomial. But the novel technics is a system of correctors which applies controlled forces at the different points of the mirror, to induce the controlled deformation of the substrate that compensates the polishing errors. With this, the resulting figure errors can be reduced below one nanometre.

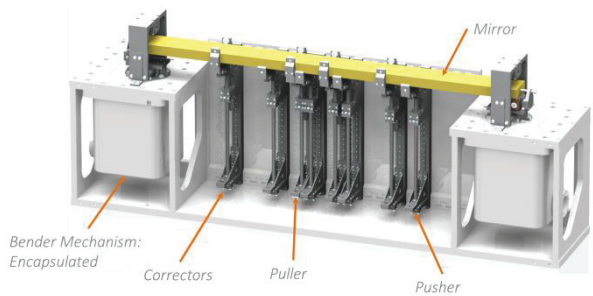


Figure 7: Nanoberder model.

The design of the correctors must be able to apply forces up to 40 N, with a resolution and stability of 0.01 N, in order to preserve the correction of the mirror. By analysing the initial mirror flatness the method calculates the force and the position of each actuator to reach ultimate correction of the mirror reflective surface and thus minimum incident wavefront aberrations and thus to be able of even incident wavefront correction.

Bender Mechanism

The mechanism for controlling the elliptic shape of the optical surface of the mirror (See Fig. 7) is based on the elastic bending of the mirror substrate under two

ISBN: 978-3-95450-188-5 doi:10.18429/JACoW-MEDSI2016-FRBA02

torques applied at its extremes. These torques are obtained by applying forces, normal to the mirror surface, at offset positions from the points where the mirror is simply supported, without embedment. The system is designed to accommodate mirrors from 300 mm to 1500 mm with a cross section of 50 mm width by 20 mm thick.

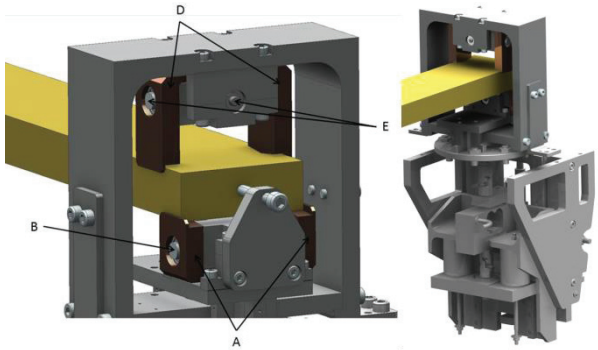


Figure 8: Bender mechanism.

The mirror support contacts the ends of the mirror at four contact points (see. Fig. 8, A). The support points have articulated mounts on the contacting parts to avoid introducing any force other than purely normal to the mirror surface. An articulated rotation (see Fig. 8, B) on the transversal direction allows the mount accommodating to the bottom face of the mirror substrate, thus avoiding introducing longitudinal components of force. Similarly, one of the two supports includes a rotation about the longitudinal direction of the mirror (see Fig. 8, C). With this, the support can accommodate to the mirror face, whose orientation is determined by the other support, which does not include this rotation. The bending forces are introduced by contact points offset 25 mm from the vertical of the supports, towards the centre of the mirror (see Fig. 3, D). The bending actuators have double articulated contacts (see Fig. 3, E) to ensure that the applied force is purely vertical. All mentioned contacts are doom shaped, to avoid excessive stress at the surface contact points. All the bearings used in the articulations are deep grove bearings, which have certain play or clearance, allowing a minimum rotation on the transverse directions of bearing axis. This helps on avoiding undesired loads. All of them are also hybrid bearings, fully Ultra High Vacuum compatible.

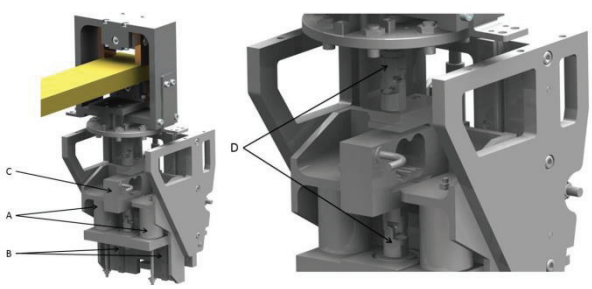


Figure 9: Bender mechanism.

The bending mechanism (see Fig. 9) is a spring based loading system that allows introducing a force up to 500 N, corresponding to a bending torque of 10.5 Nm. The spring (Fig. 9, A) is compressed by a conventional linear stage, which includes two linear guides (see Fig. 4, B) and is driven by a ball bearing nut and spindle system. The spindle is actuated by a stepper motor with a reduction factor 1:276. This allows for a resolution of 0.05 μm, equivalent to a force resolution about 0.0004 N. The spring can be compressed by 60 mm which allows for a versatile force range, and reduces in turn the system sensitivity to thermal drifts which may change the spring compression length and mirror ellipse correspondingly.

The force is transmitted to the mirror by means of a mechanical chain which includes a strain gauge (see Fig. 9, C) placed between two bearing gimbal articulations (see Fig. 4, D) which ensure that the applied force is purely vertical, and along the measuring axis of the gauge. All this mechanism is not Ultra High Vacuum compatible, and is therefore enclosed in an air volume, surrounded by vacuum. The force is transmitted through a double edge-welded bellow (see Fig. 4, E) which self-compensates vacuum forces. As shown in the next chapter the focus of the ellipse generated by this bending is independent of the figure correction.

The Correctors

The correctors deals with the slope error compensation or mirror optical surface shape correction. This small mechanism allows the introduction from 0 to 40N forces on the mirror in-between the two extremes bending mechanisms (see Fig. 7). It can be placed at any position along the mirror as function of the mirror initial flatness and its optimized correction values on force, position and number of correctors with a minimum separation of 22mm. It can be settled in pushing or pulling forces at convenience of the force value.

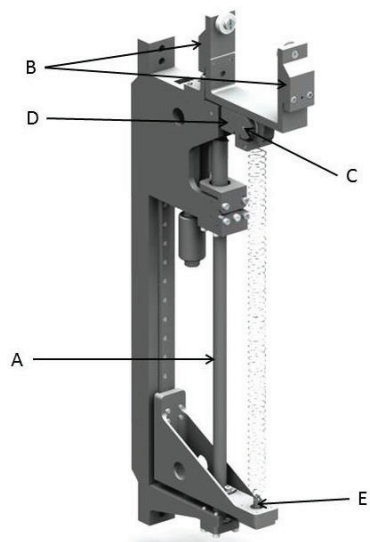


Figure 10: Corrector mechanism.

The correctors consist on a long traction spring with a very small spring constant that allows for a force

Content from this work may be used under the terms of the CC BY 3.0 licence (© 2016). Any distribution of this work must maintain attribution to the author(s), title of the work, publisher, and DOI.

ISBN: 978-3-95450-188-5 doi:10.18429/JACoW-MEDSI2016-FRBA02

Content from this work may be used under the terms of the CC BY 3.0 licence (© 2016). Any distribution of this work must maintain attribution to the author(s), title of the work, publisher, and DOI.

resolution below 0.001N (see Fig. 10). The long spring allows the system also for high robustness to thermal drifts, and allow for reproducible correction after dismounting and re-mounting the mirror.

The spring is elongated by means of lead screw (see Fig. 10, A) actuated by a stepper motor. The correction force is applied to the mirror by two deep grove bearings (see Fig. 10, B), which contact directly the mirror surface. The bearings are held on a frame that is linked to the spring by a rolled articulation (see Fig. 10, C), to accommodate both contacts without introducing any twist or torsion on the mirror. This articulation can move only in the vertical direction, as is attached itself to a pivoting beam (see Fig. 10, D). The spring end can be attached to different points of the pivoting beam, which allows converting the corrector from pusher to puller. It also allows scaling the resulting spring force to obtain higher force resolution. The bottom fixation of the spring includes a bearing to allow the spring torsion and thus to avoid any residual transverse force. A linear guide allows placing the spring fixation at the vertical of the attachment at the upper end (see Fig 10, E). 20 N is the force estimated to correct 0.5 µrad rms mirrors for errors with period down to 22 mm.

With this low spring constant correctors the crosstalk between curvature adjustment and figure correction is completely eliminated as the micron level deformation of the ellipse setting does not introduce a significant change on the corrector as it is a negligible displacement for such week spring to introduce a real change of the corrector set force.

MANUFACTURING

Detailed design and manufacturing and assembly have been performed by Sener. Two prototypes have been built first one as prove of concept and second as industrialization optimization (see Fig. 11).



Figure 11: Second prototype.

MEASUREMENTS AND RESULTS

ALBA NOM

ALBA optical laboratory includes a Nanometer Optical Metrology bench. This is a 1,5m long highly accurate scanning deflectometer guided by means air bearings (see Fig. 12).

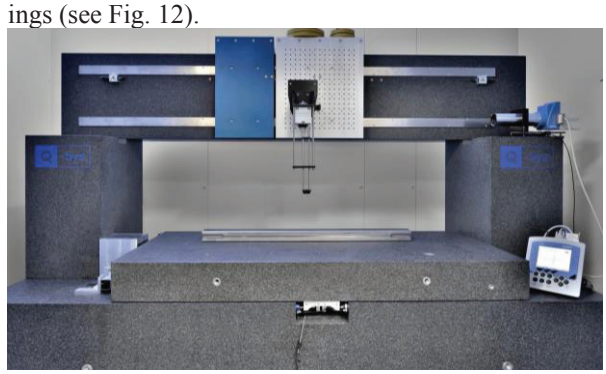


Figure 12: ALBA NOM.

The measuring axis, longitudinal, it is a smooth direct drive motion equipped with a ironless linear servo actuator.

The optical set up is composed by an autocollimator which measures directly the optical mirror surface slope and a pentaprism to deviate orthogonally the autocollimator beam from its horizontal pedestal to normal to the mirror surface eliminating at the same time pitch guidance errors.

The laboratory temperature is stabilized by means of a PID controlled post-heating system and well isolated from surrounding rooms (which are stabilized already at 1º around 23º) by means rockwood isolation. The NOM is encapsulated in a last isolation cabinet which dumps further temperature oscillation down to a hundredth of degrees.

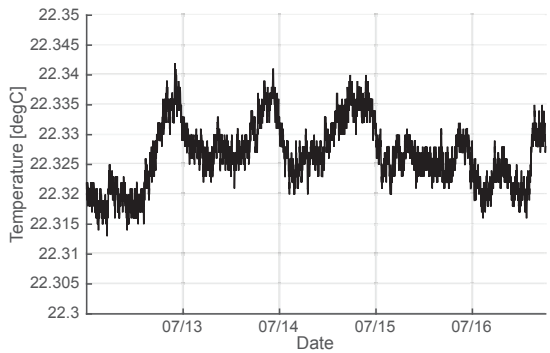


Figure 13: Optics laboratory temperature stabilization.

The ALBA-NOM can provide measurements that are accurate in the range of a few tens of nanoradians, and well below the nanometer [6].

Mathematical Deformation Model

The mathematical model is analytical an based on Euler Bernoulli-law [Eq. (1)].

$$EI\frac{d^4}{dx^4}z(x) = \sum_{n=1}^{N} F_n\,\delta(x - x_n) \tag{1}$$

The model is linear and allows superposition, thus the curvature of the deformation is a piecewise linear function and the surface curvature is a piecewise cubic polynomial.

ISBN: 978-3-95450-188-5 doi:10.18429/JACoW-MEDSI2016-FRBA02

With a theory dummy 1 meter long mirror the model predict that it is possible to correct a mirror that needs and induced deformation of 600nm, after removing the curvature, the model is accurate below 1 nm (see Fig.14).

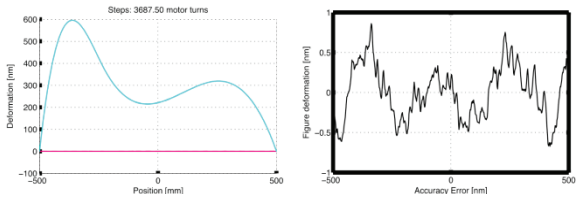


Figure 14: mirror correction mathematical model accuracy.

Bending Mechanism Performances

Table 1 shows the results of the bender mechanism.

Table 1: Bender Mechanism Performances

Performance	Figure
Bending range	0 – 500 N
Bending resolution	< 0.001 N
Strange gauge sensitivity	16 nrad (RMS)
Actuator linearity	35 nrad
Bending repeatability	15 nrad (RMS)
Stability	< 15 nrad / 5 days

Corrector Performances

Figure 15 shows the resolution homogeneity of the corrector. It is very regular around 1 mN.

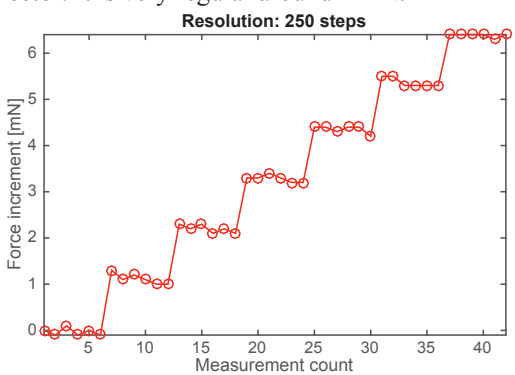


Figure 15: Corrector resolution.

The repeatability of the corrector also have been tested. By lifting the corrector contact and leaving it back to its contact position without resetting the corrector but measuring the force exerted on the mirror this is around 1 mN. Figure 16 shows the low force dispersion of the corrector.

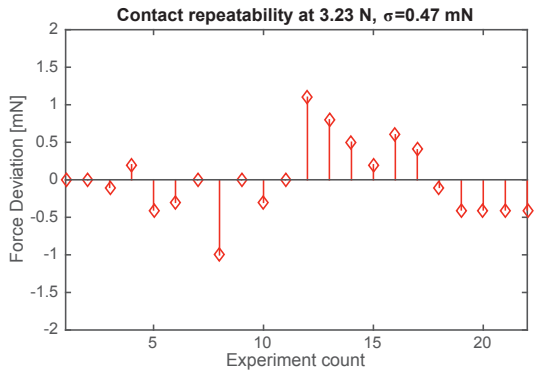


Figure 16: Corrector repeatability

Stability test shows that over 130h the stability is below ±30mN (see Fig. 17).

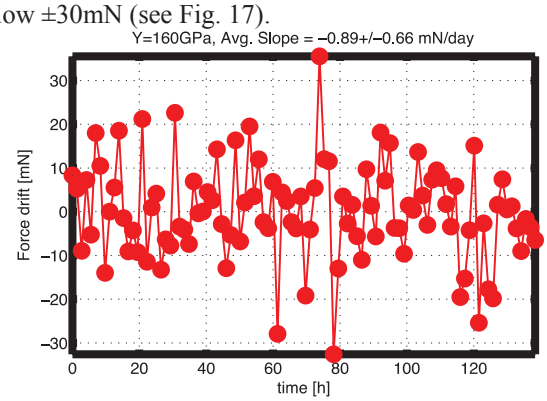


Figure 17: Corrector stability

Corrector motion repeatability is done by recovering the position from random positions, with this corrector setting repeatability is about ±20mN (see Fig. 18).

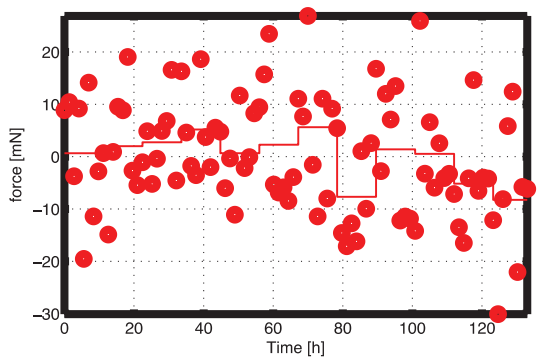


Figure 18: Corrector motion repeatability.

Table 2 summarizes the results of the corrector mechanism.

Table 2: Bender Mechanism Performances

Performance	Figure
Corrector range	±40 N
Corrector resolution	~ 0.001 N
Contact repeatability	0,47 mN (RMS)
Stability (130h)	±30mN (PTV)
Motion repeatability	±20mN (PTV)

Content from this work may be used under the terms of the CC BY 3.0 licence (© 2016). Any distribution of this work must maintain attribution to the author(s), title of the work, publisher, and DOI.

ISBN: 978-3-95450-188-5 doi:10.18429/JACoW-MEDSI2016-FRBA02

Content from this work may be used under the terms of the CC BY 3.0 licence (© 2016). Any distribution of this work must maintain attribution to the author(s), title of the work, publisher, and DOI.

Mirror Optimization

A test mirror has been optimized with the two prototypes. The figure optimization is shown in the Fig. 19 and Table 3 summarizes the final corrected mirror figures.

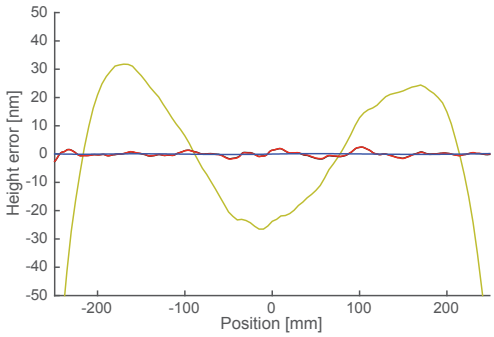


Figure 19: Test mirror optimization.

Clearly the optics mirror surface is corrected at nanometre level.

Table 3: Bender Mechanism Performances

Performance	Figure
Initial slope error	0,87 µrad (RMS)
Corrected slope error	0,115 µrad (RMS)
Initial surface error	23,2 nm (RMS)
Corrector surface error	0,858 nm (RMS)

With the mathematical model it is possible to optimize the correctors position, the force and its sense.

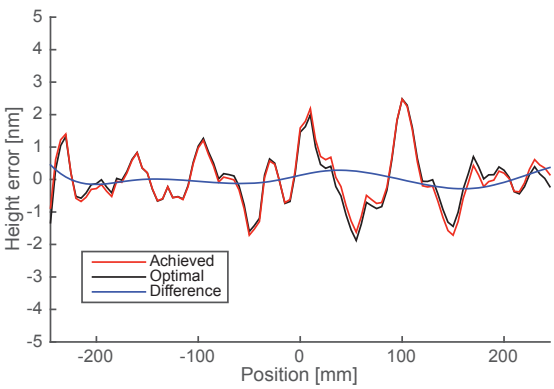


Figure 20: Test mirror height errors.

The model is able to predict the deformation of the mirror with an accuracy better than 0,08 nm RMS.

NEXT STEPS

Bender and Corrector Improvements

The corrector repeatability has already been improved with the evolution from the first and the second prototype. Nevertheless the bender mechanism it is still encapsulated complicating the hardware and its cost. Due the low rigidity of the correctors springs make the bender to be too tall and thus ending to a much bulky instrument. Thus the most relevant improvements to introduce would be:

- Remove the bender mechanics encapsulation.
- Compact the bender mechanism.
- Compact the correctors.

Bender mechanism compaction would need for new proposals while correctors could be reduced by means the already proposals with magnets stabilization concepts developed in the paper and patents [7,8,9] for spring in which the corrector spring constant could be increased as the force application could be stabilized in a range of almost 1 mm of drift, the motion have already enough resolution to absorb this reduction. This rigidity increase of the spring allows reducing its length while still maintaining its force range. The articulation bearing friction and also stability, as the bearing has some play, could be also improved by the stabilized flexures proposed in these publications.

Active Optics

The design of the mechanical system is thought to allow an easy design upgrade to an active optics bender able not only to improve mirror figure polishing errors but also able to correct incident wavefront aberrations.

For this purpose correctors must allow its adjustment after installation or even in beam line operation phase. For this purpose the correctors includes already a motorization, only it is needed to change the selected stepper motor by a UHV compatible one, market already have options on this sense.

The next issue is ensuring that force could change its sense. This could be easily solved by means mounting two spring on each level arm extreme one that could deal with the range and the opposite extreme a spring that could compensate twice the range. Optimizations shows that typically with few correctors are enough, just by mounting as much as possible, separated by the minimum needed separation, active optics must be possible as each corrector could set pushing or pulling force on its point depending on optimization request.

CONCLUSIONS

With these new proposed concepts based on high resolution and low rigidity force actuators a new bender with figure correctors have successful results at nanometre level, with an optimization mathematical model that predicts the corrected curvature down to 0,08 nm and improve mirrors slope errors easily below 0,1 µrad.

The bender mechanism with null crosstalk between curvature setting and figure correction is achieved.

The new correctors are very stable and with high force resolution to correct the mirror at nanometer level.

New –k compensated correctors have been designed and tested. They keep force constant within 1 mN in a range of motion of the mirror up to 2 mm. This will

ISBN: 978-3-95450-188-5 doi:10.18429/JACoW-MEDSI2016-FRBA02

allow friendly mirror dismantling and remounting and insensitive to drifts.

New, frictionless, torque free articulation has been designed, and is being currently tested in order to substitute the articulation bearing.

With all these bender characteristics X-Ray mirror can be curved with at the desired focus without introducing beam aberration or even correct incident beam ones.

ACKNOWLEDGEMENT

The authors thanks all involved members on the design, hardware set up and measurements. Especially the technicians head Jose Ferrer for the fine-tuned set up, Karim Maimoni and Jordi Navarro.

REFERENCES

[1] J. Nicolas, "*Dispositivo para curvar espejos*", Oficina Española de Patentes y Marcas, No. P201530735, May. 2016.

[2] J. Juanhuix, "Developments in optics and performance at BL13-XALOC, the macromolecular crystallography beamline at the Alba Synchrotron", *Journal of Synchrotron Radiation. Research Papers*, vol. 21, Part 4, p. 679-689, July 2014.

[3] Kirkpatrick, P. & Baez A.V, "Formation of Optical Images by X-Rays", J. Opt. Soc. Vol. 38, Issue 9, p. 766-774, 1948.

[4] J. Nicolas, "Focusing and defocusing using mechanically corrected mirrors at the MX beamline at Alba", J. Phys.: Conf. Ser. 425, Part 5, 2012.

[5] Goodwine, B. "Engineering differential Equations: Theory and Applications", Springer, 2011.

[6] J. Nicolas, J. & Martínez, J.C. "Characterization of the error budget of Alba-NOM", Nucl. Instr. Meth. in Phys. Res. A 710, p. 24-30, Nov. 2012.

[7] C. Colldelram, "Stabilization Methods for Force Actuators and Flexure Hinges", in *Proc. 9th Mechanical Engineering Design for Synchrotron Radiation Equipment and Instrumentation. (MEDSI'16)*, Barcelona, Spain, Sep. 2016, paper MOPE01.

[8] J. Nicolas, "*Dispositivo y metodo de aplicación de fuerza en un objeto*", Oficina Española de Patentes y Marcas, No. P201630506, Apr. 2016.

[9] C. Colldelram, "*Dispositivo de articulación*", Oficina Española de Patentes y Marcas, No. P201631142, Sep. 2016.

Content from this work may be used under the terms of the CC BY 3.0 licence (© 2016). Any distribution of this work must maintain attribution to the author(s), title of the work, publisher, and DOI.

ISBN: 978-3-95450-188-5 doi:10.18429/JACoW-MEDSI2016-FRBA03

DESIGN OF THE DIAMOND LIGHT SOURCE DMM FOR THE VMXi BEAMLINE

D. J. Butler†, J. H. Kelly, Diamond Light Source, Didcot, UK

Abstract

A Double Multilayer Monochromator (DMM) was designed in-house for the VMXi beamline. This paper describes the novel engineering solutions employed to build a high stability instrument. PiezoMotor® actuators drive sine-arm Bragg axes for both optics providing the coarse and fine motion in a single actuator. The long translation of the second multilayer is driven externally via a linear shift to eliminate in-vacuum pipe & cable motions. A high stability air bearing translates the whole DMM across the two multilayer stripes. The optics are water cooled via an Indium / Gallium eutectic alloy bath to minimise coupled vibrations. The DMM is operational on the VMXi beamline, experimental and performance data is presented.

INTRODUCTION

The in-situ Versatile Macromolecular crystallography (VMXi) beamline due to enter into service December 2016 is a high performance, high throughput autonomous upgrade to beamline I02. I02 currently operates a Double Crystal Monochromator (DCM) and the new DMM sits upstream of the DCM to allow both DCM and DMM based experiments. The DMM provides a broad energy band pass providing approximately 60x more photons to the sample. The overall design can be seen installed in the optics hutch (Fig. 1) and an isometric 3D CAD view (Fig. 2).

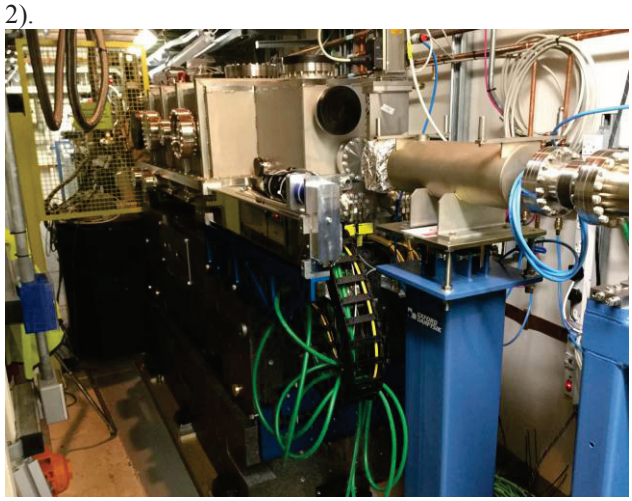


Figure 1: DMM installed in I02 optics cabin.

Stability of the beam was a critical criterion so throughout the design, care was taken to provide rigid mounting and stiff supports. Due to the shallow angles the DMM operates with, a relatively long travel in the beam axis is required. This is defined by the angular range and difference in multilayer heights. To maintain compatibility with the DCM, the DMM has a 25 mm vertical fixed offset so ML2 requires approximately 600 mm travel in the Z-direction (see Fig. 3).

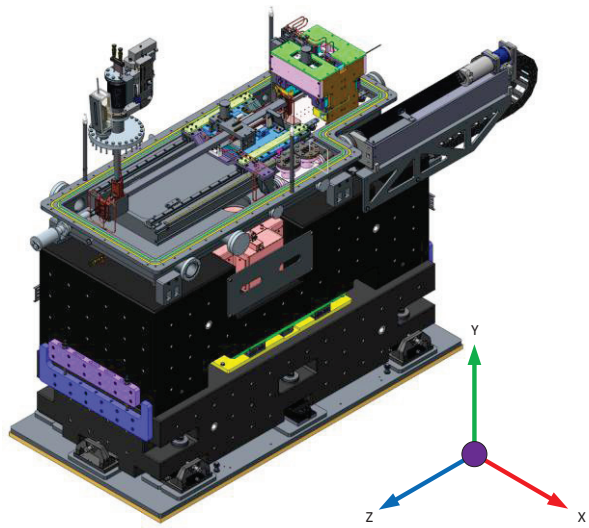


Figure 2: 3D CAD model of the VMXi DMM.

This posed a number of design challenges to maintain pitch stability over this range (the DMM is largely insensitive to roll and yaw). From previous experience with commercial DMMs and DCMs it was decided that an in-house design would be developed. The storage ring at DLS currently operates at 300 mA but future upgrade to a Cryogenic Permanent Magnet Undulator (CPMU) would increase the ring current to 500 mA. The DMM has therefore been designed with this in mind. Table 1 details the specification and achieved performance.

Table 1: DMM Specification

Incident design power (CPMU @500mA)	~590 W
Incident beam size	3.4 x 2.1 mm (max)
Deflection Geometry	25 mm down
Energy Range	10-25 keV
Beam stability (measured)	34 nrad (RMS)

DMM COMPONENTS

At the heart of the design are the multilayers – a silicon substrate on which layers of heavy and light elements are deposited. The multilayer can therefore be produced with a prescribed d-spacing and the VMXi multilayer has 2x stripes at d-spaces of 2 nm and 2.4 nm. This allows an energy range between 10-25 keV with some energy overlap between the two multilayers. To select either multilayers the whole vessel is translated in the X-direction on a granite air bearing.

† d.butler@diamond.ac.uk

Content from this work may be used under the terms of the CC BY 3.0 licence (© 2016). Any distribution of this work must maintain attribution to the author(s), title of the work, publisher, and DOI.

ISBN: 978-3-95450-188-5 doi:10.18429/JACoW-MEDSI2016-FRBA03

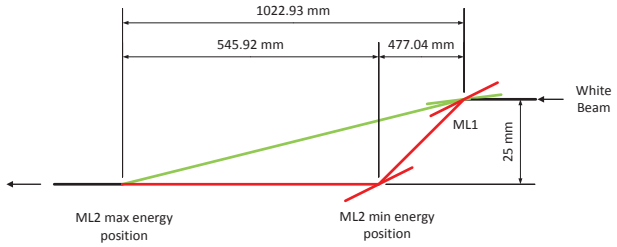


Figure 3: DMM optic geometry.

Multilayer Subassemblies

The two main subassemblies of the DMM are Multilayer 1 (ML1) and Multilayer 2 (ML2) which were designed to be assembled independently. This approach more favourably facilitated assembly, testing and commissioning at DLS. Each of the multilayer subassemblies sits on a cone, vee and 2x flats to increase stiffness while still providing repeatability in mounting. While not truly kinematic, due to the large span and relatively large mass the increased stability from 4x mounting points was preferred. The mount posts inside the vessel form a continuous solid path down to the granite and are coupled to the vessel via thin walled tubes. This allows some compliance without the need for bellows to isolate the internal components.

Multilayers

The silicon multilayers are shown in Fig. 4 with the two stripes clearly identified. ML1 (right hand multilayer) is upside down in this image. Both multilayers have troughs for cooling via an Indium-Gallium eutectic to reduce vibrations induced from the water chiller.

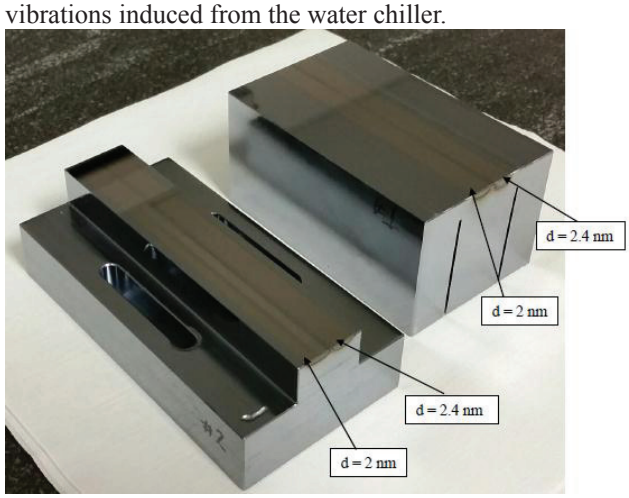


Figure 4: DMM Multilayers.

ML1 Assembly

ML1 subassembly is shown in Fig. 5 partially assembled and the 3D isometric view from CAD in Fig. 6.

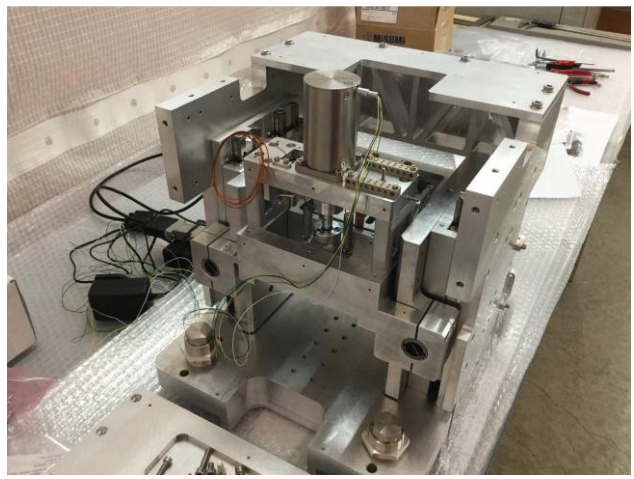


Figure 5: ML1 subassembly partially assembled.

Bragg axis

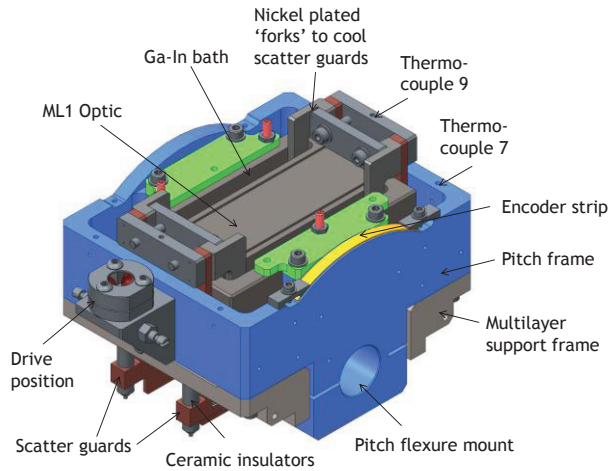


Figure 6: ML1 multilayer pitch assembly.

ML1 pitch axis is driven via a linear PiezoMotor® actuator in a sine arm configuration. The hinge consists of Riverhawk crossed flexures to minimise free play and friction of the joint. The actuator is coupled via stainless (440C) balls in a nest of 3x ruby balls. This yields a high stiffness, compact and low friction joint that has a large angular range as required for the sine arm (see section view in Fig. 7).

Table 2: Bragg Axes Performance (ML1 & ML2)

Range	-0.5 to +1.5°
Resolution	< 0.1 µrad
Bidirectional repeatability	< 5 µrad
Accuracy	< 3 µrad / 8 mrad

Measurements in Diamonds Precision Metrology Lab for the pitch axis show good resolution, accuracy and repeatability (Table 2). Figure 8 details the results of a sweep with 5 count (71 nrad) steps demonstrating a very stiff structure. This shows that the system was able to meet and exceed the defined 0.5 µrad specification with negligible stick-slip in the crossed flexures and drive rod mechanism.

Content from this work may be used under the terms of the CC BY 3.0 licence (© 2016). Any distribution of this work must maintain attribution to the author(s), title of the work, publisher, and DOI.

ISBN: 978-3-95450-188-5 doi:10.18429/JACoW-MEDSI2016-FRBA03

Content from this work may be used under the terms of the CC BY 3.0 licence (© 2016). Any distribution of this work must maintain attribution to the author(s), title of the work, publisher, and DOI.

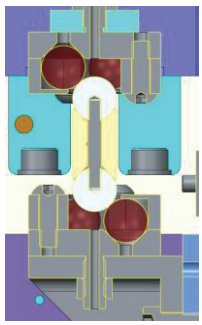


Figure 7: Section of stainless ball on nest of ruby balls.

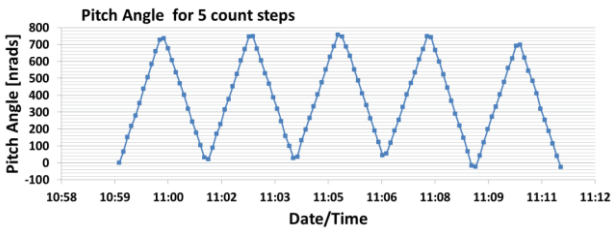


Figure 8: ML1 Bragg axis step scan measured with differential capacitive sensors [1].

Multilayer clamping and cooling To avoid distortion while still supporting the multilayer, a light preload was applied to push the multilayer against hardened stops. The optics are relatively insensitive to yaw so the horizontal stops were only positioned to standard manufacturing tolerances. The nominal roll and height however are more critical as ideally the Bragg axis would lie on the surface of the multilayer. 100TPI adjusters at 3x points on the lower surface were provided to support the multilayer and allow roll and height adjustment (Fig. 9).

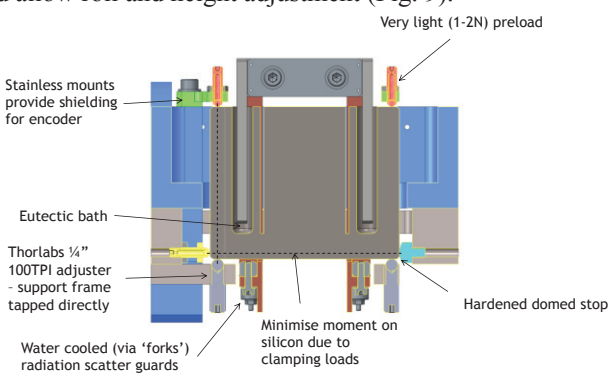


Figure 9: Section through ML1 substrate showing cooling and clamping method.

Roll axis and Y-axis To position ML1 on beam, vertical and roll axes are required. These two functions can be combined by making use of the differential position of the y-actuators. Riverhawk flexures were again utilised to provide the pin joints and a custom flexure was wire cut into the ML1 support frame to allow for the stretch of the assembly as the roll angle increased (see Figure 10).

Table 3: ML1 Y-axis Performance

Range	+5 mm – 7 mm
Resolution	0.25 µm
Bidirectional repeatability	1 µm over 0.7 mm
Parasitic pitch	50 µm over 0.7 mm

Table 4: ML1 (Virtual) Roll-axis Performance

Range	±1° (limited to ± 0.5°)
Resolution	1 µrad
Bidirectional repeatability	5.7 µrad
Parasitic pitch	175 µrad over 2°
Parasitic yaw	150 µrad over 2°

The vertical guidance for ML1 was achieved through 4x THK crossed roller tables (VRU-4205). Additional stiffness was harnessed by reducing the stroke to allow additional rollers in each bearing. This arrangement clearly leads to an over-constrained design so care was required when assembling to prevent binding. The result was an exceptionally stiff stage over the range with bidirectional repeatability measured as 0.2 µm over 0.7 mm range [2]. Table 3 and Table 4 detail the achieved specification of the Y and roll axes.

The vertical actuation for the ML1 y-axis was achieved through Huber Z-stages (5103.A10-X1) mounted on the granite outside of vacuum. These were coupled via slender flexure rods through bellows to exert a purely axial force on the assembly. The roll exhibited some non-linearity (Fig. 11) due to the flexure that allows for the stretch in the frame. The overall roll error was found to be 5.7 µrad which was just outside of our 5 µrad spec but still acceptable.

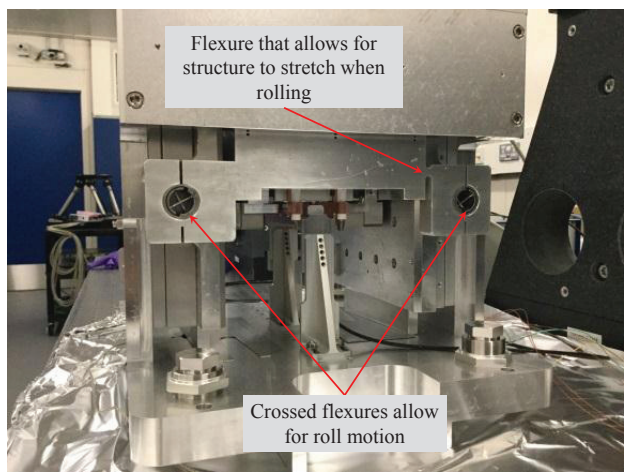


Figure 10: ML1 assembly at Diamonds Precision Metrology Lab (PML) [2].

ISBN: 978-3-95450-188-5 doi:10.18429/JACoW-MEDSI2016-FRBA03

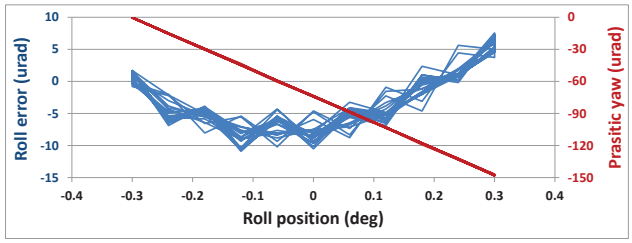


Figure 11: Parasitic pitch and yaw from roll axis [2].

ML2

The Bragg axis for ML2 is driven is the same manner as ML1 (i.e. Piezo actuator, sine arm driven through stainless on ruby spheres) so will not be discussed further.

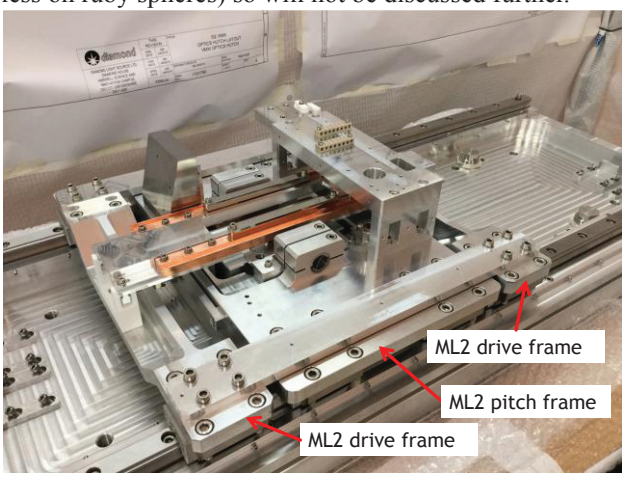


Figure 12: ML2 subassembly.

Z-axis The Z-axis is driven via an external linear shift (UHV Design HLSML64, 600mm stroke) outside of vacuum mounted from a port on the vessel. Utilising a hollow shaft, the cables and cooling hoses were passed into the moving assembly. This results in no in-vacuum rolling cables that often cause issues as they move around. A re-entrant vessel was fixed to the end of the actuator and to allow for feedthroughs and cabling access. Figure 12 shows the 2nd multilayer assembly.

Table 5: ML2 Z-axis Performance

Range	580 mm
Resolution	2 µm
Bidirectional repeatability	64.8 µm (no vacuum loads)
Parasitic pitch	110 µrad
Parasitic yaw	20 µrad
Speed	100 mm/s

This approach however required the drive force to be off-axis (in the x-direction) so a yaw moment occurs as ML2 moves. The guidance for the Z-axis is through lightly preloaded THK HSR linear bearings. To reduce the yaw effect from the drive load the ML2 pitch frame is pushed through points on axis (balls on flats) via a drive frame on the same rails. It is this frame, not the ML2 pitch assembly which is driven by the actuator so any yaw effects should be reacted by the frame and not the ML2 pitch assembly. Table 5 details the achieved performance.

Multilayer clamping and cooling Similar to ML1, the aim was to lightly clamp the multilayer to avoid distortion holding the multilayer or from thermal effects. Direct access to the underside of the multilayer was impractical so a flexure based lever adjustment method was devised to allow roll and height adjustments from above (see Fig. 13).

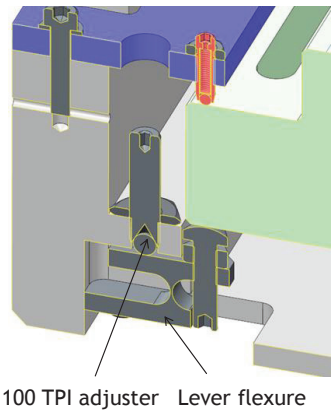


Figure 13: ML2 flexure adjusters.

X-Axis

An actuator was developed to position and guide the vessel. A flexure based design provides vertical compliance for the 50µm lift of the air bearing while remaining stiff against yaw and pitch. The design is self-contained so was assembled, wired and tested in isolation to the rest of the DMM. Figure 14 shows the actuator installed and Table 6 details the achieved performance.

Table 6: X-axis Performance

Range	±15 mm
Bidirectional repeatability	4.5 µm
Parasitic pitch	5 µrad
Parasitic roll	8 µrad
Parasitic yaw	30 µrad

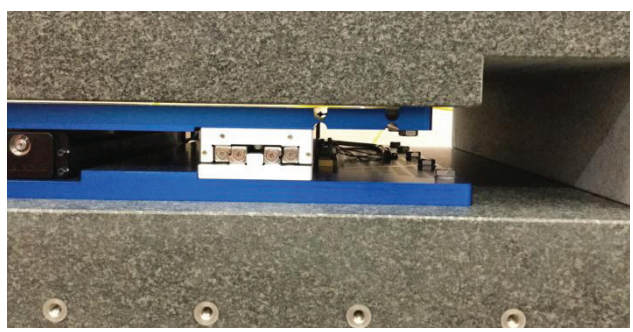


Figure 14: X-axis actuator and guidance for air bearing.

Shields, Masks and Thermal Issues

Scattered radiation causes drift of the beam position affecting stability as supports warm. Machine safety also required that the DMM could be interlocked with the

Content from this work may be used under the terms of the CC BY 3.0 licence (© 2016). Any distribution of this work must maintain attribution to the author(s), title of the work, publisher, and DOI.

ISBN: 978-3-95450-188-5 doi:10.18429/JACoW-MEDSI2016-FRBA03

Content from this work may be used under the terms of the CC BY 3.0 licence (© 2016). Any distribution of this work must maintain attribution to the author(s), title of the work, publisher, and DOI.

DCM to avoid sending DMM beam onto the DCM. A series of water cooled masks were designed to stop scattered radiation at 4x positions along the beam path:

i. A single slot front mask at beam height
ii. A mid mask between ML1 and ML2 with a large aperture for the swept beam
iii. A double slot end mask after ML2 that passes either through or the diverted DMM beam
iv. A combined beam position monitor (fluorescent screen), mask aperture and stop on a UHV linear shift to select position

Where possible, the beam path was enclosed with water cooled channels to catch scattering, heated components isolated and thermal paths minimised. Thermocouples were fitted to the assembly and show that the scatter guards around ML1 multilayer are warming. Over time this warms the ML1 pitch frame so a positional drift occurs. A future upgrade to cool the pitch and multilayer support frames is planned. It is currently not understood why this heating occurs but shows it was advantageous to enclose the beam path.

Vibration Stability

Seismometers were placed on the floor and ML2 assembly to measure the vibration amplification. Figure 15 and Fig. 16 show very low amplification factors of 1.05 in the vertical direction and 1.14 in the horizontal (Z) direction.

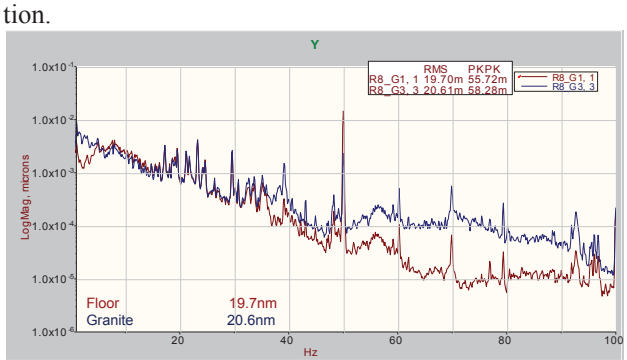


Figure 15: FFT of Vertical seismometer displacements of floor (red) and ML2 Frame (blue).

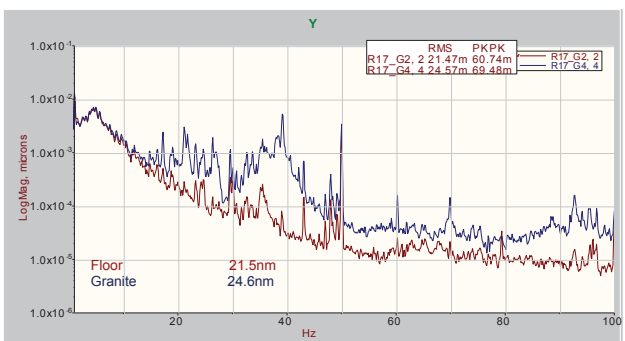


Figure 16: FFT of Horizontal seismometer displacements (Z-Direction) of floor (red) and ML2 Frame (blue).

BEAM STABILITY AT THE SAMPLE

The beam position was measured 13.5m downstream from ML1 using a 700Hz fast X-ray camera. Position vibration of approximately 2.5µm pk-pk (Fig. 17) was measured and integrating over 1-350Hz (Fig. 18), the vibration amplitude of 34 nrad RMS was calculated. One of the largest sources of vibration in monochromatic instruments is typically the cooling fluid turbulence which is significantly exacerbated by the use of flexible hydroformed hoses. This DMM design provides a smooth bore fluid path and decouples the flexible rubber pipe sections from the optic supports.

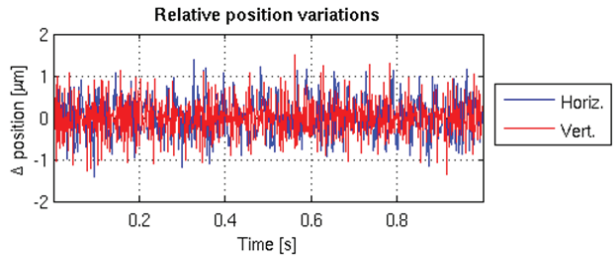


Figure 17: Beam vibration data.

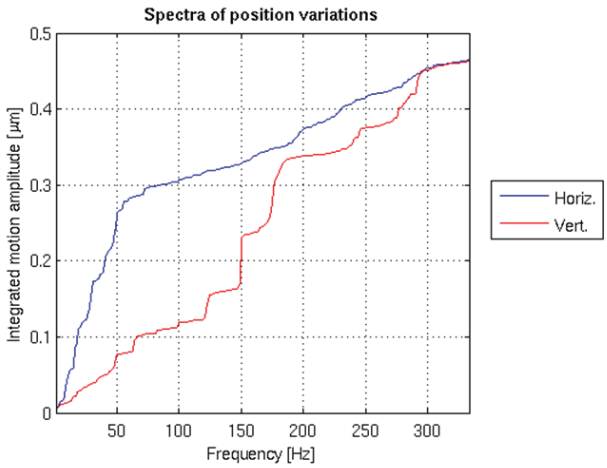


Figure 18: Integrated (RMS) position from 1-350Hz.

CONCLUSIONS

The DMM for the VMXi Beamline was designed and developed in house and installed at the end of the December shutdown 2015. It has been in operation with users and a number of improvements identified. This paper has outlined a number of the innovations and demonstrated performance figures for the instrument.

ACKNOWLEDGEMENT

Credit to Dr. Jon Kelly for project definition, design input and proof reading of this paper.

REFRERENCES

[1] Bugnar (2016), I02 DMM ML1 pitch motion and vibration metrology report, internal Diamond report
[2] Bugnar (2016), I02 DMM Metrology, internal Diamond report

ISBN: 978-3-95450-188-5

List of Authors

Bold papercodes indicate primary authors; ~~crossed out~~ papercodes indicate 'no submission'

— A —

Adam, M.J.P. MOPE26, **WEPE01**
Adamson, L.W.S. ~~**WEPE41**~~
Afzali-Far, B. ~~**MOPE04**~~
Aizpurua, G.A. ~~MOPE12~~
Al-Mohammad, H. MOPE28
Al-Najdawi, M.A. **MOPE28**
Almer, J. WEPE28
Alves, F. TUCA03
Amemiya, K. ~~WEPE13~~, ~~WEPE19~~
Amores, L. ~~FRAA02~~
Amundsen, C. TUPE31, TUPE33, WEBA03
Andi, B.A. WEPE36
André, T. WECA06
Andreazza, W. MOPE13
Andriyash, I.A. WECA06
Ansaldi, G. ~~**WEPE42**~~
Anton, J.W.J. TUAA01, TUBA04
Aoyagi, H. **WEPE10**
Appel, K. ~~WEPE43~~
Arbelaez, D. THBA01
Arbo Sangüesa, V. TUPE06
Asaoka, S. WEPE03
Assoufid, L. WEPE14

— B —

Bagnato, O.R. MOPE02, TUPE23
Barjau, A. MOPE13
Barkway, G.R. MOPE26
Barrett, S.T. ~~TUPE34~~
Bartalesi, A. ~~**WEPE11**~~
Bassan, H. TUPE33
Basset, C. WECA06
Bayer, M. ~~WEPE35~~
Beauregard, D. WEPE29
Béchu, N. TUPE40
Beckhoff, B. ~~MOPE35~~, ~~THBA02~~
Belev, G. ~~WEPE16~~, WEPE24, ~~WEPE31~~, ~~THAA01~~
Benabderrahmane, C. WECA06
Benda, E. **WEPE28**
Beno, M.A. WEPE18
Berman, L. WEPE36
Berteaud, P. WECA06
Bertwistle, D. TUPE19
Bhogadi, D.K. **WEPE36**
Biasci, J.C. ~~TUPE27~~, ~~TUPE30~~, ~~WEAA01~~, WEAA02, WEAA03, ~~WECA02~~
Bischoff, P. ~~MOPE21~~
Blasco, V. TUPE09
Bobault, S. WECA06
Bodnarchuk, C. WEPE01
Boehler, P. **WECA03**
Boire, J. ~~WEPE31~~, ~~THAA01~~
Bonnin, S. WECA06
Bouteille, J-F.B. WEAA03
Boutet, S. ~~MOPE03~~
Bouvet, F. WECA06
Boyd, E.W. ~~WEPE43~~
Brachmanski, M. MOPE40
Brajuskovic, B. ~~**MOTB02**~~, TUPE25
Bree, M. ~~WEPE31~~
Breitfeller, M.G. **WEPE05**
Briquez, F. TUPE40, WECA06
Brochard, T. TUCA06, ~~WECA02~~
Broers, C. ~~MOPE14~~
Brügger, M. WECA03
Brumund, P.M. ~~WECA02~~
Buccianti, L. MOPE08, TUPE26
Bumrungkoh, D. ~~MOPE36~~
Butler, D.J. **FRBA03**

— C —

Cacho-Nerin, F. FRAA01
Caliari, R.M. **MOPE02**, MOPE19, TUCA05
Caliebe, W.A. WEPE09
Calvi, M. WECA03
Campmany, J. TUPE14
Canova, H.F. TUPE26, WEPE06
Capatina, D. **WEPE18**
Cappadoro, P.L. TUPE04
Carballedo, A. **MOPE41**, TUPE11
Cardoso, F.H. TUPE26
Carley, R. ~~MOPE14~~
Carlucci-Dayton, M. WEPE36, ~~FRAA02~~
Carriere, S.R. **WEPE29**
Casalta Escuer, J.M. FRBA02
Casas, J.J. MOPE42, MOPE43, TUPE05, TUPE06, TUPE11, TUPE13, TUPE14
Castagna, J.C. ~~**MOPE03**~~
Cease, H. MOPE32, MOPE34, TUPE44, WEBA01
Chaichuay, S. ~~MOPE36~~
Chan, C.K. MOPE30
Chang, C.-C. MOPE30
Chang, C.-H. ~~**TUPE39**~~
Chang, C.F. **MOPE18**
Chang, C.H. **TUPE41**
Chang, C.H. MOPE05, TUPE12
Chang, C.Y. TUPE12
Chang, J.-C. **TUPE02**
Chang, S.H. MOPE05, MOPE24, TUPE12
Chang, Y.C. TUPE02
Chapman, L.D. ~~WEPE16~~, ~~WEPE31~~, ~~THAA01~~
Chapuis, L. TUPE40, WECA06

Content from this work may be used under the terms of the CC BY 3.0 licence (© 2016). Any distribution of this work must maintain attribution to the author(s), title of the work, publisher, and DOI.

ISBN: 978-3-95450-188-5

Content from this work may be used under the terms of the CC BY 3.0 licence (© 2016). Any distribution of this work must maintain attribution to the author(s), title of the work, publisher, and DOI.

Chavan, A. **TUPE28**
Chavanne, J. ~~TUPE30~~
Chen, B.Y. **MOPE24**
Chen, C. TUPE12
Chen, C.Y. MOPE05
Chen, H.-H. ~~TUPE39~~
Chen, H.Y. MOPE24
Chen, J.-R. ~~**MOPE06**~~
Chen, M.L. ~~MOPE06~~, MOPE09, MOPE11, MOPE23
Chen, S.D. TUPE41
Chen, S.Y. **TUPE19**
Cheng, C.M. MOPE09
Chiu, C.C. TUPE12
Chritin, N. MOPE13
Cianciosi, F. **TUCA06**, ~~WECA02~~
Claudiano, G.V. **TUPE23**
Clement, J.M. ~~TUBA02~~
Cocco, D. ~~WEBA02~~, ~~WEPE20~~, ~~FRAA02~~, ~~FRBA04~~
Colldelram, C. ~~MOTC01~~, **MOPE01**, MOPE41, MOPE42, MOPE43, ~~**TUAA00**~~, TUPE05, TUPE06, TUPE11, TUPE13, TUPE14, WEPE15, WEPE40, FRAA03, **FRBA02**, ~~**FRBA05**~~
Collins, J.T. MOPE32, **MOPE34**, TUPE44, WEBA01
Connatser, R.W. **WEPE30**
Costa, M.H.A. MOPE08, TUPE26
Coulon, D. ~~TUPE27~~, WEAA02
Couprie, M.-E. TUPE40, WECA06
Crisol, A. TUPE11, TUPE14, FRAA03

— D —

da Silva, L.G. MOPE08
Dabin, Y. TUCA06, ~~TUPE27~~, ~~WEAA01~~, WEAA02, WEAA03
De Jonge, M. MOPE38
de Oliveira, H.G.P. **MOPE08**, WEPE06
de Olivera, C. TUPE40, WECA06
de Souza, L.,Jr. MOPE02
Degenhardt, M. WEPE09
Dehning, B. MOPE13
Deiter, C. ~~**WEPE27**~~
Delfs, A. ~~**TUPE24**~~
Delgado, A. ~~MOPE12~~
Delitz, J.T. ~~**MOPE14**~~
Den Hartog, P.K. TUPE08, WEBA04
Deng, J. TUAA02
Deng, R.B. MOPE31, **TUPE36**
Dennetière, D. WECA06
DePaola, F.A. **TUPE31**, WEBA03
Diaz-Moreno, S. TUPE10
DiChiara, A. TUPE28
Dietrich, P. ~~THBA02~~
Dietrich, Y. WECA06
Dill, F.U. ~~**MOPE25**~~
Diot, M. WEAA03
Divitcos, J. **MOPE38**
Docker, P. TUPE10
Doehrmann, R. ~~**TUCA01**~~
Dommach, M. ~~**TUPE37**~~
Dong, Y.X. MOPE31
dos Santos, J.E. TUPE26
Dubuisson, J.M. TUPE40
Ducoing, T. ~~TUPE27~~, WEAA02
Ducotté, L. ~~**TUBA02**~~
Duller, G.M.A. **WEPE22**
Dumas, P. FRAA03
Duval, J.P. TUPE40, WECA06

— E —

Eggenstein, F. ~~**MOPE21**~~
Eisebitt, S. MOPE22
El Ajjouri, M. WECA06
El Ajjouri, T.K. WECA06
Ellis, G. FRAA03
Emery, J. MOPE13
Erko, A. ~~MOPE21~~
Escaler, X. **TUPE05**, **TUPE06**, **TUPE09**, **TUPE13**
Escudero, C. WEPE15
Esper Neto, C. MOPE08
Ewald, F. ~~TUPE27~~, WEAA02

— F —

Fan, L. MOPE29
Fang, W. TUPE38
Farvacque, L. WEAA03
Favier, F. WEAA03
Feng, J. ~~MOPE44~~
Feng, Y. ~~TUPE17~~
Fernandes, H.C. **TUPE04**
Ferrari, A. ~~WEPE43~~
Ferrater, M. **MOPE42**
Ferrer, S. WEPE15
Fischetti, R. THAA03
Fisher, M.V. **WEPE14**, WEPE18
Flaven-Bois, A. WEAA03
Fonseca, P.T. MOPE08, TUPE23, WEPE06
Fontserè Recuenco, A. WEPE40
Francisco, F.R. MOPE02, TUPE23
Freitas, P.P.S. WEPE06
Friedrich, B. **MOPE22**
Fuchs, M.R. WEPE36

— G —

Gagliardini, E. ~~**TUPE27**~~, WEAA02
Gao, F. **MOPE31**, TUPE36
García, J.R. MOPE41
Gautier, J. WECA06
Geraldes, R.R. MOPE02, MOPE08, **MOPE19**, **TUCA05**, TUPE15
Gevorgyan, A.A. FRAA03

ISBN: 978-3-95450-188-5

Gibbons, M. WEPE24
Gießel, T. ~~WEPE21~~
Gilmour, A. TUPE15, WEPE06
Giorgetta, J.L. **~~WEPE17~~**
Giraldo, J.C. TUPE29
Gleyzolle, H. ~~TUBA02~~
Gluskin, E. WECA04
Goirand, L. TUCA06, ~~TUPE30~~, ~~WEAA01~~, **~~WECA02~~**
González Fernández, J.B. **WEPE40**
González, N **WEPE15**
Got, P. FRBA01
Graceffa, R. ~~WEPE27~~
Grama, V. **WEAA04**
Grötzsch, D. **~~THBA02~~**, ~~MOPE35~~
Gudkov, D. MOPE13

— H —

Hall, D.R. WEPE22
Hammond, N.P. MOPE37
Harder, D.A. TUPE04
Hardin, C.L. **~~FRAA02~~**
Hartog, P.D. TUPE28
He, Y.Z. ~~MOPE33~~
Hendel, S. **~~WEPE21~~**
Henneberg, G.R. **MOPE26**
Herbeaux, C. TUPE40, WECA06
Hernandez-Toro, J. MOPE41
Hernikl, C.D. WEPE39
Herranz, J. **MOPE13**
Hess, C. MOPE16
Hesse, M. MOPE40, WEPE09
Heuer, J. ~~TUCA01~~
Hidas, D.A. TUPE04
Hirschi, P. WEPE37
Ho, H.C. MOPE09, MOPE11, **MOPE23**
Holz, M. MOPE27
Hong, M. MOPE24
Hong, Y.Z. MOPE29
Honkimaki, V. FRBA01
Horbach, J. ~~TUCA01~~
Howard, D. MOPE38
Hsiao, F.Z. TUPE02
Hsu, K.H. **MOPE09**, MOPE11, MOPE23
Hu, B. TUPE28
Hu, X. MOPE31, ~~MOPE33~~, TUPE38
Huang, C.Y. MOPE05
Huang, D.-G. MOPE09, MOPE11, MOPE23
Huang, J.C. ~~TUPE39~~, TUPE41
Huang, L. TUPE12
Huber, N. MOPE17, ~~WEPE16~~, ~~WEPE31~~
Hubert, N. WECA06
Huttel, E. MOPE28
Hwang, C.-S. ~~TUPE39~~, TUPE41
Hävecker, M. ~~WEPE21~~

— I —

Igarashi, N. **~~WEPE13~~**, ~~WEPE32~~
Inagaki, Y. ~~WEPE33~~
Izquierdo, M. ~~MOPE14~~
Izzo, S.J. MOPE34

— J —

Jacob, J. ~~TUPE30~~
Jacobsen, C. TUAA02
Jakoncic, J. WEPE36
James, J.H. ~~WEBA02~~
Jastrow, U. MOPE40
Jensen Jr., D.P. WECA04
Jensen, B.N. WEBA01
Jia, D. WEPE07
Jiang, Z. MOPE31
Jin, L. TUPE16
Jobert, N. **TUCA03**
Jöhri, H. **MOPE16**, TUCA02, WECA03
Jonas, A. ~~THBA02~~
Jover-Mañas, G. WEPE40
Juan Garcia, D. TUPE13
Jung, J.-Y. THBA01

— K —

Kanngießer, B. ~~MOPE35~~, ~~THBA02~~
Kao, S.P. TUPE02
Kay, J. **MOPE37**, TUPE10
Kearney, S.P. TUAA01, **TUBA01**, TUBA04
Kei, K. TUPE19
Kelez, N.M. ~~WEBA02~~, ~~WEPE20~~, ~~FRAA02~~, ~~FRBA04~~
Keller, A. WECA03
Kelly, J.H. **TUPE01**, **WECA07**, FRBA03
Kemppinen, J. **MOPE15**
Kenesei, P. WEPE28
Kersevan, R. **~~MOTB01~~**
Khojoyan, M. WECA06
Kikuchi, T. ~~WECA01~~, ~~WEPE13~~, ~~WEPE19~~
Kitégi, C.A. TUPE04
Kitel, M. ~~WEPE27~~
Knopp, J.J. WEPE18
Kodama, H. ~~WECA01~~
Kohlstrunk, N. **~~WEPE12~~**
Kortaberria, G. **~~MOPE12~~**
Kostka, Z.S. MOPE15
Kosugi, N. ~~WEPE33~~
Koyama, A. ~~WEPE32~~
Kramer, S.L. WEPE05
Kristiansen, P. **~~TUCA04~~**
Krüger, H. **WEPE09**
Krzywiński, J. ~~TUPE17~~
Kuan, C.K. MOPE09, MOPE11, MOPE23
Kubsky, S.K. TUCA03
Kubyshin, Yu.A. TUPE09
Kuhlmann, M. MOPE40
Kwo, J.R. MOPE24

Content from this work may be used under the terms of the CC BY 3.0 licence (© 2016). Any distribution of this work must maintain attribution to the author(s), title of the work, publisher, and DOI.

ISBN: 978-3-95450-188-5

Content from this work may be used under the terms of the CC BY 3.0 licence (© 2016). Any distribution of this work must maintain attribution to the author(s), title of the work, publisher, and DOI.

— L —

La Civita, D. **~~FRAA04~~**
Labat, M. WECA06
Ladrera Fernández, J. TUPE29, WEPE40
Lai, B. TUAA02, TUBA04, WEPE18
Lai, L. TUPE12
Lai, W.Y. ~~MOPE06~~, MOPE09, MOPE11, MOPE23
Lambert, G. WECA06
Lanaia, D. MOPE42
Langdon, T. WEPE36
Lara, J. WEPE36
Leclercq, N. WECA06
Lee, C.Y. MOPE24
Lee, L. TUPE12
Lee, M.H. **TUPE12**
Lee, S.H. **WEPE04**
Lemke, M. MOPE27, ~~WEPE35~~
Leontowich, A.F.G. THAA02
Lesourd, M. TUCA06
Lestrade, A. TUPE40, WECA06
Li, A. TUAA01
Li, H.C. TUPE02
Li, Y. **WEPE07**
Liao, W.R. TUPE02
Lin, B.H. MOPE24
Lin, C.J. MOPE09, MOPE11, MOPE23
Lin, J.M. MOPE05
Lin, L.X. **TUPE21**
Lincoln, F.C. WEBA03
Lipton, T.M. WEPE39
Liu, C.Y. TUPE02
Liu, D.G. MOPE05, TUPE12
Liu, W. TUBA04
Liu, Y. **~~MOPE33~~**
Liu, Z. MOPE32, MOPE34, **TUPE44**, WEBA01
Llonch, M.L. TUPE29
Locher, M. WECA03
Löhl, F. TUCA02
Lopez Nonell, D. ~~TUAA00~~
Lopez, L.C. **~~WEPE44~~**
Lorenzen, K. ~~WEPE27~~
Loulergue, A. WECA06
Lu, W. MOPE22, ~~WEPE42~~
Lubeck, J. **~~MOPE35~~**
Lurie, A.M. WEBA04
Lyndaker, A. **~~TUPE34~~**

— M —

Maag, St. **WEPE37**
Macià, L. **MOPE43**
Madacki, R. TUPE26
Madsen, A. MOPE22, ~~WEPE42~~
Magagnin, P. MOPE13
Magnin-Mattenet, M. ~~WEPE42~~, **FRBA01**
Mahn, H. MOPE40
Mainaud Durand, H. MOPE15
Mairs, T.R. **~~TUPE35~~**
Makahleh, F. MOPE28
Makarov, O. THAA03
Malfois, M. WEPE40
Malka, V. WECA06
Malzer, W. ~~THBA02~~
Mao, C. TUAA01
Marchial, T. WEAA03
Marcos, J. TUPE14
Marcouillé, O. WECA06
Marin, F.S. TUAA02
Marion, P. TUCA06, ~~TUPE27~~, **~~WEAA01~~**, WEAA02
Marlats, J.L. TUPE40
Marshall, A.R. **THAA04**
Marteau, F. WECA06
Martí, Z. **~~MOTC02~~**
Martin, D. WEAA03
Martín-Nuño Gonzalez, C. FRBA02
Martínez Guil, J.C. WEPE40
Martins, B.S. WEPE36
Martyanov, W. ~~THBA02~~
Marutzky, F. MOPE40, WEPE09
Mary, A. WECA06
Mase, K. **~~WECA01~~**, **~~WEPE19~~**
Maser, J. TUAA02, TUBA04
Mashayekhi, A. WEPE28
Mashrafi, S.T. TUAA02
Matsuoka, A. **~~WEPE32~~**
McChesney, J.L. WEPE14
McKinlay, J. MOPE38
McSweeney, S. WEPE36
Meissner, D. **MOPE40**
Meyer, B.C. MOPE08
Miller, C.D. ~~WEPE16~~, WEPE24, ~~WEPE31~~, ~~THAA01~~
Miret, M. **MOPE20**
Miyauchi, H. **WEPE03**
Miyazawa, T. ~~WEPE19~~
Monge, R. MOPE41, **TUPE29**, FRAA03
Moog, E.R. WEPE18
Moore, L. ~~WEPE27~~
Moreno, G.B.Z.L. MOPE19, TUCA05
Mori, T. ~~WEPE13~~
Morton, D.S. ~~WEBA02~~, **~~WEPE20~~**, ~~FRAA02~~, ~~FRBA04~~
Mulvey, J. WEPE04
Muñoz Horta, R. MOPE42
Murray, C. TUPE19
Musardo, M. TUPE04
Myers, S.F. WEPE36

— N —

Nakatsutsumi, M. ~~WEPE43~~
Nasiatka, J.R. **~~MOPE44~~**
Navrotski, G. **TUPE25**

ISBN: 978-3-95450-188-5

N'gotta, P. WECA06
Nicolás, J. ~~**MOTC01**~~, MOPE01, FRAA03, FRBA02
Nietzold, C. ~~THBA02~~
Nikitina, L. MOPE41, TUPE29, FRAA03
Nölle, D. MOPE27
Noll, T. **TUBA03**, MOPE22, **WEPE38**
Nowak, M.P. MOPE07, MOPE10
Nozawa, S. **WEPE26**
Nudell, J. **MOPE32**, MOPE34, TUPE44, WEBA01
Nue, L. MOPE16, WEPE37
Nutsch, A. ~~THBA02~~

— O —

Ogier, B. ~~**TUPE30**~~
Ohigashi, T. ~~**WEPE33**~~
Ohno, S. ~~WECA01~~
Okasinski, J.S. WEPE28
Okrent, F. ~~**WEPE35**~~
Okudaira, K.K. ~~WECA01~~
Olarra, A. ~~MOPE12~~
Olea, G. **MOPE17**
Ortiz, E. ~~TUPE17~~

— P —

Padmore, H.A. ~~MOPE44~~
Palombarini, E. TUPE26
Pan, Y. TUAA01
Parise, R.L. MOPE02, TUPE23
Park, J.S. WEPE28
Parker, J. FRAA01
Pasquaud, J. ~~WECA02~~
Patthey, L. MOPE16
Peach, A. **FRAA01**
Pedersen, T.M. TUPE19
Pedreira, P. FRBA02
Pedrozzi, M. TUCA02
Pei, X.T. MOPE29
Peña, G. TUPE11, TUPE14
Pereira, M.A. MOPE08, TUPE26
Pérez, F. MOPE42
Permanyer, X. ~~**TUCA07**~~
Perng, S.Y. MOPE09, MOPE11, MOPE23
Peters, H.-B. WEPE09
Peters, R. WEPE09
Phanak, M. ~~MOPE36~~
Pile, G. WECA04
Plönjes-Palm, E. MOPE40
Polack, F. WECA06
Pongampai, S. ~~MOPE36~~, ~~**WEPE34**~~
Pont, M. TUPE29
Preissner, C.A. MOPE32, MOPE34, **TUAA02**, TUPE44, **WEBA01**
Priebe, G. ~~WEPE43~~
Prieto, M. TUPE05, TUPE06, TUPE09, TUPE13
Prudente, C. MOPE08, TUPE26

— Q —

Qian, J. WEPE14
Qin, H.L. **TUPE16**
Quinn, P.D. FRAA01
Quispe, M. MOPE42, MOPE43, TUPE05, TUPE06, **TUPE11**, TUPE13, **TUPE14**, TUPE29, FRAA03

— R —

Radu, F. WEPE38
Raimondi, P. WEAA03
Ramanathan, M. WEPE04
Ranay, R. WEPE28
Rank, J. TUPE04
Regier, C.N. **WECA05**, **THAA02**
Reichardt, G. ~~WEPE21~~
Reininger, R. WEPE14
Renier, M. ~~WEPE16~~, ~~WEPE31~~, ~~THAA01~~
Ribbens, M. ~~**WEPE23**~~
Ribó, L. TUPE11, FRBA02
Ribó, L.R.M. **FRAA03**
Roca Santo, M.L. TUPE26
Rocha, A.S. WEPE06
Rodolakis, F.M. WEPE14
Rodrigues, G.L.M.P. MOPE08, WEPE06
Röhling, M. MOPE40, WEPE09
Roehrig, C. TUAA02, TUBA04, WEPE18
Romero, J.A. TUPE09
Rommeluère, P. WECA06
Ronde, M.J.C. MOPE19
Roso, L. MOPE41
Roth, T. MOPE22, ~~WEPE42~~
Roussé, J.Y. WECA06
Roussel, E. WECA06
Roux-Buisson, P. WEAA03
Rowen, M. ~~TUPE17~~
Rubeck, J.R. ~~**WEPE25**~~
Ruget, C. ~~MOTC01~~, MOPE01, FRBA02
Ruijl, T.A.M. MOPE02, MOPE19, TUCA05, TUPE15

— S —

Samuelsson, S. MOPE13
Sanchez, A. TUPE09
Sanfelici, L. MOPE08, TUCA05, **TUPE26**, WEPE06
Sano, M. WEPE02
Saveri Silva, M. MOPE02, TUCA05, **TUPE15**, WEPE06
Scharfstein, G.A. **THBA01**
Scheel, M. ~~WEPE17~~
Scherz, A. ~~MOPE14~~
Schmidt, A. ~~WEPE42~~, ~~**WEPE43**~~
Schmidt, O.A. **WECA04**
Schmidt, T. WECA03
Schmitt, T. MOPE16, WEPE37
Schneider, B.A. WEPE29

Content from this work may be used under the terms of the CC BY 3.0 licence (© 2016). Any distribution of this work must maintain attribution to the author(s), title of the work, publisher, and DOI.

ISBN: 978-3-95450-188-5

Content from this work may be used under the terms of the CC BY 3.0 licence (© 2016). Any distribution of this work must maintain attribution to the author(s), title of the work, publisher, and DOI.

Schneider, D.K. WEPE36
Schneider, R.M. MOPE19, TUCA05, TUPE15
Schulte Schrepping, H. ~~TUCA01~~
Schulte-Schrepping, H. MOPE40, WEPE09
Schulz, J. ~~WEPE27~~
Schulz, L. WECA03
Schäfers, F. ~~MOPE21~~
Schäfers, F. ~~WEPE21~~
Sebdaoui, M. TUPE40, WECA06
Senf, F. ~~MOPE21~~
Sergeev, I. ~~TUCA01~~
Sharma, S.K. MOPE30, TUPE31, **TUPE32**, TUPE33, **WEBA03**
Shastri, S.D. WEPE28
Shehab, M.M. MOPE28
Sheng, I.C. **MOPE30**
Shu, D. **TUAA01**, TUBA01, **TUBA04**
Shueh, C. MOPE30
Shvedunov, V.I. TUPE09
Sics, I. TUPE11, FRAA03, FRBA02
Silva, L.G. TUPE26
Silva, M.S. TUPE26
Sinn, H. TUBA03, ~~WEPE12~~, ~~FRAA04~~
Sirvent, J.L. MOPE13
Sokolov, A. ~~MOPE21~~
Souza Neto, N.M. TUCA05
Spataro, C.J. **TUPE33**
Srichan, S. ~~**MOPE36**~~, ~~WEPE34~~
Srinivasan, V.N. ~~FRAA02~~
Stallwood, A. WEPE22
Stapf, T. TUCA02
Steel, G.A. WEPE29
Steffen, B. WEPE09
Stepanov, S.A. THAA03
Stevens, T.A. WEPE39
Stimson, J.S. **TUPE10**
Streeck, C. ~~THBA02~~
Strelnikov, N.O. WECA04
Su, Y. TUPE12
Sullivan, S. TUAA02
Sun, S. MOPE31, TUPE38
Sunayama, R. TUPE22
Suortti, P. ~~WEPE16~~
Suthar, K.J. **TUPE08**, TUPE28, **WEBA04**, WECA04
Sutter, J. TUPE10
Sweet, R.M. WEPE36

— T —

Ta Phuoc, K. WECA06
Tahara, T. WEPE03
Takahashi, S. **WEPE02**, WEPE10
Takakuwa, J.H. **WEPE39**
Takeichi, Y. ~~WEPE13~~, ~~WEPE19~~
Tallarida, M. TUPE14
Tampigny, B. **WEAA03**
Tanabe, T. TUPE04
Tanaka, H. ~~WEPE13~~, ~~WEPE19~~
Tanaka, M. ~~WECA01~~
Tanaka, M. ~~WECA01~~
Tang, M.T. MOPE24
Tavakoli, K.T. TUPE40, **WECA06**
Tavares, D.O. MOPE02
Taylor, D.M. WEPE29, THAA02
Temnykh, A.B. ~~TUPE34~~
Thaury, C. WECA06
Thiam, F. WECA06
Thiel, A. ~~**TUPE42**~~
Thomas, F. ~~TUPE27~~, **WEAA02**, WEAA03
Thute, P. ~~WEPE27~~
Tiedtke, K.I. MOPE40
Tilmont, M. **TUPE40**
Tischler, J.Z. TUBA04
Tizzano, W. **TUPE18**
Toellner, T.S. TUBA01
Tolentino, H.C.N. TUCA05
Tomas Justribo, A. FRBA02
Toyoda, M. **TUPE22**
Toyoshima, A. ~~WEPE19~~
Trakhtenberg, E. WECA04
Trapp, A. TUBA03
Treusch, R. MOPE40
Tsai, C.W. MOPE11
Tsai, Z.-D. ~~MOPE06~~
Tseng, S.C. MOPE24
Tseng, T.C. MOPE09, **MOPE11**, MOPE23
Tuozzolo, J.L. WEBA03

— U —

Úbeda Gonzalez, D. FRBA02
Uchida, Y. ~~WEPE13~~
Unger, W. ~~THBA02~~

— V —

Valléau, M. WECA06
Van Vaerenbergh, P. ~~WECA02~~
Vasserman, I. WECA04
Veness, R. MOPE13
Venugopalan, N. THAA03
Vétéran, J. WECA06
Vilcins, S. **MOPE27**
Villanueva Guerrero, J.R. ~~**TUPE20**~~
Vivo, A. FRBA01
Vogt, S. TUAA02, WEPE18
Volpe, L.M. TUPE23, **WEPE06**

— W —

Wagner, A. WEAA04
Wang, D.-J. MOPE05
Wang, H. ~~**TUPE17**~~
Wang, H.F. ~~MOPE33~~
Wang, H.S. MOPE09, MOPE11, MOPE23
Wang, J. ~~MOPE33~~
Wang, L. MOPE31, ~~MOPE33~~, TUPE38
Wang, S.H. ~~MOPE33~~

ISBN: 978-3-95450-188-5

Wang, X. **TUCA02**, WEPE37
Wang, Y. **MOPE29**
Ward, M.C.L. TUPE10
Warwick, T. WEPE39
Watanabe, A. WEPE02
Webb, M.A. **WEPE24**
Wei, W. MOPE29
Weitkamp, T. ~~WEPE17~~
Wen, Y.M. MOPE31
Weser, J. ~~MOPE35~~
Westfahl Jr., H. TUCA05, WEPE06
White, S.M. ~~TUPE35~~
Wiebers, Ch. MOPE27
Witte, K.W. ~~THBA02~~
Wright, J. ~~TUBA02~~
Wu, J.X. MOPE24
Wu, L.H. MOPE30
Wysokinski, T.W. TUPE21, ~~**WEPE16**~~, WEPE24, ~~**WEPE31**~~, ~~**THAA01**~~

— X —

Xu, J.Z. WECA04
Xu, S. **THAA03**
Xue, S. WEPE07

— Y —

Yamada, Y. ~~WEPE32~~
Yan, H.Y. **MOPE05**, TUPE12
Yanagihara, M. TUPE22
Yang, B.X. WEPE04
Yang, C.K. TUPE41
Yang, K. TUPE16
Yang, Y.C. ~~MOPE06~~
Yin, G.C. MOPE24
Yin, L. ~~MOPE33~~, TUPE36, **TUPE38**
Yousef, I. TUPE11, FRAA03
Yu, L.Y. TUPE38
Yu, Y.T. ~~TUPE39~~

— Z —

Zastrau, U. ~~WEPE43~~
Zerbib, D. WECA06
Zeschke, T. ~~MOPE21~~
Zhang, B. MOPE29
Zhang, H. TUPE16
Zhang, L. TUCA06, ~~**WEBA02**~~, ~~WEPE20~~, ~~FRAA02~~, ~~**FRBA04**~~
Zhang, L. ~~MOPE33~~
Zhang, M. WEPE07
Zhang, W. ~~MOPE33~~, TUPE38
Zhou, Q.G. ~~MOPE33~~
Zhu, N. WEPE24
Zhu, W. TUPE16, WEPE07
Ziemianski, D.T. **MOPE07**, **MOPE10**

Content from this work may be used under the terms of the CC BY 3.0 licence (© 2016). Any distribution of this work must maintain attribution to the author(s), title of the work, publisher, and DOI.

ISBN: 978-3-95450-188-5

Content from this work may be used under the terms of the CC BY 3.0 licence (© 2016). Any distribution of this work must maintain attribution to the author(s), title of the work, publisher, and DOI.

Institutes List

ALBA-CELLS Synchrotron
Cerdanyola del Vallès, Spain
- Campmany, J.
- Carballedo, A.
- Casas, J.J.
- Colldelram, C.
- Crisol, A.
- Escudero, C.
- Ferrer, S.
- Fontserè Recuenco, A.
- García, J.R.
- Gevorgyan, A.A.
- Giraldo, J.C.
- González, N
- González Fernández, J.B.
- Jover-Mañas, G.
- Ladrera Fernández, J.
- Lanaia, D.
- Llonch, M.L.
- Lopez Nonell, D.
- Malfois, M.
- Marcos, J.
- Martínez Guil, J.C.
- Martí, Z.
- Monge, R.
- Muñoz Horta, R.
- Nicolás, J.
- Nikitina, L.
- Pedreira, P.
- Pérez, F.
- Peña, G.
- Pont, M.
- Prieto, M.
- Quispe, M.
- Ribó, L.
- Ribó, L.R.M.
- Ruget, C.
- Sics, I.
- Tallarida, M.
- Yousef, I.

ANL
Argonne, Illinois, USA
- Almer, J.
- Anton, J.W.J.
- Assoufid, L.
- Benda, E.
- Beno, M.A.
- Brajuskovic, B.
- Capatina, D.
- Cease, H.
- Collins, J.T.
- Den Hartog, P.K.
- Deng, J.
- DiChiara, A.
- Fischetti, R.
- Fisher, M.V.
- Gluskin, E.
- Hartog, P.D.
- Hu, B.
- Izzo, S.J.
- Jacobsen, C.
- Jensen Jr., D.P.
- Kearney, S.P.
- Kenesei, P.
- Knopp, J.J.
- Lai, B.
- Lee, S.H.
- Liu, W.
- Liu, Z.
- Lurie, A.M.
- Makarov, O.
- Marin, F.S.
- Maser, J.
- Mashayekhi, A.
- Mashrafi, S.T.
- McChesney, J.L.
- Moog, E.R.
- Mulvey, J.
- Navrotski, G.
- Nudell, J.
- Okasinski, J.S.
- Park, J.S.
- Pile, G.
- Preissner, C.A.
- Qian, J.
- Ramanathan, M.
- Ranay, R.
- Reininger, R.
- Rodolakis, F.M.
- Roehrig, C.
- Schmidt, O.A.
- Shastri, S.D.
- Shu, D.
- Stepanov, S.A.
- Strelnikov, N.O.
- Sullivan, S.
- Suthar, K.J.
- Tischler, J.Z.
- Toellner, T.S.
- Trakhtenberg, E.
- Vasserman, I.
- Venugopalan, N.
- Vogt, S.
- Xu, J.Z.
- Xu, S.
- Yang, B.X.

ANSTO
Menai, New South Wales, Australia
- De Jonge, M.
- Divitcos, J.
- Howard, D.
- McKinlay, J.

ASCo
Clayton, Victoria, Australia
- Adamson, L.W.S.

ISBN: 978-3-95450-188-5

BAM
Berlin, Germany
- Dietrich, P.
- Nietzold, C.
- Unger, W.

BCU
Birmingham, United Kingdom
- Stimson, J.S.
- Ward, M.C.L.

BESSY GmbH
Berlin, Germany
- Noll, T.

Bestec GmbH
Berlin, Germany
- Gießel, T.

Biotec Controle Ambiental
SÃ£o José dos Campos, SP, Brazil
- Buccianti, L.
- Costa, M.H.A.
- Palombarini, E.

BNL
Upton, Long Island, New York, USA
- Amundsen, C.
- Andi, B.A.
- Bassan, H.
- Berman, L.
- Bhogadi, D.K.
- Breitfeller, M.G.
- Cappadoro, P.L.
- Carlucci-Dayton, M.
- DePaola, F.A.
- Fernandes, H.C.
- Fuchs, M.R.
- Harder, D.A.
- Hidas, D.A.
- Jakoncic, J.
- Kitégi, C.A.
- Kramer, S.L.
- Langdon, T.
- Lara, J.
- Lincoln, F.C.
- Martins, B.S.
- McSweeney, S.
- Musardo, M.
- Myers, S.F.
- Rank, J.
- Schneider, D.K.
- Sharma, S.K.
- Spataro, C.J.
- Sweet, R.M.
- Tanabe, T.
- Tuozzolo, J.L.

CERN
Geneva, Switzerland
- Andreazza, W.
- Chritin, N.
- Dehning, B.
- Emery, J.
- Gudkov, D.
- Kemppinen, J.
- Kersevan, R.
- Kostka, Z.S.
- Magagnin, P.
- Mainaud Durand, H.
- Samuelsson, S.
- Sirvent, J.L.
- Veness, R.

Chiba University
Chiba, Japan
- Okudaira, K.K.
- Tanaka, M.

CLPU
Villamayor, Spain
- Hernandez-Toro, J.
- Roso, L.

CLS
Saskatoon, Saskatchewan, Canada
- Adam, M.J.P.
- Barkway, G.R.
- Beauregard, D.
- Belev, G.
- Bertwistle, D.
- Bodnarchuk, C.
- Bree, M.
- Carriere, S.R.
- Chapman, L.D.
- Chen, S.Y.
- Connatser, R.W.
- Henneberg, G.R.
- Kei, K.
- Leontowich, A.F.G.
- Lin, L.X.
- Miller, C.D.
- Murray, C.
- Pedersen, T.M.
- Regier, C.N.
- Schneider, B.A.
- Steel, G.A.
- Taylor, D.M.
- Webb, M.A.
- Wysokinski, T.W.
- Zhu, N.

Cornell University (CLASSE), Cornell Laboratory for Accelerator-Based Sciences and Education
Ithaca, New York, USA
- Barrett, S.T.
- Lyndaker, A.
- Temnykh, A.B.

CSIC
Madrid, Spain
- Ellis, G.

CUT
Kraków, Poland
- Ziemianski, D.T.

Content from this work may be used under the terms of the CC BY 3.0 licence (© 2016). Any distribution of this work must maintain attribution to the author(s), title of the work, publisher, and DOI.

ISBN: 978-3-95450-188-5

Content from this work may be used under the terms of the CC BY 3.0 licence (© 2016). Any distribution of this work must maintain attribution to the author(s), title of the work, publisher, and DOI.

DESY
Hamburg, Germany
- Bayer, M.
- Brachmanski, M.
- Caliebe, W.A.
- Degenhardt, M.
- Delfs, A.
- Dill, F.U.
- Doehrmann, R.
- Hesse, M.
- Heuer, J.
- Holz, M.
- Horbach, J.
- Jastrow, U.
- Krüger, H.
- Kuhlmann, M.
- Lemke, M.
- Mahn, H.
- Marutzky, F.
- Meissner, D.
- Nölle, D.
- Peters, H.-B.
- Peters, R.
- Plönjes-Palm, E.
- Röhling, M.
- Rubeck, J.R.
- Schulte Schrepping, H.
- Schulte-Schrepping, H.
- Sergeev, I.
- Steffen, B.
- Tiedtke, K.I.
- Treusch, R.
- Vilcins, S.
- Wiebers, Ch.

DLS
Oxfordshire, United Kingdom
- Butler, D.J.
- Cacho-Nerin, F.
- Diaz-Moreno, S.
- Docker, P.
- Duller, G.M.A.
- Grama, V.
- Hall, D.R.
- Hammond, N.P.
- Kay, J.
- Kelly, J.H.
- Marshall, A.R.
- Parker, J.
- Peach, A.
- Quinn, P.D.
- Stallwood, A.
- Sutter, J.
- Tizzano, W.
- Wagner, A.

Elettra-Sincrotrone Trieste S.C.p.A.
Basovizza, Italy
- Roussel, E.

ESRF
Grenoble, France
- Biasci, J.C.
- Bouteille, J-F.B.
- Brochard, T.
- Brumund, P.M.
- Chavanne, J.
- Cianciosi, F.
- Clement, J.M.
- Coulon, D.
- Dabin, Y.
- Diot, M.
- Ducoing, T.
- Ducotté, L.
- Ewald, F.
- Farvacque, L.
- Favier, F.
- Flaven-Bois, A.
- Gagliardini, E.
- Gleyzolle, H.
- Goirand, L.
- Got, P.
- Honkimaki, V.
- Jacob, J.
- Lesourd, M.
- Magnin-Mattenet, M.
- Mairs, T.R.
- Marchial, T.
- Marion, P.
- Martin, D.
- Ogier, B.
- Pasquaud, J.
- Raimondi, P.
- Renier, M.
- Roux-Buisson, P.
- Tampigny, B.
- Thomas, F.
- Van Vaerenbergh, P.
- Vivo, A.
- White, S.M.
- Wright, J.
- Zhang, L.

ESS
Lund, Sweden
- Permanyer, X.

ETH
Zurich, Switzerland
- Kemppinen, J.

European XFEL
Schenefeld, Germany
- Ansaldi, G.
- Appel, K.
- Broers, C.
- Deiter, C.
- Graceffa, R.
- Kitel, M.
- Lopez, L.C.
- Lorenzen, K.
- Lu, W.
- Moore, L.

ISBN: 978-3-95450-188-5

- Nakatsutsumi, M.
- Roth, T.
- Scherz, A.
- Schmidt, A.
- Schulz, J.
- Thute, P.
- Zastrau, U.

F.O.
Hamburg, Germany
- Okrent, F.

FHI
Berlin, Germany
- Hävecker, M.

FMB Oxford
Oxford, United Kingdom
- Kristiansen, P.

Fundación TEKNIKER
Elbr (Guipuzkoa), Spain
- Aizpurua, G.A.
- Delgado, A.
- Kortaberria, G.
- Olarra, A.

GIT/ECE
Atlanta, Georgia, USA
- Chavan, A.

Helsinki University, Department of Physics
University of Helsinki, Finland
- Suortti, P.

HUBER Diffraktiontechnik GmbH&Co.KG
Rimsting, Germany
- Huber, N.
- Olea, G.

HZB
Berlin, Germany
- Bischoff, P.
- Eggenstein, F.
- Erko, A.
- Hendel, S.
- Radu, F.
- Reichardt, G.
- Schäfers, F.
- Senf, F.
- Sokolov, A.
- Zeschke, T.

HZDR
Dresden, Germany
- Ferrari, A.

ILL
Grenoble, France
- Thomas, F.

Japan Synchrotron Radiation Research Institute (JASRI/SPring-8)
Hyogo, Japan
- Sano, M.
- Watanabe, A.

JASRI/SPring-8
Hyogo, Japan
- Aoyagi, H.
- Takahashi, S.

KEK
Tsukuba, Japan
- Amemiya, K.
- Asaoka, S.
- Igarashi, N.
- Kikuchi, T.
- Koyama, A.
- Mase, K.
- Matsuoka, A.
- Miyauchi, H.
- Mori, T.
- Nozawa, S.
- Tahara, T.
- Takeichi, Y.
- Tanaka, H.
- Toyoshima, A.
- Uchida, Y.
- Yamada, Y.

LBNL
Berkeley, California, USA
- Arbelaez, D.
- Feng, J.
- Hernikl, C.D.
- Jung, J.-Y.
- Lipton, T.M.
- Nasiatka, J.R.
- Padmore, H.A.
- Scharfstein, G.A.
- Stevens, T.A.
- Takakuwa, J.H.
- Warwick, T.

LNLS
Campinas, Brazil
- Bagnato, O.R.
- Caliari, R.M.
- Canova, H.F.
- Cardoso, F.H.
- Claudiano, G.V.
- da Silva, L.G.
- de Oliveira, H.G.P.
- de Souza, L.,Jr.
- dos Santos, J.E.
- Esper Neto, C.
- Fonseca, P.T.
- Francisco, F.R.
- Freitas, P.P.S.
- Geraldes, R.R.
- Gilmour, A.
- Madacki, R.
- Meyer, B.C.
- Moreno, G.B.Z.L.
- Parise, R.L.
- Pereira, M.A.
- Roca Santo, M.L.

Content from this work may be used under the terms of the CC BY 3.0 licence (© 2016). Any distribution of this work must maintain attribution to the author(s), title of the work, publisher, and DOI.

ISBN: 978-3-95450-188-5

Content from this work may be used under the terms of the CC BY 3.0 licence (© 2016). Any distribution of this work must maintain attribution to the author(s), title of the work, publisher, and DOI.

- Rocha, A.S.
- Rodrigues, G.L.M.P.
- Sanfelici, L.
- Saveri Silva, M.
- Silva, L.G.
- Silva, M.S.
- Souza Neto, N.M.
- Tavares, D.O.
- Tolentino, H.C.N.
- Volpe, L.M.
- Westfahl Jr., H.

LOA
Palaiseau, France
- Gautier, J.
- Lambert, G.
- Malka, V.
- Roussé, J.Y.
- Ta Phuoc, K.
- Thaury, C.

MAX IV Laboratory, Lund University
Lund, Sweden
- Afzali-Far, B.
- Bartalesi, A.
- Jensen, B.N.
- Thiel, A.

MBI
Berlin, Germany
- Eisebitt, S.
- Friedrich, B.
- Martyanov, W.
- Noll, T.

MI-Partners
Eindhoven, The Netherlands
- Ronde, M.J.C.
- Ruijl, T.A.M.
- Schneider, R.M.

MPI CEC
Mülheim an der Ruhr, Germany
- Grötzsch, D.

National Taiwan University
Taipei, Taiwan
- Hong, M.

NCTU
Hsinchu, Taiwan
- Hwang, C.-S.

NSRRC
Hsinchu, Taiwan
- Chan, C.K.
- Chang, C.-C.
- Chang, C.-H.
- Chang, C.F.
- Chang, C.H.
- Chang, C.Y.
- Chang, J.-C.
- Chang, S.H.
- Chang, Y.C.
- Chen, B.Y.
- Chen, C.Y.
- Chen, C.
- Chen, H.-H.
- Chen, H.Y.
- Chen, J.-R.
- Chen, M.L.
- Chen, S.D.
- Cheng, C.M.
- Chiu, C.C.
- Ho, H.C.
- Hsiao, F.Z.
- Hsu, K.H.
- Huang, C.Y.
- Huang, D.-G.
- Huang, J.C.
- Huang, L.
- Hwang, C.-S.
- Kao, S.P.
- Kuan, C.K.
- Lai, L.
- Lai, W.Y.
- Lee, C.Y.
- Lee, L.
- Lee, M.H.
- Li, H.C.
- Liao, W.R.
- Lin, B.H.
- Lin, C.J.
- Lin, J.M.
- Liu, C.Y.
- Liu, D.G.
- Perng, S.Y.
- Sheng, I.C.
- Shueh, C.
- Su, Y.
- Tang, M.T.
- Tsai, C.W.
- Tsai, Z.-D.
- Tseng, S.C.
- Tseng, T.C.
- Wang, D.-J.
- Wang, H.S.
- Wu, J.X.
- Wu, L.H.
- Yan, H.Y.
- Yang, C.K.
- Yang, Y.C.
- Yin, G.C.
- Yu, Y.T.

NTHU
Hsinchu, Taiwan
- Kwo, J.R.

Proactive Research and Development
Barcelona, Spain
- Herranz, J.

Prudente Engenharia Ltda.
Uberlandia, Minas Gerais, Brazil
- Prudente, C.

ISBN: 978-3-95450-188-5

PSI
Villigen PSI, Switzerland
- Boehler, P.
- Brügger, M.
- Calvi, M.
- Hess, C.
- Hirschi, P.
- Jöhri, H.
- Keller, A.
- Locher, M.
- Löhl, F.
- Maag, St.
- Nue, L.
- Patthey, L.
- Pedrozzi, M.
- Schmidt, T.
- Schmitt, T.
- Schulz, L.
- Stapf, T.
- Wang, X.

PTB
Berlin, Germany
- Beckhoff, B.
- Lubeck, J.
- Nutsch, A.
- Streeck, C.
- Weser, J.

RMD Engineering Inc.
Saskatoon, Canada
- Boire, J.

SENER
Cerdanyola del Vallès, Spain
- Casalta Escuer, J.M.
- Martín-Nuño Gonzalez, C.
- Tomas Justribo, A.
- Úbeda Gonzalez, D.

SESAME
Allan, Jordan
- Al-Mohammad, H.
- Al-Najdawi, M.A.
- Huttel, E.
- Makahleh, F.
- Shehab, M.M.

SINAP
Shanghai, People's Republic of China
- Deng, R.B.
- Dong, Y.X.
- Fang, W.
- Gao, F.
- He, Y.Z.
- Hu, X.
- Jia, D.
- Jiang, Z.
- Jin, L.
- Li, A.
- Li, Y.
- Liu, Y.
- Mao, C.
- Pan, Y.
- Sun, S.
- Wang, H.F.
- Wang, J.
- Wang, L.
- Wang, S.H.
- Wen, Y.M.
- Xue, S.
- Yin, L.
- Yu, L.Y.
- Zhang, H.
- Zhang, M.
- Zhang, W.
- Zhou, Q.G.
- Zhu, W.

SINP MSU
Moscow, Russia
- Shvedunov, V.I.

SLAC
Menlo Park, California, USA
- Amores, L.
- Boutet, S.
- Castagna, J.C.
- Cocco, D.
- Feng, Y.
- Hardin, C.L.
- James, J.H.
- Kelez, N.M.
- Krzywiński, J.
- Morton, D.S.
- Ortiz, E.
- Rowen, M.
- Srinivasan, V.N.
- Wang, H.
- Zhang, L.

SLRI
Nakhon Ratchasima, Thailand
- Bumrungkoh, D.
- Chaichuay, S.
- Phanak, M.
- Pongampai, S.
- Srichan, S.

Sokendai, The Graduate University for Advanced Studies
Tsukuba, Japan
- Miyazawa, T.

Solaris
Kraków, Poland
- Nowak, M.P.

Solaris National Synchrotron Radiation Centre, Jagiellonian University
Kraków, Poland
- Nowak, M.P.

SOLEIL
Gif-sur-Yvette, France
- Alves, F.
- André, T.
- Andriyash, I.A.

Content from this work may be used under the terms of the CC BY 3.0 licence (© 2016). Any distribution of this work must maintain attribution to the author(s), title of the work, publisher, and DOI.

ISBN: 978-3-95450-188-5

Content from this work may be used under the terms of the CC BY 3.0 licence (© 2016). Any distribution of this work must maintain attribution to the author(s), title of the work, publisher, and DOI.

- Basset, C.
- Benabderrahmane, C.
- Berteaud, P.
- Bobault, S.
- Bonnin, S.
- Bouvet, F.
- Briquez, F.
- Béchu, N.
- Chapuis, L.
- Couprie, M.-E.
- de Olivera, C.
- Dennetière, D.
- Dietrich, Y.
- Dubuisson, J.M.
- Dumas, P.
- Duval, J.P.
- El Ajjouri, M.
- El Ajjouri, T.K.
- Giorgetta, J.L.
- Herbeaux, C.
- Hubert, N.
- Jobert, N.
- Khojoyan, M.
- Kubsky, S.K.
- Labat, M.
- Leclercq, N.
- Lestrade, A.
- Loulergue, A.
- Marcouillé, O.
- Marlats, J.L.
- Marteau, F.
- Mary, A.
- N'gotta, P.
- Polack, F.
- Ribbens, M.
- Rommeluère, P.
- Scheel, M.
- Sebdaoui, M.
- Tavakoli, K.T.
- Thiam, F.
- Tilmont, M.
- Valléau, M.
- Vétéran, J.
- Weitkamp, T.
- Zerbib, D.

SSRF
Shanghai, People's Republic of China
- Qin, H.L.
- Yang, K.
- Zhang, L.

Technische Universität Berlin
Berlin, Germany
- Eisebitt, S.
- Friedrich, B.
- Grötzsch, D.
- Jonas, A.
- Kanngießer, B.
- Malzer, W.
- Witte, K.W.

THK GmbH Sucursal en España
Badalona, Spain
- Miret, M.

Tohoku University, Institute of Multidisciplinary Research for Advanced Materials
Sendai, Japan
- Sunayama, R.
- Toyoda, M.
- Yanagihara, M.

Universitat Politécnica de Catalunya
Barcelona, Spain
- Barjau, A.

University of Illinois at Chicago
Chicago, USA
- Anton, J.W.J.

University of Saskatchewan
Saskatoon, Canada
- Gibbons, M.

UPC
Barcelona, Spain
- Arbo Sangüesa, V.
- Blasco, V.
- Escaler, X.
- Ferrater, M.
- Juan Garcia, D.
- Kubyshin, Yu.A.
- Macià, L.
- Romero, J.A.
- Sanchez, A.

USTC/NSRL
Hefei, Anhui, People's Republic of China
- Fan, L.
- Hong, Y.Z.
- Pei, X.T.
- Wang, Y.
- Wei, W.
- Zhang, B.

UVSOR
Okazaki, Japan
- Inagaki, Y.
- Kosugi, N.
- Ohigashi, T.

XFEL. EU
Hamburg, Germany
- Boyd, E.W.
- Carley, R.
- Delitz, J.T.
- Dommach, M.
- Izquierdo, M.
- Kohlstrunk, N.
- La Civita, D.
- Madsen, A.
- Priebe, G.
- Sinn, H.
- Trapp, A.
- Villanueva Guerrero, J.R.

ISBN: 978-3-95450-188-5

Yokohama National University
Yokohama, Japan
- Kodama, H.
- Ohno, S.
- Tanaka, M.

Content from this work may be used under the terms of the CC BY 3.0 licence (© 2016). Any distribution of this work must maintain attribution to the author(s), title of the work, publisher, and DOI.

MEDSI 2016 Delegates

Last Name	First Name	Affiliation
Adam	Madison	Canadian Light Source
Adamson	Luke	Australian Synchrotron
Afzali Far	Behrouz	MAX IV
Agustsson	Ronald	RadiaBeam Technologies
Åhnberg	Karl	MAX IV
Alessandroni	Marco	R.M.P. Srl
Al-najdawi	Mohammad	SESAME (Synchrotron-light for Experimental Science and Applications in the Middle East)
Al-sallami	Hussein	MAX IV
Álvarez	George	Renishaw Ibérica, S.A.U.
Alvarez Fernandez	Jose Maria	ALBA Synchrotron Light Source
Amat De Cabanyes	Antoni	AMAT METALPLAST, S.A.
Andreas	Mayer	Phytron GmbH
Ansaldi	Gabriele	European XFEL
Aoyagi	Hideki	Japan Synchrotron Radiation Research Institute (JASRI)
Ayas	Esther	ALBA Synchrotron Light Source
Barkway	Gordon	Canadian Light Source
Barrett	Stephen	Cornell University
Bartalesi	Antonio	MAX IV
Baruzzo	Roberto	STRUMENTI SCIENTIFICI CINEL s.r.l.
Baurichter	Arnd	RI Research Instruments GmbH
Bellafont	Ignasi	ALBA Synchrotron Light Source
Benda	Erika	Argonne National Laboratory
Benito Santamaría	Jorge	Iberica Vacuum
Benjamin	Tampigny	ESRF
Bernard	Ogier	ESRF
Biermanns-föth	Andreas	RI Research Instruments GmbH
Bjermo	Anders	Lund University, MAX IV Laboratory
Bonfadini	Marco Maria	TERATORR TECHNOLOGIES, S.L.
Bongiovanni	Stefano	STRUMENTI SCIENTIFICI CINEL s.r.l.
Bowfield	Andrew	Instrument Design Technology
Brajuskovic	Branislav	Argonne National Laboratory
Breitfeller	Mark	Brookhaven National Laboratory
Bruck	Robert	RI Research Instruments GmbH
Butler	David	Diamond Light Source Ltd
Cadoppi	Andrea	SAES Getters S.p.A.
Calderón Terol	David	ALBA Synchrotron Light Source
Capatina	Dana	Argonne National Laboratory
Carballedo Costa	Antonio	ALBA Synchrotron Light Source
Carrera	Miguel Angel	AVS Added Value Industrial Engineering Solutions
Carriere	Shawn	Canadian Light Source
Carriere	Carey	NA
Casalta	Joan Manel	SENER Ingeniería y Sistemas SA
Casas	Joan	ALBA Synchrotron Light Source
Chang	Jui-chi	National Synchrotron Radiation Research Center
Chang	Cheng-hsiang	National Synchrotron Radiation Research Center

ISBN 978-3-95450-188-5

MEDSI 2016 Delegates

Chen	Siyue	Canadian Light Source
Chen	June-rong	National Synchrotron Radiation Research Center
Chen	Bo-yi	NSRRC
Christian	Herbeaux	Synchrotron SOLEIL
Cianciosi	Filippo	ESRF
Coleman	Russell	Edwards Ltd
Colldelram Peroliu	Carles	ALBA Synchrotron Light Source
Collins	Jeff	Argonne National Laboratory
Cometti	Roberto	Vaqtec Srl
Connatser	Robert	Canadian Light Source
Connatser	Lisa	None
Crisol Ariño	Alejandro	ALBA Synchrotron Light Source
Crofts	Thomas	FMB Oxford
Cunrath	Aymeric	IRELEC
Daniel	Meissner	DESY
Deiter	Carsten	European XFEL
Delfs	Annette	Deutsches Elektronen Synchrotron
Den Hartog	Patric	Argonne National Laboratory
Deng	Rongbing	Shanghai Institute of Applied Physics
Depaola	Frank	Brookhaven National Laboratory
Diat	Jean-luc	MEWASA
Diete	Wolfgang	Axilon AG
Dill	Frank-uwe	DESY
Divitcos	Jim	Synchrotron Light Source Aust Pty Ltd
Dolan	Gerard	Instrument Design Technology
Dommach	Martin	European XFEL
Duarte	Robert	Lawrence Berkeley National Laboratory
Dubuisson	Jean-michel	Synchrotron-SOLEIL
Duget	Anne	SYMETRIE
Duller	Graham	Diamond Light Source Ltd
Dworkowski	Florian	Paul Scherrer Institut
Eggenstein	Frank	HZB, Helmholtz-Zentrum Berlin für Materialien und Energie
Elvira Cozar	Carlos	TERATORR TECHNOLOGIES, S.L.
Eric	Gagliardini	ESRF
Escobar	Víctor	Renishaw Ibérica, S.A.U.
Etzkorn	Thomas	PI miCos GmbH
Farré París	Francesc	ALBA Synchrotron Light Source
Fernandes	Huston	Brookhaven National Laboratory
Fernández	David	ALBA Synchrotron Light Source
Fernández	Susana	NORTEMECÁNICA, S.A.
Ferrer	Salvador	ALBA Synchrotron Light Source
Fisher	Michael	Argonne National Laboratory
Fraga López	Edmundo	ALBA Synchrotron Light Source
Frank	Okrent	DESY Hamburg
Frederic	Thomas	ESRF
Friedrich	Bertram	Technische Universität Berlin

ISBN 978-3-95450-188-5

MEDSI 2016 Delegates

Fuchs	Filip	BESTEC GmbH
Gao	Fei	Shanghai Institute of Applied Physics
García	Gastón	ALBA Synchrotron Light Source
García Molinero	José Ramón	ALBA Synchrotron Light Source
Gavilán	Andoni	THK GmbH, sucursal en España
Geraldes	Renan	Brazilian Synchrotron Liight Source
Gevorgyan	Artur	ALBA Synchrotron Light Source
Gibbons	George	Renishaw Ibérica, S.A.U.
Giessel	Tatjana	BESTEC GmbH
Gilmour	Allan	LNLS
Gines	Lluis	ALBA Synchrotron Light Source
Giorgetta	Jean-luc	Synchrotron SOLEIL
Giraldo González	Juan Carlos	ALBA Synchrotron Light Source
Glynn	Lola	Kurt J Lesker Company
Goirand	Loys	ESRF
Gonzalez	Nahikari	ALBA Synchrotron Light Source
González Fernández	Joaquín	ALBA Synchrotron Light Source
Grama Visweswara	Vinay	Diamond Light Source Ltd
Grötzsch	Daniel	MAX-PLANCK-INSTITUTE FOR CHEMICAL ENERGY CONVERSION
Haase	Dorthe	MAX IV
Haimo	Joehri	Paul Scherrer Institut
Hardin	Corey	SLAC National Accelerator Laboratory
Hendel	Stefan	Helmholtz-Zentrum Berlin
Hernandez Toro	Juan	CLPU
Herold	Benjamin	FMB Feinwerk- und Meßtechnik GmbH
Herranz	Juan	Proactive Research and Development, S.L
Hsu	Keng-hao	National Synchrotron Radiation Research Center
Huber	Norman	HUBER GmbH & Co.KG
Igarashi	Noriyuki	KEK-PF
Iglesias	Jordi	ALBA Synchrotron Light Source
Jan Josua	Rubeck	Deutsches Elektronen Synchrotron
Jan Torben	Delitz	European XFEL
Jean-charles	Castagna	SLAC National Accelerator Laboratory
Jensen	Brian Norsk	MAX IV
Juanhuix	Jordi	ALBA Synchrotron Light Source
Kay	James	Diamond Light Source Ltd
Kay	Carolyn	Diamond Light Source Ltd
Kearney	Steven	Argonne National Laboratory
Kelez	Nicholas	Stanford University
Kelly	Jonathan	Diamond Light Source Ltd
Kemppinen	Juha	CERN
Kersevan	Roberto	CERN
Killham	Margo	Canadian Light Source
Kim	Bongsoo	Pohang Accelerator Laboratory
Kohlstrunk	Nicole	European XFEL
Kosugi	Nobuhiro	UVSOR Synchrotron, IMS

ISBN 978-3-95450-188-5

MEDSI 2016 Delegates

Kristiansen	Paw	FMB Oxford
Krueger	Hilmar	Deutsches Elektronen Synchrotron
La Civita	Daniele	European XFEL
Ladrera	Jon	ALBA Synchrotron Light Source
Lee	Soonhong	Argonne National Laboratory
Lee	Ming Han	National Synchrotron Radiation Research Center
Li	Yongjun	Shanghai Institute of Applied Physics
Lin	Linda	Canadian Light Source
Liu	Zunping	Argonne National Laboratory
Liu	Dingoa	NSRRC
Lopez	Luis	XFEL
López	Severino	NORTEMECÁNICA, S.A.
López Nonell	David	ALBA Synchrotron Light Source
Lubeck	Janin	Physikalisch-Technische Bundesanstalt
Ludovic	Ducotté	ESRF
Maccarrone	Cristian	TERATORR TECHNOLOGIES, S.L.
Man	Zhang	Phytron GmbH
Manotas	Juan José	ALBA Synchrotron Light Source
Manuel	Tilmont	Synchrotron SOLEIL
Marc	Ribbens	Synchrotron SOLEIL
Marquina	David	Iberica Vacuum
Marshall	Andrew	Diamond Light Source Ltd
Marsol José	Josep	Blumeprot S.L.L.
Martens	Cornelius	Deutsches Elektronen Synchrotron
Martí	Zeus	ALBA Synchrotron Light Source
Martin	Juan José	TEJASA T.C S.L
Martínez Bonillo	Ana Belén	ALBA Synchrotron Light Source
Martín-nuño	Carlos	SENER Ingeniería y Sistemas SA
Mase	Kazuhiko	High energy Accelerator Research Organization
Matilla	Oscar	ALBA Synchrotron Light Source
Matsuoka	Ai	High energy Accelerator Research Organization
Maussang	Sebastien	Renishaw Ibérica, S.A.U. and Renishaw Francia S.A.S
Milharcic	Tadej	KYMA TEHNOLOGIJA D.O.O.
Miret	Martí	THK GmbH, sucursal en España
Miyauchi	Hiroshi	High Energy Accelerator Research Organization (KEK)
Moberg	Robert	Romo Scientific representing Toyama
Monge	Raquel	ALBA Synchrotron Light Source
Morton	Simon	Lawrence Berkeley National Laboratory
Morton	Daniel	SLAC National Accelerator Laboratory
Mountford	Brad	Synchrotron Light Source Aust Pty Ltd
Müller	Frieder	FMB Feinwerk- und Meßtechnik GmbH
Muriel	Magnin-mattenet	ESRF
Murray	Paul	Instrument Design Technology
Nasiatka	Jamie	Lawrence Berkeley National Laboratory
Navarro Ábalos	Jordi	ALBA Synchrotron Light Source
Navrotski	Gary	Argonne National Laboratory

ISBN 978-3-95450-188-5

MEDSI 2016 Delegates

Neuenschwander	Regis	Brazilian Synchrotron Light Laboratory
Nicolas	Josep	SLAC National Accelerator Laboratory
Nicolas	Jobert	Synchrotron SOLEIL
Nikitin	Yury	ALBA Synchrotron Light Source
Nikitina	Liudmila	ALBA Synchrotron Light Source
Noguera	Pedro	AVS Added Value Industrial Engineering Solutions
Noire	Pierre	SYMETRIE
Noll	Tino	Max-Born-Institut
Nozawa	Shunsuke	High Energy Accelerator Research Organization
Nudell	Jeremy	Argonne National Laboratory
Ohigashi	Takuji	Institute for Molecular Science
Olea	Gheorghe	HUBER GmbH & Co.KG
Paccagnella	Massimiliano	STRUMENTI SCIENTIFICI CINEL s.r.l.
Parejo	Francisco	Renishaw Ibérica, S.A.U.
Peach	Andrew	Diamond Light Source Ltd
Pedreira	Pablo	ALBA Synchrotron Light Source
Peli	Mario	Allectra Limited
Peña	Gabirel	ALBA Synchrotron Light Source
Permanyer	Xavier	European Spallation Source
Philippe	Roulet	DMP
Philippe	Marion	ESRF
Piedra I Garcia	Gerard	Grupo Blumeprot
Pirmin Eduard	Boehler	Paul Scherrer Institut
Pongampai	Surachai	Synchrotron Light Research Institute
Portabella	Manel	ALBA Synchrotron Light Source
Portillo Recio	Xavi	Grupo Blumeprot
Prat	Jordi	ALBA Synchrotron Light Source
Preissner	Curt	Argonne National Laboratory
Prieto Moliné	María Montserrat	ALBA Synchrotron Light Source
Qin	Hongliang	Shanghai Institute of Applied Physics
Quispe Flores	Marcos	ALBA Synchrotron Light Source
Ralph	Döhrmann	DESY
Regier	Chris	Canadian Light Source
Ribó Mor	Llibert	ALBA Synchrotron Light Source
Richardson	Carl	TOYAMA Co., Ltd.
Richaud	Raphael	IRELEC
Rodriguez Fernandez	Xoan Iago	ALBA Synchrotron Light Source
Roschka	Michael	FMB Feinwerk- und Meßtechnik GmbH
Roslund	Linus	MAX IV
Ruget	Claude	
Ruijl	Theo	MI-Partners
Ruiz Molero	Yolanda	ALBA Synchrotron Light Source
Rummery	Paul	Kurt J Lesker Company
Salayet Barbera	Enric	AMAT METALPLAST, S.A.
Sanfelici	Lucas	SIRIUS/LNLS
Sapina	Emilio	TEJASA T.C S.L

ISBN 978-3-95450-188-5

MEDSI 2016 Delegates

Saveri Silva	Marlon	LNLS
Schaa	Volker Reinhard Wolfgang	GSI
Scharfstein	Gregory	Lawrence Berkeley National Laboratory
Schmidt	Oliver	Argonne National Laboratory
Schmidt	Andreas	European XFEL
Schmiedeke	Lutz	Emil-Hoffmann-Str. 55-59,
Schneider	Ronald	MI-Partners
Serra	Ignasi	ALBA Synchrotron Light Source
Sharma	Sushil	Brookhaven National Laboratory
Sharma	Madonna	None
Sheng	I Ching Albert	NSRRC
Shouman	Ahmed	Shoman For Technology
Shu	Deming	Argonne National Laboratory
Sics	Igors	ALBA Synchrotron Light Source
Sitges Carreño	Josep Maria	SINERGES TECMON, s.a.
Solanich	Mireia	ALBA Synchrotron Light Source
Soler	Aymerich	AMAT METALPLAST, S.A.
Spataro	Charles	Brookhaven National Laboratory
Srichan	Supawan	Synchrotron Light Research Institute
Stephan	Maag	Paul Scherrer Institut
Stevanato	Andrea	STRUMENTI SCIENTIFICI
Stimson	Joshua	Birmingham City University
Suthar	Kamlesh	Argonne National Laboratory
Takahashi	Sunao	SPring-8/JASRI
Takakuwa	Jeffrey	Lawrence Berkeley National Laboratory
Tang	Ling Hong	SUER & POLLON MECHANICAL
Tavakoli	Keihan	Synchrotron SOLEIL
Theodor	Keld	Copenhagen University / MaxIV Lund Sweden
Thiel	Andreas	MAX IV
Tizzano	Walter	Diamond Light Source Ltd
Tomás	Albert	SENER Ingeniería y Sistemas SA
Toyoda	Mitsunori	Tohoku Univ.
Toyoda	Wakako	Tohoku Univ.
Trevor	Mairs	ESRF
Urbano	Marco Fabrizio	SAES Getters S.p.A.
Valcarcel Fernández	Ricardo	ALBA Synchrotron Light Source
Valcarcel Fernández	Ricardo	ALBA Synchrotron Light Source
Valero-casanovas	Maurici	Abello Linde S.A.
Vanselous Barrett	Heather	Cornell University
Vilanova	Joan	ALBA Synchrotron Light Source
Vilcins	Silke	Deutsches Elektronen Synchrotron
Villanueva Guerrero	José	European XFEL
Volpe	Lucas	LNLS/Sirius
Wang	Hengzi	SLAC National Accelerator Laboratory
Wang	Yong	University of Science and Technology of China
Warwick	Tony	Lawrence Berkeley National Laboratory

ISBN 978-3-95450-188-5

MEDSI 2016 Delegates

Waterstradt	Timm	Axilon AG
Wysokinski	Tomasz	Canadian Light Source
Xinyu	Wang	Paul Scherrer Institut
Xu	Shenglan	Argonne National Laboratory
Yan	Hong-yi	National Synchrotron Radiation Research Center
Yang	Chin-kang	National Synchrotron Radiation Research Center
Yin	Lixin	Shanghai Institute of Applied Physics
Yiyong Liu	Yiyong Liu	Shanghai Institute of Applied Physics
Yves	Dabin	ESRF
Zhang	Lin	SLAC National Accelerator Laboratory
Zhang	Bo	University of Science and Technology of China
Ziemianski	Daniel	Cracow University of Technology (CUT) / Institute of Applied Mechanics (M1)
Zuzuarregui	Ignacio	Desarrollos Mecanicos de Precisión S.L.

ISBN 978-3-95450-188-5